Université de Montréal

Cyclonickellation des phosphinites dérivées de phénols et naphtols
Régiosélectivité, Mécanisme, Fonctionnalisation et Formation de nouveaux Pinceurs

Par
Loïc P. Mangin

Département de chimie, Faculté des arts et des sciences

Thèse présentée en vue de l'obtention du grade de Philosophiæ Doctor

en chimie

Décembre 2019

I

Université de Montréal

Département de chimie, Faculté des arts et des sciences

Cette thèse intitulée

Cyclonickellation des phosphinites dérivées de phénols et naphtols
Régiosélectivité, Mécanisme, Fonctionnalisation et Formation de nouveaux Pinceurs

Présentée par

Loïc P. Mangin

A été évaluée par un jury composé des personnes suivantes

Frank Schaper
Président-rapporteur

Davit Zargarian
Directeur de recherche

Christian Reber
Membre du jury

Samuel A. Johnson
Examinateur externe

Résumé

Cette thèse présente différents aspects de la cyclonickellation des phosphinites de type Aryl-OP(*i*-Pr)$_2$, leur potentiel dans la fonctionnalisation et leur utilité pour former des nouveaux types de complexes de types pincer de nickel. Le **Chapitre 1** constitue une introduction générale sur l'importance de la liaison carbone-nickel en chimie organométallique. Diverses stratégies de formation des liens C-Ni dans des composés classiques (monodentés), des composés de types pincer (tridentés) et des composé cyclonickellés (bidentés et tridentés) y sont présentées, incluant des réactions impliquant des précurseurs de Ni^0, de Ni^{II} ou de Ni^{IV}. Ce chapitre présente également la réactivité de ces composés comportant des liens C-Ni, et met l'emphase sur la réactivité des liaisons carbone-nickel, en particulier dans les processus catalytiques destinés à la fonctionnalisation des liens C-H, en utilisant des groupes directeurs. Les phosphinites sont ensuite présentées comme des groupes directeurs intéressants en catalyse, bien qu'elles aient surtout été utilisé avec d'autres métaux que le nickel. La dernière partie de ce chapitre pose les questions qui tenterons de trouver réponse dans les travaux présentés aux chapitres suivants.

Les **Chapitres 2** et **4**, basés sur des articles publiés, présentent l'isolation et la caractérisation de composés dimériques de type [{κ^P,κ^C-(*i*-Pr)$_2$POAr}Ni(μ-Br)]$_2$ issus de l'*ortho*-nickellation des phosphinites dérivées des phénols et des naphtols substitués, ainsi que de certains de leurs adduits monomériques d'acétonitrile ou du ligand lui-même. Ces discussions cherchent à répondre à la question de régiosélectivité de la cyclonickellation : on y démontre que cette réaction est gouvernée par les facteurs stériques, menant à la métallation préférablement (pour les substituants fluor) ou exclusivement (pour les substituants plus volumineux) aux carbones les moins encombrés, lorsque deux positions *ortho* sont disponibles, et que la réaction mène toujours à la formation de nickellacycles à 5 chainons. Ainsi, les phénols C3-substitués subissent la métallation au carbone C6, alors que les 1- et 2-naphtols subissent la nickellation aux positions C2 et C3, respectivement.

Ces deux chapitres démontrent que la métallation peut avoir lieu sur des carbones qui possèdent déjà un voisin encombrant (F, OMe, benzo), menant à des structures relativement distordues, mais que la nickellation n'est pas produite dans les conditions standard au voisinage des substituants Me et Cl qui sont plus volumineux, ni au carbone C8 du 1-naphtol qui mènerait à

un nickellacycle à 6 chainons. L'étude structurale permet de rationaliser les régiosélectivités observées, et les études par diverses méthodes RMN complètent la caractérisation de ces nouveaux composés.

Le **Chapitre 2** démontre que lorsque les sites potentiels de nickellation sont bloqués par des substituants *ortho* Me ou Ph, la réaction ne prend pas place sur ces substituants en raison de la formation de nickellacycles à 6 ou 7 chainons respectivement. Ceci met en lumière également l'impossibilité d'isoler les composés nickellés aux carbones sp³ des substituants *ortho*, et le **Chapitre 4** démontre par des expériences d'échange H/D que la nickellation à ces positions n'est pas seulement thermodynamiquement défavorisée, mais qu'elle est aussi cinétiquement inexistante. Ce chapitre dévoile également les réactions qui sont observables à 80 °C sont radicalement accélérées à haute température (120 ou 160 °C), et que les produits de nickellation y sont thermodynamiquement stables.

Le **Chapitre 4** présente également une réaction de fonctionnalisation *in situ* des liens carbone-nickel de la phosphinite cyclonickellée dérivée du 1-naphtol. Dans cette réaction, qui se produit à haute température en absence de base, la bromophosphine Br-P(i-Pr)$_2$ se génère *in situ* et permet l'insertion formelle d'un phosphènium [(i-Pr)$_2$P]$^+$ dans le lien carbone-nickel, menant à un complexe phosphine-phosphinite de type {κ^P,$\kappa^{P'}$-1-(i-Pr)$_2$PO-2-naphtyl-P(i-Pr)$_2$}NiBr$_2$. Lorsque la position C2 du 1-naphtol est bloquée par un substituant Et, un genre similaire de fonctionnalisation à la position C8 est observé, menant à l'obtention de 8-(i-Pr)$_2$P(O)-2-Et-1-naphtol, ainsi qu'à des sous-produits qui ont été identifiés et caractérisés. Cette réaction démontre l'accessibilité cinétique de la position C8 à haute température, mais démontre également l'instabilité du nickellaycle généré.

Les conditions réactionnelles pour l'obtention des phosphinites nickellées dévoilées au **Chapitre 2** (utilisant l'acétonitrile comme solvant) ont démontré une efficacité supérieure que celle présentée précédemment (dans le toluène). Ainsi, le **Chapitre 3**, également basé sur un article publié, cherche à décrire les aspects mécanistiques de cette cyclométallation et démontre que les espèces initialement présentes dans l'acétonitrile sont des adduits mono-phosphinites du nickel au contraire des espèces présentes dans le toluène. Cette étude démontre qu'une base externe est nécessaire pour conduire à l'isolation des composés nickellés, mais qu'elle n'est pas impliquée dans le mécanisme de métallation car la formation des liens C-Ni se produit réversiblement en

absence de base. Des suivis cinétiques indiquent que la réaction est de premier ordre et qu'un excès de base ralentit la réaction en formant des espèces non réactives, et que les bases idéales sont fortes et peu coordonnantes. Une étude mécanistique expérimentale révèle que l'étape de nickellation est de nature électrophile (pente de Hammett $\rho \approx -4$) et associative ($\Delta H^{\ddagger} = 18(1)$ kcal·mol^{-1} and $\Delta S^{\ddagger} = -27(4)$ cal·mol^{-1}·K^{-1}) et que le transfert de proton est l'étape limitante ($k_H/k_D \approx 11$). Ces résultats sont appuyés par une étude computationnelle par DFT qui démontre que la dissociation d'un ligand Br$^-$ mène à une paire d'ions comme intermédiaire, depuis lequel la déprotonation est réalisée par l'anion Br$^-$ dans un mécanisme de type CMD. Les résultats de ces calculs théoriques permettent également d'appuyer la thèse d'un état fondamental triplet pour les espèces présentes avant la nickellation dans l'acétonitrile.

Les études sur la régiosélectivité ont mené à un résultat surprenant : à la place de subir la nickellation C-H, la phosphinite dérivée du 2-vinylphénol subit une attaque nucléophile sur le groupe vinyle afin de donner un composé tridenté portant un lien C_{sp^3}-Ni. Le **Chapitre 5** présente ainsi une nouvelle stratégie de préparation des composés *pincers* par des réactions de type *Umpolung*. Le ligand 2-vinylphényl-OP(*i*-Pr)$_2$ réagit avec des amines et des phosphines portant au moins un proton, pour donner des complexes pinceurs de type 6,4-POCY-NiBr (Y = P, N). Ce chapitre dévoile l'étendue des composés qui peuvent être produits par cette méthode, et offre une caractérisation de ces composés par RMN, diffraction des rayons X et par électrochimie, afin de comparer leurs caractéristiques avec les autres *pincers* décrits dans la littérature.

Enfin, alors que le **Chapitre 6** présente quelques résultats additionnels reliés aux divers axes de recherche de cette thèse, le **Chapitre 7** rappelle les grandes lignes des découvertes présentées aux **Chapitres 2-5**. Ce chapitre de conclusion générale présente également des perspectives basées sur les résultats de la thèse, et sur les quelques résultats préliminaires. Au menu : une discussion sur la relation entre régiosélectivité et la stabilité, des nouvelles stratégies de nickellation à étudier (à partir de liens carbone-halogène), la fonctionnalisation des liens C-Ni par des composés isolobaux aux phosphèniums et des stratégies pour la fonctionnalisation des oléfines dans les composés de type alcool.

Mots-clés : Cyclonickellation, Phosphinite, Régiosélectivité, Mécanisme, Complexes *pincer*, DFT, Cinétique, Fonctionnalisation, Nickellation C-H, Diffraction des Rayons X.

Abstract

This thesis presents various aspects of the cyclonickelation of phosphinites Aryl-OP(i-Pr)$_2$, as well as their potential in functionalization processes and applications in the preparation of new types of pincer-Ni complexes. **Chapter 1** consists of a general introduction on the importance of the carbon-nickel bond in organometallic chemistry. Various strategies leading to C-Ni bonds in classical (monodentate) compounds, pincer complexes (tridentate), and cyclonickelated species (bi- and tridentate) are disclosed, including reactions implicating Ni^0, de Ni^{II} ou de Ni^{IV} precursors. This chapter also presents the reactivity of species featuring C-Ni bonds C-Ni and underlines the reactivity of C-Ni bonds, especially in catalytic processes targeting C-H bonds functionalization, through the use of directing groups. Next, phosphinites are displayed as interesting directing groups in catalysis even though they have been used mostly with metals other than nickel. The last part of this chapter outlines the questions that are meant to be addressed in the next chapters.

Chapters 2 and **4**, based on published articles, display the isolation and characterization of dimeric complexes of the type [{κ^P,κ^C-(i-Pr)$_2$POAr}Ni(μ-Br)]$_2$ arising from the *ortho*-nickelation of phosphinites derived from substituted phenols and naphthols, as well as some of their acetonitrile or phosphinite adducts. These studies are meant to address the question of regioselectivity in the cyclonickelation. The results obtained prove that when two *ortho* sites are available for reactivity, the nickelation is governed by steric factors and leads to metalation preferably (in case of F substituents) or exclusively (in case of larger substituents) at the least hidered C-H bond; moreover, the nickelation always leads to 5-membered nickelacycles. Thus, C3-substituted phenols undergo nickelation at the C6 position, while 1- and 2-naphthols undergo nickelation at C2 and C3 positions, respectively.

Together, **Chapters 2** and **4** show that metalation can take place at the carbon next to a F-, MeO- or benzo substituent, but such nickelation at the hindered sites leads to distorted structures in the products. One the other hand, nickelation never occurs at carbons neighbouring the larger Me- or Cl- substituents, nor at the C8 position of 1-naphthol which would lead to a 6-membered nickelacycle. The structural study allows us to rationalize the observed regioselectivities, and NMR studies complete the characterization of these new compounds.

Chapter 2 also reveals that when the *ortho* sites are blocked by Me or Ph functional groups, no nickelation takes places on these substituents due to the unfavored generation of 6- or 7-membered metallacycles, respectively. This finding also rationalizes why it has not been possible to isolate complexes arising from the nickelation at sp³ carbons of *ortho* substituents. This point is confirmed in the studies described in **Chapter 4**, which shows how H/D exchange experiments helped us prove that reactivity at these aliphatic C-H sites is disfavored not only thermodynamically, but also kinetically. This chapter also reveals that reactions observed at 80 °C can be accelerated dramatically at higher temperatures (120 or 160 °C), and that nickelated products are stable in these conditions.

Chapter 4 also presents some examples of *in situ* functionalization of the C-Ni bonds in cyclonickelated 1-naphthyl phosphinites. Conducting these reactions in the absence of base at high temperatures allowed the *in situ* generation of bromoposphine, Br-P(i-Pr)$_2$, that promotes the formal insertion of a phosphenium fragment [(i-Pr)$_2$P]$^+$ into the C-Ni bond, thus leading to a phosphine-phosphinite complex of Ni, of the following formula: $\{\kappa^P,\kappa^{P'}$-1-(i-Pr)$_2$PO-2-naphtyl-P(i-Pr)$_2\}$NiBr$_2$. When the C2 position in the naphthyl phosphinite is blocked by an Et substituent, a similar functionalization occurs at the C8 position leading to 8-(i-Pr)$_2$P(O)-2-Et-1-naphtol, along with by-products which have been identified and characterized. These findings demonstrated the kinetic accessibility of the C8 position at high temperatures, while proving the instability of the generated nickelacycle.

The reaction conditions used for the syntheses of cyclonickelated phosphinites displayed in **Chapter 2** (using acetonitrile as the solvent) have been proven more efficient than that previously reported (in toluene). Thus, **Chapter 3**, also based on a published article, describes the mechanistic aspects of the new procedure and reveals that acetonitrile generates more reactive species at the pre-nickelation stage, namely mono-phosphinite nickel adducts, as opposed to the bis-phosphinite nickel complexes observed in toluene. This study demonstrates that an external base is required for isolating the nickelated complexes, but that this base is not implicated in the metalation process, since the formation of the C-Ni bond occurs reversibly in the absence of base. Kinetic monitoring reveals that the reaction is 1st order and that an excess of base in fact slows down the rate by generating non-reactive species. Ideal bases for the nickelation are thus strong bases but weakly coordinating nucleophiles. An experiment-based mechanistic investigation shows that the

nickelation is of electrophilic (Hammett slope $\rho \approx -4$) and associative ($\Delta H^{\ddagger} = 18(1)$ kcal·mol^{-1} and $\Delta S^{\ddagger} = -27(4)$ cal·mol^{-1}·K^{-1}) nature, and that the proton transfer is rate limiting ($k_H/k_D \approx 11$). These results are supported by a DFT-based computational study that points towards an ion pair formation that allows the dissociated Br⁻ anion to capture the proton, in a CMD mechanism. The theoretical calculation also supported a triplet ground state in acetonitrile for the species present in the pre-nickelation mixture in acetonitrile.

Regioselectivity studies of a phosphinite bearing an *ortho*-vinyl substituent led to a surprising finding: instead of undergoing C-H nickelation, the phosphinite derived from 2-vinylphenol is attacked by nucleophiles on the vinyl moiety and give a Ni complex featuring a tridentate pincer-type ligand with a central C_{sp^3}-Ni bond. **Chapter 5** thus discloses a new Umpolung-based strategy leading to new pincer complexes. Reaction of the ligand 2-vinylphenyl-OP(i-Pr)$_2$ with primary or secondary amines and phosphines produces novel pincer-Ni complexes of the type 6,4-POC$_{sp3}$Y-NiBr (Y = P, N). This chapter discloses the variety of new complexes that can be prepared by this new synthetic strategy. The characterisation of the new complexes by NMR, XRD and electrochemical analysis allowed us to compare their structural and redox properties to pincer-Ni complexes reported in the literature.

While **Chapter 6** discloses additional results related to various research axes of this thesis, **Chapter 7** recalls the main findings revealed in **Chapters 2-5.** This conclusion also discloses research perspectives based on the results presented in this thesis, as well as phosphinite-related preliminary results gathered during my Ph. D. studies. The main proposed ideas touch on the following aspects: (a) the relationship between regioselectivity and stability towards functionalization; (b) new nickelation strategies based on the metalation of carbon-halogen bonds; (c) C-Ni functionalization by isolobal compounds to phosphenium ions; and (d) strategies towards the functionalization of alcohols bearing alkene moieties.

Keywords: Cyclonickelation, Phosphinite, Regioselectivity, Mechanism, Pincer complexes, DFT, Kinetics, Functionalization, C-H nickelation, X-Ray diffraction.

Table des matières

Liste des Schémas et Schemes

XVIII

Liste des Figures

XXXV

XLVII

Liste des Tableaux et Tables

Liste des sigles et abréviations

C-M : carbone-métal

C-Ni : carbone-nickel

C-H : carbone-hydrogène

C-X : carbone-halogène

C-N : carbone-azote

C-O : carbone-oxygène

C-C : carbone-carbone

M-H : métal-hydrure

Ni-H : nickel-hydrure

SET : *Single electron transfer* / Transfer d'électron célibataire

CMD : *Concerted metalation-deprotonation* / Métallation-déprotonation concertée

CO : monoxyde de carbone

Ar : aryle / aromatique

Ar^F : (poly)fluoroaromatique

OAc : Acétate

cod : 1,5-cycloocatdiène

^{i}Pr = i-Pr : *iso*propyl

^{t}Bu : *tert*butyl

^{n}Bu : butyl linéaire

Bn : benzyle

Bz : benzoyl

Piv : pivalate / *tert*butylcarboxylate

TEMPO : (2,2,6,6-tetramethylpipéridin-1-yl)-oxy

OTf : triflate / trifluorométhylsulfonate

OTs : tosylate / *para*-toluènesulfonate

acac : acetylacetonate

L_n : ligands de type et de nombre indéterminés

DG : *directing group* / groupe directeur

8AQ : 8-aminoquinol-N-yl

AQ : quinol-8-yl

TFE : tétrafluoroéthylène

XRD : *X-Ray diffraction* / diffraction des rayons X

RMN / NMR : résonance magnétique nucléaire / *nuclear magnetic resonance*

IR : infrarouge / *infrared*

CV : *cyclic voltammetry* / voltamperométrie cyclique

DFT : *density functional theory* / théorie de la fonctionnelle de la densité

Nu^- : nucléophile

E^+ : électrophile

Remerciements

Je tiens tout d'abord à remercier **Pr. Davit Zargarian** pour m'avoir accepté dans son groupe de recherche, et pour sa qualité de supervision tout au long de mon doctorat. Ce sont d'ailleurs son cours de chimie organométallique et sa pédagogie qui m'ont poussé à poursuivre mes études supérieures dans ce domaine de la chimie. Sa disponibilité, son ouverture et la confiance qu'il a démontré en moi m'ont permis de m'approprier ces projets de recherche en ayant un certain degré d'autonomie mais sans jamais me sentir seul. Je ressors également grandi de toutes les discussions et débats intéressants au sein de son groupe, qu'ils soient reliés ou non à la science.

Les travaux présentées dans cette thèse n'auraient pas pu être possible sans la qualité des services de recherche que l'on a à disponibilité à l'Université de Montréal. Ainsi, je tiens à remercier les membres du service RMN, et en particulier **Dr. Pedro Aguiar** qui s'est toujours montré disponible pour installer les expériences particulières dont j'avais besoin, et pour son implication à m'aider dans la résolution de problèmes reliés à la RMN que j'ai rencontrés. Je remercie également tous les membres du service d'analyse par Diffraction des Rayons X pour leur disponibilité et leur confiance en moi, et en particulier **Dr. Michel Simard** qui m'a formé à cette technique. Enfin, je remercie, pour les analyses élémentaires, **Elena Nadezhina**, **Dr. Mihaela Cibian** et **Dr. Thomas Auvray**. Je remercie d'ailleurs ce dernier pour son temps et son implication dans les analyses par ESI-MS.

Je remercie également les collègues et professeurs des groupes inorganiques, qui forment une jolie communauté. Une pensée également pour les stagiaires qui sont passé dans le groupe et qui ont été attentifs aux enseignements que j'ai pu leur apporter, en particulier **Raphaël Racine**, **Zubi Sadiq**, **Guillaume Michaud** (qui a participé aux recherches présentées dans le Chapitre 5), sans oublier **Morteza Karimzadeh** qui a été un collègue et reste ami très cher. Je tiens aussi à remercier tous les membres du groupe, incluant **Sébastien Lapointe** et **Dr. Boris Vabre** (qui m'a incité à joindre le groupe Zargarian et qui m'a formé à mes débuts). Enfin et surtout, je tiens à remercier **Dr. Jean-Philippe Cloutier** (aka J.-P.) pour toutes ces années formidables qu'on a passées ensemble dans le groupe, pour des discussions et des débats très intéressants sur la chimie, la physique, la cuisine et autres sujets philosophiques.

Enfin, je dis un grand merci à mes proches : ma sœur **Nathalie** pour m'avoir inculqué dès le plus jeune âge le gout du savoir, **mes parents** pour m'avoir toujours poussé à réaliser mes ambitions et pour leur soutien moral et financier, et bien évidemment mon copain **Stéphane** pour m'avoir soutenu pendant toutes ces années, pour toujours croire en moi et pour me rendre heureux au quotidien.

Chapitre 1 – Introduction

1.1 La liaison Carbone-Métal

La liaison carbone-métal (C-M) constitue le point central de la chimie organométallique qui étudie sa formation et sa réactivité. Plusieurs stratégies sont disponibles afin de former ces types de liens. Les métaux alcalins et alcalinoterreux ont une énergie d'ionisation qui est très faible et perdent facilement l'électron (les électrons) de leur orbitale s.[1] Les mécanismes les plus courants impliquent donc l'oxydation du métal accompagné de la réduction d'un lien carbone-halogène (échange métal/halogène) ou d'un lien carbone-hydrogène (déprotonation).[2] Parmi les métaux les plus courants, on trouve le lithium et le sodium comme représentants du groupe I et le magnésium comme représentant du groupe II, pour donner respectivement des composés organolithiens, organosodiques et organomagnésiens (ou réactifs de Grignard, ce dernier étant co-lauréat du prix Nobel de chimie en 1912). On propose généralement un mécanisme réactionnel commençant par un transfert d'électron (*single electron transfer* = SET, **Schéma 1.1**).

Schéma 1.1. Exemples de synthèse de composés organométalliques des groups I et II par métallation directe.
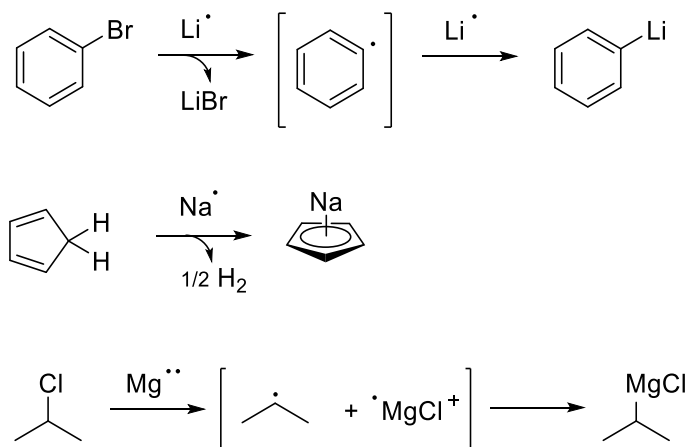
D'autres stratégies de formation des liens carbone-métal sont des métathèses impliquant un carbone déjà métallé. Un des exemples est la transmétallation, c'est-à-dire l'échange avec un autre métal déjà oxydé généralement contrebalancé par un halogène/pseudohalogène (**Schéma 1.2**). Un

autre exemple est l'échange métal/halogène, le plus souvent échange lithium/halogène, qui implique l'échange de l'ion Li$^+$ entre un organolithien et un halogénure organique.

Schéma 1.2. Exemples de synthèse de composés organométalliques par transmétallation.
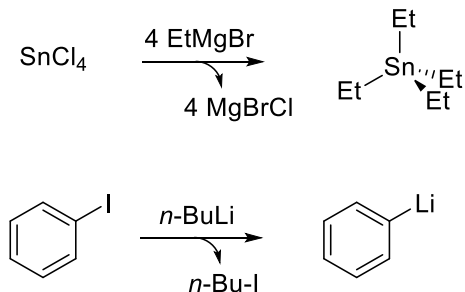
Dans les deux groupes, la liaison C-M est fortement polarisée ce qui rend le carbone très réactif et généralement nucléophile. Aussi, l'absence de contribution des orbitales d à la liaison chimique limite les types de réactions possibles et les organo-lithiens, -sodiques et -magnésiens sont des bases fortes ou des nucléophiles puissants (**Schéma 1.3**).[3]

Schéma 1.3. Réactivité des composés organométalliques des groupes I et II.
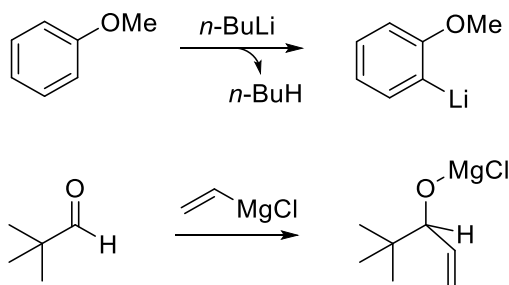
Lorsqu'on passe aux métaux de transition, pour lesquels les orbitales d sont mises à contribution, de nouvelles voies s'ouvrent en termes de stratégies de formation de liens carbone-métal mais également en termes de réactivité.[4] Les méthodes d'échange métal/halogène et de déprotonation sont toujours valables pour les métaux de transitions à un bas état d'oxydation, en particulier pour les métaux de la gauche du bloc d (*early transition metals*, groupes III-VII) car leur énergie d'ionisation est plus faible. Quant à la transmétallation, elle est commune à tous les métaux de transition et se fait généralement à partir de composés organométalliques des métaux alcalins et alcalino-terreux (en particulier le lithium et le magnésium). Lorsqu'on s'approche des métaux plus à droite du bloc d (*late transition metals*), de nouvelles stratégies voient le jour. On

2

notera par exemple l'addition oxydante concertée (**Schéma 1.4**) qui se fait le plus souvent par réaction avec des substrats portant des liens C-H ou C-X (X = halogène ou pseudohalogène) ou par substitution nucléophile sur des substrats portant des liens C-X moins encombrés (par ex. sur des carbones sp^3 peu encombrés, **Schéma 1.5**).

Schéma 1.4. Orbitales impliquées dans le processus d'addition oxydante concertée.
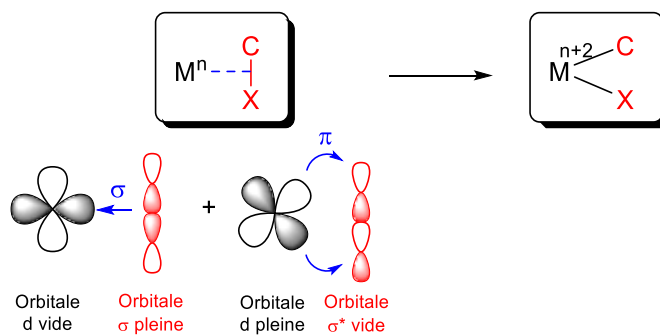
Schéma 1.5. Exemples de réactions d'addition oxydante sur les métaux de transition.
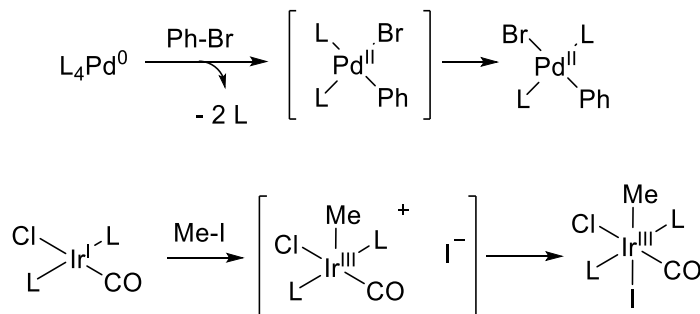
Ces réactions sont favorisées par l'oxydation du centre métallique dans des espèces à bas état d'oxydation, et sont facilitées par la coordination des liens C-H ou C-X au métal par donation σ accompagnée d'une rétro-donation π dans l'orbitale anti-liante du lien C-H/C-X. D'autres stratégies de formation de liens C-M, particulièrement pour les *late transition metals* sont appelées la métallation directe des liens C-H, qui ne modifie pas l'état d'oxydation du centre métallique. Ces procédés sont favorisés par la coordination du carbone au métal, ce qui décroit la densité électronique dans le lien C-H et permet l'éjection d'un proton en même temps que le lien C-M est formé. Ces réactions sont souvent, mais pas toujours, facilitées par la présence d'une base qui capte

le proton,[5] et constituent la classe des réactions de Métallation-Déprotonation concertée (assistée par une base) ou (*base-assisted*) *concerted metalation-deprotonation* (CMD, **Schéma 1.6**).

Schéma 1.6. Représentation du mécanisme CMD par le palladium.
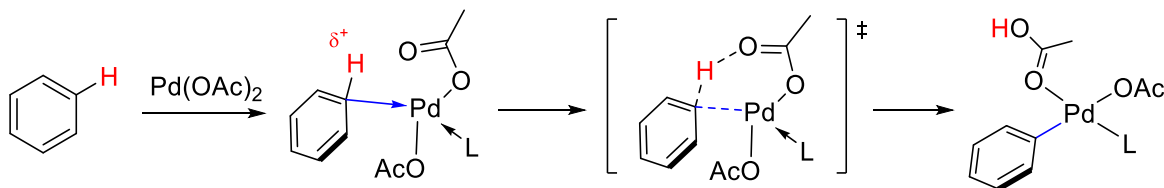
Avec les métaux de transition, qui sont plus électronégatifs que dans les organo-lithiens et -magnésiens, les liens C-M sont moins polarisés et plus robustes. En conséquence, le carbone est moins basique et nucléophile, ce qui permet d'ouvrir de nouvelles réactivités autour du lien carbone-métal. Par exemple, la contribution des orbitales d à la liaison chimique et le fait que le la sphère de coordination autour du métal peut être plus étendue permet de lier des molécules comme le monoxyde de carbone (CO), ou encore des molécules insaturées telles que les oléfines ou les alcynes. Ces dernières peuvent, par exemple réagir avec les liens C-M et M-H par insertion migratoire, et ces réactions ont été largement exploitées dans la synthèse des polymères telles que le polypropylène (insertions successives d'unités propylène, **Schéma 1.7**)[6] ou le polyacétone (insertion en alternance d'unités éthylène et CO, **Schéma 1.8**).[7]

Schéma 1.7. Mécanisme de polymérisation du propylène par un complexe cationique de zirconium.
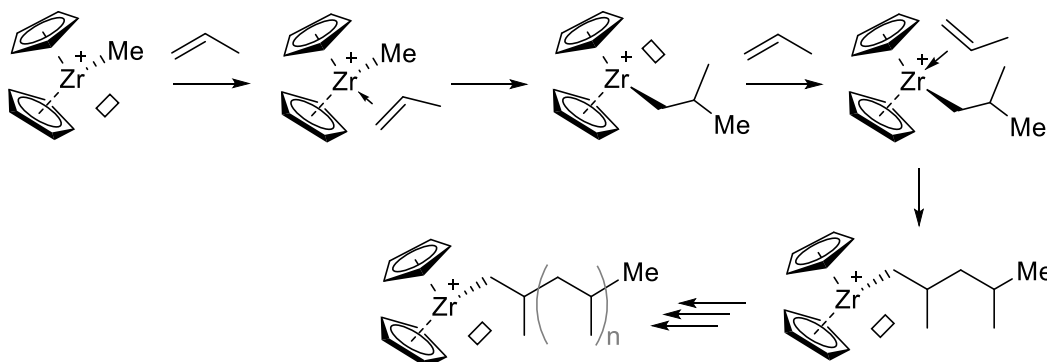
Schéma 1.8. Mécanisme de co-polymérisation du CO et de l'éthylène par un complexe cationique de palladium.
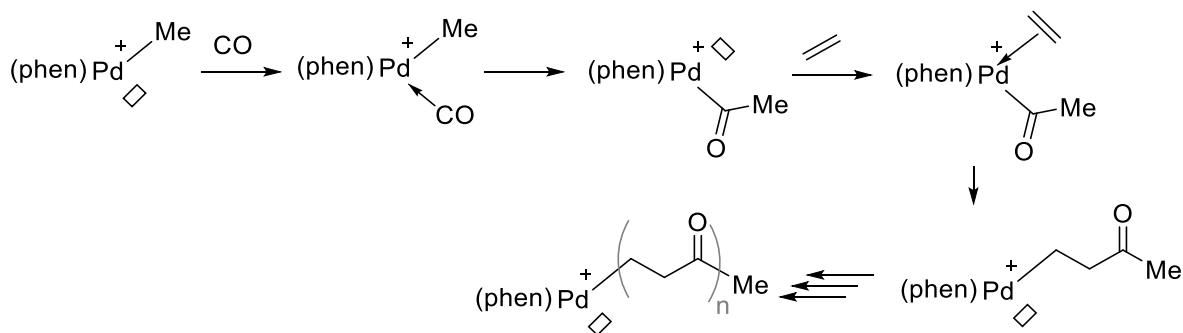
Les réactions inverses sont également une des particularités des métaux du bloc d : lorsqu'un ligand hydrocarboné est insaturé et possède des hydrogènes ou des groupes alkyles en position β, ces derniers peuvent migrer sur le métal par élimination β-H ou β-alkyle, respectivement, pour donner une oléfine et un hydrure métallique (M-H) ou un lien C-M. Ces réactions constituent généralement l'élément de terminaison dans la croissance des chaines de polymère, ou dans les cycles catalytiques de couplages (**Schéma 1.9**).[2] Finalement, lorsque le carbone lié au centre métallique est un carbène (généralement carbène de Schrock), ce lien carbène-métal peut réagir avec un autre alcène dans une réaction de métathèse (**Schéma 1.10**).[8] L'état d'oxydation du métal reste constant dans ce procédé, et cette découverte a valu à R. Grubbs le prix Nobel de chimie en 2005.

Schéma 1.9. Terminaison de la chaine en croissance du polypropylène par éliminations β-Hydrure ou β-Alkyle.
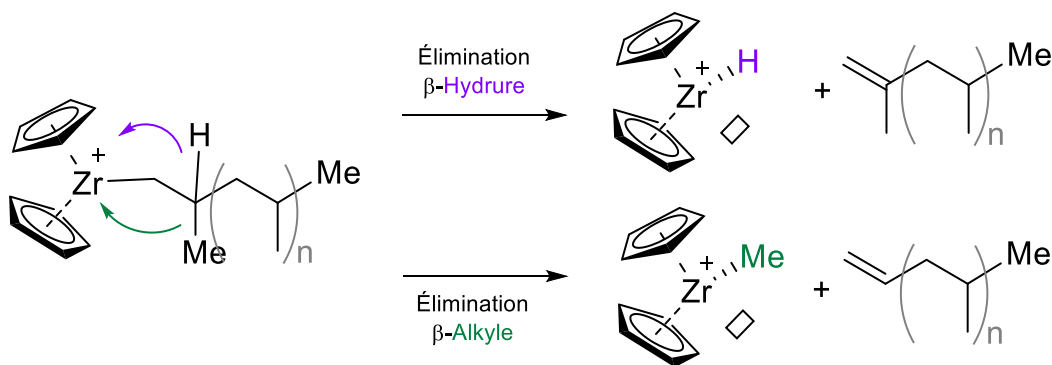
Schéma 1.10. Représentation du mécanisme de métathèse des oléfines.
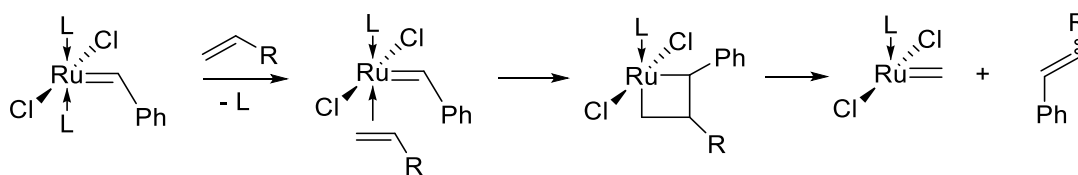
En raison de leur capacité à changer d'état d'oxydation facilement, les réactions inverses de l'addition oxydante sont également une particularité des métaux de transition, en particulier pour les métaux du milieu et de la droite du bloc d. Ces réactions sont plus facilement réalisées entre deux ligands carbones, deux ligands hydrures ou encore un ligand carbone et un hydrure. Ces propriétés ont été largement exploitées dans les couplages croisés entre des (pseudo)halogénures d'aryle/alkyle et d'autres espèces organométalliques (organo-cuprates, -magnesiens, -stannanes, -boranes, -zinciques) ou des carbonyles α,β-insaturés (**Schéma 1.11**). Ces réaction impliquant le nickel ou le palladium comme catalyseurs, ont été développées et nommées respectivement après K. Sonogashira, M. Kumada, J. K. Stille, A. Suzuki, E. Negishi et R. Heck, et a valu à ces trois derniers d'être les lauréats du prix Nobel de chimie en 2010. Plus récemment, des couplages entre des carbones et de hétéroatomes pour donner des liens C-N ou C-O, autant avec le palladium comme dans les couplages étudiés par S. L. Buchwald et J. F. Hartwig, où les états d'oxydation Pd^0, Pd^{II} et Pd^{IV} sont généralement invoqués, qu'avec le nickel qui nécessite souvent la présence d'un photo-cocatalyseur comme dans les réactions étudiées par D. W. C. MacMillan, où l'on invoque plutôt des états d'oxydation Ni^0, Ni^I, Ni^{II} et Ni^{III}.

Schéma 1.11. Représentations des mécanismes de couplage C-C ou C-N par le palladium.[9,10]
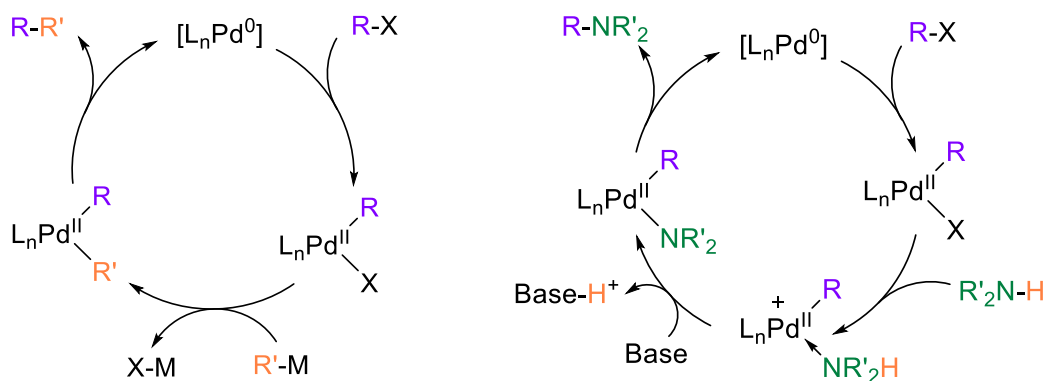
Tous ces types de couplages nécessitent généralement un substrat portant un lien C-X afin de former le lien carbone-métal réactif. Cependant, les procédés ne requérant que la présence d'un lien C-H pour générer le lien carbone-métal et obtenir un produit à plus haute valeur ajoutée sont vus comme des cibles majeures en chimie organométallique. En effet, la fonctionnalisation directe des liens C-H est avantageuse à plusieurs égards : les substrats organiques peuvent être utilisés directement nécessiter transformation des liens C-H en liens C-X plus activés, les substrats hydrocarbonés sont moins couteux que leurs parents halogénés et l'absence d'halogénures rend le processus plus écologique, en accord avec les grands axes de la chimie verte qui cherche à éviter les substrats organohalogénés.[11]

Pour réaliser ces procédés de fonctionnalisation directe des lien C-H, les métaux seconde et troisième rangée du bloc d ont été plus largement étudiés, mais l'utilisation de leurs homologues de première rangée, qui sont plus abondants, suscite de plus en plus d'intérêt.[12] Non seulement l'utilisation du nickel à la place du palladium ou du platine est très avantageuse économiquement, mais les métaux du bloc 3d ont des réactivités différentes et complémentaires à celles de leurs homologues plus lourds. Alors que le palladium réalise plutôt des changements d'état d'oxydation à deux électrons (*i.e.* Pd^0, Pd^{II} et Pd^{IV}), le nickel a une facilité à produire les états d'oxydation intermédiaires par SET (*i.e.* Ni^0, Ni^I, Ni^{II}, Ni^{III} et Ni^{IV}), ce qui permet d'ouvrir de nouvelles voies de transformations.

1.2 Fonctionnalisation directe des liens C-H par catalyse au Ni

Deux stratégies de fonctionnalisation directe des liens C-H par le nickel sont envisageables : la première consiste à former le lien carbone-nickel par addition oxydante du lien C-H sur un nickel de basse valence (souvent un précurseur de Ni^0), et la seconde par métallation directe des liens C-H sur un nickel déjà oxydé (souvent un précurseur de Ni^{II}). Dans les deux cas, le mécanisme requiert une coordination du lien C-H ou du carbone portant le proton sur le centre métallique afin de déclencher la réaction. Contrairement aux métaux de transition des blocs 4d et 5d qui forment des liens agostiques (C-H)→Métal et des liens datifs du carbone au métal (H)C→Métal relativement facilement, ces types d'interaction chez les métaux de première rangée tels que le nickel sont relativement faibles. De plus, une fois l'activation ou la métallation du lien C-H réalisée, les liens C-M et H-M sont également moins stables avec les métaux du bloc 3d qu'avec leurs

homologues de deuxième et troisième rangées. Ainsi, la formation directe des liens Carbone-Métal à partir de liens C-H avec le nickel représente un défi autant en termes de cinétique que de thermodynamique, ce qui a poussé les chimistes à trouver des stratégies bien précises pour réaliser ces réactions.

1.2.1 Ne nécessitant pas de groupes directeurs

La première approche consiste à utiliser des liens carbone-hydrogène très activés, ce qui permet de faciliter la réaction lorsque le métal et le substrat se rencontrent ainsi que de rendre leur thermodynamique plus favorable. Par exemple, les liens C_{sp^2}-H des substrats aromatiques fluorés et polyfluorés se sont révélés de bons candidats pour l'addition oxydante sur de fragments métalliques de basse valence. En effet, une étude systématique de W. D. Jones sur l'énergie de dissociation des liens Rh^{III}-Ar^F ($Ar^F = C_6F_nH_{5-n}$) a démontré que la vitesse d'élimination réductrice menant à la formation de Rh^I et de H-Ar^F diminuait rapidement avec l'augmentation du nombre de substituants F.[13] Ainsi la réaction inverse, l'addition oxydante Ar^F-H, devrait être facilitée par la substitution des hydrogènes par des fluors. Cette propriété a été transposée au nickel : des précurseurs de Ni^0 ont permis efficacement l'activation C-H des fluoroarènes et fluoropyridines pour lesquels l'addition oxydante dans les liens C-H était plus rapide que dans les liens C-F. Ainsi en 2008, T. Hiyama reportait une réaction de *cis*-hydroarylation des alcynes et des alcènes à partir de fluoro-arènes/pyridines catalysée par le nickel (**Schéma 1.12, A**).[14] Puis en 2010, S. A. Johnson reportait la stannylation des liens C-H par le vinyl-$SnBu_3$ pour les fluoroarènes et la 2,3,5,6-F_4-pyridine, également catalysée par le Ni^0.[15] Dans les deux cas, lorsque plusieurs C-H sont disponibles, la position possédant le plus de substituants *ortho*-F est favorisée ce qui permet un alcènylation ou une stannylation régiosélective (**Schéma 1.12, B**). Également, il semble que pour les deux mécanismes, l'activation C-H se produit sur une intermédiaire où l'alcyne ou l'oléfine est coordonnée au Ni^0, impliquant une métallation par transfert direct d'hydrure concerté, correspondant formellement à une étape d'addition oxydante C-H suivie d'une insertion du composé insaturé.[16,17]

Schéma 1.12. Mécanismes proposés pour l'acènylation (A) et la stannylation (B) régiosélectives des fluoroarènes.
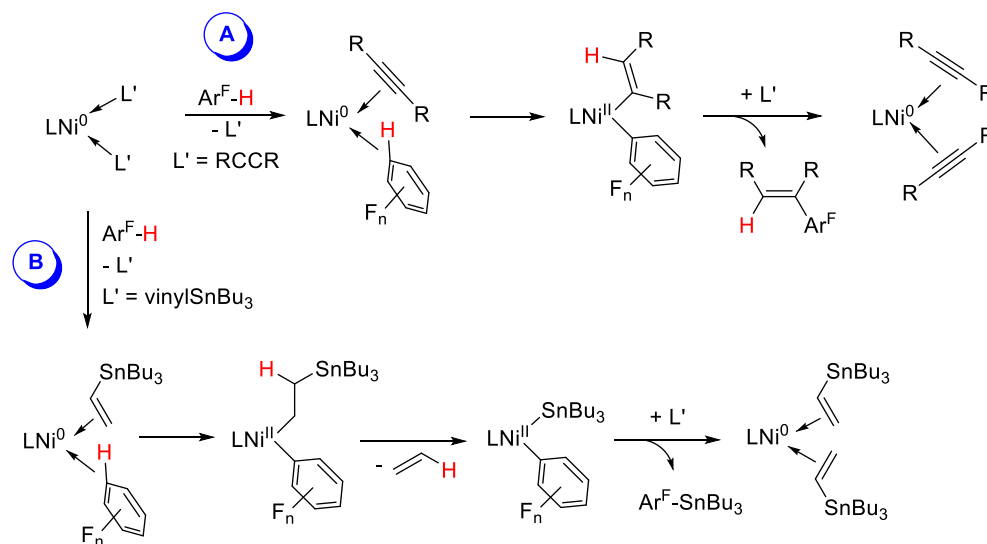
T. Hiyama a également démontré que le Ni[0] pouvait également catalyser l'acènylation et l'alkylation des pyridines non fluorées en présence d'un acide de Lewis, avec une activation C-H régiosélective pour la position 2.[18] Et en 2015, P. M. Zimmerman et J. Montgomery reportent un catalyseur de nickel également capable d'effectuer l'alcènylation par activation C-H des fluoro-arènes/pyridines,[19] et ont réussi à l'étendre plus tard aux liens C-H d'hétérocycles non fluorés tels que le benzoxaole, le benzofurane, le benzothiophène ou le N,N'-diméthyle-uracile, et ce de manière régiosélective.[20]

Dans la seconde approche ne nécessitant pas l'utilisation de groupe directeur, le lien carbone-nickel est formé à partir d'un centre métallique déjà oxydé. Même si le pré-catalyseur employé est souvent un complexe de Ni[0], le lien C-Ni est réalisé par métallation directe, après que le partenaire de couplage se soit additionné sur le métal pour donner un intermédiaire de Ni[II]. Les liens C-H qui permettent de réaliser ces réactions nécessitent d'être hautement activés et plus faciles à déprotoner : ils proviennent en général d'hétérocycles aromatiques azotés et la présence d'une base pour capter le proton issu de la nickellation est nécessaire. En 2009, K. Itami reportait un couplage croisés entre des halogénures d'aryles et des azoles tels que (benz)imidazoles, (benz)oxazoles et (benzo)thiazoles catalysé par le nickel (**Schéma 1.13**).[21] L'avantage était l'utilisation d'un précatalyseur très bon marché, *i.e.* Ni(OAc)$_2$·4H$_2$O, et une régiosélectivité sur la position 2 des azoles.

Schéma 1.13. Mécanisme proposé pour l'arylation de la position C2 des azoles.
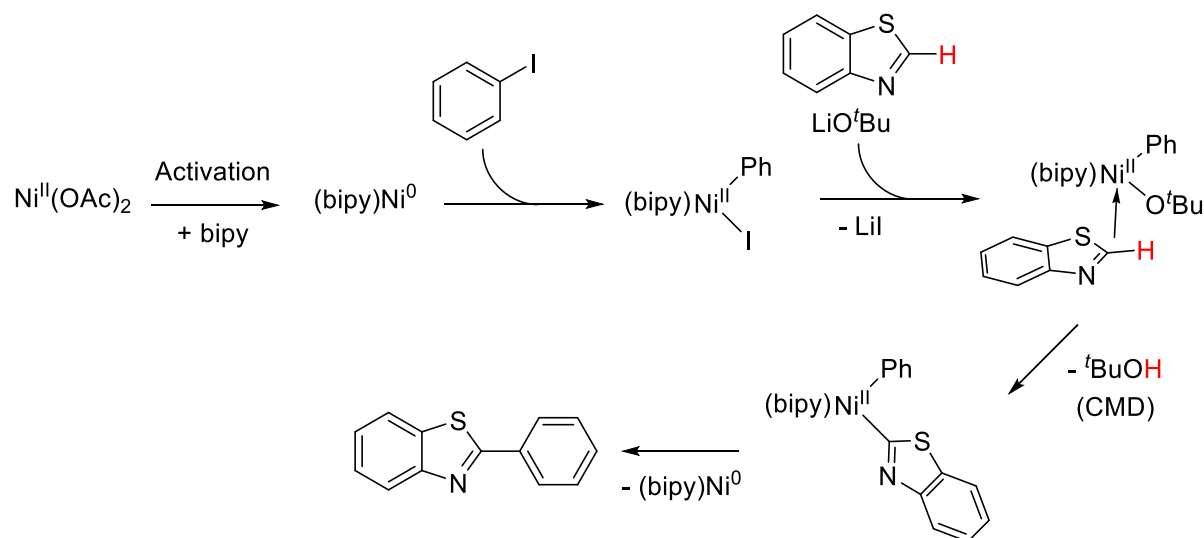
Un peu plus tard, le même groupe proposait un couplage croisé similaire impliquant des azoles, mais cette fois avec un triflates et les pivalates d'aryles comme partenaire de couplage.[22] Bien que l'utilisation des dérivés des phénols soit rentable économiquement, cet avantage est contre-balancé par la nécessité d'un précatalyseur de basse valence, *i.e.* Ni(cod)$_2$, qui est relativement dispendieux. En 2015, T. Chen et L.-B. Han ont démontré que cette dernière stratégie se révélait également efficace, pour générer des liens C$_{sp^3}$-C$_{sp^2}$ par couplage des fluoroaryles et des azoles avec des pivalates de naphtyle (**Schéma 1.14**).[23]

Schéma 1.14. Couplages des pivalates de naphtyle avec les fluoroarènes et les azoles.
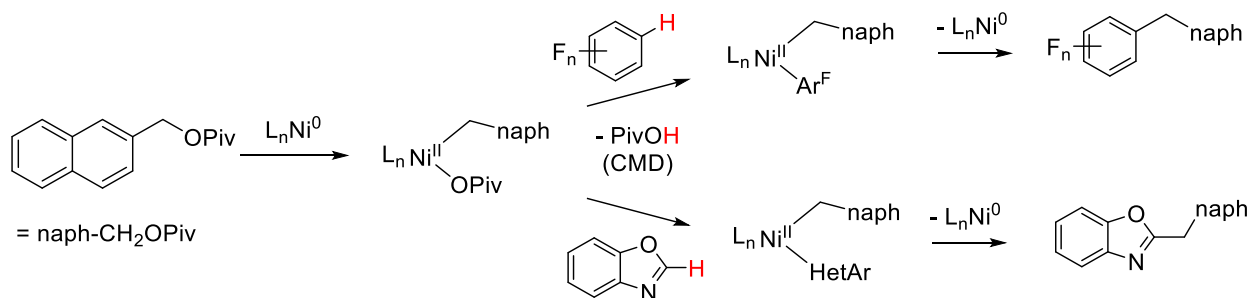
Bien que les indoles soient des composés aromatiques moins activés que les (benz)azoles, C. Cai reportait également en 2015 une réaction de couplage C_{sp^3}-C_{sp^2} entre les dérivés de l'indole et le carbone α d'éthers cycliques, en présence de peroxyde de *tert*-butyle.[24] Contrairement aux azoles qui ont une seul position activée (la position 2 entre les deux hétéroatomes), les indoles pourraient être fonctionnalisés sur le cycle A en positions 2 et 3. Ainsi, ces travaux ont montré qu'en variant l'identité du pré-catalyseur de nickel, une régiosélectivité peut s'instaurer soit sur la position 2 en utilisant NiF_2 + PPh_3, soit en position 3 lorsque $Ni(acac)_2$ + $Zn(OTf)_2$ est employé (**Schéma 1.15**). Des réactions test en présence TEMPO˙ ont montré que ce dernier couple avec le carbone α de l'éther mais ne couple pas avec l'indole. Ce résultat suggère que le lien entre le carbone de l'indole et le métal est produit par une étape de nickellation directe C-H sur un centre Ni^{II} ou encore Ni^{III}.

Schéma 1.15. Couplage des indoles avec le dioxane dans différentes conditions.
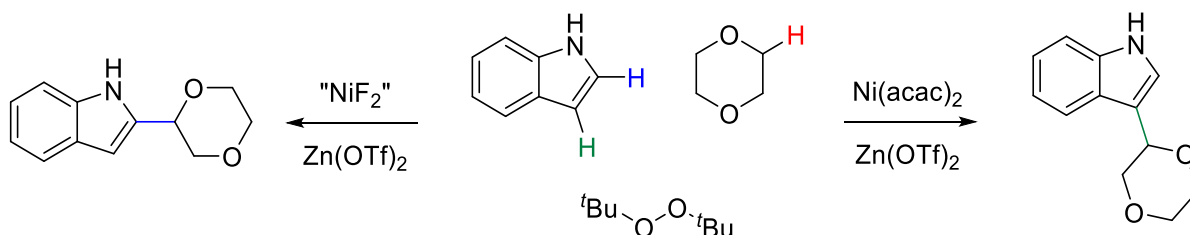
1.2.2 Nécessitant des groupes directeurs

Lorsque les liens C-H ne sont pas suffisamment activés ou acides, leur fonctionnalisation par catalyse au nickel requiert généralement l'emploi d'un groupe directeur qui est greffé, de manière réversible ou non, sur le substrat. Le groupe directeur (*directing group* ou DG) est généralement un groupe fonctionnel nucléophile qui se lie au métal afin de rapprocher le lien C-H d'intérêt du centre métallique et de faciliter le bris de ce lien, afin de donner un intermédiaire cyclique. Cette stratégie a deux avantages : d'une part elle abaisse l'énergie d'activation pour la formation du lien Carbone-Métal car la métallation devient alors unimoléculaire (facteurs entropiques favorables), et d'autre part elle permet de contrôler la régiosélectivité de la métallation car elle impose des conditions stériques pour la formation d'un métallacycle. En effet, on a vu que dans les réactions impliquant des aromatiques polyfluorés, l'activation C-H est dirigée vers le site

11

portant le maximum de substituants fluors en *ortho*; mais dans la métallation des azoles, il n'y a en réalité qu'un seul site réactif qui est la position 2. Si l'on souhaite réaliser la fonctionnalisation des liaisons C-H non-activées (*i.e.* liens C_{sp^2}-H d'oléfines ou d'arènes non fluorés ou liens C_{sp^3}-H de substrats aliphatiques) où plusieurs sites sont de caractère électronique semblable, l'utilisation d'un groupe directeur s'avère cruciale pour diriger la réaction vers un seul produit. Les DG se différencient surtout par leur denticité, qui correspond au nombre d'atomes du groupe qui se lient au centre métallique afin de réaliser la métallation du substrat qui les porte.

Les groupes directeurs monodentés mènent donc à une espèce cyclométallée (portant le lien carbone-métal) bidentée. Parmi ceux-ci, les azines se sont révélées efficaces pour la fonctionnalisation C-H catalysée par le nickel. Certains articles reportent l'efficacité de ces groupes directeurs pour la fonctionnalisation des liens C-H par addition oxydante à partir de complexes de Ni^0. Par exemple, en 2013, L. Ackermann reportait la transformation des anilines en indoles par annulation en présence d'alcynes catalysée par Ni(cod)$_2$ (**Schéma 1.16**).[25] Pour ce faire l'azote de l'aniline est muni du groupe directeur 2-pyrimidyl qui permet de lier le nickel afin de réaliser l'activation C-H en position *ortho* de l'aniline. L'insertion formelle de l'alcyne dans le lien nickel-hydrure suivie de l'élimination réductrice fournit le produit d'*ortho*-alcènylation du substrat; l'annulation prend place après activation du lien N-H par le métal, insertion de l'oléfine et deshydrogénation *in situ*. Cette réaction s'est également avérée possible lorsque le DG est un fragment 2-pyridyl, bien que plus difficile à difficile à dissocier du substrat. Un autre exemple de l'utilisation du groupe directeur 2-pyridyl a été publié en 2017 par M. Miura : greffé encore une fois sur l'azote du substrat, ce DG permet l'activation C-H de la position 6 des pyridones, suivie de l'alkylation par insertion d'alcènes (**Schéma 1.17**).[26] Le produit d'insertion Markovnikov a été trouvé comme majeur, et dans le cas où l'alcène est un diène non tendu, la seconde fonction oléfine peut s'insérer dans le lien Carbone-Nickel afin de donner des composés cycliques.

Schéma 1.16. Mécanisme de préparation des indoles par annulation des pyridines avec des alcynes.
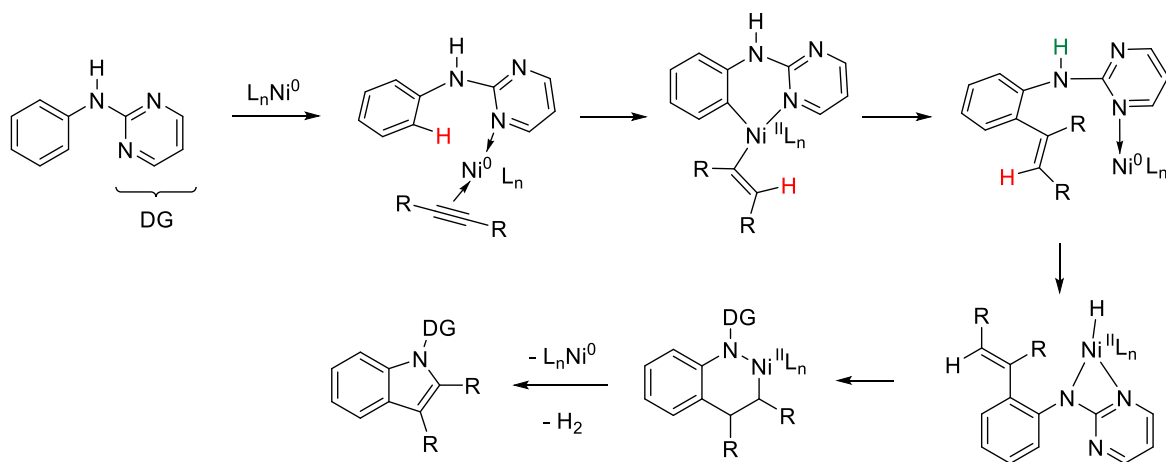
Schéma 1.17. Réaction d'alkylation des pyridones avec les alcènes.
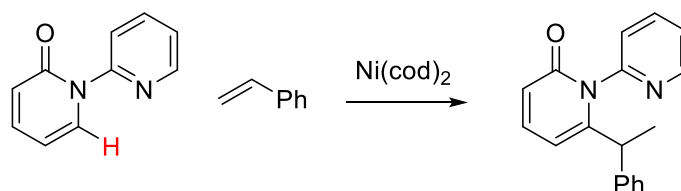
Les hétérocycles azotés se sont, en outre, révélés utiles comme groupes directeurs dans la fonctionnalisation C-H où le lien C-Ni est formé par métallation directe en présence d'une base (CMD). Ainsi, en 2016, L. Ackermann reprenait sa stratégie pour la métallation directe *ortho* des anilines par un catalyseur de Ni^{II}, cette fois ci pour réaliser l'alkylation avec des halogénures d'alkyle primaires ou secondaires (**Schéma 1.18**).[27] Également, en 2017, B. Punji reportait une réaction d'alcynylation catalytique des indoles, des (benz)imidazole, des pyrroles et des pyrrazoles avec une sélectivité en *ortho* du groupe directeur.[28] Alors que le partenaire de couplage est un bromo-alcyne, l'espèce qui semble réaliser l'étape de métallation est un complexe de Ni^{II}. Ici, tout comme pour l'*ortho*-alkylation des anilines de L. Ackermann, on propose que l'intermédiaire cyclonickellé réagit avec le bromo-alcyne par SET (pour donner une espèce Ni^{III}) ou par addition oxydante C-Br (pour donner une espèce Ni^{IV}), afin d'obtenir le produit de couplage croisé par élimination réductrice.

Schéma 1.18. Mécanismes proposés pour l'*ortho*-alkylation des anilines catalysée par Ni[II].
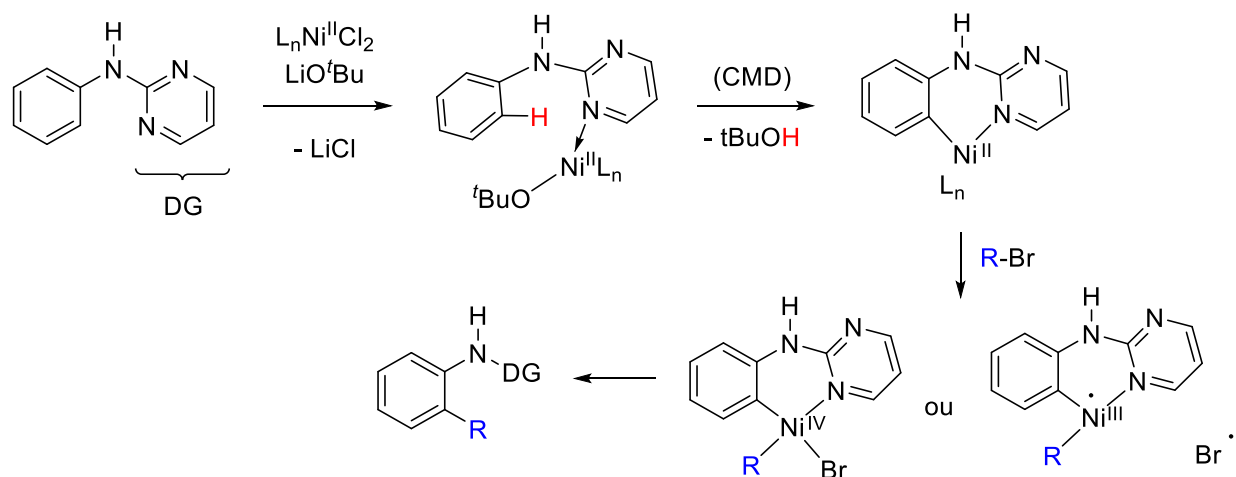
Enfin, en 2019, C. Cai a utilisé le groupe directeur 2-pyridyl greffé sur des arènes non activés pour transformer la position *ortho*-C-H du cycle aromatique en groupement C-OR (OR = OAc, OMe, OEt, OBz).[29] Ce couplage C-O réalisé par un catalyseur de Ni[II] permet l'introduction du groupement -OR soit sous forme de d'oxydant tel que PhI(OAc)₂ (pour OR = OAc), soit sous forme de sa version protonée ROH (pour OR = OMe, OEt, OBz) auquel cas l'addition d'un co-oxydant tel que les sels d'Ag[I] ou une atmosphère d'oxygène est nécessaire (**Schéma 1.19**). Les auteurs proposent ainsi que l'intermédiaire cyclométallé, alors riche en électron, est aisément oxydé pour donner le produit de couplage C-O par élimination réductrice. La valorisation des liens C-H par couplage avec des hétéroatomes et l'utilisation de l'oxygène moléculaire comme oxydant fait de ce procédé d'un grand intérêt économique.

Schéma 1.19. Couplages C-O promus par des oxydants et catalysés par le Ni[II].
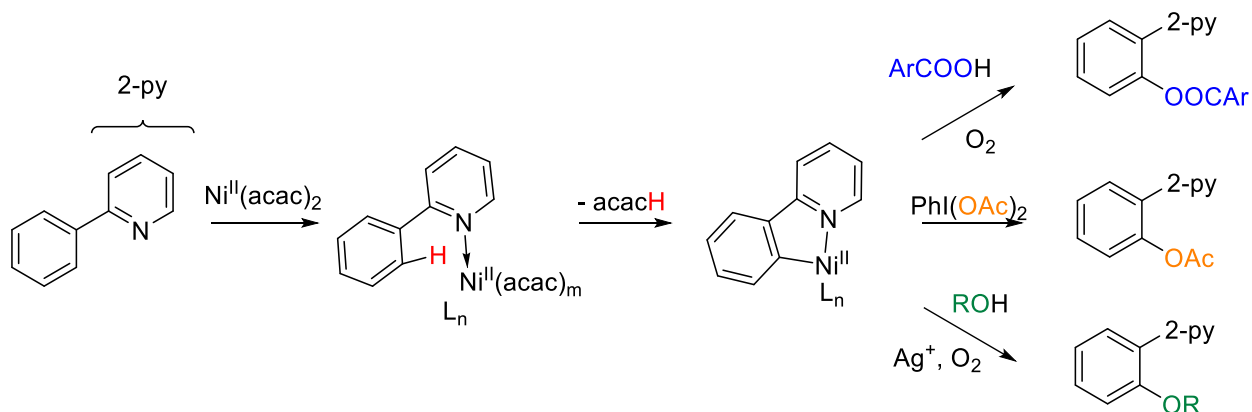
Lorsque le DG se lie au métal par deux points d'ancrage afin de faciliter la métallation du substrat, on obtient un intermédiaire cyclométallé tridenté, ce qui implique en principe une plus grande stabilité du lien carbone-métal, mais qui laisse entrevoir des transformations nécessitant des conditions réactionnelles plus agressives. La majorité des rapports dévoilant des procédés de fonctionnalisation C-H catalysés par le nickel utilisent des groupes directeurs pour lesquels la bidenticité comporte un ligand pyridine relié au substrat par une liaison amide, lequel constitue la seconde dent du DG, une fois déprotoné. Dans ces cas, le DG est greffé aux substrats portant une fonction acyle par amidification, et permet une régiosélectivité en position β du carbonyle (*i.e.* position 2 du cycle aromatique dans le cas des fragments benzoyles) pour former un intermédiaire cyclonickellé à 5 chainons. Ainsi, en 2011, N. Chatani reportait la première fonctionnalisation des liens *ortho* C-H catalysée par le nickel et assistée par un groupe directeur, obtenu par amidification avec le 2-pyridinylmethylamine (**Schéma 1.20**).[30] Après coordination des deux dents du groupe directeur au centre métallique, la nickellation C-H donne un intermédiaire tridenté où le lien C-Ni permet l'insertion d'un alcyne, après quoi une élimination réductrice permet de compléter l'annulation et résulte en une isoquinolone. Cette réaction procède sans l'utilisation d'une base externe, puisque le proton de la nickellation est capté formellement par un hydrure, lequel résulte de l'activation N-H de la fonction amide par le pré-catalyseur de Ni^0.

Schéma 1.20. Premier exemple de fonctionnalisation C-H assitée par un groupe directeur et catalysée par le nickel.
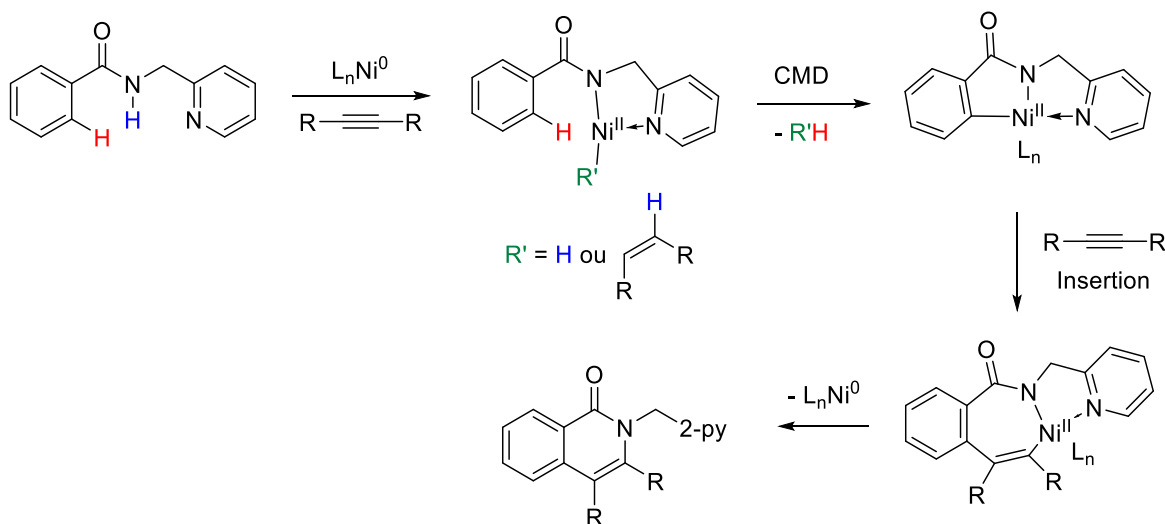
En 2013, le même chercheur reporte deux nouvelles réactions catalytiques complémentaires : tout d'abord l'alkylation des liens C_{sp^2}-H dans les benzamides et acrylamides,[31] puis l'arylation des liens C_{sp^3}-H dans les amides aliphatiques (**Schéma 1.21**).[32] Cette fois, les auteurs optent pour un groupe directeur plus rigide que celui reporté en 2011, où la fonction amide dérive de la 8-aminoquinoline (8AQ), ce DG ayant prouvé précédemment son efficacité avec des métaux plus lourds comme le palladium ou le ruthénium. De plus, on y utilise des pré-catalyseurs de Ni^{II} et le groupe directeur bidenté vient se lier au métal après une étape de déprotonation, et la métallation est formée par CMD assistée par la base, ce qui justifie l'emploi de Na_2CO_3 en quantités supra-stœchiométriques. Le partenaire de couplage dans ces deux études sont respectivement les bromures d'alkyles primaires, et les iodures d'aryles, et les auteurs proposent que le lien carbone-halogène s'additionne sur l'intermédiaire cyclonickellé pour donner un espèce Ni^{IV} qui résulte en un couplage carbone-carbone subséquemment, par élimination réductrice.

Schéma 1.21. Stratégies complémentaires d'alkylation Csp²-H et d'arylation C-sp³-H dirigées par la fonction N-8-Aminoquinolylamide.
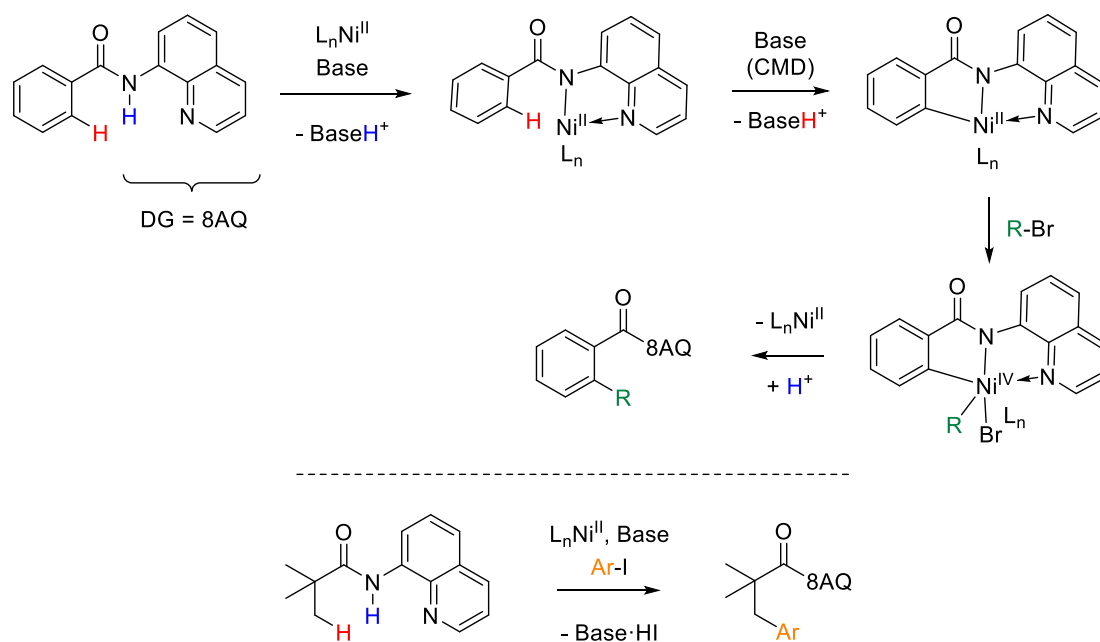
Le groupe directeur 8AQ reste un emblème de la fonctionnalisation directe des liens C-H catalysée par le nickel, car il répond bien au grand défi de faire réagir les liens C_{sp^2}-H et même C_{sp^3}-H non activés. De plus, les articles publiés par N. Chatani ainsi que d'autres auteurs qui ont suivi

ses traces démontrent que ce DG permet de valoriser le lien carbone-nickel par quasiment tout l'éventail de réactivités observées dans la chimie organométallique (**Schéma 1.22**). Dans la catégorie des liens C$_{sp^2}$-H fonctionnalisés par cette stratégie (généralement provenant de substrats arènes et hétéroarènes mais également des vinyles), on trouve l'arylation par Ar-I (N. Chatani, 2014)[33], l'akylation par des halogénoalcanes secondaires (L. Ackermann, 2014)[34]; l'amination de type Buchwald-Hartwig en présence d'un oxydant (Z. Liu et Y. Zhang, 2015)[35]; l'acynylation par des bromoalcynes (F. Li, 2015)[36]; le couplage croisés avec le C2-H des azoles en présence d'un oxydant (J. You, 2016)[37]; l'annulation en naphthyles par double insertion des alcynes (Y. Huang, 2016)[38]; l'halogénation par LiX (X = Cl, Br, I)[39] en présence d'oxydant (B.-F. Shi, 2016) ou encore l'iodination en présence d'iode moléculaire (N. Chatani, 2016).[40]

Schéma 1.22. Exemples de l'éventail des fonctionnalisations directes C-H des composés insaturés promues par le groupe directeur 8AQ.
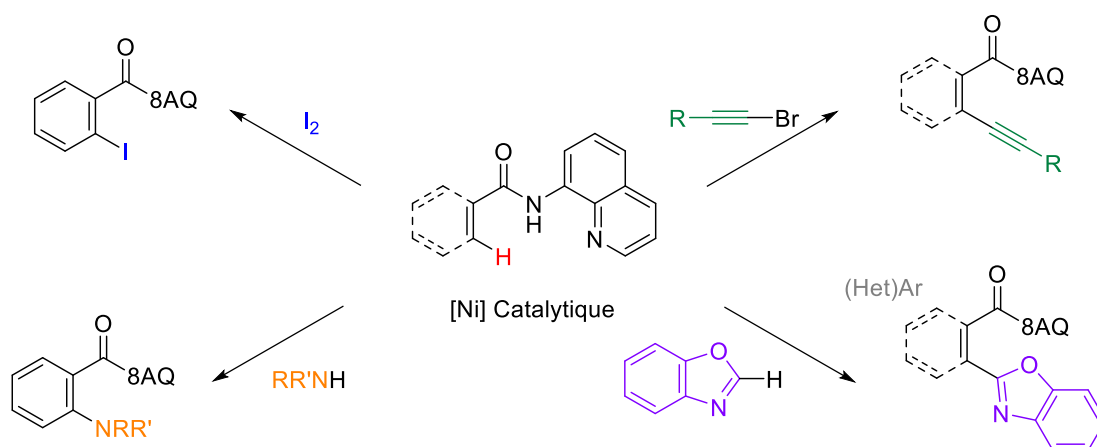
Bien que la nickellation des liens C$_{sp^3}$-H représente un défi de taille, cette stratégie prodigue des voies réactionnelles de grande variété également (**Schéma 1.23**). On y trouve des exemples de fonctionnalisation par alkylation avec les iodoalcanes primaires (H. Ge, 2014)[41]; l'amidation intramoléculaire pour générer des β-lactames en présence de TEMPO˙ (H. Ge, 2014)[42] ou d'iode moléculaire (N. Chatani, 2016)[43]; l'arylation à partir de bromoaryles (J. You, 2014)[44], la thioarylation par les oxydants disulfurés (Y. Zhang, 2015)[45], l'acènylation par des iodures de vinyles (B.-F. Shi, 2015)[46], par des alcynes internes (J. You, 2015)[47] ou par des alcynes terminaux dans un couplage de type Sonogashira donc en présence de Cu^I (Z.-J. Shi, 2016)[48] ou encore la thiophèn-2-ylation en présence de thiophènes et d'Ag^I comme oxydant (R. Qiu, Y. Xia et S.-F. Yin, 2017)[49]

17

Schéma 1.23. Exemples de l'éventail des fonctionnalisations directes C-H des composés aliphatiques promues par le groupe directeur 8AQ.
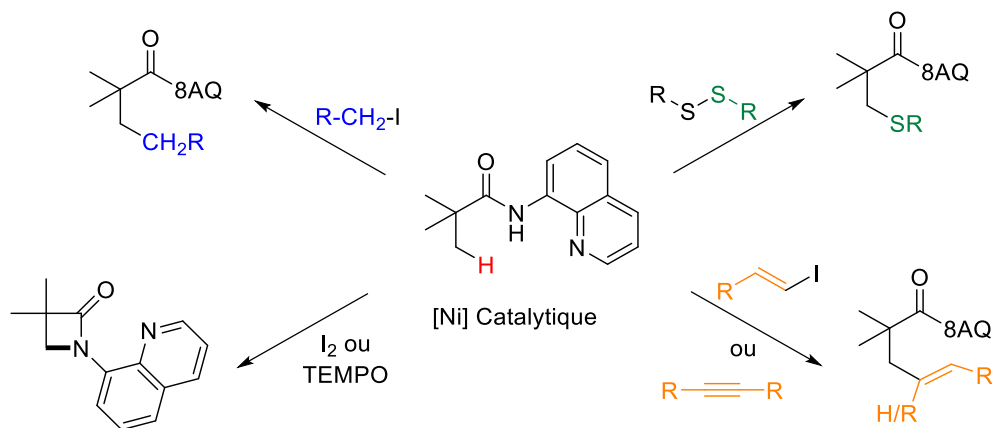
Dans tous ces exemples de fonctionnalisation C-H, l'étape de nickellation se produit sur un centre Ni^{II}, puis la réactivité du lien carbone-nickel peut ensuite passer par le même état d'oxydation, ou par des mécanismes impliquant des valences plus hautes comme Ni^{III} ou Ni^{IV}. Cependant, dans ces travaux, l'intermédiaire portant le lien carbone-nickel n'est généralement pas isolé. Ainsi, peu d'études se focalisent sur ces intermédiaires clés et cherchent à isoler le mécanisme de leur formation et leur réactivité propre. Bien que des études cinétiques sur le procédé révèlent parfois que la métallation n'est pas l'étape cinétiquement limitante, peu d'indices permettent de justifier l'utilisation de très hautes températures et des temps de réactions longs, ou d'expliquer le rôle des additifs employés. Ceci démontre une connaissance relativement faible de la nature des micro-étapes ou des espèces réellement réactives dans le cycle catalytique. Afin d'améliorer rationnellement les conditions réactionnelles, et d'offrir une connaissance fondamentale plus approfondie de ces processus, il convient donc d'étudier systématiquement les intermédiaires en les isolant afin d'en comprendre les mécanismes de leur formation et leur réactivité.

1.3 Les espèces cyclonickellées de type *pincer*

Les espèces de types *pincer* sont des espèces organométalliques tridentées dont les deux dents latérales sont constituées de donneurs neutres (E = R$_3$P, R$_3$N, R$_2$S *etc.*) et dont la dent centrale est un donneur anionique (Y = C, N, Si *etc.*). Notés selon la nomenclature (EYE)MX (M = métal, X = ligand(s) auxiliaire(s)), les trois dents forment un environnement planaire et doublement cyclométallé autour du métal, et le lien entre le donneur central et le métal a pour effet de stabiliser le ligand *pincer* sans quoi il serait sujet à protonation ou autres réactions menant à la décomposition du lien X-M. Introduits par B. L. Shaw vers les fin des années 1970,[50,51,52] ces types de ligand permettent de stabiliser une grande variété de dérivés ou d'états d'oxydation autour du métal, lui donnant ainsi des propriétés uniques par rapport aux espèces organométalliques classiques. Lorsqu'une méthode de synthèse d'un type de pinceur se révèle efficace, il est également facile d'affiner ses propriétés en faisant varier les substituants sur les donneurs E ou les substituants du squelette dans le donneur central Y. Étant plus facilement isolables car le lien Y-M est stabilité par la forte coordination tridentée de leur ligand, les complexes pinceurs portant un donneur central carboné (*i.e.* ECE) sont donc des composés modèles pour l'étude de la formation et de la réactivité des espèces organométalliques telles que celles proposées dans les procédés catalysés par le nickel.

1.3.1 Stratégies de synthèse

Les stratégies de synthèse de ces espèces sont semblables à celles utilisées pour former les espèces organométalliques plus communes. Une des méthode conventionnelle consiste en l'addition oxydante d'un lien carbone-halogène dans un métal de basse valence M^n (Rh^I, Ir^I, Ni^0 *etc.*) pour obtenir un complexe pincer du métal M^{n+2} (**Schéma 1.24, A**).[53,54] Lorsque le composé hydrure dudit *pincer* est stable, on peut également opter pour l'addition oxydante d'un lien C-H dans un précurseur métallique de basse valence (**Schéma 1.24, B**). Bien que cette stratégie ait été plutôt exploitée avec les métaux des blocs 4d et 5d, qui forment des liens métal-hydrure beaucoup plus forts qu'avec les éléments du bloc 3d, des composés *pincers* de Ni ont pu être préparés par cette méthode.[55,56] Une autre méthode consiste en la transmétallation à partir des organolithiens des ligands pinceurs, générés eux même par déprotonation du lien C-H ou par échange lithium-halogène.

Schéma 1.24. Stratégies de synthèse des composés *pincers* par addition oxydante C-X (A) ou C-H (B) avec des métaux lourds et avec le nickel.
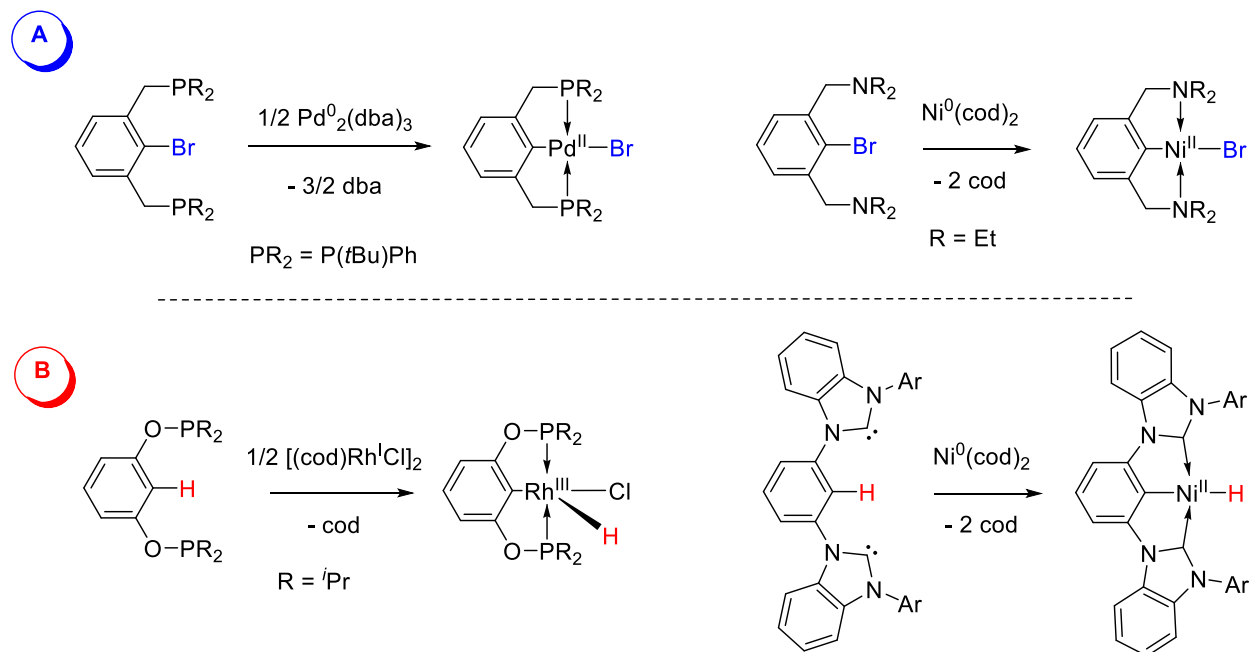
Schéma 1.25. Synthèse du pinceur NCN-NiBr par transmétallation avec le lithium.
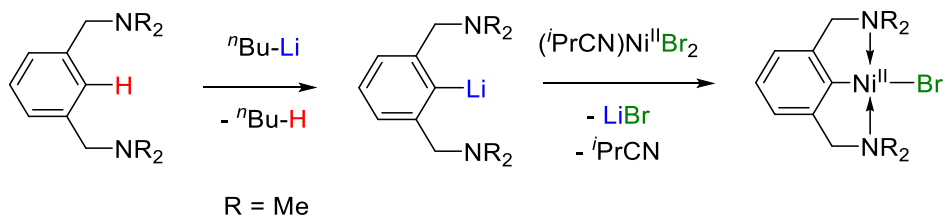
Enfin, la méthode qui semble la plus attrayante est la métallation directe C-H, car elle ne requiert pas l'utilisation d'un proligand organohalogéné ou l'utilisation d'un précurseur métallique de basse valence qui sont généralement dispendieux et sensibles à l'air, et évite une étape de lithiation comme celle requise pour les procédés par transmétallation. Cette stratégie s'est révélée être efficace pour la synthèse des complexes *pincers* de nickel : à l'instar de l'utilisation de groupes directeurs, la nickellation est facilitée par la chélation des bras latéraux du proligand pinceur, qui rapprochent le carbone central du métal et favorisent l'interaction de ce dernier avec le lien C-H, en vue de former la liaison carbone-nickel. Une base est généralement nécessaire pour capter tout

l'équivalent de protons généré lors de la métallation afin de conduire la réaction à complétion. Les exemples les plus communs (autant pour le nickel que d'autres métaux) sont des *pincers* portant au moins un donneur neutre basé sur le phosphore, tels que ceux étudiés par le groupe de D. Zargarian (**Schéma 1.26**). On y trouve par exemple des complexes symétriques tels que les composés PCP-Ni ou POCOP-Ni (basés respectivement sur des donneurs phosphines et phosphinites), pour lesquels la liaison carbone-nickel provient soit de la nickellation de liens C_{sp^2}-H ou C_{sp^3}-H.[57,58] Ces complexes subissent la métallation à température pièce (Tp) et relativement rapidement, en particulier pour ceux ayant un squelette aromatique On y trouve également des complexes non symétriques portant un donneur azoté tels que les composés POCN-Ni (portant un donneur amine ou imine, publiés également par le groupe D. Zargarian)[59,60] ou plus récemment les PCN-Ni (étudiés par O. Wendt).[61] Ces complexes portant un donneur azoté nécessitent cependant du chauffage et des temps de réaction plus longs afin de compléter la réaction. D'autres variantes portant des donneurs de type carbènes hétérocyclique (NHCCOP), imidazoliophosphines (PIMIOCOP) ou imidazolophosphines (PIMCOP) ont également été reportées par ce groupe en collaboration avec R. Chauvain.[62]

Schéma 1.26. Exemples de pincers de nickel préparés par nickellation directe C-H.
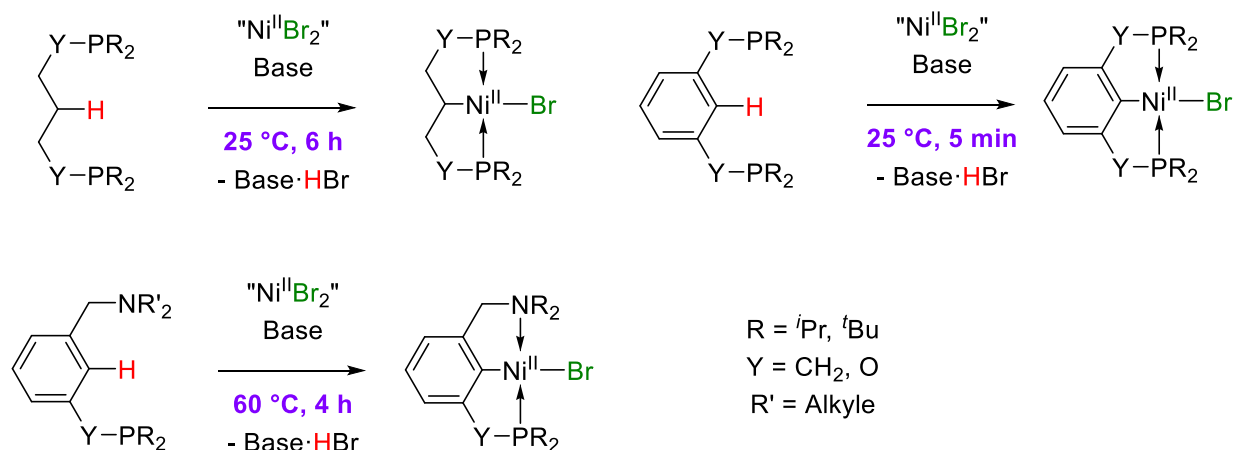
Le mécanisme de la nickellation des proligands PCP et POCOP menant aux complexes *pincers* de nickel portant des liens C_{sp^2}-H ou C_{sp^3}-H a été étudié aux niveaux expérimental et théorique par D. Zargarian et D. H. Ess.[63] Bien que les réactions soient trop rapides pour permettre

l'extraction des constantes de vitesse, des études de compétition ont permis de démontrer que les proligands aromatiques réagissent plus rapidement que leurs homologues aliphatiques, que les PCP réagissent plus vites que leurs homologues POCOP et que dans chaque catégorie, et que les squelettes portant des substituants électrodonneurs sont plus réactifs que ceux portant des substituants électroattracteurs. L'étude théorique computationnelle DFT (*density functional theory* ou théorie de la fonctionnelle de la densité) a considéré plusieurs mécanismes plausibles pour la nickellation C-H menant à ces composés. Parmi les chemins envisagés on trouve (a) l'addition oxydante du lien C-H menant à un intermédiaire Ni^{IV} suivie de l'élimination réductrice des ligands hydrudes et bromures; (b) la métahèse concertée des liens C-H et Ni-Br sans changement d'état d'oxydation; (c) la nickellation/déprotonation concertée assistée par la base après dissociation hétérolytique et (d) la nickellation promue par une espèce Ni^I après dissociation hétérolytique du lien Ni-Br. Les résultats de cette étude pointent vers le mécanisme (c) (**Schéma 1.27**) comme étant celui possédant la barrière énergétique la plus faible, et passant par des états de transitions singulets (bien que l'état fondamental ait été trouvé comme un triplet). Dans ce mécanisme, la dissociation hétérolytique d'un ligand bromure permet la coordination du carbone du lien C-H sur le métal, qui devient alors électrophile puisqu'étant le cation d'une paire d'ion, suivi de la déprotonation du C-H par le contre-anion bromure, qui constitue la base cinétique. Ces conclusion ont permis de rationaliser la nécessité d'avoir une combinaison d'un nickel électrodéficient et un carbone électroriche, puisqu'une forte coordination de ce dernier au centre métallique fait baisser l'énergie d'activation en stabilisant la paire d'ions intermédiaire.

Schéma 1.27. Nickellation électrophile par CMD dans la synthèse des composés PCP-NiBr.
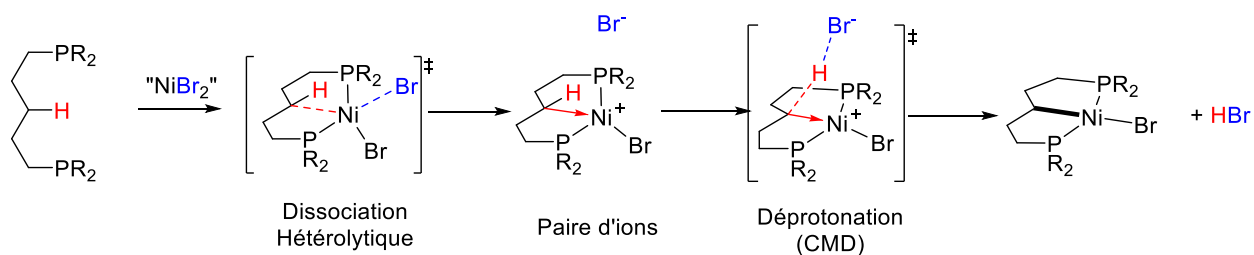
Ce mécanisme permet également d'expliquer la plus grande difficulté à faire réagir les proligands portant des donneurs azotés qui sont de plus forts donneurs que les phosphines/phosphinites : un chauffage modéré est nécessaire dans le cas des POCN et PCN, alors

que les proligands NCN requièrent un chauffage intense et prolongé dans les meilleurs cas,[64] ou ne génèrent pas de complexe pinceur dans les pires cas.

1.3.2 Réactivité des complexes pinceurs

   Étant donné leur relative stabilité et facilité d'isolation, les composés *pincers* du nickel portant un carbone comme donneur central constituent des complexes modèles pour l'étude de la réactivité des espèces cyclonickellées possédant une liaison carbone-nickel. Par exemple, on peut étudier l'étendue de possibilités des ligands ayant la capacité de se lier en position *trans* du lien C-Ni. Ainsi, bien que ces espèces soient généralement isolées sous forme d'halogénures (*i.e.* ECE-NiX où X = halogène), de nombreux dérivés ont pu être préparés par échange de ligands, tels que les complexes homologues hydrures, aryles, alkyles, siloxydes, amidures ou encore des cations. Ces dérivés ont été souvent isolés afin de démontrer qu'ils étaient des intermédiaires potentiels dans les réactions catalytiques impliquant les pinceurs.

   Les *pincers* de nickel ont en effet trouvé plusieurs applications en catalyse, à commencer par celles qui ne semblent pas impliquer d'autres états d'oxydation du métal. Les hydrures des complexes POCOP, étudiés par H. Guan, ont montré une efficacité catalytique pour l'hydrosilylation des aldéhydes et des cétones,[65] la réduction du CO_2 par des boranes,[66] l'hydrogénation des phenylacétylènes[67] alors que le *pincer* homologue Ni-CH_2CN pouvait promouvoir la cyanométhylation des aldéhydes menant à des α-cyanoalcools (**Schéma 1.28**).[68]

Schéma 1.28. Exemples de réactions catalysées par les complexes pinceurs de nickel de H. Guan.
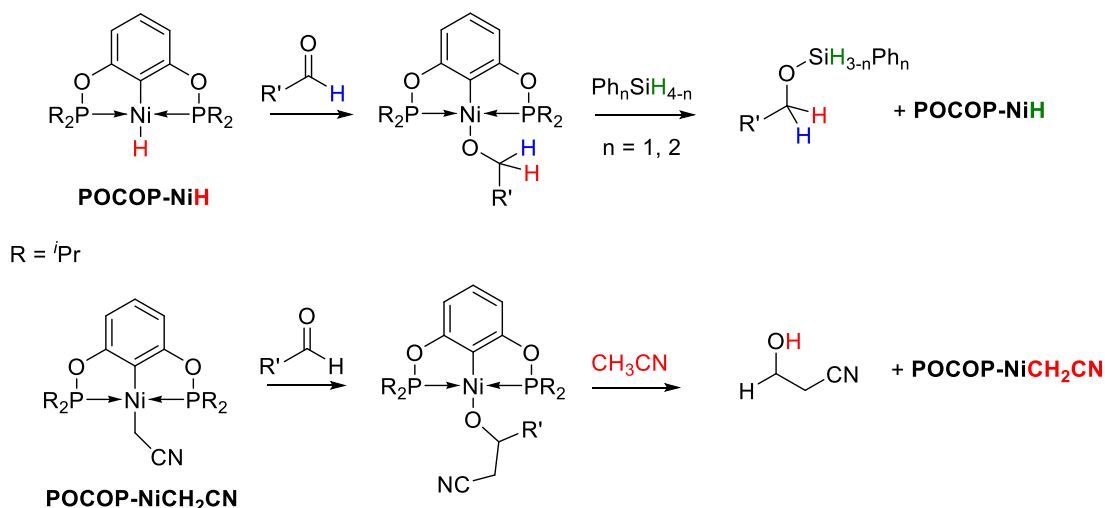
De son côté, le groupe D. Zargarian a démontré l'efficacité des homologues cationiques des complexes POCOP et PCP à promouvoir l'hydroamination des alcènes activés dérivés de l'acrylonitrile,[69] alors que les cations des pincers POCOP et POCN ont également démontré un activité dans l'hydroalkoxylation de ces mêmes acrylonitriles (**Schéma 1.29**).[70,71] Ces dernières études montrent que le *resting state* (l'intermédiaire de plus basse énergie du cycle catalytique) est un complexe cationique où le ligand auxiliaire est l'acrylonitrile, lié au métal par l'azote.[72]

Schéma 1.29. Exemples de réactions catalysées par les complexes pinceurs de nickel de D. Zargarian.
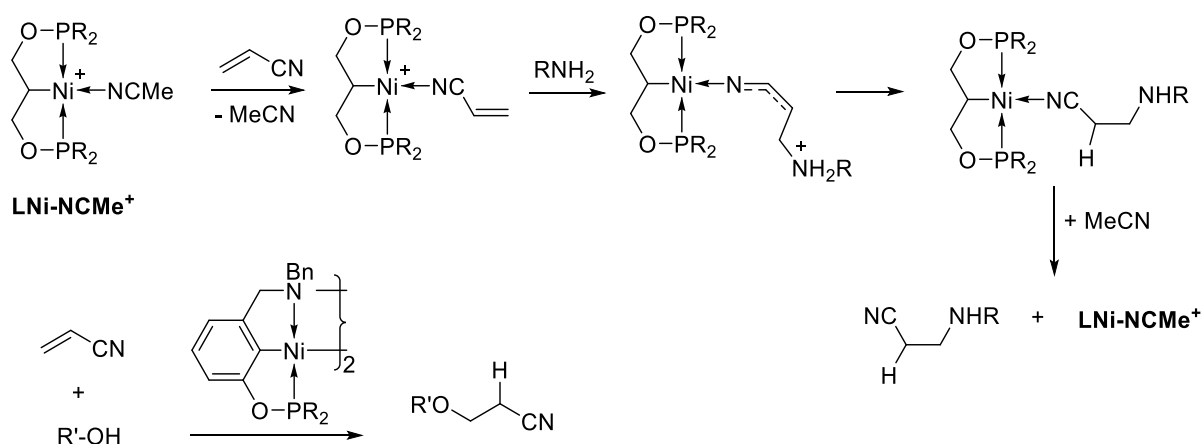
L'étude des complexes pinceurs de nickel s'est également étendue à des processus catalytiques impliquants différents états d'oxydation du centre métallique. En effet, des études électrochimiques par voltampérométrie cyclique (*cyclic voltammetry* = CV) ont permis de mettre en évidence la capacité de ces espèces à s'oxyder en Ni^{III}. Les complexes de type NCN préparé par G. C. van Koten possèdent les potentiels d'oxydation de loin les plus bas, les complexes POCN et PCP des potentiels d'oxydation intermédiaires alors que ceux de type POCOP se sont révélés les plus difficiles à oxyder. Dans ces deux dernière catégories, les espèces portant des donneurs centraux C_{sp^3} ont montré un accès plus aisé aux complexes de Ni^{III} que ceux portant des donneurs C_{sp^2}. Ainsi, bien que seuls les composés $PC_{sp^2}P$ et $POC_{sp^2}OP$ n'ont pas permis l'isolation de leurs homologues trivalents, tous les complexes divalents ont montré une activité catalytique dans des processus impliquant des états d'oxydation élevés, en particulier pour les couplages croisés

impliquant des halogénures. Un des exemples types est l'addition de Kharasch, qui met en jeu le couplage d'un poly-haolégnoalcane avec un alcène pour donner le produit d'haloalkylation anti-Markovnikov, et dont la première étape consiste en une dissociation hétérolytique d'un lien carbone-halogène assistée par le métal (**Schéma 1.30**). Les centres métalliques permettant cette réaction doivent donc être capables de capter un radical halogène pour former un espèce oxydée. Cette réaction avec les pinceurs de nickel a été d'abord démontrée par G. C. van Koten en 1988 en utilisant le complexe NCN-Ni[II] qui peut facilement générer son homologue de Ni[III].[73,74] Dans les années 2000 et 2010, D. Zargarian a donc également prouvé que les complexes de nickel trivalents basés sur les ligands phosphinites (POCOP-Ni et POCN-Ni) se montraient efficaces pour catalyser l'addition de Kharasch, et plus récemment O. Wendt a montré l'efficacité du complexe PCN-Ni dans cette même réaction.

Schéma 1.30. Mécanisme proposé pour l'addition de Kharasch catalysée par le pincer POCN-NiBr.
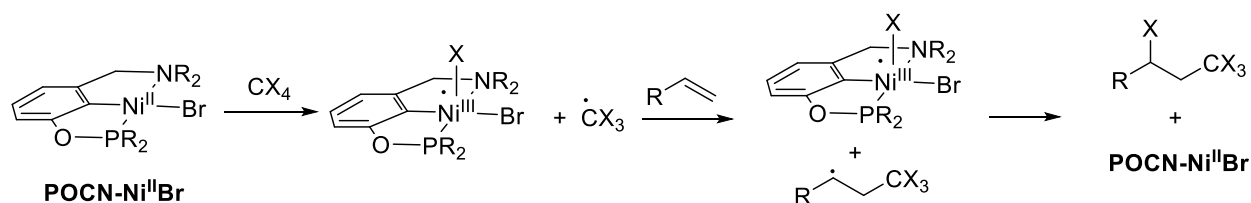
D'autre réactions impliquant des intermédiaires Ni[III] ont pu également être catalysées par les complexes *pincers*. En 2008, D. Zargarian publiait une étude des complexes PCP-Ni et montrait que le complexe Ni-Br pouvait être converti en son homologue Ni-Me, et que ce dernier réagissait avec le chlorobenzène pour donner du toluène et le complexe Ni-Cl. Ainsi, l'article démontre la capacité de ce *pincer* à catalyser le couplage de Kumada-Corriu entre un réactif de Grignard et des halogénures d'aryles (**Schéma 1.31**). La même année, K. Mitsudo et H. Tanaka démontraient également l'efficacité des pinceurs de nickel, cette fois ci de type NCN portant des oxazolines comme donneurs latéraux, dans la réaction de Heck qui couple un carbonyle α,β-insaturé avec un halogénure d'aryle pour donner le produit de β-alkylation. Deux ans plus tard, H. Guan démontrait que les complexes POCOP-Ni permettaient le couplage catalytique des halogénures d'aryles avec les thiolates pour donner les thioéthers correspondants. Dans tous ces cas, on présume que le lien

carbone-halogène se brise da manière homolytique et implique donc des intermédiaires de Ni^{III} ainsi que des intermédiaires de Ni^{I}.

Schéma 1.31. Mécanisme Ni^{II}/Ni^{III} proposé pour le couplage de Kumada-Corriu catalysé par le pincer PCP-NiBr.
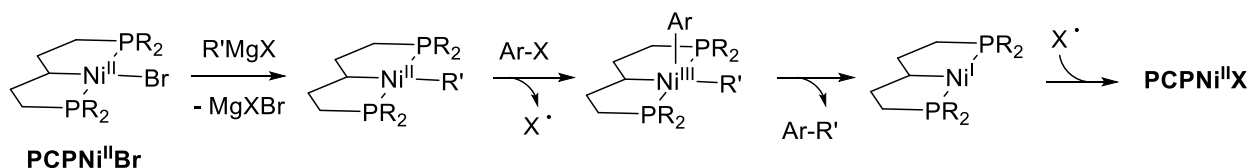
Si elles démontrent les propriétés des espèces cyclonickellées, dans les réactions présentées ci-dessus, la réactivité est centrée sur le métal et le ligand auxiliaire du complexe pincer. Cependant, des études ont montré que le ligand lui-même, en particulier le lien C-Ni central des pinceurs peut aussi être réactif afin de donner des produits de fonctionnalisation. Ces réactions sont généralement promues par des complexes haut-valents de nickel tels que les complexe de Ni^{III} et Ni^{IV} pour lesquels l'instabilité de l'état oxydé permet la réactivité des liens carbone-nickel.

Par exemple, D. Zargarian publiait en 2015 un rapport sur un nouveau pinceur de type NCN-Ni, avec des pyrazoles comme donneurs latéraux, pour lequel l'oxydation par H$_2$O$_2$ donne un couplage avec le carbone central menant à la formation d'un fragment C-OH, et pour lequel la réaction avec un excès d'amines R$_2$NH ou d'alcools ROH donne un couplage similaire menant à la formation de liens C-NR$_2$ ou C-OR sur le ligand, lorsque la réaction est conduite en présence d'oxygène. Les auteurs proposent donc que l'espèce réactive est une espèce *pincer* de Ni^{III} et que le couplage se fait via élimination réductrice C-O ou C-N comme dans les couplages de type Buchwald-Hartwig. Le pinceur NCN basé sur des pyrazoles n'ayant pas permis d'isoler l'espèce oxydée, et ayant un potentiel d'oxydation moins bon que la plateforme de G. C. van Koten, les auteurs se sont tournés vers l'étude de ce dernier dans les même types de couplages. Ils ont démontré que ce complexe permet le même type de couplages C-O et C-N, ainsi que les couplages plus difficile carbone-halogéne, à partir des complexes isolés de Ni^{III} ou de leurs homologues de Ni^{II} en présence d'oxygène (**Schéma 1.32**). Ils ont également démontré en combinant une étude expérimentale et théorique que les espèces cationiques et di-cationiques du NCN permettent une

réaction plus rapide car l'élimination réductrice est plus aisée lorsque le centre métallique est électrodéficient.

Schéma 1.32. Couplages carbone-hétéroatome entre le ligand et des composés protiques promus par l'oxydation du nickel dans les pinceurs NCN-Ni.
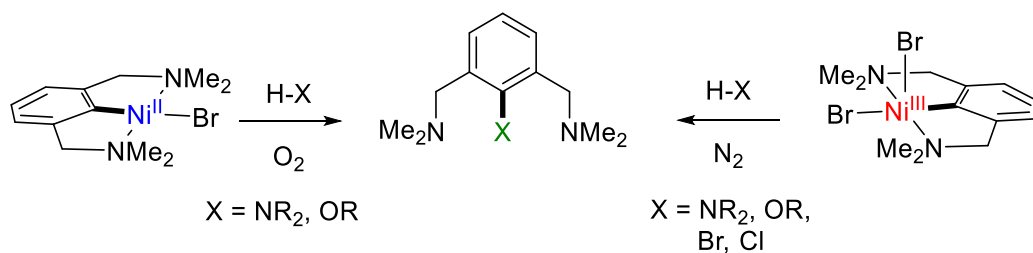
Les transformations mettant en jeu le lien C-Ni des ligands *pincers* comme réactif permettent donc de d'étudier la réactivité des espèces cyclométallées portant des liens C-Ni. Cependant, les produits de fonctionnalisation qui en résultent sont généralement de peu d'intérêt synthétique, dû à la nature des ligands utilisés. De plus, la stabilisation offerte par la multi-denticité, si elle est commode pour les études systématiques et mécanistiques, peut influer significativement sur la réactivité sur centre métallique et sur ligand. Ainsi, il est également important de comprendre la réactivité des liens C-Ni dans les espèces simplement cyclonickellées, même si leur isolation peut parfois s'avérer plus ardue.

1.4 Les nickellacycles : Isolation et réactivité

Les liens carbone-métal dans les espèces « simplement » cyclométallées ne jouissent pas de la stabilisation et de la protection offerte par les deux bras du ligand dans les plateformes de type *pincer*. Les complexes de ce type sont donc plus difficiles à isoler, car le lien C-M pourrait réagir avec des ligands se positionnant en position *cis*. Cela dit, ils sont généralement préparés par des réactions similaires que les complexes pinceurs.

1.4.1 Formés par réaction sur le Ni^0

Une première famille de procédés utilise des précurseurs métalliques de basse valence (M^n) tels que Ir^I, Rh^I, Pd^0 qui génèrent des métallacycles où le centre se retrouve oxydé à l'état M^{n+2}, l'oxydation étant une des forces motrices de la réaction. Dans cette famille, on retrouve les réactions d'additions oxydantes carbone-halogène, carbone-hydrogène et même carbone-carbone, ainsi que des réactions de cyclisation oxydante par réaction avec des composés insaturés. Avec le nickel, les précurseurs généralement employés sont le $Ni(cod)_2$ et les composés du type $Ni(PR_3)_4$ qui peuvent être générés *in situ* par réaction des dihalogénures de Ni(II) en présence de réducteurs (organomagnésiens ou organoaluminiums). Par exemple, G. Muller et M. Rocamora isolent et caractérisent en 1993 un phosphine cyclonickellée à 5 chainons par addition oxydante du lien C-Cl en position *ortho* du fragment benzyle dans le ligand $BnPPh_2$ (**Schéma 1.33**).[75] Ils montrent également que le lien C-Ni généré peut subir des réactions d'insertion de CO, de SO_2 ou d'alcynes

Schéma 1.33. Synthèse par addition oxydante d'une phosphine cyclonickellée et sa réactivité.
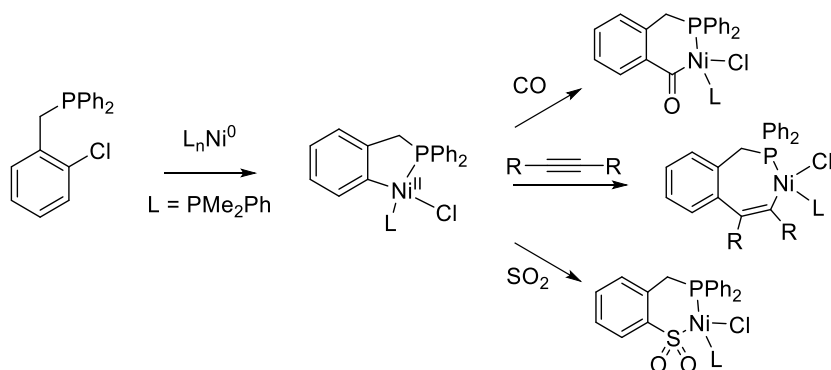
En 1995, le même groupe publie des nickellacycles à 5 chainons formés par addition oxydante de liens C-X (X = Cl, Br) dans des ligands benzylamines et benzylimines formant des nickellacycles bidentés.[76] L'année suivante, ils étendent cette réaction à ces même benzyl-amines et -imines où l'azote est substitué par une dent diméthylaminoéthylène, donnant ainsi des composés cylométallés tridentés de type NNC, et montrent que le lien C-Ni subit l'insertion d'éthylène ou d'alcynes.[77]

Cette dernière stratégie, utilisant un groupe directeur bidenté pour former le lien C-Ni a été également reprise en 2018 par M. D. Frysuk, cette fois avec des phosphores comme donneurs du

DG.[78] Ils montrent que la coordination en *cis* du lien C-Ni de ligands méthyle mène à l'élimination réductrice C-C pour donner le ligand ortho-méthylé (**Schéma 1.34**). Ils prouvent également que l'ajout de ligands éthyle ou isopropoxyde mène à l'élimination β-Hydrure et que le complexe hydrure subit l'élimination réductrice C-H pour redonner le ligand non métallé et un complexe de Ni^0. Ces travaux indiquent que l'addition oxydante C-H du ligand sur un précurseur de Ni^0 ne pourrait pas mener thermodynamiquement à la formation d'un composé cyclométallé Ni-H.

Schéma 1.34. Préparation d'un nickellacycle tridenté par addition oxydante C-Br et son instabilité face aux alkyles et aux hydrures.
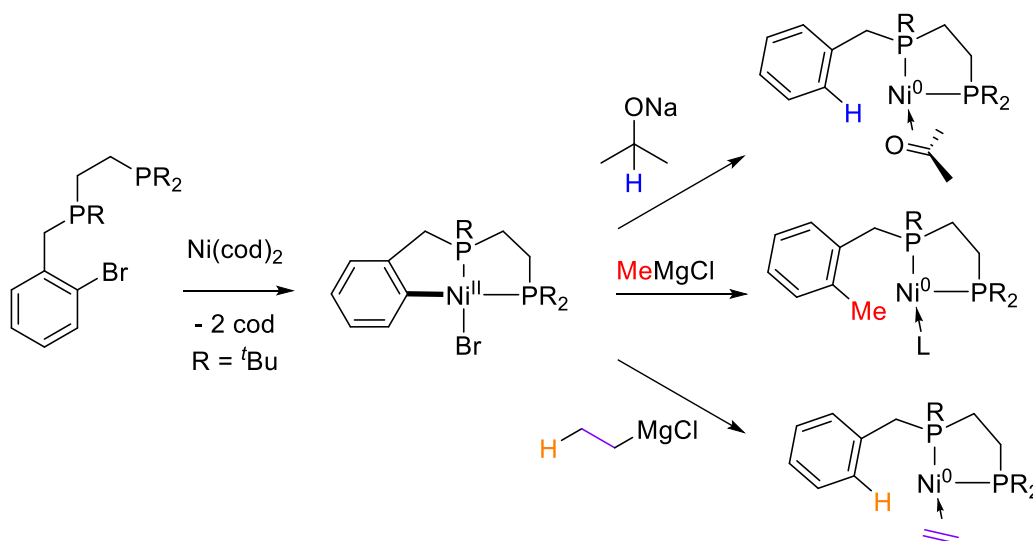
En effet, bien que la stratégie de cyclométallation par activation C-H soient courante avec les métaux des blocs 4d et 5d (car ils forment des liens M-H beaucoup plus robustes), aucun complexe cyclonickellé (hormis *pincers*) formé par activation C-H n'a été isolé. Bien que proposés comme intermédiaires dans de nombreux procédés, la formation du lien C-Ni par des précurseurs bas-valents est accompagnée de l'insertion d'un composé insaturé dans le lien nickel-hydrure.

Alors que l'élimination réductrice carbone-carbone est généralement favorable lorsque les deux ligands sont en position *cis* sur un centre de Ni^{II}, plusieurs procédés génèrent des nickellacycles par la réaction inverse, soit l'addition oxydante C-C sur des précurseurs de Ni^0. Pour que la réaction soit favorable, les substrats sont généralement des composés cycliques tendus pour lesquels la force motrice de la réaction est le relâchement de la tension de cycle. Ainsi, le nickel a déjà démontré son efficacité catalytique dans des procédés de fonctionnalisation par bris de liens

C-C sur des cyclopropanes ou méthylènecyclopropanes (tension de cycle d'environ 29 et 39 kcal/mol, respectivement), mais les intermédiaires nickellacyclobutanes n'ont jamais été isolés.[79,80] En revanche, un exemple célèbre de composé cyclonickellé généré par addition oxydante C-C provient de la réaction des complexes de Ni^0 du biphénylène, qui possède une énergie de dissociation C-C entre les deux cycles aromatiques de seulement 65 kcal/mol (**Schéma 1.35**). Le produit d'addition oxydante a été isolé et caractérisé par J. J. Eisch en 1984, et les auteurs ont démontré que chauffer ce complexe seul menait à la dimérisation en tétraphénylène, tandis que l'ajout d'un alcyne, de CO, ou d'O_2 permettait leur insertion dans le lien C-Ni et de donner par élimination réductrice un phénanthrène, de la fluorènone ou le dibenzofurane.[81]

Schéma 1.35. Isolation d'un nickellacycle par addition oxydante C-C et réactivité du lien C-Ni
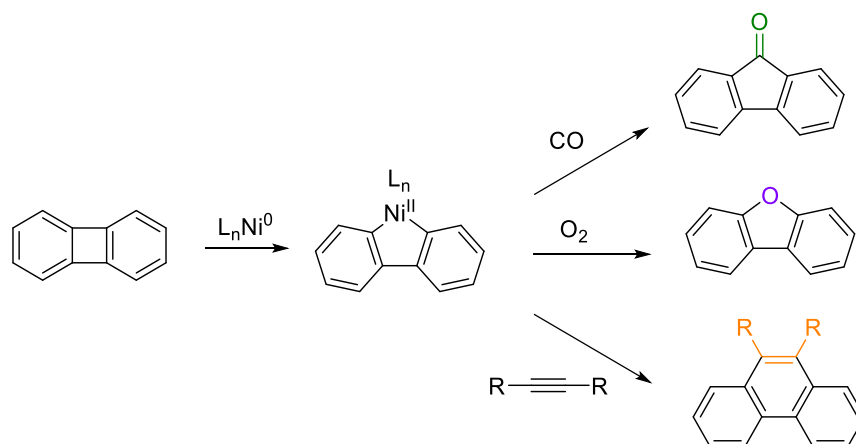
À la différence des réactions présentées ci-dessus, le dernier procédé permettant la formation d'espèces cyclométallées portant des liens C-Ni à partir de précurseurs de Ni^0 n'entraine pas le bris de liaisons σ, mais le bris de liaisons π au profit de la formation de liens σ. Si cela est très favorable enthalpiquement, ce type de réaction – la cyclisation oxydante – implique un réarrangement péricyclique entre un centre de basse valence M^n et au moins deux unités insaturées donnant lieu à un seul métallacycle dont le centre est oxydé M^{n+2}, ce qui la rend peu favorable d'un point de vue entropique (**Schéma 1.36**).

Schéma 1.36. Orbitales impliquées dans les réactions de cyclisation oxydantes.

Oribtales d* vide
et π remplies

+

Oribtales π∗ vides
et d remplies
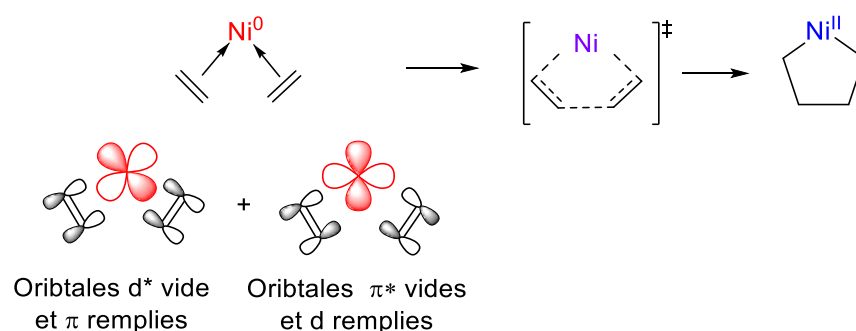
Bien que ces mécanismes aient été décrits il y a longtemps, les composés du nickel émanant de cyclisations oxydantes ont souvent été observés indirectement comme des intermédiaires dans des processus catalytiques mais ont rarement été isolés. Cependant, dans les années 1990, M. A. Bennett a isolé et caractérisé des produits cyclonickellés mettant en jeu la cyclisation oxydante d'arynes avec des composés insaturés (**Schéma 1.37**).[82] La réaction en présence de CO_2 a donné lieu au benzoate *ortho*-métallé correspondant, la réaction avec le tétrafluoroéthylène (TFE) au métallacycle bidenté correspondant. Quant à la réaction avec les acétylènes, elle ne permettait pas l'isolation du composé cyclométallé mais menait à l'insertion d'un second alcyne dans le nickellacycle pour former le polyarène correspondant par annulation.

Schéma 1.37. Réactions de cyclisation oxydante des arynes avec des composés insaturés.
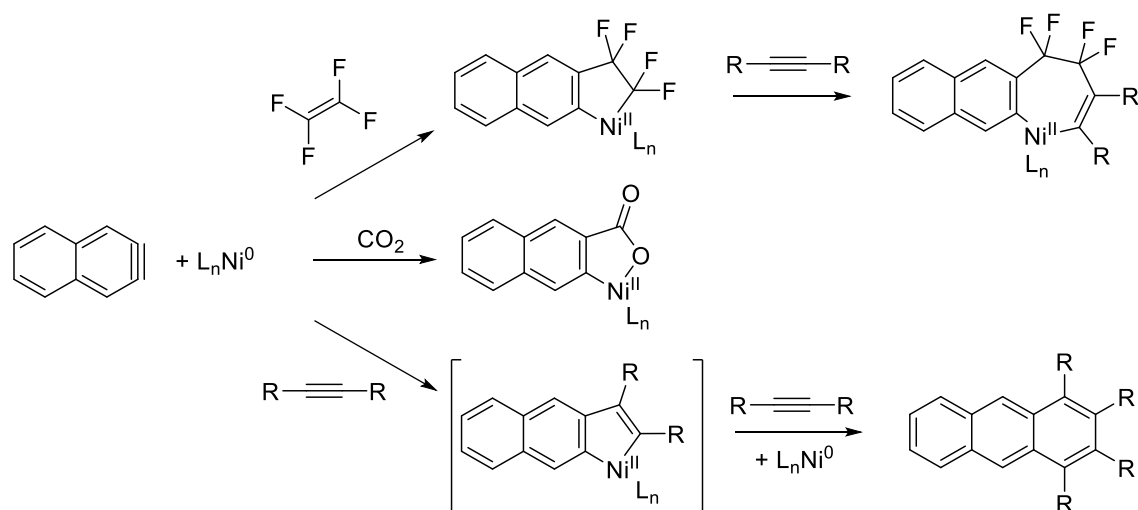
L'intermédiaire cyclométallé provenant de la réaction du benzyne avec le TFE étant isolable,[83] les auteurs ont également montré que sa réaction avec le dioxygène et le diiode menait respectivement à l'oxydation du lien C_{sp^2}-Ni ou à son iodination, respectivement (**Schéma 1.38**). Ils ont démontré également que le lien C_{sp^2}-Ni pouvait insérer une molécule de CO suivie d'une élimination réductrice ou d'une oxydation, ou insérer des alcynes pour donner des naphtalènes 1,2-difluorés.

Schéma 1.38. Réactivité d'un nickellacycle préparé par cyclisation oxydante.
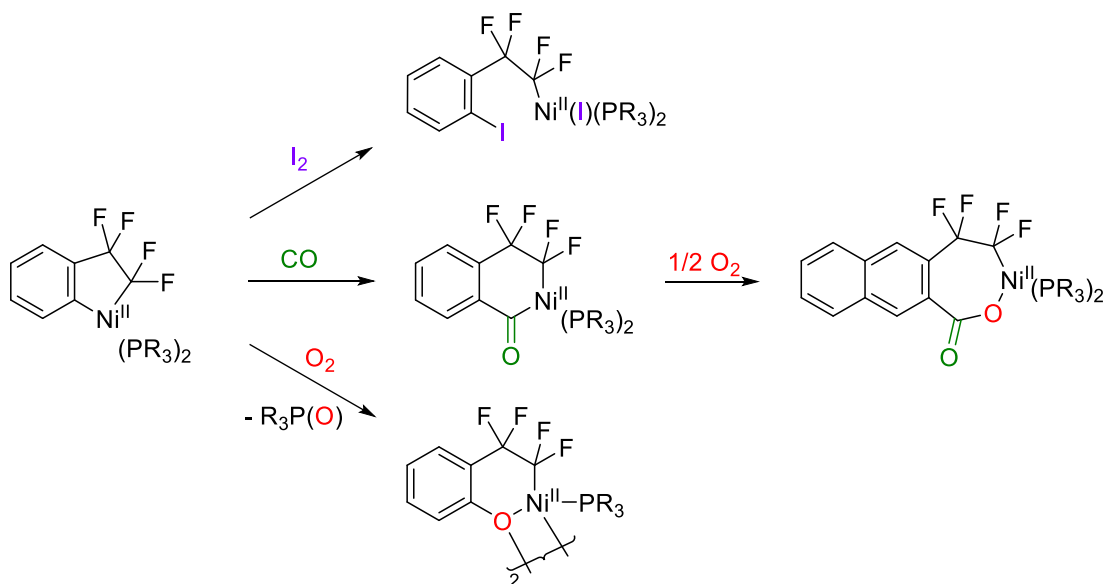
Dans les années 2010, S. Ogoshi a également utilisé ces stratégies de réactions péricycliques pour la synthèse organique catalysée par le nickel. Il a également fait un travail remarquable concernant l'isolation et la caractérisation structurale des produits de cyclisation oxydante, et même dans de nombreux cas des espèces initiales de Ni^0 coordonnant les substrats avant l'étape de cyclisation (**Schéma 1.39**). Il fut le premier, en 2004, à isoler directement le produit de nickellation issu de la cyclisation oxydante entre un aldéhyde et un alcène.[84] La réaction était favorisée par le fait que les deux groupes fonctionnels font partie de la même entité moléculaire (substrat ènal), ce qui fait de cette cyclisation une réaction bimoléculaire et réduit donc son coût entropique. Ces travaux montraient que le lien C_{sp^3}-Ni généré peut subir à Tp l'insertion de CO suivie de l'élimination réductrice C-O afin de produite une lactone.
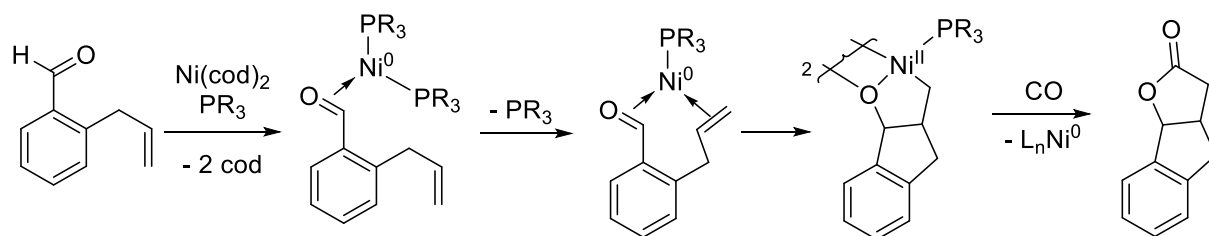
Il a plus tard montré que le même type d'intermédiaire cyclométallé (oxanickellacycle) peut mener à la formation de cétones cycliques par transfert d'hydrure intramoléculaire,[85] ou aux alcools silylés cycliques correspondants lorsque la réaction est conduite en présence de triéthylsilane (**Schéma 1.40**).[86] Le groupe de recherche a également étendu la méthode de cyclisation des alcènes avec des partenaires de couplages différents tels que le TFE en présence d'alcynes, d'alcènes ou de benzaldéhydes pour donner obtenir respectivement des diènes, des alcènes ou des cétones linéaires contenant le fragment terminal $-CF_2-CF_2H$.[87,88,89] Ils ont également isolé les produits de cyclisation des aldimines basées sur des amines électropauvres avec des alcynes et ont montré que la réaction de ces nickellacycles avec un excès d'alcyne ou de CO menait à la formation de pyridines ou de pyrrolones, respectivement (**Schéma 1.41**).[90]

Schéma 1.40. Réactivité des oxanickellacyclopentanes.
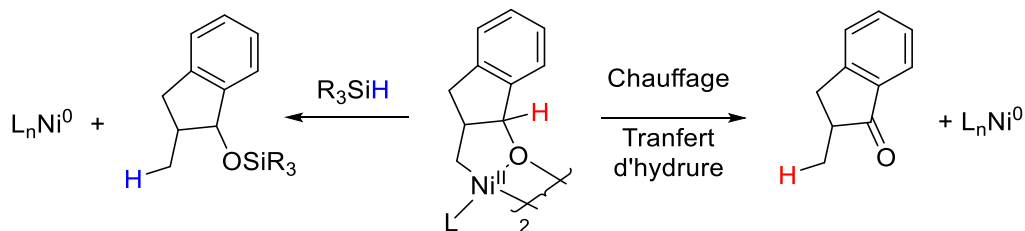
Schéma 1.41. Cyclisation oxydante des aldimine et des alcynes et réactivité par insertion.
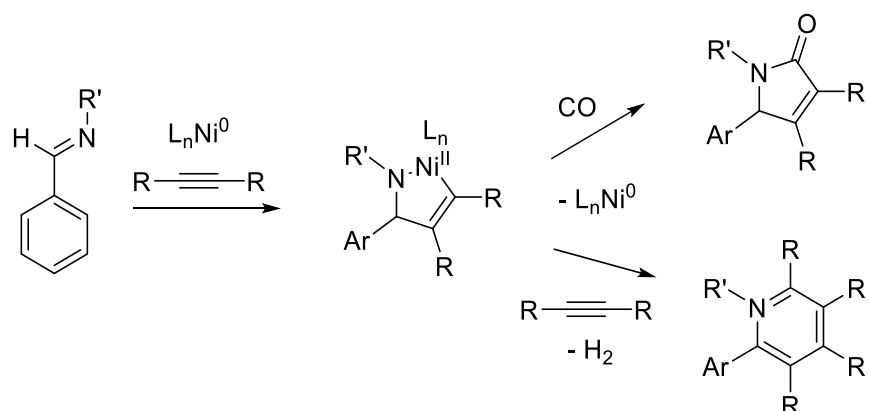
1.4.2 Espèces générées à partir de Ni^{II} et Ni^{IV}

La seconde famille de stratégies menant à des métallacycles portant des liens carbone-nickel est basée sur l'utilisation d'espèces déjà oxydées de nickel. Ainsi, tout comme pour la formation de composés non cycliques, on trouve la transmétallation à partir d'un composé déjà lié au métal. Cette méthode a été, par exemple, reportée par K. Ruhland en 1998, afin d'obtenir un composés de Ni^{II} doublement cyclométallé (**Schéma 1.42**).[91] Le ligand aryle-phosphinite portant un brome en position *ortho* réagit facilement avec le Ni(cod)$_2$ par addition oxydante C-Br afin de mener à la première cyclométallation. Le second ligand ne réalise la nickellation qu'après avoir été lithié en position *ortho* par échange lithium/halogène, menant au composé plan carré de conformation *cis*. Les auteurs montrent que la forme *trans* est thermodynamiquement plus favorable mais que l'un ou l'autre des isomères réagissent avec CO pour donner le produit d'insertion dans le lien C-Ni, puis l'élimination réductrice C-C afin de produire un ligand bis-phosphinite lié au Ni^0. Cette stratégie par transmétallation intramoléculaire est relativement rare avec le nickel, car elle requiert l'utilisation de réactifs puissants tels que les organolithiens ou les réactifs de Grignard qui pourraient réduire le centre Ni^{II} avant même qu'il y ait formation du composé cyclométallé.

34

Schéma 1.42. Cyclonickellation d'une phosphinite par transmétallation intramoléculaire et sa réactivité.
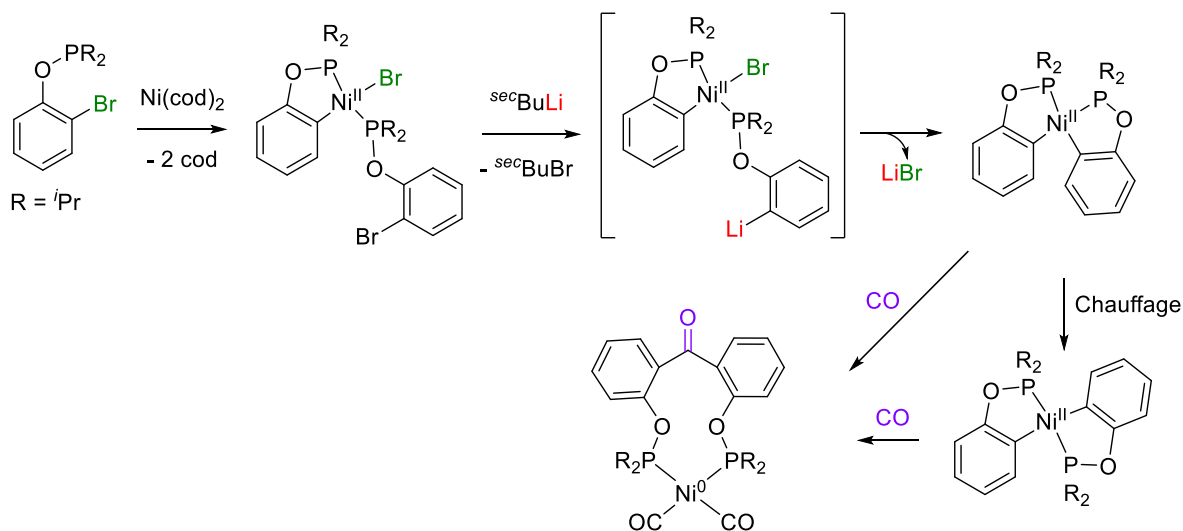
Historiquement, la synthèse des composés cyclonickellés par mécanisme CMD employait une base formelle qui est liée au métal, le plus souvent un ligand de type carbanion. Par exemple, le premier complexe cyclonickellé a été reporté en 1963 par J. P. Kleiman et M. Dubeck, formé par réaction de l'azobenzène sur le nickellocène à 135°C (**Schéma 1.43**).[92] Bien que la caractérisation par XRD n'a été publiée qu'en 1989, confirmant la liaison au nickel d'un azote et du carbone *ortho* du fragment aryle pour former un nickellacycle à 5 chainons, les auteurs de cette découverte l'ont cependant caractérisé par des moyens chimiques et par spectroscopies IR et RMN, révélant le caractère diamagnétique de ce nouveau composé.

Schéma 1.43. Premier composé cyclonickellé formé par nickellation directe sur un Ni^{II}.
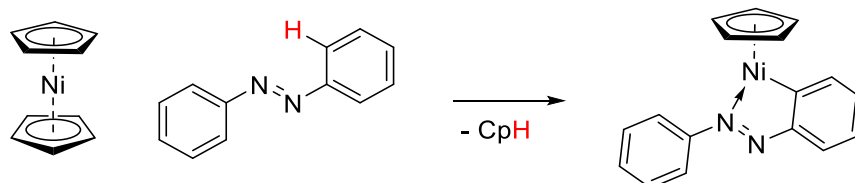
Plus tard, après avoir travaillé sur de nombreux complexes dialkyles de Ni^{II}, E. Carmona remarque en 1989 que le composés portant deux ligands 2-phényl-*iso*butyl donne un produit de cyclonickellation (**Schéma 1.44**).[93] Cette réaction est d'autant plus efficace que le nickel est supporté par un ligand bidenté qui force les alkyles à se tenir en position *cis*, menant à la formation d'un nickellacyclopentane portant un lien C_{sp^3}-Ni et un lien C_{sp^2}-Ni, ainsi que du *tert*-butylbenzène comme sous-produit issu de la protonation d'un ligand alkyle. Ils remarquent que le composé cyclométallé obtenu est stable à l'ajout d'excès de Grignard, qu'un lien C-Ni peut subir l'insertion de ligands CO ou alcyne suivie d'une élimination réductrice pour donner respectivement une cétone cyclique et un dihydronaphtalène. Bien que les produits d'insertion de ces deux réactions n'aient pas été isolés, les réactions avec le CO_2 et le formaldéhyde, eux, permettent l'isolation des composés d'insertion dans le lien C_{sp^2}-Ni. Quelques années plus tard, G. Hillhouse isole un nickellacycle homologue entièrement aliphatique et dévoile sa réaction avec un azoture donnant l'insertion formelle d'un nitrène (**Schéma 1.45**).[94,95] L'oxydation subséquente du centre métallique par un électron permet l'élimination réductrice et mène à la pyrrolidine correspondante. Il démontre aussi que le gaz N_2O permet l'insertion d'un atome d'oxygène dans le lien C-Ni, et que l'oxydation mène à la formation du THF par élimination réductrice, tandis que la réaction du complexe cyclonickellé avec CO mène à l'obtention de la δ-valérolactone.

Schéma 1.44. Préparation d'un nickellacyclopentane par métallation directe et réactivité.
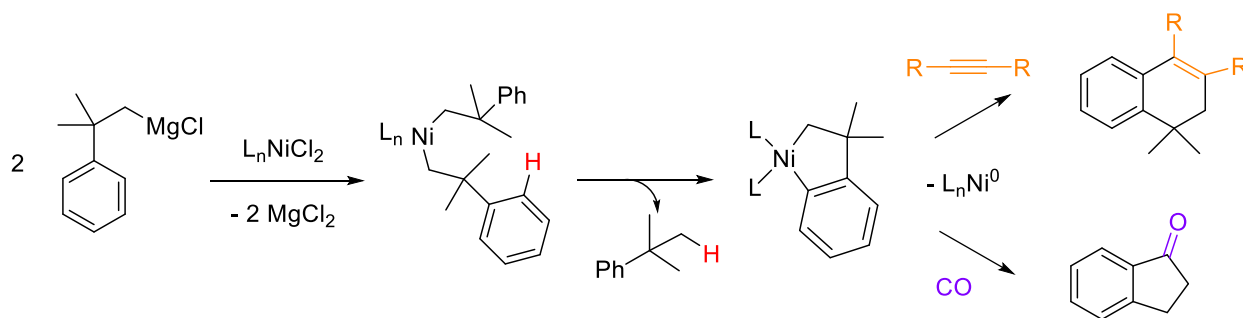
Schéma 1.45. Réactivité d'un nickellacyclopentane face à des oxydants.
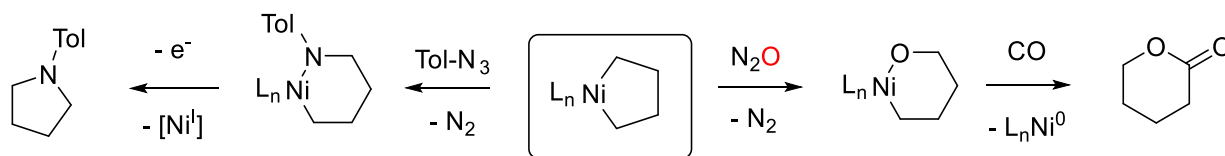
Dans les années 1990, H.-F. Klein a démontré que le lien C-H de la fonction benzaldehyde pouvait être métallé sur un centre de Ni^{II}, dans des substrats possédant un groupe directeur, menant ainsi à des nickellacycles portant une liaison nickel-acyle.[96] Ainsi, il a montré que les dérivés du salicylaldéhyde une fois la fonction phénol déprotonée et que les 2-diphénylphosphino-benzaldéhydes subissaient la cyclométallation via des composés portant un lien nickel-méthyle, et que l'émanation de méthane rendait la réaction irréversible (**Schéma 1.46**). Bien que les métallacycles aient été isolés et caractérisés complétement, la réactivité des liens nickel-acyle dans ces composés n'a pas été étudiée, mais ces travaux démontrent que le nickel permet une déprotonation formelle en position *ipso* de la fonction aldéhyde, dont le proton est extrêmement faiblement acide.

Schéma 1.46. Cyclonickellation menant lieu à la formation d'un lien Nickel-Acyle.
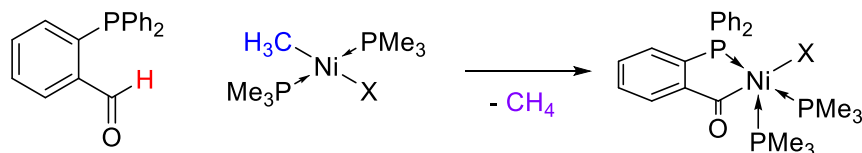
On a vu que des ligands de type pincer subissent relativement facilement la nickellation C-H à partir de simples sels de nickel, sans la nécessité d'utiliser une base forte ou des ligands alkyles très basiques. Lorsqu'on ôte un bras du ligand pour mener à la formation des espèces cyclométallées correspondantes, la disparition de l'effet chélate des deux bras latéraux diminue significativement la facilité de former le lien C-Ni. En effet, D. Zargarian publie en 2014 la cyclométallation des aryle-phosphinites, homologues au ligand POC$_{sp^2}$OP qui donne le complexe *pincer* à température de la pièce en quelques minutes. Le ligand ArOP(i-Pr)$_2$, lorsque mélangé avec un demi équivalent du précurseur de Ni^{II} (i-PrCN)NiBr$_2$ donne le complexe cyclonickellé (obtenu plus tôt par K. Ruhland à partir de Ni^0) mais nécessite un chauffage à 100 °C pendant 48 h afin d'obtenir une conversion complète à l'adduit de phosphinite (**Schéma 1.47**).[97] Les auteurs montrent également que lorsqu'une quantité super-stœchiométrique de sel de nickel est utilisé, la réaction se poursuit jusqu'à nickellation complète de toutes les phosphinites pour donner un composé dimérique. Lorsque ce dimère est chauffé avec du bromure de benzyle, le lien C-Ni se brise pour former un lien C-Bn, résultant ainsi au produit d'*ortho*-fonctionnalisation du phénol.

Schéma 1.47. Cyclonickellation d'une phosphinite par métallation directe, et fonctionnalisation du lien C-Ni.
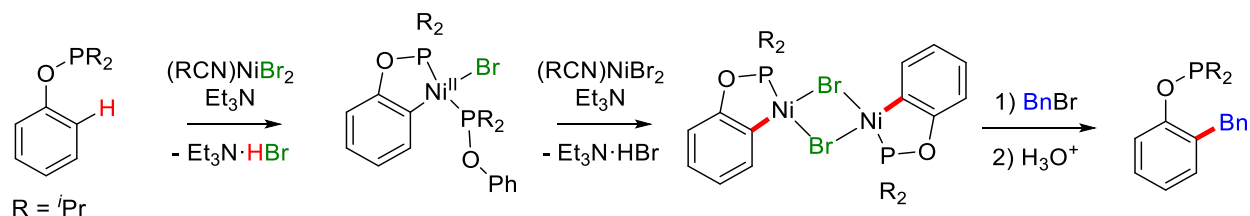
Cette stratégie a été utilisée plus tôt avec le palladium qui réalise aisément l'*ortho*-cyclométallation des benzylamines et benzylimines, pour donner des dimères pontés par des halogénures, qui peuvent ensuite donner le produit de fonctionnalisation par couplage avec des halogénures d'aryle (couplage de type Kumada/Suzuki/Stille) ou des alcènes activés (couplage de type Heck). Ces espèces cyclométallées des amines/imines benzyliques représentent un des bras des complexes pinceurs de type POCN, qui réalisent relativement aisément la nickellation directe C-H. Cependant aucune synthèse de ces nickellacycles par métallation directe C-H n'a été reportée avec ces substrats monodentés. Une étude computationnelle par DFT de J.-P. Djukic[98] datant de 2019 montre que relativement au palladium, la réaction avec le nickel a une barrière d'activation presque deux fois plus haute, et que la réaction n'est d'ailleurs pas thermodynamiquement favorable, avec une énergie de Gibbs évaluée à +15 kcal/mol quand les bases AcO⁻ et AcNH⁻ sont employées. En revanche, en 2007, P. T. Wolczanski a montré que les phényl-pyridines étaient capables de mener à la nickellation si chauffées à 180 °C en présence de sels de Ni(OTf)$_2$, et que la nickellation d'un second ligand étaient encore plus aisée et pouvait se faire à température de la pièce (**Schéma 1.48**).[99] Les auteurs ont également montré que le lien C-Ni généré pouvait réagir avec les alcynes à 100 °C, et ont isolé le produit d'insertion en résultant.

Schéma 1.48. Cyclonickelation des phénylpyridines et insertion d'alcynes.
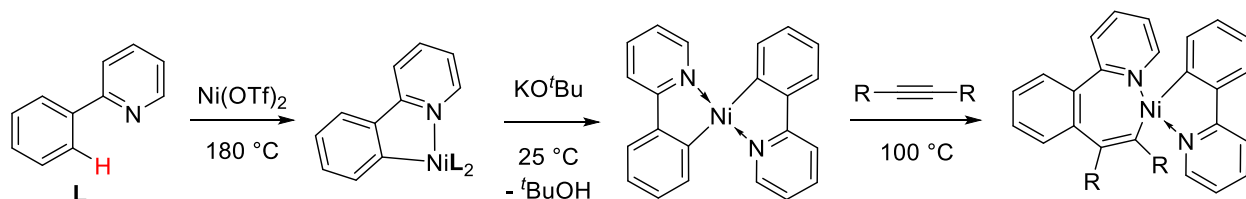
Représentant un défi plus grand que la métallation des liens C_{sp^2}-H, l'isolation des composés cyclonickellés issus du bris de liens C_{sp^3}-H est également plus rare en particulier avec des groupes directeurs monodentés. Ainsi, la métallation directe des liens C_{sp^3}-H non activés pour former des espèces cyclonickellées est souvent reportée avec des groupes directeurs bidentés, menant à la formation de composés tridentés, tel que l'exemple reporté en 2013 par G. Du (**Schéma 1.49**).[100] Dans cet exemple le groupe directeur bidenté est composé d'un squelette oxazoline-amidure qui permet l'activation du lien C-H d'un méthyle en position benzylique, capté par un ligand Ph du précurseur de Ni^{II}.

Schéma 1.49. Un groupe bidenté permet la formation d'un nickelacycle par métallation Csp^3-H.
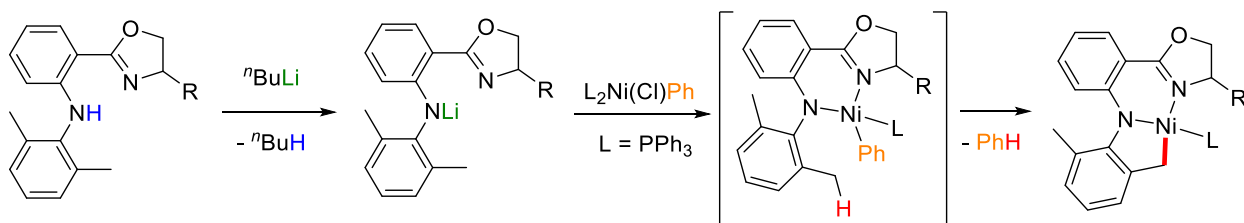
C'est également le cas des intermédiaires proposés dans les fonctionnalisations catalytiques avec les groupes directeurs 8-aminoquinoline (8AQ) proposés par N. Chatani. En 2018, L. L. Schaffer et J. A. Love ont étudié la nickellation des liens C_{sp^3}-H en utilisant comme modèles les urées tertiaires, portant d'un côté le fragment 8AQ comme groupe directeur et de l'autre côté un substituant méthyle ou benzyle qui constitue le substrat de la nickellation.[101] Les auteurs ont étudié le rôle du solvant, démontrant que la réaction est plus rapide dans un milieu polaire, ont étudié la cinétique de la réaction via des études de Hammett et de Eyring afin de démontrer que la métallation était de nature électrophile (CMD) et d'en extraire les paramètres d'activation, et ont dévoilé le rôle des additifs utilisés dans les processus catalytiques (**Schéma 1.50**). De plus, ils ont isolé les composés cyclonickellés et prouvé leur efficacité dans le couplage avec différents partenaires tels que les halogénures d'aryle ou d'alkyles, les iodoniums ou le CO, des partenaires de couplages utilisés en catalyse par N. Chatani.

L'année suivante, M. S. Sanford publiait l'isolation et l'étude des intermédiaires cyclométallés portant le groupe directeur 8AQ sur les amides aliphatiques et aromatiques correspondants, se rapprochant davantage des systèmes utilisés pour la fonctionnalisation

catalytique des liens C-H présentés par N. Chatani (**Schéma 1.51**).[102] Bien que les espèces cyclonickellées ait été isolés par des voies différentes de la métallation directe C-H (bien qu'observée dans le cas du substrat aryle, mais en de faibles rendements), l'étude a permis de démontrer que les nickellacycles étaient enclins à générer les espèces oxydées Ni^{III} dans des conditions douces. Les auteurs ont pu ainsi isoler ou détecter ces espèces de haute valence, et prouver leur implication dans les processus catalytiques menant à l'iodination par I_2 chez les substrats aromatiques et la formation de β-lactames chez les substrats aliphatiques.

Schéma 1.50. Étude des urées comme substrats modèles pour la nickellation et la fonctionnalisation des liens C_{sp^3}-H.
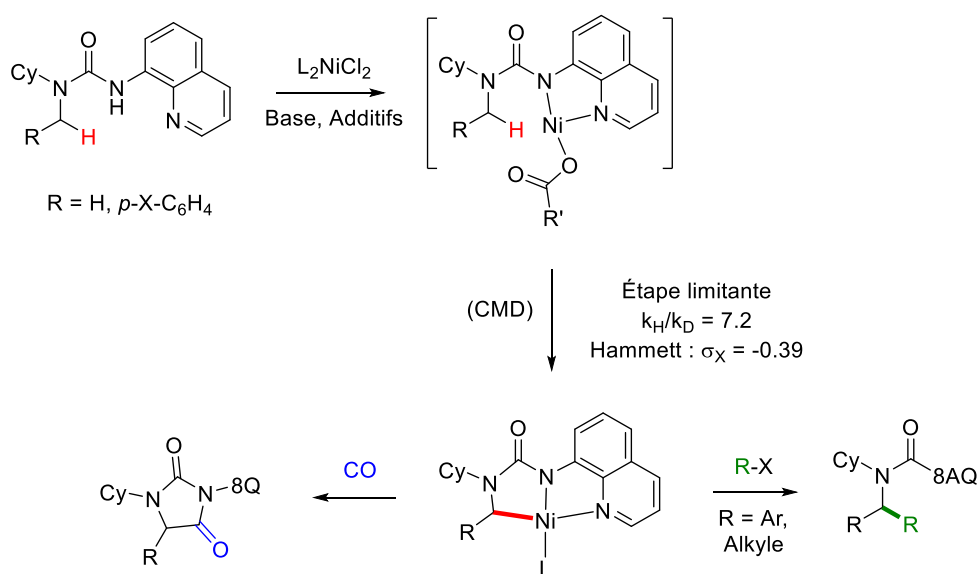
Schéma 1.51. Préparation des intermédiaires cyclonickellés supposés dans les processus catalytiques aidés par le DG 8-AQ, et preuve de leur réactivité.
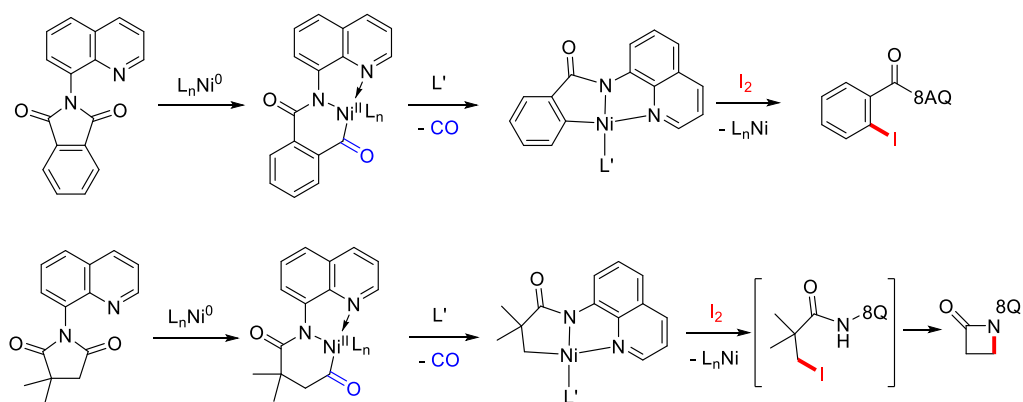
Enfin, le groupe de M. S. Sanford a également démontré récemment une stratégie unique menant à l'isolation de composés cyclonickellés par métallation directe. Cette fois, le groupe directeur était constitué d'un fragment bis-(2-pyridyl)méthane sur lequel est greffé un substrat aromatique (phényle)[103] ou un substrat aliphatique (tert-butyle).[104] Dans les deux cas, la liaison du DG sur le centre métallique Ni^{II} ne mène pas à la formation du lien C-Ni, mais c'est seulement après l'oxydation à deux électron pour donner un centre Ni^{IV} que la nickellation se produit, à température de la pièce (**Schéma 1.52**). Les études computationnelles et expérimentales mènent à la conclusion que ce type de métallation est de nature électrophile. Dans le cas du composé portant un le substrat aromatique, les auteurs n'ont pas réussi à briser le lien C$_{sp^2}$-Ni par un nucléophile, mais la réaction s'est avérée efficace avec le substrat aliphatique, menant à la réduction du Ni^{IV} en Ni^{II}. Danc ce dernier cas, la réaction a pu être élevée au niveau catalytique, menant à la fonctionnalisation directe des liens C$_{sp^3}$-H dans des conditions très douces, et avec des intermédiaires réactionnels bien définis.

Schéma 1.52. Préparation de métallacycles par nickellation C-H directe induite par l'oxydation.
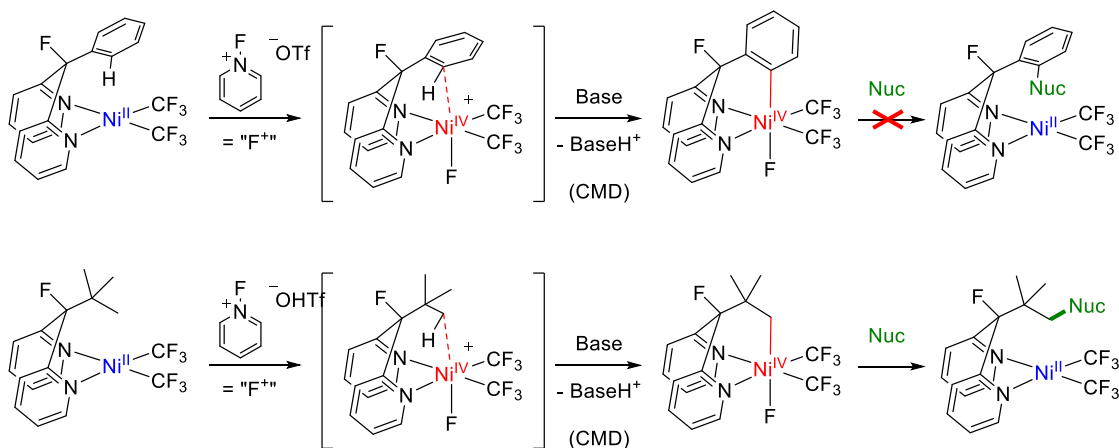
1.5 Potentiel des phosphinites comme groupe directeur pour la fonctionnalisation

Les ligands phosphorés ont généralement une bonne affinité pour les métaux de transition, mais ont surtout été utilisés comme ligands dans les précurseurs de complexes des *late transition metals*. Les phosphines ont largement été employées comme ligands de support en catalyse organométallique, et sont dans certains cas capables de donner des intermédiaires cyclométallés. Cependant, leur intérêt comme groupe directeur serait limité à la synthèse d'autres phosphines fonctionnalisées, puisque le phosphore est difficilement détachable des substituants alkyles/aryles par des méthodes douces. À l'inverse, les ligands phosphorés portant des liens phosphore-oxygène sont d'un intérêt supérieur puisque le lien P-O peut être clivé par hydrolyse (ou alcoolyse) afin de relâcher le substituant alcool (**Schéma 1.53**). Ainsi, l'étude de ces ligands comme groupes directeurs dans la fonctionnalisation des substrats organiques (en particulier des alcool) est davantage justifiée.

Schéma 1.53. Réactions d'hydrolyse et d'alcoolyse des phosphinites et des phosphites.
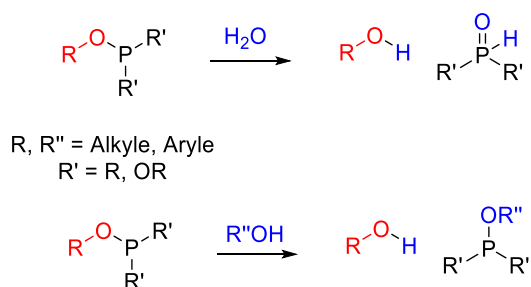
Historiquement, les premiers ligands phosphoré portant des liens P-O qui ont démontré une aptitude à la cyclométallation sont les phosphites $P(OR)_3$. À la fin des années 1960, G. W. Parshall isole des complexes possédant une phosphite cyclométallée de ruthénium (**Schéma 1.54**) et de rhodium, et lui permet de rationnaliser certaines réactions observées avec le cobalt (**Schéma 1.55**).[105] En effet, lorsque la triphénylphosphite est chauffée avec des complexes hydrures de Co^I ou de Ru^{II} en présence de deutérium moléculaire, les positions *ortho* des fragments phényles se trouvent à avoir incorporé le deutérium, impliquant une *ortho*-métallation des ligands phosphites, suivi d'échanges H/D. Le complexe de ruthénium permet même la deutération catalytique des positions *ortho* des phénols, par substitution des fragments $C_6D_2H_3O^-$ par les fragments non réagis $C_6H_5O^-$.

Schéma 1.54. Isolation de phosphites cycloruthéniées et leur implication dans l'*ortho*-deutération des phénols.

Schéma 1.55. Mécanisme proposé pour l'*ortho*-deutération des phopshites promues par le cobalt.

Plus tard, en 1986, L. N. Lewis montrera que quand les complexes de ruthénium(II) possédant un ou deux ligands triphénylphosphite cyclométallées sont chauffées en présence d'éthylène ou de propylène, les substituants Ph des ligands incorporent des substituants Et et *i*-Pr, respectivement, avec une sélectivité pour la position *ortho* (**Schéma 1.56**). Les auteurs proposent que l'insertion des alcènes dans le lien carbone-ruthénium mène à un métallacycle instable, qui joue le rôle de base dans la cylométallation d'un autre ligand phosphite. Les auteurs montrent également que ces mêmes complexes réagissent avec le styrène par insertion dans le lien carbone-ruthénium mais que les réactions d'insertion s'enchainent afin donner lieu à un polymère.

Schéma 1.56. Mécanisme proposé pour l'*ortho*-alkylation des phosphinites.
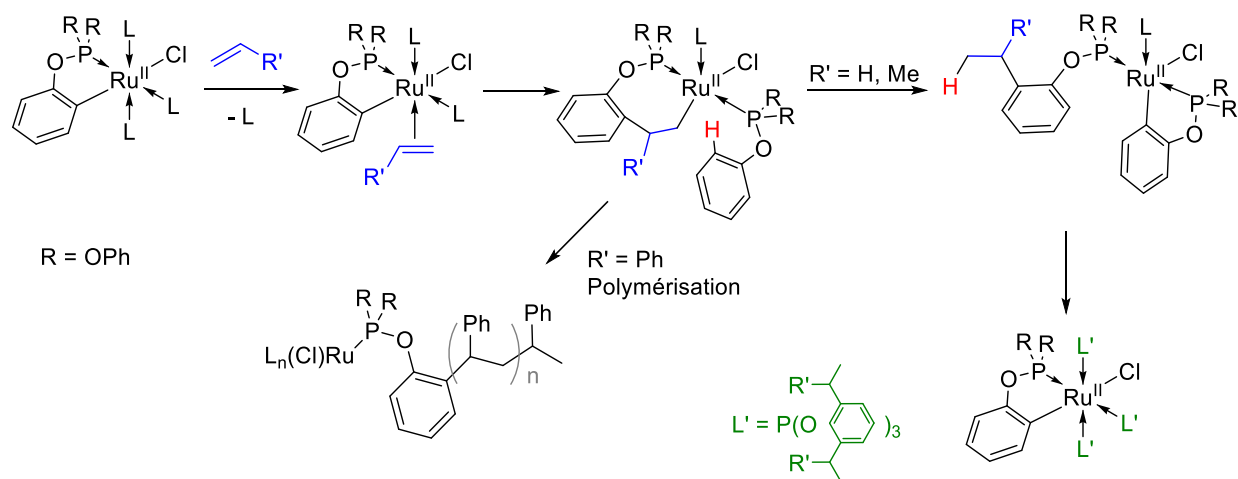
Plus tard, de nombreux complexes contenant des phosphites cyclométallées ont été isolés et caractérisés, mais rarement utilisés pour des processus de fonctionnalisation stœchiométrique ou catalytique du lien carbone-métal. Un exemple est le dimère de palladium portant une phosphite cyclométallée, pour lequel la présence d'un lien C-Pd favorise l'activation du catalyseur pour les couplages croisés. Cependant, il a été démontré plus tard que son homologue portant, cette fois ci, une phosphinite (ROPR'$_2$, R' = Aryle) cyclopalladée augmentait l'efficacité de la catalyse dans le couplage de Suzuki (**Schéma 1.57**).[106] Les aryle-phosphinites, ayant toujours la capacité de cyclométaller le fragment OAr, sont en effet de meilleurs donneurs en raison des deux substituants carbonés (aryles ou alkyles) du phosphore, bien que dans ces réactions, le ligand cyclométallé n'est pas le substrat de la fonctionnalisation.

Schéma 1.57. Mécanisme d'activation des catalyseurs de palladium basés sur des phosphi(ni)tes cyclométallées.
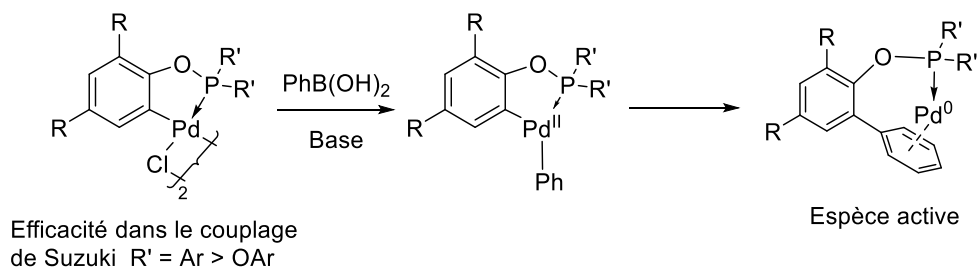
Cependant, la capacité des phosphinites à échanger les fragments alcoolate sur le phosphore a permis diverses réaction catalytiques pour la fonctionnalisation des alcools, la métallation et la régiosélectivité de celle-ci étant gouvernée par la formation de phosphinites cyclométallées. Dans ce domaine, c'est le rhodium qui a surpassé tous les autres métaux de transition, à commencer par les travaux de R. B. Bedford qui a révélé en 2003 une réaction catalytique d'*ortho*-arylation des phénols.[107] Dans cette publication, le catalyseur de Wilkinson est additionné d'un ligand phosphinite comme co-catalyseur et permet l'arylation sélective des phénols en position *ortho*, par des bromures d'aryle. Le mécanisme proposé (**Schéma 1.58**) consiste en l'addition oxydante de l'halogénure d'aryle sur le précatalyseur de Rh^I, suivi de l'*ortho*-métallation du ligand phosphinite sur le centre Rh^{III} puis de l'élimination réductrice menant au ligand phosphinite fonctionnalisé par couplage C-C. Ce dernier peut ensuite s'échanger avec un autre phénol par trans-estérification sur le phosphore et libérer le phénol fonctionnalisé.

Schéma 1.58. Mécanisme proposé pour l'*ortho*-arylation des phénols de R. B. Bedford.
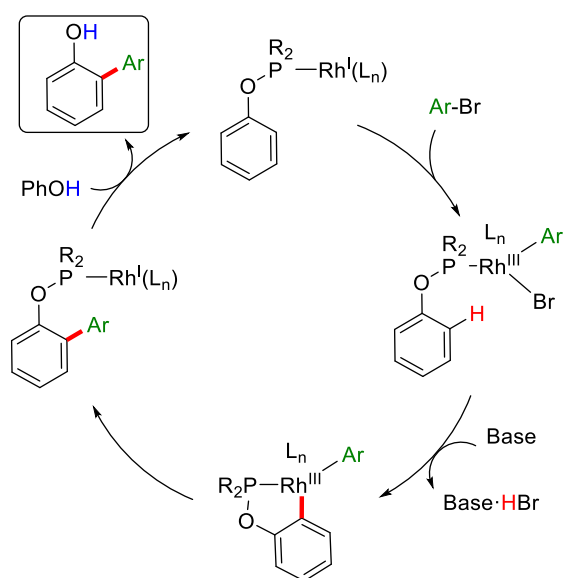
Cette stratégie est très avantageuse car non seulement le métal, mais aussi le groupe directeur est utilisé en quantité catalytique puisqu'il se greffe et se détache du substrat de manière réversible dans le milieu réactionnel. En effet, les groupes directeurs qui se greffent au substrat tels que les 8AQ exploitées par N. Chatani ou les pyrazines exploitées par L. Ackermann ne sont pas utilisés en quantités catalytiques car ils ne peuvent s'échanger dans le milieu réactionnel. Deux

étapes supplémentaires pour la fonctionnalisation sont donc à compter : le greffage du DG au substrat avant le processus catalytique et la déprotection du substrat, qui nécessite d'ailleurs des conditions rudes qui ne conviennent pas à de nombreux groupes fonctionnels (**Schéma 1.59**).

Schéma 1.59. Réactions de greffage du DG et de déprotection du substrat requises pour divers processus catalysés par le nickel.
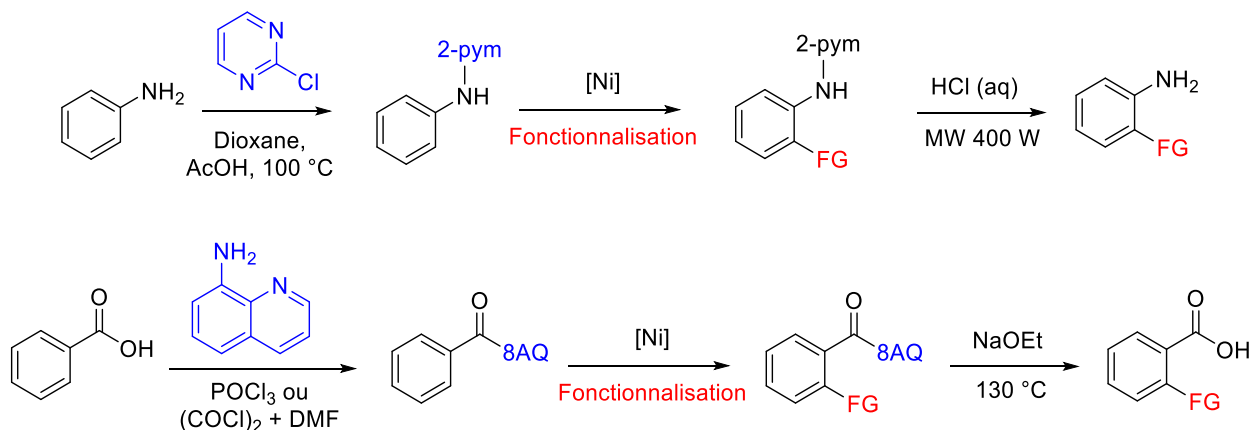
La stratégie de R. B. Bedford a ensuite été appliquée à différents processus catalytiques pour la transformation des alcools aromatiques tels que l'*ortho*-alkylation intermoléculaire par des alcènes (R. G. Bergmann et J. A. Ellman, 2005;[108] D. J. Cole-Hamilton, 2006)[109] ou encore en version intramoléculaire menant à des composés cycliques (R. G. Bergmann et J. A. Ellman) (**Schéma 1.60**). Elle s'est également étendue aux alcools aliphatiques, en particulier les alcools homoallyliques qui produisent en présence de CO et de H_2 des acétals cycliques, eux même convertis en lactones par oxydation (B. Breit, 2008, **Schéma 1.61**).[110]

Schéma 1.60. *ortho*-alkylations inter- et intra-moléculaires des phénols catalysées par le rhodium, en utilisant un phosphinite comme DG.
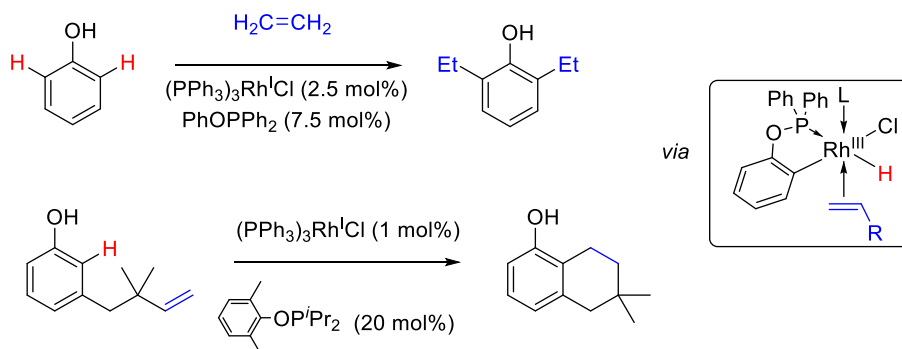
Schéma 1.61. Procédé d'hydroformylation des alcools homoallyliques couplée à la cyclisation menant à des cétals cycliques.

Ces transformations utilisant le rhodium démontrent la stabilité des phosphinites face à certains procédés, mais peuvent difficilement être transposées aux métaux 3d dans les mêmes conditions car les étapes de coordination/insertion sont beaucoup plus favorables avec les métaux lourds; En conséquence, aucun rapport ne dévoilait à ce jour de transformation catalysées par les métaux 3d assitée par un groupe directeur de type phosphinite. Cependant les travaux de D. Zargarian en 2014 sur les phosphinites cyclonickellées (hormis *pincers*) ont permis d'offrir une preuve de concept au point de vue stœchiométrique, en montrant que la cyclonickellation des phosphinites par métallation directe C-H était accessible, et que les liens C-Ni pouvaient générer des phénols dérivatisés. Cette étude constitue le point de départ de l'étude présentée dans cette thèse sur la cyclonickellation des phosphinites dérivées des alcools aromatiques.

1.6 Objectifs de la thèse

1.6.1 Étude de la régiosélectivité

Les travaux de D. Zargarian sur la nickelation des phosphinites dérivées des phosphinites de type ArO-P(*i*-Pr)$_2$ ont soulevé la question de la régiosélectivité, lorsque deux sites en position *ortho* sont disponibles mais non-équivalents. En effet, lorsque la phosphinite dérivée du 3-fluorophénol est soumise aux conditions de la métallation, deux produits sont observés dans un ratio de d'environ 6:1. L'analyse par RMN indique que produit mineur est celui issu de la nickelation du site qui se trouve en position *ortho* du substituant fluor, et le produit majeur est donc celui issu de la nickelation au site le plus éloigné du fluor, soit le site le moins encombré (**Schéma 1.62**).

Schéma 1.62. Ratio des isomères observés pour la nickellation du ligand 3-F-C$_6$H$_4$OP(i-Pr)$_2$.
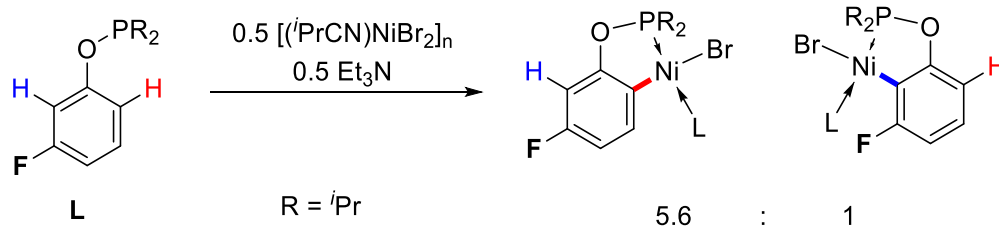
Ce résultat fait écho au ratio de régiosélectivité dans l'acetoxylation catalysée par le palladium des 2-phénylpyridines démontrée par M. S. Sanford. Cette sélectivité est inverse de ceux observées par T. Hiyama et S. A. Johnson dans la fonctionnalisation des fluoroarènes par le nickel par activation C-H. Dans les travaux menés par M. S. Sanford avec le palladium, bien que la cyclopalladation montre une sélectivité pour le site le moins encombré (**Schéma 1.63**), avec des ratios augmentant selon la taille sur substituant voisin du site de nickelation (6:1 pour *m*-F; 27:1 pour *m*-Me; 60:1 pour *m*-MeO et un seul isomère pour les substituants plus volumineux).[111] Dans les fonctionnalisation des benzamides présentées par N. Chatani, avec le groupe directeur 8-aminoquinoline, on observe également que la nickelation se produit au site *ortho* le moins encombré (**Schéma 1.64**). La régioselectivité est parfaite pour la quasi-majorité des substrats, bien que des isomères soient détectables dans les procédés d'annulation pour certains amides (*m*-CF$_3$O, 20:1 avec DG = 8AQ, et *m*-Me, 2:1 avec un DG monodenté[112]). Cependant, pour les procédés d'*ortho*-arylation, le ratio des isomères sur les benzamides *meta*-substitués n'est pas dévoilée.

Schéma 1.63. Ratio des isomères observés pour l'acétoxylation des phénylpyridines catalysée par le palladium.
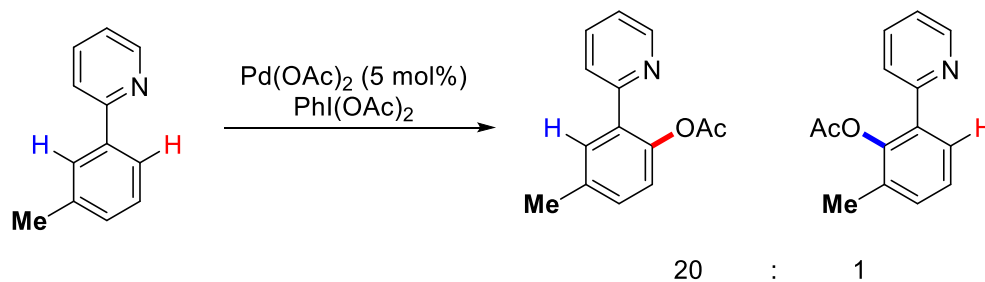
Schéma 1.64. Ratio des isomères observés pour l'annulation des benzamides catalysée par le nickel.
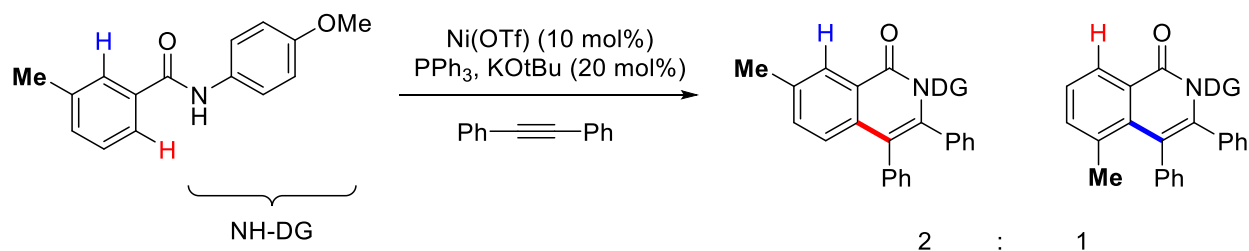
Enfin, dans les travaux de R. B. Bedford, les réactions d'*ortho*-arylation des alcools aromatique via des phosphinites cyclorhodées montre également un mélange de produits. Lorsque le substrat est un phénol *meta*-substitué, la fonctionnalisation prend place aux deux positions ortho sauf avec le substituant volumineux *tert*-butyle. De plus, lorsque le substrat possède un substituant en *ortho* qui bloque un des deux sites réactifs potentiels, non seulement le produit de simple *ortho*-arylation est observé mais la réaction se poursuit à la fonctionnalisation du nouveau substituant aryle qui vient juste d'être greffé (**Schéma 1.65**). Ceci indique que le rhodium est très réactif, car il accommode la métallation à des positions encombrées et à des métallacycles de différente taille, mais la contrepartie est un grand manque de sélectivité.

Schéma 1.65. Différents produits observés pour l'*ortho*-arylation des phénols catalysée par le rhodium.
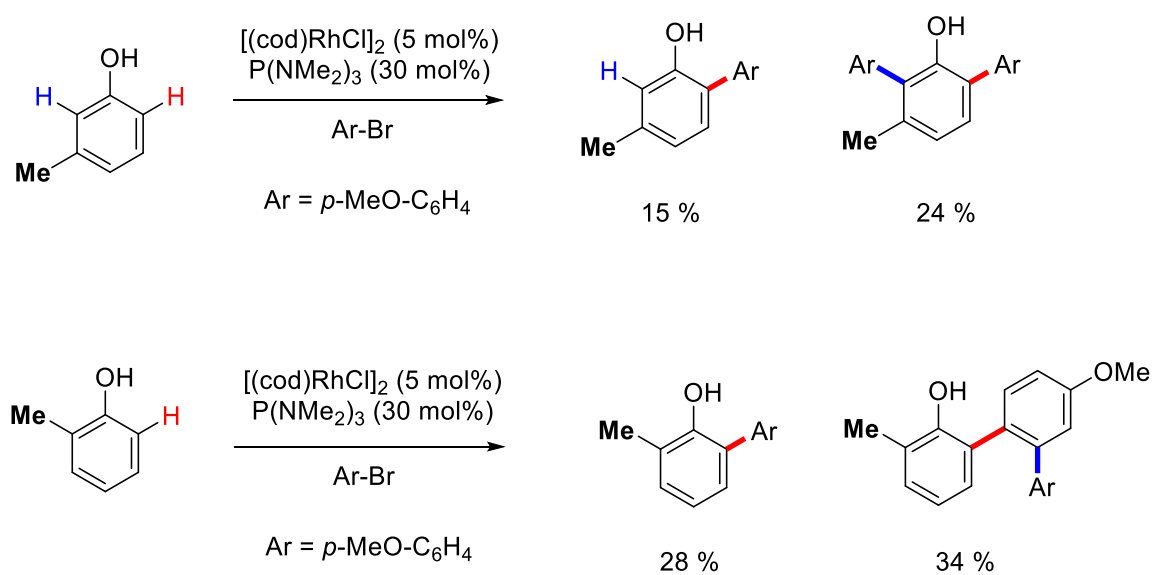
Ainsi, le **Chapitre 2**[113] de cette thèse a cherché à évaluer la préférence de la nickelation C-H pour les phosphinites dérivées des phénols *meta*-substitués. On y démontre que les substituants plus volumineux que le fluor mènent à une régiosélectivité parfaite, et seulement les espèces cyclonickelées au site le moins encombré sont observées. Afin de déterminer si cette régiosélectivité émane d'une simple préférence ou d'une impossibilité de réaliser la métallation sur la position encombrée, la réactivité des phosphinites *meta,meta*-disubstituées a été évaluée. Également, la nickelation des phosphinites *ortho*-monosubstituées ou *ortho,ortho*-disubstituées par des groupement alkyles ou aryles été évaluées afin de déterminer si des métallacycles à 6 chaisons (issus de la métallation au carbone C_{sp^3}-H) ou à 7 chainons (issus de la métallation du substituant Ph au carbone C_{sp^2}-H) pouvaient être isolés.

Le **Chapitre 4**[114] étend cette étude sur la régiosélectivité à la cyclonickelation des phosphinites dérivées des naphthols. Les 2-naphtols possèdent deux sites *ortho* potentiellement réactifs mais de propriétés électroniques et stériques différentes, alors que les 1-naphtols présentent un seul site *ortho* menant à la formation de métallacycles à 5 chainons, mais pourraient mener à la formation d'un cycle à 6 chainons dans l'éventualité d'une métallation au carbone C8. Les conditions présentées par R. B. Bedford montrent d'ailleurs que si le site *ortho* (carbone C2) est le site primaire de réactivité, l'arylation se produit également, en moindre mesure, également au carbone C8 (**Schéma 1.66**). À l'inverse, le palladium effectue l'arylation du 1-naphtol sans groupe directeur, tel que présenté par M. Miura, essentiellement à la position C8, soulignant l'importance de la taille du métallacycle intermédiaire dans la régiosélectivité.[115]

Schéma 1.66. Régiosélectivités observées pour l'arylation du 1-naphtol catalysée par le rhodium ou par le palladium.
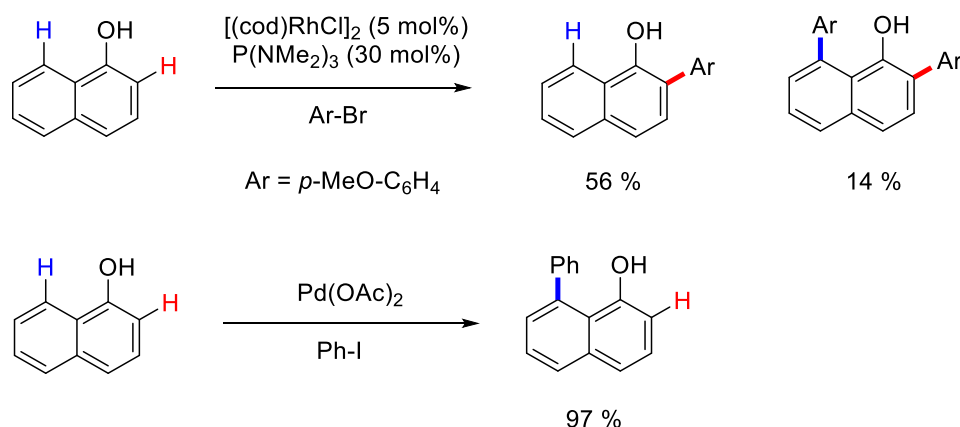
Dans ce chapitre, l'évaluation de l'accessibilité cinétique de la cyclonickelation aux substituants *ortho* portant un lien C$_{sp^3}$-H a été évaluée (**Schéma 1.67**), et cette étude a même permis de mener à l'isolation d'un complexe portant un lien C$_{sp^3}$-Ni par métallation directe, et ce dans des conditions très douces. Enfin, le **Chapitre 4** dévoile des produits de fonctionnalisation *in situ* des liens C-Ni par des fragments phosphorés, lorsque la réaction est conduite en absence de base et à haute température, révélant une trace de la nickelation au carbone C8 des 1-naphtols, bien que l'intermédiaire métallé n'est pas isolable.

Schéma 1.67. Le système phosphinite-nickel permet-il la cyclométallation des liens C$_{sp^3}$-H ?
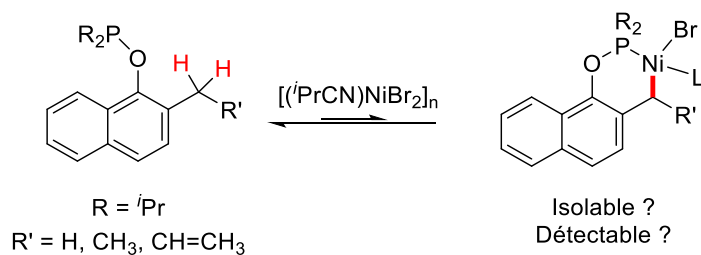
Dans les **Chapitres 2** et **4**, les produits issus des réactions de cyclonickelation ou de la fonctionnalisation sont isolés et caractérisés par RMN et par XRD. L'étude structurale permettra en particulier de rationaliser les régiosélectivités observées et de pointer vers une réaction guidée par les facteurs stériques et non par les facteurs électroniques.

1.6.2 Étude mécanistique

Le **Chapitre 2** révèle une procédure de synthèse des phosphinites cyclonickellées différente de la première procédure publiée par D. Zargarian, en particulier requérant moins d'excès de précurseur de nickel ou de base, et requérant des temps de réactions plus courts à une température plus basse. Ces avantages ont été apportés surtout par le transfert à un solvant plus polaire (*i.e.* acétonitrile) qui menait à un milieu réactionnel homogène contenant des espèces plus réactives, au contraire du toluène initialement utilisé (**Schéma 1.68**). Ainsi, le **Chapitre 3**[116] de cette thèse cherche à comprendre les intérêts de cette nouvelle méthode, en essayant d'isoler ou de détecter les espèces présentes en solution dans les différents solvants, et de comprendre leur impact sur la vitesse de la réaction.

Schéma 1.68. Différentes conditions menant à l'obtention des phosphinites cyclonickellées.
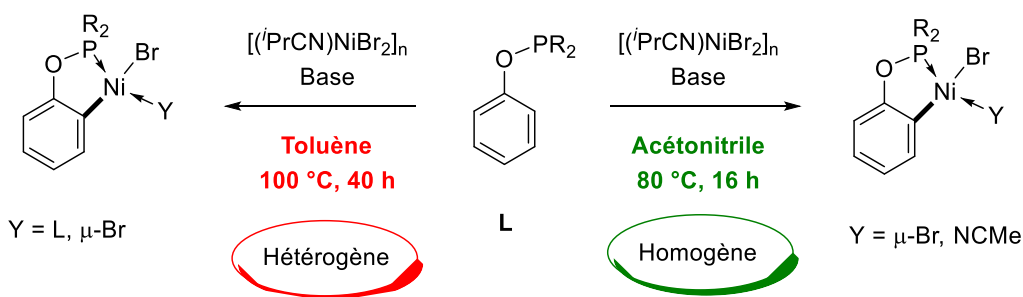
Les études menées sur les systèmes pincer correspondants ont permis de révéler le mécanisme de la nickelation pour les systèmes POCOP et PCP. Malheureusement, ces proligands subissent la métallation si rapidement qu'il est difficile d'évaluer la vitesse de réaction, limitant les études cinétiques à des réactions de compétitions (**Schéma 1.69**). Ainsi, le **Chapitre 3** cherche à déterminer le mécanisme et la nature de la cyclonickellation, pour lesquels la lenteur de la réaction permet un suivi cinétique. La première partie de ce chapitre met donc en lumière des données destinées à dévoiler l'ordre de la réaction, les paramètres d'activation, les effets cinétiques isotopiques et l'impact de la richesse électronique du substrat et sa magnitude.

Schéma 1.69. Exemples de réactions de compétitions donnant des indices sur la nickellation des ligands pincer PCP ou POCOP.
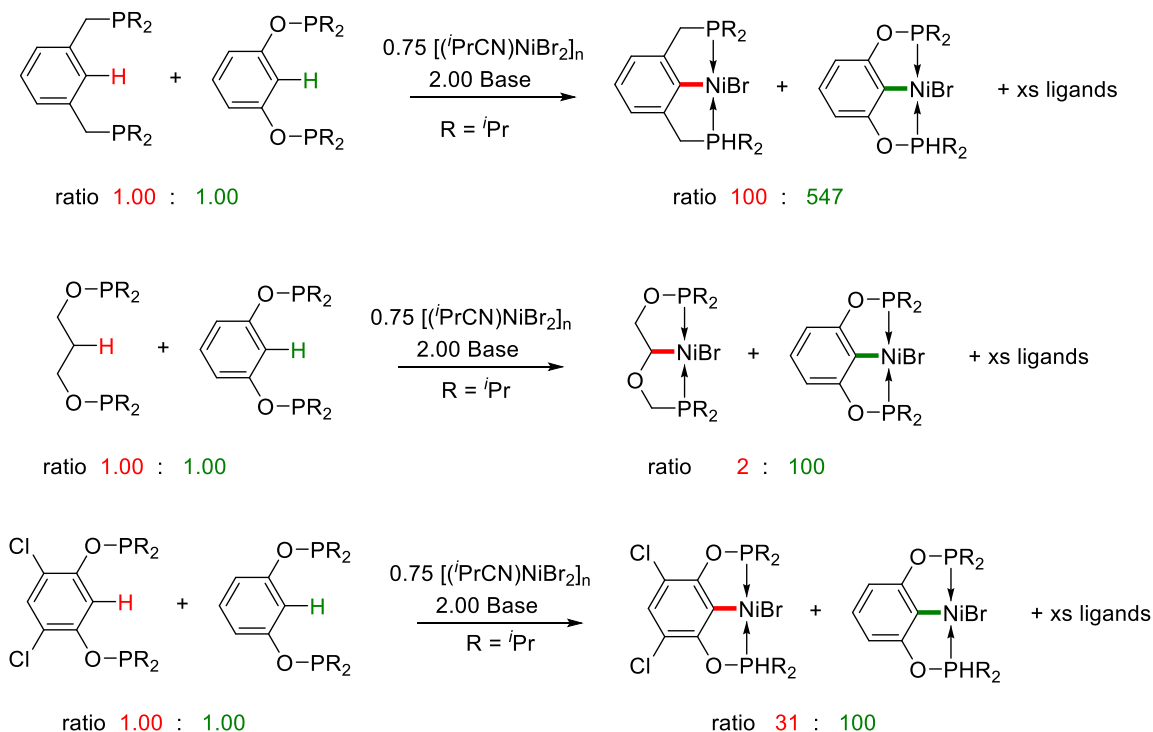
De plus, les systèmes pinceurs peuvent mener à l'observation et à l'isolation des complexes nickelés même en absence d'une base externe, et les auteurs de l'étude ont montré que le ligand non réagi peut capter le proton issu de la nickelation, mais que cela empêche la réaction d'arriver à complétion. À l'inverse, la cyclonickelation des phosphinites monodentées n'est pas observable sans l'ajout de triéthylamine (**Schéma 1.70**). La présente étude cherche donc à comprendre le rôle de la base, à savoir si elle entraine/compromet la génération d'espèces actives, et si elle a un rôle simplement thermodynamique (rendre la réaction favorable) ou si elle a également un rôle cinétique (sa présence est nécessaire à produire les espèces cyclonickellées). Des études d'échange proton/deutérium ont donc été entreprises afin de détecter si le lien carbone-nickel est formé, même réversiblement, en l'absence de triéthylamine.

Schéma 1.70. Rôle de la base externe dans l'isolation des phosphinites cyclonickellées.
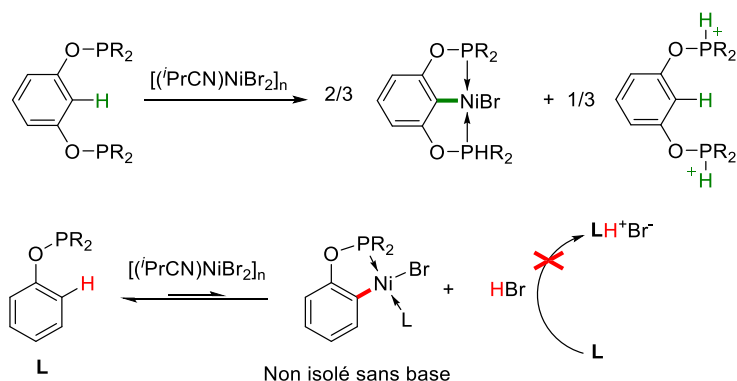
Enfin, les travaux mécanistiques sur les systèmes pincer sont agrémentés d'une étude computationnelle par DFT, ce qui a permis de montrer que c'est une ligand bromure du nickel qui capte d'abord le proton (base cinétique) et que le HBr généré est ensuite capté par la base externe (base thermodynamique). Ainsi, la seconde partie du **Chapitre 3** reproduit une étude semblable, afin de déterminer si le mécanisme de la cyclométallation des ligands monodentés est similaire à celle des proligands pinceurs, à savoir une nickelation électrophile promue par la formation d'une paire d'ions, et une étape limitante de CMD où l'ion Br⁻ joue la base. L'étude computationnelle cherchera donc à corréler les résultats expérimentaux avec les attentes théoriques, en évaluant plusieurs mécanismes de métallation potentiels. Elle permettra également de faire la lumière sur l'identité des espèces initiales dans le milieu réactionnel qui n'ont pas pu être isolées ou même détectées par des méthodes expérimentales.

1.6.3 Synthèse et caractérisation d'une nouvelle classe de composés pinceurs

Les études de la réactivité sur liens C_{sp^3}-H de substituants *ortho* des aryl-phosphinites nous ont poussé à étudier la réactivité sur un substituant en position *ortho* portant un lien C_{sp^2}-H. Non seulement la réactivité de la phosphinite dérivée du 2-vinyl-phénol pourrait ouvrir la voie à l'isolation d'un nickelacycle à 6 chainons, si elle se produit au carbone α. De plus, la nickelation à cette position représenterait un modèle du composé cylométallé au carbone C8 des 1-naphtylphosphinites, sans la rigidité du squelette aromatique que l'on pensait être en cause dans l'instabilité de l'intermédiaire proposé. Cependant, la réaction de la 2-vinylphénylphosphinite dans les conditions standards n'ont pas mené à la nickelation du carbone α, ni même à celle de la position *ortho* libre du cycle aromatique. À la place, un nouveau type de composé pinceur a été obtenu (**Schéma 1.71**), possédant une bras constitué de la phosphinite cyclonickellée, avec en son centre un lien C_{sp^3}-Ni issu du carbone α du substituant vinyle, alors que la position β est occupée par un fragment oxyde de phosphine qui constitue le second bras du *pincer*.

Schéma 1.71. Produits attendu et obtenu pour la nickelation de la 2-vinylphenyl-phosphinite.
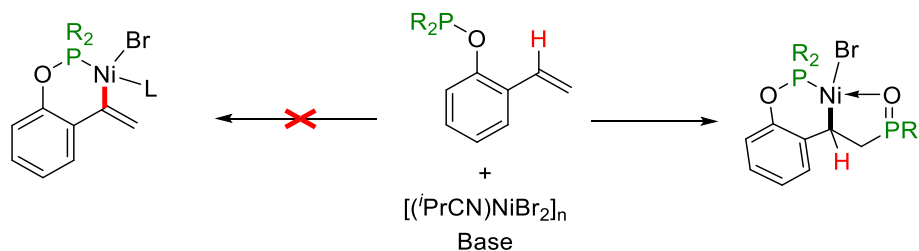
L'isolation d'un tel composé démontre que le substituant vinyle d'une phosphinite a probablement été attaqué par un autre ligand phosphinite et menait à la formation concomitante du lien carbone-nickel. C'est ainsi que nous avons compris que des nucléophiles 'Nu' pouvaient attaquer la partie oléfine, et que s'ils possédaient un lien 'Nu-H', leur déprotonation subséquente entrainerait la formation d'une nouvelle classe de pinceurs (**Schéma 1.72**). Alors que les proligands de type pincer portant des liens C_{sp^3}-H réalisent plus difficilement la réaction de nickelation, cette stratégie est novatrice puisqu'elle n'implique pas le bris de lien C-H par addition oxydante ou par métallation directe, ni l'utilisation de bases fortes tout en permettant de former des composés portant une liaison C_{sp^3}-Ni.

Schéma 1.72. Stratégie de métallation menant à une nouvelle classe de composés *pincer*-Ni.
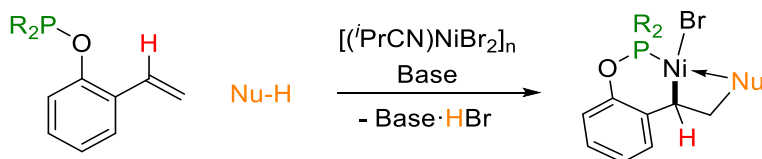
Ainsi, le **Chapitre 5** de cette thèse se consacre à l'étude de la formation de nouveaux *pincers*, par cette stratégie unique de couplage entre la 2-vinylphénylphosphinite et des nucléophiles variés basés sur des phosphines et des amines. Ce chapitre présente l'isolation et la caractérisation structurale de ces nouveaux complexes dont le dénominateur commun est un nickelacycle à 6 chainons, et dont le second nickelacycle possède seulement 4 chainons lorsque les phosphines et les amines sont employées comme nucléophile. L'étude cherche à démontrer la facilité d'obtenir des complexes variés avec la même stratégie. En outre, les ligands portant un donneur C_{sp^3} sont connus pour enrichir électroniquement le centre métallique, et faciliter leur oxydation vers des complexes de Ni^{III}. Une étude électrochimique a donc été entreprise pour déterminer les propriétés redox de ces nouveaux composés et les comparer avec les autres complexes de type *pincer* du nickel reportés dans la littérature.

1.7 Références

[1] Housecroft, C. E., & Sharpe, A. G. (2012). *Inorganic chemistry*. Harlow, England: Pearson.

[2] Cotton, F. A., & Wilkinson, G. (1988). *Advanced inorganic chemistry*. New York: Wiley.

[3] Smith, M. B., & March, J. (2007). *March's Advanced Organic Chemistry: Reactions, Mechanisms, and Structure* (6th Edition). New York: Wiley.

[4] Crabtree, R. H. (2005). *The organometallic chemistry of the transition metals*. Hoboken, N.J: John Wiley.

[5] Gorelsky, S. I.; Lapointe, D.; Fagnou, K., Analysis of the Concerted Metalation-Deprotonation Mechanism in Palladium-Catalyzed Direct Arylation Across a Broad Range of Aromatic Substrates. *Journal of the American Chemical Society* **2008,** *130* (33), 10848-10849.

[6] Kaminsky, W., Highly active metallocene catalysts for olefin polymerization. *Journal of the Chemical Society, Dalton Transactions* **1998,** (9), 1413-1418.

[7] Drent, E.; Budzelaar, P. H. M., Palladium-Catalyzed Alternating Copolymerization of Alkenes and Carbon Monoxide. *Chemical Reviews* **1996,** *96* (2), 663-682.

[8] Ogba, O. M.; Warner, N. C.; O'Leary, D. J.; Grubbs, R. H., Recent advances in ruthenium-based olefin metathesis. *Chemical Society Reviews* **2018,** *47* (12), 4510-4544.

[9] Biffis, A.; Centomo, P.; Del Zotto, A.; Zecca, M., Pd Metal Catalysts for Cross-Couplings and Related Reactions in the 21st Century: A Critical Review. *Chemical Reviews* **2018,** *118* (4), 2249-2295.

[10] Ruiz-Castillo, P.; Buchwald, S. L., Applications of Palladium-Catalyzed C–N Cross-Coupling Reactions. *Chemical Reviews* **2016,** *116* (19), 12564-12649.

[11] Anastas, P. T., & Warner, J. C. (1998). *Green chemistry: Theory and practice*. Oxford, England: Oxford University Press.

[12] Gandeepan, P.; Müller, T.; Zell, D.; Cera, G.; Warratz, S.; Ackermann, L., 3d Transition Metals for C–H Activation. *Chemical Reviews* **2019,** *119* (4), 2192-2452.

[13] Tanabe, T.; Brennessel, W. W.; Clot, E.; Eisenstein, O.; Jones, W. D., Synthesis, structure, and reductive elimination in the series Tp′Rh(PR$_3$)(ArF)H; Determination of rhodium–carbon bond energies of fluoroaryl substituents. *Dalton Transactions* **2010,** *39* (43), 10495-10509.

[14] Nakao, Y.; Kashihara, N.; Kanyiva, K. S.; Hiyama, T., Nickel-Catalyzed Alkenylation and Alkylation of Fluoroarenes via Activation of C−H Bond over C−F Bond. *Journal of the American Chemical Society* **2008,** *130* (48), 16170-16171.

[15] Doster, M. E.; Hatnean, J. A.; Jeftic, T.; Modi, S.; Johnson, S. A., Catalytic C−H Bond Stannylation: A New Regioselective Pathway to C−Sn Bonds via C−H Bond Functionalization. *Journal of the American Chemical Society* **2010,** *132* (34), 11923-11925.

[16] Kanyiva, K. S.; Kashihara, N.; Nakao, Y.; Hiyama, T.; Ohashi, M.; Ogoshi, S., Hydrofluoroarylation of alkynes with fluoroarenes. *Dalton Transactions* **2010,** *39* (43), 10483-10494.

[17] Johnson, S. A.; Doster, M. E.; Matthews, J.; Shoshani, M.; Thibodeau, M.; Labadie, A.; Hatnean, J. A., A mechanistic investigation of carbon–hydrogen bond stannylation: synthesis and characterization of nickel catalysts. *Dalton Transactions* **2012,** *41* (26), 8135-8143.

[18] Nakao, Y.; Kanyiva, K. S.; Hiyama, T., A Strategy for C−H Activation of Pyridines: Direct C-2 Selective Alkenylation of Pyridines by Nickel/Lewis Acid Catalysis. *Journal of the American Chemical Society* **2008,** *130* (8), 2448-2449.

[19] Nett, A. J.; Zhao, W.; Zimmerman, P. M.; Montgomery, J., Highly Active Nickel Catalysts for C–H Functionalization Identified through Analysis of Off-Cycle Intermediates. *Journal of the American Chemical Society* **2015,** *137* (24), 7636-7639.

[20] Nett, A. J.; Montgomery, J.; Zimmerman, P. M., Entrances, Traps, and Rate-Controlling Factors for Nickel-Catalyzed C–H Functionalization. *ACS Catalysis* **2017,** *7* (10), 7352-7362.

[21] Canivet, J.; Yamaguchi, J.; Ban, I.; Itami, K., Nickel-Catalyzed Biaryl Coupling of Heteroarenes and Aryl Halides/Triflates. *Organic Letters* **2009,** *11* (8), 1733-1736.

[22] Muto, K.; Yamaguchi, J.; Itami, K., Nickel-Catalyzed C–H/C–O Coupling of Azoles with Phenol Derivatives. *Journal of the American Chemical Society* **2012,** *134* (1), 169-172.

[23] Xiao, J.; Chen, T.; Han, L.-B., Nickel-Catalyzed Direct C–H/C–O Cross Couplings Generating Fluorobenzenes and Heteroarenes. *Organic Letters* **2015,** *17* (4), 812-815.

[24] Jin, L.-K.; Wan, L.; Feng, J.; Cai, C., Nickel-Catalyzed Regioselective Cross-Dehydrogenative Coupling of Inactive C(sp^3)–H Bonds with Indole Derivatives. *Organic Letters* **2015,** *17* (19), 4726-4729.

[25] Song, W.; Ackermann, L., Nickel-catalyzed alkyne annulation by anilines: versatile indole synthesis by C–H/N–H functionalization. *Chemical Communications* **2013,** *49* (59), 6638-6640.

[26] Miura, W.; Hirano, K.; Miura, M., Nickel-Catalyzed Directed C6-Selective C–H Alkylation of 2-Pyridones with Dienes and Activated Alkenes. *The Journal of Organic Chemistry* **2017,** *82* (10), 5337-5344.

[27] Ruan, Z.; Lackner, S.; Ackermann, L., A General Strategy for the Nickel-Catalyzed C−H Alkylation of Anilines. *Angewandte Chemie International Edition* **2016,** *55* (9), 3153-3157.

[28] Khake, S. M.; Soni, V.; Gonnade, R. G.; Punji, B., A General Nickel-Catalyzed Method for C−H Bond Alkynylation of Heteroarenes Through Chelation Assistance. *Chemistry – A European Journal* **2017,** *23* (12), 2907-2914.

[29] Li, Z.-l.; Sun, K.-k.; Cai, C., Nickel-catalyzed regioselective C–H oxygenation: new routes for versatile C–O bond formation. *Organic Chemistry Frontiers* **2019,** *6* (5), 637-642.

[30] Shiota, H.; Ano, Y.; Aihara, Y.; Fukumoto, Y.; Chatani, N., Nickel-Catalyzed Chelation-Assisted Transformations Involving Ortho C–H Bond Activation: Regioselective Oxidative Cycloaddition of Aromatic Amides to Alkynes. *Journal of the American Chemical Society* **2011,** *133* (38), 14952-14955.

[31] Aihara, Y.; Chatani, N., Nickel-Catalyzed Direct Alkylation of C–H Bonds in Benzamides and Acrylamides with Functionalized Alkyl Halides via Bidentate-Chelation Assistance. *Journal of the American Chemical Society* **2013,** *135* (14), 5308-5311.

[32] Aihara, Y.; Chatani, N., Nickel-Catalyzed Direct Arylation of C(sp^3)–H Bonds in Aliphatic Amides via Bidentate-Chelation Assistance. *Journal of the American Chemical Society* **2014,** *136* (3), 898-901.

[33] Yokota, A.; Aihara, Y.; Chatani, N., Nickel(II)-Catalyzed Direct Arylation of C–H Bonds in Aromatic Amides Containing an 8-Aminoquinoline Moiety as a Directing Group. *The Journal of Organic Chemistry* **2014,** *79* (24), 11922-11932.

[34] Song, W.; Lackner, S.; Ackermann, L., Nickel-Catalyzed C–H Alkylations: Direct Secondary Alkylations and Trifluoroethylations of Arenes. *Angewandte Chemie International Edition* **2014,** *53* (9), 2477-2480.

[35] Yan, Q.; Chen, Z.; Yu, W.; Yin, H.; Liu, Z.; Zhang, Y., Nickel-Catalyzed Direct Amination of Arenes with Alkylamines. *Organic Letters* **2015,** *17* (10), 2482-2485.

[36] Yi, J.; Yang, L.; Xia, C.; Li, F., Nickel-Catalyzed Alkynylation of a $C(sp^2)$–H Bond Directed by an 8-Aminoquinoline Moiety. *The Journal of Organic Chemistry* **2015,** *80* (12), 6213-6221.

[37] Cheng, Y.; Wu, Y.; Tan, G.; You, J., Nickel Catalysis Enables Oxidative C(sp2)–H/C(sp2)–H Cross-Coupling Reactions between Two Heteroarenes. *Angewandte Chemie* **2016,** *128* (40), 12463-12467.

[38] He, Z.; Huang, Y., Diverting C–H Annulation Pathways: Nickel-Catalyzed Dehydrogenative Homologation of Aromatic Amides. *ACS Catalysis* **2016,** *6* (11), 7814-7823.

[39] Zhan, B.-B.; Liu, Y.-H.; Hu, F.; Shi, B.-F., Nickel-catalyzed *ortho*-halogenation of unactivated (hetero)aryl C–H bonds with lithium halides using a removable auxiliary. *Chemical Communications* **2016,** *52* (27), 4934-4937.

[40] Aihara, Y.; Chatani, N., Nickel-Catalyzed Reaction of C–H Bonds in Amides with I_2: ortho-Iodination via the Cleavage of $C(sp^2)$–H Bonds and Oxidative Cyclization to β-Lactams via the Cleavage of $C(sp^3)$–H Bonds. *ACS Catalysis* **2016,** *6* (7), 4323-4329.

[41] Wu, X.; Zhao, Y.; Ge, H., Nickel-Catalyzed Site-Selective Alkylation of Unactivated $C(sp^3)$–H Bonds. *Journal of the American Chemical Society* **2014,** *136* (5), 1789-1792.

[42] Wu, X.; Zhao, Y.; Ge, H., Nickel-Catalyzed Site-Selective Amidation of Unactivated $C(sp^3)$–H Bonds. *Chemistry – A European Journal* **2014,** *20* (31), 9530-9533.

[43] Aihara, Y.; Chatani, N., Nickel-Catalyzed Reaction of C–H Bonds in Amides with I2: ortho-Iodination via the Cleavage of $C(sp^2)$–H Bonds and Oxidative Cyclization to β-Lactams via the Cleavage of $C(sp^3)$–H Bonds. *ACS Catalysis* **2016,** *6* (7), 4323-4329.

[44] Li, M.; Dong, J.; Huang, X.; Li, K.; Wu, Q.; Song, F.; You, J., Nickel-catalyzed chelation-assisted direct arylation of unactivated C(sp3)–H bonds with aryl halides. *Chemical Communications* **2014,** *50* (30), 3944-3946.

[45] Lin, C.; Yu, W.; Yao, J.; Wang, B.; Liu, Z.; Zhang, Y., Nickel-Catalyzed Direct Thioetherification of β-$C(sp^3)$–H Bonds of Aliphatic Amides. *Organic Letters* **2015,** *17* (5), 1340-1343.

[46] Liu, Y.-J.; Zhang, Z.-Z.; Yan, S.-Y.; Liu, Y.-H.; Shi, B.-F., Ni(ii)/BINOL-catalyzed alkenylation of unactivated $C(sp^3)$–H bonds. *Chemical Communications* **2015,** *51* (37), 7899-7902.

[47] Li, M.; Yang, Y.; Zhou, D.; Wan, D.; You, J., Nickel-Catalyzed Addition-Type Alkenylation of Unactivated, Aliphatic C–H Bonds with Alkynes: A Concise Route to Polysubstituted γ-Butyrolactones. *Organic Letters* **2015,** *17* (10), 2546-2549.

[48] Luo, F.-X.; Cao, Z.-C.; Zhao, H.-W.; Wang, D.; Zhang, Y.-F.; Xu, X.; Shi, Z.-J., Nickel-Catalyzed Oxidative Coupling of Unactivated $C(sp^3)$–H Bonds in Aliphatic Amides with Terminal Alkynes. *Organometallics* **2017,** *36* (1), 18-21.

[49] Wang, X.; Xie, P.; Qiu, R.; Zhu, L.; Liu, T.; Li, Y.; Iwasaki, T.; Au, C.-T.; Xu, X.; Xia, Y.; Yin, S.-F.; Kambe, N., Nickel-catalysed direct alkylation of thiophenes via double $C(sp^3)$–H/$C(sp^2)$–H bond cleavage: the importance of KH_2PO_4. *Chemical Communications* **2017,** *53* (59), 8316-8319.

[50] Al-Salem, N. A.; Empsall, H. D.; Markham, R.; Shaw, B. L.; Weeks, B., Formation of large chelate rings and cyclometalated products from diphosphines of type $But_2P(CH_2)_nPBut_2$(n= 5–8) and $Ph_2P(CH_2)_5PPh_2$ with palladium and platinum chlorides: factors affecting the stability and conformation of large chelate rings. *Journal of the Chemical Society, Dalton Transactions* **1979,** (12), 1972-1982.

[51] Moulton, C. J.; Shaw, B. L., Transition metal–carbon bonds. Part XLII. Complexes of nickel, palladium, platinum, rhodium and iridium with the tridentate ligand 2,6-bis[(di-t-butylphosphino)methyl]phenyl. *Journal of the Chemical Society, Dalton Transactions* **1976,** (11), 1020-1024.

[52] Crocker, C.; Errington, R. J.; Markham, R.; Moulton, C. J.; Odell, K. J.; Shaw, B. L., Large-ring and cyclometalated rhodium complexes from some medium-chain .alpha.,.omega.-diphosphines. *Journal of the American Chemical Society* **1980,** *102* (13), 4373-4379.

[53] Pell, C. J.; Ozerov, O. V., A Series of Pincer-Ligated Rhodium Complexes as Catalysts for the Dimerization of Terminal Alkynes. *ACS Catalysis* **2014,** *4* (10), 3470-3480.

[54] Van Beek, J. A. M.; Van Koten, G.; Ramp, M. J.; Coenjaarts, N. C.; Grove, D. M.; Goubitz, K.; Zoutberg, M. C.; Stam, C. H.; Smeets, W. J. J.; Spek, A. L., Influence of the amino substituents of potentially bis ortho chelating aryl ligands (2,6-$\{R_1R_2NCH_2\}_2C_6H_3$)- on the synthesis and properties of their organonickel(II) complexes. *Inorganic Chemistry* **1991,** *30* (15), 3059-3068.

[55] Williams, B. S.; Dani, P.; Lutz, M.; Spek, A. L.; van Koten, G., Development of the First P-Stereogenic PCP Pincer Ligands, Their Metallation by Palladium and Platinum, and Preliminary Catalysis. *Helvetica Chimica Acta* **2001,** *84* (11), 3519-3530.

[56] Matson, E. M.; Espinosa Martinez, G.; Ibrahim, A. D.; Jackson, B. J.; Bertke, J. A.; Fout, A. R., Nickel(II) Pincer Carbene Complexes: Oxidative Addition of an Aryl C–H Bond to Form a Ni(II) Hydride. *Organometallics* **2015,** *34* (2), 399-407.

[57] Pandarus, V.; Zargarian, D., New Pincer-Type Diphosphinito (POCOP) Complexes of Nickel. *Organometallics* **2007,** *26* (17), 4321-4334.

[58] Castonguay, A.; Beauchamp, A. L.; Zargarian, D., Preparation and Reactivities of PCP-Type Pincer Complexes of Nickel. Impact of Different Ligand Skeletons and Phosphine Substituents. *Organometallics* **2008,** *27* (21), 5723-5732.

[59] Spasyuk, D. M.; Zargarian, D.; van der Est, A., New POCN-Type Pincer Complexes of Nickel(II) and Nickel(III). *Organometallics* **2009,** *28* (22), 6531-6540.

[60] Spasyuk, D. M.; Gorelsky, S. I.; van der Est, A.; Zargarian, D., Characterization of Divalent and Trivalent Species Generated in the Chemical and Electrochemical Oxidation of a Dimeric Pincer Complex of Nickel. *Inorganic Chemistry* **2011,** *50* (6), 2661-2674.

[61] Mousa, A. H.; Bendix, J.; Wendt, O. F., Synthesis, Characterization, and Reactivity of PCN Pincer Nickel Complexes. *Organometallics* **2018,** *37* (15), 2581-2593.

[62] Vabre, B.; Canac, Y.; Duhayon, C.; Chauvin, R.; Zargarian, D., Nickel(ii) complexes of the new pincer-type unsymmetrical ligands PIMCOP, PIMIOCOP, and NHCCOP: versatile binding motifs. *Chemical Communications* **2012,** *48* (84), 10446-10448.

[63] Vabre, B.; Lambert, M. L.; Petit, A.; Ess, D. H.; Zargarian, D., Nickelation of PCP- and POCOP-Type Pincer Ligands: Kinetics and Mechanism. *Organometallics* **2012,** *31* (17), 6041-6053.

[64] Cloutier, J.-P.; Vabre, B.; Moungang-Soumé, B.; Zargarian, D., Synthesis and Reactivities of New NCN-Type Pincer Complexes of Nickel. *Organometallics* **2015,** *34* (1), 133-145.

[65] Chakraborty, S.; Krause, J. A.; Guan, H., Hydrosilylation of Aldehydes and Ketones Catalyzed by Nickel PCP-Pincer Hydride Complexes. *Organometallics* **2009,** *28* (2), 582-586.

[66] Chakraborty, S.; Zhang, J.; Patel, Y. J.; Krause, J. A.; Guan, H., Pincer-Ligated Nickel Hydridoborate Complexes: the Dormant Species in Catalytic Reduction of Carbon Dioxide with Boranes. *Inorganic Chemistry* **2013,** *52* (1), 37-47.

[67] Wilson, G. L. O.; Abraha, M.; Krause, J. A.; Guan, H., Reactions of phenylacetylene with nickel POCOP-pincer hydride complexes resulting in different outcomes from their palladium analogues. *Dalton Transactions* **2015,** *44* (27), 12128-12136.

[68] Chakraborty, S.; Patel, Y. J.; Krause, J. A.; Guan, H., A Robust Nickel Catalyst for Cyanomethylation of Aldehydes: Activation of Acetonitrile under Base-Free Conditions. *Angewandte Chemie International Edition* **2013,** *52* (29), 7523-7526.

[69] Castonguay, A.; Spasyuk, D. M.; Madern, N.; Beauchamp, A. L.; Zargarian, D., Regioselective Hydroamination of Acrylonitrile Catalyzed by Cationic Pincer Complexes of Nickel(II). *Organometallics* **2009,** *28* (7), 2134-2141.

[70] Spasyuk, D. M.; Zargarian, D., Monomeric and Dimeric Nickel Complexes Derived from a Pincer Ligand Featuring a Secondary Amine Donor Moiety. *Inorganic Chemistry* **2010,** *49* (13), 6203-6213.

[71] Salah, A. B.; Offenstein, C.; Zargarian, D., Hydroamination and Alcoholysis of Acrylonitrile Promoted by the Pincer Complex $\{\kappa^P,\kappa^C,\kappa^P\text{-}2,6\text{-}(Ph_2PO)_2C_6H_3\}Ni(OSO_2CF_3)$. *Organometallics* **2011,** *30* (20), 5352-5364.

[72] Lapointe, S.; Zargarian, D., On the mechanism of Ni(ii)-promoted Michael-type hydroamination of acrylonitrile and its substituted derivatives. *Dalton Transactions* **2016,** *45* (40), 15800-15810.

[73] Grove, D. M.; Van Koten, G.; Mul, P.; Zoet, R.; Van der Linden, J. G. M.; Legters, J.; Schmitz, J. E. J.; Murrall, N. W.; Welch, A. J., Syntheses and characterization of unique organometallic nickel(III) aryl species. ESR and electrochemical studies and the x-ray molecular study of square-pyramidal [Ni{$C_6H_3(CH_2NMe_2)_2$-*o,o'*}I$_2$]. *Inorganic Chemistry* **1988,** *27* (14), 2466-2473.

[74] Grove, D. M.; Van Koten, G.; Verschuuren, A. H. M., New Homogeneous Catalysts in the Addition of Polyhalogenoalkanes to Olefins; Organonickel(II) Complexes [Ni{$C_6H_3(CH_2NMe_2)_2$-*o,o'*}X] (X = Cl, Br, I). *Journal of Molecular Catalysis* **1988,** *45* (2), 169-174.

[75] Muller, G.; Panyella, D.; Rocamora, M.; Sales, J.; Font-Bardía, M.; Solans, X., Preparation and reactivity of five-membered phosphonickelocycles. *Journal of the Chemical Society, Dalton Transactions* **1993,** (19), 2959-2967.

[76] Ceder, R. M.; Granell, J.; Muller, G.; Font-Bardia, M.; Solans, X., Preparation of Five-Membered Nickelacycles of N-Donor Ligands by Activation of C-X Bonds (X = F, Cl, or Br). X-ray Crystal Structure of [NiBr{2-(CH=NCH₂Ph)C_6H_4}(2,4,6-Me₃C₅H₂N)]. *Organometallics* **1995,** *14* (12), 5544-5551.

[77] Ceder, R. M.; Granell, J.; Muller, G.; Font-Bardía, M.; Solans, X., Preparation of Five-Membered Nickelacycles with Anionic C−N−N' Terdentate Ligands. X-ray Crystal Structure of [NiCl{2-(CH=NCH₂CH₂NMe₂)-3-ClC₆H₃}]. *Organometallics* **1996,** *15* (21), 4618-4624.

[78] Zimmerman, A. C.; Fryzuk, M. D., β-Hydrogen Elimination and Reductive Elimination from a κ^3-PPC Nickel Complex. *Organometallics* **2018,** *37* (14), 2305-2318.

[79] Liu, L.; Montgomery, J., Dimerization of Cyclopropyl Ketones and Crossed Reactions of Cyclopropyl Ketones with Enones as an Entry to Five-Membered Rings. *Journal of the American Chemical Society* **2006,** *128* (16), 5348-5349.

[80] Souillart, L.; Cramer, N., Catalytic C–C Bond Activations via Oxidative Addition to Transition Metals. *Chemical Reviews* **2015,** *115* (17), 9410-9464.

[81] Eisch, J. J.; Piotrowski, A. M.; Han, K. I.; Kruger, C.; Tsay, Y. H., Organic chemistry of subvalent transition complexes. 9. Oxidative addition of nickel(0) complexes to carbon-carbon bonds in biphenylene: formation of nickelole and 1,2-dinickelecin intermediates. *Organometallics* **1985,** *4* (2), 224-231.

[82] Bennett, M. A.; Hockless, D. C. R.; Wenger, E., Generation of (2,3-.eta.)-Naphthalyne-Nickel(0) Complexes and Their Reactions with Unsaturated Molecules. *Organometallics* **1995,** *14* (4), 2091-2101.

[83] A. Bennett, M.; Glewis, M.; C. R. Hockless, D.; Wenger, E., Successive insertion of tetrafluoroethylene and CO and of tetrafluoroethylene and acetylenes into aryne–nickel(0) bonds*Journal of the Chemical Society, Dalton Transactions* **1997,** (18), 3105-3114.

[84] Ogoshi, S.; Oka, M.-a.; Kurosawa, H., Direct Observation of Oxidative Cyclization of η2-Alkene and η2-Aldehyde on Ni(0) Center. Significant Acceleration by Addition of Me₃SiOTf. *Journal of the American Chemical Society* **2004,** *126* (38), 11802-11803.

[85] Hoshimoto, Y.; Hayashi, Y.; Suzuki, H.; Ohashi, M.; Ogoshi, S., Synthesis of Five- and Six-Membered Benzocyclic Ketones through Intramolecular Alkene Hydroacylation Catalyzed by Nickel(0)/N-Heterocyclic Carbenes. *Angewandte Chemie International Edition* **2012,** *51* (43), 10812-10815.

[86] Hayashi, Y.; Hoshimoto, Y.; Kumar, R.; Ohashi, M.; Ogoshi, S., Nickel(0)-catalyzed intramolecular reductive coupling of alkenes and aldehydes or ketones with hydrosilanes. *Chemical Communications* **2016,** *52* (37), 6237-6240.

[87] Ohashi, M.; Kawashima, T.; Taniguchi, T.; Kikushima, K.; Ogoshi, S., 2,2,3,3-Tetrafluoronickelacyclopentanes Generated via the Oxidative Cyclization of Tetrafluoroethylene and Simple Alkenes: A Key Intermediate in Nickel-Catalyzed C–C Bond-Forming Reactions. *Organometallics* **2015,** *34* (9), 1604-1607.

[88] Ohashi, M.; Shirataki, H.; Kikushima, K.; Ogoshi, S., Nickel-Catalyzed Formation of Fluorine-Containing Ketones via the Selective Cross-Trimerization Reaction of Tetrafluoroethylene, Ethylene, and Aldehydes. *Journal of the American Chemical Society* **2015,** *137* (20), 6496-6499.

[89] Kawashima, T.; Ohashi, M.; Ogoshi, S., Nickel-Catalyzed Formation of 1,3-Dienes via a Highly Selective Cross-Tetramerization of Tetrafluoroethylene, Styrenes, Alkynes, and Ethylene. *Journal of the American Chemical Society* **2017,** *139* (49), 17795-17798.

[90] Ohashi, M.; Hoshimoto, Y.; Ogoshi, S., Aza-nickelacycle key intermediate in nickel(0)-catalyzed transformation reactions. *Dalton Transactions* **2015,** *44* (27), 12060-12073.

[91] Ruhland, K.; Obenhuber, A.; Hoffmann, S. D., Cleavage of Unstrained $C(sp^2)$—$C(sp^2)$ Single Bonds with Ni^0 Complexes Using Chelating Assistance. *Organometallics* **2008,** *27* (14), 3482-3495.

[92] Kleiman, J. P.; Dubeck, M., The Preparation of Cyclopentadienyl [o-(Phenylazo)Phenyl]Nickel. *Journal of the American Chemical Society* **1963,** *85* (10), 1544-1545.

[93] Carmona, E.; Gutierrez-Puebla, E.; Marin, J. M.; Monge, A.; Paneque, M.; Poveda, M. L.; Ruiz, C., Synthesis and x-ray structure of the nickelabenzocyclopentene complex [cyclic](Me₃P)2Ni(CH₂CMe₂-*o*-C₆H₄). Reactivity toward simple, unsaturated molecules and the crystal and molecular structure of the cyclic carboxylate (Me₃P)₂Ni(CH₂CMe₂-*o*-C₆H₄C(O)O). *Journal of the American Chemical Society* **1989,** *111* (8), 2883-2891.

[94] Matsunaga, P. T.; Hillhouse, G. L.; Rheingold, A. L., Oxygen-atom transfer from nitrous oxide to a nickel metallacycle. Synthesis, structure, and reactions of [cyclic] (2,2'-bipyridine)Ni(OCH₂CH₂CH₂CH₂). *Journal of the American Chemical Society* **1993,** *115* (5), 2075-2077.

[95] Koo, K.; Hillhouse, G. L., Indoline Synthesis via Coupling of Phenethyl Grignard Reagents with Organoazides Mediated by (Alkylphosphine)nickel(II) Complexes. *Organometallics* **1996,** *15* (12), 2669-2671.

[96] Klein, H.-F.; Lemke, U.; Lemke, M.; Brand, A., 2-Diphenylphosphinobenzaldehyde as Chelating Ligand in Trimethylphosphine Complexes of Cobalt and Nickel. *Organometallics* **1998,** *17* (19), 4196-4201.

[97] Vabre, B.; Deschamps, F.; Zargarian, D., Ortho Derivatization of Phenols through C–H Nickelation: Synthesis, Characterization, and Reactivities of Ortho-Nickelated Phosphinite Complexes. *Organometallics* **2014,** *33* (22), 6623-6632.

[98] Cornaton, Y.; Djukic, J.-P., A noncovalent interaction insight onto the concerted metallation deprotonation mechanism. *Physical Chemistry Chemical Physics* **2019,** *21* (36), 20486-20498.

[99] Volpe, E. C.; Chadeayne, A. R.; Wolczanski, P. T.; Lobkovsky, E. B., Heterolytic CH-bond activation in the synthesis of Ni{(2-aryl-κC^2)pyridine-κN}$_2$ and derivatives. *Journal of Organometallic Chemistry* **2007,** *692* (21), 4774-4783.

[100] Lu, Z.; Abbina, S.; Sabin, J. R.; Nemykin, V. N.; Du, G., Unexpected Formation of Chiral Pincer CNN Nickel Complexes with β-Diketiminato Type Ligands via C–H Activation: Synthesis, Properties, Structures, and Computational Studies. *Inorganic Chemistry* **2013,** *52* (3), 1454-1465.

[101] Beattie, D. D.; Grunwald, A. C.; Perse, T.; Schafer, L. L.; Love, J. A., Understanding Ni(II)-Mediated C(sp^3)–H Activation: Tertiary Ureas as Model Substrates. *Journal of the American Chemical Society* **2018,** *140* (39), 12602-12610.

[102] Roy, P.; Bour, J. R.; Kampf, J. W.; Sanford, M. S., Catalytically Relevant Intermediates in the Ni-Catalyzed C(sp^2)–H and C(sp^3)–H Functionalization of Aminoquinoline Substrates. *Journal of the American Chemical Society* **2019,** *141* (43), 17382-17387.

[103] Chong, E.; Kampf, J. W.; Ariafard, A.; Canty, A. J.; Sanford, M. S., Oxidatively Induced C–H Activation at High Valent Nickel. *Journal of the American Chemical Society* **2017,** *139* (17), 6058-6061.

[104] Roberts, C. C.; Chong, E.; Kampf, J. W.; Canty, A. J.; Ariafard, A.; Sanford, M. S., Nickel(II/IV) Manifold Enables Room-Temperature C(sp^3)–H Functionalization. *Journal of the American Chemical Society* **2019,** *141* (49), 19513-19520.

[105] Parshall, G. W.; Knoth, W. H.; Schunn, R. A., Ligand-metal hydrogen-transfer reactions in triphenyl phosphite and triphenylphosphine complexes. *Journal of the American Chemical Society* **1969,** *91* (18), 4990-4995.

[106] Adhikary, A.; Guan, H., Catalysis Involving Phosphinite-Based Metallacycles. *ACS Catalysis* **2015,** *5* (11), 6858-6873.

[107] Bedford, R. B.; Limmert, M. E., Catalytic Intermolecular Ortho-Arylation of Phenols. *The Journal of Organic Chemistry* **2003,** *68* (22), 8669-8682.

[108] Lewis, J. C.; Wu, J.; Bergman, R. G.; Ellman, J. A., Preagostic Rh−H Interactions and C−H Bond Functionalization: A Combined Experimental and Theoretical Investigation of Rhodium(I) Phosphinite Complexes. *Organometallics* **2005,** *24* (23), 5737-5746.

[109] Carrión, M. C.; Cole-Hamilton, D. J., Halide-free ethylation of phenol by multifunctional catalysis using phosphinite ligands. *Chemical Communications* **2006,** (43), 4527-4529.

[110] Grünanger, C. U.; Breit, B., Branched-Regioselective Hydroformylation with Catalytic Amounts of a Reversibly Bound Directing Group. *Angewandte Chemie International Edition* **2008,** *47* (38), 7346-7349.

[111] Kalyani, D.; Sanford, M. S., Regioselectivity in Palladium-Catalyzed C−H Activation/Oxygenation Reactions. *Organic Letters* **2005,** *7* (19), 4149-4152.

[112] Obata, A.; Ano, Y.; Chatani, N., Nickel-catalyzed C–H/N–H annulation of aromatic amides with alkynes in the absence of a specific chelation system. *Chemical Science* **2017,** *8* (9), 6650-6655.

[113] Mangin, L. P.; Zargarian, D., C–H nickellation of phenol-derived phosphinites: regioselectivity and structures of cyclonickellated complexes. *Dalton Transactions* **2017,** *46* (46), 16159-16170.

[114] Mangin, L. P.; Zargarian, D., C–H Nickelation of Naphthyl Phosphinites: Electronic and Steric Limitations, Regioselectivity, and Tandem C–P Functionalization. *Organometallics* **2019,** *38* (24), 4687-4700.

[115] Satoh, T.; Inoh, J.-i.; Kawamura, Y.; Kawamura, Y.; Miura, M.; Nomura, M., Regioselective Arylation Reactions of Biphenyl-2-ols, Naphthols, and Benzylic Compounds with Aryl Halides under Palladium Catalysis. *Bulletin of the Chemical Society of Japan* **1998,** *71* (9), 2239-2246.

[116] Mangin, L. P.; Zargarian, D., C–H Nickelation of Aryl Phosphinites: Mechanistic Aspects. *Organometallics* **2019,** *38* (7), 1479-1492.

Chapitre 2 – C–H nickelation of phenol-derived phosphinites: regioselectivity and structures of cyclonickelated complexes

Loïc P. Mangin[a] and Davit Zargarian[a]*

[a] Département de Chimie, Université de Montréal, Montréal, Canada H3T 1J4

Full paper

2.1 Abstract

This report describes the results of a study on the *ortho*-C–H nickelation of the aryl phosphinites i-Pr$_2$P(OAr) derived from the following four groups of substituted phenols: 3-R-C$_6$H$_4$OH (R = F (b), Me (c), MeO (d), Cl (e)); 3,5-R$_2$-C$_6$H$_3$OH (R = F (f), Me (g), Cl (h), OMe (i)); 2-R-C$_6$H$_4$OH (R = Me (j), Ph(k)); and 2,6-R$_2$-C$_6$H$_3$OH (R = Me (l), Ph (m)). No nickelation was observed with the phosphinites derived from the 3,5-disubstituted phenols g and h, and the 2,6-disubstituted phenols l and m; in all other cases nickelation occurred at an *ortho*-C–H to generate either the Br-bridged dimers [{κ^P,κ^C-(i-Pr)$_2$POAr}Ni(μ-Br)]$_2$ (1b–1f, 1j, and 1k) or the monomeric acetonitrile adduct {κ^P,κ^C-ArOP(i-Pr)$_2$}Ni(Br)(NCMe) (1i-NCMe). Analysis of C–H nickelation regioselectivity with 3-R-C$_6$H$_4$OH pointed to the importance of substituent sterics, not electronics: nickelation occurred at the least hindered position either exclusively (for R = Me (c), MeO(d), and Cl (e)) or predominantly (for R = F (b); 6:1). This conclusion is also consistent with the observation that C–H nickelation is possible with the 3,5-disubstituted aryl phosphinites bearing F and OMe, but not with the more bulky substituents Me or Cl. For the 2-substituted aryl phosphinites, C–H nickelation occurs at the unsubstituted *ortho*-C–H and not on the R substituent, regardless of whether the alternative C–H moiety of the substituent is sp^3 (R = Me (j)) or sp^2 (R = Ph (k)). The system thus reveals a strong preference for formation of 5-membered metallacycles. Consistent with this reactivity, no nickelation occurs with (2,6-R$_2$-C$_6$H$_3$O)P(i-Pr)$_2$. Tests with the parent dimer derived from i-Pr$_2$P(OPh) showed that conversion to the monomeric acetonitrile adduct is highly favored, going to completion with only a small excess of MeCN. All new cyclonickelated complexes reported in this study were fully characterized, including by single crystal X-ray diffraction studies. The solid state structures of the dimers 1b and 1d showed an unexpected feature: two halves of the dimers displayed non-coplanar conformations that place the two Ni(II) centers at shortened distances from each other (2.94–3.16 Å). Geometry optimization studies using DFT have shown that such non-coplanar conformations stabilize the complex, implying that the "bending" observed in these complexes is not caused by packing forces. Indeed, it appears that the occurrence of coplanar conformations in the solid state structures of these dimers is a simple consequence of packing forces rather than an intrinsic property of the compound.

2.2 Introduction

Chelation-assisted C-H metalation and derivatization is an attractive methodology for the sustainable synthesis of complex organic molecules.[1] This approach is generally considered to be even more powerful when (i) simple salts or derivatives of the more abundant 3d metals can serve as required metallic precursors, and (ii) the directing functional group(s) required for chelation can be installed and removed easily ("traceless functionalization").[2] From a practical point of view, another desired feature of metalation-functionalization protocols is that they proceed in a one-pot manner, thus bypassing the isolation and manipulation of the cyclometalated species that are thought to be intermediates in these processes. On the other hand, intercepting such key intermediates of the catalytic cycle and probing their properties can be potentially advantageous for rational design of new metalation-functionalization processes and their optimization. For instance, isolation of the cyclometalated species arising from the C-H metalation can facilitate the modelling of this step and allow a systematic study of the functionalization step as well.

The emergence over the past decade of an increasing number of reports on nickel-catalyzed C-H functionalization reactions has demonstrated that in this context Ni precursors can be viable alternatives to their more widely-used Pd counterparts.[3] These developments and our longstanding interest in organonickel chemistry,[4] including the synthesis and reactivities of pincer-type nickel complexes,[5] led us to prepare nickelacyclic complexes via C-H nickelation and study their structures, stabilities, and functionalization aptitudes. The preparation of the orthonickelated phosphinite complexes $[\{\kappa^P,\kappa^C\text{-}(i\text{-Pr})_2\text{POAr}\}\text{Ni}(\mu\text{-Br})]_2$ or $trans\text{-}\{\kappa^P,\kappa^C\text{-} \text{ArOP}(i\text{-Pr})_2\}\text{NiBr}\{i\text{-Pr}_2\text{P(OAr)}\}$ derived from substituted phenols, R-C$_6$H$_4$OH, was reported recently (**Scheme 2.1**).[6,7]

Scheme 2.1. Alternative protocols for preparation of orthonickelated complexes from aryl phosphinites.
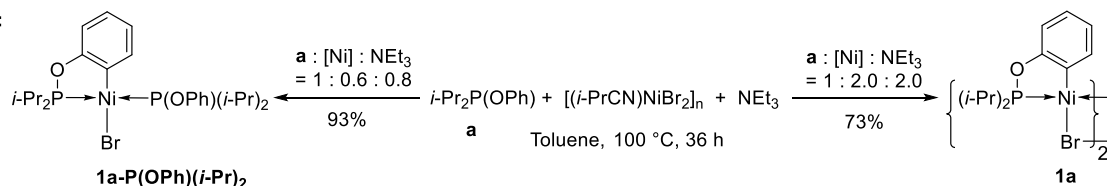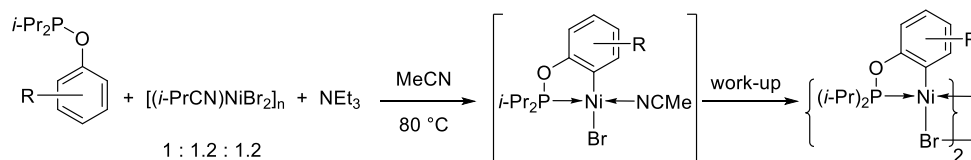
This first report outlined the impact of substituent R on relative cyclonickelation rates for R-$C_6H_4OP(i\text{-}Pr)_2$ (COOMe < Me < OMe), indicating that the C-H nickelation step follows an electrophilic mechanism; this finding was consistent with our postulates on how POCOP-type pincer ligands undergo C-H nickelation.[8] This report also showed that the cyclonickelated complexes in question can be benzylated at the nickelated carbon, thus providing a proof of concept for the functionalization step.[6] On the other hand, our initial results did not provide much insight on the regioselectivity of cyclonickelation, nor did they result in a broad scope for the functionalization step. It was thus evident that much was left to do to develop a better understanding of the factors that govern C-H nickelation and the reactivities of the resulting species.

As a continuation of our initial studies, we have examined the regioselectivity of C-H nickelation with aryl phosphinites $R_nC_6H_{(5\text{-}n)}OP(i\text{-}Pr)_2$ derived from substituted phenols. The results presented herein show that C-H nickelation of substrates derived from 3-R-C_6H_4OH (R = Me, OMe, Cl) takes place selectively at the less hindered *ortho* position, whereas nickelation of substrates derived from 2-R-C_6H_4OH (R = Me, Ph) takes place at the unsubstituted *ortho* C-H of the phenol ring, and not on the ring substituents. In contrast to the reactivity of these mono-substituted substrates, no nickelation takes place with disubstituted phosphinites derived from 2,6-R_2-C_6H_3OH (R = Me, Ph) or 3,5-R_2-C_6H_3OH (R = Me, Cl), whereas the less bulky analogues of the latter phosphinites (R = F, OMe) did undergo nickelation. The observed nickelation reactions led to the dimeric species $[\{\kappa^P,\kappa^C\text{-}(i\text{-}Pr)_2POAr\}Ni(\mu\text{-}Br)]_2$ in every case except with 3,5-$(MeO)_2$-$C_6H_3OP(i\text{-}Pr)_2$, which

produced the monomeric acetonitrile adduct *trans*-{κ^P,κ^C-3,5-(MeO)$_2$-C$_6$H$_3$OP(*i*-Pr)$_2$}NiBr(NCMe). The present report discusses these results in terms of the steric and electronic properties of the R-substituents, and describes the solid state structures and NMR spectra of the various cyclonickelated complexes obtained.

2.3 Results & Discussion

2.3.1 Revised procedure for cyclonickelation of arylphosphinites

Vabre et al.[6] have reported that extended heating of the Ni(II) precursor {(*i*-PrCN)NiBr$_2$}$_n$ in toluene with *i*-Pr$_2$P(OPh), a, and NEt$_3$ facilitates direct *ortho*-C-H nickelation; this reaction generated both the Br-bridged dinickel complex {κ^P,κ^C-C$_6$H$_4$OP(*i*-Pr)$_2$}NiBr}$_2$ (1a) and its monomeric *i*-Pr$_2$P(OPh) adduct bearing a non-cyclometalated phosphinite, *trans*-{{κ^P,κ^C-C$_6$H$_4$OP(*i*-Pr)$_2$}Ni{*i*-Pr$_2$P(OPh)}Br (1a-P(OPh)(*i*-Pr)$_2$) (Scheme 1). Controlling the precise phosphinite: Ni-precursor ratio in this protocol allowed the exclusive or predominant formation of one or the other of the two products. For example, using a 1.0 : 0.6 ratio gave the thermodynamically more favored mononickel adduct exclusively, whereas a 1 : 2 ratio gave the dinickel species.6

To improve the atom-efficiency of the orthonickelation reaction under discussion, we probed the influence of various solvents with a view to favoring the formation of the dimeric species **1a**. Our tests showed that using acetonitrile as solvent led to orthonickelation at lower temperatures and over a shorter reaction time. This modified protocol also required only a small excess of the Ni(II) precursor to smoothly generate the monomeric MeCN adduct as a stable intermediate species, from which we could obtain the target Br-bridged dimer after work-up (**Scheme 2.1**). In contrast, conducting the nickelation reactions in THF or ethyl acetate showed rates that were intermediate between those observed in toluene and acetonitrile, such that the nickelation was incomplete after 24 h.

We believe that the main advantages of using acetonitrile in this C-H nickelation protocol, i.e., exclusive access to the dimeric species over shorter reaction times, can be attributed to two factors. First, acetonitrile reaction mixtures remain homogeneous throughout the entire reaction span, thus

providing a greater effective concentration of Ni and maintaining a Ni : phosphinite ratio of $\approx 1 :$ 1. Second, formation of the undesired adduct 1a-P(OPh)(i-Pr)$_2$ during the reaction is circumvented by the facile formation of the analogous acetonitrile adduct, as illustrated in Scheme 1. This assertion was confirmed by the ^{31}P{^{1}H} NMR spectra recorded for toluene solutions of the authenticated dimeric species 1a to which were added various amounts of acetonitrile (**Figure 2.1**). These spectra show that portion-wise addition of acetonitrile to the dimeric species (represented by the P singlet at 196.7 ppm) converts it into the monomeric acetonitrile adduct **1a-NCMe** (represented by a new singlet at ca. 193.5 ppm).
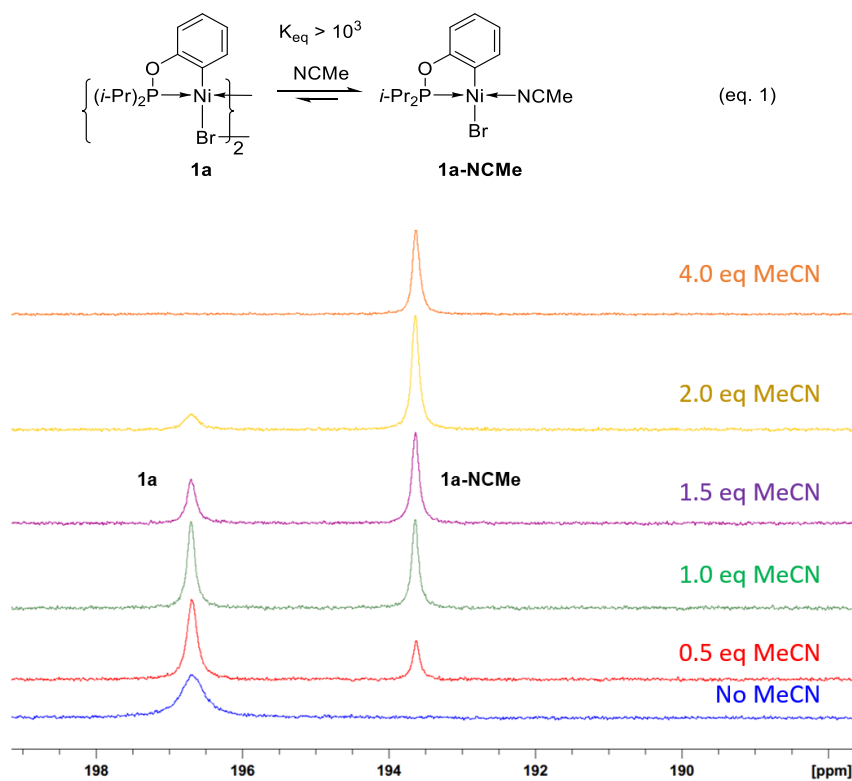
Figure 2.1. ^{31}P{1H} NMR (162 MHz, 25 mM in PhMe) spectra of **1a** upon portion-wise addition of MeCN

The identity of **1a-NCMe** was confirmed by its direct synthesis, which was done as follows. Addition of 10 equiv of MeCN to a suspension of **1a** in Et$_2$O led to an immediate color change from orange to yellow, and evaporation gave the adduct **1a-NCMe** as a yellow powder that could be isolated in 86 % yield. The ^{1}H NMR spectrum of this solid in CD$_3$CN matched that of **1a** in CD$_3$CN, and the structural assignment was confirmed by single crystal diffraction studies (vide infra). That more than 2 equiv of MeCN are required for a complete transformation of **1a** to **1a-**

NCMe suggests a dimer⇌monomer equilibrium (eq. 1). Integration of the ^{31}P signals for the two species (**Figure 2.1**) allowed us to estimate a large equilibrium constant ($K_{eq} \approx 10^3\text{-}10^4$), which implies a strong preference for the monomeric adduct. A similar conclusion was drawn from the UV-vis spectra recorded for a toluene solution of **1a** before and after addition of 10 equiv acetonitrile: the orange solution of the dimer (λ_{max} = 434 nm; $\varepsilon_{[Ni]}$ = 737 M^{-1}·cm^{-1}) turned yellow (λ_{max} = 403 nm, $\varepsilon_{[Ni]}$ = 1414 M^{-1}·cm^{-1}) as a result of the formation of **1a-NCMe**. (See Figure **S2.1** for these spectra.) The greater thermodynamic preference for the acetonitrile adduct also explains why it proved difficult to isolate analytically pure samples of the dimer from acetonitrile solutions; indeed, most samples showed the presence of traces of nitrogen (<0.10 %) unless they were subjected to multiple recrystallizations and extended evaporation under vacuum.

2.3.2 Regioselectivity of C-H nickelation with new aryl phosphinites derived from 3-substituted phenols

Having optimized the protocol for the synthesis of **1a**, we set out to test our new, acetonitrile-based synthetic protocol for the C-H nickelation of phosphinites derived from substituted phenols. The first substrate we tested was 3-F-C$_6$H$_4$OP(*i*-Pr)$_2$ (**b**) for which cyclonickelation via the toluene-based protocol had given the two regioisomers of *trans*-{{κ^P,κ^C-F-C$_6$H$_4$OP(*i*-Pr)$_2$}Ni{*i*-Pr$_2$P(OAr)}Br in a 5.6:1 ratio, the major isomer arising from the metalation at the less hindered position (*para* to the C-F moiety.[6] Applying the new protocol to this phosphinite gave the anticipated dimers with a comparable regioselectivity (**Scheme 2.2**).[9]

Scheme 2.2. Orthonickelation of 3-F-C$_6$H$_4$OH in acetonitrile.

Combined isolated yield after work-up: 52%
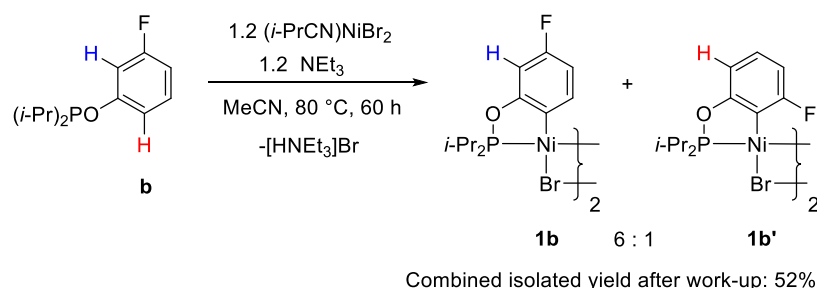
Next, we used the acetonitrile-based protocol to expand our investigation of the nickelation regioselectivity beyond 3-F-C$_6$H$_4$OH. As shown in Scheme 3, cyclonickelation of aryl phosphinites derived from 3-Me-, 3-MeO-, and 3-Cl-C$_6$H$_4$OH occurs exclusively at the *ortho* position farthest

from the substituent. Analysis of the reaction mixtures by ^{31}P NMR spectroscopy helped signal complete conversion of the starting materials to the nickelated species (singlet at ca. 190–200 ppm), and established the regioselectivities shown in **Scheme 2.3**. Work-up furnished the new cyclonickelated species 1c-1e as orange solids, which were completely characterized by NMR spectroscopy and single crystal diffraction studies; these results will be presented later, following the discussion of the regioselectivity issues.

Scheme 2.3. Cyclonickelation of 3-substituted and 3,5-disubstituted aryl phosphinites

	R	R'	time (h)	%yield
c:	Me	H	16	67
d:	OMe	H	16	60
e:	Cl	H	40	71
f:	F	F	60	62
g:	Me	Me	60	nr
h:	Cl	Cl	60	nr
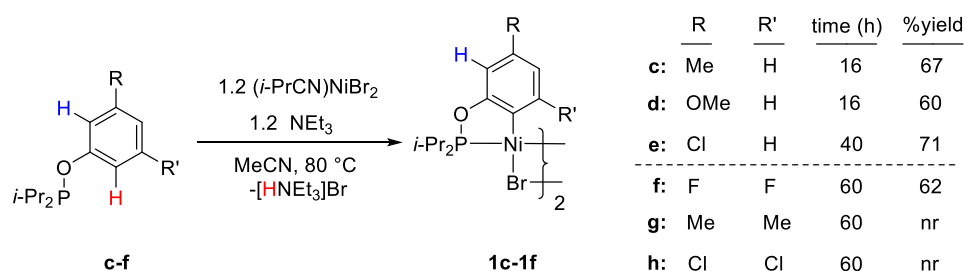
In light of the observation that the C-H nickelation reactions in question are regioselective regardless of the electron-donating or electron-withdrawing nature of the substituents, we conclude that the main determinant of regioselectivity is sterics, not electronics. This would explain why nickelation is regiospecific with substrates **c** and **e** bearing substituents Me and Cl, respectively, which are of opposite electronic properties but very similar van der Waals spherical volumes.[10] Moreover, substrate **b** bearing the smallest non-hydrogen substituent, F, is the only case where the nickelation regioselectivity is less than 100% (6:1).

2.3.3 Cyclonickelation of aryl phosphinites derived from 3,5-disubstituted phenols

In order to establish whether the regioselectivities observed with substrates **b-e** reflect a mere *preference* for the least hindered C-H bond, or whether the sterically hindered C-H bond is simply *inaccessible*, we tested the cyclometalation of the disubstituted substrates 3,5-R$_2$-C$_6$H$_3$OP(i-Pr)$_2$ (R= F (**f**), Me (**g**), Cl (**h**), MeO (**i**)). These tests showed that cyclonickelation occurs with the substrates bearing the smaller substituents F and OMe (**f** in **Scheme 2.3** and **i** in **Scheme 2.4**),10 whereas substrates **g** and **h** bearing the larger Me or Cl substituents did not metalate even after 5 days of heating (**Scheme 2.3**).

The above observations confirm the crucial importance of substituent size on C-H nickelation in our system, and suggest that Me and Cl substituents are beyond the steric limits of cyclonickelation. Another noteworthy insight gained from these tests concerns the rate of nickelation, which was quite rapid with the MeO-bearing substrate **i** and much slower with the F-bearing substrate **f** (16 vs. 60 h for >90% conversion). A similar trend was evident in the nickelation rates of substrates **c** and **d** *vs.* substrate **e** (16 *vs.* 40 h, **Scheme 2.3**). These observations are consistent with the presumed electrophilic nature of the C-H nickelation.8

Finally, tests conducted on substrate **i** showed that steric bulk influences not just regioselectivity of C-H nickelation but also the structure of the resulting cyclonickelated product. As shown in Scheme 4, nickelation of substrate **i** followed by the usual workup failed to give the anticipated μ-Br dimeric species, giving instead the monomeric MeCN adduct **1i-NCMe**. This result raised the question of whether the dimeric structure is altogether inaccessible for this substrate, or is it merely less stable for substrate **i** in comparison to other less bulky substrates. To answer this question, we attempted to drive off the coordinated acetonitrile from the monomeric acetonitrile adduct and generate the putative dimer. However, **1i-NCMe** remained unchanged after heating a toluene solution of it to 60 °C and evaporation to dryness under reduced pressure (**Scheme 2.4**). This observation indicated that the steric hindrance engendered by the two MeO substituents in substrate **i** strongly disfavors dimerization of its cyclonickelated derivative, thus favoring the formation of **1i-NCMe**.

Scheme 2.4. Formation of 1i-NCMe from cyclonickelation of **i**.
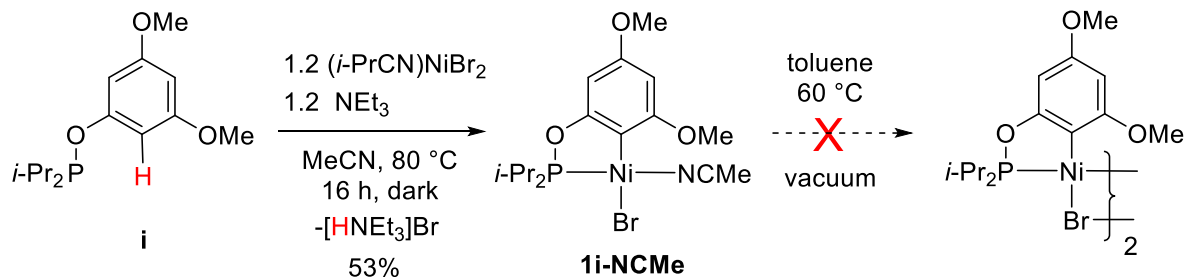
2.3.4 Cyclonickelation of 2-substituted aryl phosphinites

Our investigation of nickelation regioselectivity continued with phosphinites derived from 2-substituted phenols (Scheme 5). We first examined the reaction of $\{(i\text{-PrCN})NiBr_2\}_n$ with phosphinite j (derived from *ortho*-cresol) to test if nickelation at the C_{sp3}-H of the 2-Me substituent might be competitive with the anticipated *ortho*-nickelation at the unsubstituted position. The results confirmed, however, exclusive reactivity at the unsubstituted *ortho*-C-H position. That the outcome of this reaction is not necessarily due to the intrinsically more favorable nickelation of sp^2 vs sp^3 C-H moieties was inferred from the nickelation of phosphinite k (derived from 2-phenylphenol), which also occurred at the unsubstituted *ortho*-C-H position of the main aryl ring and not the sp^2 C-H moiety of the substituent (**Scheme 2.5**).

Scheme 2.5. Cyclonickelation of various mono- or di-ortho-substituted aryl phosphinites

	R	R'	R"	time (h)	%yield
j:	Me	H	H	16	64
k:	Ph	H	H	16	74
l:	Me	Me	Me	60	nr
m:	Ph	Ph	H	60	nr
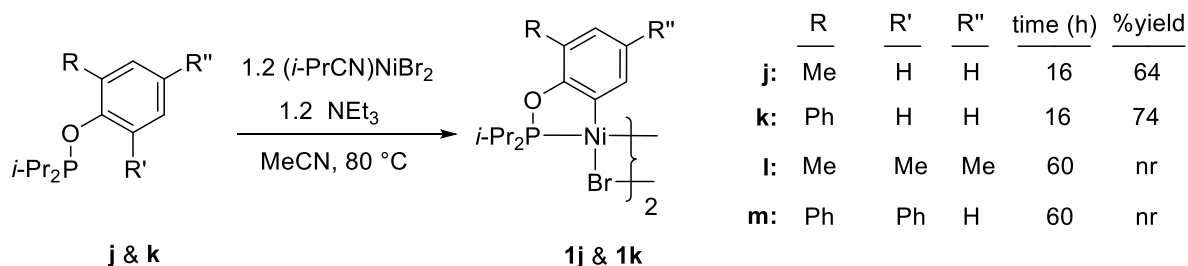
The above-discussed reactivity, i.e., exclusive nickelation at the unsubstituted *ortho*-C-H position of the phenol ring as opposed to the C-H moiety of the methyl or phenyl substituent, is presumably a result of the more favorable energetics of the 5-membered metallacycles that form at the transition state versus the alternative 6- or 7-membered metallacycles. Comparison of these results to related literature reports reveals that the regioselectivity under discussion is a function of the metal precursor; it also depends on whether the substrate ArOH is derivatized or not. For instance, using a Rh(I) pre-catalyst along with $ArOPR_2$ leads to metalation/coupling with aryl halides at the *ortho*-C-H of both the main ring (5-membered metallacycle) and the Ph substituent at the *ortho* position (7-membered metallacycle),[11] whereas metalation/coupling of underivatized 2-aryl phenols with $Pd(OAc)_2/Cs_2CO_3$ as pre-catalyst occurs only at the *ortho*-C-H of the Ph substituent (6-membered metallacycle).[12]

Two other reactions were carried out with ligands bearing substituents at both *ortho* positions to test if nickelation can be forced on a substituent C-H site. Thus, reactions with ligands **l** (derived from 2,4,6-Me$_3$-C$_6$H$_2$OH)[13] and **m** (derived from 2,6-Ph$_2$- C$_6$H$_3$OH) were examined, but neither showed any nickelation even after 5 days of heating. To establish whether this lack of reactivity is due to the inability of these phosphinites to coordinate to the Ni center, we examined the reactivity of the Ni precursor with two equivalents of ligand **m** in the absence of added base. Similarly to what had been observed with all other less hindered phosphinites, no coordination was observed at r.t., but heating the reaction mixture to 80 °C for one hour led to a brownish mixture that showed a new ^{31}P resonance at 134 ppm, which is in a region characteristic of the bis-phosphinite complexes *trans*-(*i*-Pr$_2$POAr)$_2$NiBr$_2$. We conclude that sterically hindered phosphinites can coordinate to Ni(II), at least in the absence of other nucleophiles. This implies in turn that the observed failure to induce C-H nickelation in disubstituted ligands **l** and **m**, even after extended heating, likely reflects the strong energetic preference for transition states leading to formation of 5-membered nickelacycles.

2.3.5 Solid state structures of the new complexes

Solid state structures were determined for 9 new cyclonickelated complexes, of which two are monomeric adducts and 7 dimers. The results of these analyses allowed us to unequivocally establish the identities of all complexes. In the case of complex 1k, resolution of the structural data was problematic due to the twinned crystals obtained;[14] hence, structural discussion in this case will be limited to those features that are established with confidence. The pertinent structural parameters for all complexes are listed in **Table 2.1** and **Tables S2.2─S2.3**, the molecular drawings are shown in **Figures 2─5** and Figures **S2.86─S2.90**, and the main findings are discussed below. Complex **1a-NCMe** (**Figure 2.2**), the mononuclear acetonitrile adduct obtained from cyclonickelation of unsubstituted phosphinite **a**, showed a fairly unremarkable solid state structure in which the largest distortion is the smaller-than-ideal bite angle of the metalated phosphinite moiety (83°). By comparison, relatively major angular distortions were noted in the analogous monomeric adduct **1i-NCMe** obtained from nickelation of the phosphinite derived from 3,5-methoxy-phenol (**Figure 2.2**). Thus, the two *trans* angles are compressed to 166° and 164°, and the C-Ni-N *cis* angle is enlarged to 100°. These non-ideal angles translate into a much more pronounced tetrahedral distortion in **1i-NCMe** vs. **1a-NCMe**, as reflected in τ_4 values of 0.20 and

0.07, respectively.[15] We conclude, therefore, that the presence of a non-hydrogen substituent vicinal to the nickelation site distorts the solid state structure of these complexes.

Table 2.1. Selected structural parameters for dimers and MeCN adducts.[a]

	Ni-C	Ni-P	*trans*-Ni-Br[b]	*cis*-Ni-L[b]	C-Ni-P	Br-Ni-L	Ni-Br-Ni	Ni---Ni	τ_4
1a	1.914(4)	2.095(1)	2.37	2.3641(7)	82	88	92	3.42	0.06
1b	1.911(4)	2.106(1)	2.3736(8)	2.3781(7)	84	87	83	3.16	0.06
1c	1.920(3)	2.0963(7)	2.39	2.3815(5)	82	88	92	3.44	0.04
1d[c]	1.914(2); 1.88(3); 1.95(3)	2.0985(5); 2.0972(5)	2.3803(3); 2.3851(3)	2.3857(3); 2.3875(3)	79; 83; 87	87	76	2.9406(3)	0.05; 0.11; 0.12
1e	1.914(2)	2.0987(7)	2.38	2.3796(5)	82	88	92	3.44	0.04
1f	1.931(2)	2.1017(5)	2.3743(3)	2.39	82	86	94	3.49	0.10
1j	1.911(2)	2.0936(4)	2.3759(3)	2.39	83	87	93	3.44	0.06
1k[d]	1.894(10)— 1.926(10)	2.098(3)— 2.105(3)	2.357(2)— 2.389(2)	2.387(2)— 2.398(2)	81—83	86—87	93—94	3.46— 3.47	0.03— 0.08
1a-NCMe	1.916(2)	2.1018(6)	2.3533(4)	1.913(2)	83	91	-	-	0.07
1i-NCMe	1.932(2)	2.1000(6)	2.3613(4)	1.915(2)	83	91	-	-	0.20

a) The values for angles have been rounded up to the nearest degree. b) Designation of *cis*- and *trans*-Ni-Br bonds is with respect to the Ni-C2 bond. c) In this nonsymmetrical structure, two different values are observed for all parameters except the Ni-C distance and C-Ni-P angle for which three different values are observed due to the presence of disorder in one half of the dimer. d) These ranges represent the bond distances and angles observed in the four molecules present in the asymmetric unit.
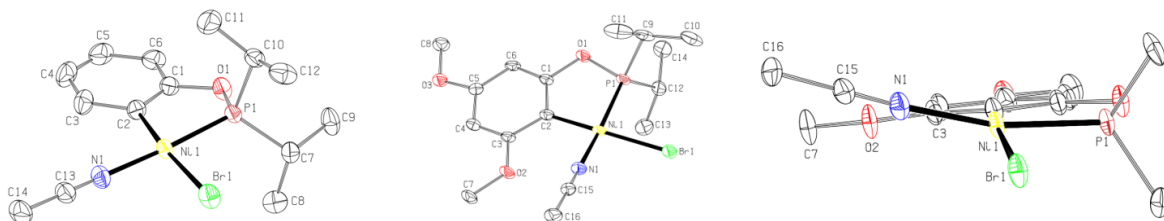
Figure 2.2. Top views of the molecular diagrams for complexes **1a-NCMe** (left) and **1i-NCMe** (middle), and side view for complex **1i-NCMe** (right). Thermal ellipsoids are shown at the 50% probability level. Hydrogen atoms in all diagrams and Me groups in the side view of **1i-NCMe** have been omitted for clarity.

In the crystal structures of the dimeric species **1b-1f**, **1j**, and **1k** (**Figures 2.3─2.5** and **S2.86─S2.90**), both Ni centers adopt nearly ideal square planar geometries, indicating that neither the steric bulk nor the substituent position has any significant bearing on the overall coordination geometry of the dimeric complexes.
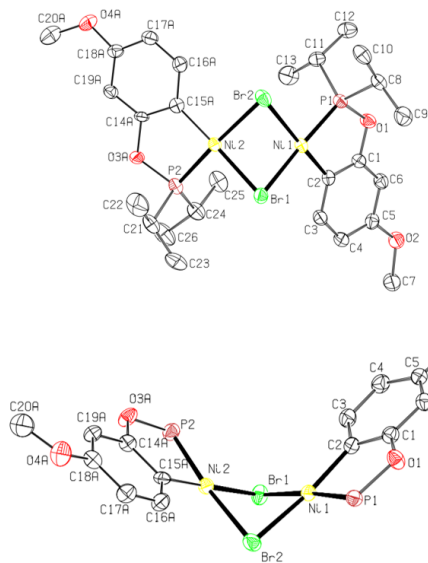
Figure 2.3. Top and side views of the molecular diagram for complex **1d**. Thermal ellipsoids are shown at the 50% probability level; hydrogens in both views and the P-substituents in the side view have been omitted for clarity.
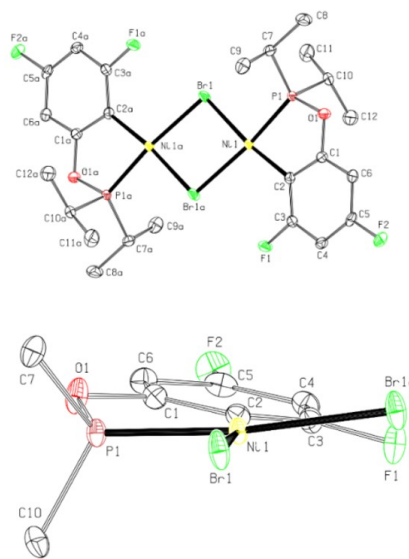
Figure 2.4. Top view of the molecular diagram for complex **1f** and side view for a portion of the dimer. Thermal ellipsoids are shown at the 50% probability level; hydrogens are omitted for clarity. The side view shows the ligands around only one Ni atom.
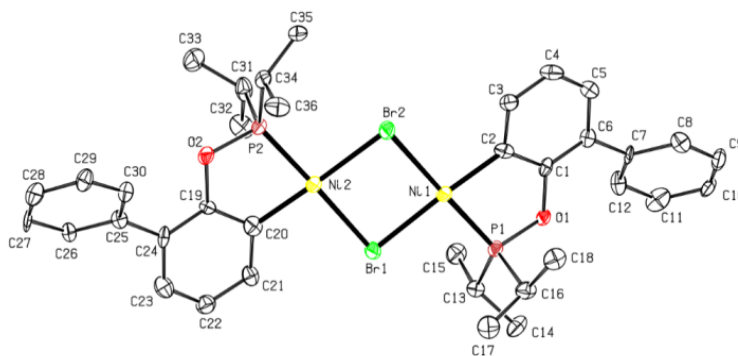
Figure 2.5. Top view of the molecular diagram for complex **1k**. Thermal ellipsoids are shown at the 50% probability level; hydrogens are omitted for clarity.

To be sure, some degree of tetrahedral distortion is evident in all dimeric complexes studied here, but these are fairly insignificant as can be deduced from the small τ_4 values that define these distortions15 (0.03 to 0.12; **Tables 2.1** and **S2.2−S2.3**). It should also be noted here that the presence in **1f** of an F substituent vicinal to the nickelation site causes little distortion ($\tau_4 = 0.102$), whereas major structural distortions are evident in **1i-NCMe** due to the presence of MeO (*vide supra*). This difference is likely a reflection of the smaller van der Waals volume of F compared to that of MeO.

The nature of the substituents also has little or no impact on bond distances found in the dimeric complexes: the values for Ni-P (2.094−2.106 Å), Ni-C (1.911−1.931 Å), and Ni-Br (2.374−2.393 Å) fall within the normal range for related Ni(II) complexes. Comparing these values to the corresponding distances in the related resorcinol-based pincer complexes (R$_n$-POCOP$^{i\text{-}Pr}$)NiBr reveals that the cyclonickelated compounds under discussion here feature somewhat longer distances for Ni-C (1.91 vs 1.89 Å) and Ni-Br(2.36-2.39 vs 2.323 Å), but slightly shorter P-Ni bond distances (2.10 vs 2.142/2.153 Å).[16]

One unexpected and fairly significant structural distortion that was observed in some dimeric complexes regards the relative spatial orientations of the two halves of these molecules. As expected, dimers possessing an inversion center adopt a structure wherein the two halves of the dimer are coplanar, whereas dimers that do not crystallize on an inversion center display various degrees of deviation from co-planarity. The extent of the "bending" of the two halves of the dimers is conveniently quantified by the torsion angles Ni1-μ-Br1-μ-Br2-Ni2 atoms, which would be 180° in a coplanar arrangement (no bending at all). The measured values of this torsion angle ranged from 170−172°[17] in **1k** to 133° in **1b** and 116° in **1d**. One consequence of the "bending" represented by the torsion angles for **1b** and **1d** is a shrinking of the Ni-Br-Ni angle, which is 83° in **1b** and 76° in **1d**, compared to angles of $\geq$ 92° in all coplanar dimers. A potentially even more significant structural consequence of the bending is that it brings the two Ni centers closer to each other; thus, the Ni---Ni distances are 3.16 Å in **1b** and 2.94 Å in **1d**, compared to > 3.4 Å in coplanar dimers. Of course, such shortened distances do not necessarily imply bonding interactions as they are still longer than the sum of covalent radii for two Ni(II) atoms ($\approx$ 2.50 Å)[18], but they are still shorter than the sum of two van der Waals radii ($\approx$ 3.26 Å).

Indeed, such interactions would be rather surprising given that the filled d_{z^2} orbitals in these d^8 centers are expected to favor a conformation that would minimize any orbital interactions. On this basis alone, a coplanar conformation (torsion angle = 180°) would have been optimal in the absence of packing forces. We have probed this phenomenon using DFT calculations to identify the optimal geometries for the dimeric complex **1d** in toluene. All optimizations were carried out using Gaussian 16 with M06 functional method in implicit toluene solvent using the SMD model. The experimentally obtained solid state structure for **1d** was used as the beginning point for the first geometry optimizations; these led to a bent structure featuring Ni---Ni bond distances and torsion angles very similar to those found in the solid state structure (2.75 Å vs. 2.94 Å; 102° vs 116° respectively). The geometry was then allowed to unfold to a structure displaying a coplanar conformation around Ni1-Br1-Br2-Ni2. Optimization of this coplanar geometry led to a local minimum, which was found to be less stable than the bent structure: $\Delta G°_{bending}$ = -6.5 kJ/mol.

DFT optimizations were also applied to **1a**, the parent dimer that crystallizes on an inversion center and hence adopts a coplanar structure in the solid state. In this case, too, the planar structure obtained after initial optimizations appeared to be only a local minimum, because optimizations carried out on starting structures featuring non-coplanar Ni_2Br_2 cores led to a bent geometry that was more stable relative to the coplanar structure: torsion angle of 104°; Ni---Ni bond distance of 2.77 Å; $\Delta G°_{bending}$ = -5.7 kJ/mol.

In order to avoid local minima resulting from the different possible orientations of the *i*-Pr groups in the P(*i*-Pr)$_2$ moieties, further optimizations were carried out on the PMe$_2$ analogues of **1a** and **1d**. As a further measure for ensuring the reliability of our optimization studies, the PMe$_2$ analogue of **1d** was allowed to adopt the three possible conformations due to the two orientations of the MeO substituents observed in the crystal structure of **1d**. (See SI for details of these structures.) In all four cases, optimizations generated bent structures for these PMe$_2$ analogues of **1a** and **1d**, with structural parameters very similar to those seen in the solid state structure of the P(*i*-Pr)$_2$ complexes: torsion angles ≈ 100–103°; Ni---Ni distances ≈ 2.68 - 2.70 Å. As before, freezing the torsion angles at 180° (coplanar structures) during optimization yielded a local minimum for each structure, but these were always less stable than the bent ones by 1.3 - 3.8 kJ·mol^{-1}.

Altogether, the results of our DFT studies imply that this family of dimeric Ni(II) complexes must have an intrinsic preference for adopting non-coplanar conformations. The underlying causes for

this preference for bent conformations cannot be identified at this point. Indeed, it is still unclear whether this tendency is driven by stabilizing interactions between the two d^8 centers, or whether the shortened Ni---Ni distances observed are simply the consequence of the bending, as opposed to being its cause. What seems clear at this point is that no simple correlation exists between the degree of bending and Ni---Ni distances in complexes studied, on the one hand, and the electron-withdrawing or -releasing properties of their ring substituents (3-F, 3-MeO) on the other. This phenomenon will be probed in future investigations.

2.3.6 NMR characterization of the cyclonickelated dimers

All attempts to record informative NMR spectra using $CDCl_3$, CD_2Cl_2, or C_6D_6 solutions of the dimeric complexes resulted in poorly resolved spectra featuring low signal-to-noise ratios. In contrast, CD_3CN solutions gave high-quality spectra that facilitated solution characterization of these complexes. This difference in the spectral quality as a function of solvent nucleophilicity is presumably due to a relatively slow dynamic process occurring in non-nucleophilic solvents (e.g., the flipping up and down of the dimer), whereas complete dissociation of the dimers takes place in acetonitrile to give monomeric acetonitrile adducts that do not experience this fluxionality.[19] To shed some light on this issue, we carried out a computational study to estimate the energy barrier required for the flipping motion of a simplified model (Me_2P instead of i-Pr_2) for the bent dimer **1a**. (See SI for technical details on this study.) The energy barrier obtained for flipping **1a-PMe₂** via a coplanar transition state was only 11.6 kJ/mol, which is easily accessible at room temperature. This result implies that the relatively slow up and down flipping of dimers in solution might well be the cause of the poorly-resolved NMR spectra alluded to above.[20] Regardless of the precise reason(s) for these observations, it should be emphasized that the well-resolved spectra discussed below are those of the monomeric acetonitrile adducts $\{\kappa^P,\kappa^C$-R-ArOP(i-Pr)$_2\}$NiBr(NCCD$_3$) derived from each dimer.

The ^{31}P$\{^1$H$\}$ NMR spectra recorded for the CD_3CN samples of all dimers displayed a singlet resonance at 190-198 ppm. The corresponding ^{1}H NMR spectra were also consistent with the loss of one aromatic proton as a result of nickelation, and featured the characteristic signals for i-Pr protons (two dd for the diastereotopic Me groups, and a pseudo-octuplet for the methyne C-H). For the dimeric complex **1f**, the assignments of the H-P and H-F couplings were facilitated thanks to the selectively decoupled ^{1}H$\{^{31}$P$\}$ and ^{1}H$\{^{19}$F$\}$ spectra (See **Figures 2.6** and **S2.50–S2.52**). Further

evidence for nickelation was also obtained from the $^{13}C\{^1H\}$ NMR spectra featuring doublets at 105 – 130 ppm ($^2J_{CP}$ = 30–40 Hz) and 160–168 ppm ($^2J_{CP}$ = 11–15 Hz) for the nickelated carbon C2 and the O-bearing carbon C1, respectively. In some cases, P-C coupling was also visible for other aromatic carbons, but these showed generally much smaller coupling constants ($^3J_{CP}$ and $^4J_{CP}$ < 5 Hz). The NMR spectra of the CD₃CN solutions of dimers 1b/1b', 1f, and 1k showed particularly intriguing coupling patterns and provided a wealth of information about the various coupling interactions.
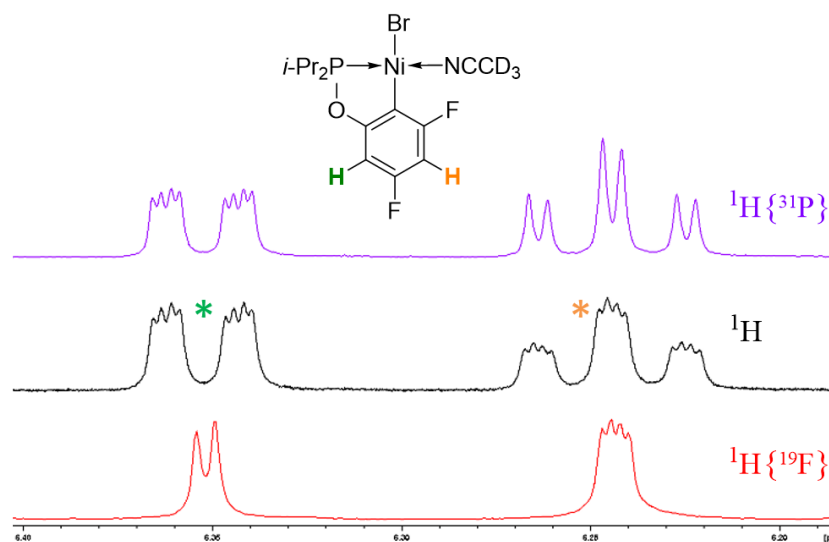
Figure 2.6. Aromatic region of the ^1H, $^1H\{^{19}F\}$, and $^1H\{^{31}P\}$ NMR spectra of **1f**, disclosing J$_{HF}$, J$_{HH}$ and J$_{HP}$ couplings.

For example, the ^{19}F NMR spectrum for the mixture of the two regioisomers **1b** and **1b'** displayed a pseudo-quartet at -118 ppm for the major isomer with *para*-F ($^3J_{HF} \approx {}^4J_{HF} \approx$ 9 Hz) and a doublet of doublets at -95 ppm for the minor isomer with *ortho*-F ($^3J_{HF}$ = 9 Hz, $^4J_{HF}$ = 6 Hz). Correlating these chemical shifts with those of the two ^{19}F resonances found at -116.4 (q, $^3J_{HF} = {}^3J_{H'F} = {}^4J_{FF}$ = 9 Hz) and -93 (t, $^3J_{HF} = {}^4J_{FF}$ = 9 Hz) for dimer **1f** allowed an unambiguous identification of the two F nuclei.

The ^{13}C NMR spectrum of **1f**/NCCD₃ was also quite informative: two ^{13}C doublets of doublets featuring large $^1J_{FC}$ coupling constants (ca. 240 Hz) were readily attributed to the two F-bearing carbon nuclei C5 and C3 (see **Figure S2.53** in SI). However, the doublets in question did not

display any J_{C-P} coupling, which precluded their assignment to the specific nuclei C3 and C5. On the other hand, the data allowed exact assignments for the remaining carbon nuclei of the aromatic ring in 1f. Thus, C2 and C6 showed (**Figure 2.7**) both $^2J_{CP}$ (39 Hz) and $^3J_{CP}$ (13 Hz) as well as $^2J_{CF}$ (36 and 24 Hz, respectively) and even $^4J_{CF}$ coupling constants (3 and 4 Hz, respectively). A ddd ^{13}C resonance at 168 ppm was attributed to C1 ($^3J_{CF} = 25$ Hz; $^3J_{CF'} = 14$ Hz; $^2J_{CP} = 11$ Hz), while another ddd was observed for C4 and attributed to two different $^2J_{CF}$ couplings: 36 and 25 Hz. Finally, it is noteworthy that we observe P-C6 coupling but no P-H6 coupling, whereas the opposite is the case for C4, i.e., we observe P-H4 coupling but no P-C4 coupling.
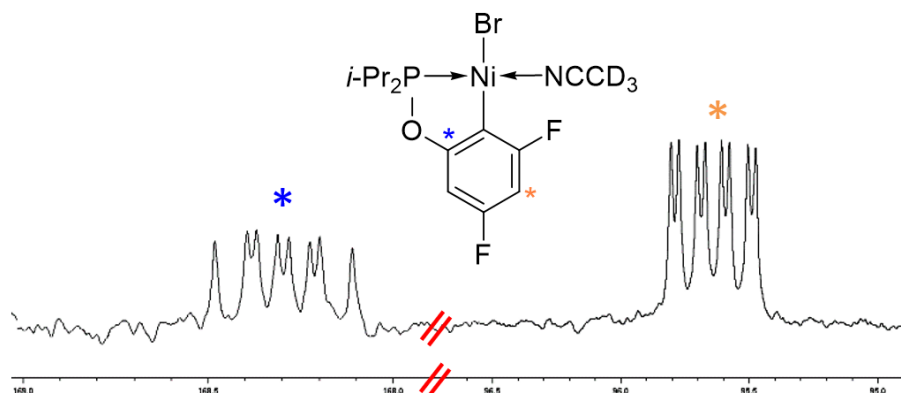
Figure 2.7. Selected regions in the ^{13}C{^{1}H} NMR of 1f displaying J_{CF} and J_{CP} couplings.

2.4 Conclusions

The following are the main findings of this study with respect to C-H nickelation regioselectivity: (a) the aryl phosphinites i-Pr$_2$POAr undergo C-H nickelation when heated in acetonitrile solutions containing the nickel precursor [(i-PrCN)NiBr$_2$]$_n$ and NEt$_3$, giving the acetonitrile adducts $trans$-{ κ^P,κ^C-ArOP(i-Pr)$_2$}Ni(NCMe)Br that upon work-up yield the dimeric species { κ^P,κ^C-ArOP(i-Pr)$_2$}$_2$Ni$_2$Br$_2$ for every substrate tested except that with Ar= 3,5-(OMe)$_2$-C$_6$H$_3$ that gave the acetonitrile adduct { κ^P,κ^C-3,5-(OMe)$_2$-C$_6$H$_3$ OP(i-Pr)$_2$}NiBr(NCMe); (b) the C-H nickelation of all but one of the phosphinites derived from 3-R-C$_6$H$_4$OH occurs regioselectively at the less hindered $ortho$ position, the only exception being observed with substrate (3-F-C$_6$H$_4$O)P(i-Pr)$_2$ that gives a 6:1 mixture of regioisomers (major one nickelated at the less hindered $ortho$ position); (c) the C-H nickelation of both phosphinites derived from 2-R-CH$_4$OH (R= Me, Ph) also occurs

regioselectively at the only available *ortho* C-H of the phenol ring, not at the substituent C-H moiety; (d) no C-H nickelation occurs with the disubstituted phosphinites derived from 2,6-R_2-C_6H_3OH (R= Me, Ph), whereas for those derived from 3,5-R_2-C_6H_3OH C-H nickelation was possible with R= F or OMe but not Me or Cl.

The above results indicate that the reactivity with 3-substituted is highly sensitive to the steric size of the phenol substituent(s), nickelation occurring exclusively or preferentially at the less congested site, whereas C-H nickelation with the 3,5-disubstituted substrates is altogether inaccessible with the substituents Me and Cl. Another important factor is the size of the resulting nickelacycles: the greater preference for a 5-membered nickelacycle precludes nickelation at the phenol substituent C-H sites in 2-substituted and 2,6-disubstitued substrates.

Other interesting findings of this study include the confirmation of a previously noted observation that C-H nickelation of these substrates occurs more readily with electron-rich substrates (R = Me, OMe), and also the observation that the dimers adopt more stable bent conformations and they break apart into monomeric adducts in the presence of acetonitrile. This latter reactivity should open the way to potentially interesting functionalization pathways, which we intend to explore. Our future studies will also focus on elucidating the mechanism of C-H nickelation.

2.5 Experimental section

General considerations. All manipulations were carried out under a nitrogen atmosphere using standard Schlenk techniques and an inert-atmosphere box. The solvents were dried by passage over a column of activated alumina, collected under nitrogen, and stored over 4 Å molecular sieves. Triethylamine was dried over CaH_2. Synthesis of the nickel precursor $\{(i\text{-PrCN})NiBr_2\}_n$ used throughout this study has been described previously.[21] 3,5-dichlorophenol was synthesized from demethylation of 3,5-dichloroanisole in refluxing 48 % aq. HBr. All other reagents were purchased from Sigma-Aldrich and used without further purification.

Unless otherwise specified, all 1D NMR spectra were recorded at 500 MHz (^{1}H), 125.72 MHz (^{13}C), 202.4 MHz (^{31}P) and 470.4 MHz (^{19}F), whereas the HSQC experiments were recorded at 400 MHz (^{1}H) and 100.6 MHz (^{13}C). Chemical shift values are reported in ppm (δ) and referenced internally to the residual solvent signals (^{1}H and ^{13}C: 1.94 and 118.26 ppm for C*H*D$_2$C*N*) or externally (^{31}P, H_3PO_4 in D_2O, $\delta = 0$; ^{19}F, $CFCl_3$, $\delta = 0$). The values for *J* coupling are given in Hz.

The NMR data obtained for CD$_3$CN solutions of the dimeric complexes correspond to the corresponding monomeric NCCD$_3$ adducts.

General procedure for the synthesis of cyclonickelated phosphinite dimers. To a solution of ArOH (2.00 mmol) in 20 mL dry THF was added Et$_3$N (2.20 mmol, 307 μL, 1.10 equiv) and then ClP(i-Pr)$_2$ (2.10 mmol, 334 μL, 1.05 equiv) after which salt precipitation started. The mixture was stirred at room temperature until the reaction was complete (from 0.5 to 20 h, as monitored by ^{31}P NMR). The solvent was removed under vacuum, the residues extracted with Et$_2$O (3x15 mL), and evaporated to yield a colorless to pale yellow oil. To the latter was added dry MeCN (20 mL), {(i-PrCN)NiBr$_2$}$_n$ (2.40 mmol, 691 mg, 1.2 equiv), and Et$_3$N (2.40 mmol, 335 μL, 1.2 equiv). The resulting green to brownish-green homogeneous mixture was stirred at 80 °C until the reaction was complete (monitored by the disappearance of the starting material ^{31}P signal at 135 ppm). The solvent was then removed under vacuum and the residues were extracted with toluene by filtration through Celite®. The toluene was removed under vacuum and the residues (deliquescent solids or dark orange pasty products) were dissolved in a minimum of Et$_2$O, precipitated with hexanes, filtered off and the solids washed with a minimum of hexanes to complete removal of impurities. The remaining solid was dried under vacuum to yield a bright to dull orange powder. Single crystals were obtained by slow evaporation of an Et$_2$O solution kept under N$_2$.

[{κ^P,κ^C-(i-Pr)$_2$PO-C$_6$H$_4$}Ni(μ-Br)]$_2$ (1a). This compound has been synthesized previously via a different procedure.[6] The revised general procedure described above was applied on a 5.00 mmol scale in MeCN over 16 h at 80 °C. Yield of the bright orange powder obtained: 1.514 g (2.17 mmol, 87 %). The NMR spectroscopic data in CD$_3$CN confirmed the identity of the compound. ^{1}H NMR (500 MHz, 20 °C, CD$_3$CN): δ 1.31 (dd, 6H, CH(CH_3)(CH$_3$), $^3J_{HH}$ = 7.0, $^3J_{HP}$ = 14.9), 1.46 (dd, 6H, CH(CH$_3$)(CH_3), $^3J_{HH}$ = 7.2, $^3J_{HP}$ = 17.5), 2.44 (oct, 2H, CH(CH$_3$)$_2$, $^3J_{HH} \approx {}^2J_{HP}$ = 7.1), 6.63 (dd, 1H, C6$_{Ar}$-H, $^3J_{HH}$ = 7.9, $^4J_{HH}$ = 1.3), 6.68 (tt, 1H, C4$_{Ar}$-H, $^3J_{HH}$ = 7.4, $^4J_{HH} \approx {}^5J_{HP}$ = 1.1), 6.98 (tm, 1H, C5$_{Ar}$-H, $^3J_{HH}$ = 7.5, $^4J_{HH}$ = 1.4), 7.16 (dt, 1H, C3$_{Ar}$-H, $^3J_{HH}$ = 7.6, $^4J_{HH} \approx {}^4J_{HP}$ = 1.4). ^{13}C{^{1}H} NMR (125.7 MHz, 20 °C, CD$_3$CN): δ 16.88 (d, 2C, CH(CH_3)(CH$_3$), $^2J_{CP}$ = 1.9), 18.50 (d, 2C, CH(CH$_3$)(CH$_3$), $^2J_{CP}$ = 2.7), 29.07 (d, 2C, CH(CH$_3$)(CH$_3$), $^1J_{CP}$ = 29.0), 110.60 (d, 1C, $C6_{Ar}$-H, $^3J_{CP}$ = 13.2), 121.43 (d, 1C, $C4_{Ar}$-H, $^4J_{CP}$ = 2.0), 127.56 (s, 1C, $C5_{Ar}$-H), 133.78 (d, 1C, $C2_{Ar}$-Ni, $^2J_{CP}$ = 33.9), 139.11 (d, 1C, $C3_{Ar}$-H, $^3J_{CP}$ = 2.6), 167.66 (d, 1C, $C1_{Ar}$-OP, $^2J_{CP}$ = 11.9). ^{31}P{^{1}H} NMR (202.4 MHz, 20 °C, CD$_3$CN): δ 196.21 (s, 1P).

[{κ^P,κ^C-(*i*-Pr)$_2$PO-(5-F-C$_6$H$_3$)}Ni(μ-Br)]$_2$ (1b) and κ^P,κ^C-(*i*-Pr)$_2$PO-(3-F-C$_6$H$_3$)Ni(μ-Br)]$_2$ (1b'). Applying the general procedure given above (at 80 °C for 36 h) gave a bright orange powder. Yield: 382 mg (0.522 mmol). This solid was shown by ^{31}P{^{1}H} and ^{19}F NMR spectra to contain the two isomers **1b** (major, metalated *para* to F) and **1b'** (minor, metalated *ortho* to F) in a 6.5 : 1 ratio. Spectroscopic data for **1b** :^{1}H NMR (500 MHz, 20 °C, CD$_3$CN): δ 1.30 (dd, 6H, CH(C*H*$_3$)(CH$_3$), $^3J_{HH}$ = 7.2, $^3J_{HP}$ = 15.1), 1.46 (dd, 6H, CH(CH$_3$)(C*H*$_3$), $^3J_{HH}$ = 7.2, $^3J_{HP}$ = 17.6), 2.44 (oct, 2H, C*H*(CH$_3$)$_2$, $^3J_{HH} \approx {}^2J_{HP}$ = 7.2), 6.45 (dd, 1H, C6$_{Ar}$-*H*, $^3J_{HF}$ = 10.2, $^4J_{HH}$ = 2.6), 6.48 (tdd, 1H, C4$_{Ar}$-*H*, $^3J_{HH} \approx {}^3J_{HF}$ = 9.4, $^4J_{HH}$ = 2.7, $^5J_{HP}$ = 0.9), 7.11 (tm, 1H, C3$_{Ar}$-*H*, $^3J_{HH} \approx {}^4J_{HF}$ = 7.3, $^4J_{HP}$ = 0.8). ^{13}C{^{1}H} NMR (125.7 MHz, 20 °C, CD$_3$CN): δ 18.04 (d, 2C, CH(*C*H$_3$)(CH$_3$), $^2J_{CP}$ = 1.9), 18.65 (d, 2C, CH(CH$_3$)(*C*H$_3$), $^2J_{CP}$ = 2.7), 29.34 (d, 2C, *C*H(CH$_3$)(CH$_3$), $^1J_{CP}$ = 29.0), 98.89 (dd, 1C, *C6*$_{Ar}$-H, $^2J_{CF}$ = 24.7, $^3J_{CP}$ = 13.9), 108.01 (dd, 1C, *C4*$_{Ar}$-H, $^2J_{CF}$ = 19.6, $^4J_{CP}$ = 1.7), 128.20 (d, 1C, *C2*$_{Ar}$-Ni, $^2J_{CP}$ = 34.2), 139.60 (dd, 1C, *C3*$_{Ar}$-H, $^3J_{CF}$ = 8.5, $^3J_{CP}$ = 3.1), 163.53 (d, 1C, *C5*$_{Ar}$-F, $^2J_{CF}$ = 240.8), 167.84 (dd, 1C, *C1*$_{Ar}$-OP, $^3J_{CF}$ = 13.2, $^2J_{CP}$ = 11.2). ^{31}P{^{1}H} NMR (202.4 MHz, 20 °C, CD$_3$CN): δ 197.72 (s, 1P). ^{19}F NMR (470.4 MHz, 20 °C, CD$_3$CN): δ -118.39 (q, 1F, C5$_{Ar}$-F, $^3J_{HF} \approx {}^4J_{HF}$ = 9.4). Spectroscopic data for **1b'** : ^{1}H NMR (500 MHz, 20 °C, CD$_3$CN): δ 1.30 (dd, 6H, CH(C*H*$_3$)(CH$_3$), $^3J_{HH}$ = 7.2, $^3J_{HP}$ = 15.1), 1.47 (dd, 6H, CH(CH$_3$)(C*H*$_3$), $^3J_{HH}$ = 7.1, $^3J_{HP}$ = 17.7), 2.44 (oct, 2H, C*H*(CH$_3$)$_2$, $^3J_{HH} \approx {}^2J_{HP}$ = 7.2), 6.38 (1H, tm, C4$_{Ar}$-*H*, $^3J_{HH} \approx {}^3J_{HF}$= 8.5, $^4J_{HH}$ = 1.1), 6.51 (1H, dd, C6$_{Ar}$-*H*, $^3J_{HH}$ = 7.9, $^4J_{HH}$ = 1.1), 6.98 (1H, qm, C5$_{Ar}$-*H*, $^3J_{HH}$ = 7.9, $^4J_{HF}$ = 6.2, $^5J_{HP}$ = 1.1). ^{13}C{^{1}H} NMR (125.7 MHz, 20 °C, CD$_3$CN): δ 18.09 (d, 2C, CH(*C*H$_3$)(CH$_3$), $^2J_{CP}$ = 2.2), 18.78 (d, 2C, CH(CH$_3$)(*C*H$_3$), $^2J_{CP}$ = 2.2), 29.75 (d, 2C, *C*H(CH$_3$)(CH$_3$), $^1J_{CP}$ = 30.0), 107.40 (dd, 1C, *C6*$_{Ar}$-H, $^3J_{CP}$ = 12.2, $^4J_{CF}$ = 2.6), 109.24 (dd, 1C, *C4*$_{Ar}$-H, $^3J_{CF}$ = 29.7, $^4J_{CP}$ = 1.4), 128.91 (d, 1C, *C5*$_{Ar}$-H, $^3J_{CF}$ = 10.2), 168.82 (m, 1C, *C1*$_{Ar}$-OP), 171.68 (d, 1C, *C3*$_{Ar}$-F, $^1J_{CF}$ = 238.8), *C2*$_{Ar}$-Ni was not detected. ^{31}P{^{1}H} NMR (202.4 MHz, 20 °C, CD$_3$CN): δ 192.04 (s, 1P). ^{19}F NMR (470.4 MHz, 20 °C, CD$_3$CN): δ -95.55 (dd, 1F, C3$_{Ar}$-F, $^3J_{HF}$ = 9.3, $^4J_{HF}$ = 6.2). Anal. Calc. for C$_{24}$H$_{34}$F$_2$O$_2$P$_2$Ni$_2$Br$_2$: C, 39.40; H, 4.68. Found: C, 38.61; H, 4.86; N, 0.24. The elemental analysis performed on the powder shows an excess of carbon contents, likely due to residual solvent which we were not able to remove, even after extended heating under vacuum.

[{κ^P,κ^C-(*i*-Pr)$_2$PO-(5-Me-C$_6$H$_3$)}Ni(μ-Br)]$_2$ (1c). Applying the general procedure given above (at 80 °C for 16 h) gave a dull orange powder. Yield: 487 mg (0.673 mmol, 67%). ^{1}H NMR (500 MHz, 20 °C, CD$_3$CN): δ 1.29 (dd, 6H, CH(C*H*$_3$)(CH$_3$), $^3J_{HH}$ = 7.0, $^3J_{HP}$ = 14.9), 1.45 (dd, 6H, CH(CH$_3$)(C*H*$_3$), $^3J_{HH}$ = 7.2, $^3J_{HP}$ = 17.5), 2.19 (s, 3H, Ar-C*H*$_3$), 2.42 (oct, 2H, C*H*(CH$_3$)$_2$, $^3J_{HH} \approx$

$^2J_{HP}$ = 7.2), 6.49 (s, 1H, C6$_{Ar}$-*H*), 6.52 (d, 1H, C4$_{Ar}$-*H*, $^3J_{HH}$ = 7.8), 7.01 (d, 1H, C3$_{Ar}$-*H*, $^3J_{HH}$ = 7.8), ^{13}C{^{1}H} NMR (125.7 MHz, 20 °C, CD$_3$CN): δ 17.75 (d, 2C, CH(*C*H$_3$)(CH$_3$), $^2J_{CP}$ = 1.8), 18.37 (d, 2C, CH(CH$_3$)(*C*H$_3$), $^2J_{CP}$ = 2.8), 20.46 (s, 1C, Ar-*C*H$_3$), 28.87 (d, 2C, *C*H(CH$_3$)(CH$_3$), $^1J_{CP}$ = 29.0), 111.28 (d, 1C, *C6*$_{Ar}$-H, $^3J_{CP}$ = 13.2), 122.24 (d, 1C, C4$_{Ar}$-H, $^4J_{CP}$ = 1.8), 129.33 (d, 1C, *C2*$_{Ar}$-Ni, $^2J_{CP}$ = 34.4), 137.59 (s, 1C, *C5*$_{Ar}$-Me), 138.64 (d, 1C, *C3*$_{Ar}$-H, $^3J_{CP}$ = 2.7), 167.50 (d, 1C, *C1*$_{Ar}$-OP), $^2J_{CP}$ = 12.3). ^{31}P{^{1}H} NMR (202.4 MHz, 20 °C, CD$_3$CN): δ 195.79 (s, 1P). Anal. Calc. for C$_{26}$H$_{40}$O$_2$P$_2$Ni$_2$Br$_2$: C, 43.15; H, 5.57. Found: C, 42.88; H, 5.69; N, 0.03.

[{κ^P,κ^C-(*i*-Pr)$_2$PO-(5-MeO-C$_6$H$_3$)}Ni(μ-Br)]$_2$ (1d). Applying the general procedure given above (at 80 °C for 16 h) gave a dull orange powder. Yield: 452 mg (0.598 mmol, 60%). ^{1}H NMR (500 MHz, 20 °C, CD$_3$CN): δ 1.30 (dd, 6H, CH(C*H*$_3$)(CH$_3$), $^3J_{HH}$ = 7.1, $^3J_{HP}$ = 14.9), 1.45 (dd, 6H, CH(CH$_3$)(C*H*$_3$), $^3J_{HH}$ = 7.2, $^3J_{HP}$ = 17.5), 2.42 (oct, 2H, C*H*(CH$_3$)$_2$, $^3J_{HH}$ ≈ $^2J_{HP}$ = 7.2), 3.69 (s, 3H, Ar-OC*H*$_3$), 6.28 (d, 1H, C6$_{Ar}$-*H*, $^4J_{HH}$ = 2.6), 6.31 (ddd, 1H, C4$_{Ar}$-*H*, $^3J_{HH}$ = 8.5, $^4J_{HH}$ = 2.6, $^5J_{HP}$ = 0.9), 7.00 (dd, 1H, C3$_{Ar}$-*H*, $^3J_{HH}$ = 8.5, $^4J_{HH}$ = 1.0). ^{13}C{^{1}H} NMR (125.7 MHz, 20 °C, CD$_3$CN): δ 16.85 (d, 2C, CH(*C*H$_3$)(CH$_3$), $^2J_{CP}$ = 2.0), 18.47 (d, 2C, CH(CH$_3$)(*C*H$_3$), $^2J_{CP}$ = 2.8), 28.98 (d, 2C, *C*H(CH$_3$)(CH$_3$), $^1J_{CP}$ = 28.8), 55.45 (s, 1C, Ar-O*C*H$_3$), 97.42 (d, 1C, *C6*$_{Ar}$-H, $^3J_{CP}$ = 14.0), 107.28 (d, 1C, *C4*$_{Ar}$-H, $^4J_{CP}$ = 1.7), 122.96 (d, 1C, *C2*$_{Ar}$-Ni, $^2J_{CP}$ = 35.5), 139.03 (d, 1C, *C3*$_{Ar}$-H, $^3J_{CP}$ = 3.0), 160.59 (s, 1C, *C5*$_{Ar}$-OCH$_3$), 168.04 (d, 1C, *C1*$_{Ar}$-OP, $^2J_{CP}$ = 13.4). ^{31}P{^{1}H} NMR (202.4 MHz, 20 °C, CD$_3$CN): δ 196.07 (s, 1P). Anal. Calc. for C$_{26}$H$_{40}$O$_4$P$_2$Ni$_2$Br$_2$: C, 41.32; H, 5.34. Found: C, 41.09; H, 5.44; N, 0.05.

[{κ^P,κ^C-(*i*-Pr)$_2$PO-(5-Cl-C$_6$H$_3$)}Ni(μ-Br)]$_2$ (1e). Applying the general procedure given above (at 80 °C for 60 h) gave a dull orange powder. Yield: 542 mg (0.709 mmol, 71%). ^{1}H NMR (500 MHz, 20 °C, CD$_3$CN): δ 1.31 (dd, 6H, CH(C*H*$_3$)(CH$_3$), $^3J_{HH}$ = 7.0, $^3J_{HP}$ = 15.2), 1.46 (dd, 6H, CH(CH$_3$)(C*H*$_3$), $^3J_{HH}$ = 7.2, $^3J_{HP}$ = 17.6), 2.45 (oct, 2H, C*H*(CH$_3$)$_2$, $^3J_{HH}$ ≈ $^2J_{HP}$ = 7.2), 6.69 (s, 1H, C6$_{Ar}$-*H*), 6.70 (ddd, 1H, C3$_{Ar}$-*H*, $^3J_{HH}$ = 8.0, $^4J_{HP}$ = 2.1, , $^5J_{HH}$ = 1.0), 7.12 (dd, 1H, C4$_{Ar}$-*H*, $^3J_{HH}$ = 8.0, $^5J_{HP}$ = 1.0). ^{13}C{^{1}H} NMR (125.7 MHz, 20 °C, CD$_3$CN): δ 16.39 (d, 2C, CH(*C*H$_3$)(CH$_3$), $^2J_{CP}$ = 1.9), 18.00 (d, 2C, CH(CH$_3$)(*C*H$_3$), $^2J_{CP}$ = 2.7), 28.73 (d, 2C, *C*H(CH$_3$)(CH$_3$), $^1J_{CP}$ = 28.8), 110.44 (d, 1C, *C6*$_{Ar}$-H, $^3J_{CP}$ = 13.5), 120.66 (d, 1C, *C3*$_{Ar}$-H, $^3J_{CP}$ = 1.6), 131.74 (s, 1C, *C5*$_{Ar}$-Cl), 132.09 (d, 1C, *C2*$_{Ar}$-Ni, $^2J_{CP}$ = 34.2), 139.43 (d, 1C, *C4*$_{Ar}$-H, $^4J_{CP}$ = 2.7), 167.35 (d, 1C, *C1*$_{Ar}$-OP, $^2J_{CP}$ = 12.8). ^{31}P{^{1}H} NMR (202.4 MHz, 20 °C, CD$_3$CN): δ 198.12 (s, 1P). Anal. Calc. for C$_{24}$H$_{34}$O$_2$P$_2$Cl$_2$Ni$_2$Br$_2$: C, 37.70; H, 4.48. Found: C, 37.38; H, 4.56, N, 0.18.

[{κ^P,κ^C-(*i*-Pr)₂PO-(3,5-F₂-C₆H₂)}Ni(μ-Br)]₂ (1f). Applying the general procedure given above (at 80 °C for 80 h) gave a deep orange powder. Yield: 475 mg (0.618 mmol, 62%). ¹H NMR (500 MHz, 20 °C, CD₃CN): δ 1.31 (dd, 6H, CH(CH_3)(CH₃), ³J_{HH} = 7.1, ³J_{HP} = 15.4), 1.48 (dd, 6H, CH(CH₃)(CH_3), ³J_{HH} = 7.1, ³J_{HP} = 17.6), 2.45 (oct, 2H, CH(CH₃)₂, ³J_{HH} ≈ ²J_{HP} = 7.1), 6.24 (tdd, 1H, C4$_{Ar}$-H, ³J_{HF} = ³$J_{HF'}$ = 9.9, ⁴J_{HH} = 2.5, ⁵J_{HP} = 1.1), 6.35 (ddd, 1H, C6$_{Ar}$-H, ³J_{HF} = 9.6, ⁴J_{HH} = 2.4, ⁵J_{HF} = 1.1). ¹³C{¹H} NMR (125.7 MHz, 20 °C, CD₃CN): δ 16.82 (d, 2C, CH(CH_3)(CH₃), ²J_{CP} = 2.4), 18.52 (d, 2C, CH(CH₃)(CH_3), ²J_{CP} = 2.2), 29.58 (d, 2C, CH(CH₃)(CH₃), ¹J_{CP} = 29.8), 95.64 (ddd, 1C, $C6_{Ar}$-H, ²J_{CF} = 24.7, ³J_{CP} = 13.0, ⁴$J_{CF'}$ = 3.9), 97.16 (dd, 1C, $C4_{Ar}$-H, ²J_{CF} = 36.0, ²$J_{CF'}$ = 25.0), 112.53 (ddd, 1C, $C2_{Ar}$-Ni, ²J_{CP} = 39.4, ²J_{CF} = 36.2, ⁴$J_{CF'}$ = 3.3), 163.13 (dd, 1C, $C3_{Ar}$-F or $C5_{Ar}$-F, ¹J_{CF} =240.7, ³J_{CF} = 15.6), 168.29 (ddd, 1C, $C1_{Ar}$-OP, ³J_{CF} = 25.3, ³$J_{CF'}$ = 14.3, ²J_{CP} = 10.9), 171.05 (dd, 1C, $C3_{Ar}$-F or $C5_{Ar}$-F, ¹J_{CF} = 239.7, ³J_{CF} = 14.2). ³¹P{¹H} NMR (202.4 MHz, 20 °C, CD₃CN): δ 193.52 (s, 1P). ¹⁹F NMR (470.4 MHz, 20 °C, CD₃CN): δ -116.38 (q, 1F, C5$_{Ar}$-F, ³J_{HF} ≈ ³$J_{H'F}$ ≈ ⁴J_{FF} = 9.0), -92.62 (t, C3$_{Ar}$-F, ³J_{HF} ≈ ⁴J_{FF} = 9.0). Anal. Calc. for C₂₄H₃₂O₂P₂F₄Ni₂Br₂: C, 37.55; H, 4.20. Found: C, 37.75; H, 4.01; N, 0.07.

{κ^P,κ^C-(*i*-Pr)₂PO-(3,5-(MeO)₂-C₆H₂)}NiBr(NCMe) (1i-NCMe). The general procedure given above was applied at 70 °C for 16 h gave a dull orange powder. It is important to emphasize that these reaction mixtures were protected from ambient light with aluminum foil during the reaction and during the extraction. Failure to keep out ambient light at all moment, including during work-up, hindered the cyclonickelation reaction. Yield: 480 mg (1.07 mmol, 53%). ¹H NMR (500 MHz, 20 °C, CD₃CN): δ 1.27 (dd, 6H, CH(CH_3)(CH₃), ³J_{HH} = 7.1, ³J_{HP} = 14.9), 1.47 (dd, 6H, CH(CH₃)(CH_3), ³J_{HH} = 7.3, ³J_{HP} = 17.4), 1.96 (s, 3H, free CH_3CN), 2.38 (oct, 2H, CH(CH₃)₂, ³J_{HH} ≈ ²J_{HP} = 7.2), 3.67 (s, 1H, ArO-CH_3), 3.69 (s, 1H, ArO-CH_3), 5.90 (m, 1H, C4$_{Ar}$-H), 5.97 (d, 1H, C6$_{Ar}$-H, ⁴J_{HH} = 2.3 Hz). ¹³C{¹H} NMR (125.7 MHz, 20 °C, CD₃CN): δ 16.60 (d, 2C, CH(CH_3)(CH₃), ²J_{CP} = 2.2), 18.28 (d, 2C, CH(CH₃)(CH_3), ²J_{CP} = 2.4), 29.00 (d, 2C, CH(CH₃)(CH₃), ¹J_{CP} = 29.2), 55.14 (s, 1C, ArO-CH₃), 55.49 (s, 1C, ArO-CH₃), 90.17 (d, 1C, $C6_{Ar}$-H, J_{CP} = 13.3), 92.58 (s, 1C, $C4_{Ar}$-H), 107.98 (d, 1C, $C2_{Ar}$-Ni, ²J_{CP} = 38.4), 161.12 (s, 1C, $C5_{Ar}$-OMe), 167.24 (d, 1C, $C1_{Ar}$-OP, ²J_{CP} = 11.3), 168.22 (d, 1C, $C3_{Ar}$-OMe, ³J_{CP} = 2.0). ³¹P{¹H} NMR (202.4 MHz, 20 °C, CD₃CN): δ 189.97 (s, 1P). Anal. Calc. for C₂₆H₄₀O₂P₂Ni₂Br₂: C, 42.81; H, 5.61; N, 3.12. Found: C, 41.39; H, 5.55; N, 1.69. The lower C- and N-contents of this sample indicate some contamination of the title compound. We have used careful NMR analysis of various samples to rule out the possibility of contamination by the phosphinite adduct **1i-L** or the

anticipated dimer. On the other hand, we have noted that this compound appears to be light-sensitive, which might explain the presence of impurities; unfortunately, we have not been able to identify the process of the side-products it might generate.

[{κ^P,κ^C-(i-Pr)$_2$PO-(6-Me-C$_6$H$_3$)}Ni(μ-Br)]$_2$ (1j). Applying the general procedure given above (at 80 °C for 16 h) gave a dull yellowish-orange powder. Yield: 465 mg (0.642 mmol, 64%). ^{1}H NMR (500 MHz, 20 °C, CD$_3$CN): δ 1.32 (dd, 6H, CH(CH_3)(CH$_3$), $^3J_{HH}$ = 7.0, $^3J_{HP}$ = 14.6), 1.35 (dd, 6H, CH(CH$_3$)(CH_3), $^3J_{HH}$ = 7.2, $^3J_{HP}$ = 17.5), 2.14 (s, 3H, Ar-CH_3), 2.45 (oct, 2H, CH(CH$_3$)$_2$, $^3J_{HH}$ ≈ $^2J_{HP}$ = 7.1), 6.58 (t, 1H, C4$_{Ar}$-H, $^3J_{HH}$ = 7.3), 6.82 (d, 1H, C5$_{Ar}$-H, $^3J_{HH}$ = 7.3), 6.97 (d, 1H, C3$_{Ar}$-H, $^3J_{HH}$ = 7.6). ^{13}C{^{1}H} NMR (125.7 MHz, 20 °C, CD$_3$CN): δ 16.05 (m, 2C, CH(CH_3)(CH$_3$) + Ar-CH_3), 17.79 (d, 2C, CH(CH$_3$)(CH_3), $^2J_{CP}$ = 2.7), 28.27 (d, 2C, CH(CH$_3$)(CH$_3$), $^1J_{CP}$ = 29.2), 119.82 (d, 1C, $C6_{Ar}$-Me, $^4J_{CP}$ = 12.5), 120.82 (d, 1C, $C4_{Ar}$-H, $^4J_{CP}$ = 2.1), 128.01 (s, 1C, $C5_{Ar}$-H), 132.52 (d, 1C, $C2_{Ar}$-Ni, $^2J_{CP}$ = 34.1), 135.80 (d, 1C, $C3_{Ar}$-H, $^4J_{CP}$ = 2.5), 165.10 (d, 1C, $C1_{Ar}$-OP, $^3J_{CP}$ = 12.1). ^{31}P{^{1}H} NMR (202.4 MHz, 20 °C, CD$_3$CN): δ 193.78 (s, 1P). Anal. Calc. for C$_{26}$H$_{40}$O$_2$P$_2$Ni$_2$Br$_2$: C, 43.15; H, 5.57. Found: C, 42.75; H, 5.51; N, 0.06.

[{κ^P,κ^C-(i-Pr)$_2$PO-(6-Ph-C$_6$H$_3$)}Ni(μ-Br)]$_2$ (1k). Applying the general procedure given above (at 80 °C for 16 h) gave a dull yellowish-orange powder. Yield: 625 mg (0.737 mmol, 74%). ^{1}H NMR (500 MHz, 20 °C, CD$_3$CN): δ 1.26 (dd, 6H, CH(CH_3)(CH$_3$), $^3J_{HH}$ = 7.3, $^3J_{HP}$ = 15.0), 1.48 (dd, 6H, CH(CH$_3$)(CH_3), $^3J_{HH}$ = 7.3, $^3J_{HP}$ = 17.6), 2.41 (oct, 2H, CH(CH$_3$)$_2$, $^3J_{HH}$ ≈ $^2J_{HP}$ = 7.3), 6.77 (td, 1H, C4$_{Ar}$-H, $^3J_{HH}$ = 7.6, $^5J_{HP}$ = 0.9), 7.06 (dt, 1H, C3$_{Ar}$-H, $^3J_{HH}$ = 7.6, $^4J_{HH}$ = $^4J_{HP}$ = 1.4), 7.17 (dm, 1H, C5$_{Ar}$-H, $^3J_{HH}$ = 7.7), 7.29 (tt, 1H, p-C$_{Ar}$-H (Ph), $^3J_{HH}$ = 7.3, $^4J_{HH}$ = 1.3), 7.38 (t, 2H, m-C$_{Ar}$-H (Ph), $^3J_{HH}$ = 7.4), 7.49 (dm, 2H, o-C$_{Ar}$-H (Ph), $^3J_{HH}$ = 7.3). ^{13}C{^{1}H} NMR (125.7 MHz, 20 °C, CD$_3$CN): δ 16.98 (d, 2C, CH(CH_3)(CH$_3$), $^2J_{CP}$ = 1.9), 18.50 (d, 2C, CH(CH$_3$)(CH_3), $^2J_{CP}$ = 2.7), 29.14 (d, 2C, CH(CH$_3$)(CH$_3$), $^1J_{CP}$ = 29.4), 122.21 (d, 1C, $C4_{Ar}$-H, $^4J_{CP}$ = 1.9), 125.16 (d, 1C, $C3_{Ar}$-H, $^3J_{CP}$ = 12.1), 127.99 (d, 2C, m-C$_{Ar}$-H (Ph), J_{CP} = 139.5), 129.12 (d, 2C, o-C$_{Ar}$-H (Ph), J_{CP} = 106.8), 135.65 (d, 1C, $C2_{Ar}$-Ni, $^2J_{CP}$ = 33.0), 138.64 (d, 1C, $C5_{Ar}$-H, $^5J_{CP}$ = 2.7), 139.78 (s, 1C, p-C$_{Ar}$-H (Ph)), 163.78 (d, 1C, $C1_{Ar}$-OP, $^2J_{CP}$ = 12.6), C_{qAr}-Ar were not detected. ^{31}P{^{1}H} NMR (202.4 MHz, 20 °C, CD$_3$CN): δ 196.11 (s, 1P). Anal. Calc. for C$_{36}$H$_{44}$O$_2$P$_2$Ni$_2$Br$_2$: C, 51.00; H, 5.23. Found: C, 50.67; H, 5.44; N, 0.05.

{κ^P,κ^C-(i -(i-Pr)$_2$PO-C$_6$H$_4$)}NiBr(NCMe) (1a-NCMe). 278 mg (400 µmol) of **1a** was suspended in 10 mL Et$_2$O, and 209 µL MeCN (4.00 mmol, 10 eq) was added. The solid readily dissolved to

give a yellow solution which was stirred at room temperature for 30 min. Removal of the solvent under vacuum gave a yellow powder (267 mg, 687 µmol, 86 %). ^{1}H NMR data in CD$_3$CN matched the data reported for the dimeric species **1a** in CD$_3$CN (+ 3H for free C*H*$_3$CN), and crystallization confirmed the identity of the MeCN adduct.

2.6 Acknowledgements

2.7 References

[1] For representative reviews on the subject of C-H functionalization see: (a) Kakiuchi, F.; Kochi, T. *Synthesis* **2008**, 3013. (b) Ackermann, L. *Chem. Rev.* **2011**, 111, 1315. (c) Yamaguchi, J.; Yamaguchi, A. D.; Itami, K. *Angew. Chem. Int. Ed.* **2012**, 51, 8960. (d) Ackermann, L. *Chem. Commun.* **2010**, 46, 4866. (e) Chen, D. Y.-K.; Youn, S. W. *Chem. Eur. J.* **2012**, 18, 9452. (f) Arockiam, P. B.; Bruneau, C.; Dixneuf, P. H. *Chem. Rev.* **2012**, 112, 5879. (g) Colby, D. A.; Bergman, R. G.; Ellman, J. A. *Chem. Rev.* **2010**, 110, 624. (h) Rouquet, G.; Chatani, N. *Angew. Chem. Int. Ed.* **2013**, 52, 11726. (i) Lyons, T. W.; Sanford, M. S. *Chem. Rev.* **2010**, 110, 1147. (j) Xu, L.-M.; Li, B.-J.; Yang, Z.; Shi, Z.-J. *Chem. Soc. Rev.* **2010**, 39, 712. (k) Sehnal, P.; Taylor, R. J. K.; Fairlamb, I. J. S. *Chem. Rev.* **2010**, 110, 824.

[2] Gulevich, A. V.; Melkonyan, F. S.; Sarkar, D.; Gevorgyan, V. J. Am. Chem. Soc. **2012**, 134, 5528.

[3] (a) Kanyiva, K. S.; Nakao, Y.; Hiyama, T. Angew. Chem. Int. Ed. **2007**, 46, 8872. (b) Nakao, Y.; Kanyiva, K. S.; Hiyama, T. J. Am. Chem. Soc. **2008**, 130, 2448. (c) Tobisu, M.; Hyodo, I.; Chatani, N. J. Am. Chem. Soc. **2009**, 131, 12070. (d) Shacklady-McAtee, D. M.; Dasgupta, S.; Watson, M. P. Org. Lett. **2011**, 13, 3490. (e) Ogata, K.; Atsuumi, Y.; Shimada, D.; Fukuzawa, S. Angew. Chem. Int. Ed. **2011**, 50, 5896. (f) Shiota, H.; Ano, Y.; Aihara, Y.; Fukumoto, Y.; Chatani, N. J. Am. Chem. Soc. **2011**, 133, 14952. (g) Aihara, Y.; Chatani, N. J. Am. Chem. Soc. **2013**, 135, 5308. (h) Song, W.; Lackner, S.; Ackermann, L. Angew. Chem. Int. Ed. **2014**, 53, 2477.

[4] (a) Baho, N.; Zargarian, D. Inorg. Chem. **2007**, 46, 299-308. (b) Groux, L. F.; Zargarian, D. Organometallics **2003**, 22, 4759-4769. (c) Groux, L. F.; B.-Gariépy, F.; Zargarian, D.; Vollmerhaus, R. Organometallics **2000**, 19, 1507. (d) Fontaine, F.-G.; Kadkhodazadeh, T.; Zargarian, D. J. Chem. Soc., Chem. Commun. **1998**, 1253-1254.

[5] (a) Hao, J.; Mougang-Soumé, B; Vabre, B.; Zargarian, D. Angew. Chem. Int. Ed. **2014**, 53, 3218-3222. (b) Hao, J.; Vabre, B.; Mougang-Soumé, B; Zargarian, D. Chem. Eur. J. **2014**, 20, 12544-12552. (c) Vabre, B.; Petiot, P.; Declercque, R.; Zargarian, D. Organometallics **2014**, 33, 5173-5184. (d) Vabre, B.; Lindeperg, F.; Zargarian, D. Green Chem. **2013**, 15, 3188. (e) Zargarian, D.; Castonguay, A.; Spasyuk, D. M. "ECE-Type Pincer Complexes of Nickel", in Top. Organomet. Chem. **2013**, 40, 131-174. Eds. G. van Koten and D. Milstein. DOI: 10.1007/978-3-642-31081-2_5. Springer-Verlag, Berlin Heidelberg. (f) Vabre, B.; Canac, Y.; Duhayon, C.; Chauvin, R.; Zargarian, D. Chem. Comm. **2012**, 48, 10446 – 10448. (g) Spasyuk, D. M.; Gorelsky, S. I.; van der Est, A.; Zargarian, D. Inorg. Chem. **2011**, 50, 2661-2674. (h) Castonguay, A.; Beauchamp, A. L.; Zargarian, D. Inorg. Chem. **2009**, 48, 3177-3184.

[6] Vabre, B.; Deschamps, F.; Zargarian, D. Organometallics **2014**, 33, 6623–6632.

[7] The analogous Pd dimers have been reported by Bedford's group: Bedford, R. B.; Hazelwood (née Welch), S. L.; Horton, P. N.; Hursthouse, M. B. Dalton Trans. **2003**, 4164-4174.

[8] *A combined kinetic and DFT study on C-H nickellation of POCOP- and PCP-type pincer ligands has established that the C-H nickellation step proceeds via an electrophilic mechanism: Vabre, B; Lambert, M. L.; Petit, A.; Ess, D. H.; Zargarian, D. Organometallics 2012, 31, 6041−6053.*

[9] It should be noted that the regioselectivity of C-H metalation observed in our system seems to be similar to that reported for palladation of 2-(3-F-Ph)-pyridine (Kalyani, D.; Sanford, M. S. Org. Lett. **2005**, 7, 4149), but opposite of C-H activation reaction by Ni(0) (Doster, M. E.; Hatnean, J. A.; Jeftic, T.; Modi, S.; Johnson, S. A. J. Am. Chem. Soc. **2009**, 132, 11923-11925). Interestingly, sterics also seem to be important in the reaction of fluorobenzenes with Rh(I) in that the kinetic products are those involving less congested C-H moieties, whereas heating the product mixture favors the products featuring Rh-C bonds adjacent to fluoro-substituted sites: Evans, M. E.; Burke, C. L.; Yaibuathes, S.; Clot, E.; Eisenstein, O.; Jones, W. D. J. Am. Chem. Soc. **2009**, 131, 13464-13473.

[10] The estimated vdW volumes (in cm^3/mol) of these fragments increase in the following order: F (5.0) < OH (8.0) < Cl (12.0) < Me (13.7). (a) Bondi, A. J. Phys. Chem. **1964**, 68, 441. (b) Pauling, L. "Nature of the Chemical Bond and the Structure of Molecules and Crystals: An Introduction to Modern Structural Chemistry", third edition, Cornel University Press, 1960, pp. 260-261.

[11] Bedford, R. B.; Limmert, M. E. J. Org. Chem. 2003, **68**, 8669-8682.

[12] Satoh, T.; Kawamura, Y.; Miura, M.; Nomura, M. Angew. Chem., Int. Ed. Engl. 1997, **36**, 1740.

[13] *When electing to probe the reactivities of substrate* **l**, *we were also mindful of the difficult but not impossible activation of a C-Me bond in this substrate. See Milstein's report for a precedent on this type of reactivity with Ni(II): van der Boom, M. E.; Liou, S.-Y.; Shimon, L. J. W.; Ben-David, Y.; Milstein, D. Inorg. Chim. Acta 2004, 357, 4015–4023.*

[14] Complex **1k** crystallized in $P2_1$ space group, but very close to $P2_1$/a or orthorhombic due to pseudo-symmetry. The non-restrained refinement process yielded one non-positive definite atom and several atoms featuring ellipsoids with high ratios of atomic displacement parameters. A highly restrained RIGU command was thus applied to all atoms to sort out these issues. It should be noted that data collected at two different temperatures (100 and 150 K) gave very similar results, suggesting that the resolution problems mentioned above are not due to a phase transition at or near the data collection temperature.

[15] The*se values were derived by applying the following equation τ4 = {360 – (α + β)]/141 wherein α and β are the greater bond angles in the given structure. This approach generates values ranging from 0 for an ideal square plane to 1 for an ideal tetrahedron. For a discussion of this topic see the following reports: (a) Yang, L.; Powell, D. R.; Houser, R. P. Dalton Trans. 2007, 955. (b) Okuniewski, A.; Rosiak, D.; Chojnacki, J.; Becker, B. Polyhedron 2015 90, 47–57.*

[16] (a) Lefèvre, X.; Spasyuk, D. M.; Zargarian, D. J. Organomet. Chem. **2011**, 696, 864. (b) Lefèvre, X.; Durieux, G.; Lesturgez, S.; Zargarian, D. J. Mol. Catal. A **2011**, 335, 1. (c) Lapointe, S.; Vabre, B.; Zargarian, D. Organometallics 2015, 34, 3520–3531. (d) Salah, A.; Corpet, M.; Khan, N. u-H.; Zargarian, D.; Spasyuk, D. New J. Chem. **2015**, 39, 6649–6658.

[17] This value represents the range of torsion angles in the 4 independent molecules in the unit cell of this compound.

[18] Cordero, B.; Gómez, V.; Platero-Prats, A. E.; Revés, M.; Echeverría, J.; Cremades, E.; Barragán, F.; Alvarez, C. *Dalton Trans.* **2008**, 2832.

[19] We recognize that monomeric acetonitrile adducts likely exchange rapidly with CD_3CN solvent, but we have not attempted to confirm the occurrence of these processes.

[20] A reviewer of our manuscript suggested that the exchange process in question might occur via an s-trans-to-s-cis isomerization process proceeding via one or the other of the following alternative pathways, a conformational isomerization (square-planar⇆tetrahedral) or a Ni-Br bond scission followed by rotation around the remaining Ni-□-Br bond. We have probed these scenarios briefly using DFT studies carried out on the title dimeric complexes. These studies showed that the isolated s-trans dimers are more stable than both the s-cis isomer (by 10.0 kJ/mol) and the proposed tetrahedral intermediate/transition-state (by 68.3 kJ/mol). (See SI for details.) Thus, the putative s-cis dimer seems feasible, but the proposed conformational isomerization pathway passing through a tetrahedral intermediate/ transition sate seems thermally inaccessible at r.t. We also remain skeptical with respect to an isomerization pathway involving a Ni-Br bond scission, which would generate a 3-coordinate, 14-electron intermediate. Attempts to estimate the energy of such an intermediate by DFT were unsuccessful, implying that it is thermally inaccessible

[21] Vabre, B.; Spasyuk, D. M.; Zargarian, D. Organometallics **2012**, 31, 8561−8570.

Chapitre 2 – Annexes

S2.1 General information and references

All NMR 1D spectra were recorded on a Bruker AV500 spectrometer and the HSQC experiments were recorded on a Bruker AV400 spectrometer, with access provided by Centre régional de résonance magnétique nucléaire de l'Université de Montréal. The elemental analyses were performed by the Laboratoire d'Analyse Élementaire, Département de chimie, Université de Montreal, on a Fisons EA 1108, CHNS instrument. All DFT calculations were performed using Gaussian16 Revision A03[1] on Grex cluster server form Westgrid computational facilities, with access provided by Compute Canada – Calcul Canada. The crystallographic data for all resolved structures were collected either on a Bruker Microsource (Cu source) or a Bruker Venture Metaljet (Ga source) via the Bruker APEX II or APEX III[2] softwares. Cell refinement and data reduction were performed using SAINT[3]. An empirical absorption correction, based on multiple measurements of equivalent reflections, was applied using the program SADABS[4]. The space group was confirmed by the XPREP[5] routine in APEX. The structures were solved in OLEX[6] using the SHELX[7] suite and refined by full-matrix least squares with SHEXL[8]. All non-hydrogen atoms were refined with anisotropic displacement parameters, whereas hydrogen atoms were set in

[1] Gaussian 16, Revision A.03, M. J. Frisch, G. W. Trucks, H. B. Schlegel, G. E. Scuseria, M. A. Robb, J. R. Cheeseman, G. Scalmani, V. Barone, G. A. Petersson, H. Nakatsuji, X. Li, M. Caricato, A. V. Marenich, J. Bloino, B. G. Janesko, R. Gomperts, B. Mennucci, H. P. Hratchian, J. V. Ortiz, A. F. Izmaylov, J. L. Sonnenberg, D. Williams-Young, F. Ding, F. Lipparini, F. Egidi, J. Goings, B. Peng, A. Petrone, T. Henderson, D. Ranasinghe, V. G. Zakrzewski, J. Gao, N. Rega, G. Zheng, W. Liang, M. Hada, M. Ehara, K. Toyota, R. Fukuda, J. Hasegawa, M. Ishida, T. Nakajima, Y. Honda, O. Kitao, H. Nakai, T. Vreven, K. Throssell, J. A. Montgomery, Jr., J. E. Peralta, F. Ogliaro, M. J. Bearpark, J. J. Heyd, E. N. Brothers, K. N. Kudin, V. N. Staroverov, T. A. Keith, R. Kobayashi, J. Normand, K. Raghavachari, A. P. Rendell, J. C. Burant, S. S. Iyengar, J. Tomasi, M. Cossi, J. M. Millam, M. Klene, C. Adamo, R. Cammi, J. W. Ochterski, R. L. Martin, K. Morokuma, O. Farkas, J. B. Foresman, and D. J. Fox, Gaussian, Inc., Wallingford CT, 2016.
[2] Bruker (2012). APEX2 / Bruker (2016) APEX3, Bruker AXS Inc., Madison, WI, USA.
[3] Bruker (2012). "SAINT Integration Software for Single Crystal Data", Bruker AXS Inc., Madison, WI, USA.
[4] Sheldrick, G. M., "Comparison of silver and molybdenum microfocus X-ray sources for single crystal structure determination", *J. Appl.Cryst.*, 2015, *48*, 3-10
[5] Bruker (2012). Data Preparation and Reciprocal Space Exploration Program, Bruker AXS Inc., Madison, WI, USA.
[6] A: O. V. Dolomanov, L. J. Bourhis, R. J. Gildea, J. A. K. Howard and H. Puschmann. "OLEX2: a complete structure solution, refinement and analysis program". *J. Appl. Cryst.* 2009, *42*, 339-341.
[7] Sheldrick, G. M., "SHELXT - Integrated space-group and crystal structure determination", *Acta Cryst.*, 2015, A71, 3-8.
[8] Sheldrick, G. M., Crystal structure refinement with SHELXL, *Acta Cryst.*, 2015, C71, 3-8.

calculated positions and refined as riding atoms, with thermal parameters being 1.5 times that of the carbon bearing the H in question. All thermal ellipsoid plots were drawn using Platon[9].

S2.2 UV-vis Spectra for 1a and 1a-NCMe
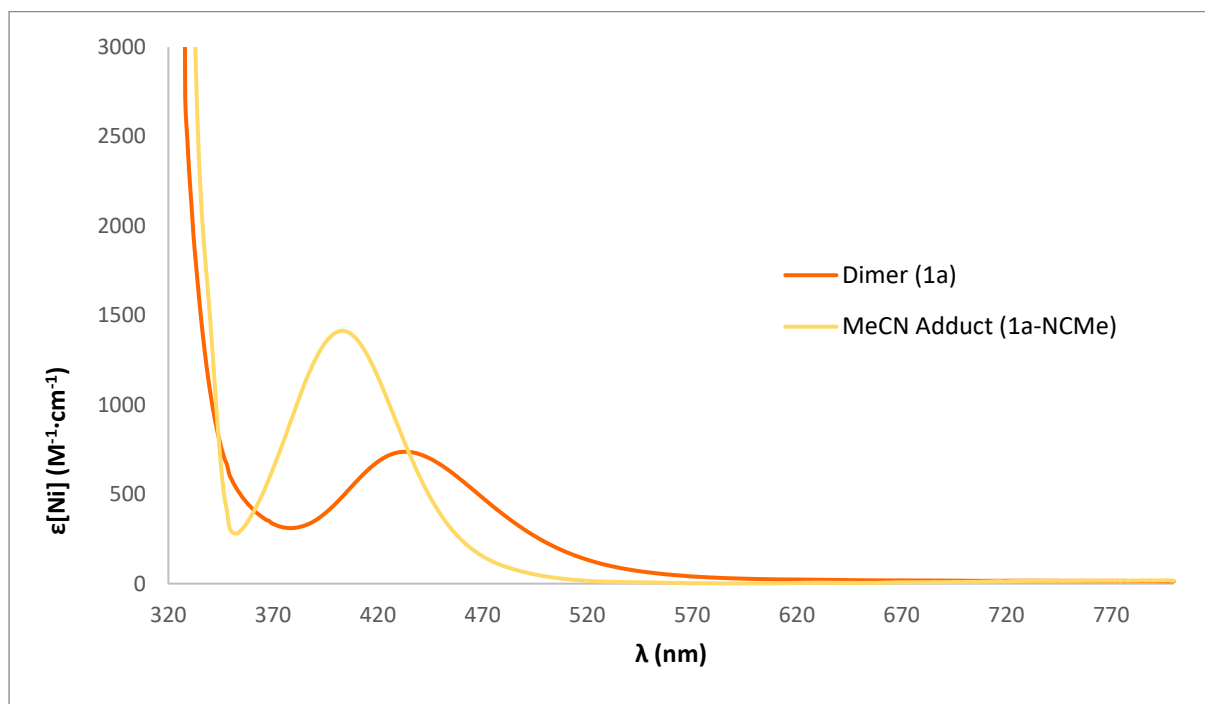
Figure S2.1: UV-vis Spectra of the dimer derived from PhOP(i-Pr)$_2$ ([Dimer] = ½ [Ni] = 0.833 mM) and of the MeCN adduct ([Monomer] = 0.555 mM) generated by addition of 10 eq. MeCN in Toluene at 22 °C

S2.3 Estimation of K$_{eq}$ for 1a ⇆ 1a-NCMe

---
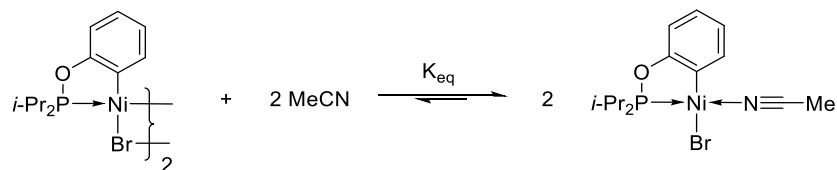
[9] Spek, A. L., *Acta Cryst.*, 2009, D65, 148-155

Table S2.1: ^{31}P NMR estimation of the constants for equilibration of **1a** and **1a-NCMe**

eq$_{(MeCN)}$	%Dimer	%Monomer	[Dimer] (M)	[Monomer] (M)	[MeCN]$_{free}$ (M)	K$_{eq}$
0.5	0.7583	0.2417	0.0189575	0.012085	0.000415	4.5E+04
1	0.5276	0.4724	0.01319	0.02362	0.00138	2.2E+04
1.5	0.3746	0.6254	0.009365	0.03127	0.00623	2.7E+03
2	0.1887	0.8113	0.0047175	0.040565	0.009435	3.9E+03

S2.4 NMR Spectra for compounds 1a-1f, 1i-NCMe and 1j-1k in CD₃CN
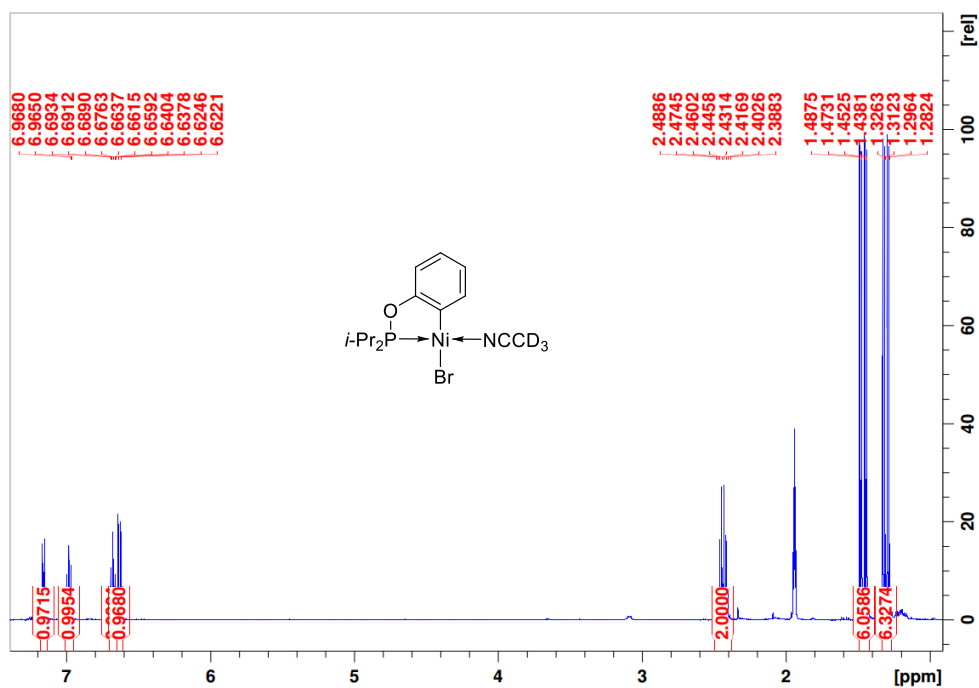
Figure S2.2: Full ^{1}H NMR spectrum of **1a** in CD₃CN
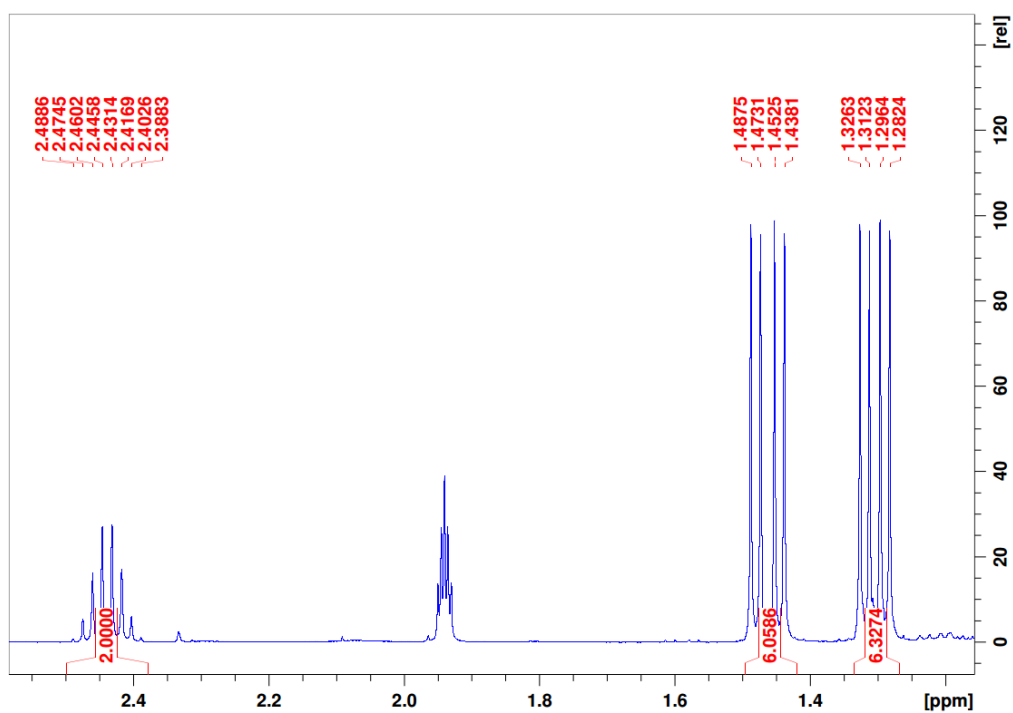
Figure S2.3: ^{1}H NMR spectrum of **1a** in CD₃CN; focus on aliphatic region
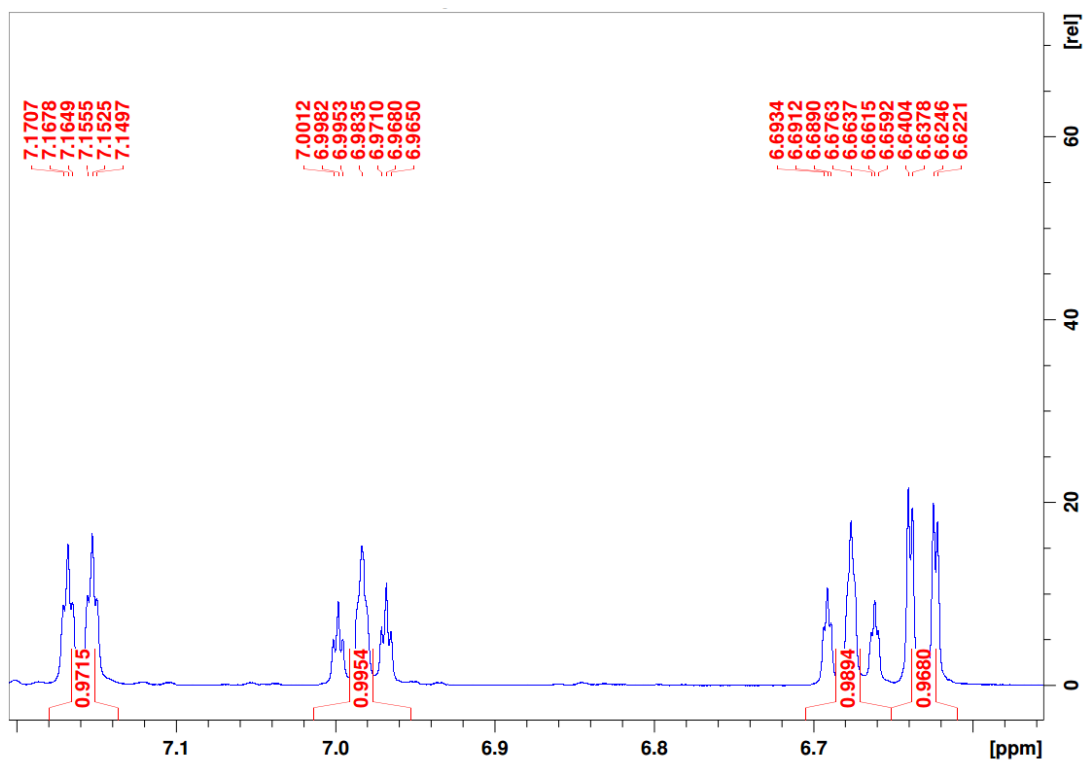
Figure S2.4: ^{1}H NMR spectrum of **1a** in CD$_3$CN; focus on aromatic region
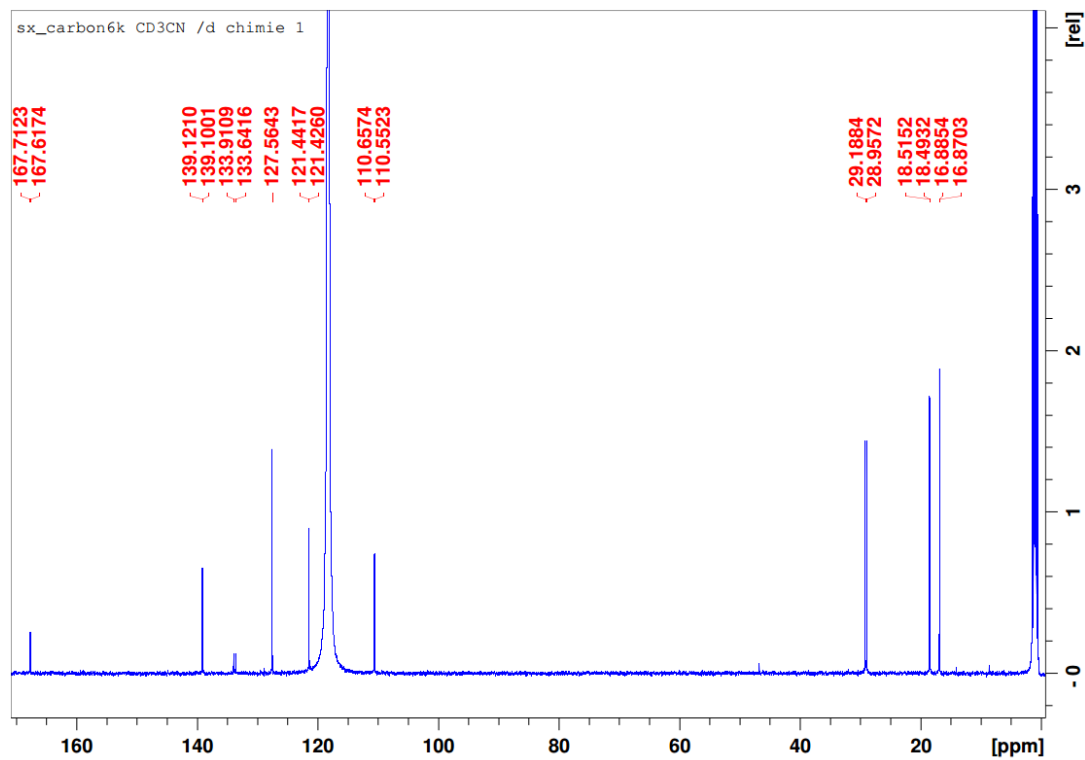
Figure S2.5: Full ^{13}C{1H} NMR spectrum of **1a** in CD$_3$CN

91
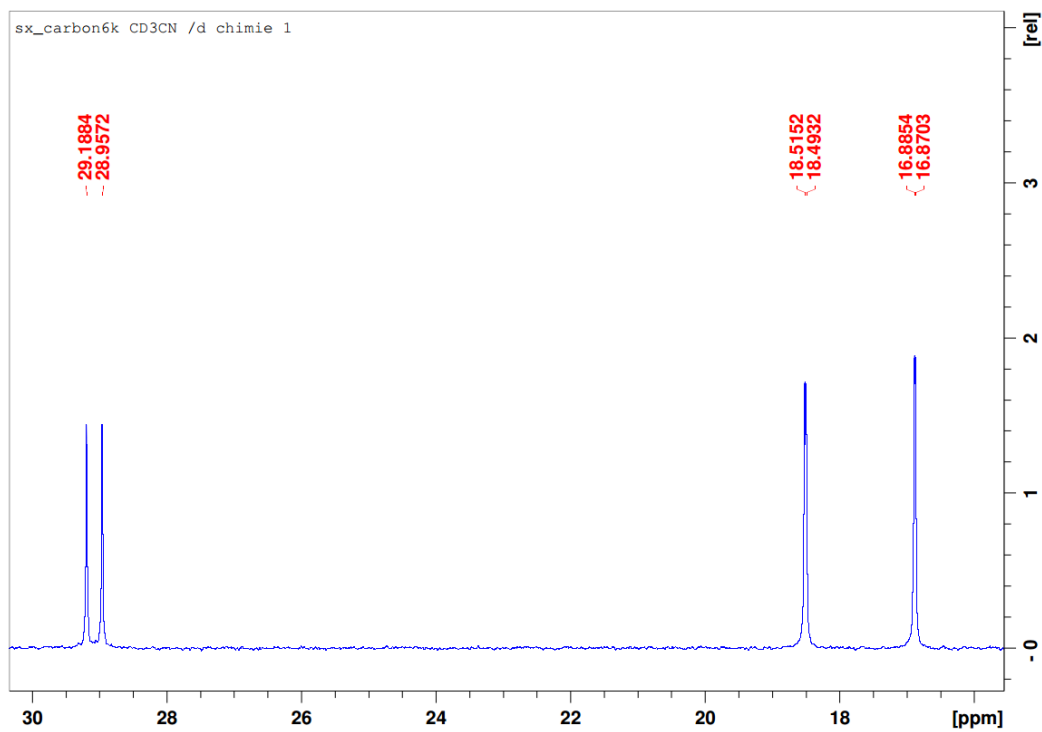
Figure S2.6: $^{13}C\{^{1}H\}$ NMR spectrum of **1a** in CD$_3$CN; focus on aliphatic region
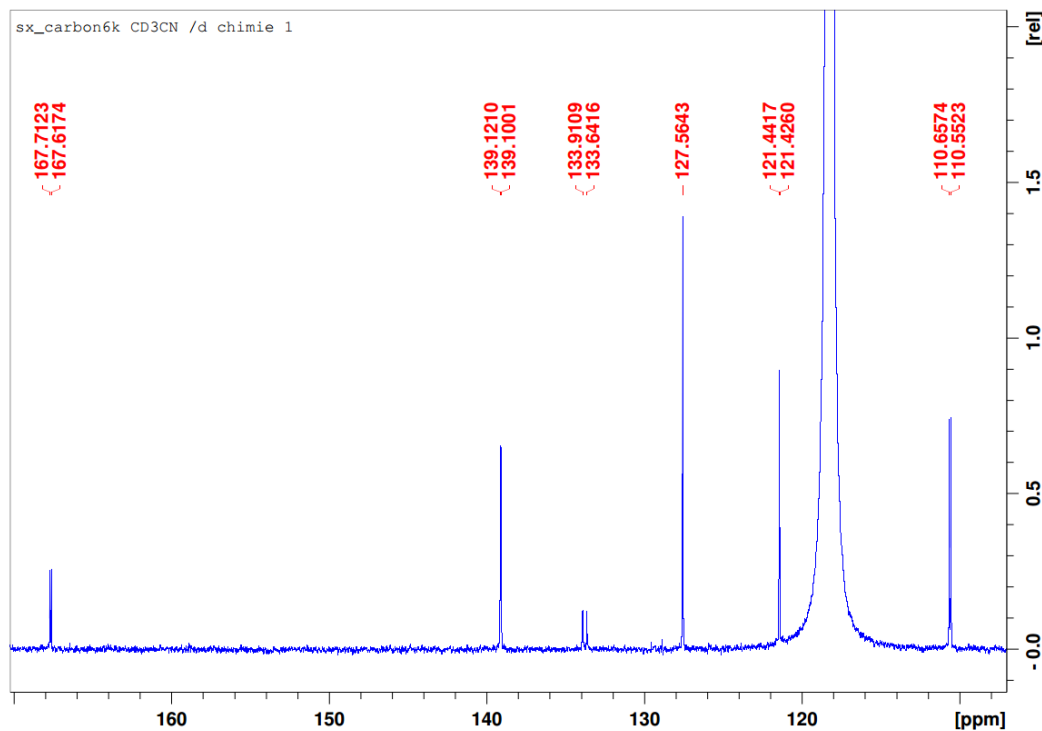
Figure S2.7: $^{13}C\{^{1}H\}$ NMR spectrum of **1a** in CD$_3$CN; focus on aromatic region
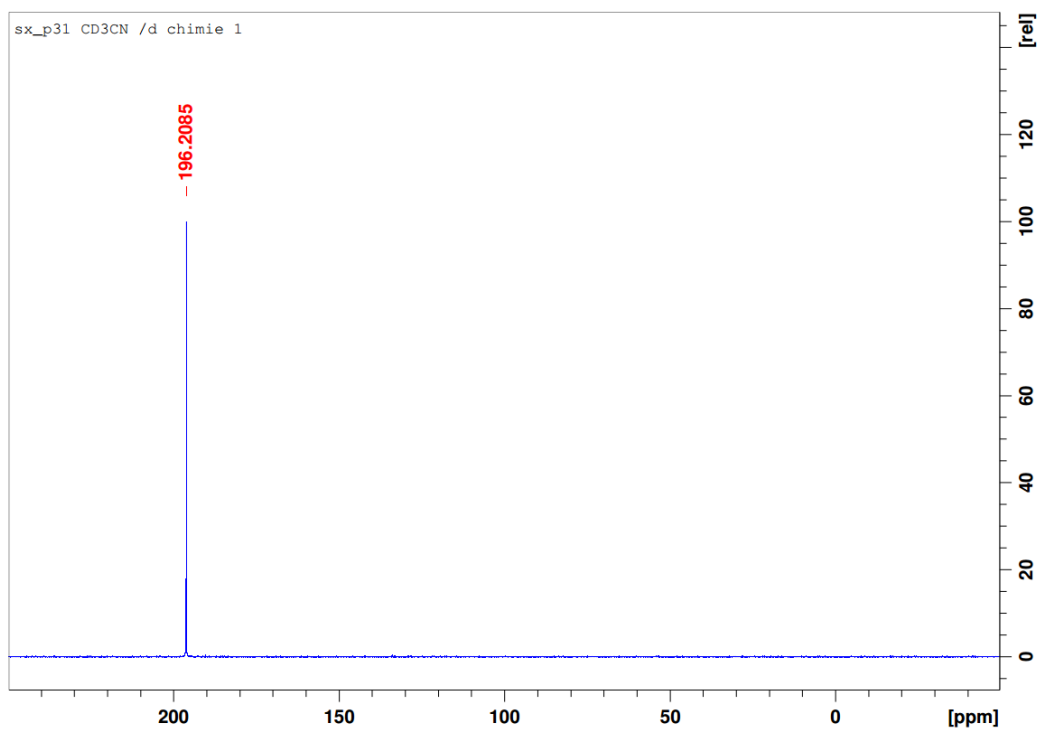
Figure S2.8: $^{31}P\{^1H\}$ NMR spectrum of **1a** in CD$_3$CN
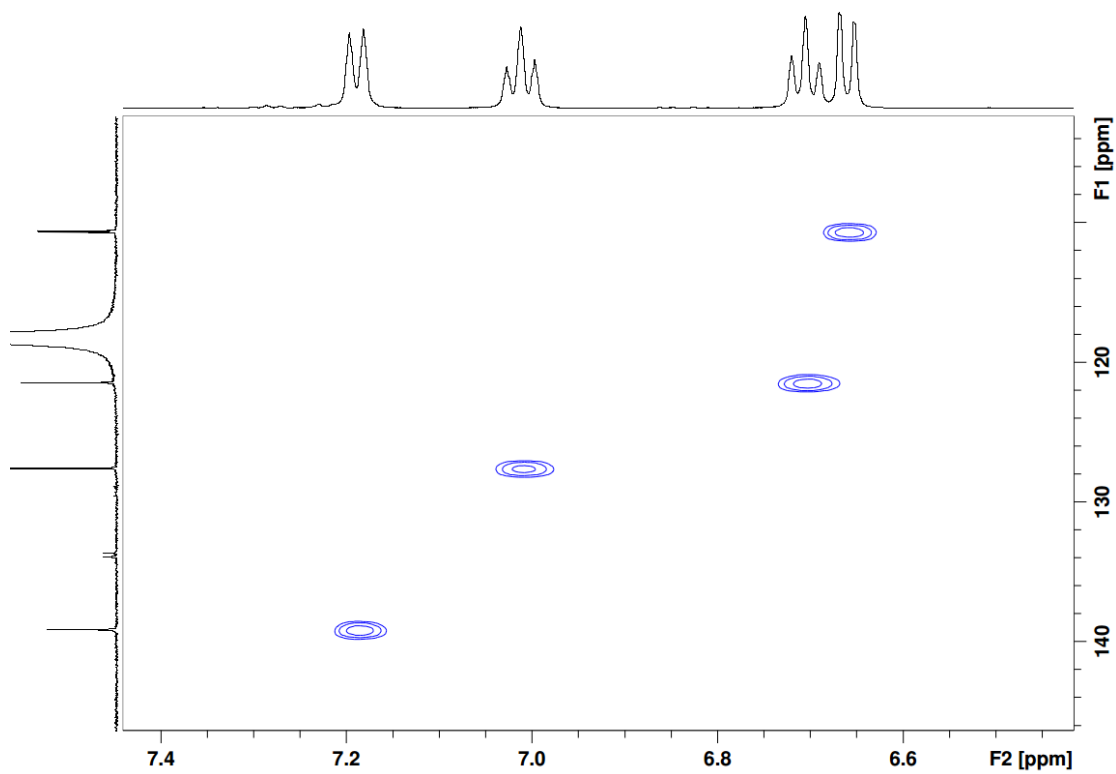
Figure S2.9: HSQC spectrum of **1a** in CD$_3$CN; focus on aromatic region

1b+1b'
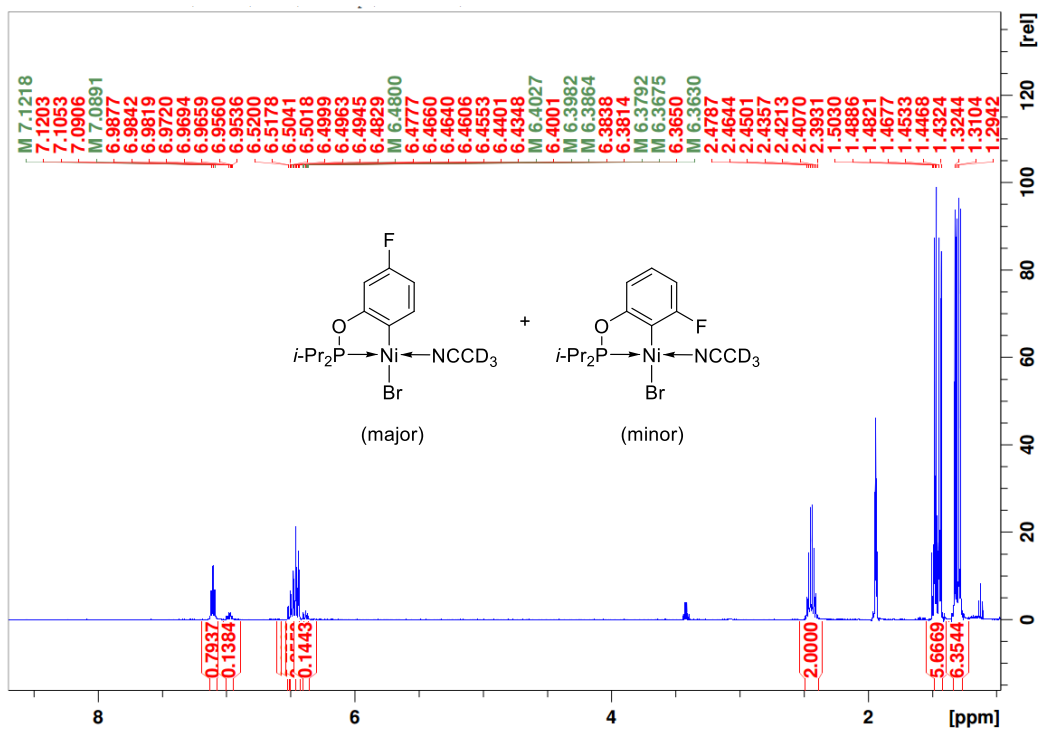
Figure S2.10: Full ^{1}H NMR spectrum of **1b**(major)+**1b'**(minor) in CD$_3$CN
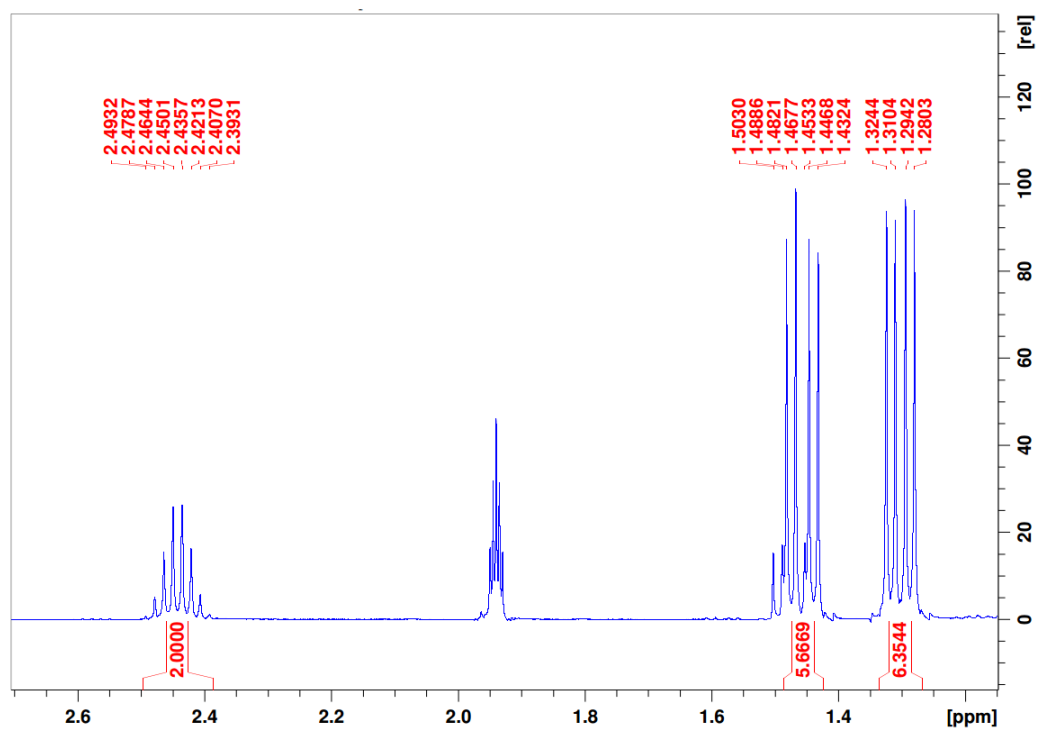
Figure S2.11: ^{1}H NMR spectrum of **1b**+**1b'** in CD$_3$CN; focus on aliphatic region
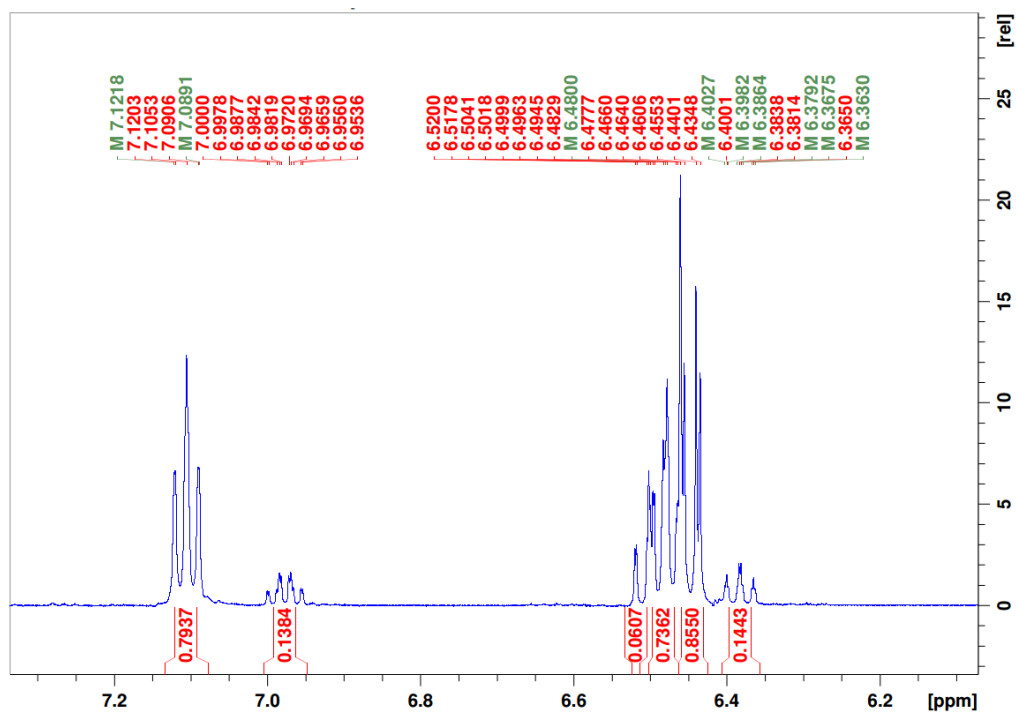
Figure S2.12: ^{1}H NMR spectrum of **1b**+**1b'** in CD$_3$CN; focus on aromatic region
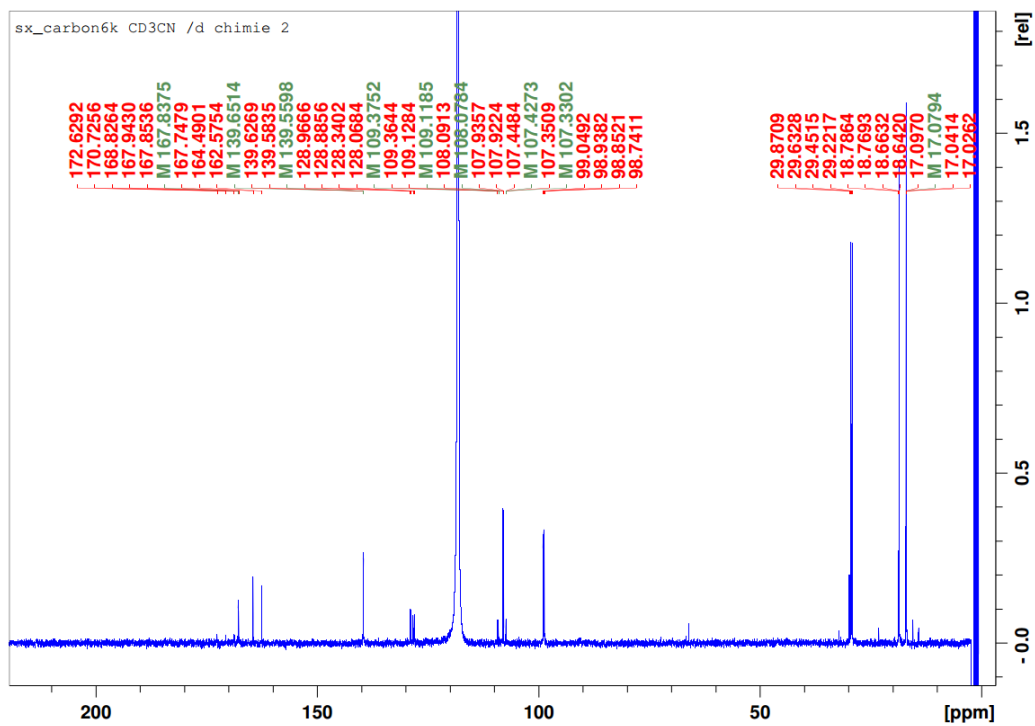
Figure S2.13: Full ^{13}C{^{1}H} NMR spectrum of **1b**+**1b'** in CD$_3$CN
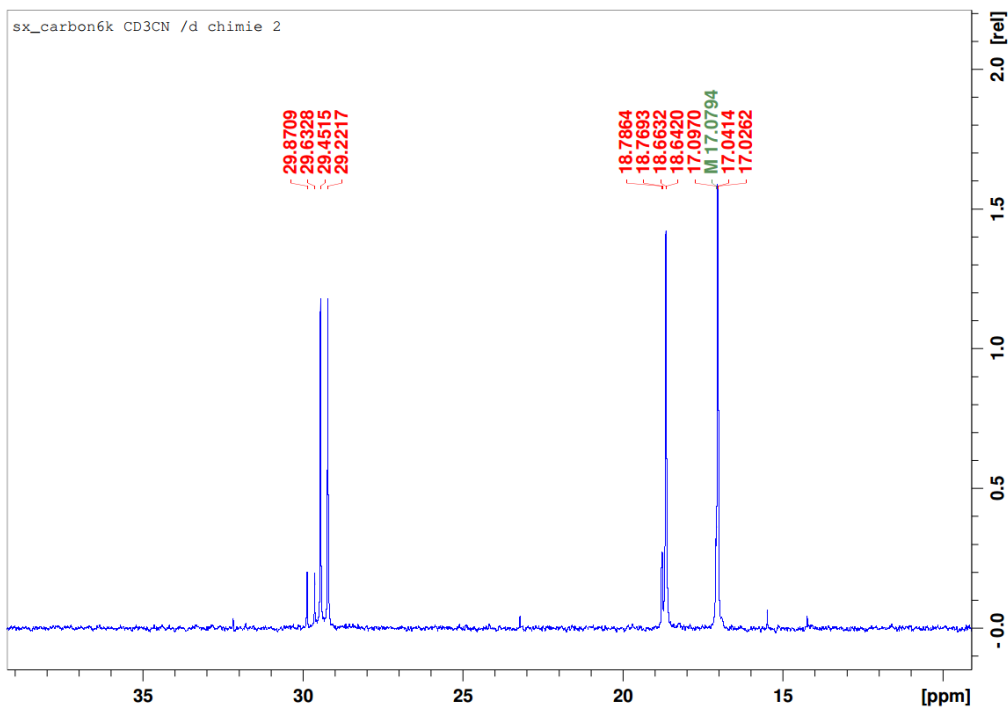
Figure S2.14: $^{13}C\{^1H\}$ NMR spectrum of **1b+1b'** in CD$_3$CN; focus on aliphatic region
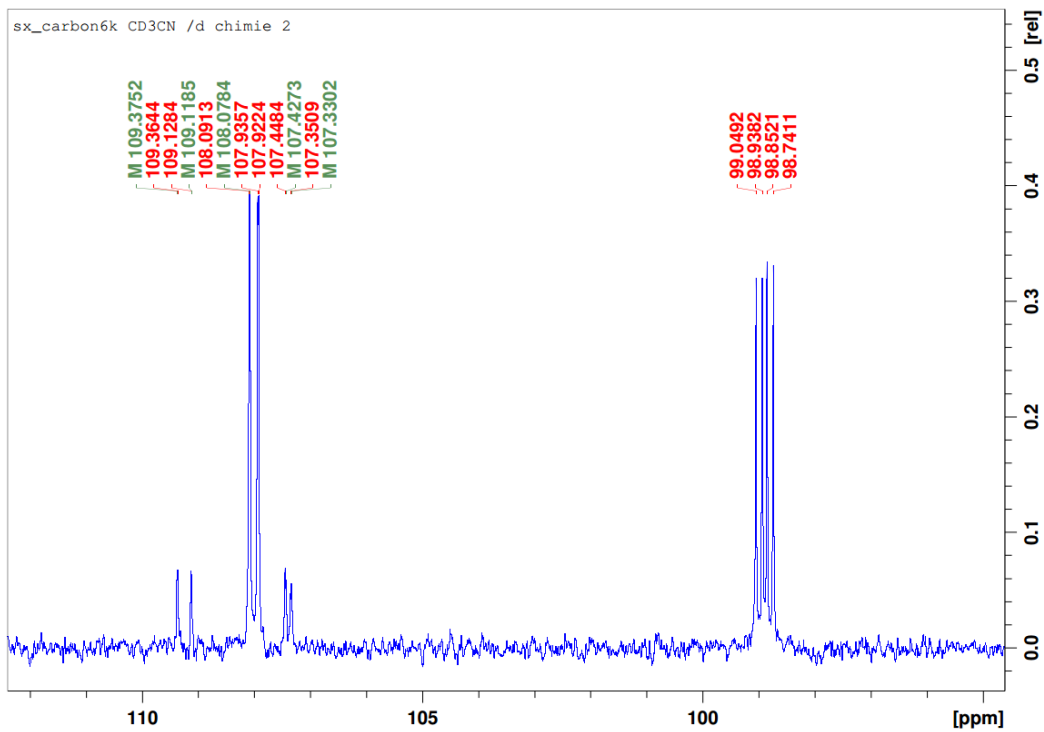
*Figure S2.15: $^{13}C\{^1H\}$ NMR spectrum of **1b+1b'** in CD$_3$CN; focus on aromatic region (I)*

96
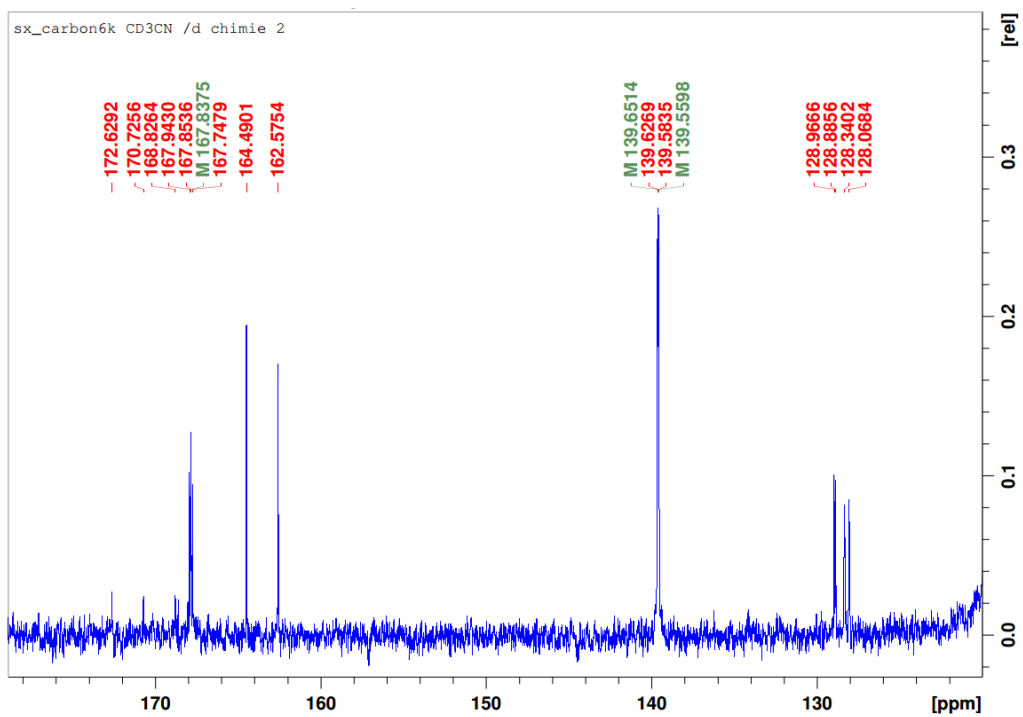
Figure S2.16: $^{13}C\{^{1}H\}$ NMR spectrum of **1b**+**1b'** in CD$_3$CN; focus on aromatic region (II)
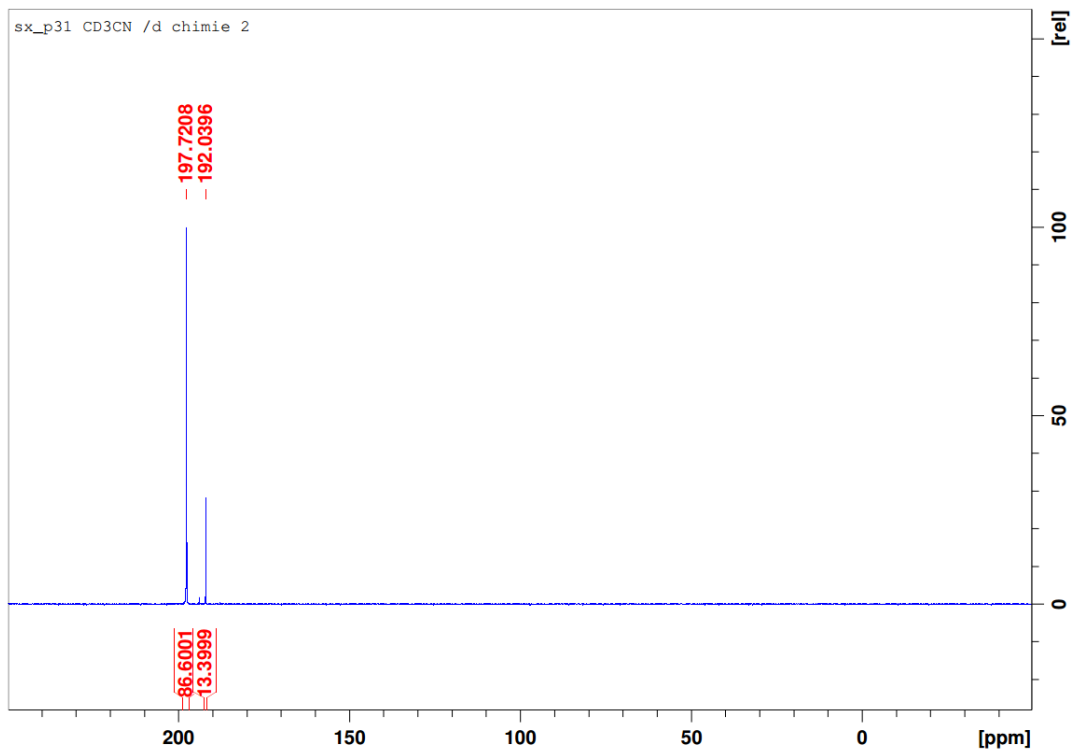
Figure S2.17: $^{31}P\{^{1}H\}$ NMR spectrum of **1b**+**1b'** in CD$_3$CN

97
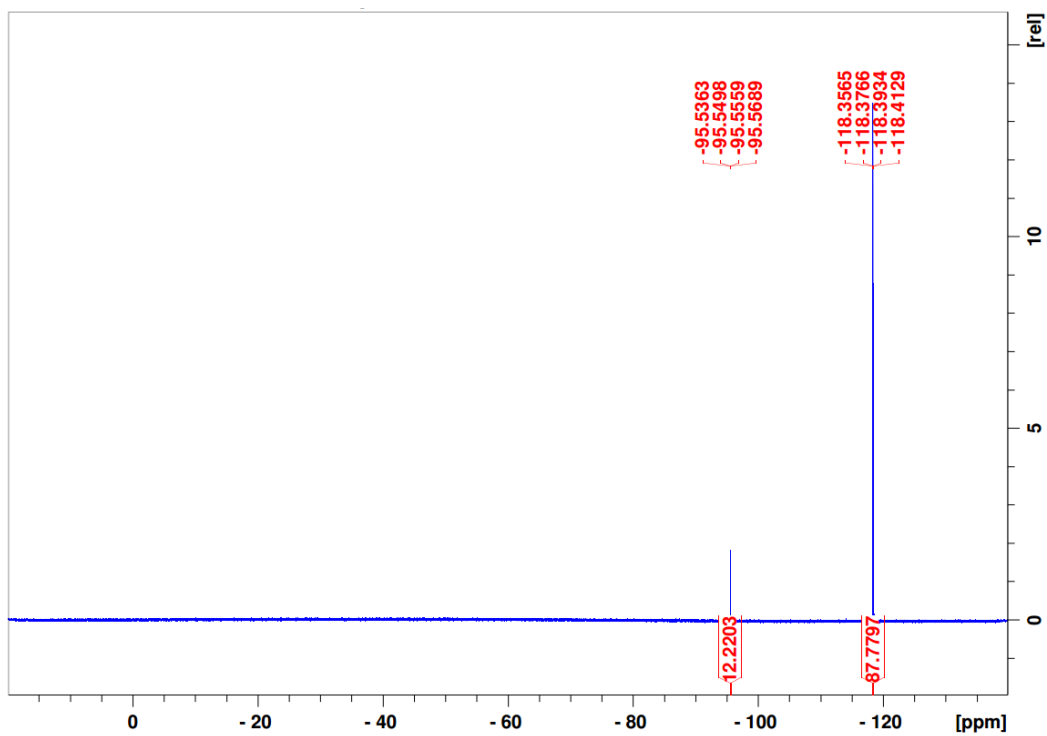
Figure S2.18: ^{19}F NMR spectrum of **1b**+**1b'** in CD$_3$CN
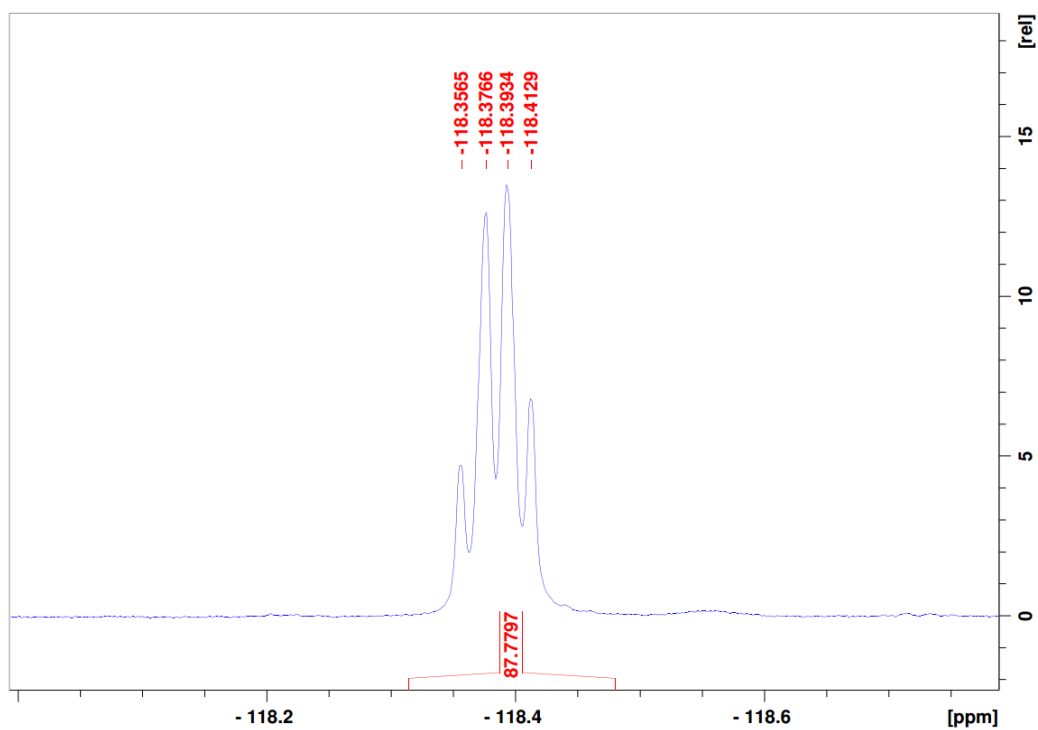
Figure S2.19: ^{19}F NMR spectrum of **1b**+**1b'** in CD$_3$CN; focus on **1b**

98
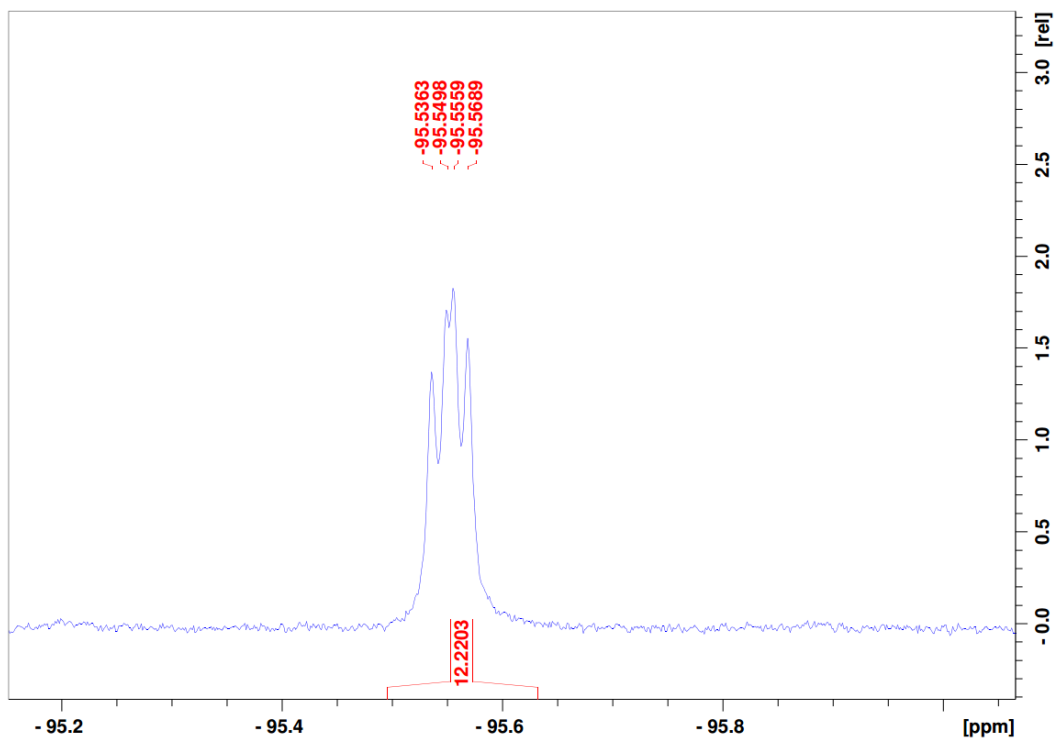
Figure S2.20: ^{19}F NMR spectrum of **1b**+**1b'** in CD$_3$CN; focus on **1b'**
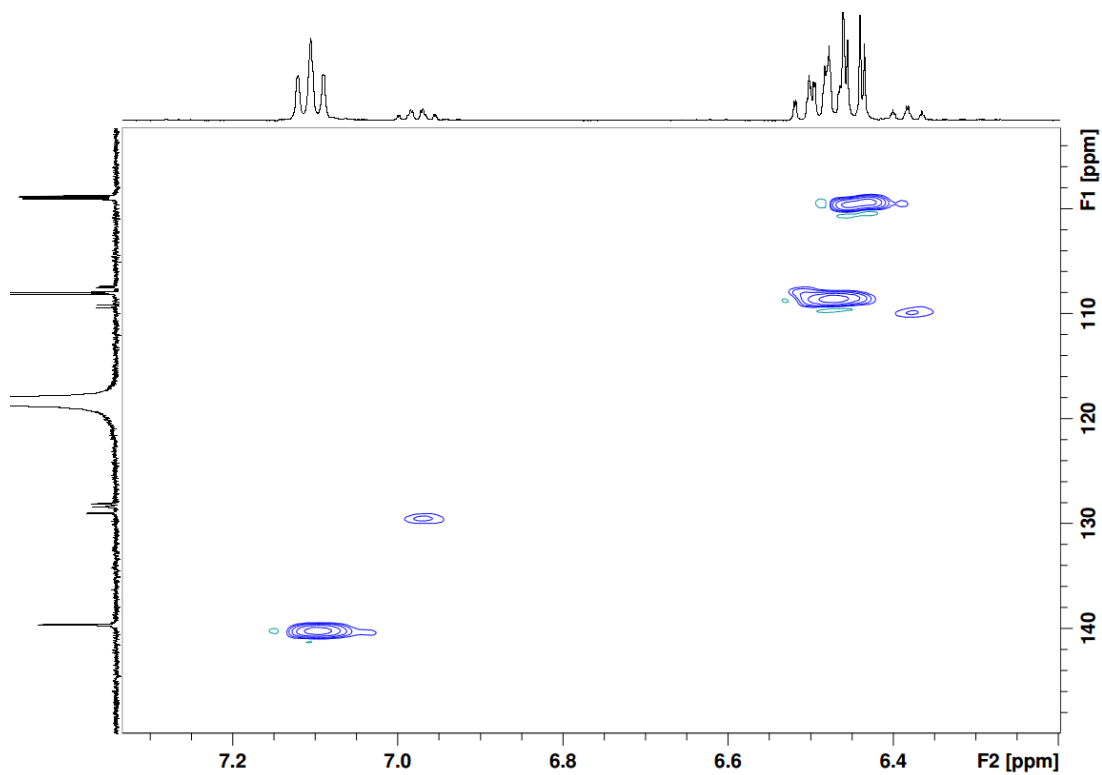
Figure S2.21: HSQC spectrum of **1b**+**1b'** in CD$_3$CN; focus on aromatic region

1c
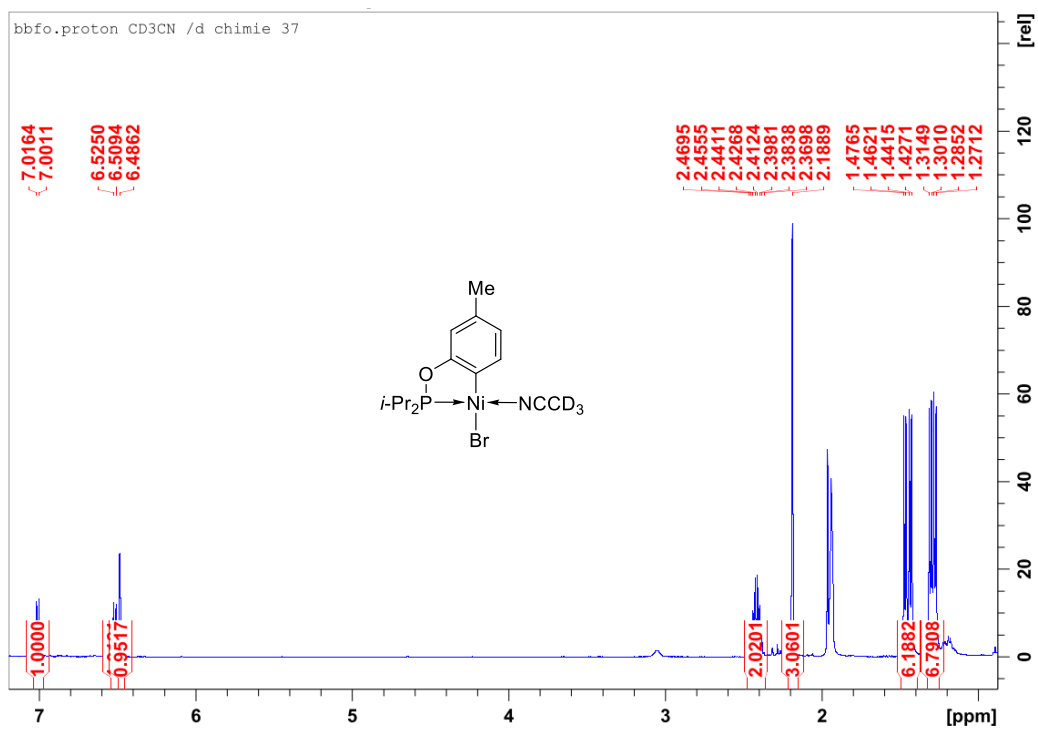
Figure S2.22: Full ^{1}H NMR spectrum of **1c** in CD$_3$CN
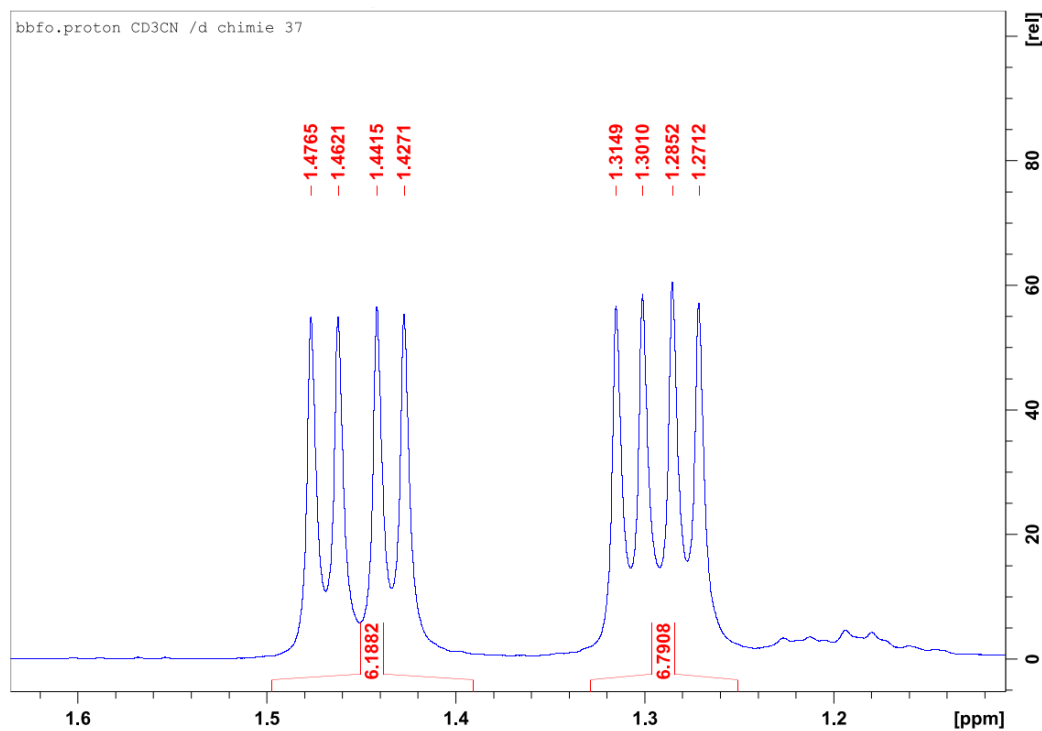
Figure S2.23: ^{1}H NMR spectrum of **1c** in CD$_3$CN; focus on aliphatic region (I)
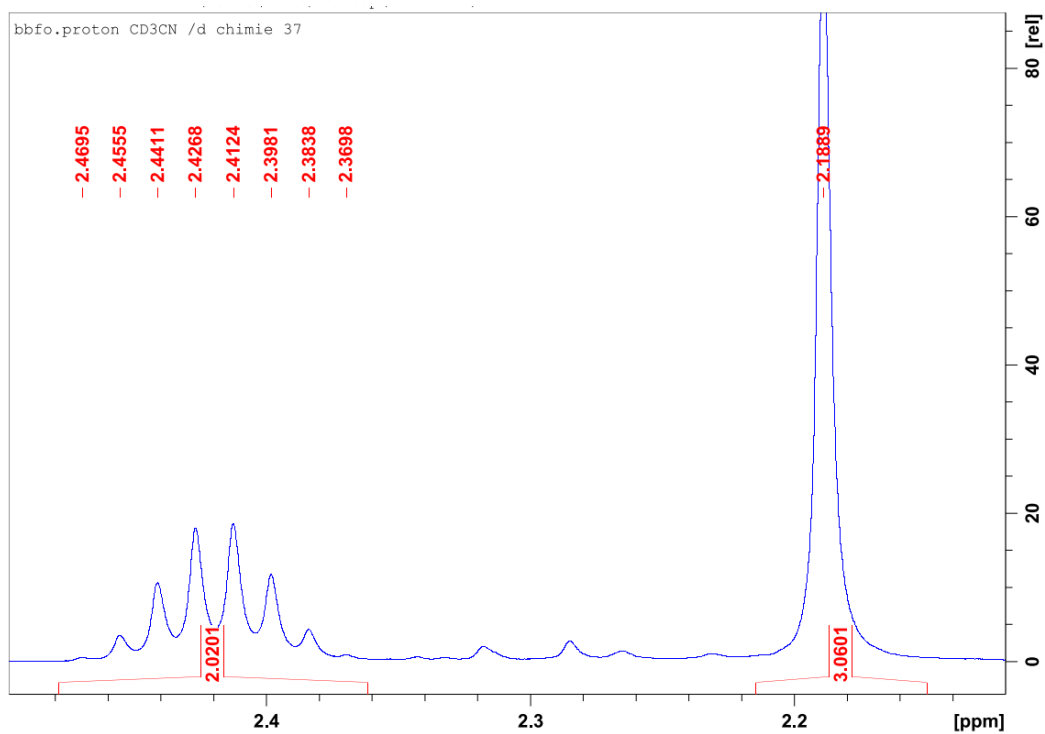
Figure S2.24: ^{1}H NMR spectrum of **1c** in CD$_3$CN; focus on aliphatic region (II)
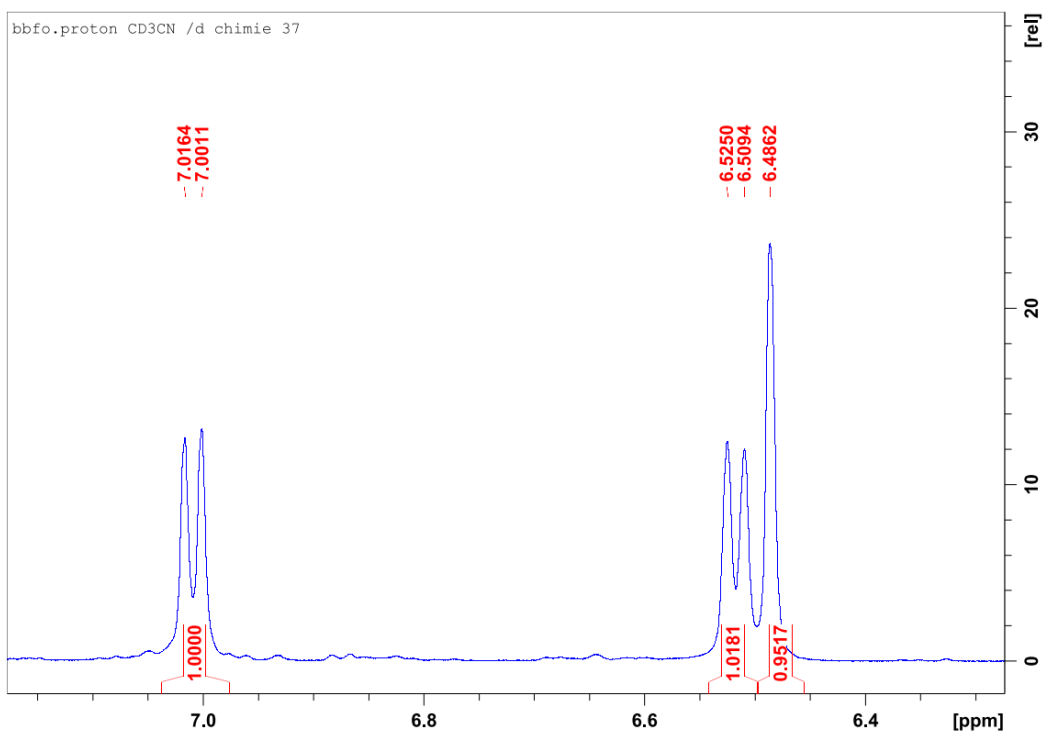
Figure S2.25: ^{1}H NMR spectrum of **1c** in CD$_3$CN; focus on aromatic region
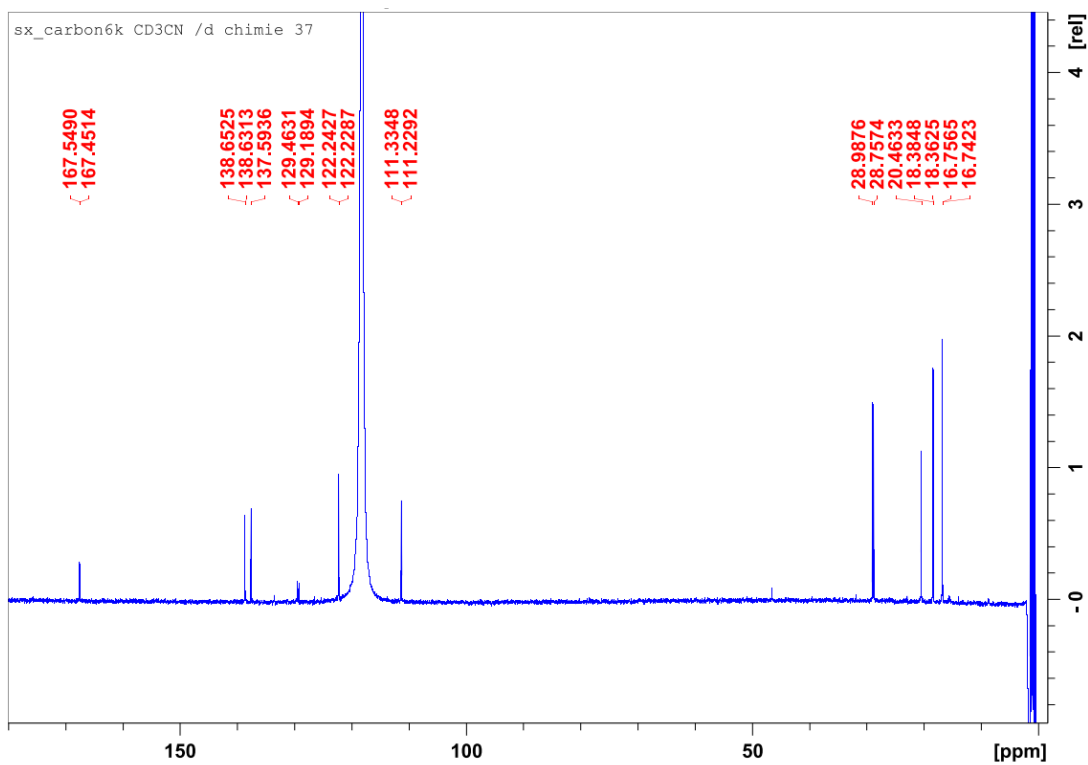
Figure S2.26: Full $^{13}C\{^1H\}$ NMR spectrum of **1c** in CD$_3$CN
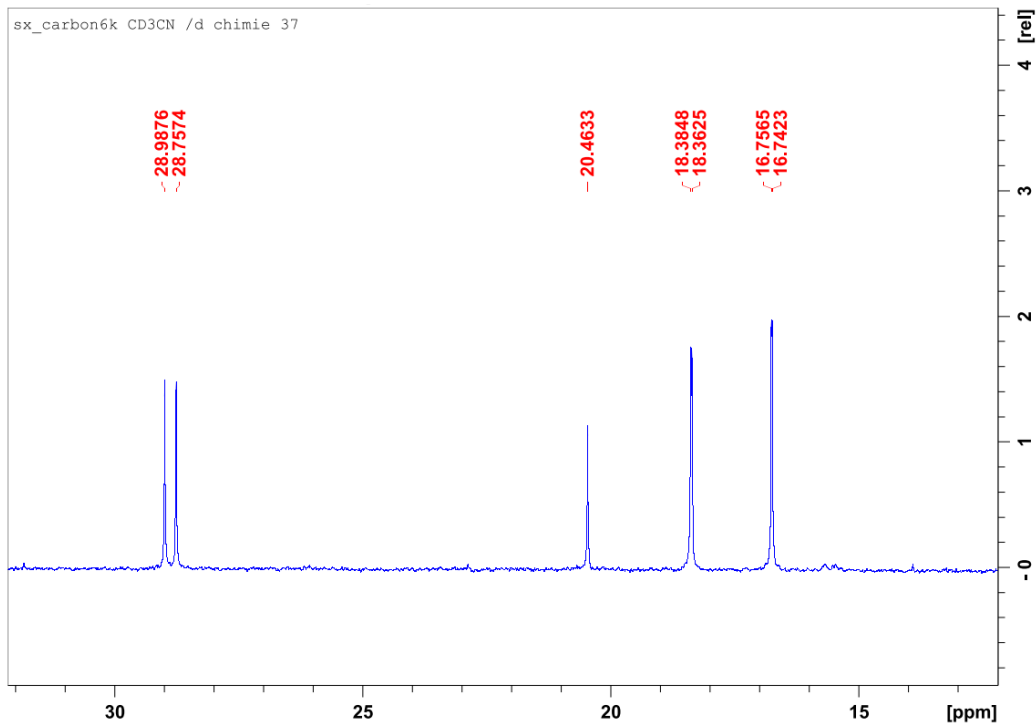
Figure S2.27: $^{13}C\{^1H\}$ NMR spectrum of **1c** in CD$_3$CN; focus on aliphatic region
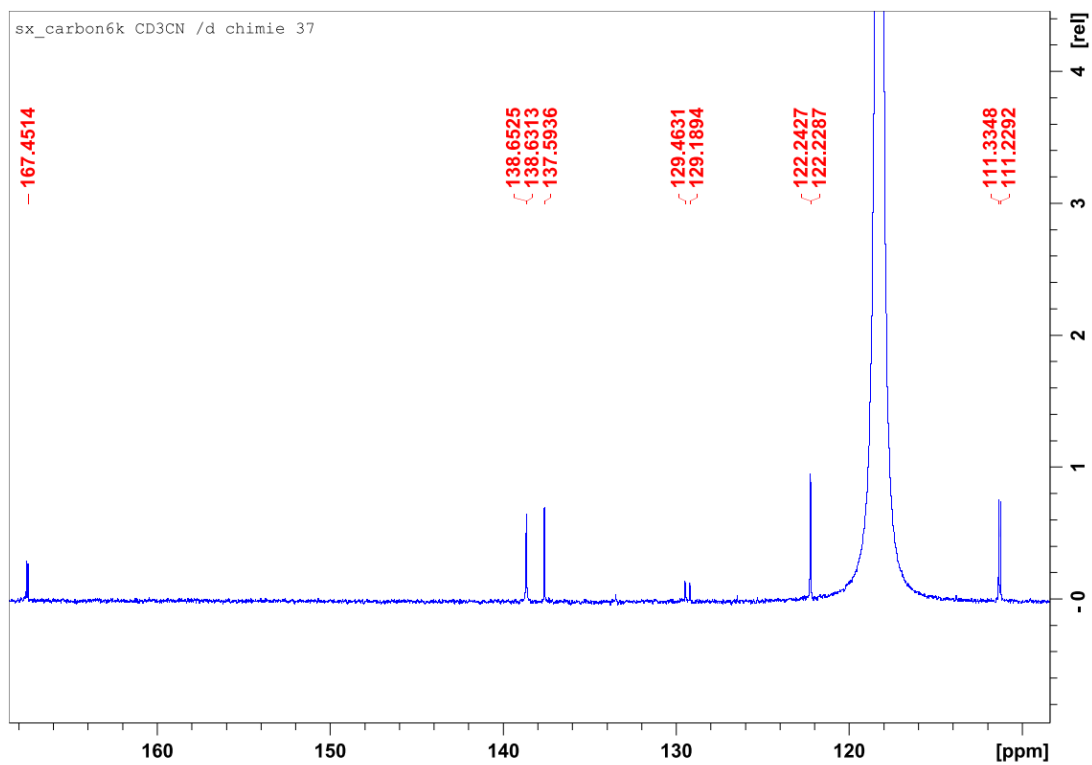
Figure S2.28: $^{13}C\{^1H\}$ NMR spectrum of **1c** in CD_3CN; focus on aromatic region
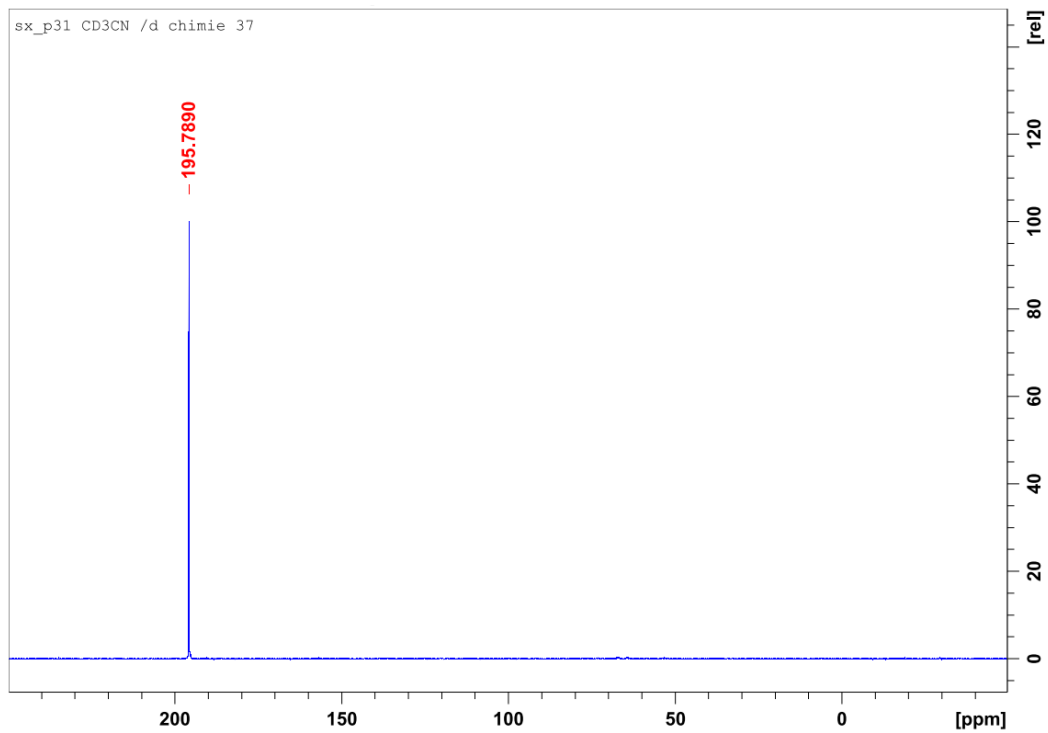
Figure S2.29: $^{31}P\{^1H\}$ NMR spectrum of **1c** in CD_3CN
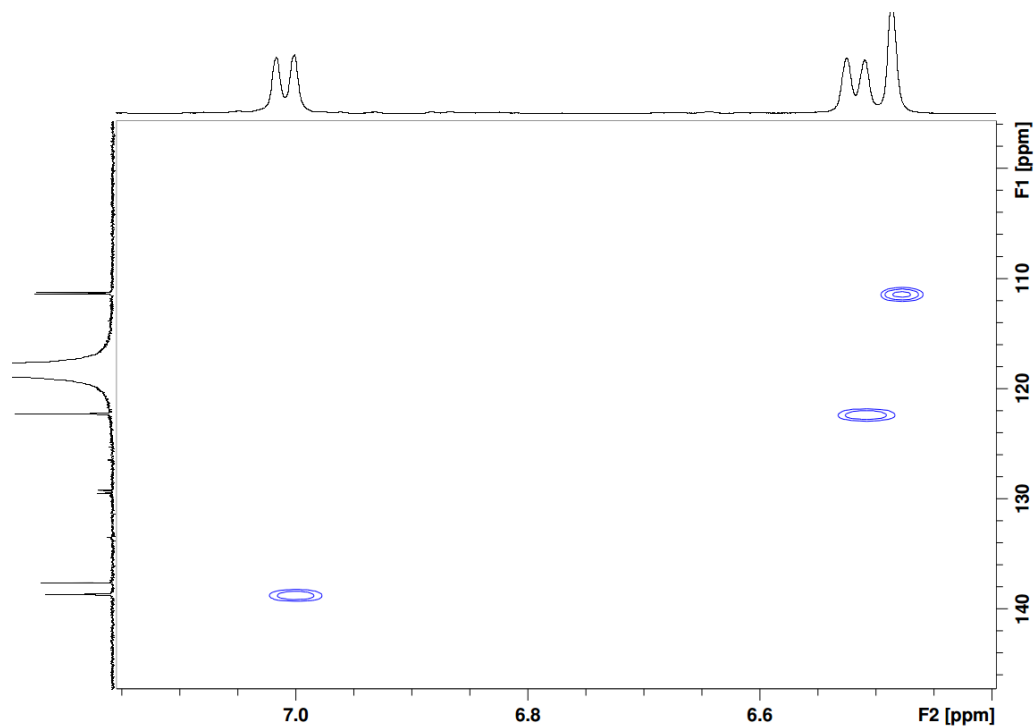
Figure S2.30: HSQC spectrum of **1c** in CD$_3$CN

1d
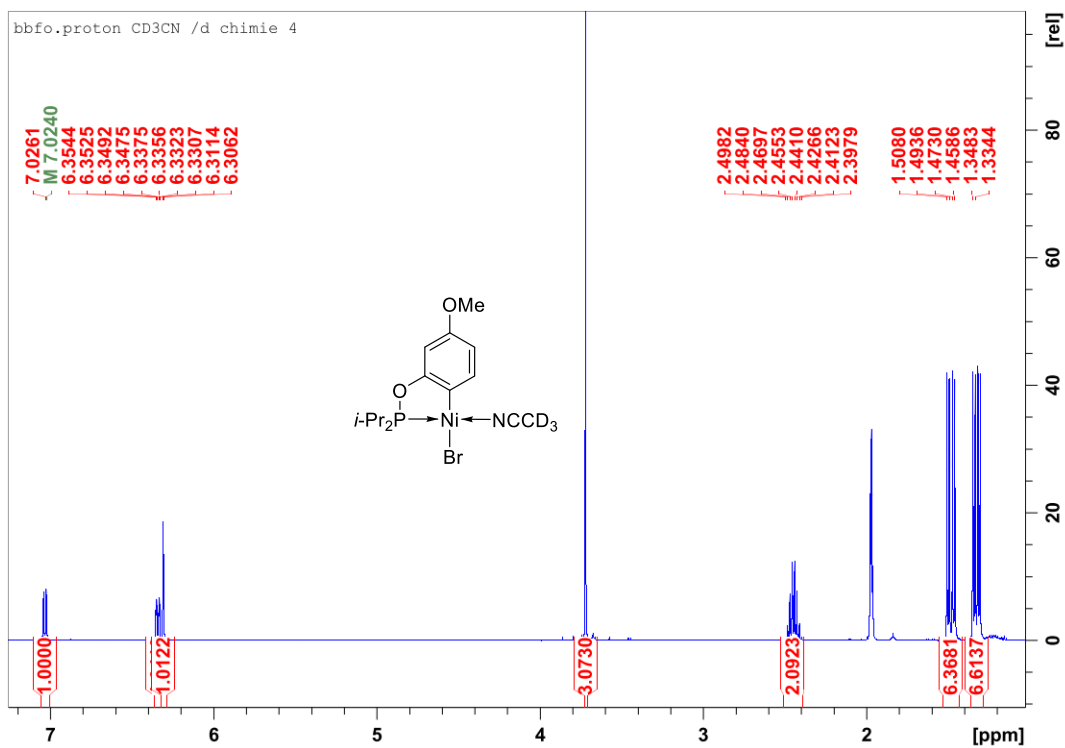
Figure S2.31: Full ^{1}H NMR spectrum of **1d** in CD$_3$CN
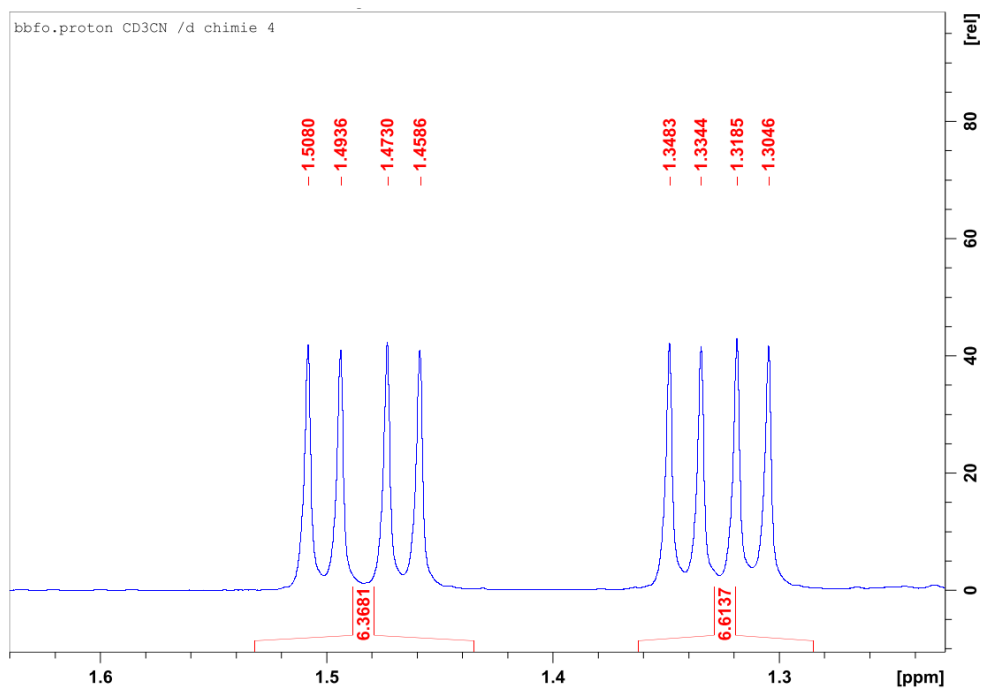
Figure S2.32: ¹H NMR spectrum of **1d** in CD₃CN; focus on aliphatic region (I)
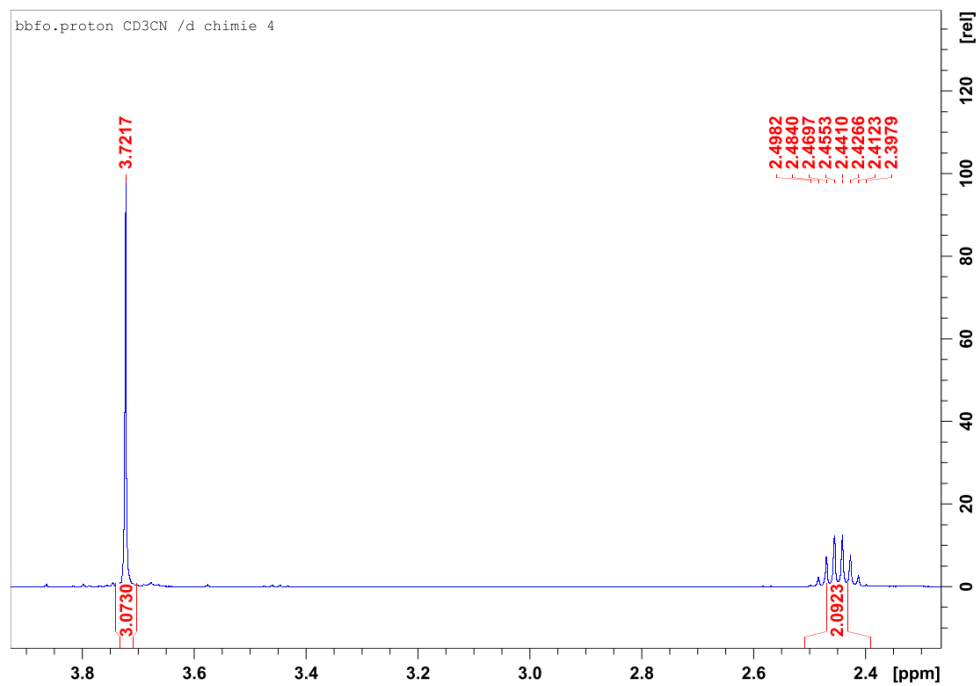
Figure S2.33: ¹H NMR spectrum of **1d** in CD₃CN; focus on aliphatic region (II)
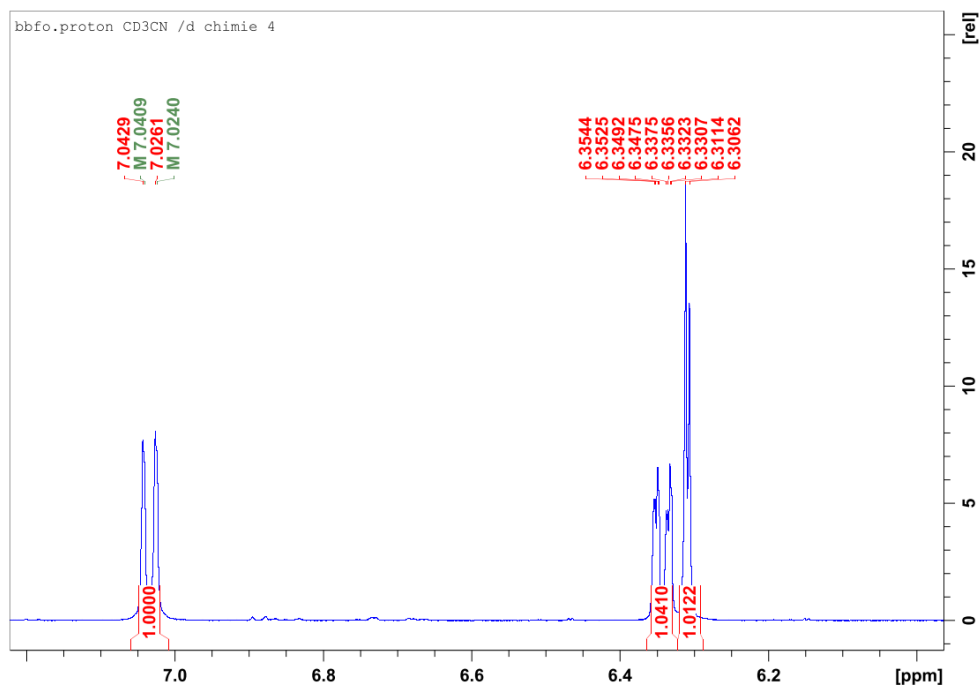
Figure S2.34: ^{1}H NMR spectrum of **1d** in CD$_3$CN; focus on aromatic region
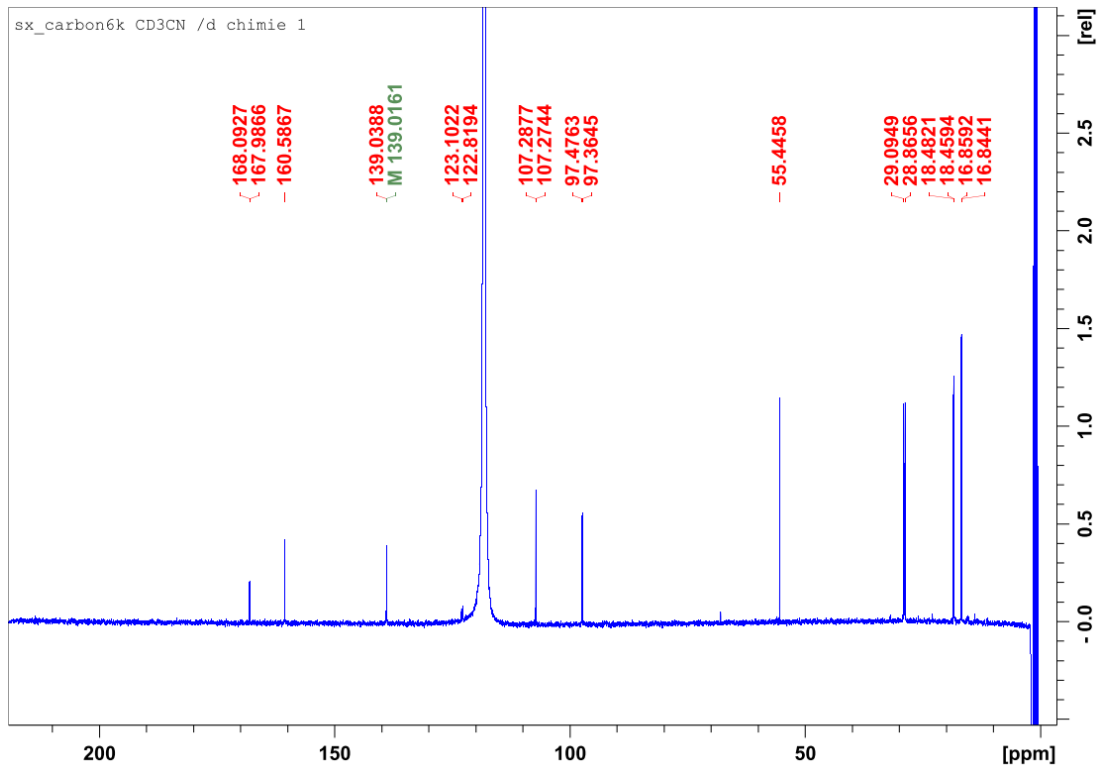
Figure S2. 35: Full ^{13}C{1H} NMR spectrum of **1d** in CD$_3$CN
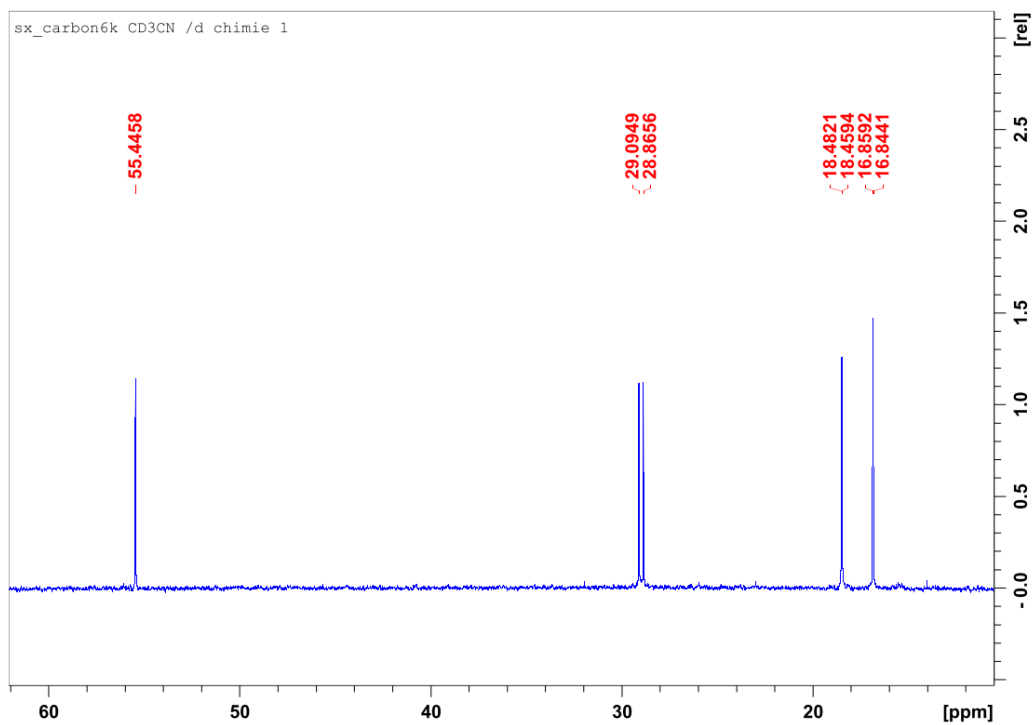
Figure S2.36 ^{13}C{^{1}H} NMR spectrum of **1d** in CD$_3$CN; focus on aliphatic region
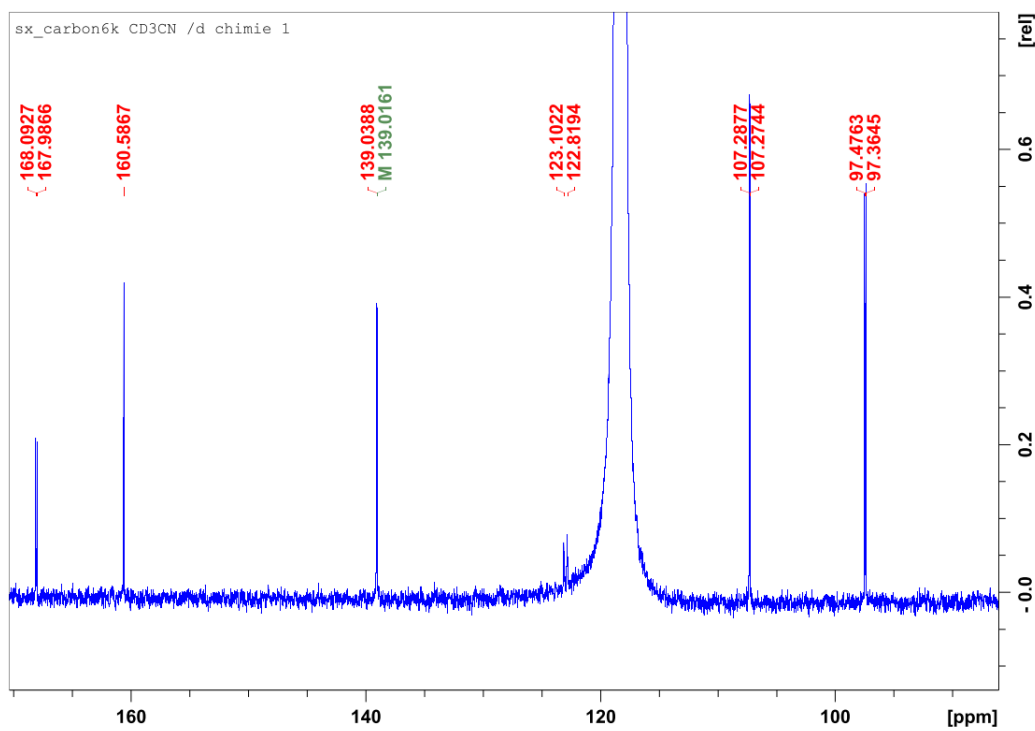
Figure S2.37: ^{13}C{^{1}H} NMR spectrum of **1d** in CD$_3$CN; focus on aromatic region

107

— 196.0664
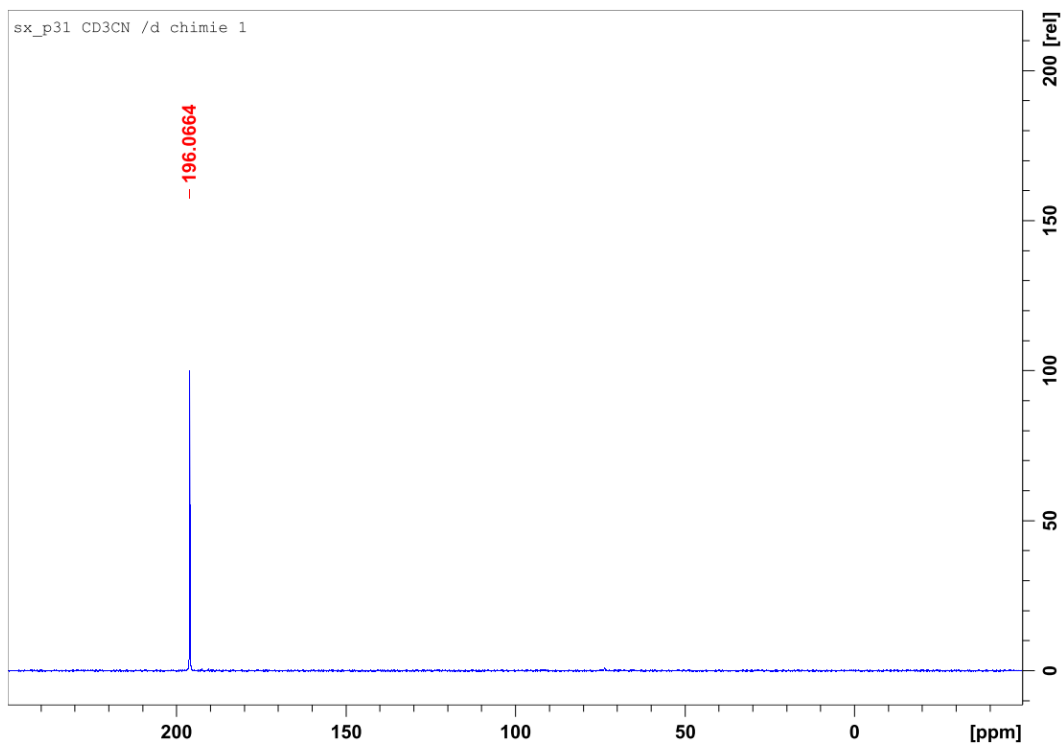
Figure S2.38: $^{31}P\{^1H\}$ NMR spectrum of **1d** in CD$_3$CN
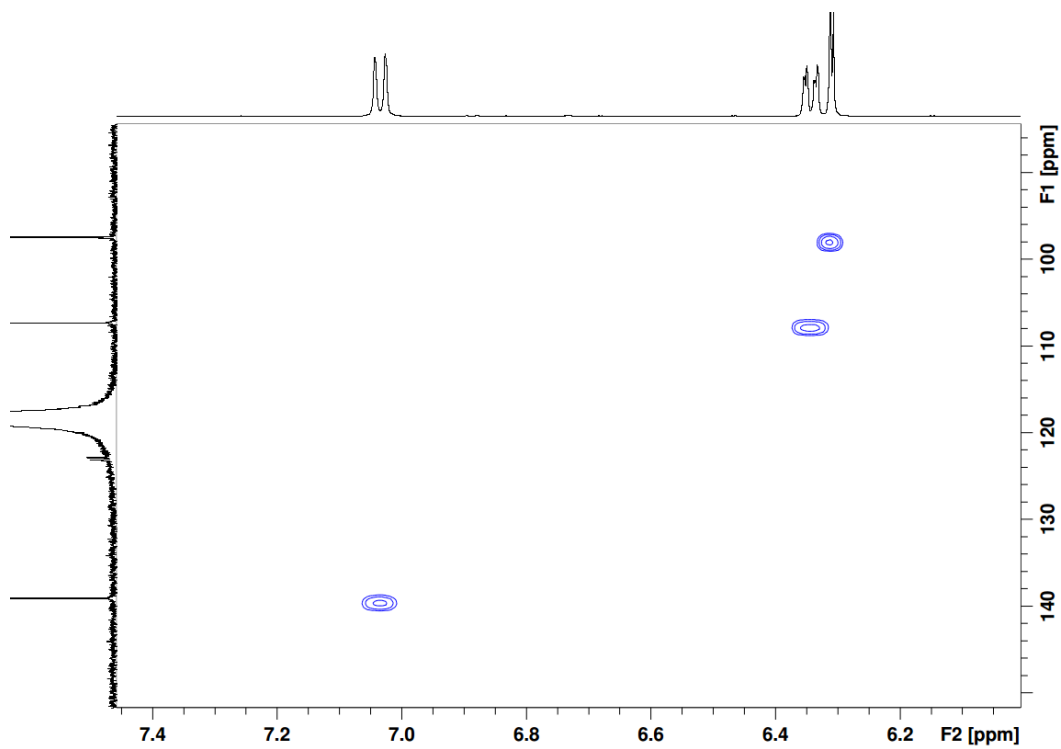
Figure S2.39: HSQC spectrum of **1d** in CD$_3$CN; focus on aromatic region

1e
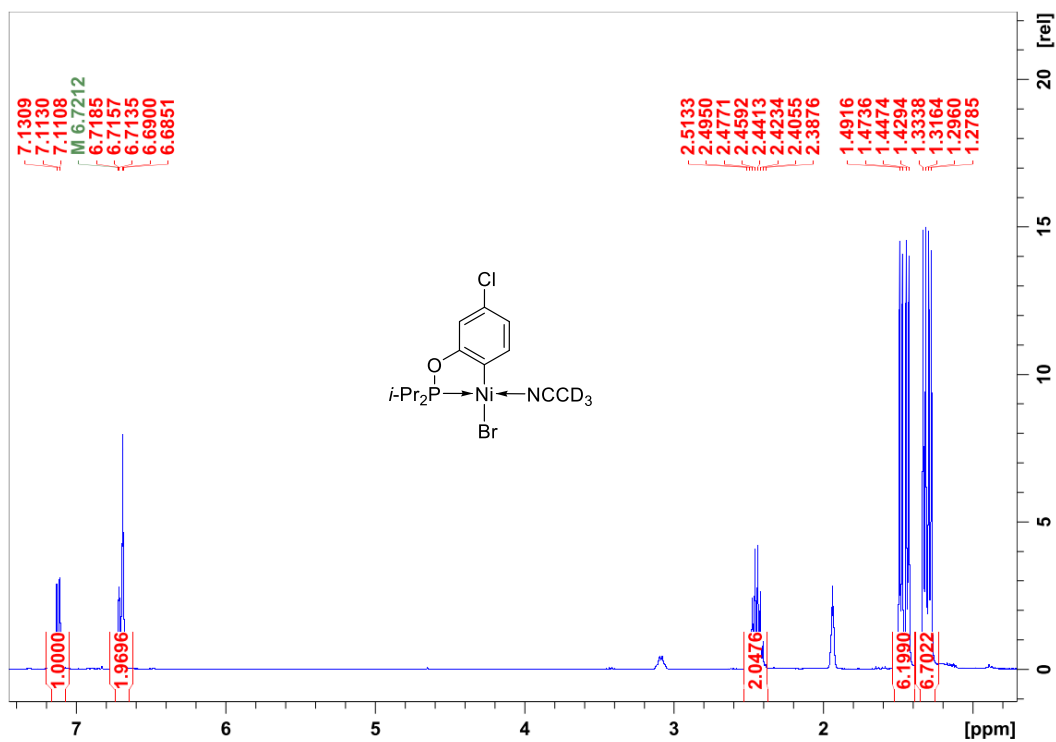
Figure S2.40: Full ^{1}H NMR spectrum of **1e** in CD$_3$CN
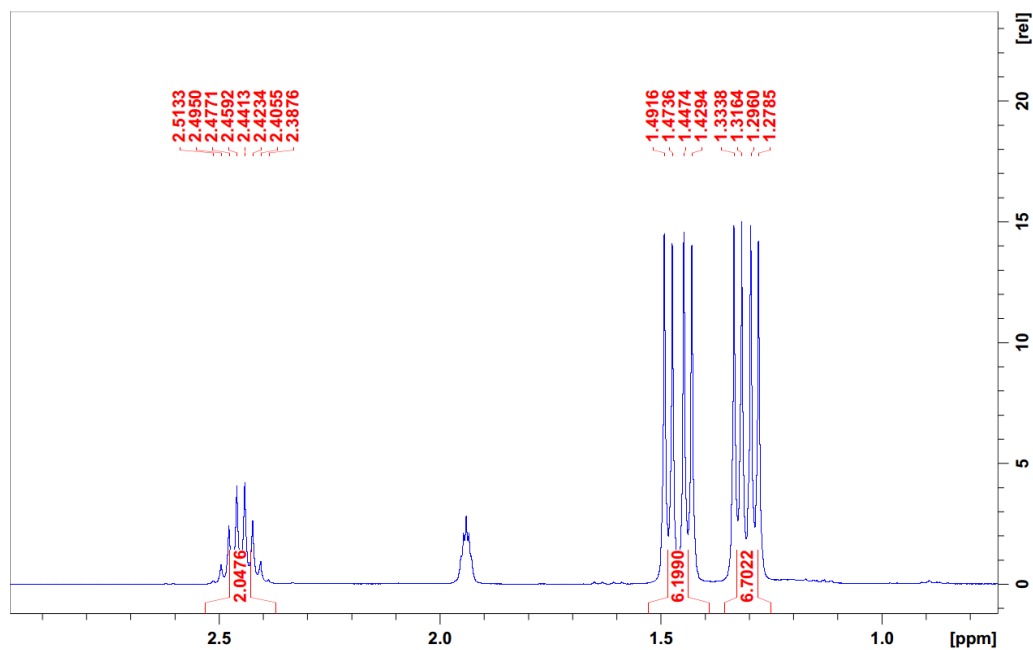
Figure S2.41: ^{1}H NMR spectrum of **1e** in CD$_3$CN; focus on aliphatic region
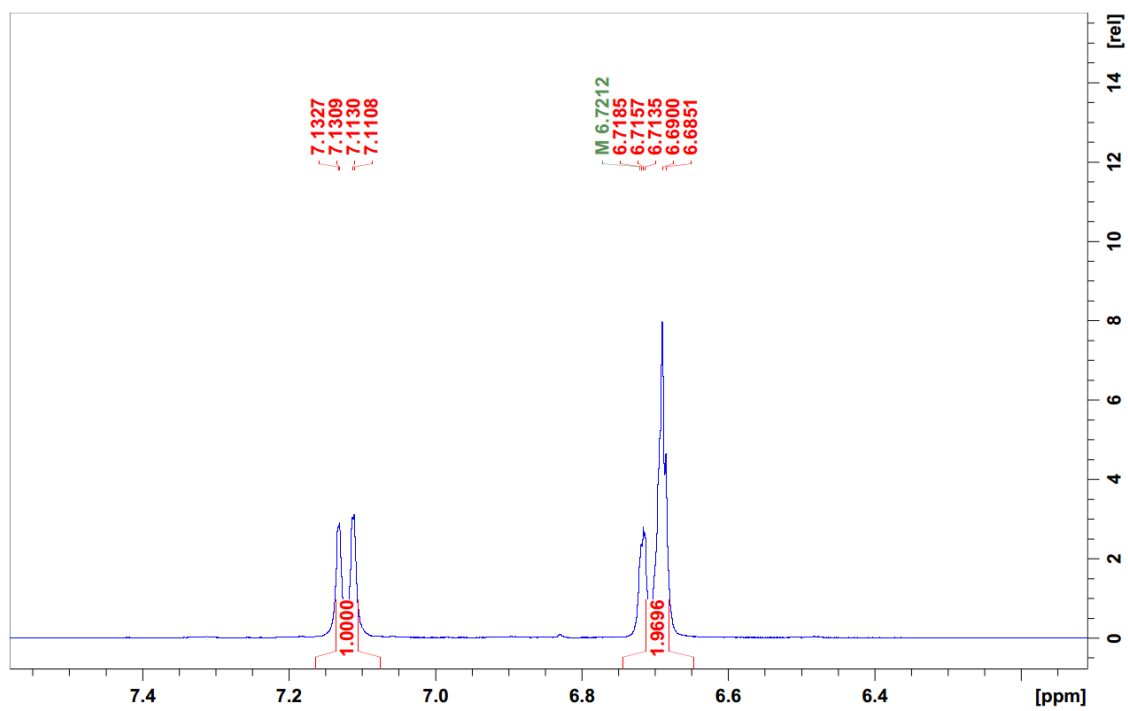
Figure S2.42: ^{1}H NMR spectrum of **1e** in CD$_3$CN; focus on aromatic region
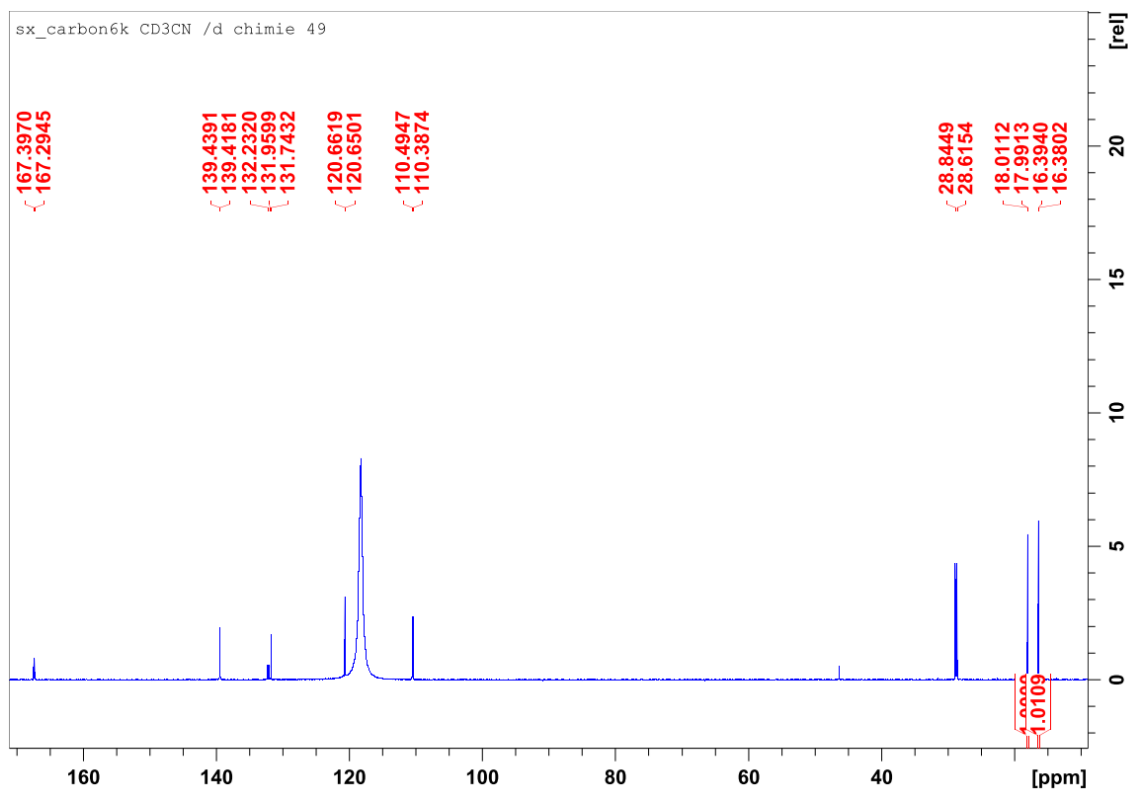
Figure S2.43: Full ^{13}C{^{1}H} NMR spectrum of **1e** in CD$_3$CN
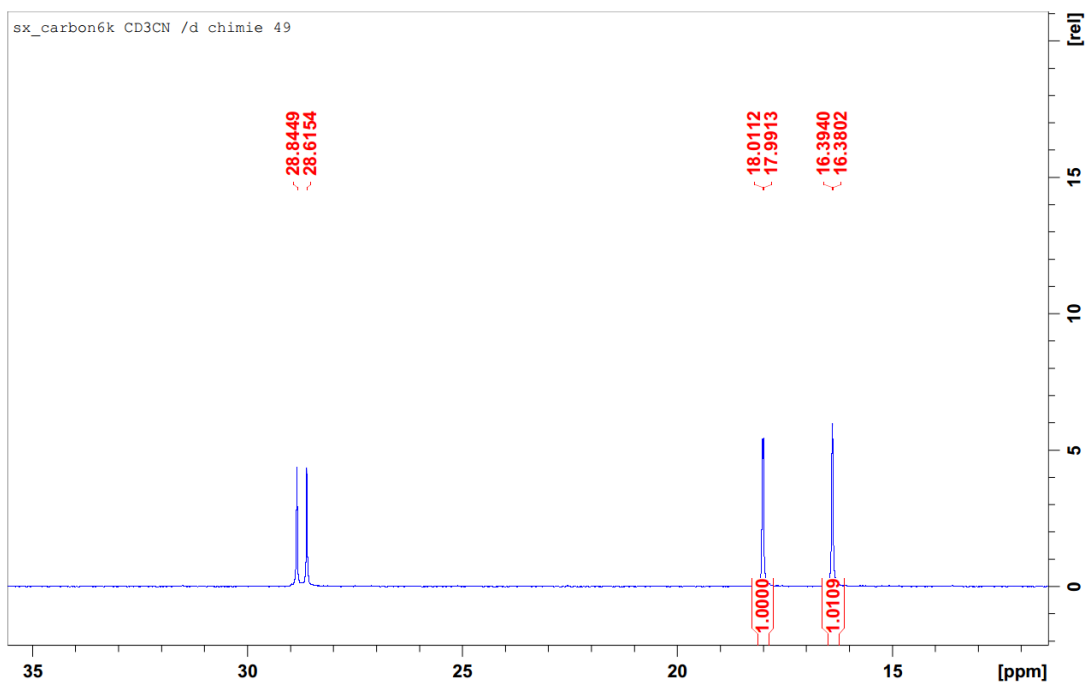
Figure S2.44: $^{13}C\{^1H\}$ NMR spectrum of **1e** in CD$_3$CN; focus on aliphatic region
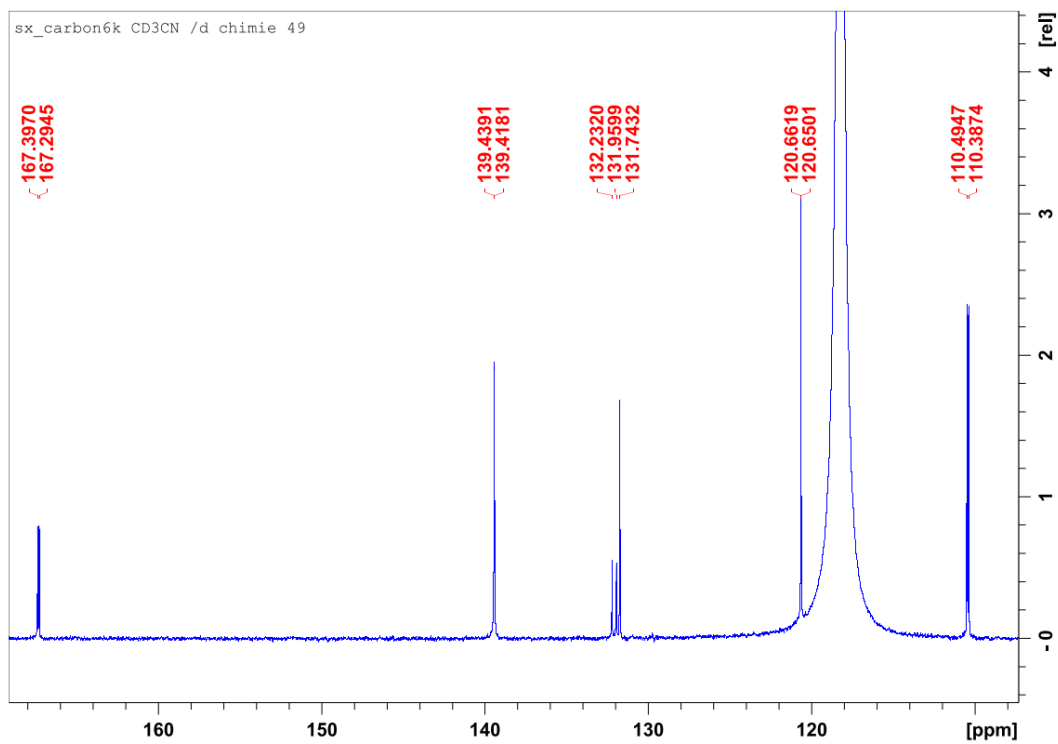
Figure S2.45: $^{13}C\{^1H\}$ NMR spectrum of **1a** in CD$_3$CN; focus on aromatic region
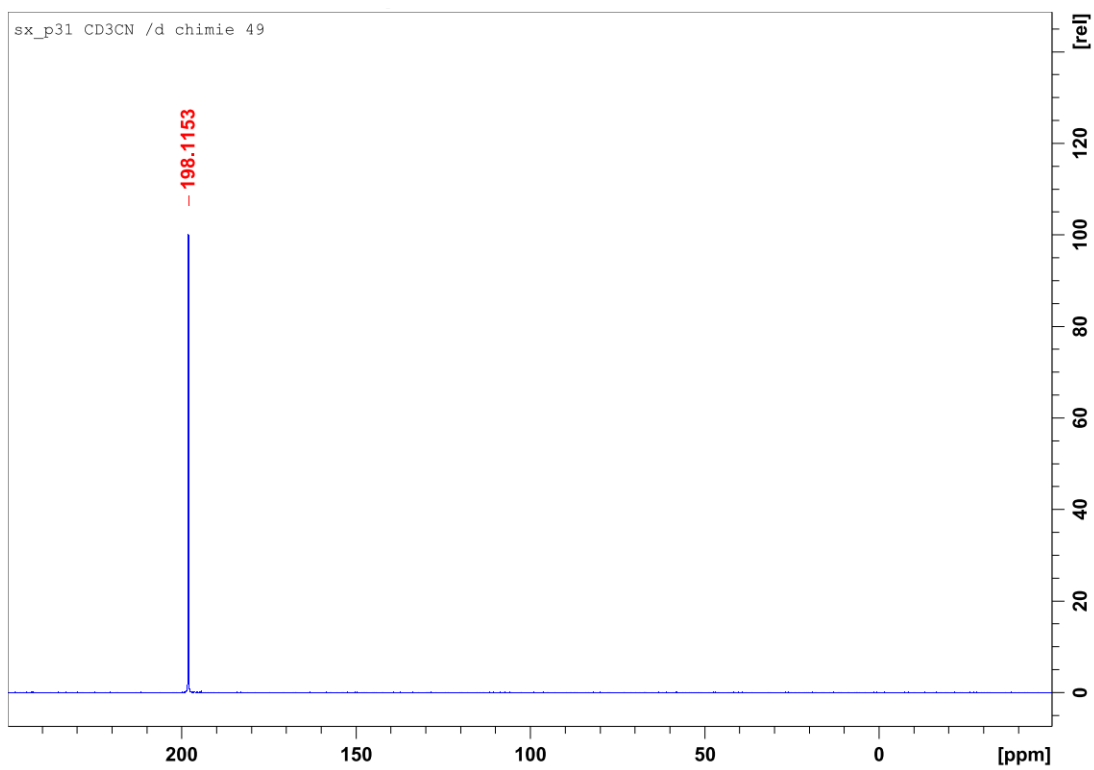
Figure S2.46: $^{31}P\{^1H\}$ NMR spectrum of **1e** in CD$_3$CN
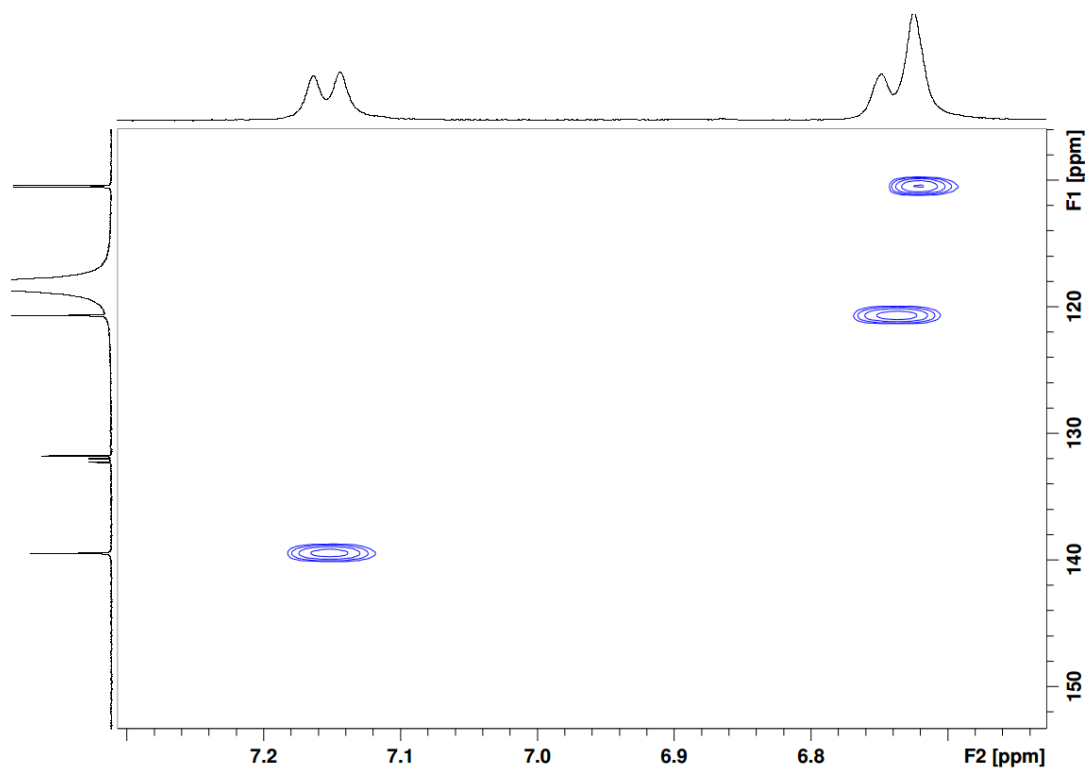
Figure S2.47: HSQC spectrum of **1a** in CD$_3$CN; focus on aromatic region

112

1f
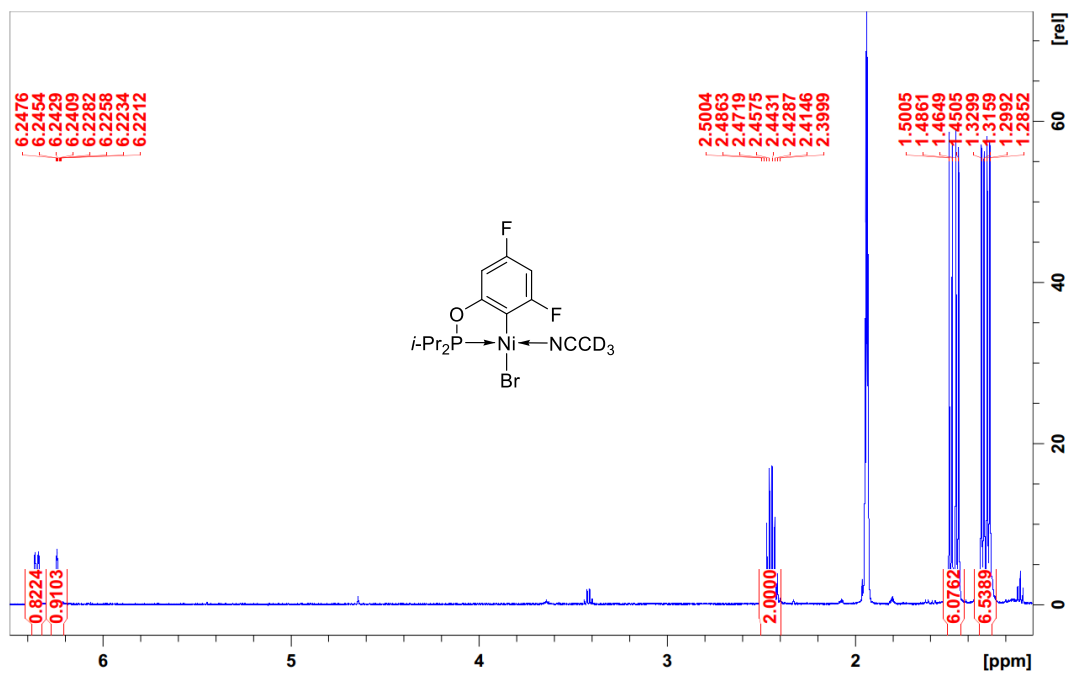
Figure S2.48: Full ^{1}H NMR spectrum of **1f** in CD$_3$CN
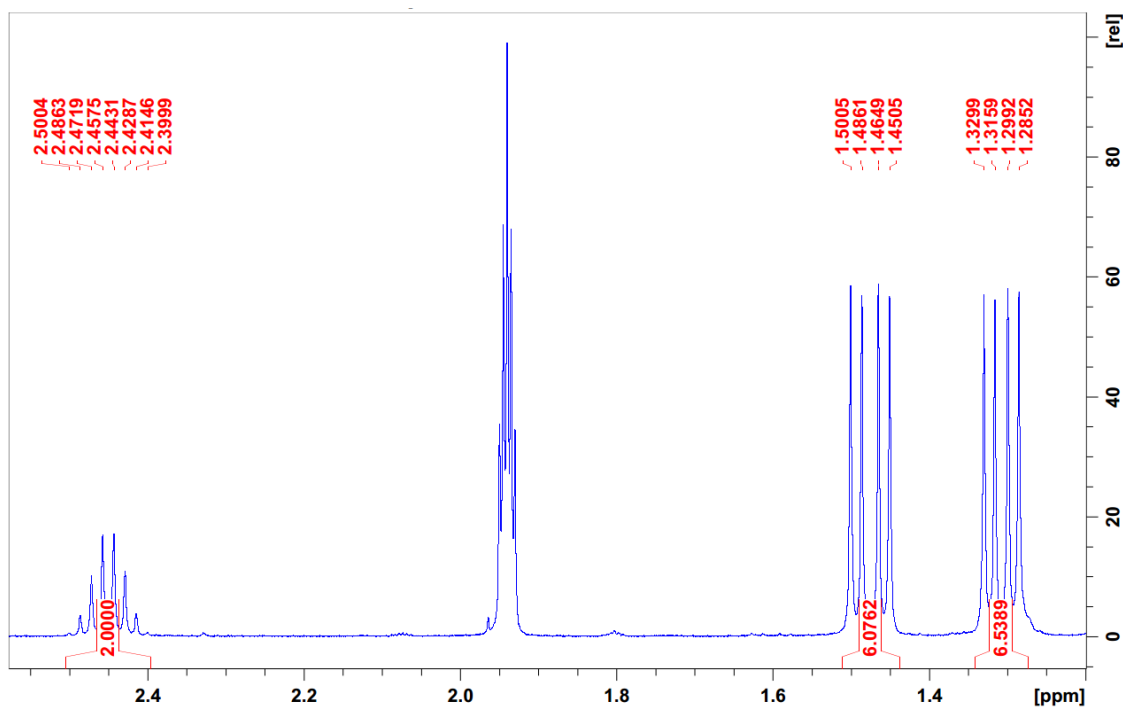
Figure S2.49: ^{1}H NMR spectrum of **1f** in CD$_3$CN; focus on aliphatic region

113
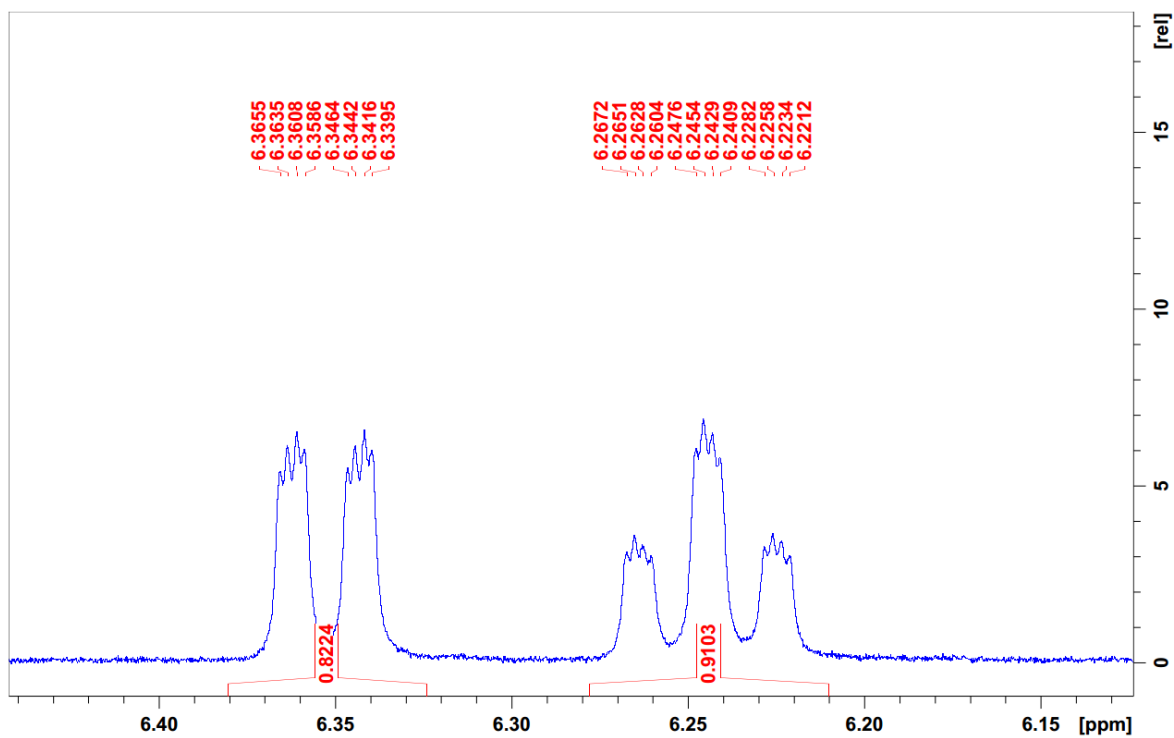
Figure S2.50: ^{1}H NMR spectrum of **1f** in CD$_3$CN; focus on aromatic region
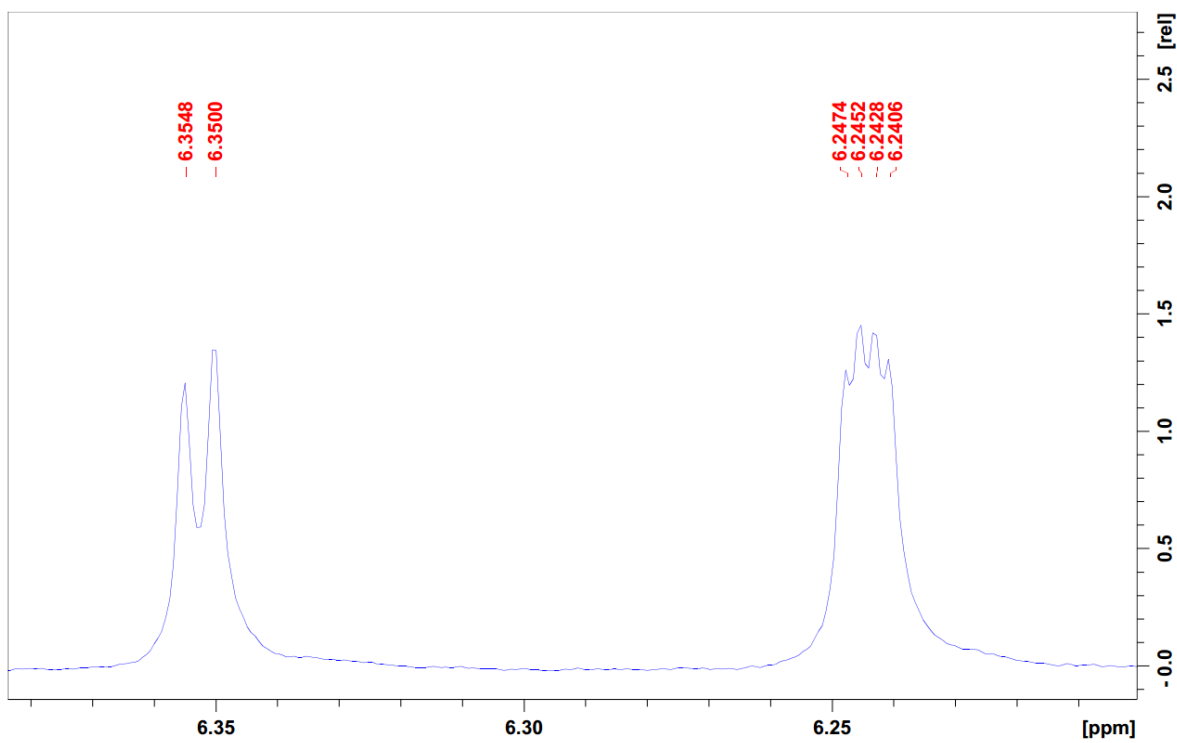
Figure S2.51: ^{1}H{^{19}F} NMR spectrum of **1f** in CD$_3$CN; focus on aromatic region
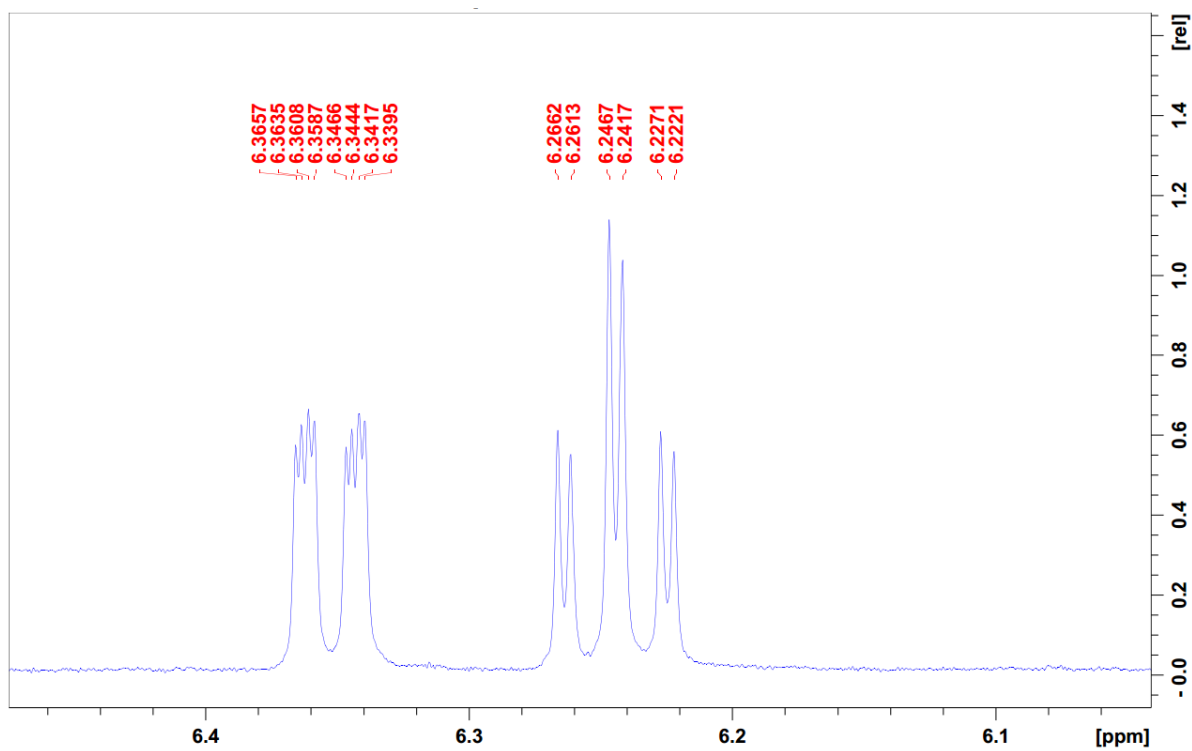
Figure S2.52: ^{1}H{^{19}F} NMR spectrum of **1f** in CD$_3$CN; focus on aromatic region
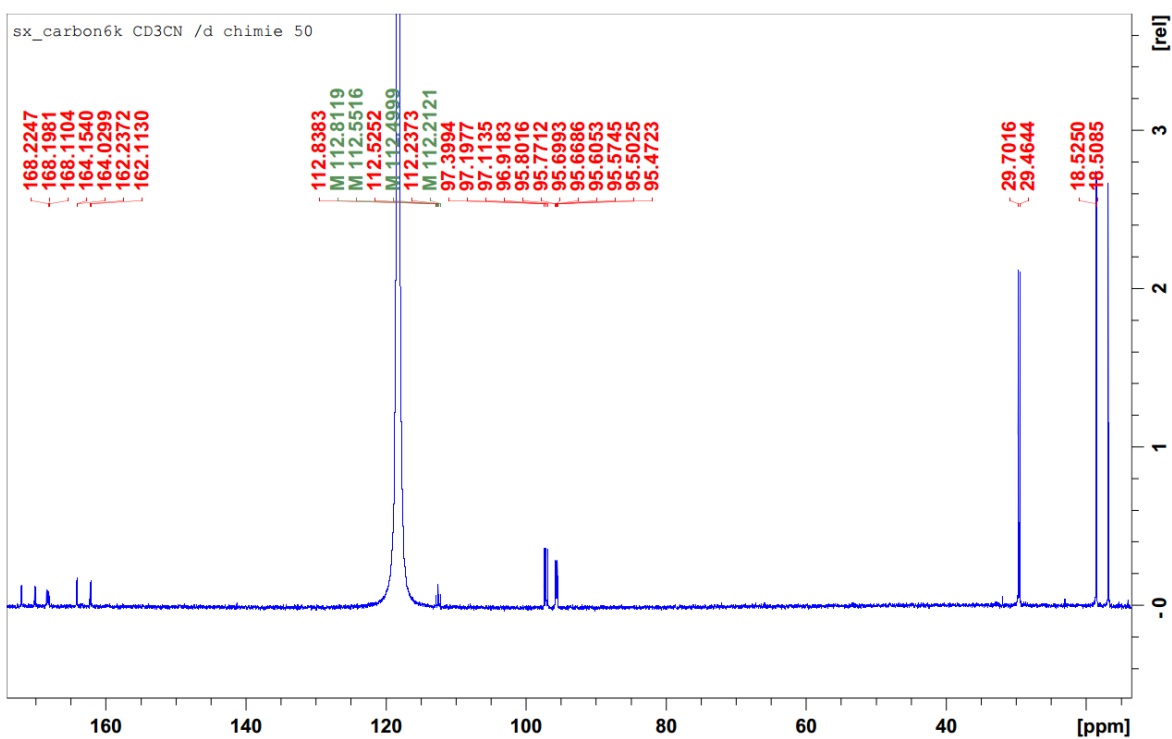
Figure S2.53: Full ^{13}C{^{1}H} NMR spectrum of **1f** in CD$_3$CN
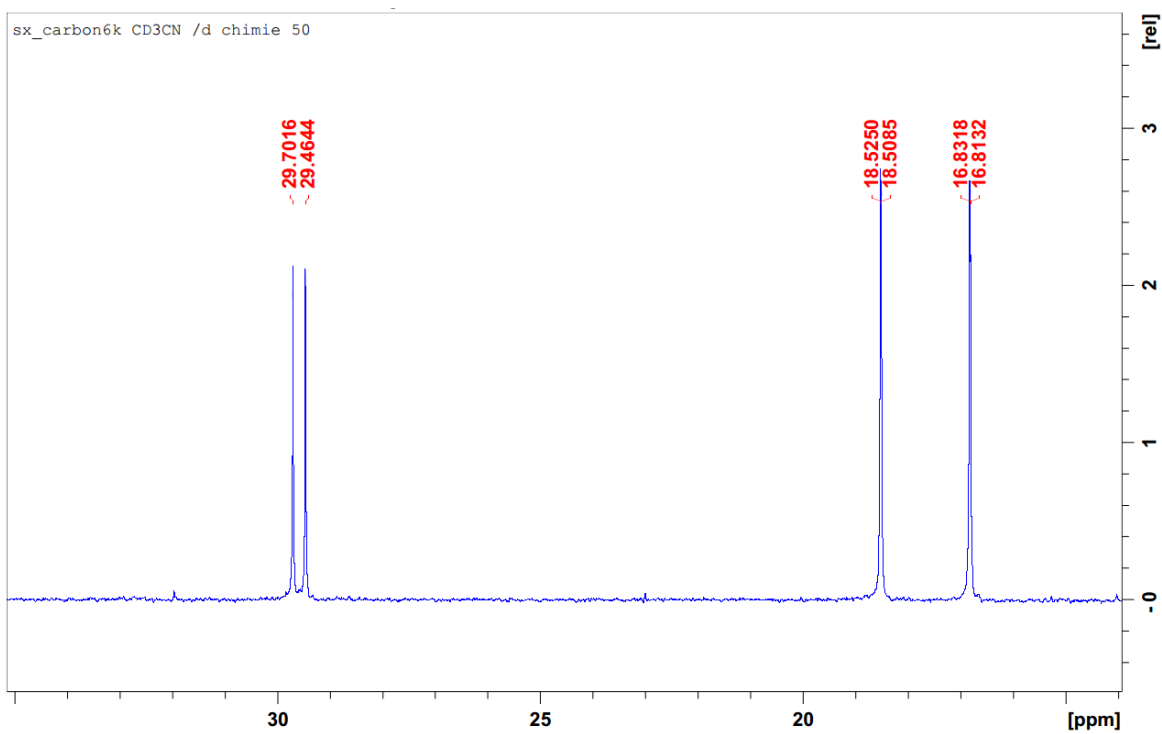
Figure S2.54: $^{13}C\{^1H\}$ NMR spectrum of **1f** in CD$_3$CN; focus on aliphatic region
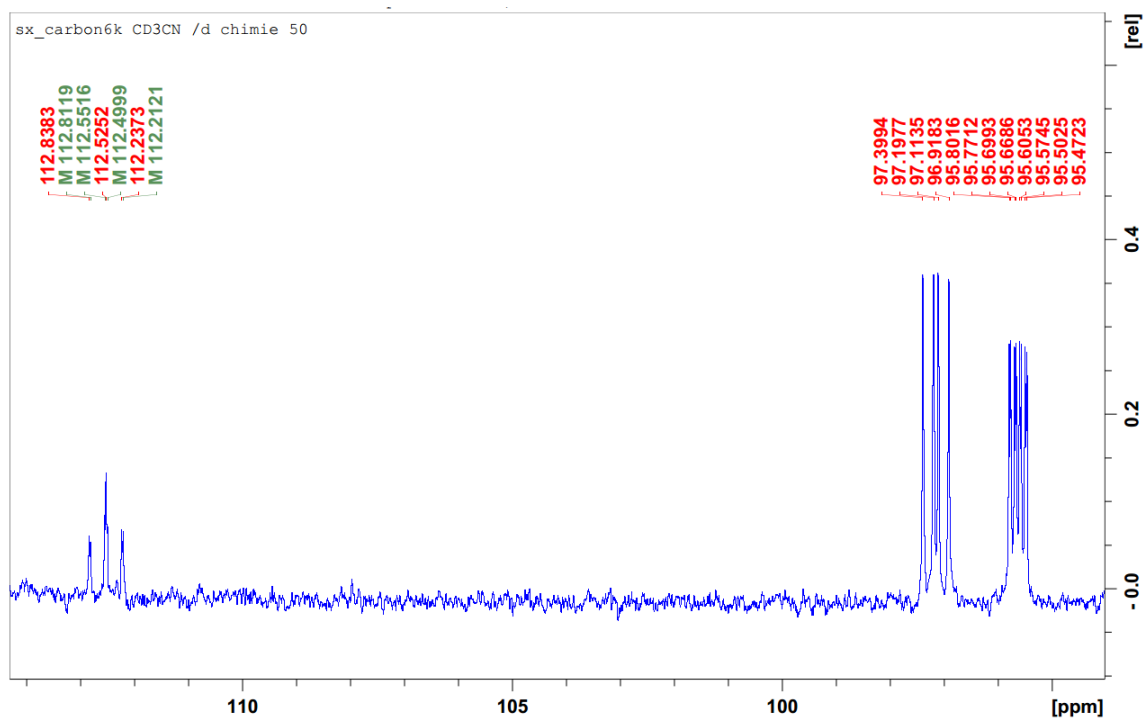
Figure S2.55: $^{13}C\{^1H\}$ NMR spectrum of **1f** in CD$_3$CN; focus on aromatic region (I)
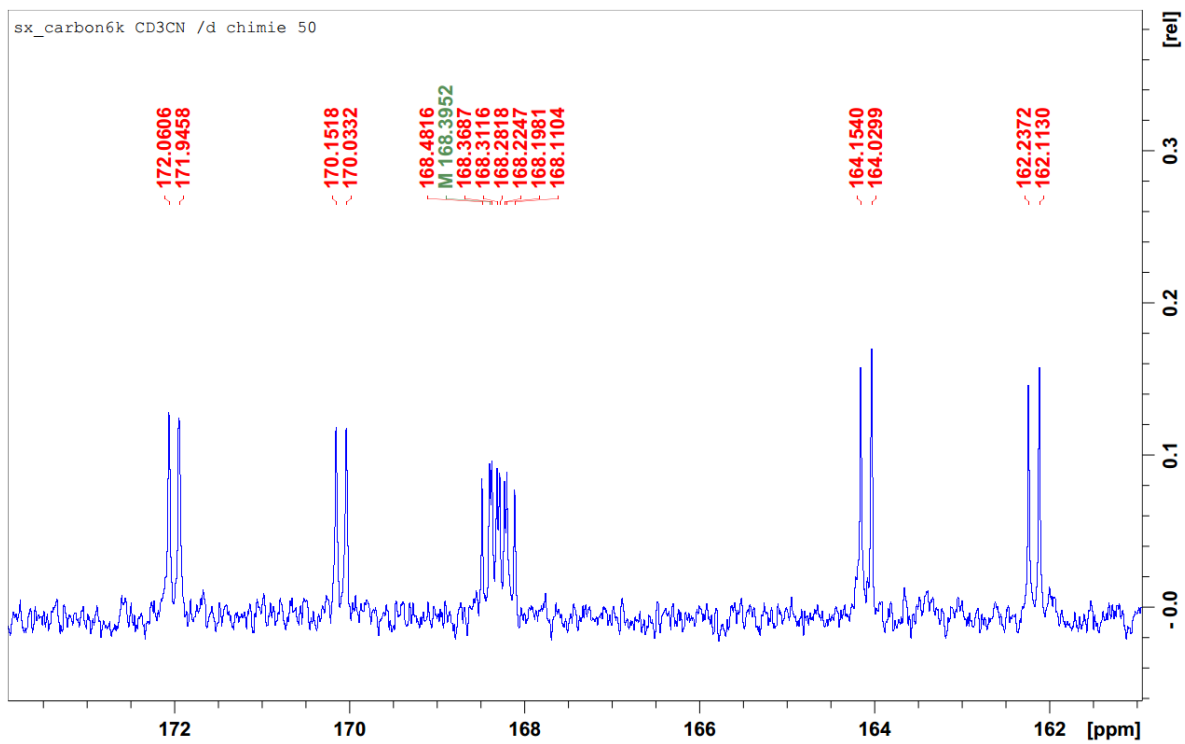
Figure S2.56: $^{13}C\{^1H\}$ NMR spectrum of **1f** in CD₃CN; focus on aromatic region (II)
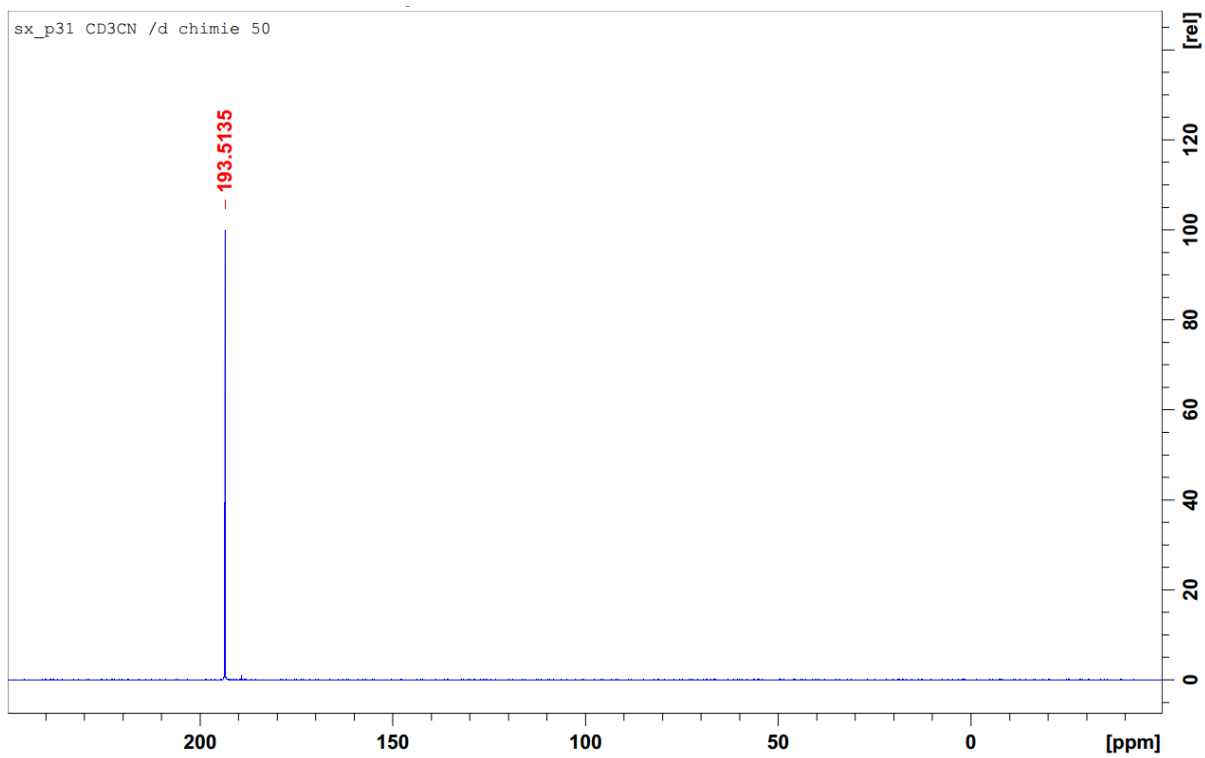
Figure S2.57: $^{31}P\{^1H\}$ NMR spectrum of **1f** in CD₃CN
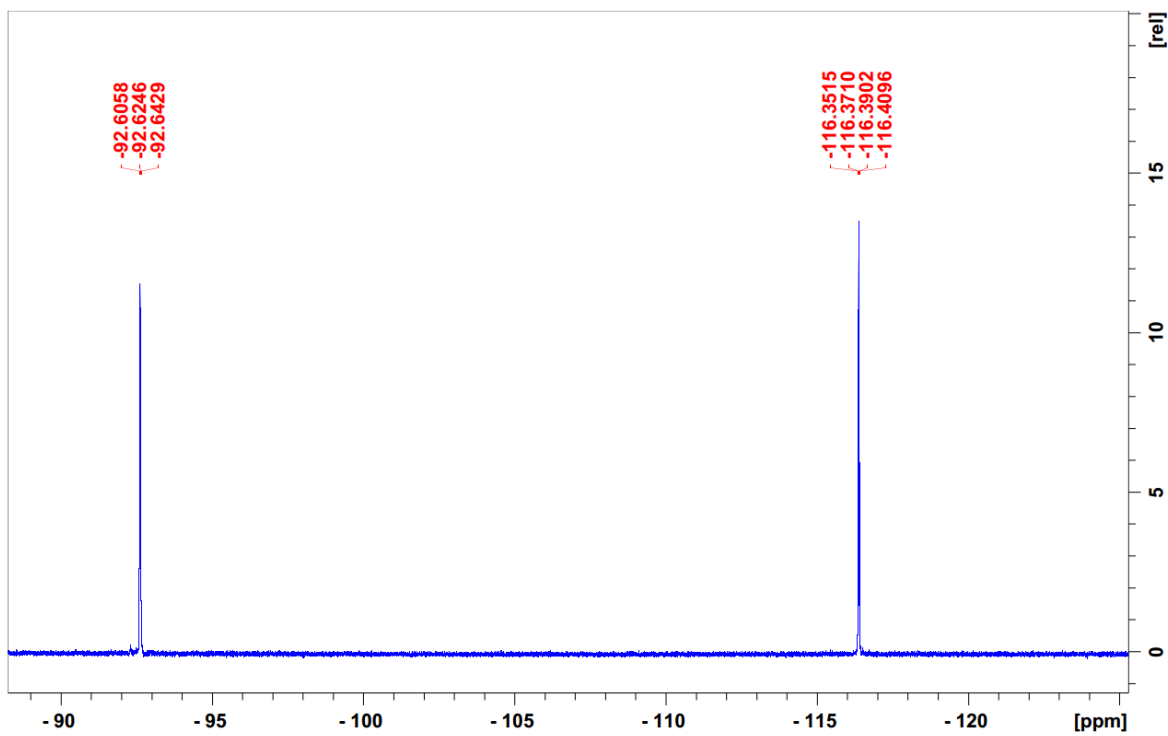
Figure S2.58: ^{31}F{^{1}H} NMR spectrum of **1f** in CD$_3$CN
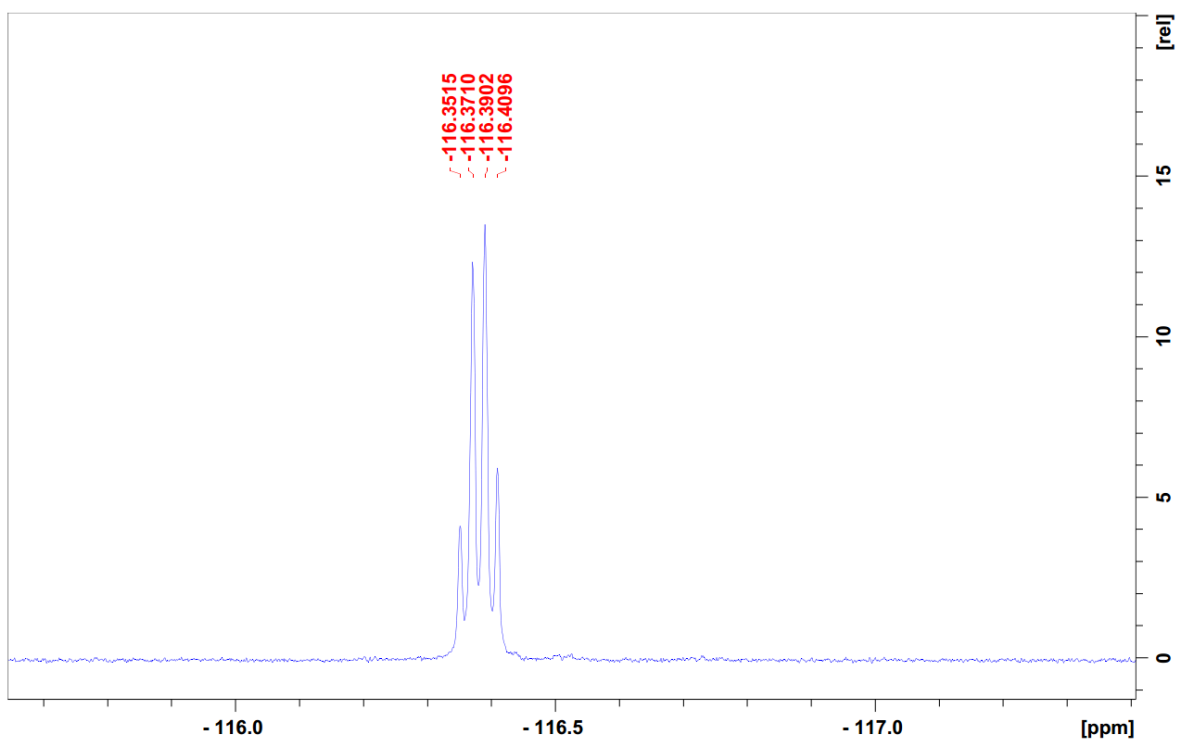
Figure S2.59: ^{31}F{^{1}H} NMR spectrum of **1f** in CD$_3$CN; focus on C5$_{Ar}$-F
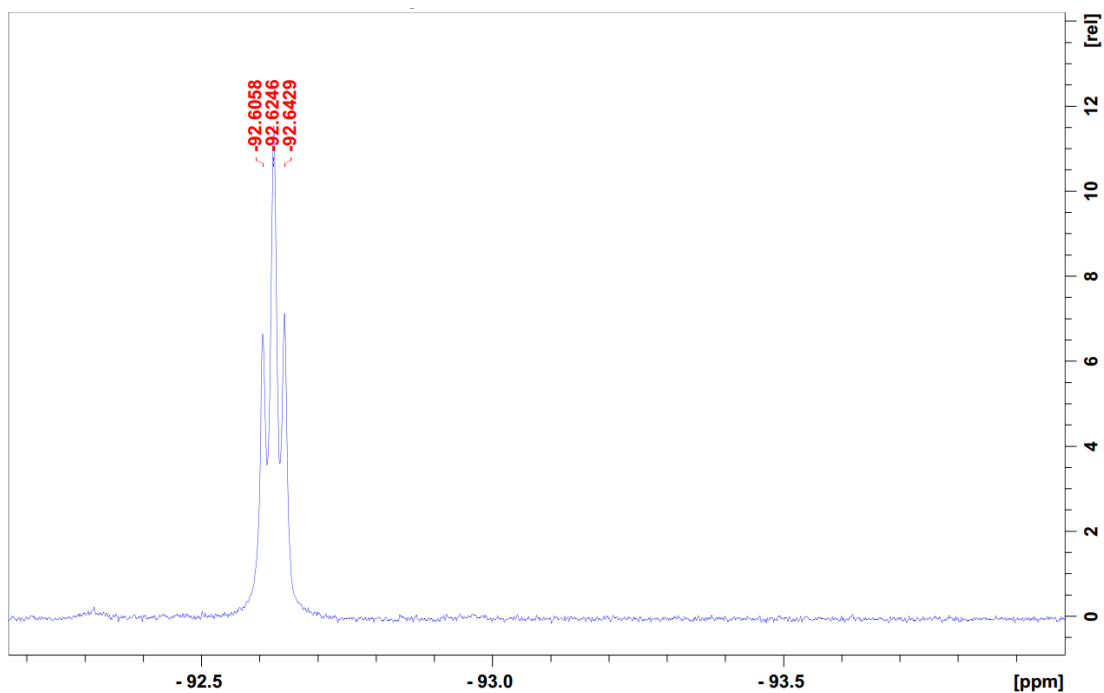
Figure S2.60: ^{31}F{^{1}H} NMR spectrum of **1f** in CD$_3$CN; focus on C3$_{Ar}$-F
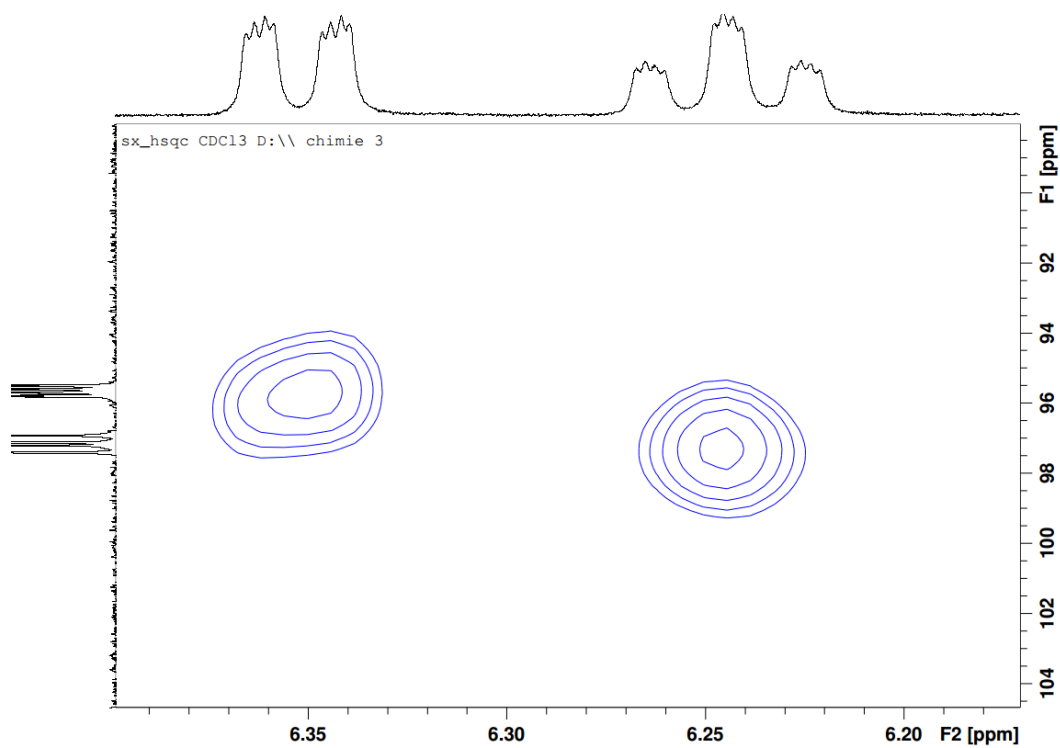
Figure S2.61: HSQC spectrum of **1f** in CD$_3$CN; focus on aromatic region

1i-NCMe
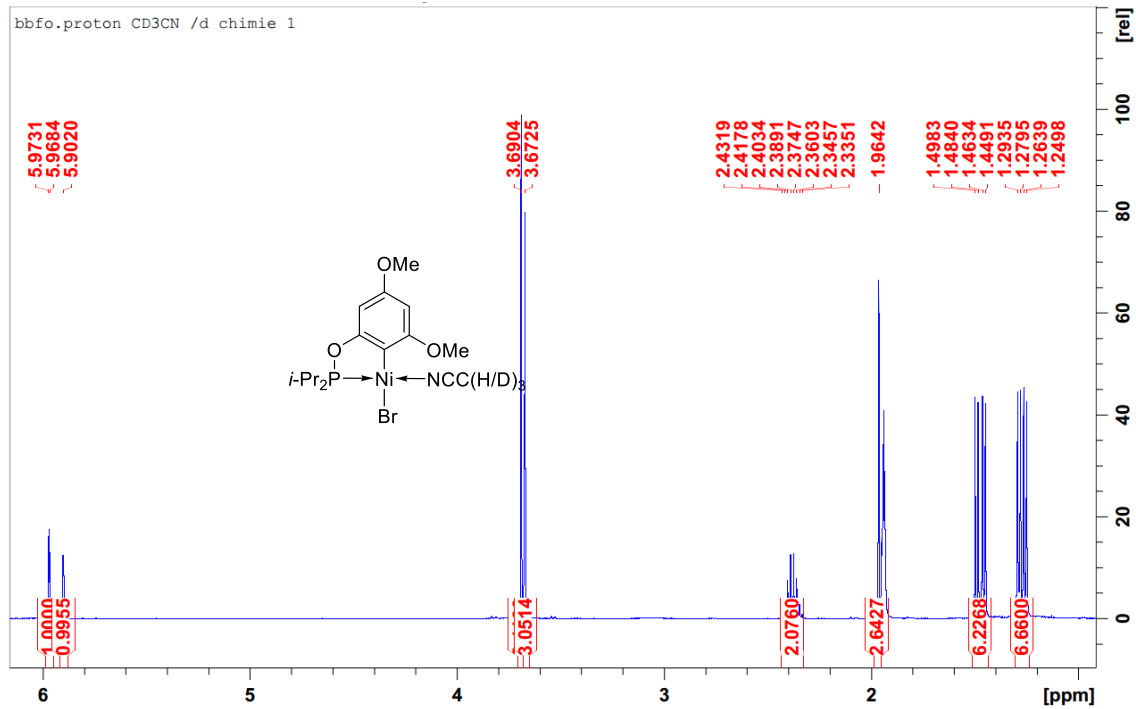
Figure S2.62: Full ^{1}H NMR spectrum of **1i-NCMe** in CD$_3$CN
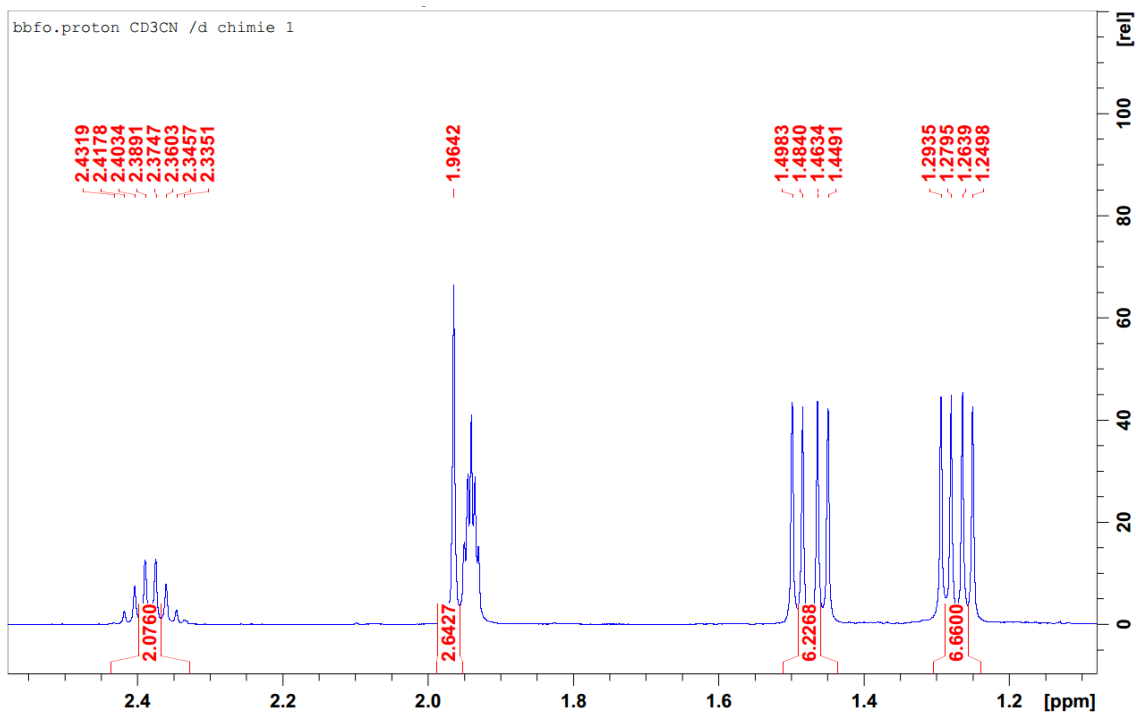
Figure S2.63: ^{1}H NMR spectrum of **1i-NCMe** in CD$_3$CN; focus on aliphatic region

Figure S2.64: ^{1}H NMR spectrum of **1i-NCMe** in CD$_3$CN; focus on O-CH$_3$ and aromatic region

Figure S2.65: Full ^{13}C{^{1}H} NMR spectrum of **1i-NCMe** in CD$_3$CN
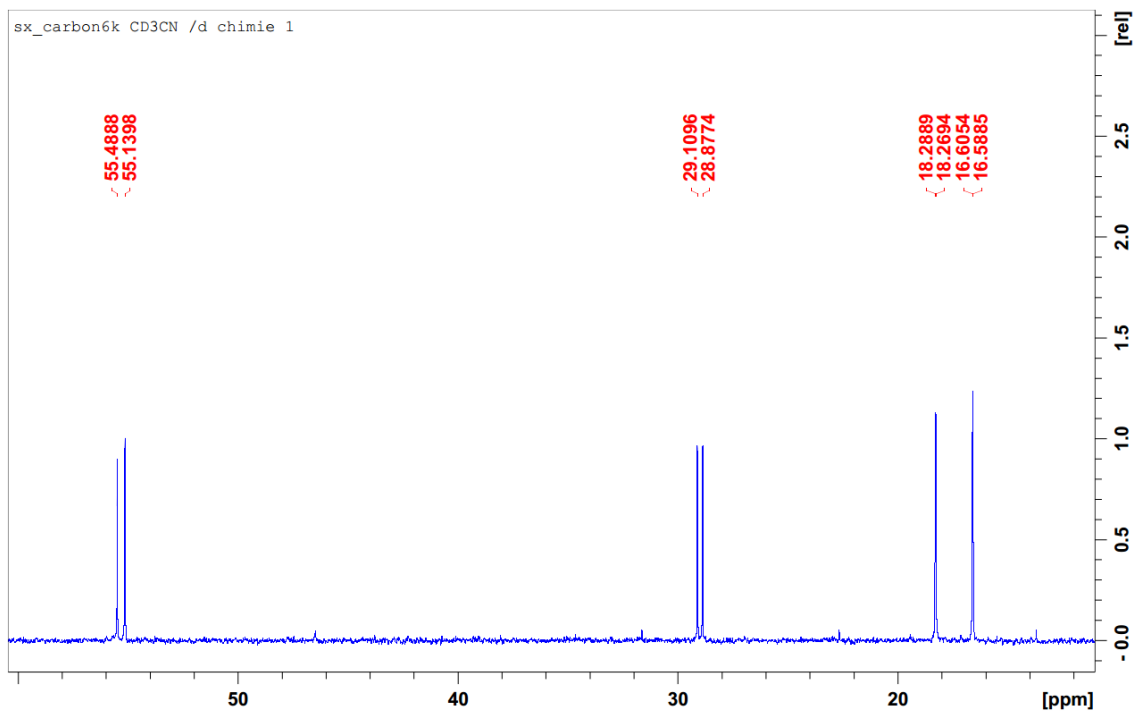
Figure S2.66: $^{13}C\{^1H\}$ NMR spectrum of **1i-NCMe** in CD$_3$CN; focus on aliphatic region
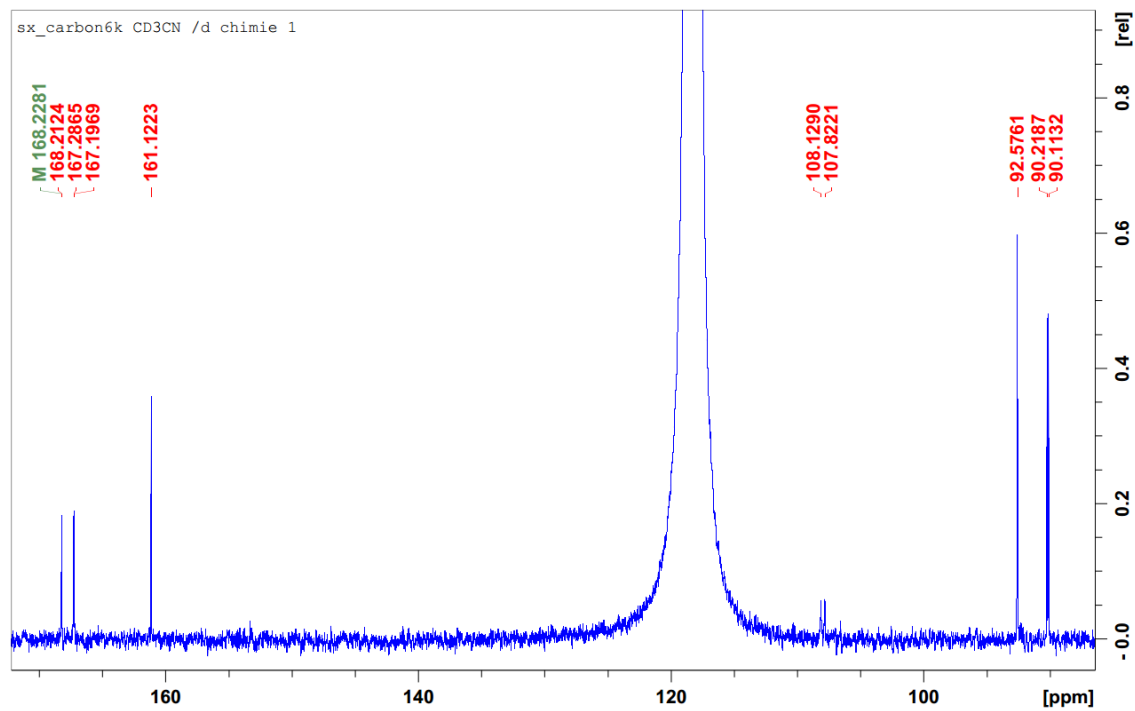
Figure S2.67: $^{13}C\{^1H\}$ NMR spectrum of **1i-NCMe** in CD$_3$CN; focus on aromatic region
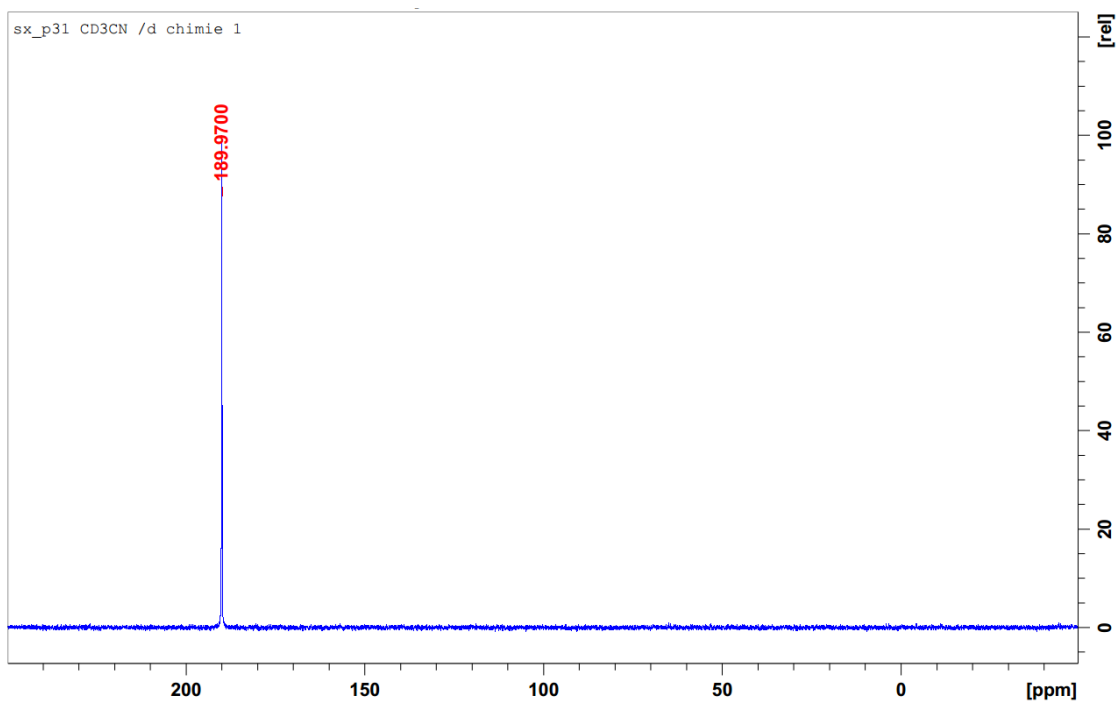
Figure S2.68: $^{31}P\{^1H\}$ NMR spectrum of **1i-NCMe** in CD$_3$CN
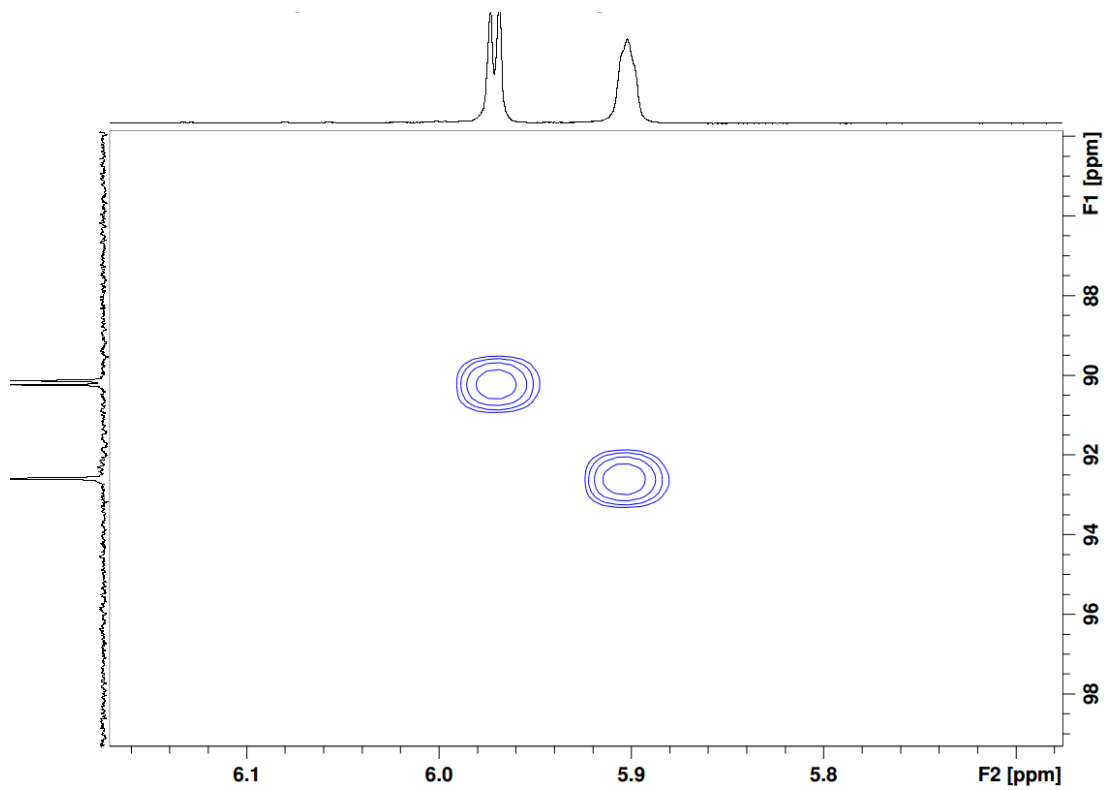
Figure S2.69: HSQC spectrum of **1i-NCMe** in CD$_3$CN; focus on aromatic region

1j
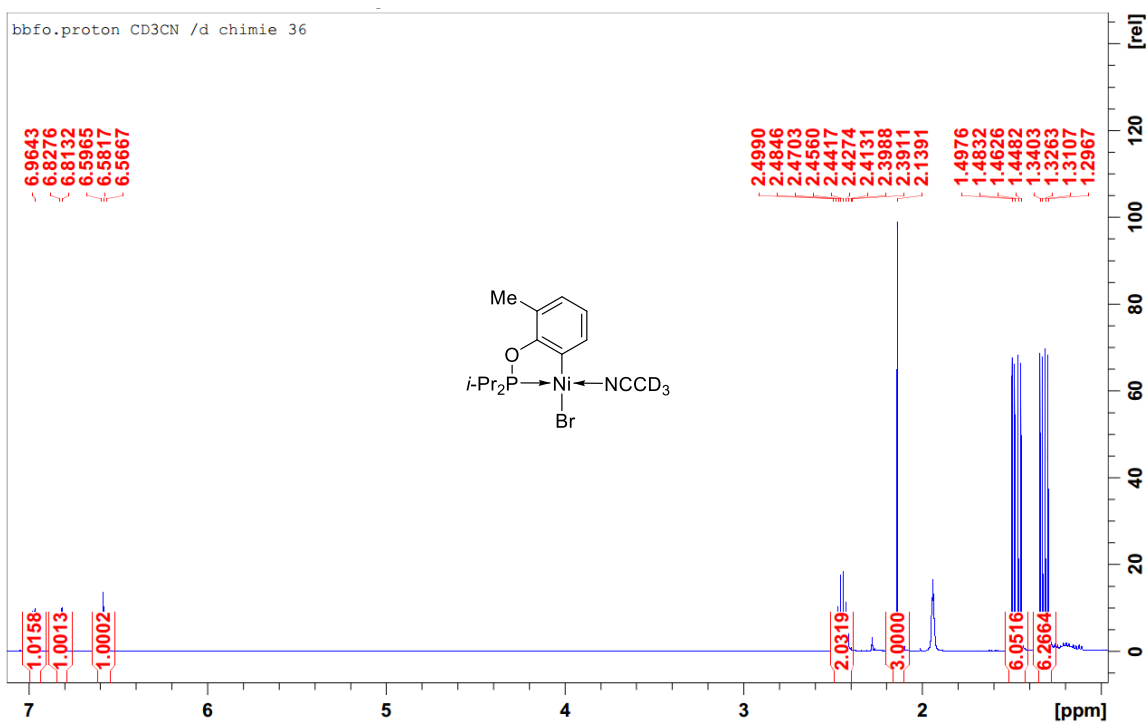
Figure S2.70: Full ^{1}H NMR spectrum of **1j** in CD$_3$CN
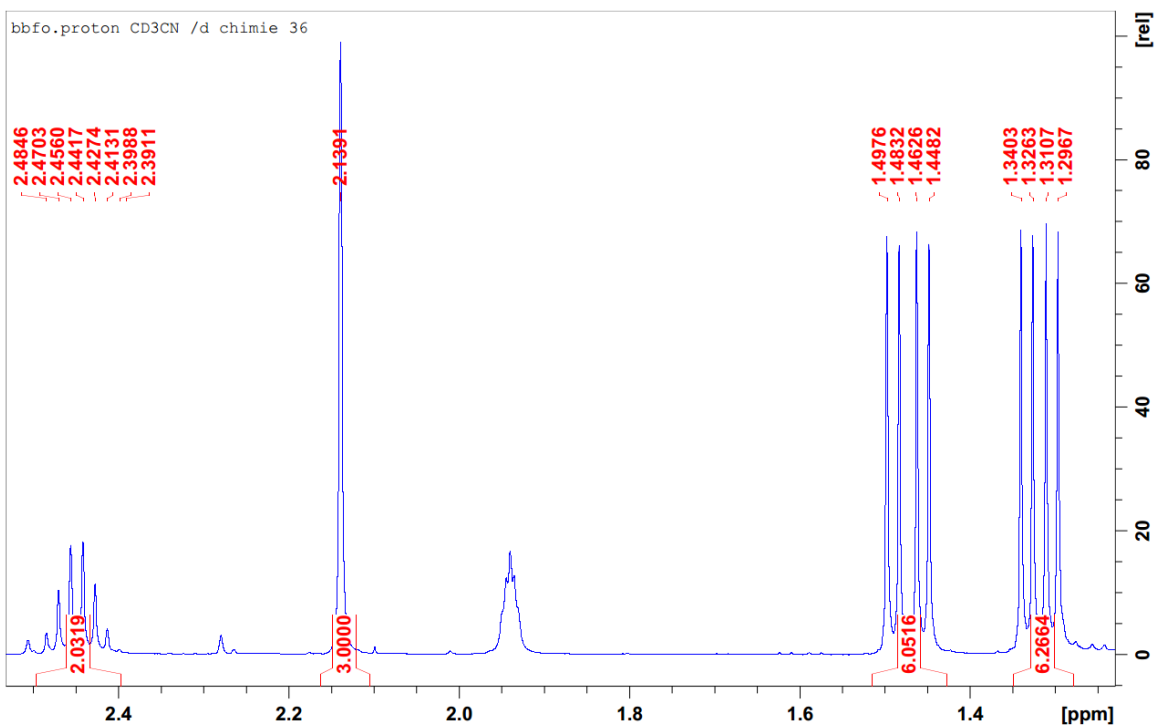
Figure S2.71: ^{1}H NMR spectrum of **1j** in CD$_3$CN; focus on aliphatic region
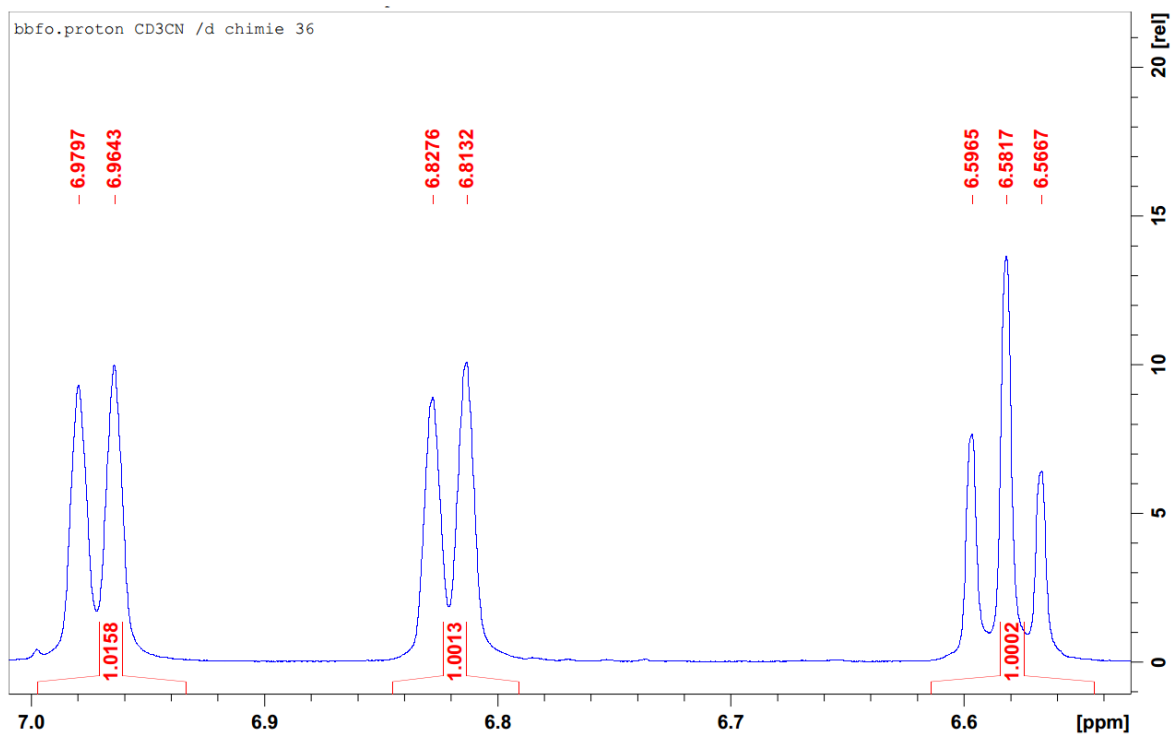
Figure S2.72: ^{1}H NMR spectrum of **1j** in CD$_3$CN; focus on aromatic region
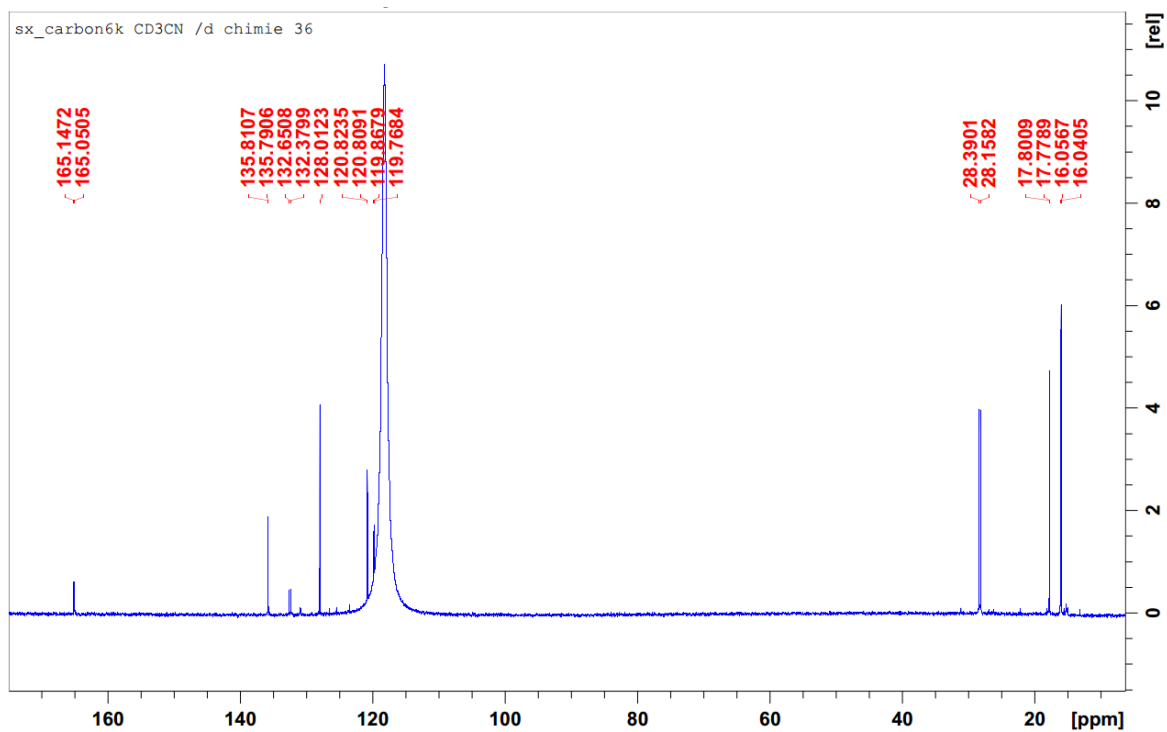
Figure S2.73: Full ^{13}C{^{1}H} NMR spectrum of **1j** in CD$_3$CN
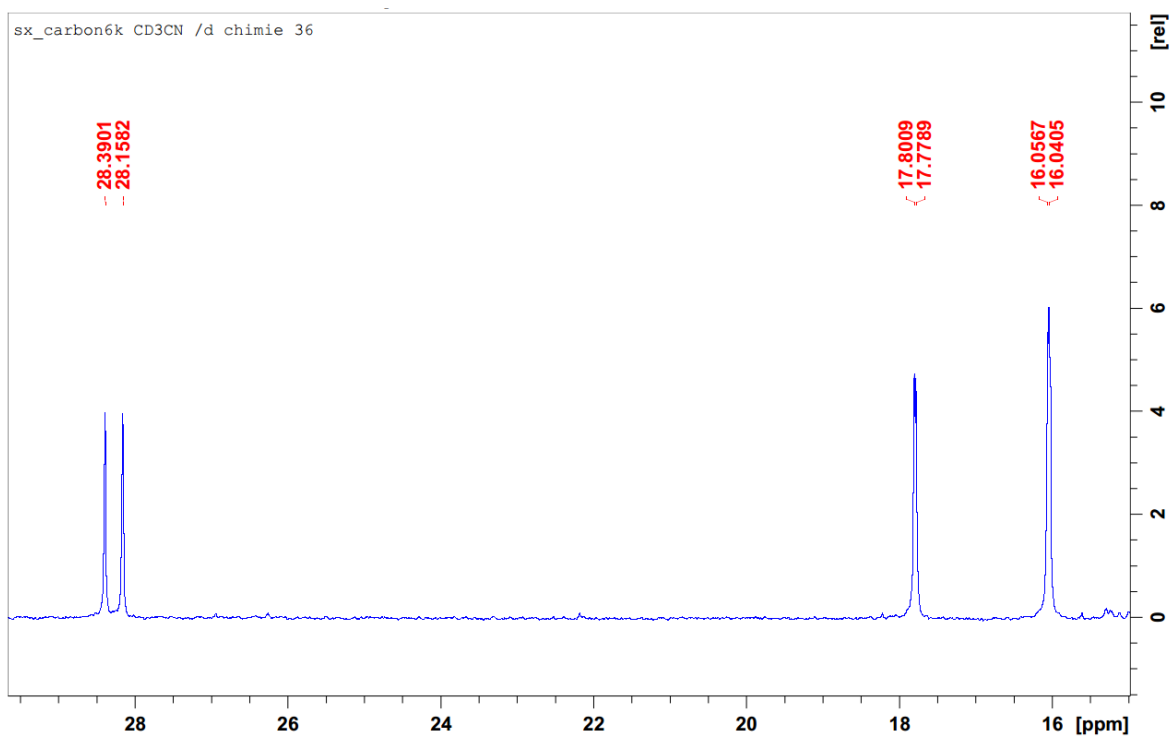
Figure S2.74: $^{13}C\{^1H\}$ NMR spectrum of **1a** in CD$_3$CN; focus on aliphatic region
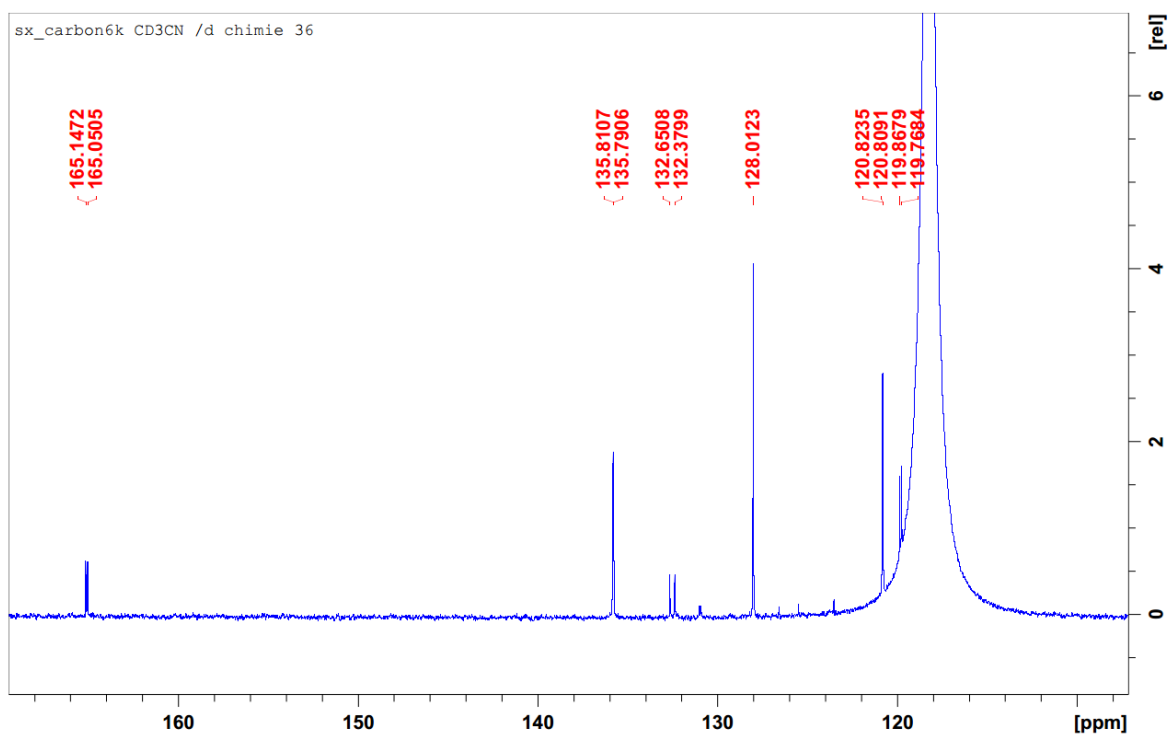
Figure S2.75: $^{13}C\{^1H\}$ NMR spectrum of **1j** in CD$_3$CN; focus on aromatic region
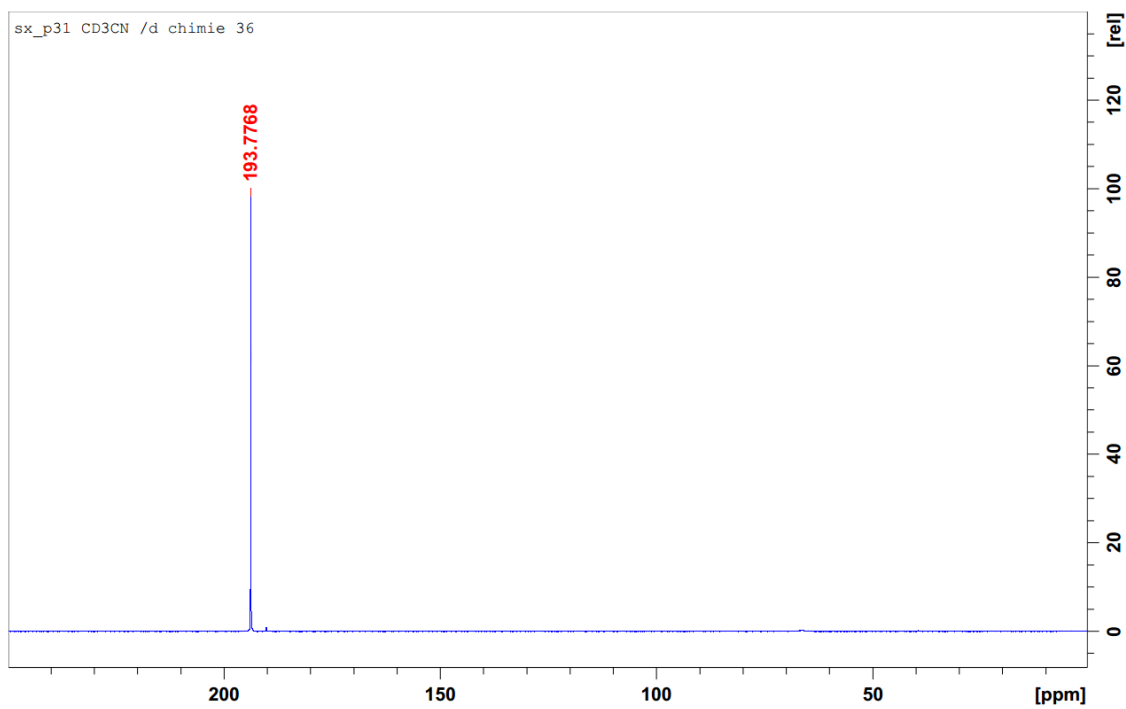
Figure S2.76: $^{31}P\{^{1}H\}$ NMR spectrum of **1j** in CD$_3$CN
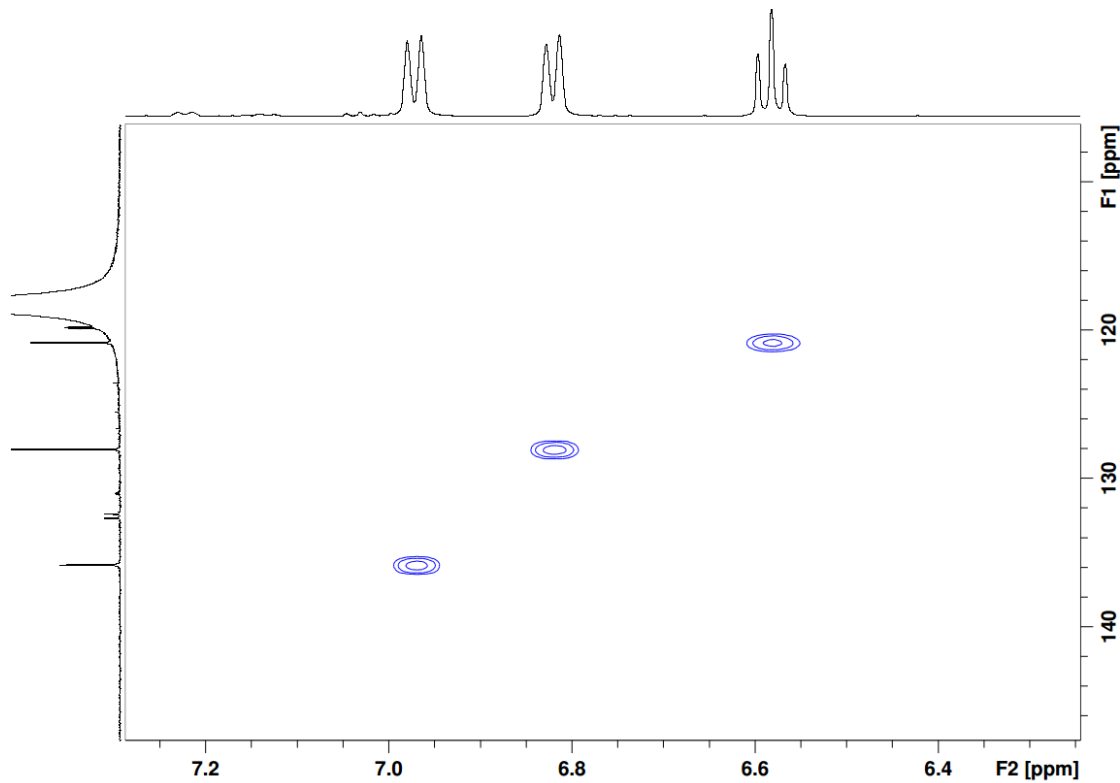
Figure S2.77: HSQC spectrum of **1j** in CD$_3$CN; focus on aromatic region

1k
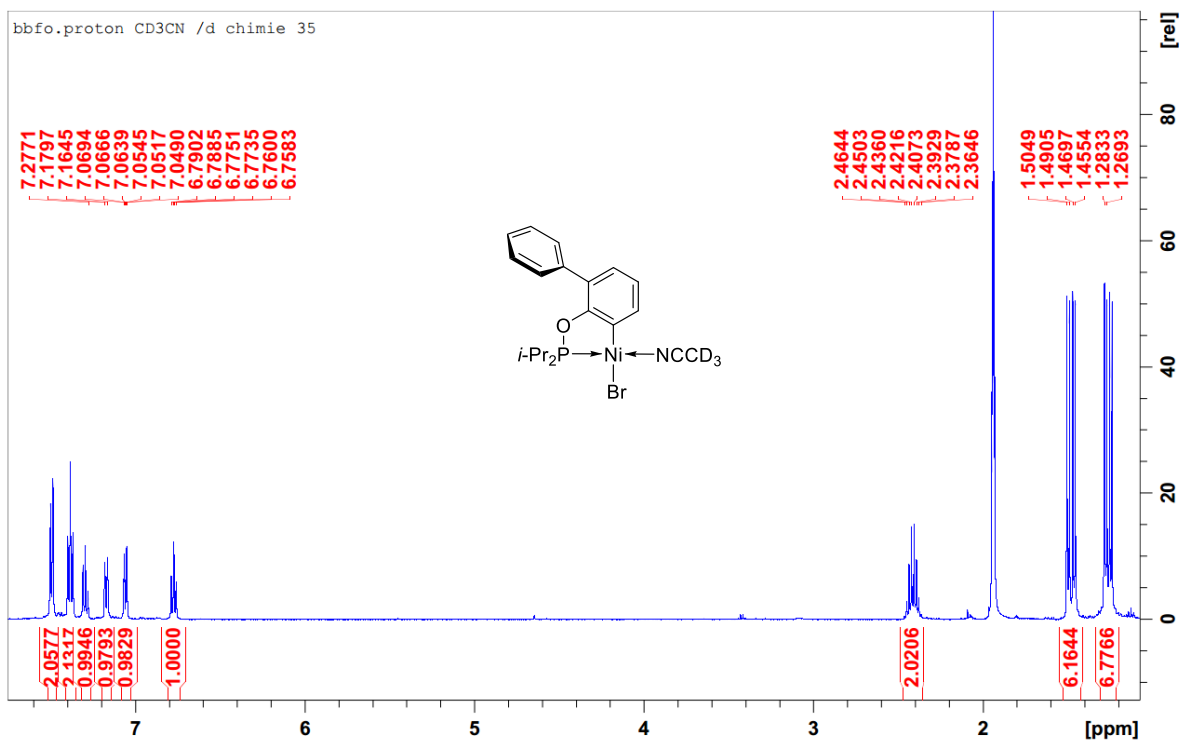
Figure S2.78: Full ^{1}H NMR spectrum of **1k** in CD$_3$CN
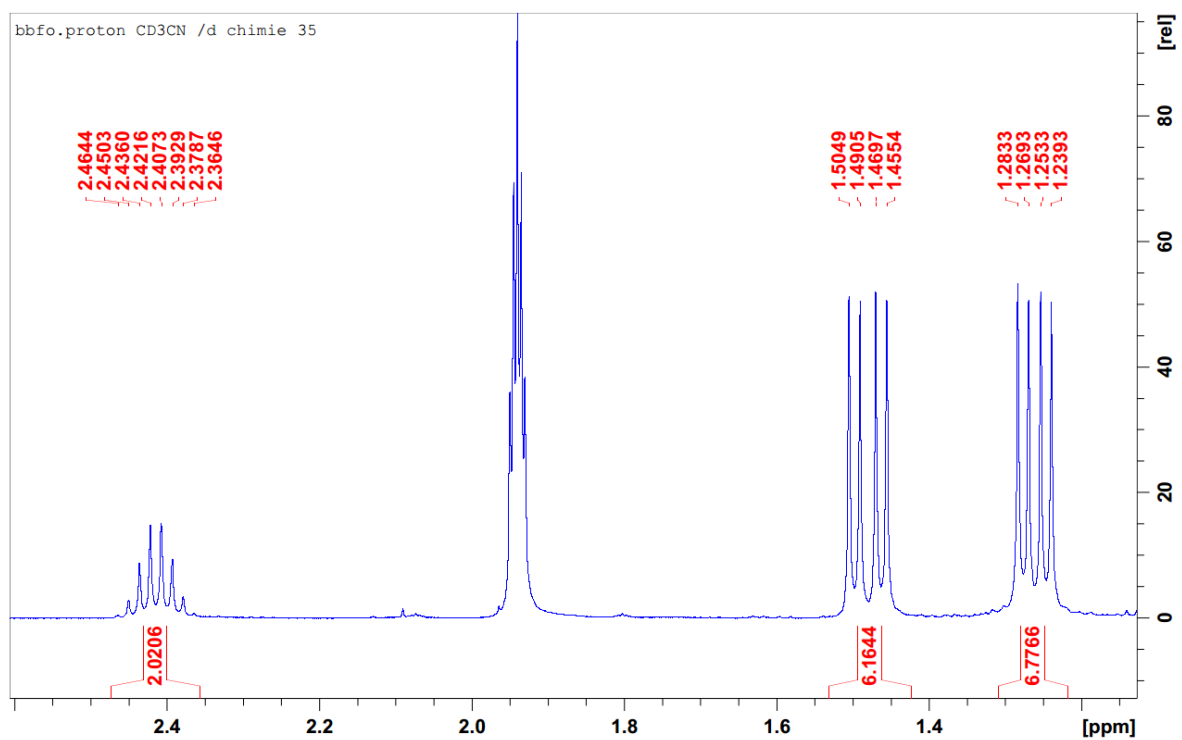
Figure S2.79: ^{1}H NMR spectrum of **1k** in CD$_3$CN; focus on aliphatic region
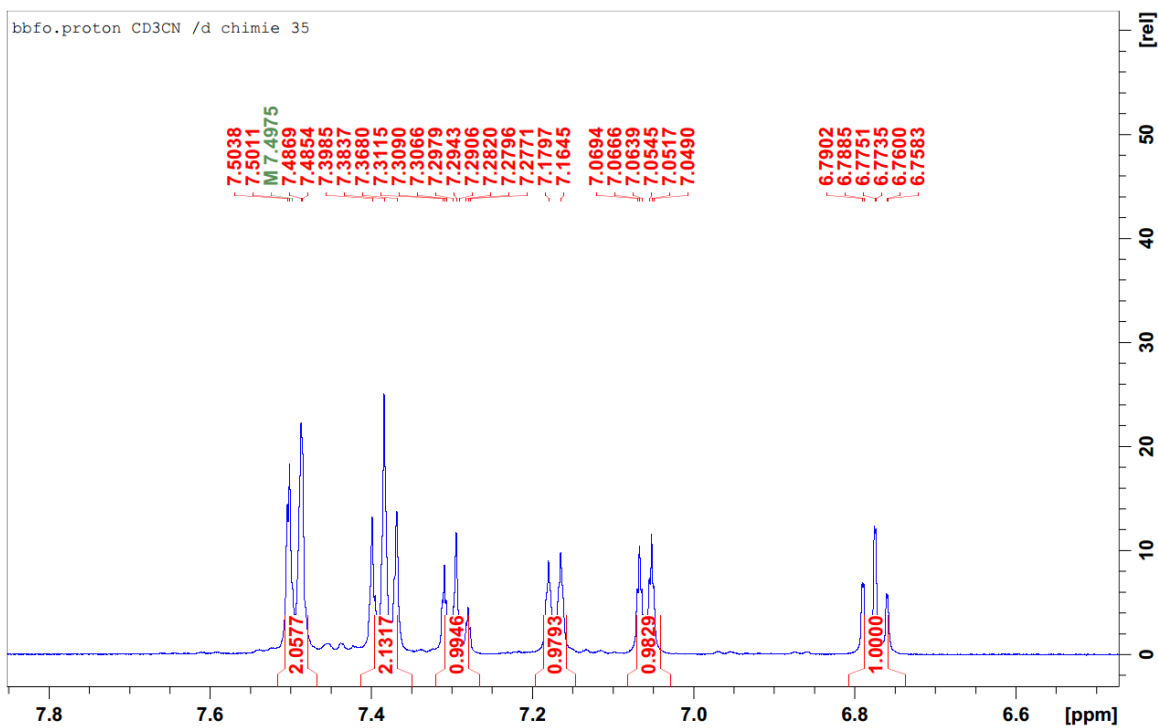
Figure S2.80: ^{1}H NMR spectrum of **1k** in CD$_3$CN; focus on aromatic region
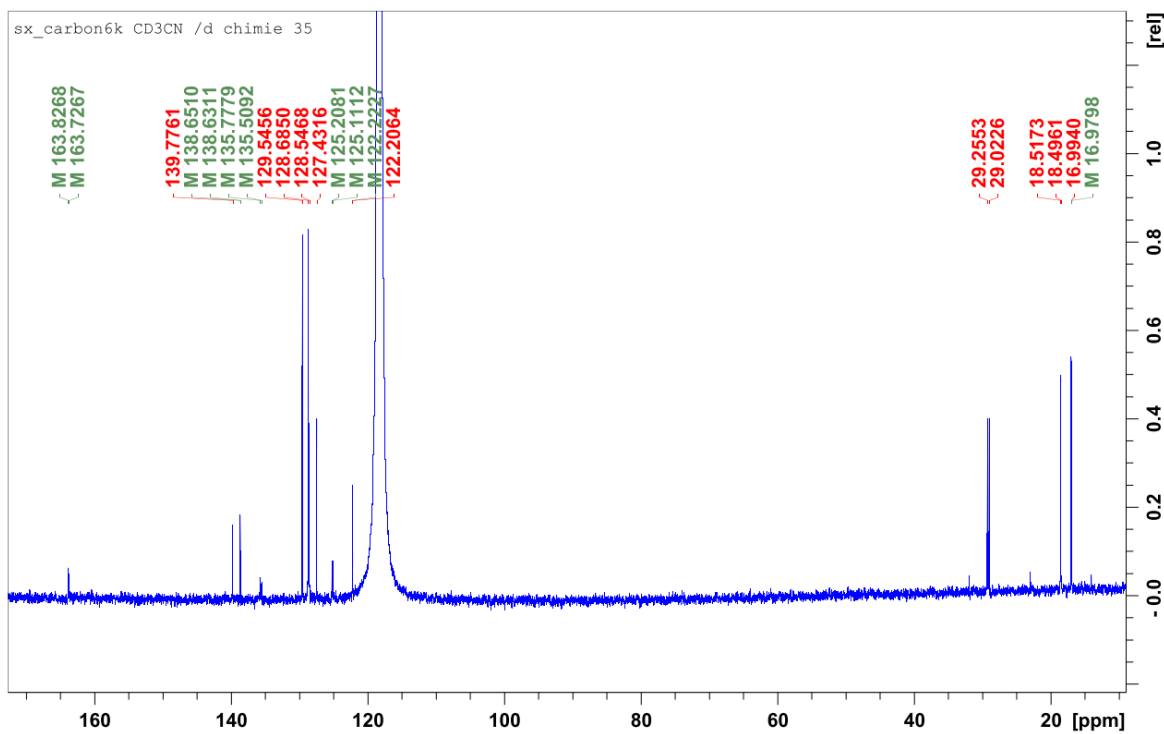
Figure S2.81: Full ^{13}C{^{1}H} NMR spectrum of **1k** in CD$_3$CN
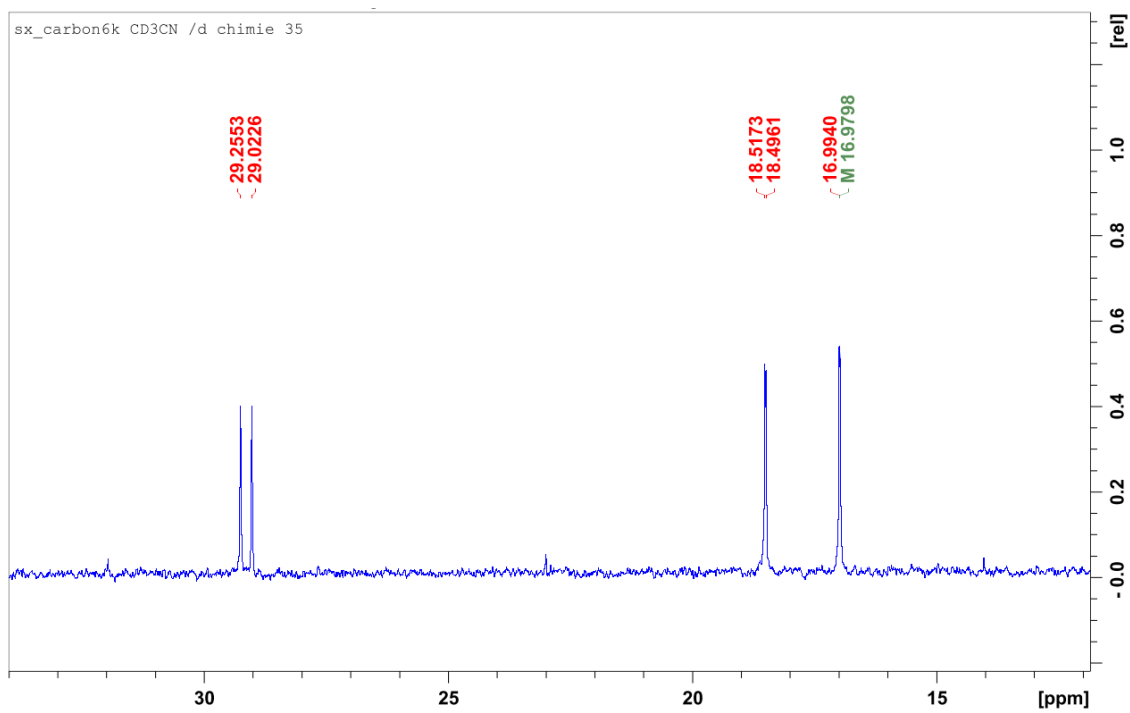
Figure S2.82: $^{13}C\{^1H\}$ NMR spectrum of **1k** in CD$_3$CN; focus on aliphatic region
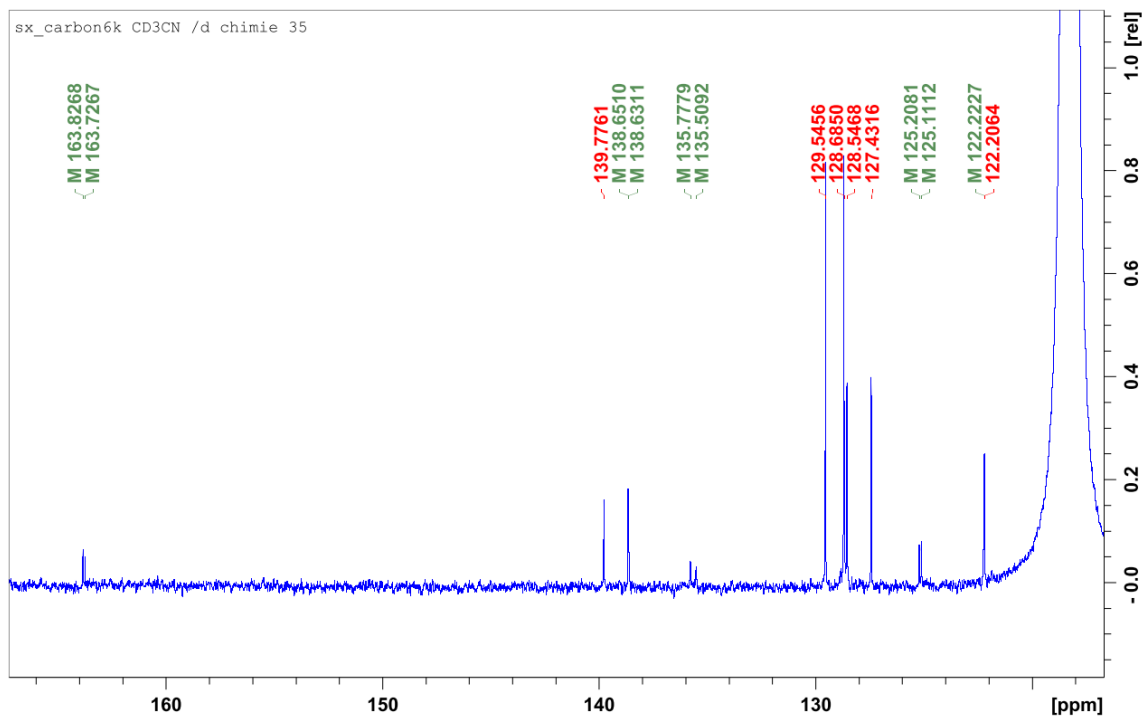
Figure S2.83: $^{13}C\{^1H\}$ NMR spectrum of **1k** in CD$_3$CN; focus on aromatic region
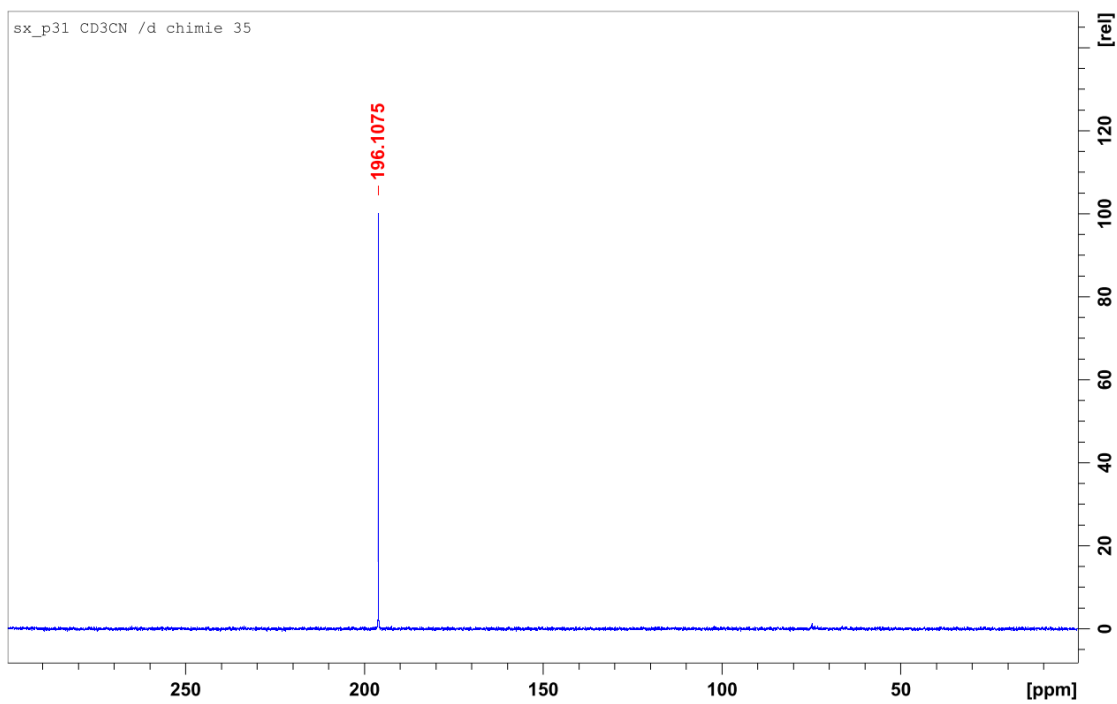
Figure S2.84: $^{31}P\{^1H\}$ NMR spectrum of **1k** in CD_3CN
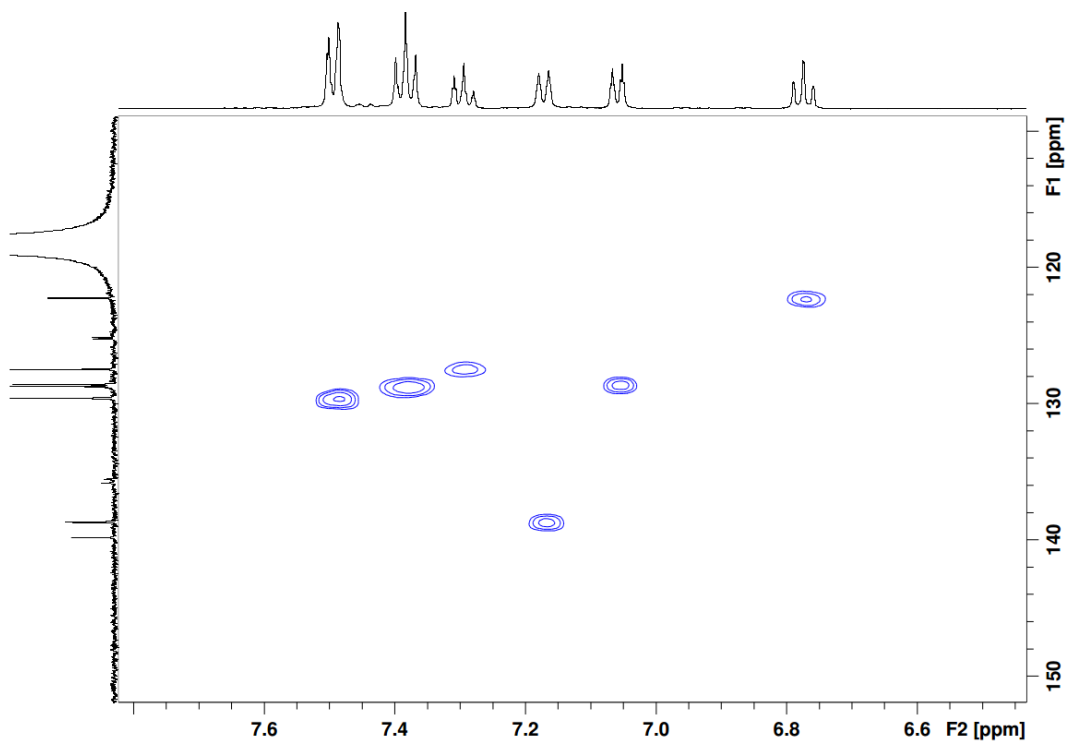
Figure S2.85: HSQC spectrum of **1k** in CD_3CN; focus on aromatic region

S2.5 Additional Thermal Ellipsoid plots

1a-NCMe
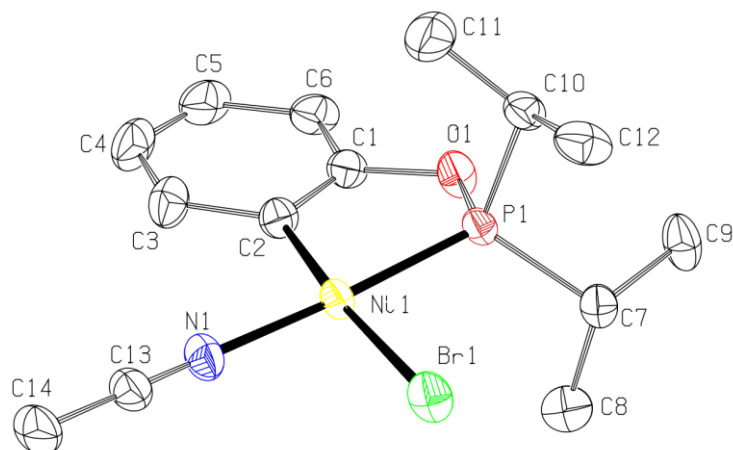
Figure S2.86: Solid state structure of **1a-NCMe**. Thermal ellipsoids are shown at the 50% probability level; hydrogen atoms are omitted for clarity.

1b
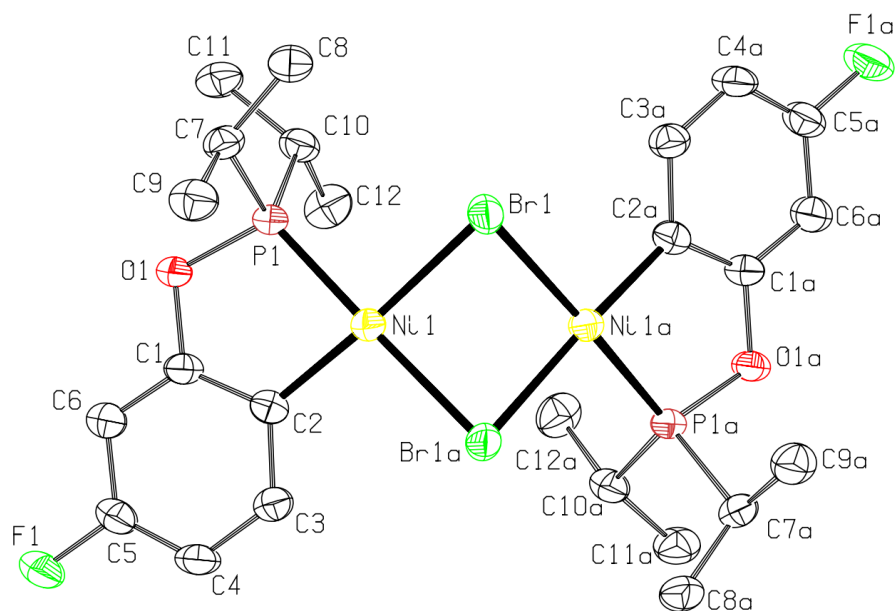
Figure S2.87: Solid state structure of **1b**. Thermal ellipsoids are shown at the 50% probability level; hydrogen atoms are omitted for clarity
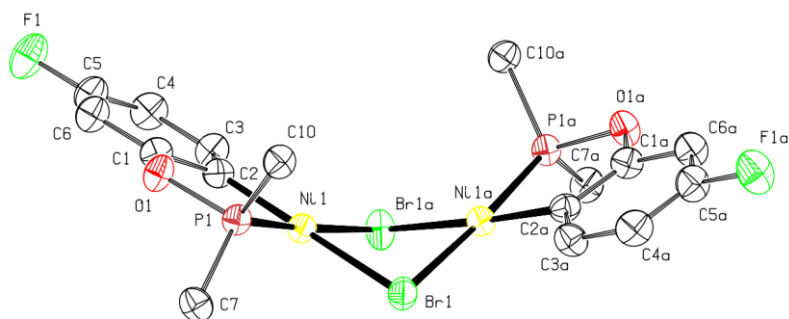
Figure S2.88: Side view of **1b**. Thermal ellipsoids are shown at the 50% probability level; hydrogen atoms and isopropyl substituents are omitted for clarity

1c
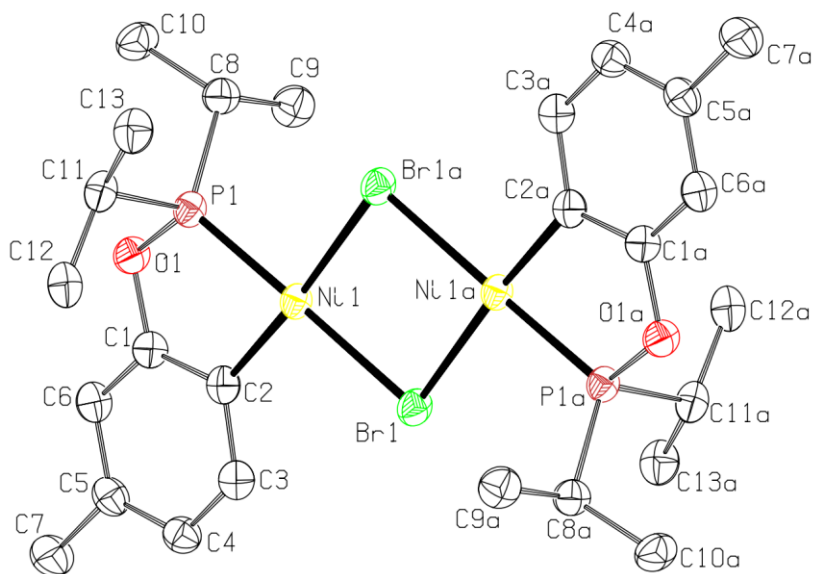
Figure S2.89: Solid state structure of **1c**. Thermal ellipsoids are shown at the 50% probability level; hydrogen atoms are omitted for clarity

1e
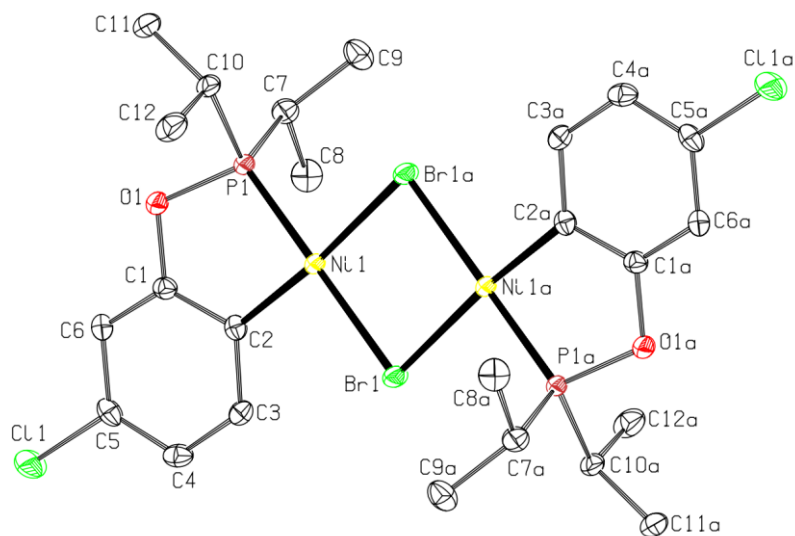
Figure S2.90: Solid state structure of **1e**. Thermal ellipsoids are shown at the 50% probability level; hydrogen atoms are omitted for clarity

1j
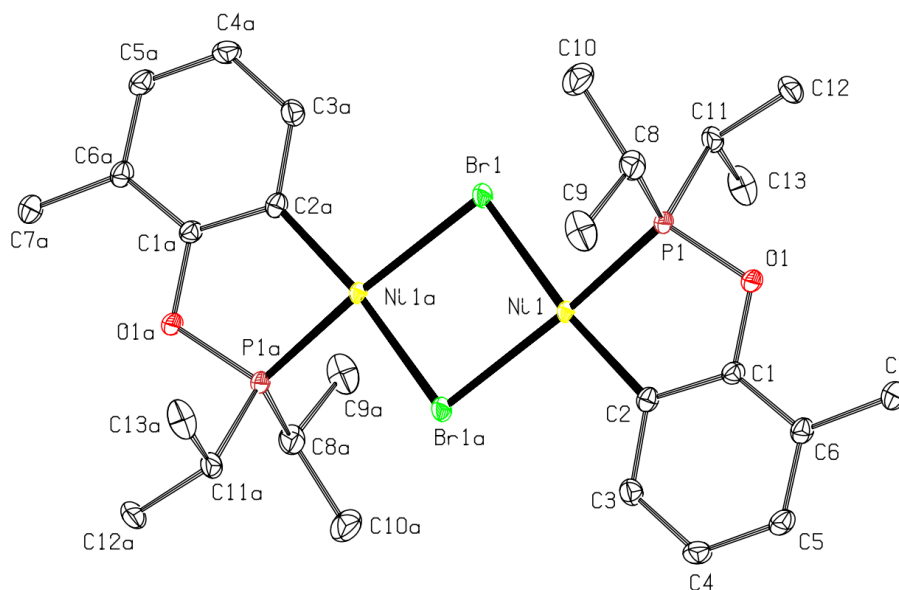
Figure S2.91: Solid state structure of **1j**. Thermal ellipsoids are shown at the 50% probability level; hydrogen atoms are omitted for clarity

S2.6 Crystallographic data

Table S2.2: Additional bond distances and angles around the nickel centre for compounds **1a-1e**

Compound	1a	1b	1c	1d	1e
cis **Ni-Br**	2.3641 (7)	2.3781 (7)	2.3815 (5)	2.3875 (3)	2.3796 (5)
trans **Ni-Br**	2.38	2.3736 (8)	2.39	2.3851 (3)	2.382
Ni-C2	1.914 (4)	1.911 (4)	1.920 (3)	1.9140 (17)	1.914 (2)
Ni-P1	2.0953 (10)	2.1056 (12)	2.0963 (7)	2.0985 (5)	2.0987 (7)
τ_4	0.06	0.06	0.04	0.12	0.04
Ni-Br-Ni	92	83	88	76.159 (10)	92
P1-Ni-C2	82.07 (12)	83.60 (13)	82.29(8)	82.97 (5)	82.38 (8)
C2-Ni-Br	97.61 (12)	94	97.39(8)	98.90 (5)	97.49 (8)
Br-Ni-Br	88	87	88	86.79 (1)	88
Br-Ni-P	93	92.56 (4)	93	92.297 (15)	92.483
trans C-Ni-Br	174	175.96 (13)	175	169.34 (5)	175
trans P-Ni-Br	176.19 (4)	176	178.82(3)	173.927 (17)	179.79 (3)

Table S2.3: Additional bond distances and angles around the nickel centre for compounds **1f**, **1j**, **1k**, **1a-NCMe** and **1i-NCMe**

Compound	1f	1j	1k	1a(NCMe)	1i-NCMe
cis **Ni-Br**	2.39	2.39	2.393(2)	1.913 (2)	1.9149 (19)
trans **Ni-Br**	2.3743(3)	2.3759(3)	2.390(2)	2.3533 (4)	2.3613 (4)
Ni-C2	1.9313(16)	1.9113(15)	1.919(12)	1.916 (2)	1.932 (2)
Ni-P1	2.1017(5)	2.0936(4)	2.104(3)	2.1018 (6)	2.1000 (6)
τ_4	0.10	0.06	0.06	0.03	0.20
Ni-Br-Ni	94	93	92.76(7)	x	x
P1-Ni-C2	82.41(5)	82.51(5)	81.5(4)	82.51 (7)	83.23 (6)
C2-Ni-Br	101	98	96.5(4)	96.03 (10)	100.20 (8)
Br-Ni-Br	83	87	86.51(7)	90.92 (7)	91.18 (6)
Br-Ni-P	90.636 (15)	92.931(13)	96	90.681 (19)	88.17 (2)
trans C-Ni-Br	173.04(5)	171.33(5)	175.9(4)	172.62 (7)	164.43 (6)
trans P-Ni-Br	172	180	175.36(12)	176.66 (6)	166.40 (6)

Table S2.4: Crystal information for compounds **1b-1d.**

	1b	1c	1d	
chemical formula	$C_{24}H_{34}Br_2F_2Ni_2O_2P_2$	$C_{26}H_{40}Br_2Ni_2O_2P_2$	$C_{26}H_{40}Br_2Ni_2O_4P_2$	a
crystal color	Orange	Orange	Orange	
_Fw_; _F_(000)	365.84; 1472	361.88; 736	755.76; 1536	
_T_ (K)	100	100	100	
wavelength (Å)	1.54178	1.54178	1.34139	
space group	C_2/c	$P2_1/n$	$P2_1/c$	
_a_ (Å)	12.7913(5)	11.1846(11)	24.6811(8)	
_b_ (Å)	11.7694(5)	11.1021(11)	8.6173(3)	
_c_ (Å)	19.0246(7)	12.8093(13)	15.0729(5)	
α (deg)	90	90	90	
β (deg)	103.6270(10)	109.753(3)	104.9950(10)	
γ (deg)	90	90	90	
_Z_	4	2	4	
_V_ (Å³)	2783.45(19)	1497.0(3)	3096.61(18)	
ρ_{calcd} (g·cm⁻³)	1.746	1.606	1.621	
μ (mm⁻¹)	6.418	5.859	9.686	
θ range (deg); completeness	5.175 − 72.160; 0.998	5.792 − 72.082; 0.999	1.612 − 60.765; 0.998	
collected reflections; R_σ	55870; 0.0135	39328; 0.0209	52360; 0.0262	
unique reflections; R_{int}	2744; 0.0400	2941; 0.0548	7083; 0.0421	
R1ᵃ; wR2ᵇ [I > 2σ(I)]	0.0365; 0.1064	0.0358; 0.1020	0.0233; 0.0572	
R1; wR2 [all data]	0.0367; 0.1065	0.0361; 0.1024	0.0244; 0.0601	
GOF	1.271	1.093	1.067	
largest diff peak and hole	0.739 and -0.473	1.233 and -0.699	0.682 and -0.532	

$R_1=\Sigma(||F_o|-|F_c||)/\Sigma|F_o|$

ᵇ $wR_2=\{\Sigma[w(F_o^2-F_c^2)^2]/\Sigma[w(F_o^2)^2]\}^{1/2}$

Table S2.5: Crystal information for compounds **1e-1f** and **1i-NCMe**

	1e	1f	1i-NCMe
chemical formula	$C_{24}H_{34}Br_2Cl_2Ni_2O_2P_2$	$C_{24}H_{32}Br_2F_4Ni_2O_2P_2$	$C_{16}H_{25}BrNNiO_3P$
crystal color	Orange	Red	Orange
Fw; $F(000)$	764.59; 768	383.84; 768	448.96; 920
T (K)	100	100	100
wavelength (Å)	1.54178	1.54178	1.54178
space group	$P2_1/n$	$P2_1/n$	$P2_1/c$
a (Å)	11.0573(3)	10.45540(10)	12.7532(3)
b (Å)	11.0873(3)	12.15070(10)	13.1865(3)
c (Å)	12.8018(3)	11.12550(10)	11.4773(3)
α (deg)	90	90	90
β (deg)	108.8690(10)	93.38	97.3600(10)
γ (deg)	90	90	90
Z	2	2	4
V (Å³)	1485.10(7)	1410.92(2)	1914.24(8)
ρ_{calcd} (g·cm⁻³)	1.710	1.807	1.558
μ (mm⁻¹)	7.561	6.472	4.802
θ range (deg); completeness	5.814 − 72.041; 0.997	5.588 − 72.151; 0.997	3.494 − 72.162; 0.999
collected reflections; R_σ	58307; 0.0085	19280; 0.0112	75144; 0.0191
unique reflections; R_{int}	2914; 0.0272	2760; 0.0205	3778; 0.0504
R1[a]; wR2[b] [I > 2σ(I)]	0.0274; 0.0735	0.0200; 0.0506	0.0378; 0.1050
R1; wR2 [all data]	0.0275; 0.0735	0.0202; 0.0507	0.0386; 0.1061
GOF	1.128	1.158	1.083
largest diff peak and hole	0.642 and -0.427	0.352 and -0.339	1.643 and -0.485

[a] $R_1 = \Sigma(||F_o|-|F_c||)/\Sigma|F_o|$

[b] $wR_2 = \{\Sigma[w(F_o^2 - F_c^2)^2]/\Sigma[w(F_o^2)^2]\}^{\frac{1}{2}}$

Table S2.6: Crystal information for compounds **1j-1k** and **1a-NCMe**

	1j	1k	1a-NCMe
chemical formula	$C_{26}H_{40}Br_2Ni_2O_2P_2$	$C_{36}H_{44}Br_2Ni_2O_2P_2$	$C_{14}H_{21}BrNNiOP$
crystal color	Yellow	Orange	Yellow
***Fw**; **F**(000)*	1447.52; 736	847.89; 3456	388.91; 396
***T* (K)**	100	100	150
wavelength (Å)	1.34139	1.54178	1.34139
space group	$P2_1/n$	$P2_1$	P-1
***a* (Å)**	10.4265(2)	15.6693(4)	7.4137(4)
***b* (Å)**	14.2437(3)	12.3783(3)	9.6993(5)
***c* (Å)**	10.4603(2)	36.7303(10)	12.7577(7)
α (deg)	90	90	97.074(2)
β (deg)	105.6540(10)	91.6650(10)	101.279(2)
γ (deg)	90	90	111.252(2)
Z	2	8	2
***V* (Å³)**	1495.86(5)	7121.2(3)	819.36(8)
ρ$_{calcd}$ (g·cm⁻³)	1.607	1.582	1.576
μ (mm⁻¹)	9.974	5.028	9.146
θ range (deg); completeness	4.678 − 60.586; 0.999	1.203 − 72.189; 0.996	3.145 − 60.638; 0.999
collected reflections; R$_\sigma$	23556; 0.0240	149169; 0.0532	19653; 0.0311
unique reflections; R$_{int}$	3438; 0.0422	14686; 0.0409	3772; 0.0502
R1ᵃ; wR2ᵇ [I > 2σ(I)]	0.0222; 0.0589	0.0489; 0.1295	0.0384; 0.1080
R1; wR2 [all data]	0.0224; 0.0592	0.0499; 0.1303	0.0389; 0.1087
GOF	1.102	1.034	1.251
largest diff peak and hole	0.578 and -0.630	1.878 and -0.698	0.630 and -1.540

ᵃ $R_1 = \Sigma(||F_o|-|F_c||)/\Sigma|F_o|$

ᵇ $wR_2 = \{\Sigma[w(F_o^2-F_c^2)^2]/\Sigma[w(F_o^2)^2]\}^{\frac{1}{2}}$

S2.7 Details on DFT optimizations

All DFT calculations were performed using Gaussian 16 on Grex server from Westgrid (provided by Compute Canada/Calcul Canada). Optimizations were carried out using 6-31g** for all light atoms (C, H, O P) and def2TZVP for Ni and Br basis sets. The M06 functional was exploited in implicit toluene solvent using the SMD model. Local minima were assessed by convergence and the absence of imaginary frequencies in the frequency calculation. The electronic energy was computed with def2TZVP for all atoms, from the optimized geometry. The thermal energy was calculated by the sum of the electronic energy and the thermal correction to Gibbs free energy outputted from the frequency calculations.

Calculations on di-isopropylphosphinites compounds **1a** and **1d** were carried out as follows. **1a** was optimized (a) from its crystal structure geometry, leading to a perfectly coplanar structure (dihedral angle Ni1-μ-Br1-μ-Br2-Ni2 = 180.00000°) and (b) from a bent geometry where the dihedral angle was set to 116° (in line with the solid state structure of **1d**), leading to a bent geometry with dihedral angle Ni1-μ-Br1-μ-Br2-Ni2 = 104°. **1d** was optimized (a) using structural parameters obtained from the crystal structure (bent conformation; dihedral angle of 102°) and (b) from the crystal structure unfolded to a coplanar structure (dihedral angle of 180°), leading to a nearly planar structure.

Calculations on model compounds featuring simplified Me$_2$POAr moieties were carried out as follows. The Me$_2$P analogue of the unsubstituted complex **1a** was called ModelPhenol. Three conformations were considered for the Me$_2$P analogue of complex **1d**: one with both methoxy methyls pointing towards C4 (ModelConf1), one with both Me pointing towards C6 (ModelConf2), and one with one Me pointing towards C4 and the other towards C6 (ModelConf3). For each of these models, optimizations were started from both a coplanar structure (derived from the crystal structure of **1a**) and a bent structure (derived from the crystal structure of **1d**). All optimizations starting from either a bent or a coplanar geometry ended up as bent compounds. Freezing the dihedral angle to 180° allowed us to find a planar local minimum for each compound, for the

139

purposes of comparison. Only ModelConf2 could converge into a local coplanar minimum without requiring freezing; this model gave a structure featuring a dihedral angle of 178°.

In all six cases, the optimized bent structures were found to be lower in energy than the coplanar local minima, with stabilizations of 5.7 kJ/mol for **1a** and 6.5 kJ/mol for **1d**. It should be noted here that although the located minima are close to the global minimum, they could be local minima due to the rotation of the *i*-Pr groups. In the model compounds, stabilisations between the bent structures (absolute minimum) and the corresponding coplanar structures were as follows (all values in kJ/mol): ModelPhenol, 2.8; ModelConf1, 1.3; ModelConf2, 3.8; and ModelConf3, 3.3.

The transition state for flipping the dimer from one bent conformation to the other was found using the QST2 routine with input geometries coming from the optimized structures found with ModelPhenol and its mirror image leading to the structure bent the other way. This process yielded a nearly coplanar geometry as transition state, with one single imaginary frequency for which the vectors directed a bend towards one or the other faces of the dimer. The Internal Reaction Coordinate (IRC) confirmed the identity of the transition state as being the link between the two opposite bent structures. The energy of this transition state was found to be 11.6 kJ/mol higher than the optimized bent structures.

The possibility of a *s*-trans to s-*cis* isomerization suggested by a reviewer was also performed on the model complex ModelPhenol. The geometry minimization of the s-*cis* isomer (ModelPhenolCis) led to a bent structure which was 10.0 kJ/mol higher in energy than the s-*trans* isomer. The mixed square planar-tetrahedral dinuclear species (ModelPhenolMix) proposed to be the intermediate/transition state for this isomerization s intermediate : it was computed as a triplet and found to be 68.3 kJ/mol higher than the *s-trans* bent dimer. The transition state leading to this intermediate was thus not investigated, as it should be much higher than the barrier required for the above described flipping mechanism.

S2.8 Geometries of the optimized structures

a) Coplanar local minimum and bent optimized structures of **1a**

Table S2.7: Coordinates for optimized 1a-plane and 1a-bent

Plane structure				Bent structure			
Br	1.504573	-0.537126	-0.385582	Br	-0.424022	-1.557051	-1.804923
Ni	0.68079	0.966794	1.285711	Ni	1.359062	-0.350519	-0.725332
Br	-1.504573	0.537126	0.385582	Br	0.429147	1.617932	-1.756217
Ni	-0.68079	-0.966794	-1.285711	Ni	-1.316992	0.372456	-0.663208
P	0.073775	-2.343543	-2.737987	P	-2.795096	-0.820576	0.319267
P	-0.073775	2.343543	2.737987	P	2.804127	0.80899	0.339864
O	1.194955	2.76708	3.710688	O	3.524514	-0.212588	1.426931
O	-1.194955	-2.76708	-3.710688	O	-3.714906	0.21856	1.224856
C	2.355764	1.338085	2.167479	C	2.158646	-1.801728	0.253517
C	-0.749516	0.380589	4.519878	C	1.048679	1.573392	2.300641
H	0.184397	0.551881	5.070707	H	1.425365	0.78504	2.966128
H	-0.549489	-0.361314	3.737284	H	0.236288	1.156645	1.691081
H	-1.474105	-0.052468	5.219757	H	0.618069	2.365839	2.925274
C	3.524315	2.493926	4.004787	C	3.712269	-2.489256	2.038611
H	3.455868	3.160552	4.861401	H	4.445413	-2.1906	2.784384
C	-1.293539	1.685465	3.947163	C	2.167436	2.143163	1.435181
H	-2.195522	1.469041	3.354171	H	1.740153	2.891366	0.750512
C	3.5961	0.804497	1.797363	C	1.844253	-3.157231	0.088219
H	3.665433	0.140233	0.938774	H	1.124194	-3.451834	-0.672059
C	-1.620686	2.690512	5.04538	C	3.270869	2.772953	2.277098
H	-2.315452	2.238154	5.763686	H	2.835845	3.525978	2.945654

141

H	-2.093027	3.601716	4.660841	H	4.03467	3.274391	1.671701
H	-0.716756	2.978727	5.595956	H	3.766876	2.021916	2.904178
C	2.376999	2.185998	3.286042	C	3.119333	-1.520933	1.238792
C	4.76748	1.093509	2.497116	C	2.425633	-4.153636	0.872444
H	5.708927	0.654322	2.173198	H	2.149244	-5.19379	0.71156
C	4.732677	1.9371	3.601775	C	3.353166	-3.81958	1.853348
H	5.643178	2.165306	4.151667	H	3.80636	-4.59211	2.470789
C	-0.650213	4.001674	2.181331	C	4.270065	1.461793	-0.562815
H	-0.628716	4.607361	3.101745	H	4.983791	1.707968	0.239844
C	-2.059906	3.989272	1.606871	C	3.95765	2.709145	-1.377379
H	-2.358439	5.013217	1.350762	H	4.879057	3.08659	-1.837362
H	-2.805456	3.594073	2.307157	H	3.530803	3.520346	-0.775893
H	-2.109767	3.393108	0.687562	H	3.253953	2.485537	-2.188763
C	0.357441	4.566403	1.186866	C	4.856098	0.355864	-1.432113
H	0.371875	3.970568	0.26435	H	4.153315	0.068672	-2.225805
H	1.375685	4.586851	1.59202	H	5.100335	-0.54296	-0.854747
H	0.082577	5.593745	0.918143	H	5.777914	0.706804	-1.912007
C	-2.355764	-1.338085	-2.167479	C	-2.158997	1.804866	0.311433
C	0.749516	-0.380589	-4.519878	C	-4.542917	-0.575669	-1.775552
H	-0.184397	-0.551881	-5.070707	H	-5.028932	0.267229	-1.267034
H	0.549489	0.361314	-3.737284	H	-3.726461	-0.175103	-2.388661
H	1.474105	0.052468	-5.219757	H	-5.28127	-1.027793	-2.448678
C	-3.524315	-2.493926	-4.004787	C	-3.937017	2.477824	1.879836
H	-3.455868	-3.160552	-4.861401	H	-4.783715	2.177259	2.492723
C	1.293539	-1.685465	-3.947163	C	-4.051114	-1.610855	-0.769391

Atom	X	Y	Z
H	2.195522	-1.469041	-3.354171
C	-3.5961	-0.804497	-1.797363
H	-3.665433	-0.140233	-0.938774
C	1.620686	-2.690512	-5.04538
H	2.315452	-2.238154	-5.763686
H	2.093027	-3.601716	-4.660841
H	0.716756	-2.978727	-5.595956
C	-2.376999	-2.185998	-3.286042
C	-4.76748	-1.093509	-2.497116
H	-5.708927	-0.654322	-2.173198
C	-4.732677	-1.9371	-3.601775
H	-5.643178	-2.165306	-4.151667
C	0.650213	-4.001674	-2.181331
H	0.628716	-4.607361	-3.101745
C	2.059906	-3.989272	-1.606871
H	2.358439	-5.013217	-1.350762
H	2.805456	-3.594073	-2.307157
H	2.109767	-3.393108	-0.687562
C	-0.357441	-4.566403	-1.186866
H	-0.371875	-3.970568	-0.26435
H	-1.375685	-4.586851	-1.59202
H	-0.082577	-5.593745	-0.918143

re 1. –

$$E_{Gibbs} = E_{def2TZVP} + Corr_{EGibbs}$$

$$= -9933.9727553 + 0.475031$$

$$= -9933.4977243 \text{ Ha}$$

Atom	X	Y	Z
H	-3.506119	-2.404393	-1.303123
C	-1.758472	3.147586	0.28537
H	-0.909689	3.442553	-0.327225
C	-5.204182	-2.213397	0.024982
H	-5.939252	-2.645759	-0.664912
H	-4.882921	-3.010402	0.705199
H	-5.716587	-1.444717	0.616046
C	-3.262154	1.521034	1.132424
C	-2.414237	4.130962	1.025522
H	-2.069915	5.161997	0.973267
C	-3.50409	3.797365	1.822598
H	-4.019613	4.560832	2.401253
C	-2.314772	-2.038895	1.617477
H	-3.244057	-2.146177	2.20075
C	-1.890583	-3.397183	1.077957
H	-1.707921	-4.078216	1.918446
H	-2.647696	-3.86074	0.434512
H	-0.957177	-3.322505	0.508203
C	-1.236763	-1.430663	2.507389
H	-0.289597	-1.33106	1.958222
H	-1.52138	-0.443889	2.892982
H	-1.051804	-2.085516	3.367783

re 2. –

$$E_{Gibbs} = E_{def2TZVP} + Corr_{EGibbs}$$

$$= -9933.9780433 + 0.478159$$

$$= - -9933.4998843 \text{ Ha}$$

$\Delta G_{bending}$ = -0.0021600 Ha = -5.67 kJ/mol

b) Coplanar local minimum and bent optimized structures of **1d**

Table S2.8: Coordinates for optimized 1d-plane and 1d-bent

Plane structure

Bent structure

Br	-0.304198	1.615779	-0.339206	Br	0.560944	1.544178	-2.101098
Br	0.304397	-1.616227	-0.336809	Br	-0.561129	-1.545744	-2.100197
Ni	-1.703448	-0.315135	-0.120295	Ni	1.292893	-0.466536	-0.994635
Ni	1.703554	0.314917	-0.120432	Ni	-1.292878	0.465527	-0.994782
P	-2.93224	-2.047282	0.119057	P	1.793232	-2.247127	0.074839
P	2.931982	2.047271	0.119458	P	-1.792464	2.246873	0.073837
O	-4.506298	-1.534021	0.133476	O	2.936743	-1.826505	1.198958
O	-7.255361	2.257455	0.057446	O	5.646492	1.674124	2.727035
C	-4.589573	-0.156842	0.057543	C	3.315742	-0.505838	1.066958
C	-3.401166	0.59025	-0.036261	C	2.720676	0.275431	0.058845
C	-3.58509	1.973477	-0.090509	C	3.199848	1.585713	-0.026529
H	-2.721171	2.631148	-0.158087	H	2.801023	2.253625	-0.786587
C	-4.843603	2.578881	-0.062335	C	4.174288	2.098599	0.833095
H	-4.913694	3.661799	-0.110177	H	4.502515	3.126948	0.71123
C	-5.985871	1.784374	0.024944	C	4.707936	1.283518	1.831268
C	-5.857302	0.395181	0.08797	C	4.276489	-0.039714	1.946438
H	-6.741503	-0.232598	0.160436	H	4.697381	-0.686539	2.711728
C	-7.434957	3.652059	-0.003735	C	6.122368	2.996101	2.641843
H	-6.965557	4.163239	0.849106	H	6.609816	3.194466	1.676524

144

Atom	X	Y	Z	Atom	X	Y	Z
H	-8.512873	3.829333	0.029928	H	6.86021	3.113739	3.439376
H	-7.035582	4.075651	-0.936408	H	5.318519	3.731147	2.792348
C	-2.865543	-2.985387	1.702274	C	2.662049	-3.602134	-0.819544
H	-3.805488	-3.560642	1.704111	H	3.079007	-4.225856	-0.012586
C	-2.8813	-1.997159	2.862564	C	3.80494	-3.010157	-1.635301
H	-1.963274	-1.394294	2.874215	H	3.420579	-2.359667	-2.432455
H	-2.939549	-2.538553	3.814813	H	4.381893	-3.814429	-2.108137
H	-3.735115	-1.311597	2.813634	H	4.493762	-2.42041	-1.02004
C	-1.6796	-3.935613	1.79018	C	1.727859	-4.434591	-1.686149
H	-1.650289	-4.662067	0.969177	H	0.889443	-4.864105	-1.125228
H	-1.732855	-4.500394	2.72903	H	2.286726	-5.264645	-2.13533
H	-0.730017	-3.386814	1.78908	H	1.312329	-3.836843	-2.506872
C	-2.928332	-3.257825	-1.265664	C	0.490585	-3.004706	1.134452
H	-1.916646	-3.692325	-1.260468	H	-0.283815	-3.348295	0.431565
C	-3.967697	-4.357326	-1.081446	C	1.021633	-4.180678	1.946157
H	-3.784755	-4.971931	-0.192642	H	1.361903	-5.013112	1.319607
H	-3.954689	-5.025632	-1.951306	H	0.226244	-4.563732	2.597323
H	-4.977011	-3.934777	-1.004656	H	1.854426	-3.872006	2.590212
C	-3.137272	-2.49825	-2.571801	C	-0.103578	-1.924159	2.032223
H	-4.11904	-2.007595	-2.588284	H	0.652605	-1.51852	2.717613
H	-3.097865	-3.192528	-3.419687	H	-0.915505	-2.34605	2.638098
H	-2.372049	-1.728217	-2.728027	H	-0.526943	-1.097748	1.448151
C	2.863347	2.985796	1.702348	C	-2.659538	3.602649	-0.821102
H	3.803491	3.560729	1.705335	H	-3.076857	4.226341	-0.014308
C	2.877196	1.997786	2.862851	C	-3.802024	3.01148	-1.638015

H	1.958854	1.395384	2.873499	H	-3.41725	2.361143	-2.435098
H	2.934569	2.539324	3.815071	H	-4.37825	3.816165	-2.111031
H	3.730718	1.311772	2.815076	H	-4.491585	2.421784	-1.02354
C	1.677608	3.936439	1.788487	C	-1.724248	4.435021	-1.686579
H	1.649639	4.662781	0.967341	H	-0.885934	4.863629	-1.124807
H	1.72979	4.501346	2.727322	H	-2.282289	5.265733	-2.135581
H	0.727842	3.387961	1.786209	H	-1.308525	3.83756	-2.50741
C	2.929662	3.257418	-1.2656	C	-0.489737	3.003282	1.134214
H	1.918004	3.692007	-1.261553	H	0.285255	3.346381	0.431737
C	3.139926	2.497521	-2.571328	C	0.103214	1.922176	2.032091
H	4.121686	2.006804	-2.586663	H	-0.653533	1.51713	2.717231
H	3.101467	3.191601	-3.419423	H	0.915408	2.343256	2.63818
H	2.374826	1.727495	-2.728174	H	0.525975	1.095456	1.448044
C	3.968929	4.356881	-1.080552	C	-1.020248	4.179557	1.945836
H	3.785217	4.971608	-0.191989	H	-1.359483	5.012381	1.319233
H	3.956787	5.025085	-1.950503	H	-0.2249	4.56184	2.597512
H	4.978131	3.934255	-1.002757	H	-1.853656	3.87146	2.589364
O	4.506048	1.534071	0.136072	O	-2.937285	1.827565	1.197127
O	7.255813	-2.256849	0.058207	O	-5.649416	-1.67086	2.725937
C	4.58957	0.156966	0.059182	C	-3.316619	0.506925	1.065882
C	3.401342	-0.590268	-0.035859	C	-2.721007	-0.275385	0.058904
C	3.585568	-1.973398	-0.091437	C	-3.200235	-1.585721	-0.02547
H	2.721823	-2.631176	-0.160188	H	-2.80083	-2.254455	-0.784511
C	4.844177	-2.578599	-0.063204	C	-4.175481	-2.097586	0.833847
H	4.914481	-3.661453	-0.11213	H	-4.503736	-3.126017	0.712774

C	5.986249	-1.783971	0.025495	C	-4.709893	-1.28138	1.83069
C	5.857384	-0.394862	0.089759	C	-4.278247	0.04186	1.94496
H	6.741433	0.233021	0.163189	H	-4.699609	0.689482	2.709319
C	7.435702	-3.651362	-0.004215	C	-6.125457	-2.992832	2.641689
H	6.965875	-4.163449	0.847845	H	-6.612091	-3.192118	1.676149
H	8.51363	-3.828473	0.029926	H	-6.864022	-3.109513	3.438695
H	7.036969	-4.074123	-0.937539	H	-5.321881	-3.727864	2.793673

ire 3. –

$$E_{Gibbs} = E_{def2TZVP} + Corr_{EGibbs}$$

$$= -10162.988461 + 0.535439$$

$$= -10162.45302 \text{ Ha}$$

ire 4. –

$$E_{Gibbs} = E_{def2TZVP} + Corr_{EGibbs}$$

$$= -10162.99390 + 0.538414$$

$$= -10162.45549 \text{ Ha}$$

$$\Delta G_{bending} = -0.002469 \text{ Ha} = -6.48 \text{ kJ/mol}$$

c) Coplanar local minimum and bent optimized structures of ModelPhenol

Table S2.9: Coordinates for optimized ModelPhenol-plane and ModelPhenol-bent

Plane structure				Bent structure			
Br	-0.184678	-1.64646	0.062125	Br	-0.45081	-1.598388	-1.7625
Ni	-1.720062	0.186585	0.026995	Ni	-1.303838	0.357053	-0.656494
Br	0.185931	1.64819	0.066747	Br	0.450795	1.598615	-1.762376
Ni	1.721321	-0.184808	0.032392	Ni	1.303827	-0.35692	-0.656486
P	3.045895	-1.840966	-0.058236	P	1.731753	-2.042345	0.553602
P	-3.048569	1.84016	-0.054453	P	-1.731888	2.04236	0.553716
O	-4.581961	1.253028	-0.194548	O	-3.016737	1.656871	1.516922
O	4.5858	-1.257656	-0.117728	O	3.016717	-1.657101	1.516752
C	-3.369348	-0.81163	0.011904	C	-2.754039	-0.419352	0.337136
C	-5.829065	-0.756803	-0.126897	C	-4.48679	-0.117119	2.061345
H	-6.731717	-0.157313	-0.218879	H	-4.952312	0.539043	2.793092
C	-3.465073	-2.204426	0.114159	C	-3.235531	-1.723052	0.162015
H	-2.562134	-2.803245	0.212715	H	-2.768889	-2.37355	-0.574278
C	-4.591381	-0.129885	-0.102098	C	-3.423258	0.351405	1.302037
C	-4.692906	-2.865294	0.093906	C	-4.306576	-2.219603	0.904494
H	-4.720734	-3.950108	0.17402	H	-4.653638	-3.236702	0.733747
C	-5.874695	-2.142889	-0.029435	C	-4.929835	-1.418849	1.855838
C	3.371176	0.81233	0.014864	C	2.754056	0.419276	0.337249
C	5.832975	0.75221	-0.079586	C	4.486952	0.116719	2.061255
H	6.736301	0.149755	-0.140288	H	4.952503	-0.53956	2.792878
C	3.466839	2.207537	0.077142	C	3.235623	1.722971	0.162233
H	2.562984	2.809735	0.140277	H	2.768951	2.373592	-0.573919

C	4.594284	0.127046	-0.060173		C	3.423312	-0.35164	1.301999
C	4.695616	2.866747	0.06152		C	4.306781	2.219351	0.904666
H	4.723137	3.953392	0.111452		H	4.653909	3.236442	0.734003
C	5.878714	2.140316	-0.018348		C	4.930078	1.418435	1.855845
C	-2.934871	2.98736	-1.451567		C	-2.242269	3.623442	-0.166001
H	-3.807955	3.650289	-1.456006		H	-2.59617	4.289129	0.629794
H	-2.023431	3.588443	-1.365819		H	-1.393142	4.087981	-0.67763
H	-2.899416	2.423602	-2.388473		H	-3.047008	3.459024	-0.888443
C	2.962158	-2.913927	-1.515855		C	2.242104	-3.623295	-0.166423
H	3.821012	-3.595115	-1.524941		H	2.596073	-4.289125	0.629228
H	2.035265	-3.496976	-1.49454		H	1.393014	-4.08778	-0.678152
H	2.97222	-2.301072	-2.422136		H	3.04684	-3.458671	-0.888825
C	3.096	-2.986015	1.345774		C	0.43493	-2.470399	1.745209
H	2.162898	-3.557964	1.391786		H	-0.435656	-2.873203	1.216482
H	3.940484	-3.67579	1.232375		H	0.812186	-3.213454	2.457447
H	3.208867	-2.419711	2.275146		H	0.126793	-1.569189	2.285809
C	-3.142852	2.90935	1.406327		C	-0.43505	2.47025	1.745381
H	-2.203077	3.459695	1.524342		H	0.435637	2.872907	1.216713
H	-3.970583	3.619821	1.297327		H	-0.812223	3.213366	2.4576
H	-3.304094	2.293205	2.296207		H	-0.127109	1.568989	2.286011
H	-6.834606	-2.654303	-0.047185		H	5.764371	1.802345	2.438835
H	6.839438	2.650319	-0.032041		H	-5.764036	-1.802895	2.43887

re 5. –   re 6. –

$E_{Gibbs} = E_{def2TZVP} + Corr_{EGibbs}$ $E_{Gibbs} = E_{def2TZVP} + Corr_{EGibbs}$

= -9619.6064987 + 0.263190   = -9619.6027336 + 0.260489

= -9619.3433087 Ha   = -9619.3422446 Ha

$\Delta G_{bending}$ = -0.00106413 Ha = -2.79 kJ/mol

d) Coplanar local minimum and bent optimized structures of ModelConf1

Table S2.10: Coordinates for optimized ModelConf1-plane and ModelConf1-bent

Plane structure

Bent structure

Br	-0.558513	1.562276	0.012071	Br	0.859774	-1.528809	1.963661
Ni	-1.6325	-0.575607	0.002049	Ni	1.163251	0.63078	0.948209
Br	0.558577	-1.562311	-0.011981	Br	-0.842115	1.324872	2.110271
Ni	1.632493	0.575495	-0.001959	Ni	-1.159491	-0.726513	0.897415
P	2.549724	2.48794	-0.000841	P	-1.164018	-2.419534	-0.373276
P	-2.549831	-2.487986	0.001183	P	1.117979	2.410193	-0.197938
O	-4.185048	-2.274914	0.027402	O	2.46799	2.435359	-1.150804
O	4.184937	2.274888	-0.025582	O	-2.503621	-2.328919	-1.337628
C	-3.464314	0.015934	0.003457	C	2.751969	0.306108	-0.077855
C	-5.850876	-0.606518	0.015623	C	4.337205	1.139295	-1.77216
H	-6.614444	-1.379692	0.02481	H	4.635718	1.916099	-2.471077
C	-3.882948	1.347824	-0.010384	C	3.558801	-0.830421	0.022237
H	-3.144098	2.146293	-0.021573	H	3.284744	-1.622394	0.715907
C	-4.506825	-0.929016	0.015529	C	3.19854	1.272131	-0.999481
C	-5.22769	1.724496	-0.010872	C	4.72174	-1.004994	-0.731232
H	-5.483788	2.780022	-0.021522	H	5.309946	-1.90887	-0.600648
C	-6.216764	0.74143	0.002507	C	5.111095	-0.015421	-1.634118
C	3.464317	-0.016025	-0.003499	C	-2.743559	-0.289415	-0.094195
C	5.850884	0.606651	-0.014853	C	-4.337384	-0.93951	-1.858668
H	6.61439	1.379901	-0.02337	H	-4.65077	-1.648194	-2.620609
C	3.883011	-1.34788	0.009428	C	-3.52263	0.854924	0.095228

H	3.144257	-2.146454	0.019943	H	-3.235035	1.578684	0.854676
C	4.506812	0.929004	-0.014727	C	-3.207535	-1.164882	-1.094353
C	5.227815	-1.72443	0.00987	C	-4.674409	1.122206	-0.648457
H	5.484033	-2.779921	0.019889	H	-5.239241	2.027824	-0.446598
C	6.216816	-0.741257	-0.002679	C	-5.082086	0.220457	-1.631564
C	-2.264793	-3.583054	1.41691	C	1.161225	4.049868	0.569006
H	-2.939039	-4.445656	1.361117	H	1.322742	4.809113	-0.205087
H	-1.226388	-3.931392	1.411865	H	0.211887	4.245056	1.077995
H	-2.448239	-3.035099	2.345998	H	1.97407	4.095543	1.299777
C	2.301266	3.550656	1.446235	C	-1.280704	-4.097373	0.297957
H	2.972079	4.416026	1.392386	H	-1.454158	-4.808566	-0.517898
H	1.262338	3.89631	1.477288	H	-0.348988	-4.3537	0.812619
H	2.510758	2.981758	2.357102	H	-2.108159	-4.15173	1.011633
C	2.265628	3.582256	-1.417363	C	0.197447	-2.489291	-1.567836
H	1.2276	3.931717	-1.412385	H	1.139149	-2.684325	-1.043496
H	2.940803	4.44418	-1.362267	H	0.010742	-3.281213	-2.302662
H	2.448357	3.033467	-2.346098	H	0.27968	-1.525286	-2.08078
C	-2.302432	-3.549922	-1.446645	C	-0.236097	2.494953	-1.400336
H	-1.263198	-3.894523	-1.479297	H	-1.193479	2.594339	-0.876935
H	-2.972307	-4.415979	-1.392212	H	-0.087821	3.348824	-2.071924
H	-2.513749	-2.980847	-2.356981	H	-0.256552	1.569084	-1.984967
O	-7.548995	0.987074	0.003022	O	6.214071	-0.078334	-2.417343
O	7.549039	-0.986844	-0.003212	O	-6.176047	0.374377	-2.414635
C	-7.965871	2.331631	-0.010718	C	7.035228	-1.216318	-2.301571
H	-7.619589	2.858144	-0.91166	H	6.497889	-2.137541	-2.568862

151

H	-9.058644	2.319237	-0.008652		H	7.862334	-1.07584	-3.001774
H	-7.61632	2.877308	0.877467		H	7.444562	-1.323643	-1.286945
C	7.966006	-2.331382	0.009707		C	-6.967598	1.522296	-2.218916
H	9.058772	-2.318803	0.007734		H	-7.792829	1.456276	-2.932271
H	7.619639	-2.858459	0.910285		H	-7.381541	1.565303	-1.20143
H	7.616587	-2.876513	-0.878851		H	-6.404275	2.446077	-2.414343

re 7. –

$E_{Gibbs} = E_{def2TZVP} + Corr_{EGibbs}$

$= -9848.6184623 + 0.319498$

$= -9848.2989643$ Ha

re 8. –

$E_{Gibbs} = E_{def2TZVP} + Corr_{EGibbs}$

$= -9848.6221453 + 0.322696$

$= -9848.2994493$ Ha

$\Delta G_{bending} = -0.00048501$ Ha $= -1.27$ kJ/mol

e) Coplanar local minimum and bent optimized structures of ModelConf2

Table S2.11: Coordinates for optimized ModelConf2-plane and ModelConf2-bent

Plane structure

Bent structure

Br	0.437604	-1.598788	-0.06472		Br	0.694373	-1.885046	-1.795634
Ni	1.669889	0.449402	-0.023518		Ni	1.225644	0.348538	-1.070694
Br	-0.438559	1.601496	-0.03924		Br	-0.681421	1.08976	-2.360405
Ni	-1.670584	-0.447684	-0.020989		Ni	-1.22518	-0.727671	-0.882131
P	-2.73408	-2.282046	0.024305		P	-1.424168	-2.219297	0.606693
P	2.736425	2.282264	0.001519		P	1.359612	2.256147	-0.163529
O	4.346808	1.938658	0.11115		O	2.735806	2.287419	0.752601
O	-4.348502	-1.941754	-0.009361		O	-2.699505	-1.803248	1.574681
C	3.450238	-0.28354	-0.011364		C	2.755389	-0.001017	0.03432
C	5.883003	0.151405	0.082414		C	4.431067	0.894901	1.616171
H	6.671251	0.895948	0.138538		H	4.787459	1.757311	2.171147

152

	Left				Right		
C	3.766008	-1.649932	-0.066587	C	3.413086	-1.237417	0.140451
H	2.968155	-2.38706	-0.127037	H	3.043744	-2.090759	-0.424105
C	4.55711	0.570795	0.059484	C	3.314002	1.031921	0.79844
C	5.072236	-2.117449	-0.0462	C	4.533373	-1.419847	0.938635
H	5.292447	-3.181662	-0.087783	H	5.033717	-2.383612	0.999386
C	6.13879	-1.217533	0.030259	C	5.048268	-0.352979	1.6813
C	-3.45116	0.283641	0.006765	C	-2.744595	0.020967	0.018873
C	-5.885055	-0.154904	0.016107	C	-4.369254	-0.164223	1.872501
H	-6.673742	-0.901094	0.013505	H	-4.707059	-0.734818	2.73239
C	-3.766817	1.65105	0.025062	C	-3.407527	1.200413	-0.357432
H	-2.968462	2.39008	0.030268	H	-3.061036	1.756559	-1.225516
C	-4.558591	-0.572924	0.00481	C	-3.27778	-0.623801	1.142323
C	-5.073622	2.117257	0.03641	C	-4.501973	1.694862	0.337944
H	-5.29375	3.182211	0.048933	H	-5.004061	2.60827	0.027352
C	-6.140832	1.21494	0.031032	C	-4.986758	1.015139	1.459207
C	2.484163	3.432903	1.378091	C	0.045468	2.58174	1.042873
H	3.250868	4.21589	1.351392	H	0.259696	3.503529	1.59642
H	1.493346	3.892893	1.298946	H	-0.918378	2.671828	0.529135
H	2.547179	2.891292	2.326539	H	-0.014513	1.740109	1.74152
C	-2.565942	-3.310965	1.507133	C	-0.051745	-2.352188	1.782498
H	-3.284945	-4.137669	1.472714	H	-0.35102	-2.972781	2.635216
H	-1.549169	-3.714337	1.565525	H	0.815259	-2.800732	1.285993
H	-2.753174	-2.699592	2.395185	H	0.229226	-1.354141	2.133923
C	-2.544166	-3.441305	-1.355326	C	-1.81216	-3.929706	0.154126
H	-1.544285	-3.887651	-1.329274	H	-0.957158	-4.376326	-0.364044

Atom	x	y	z	Atom	x	y	z
H	-3.297564	-4.234034	-1.279996	H	-2.035301	-4.510643	1.056563
H	-2.667792	-2.907988	-2.302577	H	-2.679002	-3.944375	-0.513274
C	2.640686	3.32082	-1.48119	C	1.505797	3.789501	-1.114374
H	1.627847	3.724413	-1.586849	H	0.548839	4.017064	-1.594587
H	3.356853	4.147306	-1.406501	H	1.778054	4.609209	-0.439198
H	2.871537	2.714433	-2.362431	H	2.274758	3.680495	-1.884663
O	7.380068	-1.758589	0.046316	O	6.141355	-0.619704	2.433886
O	-7.382736	1.754786	0.042285	O	-6.054691	1.568672	2.080082
C	8.477239	-0.880547	0.124493	C	6.697596	0.435569	3.181658
H	8.458163	-0.283437	1.047695	H	5.989189	0.827832	3.925465
H	9.375722	-1.502529	0.126366	H	7.564439	0.024234	3.704545
H	8.519367	-0.200626	-0.738717	H	7.031835	1.261208	2.537077
C	-8.480545	0.874146	0.03722	C	-6.577661	0.903195	3.205127
H	-9.379558	1.495277	0.046415	H	-7.425458	1.498084	3.553605
H	-8.495046	0.24386	-0.863757	H	-6.932998	-0.106524	2.953964
H	-8.489109	0.225987	0.925537	H	-5.839473	0.829714	4.016793

re 9. –   re 10. –

$E_{Gibbs} = E_{def2TZVP} + Corr_{EGibbs}$

$= -9848.6182629 + 0.319331$

$= -9848.2989319$ Ha

$E_{Gibbs} = E_{def2TZVP} + Corr_{EGibbs}$

$= -9848.6220184 + 0.321634$

$= -9848.3003844$ Ha

$\Delta G_{bending} = -0.0014525$ Ha $= -3.81$ kJ/mol

f)   Coplanar local minimum and bent optimized structures of ModelConf3

Table S2.12: Coordinates for optimized ModelConf3-plane and ModelConf3-bent

Plane structure   Bent structure

Atom	x	y	z	Atom	x	y	z
Br	0.478124	1.639666	0.013174	Br	0.815652	-0.842123	2.353836
Ni	1.634749	-0.453413	0.001085	Ni	1.210216	0.890733	0.732722

Atom	x	y	z	Atom	x	y	z
Br	-0.51553	-1.525114	-0.008995	Br	-0.731899	2.013107	1.641095
Ni	-1.672475	0.570143	0.003108	Ni	-1.174993	-0.288478	1.096187
P	-2.66661	2.443939	-0.007806	P	-1.250805	-2.262766	0.3374
P	2.633334	-2.324261	0.009121	P	1.260748	2.266382	-0.876504
O	4.258142	-2.041616	-0.050064	O	2.533665	1.860655	-1.850907
O	-4.291684	2.164952	0.043724	O	-2.630166	-2.410267	-0.562673
C	3.440686	0.213271	0.006957	C	2.740206	0.162948	-0.167
C	5.857526	-0.309612	-0.030369	C	4.287616	0.299511	-2.080652
H	6.619722	-1.082399	-0.055223	H	4.598985	0.791617	-2.998247
C	3.803934	1.568401	0.036778	C	3.482404	-0.937226	0.27005
H	3.032362	2.334743	0.064656	H	3.197035	-1.445144	1.188705
C	4.517263	-0.681314	-0.02379	C	3.199115	0.754055	-1.3594
C	5.126204	1.988911	0.031383	C	4.592472	-1.427975	-0.421309
H	5.383524	3.045347	0.053127	H	5.13035	-2.284743	-0.025524
C	6.160992	1.050319	-0.003645	C	4.994084	-0.807759	-1.604376
C	-3.47926	-0.09429	-0.001827	C	-2.763285	-0.091914	0.038323
C	-5.888848	0.430379	0.02706	C	-4.433186	-1.165597	-1.434835
H	-6.683382	1.171533	0.046179	H	-4.754002	-2.075154	-1.93353
C	-3.843206	-1.44197	-0.025104	C	-3.500366	1.095377	-0.100655
H	-3.072339	-2.209439	-0.046855	H	-3.16578	1.99631	0.408738
C	-4.559133	0.807574	0.022642	C	-3.283344	-1.194297	-0.65208
C	-5.171579	-1.87327	-0.02116	C	-4.656041	1.169835	-0.86484
H	-5.384921	-2.938201	-0.038512	H	-5.217199	2.097306	-0.95296
C	-6.199377	-0.931236	0.005909	C	-5.127283	0.038674	-1.538084
C	2.378799	-3.462051	-1.378078	C	1.534118	4.033175	-0.586687

155

H	3.101176	-4.284615	-1.320754
H	1.362439	-3.868517	-1.341618
H	2.510117	-2.924852	-2.322102
C	-2.477463	3.482951	-1.480975
H	-3.168424	4.332491	-1.430405
H	-1.44838	3.853107	-1.543996
H	-2.6931	2.888764	-2.374178
C	-2.41366	3.578685	1.382073
H	-1.396143	3.982627	1.349902
H	-3.13383	4.403065	1.323026
H	-2.55023	3.040699	2.324891
C	2.453325	-3.361694	1.484736
H	1.423927	-3.729707	1.555466
H	3.142299	-4.212642	1.43106
H	2.675747	-2.766119	2.375395
O	7.421103	1.546208	-0.007872
O	-7.520667	-1.229944	0.012411
C	8.487398	0.628221	-0.044439
H	8.464094	0.010131	-0.953653
H	9.407369	1.217895	-0.043549
H	8.489446	-0.031893	0.835061
C	-7.884292	-2.589684	-0.00783
H	-8.9767	-2.62018	0.001348
H	-7.5235	-3.096187	-0.914539
H	-7.50758	-3.126937	0.87437

re 11. –

H	1.698495	4.542363	-1.543418
H	0.658565	4.464574	-0.090472
H	2.409798	4.170074	0.054615
C	-1.342523	-3.712461	1.418417
H	-1.572302	-4.600914	0.818709
H	-0.382781	-3.854154	1.925727
H	-2.124528	-3.567058	2.169359
C	0.062705	-2.651822	-0.850306
H	1.032032	-2.667112	-0.339676
H	-0.126904	-3.624833	-1.318636
H	0.09177	-1.874132	-1.621149
C	-0.15367	2.196527	-2.007297
H	-1.042237	2.602931	-1.51261
H	0.064011	2.775745	-2.91231
H	-0.354201	1.15465	-2.277551
O	6.048256	-1.197213	-2.360019
O	-6.258335	0.202942	-2.26343
C	6.799088	-2.30286	-1.917382
H	6.189622	-3.21642	-1.864568
H	7.594587	-2.452649	-2.651446
H	7.254845	-2.120751	-0.933679
C	-6.76975	-0.916673	-2.946659
H	-7.674197	-0.582306	-3.460681
H	-6.059483	-1.299667	-3.693553
H	-7.034754	-1.730448	-2.256452

re 12. –

$$E_{Gibbs} = E_{def2TZVP} + Corr_{EGibbs} \qquad\qquad E_{Gibbs} = E_{def2TZVP} + Corr_{EGibbs}$$

$$= \text{-9848.6183918} + 0.320247 \qquad\qquad = \text{-9848.6220727} + 0.322662$$

$$= \text{-9848.2981448 Ha} \qquad\qquad = \text{-9848.2994107 Ha}$$

$$\Delta G_{bending} = \text{-0.00126594 Ha} = \text{-3.23 kJ/mol}$$

g) Geometry of the transition state for the flipping

Table S2.13: Coordinates for the optimized transition state of ModelPhenol flipping

ModelPhenol – Transition state

Br	-0.18607591	-1.64807091	0.04364467
Ni	-1.71931291	0.18668009	0.01022167
Br	0.18607509	1.64806609	0.04379567
Ni	1.71931209	-0.18668191	0.01019067
P	3.05429509	-1.83654291	-0.00462233
P	-3.05429391	1.83654409	-0.00443233
O	-4.57605391	1.25378709	-0.25000133
O	4.57605109	-1.25376291	-0.25017033
C	-3.36977591	-0.81090391	-0.01668833
C	-5.82662691	-0.75571991	-0.20142033
H	-6.72726491	-0.15615191	-0.31101533
C	-3.46786091	-2.20316891	0.09068767
H	-2.56710891	-2.80158591	0.20983767
C	-4.58938691	-0.12918991	-0.15485833
C	-4.69522491	-2.86376091	0.04744167
H	-4.72491891	-3.94838191	0.12959167
C	-5.87422391	-2.14164191	-0.10216833
C	3.36977509	0.81090409	-0.01663633

C	5.82662409	0.75573909	-0.20139533
H	6.72726209	0.15618209	-0.31105833
C	3.46786109	2.20315809	0.09087967
H	2.56711009	2.80156309	0.21009867
C	4.58938509	0.12920409	-0.15488633
C	4.69522409	2.86375509	0.04768867
H	4.72491909	3.94836809	0.12994767
C	5.87422209	2.14165109	-0.10200533
C	-2.91724891	3.11412509	-1.27998033
H	-3.81424091	3.74414309	-1.26427033
H	-2.03546891	3.73469109	-1.08855533
H	-2.81476791	2.64782709	-2.26414933
C	2.91723109	-3.11402291	-1.28026833
H	3.81422809	-3.74403491	-1.26463133
H	2.03546109	-3.73461291	-1.08887033
H	2.81472109	-2.64764891	-2.26439833
C	3.19632609	-2.75821091	1.55063667
H	2.25439909	-3.27683891	1.76089067
H	4.01038409	-3.48932591	1.48406567
H	3.40014409	-2.05634891	2.36550567
C	-3.19629391	2.75809209	1.55090067
H	-2.25436991	3.27672309	1.76116167
H	-4.01036691	3.48919809	1.48440767
H	-3.40007391	2.05616909	2.36572567
H	6.83360809	2.65310209	-0.13781533

| H | -6.83361091 | -2.65308891 | -0.13802133 |

re 13. –

$$E_{Gibbs} = E_{def2TZVP} + Corr_{EGibbs}$$

= -9619.60268 + 0.263779

= -9619.338898 Ha
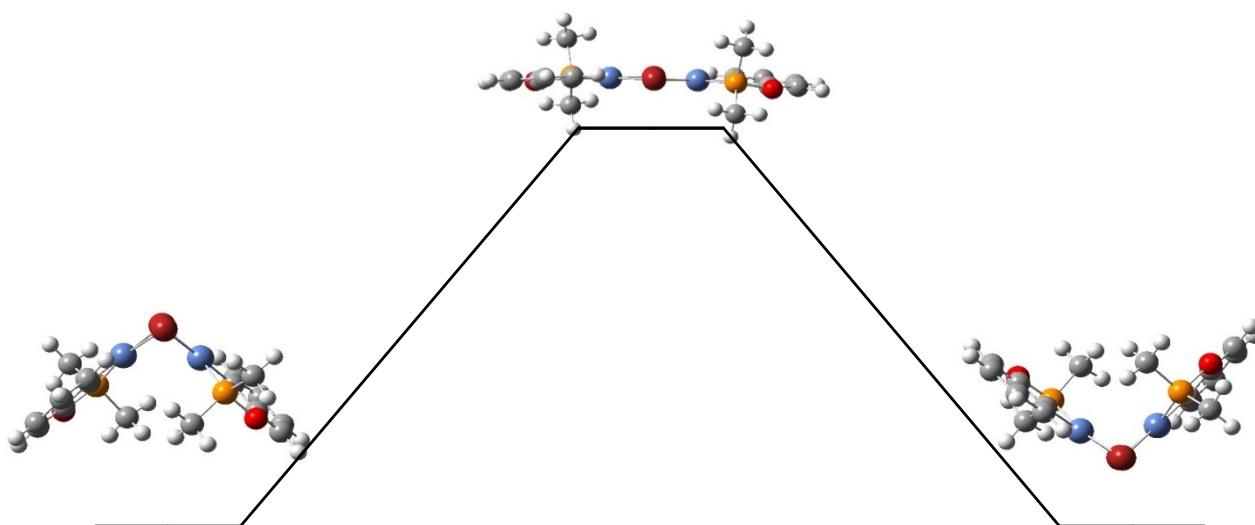
Figure S2.92: Proposed energy surface for the inversion of the bending in ModelPhenol

h) Geometry of the *s*-cis isomer and the mixed square planar-tetrahedral dinuclear intermediate

Table S2.14: Coordinates for the optimized transition state of ModelPhenol flipping

ModelPhenolCis

Ni	-1.479321	-0.08185	-0.464563
Br	0.011471	1.401719	-1.560551
Ni	1.474916	-0.102671	-0.457045
Br	-0.013023	-1.895791	-1.139416
P	-2.747358	-1.460018	0.54016
P	2.698325	-1.487157	0.59346
O	3.868833	-0.631804	1.376982
O	-4.060853	-0.6303	1.088401
C	2.805976	1.147271	0.157581
C	4.840243	1.52284	1.496022

ModelPhenolMix

Ni	-1.300403	0.735936	0.364086
Ni	1.318597	0.400763	0.002088
Br	0.222379	0.354496	2.190421
Br	0.140462	2.513227	-0.499439
P	-2.402239	0.846852	-1.452308
P	3.579312	0.319929	0.309392
O	3.984769	-0.952419	-0.678225
O	-3.662337	-0.212123	-1.340868
C	1.616371	-1.420519	-0.688673
C	3.248242	-3.025031	-1.561909

H	5.60272	1.102221	2.147477	H	4.288069	-3.27001	-1.7677
C	2.850994	2.50393	-0.185585	C	0.608448	-2.347174	-0.97515
H	2.087508	2.920413	-0.837342	H	-0.427907	-2.106446	-0.722833
C	3.835482	0.702481	1.002621	C	2.928256	-1.804984	-0.977629
C	3.848385	3.353078	0.291993	C	0.896331	-3.579184	-1.561826
H	3.843179	4.401915	0.002599	H	0.094432	-4.281767	-1.779574
C	4.840814	2.865198	1.134996	C	2.216416	-3.909657	-1.860392
C	-2.775945	1.189391	0.181781	C	-2.6225	-0.59734	0.791883
C	-4.905513	1.562247	1.364039	C	-4.641792	-1.820866	0.090028
H	-5.753443	1.128571	1.889044	H	-5.393482	-1.991874	-0.676927
C	-2.691213	2.577321	0.017222	C	-2.671832	-1.316832	1.992497
H	-1.835723	3.006788	-0.497352	H	-1.91305	-1.14861	2.751788
C	-3.909387	0.730447	0.872155	C	-3.638907	-0.88749	-0.133634
C	-3.676026	3.438903	0.498827	C	-3.670899	-2.254818	2.247903
H	-3.571434	4.511047	0.345678	H	-3.67407	-2.790098	3.19508
C	-4.783989	2.933235	1.16977	C	-4.653631	-2.509437	1.297328
C	3.643766	-2.681282	-0.391256	C	4.090288	-0.263711	1.953157
H	4.343529	-3.228717	0.250886	H	5.145625	-0.559635	1.94859
H	2.961333	-3.389	-0.874276	H	3.932699	0.530069	2.692235
H	4.201635	-2.146282	-1.166207	H	3.472535	-1.124361	2.232292
C	-2.093257	-2.234034	2.045512	C	-1.53321	0.287784	-2.941436
H	-2.89614	-2.762198	2.57293	H	-2.247908	0.183072	-3.766194
H	-1.302391	-2.944382	1.781463	H	-0.760342	1.013673	-3.214824
H	-1.678093	-1.458719	2.697526	H	-1.054489	-0.678402	-2.746939
C	-3.507453	-2.825817	-0.376222	C	-3.23018	2.381401	-1.943396

H	-2.749268	-3.575146	-0.626476	H	-2.488386	3.124149	-2.252985
H	-4.288093	-3.290559	0.237182	H	-3.909869	2.173827	-2.778053
H	-3.950018	-2.446606	-1.302121	H	-3.801472	2.778799	-1.09924
C	1.984228	-2.477464	1.934074	C	4.871677	1.504539	-0.158505
H	1.385535	-3.290558	1.510622	H	4.851227	2.347922	0.540412
H	2.791619	-2.902966	2.541379	H	5.85781	1.027456	-0.12266
H	1.349406	-1.846661	2.564061	H	4.687861	1.882297	-1.168491
H	5.619058	3.525385	1.511559	H	2.449602	-4.869039	-2.317699
H	-5.55421	3.602553	1.546727	H	-5.43175	-3.244346	1.491473

e 14. –

$E_{Gibbs} = E_{def2TZVP} + Corr_{EGibbs}$

$= -9619.6022461 + 0.262749$

$= -9619.3394971$ Ha

$\Delta G_{s\text{-}cis} - \Delta G_{s\text{-}trans} = +0.00381164$ Ha $= +10.0$ kJ/mol

e 15. –

$E_{Gibbs} = E_{def2TZVP} + Corr_{EGibbs}$

$= -9619.5757152 + 0.258432$

$= -9619.3172832$ Ha

$\Delta G_{mix\text{-}triplet} - \Delta G_{s\text{-}trans} = +0.02602554$ Ha $= +68.3$ kJ/mol

Chapitre 3 – C-H Nickelation of Aryl Phosphinites: Mechanistic Aspects

Loïc P. Mangin[a] and Davit Zargarian[a]*

[a] Département de Chimie, Université de Montréal, Montréal, Canada H3T 1J4

Full paper

3.1 Abstract

The present report describes the results of a combined experimental and computational study on the mechanism of aryl phosphinite cyclonickelation. The reaction of ArOP(i-Pr)$_2$ with [(i-PrCN)NiBr$_2$]$_n$ proceeds more readily in acetonitrile relative to toluene; this is because the greater nucleophilicity of acetonitrile towards Ni stabilizes a more reactive acetonitrile adduct bearing one (as opposed to two) phosphinite ligands. A sufficiently strong external base such as Et$_3$N serves to quench the HBr generated at the nickelation step, thus allowing isolation of the cyclonickelated species. However, nickelation tests conducted in the absence of external base revealed that D/H scrambling occurs at the *ortho* positions of C$_6$D$_5$OP(i-Pr)$_2$, implying that the cyclonickelation proceeds independently of the base. Thus, the main role of the external base is to prevent protonation of the Ni-aryl moiety formed via C-H nickelation. Tests have also shown that nickelation rates are affected by the quantity of the base used: the presence of more than one equivalent of Et$_3$N generates the less reactive bi-phosphinite complex *trans*-{PhOP(i-Pr)$_2$}$_2$NiBr$_2$, thus inhibiting the desired C-H nickelation. Experimental studies have shown that nickelation is faster with aryl phosphinites bearing electron donating substituents (Hammett slope $\rho \approx -4$) and the proton transfer is rate limiting (KIE $\approx$ 11). The activation parameters were found to be $\Delta H^{\ddagger} = 18(1)$ kcal·mol^{-1} and $\Delta S^{\ddagger} = -27(4)$ cal·mol^{-1}·K^{-1}. DFT analyses have provided support for these findings and suggest that aryl phosphinite C-H nickelation proceeds via an ion pair-assisted deprotonation.

3.2 Introduction

The past decade has witnessed an increasing number of reports that disclose Ni(II)-catalyzed protocols for the direct functionalization of unactivated C-H moieties. Such non-redox type C-H metalation processes, followed by functionalization, are facilitated by the use of at least one directing group (DG) that serves the purpose of binding to the Ni(II) center and facilitating its encounter with the C-H moiety. This type of metalation by chelation also helps determine the regiochemistry of the functionalization, which is likely controlled by the relative stabilities of the nickelacycles generated in the C-H nickelation step. In this context, the most commonly used DG's are mono- and bidentate auxiliaries based on imine-type donors, such as 2-pyrimidyl anilines (monodentate)[1] and benzamido quinolones and pyridines (bidentate),[2] which were popularized by the groups of Ackermann and Chatani, respectively. Another effective DG is pyridine oxide.[3]

In contrast to the significant progress registered in Ni(II)-catalyzed direct functionalization of unactivated C-H bonds, however, there is relatively little concrete mechanistic knowledge on how these processes work.[4] The main reason for this paucity of mechanistic knowledge is that most efforts to date have focused on developing one-pot protocols that combine the chelation, metalation, and functionalization steps. While such a one-pot approach is attractive from a practical point of view, it bypasses the detection and isolation of reaction intermediates and forgoes the chance to improve our understanding of reaction mechanisms. Ideally, therefore, systematic efforts are needed to isolate model cyclonickelated complexes and delineate the factors that favor various steps of the C-H functionalization process.

The above considerations and our group's long-standing interest in organonickel chemistry[5] inspired us to investigate the preparation of thermally stable cyclonickelated species via C-H nickelation and study the direct functionalization of the resulting Ni-hydrocarbyl moiety. A search of the literature revealed that most cyclonickelated complexes accessible via C-H nickelation are stabilized by pincer-type ligands.[6] Our experience with the facile C-H nickelation of POCOP-type pincer ligands featuring aryl- and alkyl-phosphinite donor moieties[7] encouraged us to test the reactivities of substrates bearing a single phosphinite DG. Initial tests showed that alkyl phosphinites are insufficiently reactive, whereas aryl phosphinites underwent relatively facile C-H nickelation. Thus, we succeeded in accessing the isolable and thermally stable *ortho*-metalated complexes {(κ^P,κ^C-ArOPR$_2$)Ni(μ-Br)}$_2$ and (κ^P,κ^C-ArOPR$_2$)Ni(L)Br (**Chart 3.1**; R = *i*-Pr) and studying their structures, stabilities, and reactivities with electrophiles.[8]

Chart 3.1. Cyclonickelated species derived from aryl phosphinites.
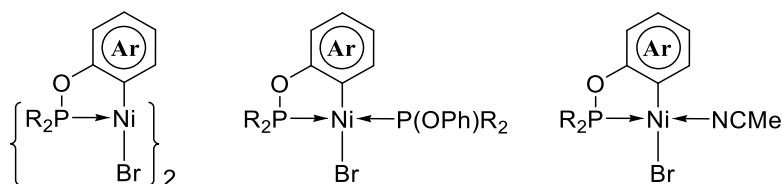
In addition to the above-mentioned promising reactivities of aryl phosphinites, we should also note that these substrates present many advantages in the context of the proposed studies: they are derived from phenols, which are inexpensive and ubiquitous in organic synthesis; the PR$_2$ directing group is easily grafted onto phenols by reaction with ClPR$_2$; ^{31}P NMR spectroscopy provides a convenient and powerful method for monitoring reactions and detecting intermediates. These

advantages compelled us to undertake detailed mechanistic studies on C-H cyclonickelation of aryl phosphinites. In a recent report,[9] we presented an optimized synthetic protocol for the preparation of cyclonickelated complexes shown in **Chart 3.1**, and provided a detailed analysis of the electronic and steric impact of phenol substituents on cyclonickelation rates, regiochemistry, and solid state structures of the cyclonickelated complexes.

The present contribution reports on our continued investigations on the reactivities of Ni(II) precursors with aryl phosphinites. The focus of this report is identification of the *in-situ* generated Ni species that promote the C-H nickelation step. Our investigation of the reaction conditions affecting the rate of this step has revealed a crucial role for the solvent, as well as the type and quantity of amine bases used. Deuterium labelling experiments have revealed that the C-H/C-D nickelation step occurs in the absence of base, but isolation of the cyclonickelated product arising from this reaction requires a relatively strong base. Kinetic studies and a Hammett analysis have - provided quantitative data about the rate and nature of the C-H nickelation step. Finally, DFT studies have supported the mechanistic insights obtained from experimental studies.

3.3 Results and Discussion

3.3.1 Impact of solvent on cyclonickelation

We have reported previously that *ortho*-C-H nickelation of aryl phosphinites is faster in acetonitrile relative to toluene, THF, and EtOAc.9 Initially, we attributed this observation to the greater ability of a polar solvent like acetonitrile for stabilizing the nickelation transition state, which is believed to involve significant charge separation over the reacting moieties $C^{\delta-}$---$H^{\delta+}$ and $Ni^{\delta+}$---$Br^{\delta-}$.[10] However, on reflection it occurred to us that another reason for the more facile cyclonickelation in acetonitrile might be this solvent's greater nucleophilicity towards Ni(II).[11] Thus, the more favorable MeCN→Ni coordination could conceivably generate a solvent adduct such as (L)(MeCN)NiBr$_2$ (**1a**, L = PhOP(*i*-Pr)$_2$) that would be more reactive toward cyclonickelation relative to the bi-phosphinite complex *trans*-L$_2$NiBr$_2$ (**1b**) present in toluene.[12]

The assertion that a different intermediate might form in acetonitrile was consistent with the observation of differently colored initial reaction mixtures as a function of solvent. For instance, stirring the insoluble Ni precursor [(*i*-PrCN)NiBr$_2$]$_n$ in toluene solutions of PhOP(*i*-Pr)$_2$ at r.t. generates the toluene-soluble bi-phosphinite adduct **1b**. The deep-red color of this complex

dominates the heterogeneous mixture that forms in the presence of less than 2 equiv of L, whereas a homogeneous deep-red solution is observed with two or more equiv of L. In other words, the L:Ni ratio affects the homogeneity of these toluene mixtures, but not their color. The ^{31}P NMR spectrum of the latter mixtures displayed, independently of the L:Ni ratio, a fairly broad peak spanning the chemical shift interval 132 – 138 ppm, which could be attributed to dynamic exchange. Recording the ^{31}P spectrum at –30 °C gave significant peak sharpening (**Fig. S3.15**), and displayed a major peak at 135 ppm, along with a minor peak at 130 ppm which can be attributed to a different conformer of **1b** (*i.e.* C2 symmetric *vs.* centrosymmetric).

Repeating the above experiment in acetonitrile revealed two different color regimes depending on the L:Ni ratio. Thus, addition of one equiv of phosphinite to the acetonitrile suspension of [(*i*-PrCN)NiBr$_2$]$_n$ gave a homogeneous green solution displaying no ^{31}P signal at all, whereas adding a second equiv of L led to a deep-red solution displaying a very broad ^{31}P signal spanning the chemical shift range of 120 – 150 ppm. This latter signal was confirmed to be due to **1b** by recording the ^{31}P NMR spectrum of an authentic sample of this compound in acetonitrile. Recording the ^{31}P spectrum of **1b** at –30 °C revealed sharp peaks at 135 ppm (major) and 130 ppm (minor), as well as a peak at 150 ppm corresponding to the free ligand. This indicates that MeCN is nucleophilic enough to allow displacement of the phosphinite, and that lowering the temperature slows down the exchange process sufficiently to allow us to detect the species involved in the exchange (**Fig. S16**). Moreover, when the green 1:1 L:Ni mixture was subjected to the same analysis, the only detectable peaks were at 135 ppm (major) and 130 ppm (minor, **Fig. S3.17**); this implies that **1b** also exchanges with the bi-phosphinite species, even though the latter is present to a significantly smaller extent in MeCN than in non-polar solvents.

The above observations allow us to propose the sequence of events shown in **Scheme 1** for rationalizing how PhOP(*i*-Pr)$_2$ and [(*i*-PrCN)NiBr$_2$]$_n$ interact prior to the cyclonickelation stage. We believe that dynamic equilibria are taking place in both solvents at r.t. In toluene, these equilibria always favor the deep-red bi-phosphinite species **1b**, whereas in acetonitrile it is the green mono-phosphinite adduct **1a** that is dominant in the presence of one equiv of phosphinite. The stability of the mono-phosphinite species **1a** is presumably due to the nucleophilic character of acetonitrile, whereas related mono-phosphinite intermediates do not appear to be stable in toluene, THF or EtOAc.[13]

Scheme 3.1. The different Ni species postulated to exist in toluene and acetonitrile prior to the nickelation of PhOP(*i*-Pr)$_2$.
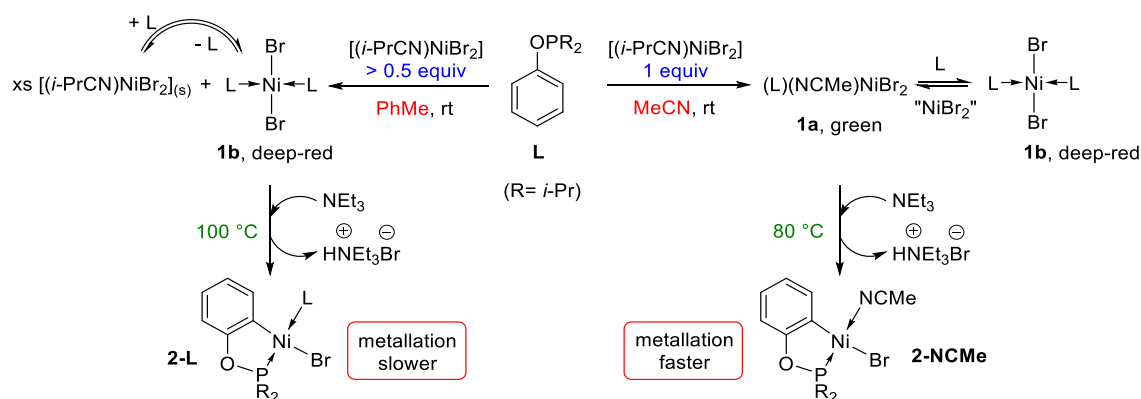
Furthermore, given the broadness of the ^{1}H and ^{31}P signals for the acetonitrile solutions of **1b**, it is reasonable to infer that the competitive binding of the solvent could lead to exchange between bi- and mono-phosphinite species, and that the latter would exist as a paramagnetic tetrahedral form.

Having established that r.t. reaction mixtures contain different Ni-phosphinite species **1a** and **1b** depending on solvent and L:Ni ratio, we proceeded to measure how easily each of these species undergoes cyclonickelation. Thus, heating a 1:1:1 mixture of L:Ni:Et$_3$N in acetonitrile at 80 °C gave complete cyclonickelation in 16 h, whereas only 50% conversion was observed in toluene under analogous conditions; even heating the toluene mixture at 100 °C gave only 75% conversion.[14] A similar result was obtained when we measured the cyclo-nickelation rates in the presence of 2:1 L:Ni ratio. Indeed, heating 1:1 solutions of **1b**:Et$_3$N at 80 °C for 16 h showed complete cyclonickelation in acetonitrile, but only 40% in toluene; the latter mixture required heating to 100 °C to achieve 90% conversion.[15] It appears, therefore, that cyclonickelation is faster in acetonitrile likely because of the reactive mono-phosphinite intermediate **1a** formed in this solvent (**Scheme 1**). Conversely, metalation is slower in toluene because the predominant species in this solvent is the bi-phosphinite complex **1b**; the latter is less reactive since it requires the dissociation of one phosphinite to promote the C-H nickelation. This scenario is also consistent with the observation that presence of excess L slows down the cyclonickelation reaction.[8]

3.3.2 Role and influence of base on C-H nickelation

Our previous studies had shown that the presence of Et$_3$N is essential for successful cyclonickelation of aryl phosphinites; this was attributed to the quenching of the *in-situ* generated HBr.[8,9] However, a more careful analysis of the reaction mixtures prior to cyclonickelation (*i.e.*, prior to heating) gave indications that Et$_3$N might hinder the desired reaction. Thus, although the 1:1 mixture of L:Ni in MeCN gives a green solution that is NMR-silent, addition of one equiv of Et$_3$N to this solution turned it brownish, and gave a broad ^{31}P signal (120 – 150 ppm) characteristic of bi-phosphinite complex **1b** in acetonitrile. We also detected a sharp and minor peak (< 2%) on top of the initial broad peak at 135 ppm, but we were unable to identify the species responsible for this resonance. Addition of 3 more equiv of Et$_3$N led to a small amount of free phosphinite (151 ppm), suggesting that competitive binding of the base would hinder the reaction.

To confirm that the observed changes result from the coordination of the base to Ni, we added 1 equiv of the bulkier and less nucleophilic amine *i*-Pr$_2$NEt (Hünig's base) to a green, 1:1 mixture of L:Ni in acetonitrile. This mixture showed no color change and its ^{31}P NMR spectrum displayed only the very minor sharp peak at 135 ppm, but not the broad signal at 120 – 150 ppm attributed to **1b**.

The above observations imply that the NMR-silent feature of the 1:1 L:Ni acetonitrile mixture as well as its green color can be reasonably ascribed to the formation of a paramagnetic tetrahedral mono-phosphinite adduct such as **1a**. Alternatively, the absence of NMR signals could also indicate a dynamic exchange process, for instance involving various mono- and bi-phosphinite adducts. Regardless of which interpretation is more probable, addition of a sufficiently nucleophilic amine such as Et$_3$N can lead to a competition for binding to Ni, thus reducing the effective concentration of Ni available for interaction with the phosphinite. In other words, Et$_3$N leads to an effective L:Ni ratio greater than 1:1, thereby leading to the formation of **1b**, which is known to hinder the cyclonickelation reaction. We conclude, therefore, that although Et$_3$N is necessary for driving the reaction to completion by capturing the *in-situ* generated HBr, it also retards the cyclonickelation by promoting the formation of **1b**.

The seemingly counteracting roles of Et$_3$N prompted us to conduct kinetic studies aimed at measuring the impact of [amine] on cyclonickelation of PhOP(*i*-Pr)$_2$. The conversion *vs.* time plots revealed that the C-H nickelation of PhOP(*i*-Pr)$_2$ is faster with 1 equiv of Et$_3$N than with 4 equiv

(**Fig. S3.38**). Plotting ln(1-conversion) *vs.* time over the first 3 h of the reaction produced fairly straight lines (**Fig. 3.1**), revealing that the C-H nickelation follows approximatively first-order rates. The regression gave rate constants of 0.19 and 0.15 h^{-1}, respectively, implying a smaller than zero-th order for the base. This finding is consistent with the above-mentioned proposal that competitive $Et_3N{\rightarrow}Ni$ coordination can diminish the concentration of the species responsible for the C-H nickelation. Moreover, when 1 equiv of base was used, the reaction was faster with *i*-Pr_2NEt relative to Et_3N (0.22 vs. 0.19 h^{-1}), which is also consistent with the diminished inhibitory effect of a more hindered amine on the cyclonickelation.
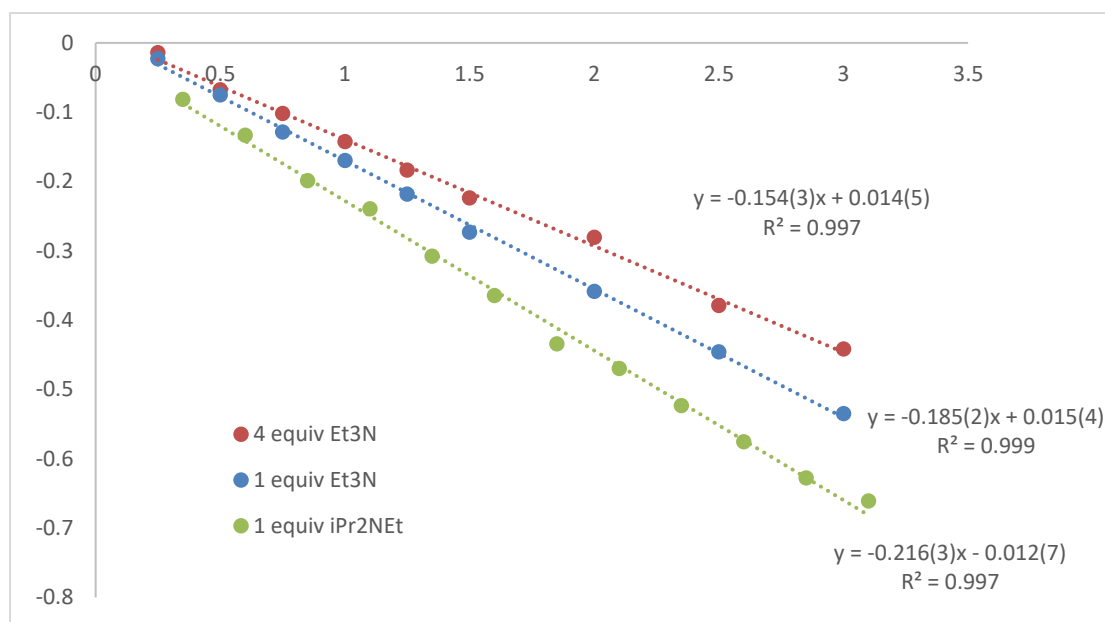
Figure 3.1. Plot of ln(1-conv.) as a function of time, and rate constants under the assumption of a 1st order cyclonickelation in MeCN at 70 °C with various amines and [amine].

To further investigate the impact of external base on cyclonickelation, we studied the reaction of [(*i*-PrCN)NiBr$_2$]$_n$ with PhOP(*i*-Pr)$_2$ in the presence of other amines. This reaction was found to be very sensitive to the specific choice of external base, strong bases of weak nucleophilic character being ideal candidates. Thus, little or no reactivity was observed with amines that are weakly basic (e.g., aniline and *N,N*-diethylaniline) or strongly coordinating (e.g., pyridine, imidazole, pyrazole, and DBU). In the case of the latter amines, immediate color changes were observed upon addition of the amine, confirming the competitive coordination of the amine, thus hindering the metalation. These findings can be summed up as follows: external bases can hinder cyclonickelation of aryl

phosphinites if they are strongly coordinating and/or present in super-stoichiometric amounts; nevertheless, they play an essential role in the fate of cyclonickelation, one that cannot be fulfilled by excess phosphinite, which is insufficiently basic to quench HBr.

3.3.3 Reversibility of the nickelation

It occurred to us that the requirement for a strong base could be understood if the nickelated complex was easily protonated. In such a scenario, protonation of weak bases (including phosphinites) by the *in-situ* generated HBr would give rise to a strong conjugate acid capable of protonating the newly formed Ni-C bond, thus reversing the nickelation step. Conversely, reaction of strong external bases with HBr would form weak conjugate acids that would not be effective for protonating the Ni-C moiety; this would drive the cyclonickelation forward. To determine the validity of this hypothesis, we tested the stability of the independently prepared and authenticated complexes [{κ^P,κ^C-C$_6$H$_4$OP(i-Pr)$_2$}Ni(μ-Br)]$_2$ (**2-μBr**) and **2-NCMe** in the presence of a relatively strong proton source, as described below in **Scheme 3.2**.

Scheme 3.2. Protonation of the aryl moiety by AcOH.

X = Br or OAc; L = PhOPR$_2$
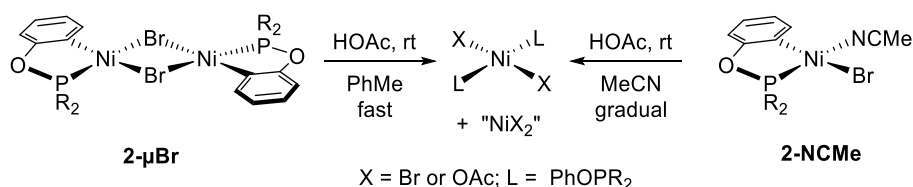
Addition of one equiv of acetic acid to the r.t. acetonitrile solution of **2-NCMe** caused a gradual color change to a deeper red, and the original ^{31}P signal at 196 ppm was partially replaced over a few hours by a broad signal at 135 ppm; this is the signal for the non-metalated complexes *trans*-L$_2$NiX$_2$ (X= Br, OAc). A similar reactivity was observed when two equiv of acetic acid were added to the toluene solution of **2-μBr** at r.t., but in this case the color change took place in the time of mixing, and the ^{31}P NMR spectrum recorded within 10 min confirmed complete disappearance of the starting material. These observations indicate that the C-H nickelation of aryl phosphinites is reversible even in the presence of a relatively weak organic acid. Moreover, tests also showed that the phosphinite could not be protonated in the presence of acetic acid or an even stronger acid such

as 3-Cl-C$_6$H$_4$COOH, demonstrating that the conjugate acid, $[i$-Pr$_2$P(H)OPh$]^+$ must be a sufficiently strong acid to reverse the cyclonickelation step.

The above results indicate that the cyclonickelated complex is thermodynamically unstable towards re-protonation by HBr, but it should be kinetically accessible even in the absence of a base. To prove this, we sought evidence for H/D scrambling between a phosphinite and its deuterated analogue under the conditions of C-H nickelation; if the cyclonickelated species arising from these phosphinites could survive in the medium long enough, the ensuing re-protonation by HBr/DBr should leave a trace of the cyclonickelation event.

The above hypothesis was tested by refluxing a 1:1 mixture of *trans*-(C$_6$D$_5$OPR$_2$)$_2$NiBr$_2$ (R= *i*-Pr, **1b-d$_5$**) and *trans*-(4-Cl- C$_6$H$_4$OPR$_2$)$_2$NiBr$_2$ (**1b-Cl**) in *d$_0$*-acetonitrile over 24 h in the absence of added base (**Scheme 3.3**). The nickel complexes present in the final reaction mixture were isolated by crystallization and analyzed by ^{1}H NMR in CDCl$_3$, which showed H-incorporation into the *ortho* position of the deuterated ligand but none into *meta*/*para* positions. Surprisingly, however, there was no significant decrease in the ^{1}H signal for the *ortho* H in **1b-Cl**, indicating that this compound was not the source of the protons incorporated into **1b-d$_5$**. This raised the question of whether the H/D scrambling occurs with the solvent. In such a scenario, scrambling of phosphinite *ortho* positions with C*H$_3$*CN would occur for both complexes, but would be detectable in the deuterated ligand only.

Scheme 3.3. Observed ortho H/D scrambling between complexes 1b-d5 and 1b-Cl in MeCN.
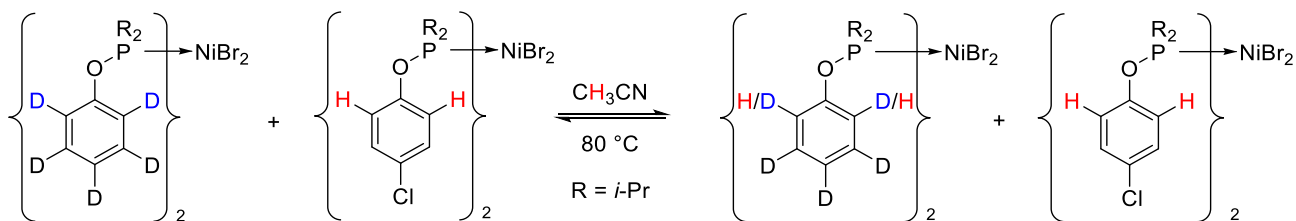
To test this second hypothesis, we refluxed the deuterated complex **1b-d$_5$** alone in CH$_3$CN for 24 h and analyzed the final product as above, which showed that the ligand had incorporated 17% H into the ortho positions only (Scheme 4). However, ^{2}H{^{1}H} NMR of the sample in CHCl$_3$ revealed signals corresponding to ortho D in the ligand above natural abundance. Although the signal was too small to be accurately quantified, comparison with the natural abundance of CDCl$_3$ in CHCl$_3$

allowed us to evaluate that the extent of D incorporation is well below 1% (**Fig. S3.29**). These results can be rationalized by invoking H/D exchange between the *in-situ* generated DBr and the reaction solvent to generate HBr (Eq. 1). The HBr will then protonate the newly formed Ni-C bond (Eq. 2), thus accounting for H-incorporation into **1b-d$_5$** (**Scheme 3.4**). We should note as well that ^{13}C{^{1}H} NMR analysis of the final material (**Fig. S3.32**-3.**33**) showed that the *i*-Pr moieties of the ligand have not incorporated any D as we detected no signal for *CD*Me$_2$ or CHMe(*CD*H$_2$); this confirms that the H/D exchange takes place with the solvent. This sequence of reactions takes place because the H/D exchange between the *in-situ* generated DBr and CH$_3$CN (Eq 1) proceeds with a rate that is similar to the protonation of the newly formed C-Ni bond by the HBr generated in the exchange (Eq. 2). In contrast, the analogous H/D exchange between **1b** and CD$_3$CN is not observed, probably because the H/D exchange in CD$_3$CN (Eq. 3) is slower than the protonation of the C-Ni bond (Eq 2).

$$CH_3CN + DBr \quad \rightleftharpoons \quad CH_3CND^+ + Br^- \quad \rightleftharpoons \quad CH_2DCNH^+ + Br^- \quad \rightleftharpoons \quad CH_2DCN + HBr \qquad \text{(Eq 1)}$$

$$HBr_{(solv.)} + \textbf{2-L} \rightarrow \textbf{1b} \qquad\qquad \text{(fast)} \qquad\qquad\qquad\qquad\qquad\qquad\qquad\qquad \text{(Eq 2)}$$

$$CD_3CN + HBr \quad \rightleftharpoons \quad CD_2HCN + DBr \quad \text{(slow)} \qquad\qquad\qquad\qquad\qquad \text{(Eq 3)}$$
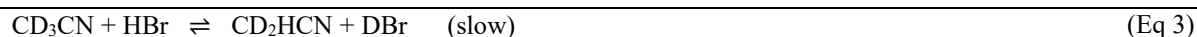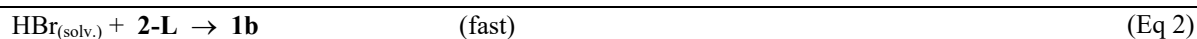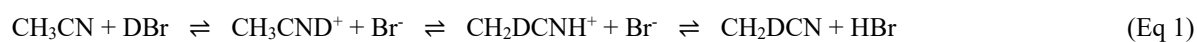
Scheme 3.4. Proposed mechanism for the role of solvent in the incorporation of H into deuterio ligand.
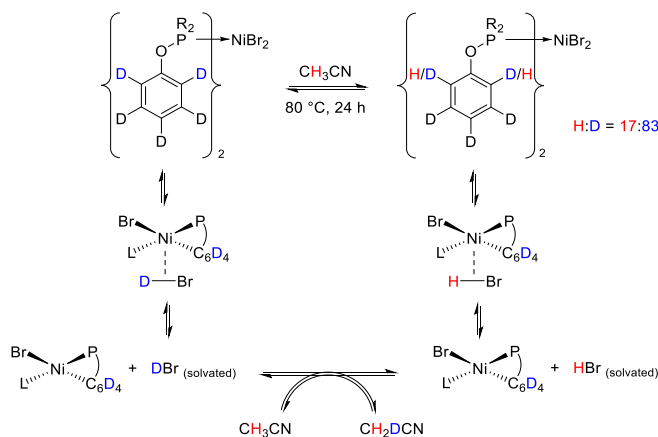
Repeating the above experiments in toluene gave similar results. Heating **1b-d$_5$** in the absence of a base for 24 h at 100 °C in *d$_0$*-toluene showed 23 % H incorporation into the ortho position of the ligand under the same conditions (and no D incorporation into the *i*-Pr moieties); moreover, ^{2}H{^{1}H}

NMR did not show *ortho* D incorporation into the ligand, suggesting this to be below the detection limit (< 0.1 %). In this case, the H/D exchange between in-situ generated DBr and toluene is conceivably going through a protonated arene such as a Wheland intermediate (Eq 4).

$$C_6H_5CH_3 + DBr \rightleftharpoons [C_6H_5(D)CH_3]^+ + Br^- \rightleftharpoons C_6H_4DCH_3 + HBr \qquad (Eq\ 4)$$

As was discussed for the analogous reactivity in CD_3CN, no H/D exchange is observed in d_8-toluene owing to slow exchange with this solvent. Although the nickelation is known to be slower in toluene than in acetonitrile, more H-incorporation has been observed in toluene (23% vs. 17%); this indicates that the exchange of DBr with toluene is faster than that with acetonitrile, and that the rate limiting step in acetonitrile is this exchange, and not the nickelation step.

Altogether, the results of the above-described D/H exchange experiments confirm that the C-H nickeallation of aryl phosphinite can take place in the absence of an external base. Significantly, these observations also imply that capture of the acid formed in the immediate aftermath of the C-H nickelation step by the base takes place outside the coordination sphere.

3.3.4 Kinetics of aryl phosphinite cyclonickelation

The observations described in the above sections established that the most favorable conditions for cyclonickelation of aryl phosphinites are the following: running the reactions in acetonitrile with the phosphinite ligand, our Ni precursor, and *i*-Pr$_2$NEt in a 1:1:1 ratio. Monitoring the reaction under these conditions at 80 °C and plotting ln(1-conv) against time revealed first order kinetics for the cyclonickelation up to 90% conversion, although a somewhat faster rate is evident at the beginning of the reaction (**Fig. 3.2**). The observed 1st order C-H nickelation is consistent with the previously stated proposal that the base plays no role in the rate determining step. In an effort to shed some light on the possible reaction pathways, we conducted a Hammett analysis on the cyclonickelation of substituted aryl phosphinites. Monitoring the cyclo-nickelation of various *meta*-substituted aryl phosphinites 3-X-C$_6$H$_5$OP(*i*-Pr)$_2$ (X = COOMe, Cl, H, Me or OMe) at 80 °C revealed a strong dependence on the electron-withdrawing (EW) or electron-donating (ED) character of the substituent (**Fig. 3.3**). Indeed, the Hammett plot displays a strongly negative slope ($\rho \approx -4$, **Fig. 3.4**), indicating a much faster C-H nickelation rate for substrates bearing ED substituents.

174
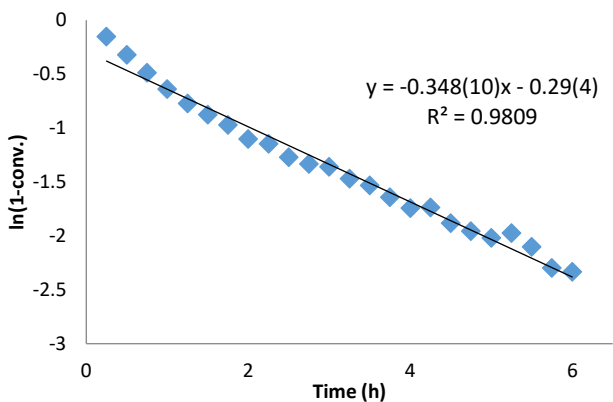
Figure 3.2. Plot of ln(1-conv.) as a function of time for the cyclonickelation of PhOP(i-Pr)$_2$ with 1 equiv Ni precursor and 1equiv i-Pr$_2$NEt in MeCN at 80 °C.
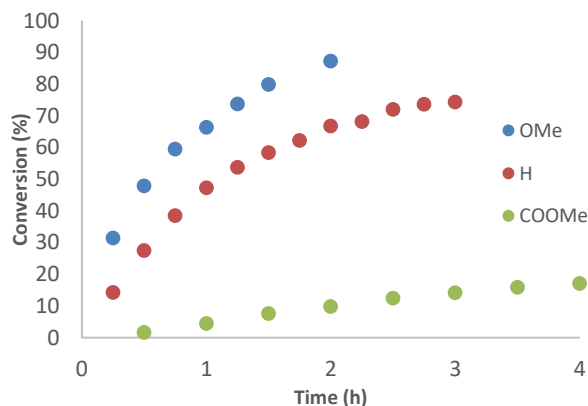
Figure 3.3. Nickelation rates of various 3-X-C$_6$H$_5$OP(i-Pr)$_2$ species in MeCN at 80 °C.

The fastest rate, obtained for the cyclonickelation of 3-MeO-C$_6$H$_4$OP(i-Pr)$_2$, is 20 times greater than that of the slowest rate, obtained for the cyclonickelation of 3-COOMe-C$_6$H$_4$OP(i-Pr)$_2$. Consistent with these results, cyclonickelation of the highly electron-rich substrate 3-Me$_2$N-C$_6$H$_4$OP(i-Pr)$_2$ proved too fast to be measured conveniently at 80 °C (> 70% conversion within 15 min); indeed, this reaction proceeded to completion even at r.t., over 16 h. Finally, the cyclometalation of sterically hindered 3,5-(MeO)$_2$-C$_6$H$_5$)OP(i-Pr)$_2$ was found to be faster than the analogous reaction with the unsubstituted PhOP(i-Pr)$_2$ (**Fig. S3.41**), demonstrating that favorable electronic factors can overcome unfavorable steric effects.

The favorable impact of ED substituents on cyclonickelation of aryl phosphinites indicates that a positive charge develops on the Ni center at the transition state, which is stabilized by the coordination of the C-H moiety. This argues in favor of an electrophilic C-H metalation. To determine the importance of the proton transfer on the overall C-H nickelation rate, we examined the relative reaction rates for the cyclonickelation of C$_6$H$_5$OP(i-Pr)$_2$ and its deuterio analogue C$_6$D$_5$OP(i-Pr)$_2$. The reaction with the latter was much slower and we observed a $k_H/k_D \approx 11$ (**Fig. S3.42**). The large value for the kinetic isotope effect suggests that the C-H bond breaking is involved in the rate limiting step.
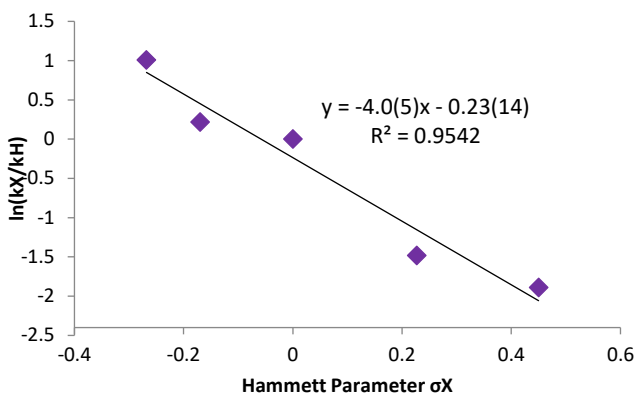
Figure 3.4. Hammett plot for the nickelation of 3-X-C$_6$H$_5$OP(i-Pr)$_2$ species in MeCN at 80 °C.
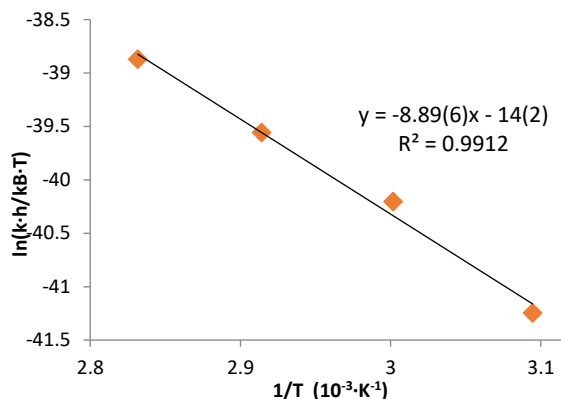
Figure 3.5. Eyring plot displaying rates at 50, 60, 70 and 80 °C for the metalation of PhOP(i-Pr)$_2$ in MeCN.

Next, we studied metalation rates of PhOP(i-Pr)$_2$ between 50 and 80 °C. The linear regression of the Eyring plot (**Fig. 3.5**) allowed us to extract the idealized kinetic parameters according to the transition state theory: $\Delta H^\ddagger$ = 18(1) kcal·mol^{-1} and $\Delta S^\ddagger$ = –27(4) cal·mol^{-1}·K^{-1}. The large and negative $\Delta S^\ddagger$ suggests a rate limiting step with fewer degrees of freedom, *i.e.*, a highly ordered transition state. This finding implies that the pathway from the resting state of the active species to the transition state for C-H nickelation must involve association as opposed to dissociation.

3.3.5 Attempts to isolate reaction intermediates in acetonitrile

3.3.5.1 Identification of Et$_3$N→Ni intermediates.

The above-mentioned findings on the formation of the less reactive bi-phosphinite complex **1b** being favored in the presence of excess Et$_3$N prompted us to probe how binding of Et$_3$N to Ni can impact the latter's reactivity with aryl phosphinites. To do so, we set out to isolate Et$_3$N→Ni adducts in the absence of the phosphinite, as follows.

Adding 2 equiv of Et$_3$N to the green suspension of [(i-PrCN)NiBr$_2$]$_n$ in acetonitrile caused an instantaneous color change to deep blue and rendered the mixture homogenous; addition of Et$_2$O and cooling to –35 °C for a few hours yielded large, royal blue crystals. Exposing these crystals to ambient air for even a few seconds led to formation of a green crust on the crystal, presumably hydrates. Crystallographic analysis of the material proved challenging due to significant

decomposition during crystal mounting and data collection; nevertheless, the collected data allowed us to unambiguously identify the main blue species as the homonuclear salt [Ni(NCMe)$_6$][(Et$_3$N)NiBr$_3$]$_2$ (**Scheme 3.5**).

Scheme 3.5 Isolation of Et$_3$N adducts of Ni.
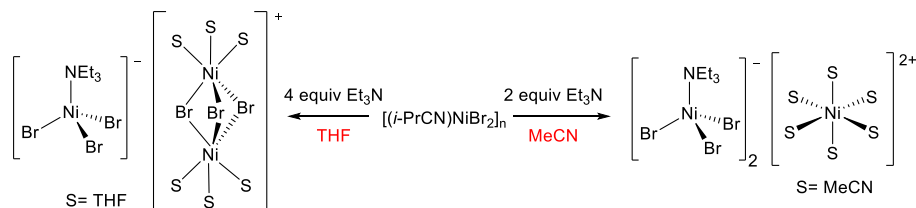
To determine if new, acetonitrile-free species could form in the presence of Et$_3$N, we repeated the above experiment in the less nucleophilic solvent THF. Adding 4 equiv of Et$_3$N to [(*i*-PrCN)NiBr$_2$]$_n$ in THF at r.t. also gave a blue solution that yielded blue crystals upon addition of Et$_2$O and cooling to −35 °C. Analysis of these crystals revealed the formation of another homonuclear salt featuring the same anion, [(Et$_3$N)NiBr$_3$]⁻, but a different cationic species, namely the μ-Br bridged dinuclear adduct of THF (**Scheme 3.5** and **Fig. 3.6**). It appears, therefore, that formation of the tetrahedral anion [(Et$_3$N)NiBr$_3$]⁻ is strongly favored and that this species serves to divert some of the Ni (in a reversible manner) from the main path of the cyclonickelation reaction. This finding allows us to propose the scenario depicted in **Scheme 3.6** for the speciation of Ni in the initial stages of the cyclonickelation.
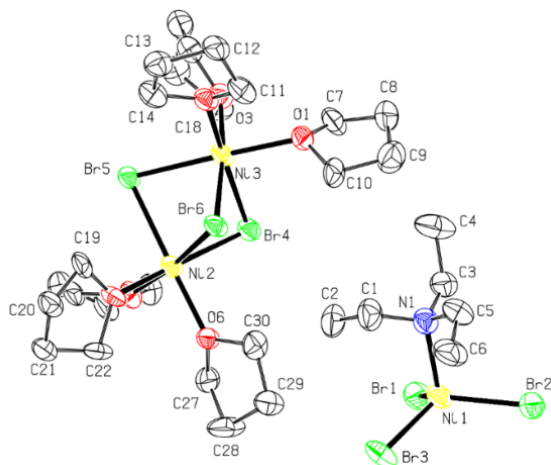
Figure 3.6. Molecular diagram of [(THF)$_6$Ni$_2$(μ-Br)$_3$][(Et$_3$N)NiBr$_3$]. Thermal ellipsoids are shown at the 50% probability level. Hydrogen atoms have been omitted for clarity.

Scheme 3.6. Postulated mechanism of action of Et$_3$N in slowing down cyclonickelation in MeCN.
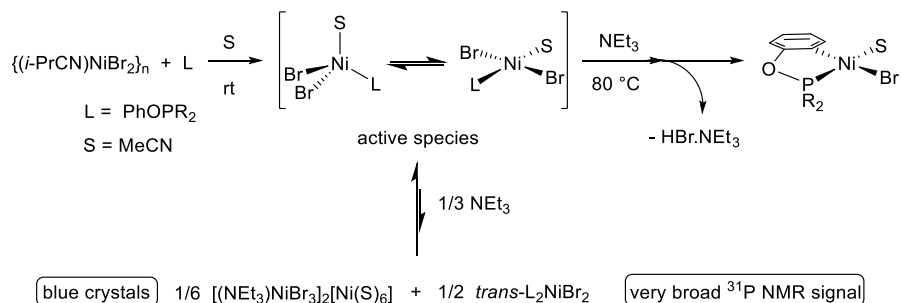
3.3.5.2 Isolation of a proposed mono-phosphinite intermediate.

In an effort to isolate the cyclonickelation active mono- phosphinite species depicted in **Scheme 6**, we stirred an equimolar acetonitrile solution of [(i-PrCN)NiBr$_2$]$_n$ (0.1 M) and PhOP(i-Pr)$_2$, and cooled the resulting green mixture at –35 °C. This gave deep red crystals of the bi-phosphinite complex **1b** and the green-yellow crystals that were identified as the coordination polymer of the formula [NiBr$_2$(NCMe)$_2$]$_n$. The failure to isolate the target mono-phosphinite species is attributed to the propensity of **1b** and [NiBr$_2$(NCMe)$_2$]$_n$ to equilibrate readily, and also to their limited solubility in acetonitrile at lower temperatures.

In a second effort to isolate the putative mono-phosphinite adduct, we prepared the parent charge-tagged phosphinite salt [3-Me$_3$N-C$_6$H$_4$OP(i-Pr)$_2$]X, L'$^+$X$^-$ (X = Cl, I) and repeated the above experiment. To avoid potential complications arising from the presence of different halides, we treated L'$^+$X$^-$ with 2 equiv of Ag(OTs) (Ts = p-Me-C$_6$H$_4$SO$_2$) in order to replace Cl$^-$ and I$^-$ anions by the less coordinating tosylate anion. This led to immediate precipitation of a white solid (presumably silver salts), which was filtered off. Subsequent addition of one equiv of the Ni precursor to the filtrate and stirring at r.t. led to a green solution that displayed broad ^{31}P NMR signals at 161 ppm (major) and 135 ppm (minor). Allowing this green solution to stand at r.t. gave only colorless crystals that turned out to be the dimeric silver salt [(L'$^+$Ag)$_2$(μ-Br)$_3$]Br (**Scheme 3.7**; see **Fig. S3.36** for molecular diagram). It is worth emphasizing that the anticipated Ni compound was not isolated even after cooling the green filtrate at –35 °C forseveral days. Evidently, the greater affinity of the phosphinite for Ag(I) appears to circumvent the isolation of Ni-phosphinite species.

Scheme 3.7. Species obtained from reactions of a charge tagged ligand with Ni-precursor.

Finally, we treated the *in-situ* generated L'$^+$X$^-$ directly with one equiv of [(*i*-PrCN)NiBr$_2$]$_n$ in MeCN at r.t. and analyzed the green solution by ESI-MS. The result was most consistent with the formation of (MeCN)$_n$(L'$^+$)NiBr$_2$ species (n = 1, 2).[16] Cooling this solution to –35 °C overnight gave deep green crystals that turned out to be the zwitterionic, mono-phosphinite adduct {3-Me$_3$N-C$_6$H$_4$OP(i-Pr)$_2$)}NiX$_3$ (X= Cl, Br, **Scheme 3.7**; see **Fig. S3.37** for molecular diagram). The unanticipated formation of an anionic trihalide species can be ascribed to the high halide:Ni ratio of 4:1 in this mixture vs. the 2:1 ratio present in the usual conditions of cyclonickelation.

In conclusion, our attempts to isolate or detect the putative cyclonickelation intermediate were unsuccessful. Nevertheless, the existence of a reactive, mono-phopsphinite species in acetonitrile mixtures of the Ni precursor and phosphinites is supported by (a) isolation of the mono-phopsphinite zwitterionic complex illustrated in **Scheme 3.7**, and (b) the fact that this tetrahedral compound has the same color (green) as the species generated in the equimolar solution of [(*i*-PrCN)NiBr$_2$]$_n$ and PhOP(*i*-Pr)$_2$. Further support for the intermediacy of such species in the cyclonickelation process was provided by the DFT calculations presented in the following section.

3.3.6 DFT computational analysis

Our DFT calculations started with model compounds based on the simpler phosphinite PhOPMe$_2$. This simplification allowed us to explore a larger range of mechanistic scenarios at a lower computational cost, and eventually eliminate the least realistic pathways; subsequent DFT studies were then undertaken with PhOP(*i*-Pr)$_2$ phosphinites in order to describe our system more

accurately. All energies discussed in the following sections for local minima and for transition states are calculated Gibbs free energies.

3.3.6.1 Ground State

M06 was used to start the optimization of the tetracoordinated, 16-electron model compound $(PhOPMe_2)NiBr_2(NCMe)$, which was allowed to adopt the *cis* or *trans* square planar singlet geometries (^1cis-**1** and ^1trans-**1**), or a tetrahedral triplet geometry (^1tet-**1**). For each of these, we considered as starting points different rotamers (rotation around the Ni-P bond) as well as different orientations for the Ph moiety, pointing away from the Ni center or pointing towards it. In each of the three geometries considered, several local minima were found within a range of 1 – 2 kcal/mol, with those that featured the Ph group pointing towards the Ni atom being more stable. Taking into account the more stable rotamer found for each geometry (**Fig. 3.7**), ^1trans-**1** was found to be the most stable, followed closely by ^3tet-**1** (1.0 kcal/mol higher) and ^1cis-**1**, which was significantly less stable (4.7 kcal/mol higher).

| ^{1}trans-1 | ^{3}*tet*-1 | ^{1}*cis*-1 |
| 0.0 | + 1.0 | + 4.7 |
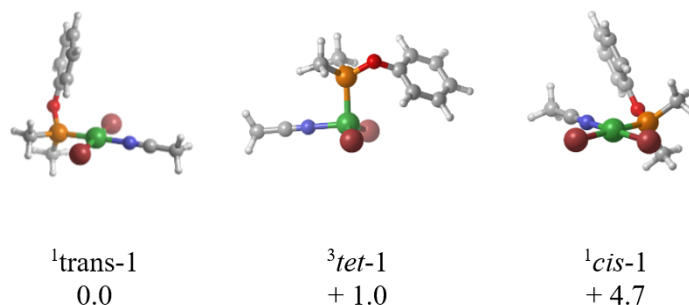
Figure 3.7. Energies (calculated at the M06 level of theory and expressed in kcal/mol) for optimized structures of the potential ground states for the model compound $(PhOPMe_2)NiBr_2(NCMe)$.

For completeness sake, we also probed the viability of the pentacoordinated 18-electron species $(PhOPMe_2)Br_2Ni$- $(NCMe)_2$, optimizing it as a square pyramidal singlet or a trigonal bipyramidal (*tbp*) triplet. The first approach led to dissociation of the apical acetonitrile, implying that this option is unlikely (**Fig. 3.8**). The second approach led to two distinct options featuring equatorial Br ligands and the phosphinite occupying either an equatorial (^3tbp-**1-eq**) or an axial position (^3tbp-**1-ax**). Both of these species proved to be less stable (by 7 kcal/mol) with respect to ^1trans-**1**, implying that the latter four-coordinated species is the most realistic option.

^{3}*tbp*-1-ax ^{1}*trans*-1 + MeCN ^{3}*tbp*-1-eq
+ 6.7   + 6.6

Figure 3.8. Energies (calculated at the M06 level of theory and expressed in kcal/mol) for optimized structures as the potential ground states for the pentacoordinated model compound (PhOPMe$_2$)NiBr$_2$(NCMe)$_2$.

Optimization of the above-discussed geometries with B3LYP led to different conclusions. The ground state was found to be ^{3}*tet*-1, whereas ^{1}*trans*-1 and to ^{1}*cis*-1 were found more energetic by 8.3 and 11.6 kcal/mol, respectively. It should be noted here that the much greater stability observed for the triplet tetrahedral isomer likely results from B3LYP's propensity to artificially stabilize high spin over low spin states[17]. Finally, the *tbp* geometries were disfavored by more than 11 kcal/mol.

3.3.6.2 Mechanistic pathways

In accordance with our experimental data, we tested three plausible mechanistic scenarios: (a) C-H oxidative addition followed by H-Br reductive elimination; (b) concerted σ bond metathesis; (c) ion pair assisted electrophilic C-H deprotonation/metalation. To examine the premises of the first scenario, we evaluated the kinetic accessibility of the Ni(IV) intermediates originating from a C-H bond oxidative addition. The three octahedral species shown in **Fig. 3.9** were considered as probable intermediates differing by the relative position of the MeCN relative to the aryl moiety.

All attempts to minimize ^{1}**Oxadd-1-m*cis*eq** with M06 converged to its precursor Ni(II) square planar species ^{1}***trans*-1**, suggesting that this species is not viable. Optimization of the species ^{1}**Oxadd-1-m*cis*ax** and ^{1}**Oxadd-1-m*trans*** did converge to local minima, albeit at very high energies of 43.9 and 48.2 kcal/mol, respectively. The transition states for accessing these intermediates were found quite close in geometry and displayed barriers of 44.6 and 48.5 kcal/mol, respectively. Using B3LYP also gave very high energies for barriers and intermediates (> 52 kcal/mol above ground state). The very high energies found for the mechanisms involving Ni(IV) species thus rule out scenario a.

	[1]Oxadd-mciseq	[1]Oxadd-mcisax	[1]Oxadd-mtrans
E vs. GS (barrier)	N/A	43.9 (44.6)	48.2 (48.5)

Figure 3.9. Energies and kinetic barriers (calculated at the M06 level of theory and expressed in kcal/mol) for the species resulting from C-H oxidative addition.

Next, we considered scenario b. Proceeding with M06 in the search for a transition state for the concerted σ bond metathesis always led to a transition state for the ion pair-assisted deprotonation, implying that scenario b is also unlikely. In contrast, the search for an ion pair assisted deprotonation (scenario c) led to proton transfer transition states for each of the precursor geometries [1]*trans*, [1]*cis* and [3]*tet* (**Fig. 10**). The energy barriers found with M06 were 26.4 kcal/mol for [1]**TS-*trans*-dep** and 32.2 kcal/mol for [1]**TS-*cis*- dep**. These transition states were linked by the Intrinsic Reaction Coordinate (IRC) path to the nickelated species and HBr (respectively [1]***trans*-2** + HBr and [1]***cis*-2** + HBr) and to the non metalated complexes ([1]***trans*-1** and [1]***cis*-1**, respectively), albeit without finding ion pairs as local minima.

Exploration of the ion pair-assisted deprotonation scenario on the triplet surface gave the following results (**Fig. 3.10**). A transition state was found for this pathway at a barrier of 45.8 kcal/mol ([3]**TS-*tet*-1-dep**). The IRC path revealed an ion pair as a local minimum at 36.1 kcal/mol, which can be considered an intermediate ([3]***tet*-1-Ionpair**) for the heterolytic dissociation step (leading to the ion pair). Moreover, no transition state was found for the heterolytic dissociation of the bromide ligand, i.e. [3]***tet*-1** → [3]***tet*-1-Ionpair**, suggesting a TS very close to the ion pair. It is worth emphasizing here that the ion pair on the triplet surface is 5 – 10 kcal/mol higher in energy than the two deprotonation barriers on the singlet surfaces. Exploring scenario b with B3LYP (**Scheme S3.2**) gave transition states on the triplet surface as high as 34.1 kcal/mol for [1]**TS-*trans*-1-dep** and 39.5 kcal/mol for [1]**TS-*cis*-1-dep**. The IRC path of the latter provided [1]***cis*-1-Ionpair** as a local mini-mum 36.5 kcal/mol above ground state; as was the case with M06, no ion pair was found on the [1]*trans* pathway. The deprotonation on the triplet surface going through [3]***tet*-1-Ionpair** (32.2 kcal/mol)

182

was, once again, found prohibitive, with **³TS-*tet*-1-dep** being as high as 47.2 kcal/mol. Overall, both M06 and B3LYP favor the ion pair assisted deprotonation process on the ¹*trans* pathway.
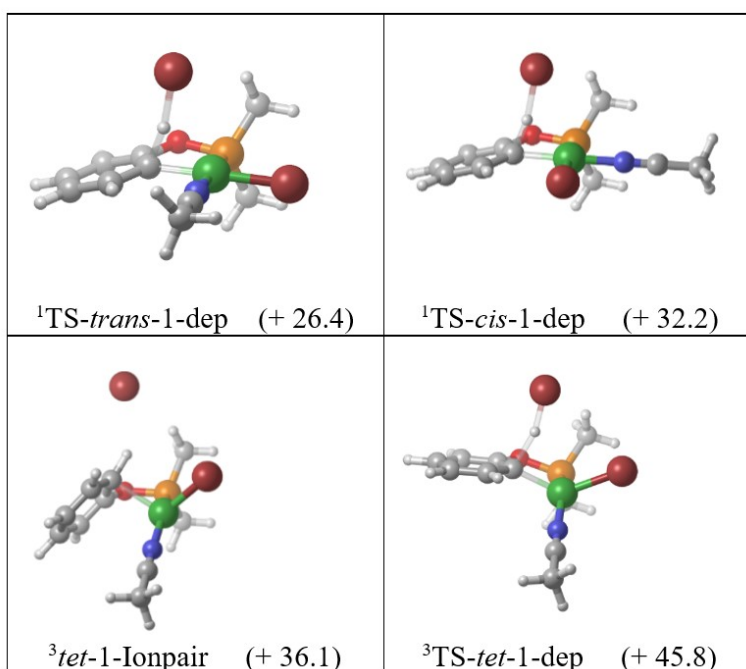
Figure 3.10. Energies (calculated at the M06 level of theory and expressed in kcal/mol) of the optimized transition states for the deprotonation on the ¹*cis*, ¹*trans* and ³*tet* surfaces as well as the ion pair on the triplet surface.

3.3.6.3 Thermodynamic considerations.

Scheme 8 summarizes the M06 analysis of the cyclonickelation reaction in acetonitrile leading to **2** + HBr. This was found to be an endergonic process with the following ΔG values (in kcal/mol with respect to ¹*trans*-**1**): ¹*trans*-**2** + HBr, 15.8; ¹*cis*-**2** + HBr, 21.4; ³*tet*-**2** + HBr, 33.2. The endergonic character of this process echoes the need for a sufficiently strong base to quench the *in-situ* generated HBr and driving the C-H nickelation to completion. Given the Gibbs free energy of 18.1 kcal/mol for the experimental ΔG for protonation of Et₃N by HBr in acetonitrile,[18] we can conclude that this is an effective base for rendering the overall C-H nickelation process exergonic by 2.3 kcal/mol. This accounts for the feasibility of the nickelation in the presence of Et₃N. In contrast, the value of − 9.7 kcal/mol we obtained by DFT calculation of the ΔG for phosphinite protonation by HBr would be insufficient (by 6 kcal/mol) for rendering the overall nickelation exergonic.

The ΔG values of the nickelation process computed using B3LYP revealed the same trend as above (in kcal/mol with respect to ³*tet*-2): ¹*trans*-2 + HBr, 21.7; ¹*cis*-2 + HBr, 25.2; ³*tet*-2 + HBr, 31.3 kcal/mol. However, in this case the process is more endergonic, such that nickelation would not proceed even in the presence of Et₃N. We infer here that the thermodynamics is biased by the over-stabilized ³*tet*-1.

Scheme 3.8. Proposed energy surface for the nickelation of PhOPMe₂. Energies were calculated at the M06 level of theory and are expressed in kcal/mol.
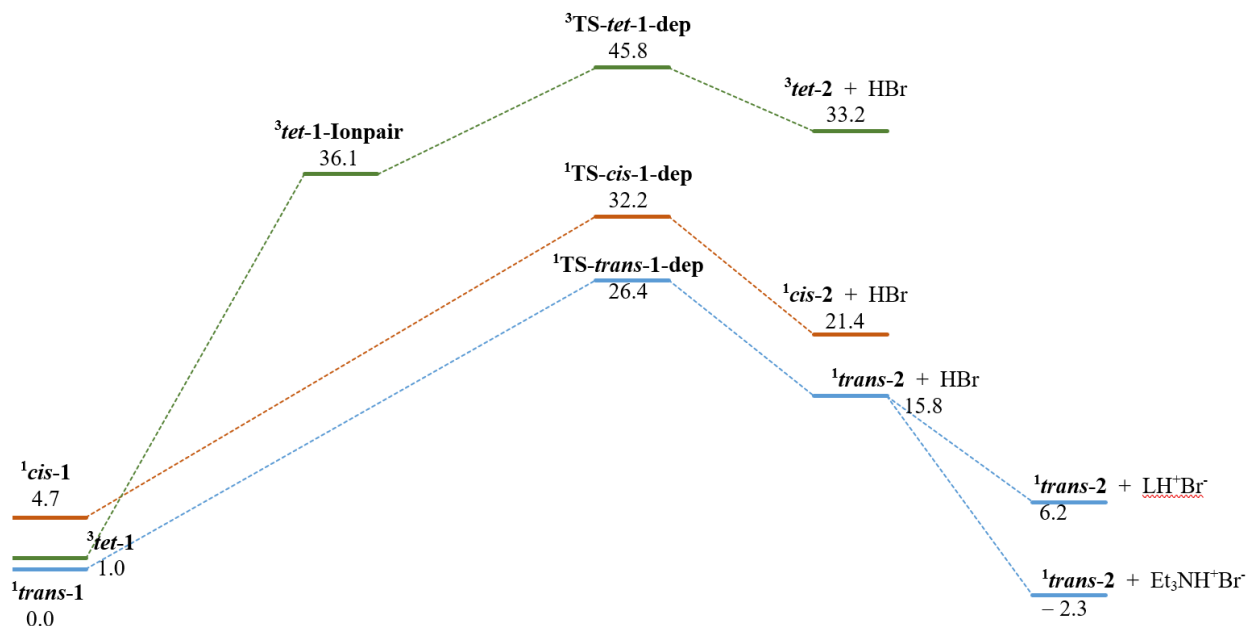
3.3.6.4 Reaction surface with P-substituents *i*-Pr.

Having completed the analysis of the C-H nickelation pathway with the PMe₂ model, we set out to explore the analogous reaction surface for the PhOP(*i*-Pr)₂ species. The above results for the PMe₂ model served to guide our study on the P(*i*-Pr)₂ species. Specifically, we focused on the four-coordinated species only and considered the ion-pair assisted deprotonation pathway as the most viable reaction mechanism. To prevent falling into local minima defined by various rotamers arising from rotation of the *i*-Pr moieties, we studied the different conformations of these substituents. Among all possible intermediates studied, the more stable conformations were always those that minimize the Me-Me steric interactions, as observed in the crystal structures for {ArOP(*i*-Pr)₂}-Ni complexes.

184

As was the case with the simplified PMe$_2$ model, analysis of the ground state with M06 showed that the *cis* isomer (**^{1}*cis*-iPr-1**) was higher in energy than the *trans* isomer (**^{1}*trans*-iPr-1**, **Fig. 3.11**). However, the triplet tetrahedral species (**^{3}*tet*-iPr-1**) is significantly more stable than the square planar forms for the P(*i*-Pr)$_2$ system, presumably because of the greater importance of steric demands of the *i*-Pr substituents. This result is also more consistent with the fact that the 1:1 L:Ni mixture is green and NMR-silent, features usually observed for tetrahedral Ni(II) compounds such as the emerald green zwitterionic complex {Me$_3$N-PhOP(*i*-Pr)$_2$}NiX$_3$ (*vide supra*, **Scheme 3.7**). Ion pair intermediates were found for each of these geometries, with **^{1}*trans*-iPr-1-Ionpair** being the more stable, 24.7 kcal/mol above the ground state, followed by **^{1}*cis*-iPr-1- Ionpair** (29.1 kcal/mol) and **^{3}*tet*-iPr-1-Ionpair** (34.1 kcal/mol) (**Fig. 3.12**).

^{3}*tet*-iPr-1 ^{1}*trans*-iPr-1 ^{1}*cis*-iPr-1
0.0   + 3.7   + 5.5
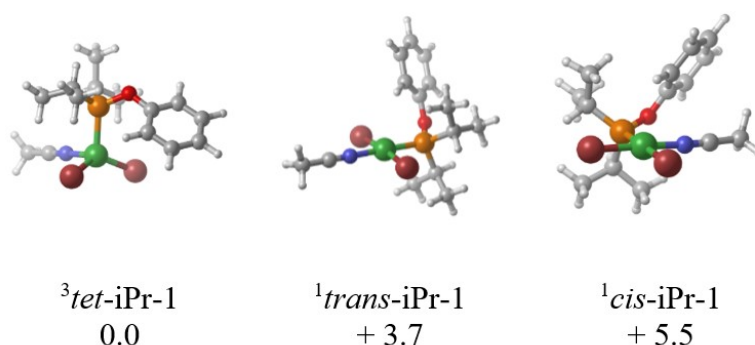
Figure 3.11. Optimized structures for the {PhOP(*i*-Pr)$_2$}NiBr$_2$(NCMe) isomers and their energies calculated at the M06 level of theory. Energies are expressed in kcal/mol.

Analysis of the nickelation thermodynamics gave the following ΔG values for the formation of **iPr-2** + HBr (in kcal/mol with respect to **^{3}*tet*-iPr-2**): **^{1}*trans*-iPr-2** + HBr, 15.2; **^{1}*cis*-iPr-2** + HBr, 18.1; **^{3}*tet*-iPr-2** + HBr, 31.1. **Scheme 3.9** gives a brief analysis of the metalation process for the *i*-Pr species. Thus, conversion of the ^{1}*trans* isomer to **^{1}*trans*-iPr-1-Ionpair** via Br$^-$ dissociation revealed a transition state at 25.7 kcal/mol, and the deprotonation from the latter ion pair towards the **^{2}*trans*-iPr-2** + HBr went through a slightly higher transition state (26.5 kcal/mol, **Fig 3.12**).
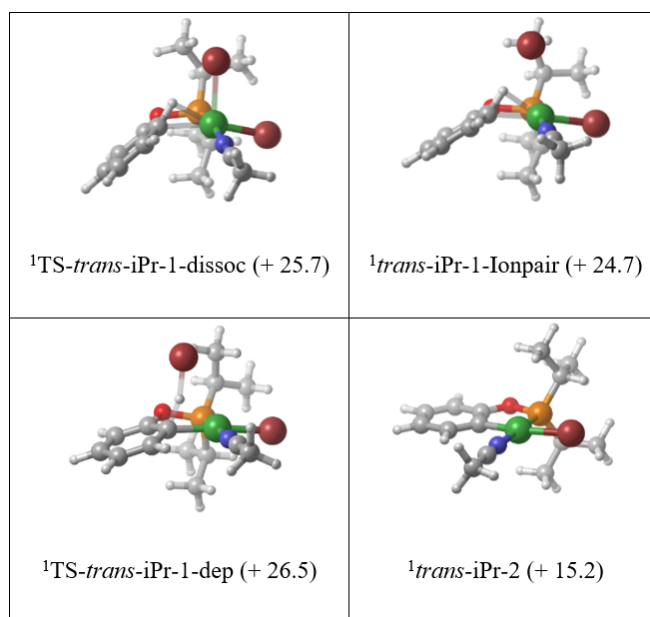
Figure 3.12. Optimized structures for the P(i-Pr)$_2$ intermediates on the ^{1}*trans* surface and their energies calculated at the M06 level of theory. Energies are expressed in kcal/mol.

The ion pairs for the ^{1}*cis* and ^{3}*tet* geometries were also found to be higher than **^{1}TS-*trans*-iPr-1-dep**, suggesting that the surface via ^{1}*trans* is the most probable. Although the strongly negative slope of the Hammett plot is consistent with this pathway, this finding on its own does not allow us to determine if the rate-limiting step is the dissociation or the deprotonation. To settle this question, we resorted to calculating the KIE values associated with different steps to see which would give a KIE value closer to the experimentally determined value.

Frequency calculations on the ^{1}*trans* surface with the aromatic protons replaced by deuterons allowed us to evaluate the magnitude of the kinetic isotope effect for both dissociation and deprotonation barriers. According to the transition state theory, the k_H/k_D at 25 °C was found to be 1.2 (1.1 at 80 °C) for the heterolytic Ni-Br dissociation (*i.e.* the formation of the ion pair) but 8.4 (6.0 at 80 °C) for the deprotonation.

Scheme 3.9. Proposed energy surface for the nickelation of PhOP(i-Pr)$_2$ on the ^{1}*trans* surface and local minima on the ^{1}*cis* and ^{3}*tet* surfaces at the M06 level of theory. Energies are expressed in kcal/mol.
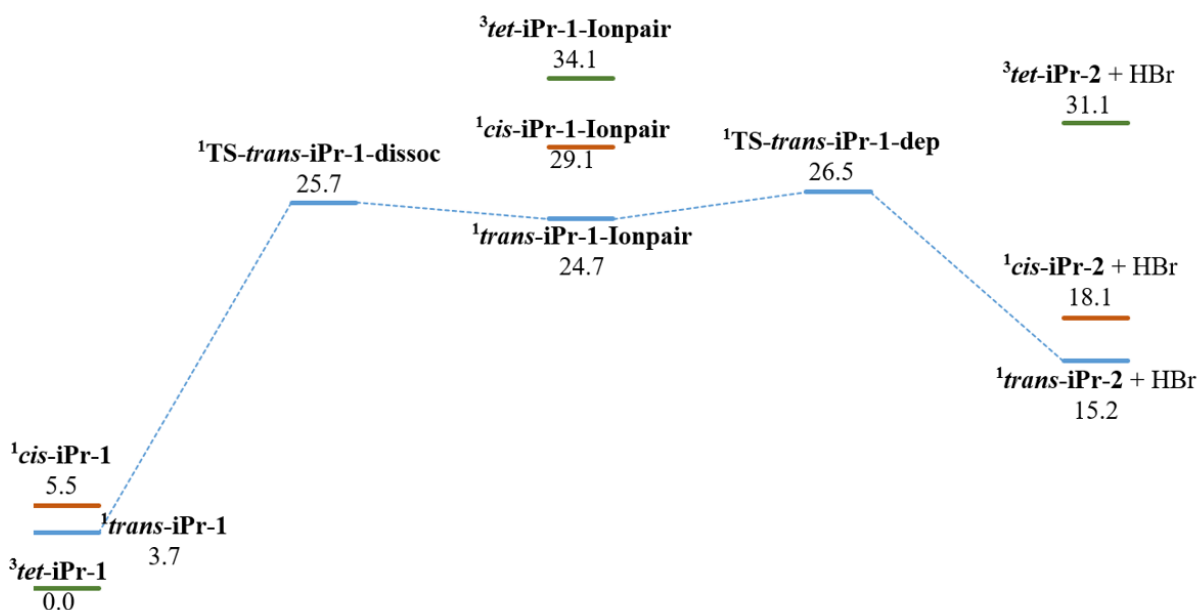
The finding that this last step gives a much closer value to the experimentally determined k_H/k_D of 11 suggests that the rate limiting step responsible for the observed high KIE is indeed the deprotonation and not the dissociation.

The C-H nickelation process is still endergonic by 15.2 kcal/mol, and the protonation of the ligand PhOP(i-Pr)$_2$ by HBr in MeCN was computed to be exergonic by only 9.7 kcal/mol. Therefore, the quenching of HBr by Et$_3$N ($-$ 18.1 kcal/mol) is necessary in order to make the overall reaction exergonic by 2.9 kcal/mol. The MECP between the singlet pathways involving ^{1}***trans***/^{1}***cis*-iPr-1** and the triplet surface involving ^{3}***tet*-iPr-1** was not sought since the experimental observations suggest that the system intercrossing would not be rate limiting in the reaction.

As was the case with the M06 calculations, the metalation reaction analyzed with B3LYP was found to be endergonic, with nickelated adducts **iPr-2** + HBr reaching 18.4, 21.0 and 27.0 kcal/mol above ground state for the ^{1}*trans*, ^{1}*cis* and ^{3}*tet*. The computational analysis with B3LYP also showed that the ground state is ^{3}***tet*-iPr-1**, its stability being greater than ^{1}***trans*-iPr-1** (by 9.7 kcal/mol) and ^{1}***cis*-iPr-1** (by 10.6 kcal/mol). The ion pairs for each geometry were shown to follow the same trend as the starting material, with ^{1}***trans*-iPr-1-Ionpair**, ^{1}***cis*-iPr-1-Ionpair** and ^{3}***tret*-iPr-1-Ionpair** found at 33.0, 34.0 and 27.30 kcal/mol above ground state. On the ^{1}*trans* pathway,

the barrier for the dissociation of the bromide to yield the ion pair reached 31.4 kcal/mol and the proton transfer was also found as the rate limiting step with a barrier of 33.4 kcal/mol. surfaces, respectively. The quenching of HBr by the ligand PhOP(i-Pr)$_2$ turned out to be exergonic by only 8.5 kcal/mol. Indeed, these calculations showed that even Et$_3$N would barely drive the reaction on the ^{1}*trans* pathway, which reflects the overestimated stability of the high spin ground state with B3LYP.

3.4 Conclusion

This report has established that C-H nickelation of aryl phosphinites is facilitated when this reaction is conducted in acetonitrile and in the presence of an equimolar quantity of NEt$_3$ or its less nucleophilic homologue i-Pr$_2$NEt. The bene- ficial role of acetonitrile is believed to originate from the greater nucleophilic character of this solvent (relative to toluene, THF, or EtOAc), which leads to the stabilization of a reactive, mono(phosphinite) intermediate. In contrast, the nucleophilic character of a base such as NEt$_3$ hinders the C-H nickelation by generating various unproductive amine species such as [(Et$_3$N)NiBr$_3$]$^-$ and the bi-phosphinite species (ArOPR$_2$)$_2$NiBr$_2$ that is less reactive towards C-H nickelation. DFT calculations have provided support for these conclusions by showing that tetrahedral (and hence NMR-silent) mono-phosphinite Ni(II) complexes are viable species.

Kinetic studies demonstrated that the C-H nickelation reaction in our system is favored by the presence of electron-donating substituents on the phosphinite aryl ring, thus underlining the importance of the latter's coordination to the electrophilic Ni(II) center. This conclusion is also consistent with the importance of directing groups (the phosphinite moiety in this case) in promoting the C-H nickelation process. The kinetic studies also revealed a very large KIE ($\approx$ 11 at 80 °C), suggesting that C-H bond breaking is rate limiting. A DFT analysis has suggested that the C-H nickelation proceeds through an ion-pair mechanism involving a Ni(II) intermediate.

Another interesting finding touched on the thermodynamics of the C-H nickelation step: H/D exchange studies in deuterio- and protio-solvents confirmed that C-H nickelation does take place under base-free conditions via an uphill equilibrium, but the newly formed cyclonickelated species is unstable in the absence of a sufficiently strong external base that can quench the in-situ generated HBr. The finding that the metalated intermediate is generated in the absence of Et$_3$N and can survive long enough (before re-protonation) to allow H/D scrambling with the solvent implies that

such species are kinetically accessible and should be susceptible to functionalization of the Ni-C moiety in the presence of suitable reagents. This lead will be exploited in our future studies to develop new *ortho*-functionalization strategies for phenols.

3.5 Experimental Section

All manipulations were carried out under a nitrogen atmosphere using standard Schlenk techniques and an inert-atmosphere box. Solvents were dried by passage over a column of activated alumina, collected under nitrogen, and stored over 4 Å molecular sieves. Triethylamine was dried over CaH_2. Synthesis of the nickel precursor $[(i\text{-PrCN})NiBr_2]_n$ used throughout this study has been described previously.[19] All other reagents, including deuterated phenol, were purchased from Sigma-Aldrich and used without further purification. All kinetic measurements or studies were conducted by NMR on a Bruker AV400 instrument equipped with a cryoprobe cooled to liquid N_2. All other NMR spectra were recorded on regular Bruker AV400 or AV500 spectrometers. The C-H nickelation progress was followed by monitoring the ^{31}P NMR signal for $\{\kappa^P,\kappa^C\text{-ArOP}(i\text{-Pr})_2\}Ni(NCMe)Br$ (resonance around 196 ppm in CH_3CN), using $TBAPF_6$ as the internal standard (septet around − 150 ppm). The substituted aryl phosphinites were synthesized directly from commercially available phenols and $ClP(i\text{-Pr})_2$ using a reported protocol.[9]

[3-Me₃N-C₆H₄OH]I. 3-*N,N*-dimethylaminophenol (686 mg, 5.0 mmol) was dissolved in 20 mL CH_3CN to give a deep red solution. MeI (3.11 mL, 50 mmol, 2 equiv.) was added slowly and the mixture stirred at r.t. for 20 h after which a solid formed. 30 mL Et_2O were added in order to complete precipitation, and the product was filtered, washed with 2 × 15 mL Et_2O and dried *in vacuo* to yield 1.25 g (4.5 mmol, 90%) of a pale purple powder which was found to be pure as assessed by the ^1H NMR in DMSO-d_6 which matched that of the literature.[20]

***trans*-{PhOP(*i*-Pr)₂}₂NiBr₂ (1b).** PhOP(*i*-Pr)₂ (210 mg, 1.0 mmol) was added to a suspension of $[(i\text{-PrCN})NiBr_2]_n$ (287 mg, 1.0 mmol, 1.0 equiv.) in 20 mL Et_2O. The mixture turned rapidly dark red and was stirred at room temperature for 1 h. The excess Ni precursor was removed by cannula filtration and the residues extracted twice with 10 mL Et_2O. Evaporation of the ethereal phase gave 243 mg (0.38 mmol, 76%) of a deep red solid, which was shown to be pure by ^{31}P and ^1H NMR in $CDCl_3$. *Purification.* The crude compound was dissolved in a minimum amount of MeCN at r.t. and then cooled down to −35 °C for 20 h. The deep red crystals were washed twice with cold

acetonitrile (–35 °C) prior to drying under vacuum. The spectroscopic data in CDCl$_3$ matched literature data.[8]

***trans*-{C$_6$D$_5$OP(*i*-Pr)$_2$}$_2$NiBr$_2$ (1b-d$_5$)** This compound was synthesized using the same procedure as described above for **1b**, except for the use of deuterated phenol. The crude powder was directly purified as described above yielding deep red crystals (330 mg, 0.51 mmol, 51%) . The ^{31}P and ^{1}H NMR spectra in CDCl$_3$ matched those of the related non-deuterated complex, with absence of the aromatic protons.

***trans*-{4-Cl-C$_6$H$_4$OP(*i*-Pr)$_2$}$_2$NiBr$_2$ (1b-Cl).** This compound was synthesized using the same procedure described above for **1b**, except for the use of 4-Cl-phenol. The crude product (dark red powder) was directly purified as described above for **1b** to give deep red crystals (yield= 349 mg, 0.59 mmol, 49%). ^{1}H NMR (500 MHz, 20 °C, CDCl$_3$): δ 1.39 (d, 6H, CH(C*H$_3$*)(CH$_3$), $^3J_{HH}$ = 6.5), 1.52 (d, 6H, CH(CH$_3$)(C*H$_3$*), $^3J_{HH}$ = 6.6), 2.75 (sept, 2H, C*H*(CH$_3$)$_2$, $^3J_{HH}$ = 7.3), 7.28 (dm, 2H, C$_{orhto}$-*H* or C$_{meta}$-*H*, $^3J_{HH}$ = 8.9, correlated to ^{13}C at δ 129), 7.49 (dm, 2H, C$_{orhto}$-*H* or C$_{meta}$-*H*, $^3J_{HH}$ = 8.9, correlated to ^{13}C δ 121). ^{13}C{^{1}H} NMR (125.7 MHz, 20 °C, CDCl$_3$): δ 18.19 (s, 2C, CH(*C*H$_3$)(CH$_3$)), 19.52 (s, 2C, CH(CH$_3$)(*C*H$_3$)), 29.76 (s, 2C, *C*H(CH$_3$)(CH$_3$)), 121.41 (s, 2C, C$_{orhto}$-H or C$_{meta}$-H), 128.01 (s, 1C, *C*-Cl), 129.10 (s, 2C, C$_{orhto}$-H or C$_{meta}$-H), 153.64 (s, 1C, *C*-OP). ^{31}P{^{1}H} NMR (202.4 MHz, 20 °C, CDCl$_3$): δ 138 (br s).

H/D Scrambling attempt between 1b-d$_5$ and 1b-Cl. A Schlenk tube was charged with 100 mg of **1b-Cl** and 100 mg of **1b-d$_5$** and 2 mL MeCN. The deep red mixture was heated for 24 h at 80 °C, and then cooled at –35 °C for 20 h, leading to the formation of deep red crystals. These were filtered off, washed with 2 × 1.5 mL cold MeCN (–35 °C), and then dried under vacuum. The crystals were analyzed by ^{1}H NMR analysis in CDCl$_3$ and the spectrum compared to the spectra of approximately equimolar mixtures of crystalline **1b** + **4-Cl-1b** and to equimolar mixtures of crystalline **1b-d$_5$** + **4-Cl-1b**. This comparison confirmed the appearance of only the *ortho* aromatic protons of **1b**, and showed no decrease of the integration for the aromatic protons of **4-Cl-1b**.

Protocol for H/D scrambling with acetonitrile. A Schlenk tube was charged with 200 mg of the compound (**1b-d$_5$** or **1b**) and 2 mL solvent (CH$_3$CN or CD$_3$CN, respectively). The mixture was heated at 80 °C for 24 h and then cooled at –35°C for 20 h to give crystals, which were isolated and washed twice with 1 mL cold acetonitrile, dried under vacuum and analysed by ^{1}H NMR in CDCl$_3$.

Protocol for H/D scrambling with toluene. A Schlenk tube was charged with 200 mg of the compound (**1b-d₅** or **1b**) and 2 mL solvent ($C_6H_5CH_3$ or $C_6D_5CD_3$, respectively). The mixture was heated at 100 °C for 24 h and the solvent evaporated. The residues were re-dissolved in 2 mL acetonitrile and cooled at –35 °C for 20 h to give crystals, which were isolated and washed twice with 1 mL cold acetonitrile, dried under vacuum and analysed by ^{1}H NMR in $CDCl_3$.

Protocol for kinetic measurements. To a solution of $ArOP(i\text{-}Pr)_2$ (200 µmol), $[(i\text{-}PrCN)NiBr_2]_n$ (58 mg, 200 µmol, 1.00 equiv) and $(i\text{-}Pr)_2NEt$ (34.8 µL, 200 µmol, 1.00 equiv) in 2.500 mL MeCN was added a known amount of the standard $TBAPF_6$ (typically 50 – 100 mg). A 500 µL aliquot of the solution was placed in a J-Young NMR tube. This sample was used for the kinetic measurements by one of the following protocols: (i) the NMR tube was placed in the spectrometer probe and heated to the desired temperature before recording the NMR spectra over the required time interval; (ii) the NMR tube was heated in an oil bath at the desired temperature and for the required time interval before immersing it into a cold-water bath to cool the sample, recording the NMR spectra at room temperature, and repeating the heat-cool-record cycle.

For reactions that went to completion within a reasonable time, the conversion (a number between 0 and 1) at each time t (*conv.(t)*) was determined by the ratio of integrals in ^{31}P NMR for the metalated species ($A_P(t)$) and the central peak corresponding to PF_6^- ($A_S(t)$), over the same ratio at the end of the reaction (t_{inf}), as follows:

$$\text{conv.}(t) = \frac{A_P(t)}{A_S(t)} \Big/ \frac{A_P(t_{inf})}{A_S(t_{inf})}$$

When the reaction was too slow to reach completion within a reasonable time, *conv(t)* was determined by the amount of $TBAPF_6$ added, where A_{Stot} is the total area of the peak for the standard (thus $A_{Stot} = (64/20) \cdot A_S$) and n_{Stot} the exact amount of $TBAPF_6$ added, in µmol, as follows:

$$conv.(t) = \frac{n_P(t)}{n^0_{substrate}} = \frac{n_P(t)}{200\mu mol} = \frac{1}{200\mu mol} \cdot \frac{A_P(t)}{A_{Stot}(t)} \cdot n_{Stot}$$

$$= \frac{1}{200\mu mol} \cdot \frac{A_P(t)}{A_S(t) \cdot \frac{64}{20}} \cdot n_{Stot}$$

The first order rate constants were determined by plotting ln(1-*conv.*) *vs* the time, giving a slope corresponding to –k, where k is the rate constant.

Computational details. The DFT calculations were carried out in implicit MeCN solvent using the SMD model. The basis sets employed for all geometry optimizations and frequency calculations were 6-31g** for light atoms and def2TZVP for Ni and Br, whereas the electronic energy was computed with def2TZVP for all atoms. The optimizations started with the M06 functional[21], which is known to properly handle ligand-metal bonds and give accurate results on bond dissociation energies.[22] For comparison purposes, the local minima and saddle points were further re-optimized with B3LYP, which is widely used for various DFT computational analyses.[23] High resolution representations of 3D models were generated by CYLview[24]. Additional computational details as well as the coordinates/energies for all intermediates and transition states are given in ESI.

3.6 Acknowledgements

1.7 References

[1] (a) Song, W.; Ackermann, L., Nickel-catalyzed alkyne annulation by anilines: versatile indole synthesis by C–H/N–H functionalization. *Chemical Communications* **2013**, *49* (59), 6638-6640. (b) Ruan, Z.; Lackner, S.; Ackermann, L., A General Strategy for the Nickel-Catalyzed C−H Alkylation of Anilines. *Angewandte Chemie International Edition* **2016**, *55* (9), 3153-3157.

[2] (a) Shiota, H.; Ano, Y.; Aihara, Y.; Fukumoto, Y.; Chatani, N., Nickel-Catalyzed Chelation-Assisted Transformations Involving Ortho C–H Bond Activation: Regioselective Oxidative Cycloaddition of Aromatic Amides to Alkynes. *Journal of the American Chemical Society* **2011**, *133* (38), 14952-14955. (b) Aihara, Y.; Chatani, N., Nickel-Catalyzed Direct Alkylation of C–H Bonds in Benzamides and Acrylamides with Functionalized Alkyl Halides via Bidentate-Chelation Assistance. *Journal of the American Chemical Society* **2013**, *135* (14), 5308-5311. (c) Aihara, Y.; Chatani, N., Nickel-Catalyzed Direct Arylation of C(sp^3)–H Bonds in Aliphatic Amides via Bidentate-Chelation Assistance. *Journal of the American Chemical Society* **2014**, *136* (3), 898-901. (d) Aihara, Y.; Tobisu, M.; Fukumoto, Y.; Chatani, N., Ni(II)-Catalyzed Oxidative Coupling between C(sp^2)–H in Benzamides and C(sp^3)–H in Toluene Derivatives. *Journal of the American Chemical Society* **2014**, *136* (44), 15509-15512.

(e) Song, W.; Lackner, S.; Ackermann, L., Nickel-Catalyzed C-H Alkylations: Direct Secondary Alkylations and Trifluoroethylations of Arenes. *Angewandte Chemie International Edition* **2014**, *53* (9), 2477-2480. (f) Wu, X.; Zhao, Y.; Ge, H., Nickel-Catalyzed Site-Selective Alkylation of Unactivated C(sp^3)–H Bonds. *Journal of the American Chemical Society* **2014,** *136* (5), 1789-1792. (g) Landge, V. G.; Shewale, C. H.; Jaiswal, G.; Sahoo, M. K.; Midya, S. P.; Balaraman, E., Nickel-catalyzed direct alkynylation of C(sp^2)–H bonds of amides: an "inverse Sonogashira strategy" to ortho-alkynylbenzoic acids. *Catalysis Science & Technology* **2016**, *6* (6), 1946-1951. (h) Yi, J.; Yang, L.; Xia, C.; Li, F., Nickel-Catalyzed Alkynylation of a C(sp^2)–H Bond Directed by an 8-Aminoquinoline Moiety. *The Journal of Organic Chemistry* **2015**, *80* (12), 6213-6221. (i) Liu, Y.-J.; Liu, Y.-H.; Yan, S.-Y.; Shi, B.-F., A sustainable and simple catalytic system for direct alkynylation of C(sp^2)–H bonds with low nickel loadings. *Chemical Communications* **2015**, *51* (29), 6388-6391. (j) Yan, S.-Y.; Liu, Y.-J.; Liu, B.; Liu, Y.-H.; Zhang, Z.-Z.; Shi, B.-F., Nickel-catalyzed direct thiolation of unactivated C(sp3)–H bonds with disulfides. *Chemical Communications* **2015**, *51* (34), 7341-7344. (k) Liu, Y.-H.; Liu, Y.-J.; Yan, S.-Y.; Shi, B.-F., Ni(ii)-catalyzed dehydrative alkynylation of unactivated (hetero)aryl C–H bonds using oxygen: a user-friendly approach., *Chemical Communications* **2015**, *51* (58), 11650-11653.

[3] Zheng, X.-X.; Du, C.; Zhao, X.-M.; Zhu, X.; Suo, J.-F.; Hao, X.-Q.; Niu, J.-L.; Song, M.-P., Ni(II)-Catalyzed C(sp^2)–H Alkynylation/Annulation with Terminal Alkynes under an Oxygen Atmosphere: A One-Pot Approach to 3-Methyleneisoindolin-1-one. *The Journal of Organic Chemistry* **2016**, *81* (10), 4002-4011.

[4] See the following report for a rare mechanistic study on this subject: Beattie, D. D.; Grunwald, A. C.; Perse, T.; Schafer, L. L.; Love, J. A., Understanding Ni(II)-Mediated C(sp^3)–H Activation: Tertiary Ureas as Model Substrates. *Journal of the American Chemical Society* **2018**, *140* (39), 12602-12610.

[5] (a) Fontaine, F.-G.; Kadkhodazadeh, T.; Zargarian, D., Nickel indenyl complexes as precatalysts for dehydropolymerization of phenylsilane. *Chemical Communications* **1998**, (12), 1253-1254. (b) Groux, L. F.; Bélanger-Gariépy, F.; Zargarian, D.; Vollmerhaus, R., Preparation and Characterization of Nickel Complexes with η-Indenyl Ligands Bearing a Pendant Aminoalkyl Chain. *Organometallics* **2000**, *19* (8), 1507-1513. (c) Groux, L. F.; Bélanger-Gariépy, F.; Zargarian, D., Phosphino-indenyl complexes of nickel(II). *Canadian Journal of Chemistry* **2005**, *83* (6-7), 634-639. (d) Chen, Y.; Sui-Seng, C.; Zargarian, D., Tetraphenylborate as a Novel Bridging Ligand in a Zwitterionic Nickel(I) Dimer. *Angewandte Chemie International Edition* **2005**, *44* (47), 7721-7725. (e) Baho, N.; Zargarian, D., Syntheses, Structures, Spectroscopy, and Chromotropism of New Complexes Arising from the Reaction of Nickel(II) Nitrate with Diphenyl(dipyrazolyl)methane. *Inorganic Chemistry* **2007**, *46* (1), 299-308.

[6] For examples of Ni complexes based on various symmetrical or unsymmetrical pincer ligands see the following review and primary reports. (a) Haenel, M. W.; Jakubik, D.; Krüger, C.; Betz, P., 1,8-Bis(diphenylphosphino)anthracene and Metal Complexes1). *Chemische Berichte* **1991**, *124* (2), 333-336. (b) Gómez-Benítez, V.; Baldovino-Pantaleón, O.; Herrera-Álvarez, C.; Toscano, R. A.; Morales-Morales, D., High yield thiolation of iodobenzene catalyzed by the phosphinite nickel PCP pincer complex: [NiCl{C$_6$H$_3$-2,6-(OPPh$_2$)$_2$}]. *Tetrahedron Letters* **2006**, *47* (29), 5059-5062. (c) Gutsulyak, D. V.; Piers, W. E.; Borau-Garcia, J.; Parvez, M., Activation of Water, Ammonia, and Other Small Molecules by PCcarbeneP Nickel Pincer Complexes. *Journal of the American Chemical Society* **2013**, *135* (32), 11776-11779. (d) Jonasson, K. J.; Wendt, O. F., Synthesis and Characterization of a Family of POCOP Pincer Complexes with Nickel: Reactivity Towards CO$_2$ and Phenylacetylene. *Chemistry – A European Journal* **2014**, *20* (37), 11894-11902. (e) Jonasson, K. J.; Wendt, O. F., Synthesis and characterisation of new PCsp^{3}P-supported nickel complexes. *Journal of Organometallic Chemistry* **2014,** *759*, 15-18. (f) Mousa, A. H.; Bendix, J.; Wendt, O. F., Synthesis, Characterization, and Reactivity of PCN Pincer Nickel Complexes. *Organometallics* **2018**, *37* (15), 2581-2593. (g) Zargarian, D.; Castonguay, A.; Spasyuk, D. M., ECE-Type Pincer Complexes of Nickel. In *Organometallic Pincer Chemistry*, van Koten, G.; Milstein, D., Eds. Springer Berlin Heidelberg: Berlin, Heidelberg, 2013; pp 131-173. (h) Castonguay, A.; Beauchamp, A. L.; Zargarian, D., New Derivatives of PCP-Type Pincer Complexes of Nickel. *Inorganic Chemistry* **2009**, *48* (7), 3177-3184. (i) Vabre, B.; Canac, Y.; Duhayon, C.; Chauvin, R.; Zargarian, D., Nickel(II) complexes of the new pincer-type unsymmetrical ligands PIMCOP, PIMIOCOP, and NHCCOP: versatile binding motifs. *Chemical Communications* **2012**, *48* (84), 10446-10448. (j) Hao, J.; Mougang-

Soumé, B.; Vabre, B.; Zargarian, D., On the Stability of a POCsp³OP-Type Pincer Ligand in Nickel(II) Complexes. *Angewandte Chemie* **2014**, *126* (12), 3282-3286. (k) Vabre, B.; Petiot, P.; Declercq, R.; Zargarian, D., Fluoro and Trifluoromethyl Derivatives of POCOP-Type Pincer Complexes of Nickel: Preparation and Reactivities in SN₂ Fluorination and Direct Benzylation of Unactivated Arenes. *Organometallics* **2014**, *33* (19), 5173-5184.

[7] (a) Lefèvre, X.; Durieux, G.; Lesturgez, S.; Zargarian, D., Addition of amines and phenols to acrylonitrile derivatives catalyzed by the POCOP-type pincer complex [{κ^P,κ^C,κ^P-2,6-(*i*-Pr₂PO)₂C₆H₃}Ni(NCMe)][OSO₂CF₃]. *Journal of Molecular Catalysis A: Chemical* **2011**, *335* (1), 1-7. (b) Hao, J.; Vabre, B.; Mougang-Soumé, B.; Zargarian, D., Small Molecule Activation by POCOP-Nickel Complexes. *Chemistry – A European Journal* **2014**, *20* (39), 12544-12552. (c) Salah, A.; Corpet, M.; ul-Hassan Khan, N.; Zargarian, D.; Spasyuk, D. M., Synthesis of unsymmetrical 5,6-POCOP′-type pincer complexes of nickel(ii): impact of nickelacycle size on structures and spectroscopic properties. *New Journal of Chemistry* **2015**, *39* (8), 6649-6658.

[8] Vabre, B.; Deschamps, F.; Zargarian, D., Ortho Derivatization of Phenols through C–H Nickelation: Synthesis, Characterization, and Reactivities of Ortho-Nickelated Phosphinite Complexes. *Organometallics* **2014**, *33* (22), 6623-6632.

[9] Mangin, L. P.; Zargarian, D., C–H nickellation of phenol-derived phosphinites: regioselectivity and structures of cyclonickellated complexes. *Dalton Transactions* **2017**, *46* (46), 16159-16170.

[10] Vabre, B.; Lambert, M. L.; Petit, A.; Ess, D. H.; Zargarian, D., Nickelation of PCP- and POCOP-Type Pincer Ligands: Kinetics and Mechanism. *Organometallics* **2012**, *31* (17), 6041-6053.

[11] (a) Baho, N.; Zargarian, D., Diphenyl(dipyrazolyl)methane Complexes of Ni: Synthesis, Structural Characterization, and Chromotropism of NiBr₂ Derivatives. *Inorganic Chemistry* **2007**, *46* (18), 7621-7632. (b) Lapointe, S.; Vabre, B.; Zargarian, D. POCOP-Type Pincer Complexes of Nickel: Synthesis, Characterization, and Ligand Exchange Reactivities of New Cationic Acetonitrile Adducts. *Organometallics* **2015**, *34* (14), 3520–3531. (c) Lefèvre, X.; Spasyuk, D. M.; Zargarian, D. *Journal of Organometallic Chemistry* **2011**, *696*, 864-870. (d) Wang, R.; Groux, L. F.; Zargarian, D., Nickel-Triflate Complexes as Precursors to Reactive Cations: Preparation and Reactivities of (1-R-indenyl)Ni(PPh₃)(OSO₂CF₃). *Organometallics* **2002**, *21* (25), 5531-5539. (e) Spasyuk, D. M.; Gorelsky, S. I.; van der Est, A.; Zargarian, D. Characterization of Divalent and Trivalent Species Generated in the Chemical and Electrochemical Oxidation of a Dimeric Pincer Complex of Nickel. *Inorganic Chemistry* **2011**, *50*, 2661–2674. (f) Groux, L. F.; Zargarian, D., Aminoalkyl-Substituted Indenyl−Nickel Compounds: Tuning Reactivities as a Function of the Pendant, Hemilabile Moiety. *Organometallics* **2003**, *22* (15), 3124-3133.

[12] This complex has been shown to adopt a square planar structure in the solid state. See ref. 8 for its preparation, isolation, and solid-state characterization.

[13] It should be noted that EtOAc and THF mixtures showed the same colours as the toluene mixtures; to simplify the discussion, we have focused on toluene mixtures.

[14] The rates of these reactions were monitored by observing the emergence of ³¹P signals characteristic of the cyclonickellated complexes, a singlet at 196 ppm in acetonitrile for (κ^P,κ^C-*i*-Pr₂POC₆H₄)Ni(NCMe)Br, and AB doublets at 184 and 151 ppm in toluene for (κ^P,κ^C-*i*-Pr₂POC₆H₄)Ni(*i*-Pr₂POPh)Br. Complete conversion was noted by complete disappearance of the broad signals due to the non-metalated phosphinite adducts, whereas partial conversions were estimated by integration of the signals for the metalated and non-metalated species.

[15] Since toluene samples of both the starting material *trans*-L₂NiBr₂ and the cyclometalated product (κ^P,κ^C-*i*-Pr₂POC₆H₄)Ni(*i*-Pr₂POPh)Br display sharp ³¹P signals, the extent of cyclometallation in toluene mixtures could be determined in a straight forward manner based on NMR. In the case of the reactions conducted in acetonitrile, however, determination of conversion is complicated by the fact that the ³¹P NMR spectrum of the reaction mixture displays no signals due to the ligand substitution reaction between the cyclometalated complex and the solvent. In this case, conversions were determined by evaporating the final mixture, dissolving the solid residues in toluene, and recording the ³¹P NMR of this sample.

[16] It should be noted that the experimental m/z values obtained from this analysis correspond to "M⁺ – 1" for the parent ion with one Ni-bound MeCN, M⁺ = [C₁₇H₃₀Br₂N₂NiOP]⁺ = 526.98, and to "M⁺ + 2" for the parent ion with two Ni-bound MeCN, M⁺ = [C₁₉H₃₃Br₂N₃NiOP]⁺ = 568.01. Of course, we are mindful of the fact that the highly dilute solutions required for ESI-MS experiments would be expected to affect the equilibria governing the speciation of Ni, which might cast doubt on the relevance of this result for the overall reaction mechanism under realistic reaction conditions. This result is nevertheless significant, because it supports the viability of a mono-phosphinite adduct in MeCN.

[17] (a) Paulsen, H.; Duelund, L.; Winkler, H.; Toftlund, H.; Trautwein, A. X., Free Energy of Spin-Crossover Complexes Calculated with Density Functional Methods. *Inorganic Chemistry* **2001**, *40* (9), 2201-2203. (b) Reiher, M.; Salomon, O.; Artur Hess, B., Reparameterization of hybrid functionals based on energy differences of states of different multiplicity. *Theoretical Chemistry Accounts* **2001**, *107* (1), 48-55. (c) Reiher, M., Theoretical Study of the Fe(phen)₂(NCS)₂ Spin-Crossover Complex with Reparametrized Density Functionals. *Inorganic Chemistry* **2002**, *41*

(25), 6928-6935. (d) Conradie, J.; Ghosh, A., DFT Calculations on the Spin-Crossover Complex Fe(salen)(NO): A Quest for the Best Functional. *The Journal of Physical Chemistry B* **2007**, 111 (44), 12621-12624.

[18] See calculation on page S23 of ESI, which were based on these references: (a) Raamat, E.; Kaupmees, K.; Ovsjannikov, G.; Trummal, A.; Kütt, A.; Saame, J.; Koppel, I.; Kaljurand, I.; Lipping, L.; Rodima, T.; Pihl, V.; Koppel, I. A.; Leito, I., Acidities of strong neutral Brønsted acids in different media. *Journal of Physical Organic Chemistry* **2013**, *26* (2), 162-170. (b) Kaljurand, I.; Kütt, A.; Soováli, L.; Rodima, T.; Mäemets, V.; Leito, I.; Koppel, I. A., Extension of the Self-Consistent Spectrophotometric Basicity Scale in Acetonitrile to a Full Span of 28 pKa Units: Unification of Different Basicity Scales. *The Journal of Organic Chemistry* **2005**, *70* (3), 1019-1028.

[19] (a) Vabre, B.; Spasyuk, D. M.; Zargarian, D., Impact of Backbone Substituents on POCOP-Ni Pincer complexes: A Structural, Spectroscopic and Electrochemical Study, *Organometallics* **2012**, *31* (24), 8561-8570. (b) Vabre, B.; Lindeperg, F.; Zargarian, D., Direct, one-pot synthesis of POCOP-type pincer complexes from metallic nickel, *Green Chemistry* **2013**, *15* (11), 3188-3194.

[20] Ortega, P.; Copa-Patiño, J. L.; Muñoz-Fernandez, M. a. A.; Soliveri, J.; Gomez, R.; de la Mata, F. J., Amine and ammonium functionalization of chloromethylsilane-ended dendrimers. Antimicrobial activity studies. *Organic & Biomolecular Chemistry* **2008,** *6* (18), 3264-3269.

[21] Zhao, Y.; Truhlar, D. G., The M06 suite of density functionals for main group thermochemistry, thermochemical kinetics, noncovalent interactions, excited states, and transition elements: two new functionals and systematic testing of four M06-class functionals and 12 other functionals. *Theoretical Chemistry Accounts* **2008**, *120* (1), 215-241.

[22] Raju, R. K.; Bengali, A. A.; Brothers, E. N., A unified set of experimental organometallic data used to evaluate modern theoretical methods. *Dalton Transactions* **2016**, *45* (35), 13766-13778.

[23] (a) Lee, C.; Yang, W.; Parr, R. G., Development of the Colle-Salvetti correlation-energy formula into a functional of the electron density. *Physical Review B* **1988**, *37* (2), 785-789. (b) Becke, A. D., Density-functional thermochemistry. III. The role of exact exchange. *The Journal of Chemical Physics* **1993**, *98* (7), 5648-5652.

[24] CYLview, 1.0b; Legault, C. Y., Université de Sherbrooke, **2009** (http://www.cylview.org)

Chapitre 3 – Annexes

S3.1 General information and references

All ^{31}P kinetic monitoring experiments were recorded on a Bruker AV400 equipped with a cryoprobe cooled to liquid N_2 in order to reduce the noise, whereas other spectra were recorded on regular Bruker AV400 or AV500 spectrometers with access provided by Centre régional de résonance magnétique nucléaire de l'Université de Montréal. All DFT calculations were performed using Gaussian16 Revision A03[1] on Grex cluster server from Westgrid computational facilities, with access provided by Compute Canada – Calcul Canada.

The crystallographic data for all resolved structures were collected either on a Bruker Microsource (Cu source) or a Bruker Venture Metaljet (Ga source) via the Bruker APEX II or APEX III[2] softwares. Cell refinement and data reduction were performed using SAINT[3]. An empirical absorption correction, based on multiple measurements of equivalent reflections, was applied using the program SADABS[4]. The space group was confirmed by the XPREP[5] routine in APEX. The structures were solved in OLEX[6] using the SHELX[7] suite and refined by full-matrix least squares with SHEXL[8]. All non-hydrogen atoms were refined with anisotropic displacement parameters,

[1] Gaussian 16, Revision A.03, M. J. Frisch, G. W. Trucks, H. B. Schlegel, G. E. Scuseria, M. A. Robb, J. R. Cheeseman, G. Scalmani, V. Barone, G. A. Petersson, H. Nakatsuji, X. Li, M. Caricato, A. V. Marenich, J. Bloino, B. G. Janesko, R. Gomperts, B. Mennucci, H. P. Hratchian, J. V. Ortiz, A. F. Izmaylov, J. L. Sonnenberg, D. Williams-Young, F. Ding, F. Lipparini, F. Egidi, J. Goings, B. Peng, A. Petrone, T. Henderson, D. Ranasinghe, V. G. Zakrzewski, J. Gao, N. Rega, G. Zheng, W. Liang, M. Hada, M. Ehara, K. Toyota, R. Fukuda, J. Hasegawa, M. Ishida, T. Nakajima, Y. Honda, O. Kitao, H. Nakai, T. Vreven, K. Throssell, J. A. Montgomery, Jr., J. E. Peralta, F. Ogliaro, M. J. Bearpark, J. J. Heyd, E. N. Brothers, K. N. Kudin, V. N. Staroverov, T. A. Keith, R. Kobayashi, J. Normand, K. Raghavachari, A. P. Rendell, J. C. Burant, S. S. Iyengar, J. Tomasi, M. Cossi, J. M. Millam, M. Klene, C. Adamo, R. Cammi, J. W. Ochterski, R. L. Martin, K. Morokuma, O. Farkas, J. B. Foresman, and D. J. Fox, Gaussian, Inc., Wallingford CT, 2016.
[2] Bruker (2012). APEX2 / Bruker (2016) APEX3, Bruker AXS Inc., Madison, WI, USA.
[3] Bruker (2012). "SAINT Integration Software for Single Crystal Data", Bruker AXS Inc., Madison, WI, USA.
[4] Sheldrick, G. M., "Comparison of silver and molybdenum microfocus X-ray sources for single crystal structure determination", *J. Appl.Cryst.*, 2015, *48*, 3-10
[5] Bruker (2012). Data Preparation and Reciprocal Space Exploration Program, Bruker AXS Inc., Madison, WI, USA.
[6] A: O. V. Dolomanov, L. J. Bourhis, R. J. Gildea, J. A. K. Howard and H. Puschmann. "OLEX2: a complete structure solution, refinement and analysis program". *J. Appl. Cryst.* 2009, *42*, 339-341.
[7] Sheldrick, G. M., "SHELXT - Integrated space-group and crystal structure determination", *Acta Cryst.*, 2015, A71, 3-8.
[8] Sheldrick, G. M., Crystal structure refinement with SHELXL, *Acta Cryst.*, 2015, C71, 3-8.

whereas hydrogen atoms were set in calculated positions and refined as riding atoms, with thermal parameters being 1.5 times that of the carbon bearing the H in question. All Thermal Ellipsoid Plots were drawn using Platon[9].

S3.2 Relevant NMR Spectra

S3.2.1 Characterization and NMR behaviour of L_2NiBr_2 complexes in various solvents

Figure S3.1: ^1H spectrum of $\{C_6H_5OP(i\text{-}Pr)_2\}_2NiBr_2$ in $CDCl_3$

---

[9] Spek, A. L., *Acta Cryst.*, 2009, D65, 148-155

198

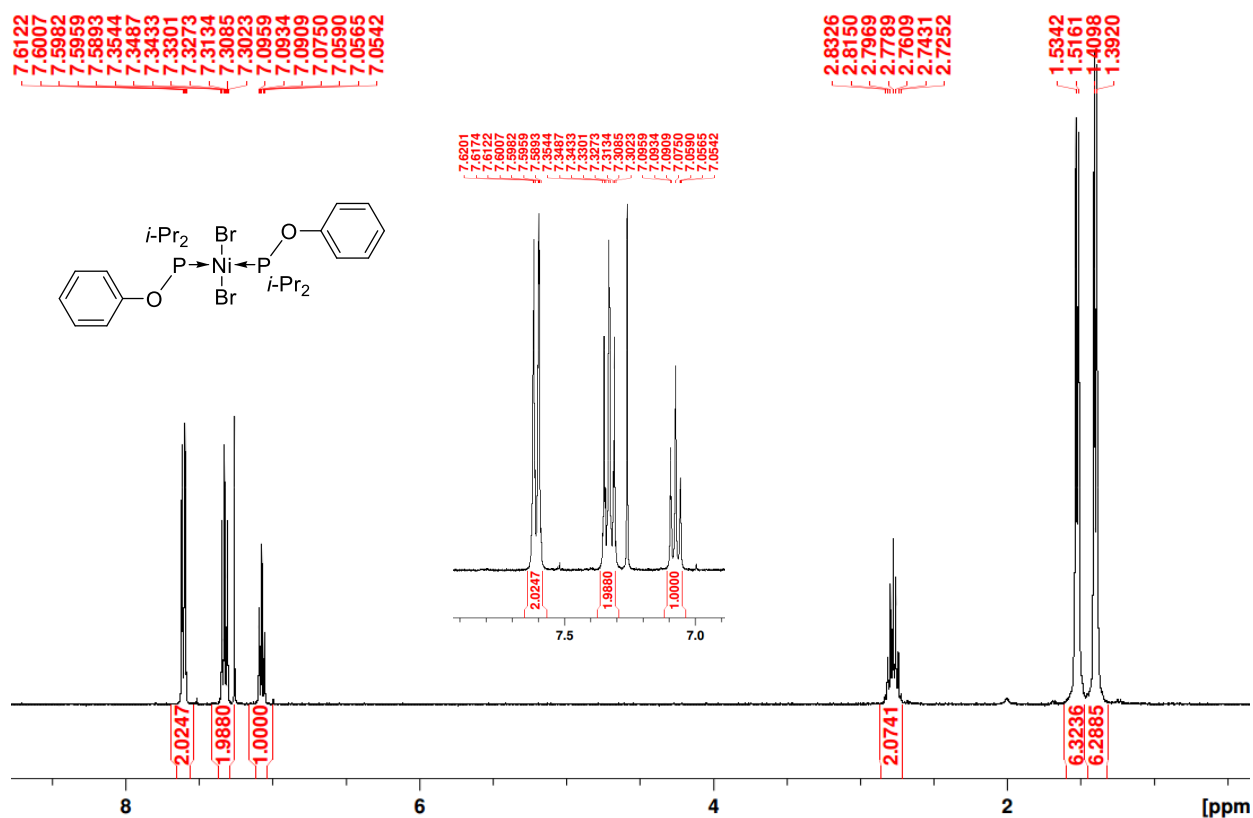
[9] Spek, A. L., *Acta Cryst.*, 2009, D65, 148-155
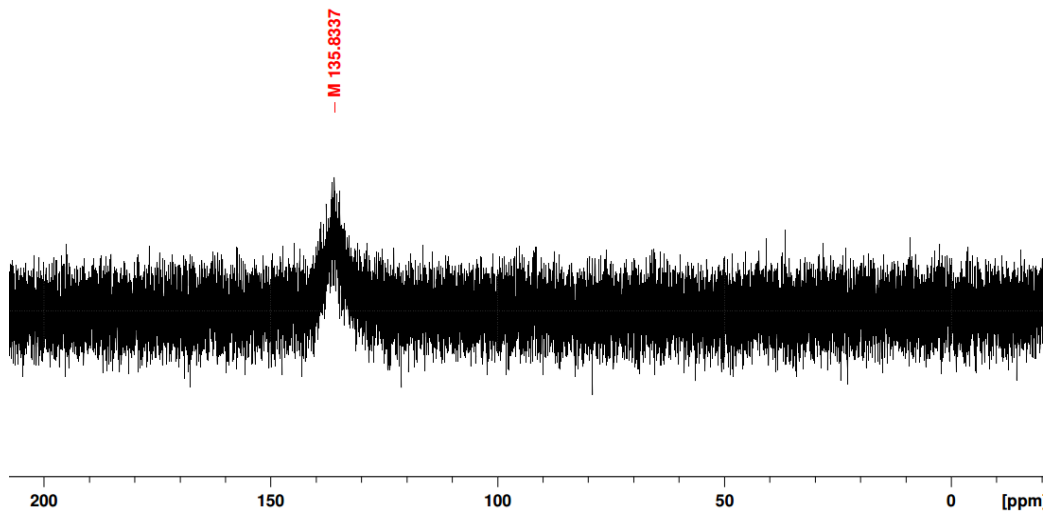
Figure S3.2: ^{31}P spectrum of $\{C_6H_5OP(i\text{-}Pr)_2\}_2NiBr_2$ in $CDCl_3$
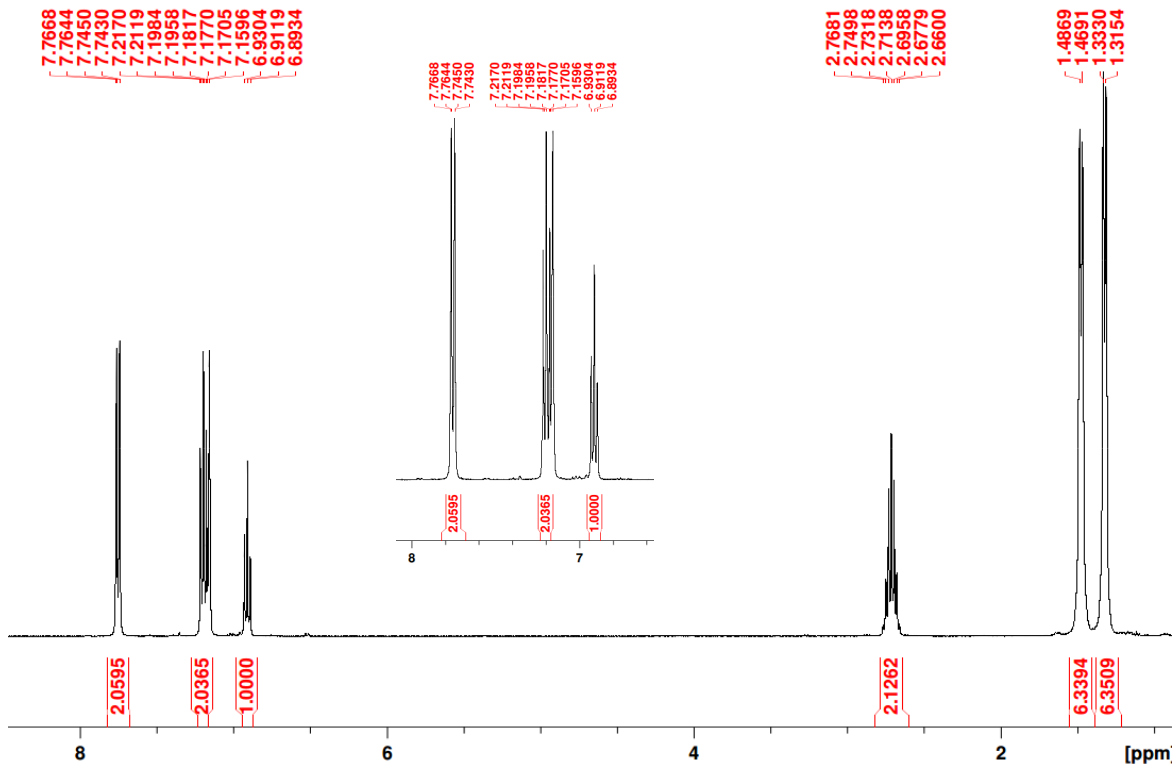
Figure S3.3: ^{1}H spectrum of $\{C_6H_5OP(i\text{-}Pr)_2\}_2NiBr_2$ in C_6D_6
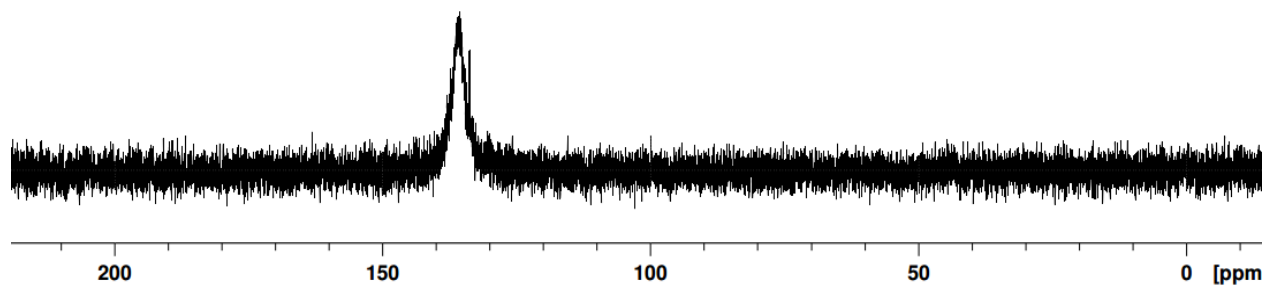
Figure S3.4: ^{31}P spectrum of $\{C_6H_5OP(i\text{-}Pr)_2\}_2NiBr_2$ in C_6D_6
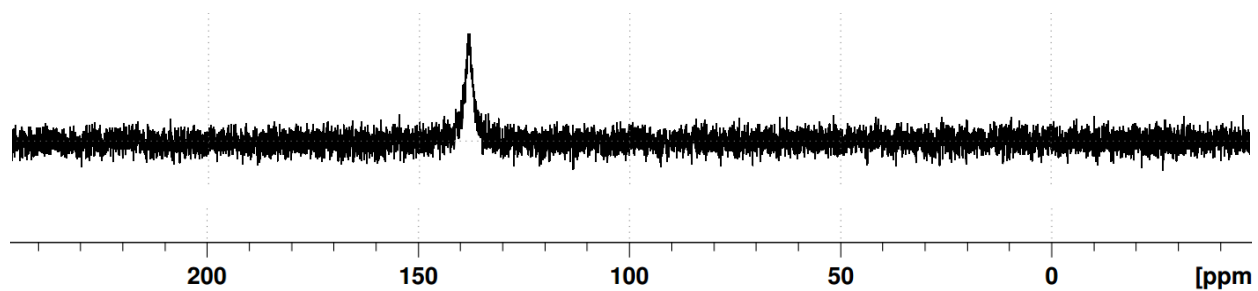
Figure S3.5: ^{31}P spectrum of $\{C_6H_5OP(i\text{-}Pr)_2\}_2NiBr_2$ in PhMe
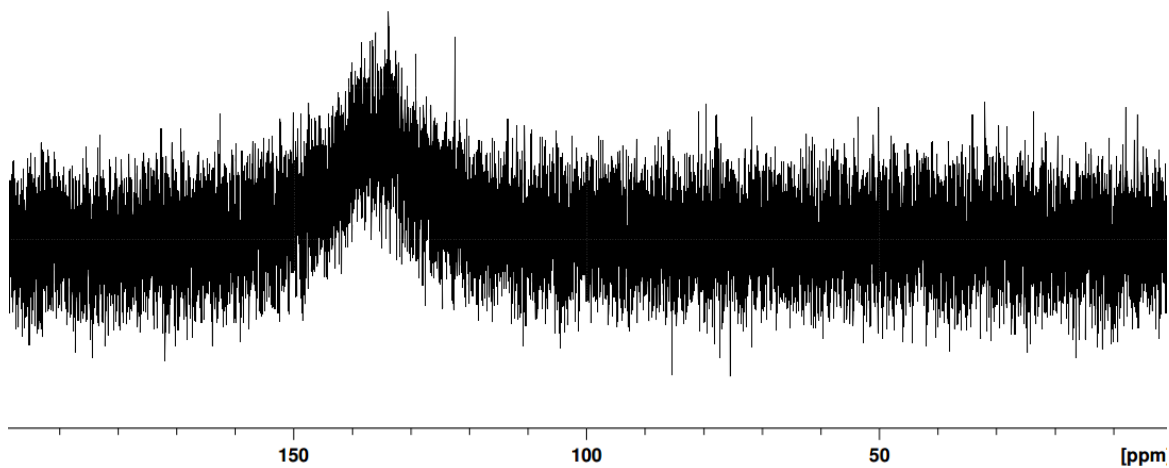
Figure S3.6: ^{31}P spectrum of $\{C_6H_5OP(i\text{-}Pr)_2\}_2NiBr_2$ in CD_3CN
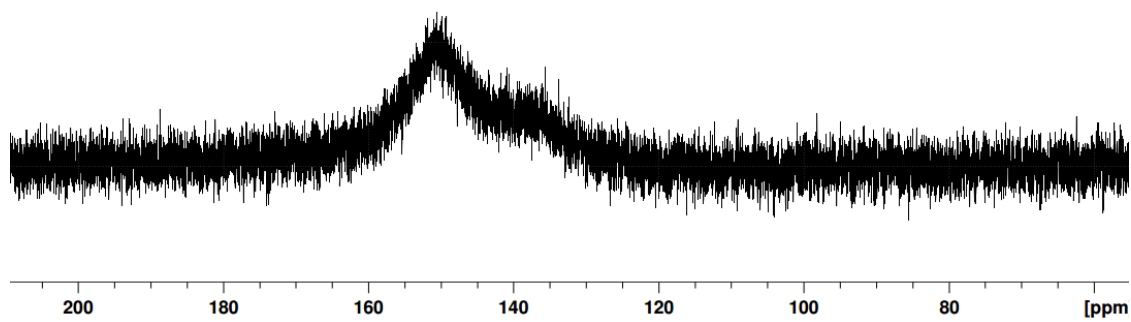
Figure S3.7: ^{31}P NMR spectrum of {$C_6H_5OP(i\text{-}Pr)_2$}$_2$NiBr$_2$ + excess $C_6H_5OP(i\text{-}Pr)_2$ ligand in MeCN
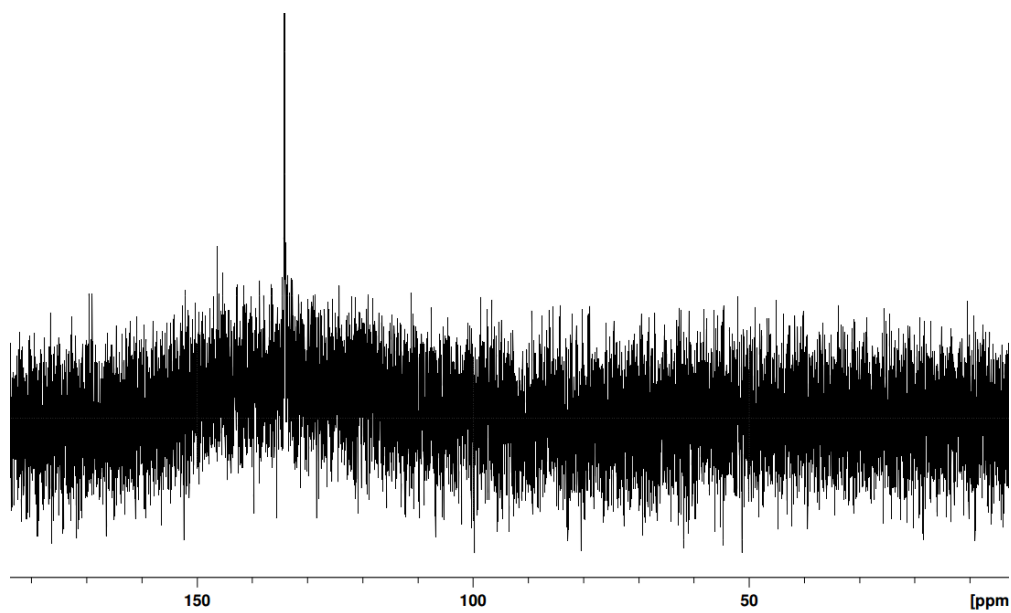
Figure S3.8: ^{31}P NMR spectrum of {$C_6H_5OP(i\text{-}Pr)_2$}$_2$NiBr$_2$ + excess Et$_3$N in MeCN
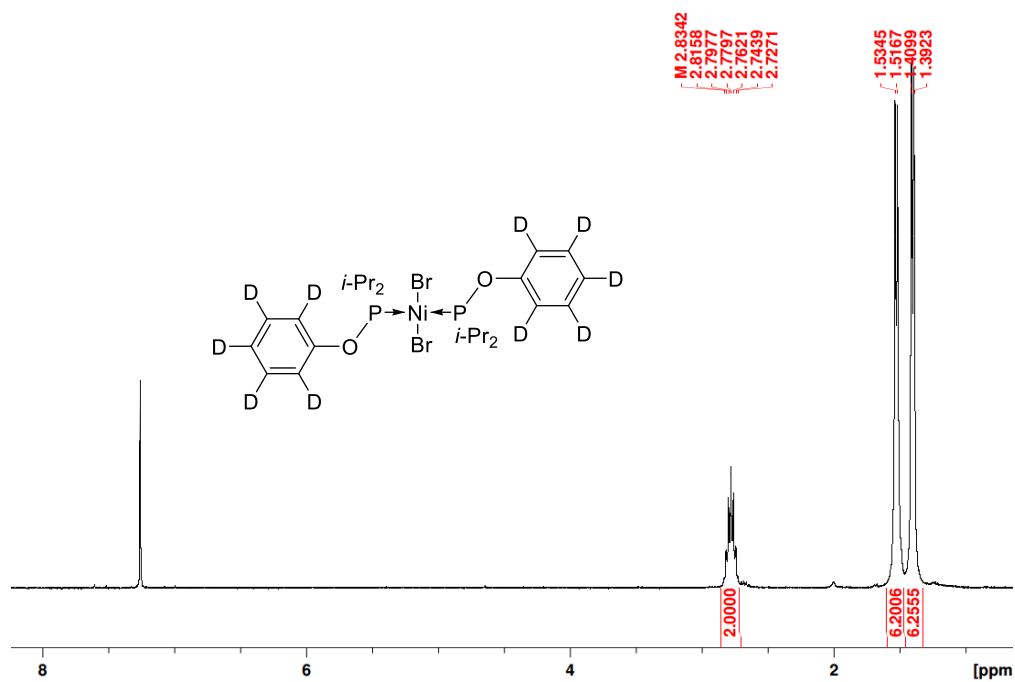
Figure S3.9: ^{1}H NMR spectrum of $\{C_6D_5OP(i\text{-}Pr)_2\}_2NiBr_2$ in CDCl$_3$
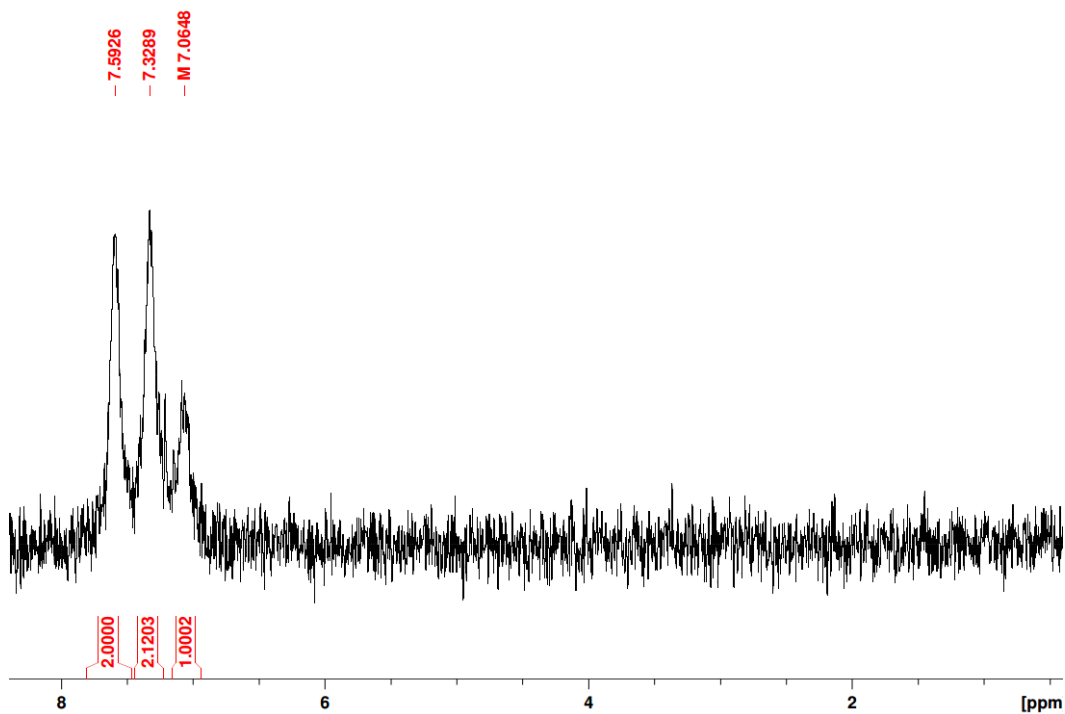
Figure S3.10: ^{2}H NMR spectrum of $\{C_6D_5OP(i\text{-}Pr)_2\}_2NiBr_2$ in CHCl$_3$
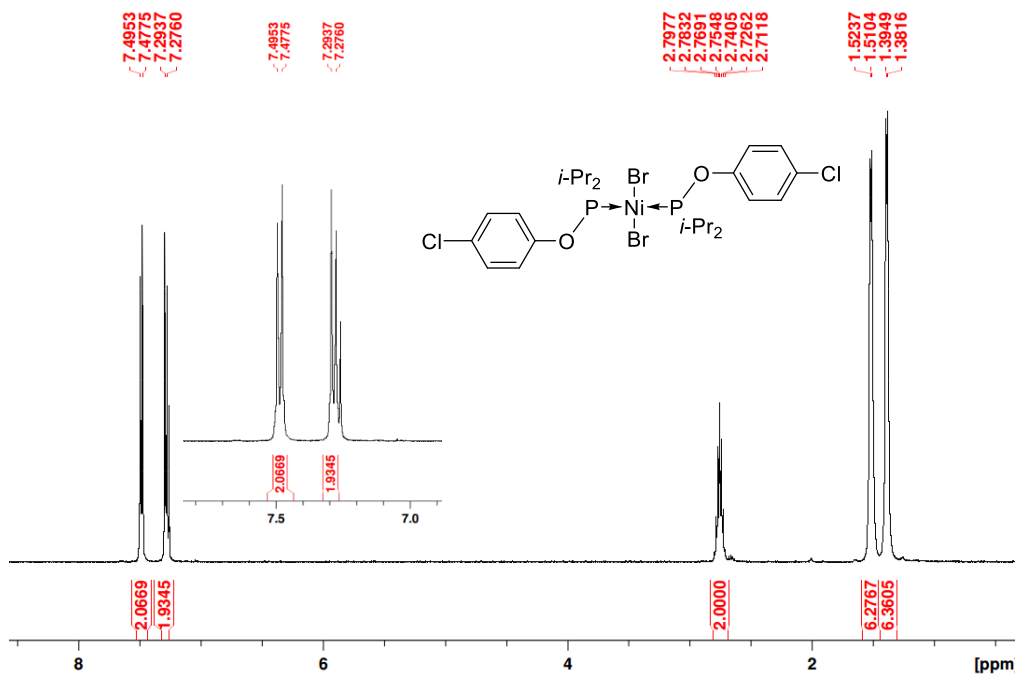
Figure S3.11: ^{1}H NMR spectrum of {4-Cl-C$_6$H$_4$-OP(i-Pr)$_2$}$_2$NiBr$_2$ in CDCl$_3$.
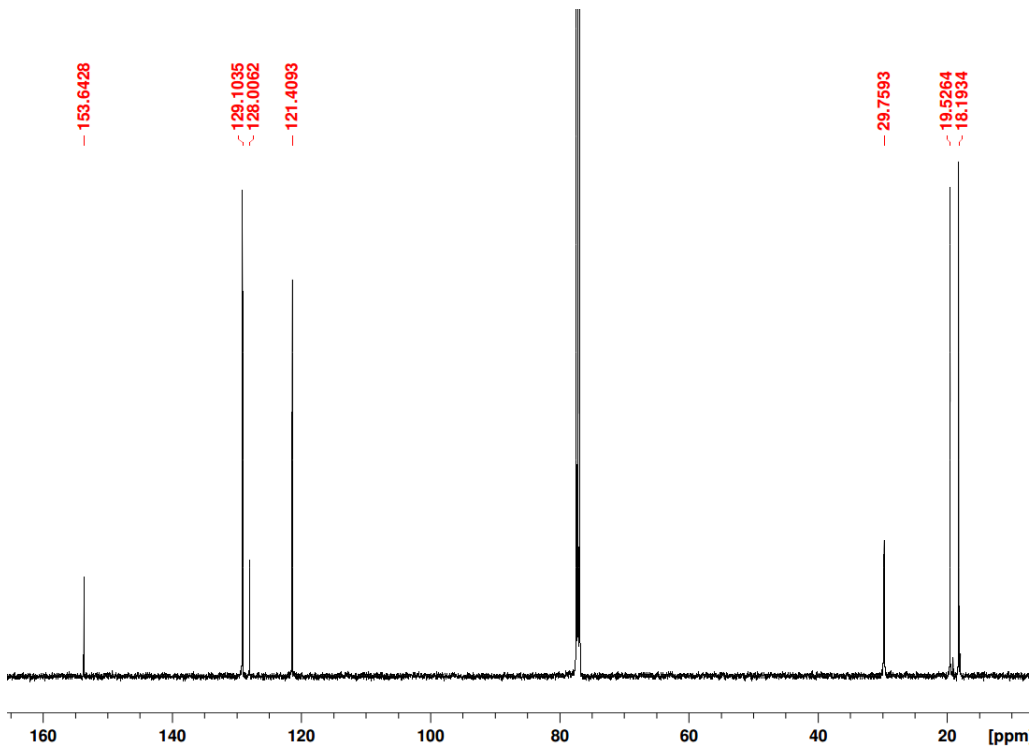
Figure S3.12: ^{13}C NMR spectrum of {4-Cl-C$_6$H$_4$-OP(i-Pr)$_2$}$_2$NiBr$_2$ in CDCl$_3$.
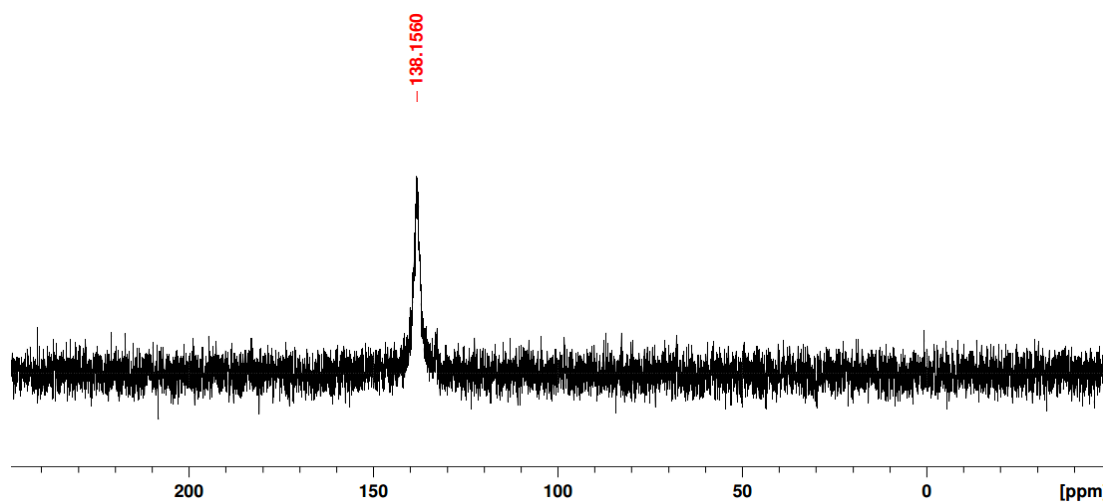
Figure S3.13: ^{31}P NMR spectrum of {4-Cl-C$_6$H$_4$-OP(i-Pr)$_2$}$_2$NiBr$_2$ in CDCl$_3$.
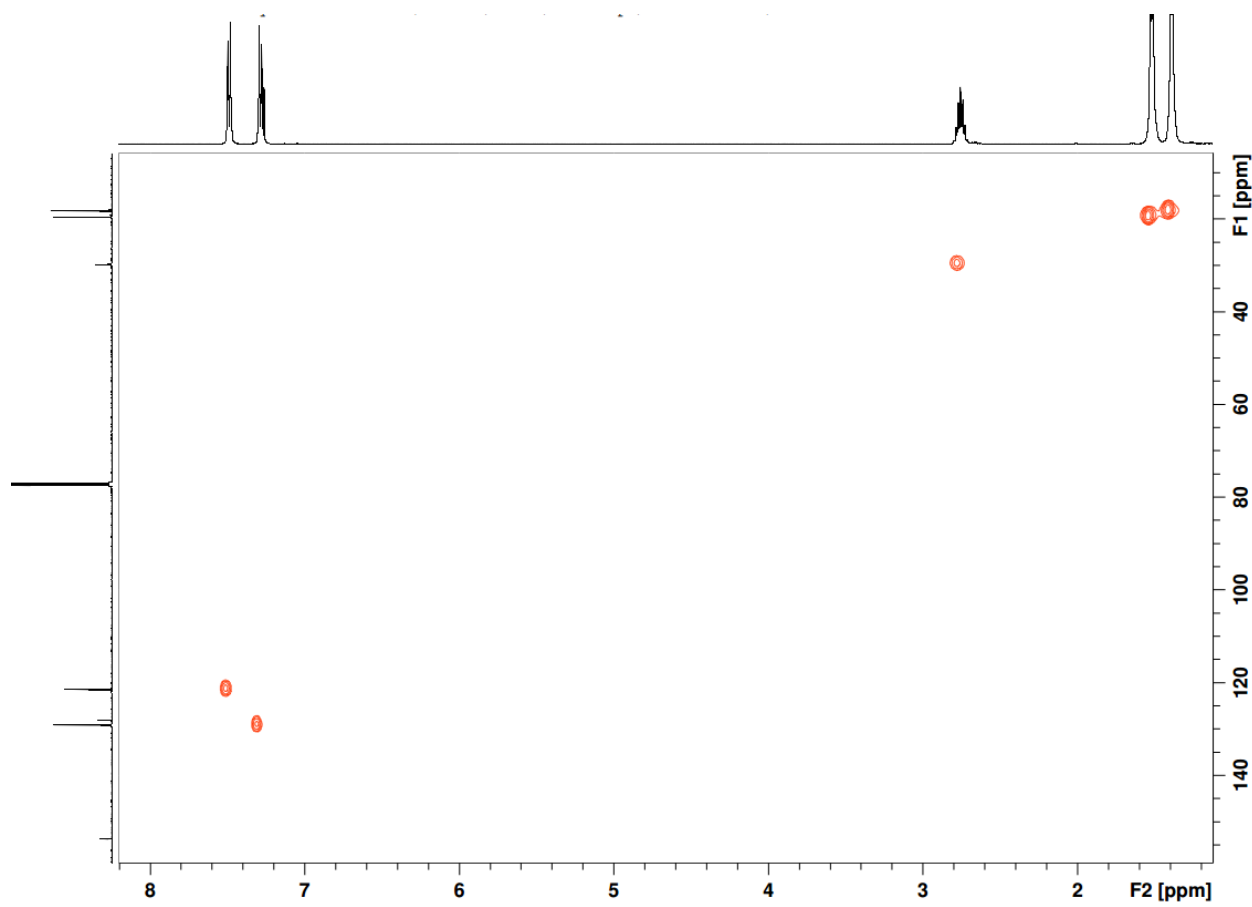
Figure S3.14: HSQC spectrum of {4-Cl-C$_6$H$_4$-OP(i-Pr)$_2$}$_2$NiBr$_2$ in CDCl$_3$.

204

S3.2.2 ^{31}P NMR spectra recorded at –30°C
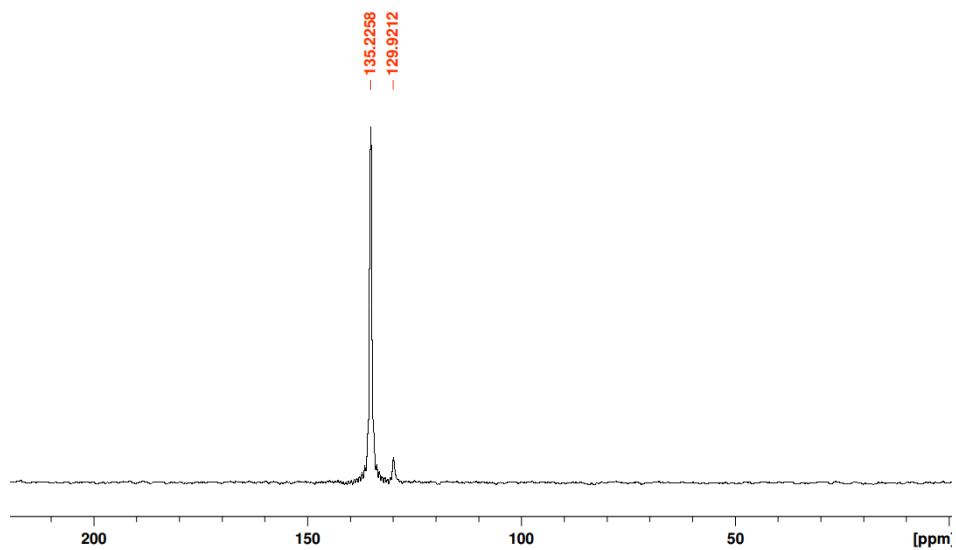
Figure S3.15: ^{31}P NMR spectrum of {C$_6$H$_5$-OP(i-Pr)$_2$}$_2$NiBr$_2$ in C$_6$D$_5$CD$_3$ at –30 °C
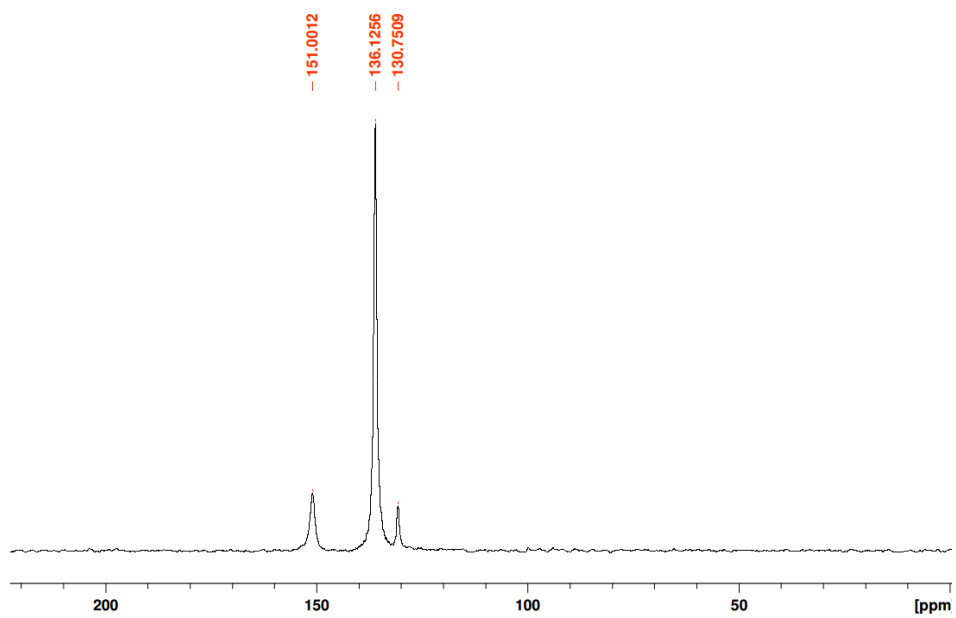
Figure S3.16: ^{31}P NMR spectrum of {C$_6$H$_5$-OP(i-Pr)$_2$}$_2$NiBr$_2$ in CD$_3$CN at –30 °C
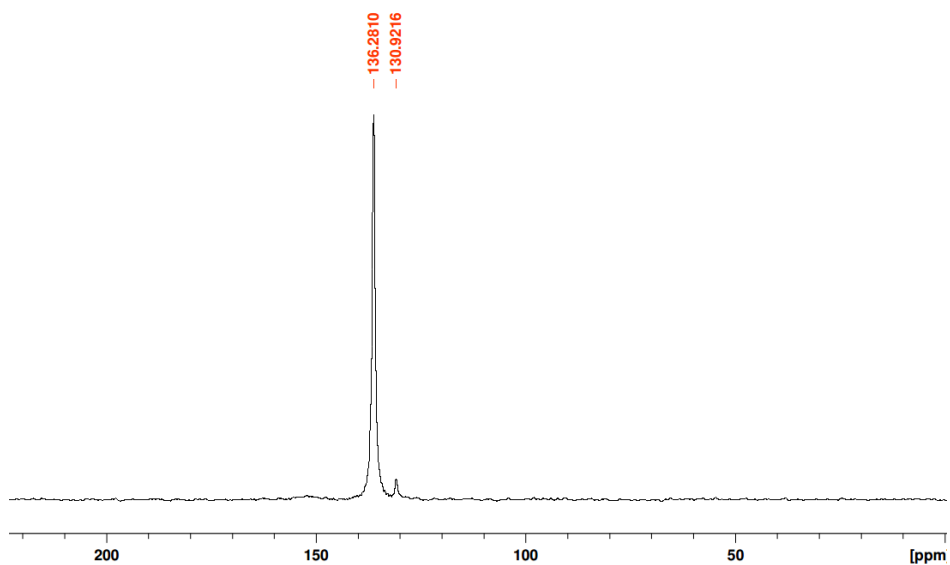
Figure S3.17: ^{31}P NMR spectrum of a 1:1 mixture of C$_6$H$_5$-OP(i-Pr)$_2$ and (i-PrCN)NiBr$_2$ in CD$_3$CN at –30 °C

S3.2.3 Conversion rates in PhMe with various L *vs.* Ni ratios at 80 and 100 °C
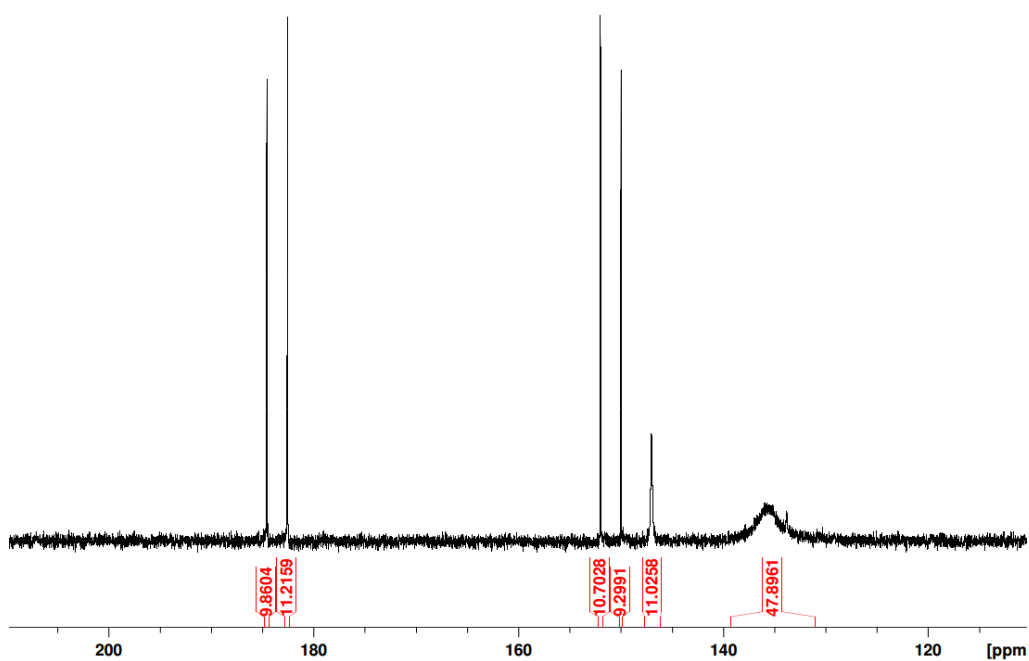
Figure S3.18: Crude mixture of {C$_6$H$_5$-OP(i-Pr)$_2$}$_2$NiBr$_2$ + 1 equiv. Et$_3$N in PhMe heated at 80 °C for 16 h
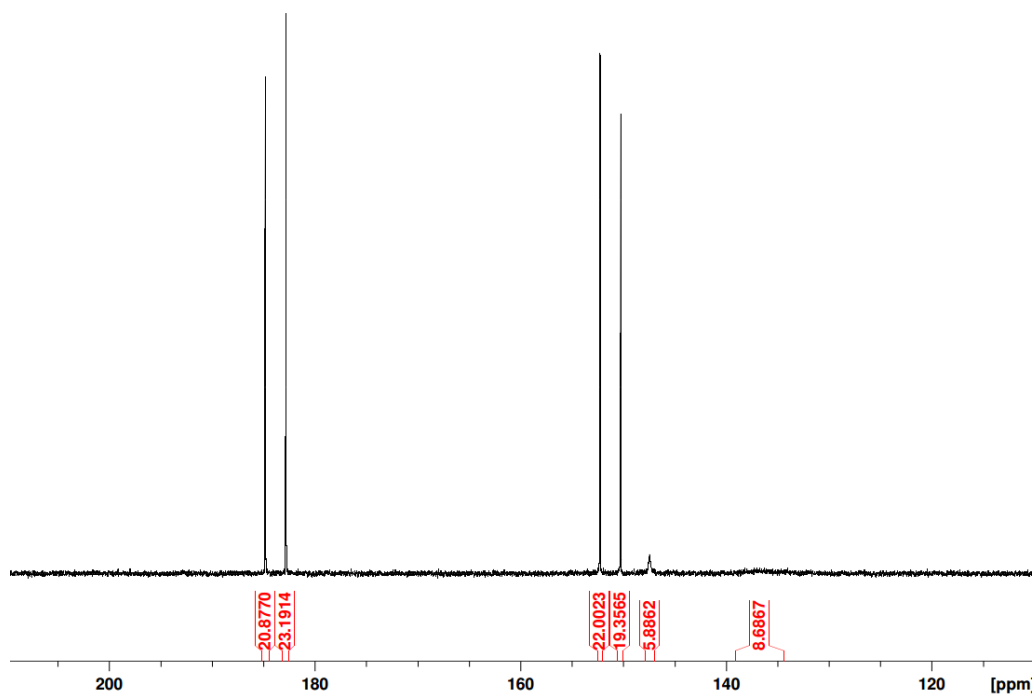
Figure S3.19: Crude mixture of {C$_6$H$_5$-OP(i-Pr)$_2$}$_2$NiBr$_2$ + 1 equiv. Et$_3$N in PhMe heated at 100 °C for 16 h
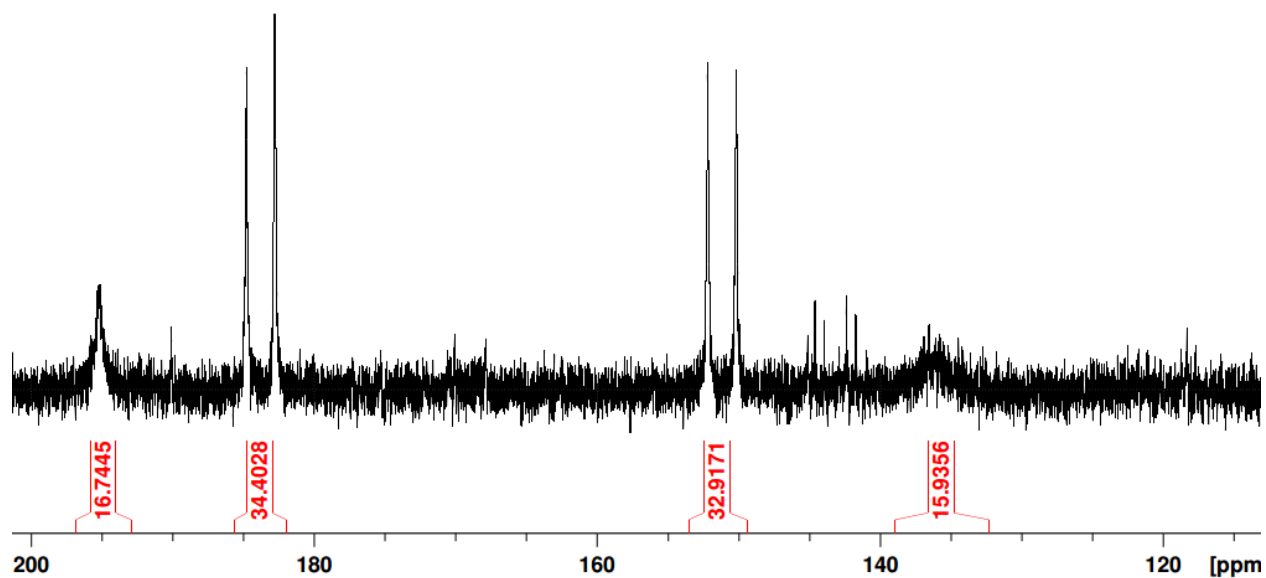
Figure S3.20: Crude mixture of C$_6$H$_5$-OP(i-Pr)$_2$ + 1 equiv. (i-PrCN)NiBr$_2$ + 1 equiv. Et$_3$N in PhMe heated at 80 °C for 16 h
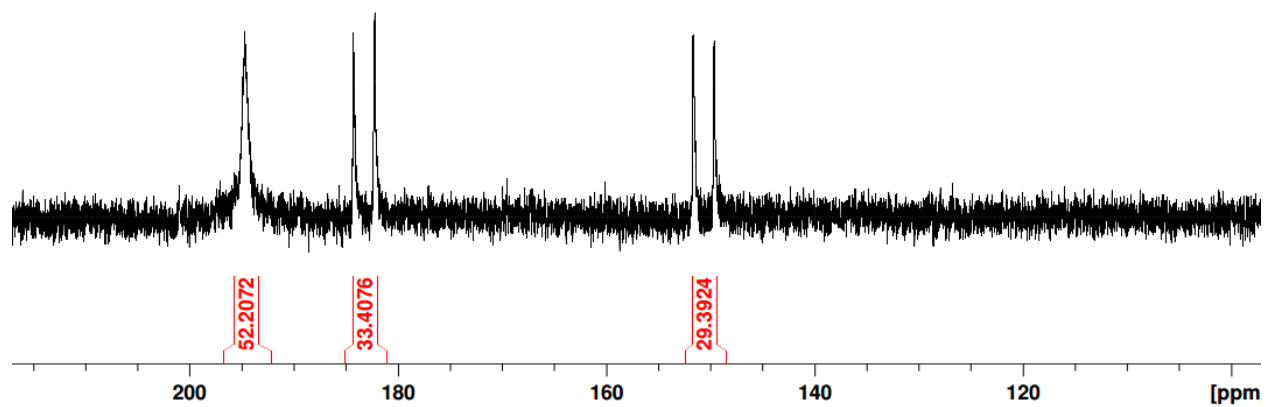
Figure S3.21: Crude mixture of C6H5-OP(i-Pr)2 + 1 equiv. (i-PrCN)NiBr2 + 1 equiv. Et3N in PhMe heated at 100 °C for 16 h

S3.2.4 ^{31}P kinetic monitoring of the reaction in MeCN at 70 °C at the beginning and end of the reaction
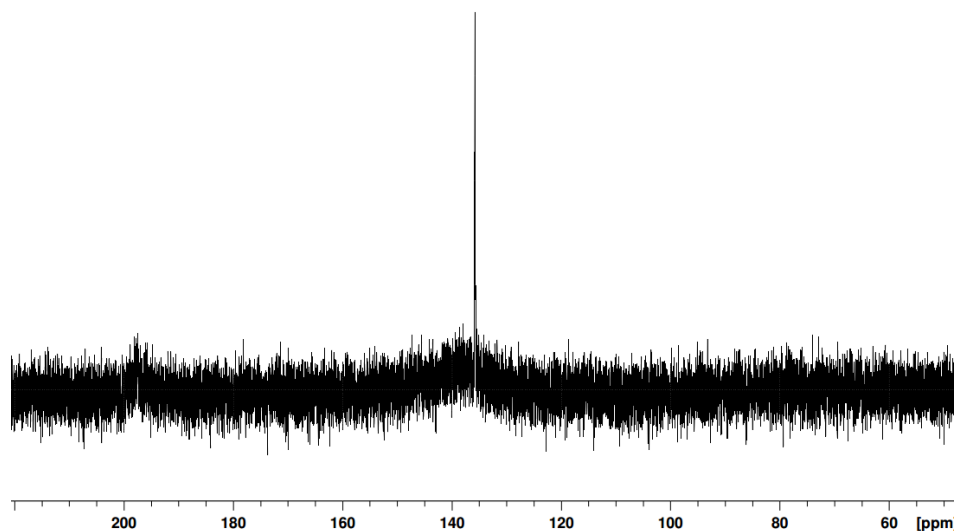
Figure S3.22: ^{31}P spectrum of the reaction mixture after 15 mins with 1 equiv. Et$_3$N. Focus on the Ni-complex region
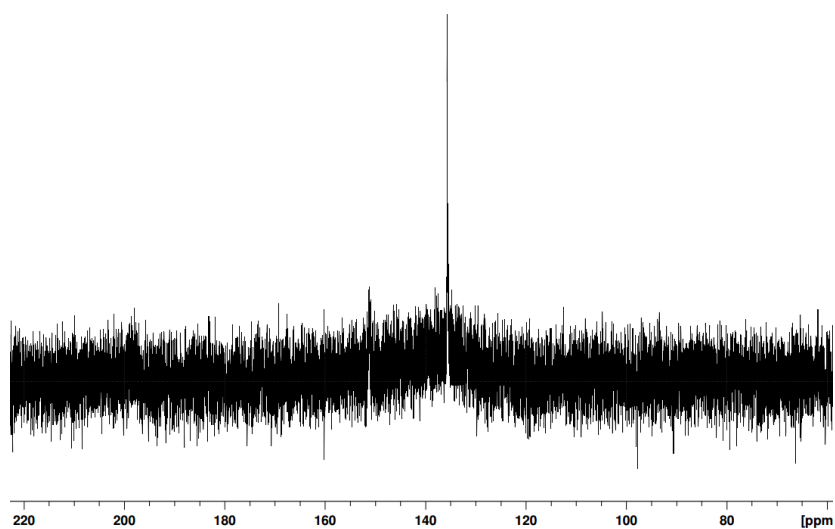
Figure S3.23: ^{31}P spectrum of the reaction mixture after 15 mins with 4 equiv. Et$_3$N. Focus on the Ni-complex region
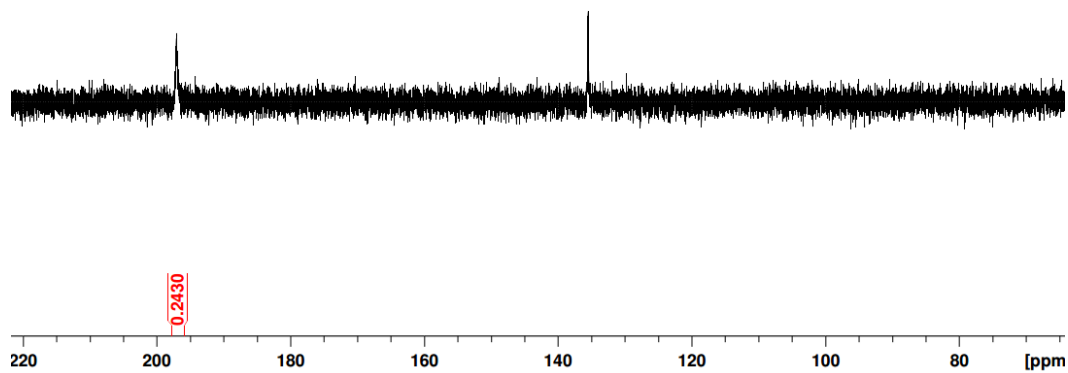
Figure S3.24: ^{31}P spectrum of the reaction mixture after 15 mins with 1 equiv. i-Pr$_2$NEt. Focus on the Ni-complex region
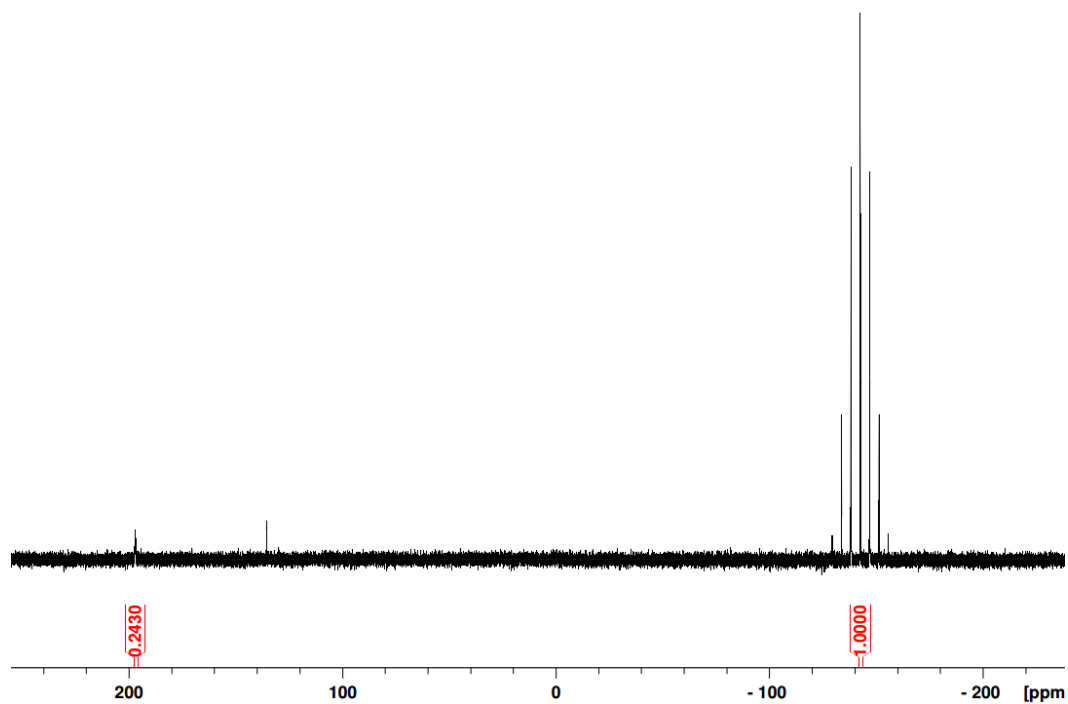
Figure S3.25: ^{31}P spectrum of the reaction mixture after 15 mins with 1 equiv. i-Pr$_2$NEt. Full spectrum.
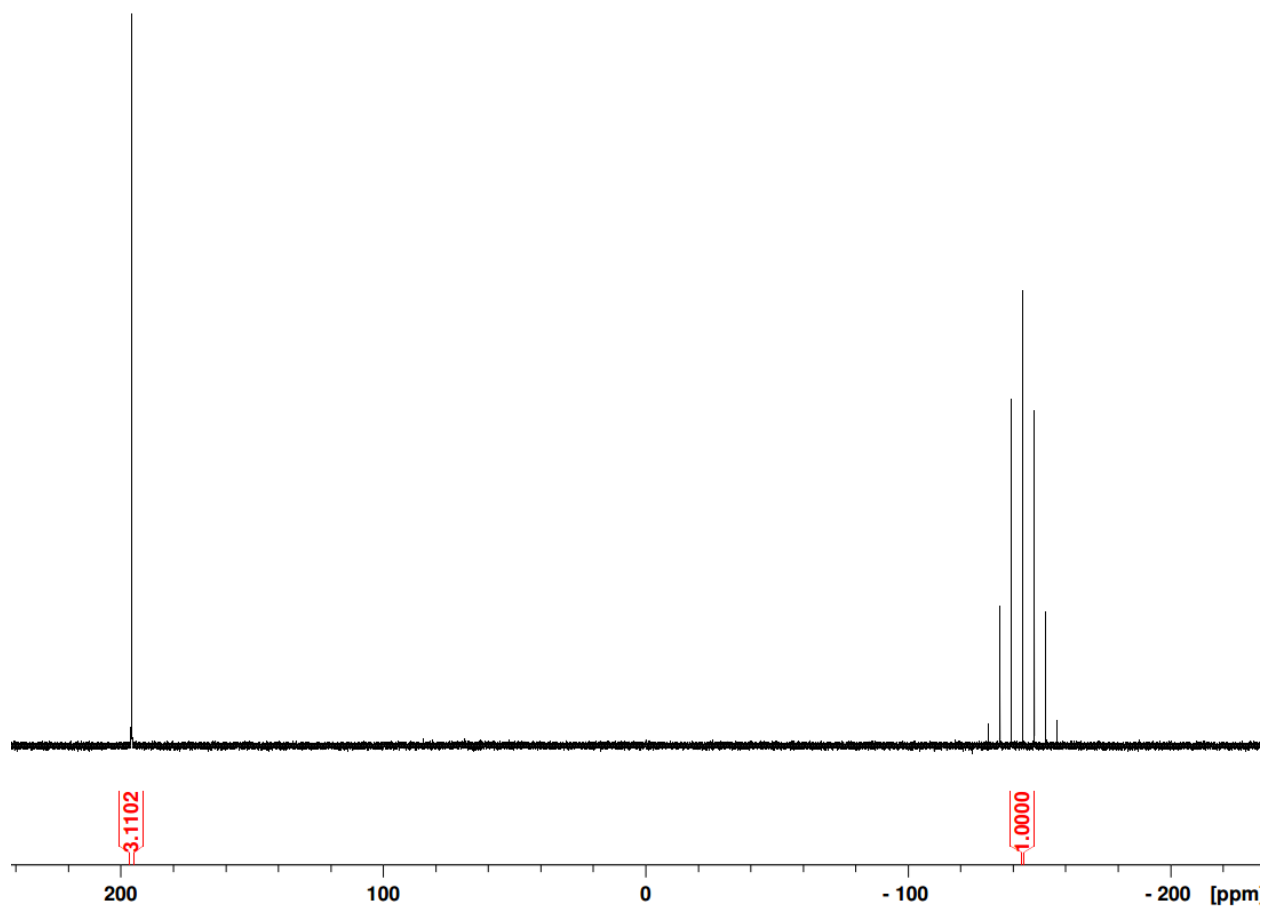
Figure S3.26: ^{31}P spectrum of the reaction mixture at the end of the reaction with 1 equiv. i-Pr$_2$NEt. Full spectrum.

S3.2.5 Results of *ortho*-H/D scrambling

Figure S3.27: ^{1}H NMR spectra in CDCl_3 of various mixtures of L_2NiBr_2 and of the H/D scrambling experiment. Focus on the aromatic region.

Scheme S3.1: The mixture between L_2NiBr_2 complexes rapidly reaches an isothermal equilibrium in (See ^{31}P NMR in Fig. S3.23).
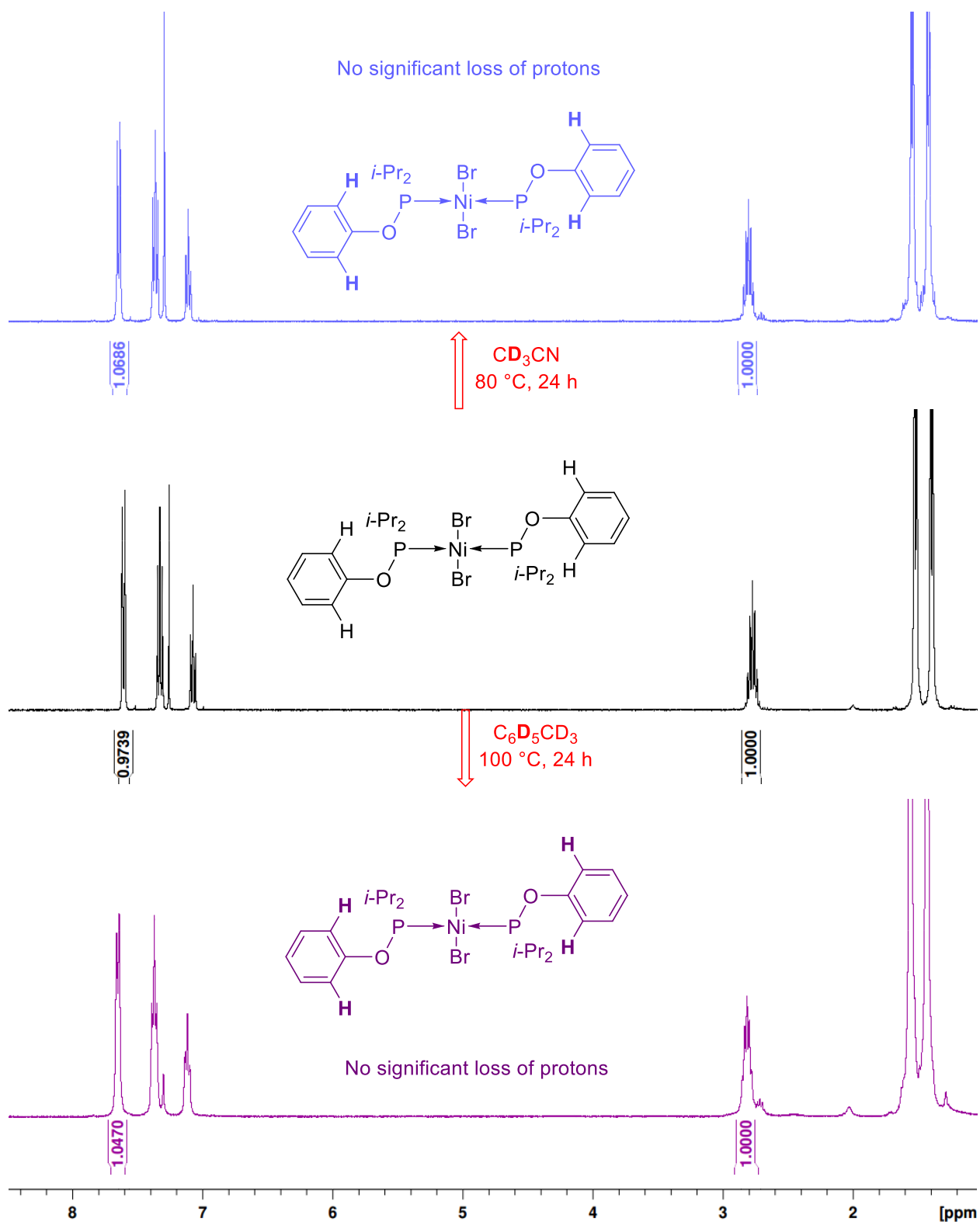
Figure S3.28: Heating $\{C_6H_5OP(i\text{-}Pr)_2\}_2NiBr_2$ in CD_3CN or $C_6D_5CD_3$ shows no ortho-D incorporation on the ligand.
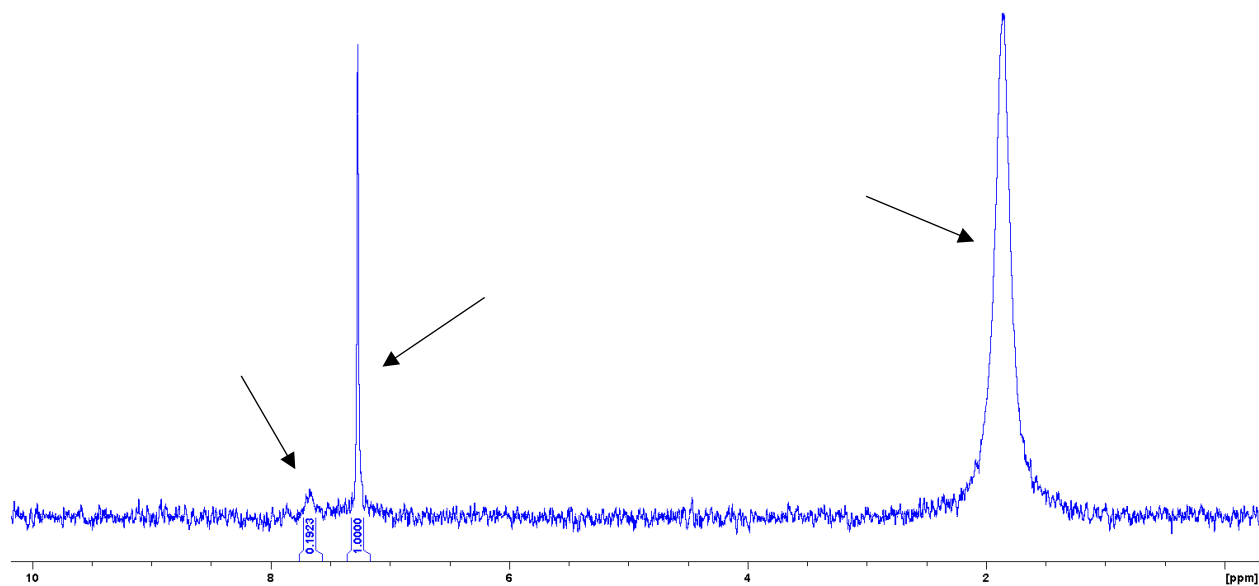
Figure S3.29: $^2H\{^1H\}$ NMR spectrum of the crystals arising from the scrambling of $\{C_6H_5OP(i\text{-}Pr)_2\}_2NiBr_2$ with CD_3CN, showing <1% D incorporation into the *ortho* positions.
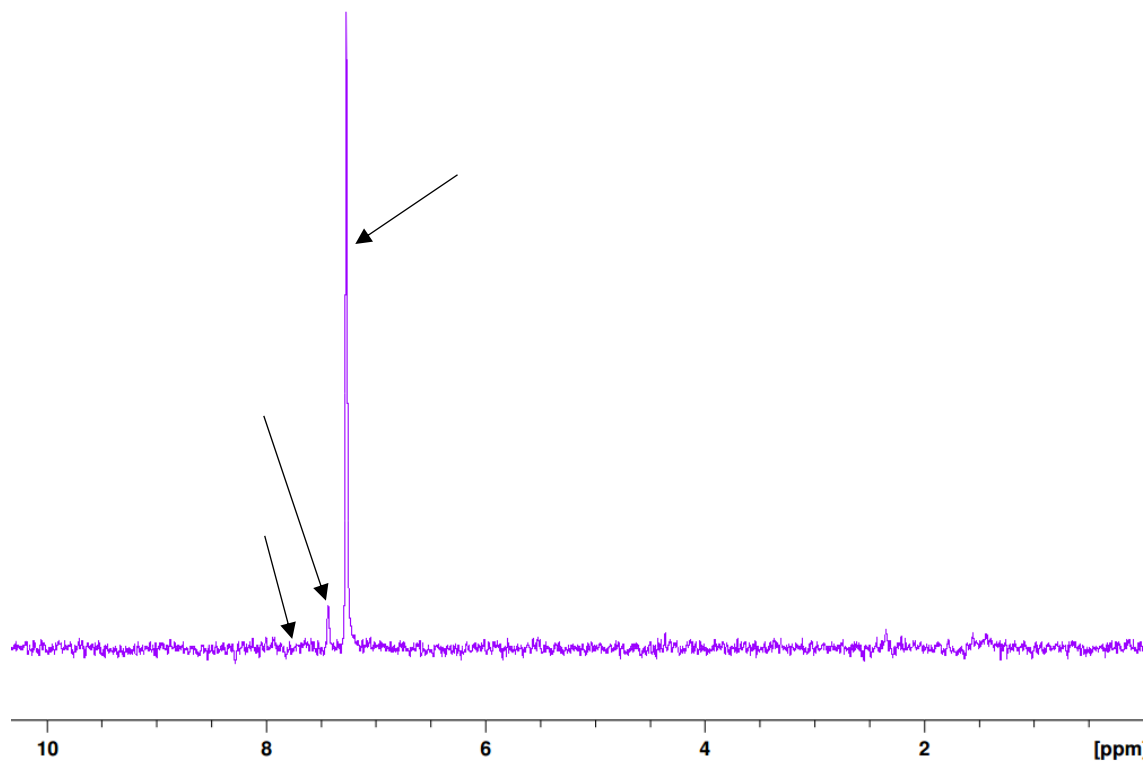
Figure S3.30: $^2H\{^1H\}$ NMR spectrum of the crystals arising from the scrambling of $\{C_6H_5OP(i\text{-}Pr)_2\}_2NiBr_2$ with $C_6D_5CD_3$, where ortho D could not be detected.
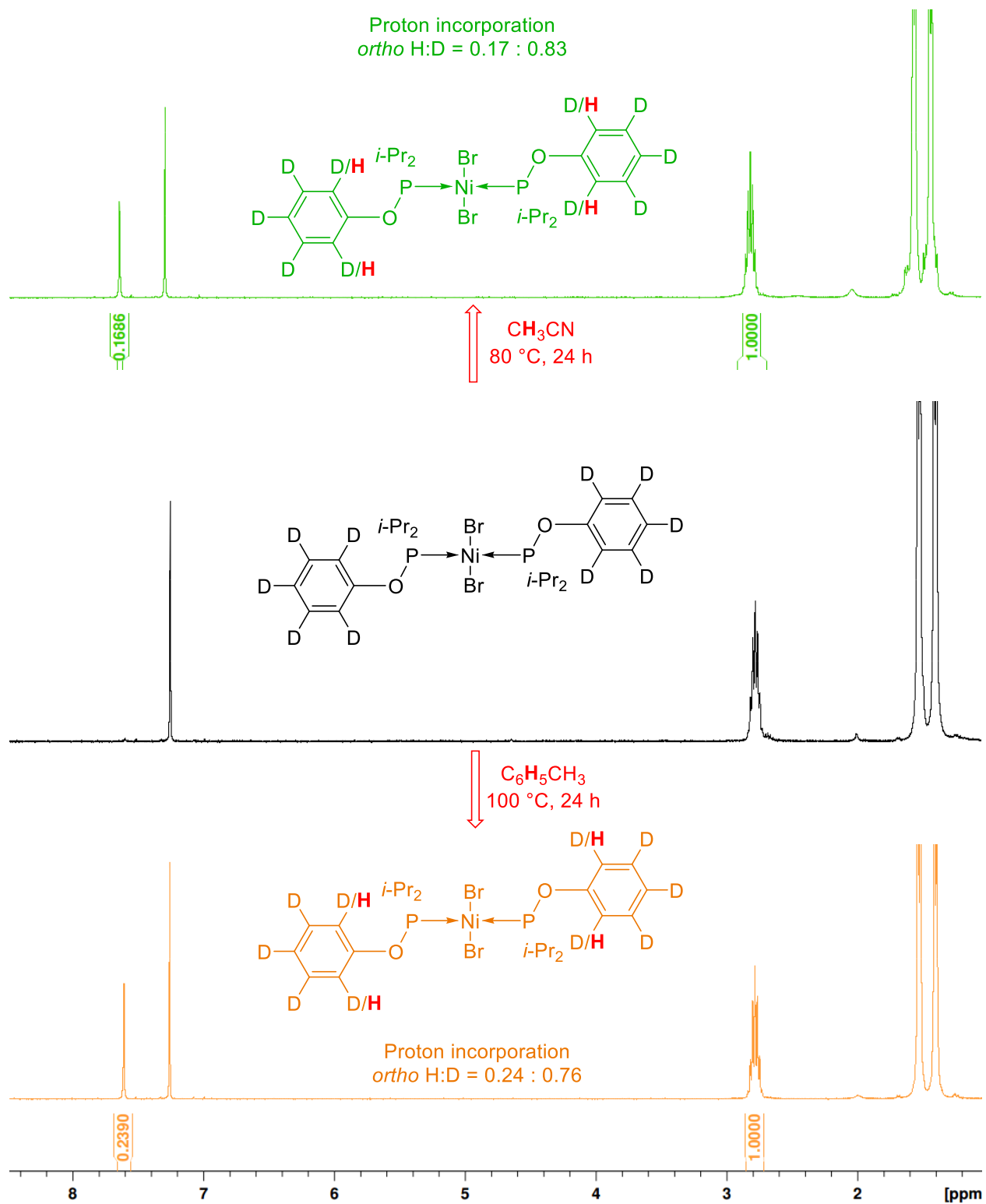
Figure S3.31: Heating {C$_6$D$_5$OP(i-Pr)$_2$}$_2$NiBr$_2$ in CH$_3$CN or C$_6$H$_5$CH$_3$ shows ortho-H incorporation on the ligand via H/D scrambling with the solvent.
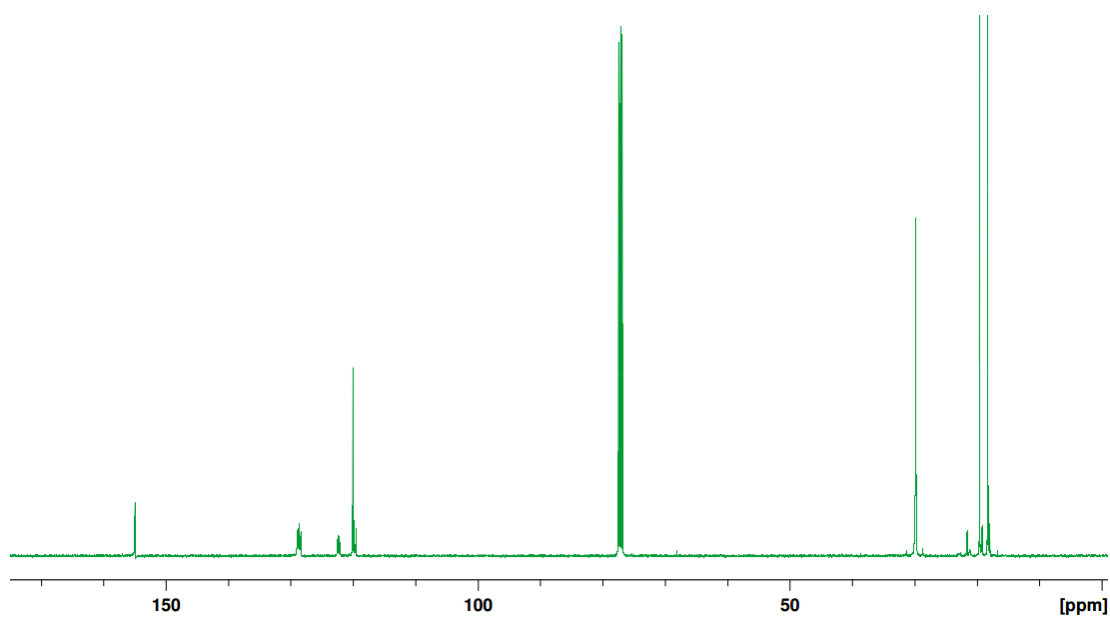
Figure S3.32: $^{13}C\{^1H\}$ NMR spectrum of the crystals arising from the scrambling of $\{C_6D_5OP(i\text{-}Pr)_2\}_2NiBr_2$ with CH_3CN, showing no D incorporation into the i-Pr moiety of the ligand.
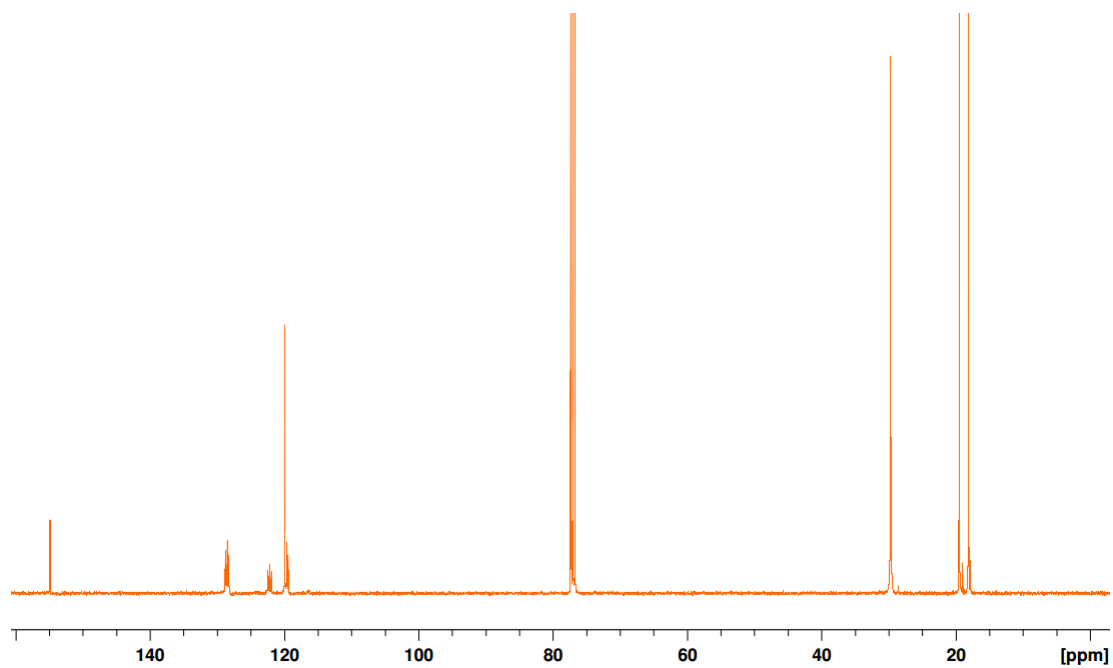
Figure S3.33: $^{13}C\{^1H\}$ NMR spectrum of the crystals arising from the scrambling of $\{C_6D_5OP(i\text{-}Pr)_2\}_2NiBr_2$ with $C_6H_5CH_3$, showing no D incorporation into the i-Pr moiety of the ligand.

S3.3 Attempts to detect the resting state(s) by ESI-MS
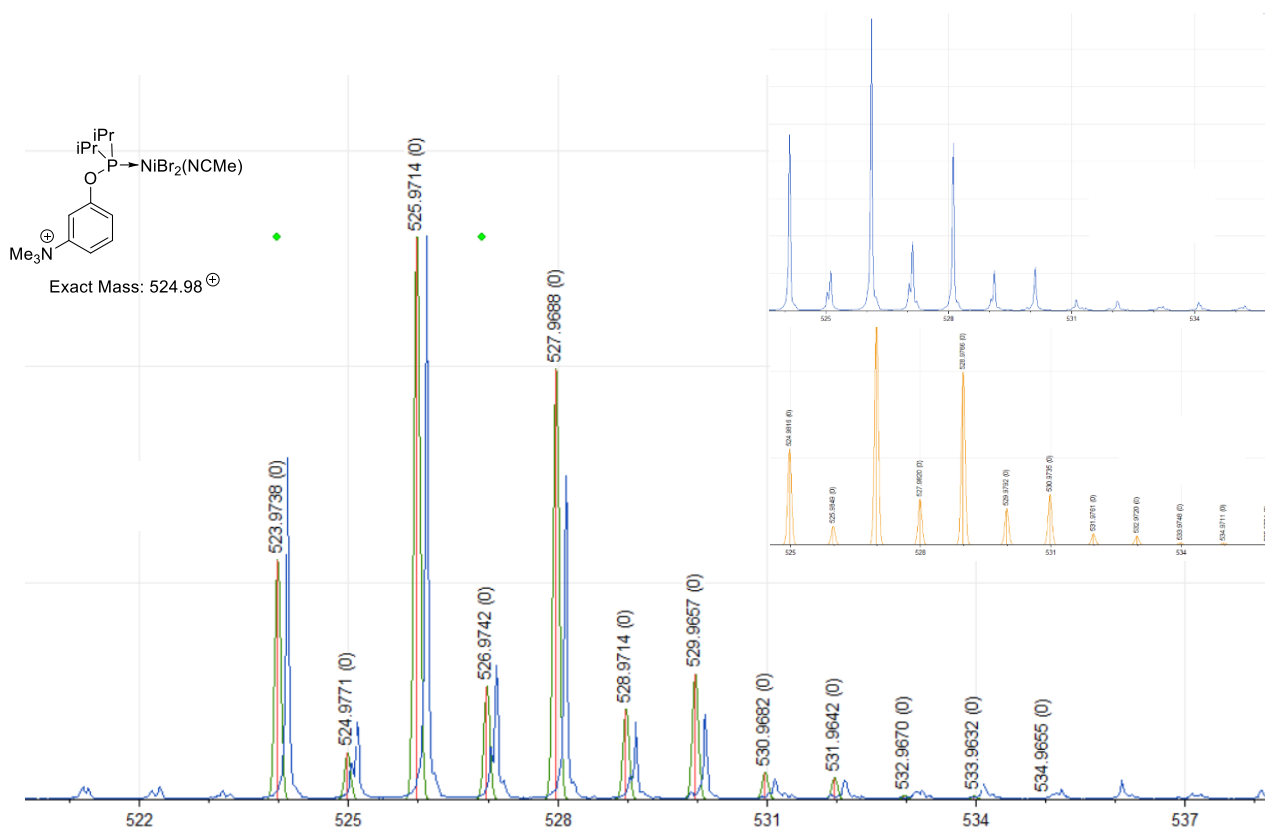
Figure S3.34: ESI-MS mass pattern in the sample (a), theoretical mass pattern for the expected $M^+ = [C_{17}H_{30}Br_2N_2NiOP]^+$ (b), and overlap of the experimental pattern and $M^+ - 1$ (c)
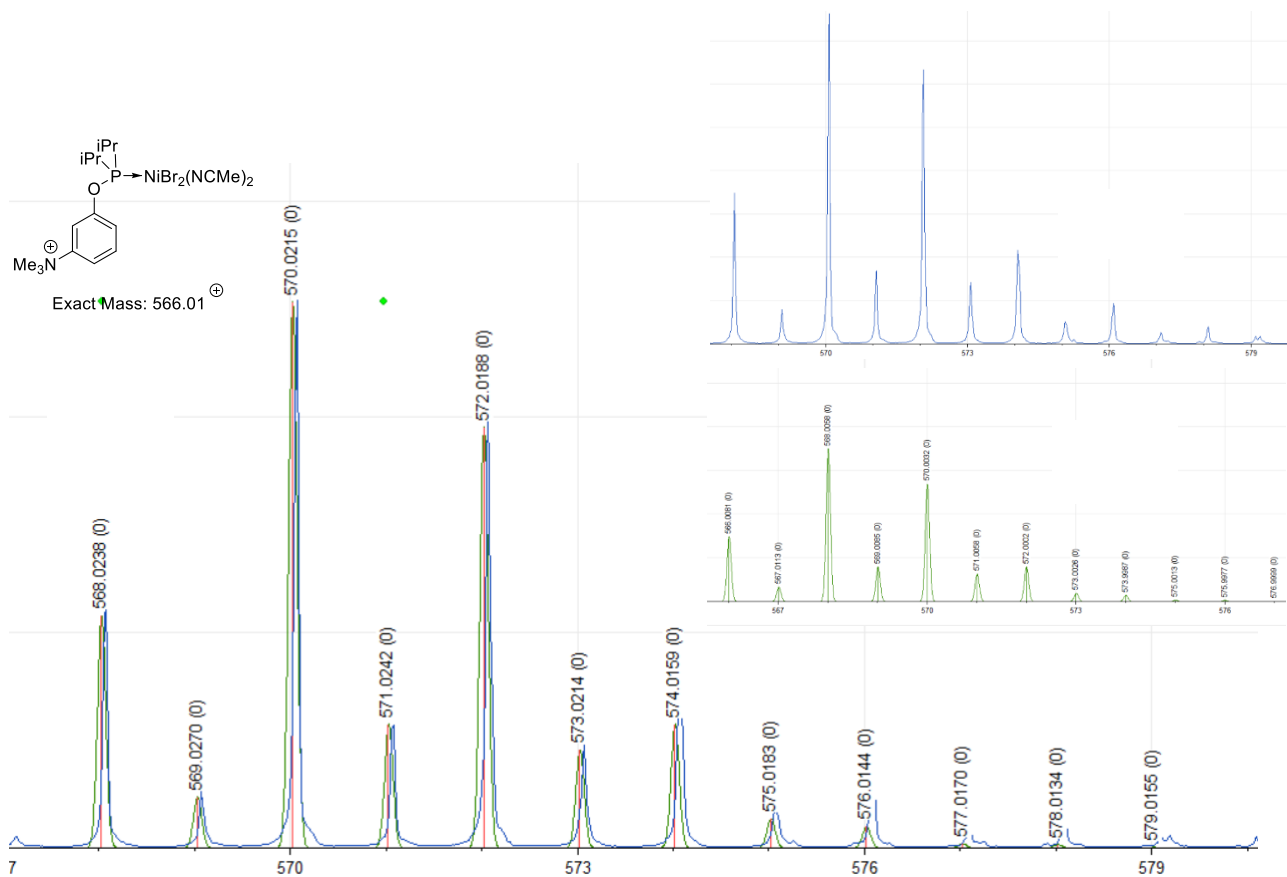
Figure S3.35: ESI-MS mass pattern in the sample (a), theoretical mass pattern for the expected $M^+ = [C_{19}H_{33}Br_2N_3NiOP]^+$ (b), and overlap of the experimental pattern and $M^+ + 2$ (c).

S3.4 Crystallographic data and additional Thermal ellipsoid plots

Table S3.1: Crystal description and refinement indicators for compounds [(THF)$_6$Ni$_2$(μ-Br)$_3$][(Et$_3$N)NiBr$_3$], [(Me$_3$N-PhOPR$_2$)$_2$Ag(μ-Br)$_3$]Br and (Me$_3$N-PhOPR$_2$)NiX$_3$.

	[(THF)$_6$Ni$_2$(μ-Br)$_3$][(Et$_3$N)NiBr$_3$]	[(Me$_3$N-PhOPR$_2$)$_2$Ag(μ-Br)$_3$]Br	(Me$_3$N-PhOPR$_2$)NiX$_3$
chemical formula	C$_6$H$_{15}$Br$_3$NNi,C$_{24}$H$_{48}$Br$_3$Ni$_2$O$_6$	C$_{30}$H$_{54}$Ag$_2$Br$_3$N$_2$O$_2$P$_2$,Br,2(C$_2$H$_3$N)	C$_{15}$H$_{27}$Br$_{1.94}$Cl$_{1.06}$NNiOP
crystal color	blue	colorless	green
crystal size (mm)	0.22 × 0.06 × 0.04	0.18 × 0.16 × 0.14	0.11 × 0.10 × 0.06
index ranges	-13 ≤ h ≤ 13 -15 ≤ k ≤ 14 -19 ≤ l ≤ 18	-23 ≤ h ≤ 23 -26 ≤ k ≤ 26 -14 ≤ l ≤ 14	-12 ≤ h ≤ 18 -11 ≤ k ≤ 10 -21 ≤ l ≤ 19
Fw; *F*(000)	1189.40; 1184	1154.18; 2288	519.77; 1044
T (K)	100	100	150
wavelength (Å)	1.54178	1.54178	1.34139
space group	P-1	C2/c	P2$_1$/c
a (Å)	11.2474(3)	19.0853(5)	14.0955(7)
b (Å)	12.5057(4)	21.4718(6)	8.8820(4)
c (Å)	15.8827(4)	11.6100(3)	16.7836(8)
α (deg)	100.186(2)	90	90
β (deg)	99.618(2)	108.9840(10)	93.698(2)
γ (deg)	95.972(2)	90	90
Z	2	4	4
V (Å^3)	2147.25(11)	4499.0(2)	2096.87(17)
ρ$_{calcd}$ (g·cm^{-3})	1.840	1.704	1.646
μ (mm^{-1})	8.366	12.070	9.472
θ range (deg); completeness	2.879 − 72.203; 0.952	3.199 − 72.307; 0.997	2.733 − 60.677; 0.993
collected reflections; R$_σ$	19319; 0.1193	48348; 0.0145	20671; 0.0397
unique reflections; R$_{int}$	7829; 0.0956	4424; 0.0334	4798; 0.0507
R1[a]; wR2[b] [I > 2σ(I)]	0.0919; 0.2507	0.0279; 0.0749	0.0380; 0.0914
R1; wR2 [all data]	0.1257; 0.2751	0.0283; 0.0754	0.0443; 0.0952
GOOF	1.042	1.071	1.032
largest diff peak and hole	2.057 and -1.303	1.336 and -0.703	1.216 and -0.936

[a] **R$_1$=Σ(||F$_o$|-|F$_c$||)/Σ|F$_o$|**

[b] **wR$_2$={Σ[w(F$_o^2$–F$_c^2$)^2]/Σ[w(F$_o^2$)^2]}^{½}**
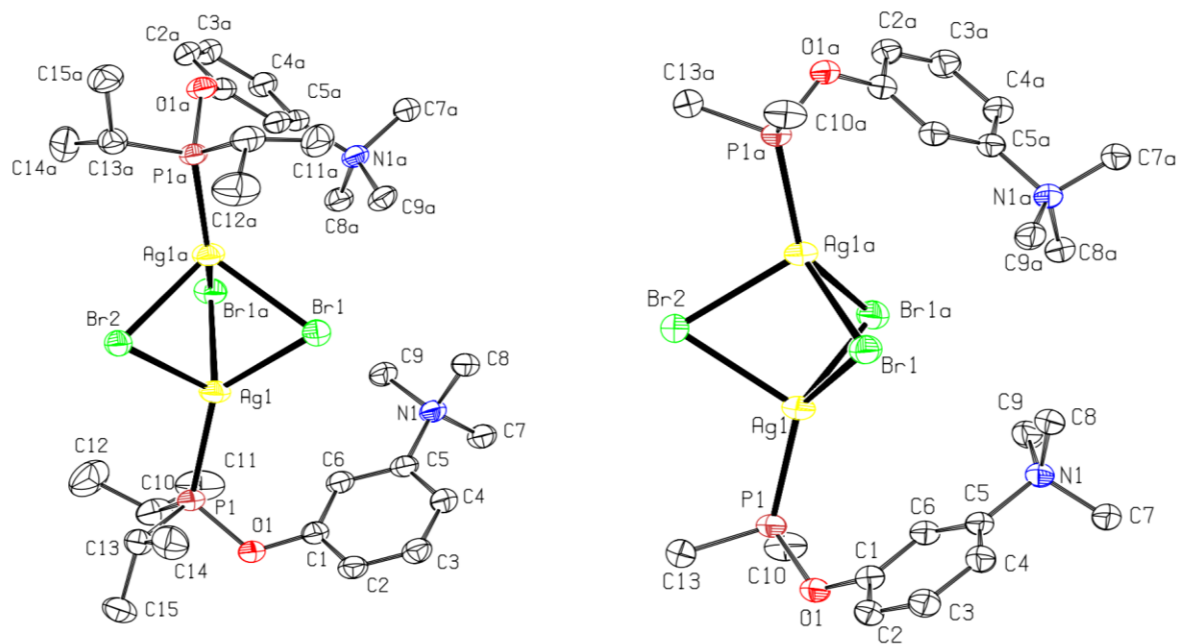
Figure S3.36: Molecular diagram for the bimetallic cation [(Me₃N-PhOPR₂)₂Ag(μ-Br)₃] (the counter anion is Br⁻). Thermal ellipsoids are shown at the 50% probability level. Hydrogens atoms have been omitted for clarity and the Methyls of the *i*-Pr in the diagram on the right.
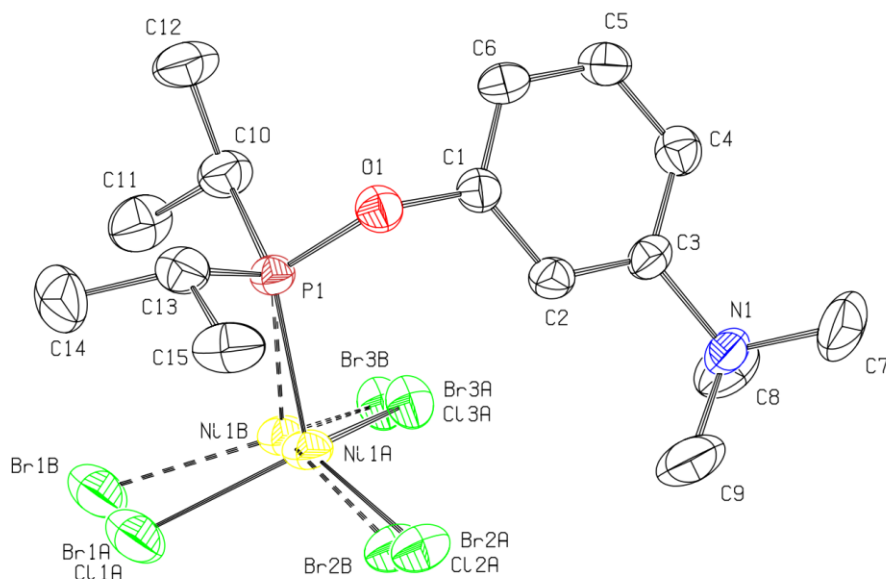
Figure S3.37: Molecular diagram for the zwitterionic compound (Me₃N-PhOPR₂)NiX₃. Thermal ellipsoids are shown at the 50% probability level. Hydrogen atoms have been omitted for clarity.

S3.5 Additional Kinetic Plots
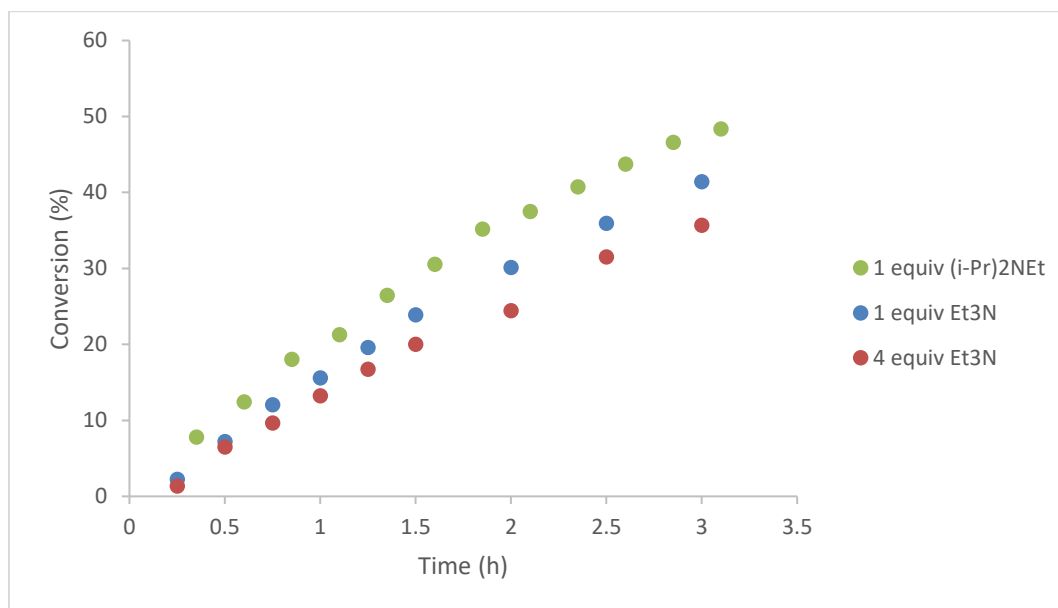
Figure S3.38: Time profile for the cyclonickelation in MeCN at 70 °C in the presence of various equivalents of amine.
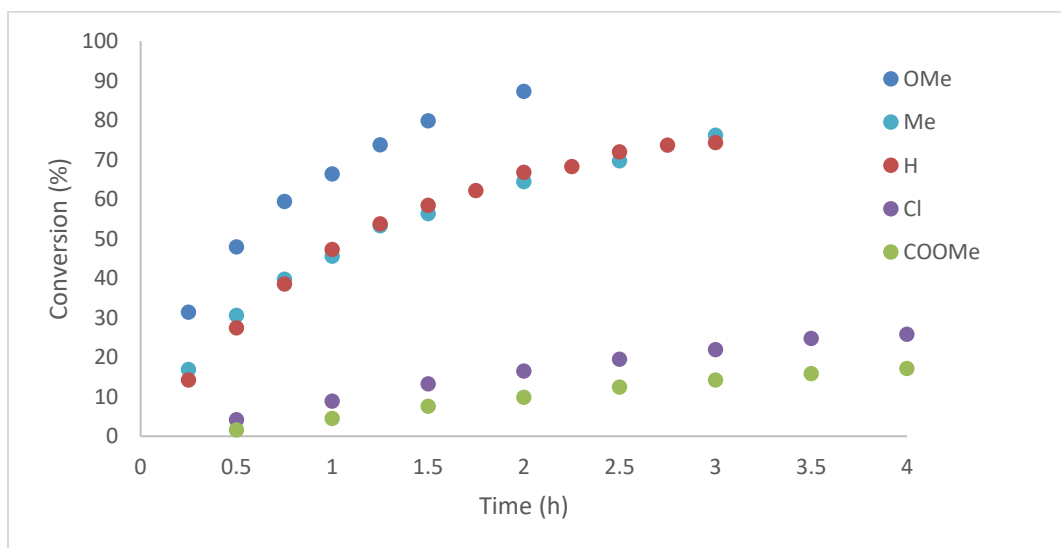
Figure S3.39: Progress of the cyclonickelation for various 3-X-$C_6C_4OP(i$-Pr$)_2$ in MeCN at 80 °C (X = OMe, Me, H, Cl and COOMe).

Figure S3.40: Plot of ln(1-conv.) as a function of time, and rate constants for various 3-X-$C_6H_4OP(i\text{-}Pr)_2$ in MeCN at 80 °C (X = OMe, Me, H, Cl and COOMe).
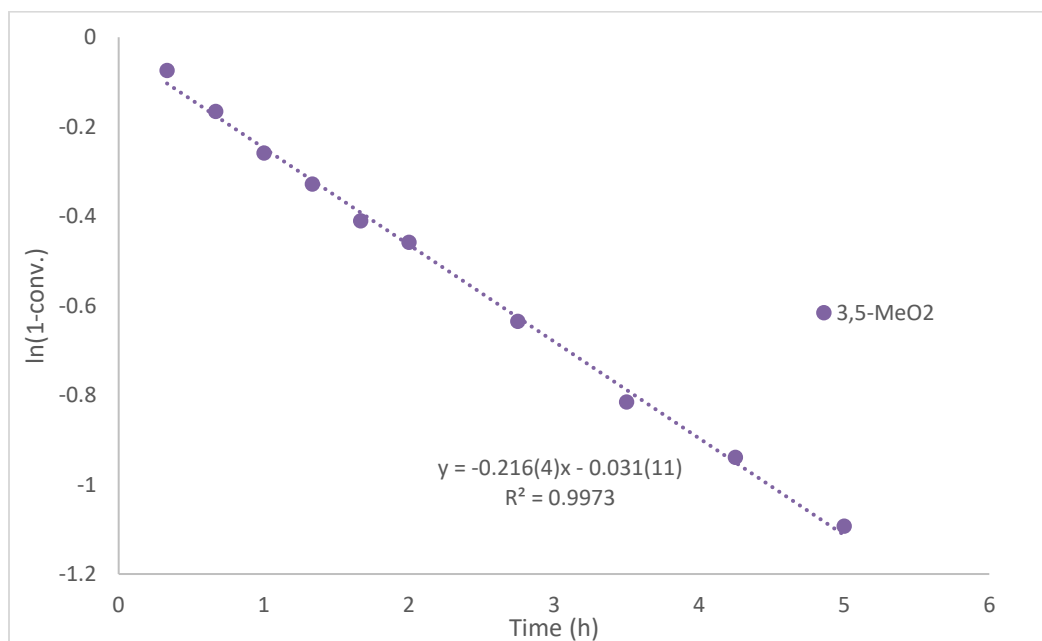
Figure S3.41: Plot of ln(1-conv.) as a function of time, and rate constant for the di-substituted ligand 3,5-MeO_2-$C_6H_3OP(i\text{-}Pr)_2$ in MeCN at 70 °C.
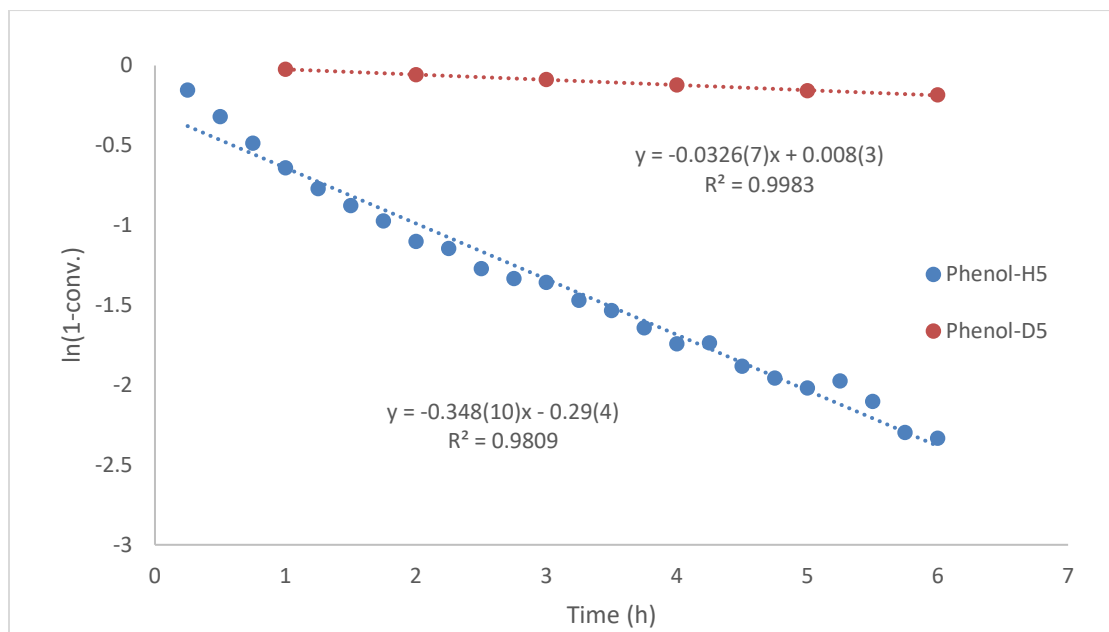
Figure S3.42: Plot of ln(1-conv.) as a function of time and rate constants for the cyclonickelation of $C_6H_5OP(i\text{-}Pr)_2$ and its deuterated parent $C_6D_5OP(i\text{-}Pr)_2$ in MeCN at 80 °C displaying a high Kinetic Isotope Effect.
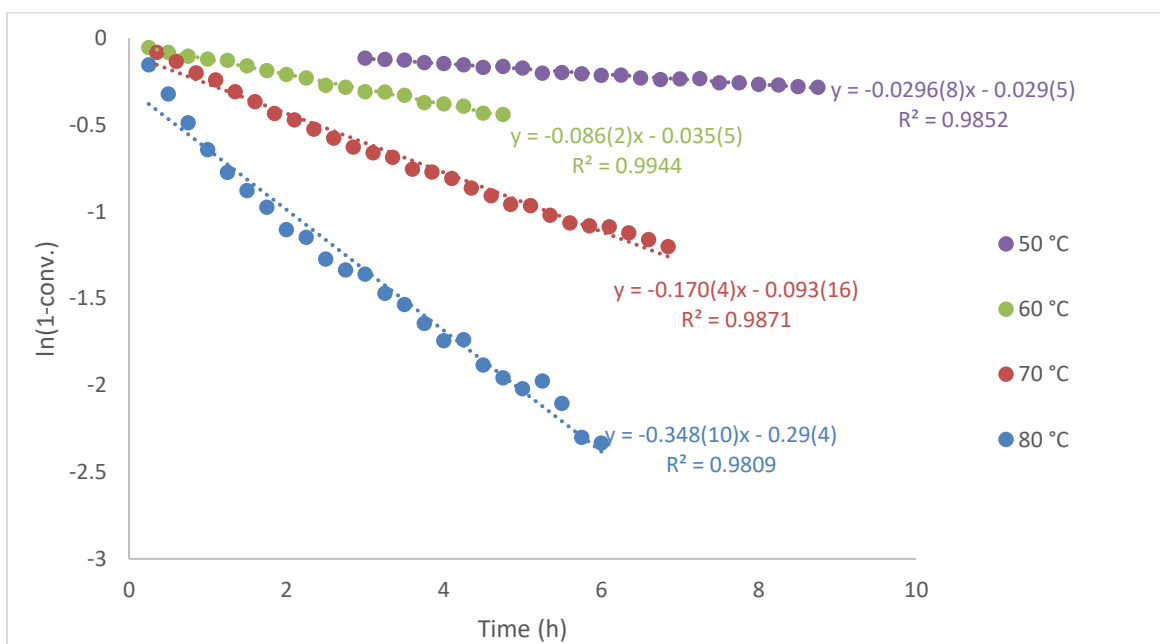
Figure S3.43: Plot of ln(1-conv.) as a function of time and rate constants for the cyclonickelation of $C_6H_5OP(i\text{-}Pr)_2$ in MeCN at temperatures ranging from 50 °C to 80 °C.

S3.6 Details on DFT analysis

a. General information

Procedure for the optimization and determination of the Gibbs energy

All DFT calculations were performed using Gaussian 16 on Grex server from Westgrid (provided by Compute Canada/Calcul Canada). Geometry optimizations were carried out using the mixed basis set 6-31g** for all light atoms (C, H, O, P, N) and def2TZVP for Ni and Br. The M06 functional was exploited in implicit acetonitrile solvent using the SMD model. Local minima were assessed by convergence and the absence of imaginary frequencies in the frequency calculation. Transition states were assessed by the existence of a single imaginary frequency along the expected reaction coordinate and have been linked to intermediates by the Intrinsic reaction coordinates routine[10]. The Gibbs free energy was calculated by the sum of correction to Gibbs free energy outputted from the frequency calculation and the electronic energy found by a single point calculation with def2TZVP for all atoms on the optimized geometries. Re-optimization with B3LYP were started from the geometries optimized with M06, using the same basis sets and methods to determine the Gibbs free energies.

Special cases of the thermochemistry of ^{1}TS-oa-x.

For the transition states leading to the products of oxidative addition, the thermal energy was found slightly below that of the related products of oxidative addition, which is unrealistic. Since the structures are really close geometrically as well as energetically, this is likely an effect of the under-estimation of the thermal correction to Gibbs free energy on the saddle point. To solve this problem, we calculated the energy of the transition states from their related Ni(IV) intermediates considering only the difference in the electronic energy computed with def2TZVP for all atoms.

That is to say: $G(TS^{\ddagger}) = G(Oxadd) + \Delta E_{electronic} = G(Oxadd) + E_{electronic}(TS^{\ddagger}) - E_{electronic}(Oxadd)$

In other words, we applied the same Gibbs free energy correction to the transition state and to the closely related intermediate.

---

[10] In order to overcome the flatness of the surface around the saddle point for ^{1}TS-*trans*-iPr-1-dissoc, the step size for the IRC analysis was raised to 0.5 Bohr (as compared to 0.1 Bohr as default).

Calculation of the basicity of the ligands.

The experimental pK$_a$s of HBr[11] and [Et$_3$NH$^+$][12] have been reported to be 5.5 and 18.8 respectively. Thus, the protonation of Et$_3$N by HBr at 298 K in MeCN was determined to be exergonic with:

$$\Delta G_{Et3N\cdot HBr} = -RT \cdot \ln(10^{pKa_{Et3NH+}-pKa_{HBr}}) = -8.314 \cdot 298 \cdot \ln(10^{18.8-5.5})$$

$$= -75847 \, J.mol^{-1} = -18.1 \, kcal.mol^{-1}$$

For consistency, we used this experimental value in order to determine the exergonicity of the quenching of HBr by the ligands L. To do so, and to limit the errors on invoking very different species, we exploited the following Hess law which allowed us to only compute Et$_3$N, Et$_3$NH$^+$ as well as L and LH$^+$:

$$Et_3N \ + \ HBr \ \leftrightarrow \ Et_3NH^+ \ + \ Br^- \qquad \Delta G_{Et3N\cdot HBr}$$

$$Et_3NH^+ \ + \ L \ \leftrightarrow \ Et_3N \ + \ LH^+ \qquad \Delta G_{Et3NH\cdot L}$$

$$\overline{L \ + \ HBr \ \leftrightarrow \ LH^+ \ + \ Br^- \qquad\qquad \Delta G_{L\cdot HBr}}$$
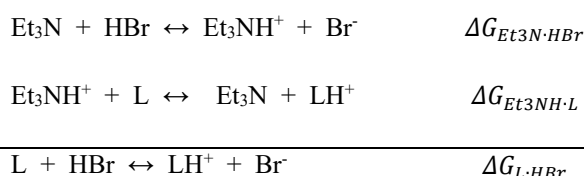
The Gibbs free energy for the protonation of ligands L with HBr was thus computed by:

$$\Delta G_{(L\cdot HBr)} = \Delta G_{(Et3N\cdot HBr)} - \Delta G_{(E3NH\cdot L)} = \Delta G_{(Et3N\cdot HBr)} - [G_{Et3N} + G_{LH+} - G_{Et3NH+} - G_L]$$

Table S3.2 Computed free Gibbs energies of protonation of the PMe$_2$ and P(i-Pr)$_2$ ligands with HBr

		M06		B3LYP	
		L = PhOPMe$_2$	L = PhOP(i-Pr)$_2$	L = PhOPMe2	L = PhOP(i-Pr)$_2$
G (Ha)	Et3N	-292.1219604		-292.3644312	
	Et3NH$^+$	-292.5766442		-292.8248255	
	L	-727.8004964	-884.8754323	-728.1294082	-885.3291508
	LH$^+$	-728.2417720	-885.3166771	-728.5734083	-885.7744803
ΔG(Et3NH-L) (Ha)		0.0134082	0.0134390	0.0163943	0.0150648
ΔG(Et3NH-L) (kcal/mol)		8.41	8.43	10.29	9.45
ΔG(L-HBr) (kcal/mol)		-9.69	-9.67	-7.81	-8.65

[11] Raamat, E.; Kaupmees, K.; Ovsjannikov, G.; Trummal, A.; Kütt, A.; Saame, J.; Koppel, I.; Kaljurand, I.; Lipping, L.; Rodima, T.; Pihl, V.; Koppel, I. A.; Leito, I., Acidities of strong neutral Brønsted acids in different media. *Journal of Physical Organic Chemistry* **2013,** *26* (2), 162-170.

[12] Kaljurand, I.; Kütt, A.; Sooväli, L.; Rodima, T.; Mäemets, V.; Leito, I.; Koppel, I. A., Extension of the Self-Consistent Spectrophotometric Basicity Scale in Acetonitrile to a Full Span of 28 pKa Units: Unification of Different Basicity Scales. *The Journal of Organic Chemistry* **2005,** *70* (3), 1019-1028.

Determination of the Kinetic Isotope Effect.

The ground state ^{3}*tet*-iPr-1 and the kinetic barriers ^{1}TS-*trans*-iPr-1-dissoc and ^{1}TS-*trans*-iPr-1-dep were subjected to a frequency analysis with all 5 aromatic protons replaced by deuterons. Revision of the thermal correction to Gibbs energy for each of them allowed us to determine the barriers $\Delta G_D^{\ddagger}$ with the deuterated species. According to the transition state theory, the first order rate constant is:

$$k = \kappa \frac{k_B T}{h} e^{\frac{-\Delta G^{\ddagger}}{RT}}$$

Thus, the KIE was calculated as: $\frac{k_H}{k_D} = \exp\left(\frac{-\Delta G_H^{\ddagger} + \Delta G_D^{\ddagger}}{RT}\right)$

Table S3.3: Determination of the KIE for the dissociation and the deprotonation on the 1trans-iPr surface, at 298.15 K, at the M06 level of theory

	^{3}*tet*-1	^{1}TS-*trans*-iPr-1-dissoc	^{1}TS-*trans*-iPr-1-dep
$E_{electronic}$ (Ha)	-7674.426148	-7674.390054	-7674.382380
Corr. To G_H (Ha)	0.270253	0.275201	0.268660
Corr. To G_D (Ha)	0.253475	0.258590	0.253896
$\Delta G_H^{\ddagger}$ (Ha)		0.041043	0.042176
$\Delta G_D^{\ddagger}$ (Ha)		0.041210	0.044190
$\Delta G_H^{\ddagger}$-$\Delta G_D^{\ddagger}$ (Ha)		-0.000167	-0.002014
$\Delta G_H^{\ddagger}$-$\Delta G_D^{\ddagger}$ (kJ)		-0.4385	-5.2878
k_H/k_D		1.19	8.44

b. Energies for intermediates and transition states optimized with M06

	Corr. To E_{Gibbs}	$E_{electronic}$	G (Ha)	ΔG (Ha)	ΔG (kcal/mol)
MeCN	0.022149	-132.719325369	-132.69717637		
Et$_3$N	0.170306	-292.292266372	-292.12196037		
Et$_3$NH$^+$	0.184979	-292.761623230	-292.57664423		
HBr	-0.013249	-2574.66935869	-2574.68260769		
PhOPMe$_2$	0.132611	-727.933107359	-727.80049636		
PhOPMe$_2$H$^+$	0.144708	-728.386480011	-728.24177201		
PhOP(i-Pr)$_2$	0.238682	-885.114114279	-884.875432279		
PhOP(i-Pr)$_2$H$^+$	0.249999	-885.566676129	-885.316677129		
^{1}*trans*-1	0.166649	-7517.24979495	-7517.08314595	0	0
^{1}*cis*-1	0.169492	-7517.24515170	-7517.07565970	0.00748625	4.70
^{3}*tet*-1	0.164069	-7517.24559958	-7517.08153058	0.00161537	1.01
^{3}*tbp*-1-eq	0.201031	-7649.97084649	-7649.76981549	0.01050683	6.59
^{3}*tbp*-1-ax	0.199464	-7649.96917307	-7649.76970907	0.01061325	6.66
^{1}Oxadd-1-m*cis*ax	0.16548	-7517.1787030	-7517.01322302	0.06992293	43.88
^{1}TS-oa-1-m*cis*ax	0.16548	-7517.1775531	-7517.01207305	0.07107290	44.60
^{1}Oxadd-1-m*trans*	0.165141	-7517.1714218	-7517.00628077	0.07686518	48.23
^{1}TS-oa-1-m*trans*	0.165141	-7517.1710226	-7517.00588157	0.07726438	48.48
^{1}TS-*trans*-1-dep	0.161054	-7517.20215390	-7517.04109990	0.04204605	26.38
^{1}TS-*cis*-1-dep	0.161536	-7517.19329327	-7517.03175727	0.05138868	32.25
^{3}TS-*tet*-1-dep	0.155616	-7517.16574949	-7517.01013349	0.07301246	45.82
^{3}*tet*-1-Ionpair	0.161764	-7517.18738484	-7517.02562084	0.05752511	36.10
^{1}*trans*-2	0.158181	-4942.533516	-4942.37533473	0.02520353	15.82
^{1}*cis*-2	0.159902	-4942.52631	-4942.36640759	0.03413067	21.42
^{3}*tet*-2	0.153419	-4942.501081	-4942.34766200	0.05287626	33.18
^{1}*cis*-iPr-1	0.276973	-7674.42408175	-7674.14710875	0.00878673	5.51
^{1}*trans*-iPr-1	0.27522	-7674.42526810	-7674.15004810	0.00584738	3.67
^{3}*tet*-iPr-1	0.270253	-7674.426148	-7674.15589548	0	0
^{1}TS-iPr-1-dissoc	0.275201	-7674.390054	-7674.11485264	0.04104284	25.75
^{1}*trans*-iPr-1-Ionpair	0.272957	-7674.389478	-7674.11652056	0.03937492	24.71
^{1}*cis*-iPr-1-Ionpair	0.271853	-7674.38070844	-7674.10885544	0.04704004	29.52
^{1}TS-iPr-1-dep	0.268660	-7674.38237975	-7674.11371975	0.04217573	26.47
^{3}*tet*-iPr-1-Ionpair	0.267148	-7674.36869922	-7674.10155122	0.05434426	34.10
^{1}*trans*-iPr-2	0.267515	-5099.71663180	-5099.44911680	0.02417099	15.17
^{1}*cis*-iPr-2	0.266196	-5099.71057084	-5099.44437484	0.02891295	18.14
^{3}*tet*-iPr-2	0.261033	-5099.68467620	-5099.42364320	0.04964459	31.15

c. Energies of re-optimized structures with B3LYP

	Corr. To E_{Gibbs}	$E_{electronic}$	G (Ha)	ΔG (Ha)	ΔG (kcal/mol)
MeCN	0.022363	-132.8205387	-132.7981757		
Et$_3$N	0.171351	-292.5357822	-292.3644312		
Et$_3$NH$^+$	0.186995	-293.0118205	-292.8248255		
HBr	-0.013316	-2574.792702	-2574.806018		
PhOPMe$_2$	0.13296	-728.2623682	-728.1294082		
PhOPMe$_2$H$^+$	0.144544	-728.7179523	-728.5734083		
PhOP(i-Pr)$_2$	0.239285	-885.5684358	-885.3291508		
PhOP(i-Pr)$_2$H$^+$	0.250676	-886.0251563	-885.7744803		
^{1}*trans*-1	0.167432	-7517.994523	-7517.827091	0.01315193	8.25
^{1}*cis*-1	0.168526	-7517.990344	-7517.821818	0.01842482	11.56
^{3}*tet*-1	0.161826	-7518.002069	-7517.840243	0	0
^{3}*tbp*-1-eq	0.201558	-7650.820275	-7650.618717	0.019701357	12.36
^{3}*tbp*-1-ax	0.201312	-7650.821128	-7650.619816	0.018602167	11.67
^{1}Oxadd-1-m*cis*ax	0.166763	-7517.924489	-7517.757726	0.08251623	51.78
^{1}TS-oa-1-m*cis*ax	0.164446	-7517.923326	-7517.75888	0.08367982	52.51
^{1}Oxadd-1-m*trans*	0.165976	-7517.917688	-7517.751712	0.0885302	55.55
^{1}TS-oa-1-m*trans*	0.16523	-7517.916576	-7517.751346	0.08964308	56.25
^{1}Oxadd-1-m*cis*eq	0.166989	-7517.923664	-7517.756675	0.08356735	52.44
^{1}TS-oa-1-m*cis*eq	0.166411	-7517.923563	-7517.757152	0.0836691	52.50
^{1}TS-*trans*-1-dep	0.160817	-7517.946721	-7517.785904	0.05433873	34.10
^{1}TS-*cis*-1-dep	0.161876	-7517.939239	-7517.777363	0.06287936	39.46
^{1}*cis*-Ionpair	0.166186	-7517.948284	-7517.782098	0.05814496	36.49
^{3}TS-*tet*-1-dep	0.156559	-7517.921618	-7517.765059	0.0751838	47.18
^{3}*tet*-1-Ionpair	0.160605	-7517.949488	-7517.788883	0.05136002	32.23
^{1}*trans*-2	0.159983	-4943.159661	-4942.999678	0.03454634	21.68
^{1}*cis*-2	0.159497	-4943.153574	-4942.994077	0.04014827	25.19
^{3}*tet*-2	0.155093	-4943.139318	-4942.984225	0.04999964	31.38
^{1}*cis*-iPr-1	0.275834	-7675.290256	-7675.014422	0.01693887	10.63
^{1}*trans*-iPr-1	0.275355	-7675.291193	-7675.015838	0.01552206	9.74
^{3}*tet*-iPr-1	0.271305	-7675.302665	-7675.03136	0	0.00
^{1}TS-iPr-1-dissoc	0.275683	-7675.257034	-7674.981351	0.0500099	31.38
^{1}*trans*-iPr-1-Ionpair	0.273365	-7675.256867	-7674.983502	0.04785848	30.03
^{1}*cis*-iPr-1-Ionpair	0.271689	-7675.248946	-7674.977257	0.05410325	33.95
^{1}TS-iPr-1-dep	0.269817	-7675.24793	-7674.978113	0.05324742	33.41
^{3}*tet*-iPr-1-Ionpair	0.265679	-7674.979852	-7674.714173	0.04350028	27.30
^{1}*trans*-iPr-2	0.267874	-5100.463894	-5100.19602	0.02932221	18.40
^{1}*cis*-iPr-2	0.267514	-5100.459406	-5100.191892	0.03345112	20.99
^{3}*tet*-iPr-2	0.261769	-5100.444073	-5100.182304	0.04303814	27.01

Scheme S3.2: Proposed energy surface for the nickelation of PhOPMe₂ at the B3LYP level of theory. Energies are expressed in kcal/mol.
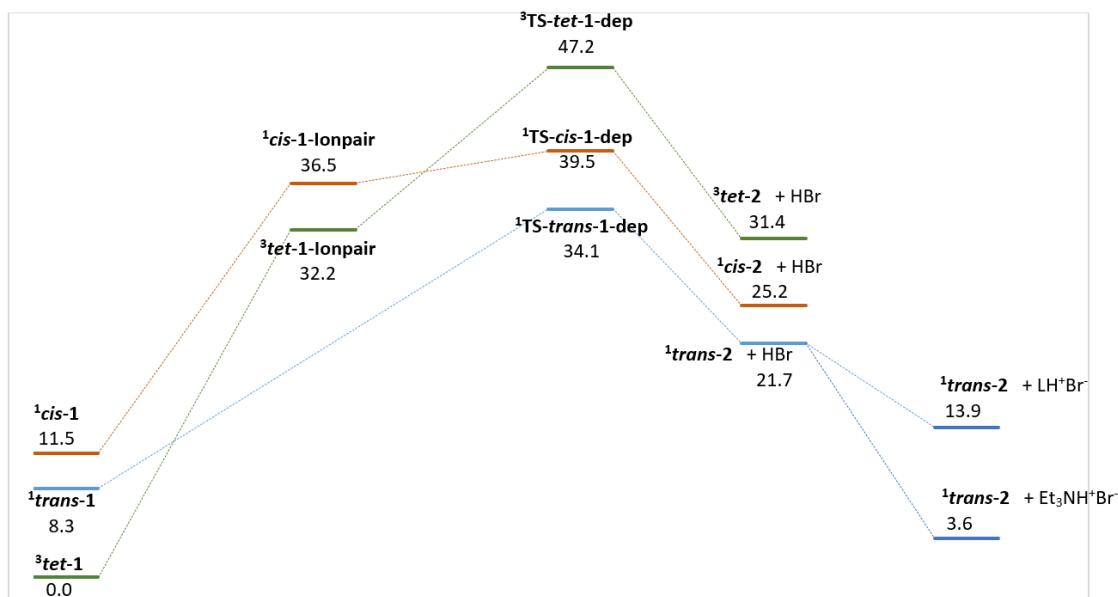
Scheme S3.3 Proposed energy surface for the nickelation of PhOP(*i*-Pr)₂ at the B3LYP level of theory. Energies are expressed in kcal/mol.
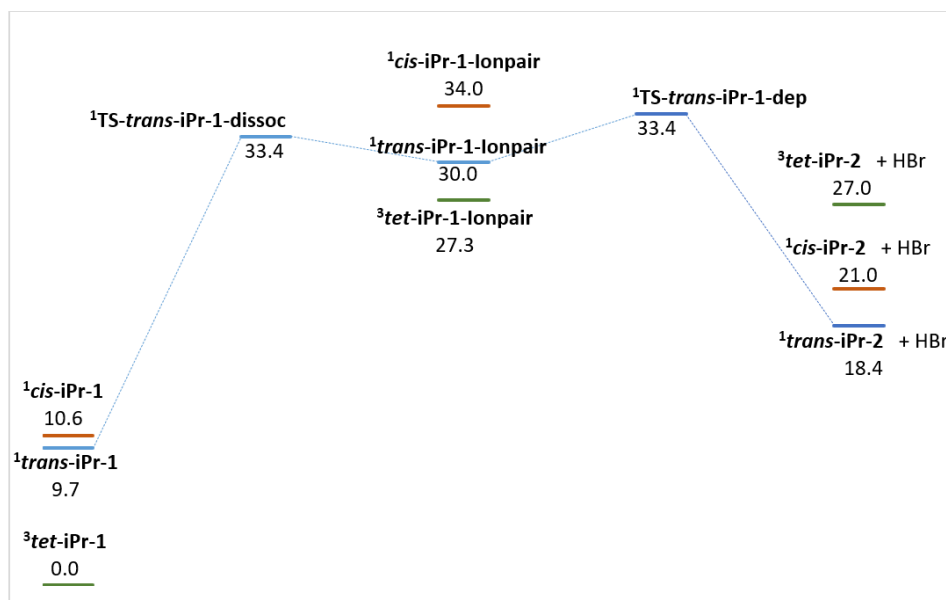
Chapitre 4 – C−H Nickelation of Naphthyl Phosphinites: Electronic and Steric Limitations, Regioselectivity, and Tandem C−P Functionalization

Loïc P. Mangin[a] and Davit Zargarian[a]*

[a] Département de Chimie, Université de Montréal, Montréal, Canada H3T 1J4

4.1 Abstract

This report describes the results of a study on the C−H nickelation of phosphinites derived from variously substituted 1- and 2-naphthols, as well as the C−P functionalization of the Ni-naphthyl moiety arising from the C−H cyclonickelation. Refluxing 4-X-1-naphthyl phosphinites (X = H, **1a**; MeO, **1b**; Cl, **1c**) with $\{(i\text{-PrCN})NiBr_2\}_n$ and Et_3N in acetonitrile gave the nickelacyclic complexes $\{(\kappa^P,\kappa^C\text{-}4\text{-X-1-OP}(i\text{-Pr})_2\text{-naphth-2-yl})Ni(\mu\text{-Br})\}_2$, **2a-c**, resulting from cyclonickelation at the C2−H, whereas cyclonickelation of the 2-naphthyl phosphinite analogue **1e** under the same conditions occurred at C3−H. Placing a Me substituent at the C3 position of a 2-naphthyl

phosphinite (**1f**) led to a very sluggish nickelation at the C1−H position, whereas 2-ethyl-1-naphthyl phosphinite (**1d**) failed to nickelate at C8−H. H/D scrambling tests conducted on the deuterated analogue of **1a** (**1a-D7**) confirmed that nickelation occurs exclusively at C2. Similar tests conducted on deuterated analogues of alkyl-substituted 1- and 2-naphthyl phosphinites showed that no nickelation takes place at C_{sp^3}−H sites of the alkyl substituents. In contrast, very facile C−H nickelation was observed with 2-allyl-1-naphthyl phosphinite **1g** to give a product featuring a π-allyl-Ni moiety. A series of tests have shown that the nickelation of substrates **1a**, **1e**, and **1f** can be accelerated dramatically at 120-160 °C. On the other hand, conducting the high temperature reaction of **1a** in the absence of Et$_3$N resulted in an unanticipated and interesting C−P functionalization of the C2−H site, thus generating a *i*-Pr$_2$P-substituted bidentate phosphine-phosphinite. A similar tandem C−H nickelation/C−P(O) functionalization was also observed at the C8−H position of substrate **1d**. The mechanisms of these functionalization reactions have been probed and outlined.

4.2 Introduction

Catalytic processes based on non-redox-type C−H metalation and tandem functionalization have gained increasing prominence in the drive toward sustainable chemical synthesis.[1] Historically, the early success of these processes was due in large part to the use of noble metal-based precursors, and to some extent the supremacy of these metals continues today.[2] However, the past decade has witnessed the development of many efficient C−H functionalization processes that are catalyzed by precursors based on the more abundant 3d metals.[3] In addition to the potential cost advantages of the latter relative to their 4d and 5d congeners, continued investigations of C−H metalation-functionalization chemistry based on 3d metals also open the door to the discovery of new and complementary reactivity patterns which can be exploited to create exciting opportunities in commercial developments.

Our group's contributions to this field have focused on the C−H nickelation of phosphinites derived from phenol and its substituted derivatives. In an initial report, we showed that orthometalation of ArOP(*i*-Pr)$_2$ is feasible with the Ni(II) precursor {(*i*-PrCN)NiBr$_2$}$_n$.[4] The isolation and structural characterization of the resulting cyclonickelated species have allowed us to gain some understanding of their thermal stabilities and reactivities in C−C and C−heteroatom functionalization (**Scheme 4.1**, **A**).

Scheme 4.1. C−H nickelation with Aryl Phosphinites.
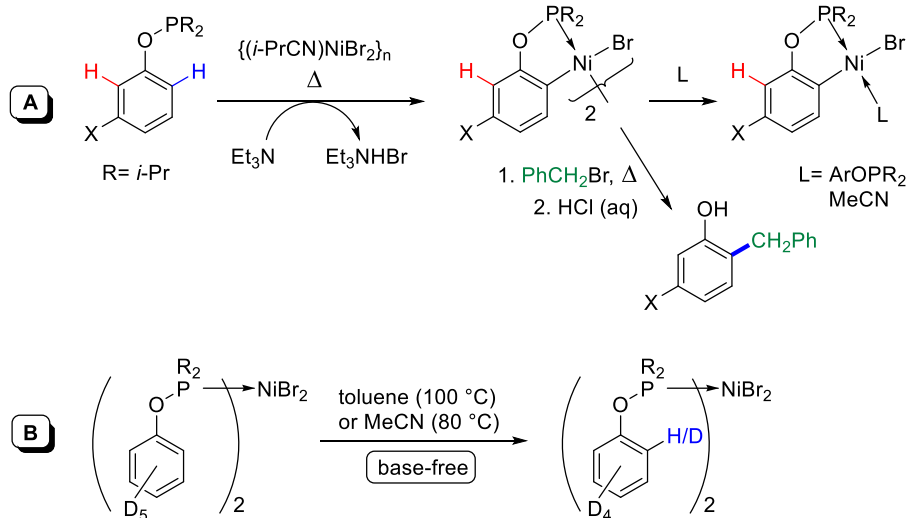
We have also delineated the impact of reaction solvent, external base, and aryl substituents on the kinetics and energetics of C−H nickelation.[5] It was found, for instance, that C−H bond rupture is rate determining ($k_H/k_D \approx 11$), and that nickelation proceeds faster with substrates bearing electron-releasing substituents.[6] Significantly, D-labelling studies and rate measurements indicated that the C−H nickelation step occurs reversibly and independently of the presence of an external base (**Scheme 4.1**, **B**). On the other hand, *isolation* of the nickelacyclic complex resulting from the C−H metalation step requires a sufficiently strong external base, because the acid generated during the nickelation step protonates the newly formed Ni-aryl moiety to reverse the C−H nickelation.[5] Finally, studying the C−H nickelation of aryl phosphinites based on 3-substituted phenols has revealed that the regiochemistry of orthonickelation is strongly influenced by steric factors.[6]

In continuation of our previous investigations, we have begun to examine the C−H nickelation of phosphinites derived from 1- and 2-napththols. These substrates offer two potentially reactive C−H sites, but the steric and electronic properties of these sites of reactivity are more dissimilar than in phosphinites derived from phenol. For instance, nickelation of 1-naphthyl phosphinite at C2 would give a 5-membered nickelacycle, whereas reaction at C8 would generate a 6-membered nickelacycle. In the case of 2-naphthyl phosphinite, nickelation at both *ortho* C−H sites (C1 and C3) would generate 5-membered nickelacycles, but these two products would be reasonably expected to display different reactivities based on their steric and electronic differences.

There is scant literature on the metalation of naphthyl phosphinites, but the few precedents that exist do offer us an indication of which C−H site might be more favorable to metalation. Bedford has shown, for example, that metalation of 1-naphthyl phosphinites with Rh occurs mainly at the C2−H site, but it can also take place to a lesser extent at the C8 site to give a 6-membered rhodacycle.[7] The analogous reactivity with 2-naphthyl phosphinites takes place at both C1−H and C3−H sites.[9] In the case of Pd, metalation of 1-naphthoxide (as opposed to its phosphinite) has been reported to occur at C8−H, whereas palladation of 2-naphthoxides takes place exclusively at C1, presumably generating a 4-membered palladacycle.[8] The above considerations prompted us to study the nickelation of naphthyl phosphinites and compare the results to the nickelation of phenyl phosphinites.

The present contribution reports the cyclonickelation of 1- and 2-naphthyl phosphinites and some of their substituted derivatives. We have found that nickelation of 1-naphthyl phosphinites occurs at C2 in preference over C8, whereas the C3 site is favored over C1 for 2-naphthyl phosphinites. In the latter case, blocking the favored pathway allowed us to induce nickelation at the less favored C1−H site, but a similar strategy was much less successful for 1-naphthyl phosphinite. In some cases, conducting the reactions at high temperatures led to accelerated C−H nickelation rates and a potentially useful tandem C−P functionalization.

4.3 Results and Discussion

4.3.1 C−H nickelation of 1-naphthyl phosphinites

Our studies began by examining the reactivities of 1-naphthyl phosphinites under the reaction conditions optimized for the C−H nickelation of substrates derived from substituted phenols. Thus, the substrate being studied was refluxed in acetonitrile in the presence of $\{(i\text{-PrCN})NiBr_2\}_n$ and Et_3N, the latter serving the purpose of quenching the HBr generated in-situ at the C−H nickelation step. **Scheme 4.2** shows the acetonitrile adducts of the cyclonickelated products generated from 1-naphtyl phosphinites **1a-1c**.

Scheme 4.2. The Nickelation of 4-X-1-Naphthyl Phosphinites.

X = H (**1a**)
OMe (**1b**)
Cl (**1c**)

2a : 16 h, 74%
2b : 20 h, 84%
2c : 30 h, 77%

Not observed
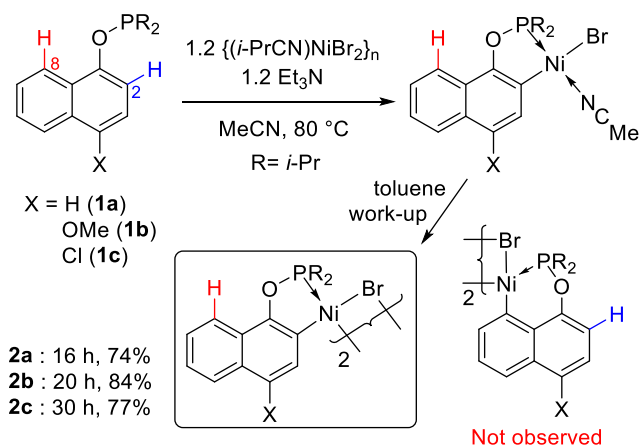
Complete conversions took place over 16-30 h, which was confirmed by the ^{31}P NMR spectra of the final reaction mixtures displaying new singlet resonances at 194-197 ppm, the chemical shift region characteristic of cyclonickelated ArOP(i-Pr)$_2$.[5] The green reaction mixtures containing the cyclonickelated products were then worked up in toluene to give the target dimeric complexes as orange powders in 74-84% isolated yields. Complete characterization of **2a-2c** by NMR and single crystal XRD confirmed that the desired cyclonickelation had taken place at the C2 to give 5-membered nickelacycles (**Fig. 4.1**); the putative compounds arising from nickelation at the C8 position and featuring 6-membered nickelacycles were not observed.
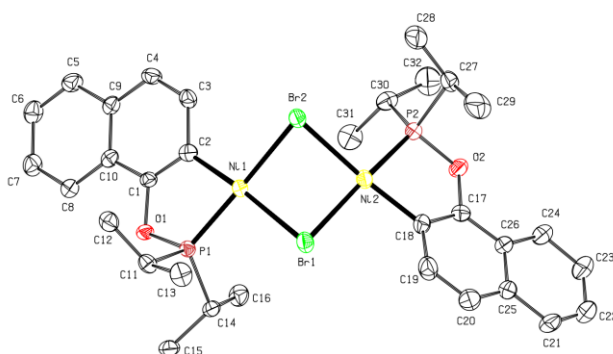
Figure 4.1. Top view of the molecular diagram for complex **2a**. Thermal ellipsoids are shown at the 50% probability level; hydrogen atoms are omitted for clarity.

The solid-state structures of **2a-c** will be discussed in the last section of this report, but the reaction times required for their formation and the isolated yields merit some comment here. The yields obtained for complexes **2a-2c** are somewhat higher than those obtained for the analogous dimeric complexes derived from phenol (67%), 3-MeO-phenol (60%), and 3-Cl-phenol (71%). We believe that these higher yields are due to the lower solubility of these complexes in Et_2O and Hexanes, which facilitates product isolation by precipitation from these solvents.

As for the different reaction times required for the formation of **2a-2c**, although we have not made systematic measurements of reaction rates in this study, monitoring the ^{31}P NMR spectra of the reaction mixtures showed that the nickelation times varied as a function of substituents X, going to completion within 20 h for X = H and OMe, but requiring longer times for X = Cl. The observation of faster nickelation for **2a** and **2b** echoes our previous results on the faster nickelation of aryl phosphinites bearing electron-rich substrates (Hammett slope of –4).6

The observation of exclusive nickelation at C2 for **1a-1c** prompted us to ask if the nickelation can be forced to occur at the alternative C8 site. This was examined by testing the C−H nickelation of 2-Et-1-naphthyl phosphinite, **1d**,[9] in which the C2 site is blocked by a substituent. This substrate was subjected to the standard cyclonickelation conditions at 80 °C for 3 days, to no avail: analysis of the final reaction mixture by ^{31}P NMR spectroscopy showed no signal in the 190–210 ppm range, implying no nickelation (**Scheme 4.3**).

Scheme 4.3. Inertness of 2-Ethyl-1-Naphthyl Phosphinite Toward Nickelation.
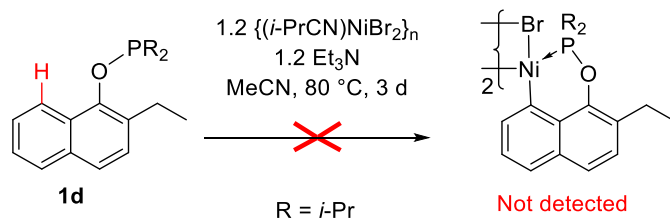
The issue of cyclonickelation regioselectivity with 1-naphthyl phosphinites, i.e., reactivity at C2 vs C8 sites, was further examined using H/D scrambling experiments. This idea was inspired from H/D scrambling experiments we carried out in a previous study on the cyclonickelation mechanism of aryl phosphinites.6 Thus, heating $C_6D_5OPR_2$ and $\{(i\text{-PrCN})NiBr_2\}_n$ in CH_3CN or protio-toluene in the absence of external base led to partial incorporation of H into the *ortho* C−D sites of the

phosphinite (**Scheme 4.1, B**). This allowed us to conclude that nickelation occurs independently of external base, but the in-situ generated DBr can undergo D/H exchange with the solvent to generate HBr, which then protonates the cyclonickelated species to generate $2\text{-H-}C_6D_4OPR_2$ (reversible nickelation).

By analogy to the above approach, we set out to conduct a D/H scrambling experiment aimed at establishing whether nickelation of 1-naphthyl phosphinite might be taking place at the C8−H position. To do this, we prepared D_7-1-naphthyl-$OP(i\text{-Pr})_2$ (**1a-D₇**)[9] and used it to prepare the precursor complex *trans*-$\{(D_7$-1-naphthyl-$OP(i\text{-Pr})_2\}_2NiBr_2$ (**3a-D₇**), which was subsequently heated in CH_3CN for 1 day at 80 °C (**Scheme 4.4**).

Scheme 4.4. Testing D/H Scrambling In 1-Naphthyl Phosphinite.
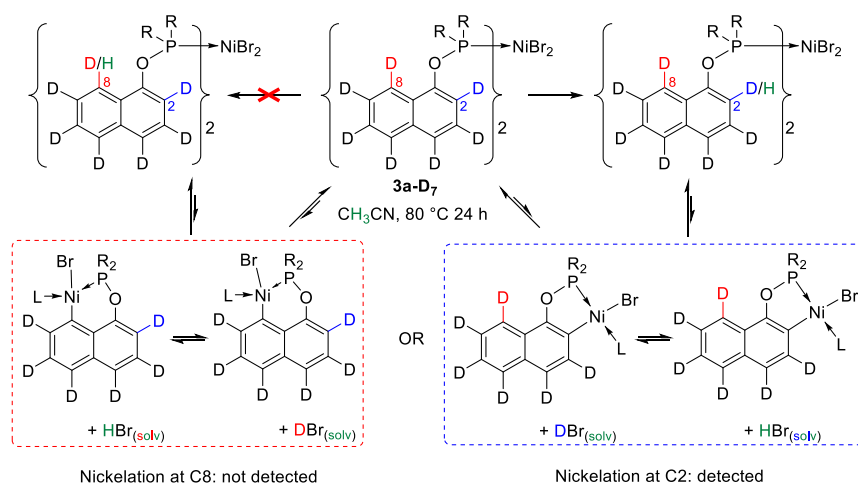
Cooling the final reaction mixture to –35 °C allowed us to isolate the product by crystallization, and ¹H NMR analysis in $CDCl_3$ revealed 53% H-incorporation into the C2 position (**Fig. S137**).[10] H-incorporation into C8 was not detected even after 3 days of heating. This establishes that the formation of the expected 6-membered nickelacycle is either kinetically not allowed in these conditions or, if nickelation does take place at C8−H, the in-situ generated DBr reacts with the resulting Ni-C moiety to reverse nickelation faster than D/H exchange with the solvent.

4.3.2 C−H nickelation of 2-naphthyl phosphinites

Cyclonickelation of 2-naphthyl phosphinite, **1e**, proceeded even more sluggishly than the analogous nickelation of 1-naphthyl phosphinites **1a-1c**, requiring 60 h at 80 °C to go to completion (**Scheme 5**). Nevertheless, the ³¹P NMR spectrum of the final reaction mixture confirmed a clean

conversion of **1e** to a new species displaying a singlet at 197 ppm. Cooling the reaction mixture to room temperature gave yellow crystals, which were identified by XRD analysis as the acetonitrile adduct of the cyclonickelated compound (**2e-NCMe** in **Scheme 4.5**).

Scheme 4.5. Nickelation of 2-Naphthyl Phosphinite.
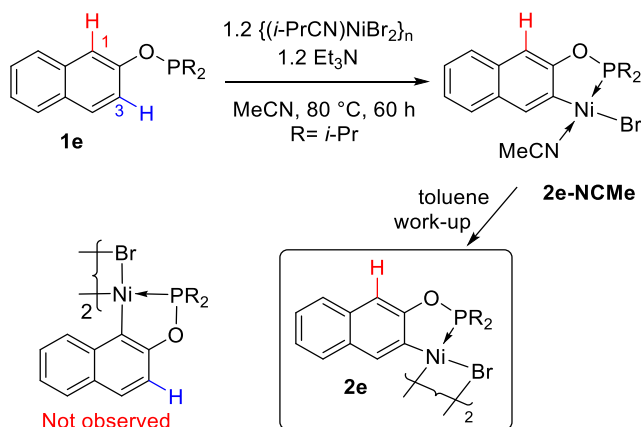
On the other hand, isolation of the corresponding dimeric complex **2e** by the usual work-up protocol was hampered by its limited solubility in toluene. Conducting the extraction process using hot toluene dissolved more of **2e-NCMe**, thus allowing us to isolate **2e** with 54% yield. However, despite multiple attempts to purify the crops of **2e** obtained from this approach, they always contained residual toluene impurities, whereas pure samples of the acetonitrile adduct **2e-NCMe** could be obtained from these in 80% yield.

C−H nickelation of **1e** could, in principle, occur at one of the two *ortho* C−H positions C1 and C3, but NMR characterization and XRD analyses of **2e** and **2e-NCMe** revealed C3 to be the only site of reactivity (**Scheme 4.5**, **Fig. 4.2**).
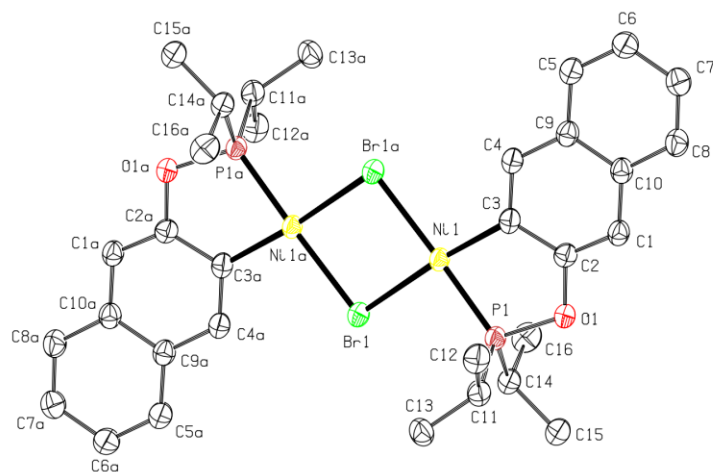
Figure 4.2. Top view of the molecular diagram for complex **2e**. Thermal ellipsoids are shown at the 50% probability level; hydrogen atoms are omitted for clarity.

This raised the question of whether the observed preference for nickelation at C3 vs. C1 originates from steric or electronic factors. Our previous investigations on the nickelation of phosphinites derived from 3-R-phenols had demonstrated that electronic factors can influence nickelation rates but not regioselectivity, whereas steric hindrance is the main determinant of which C−H is nickelated.[11,12] By analogy, it seems reasonable to conclude that the observed preference for nickelation of **1e** at C3 is due to lower steric hindrance at this site relative to C1. On the other hand, the much *slower* nickelation of this substrate compared to the analogous reactions with 1-naphthyl phosphinites **1a-1c** is likely caused by unfavorable electronic factors, the C3 position in 2-naphthols being less electron-rich relative to the C1 position.[13]

Similarly to the above-described probe of regioselectivity with substrate **1d** (**Scheme 4.3**), we examined the C−H nickelation of 3-Me-2-naphthyl phosphinite, **1f**, in which the more reactive C3 site has been blocked in order to see if C−H nickelation can be forced to occur at the less favored C1 site (**Scheme 4.6**).

Scheme 4.6. Nickelation of the 3-Me-2-Naphthyl Phosphinite **1f** and Molecular Diagram[a] of **2f-L**.
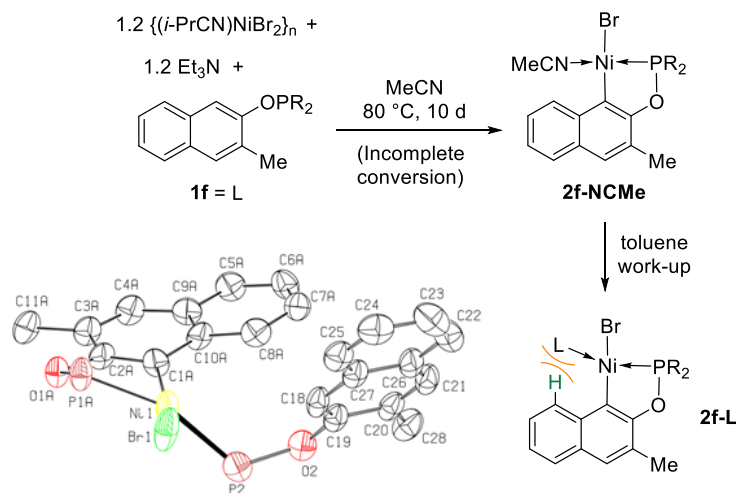
[a]Thermal ellipsoids are shown at the 50% probability level; hydrogen atoms and *P*-substituents are omitted for clarity.

Refluxing the emerald green acetonitrile mixture resulting from mixing **1f** with $\{(i\text{-PrCN})\text{NiBr}_2\}_n$ and Et_3N led to formation of a new species, but complete conversion was not achieved even after 10 days. NMR monitoring of the reaction progress showed a new ^{31}P singlet at 192 ppm, which we tentatively assign to **2f-NCMe** (**Scheme 4.6**). Integrating this peak against that of the internal standard $[n\text{-Bu}_4\text{N}][\text{PF}_6]$ showed conversions of about 10% and 16% after 3 and 7 days, respectively. Unfortunately, the standard work-up of the reaction mixture in toluene was complicated by the presence of significant quantities of the unreacted starting material; as a result, we obtained only a small quantity of crystals. Nevertheless, XRD analysis conducted on these crystals showed that this reaction generated a phosphinite adduct of the cyclonickelated species **2f-L** wherein nickelation of **1f** had taken place at C1 (**Scheme 4.6**).

Comparison of the C−H nickelation regioselectivities observed for the 2-naphthyl phosphinites **1e** and **1f** and the relative facility/sluggishness of these reactions inform us on the relative importance of sterics and electronics for these reactions. Thus, in substrate **1e** wherein C−H nickelation is, in principle, possible at both sites, reactivity takes place at C3 in preference over the more electron-rich C1 site; moreover, the nickelation of this substrate required 60 h. In contrast, with substrate **1f** wherein the C3 site is blocked by the Me substituent, the nickelation occurred at the alternative C1 site, but at a very sluggish pace.

We believe that the sluggishness of nickelation with **1f** results from the steric congestion at the C1 site. Consistent with this, the molecular diagram of **2f-L** (**Scheme 4.6**) revealed a very distorted structure in which the steric repulsion between C8−H and the phosphinite has caused a significant twist around the Ni−C1 axis. Indeed, the tetrahedral distortion parameter τ_4[14] around the Ni center was found to be 0.30 – 0.35, caused primarily by the out-of-plane displacement of the non metalated naphthyl phosphinite ligand. As a result, the dihedral angle of 50° for C10A-C1A-Ni1-P2 represents a significant out-of-plane rotation of the nickelated naphthyl ring.

4.3.3 Reactivity of *ortho* substituents

In the above discussions on the regioselectivity of C−H nickelation with alkyl-substituted 1- and 2-naphthyl phosphinites, the possibility of nickelation at the alkyl substituents was not considered. Discounting this possibility might be justified, because metalation of C_{sp^3}−H bonds is usually more difficult, and the resulting Ni-C_{sp^3} bonds are known to be less stable than Ni-C_{sp^2} bonds arising from metalation of C_{sp2}−H. Nevertheless, it seemed important to determine if C_{sp^3}−H nickelation can be kinetically accessible in naphthyl phosphinites bearing *ortho*-alkyl substituents. We have probed this possibility by using a H/D scrambling test analogous to the one shown in **Scheme 4.4** for studying C−H nickelation at C8 in **1a**.

Scheme 4.7. D/H Scrambling Tests with 1- and 2-Phosphinites Bearing α-Deuterated Alkyl Substituents.
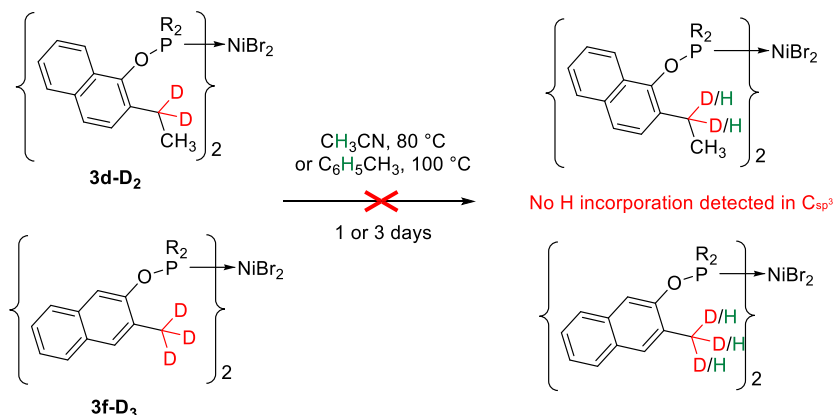
Stirring the deuterated analogue of **1d** with $\{(i\text{-PrCN})NiBr_2\}_n$ in dichloromethane at r.t. gave the target compound $\{2\text{-}CH_3CD_2\text{-}1\text{-naphthyl-OP}(i\text{-Pr})_2\}_2NiBr_2$,[9] **3d-D₂** (**Scheme 4.7**). Refluxing the latter in acetonitrile or toluene over extended reaction times (up to 3 days), followed by gradual cooling to –35 °C gave crystals after one day. Analysis of these crystals by ^{1}H NMR (CDCl₃)

confirmed that no H-incorporation had taken place into the α C_{sp^3}-D positions (**Scheme 4.7**). The analogous scrambling test was also conducted for the deuterated analogue of **1f**,[9] with the same results: ^{1}H NMR analysis of crystals of **3f-D$_3$** obtained after heating showed no H-incorporation into the α C_{sp^3}-D site (**Scheme 4.7**). We conclude, therefore, that nickelation of the C_{sp^3}H(D) sites in alkyl-substituted 1- or 2-naphthyl phosphinites is either not happening in our system or, if it is, the resulting nickelated product is simply too high in energy and reverts back to its starting form faster than the competing H/D exchange with the solvent.

The observed inertness of the alkyl substituents in **1d** and **1f** prompted us to ask if a more activated allylic/benzylic CH$_2$ moiety would get nickelated. To answer this question, we prepared substrate **1g**[9] and tested its C−H nickelation with {(*i*-PrCN)NiBr$_2$}$_n$ and Et$_3$N (**Scheme 4.8**: acetonitrile, 80 °C, 2h).

Scheme 4.8. C−H Nickelation of 2-Allyl-1-Naphthyl Phosphinite **1g** and Molecular Diagram[a] of **2g**.
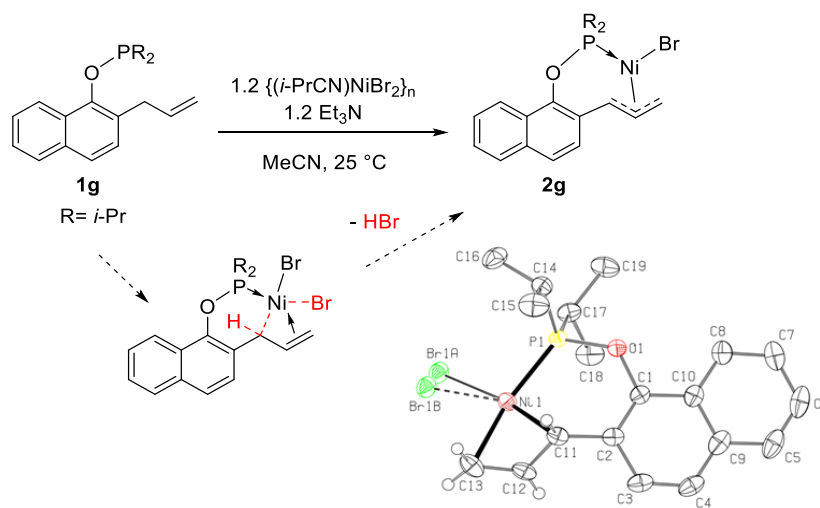
[a]Thermal ellipsoids are shown at the 50% probability level; non allylic hydrogen atoms are omitted for clarity.

This reaction did give a new species represented by a ^{31}P singlet at 201 ppm, which we ascribed to a nickelated species. However, there were also significant amounts of Ni black deposited on the walls of the reaction flask, implying that some of the putative nickelated complexes are prone to decomposition. Repeating the reaction at lower temperatures allowed us to promote the nickelation while avoiding thermal degradation. For instance, conducting the reaction with one equiv of Ni precursor and two equiv of Et$_3$N at r.t. over 16 h led to a cleaner nickelation. Work-up of the final

reaction mixture followed by crystallization in Et$_2$O/pentane gave orange crystals that were shown by XRD to be the monomeric complex **2g** featuring an η^3-π-allyl moiety (**Scheme 4.8**).

Complex **2g** features a 6-membered nickelacycle with a significantly longer Ni-C11 (1.983 and 1.972 Å)[15] and Ni-P bonds (2.145 and 2.134 Å) relative to other dimers featuring 5-membered nickelacycles. Moreover, the allyl moiety is less symmetrical than in 'free' π-allyl complexes of Ni(II)Br, and the naphthalene ring bends out of the mean plane around Ni by 25 – 37°.

Evidently, C−H nickelation at a methylenic C−H in **1g** is feasible and fairly facile, presumably due to the binding of the terminal olefin moiety of the substituent to the Ni(II) center; this would be akin to the C−H nickelation of a LXL′ pincer ligand, which is often more facile than a simple cyclonickelation.[16] Unfortunately, efforts to isolate the putative bidentate phosphinite-olefin intermediate shown in **Scheme 8** from 1:1 mixtures of **1g**:{(i-PrCN)NiBr$_2$}$_n$ yielded only the bis-phosphinite L$_2$NiBr$_2$ complex (**3g**).

4.3.4 Acceleration of C−H nickelation at high temperatures

The generally sluggish rate of C−H nickelation for 1- and 2-naphthyl phosphinites (16 h of refluxing in MeCN in the most favorable case) spurred us to find a way to accelerate these reactions. Tests showed that much faster C−H nickelation is possible with some substrates by conducting the reactions in a thermostated autoclave that allows us to safely attain reaction temperatures above the boiling point of the solvent. For instance, using this approach led to near complete nickelation of **1a** in only 30 min at 160 °C, which is significantly faster than the 16 h required for the analogous nickelation to occur in a Schlenk tube at 80 °C (**Scheme 4.9**).

Scheme 4.9. C−H nickelation of 1- and 2-Naphthyl Phosphinites at 160 °C.
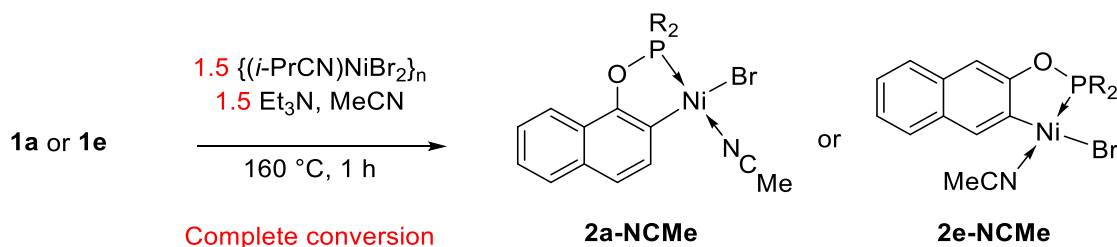
Driving the nickelation of **1a** to completion necessitated a larger excess of the precursor {(i-PrCN)NiBr$_2$}$_n$, because this compound decomposes partially at 160 °C to give Ni black deposition on the walls of the reaction flask and on the stir bar.[17] Thus, using 1.5 equiv of both {(i-

PrCN)NiBr$_2$}$_n$ and Et$_3$N led to complete nickelation of **1a** within 1 h at 160 °C. An even greater acceleration was noted for the much more sluggish nickelation of 2-naphthyl phosphinite **1e**: applying the above reaction conditions (i.e., 50% excess Ni precursor, 160 °C) led to complete conversion to the nickelation product **2e** in 1 h, much faster than the 60 h required for complete nickelation of this substrate at 80 °C (**Scheme 4.9**).

Having identified optimal conditions for the high temperature nickelation of **1a** and **1e**, we conducted a few small scale test reactions (0.2 mmol) to see if the very sluggish nickelation of **1f** (> 10 d at 80 °C, **Scheme 4.6**) can be accelerated at higher temperatures. Unfortunately, these attempts were unsuccessful as we obtained mostly Ni black and other undesired side-products (**Fig. S4.127**). For instance, conducting the reaction at 160 °C over 2 h gave a mixture in which the desired cyclonickelated species **2f-NCMe** showed only a minor ^{31}P signal at 192 ppm. Numerous additional signals were also observed, including some in the 50-100 ppm range believed to be phosphinite and phosphine oxides (Ni-bound or free) and an unassigned sharp signal at 123 ppm, in addition to signals around 135 ppm attributed to adducts of the unreacted phosphinite.

On the other hand, lowering the reaction temperature reduced the extent of thermal degradation and gave higher conversions to the target product over shorter reaction times (**Scheme 4.10**). For instance, conducting the reaction at 120 °C (1.2 equiv each of {(*i*-PrCN)NiBr$_2$}$_n$ and Et$_3$N) gave **2f-NCMe** in 43% after 3 h (**Fig. S4.135**).[18] These results should be compared to 16 % yield for the same nickelated product when the reaction is conducted over 7 days at 80 °C. The above encouraging results prompted us to see if conducting mmol scale reactions at 120 °C would allow us to isolate the cyclonickelated MeCN adduct **2f-NCMe** and eventually work it up into its corresponding dimeric complex **2f**. Indeed, heating **1f** with 1.2 equiv of both Et$_3$N and {(*i*-PrCN)NiBr$_2$}$_n$ at 120 °C for 16 h gave mostly the desired **2f-NCMe**, as inferred from the observation of a very major peak at 192 ppm assigned to this compound.

An initial attempt to isolate the dimeric species **2f** failed, however, because the work-up in toluene led to re-protonation of the nickelated species with Et$_3$N·HBr, giving back the non-nickelated complex (**Scheme 10**). To circumvent this reversal of the nickelation step, the crude reaction mixture was cooled to –35 °C to allow crystallization of unreacted **3f** and of some Et$_3$N·HBr. The green supernatant was then evaporated, extracted with toluene, and evaporated to give an orange

solid, which was recrystallized from Et$_2$O to give orange crystals that were identified as **2f**. As will be discussed below, this compound displayed a strong structural distortion.

Scheme 4.10. Nickelation of Phosphinite **1f** at 160 °C and protonation of **2f-L** in toluene.
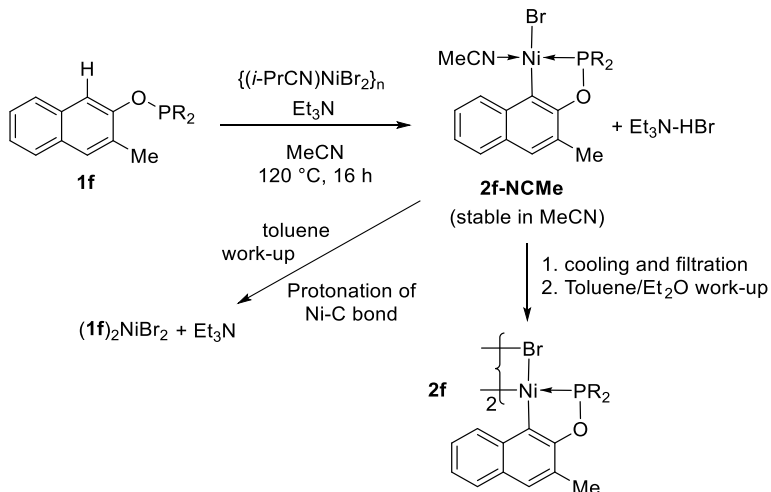
Lastly, we conducted a few experiments to see if substrate **1d**, which could not be induced to undergo nickelation under the standard reaction conditions at 80 °C, might be nickelated at high temperatures. Unfortunately, the ^{31}P NMR spectrum of the final mixture obtained from the 160 °C reaction of **1d** with {(*i*-PrCN)NiBr$_2$}$_n$ and Et$_3$N did not show the anticipated signals for a nickelation product. We found instead a major species at 123 ppm as well as a number of minor signals in the 90-110 and 160–170 ppm regions. Moreover, much Ni black was found deposited on the walls of the reaction vial, and this after only 1 h of reaction. As before, control experiments showed that no degradation of **1d** occurs after 1 h of heating at 160 °C in MeCN, implying that the degradation likely involves the putative nickelated product. Lowering the nickelation temperature to 120 °C led to less thermal degradation but the make-up of the reaction mixture remained fairly unchanged.

4.3.5 Interception of unanticipated C−P functionalized products

The results discussed in the previous section showed us that high temperatures can have dramatically different impacts on the C−H nickelation of different substrates. With substrates such as **1a** and **1e** that undergo slow C−H nickelation at 80 °C, high temperatures accelerated the cyclonickelation significantly. On the other hand, with a substrate such as **1d** that does not undergo C−H nickelation at 80 °C, high temperatures resulted in a great deal of decomposition. This

245

observation suggested that disrupting the formation of stable cyclonickelated products at high temperatures might open new reactivity pathways. To test this assertion, we set out to conduct the high temperature nickelation of **1a** in the absence of base, which we reasoned would suppress formation of the normal nickelation product **2a-NCMe** and divert the reaction toward alternative pathways.

Thus, heating an acetonitrile solution of 1-naphthyl-phosphinite **1a** and 1.2 equiv of {(*i*-PrCN)NiBr$_2$}$_n$ at 160 °C over 4 h in the absence of Et$_3$N gave a red mixture that displayed two major sets of ^{31}P NMR resonances not observed previously, namely: a set of AB doublets at 180 and 30 ppm ($J_{PP}\sim$ 69 Hz), and a singlet at 121 ppm. A few other species were also detected, including the non-nickelated phosphinite adduct **3a** represented by a broad signal at 135 ppm. Cooling the mixture to r.t. caused the precipitation of unreacted starting material, **3a**, which was removed by filtration. Cooling the filtrate to –35 °C overnight afforded red crystalline blocks, which were shown via XRD analysis to contain the new compound *cis*-(κ^P,$\kappa^{P'}$-2-P(*i*-Pr)$_2$-1-naphhtyl-OP(*i*-Pr)$_2$)NiBr$_2$, **4**, shown in **Scheme 4.11**.

Scheme 4.11. C-P Functionalization of **1a**.
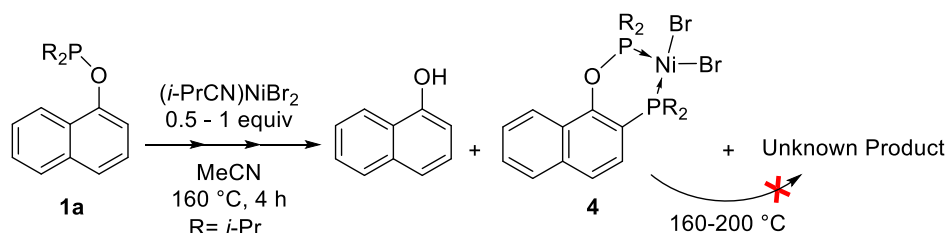
The unanticipated formation of the new phosphinite/phosphine compound **4** can be viewed as the formal insertion of P(*i*-Pr)$_2$ into the C-Ni bond generated from C−H nickelation of ligand **1a**. It occurred to us that the presence of an excess of substrate might favor this pathway, because transformation of **1a** to **4** requires a 2:1 molar ratio of **1a**:Ni. Indeed, repeating the above reaction with twice as much **1a** as before gave a red mixture for which the ^{31}P NMR spectrum seemed cleaner than the spectrum obtained from the first reaction, even though the reaction was not complete after 4 h. Increasing the reaction temperature to 200 °C resulted in complete consumption of the starting material within 1 h.[19]

Cooling the final reaction mixture overnight to –35 °C yielded a crop of thin needles consisting of elongated plates stuck together. XRD analysis of a crystal obtained from this batch showed it to be poorly diffracting and twinned; nevertheless, the data allowed us to establish that it contained compound **4** and ½ molecule of free 1-naphthol (**Scheme 4.11**, **Fig. S4.182**). As will be discussed below, the in-situ formation of 1-napththol in this reaction is significant, because it provides a significant clue for the reaction mechanism. Another mechanistically relevant observation was that heating a MeCN solution of the co-crystals isolated from this reaction to 160 – 200 °C showed only the ^{31}P resonances assigned to **4** (two ^{31}P doublets at 180 and 30 ppm), no trace of the unidentified peak at 121 ppm being detected. This implied that the unidentified species is the product of a different side reaction and does not arise from thermal degradation of **4**.

Combining the above clues suggested that the conversion of **1a** to **4** proceeds by the following sequence of steps: (a) cyclonickelation would initially generate HBr and **2a-NCMe**; (b) substitution of MeCN in the latter species by the non nickelated phosphinite **1a** would give the phosphinite adduct **2a-L**;[20] (c) this intermediate would then undergo a rearrangement to initiate the C−P bond forming process; (d) the naphthoxide leaving group generated in this last step would capture the proton produced at the nickelation step (a) to give the naphthol molecule co-crystallized with **4**.

To test the validity of the above postulate, we generated **2a-NCMe** in-situ by dissolving the independently prepared dimeric complex **2a** in MeCN, and heated it in the presence of one equiv of the phosphinite **1a** at 160 °C for 1 h. Analysis of the final red mixture by ^{31}P NMR showed only a trace of the diagnostic AB doublet for **4**, in addition to broadened signals for unreacted **2a-NCMe** and **1a**, as well as minor peaks in the region of phosphine and phosphinite oxides. This experiment showed that the formation of **4** does not proceed to any appreciable extent from the treatment of **2a-NCMe** with **1a**.

Upon reflection, it occurred to us that the main difference between the reaction depicted in **Scheme 11** and the above test is the use of independently prepared **2a-NCMe** in the latter case vs. its formation via in-situ cyclonickelation in the former case. Given that in-situ cyclonickelation generates HBr as a co-product, we reasoned that this might be an important factor for transformation of **2a-NCMe** into **4**. For instance, the presence of in-situ generated HBr might convert the phosphinite **1a** into BrP(i-Pr)$_2$, and this might be more reactive for transforming **2a-NCMe** into **4**.

To test the above possibility, we prepared BrP(i-Pr)$_2$[9] and heated it with independently prepared **2a-NCMe** (MeCN, 160 °C, 1 h). The ^{31}P NMR spectrum of the resulting red mixture showed complete disappearance of the starting material and formation of the anticipated AB signals of **4** as the major component of the mixture (**Fig. S4.146**). This result supports the putative mechanism shown in **Scheme 4.12**. We speculate that the C−P bond formation step involves a nucleophilic attack by the Ni-bound aryl moiety on the P nucleus of the coordinated BrP(i-Pr)$_2$, but other pathways can also be envisaged.

Scheme 4.12. Postulated mechanism for formation of **4**.
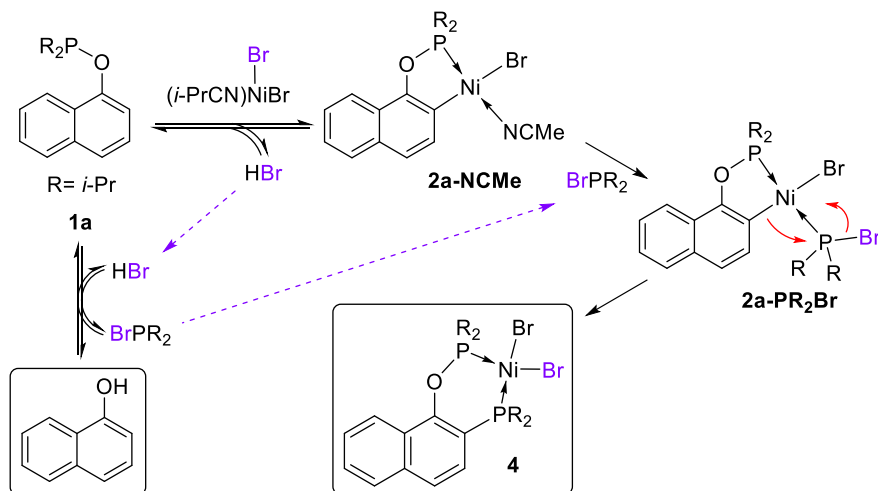
Having identified complex **4** and proposed a plausible mechanism for its formation from **1a**, we set out to identify the other product observed during this transformation, i.e., the minor species represented by the ^{31}P singlet at 121 ppm. As mentioned above, we concluded that this species does not arise from the thermal degradation of **4**. We posited that it might also be a C−P functionalization product, but one that arises via a competing C−H nickelation at C8. To test this possibility, we examined the analogous reaction of substrate **1d** at 160 °C and in the absence of Et$_3$N, based on the reasoning that the ethyl substituent in **1d** would block C−H nickelation at C2, thereby suppressing the reactivity pathway leading to **4**. Thus, heating a 1 : 1.2 MeCN mixture of **1d** and (i-PrCN)NiBr$_2$ at 160 °C for 1 h gave an emerald green suspension and a Ni mirror on the reactor walls.[21] Filtration of this suspension gave a mixture of Ni black and a mass of light green/yellowish solid, which was identified as {NiBr$_2$(NCMe)$_2$}$_n$. Analysis of the emerald green filtrate by ^{31}P

NMR spectroscopy showed a major singlet at 123 ppm, plus very minor resonances at 135, 95, and 45 ppm.

The above filtrate was cooled and filtered to remove more of $\{NiBr_2(NCMe)_2\}_n$ in addition to a few deep-red crystals, which were revealed by XRD analysis to be cis-(i-Pr$_2$PH)$_2$NiBr$_2$.[22] Evaporation of the supernatant gave a green oil, which was washed with toluene and analyzed by NMR (CD$_3$CN, **Fig. S4.151**). The ^{31}P NMR spectrum of this sample showed the expected singlet at 123 ppm, whereas its ^{1}H NMR spectrum showed two components, the minor one being identified as 2-Et-1-naphthol and the major one displaying the characteristic signals for the P(i-Pr)$_2$ moiety and the Et substituent in addition to only 5 resonances in the aromatic region (instead of 6 that would be expected for a mono-substituted naphthol derivative). Adding Et$_2$O to this NMR sample afforded colorless crystals that were identified by XRD analysis as 2-Et-8-(i-Pr$_2$P(O))-1-naphthol (compound **5** in **Scheme 4.13**), co-crystallized with ½ molecule of 2-Et-1-naphthol itself. It should be mentioned that we also obtained crystals for **5·HBr** (**Fig. S4.189**).

Scheme 4.13 Tandem C−H nickelation/C-P functionalization at C8−H of **1d**.[a]
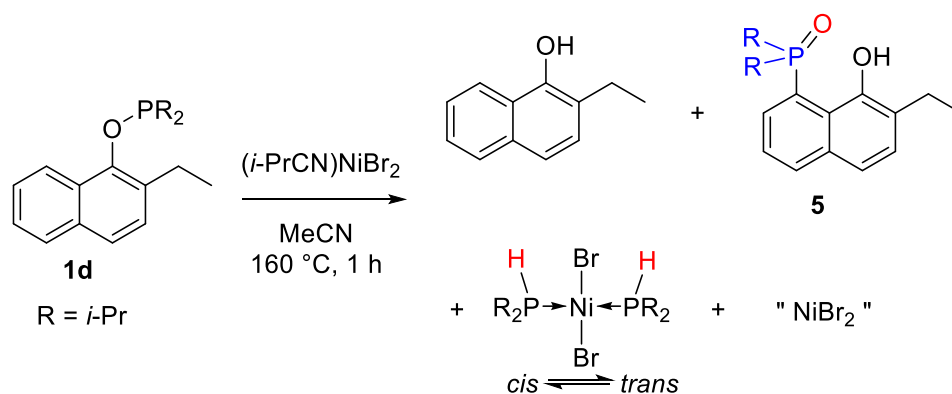
[a] For Molecular Diagrams of (i-Pr$_2$PH)$_2$NiBr$_2$ and **5**·(2-Et-1-naphthol)$_{0.5}$, see **Figs. S4.187** and **S4.188.**

The question arises whether the ^{31}P resonance at 123 ppm detected for the side-product of the high temperature reaction of **1d** represents the phosphine oxide **5** or its Ni complex. To shed some light on this question, we repeated the reaction of **1d** with $\{(i-PrCN)NiBr_2\}_n$ (1:1; MeCN, 160 °C, 1h), added 2 equiv of PPh$_3$ to the crude reaction mixture, and then recorded its ^{31}P NMR spectrum. This showed only the peak at 123 ppm and no new peak for free PPh$_3$, which implies the in-situ formation of the tetrahedral (and NMR-silent) (PPh$_3$)$_2$NiBr$_2$ from the reaction of free NiBr$_2$ with

added PPh$_3$. We infer, therefore, that the phosphine oxide **5** generated in this reaction is not Ni-bound. Moreover, solubility tests showed that **5** is soluble in MeCN but insoluble in toluene; the same pattern of solubility was found for the unidentified species generated from the reaction of **1a** (**Scheme 4.11**) and represented by a ^{31}P singlet at 121 ppm. The latter has also been analyzed by GC/MS, thus allowing us to identify it as 8-(i-Pr$_2$P(O))-1-naphthol.

We propose, therefore, that the formation of the phosphine oxides discussed above, **5** from **1d** and the unidentified species in **Scheme 4.11**, involves C−H nickelation at C8, followed by the formal insertion of a "P(i-Pr)$_2$" into the C−Ni bond. The 7-membered nickelacycles present in the resulting species would likely be thermally unstable and prone to decomposition. The main aspect that still remains obscure is how the phosphinite moiety at C1 is transformed into (i-Pr$_2$PH)$_2$NiBr$_2$ (**Scheme 4.14**).

Scheme 4.14. Postulated Mechanism for Formation of **5**.
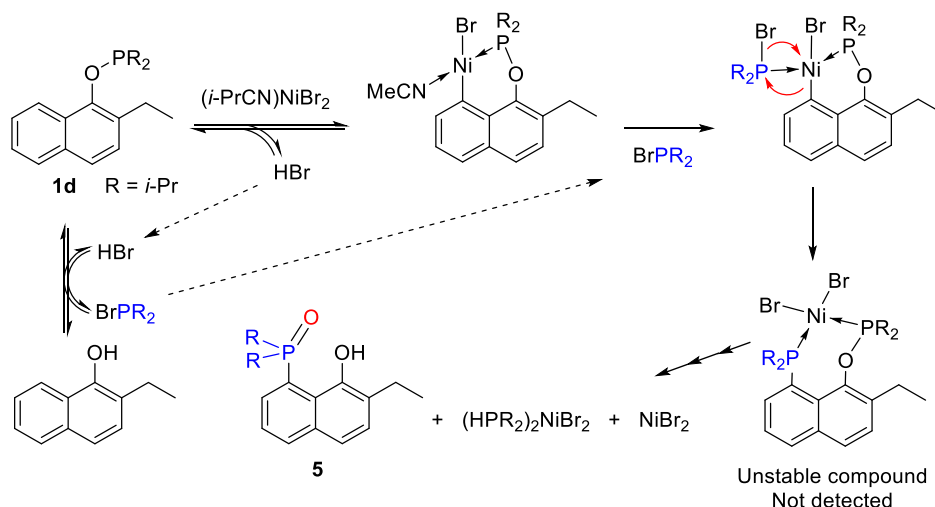
4.3.6 Solid state structures of dimers and complex 4[23]

The solid state structures of the dimeric complexes **2a**, **2b**, **2c** and **2e** (**Fig. 4.3**) share some of the main features found in the structures of the analogous dimeric complexes derived from phenyl phosphinites.[5] Thus, the Ni centers in all dimers adopt a geometry that is very close to square planar, with τ$_4$ values[14] ranging from 0.05 – 0.07 for dimers sitting on an inversion center (**2c** and **2e**) and 0.08 – 0.13 for those not generated by a symmetry operation (**2a** and **2b**). However, the Ni−μ-Br−Ni angle in **2a** was found significantly smaller than the others (85 – 87° vs. < 92°), which translates into a non-coplanarity of the two halves of the dimer (**Table 4.1**).
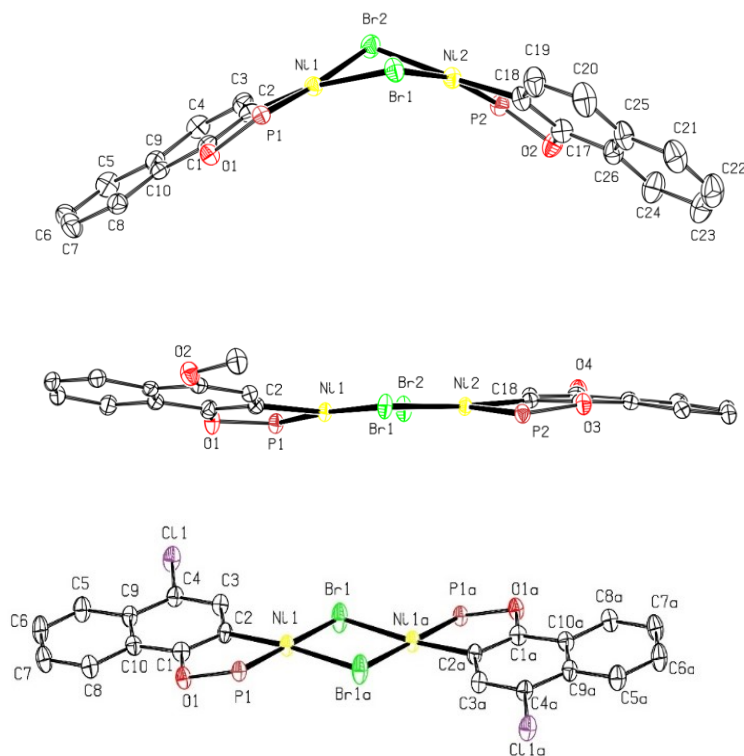
Figure 4.3. Side views of the molecular diagrams for complexes **2a** (top), **2b** (middle) and **2c** (bottom). Thermal ellipsoids are shown at the 50% probability level; hydrogen atoms and *P*-substituents are omitted for clarity.

Table 4.1. Selected structural parameters, bond distances (Å), and bond angles (°) for cyclonickelated dimers.

	Space Group	Ni–C	Ni–P1	*trans*-Ni-Br[a]	*cis*-Ni-Br[a]	C-Ni-P1	Br-Ni-L	τ_4
2a	Pca2₁	1.914(5)	2.1050(14)	2.3868(9)	2.3975(9)	81.8	87.0	0.10
		1.908(5)	2.1031(15)	2.3818(10)	2.3810(9)	81.8	87.5	0.13
		1.911(5)	2.1006(15)	2.3853(10)	2.3819(9)	82.0	87.2	0.11
		1.917(5)	2.1028(14)	2.3978(9)	2.3854(9)	82.1	86.9	0.12
2b	Pbca	1.908(2)	2.1063(7)	2.34241(4)	2.4133(4)	83.1	86.9	0.10
		1.915(2)	2.1105(7)	2.4021(4)	2.3751(5)	82.1	86.4)	0.08
2c	P-1	1.912(4)	2.1036(11)	2.3685(8)	2.3642(7)	82.1	87.4	0.07
		1.914(4)	2.1062(11)	2.3647(7)	2.3714(7)	82.6	87.4	0.05
2e	P2₁/n	1.921(2)	2.0992(6)	2.3862(4)	2.39	82.8	86.9	0.05
2f	P2₁/n	1.923(2)	2.0872(5)	2.3880(3)	2.41	80.7	88.3	0.22

[a]*cis* and *trans* positions are relative to the Ni−C bond.

Indeed, the hinge angle between the two halves (the dihedral angle Ni1−Br1−Br2−Ni2) was found to be 140° with **2a**, which strongly deviates from the 180° observed in symmetric structures **2c** and **2e**, and from the 177° observed in **2b**. The two Ni centers in **2a** are thus brought closer to each other with a Ni---Ni distance of less than 3.3 Å, shorter than the Ni−Ni distance of 3.4 Å in the planar complexes. These features have already been observed in cyclometalated phenyl phosphinite complexes of Ni[5] and cylometalated phosphines of Pd;[24] in the case of Ni, this "bent" conformation is thought to be more stable in solution than the planar one observed in crystallized centrosymmetrical complexes.

The data in **Table 4.1** also show fairly narrow ranges for the bond distances C−Ni (1.908 – 1.921(2) Å) and P−Ni (2.099(1) – 2.111(1)), and also for the C−Ni−P bite angles (82° – 83°); evidently, the different electronic character of the naphthol substituents appears to have little or no impact on these parameters. The Ni−Br bonds also showed a fairly narrow range of distances in complexes **2a**, **2c** and **2e**: 2.365 – 2.398 Å over all 14 bonds *trans* or *cis* to the C−Ni bonds. The outlier in this category is complex **2b**, the only 'flat' dimer not generated by a symmetry element, which shows greater differences for the Ni−Br distances *trans* or *cis* to Ni−C bond: 2.342 vs. 2.413 Å; 2.402 vs. 2.375 Å respectively.

One structure that justifies an individual discussion here is that of **2f** (**Fig. 4.4**), the naphthyl phosphinite adduct of the cyclometalated complex derived from **1f**, because it can help rationalize the C3/C1 regioselectivity observed in the C−H nickelation of 2-naphthyl phosphinite **1e**. The solid state structure of **2f** displays a significantly acute *trans* angle for P−Ni−Br (156°), a tetrahedral distortion with a τ_4 value of 0.22, and a naphthalene ring that bends out of the ideal plane around Ni to give a C10−C1−Ni−Br dihedral of 47° (as opposed to an aromatic plane twisted by less than 10° in similar dimeric compounds).

We believe that the tetrahedral distortion referred to above serves the purpose of minimizing any steric contact of the C8−H moiety of the rigid naphthalene ring with the ligand *cis* to C1−Ni (μ-Br for **2f** and P for **2f-L**). Moreover, it is reasonable to conclude that this steric hindrance would lead to a higher energy barrier for the nickelation of **1e** at C1−H, thus explaining the observed preference for nickelation at C3−H.
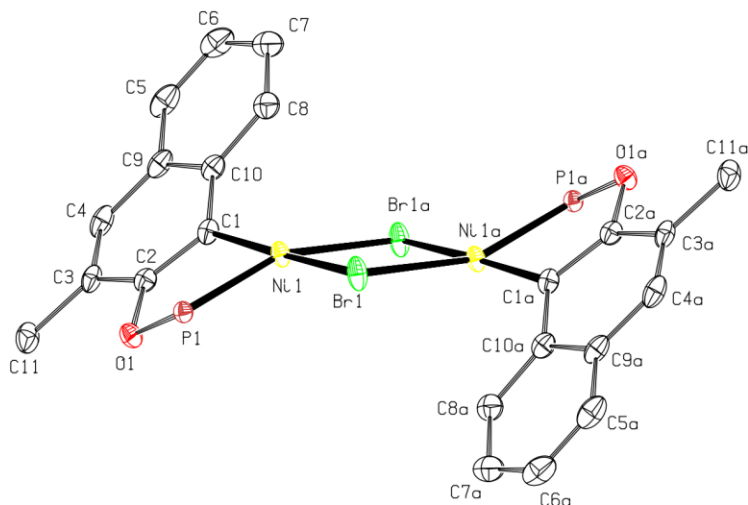
Figure 4.4. Side view of the molecular diagram for complex **2f**. Thermal ellipsoids are shown at the 50% probability level; hydrogen atoms and *P*-substituents are omitted for clarity.

Finally, the structure of the bis-phosphine/phosphinite complex **4** is worth discussing because the bidentate ligand creates a 6-membered chelating environment around Ni. Although the P1−Ni1−P2 bite angle of 94° is close to the ideal value, this brings about a significant tetrahedral distortion with a τ_4 of 0.29, and the naphthalene ring is pushed out of the mean plane around Ni by 46° (**Fig. 5**).
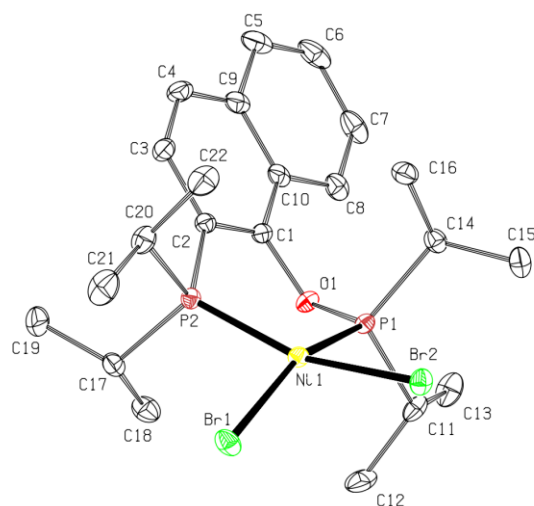
Figure 4.5. Molecular diagram for complex **4**. Thermal ellipsoids are shown at the 50% probability level; hydrogen atoms are omitted for clarity.

The Ni1−P1 distance of 2.1247(5) Å is longer than in the corresponding distances in *ortho*nickelated phosphinites, but still much shorter than the Ni-phosphinite distances of ≥ 2.23 Å observed in L_2NiBr_2 complexes featuring non cyclonickelated phosphinites; this is presumably due to the chelate effect in **4**. Similarly, the Ni1−P2 distance of 2.1767(5) Å is longer than P1−Ni1, but still shorter than the corresponding Ni−P distances of 2.23 – 2.33 Å seen for monodentate (*i*-Pr)$_2$PPh; it is also comparable to the Ni−P distances in *cis*-(diphosphine)NiX$_2$ complexes (2.137 – 2.176 Å). The two *cis* Ni−Br bonds were found to be 2.3390(3) and 2.3405(3) Å, thus not significantly different; on the other hand, these distances are significantly longer than those in *trans*-(phosphinite)$_2$NiBr$_2$ complexes characterized throughout this study.

4.4 Conclusion

This study has established that phosphinites derived from 1- and 2-naphthol undergo C−H nickelation when treated with the Ni^{II} precursor {(*i*-PrCN)NiBr$_2$}$_n$. When these reactions are conducted in the presence of Et$_3$N, the cyclonickelated products can be isolated in the form of bromo-bridged dimers or adducts of either acetonitrile or the phosphinite ligand itself. Experimentation allowed us to optimize these reactions as a function of phosphinite:Ni:Et$_3$N molar ratios, reaction temperature, and also the electronic properties of substituents placed at the *para* position of 1-naphthol. The results of these studies showed that reaction temperature has a great influence on C−H nickelation rates. For instance, the 2-naphthyl phosphinite **1e** is quantitatively converted to the dimeric cyclonickelated complex **2e** in 1 h at 160 °C, whereas the analogous reaction at 80 °C requires 60 h.

Another major issue that was addressed in this study was the regioselectivity of C−H nickelation in our system. Of the two potential C−H sites in 1- and 2-naphthyl phosphinites not bearing substituents in the *ortho* positions, the favored site for cyclonickelation is C2 (not C8) with 1-naphthyl phosphinite and C3 (not C1) in 2-naphthyl phosphinite. It is also important to emphasize that a 2-naphthyl phosphinite bearing a Me substituent at the 3-position can undergo nickelation at the alternative C1−H site at the same temperature (albeit more sluggishly), whereas blocking the favored site in 1-naphthyl phosphinite by an alkyl substituent at the C2−H position does not facilitate cyclonickelation at C8.

The observation of exclusive nickelation at the C2 site of 1-naphthyl phosphinites is in contrast to the regioselectivity of 1-naphthyl metalation-functionalization with other metals. With Rh, for

instance, these substrates react preferentially at C2, but metalation also occurs to some extent at C8.[7] We speculate that the observed inertness of the C8 site toward nickelation can be attributed to two factors. First, the shorter Ni(II) radius (relative to Rh(III)) likely results in a Ni---C8 distance that would be longer than optimal for initiating the C→Ni interaction and the ensuing deprotonation step.[6] Alternatively (or additionally), the putative 6-membered nickelacycle intermediate that would result from C−H nickelation at C8 might be thermodynamically less stable (especially at high temperatures) relative to the 5-membered metallacyclic transition state that leads to the observed products **2a-2c**.

Perhaps the most unexpected result of the present study has been the serendipitous discovery of a tandem C−P functionalization reaction that leads to the "insertion" of a i-Pr$_2$P or i-Pr$_2$P(O) moiety into the Ni−C site generated by cyclonickelation of the phosphinites derived from 1-naphthol or 2-Et-1-naphthol, respectively. In the first case, the functionalization requires conducting the C−H nickelation at high temperatures 160 – 200 °C) and in the absence of Et$_3$N. The available mechanistic information indicates that the C−P bond formation in this case proceeds via a nucleophilic attack by the Ni−C moiety on in-situ generated BrP(i-Pr)$_2$. This C−P functionalization reaction product provides further support for the conclusions we have drawn from during our earlier studies, namely: (a) C−H nickelation can take place in the absence of external base, and (b) HBr generated in-situ in the C−H nickelation step can leave the coordination sphere of the Ni center and linger in the reaction medium long enough to allow it to react with other species, including H/D exchange with the solvent.

A more complex "insertion"-type C−P functionalization occurs during the high temperature C−H nickelation of the phosphinite derived from 2-Et-1-naphthol. In this case, the "insertion" takes place at C8 and the product is 2-Et-8-(i-Pr$_2$P(O))-1-naphthol, **5**. A related though not identical side-reaction also takes place during the high temperature C−H nickelation of 1-naphthyl phosphinite, but the product of this insertion at C8 is a minor component of the final mixture.

Future investigations will aim to improve our understanding of these interesting functionalization reactions. We will also explore the potential reactivities of the cyclonickelated compounds described herein for oxidation-induced C−heteroatom functionalization reactions. These studies will draw inspiration from recently reported model systems based on NCN-type pincer-Ni^{III} complexes that promote C−N, C−O, and C−halide bond formation reactions.[25]

4.5 Experimental Section

General considerations. All manipulations were carried out under a nitrogen atmosphere using standard Schlenk techniques and an inert-atmosphere box. The reactions conducted in acetonitrile at temperatures above its boiling point (120 - 200 °C) were carried out in a conductively heated, sealed vessel autoclave with a reaction volume of 5 mL (Anton-Paar Monowave 50).[26] The heating program allowed the reaction mixtures to rapidly attain the target temperature and maintain it for the desired reaction time. Solvents were dried by passage over a column of activated alumina, collected under nitrogen, and stored over 3 Å molecular sieves. Triethylamine was dried over CaH_2. Synthesis of the nickel precursor $\{(i\text{-}PrCN)NiBr_2\}_n$ used throughout this study has been described previously.[27] D_8-1-naphthol was purchased from CDN Isotopes, whereas other reagents were purchased from Sigma-Aldrich or Fisher Sci. and used without further purification.

The NMR spectra were recorded at 500 MHz (^{1}H), 125.72 MHz (^{13}C), and 202.4 MHz (^{31}P). Chemical shift values are reported in ppm (δ) and referenced internally to the residual solvent signals (^{1}H and ^{13}C: 1.94 and 118.26 ppm for CD_3CN; 7.26 and 77.16 for $CDCl_3$; 7.16 and 128.06 for C_6D_6) or externally (^{31}P: H_3PO_4 in D_2O, $\delta = 0$). J coupling values are given in Hz. The NMR spectroscopic data for the dimers correspond to the monomeric $NCCD_3$ adducts in CD_3CN. The elemental analyses were performed by the Laboratoire d'Analyse Élementaire, Département de chimie, Université de Montreal.

Single crystals of the structurally characterized complexes were grown as follows: by slow evaporation of an Et_2O solution under inert atmosphere for the dimeric complexes **2a**, **2b**, **2c**, **2e** and **2f**; from hot acetonitrile for **2e-NCMe**, **3a**, **3d**, **3f**, **3g**, and **4**; from an acetonitrile solution cooled to – 35 °C for $(i\text{-}Pr_2PH)_2NiBr_2$; from a toluene solution cooled to – 35 °C for **3f-L**; from slow diffusion of pentane into an Et_2O solution at – 35 °C for **2g**.

Synthesis of the dimers derived from naphthols. To a solution of the desired naphthol (2.00 mmol) in 20 mL dry THF was added 1.10 eq Et_3N (2.20 mmol, 307 μL), followed by 1.05 eq $ClP(i\text{-}Pr)_2$ (2.10 mmol, 334 μL); salt precipitation started almost instantaneously. The mixture was stirred at room temperature for 0.5 to 4 h until reaction was complete (monitoring by ^{31}P NMR). The solvent was then removed under vacuum, and the residues were extracted with Et_2O (3 x 15 mL) and evaporated to yield a colorless to pale yellow oil, to which was added 15 mL dry MeCN, 1.2 eq $\{(i\text{-}PrCN)NiBr_2\}_n$ (2.40 mmol, 691 mg) and 1.2 eq Et_3N (2.40 mmol, 335 μL). The brownish-

256

green homogeneous mixture was stirred at 80 °C until the reaction was complete (monitored by the disappearance of the starting material at 135 ppm in ^{31}P NMR). The solvent was then removed under vacuum, the residues were extracted with toluene through filtration on Celite®. The filtrate was evaporated under vacuum, the residues were extracted into a few mL Et$_2$O (sonication), hexanes added to precipitate the product, followed by filtration and washing with a minimum of hexanes to complete removal of unreacted material/toluene. The solid was dried under vacuum to yield an orange powder. Single crystals were obtained from slow evaporation in Et$_2$O under N$_2$.

{(κ^P,κ^C-1-OP(i-Pr)$_2$-naphth-2-yl)Ni(μ-Br)}$_2$ (2a). Yield: 587 mg of an orange powder (0.738 mmol, 74 %). ^{1}H NMR (500 MHz, 20 °C, CD$_3$CN): δ 1.37 (dd, 6H, CH(C*H$_3$*)(CH$_3$), $^3J_{HH}$ = 7.0, $^3J_{HP}$ = 14.9), 1.50 (dd, 6H, CH(CH$_3$)(C*H$_3$*), $^3J_{HH}$ = 7.2, $^3J_{HP}$ = 17.6), 2.55 (oct, 2H, C*H*(CH$_3$)$_2$, $^3J_{HH}$ $\approx$ $^2J_{HP}$ = 7.2), 7.23 (d, 1H, C4$_{Ar}$-*H*, $^3J_{HH}$ = 8.3), 7.33 (dd, 1H, C3$_{Ar}$-*H*, $^3J_{HH}$ = 8.5, $^4J_{HP}$ = 1.3), 7.36-7.40 (m, 2H, C6$_{Ar}$-*H* and C7$_{Ar}$-*H*), 7.72-7.78 (m, 1H, C5$_{Ar}$-*H*), 7.87-7.92 (m, 1H, C8$_{Ar}$-*H*). ^{13}C{^{1}H} NMR (125.7 MHz, 20 °C, CD$_3$CN): δ 16.82 (d, 2C, CH(*C*H$_3$)(CH$_3$), $^2J_{CP}$ = 2.0), 18.43 (d, 2C, CH(CH$_3$)(*C*H$_3$), $^2J_{CP}$ = 2.8), 29.14 (d, 2C, *C*H(CH$_3$)(CH$_3$), $^1J_{CP}$ = 28.8), 120.28 (d, 1C, *C*4$_{Ar}$-H, $^4J_{CP}$ = 1.6), 121.54 (d, 1C, *C*$_{quat}$, $^4J_{CP}$ = 12.5), 122.50 (d, 1C, *C*8$_{Ar}$-H), 125.69 (s, 2C, *C*6$_{Ar}$-H and *C*7$_{Ar}$-H), 127.70 (s, 1C, *C*5$_{Ar}$-H), 127.68 (d, 1C, *C*2$_{Ar}$-Ni, $^2J_{CP}$ = 34.7), 134.03 (s, 1C, *C*$_{quat}$), 134.87 (d, 1C, *C*3$_{Ar}$-H, $^3J_{CP}$ = 2.7), 161.95 (d, 1C, *C*1$_{Ar}$-OP, $^3J_{CP}$ = 12.6). ^{31}P{^{1}H} NMR (202.4 MHz, 20 °C, CDCl$_3$): δ 195.77. Anal. Calc. for C$_{32}$H$_{40}$Br$_2$Ni$_2$O$_2$P$_2$: C, 48.30; H, 5.07. Found: C, 47.73; H, 5.00; N, 0.06.

{(κ^P,κ^C-4-MeO-1-OP(i-Pr)$_2$-naphth-2-yl)Ni(μ-Br)}$_2$ (2b). Yield: 721 mg of an orange powder (0.842 mmol, 84 %). ^{1}H NMR (500 MHz, 20 °C, CD$_3$CN): δ 1.36 (dd, 6H, CH(C*H$_3$*)(CH$_3$), $^3J_{HH}$ = 7.0, $^3J_{HP}$ = 14.9), 1.49 (dd, 6H, CH(CH$_3$)(C*H$_3$*), $^3J_{HH}$ = 7.2, $^3J_{HP}$ = 17.6), 2.52 (oct, 2H, C*H*(CH$_3$)$_2$, $^3J_{HH}$ $\approx$ $^2J_{HP}$ = 7.2), 3.93 (s, 3H, C4$_{Ar}$-OC*H$_3$*), 6.69 (s, 1H, C3$_{Ar}$-*H*), 7.35-7.45 (m, 2H, C6$_{Ar}$-*H* and C7$_{Ar}$-*H*, $^3J_{HH}$ $\approx$ 7.0, $^4J_{HH}$ $\approx$ 1.6), 7.81 (dm, 1H, C8$_{Ar}$-*H*, $^3J_{HH}$ = 7.6), 8.03 (dm, 1H, C5$_{Ar}$-*H*, $^3J_{HH}$ = 7.6). ^{13}C{^{1}H} NMR (125.7 MHz, 20 °C, CD$_3$CN): δ 17.05 (d, 2C, CH(*C*H$_3$)(CH$_3$), $^2J_{CP}$ = 2.0), 18.69 (d, 2C, CH(CH$_3$)(*C*H$_3$), $^2J_{CP}$ = 2.7), 29.36 (d, 2C, *C*H(CH$_3$)(CH$_3$), $^1J_{CP}$ = 28.9), 56.04 (s, 1C, C4$_{Ar}$-O*C*H$_3$), 113.30 (d, 1C, *C*3$_{Ar}$-H, $^3J_{CP}$ = 3.0), 121.89 (d, 1C, *C*$_{quat}$, $^4J_{CP}$ = 12.7), 122.38 (s, 1C, *C*5$_{Ar}$-H), 122.72 (s, 1C, *C*8$_{Ar}$-H), 125.18 (s, 1C, *C*6$_{Ar}$-H), 125.69 (s, 1C, *C*$_{quat}$), 126.50 (s, 1C, *C*7$_{Ar}$-H), 124.18 (d, 1C, *C*2$_{Ar}$-Ni, $^2J_{CP}$ = 35.2), 148.71 (d, 1C, *C*4$_{Ar}$-OCH$_3$, $^4J_{CP}$ = 2.6), 156.38 (d, 1C,

$C1_{Ar}$-OP, $^3J_{CP}$ = 12.3). ^{31}P{^{1}H} NMR (202.4 MHz, 20 °C, CDCl$_3$): δ 193.60. Anal. Calc. for C$_{34}$H$_{44}$Br$_2$Ni$_2$O$_4$P$_2$: C, 47.71; H, 5.18. Found: C, 47.19; H, 5.18; N, 0.12.

{(κ^P,κ^C-4-Cl-1-OP(i-Pr)$_2$-naphth-2-yl)Ni(μ-Br)}$_2$ (2c). Yield: 633 mg of an orange powder (0.767 mmol, 77 %). ^{1}H NMR (500 MHz, 20 °C, CD$_3$CN): δ 1.37 (dd, 6H, CH(C*H*$_3$)(CH$_3$), $^3J_{HH}$ = 7.0, $^3J_{HP}$ = 15.1), 1.50 (dd, 6H, CH(CH$_3$)(C*H*$_3$), $^3J_{HH}$ = 7.2, $^3J_{HP}$ = 17.8), 2.56 (oct, 2H, C*H*(CH$_3$)$_2$, $^3J_{HH}$ ≈ $^2J_{HP}$ = 7.2), 7.36 (d, 1H, C3$_{Ar}$-*H*, $^4J_{HH}$ = 0.9), 7.47 (ddd, 1H, C7$_{Ar}$-*H*, $^3J_{HH}$ = 8.3, $^3J_{HH'}$ = 7.6, $^4J_{HH}$ = 1.4), 7.53 (tm, 1H, C6$_{Ar}$-*H*, $^3J_{HH}$ = 8.2, $^3J_{HH'}$ = 7.6, $^4J_{HH}$ = 1.4), 7.94 (dm, 1H, C8$_{Ar}$-*H*, $^3J_{HH}$ = 8.4), 8.07 (dm, 1H, C5$_{Ar}$-*H*, $^3J_{HH}$ = 8.4). ^{13}C{^{1}H} NMR (125.7 MHz, 20 °C, CD$_3$CN): δ 17.15 (d, 2C, CH(*C*H$_3$)(CH$_3$), $^2J_{CP}$ = 2.2), 18.74 (d, 2C, CH(CH$_3$)(*C*H$_3$), $^2J_{CP}$ = 2.6), 29.64 (d, 2C, *C*H(CH$_3$)(CH$_3$), $^1J_{CP}$ = 28.8), 122.54 (d, 1C, *C*$_{quat}$ or *C*4$_{Ar}$-Cl, $^4J_{CP}$ = 3.1), 122.66 (d, 1C, *C*$_{quat}$, $^4J_{CP}$ = 12.2), 123.70 (s, 1C, *C*8$_{Ar}$-H), 124.73 (s, 1C, *C*5$_{Ar}$-H), 127.01 (s, 1C, *C*7$_{Ar}$-H), 127.28 (s, 1C, *C*6$_{Ar}$-H), 128.48 (d, 1C, *C*2$_{Ar}$-Ni, $^2J_{CP}$ = 33.7), 130.71 (s, 1C, *C*$_{quat}$ or *C*4$_{Ar}$-Cl), 135.31 (d, 1C, *C*3$_{Ar}$-H, $^3J_{CP}$ = 2.5), 161.66 (d, 1C, *C*1$_{Ar}$-OP, $^3J_{CP}$ = 12.5). ^{31}P{^{1}H} NMR (202.4 MHz, 20 °C, CDCl$_3$): δ 196.48. Anal. Calc. for C$_{32}$H$_{38}$Br$_2$Cl$_2$Ni$_2$O$_2$P$_2$: C, 44.45; H, 4.43. Found: C, 44.57; H, 4.49.

{(κ^P,κ^C-2-OP(i-Pr)$_2$-naphth-3-yl)Ni(μ-Br)}$_2$ (2e). This compound required a modified work-up procedure for optimal yields. After evaporation of the crude reaction mixture, 25 mL toluene was added, the mixture stirred at 80 °C for 30 min, followed by filtration (while hot), evaporation and washing of the solids with Et$_2$O and hexanes. Yield: 431 mg of an orange powder (0.542 mmol, 54 %). The ^{1}H NMR of the final powder showed that it still contained toluene (2 – 5 % w/w). Even after extended drying *in vacuo* at 80 °C, trituration in hexanes, and trituration in Et$_2$O or Et$_2$O:CH$_2$Cl$_2$ 1:1, traces of toluene were still found although it decreased to 1 % w/w (5 mol% *vs.* Ni). The elemental analysis of this solid showed fair purity. Conversion into the MeCN adduct removed all toluene and resulted in higher NMR purity. ^{1}H NMR (500 MHz, 20 °C, CD$_3$CN): δ 1.33 (dd, 6H, CH(C*H*$_3$)(CH$_3$), $^3J_{HH}$ = 7.0, $^3J_{HP}$ = 15.0), 1.48 (dd, 6H, CH(CH$_3$)(C*H*$_3$), $^3J_{HH}$ = 7.2, $^3J_{HP}$ = 17.6), 2.50 (oct, 2H, C*H*(CH$_3$)$_2$, $^3J_{HH}$ ≈ $^2J_{HP}$ = 7.1), 7.01 (s, 1H, C1$_{Ar}$-*H*), 7.25 (ddd, 1H, C6$_{Ar}$-*H* , $^3J_{HH}$ = 8.1, $^3J_{HH'}$ = 6.8, $^4J_{HH}$ = 1.3), 7.32 (ddd, 1H, C7$_{Ar}$-*H*, $^3J_{HH}$ = 8.1, $^3J_{HH'}$ = 6.8, $^4J_{HH}$ = 1.3), 7.61 (d, 1H, C8$_{Ar}$-*H*, $^3J_{HH}$ = 8.1), 7.66 (s, 1H, C4$_{Ar}$-*H*), 7.71 (d, 1H, C1$_{Ar}$-*H*, $^3J_{HH}$ = 8.1). ^{13}C{^{1}H} NMR (125.7 MHz, 20 °C, CDCl$_3$): δ 17.18 (d, 2C, CH(*C*H$_3$)(CH$_3$), $^2J_{CP}$ = 2.0), 18.79 (d, 2C, CH(CH$_3$)(*C*H$_3$), $^2J_{CP}$ = 2.7), 29.54 (d, 2C, *C*H(CH$_3$)(CH$_3$), $^1J_{CP}$ = 29.2), 104.98 (d, 1C, *C*1$_{Ar}$-H, $^4J_{CP}$ = 13.1), 124.18 (s, 1C, *C*6$_{Ar}$-H), 126.14 (s, 1C, *C*7$_{Ar}$-H), 127.03 (s, 1C, *C*8$_{Ar}$-H), 127.73 (s,

1C, $C5_{Ar}$-H), 130.36 (d, 1C, C_{quat}, $^4J_{CP}$ = 2.1), 134.60 (s, 1C, C_{quat}), 138.10 (d, 1C, $C3_{Ar}$-Ni, $^2J_{CP}$ = 36.0), 138.99 (d, 1C, $C4_{Ar}$-H, $^3J_{CP}$ = 2.7), 166.62 (d, 1C, $C1_{Ar}$-OP, $^3J_{CP}$ = 12.1). $^{31}P\{^1H\}$ NMR (202.4 MHz, 20 °C, CDCl$_3$): δ 197.33. Anal. Calc. for $C_{32}H_{40}Br_2Ni_2O_2P_2$: C, 48.30; H, 5.07. Found: C, 48.25; H, 5.21.

{(κ^P,κ^C-3-Me-2-OP(i-Pr)$_2$-naphth-1-yl)Ni(μ-Br)}$_2$ (2f). To a solution of 274 mg 3-Me-2-naphthyl-OP(i-Pr)$_2$ (1.00 mmol) in 5 mL MeCN were added 345 mg {(i-PrCN)NiBr$_2$}$_n$ (1.20 mmol, 1.2 equiv) and 167 μL Et$_3$N (1.20 mmol, 1.2 equiv). The resulting dark greenish solution that contained a red precipitate of **3f** was heated at 120 °C for 16 h in the Monowave 50. The crude mixture was cooled at – 35 °C overnight resulting in crystallization of unreacted **3f** and Et$_3$N·HBr. The green supernatant was evaporated, extracted with toluene, and the volatiles removed under vacuum at 60 °C. The orange residues were treated with 3 mL Et$_2$O and filtered, and then the dark orange filtrate cooled at –35 °C overnight to give some orange precipitate. These were removed manually and dried under vacuum to allow NMR characterization, which showed some impurities. Elemental analysis was not performed on this sample. ^1H NMR (500 MHz, 20 °C, CD$_3$CN): δ 1.24 (dd, 6H, CH(CH_3)(CH$_3$), $^3J_{HH}$ = 7.0, $^3J_{HP}$ = 14.7), 1.48 (dd, 6H, CH(CH$_3$)(CH_3), $^3J_{HH}$ = 7.2, $^3J_{HP}$ = 17.7), 2.29 (d, 3H, Ar-CH_3, $^6J_{HH}$ = 0.7), 2.44 (oct, 2H, CH(CH$_3$)$_2$, $^3J_{HH}$ ≈ $^2J_{HP}$ = 7.2), 7.21 (ddd, 1H, C6$_{Ar}$-H, $^3J_{HH}$ = 8.0, $^3J_{HH'}$ = 6.8, $^4J_{HH}$ = 1.2), 7.28 (s, overlapping with δ 7.29, 1H, C4$_{Ar}$-H), 7.29 (ddd, overlapping with δ 7.28, C7$_{Ar}$-H, 1H, $^3J_{HH}$ = 8.3, $^3J_{HH'}$ = 6.8, $^4J_{HH}$ = 1.4), 7.57 (d, 1H, C5$_{Ar}$-H, $^3J_{HH}$ = 8.3), 8.19 (d, 1H, C8$_{Ar}$-H, $^3J_{HH}$ = 8.6). $^{13}C\{^1H\}$ NMR (125.7 MHz, 20 °C, CDCl$_3$): δ 17.22 (d, 2C, CH(CH$_3$)(CH$_3$), $^2J_{CP}$ = 2.5), 17.60 (s, 1C, Ar-CH$_3$), 18.76 (d, 2C, CH(CH$_3$)(CH$_3$), $^2J_{CP}$ = 2.8), 29.71 (d, 2C, CH(CH$_3$)(CH$_3$), $^1J_{CP}$ = 27.5), 123.22 (d, 1C, $C3_{Ar}$-Me, $^4J_{CP}$ = 11.4), 123.65 (s, 1C, $C6_{Ar}$-H), 124.36 (s, 1C, $C7_{Ar}$-H), 127.65 (d, 1C, $C1_{Ar}$-Ni, $^2J_{CP}$ = 36.6), 128.29 (s, 1C, $C4_{Ar}$-H), 128.32 (s, 1C, $C5_{Ar}$-H), 130.09 (s, 1C, $C8_{Ar}$-H), 131.85 (s, 1C, C_{quat}), 141.09 (d, 1C, C_{quat}, $^3J_{CP}$ = 4.1), 161.65 (d, 1C, $C2_{Ar}$-OP, $^3J_{CP}$ = 10.1). $^{31}P\{^1H\}$ NMR (202.4 MHz, 20 °C, CDCl$_3$): δ 189.85.

(κ^P,κ^C-2-OP(i-Pr)$_2$-naphth-3-yl)NiBr(NCMe) (1e-NCMe). *Method A:* 200 mg (250 μmol) of **1e** containing 2 – 5 % w/w residual toluene were dissolved in a minimum amount of MeCN at 80 °C (12 mL). The resulting yellow solution was slowly cooled down to room temperature, kept in a fridge at – 10 °C for 4 h to induce gradual crystallization, and subsequently kept at –35 °C overnight. The resulting yellow crystals were isolated and washed with cold MeCN (2 x 2.5 mL) and dried under vacuum. Yield: 168 mg of yellow crystals (383 μmol, 77 %). *Method B:* 200 mg

(250 μmol) of **1e** containing 2 – 5 % w/w residual toluene were suspended in 10 mL Et$_2$O. Addition of 130 μL MeCN (2.5 mmol, 10 equiv) turned the orange suspension yellow. The mixture was stirred at r. t. for 30 min and the residues were isolated by cannula filtration, washed with 2 x 5 mL Et$_2$O and dried under vacuum. Yield: 174 mg of yellow microcrystalline material (396 μmol, 79 %). Anal. Calc. for C$_{18}$H$_{23}$BrNiOP: C, 49.25; H, 5.28; N, 3.19. Found: C, 49.13; H, 5.44; N, 3.15.

(κ^P,$\kappa^{C\alpha}$,$\kappa^{C\gamma}$-2-CH$_2$=CH-CH-1-naphtyl-OP(*i*-Pr)$_2$)NiBr (2g). To a solution of 600 mg **1g** (2.00 mmol) in 10 mL acetonitrile were added 575 mg {(*i*-PrCN)NiBr$_2$}$_n$ (2.00 mmol, 1.00 equiv) and 558 μL Et3N (4.00 mmol, 2.00 equiv), and the green mixture was stirred overnight at r.t. The resulting red mixture was evaporated, the residues were re-dissolved in 6 mL THF, and 10 mL Hexanes added to induce precipitation. Filtration and evaporation gave residues, which were treated with 10 mL Et$_2$O, filtered and evaporated. The resulting residues were dissolved in 2 mL Et$_2$O, diluted with 2 mL pentane, filtered, and kept at –35 °C overnight. The mixture of orange crystals and other precipitate was evaporated, washed with cold pentane (2 x 2 mL), and dried under vacuum. NMR characterization showed some impurities. Elemental analysis was not performed on this sample. ^{1}H NMR (500 MHz, 20 °C, CD$_3$CN): δ 0.88 (dd, 3H, P[CH(CH_3)(CH$_3$)][CH(CH$_3$)(CH$_3$)], $^3J_{HH}$ = 7.1, $^3J_{HP}$ = 13.6), 0.99 (dd, 3H, P[CH(CH$_3$)(CH_3)][CH(CH$_3$)(CH$_3$)], $^3J_{HH}$ = 7.2, $^3J_{HP}$ = 17.1), 1.24 (dd, 3H, P[CH(CH$_3$)(CH$_3$)][CH(CH_3)(CH$_3$)], $^3J_{HH}$ = 7.0, $^3J_{HP}$ = 14.7), 1.55 (dd, 3H, P[CH(CH$_3$)(CH$_3$)][CH(CH$_3$)(CH_3)], $^3J_{HH}$ = 7.2, $^3J_{HP}$ = 17.4), 2.32 (hept, 1H, P[CH(CH$_3$)$_2$][CH(CH$_3$)$_2$], $^3J_{HH}$ = 7.1), 2.47 (oct, 1H, P[CH(CH$_3$)$_2$][CH(CH$_3$)$_2$], $^3J_{HH}$ ≈ $^2J_{HP}$ = 7.7), 3.16-3.26 (m, 2H, Ar-C$_\alpha$$H$(Ni) and Ar-C$_\alpha$H(Ni)-C$_\beta$H=C(*H*a)(Hb) *cis* to C$_\beta$*H*), 4.36 (dd, 1H, Ar-C$_\alpha$H(Ni)-C$_\beta$H=C(Ha)(*H*b) *trans* to C$_\beta$*H*), $^3J_{HH}$ = 7.2, $^2J_{HH'}$ = 4.3), 4.95 (ddd, 1H, Ar-C$_\alpha$H(Ni)-C$_\beta$*H*=CH$_2$), 7.13 (d, 1H, C3$_{Ar}$-*H*, $^3J_{HH}$ = 8.4), 7.22-7.28 (m, 2H, C4$_{Ar}$-*H* and C6$_{Ar}$-*H*), 7.32 (t, 1H, C7$_{Ar}$-*H*, $^3J_{HH}$ = 7.4), 7.59 (d, 1H, C5$_{Ar}$-*H*, $^3J_{HH}$ = 8.1), 8.19 (d, 1H, C4$_{Ar}$-*H*, $^3J_{HH}$ = 8.3). ^{13}C{^{1}H} NMR (125.7 MHz, 20 °C, CDCl$_3$): δ 15.72 (d, 1C, P[CH(CH_3)(CH$_3$)][CH(CH$_3$)(CH$_3$)], $^2J_{CP}$ = 1.8), 17.72 (s, 1C, P[CH(CH$_3$)(CH$_3$)][CH(CH_3)(CH$_3$)]), 17.99 (d, 1C, P[CH(CH$_3$)(CH_3)][CH(CH$_3$)(CH$_3$)], $^2J_{CP}$ = 3.6), 18.10 (d, 1C, P[CH(CH$_3$)(CH$_3$)][CH(CH$_3$)(CH_3)], $^2J_{CP}$ = 6.3), 29.48 (d, 1C, P[CH(CH$_3$)$_2$][CH(CH$_3$)$_2$], $^1J_{CP}$ = 26.6), 30.41 (d, 1C, P[CH(CH$_3$)$_2$][CH(CH$_3$)$_2$], $^1J_{CP}$ = 15.9), 59.07 (d, 1C, Ar-C$_\alpha$H(Ni), $^2J_{CP}$ = 5.5), 77.48 (d, 1C, Ar-C$_\alpha$H(Ni)-C$_\beta$H=CH$_2$, $^2J_{CP}$ = 20.8), 110.92 (d, 1C, Ar-C$_\alpha$H(Ni)-C_βH=CH$_2$, $^3J_{CP}$ = 2.5), 120.62 (d, 1C, C2$_{Ar}$-C$_\alpha$H(Ni), $^3J_{CP}$ = 6.5), 122.23 (s, 1C, C8$_{Ar}$-H), 122.61 (s, 1C, C4$_{Ar}$-H), 126.03 (d, 1C, C_{quat},

$^5J_{CP}$ = 2.9), 126.61 (s, 2C, $C6_{Ar}$-H and $C7_{Ar}$-H), 126.92 (s, 1C, $C3_{Ar}$-H), 128.27 (s, 1C, C5Ar-H, hidden under the peak for C_6D_6), 134.46 (s, 1C, C_{quat}), 151.41 (s, 1C, $C1_{Ar}$-OP). $^{31}P\{^1H\}$ NMR (202.4 MHz, 20 °C, CDCl₃): δ 199.72.

Synthesis of bis-phosphinite-NiBr₂ complexes 3. To a solution of 2.00 mmol of the desired naphthyl phosphinite in 15 mL CH₂Cl₂ was added 403 mg of {(*i*-PrCN)NiBr₂}ₙ (1.40 mmol, 0.7 equiv). The resulting dark red mixture was stirred at r.t. for 30 min. The excess NiBr₂ was separated by cannula filtration and the residues extracted with an extra 2 x 15 mL CH₂Cl₂. The combined extracts were evaporated to give orange to red brownish powders that were crystallized from hot MeCN, cooled to room temperature first and then to – 10 °C for 3 – 4 h, and finally placed overnight in a freezer at – 35 °C. The resulting dark red crystals were washed with cold MeCN (3 x 5–10 mL), and dried under vacuum. Their purity was established by elemental analysis, whereas ^{31}P and ^1H NMR spectra in CDCl₃ suggested they exist as 2 isomers in solution in a 1:9 ratio; we infer that the centrosymmetric structure is the major isomer while the minor one is a C2-symmetric structure or else the cis isomer. For instance, in compound **3f**, both isomers have also been detected in the solid state ^{31}P NMR (see **Fig. S103**) at δ 137.10 (major) and 132.45 ppm (minor). In the case of deuterated ligands, the complexes were used as powders in H/D scrambling experiments without crystallization.

***trans*-{1-naphthyl-OP(*i*-Pr)₂}₂NiBr₂·CH₃CN (3a·CH₃CN).** This complex co-crystallized with 1 molecule of MeCN per nickel center, yielding 618 mg of dark red crystals (0.79 mmol, 79%). ^1H NMR (500 MHz, 20 °C, CDCl₃): δ 1.48 (m, 6H, CH(C*H₃*)(CH₃), $^3J_{HH}$ = 6.3), 1.59 (3, 6H, CH(CH₃)(C*H₃*), $^3J_{HH}$ = 6.3), 2.1.99(br s, 1.5H, C*H₃*CN), 2.84 (hept, 2H, C*H*(CH₃)(CH₃), $^3J_{HH}$ = 7.0, minor), 2.92 (hept, 2H, C*H*(CH₃)(CH₃), $^3J_{HH}$ = 7.2, major), 7.40-7.48 (m, 2H, C6_{Ar}-*H* and C7_{Ar}-*H*, $^3J_{HH} \approx$ 6.9), 7.50 (t, 1H, C3_{Ar}-*H*, $^3J_{HH}$ = 7.9), 7.59 (d, 1H, C4_{Ar}-*H*, $^3J_{HH}$ = 8.2), 7.81 (d, 1H, C5_{Ar}-*H*, $^3J_{HH}$ = 7.2), 8.10 (d, 1H, C8_{Ar}-*H*, $^3J_{HH}$ = 7.5), 8.42 (d, 1H, C2_{Ar}-*H*, $^3J_{HH}$ = 7.5, major), 8.46 (d, 1H, C2_{Ar}-*H*, $^3J_{HH}$ = 7.6, minor). $^{13}C\{^1H\}$ NMR (125.7 MHz, 20 °C, CDCl₃): δ 2.06 (s, 0.5C, C*H₃*CN), 18.19 (s, 2C, CH(C*H₃*)(CH₃), minor), 18.48 (s, 2C, CH(C*H₃*)(CH₃), major), 19.26 (s, 2C, CH(CH₃)(C*H₃*), minor), 19.77 (s, 2C, CH(CH₃)(C*H₃*), major), 28.91 (s, 2C, C*H*(CH₃)(CH₃), minor), 29.98 (s, 2C, C*H*(CH₃)(CH₃), major), 113.78 (s, 1C, C2_{Ar}-H, minor), 113.95 (s, 1C, C2_{Ar}-H, major), 116.53 (s, 1C, CH₃*C*N), 122.16 (s, 1C, C8_{Ar}-H), 122.59 (s, 1C, C4_{Ar}-H), 125.11 (s, 1C, C3_{Ar}-H, major), 125.3 (s, 1C, C3_{Ar}-H, minor), 125.76 (s, 1C, C7_{Ar}-H), 126.51 (s, 1C, C6_{Ar}-H),

126.60 (s, 1C, C_{quat}), 127.78 (s, 1C, $C5_{Ar}$-H), 134.79 (s, 1C, C_{quat}), 150.84 (s, 1C, $C1_{Ar}$-OP). ^{31}P{^{1}H} NMR (202.4 MHz, 20 °C, CDCl$_3$): δ 130.37 (s, 1P, minor), 135.65 (s, 1P, major). Anal. Calc. for C$_{34}$H$_{45}$Br$_2$NNiO$_2$P$_2$: C, 52.34; H, 5.81; N, 1.80. Found: C, 52.64; H, 5.97; N, 1.75.

trans-{2-Et-1-naphthyl-OP(*i*-Pr)$_2$}$_2$NiBr$_2$ (3d). Yield : 439 mg of dark red crystals (0.55 mmol, 55%). ^{1}H NMR (500 MHz, 20 °C, CDCl$_3$): δ 1.08 (m, 6H, CH(C*H*$_3$)(CH$_3$), $^3J_{HH}$ = 8.0), 1.21 (t, 3H, Ar-CH$_2$C*H*$_3$, $^3J_{HH}$ = 7.6), 1.33 (m, 6H, CH(CH$_3$)(C*H*$_3$), $^3J_{HH}$ = 6.6), 2.91 (q, 2H, Ar-C*H*$_2$CH$_3$, $^3J_{HH}$ = 7.6), 3.04 (m, 2H, C*H*(CH$_3$)(CH$_3$), J = 7.0, minor), 3.19 (m, 2H, C*H*(CH$_3$)(CH$_3$), J = 6.7, major), 7.27 (d, 1H, C3$_{Ar}$-*H*, $^3J_{HH}$ = 8.5), 7.43 (t, 1H, C6$_{Ar}$-*H*, $^3J_{HH}$ = 7.4), 7.53 (t, 1H, C7$_{Ar}$-*H*, $^3J_{HH}$ = 7.6), 7.56 (d, 1H, C4$_{Ar}$-*H*, $^3J_{HH}$ = 8.5), 7.79 (d, 1H, C5$_{Ar}$-*H*, $^3J_{HH}$ = 8.1), 8.33 (d, 1H, C8$_{Ar}$-*H*, $^3J_{HH}$ = 8.3). ^{13}C{^{1}H} NMR (125.7 MHz, 20 °C, CDCl$_3$): δ 14.76 (s, 1C, Ar-CH$_2$*C*H$_3$), 17.59 (s, 2C, CH(*C*H$_3$)(CH$_3$), minor), 17.74 (s, 2C, CH(*C*H$_3$)(CH$_3$), major), 17.98 (s, 2C, CH(CH$_3$)(*C*H$_3$)), 24.54 (s, 1C, Ar-*C*H$_2$CH$_3$, minor), 25.67 (s, 1C, Ar-*C*H$_2$CH$_3$, major), 29.97 (m, 2C, *C*H(CH$_3$)(CH$_3$), minor), 31.34 (vt/pt, 2C, *C*H(CH$_3$)(CH$_3$), $^1J_{CP}$ = 10.3,major), 123.44 (s, 1C, *C*8$_{Ar}$-H), 123.91 (s, 1C, *C*4$_{Ar}$-H), 125.42 (s, 1C, *C*6$_{Ar}$-H), 126.18 (s, 1C, *C*7$_{Ar}$-H), 127.36 (s, 1C, *C*3$_{Ar}$-H), 127.84 (s, 1C, C$_{quat}$), 127.92 (s, 1C, *C*5$_{Ar}$-H), 131.29 (s, 1C, C$_{quat}$), 133.78 (s, 1C, C$_{quat}$), 149.16 (s, 1C, *C*1$_{Ar}$-OP). ^{31}P{^{1}H} NMR (202.4 MHz, 20 °C, CDCl$_3$): δ 131.50 (s, 1P, minor), 136.10 (s, 1P, major). Anal. Calc. for C$_{36}$H$_{50}$Br$_2$NiO$_2$P$_2$: C, 54.37; H, 6.34. Found: C, 54.58; H, 6.67; N, 0.05.

trans-{3-Me-2-naphthyl-OP(*i*-Pr)$_2$}$_2$NiBr$_2$ (3f). Yield: 465 mg of dark red crystals (0.61 mmol, 61%). ^{1}H NMR (500 MHz, 20 °C, CDCl$_3$): δ 1.35 (m, 6H, CH(C*H*$_3$)(CH$_3$), $^3J_{HH}$ = 6.8), 1.52 (m, 6H, CH(CH$_3$)(C*H*$_3$), $^3J_{HP}$ = 6.8), 2.34 (s, 3H, Ar-C*H*$_3$), 2.76 (hept, 2H, C*H*(CH$_3$)(CH$_3$), $^3J_{HH}$ = 7.0, minor), 2.84 (hept, 2H, C*H*(CH$_3$)(CH$_3$), $^3J_{HH}$ = 7.2, major), 7.33-7.42 (m, 2H, C6$_{Ar}$-*H* and C7$_{Ar}$-*H*, $^3J_{HH} \approx$ 7.8, $^4J_{HH} \approx$ 1.9), 7.57 (s, 1H, C4$_{Ar}$-*H*), 7.72 (d, 1H, C5$_{Ar}$-*H*, $^3J_{HH}$ = 8.0), 7.75 (d, 1H, C8$_{Ar}$-*H*, $^3J_{HH}$ = 8.1), 8.51 (s, 1H, C1$_{Ar}$-*H*,), major), 8.55 (s, 1H, C1$_{Ar}$-*H*,), minor). ^{13}C{^{1}H} NMR (125.7 MHz, 20 °C, CDCl$_3$): δ 17.58 (s, 1C, Ar-*C*H$_3$), 18.01 (s, 2C, CH(*C*H$_3$)(CH$_3$), minor), 18.28 (s, 2C, CH(*C*H$_3$)(CH$_3$), major), 19.12 (s, 2C, CH(CH$_3$)(*C*H$_3$), minor), 19.67 (s, 2C, CH(CH$_3$)(*C*H$_3$), major), 28.56 (s, 2C, *C*H(CH$_3$)(CH$_3$), minor), 29.59 (s, 2C, *C*H(CH$_3$)(CH$_3$), major), 114.43 (s, 1C, *C*1$_{Ar}$-H), 124.43 (s, 1C, *C*6$_{Ar}$-H or *C*7$_{Ar}$-H), 125.55 (s, 1C, *C*6$_{Ar}$-H or *C*7$_{Ar}$-H), 126.94 (s, 1C, *C*8$_{Ar}$-H), 127.05 (s, 1C, *C*5$_{Ar}$-H), 129.10 (s, 1C, *C*4$_{Ar}$-H), 129.60 (s, 1C, C$_{quat}$), 130.14 (s, 1C, C$_{quat}$), 132.74 (s, 1C, C$_{quat}$), 152.35 (s, 1C, *C*2$_{Ar}$-OP). ^{31}P{^{1}H} NMR (202.4 MHz, 20 °C, CDCl$_3$): δ 129.30

(s, 1P, minor), 134.55 (s, 1P, major). Anal. Calc. for $C_{34}H_{46}Br_2NiO_2P_2$: C, 53.23; H, 6.04. Found: C, 53.36; H, 6.35.

***trans*-{D₇-1-naphthyl-OP(*i*-Pr)₂}₂NiBr₂ (3a-D₇).** D_8-1-naphthol (152 mg, 1.00 mmol) was converted to the corresponding phosphinite and all of the recovered ligand was used to prepare the title complex. Yield: 348 mg of an orange powder (0.462 mmol, 92 %).

***trans*-{2-CH₃CD₂-1-naphthyl-OP(*i*-Pr)₂}₂NiBr₂·CH₃CN (3d-D₂).** 2-CH₃CD₂-1-naphthol (348 mg, 2.00 mmol) was converted to the corresponding phosphinite and all of the recovered ligand was used to prepare the title complex. Yield: 727 mg of a dark red powder (0.910 mmol, 91 %).

***trans*-{3-CD₃-2-naphthyl-OP(*i*-Pr)₂}₂NiBr₂ (3f-D₃).** 3-CD₃-2-naphthol (322 mg, 2.00 mmol) was converted to the corresponding phosphinite and all of the recovered ligand was used to prepare the title complex. Yield: 681 mg of a red powder (0.881 mmol, 88 %).

H/D scrambling experiments. *In acetonitrile:* Deuterated complexes (100 mg) were heated at 80 °C in 2 mL CH_3CN for the required time (1 or 3 days). The final mixtures were cooled down to room temperature and placed overnight in a freezer at –35 °C. The resulting crystals were collected, washed with cold CH_3CN (2 x 1.5 mL) and dried under vacuum. The material was analyzed by ^1H NMR in $CDCl_3$ and the integration of the incorporated protons into D positions (if any) was compared to the integration of the methyne in $P(CH(CH_3)_2)_2$ to determine the amount of protons at D positions. *In toluene:* Deuterated complexes (100 mg) were heated at 100 °C in 2 mL $C_6H_5CH_3$ for the required time (1 or 3 days). Evaporation of the solvent under vacuum, re-dissolution in CH_3CN at r.t., filtration and cooling overnight in a freezer at –35 °C afforded crystals, which were collected, washed with cold CH_3CN (2 x 1.5 mL) and dried under vacuum. The material was analyzed by ^1H NMR and the integration of the incorporated protons into D positions (if any) was compared to the integration of the methyne in $P(CH(CH_3)_2)_2$ to determine the ratio of protons at D positions.

***cis*-(κ^P,$\kappa^{P'}$-2-P(*i*-Pr)₂-1-naphtyl-OP(*i*-Pr)₂)NiBr₂ (4).** To a solution of 260 mg of 1-naphthyl-OP(*i*-Pr)₂ (1.00 mmol) in 4 mL acetonitrile was added 288 mg of {(*i*-PrCN)NiBr₂}$_n$ (0.50 mmol, 0.50 equiv). This gave a red mixture containing an orange precipitate of **3a** which was subsequently heated at 200 °C for 1 h in the Monowave 50. The resulting dark red solution was evaporated, and the residues were treated in 6 mL toluene and filtered to remove the insoluble residues. Evaporation

of the filtrate gave a red, sticky material that was re-dissolved in 3 mL acetonitrile, filtered and placed in a freezer at –35 °C for 48 h. The red crystals were isolated and washed with cold acetonitrile (3 x 1.5 mL) and dried under vacuum to give 56 mg of crystalline material. ^{1}H NMR (500 MHz, 20 °C, C_6D_6): δ 1.00-1.14 (m, 12H, C1$_{Ar}$-OP[CH(CH_3)(CH$_3$)]$_2$ and C2$_{Ar}$-P[CH(CH_3)(CH$_3$)]$_2$), 1.40 (dd, 6H, C1$_{Ar}$-OP[CH(CH$_3$)(CH_3)]$_2$, $^3J_{HH}$ = 6.9, $^3J_{HP}$ = 16.8), 1.66 (dd, 6H, C2$_{Ar}$-P[CH(CH$_3$)(CH_3)]$_2$, $^3J_{HH}$ = 7.0, $^3J_{HP}$ = 15.7), 2.61 (hept, 2H, C2$_{Ar}$-P[CH(CH$_3$)$_2$]$_2$, $^3J_{HH}$ = 7.0), 2.83 (oct, 2H, C1$_{Ar}$-OP[CH(CH$_3$)$_2$]$_2$, $^3J_{HH}$ ≈ $^2J_{HP}$ = 7.2), 6.93 (d, 1H, C3$_{Ar}$-H, $^3J_{HH}$ = 8.2), 7.19 (d, 1H, C4$_{Ar}$-H, $^3J_{HH}$ = 8.7), 7.21-7.26 (m, 2H, C6$_{Ar}$-H and C7$_{Ar}$-H), 7.46-7.52 (m, 1H, C5$_{Ar}$-H), 8.03-8.09 (m, 1H, C8$_{Ar}$-H). ^{13}C{^{1}H} NMR (125.7 MHz, 20 °C, C_6D_6): δ 18.80 (s, 2C, C1$_{Ar}$-OP[CH(CH_3)(CH$_3$)]$_2$ or C2$_{Ar}$-P[CH(CH_3)(CH$_3$)]$_2$), 18.86 (s, 2C, C1$_{Ar}$-OP[CH(CH_3)(CH$_3$)]$_2$ or C2$_{Ar}$-P[CH(CH_3)(CH$_3$)]$_2$), 20.04 (s, 2C, C1$_{Ar}$-OP[CH(CH$_3$)(CH_3)]$_2$), 21.00 (s, 2C, C2$_{Ar}$-P[CH(CH$_3$)(CH_3)]$_2$), 26.31 (d, 2C, C1$_{Ar}$-OP[CH(CH$_3$)$_2$]$_2$, $^2J_{CP}$ = 27.7), 34.50 (d, 2C, C2$_{Ar}$-P[CH(CH$_3$)$_2$]$_2$, $^2J_{CP}$ = 26.5), 122.86 (d, 1C, C4$_{Ar}$-H), 122.96 (d, 1C, C8$_{Ar}$-H), 126.57 (d, 1C, C3$_{Ar}$-H), 127.41 (d, 1C, C6$_{Ar}$-H or C7$_{Ar}$-H), 128.26 (s, 1C, C5$_{Ar}$-H, hidden under the peak for C_6D_6), 129.12 (s, 1C, C6$_{Ar}$-H or C7$_{Ar}$-H), 135.98 (s, 1C, C2$_{Ar}$-P), 157.20 (s, 1C, C1$_{Ar}$-OP). ^{31}P{^{1}H} NMR (202.4 MHz, 20 °C, C_6D_6): δ 29.33 (d, 1P, C2$_{Ar}$-P, 64.8), 176.77 (d, 1P, C1$_{Ar}$-OP, 65.4).

(i-Pr$_2$PH)$_2$NiBr$_2$. To a solution of 288 mg of 2-Et-1-naphthyl-OP(i-Pr)$_2$ (1.00 mmol) in 4 mL acetonitrile was added 316 mg of {i-PrCN)NiBr$_2$}$_n$ (1.10 mmol, 1.10 equiv). The resulting dark greenish solution that contained a red precipitate of **3d** was heated at 160 °C for 1 h in the Monowave 50. The resulting emerald green solution was left to stand at room temperature for 1 h during which time a pale green precipitate formed. The solution was separated by filtration and kept overnight in a –35 °C freezer to give red crystals and some additional precipitate {NiBr$_2$(MeCN)$_x$}$_n$. The latter was removed by washing the solid residues with 3 x 2 mL H$_2$O, and the water was removed by washing with 3 x 1.5 mL cold acetonitrile. After drying under vacuum, 44 mg of red crystals were collected. While the crystal structure discloses the *cis* isomer of the complex (with a solid state ^{31}P NMR with δ 30.34 ppm, see **Fig. S122**), the solution NMR of the complex in C_6D_6 is rather in accordance with the *trans* isomer, as proven by the correlation between the experimental spectrum and the simulation realized with a $^vJ_{P\text{-}H}$ coupling constant of 300 - 400 Hz. ^{1}H NMR (500 MHz, 20 °C, C_6D_6): δ 1.09 (br s, 12H, CH(CH_3)(CH$_3$)), 1.50 (br s, 12H, CH(CH$_3$)(CH_3)), 2.07 (br s, 4H, CH(CH$_3$)$_2$), 3.79 (br m, 2H, P-H, ^vJ = 345). ^{13}C{^{1}H} NMR (125.7

MHz, 20 °C, C$_6$D$_6$): δ 20.59 (s, CH(*CH$_3$*)(CH$_3$)), 21.25 (s, CH(CH$_3$)(*CH$_3$*)), 21.98 (br s, *CH*(CH$_3$)$_2$). ^{31}P{^{1}H} NMR (202.4 MHz, 20 °C, C$_6$D$_6$): δ 41.74.

4.6 Acknowledgements

4.7 References

[1] (a) Kakiuchi, F.; Kochi, T., Transition-Metal-Catalyzed Carbon-Carbon Bond Formation via Carbon-Hydrogen Bond Cleavage. *Synthesis* **2008**, *2008* (19), 3013-3039. (b) Ackermann, L., Carboxylate-Assisted Transition-Metal-Catalyzed C−H Bond Functionalizations: Mechanism and Scope. *Chemical Reviews* **2011**, *111* (3), 1315-1345. (c) Yamaguchi, J.; Yamaguchi, A. D.; Itami, K., C−H Bond Functionalization: Emerging Synthetic Tools for Natural Products and Pharmaceuticals. *Angewandte Chemie International Edition* **2012**, *51* (36), 8960-9009. (d) Ackermann, L., Metal-catalyzed direct alkylations of (hetero)arenes via C−H bond cleavages with unactivated alkyl halides. *Chemical Communications* **2010**, *46* (27), 4866-4877. (e) Chen, D. Y. K.; Youn, S. W., C−H Activation: A Complementary Tool in the Total Synthesis of Complex Natural Products. *Chemistry – A European Journal* **2012**, *18* (31), 9452-9474.

[2] (a) Klei, S. R.; Tan, K. L.; Golden, J. T.; Yung, C. M.; Thalji, R. K.; Ahrendt, K. A.; Ellman, J. A.; Tilley, T. D.; Bergman, R. G., C—H Bond Activation by Iridium and Rhodium Complexes: Catalytic Hydrogen—Deuterium Exchange and C—C Bond-Forming Reactions. In Activation and Functionalization *of C−H Bonds*, American Chemical Society: 2004; Vol. 885, pp 46-55. (b) Colby, D. A.; Bergman, R. G.; Ellman, J. A., Rhodium-Catalyzed C−C Bond Formation via Heteroatom-Directed C−H Bond Activation. *Chemical Reviews* **2010**, *110* (2), 624-655. (c) Rouquet, G.; Chatani, N., Catalytic Functionalization of C(sp^2)−H and C(sp^3)−H Bonds by Using Bidentate Directing Groups. *Angewandte Chemie International Edition* **2013**, *52* (45), 11726-11743. (d) Arockiam, P. B.; Bruneau, C.; Dixneuf, P. H., Ruthenium(II)-Catalyzed C–H Bond Activation and Functionalization. *Chemical Reviews* **2012**, *112* (11), 5879-5918. (e) Lyons, T. W.; Sanford, M. S., Palladium-Catalyzed Ligand-Directed C−H Functionalization Reactions. *Chemical Reviews* **2010**, *110* (2), 1147-1169. (f) Xu, L.-M.; Li, B.-J.; Yang, Z.; Shi, Z.-J., Organopalladium(iv) chemistry. *Chemical Society Reviews* **2010**, *39* (2), 712-733. (g) Sehnal, P.; Taylor, R. J. K.; Fairlamb, I. J. S., Emergence of Palladium(IV) Chemistry in Synthesis and Catalysis. *Chemical Reviews* **2010,** *110* (2), 824-889.

[3] (a) Castro, L. C. M.; Chatani, N., Nickel Catalysts/N,N′-Bidentate Directing Groups: An Excellent Partnership in Directed C–H Activation Reactions. Chemistry Letters 2015, 44 (4), 410-421. (b) Gandeepan, P.; Müller, T.; Zell, D.; Cera, G.; Warratz, S.; Ackermann, L., 3d Transition Metals for C–H Activation. *Chemical Reviews* **2019**, *119* (4), 2192-2452. (c) Beattie, D. D.; Grunwald, A. C.; Perse, T.; Schaefer, L. L. ; Love, J. A., Understanding Ni(II)-Mediated C(sp^3)-H Activation: Tertiray Ureas as Model Substrates. *Journal of the American Chemical Society* **2018**, *140*, 12602-12610. (d) Roy, P.; Bour, J. R.; Kampf, J. W.; Sanford, M. S., Catalytically Relevant Intermediates in the Ni-Catalyzed C(sp^2)−H and C(sp^3)−H Functionalization of Aminoquinoline Substrates. *Journal of the American Chemical Society* **2019**, *141*, 17382-17387.

[4] Vabre, B.; Deschamps, F.; Zargarian, D., Ortho Derivatization of Phenols through C–H Nickelation: Synthesis, Characterization, and Reactivities of Ortho-Nickelated Phosphinite Complexes. *Organometallics* **2014**, *33* (22), 6623-6632.

[5] Mangin, L. P.; Zargarian, D., C–H nickellation of phenol-derived phosphinites: regioselectivity and structures of cyclonickellated complexes. *Dalton Transactions* **2017,** *46* (46), 16159-16170.

[6] Mangin, L. P.; Zargarian, D., C–H Nickelation of Aryl Phosphinites: Mechanistic Aspects. *Organometallics* **2019**, *38* (7), 1479-1492.

[7] Bedford, R. B.; Limmert, M. E., Catalytic Intermolecular Ortho-Arylation of Phenols. *The Journal of Organic Chemistry* **2003**, *68* (22), 8669-8682.

[8] Satoh, T.; Inoh, J.-i.; Kawamura, Y.; Kawamura, Y.; Miura, M.; Nomura, M., Regioselective Arylation Reactions of Biphenyl-2-ols, Naphthols, and Benzylic Compounds with Aryl Halides under Palladium Catalysis. *Bulletin of the Chemical Society of Japan* **1998**, *71* (9), 2239-2246.

[9] This compound was prepared in-house. For synthetic details see ESI.

[10] It should be noted here that a lower H-incorporation had been observed with the $C_6D_5OPR_2$ analogue mentioned above, indicating a smoother reaction with **1a-D$_7$**.

[11] For instance, C−H nickelation of 3-R-$C_6H_4OP(i$-Pr)$_2$ occurs at C6 either exclusively (R = Me, Cl, OMe, NMe$_2$) or predominantly (R= F; C6:C1= 6:1). Moreover, C−H nickelation is facilitated by electron-releasing substituents. Similar observations were made in the case of phosphinites derived from 3,5-R$_2$-phenols: C−H nickelation does not take place at all with R = Me and Cl, whereas with R = OMe it does proceed, albeit very sluggishly. See ref. 6 for these results.

[12] The impact of substituent electronics on C−H nickelation has also been probed in the case of pincer-type ligands featuring two donor moieties such as phosphinites or phosphines. See these reports for details: (a) Vabre, B.; Lambert, M. L.; Petit, A.; Ess, D. H.; Zargarian, D. *Organometallics* **2012**, *31*, 6041. (b) Castonguay, D. Spasyuk, N. Madern, A. L. Beauchamp, and D. Zargarian, "Regioselective Hydroamination of Acrylonitrile Catalyzed by Cationic Pincer Complexes of Nickel(II)" *Organometallics* **2009**, *28*, 2134-2141.

[13] The contention that the C1 position is more electron-rich is based on literature reports on the greater reactivity of this site in the Claisen rearrangement, a reaction that is more sensitive to electronic as opposed to steric factors. For instance, the rearrangement of *O*-allyl-2-naphthol takes place with a C1:C3 regioselectivity of 98:2: Gozzo, F. C.; Fernandes, S. A.; Rodrigues, D. C.; Eberlin, M. N.; Marsaioli, A. J., Regioselectivity in Aromatic Claisen Rearrangements. *The Journal of Organic Chemistry* **2003**, *68* (14), 5493-5499.

[14] These values were derived by applying the following equation $\tau_4 = \{360 - (\alpha+\beta)]/141$ wherein α and β are the largest bond angles in the given structure. This approach generates values ranging from 0 for an ideal square plane to 1 for an ideal tetrahedron. For a discussion of this topic see the following reports: (a) Yang, L.; Powell, D. R.; Houser, R. P., Structural variation in copper(i) complexes with pyridylmethylamide ligands: structural analysis with a new four-coordinate geometry index, $\tau4$. *Dalton Transactions* **2007,** 955-964. (b) Rosiak, D.Okuniewski, A.; Chojnacki, J., Copper(I) iodide ribbons coordinated with thiourea derivative, *Acta Crystallographica Section C* **2018,** 74 (12), 1650-1655.

[15] The mounted crystal of **2g** was found to be a 2-component twin and the Br ligand was found disordered in both the complexes of the asymmetric unit.

[16] (a) Spasyuk, D. M.; Gorelsky, S. I.; van der Est, A.; Zargarian, D., Characterization of Divalent and Trivalent Species Generated in the Chemical and Electrochemical Oxidation of a Dimeric Pincer Complex of Nickel. *Inorganic Chemistry* **2011**, *50* (6), 2661-2674. (b) Vabre, B.; Lambert, M. L.; Petit, A.; Ess, D. H.; Zargarian, D., Nickelation of PCP- and POCOP-Type Pincer Ligands: Kinetics and Mechanism. *Organometallics* **2012**, *31* (17), 6041-6053. (c) Lefèvre, X.; Spasyuk, D. M.; Zargarian, D., New POCOP-Type Pincer Complexes of Nickel(II), *J. Organomet. Chem.* **2011**, *696* (4), 864-870.

[17] In contrast, control experiments showed no decomposition at 160 °C for the free phosphinite **1a** or the cyclonickelated product **2a**.

[18] Quantification of this C−H nickelation reaction was done by integrating the ^{31}P singlet at 192 ppm against the signal for [*n*-Bu$_4$N][PF$_6$] used as an internal standard.

[19] The major resonances present in the ^{31}P{^{1}H} NMR spectrum of this mixture were the same as in the spectrum for the analogous reaction with one equivalent of **1a** (i.e., AB doublets arising from compound **4** and the singlet at 121 ppm), but in this case we observed an additional minor resonance, a set of doublets at 167 and 150 ppm with J ≈ 27 ppm.

[20] Recall that isolation and full characterization of phosphinite adducts of the cyclonickelated complexes has been reported previously: See ref 4.

[21] Monitoring the thermal profile of this reaction revealed an exothermic reaction as soon as it reached 150 °C.

[22] It is worth noting that the ^{1}H NMR (C_6D_6) spectrum of (i-Pr_2PH)$_2NiBr_2$ crystals indicated that it adopts a *trans* conformation in solution: simulations established that the broadened multiplet detected at ca. 3.79 ppm for the P-*H* protons arises from a virtual coupling with *trans* P nuclei featuring $^vJ_{PH}$ of 300 - 400 Hz.

[23] Complete crystallographic data for all compounds structurally characterized in this study, including the molecular diagrams not included here, are presented in Electronic Supporting Information.

[24] (a) Ng, J. K.-P.; Tan, G.-K.; Vittal, J. J.; Leung, P.-H., Optical Resolution and the Study of Ligand Effects on the Ortho-Metalation Reaction of Resolved (±)-Diphenyl[1-(1-naphthyl)ethyl]phosphine and Its Arsenic Analogue. *Inorganic Chemistry* **2003**, *42* (23), 7674-7682. (b) Ding, Y.; Chiang, M.; Pullarkat, S. A.; Li, Y.; Leung, P.-H., Synthesis, Coordination Characteristics, Conformational Behavior, and Bond Reactivity Studies of a Novel Chiral Phosphapalladacycle Complex. *Organometallics* **2009**, *28* (15), 4358-4370. (c) Li, X.-R.; Yang, X.-Y.; Li, Y.; Pullarkat, S. A.; Leung, P.-H., Efficient access to a designed phosphapalladacycle catalyst via enantioselective catalytic asymmetric hydrophosphination. *Dalton Transactions* **2017**, *46* (4), 1311-1316. (d) Li, X.-R.; Chen, Y.; Pang, B. P.; Tan, J.; Li, Y.; Pullarkat, S. A.; Leung, P.-H., Efficient Synthesis of Malonate Functionalized Chiral Phosphapalladacycles and their Catalytic Evaluation in Asymmetric Hydrophosphination of Chalcone. *European Journal of Inorganic Chemistry* **2018**, *2018* (39), 4385-4390.

[25] (a) Cloutier, J.-P.; Zargarian, D., Functionalization of the Aryl Moiety in the Pincer Complex (NCN)Ni^{III}Br$_2$: Insights on Ni^{III}-Promoted Carbon–Heteroatom Coupling. *Organometallics* **2018**, *37* (9), 1446-1455. (b) Cloutier, J.-P.; Rechignat, L.; Canac, Y.; Ess, D. H.; Zargarian, D., C–O and C–N Functionalization of Cationic, NCN-Type Pincer Complexes of Trivalent Nickel: Mechanism, Selectivity, and Kinetic Isotope Effect. *Inorganic Chemistry* **2019**, *58* (6), 3861-3874.

[26] Obermayer, D.; Znidar, D.; Glotz, G.; Stadler, A.; Dallinger, D.; Kappe, C. O., Design and Performance Validation of a Conductively Heated Sealed-Vessel Reactor for Organic Synthesis. *The Journal of Organic Chemistry* **2016**, *81* (23), 11788-11801.

[27] (a) Vabre, B.; Spasyuk, D. M.; Zargarian, D., Impact of Backbone Substituents on POCOP-Ni Pincer complexes: A Structural, Spectroscopic and Electrochemical Study, *Organometallics* **2012**, *31* (24), 8561-8570. (b) Vabre, B.; Lindeperg, F.; Zargarian, D., Direct, one-pot synthesis of POCOP-type pincer complexes from metallic nickel. *Green Chemistry* **2013**, *15* (11), 3188-3194.

Chapitre 4 – Annexes

S4.1 General information and references

The crystallographic data for all resolved structures were collected either on a Bruker Microsource (Cu source) or a Bruker Venture Metaljet (Ga source) via the Bruker APEX II or APEX III[1] softwares. Cell refinement and data reduction were performed using SAINT[2]. An empirical absorption correction, based on multiple measurements of equivalent reflections, was applied using the program SADABS[3]. The space group was confirmed by the XPREP[4] routine in APEX. The structures were solved in OLEX[5] using the SHELX[6] suite and refined by full-matrix least squares with SHEXL[7]. All non-hydrogen atoms were refined with anisotropic displacement parameters, whereas hydrogen atoms were set in calculated positions and refined as riding atoms, with thermal parameters being 1.5 times that of the carbon bearing the H in question. All Thermal Ellipsoid Plots were drawn using Pluton[8].

S4.1 Experimental procedure for the synthesis of organic precursors

3-Me-2-naphthol. *2-MeO-naphthalene:* In a round bottom flask purged with N_2, 2.88 g 2-naphthol (20 mmol) were dissolved in 20 mL DMF. 4.14 g K_2CO_3 (30 mmol, 1.5 equiv) was added and then dropwise 1.87 mL MeI (30 mmol, 1.5 equiv). The mixture was stirred at room temperature for 2 h after which monitoring by TLC showed disappearance of the starting material. The K_2CO_3/base was quenched with addition of HCl until no more CO_2 evolved form the mixture. 100 mL H2O were added, and the aqueouse slurry was extracted 3x with a 1:2 mixture of Et_2O:Hexanes. The organic phase was washed with 2x 30 mL dilute $Na_2S_2O_3$, 2x 20 mL H_2O and dried with $MgSO_4$.

[1] Bruker (2012). APEX2 / Bruker (2016) APEX3, Bruker AXS Inc., Madison, WI, USA.

[2] Bruker (2012). "SAINT Integration Software for Single Crystal Data", Bruker AXS Inc., Madison, WI, USA.

[3] Sheldrick, G. M., "Comparison of silver and molybdenum microfocus X-ray sources for single crystal structure determination", *J. Appl.Cryst.*, **2015**, *48*, 3-10

[4] Bruker (2012). Data Preparation and Reciprocal Space Exploration Program, Bruker AXS Inc., Madison, WI, USA.

[5] A: O. V. Dolomanov, L. J. Bourhis, R. J. Gildea, J. A. K. Howard and H. Puschmann. "OLEX2: a complete structure solution, refinement and analysis program". *J. Appl. Cryst.* **2009**, *42*, 339-341.

[6] Sheldrick, G. M., "SHELXT - Integrated space-group and crystal structure determination", *Acta Cryst.*, 2015, A71, 3-8.

[7] Sheldrick, G. M., Crystal structure refinement with SHELXL, *Acta Cryst.*, **2015**, C71, 3-8.

[8] Spek, A. L., *Acta Cryst.*, 2009, D65, 148-155

Evaporation of the organic phase and drying under vacuum afforded 3.14 g of a pale beige powder which ^{1}H spectrum matched that of literature[9] (19.8 mmol, 99 %). *3-Me-2-MeO-naphthalene:* To a solution of 2.37 g 2-MeO-naphthalene (15.0 mmol) in 40 mL THF cooled to – 78 °C were added dropwise 7.2 mL of a 2.5 M BuLi solution in hexanes (18.0 mmol, 1.2 equiv) and the mixture was slowly warmed to 0 °C over a 16-hour period. The resulting red solution was cooled again at – 40 °C and 1.40 mL MeI (22.5 mmol, 1.5 equiv) was added dropwise. The clear yellow mixture was allowed to come back to room temperature, and the volatiles evaporated. 100 mL water was added and the compound extracted with 3x 50 mL Et_2O. The ethereal phase was dried with $MgSO_4$ and evaporated. The off-white residues were purified over silica gel with 3:97 AcOEt:Hexanes as eluent yielding 1.83 g of a pure white solid which ^{1}H NMR spectrum matched that of literature[10] (10.6 mmol, 70 %). *3-Me-2-naphthol*: To a solution 1.72 g of 3-Me-2-MeO-naphthalene (10.0 mmol) in 30 mL AcOH were added 8 mL of 48 % w/w aqueous HBr (71 mmol, 7.1 equiv). The Schlenk flask was covered with aluminium foil and the mixture heated at 120 °C for 16 hours. After removal of the volatiles under vacuum, 50 mL H_2O and 25 mL Et_2O were added and vigorously stirred for 5 minutes at rt. The ethereal phase was separated, and the aqueous phase extracted with and extra 2x 25mL Et2O. The combined organic phase was washed with 3x 30 mL 5 % aqueous $Na_2S_2O_3$ until no precipitation was observed anymore in the aqueous phase. Further washing of the ethereal phase with 2x 30 mL H_2O, drying over $MgSO_4$, evaporation and drying under vacuum yielded 1.49 g of an off-white powder which ^{1}H NMR spectrum matched that of literature[11] (1.49 g, 94 %). The product shown to be > 98 % pure and was used as it, without requiring further purification.

3-CD₃-2-naphthol. This compound was prepared according to the same procedure as for protio 3-Me-2-naphthol, but the using CD_3I in the second step. Starting from 1.44 g 2-naphthol (10.0 mmol) afforded 775 mg of the title compound (4.81 mmol, 48 % over 3 steps). No protons were detected on the methyl group by ^{1}H NMR.

2-Et-1-naphthol. A zinc amalgam was prepared by adding 5.00 g zinc dust (76 mmol) and 500 mg $HgCl_2$ (1.8 mmol) in 10 mL H_2O and 250 µL conc. HCl, and stirring for 10 mins at rt. To the

[9] Leowanawat, P.; Zhang, N.; Percec, V., Nickel Catalyzed Cross-Coupling of Aryl C–O Based Electrophiles with Aryl Neopentylglycolboronates. *The Journal of Organic Chemistry* **2012,** *77* (2), 1018-1025.

[10] Zarate, C.; Nakajima, M.; Martin, R., A Mild and Ligand-Free Ni-Catalyzed Silylation via C–OMe Cleavage. *Journal of the American Chemical Society* **2017,** *139* (3), 1191-1197.

[11] Zhang, W.; Ready, J. M., The Ketene-Surrogate Coupling: Catalytic Conversion of Aryl Iodides into Aryl Ketenes through Ynol Ethers. *Angewandte Chemie International Edition* **2014,** *53* (34), 8980-8984.

amalgam was added 2.79 g of 2-Ac-1-naphthol (15.0 mmol) dissolved in 30 mL dioxane. 10 mL conc. HCl were added dropwise over a period of 15 minutes, to prevent overheating of the exothermic reaction. The mixture was then brought to reflux for 16 hours. After cooling down to rt, 50 mL H_2O were added, and the mixture extracted with 3x 50 mL Et_2O. The combined ethereal phase was dried over $MgSO_4$ and evaporated. The light yellow oily residues were purified over silica gel with 1:9 AcOEt:Hexanes as eluent, yielding 2.30 g of a light pink solid which ^{1}H NMR data matched that of literature[12] (13.4 mmol, 89 %). The compound was shown to decompose to a dark reddish slurry if stored at room temperature and exposed to light, whereas it remained clean over months when stored in a fridge at – 10 °C and protected from light.

2-CH₃CD₂-1-naphthol. This compound was prepared according to the same as for protio 2-Et-1-naphthol, but using DCl/D_2O. Starting from 931 mg 2-Ac-1-naphthol (5.00 mmol) afforded 827 mg of the title compound (4.74 mmol, 95 %). The ^{1}H NMR spectrum displayed a singlet for the terminal methyl (with minor satellites: $^3J_{HH} = 7.8$), and a minor quadruplet of triplet corresponding to -C*H*(D)CH₃ ($^3J_{HH} = 7.8$, $^2J_{HD} = 2.1$). Integration of the latter revealed a 95.5 % abundance of D into the α position.

2-allyl-1-naphthol. *1-allyloxy-naphthalene.* 2.88 g 1-naphthol (20.0 mmol) and 3.32 g powdered K_2CO_3 (24.0 mmol, 1.20 equiv) were stirred in 20 mL DMF for 10 minutes. 1.82 mL allyl bromide (21.0 mmol, 1.05 equiv) was added dropwise and the mixture stirred at r.t. for 2 h. After pouring in 100 mL H_2O and stirring for 15 min, the compound was extracted by 3x 50 mL of a 1:2 Et2O Hexanes mixture. The organic phase was washed with 3x 50 mL H_2O, dried over MgSO4 and the solvent evaporated under reduced pressure. ^{1}H NMR analysis of the light-yellow oil matched that of the literature[13] and the latter was found to be > 97 % pure, allowing its use without further purification in the next step. *2-allyl-1-naphthol.* The oil obtained in the previous step was heated neat in the sand bath at 180 – 190 °C for 1 h. After cooling, it was purified on silica gel with 5:95 AcOEt:Hexanes as eluent, yielding 1.64 g (8.92 mmol, 45 %) of a light yellow oil. The final product

[12] Odedra, A.; Wu, C.-J.; Pratap, T. B.; Huang, C.-W.; Ran, Y.-F.; Liu, R.-S., Ruthenium-Catalyzed Aromatization of Enediynes via Highly Regioselective Nucleophilic Additions on a π-Alkyne Functionality. A Useful Method for the Synthesis of Functionalized Benzene Derivatives. *Journal of the American Chemical Society* **2005,** *127* (10), 3406-3412.

[13] Mao, Y.; Liu, Y.; Hu, Y.; Wang, L.; Zhang, S.; Wang, W., Pd-Catalyzed Debenzylation and Deallylation of Ethers and Esters with Sodium Hydride. *ACS Catalysis* **2018,** *8* (4), 3016-3020.

matched that of literature[14] although it usually contained 2 – 6 % impurity due to the *para* Claisen rearrangement.

Bromodiisopropylphosphine. This compound has been prepared by a modification of a reported procedure.[15] To a solution of ClP(i-Pr)$_2$ (1.00 mL, 6.28 mmol, 1.00 equiv) in 6 mL toluene was added LiBr (2.73 g, 31.4 mmol, 5.00 equiv) and the resulting mixture stirred overnight at room temperature. The final mixture was filtered to remove lithium salts, and the solvent removed under vacuum, yielding a light yellow oil (676 mg, 3.43 mmol, 55 %).

S4.3 NMR spectra of characterized compounds

    a.   Compound **2a**
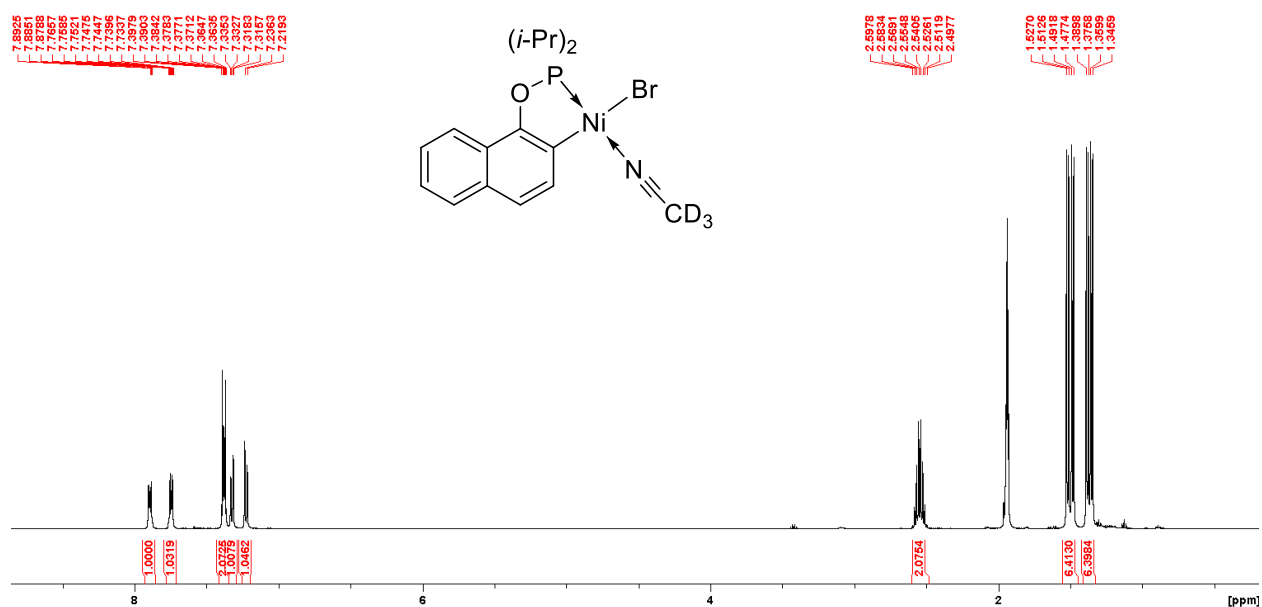
Figure S4.1: Full ^{1}H NMR spectrum of **2a** in CD$_3$CN.

---

[14] Yoshida, M.; Higuchi, M.; Shishido, K., Stereoselective Construction of Substituted Chromans by Palladium-Catalyzed Cyclization of Propargylic Carbonates with 2-(2-Hydroxyphenyl)acetates. *Organic Letters* **2009,** *11* (20), 4752-4755.

[15] Shih, W.-C.; Ozerov, O. V., One-Pot Synthesis of 1,3-Bis(phosphinomethyl)arene PCP/PNP Pincer Ligands and Their Nickel Complexes. *Organometallics* **2015,** *34* (18), 4591-4597.

Figure S4.2: ^{1}H NMR spectrum of **2a** in CD$_3$CN, focus on the aliphatic region.

Figure S4.3: ^{1}H NMR spectrum of **2a** in CD$_3$CN, focus on the aromatic region.

Figure S4.4: Full $^{13}C\{^1H\}$ NMR spectrum of **2a** in CD$_3$CN.

Figure S4.5: $^{13}C\{^1H\}$ NMR spectrum of **2a** in CD$_3$CN, focus on the aliphatic region.

Figure S4.6: $^{13}C\{^1H\}$ NMR spectrum of **2a** in CD$_3$CN, focus on the aromatic region.

Figure S4.7: COSY NMR spectrum of **2a** in CD$_3$CN, focus on the aromatic region.

Figure S4.8: NOESY NMR spectrum of **2a** in CD₃CN, focus on the aromatic/aromatic interactions.

Figure S4.9: HSQC NMR spectrum of **2a** in CD₃CN, focus on the aromatic region.

Figure S4.10: {^{1}H}^{31}P NMR spectrum of **2a** in CD$_3$CN.

b. Compound **2b**

Figure S4.11: Full ^{1}H NMR spectrum of **2b** in CD$_3$CN, focus on the aromatic region.
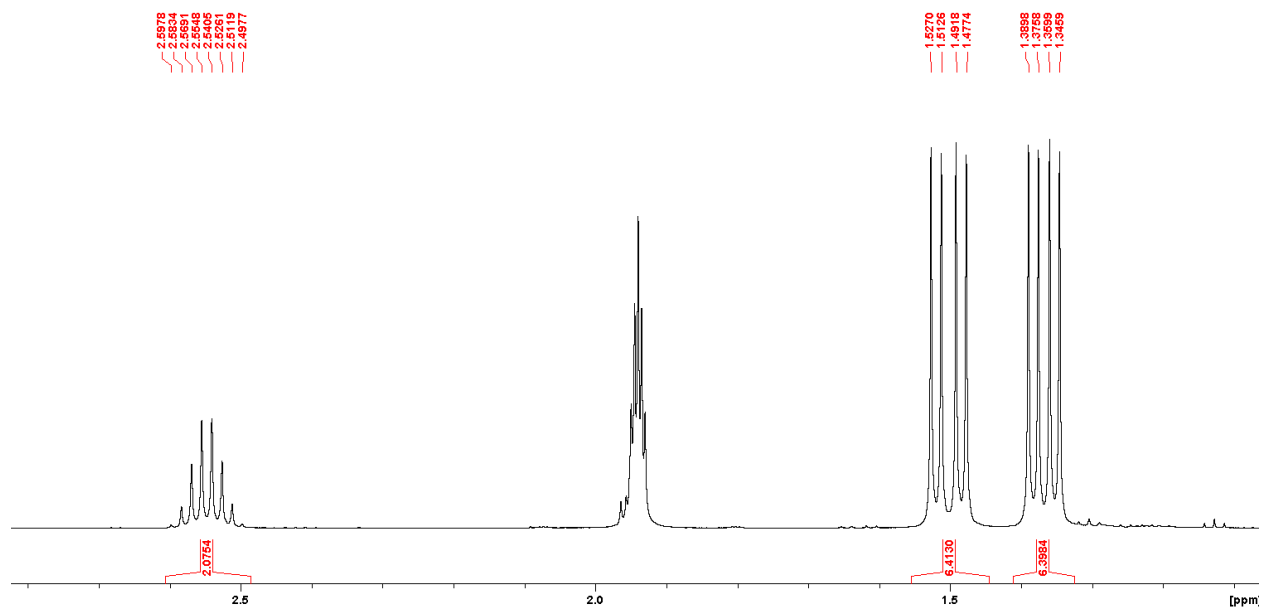

Figure S4.12: ^{1}H NMR spectrum of **2b** in CD$_3$CN, focus on the aliphatic region.

Figure S4.13: ^{1}H NMR spectrum of **2b** in CD$_3$CN, focus on the aromatic region.

Figure S4.14: Full ^{13}C{^{1}H} NMR spectrum of **2b** in CD$_3$CN.

Figure S4.15: $^{13}C\{^1H\}$ NMR spectrum of **2b** in CD$_3$CN, focus on the aliphatic region.

Figure S4.16: $^{13}C\{^1H\}$ NMR spectrum of **2b** in CD$_3$CN, focus on the aromatic region.
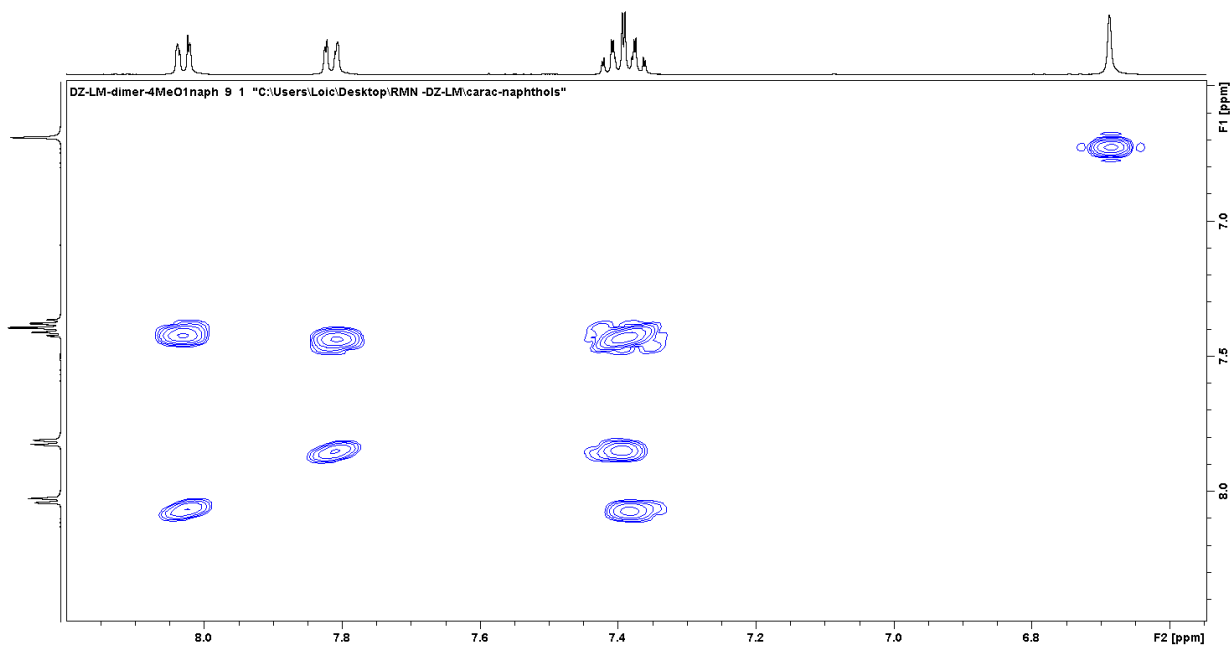
Figure S4.17: COSY NMR spectrum of **2b** in CD$_3$CN, focus on the aromatic region.
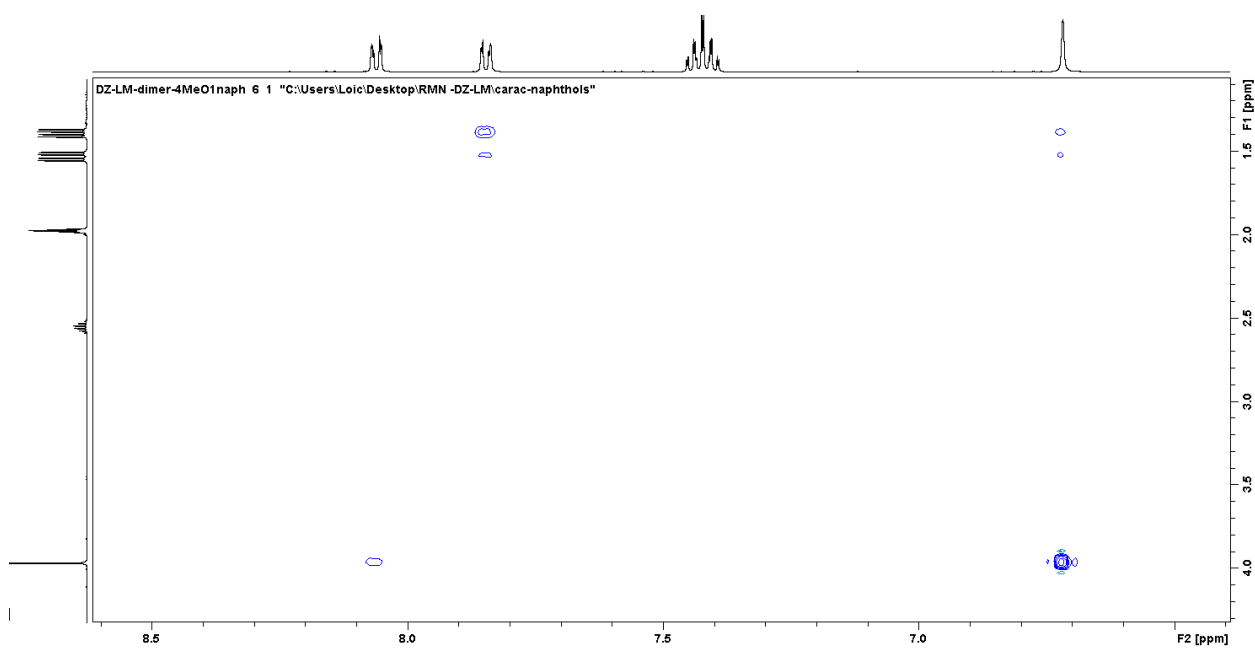
Figure S4.18: NOESY NMR spectrum of **2b** in CD$_3$CN, focus on the aliphatic/aromatic interactions.
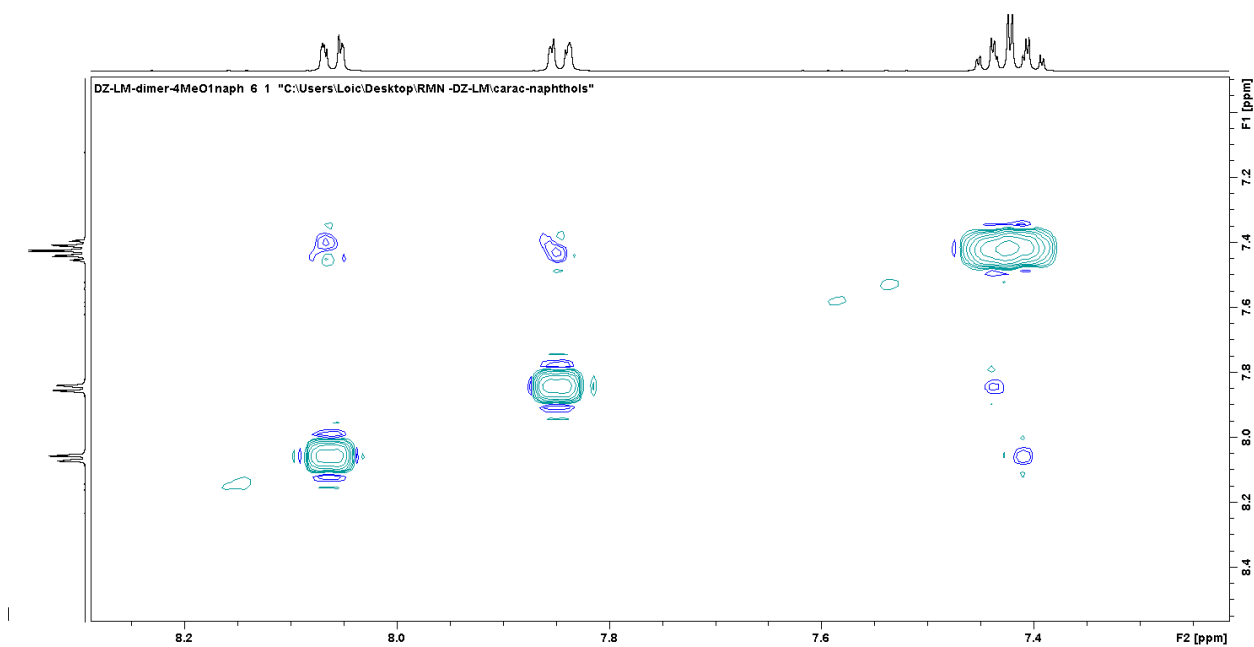
Figure S4.19: NOESY NMR spectrum of **2b** in CD$_3$CN, focus on the aromatic/aromatic interactions.
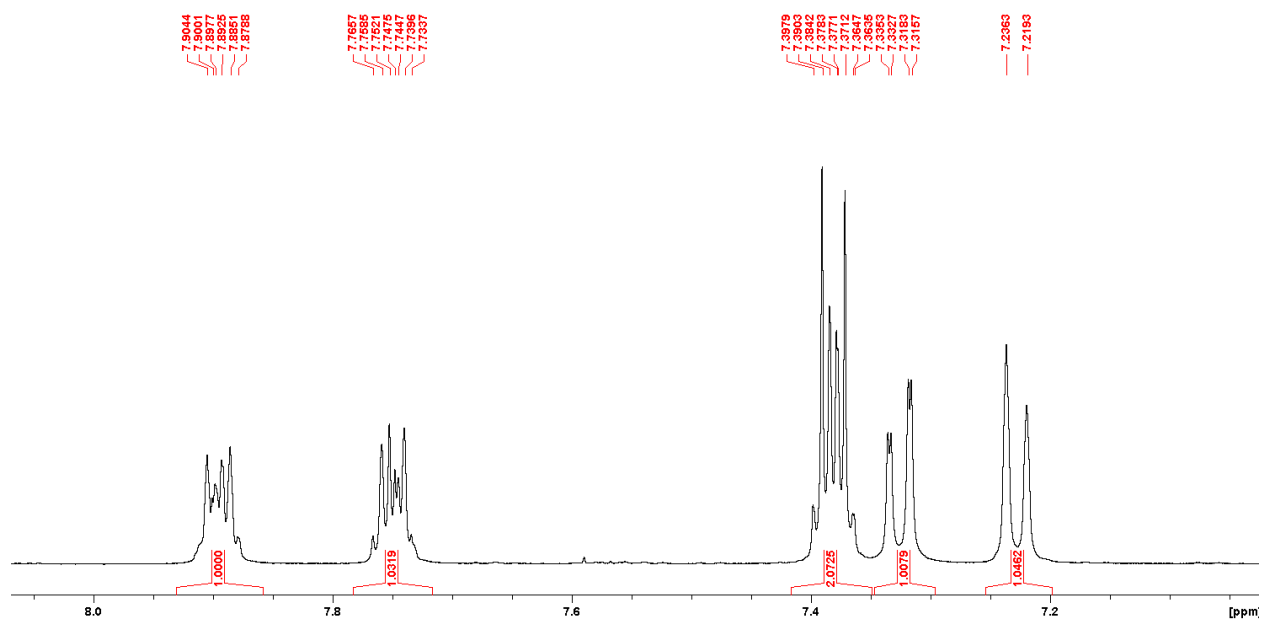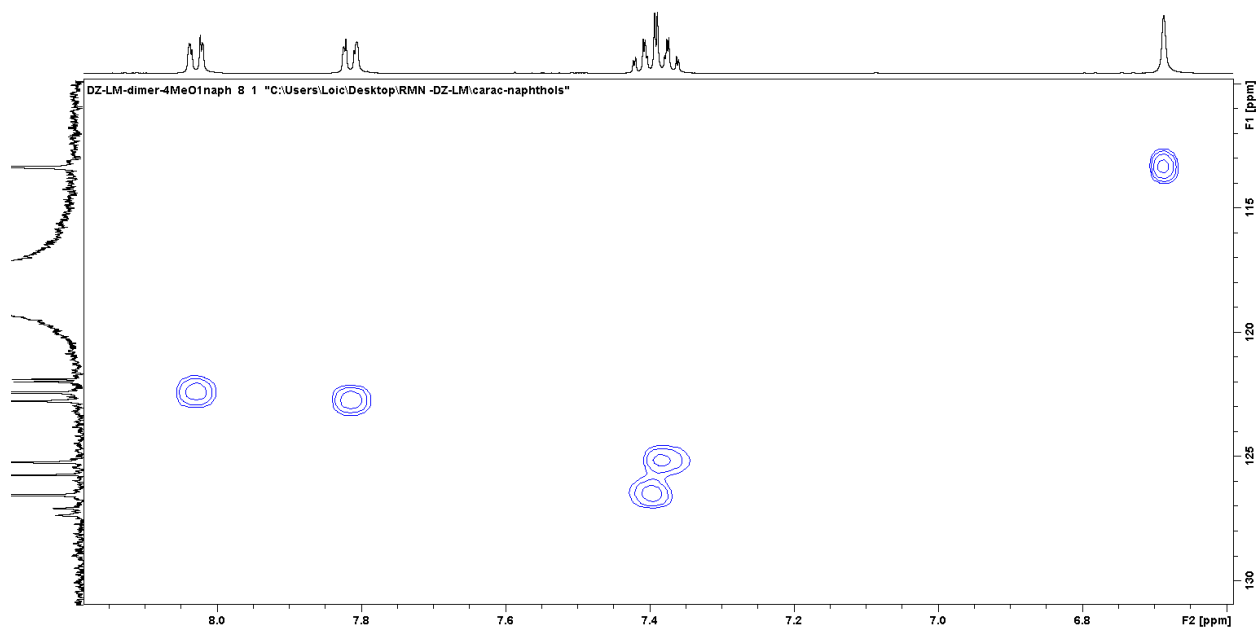

Figure S4.20: HSQC NMR spectrum of **2b** in CD$_3$CN, focus on the aromatic region.
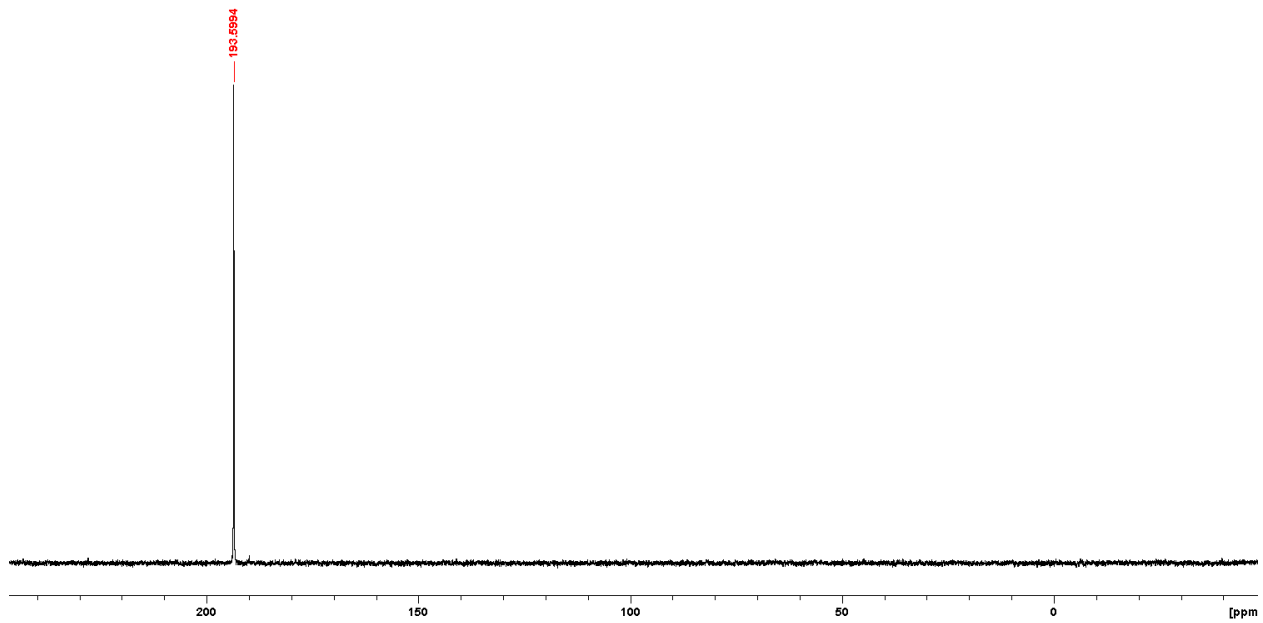
Figure S4.21: $^{31}P\{^1H\}$ NMR spectrum of **2b** in CD_3CN.

c. Compound **2c**
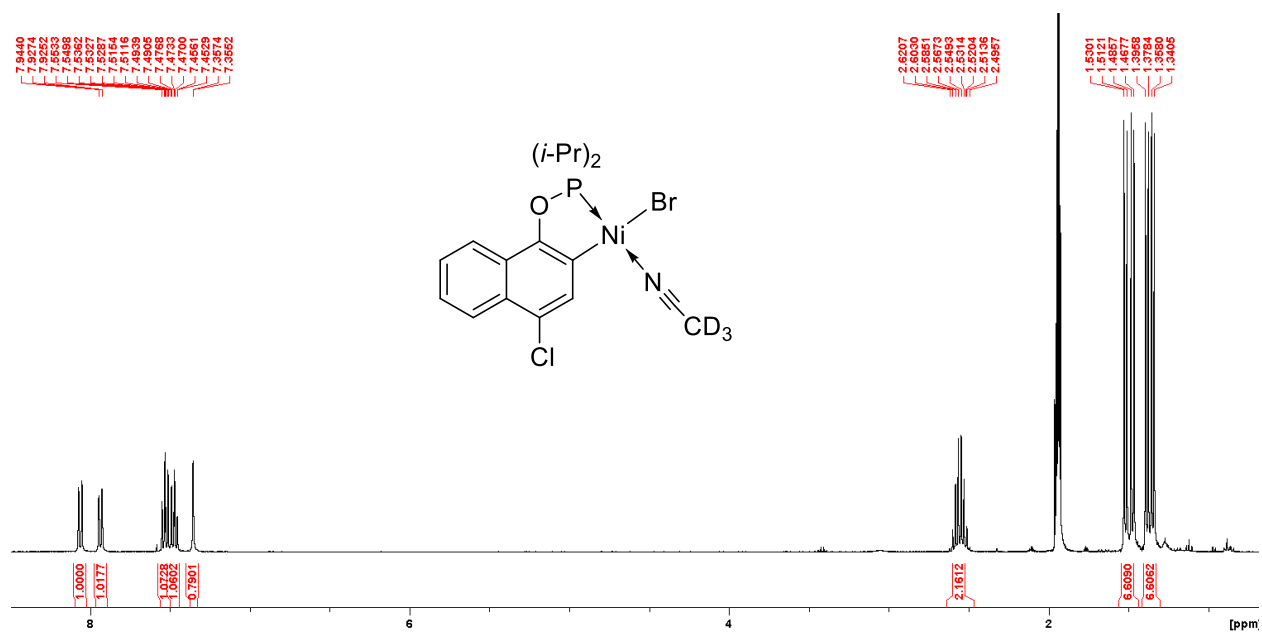
Figure S4.22: Full ^{1}H NMR spectrum of **2c** in CD$_3$CN.
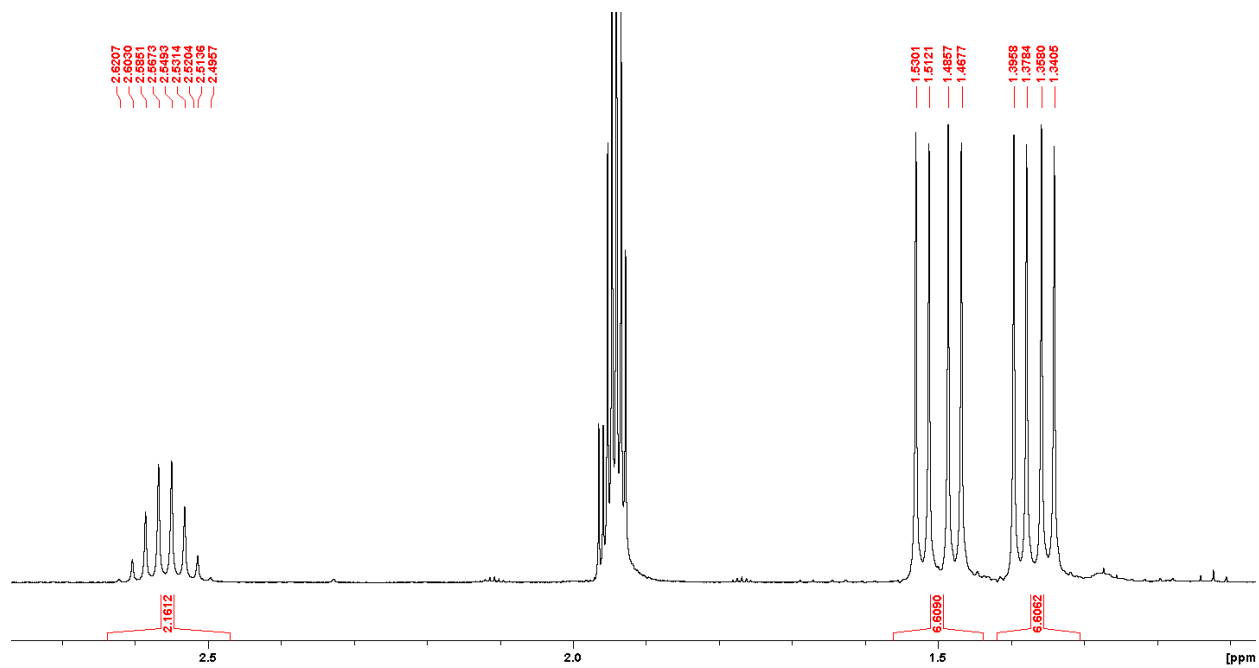
Figure S4.23: ^{1}H NMR spectrum of **2c** in CD$_3$CN, focus on the aliphatic region.
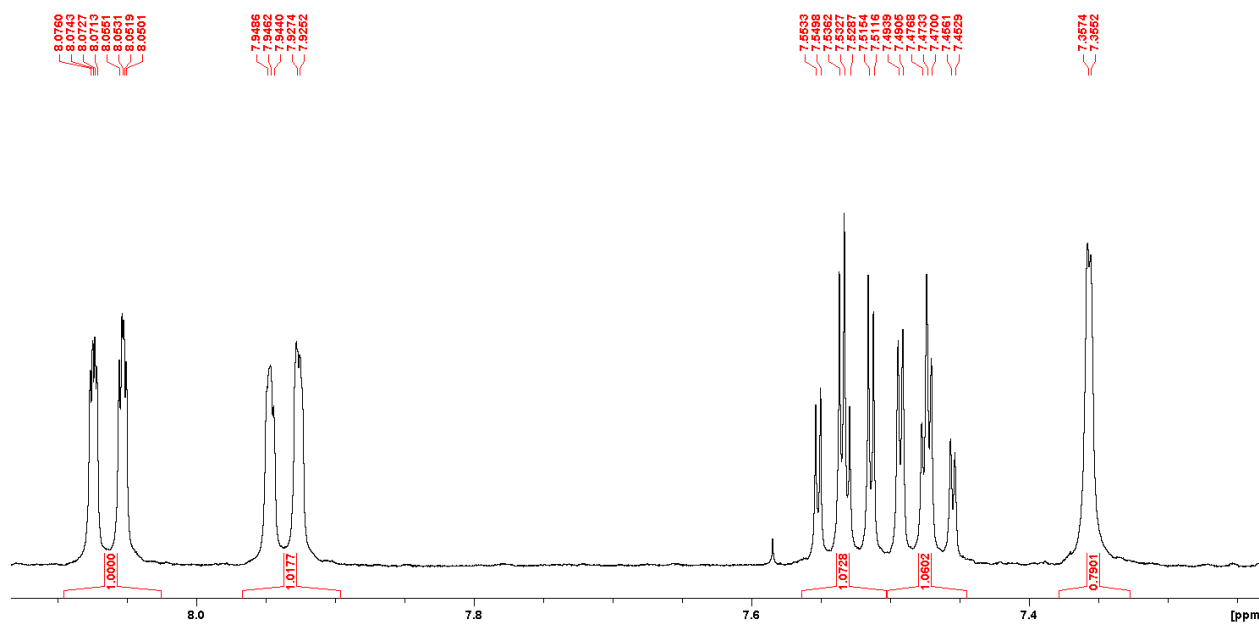
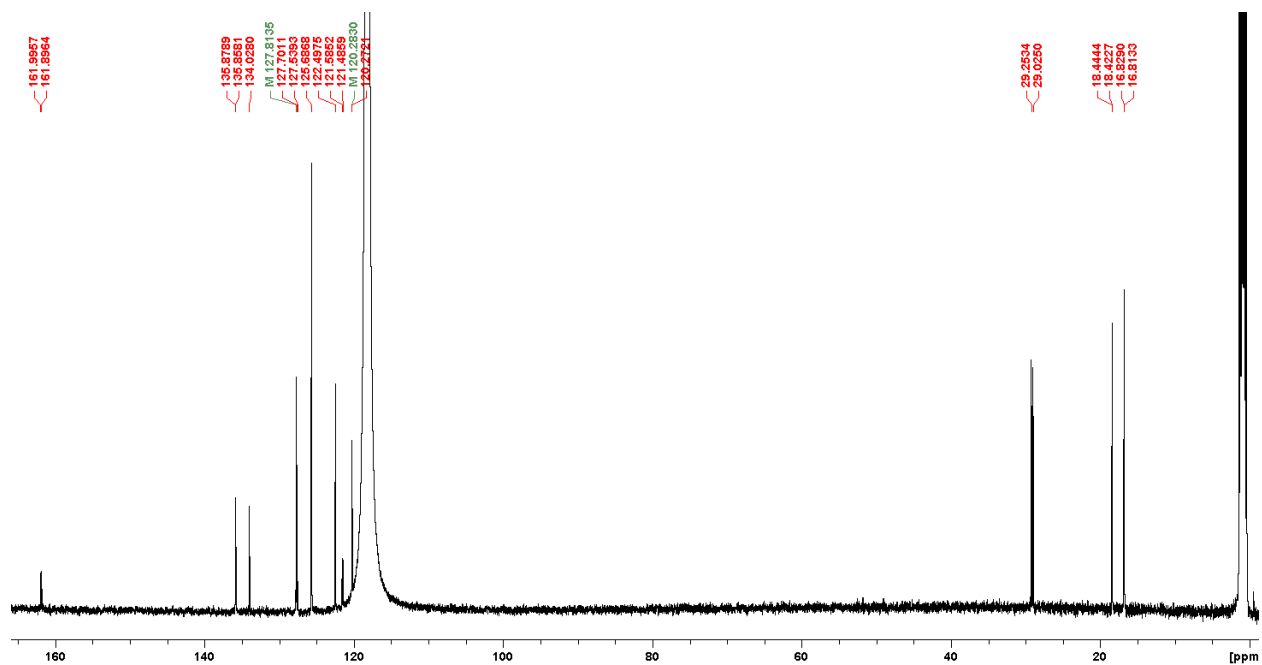Figure S4.24: ^{1}H NMR spectrum of **2c** in CD$_3$CN, focus on the aromatic region.
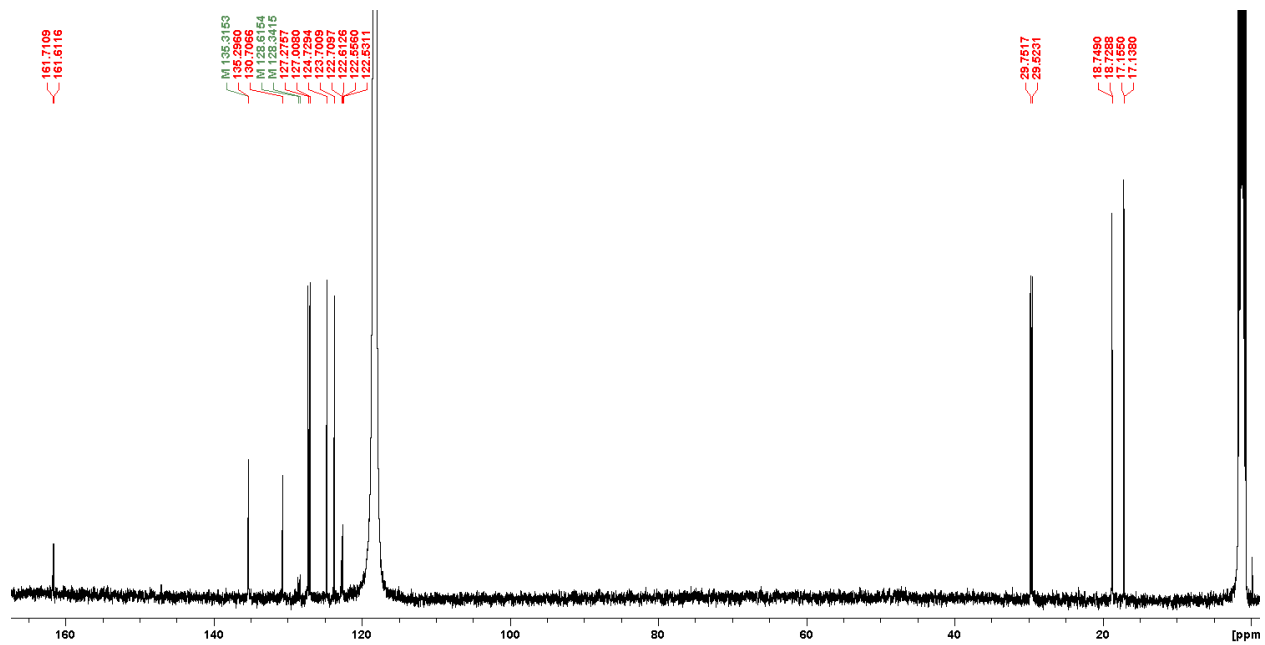
Figure S4.25: Full $^{13}C\{^1H\}$ NMR spectrum of **2c** in CD$_3$CN.
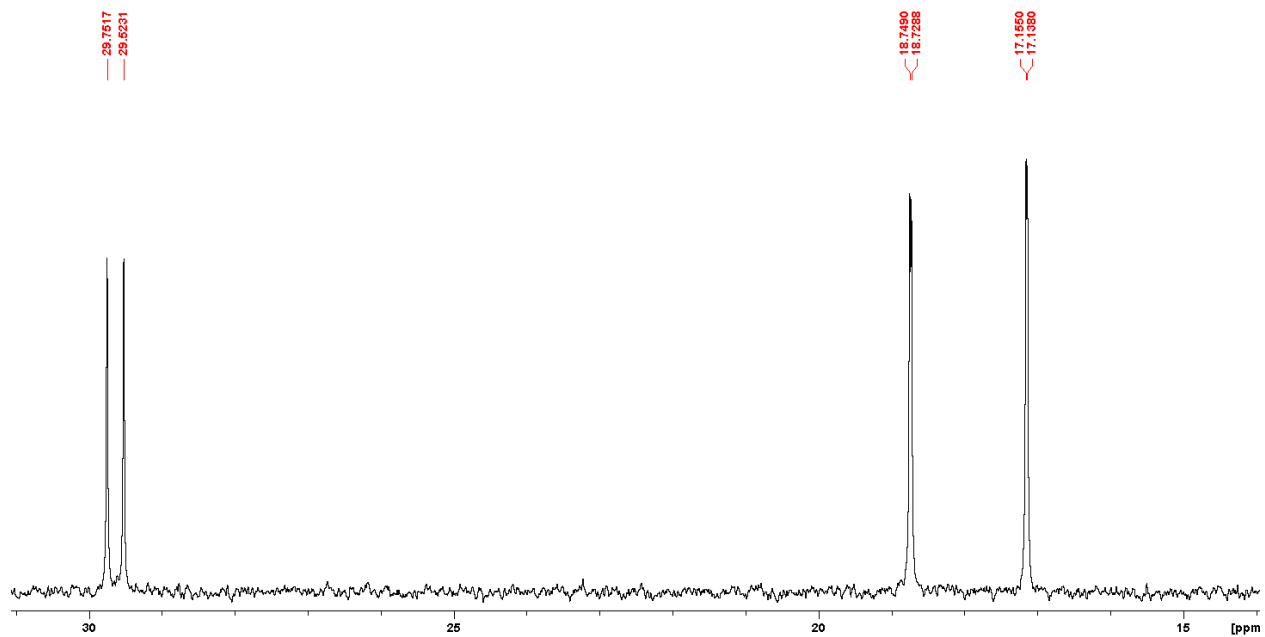
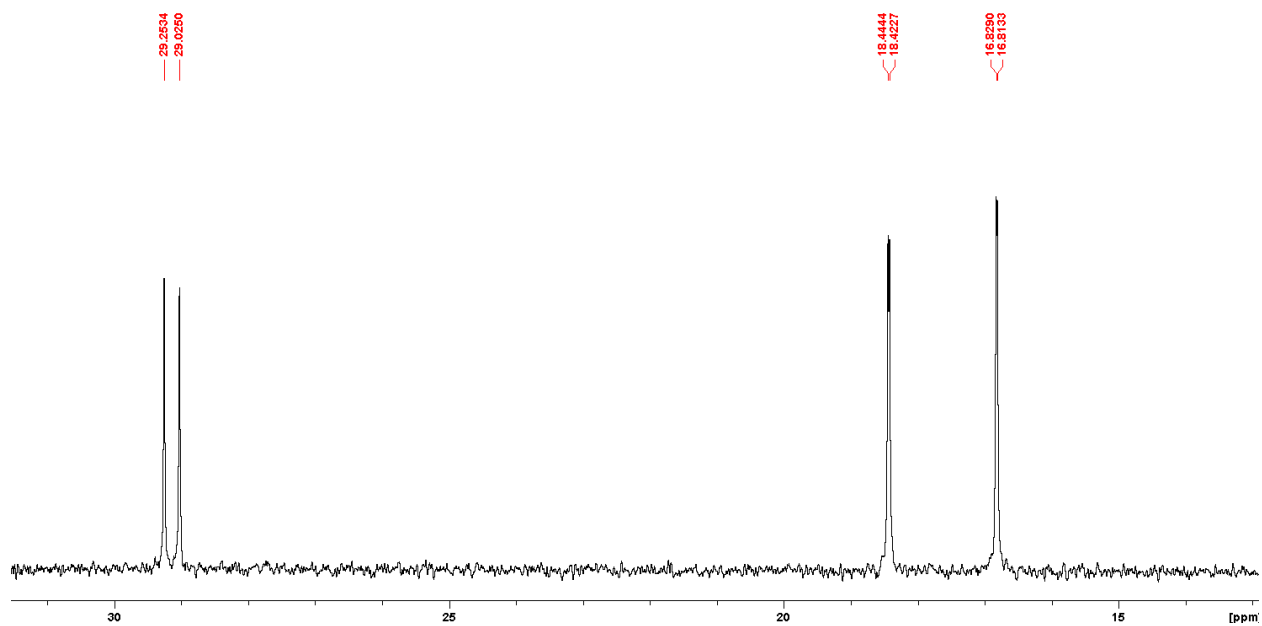Figure S4.26: $^{13}C\{^1H\}$ NMR spectrum of **2c** in CD$_3$CN, focus on the aliphatic region.
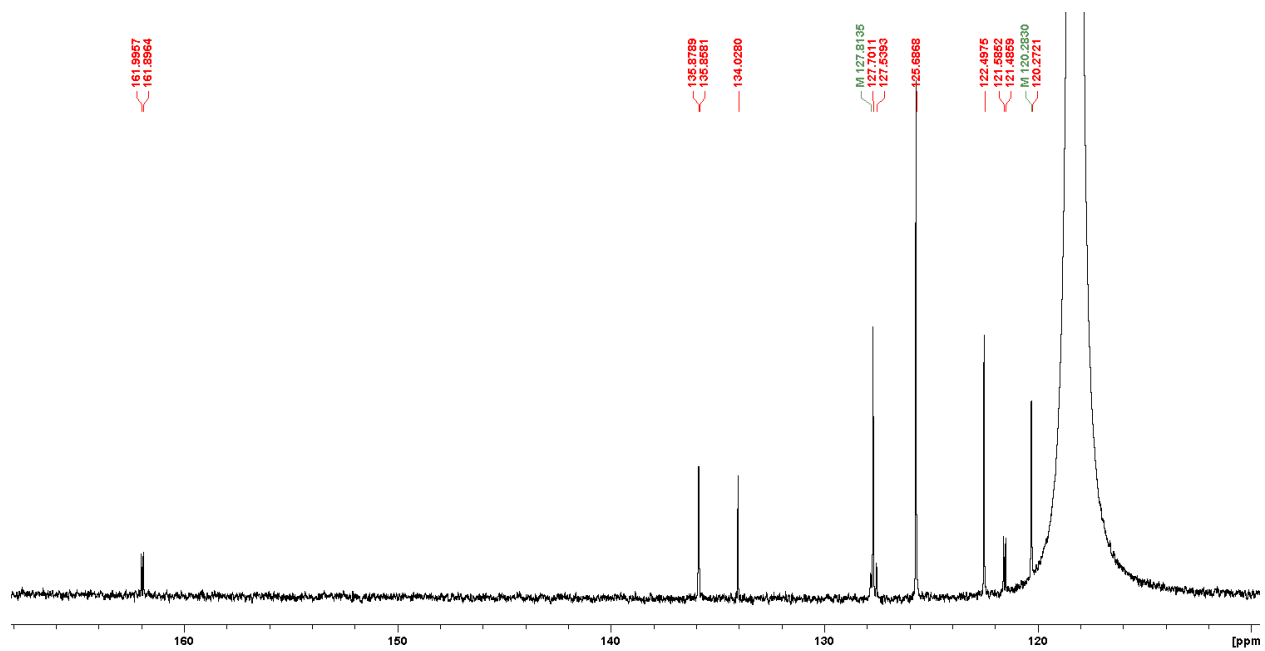
Figure S4.27: $^{13}C\{^1H\}$ NMR spectrum of **2c** in CD$_3$CN, focus on the aromatic region.
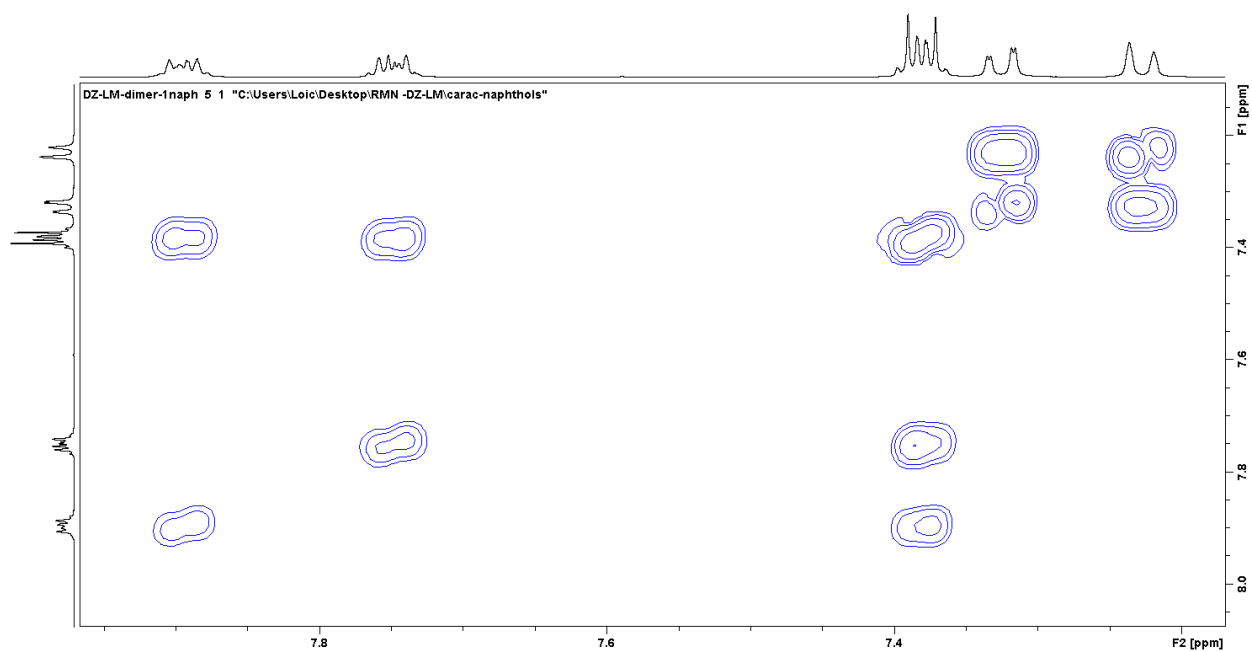

Figure S4.28: COSY NMR spectrum of **2c** in CD$_3$CN, focus on the aromatic region.
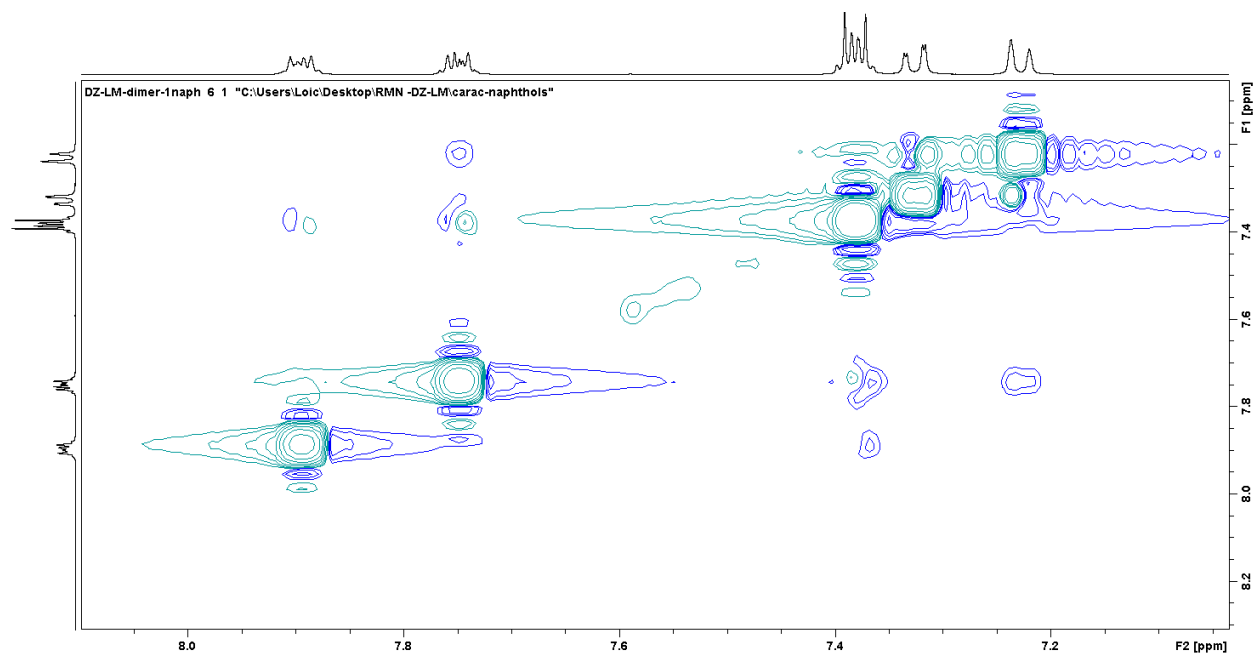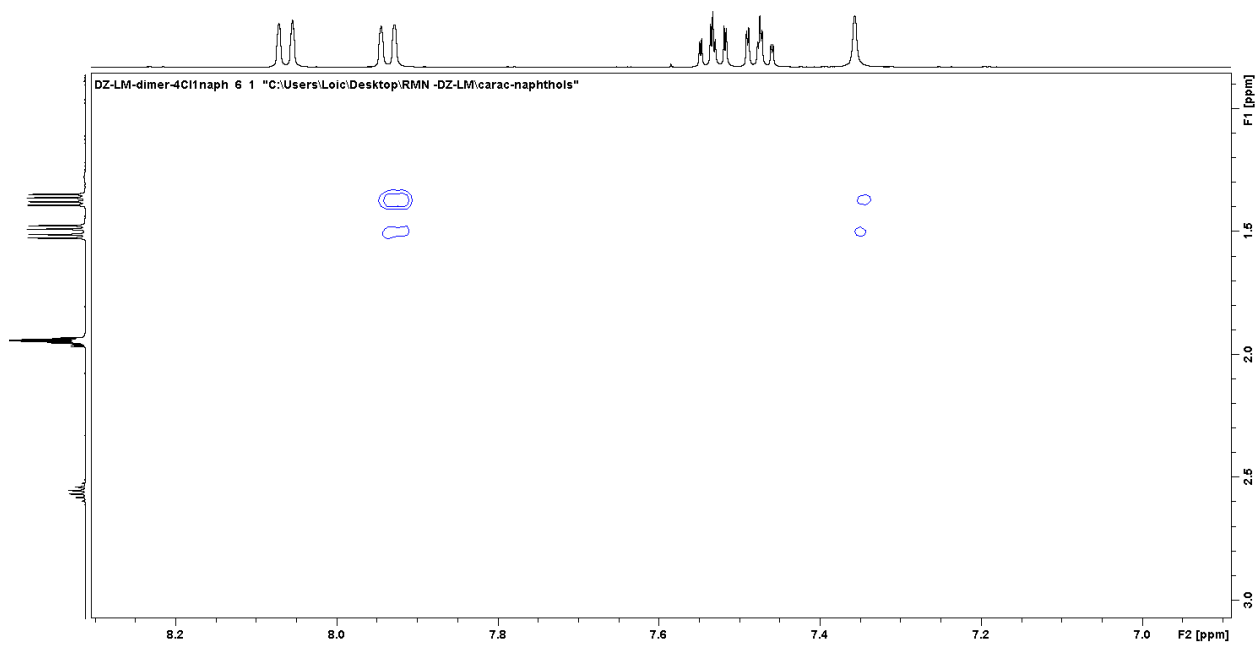
Figure S4.29: NOESY NMR spectrum of **2c** in CD$_3$CN, focus on the aliphatic/aromatic interactions.
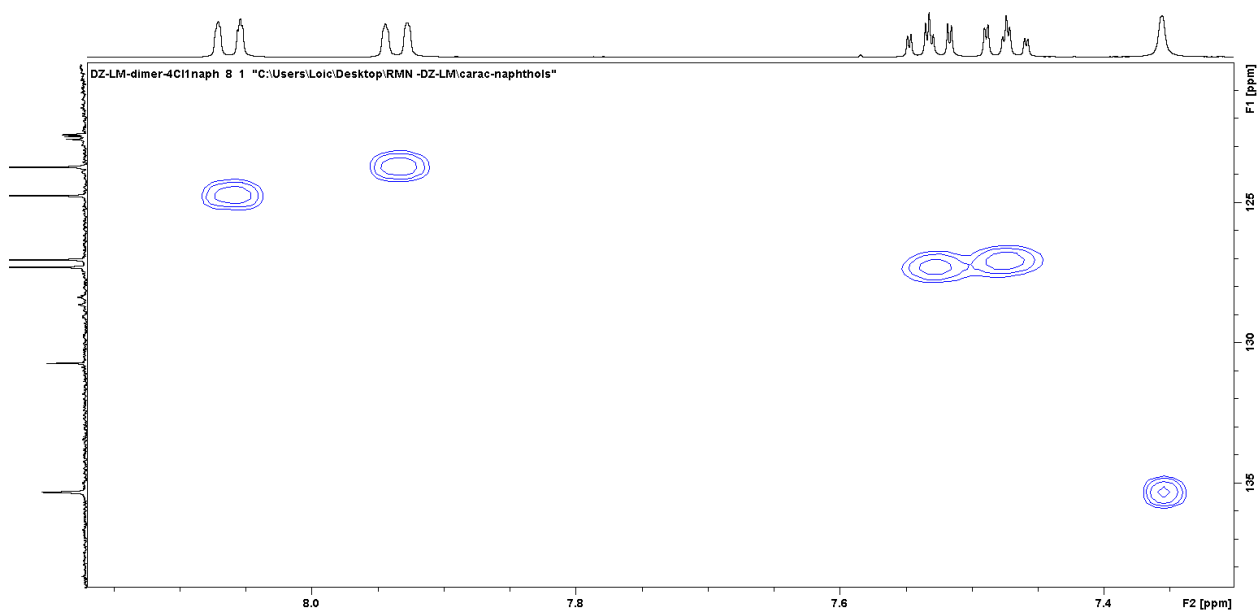
Figure S4.30: HSQC NMR spectrum of **2c** in CD$_3$CN, focus on the aromatic region.
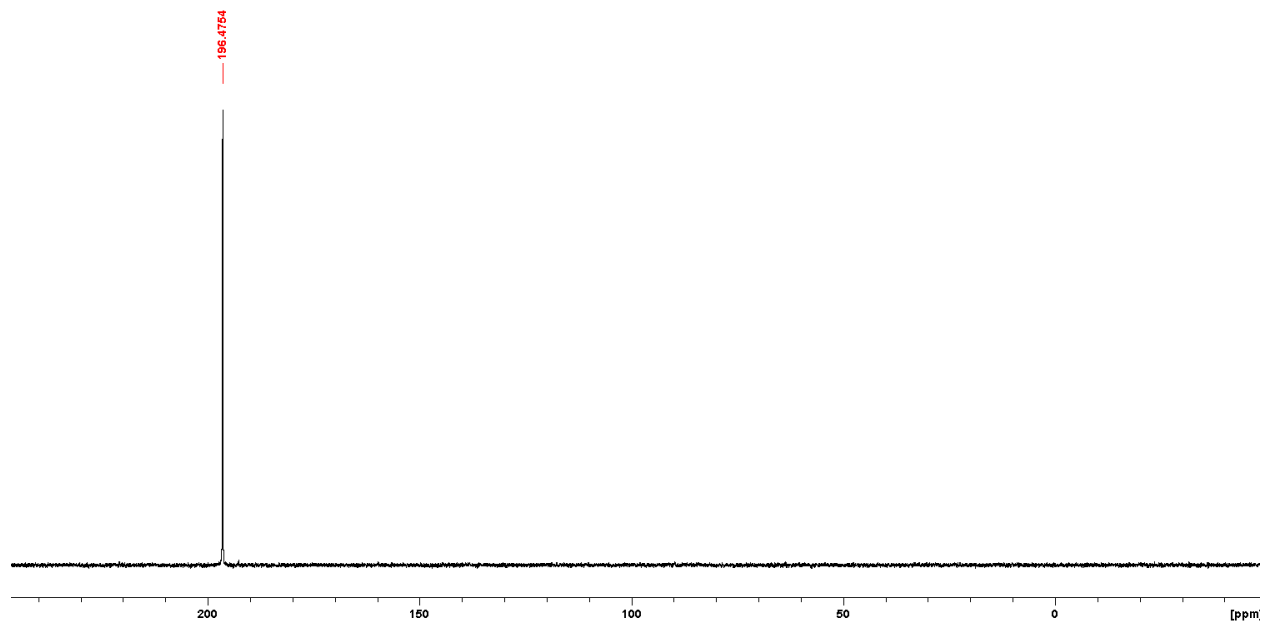
Figure S4.31: $^{31}P\{^1H\}$ NMR spectrum of **2c** in CD$_3$CN.
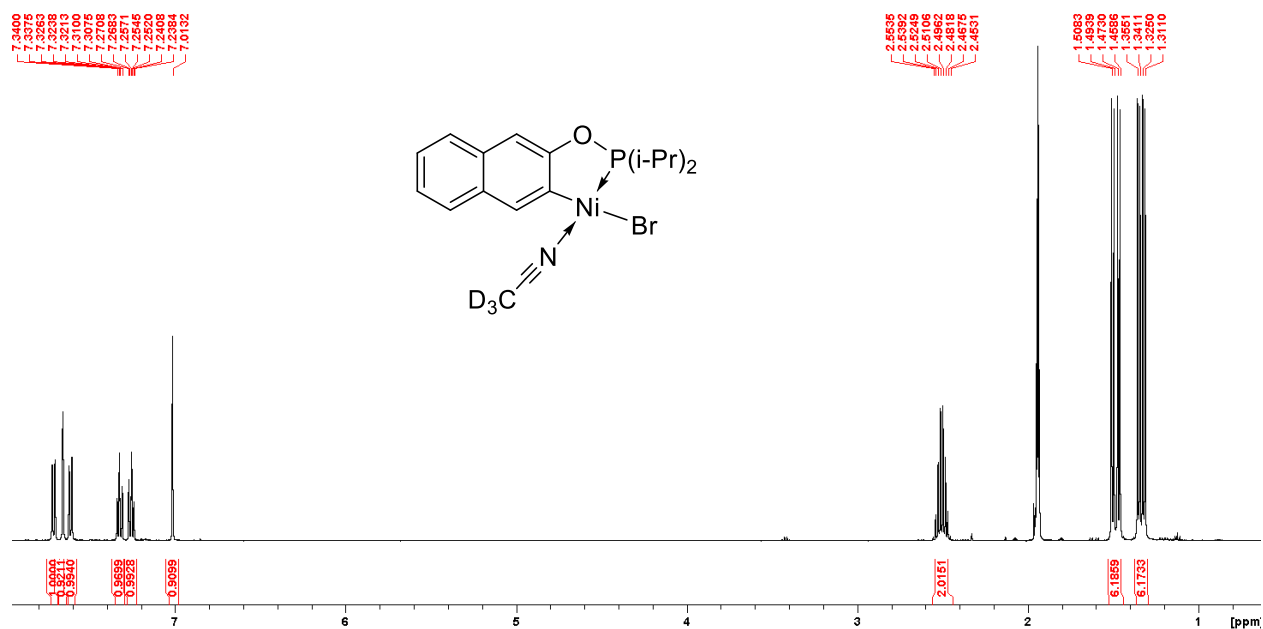
Figure S4.32: Full ^{1}H NMR spectrum of **2e** in CD$_3$CN.
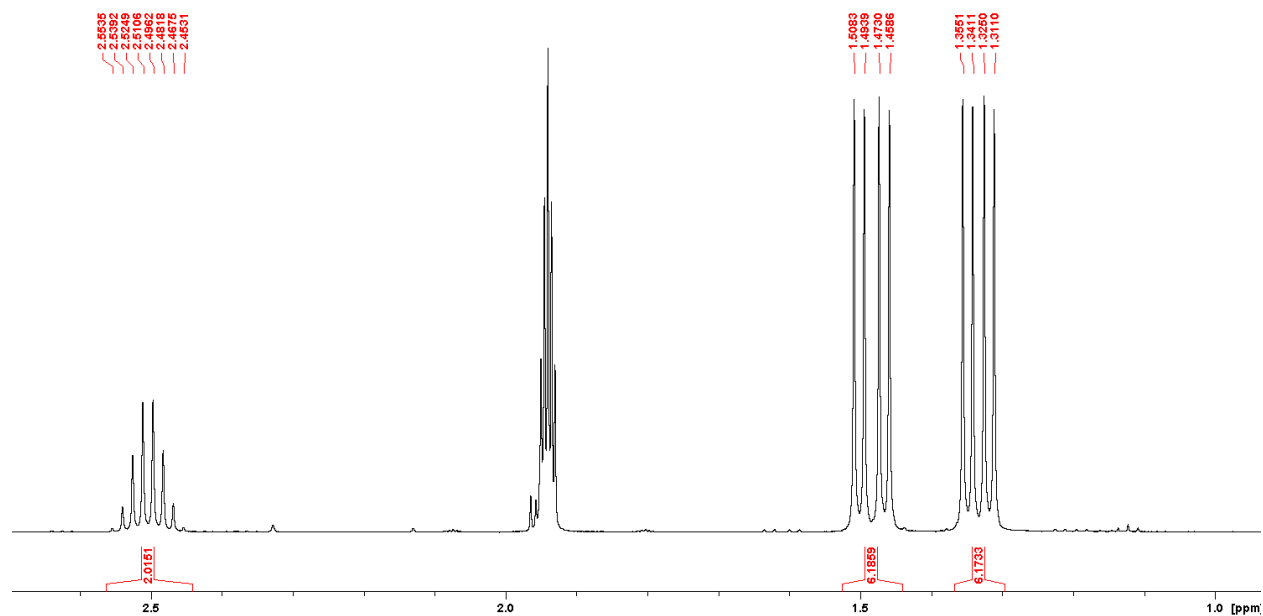
Figure S4.33: ^{1}H NMR spectrum of **2e** in CD$_3$CN, focus on the aliphatic region.

Figure S4.34: ^{1}H NMR spectrum of **2e** in CD$_3$CN, focus on the aromatic region.

Figure S4.35: Full ^{13}C{^{1}H} NMR spectrum of **2e** in CD$_3$CN.
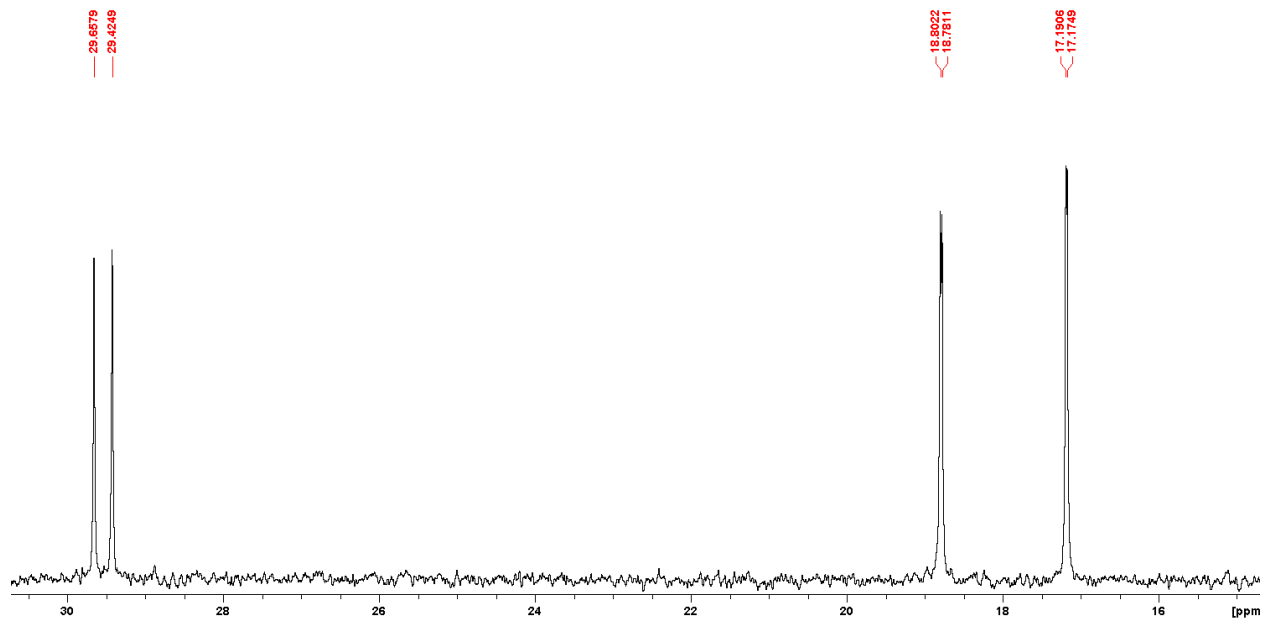
Figure S4.36: $^{13}C\{^1H\}$ NMR spectrum of **2e** in CD$_3$CN, focus on the aliphatic region.

Figure S4.37: $^{13}C\{^1H\}$ NMR spectrum of **2e** in CD$_3$CN, focus on the aromatic region.

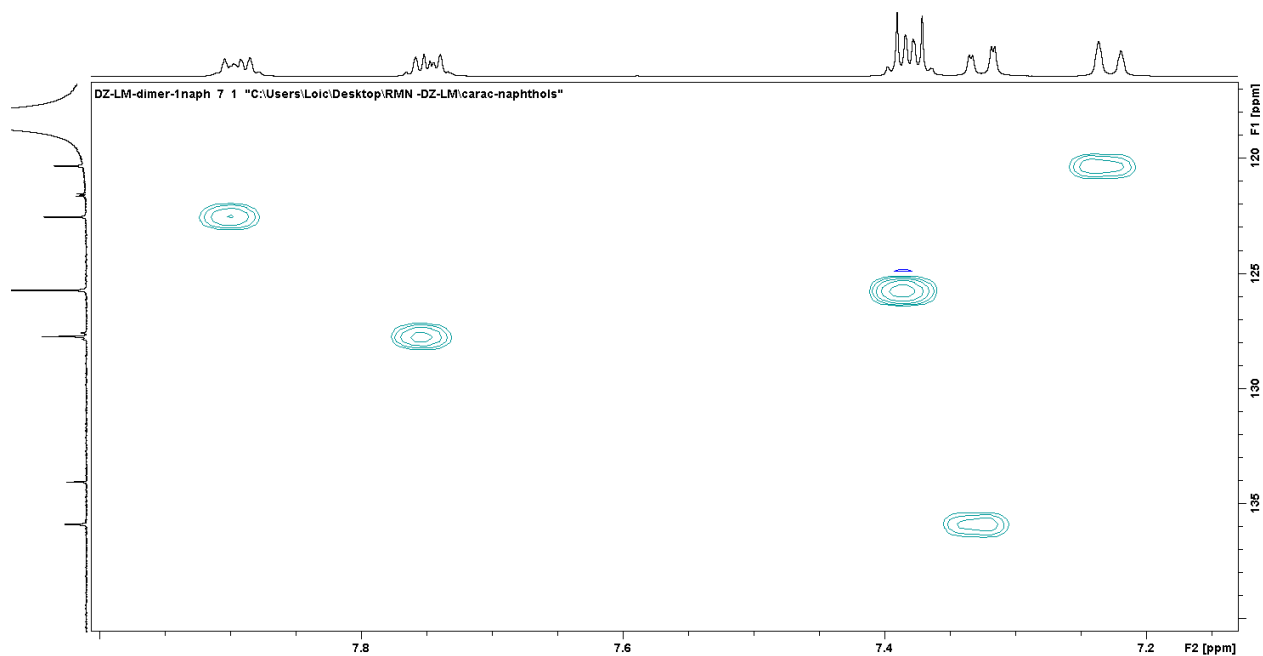Figure S4.38: COSY NMR spectrum of **2e** in CD₃CN, focus on the aromatic region.
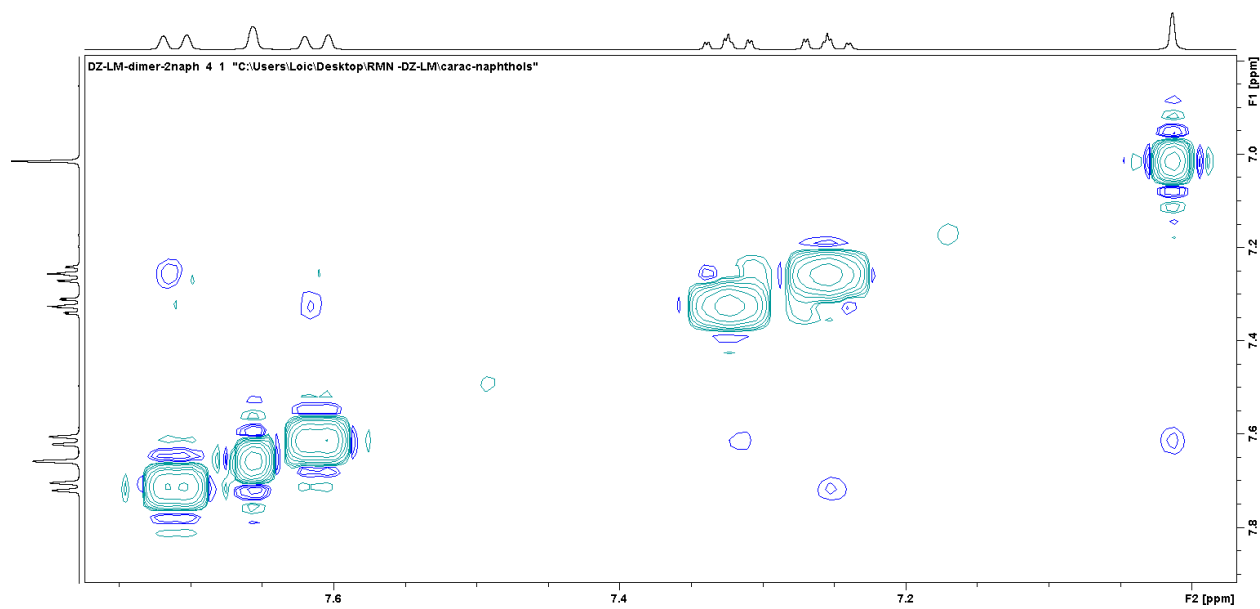
Figure S4.39: COSY NMR spectrum of **2e** in CD₃CN, focus on the aromatic/aromatic interactions.
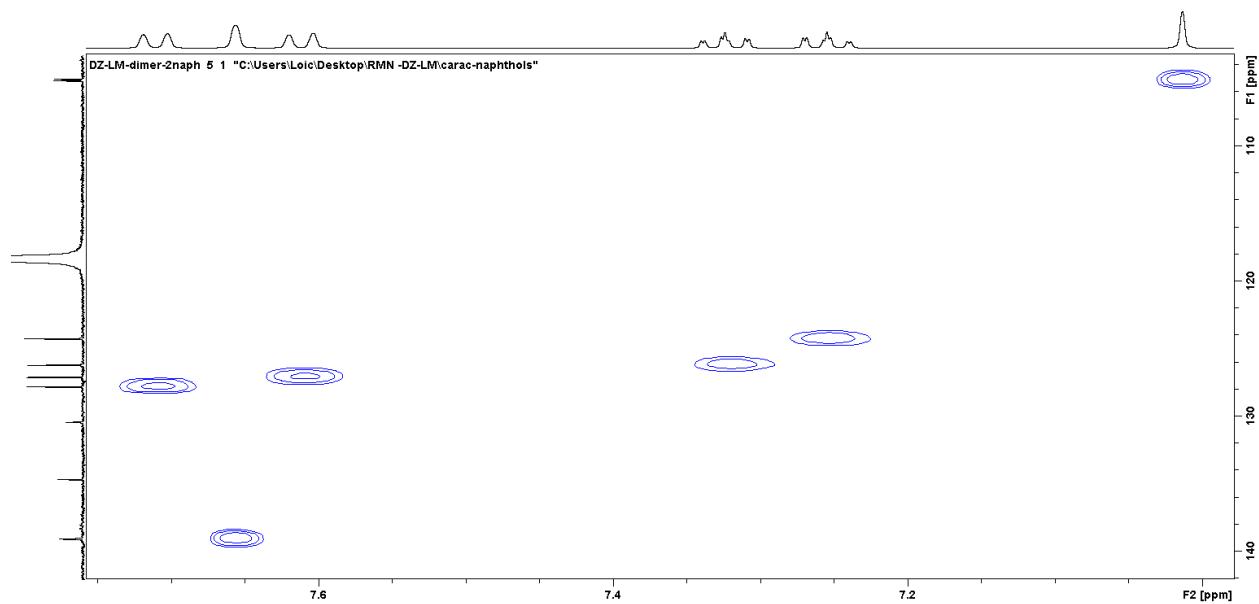
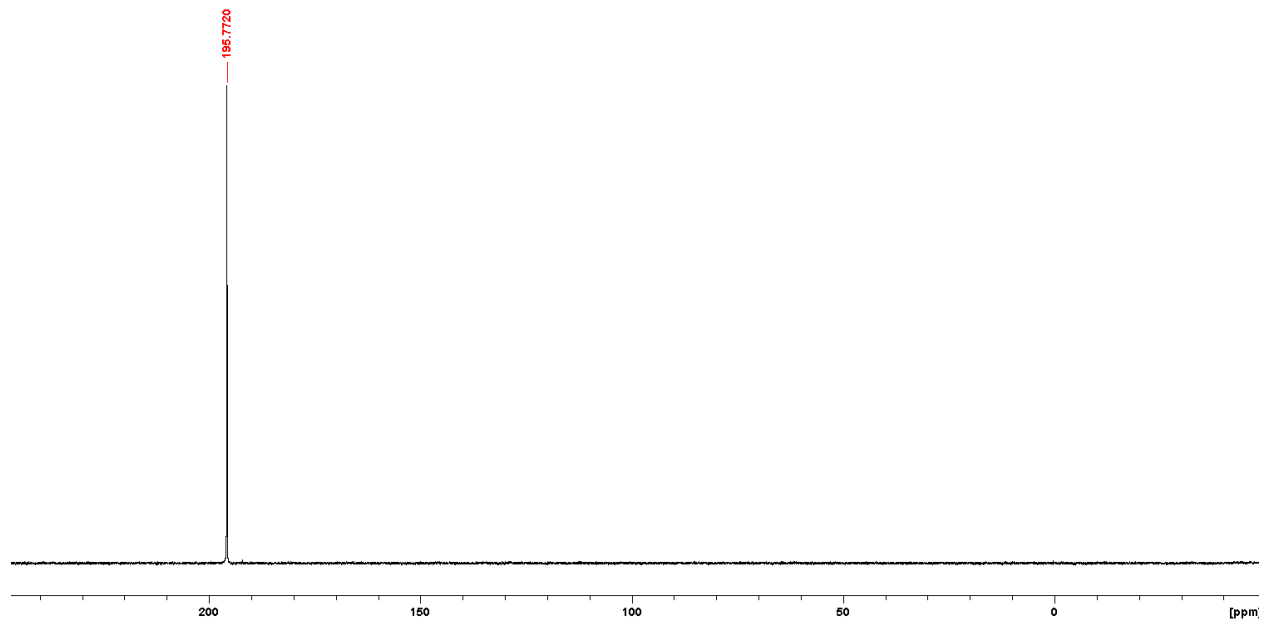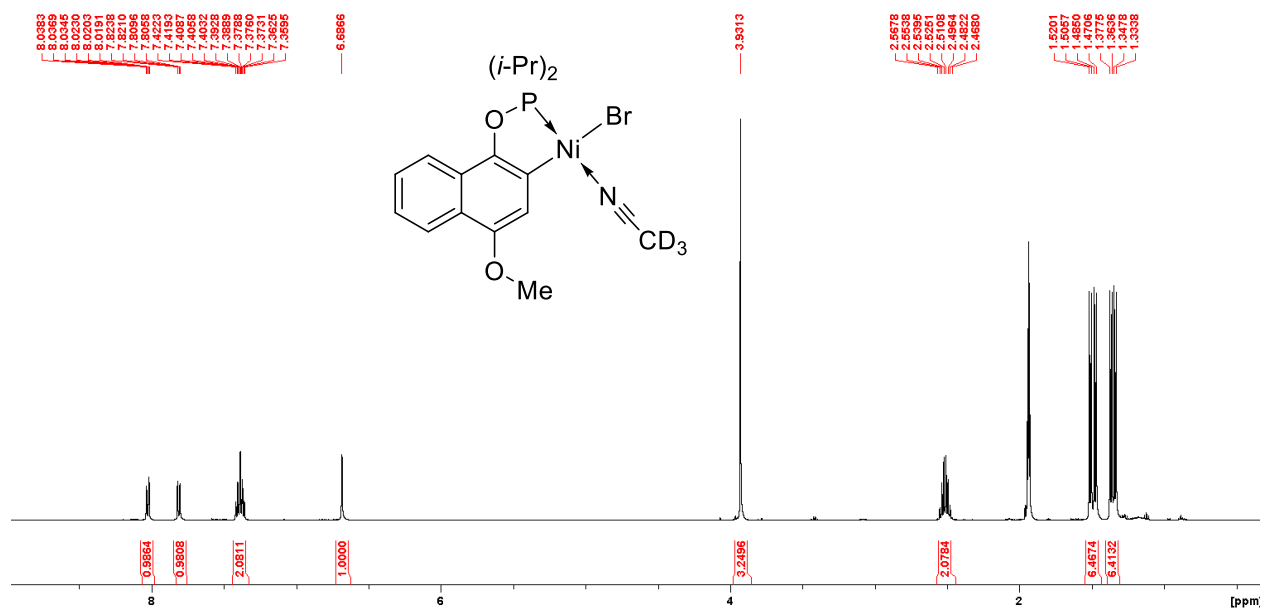Figure S4.40: HSQC NMR spectrum of **2e** in CD$_3$CN, focus on the aromatic region.
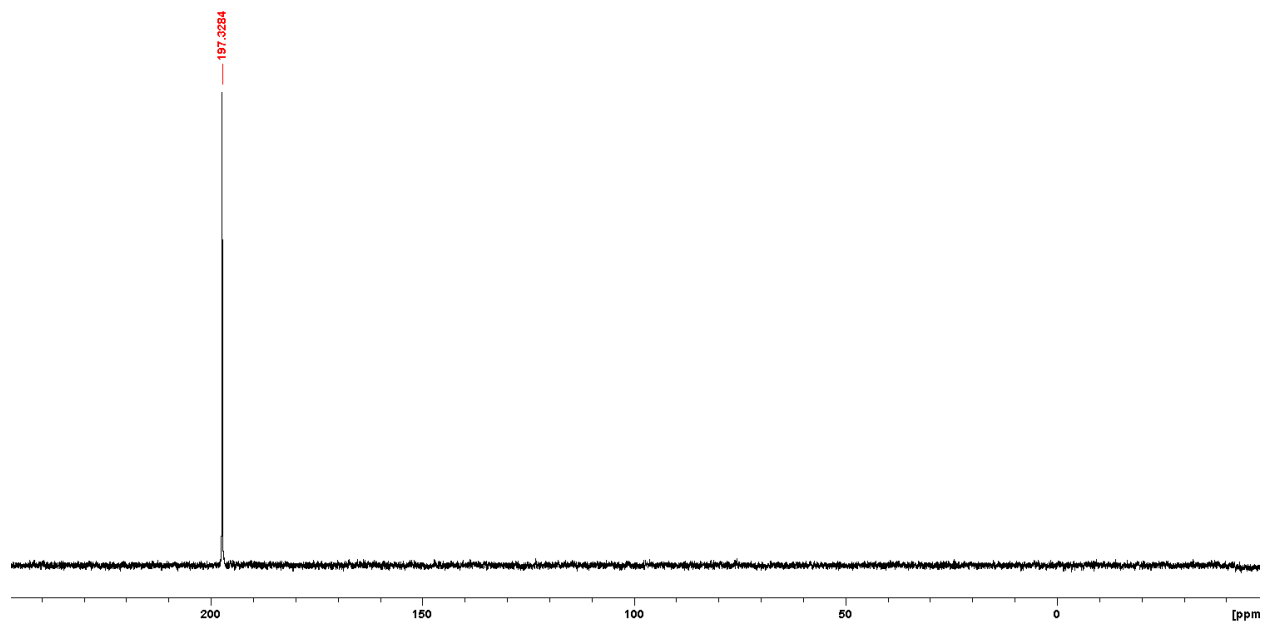
Figure S4.41: ^{31}P{^{1}H} NMR spectrum of **2e** in CD$_3$CN.

e. Compound **2f**
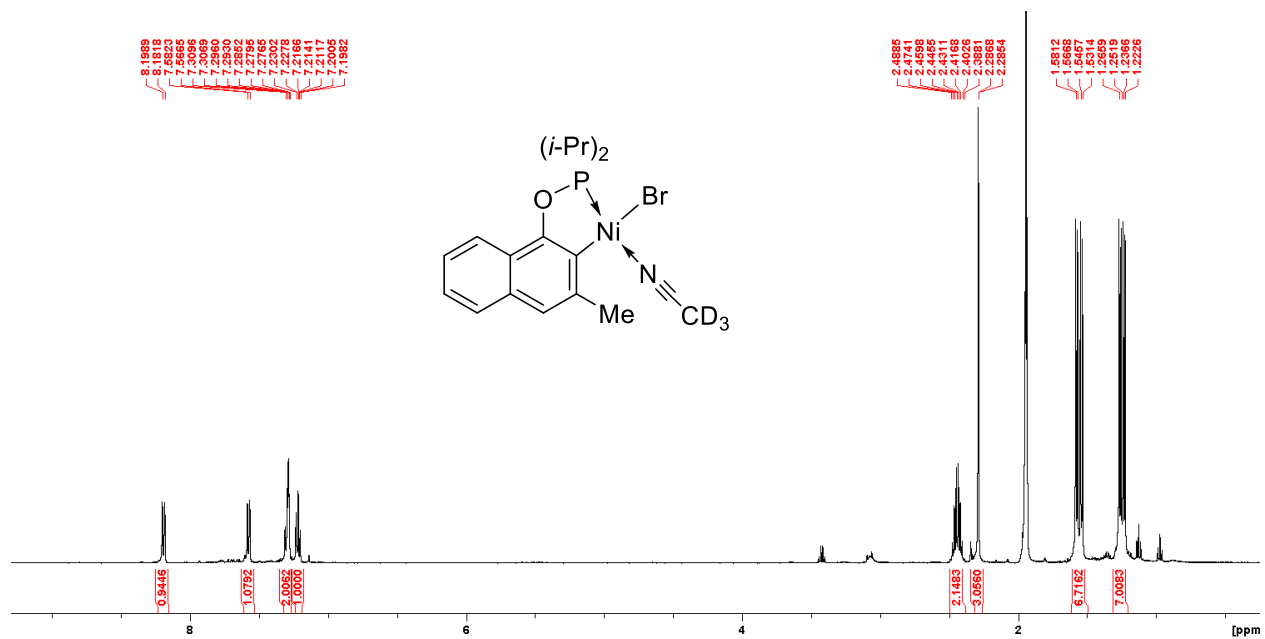
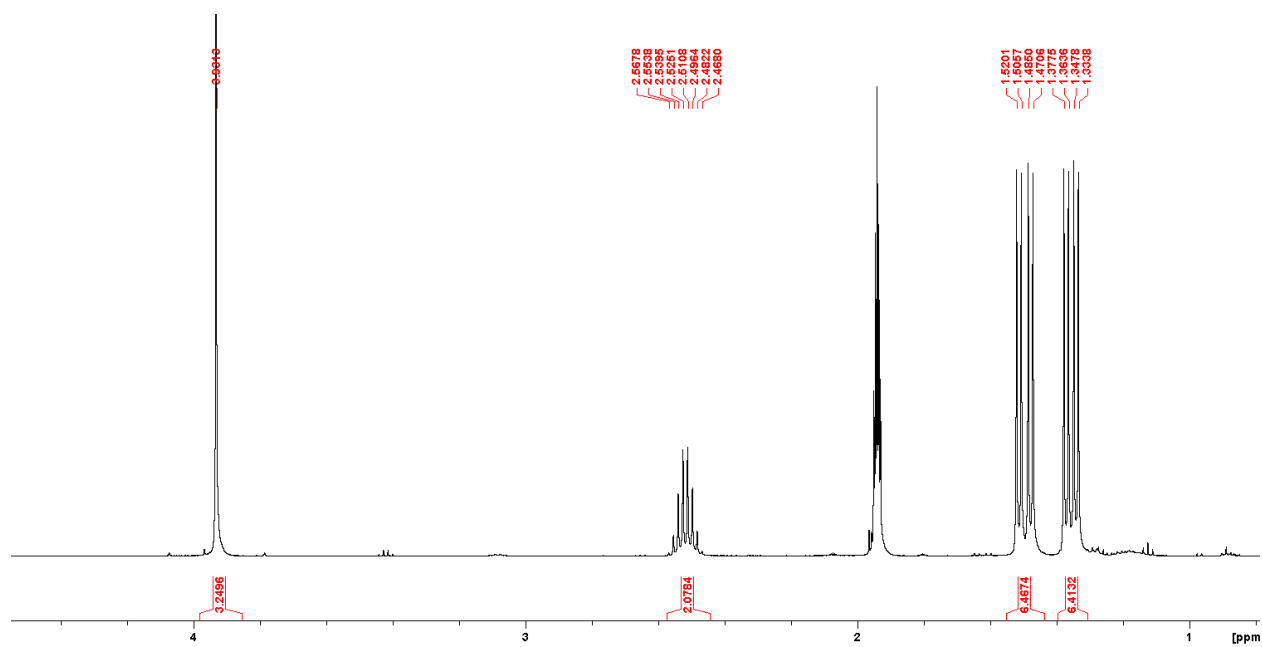Figure S4.42: Full ^{1}H NMR spectrum of **2f** in CD$_3$CN.
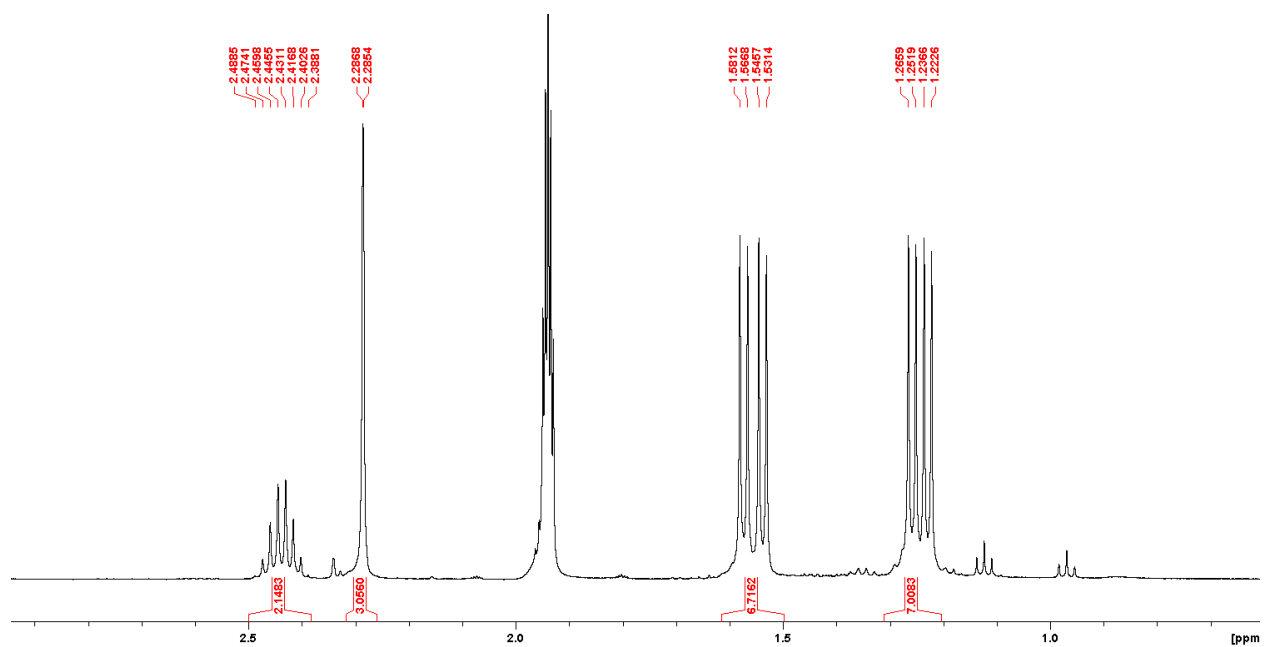
Figure S4.43: ^{1}H NMR spectrum of **2f** in CD$_3$CN, focus on the aliphatic region.
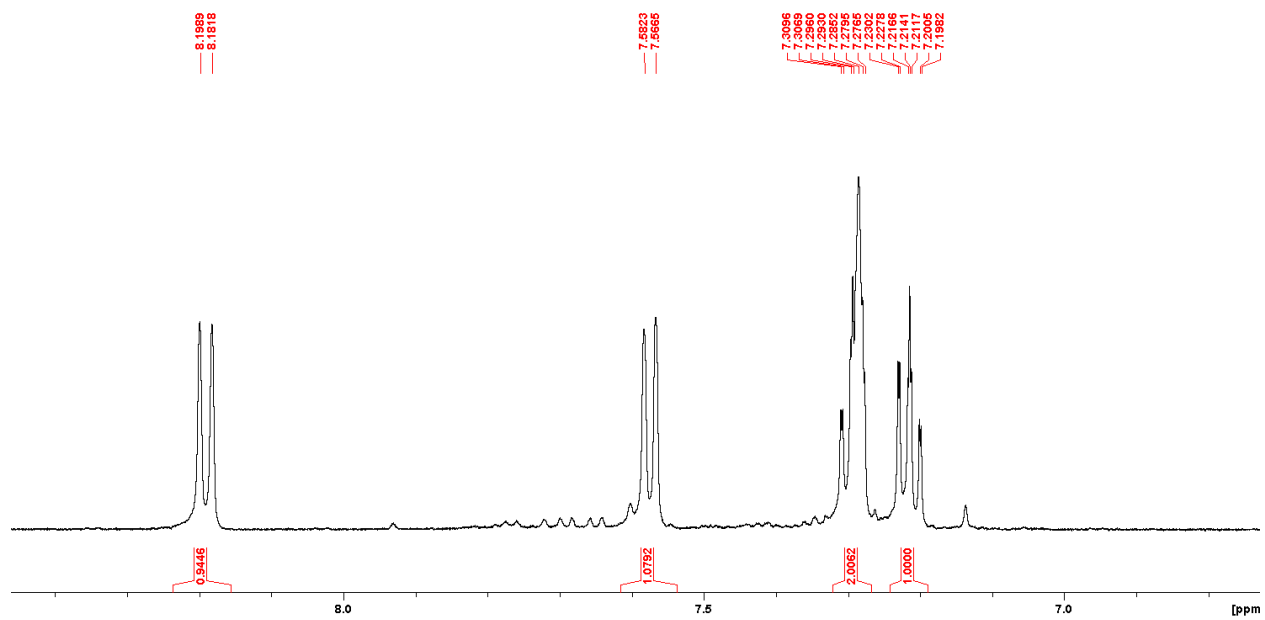
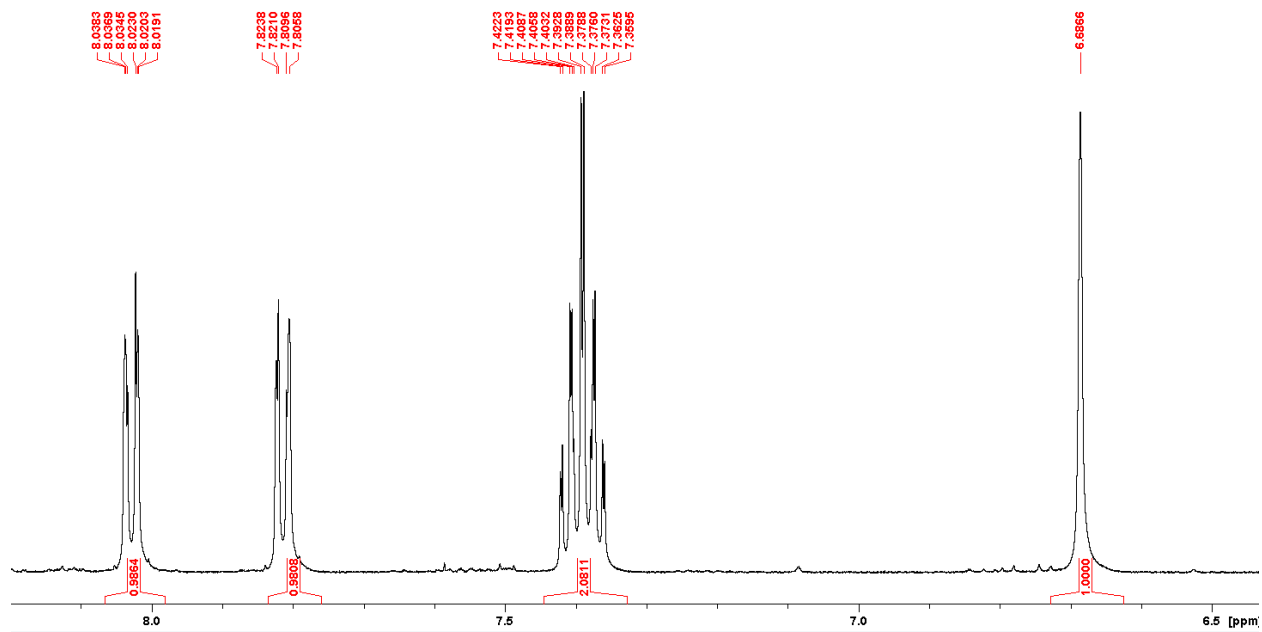Figure S4.44: ^{1}H NMR spectrum of **2f** in CD$_3$CN, focus on the aromatic region.
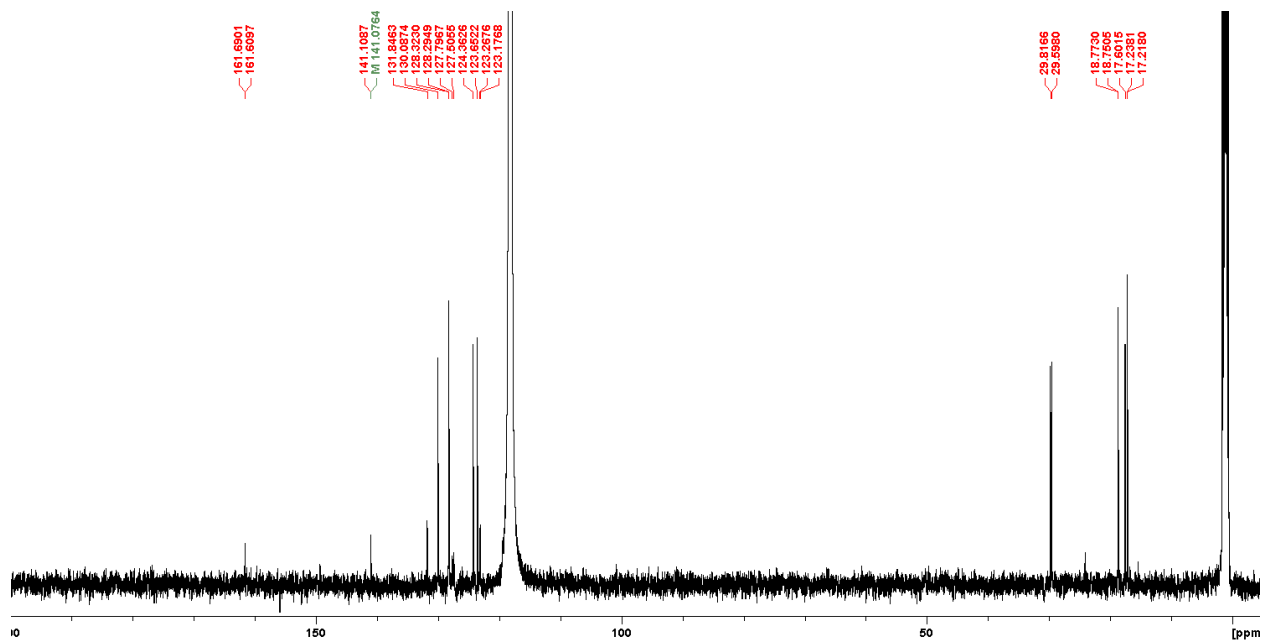
Figure S4.45: Full ^{13}C{^{1}H} NMR spectrum of **2f** in CD$_3$CN.
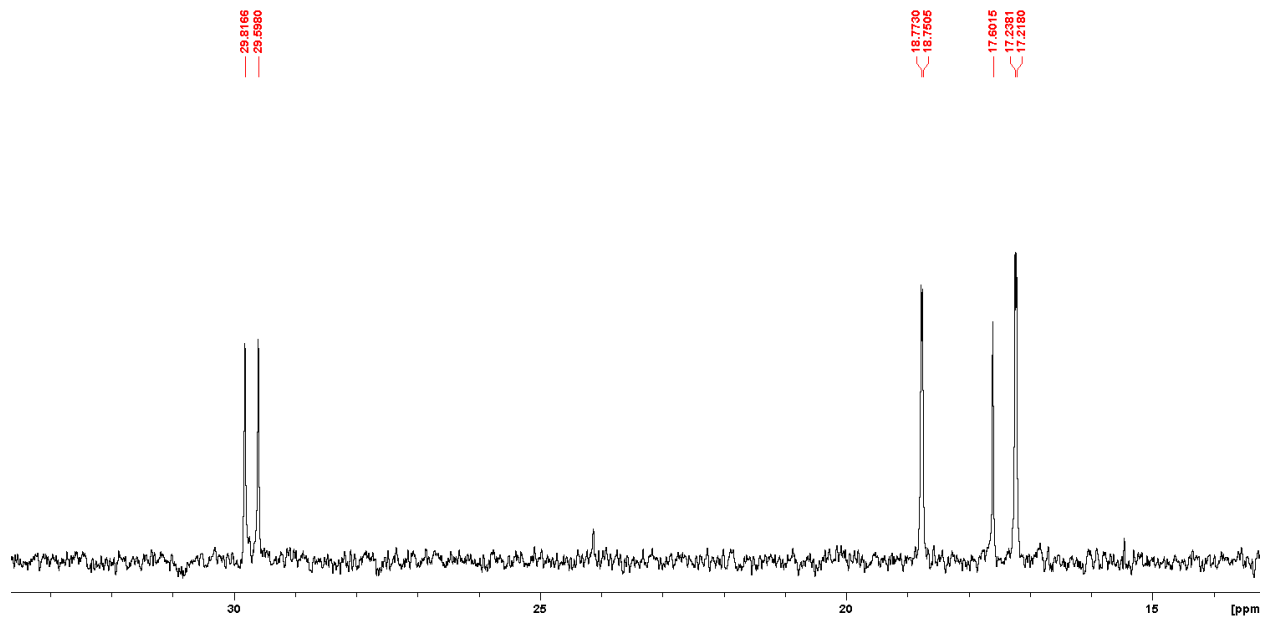
Figure S4.46: $^{13}C\{^{1}H\}$ NMR spectrum of **2f** in CD_3CN, focus on the aliphatic region.
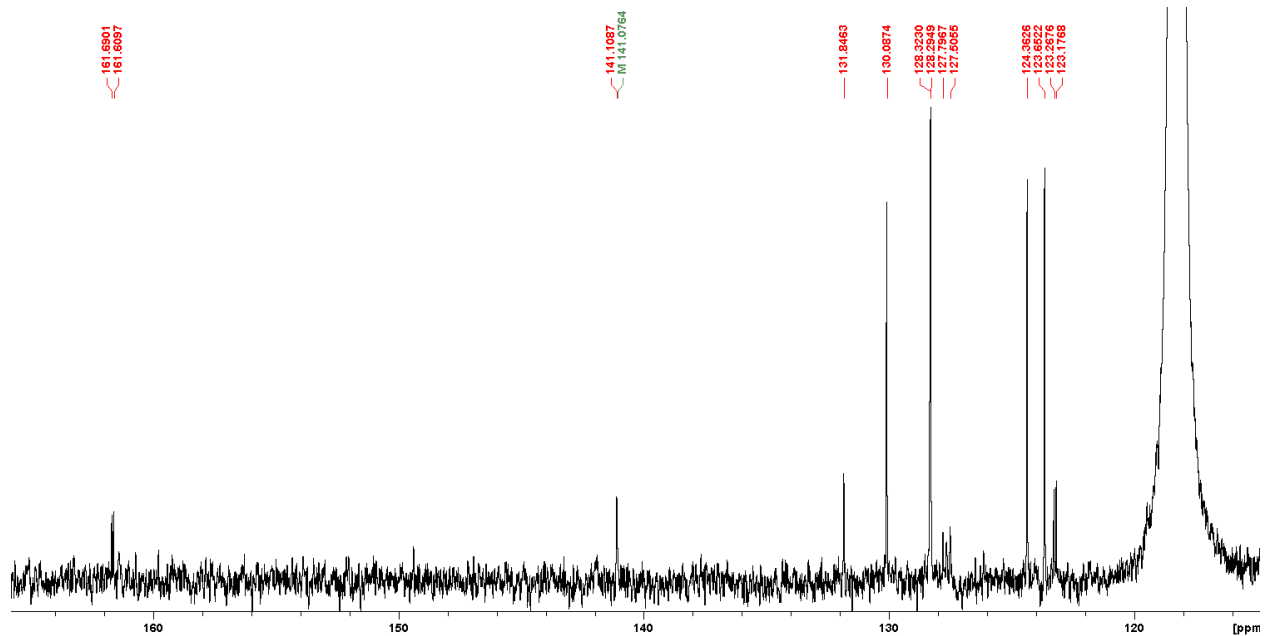
Figure S4.47: $^{13}C\{^{1}H\}$ NMR spectrum of **2f** in CD_3CN, focus on the aromatic region.
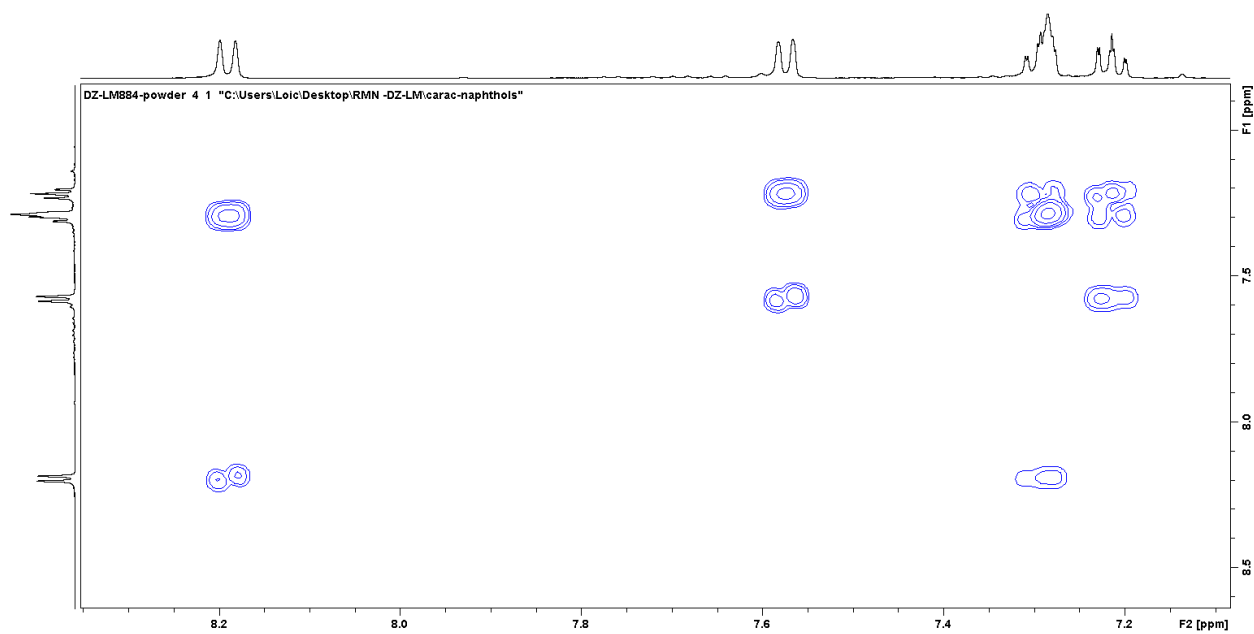
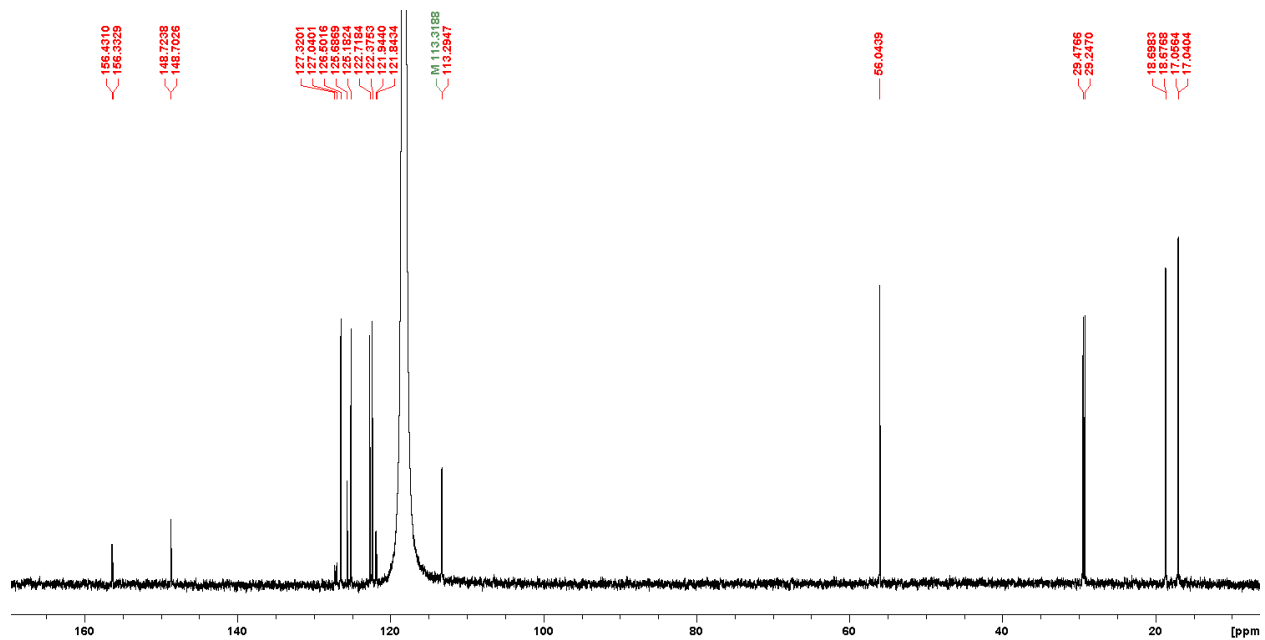Figure S4.48: COSY NMR spectrum of **2f** in CD₃CN, focus on the aromatic region.
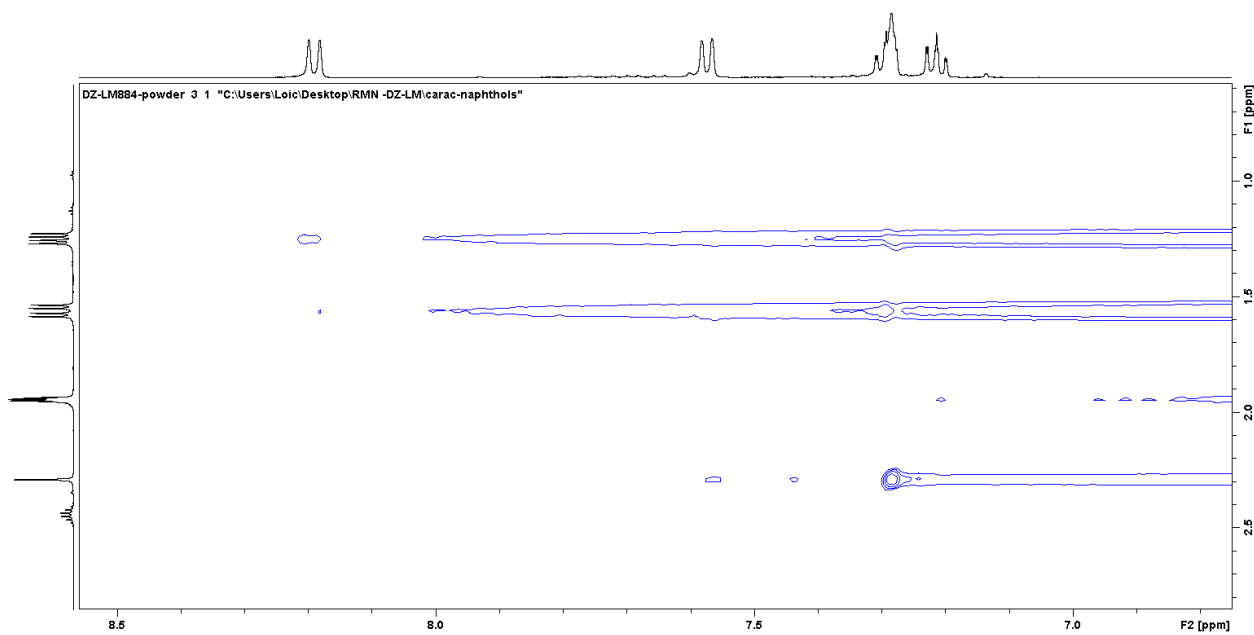
Figure S4.49: NOESY NMR spectrum of **2f** in CD₃CN, focus on the aliphatic/aromatic interactions.
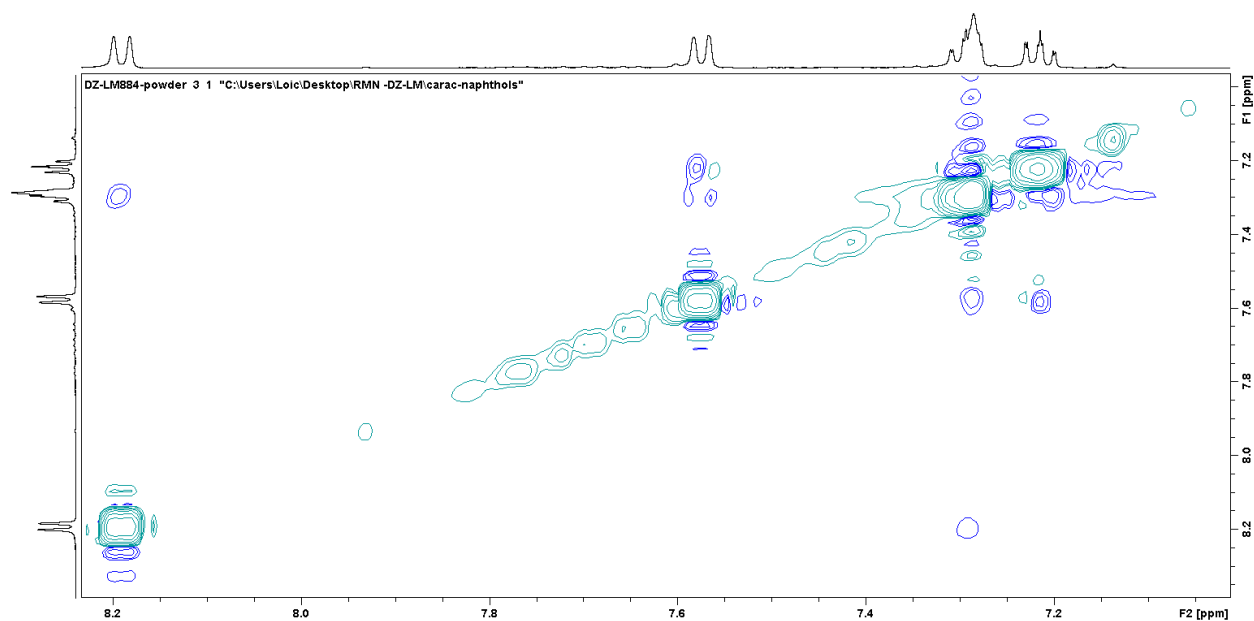
Figure S4.50: NOESY NMR spectrum of **2f** in CD$_3$CN, focus on the aromatic/aromatic interactions.
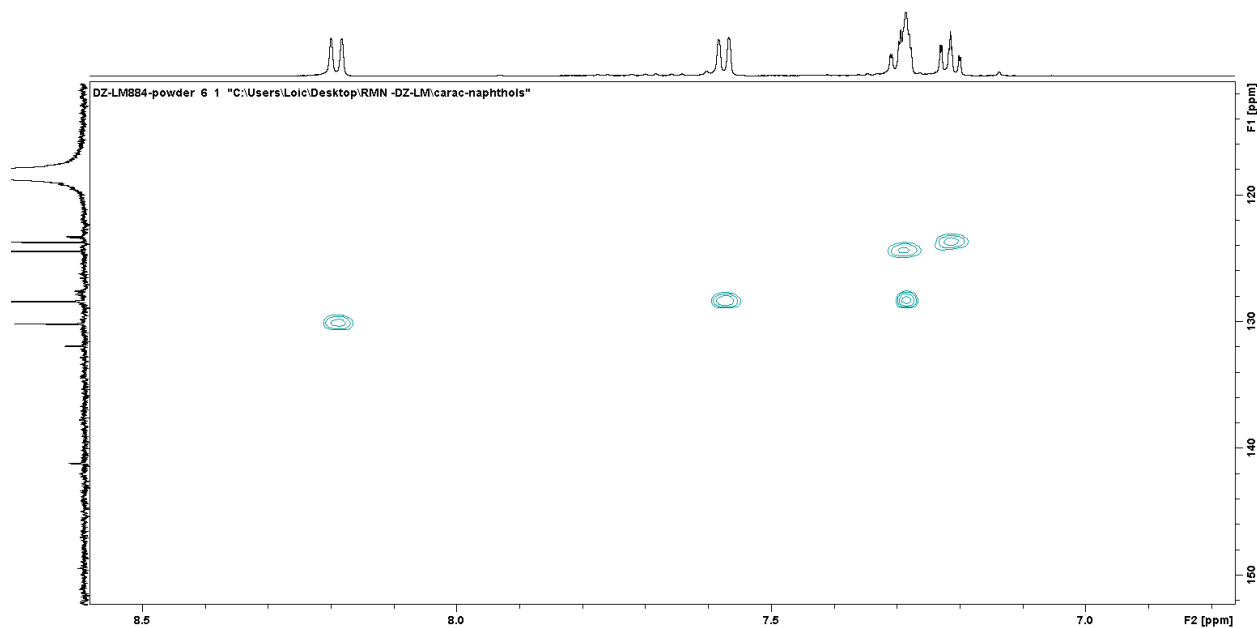
Figure S4.51: HSQC NMR spectrum of **2f** in CD$_3$CN, focus on the aromatic region.
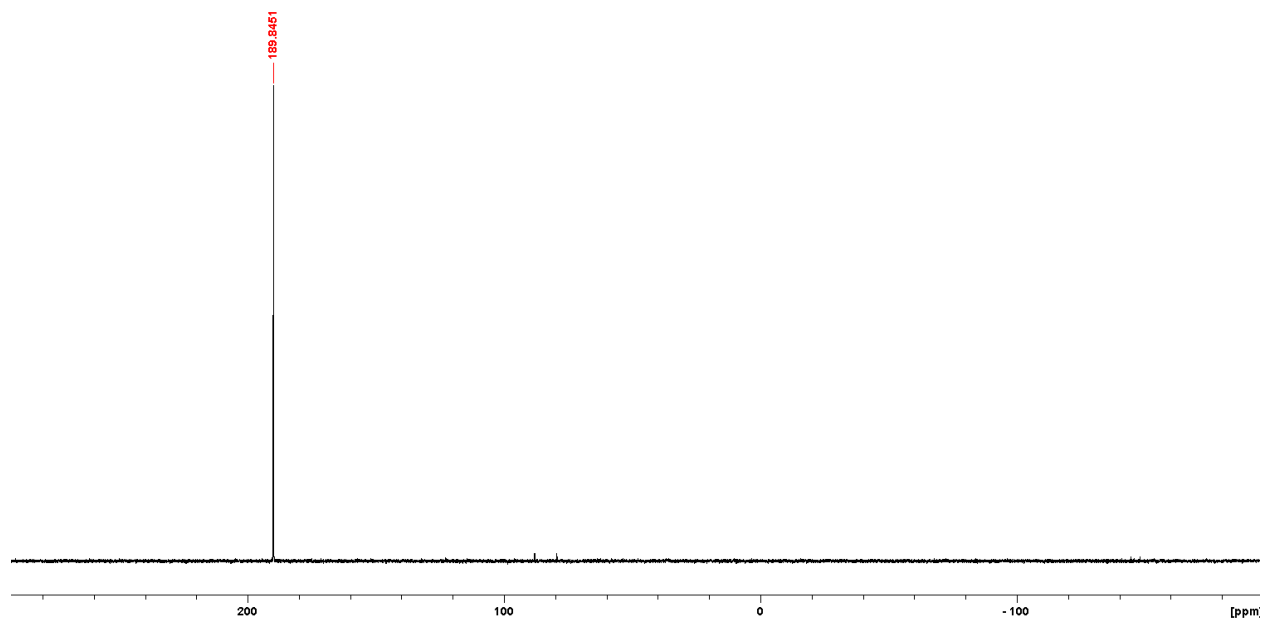
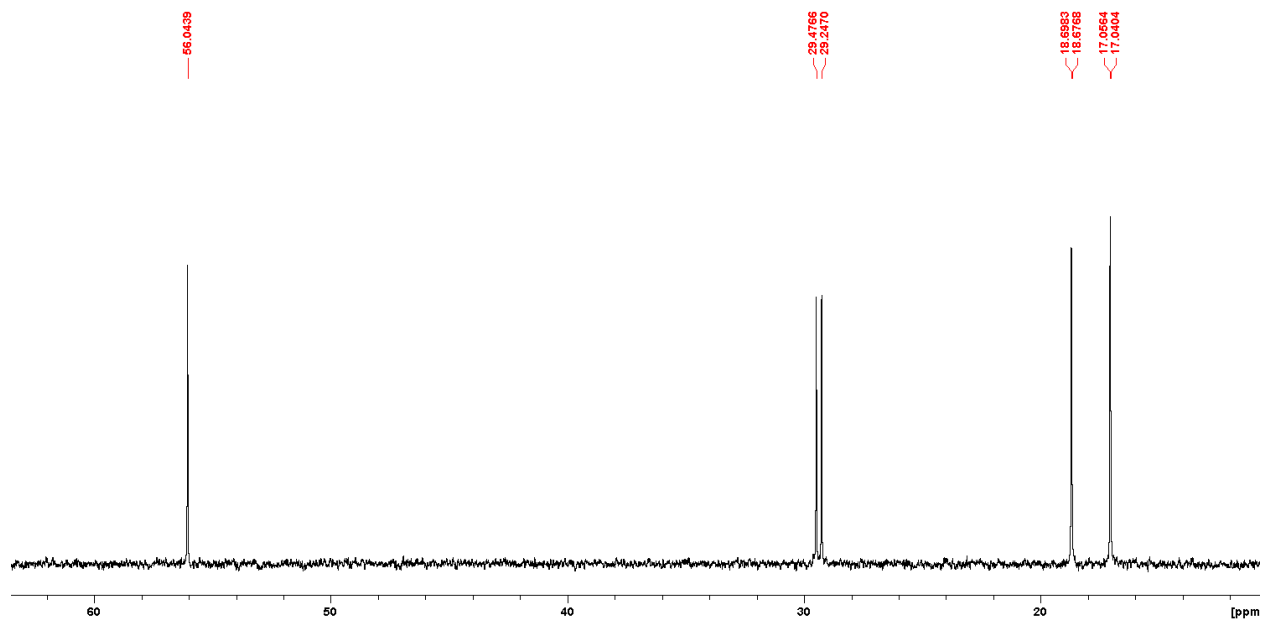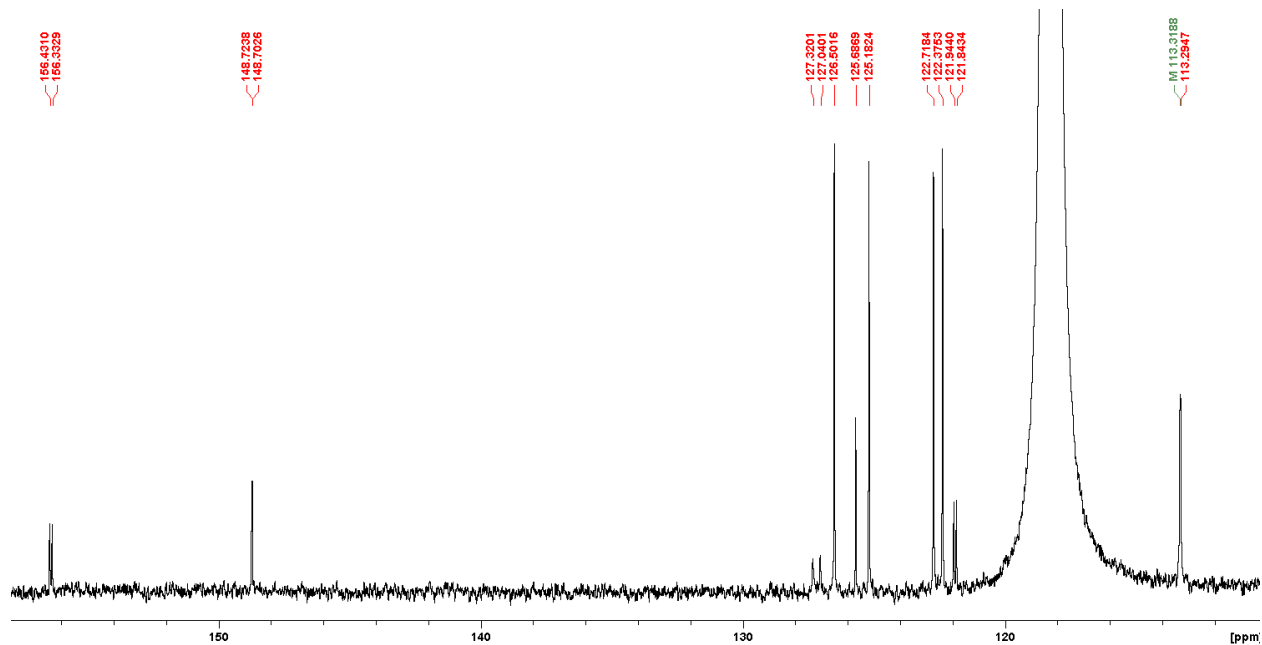Figure S4.52: $^{31}P\{^1H\}$ NMR spectrum of **2f** in CD$_3$CN.

f.   Compound **2g**
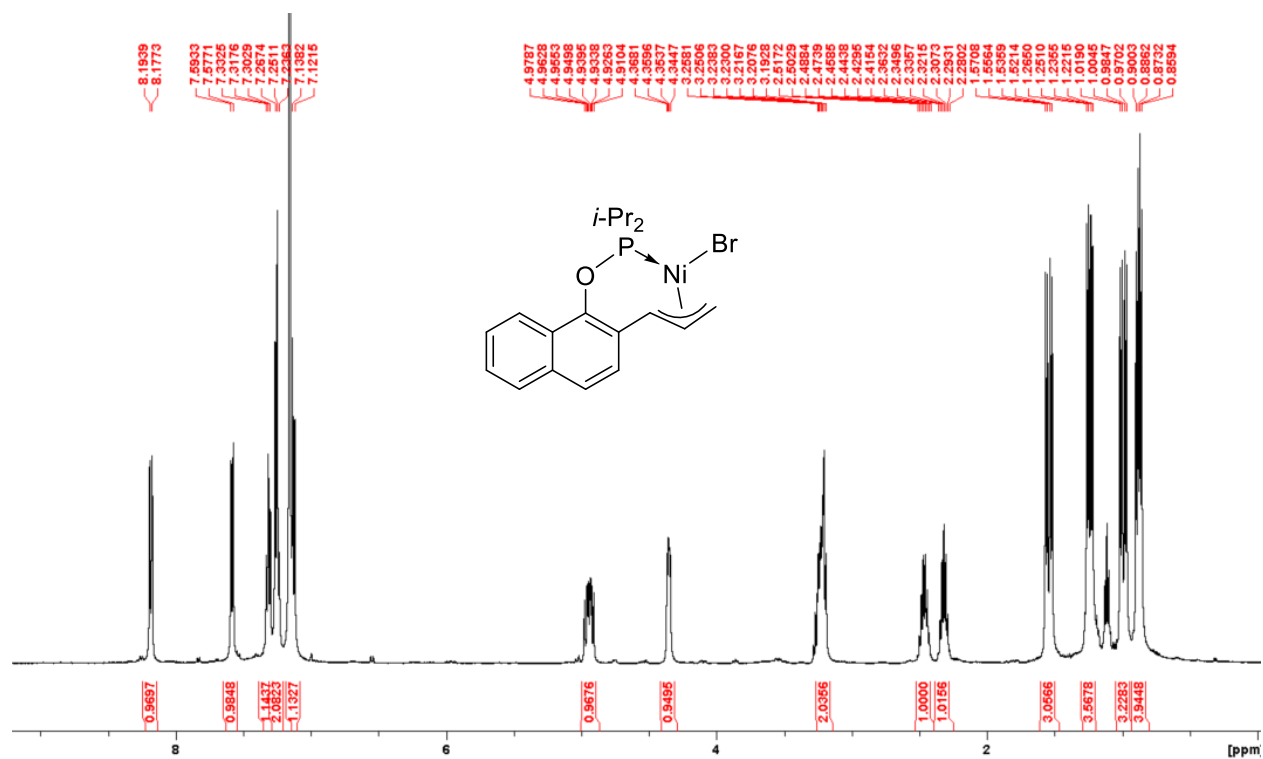
Figure S4.53: Full ^{1}H NMR spectrum of **2g** in C_6D_6.
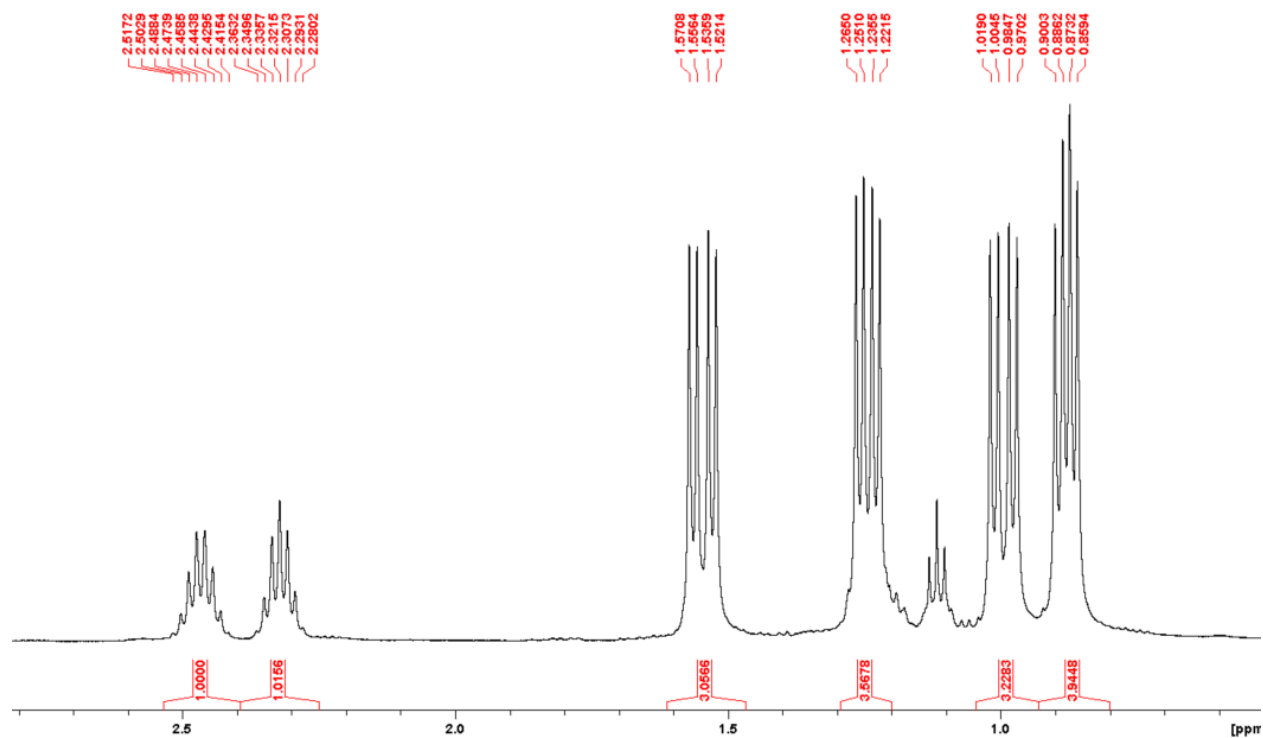
Figure S4.54: ^{1}H NMR spectrum of **2g** in C_6D_6, focus on the aliphatic region.
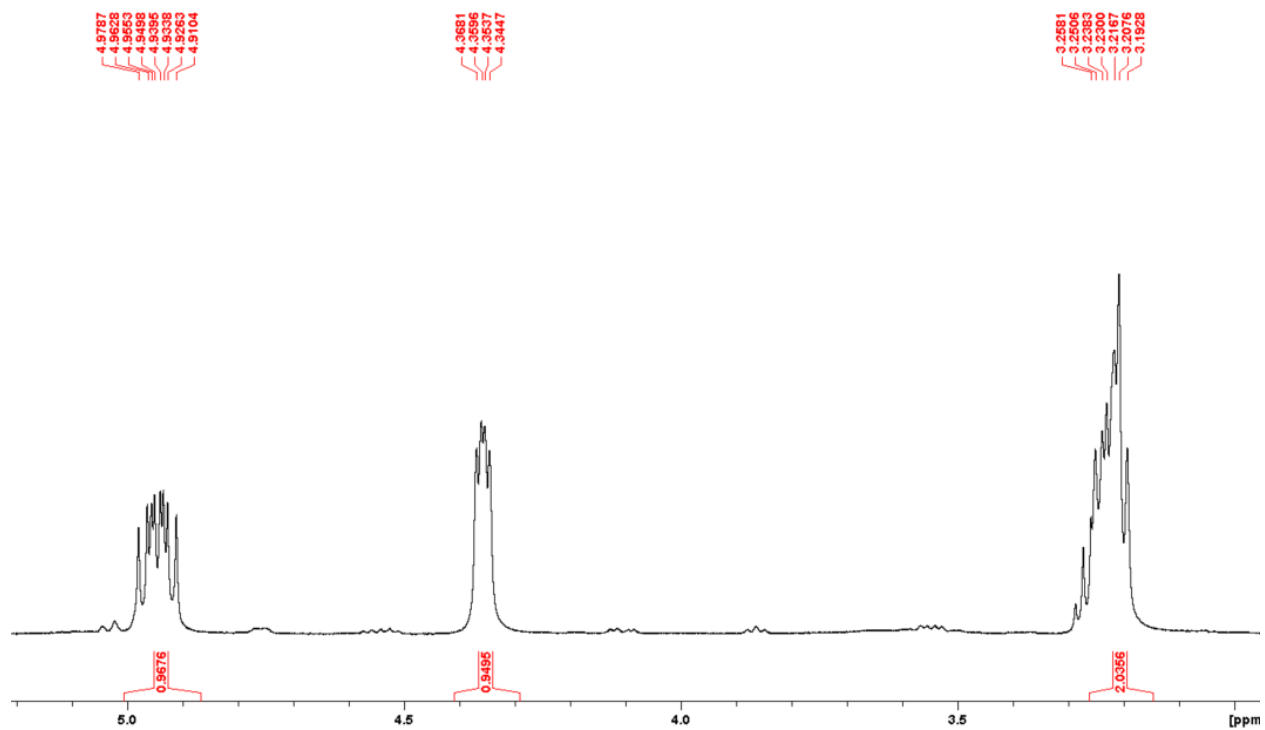
Figure S4.55: ^{1}H NMR spectrum of **2g** in C_6D_6, focus on the allylic region.
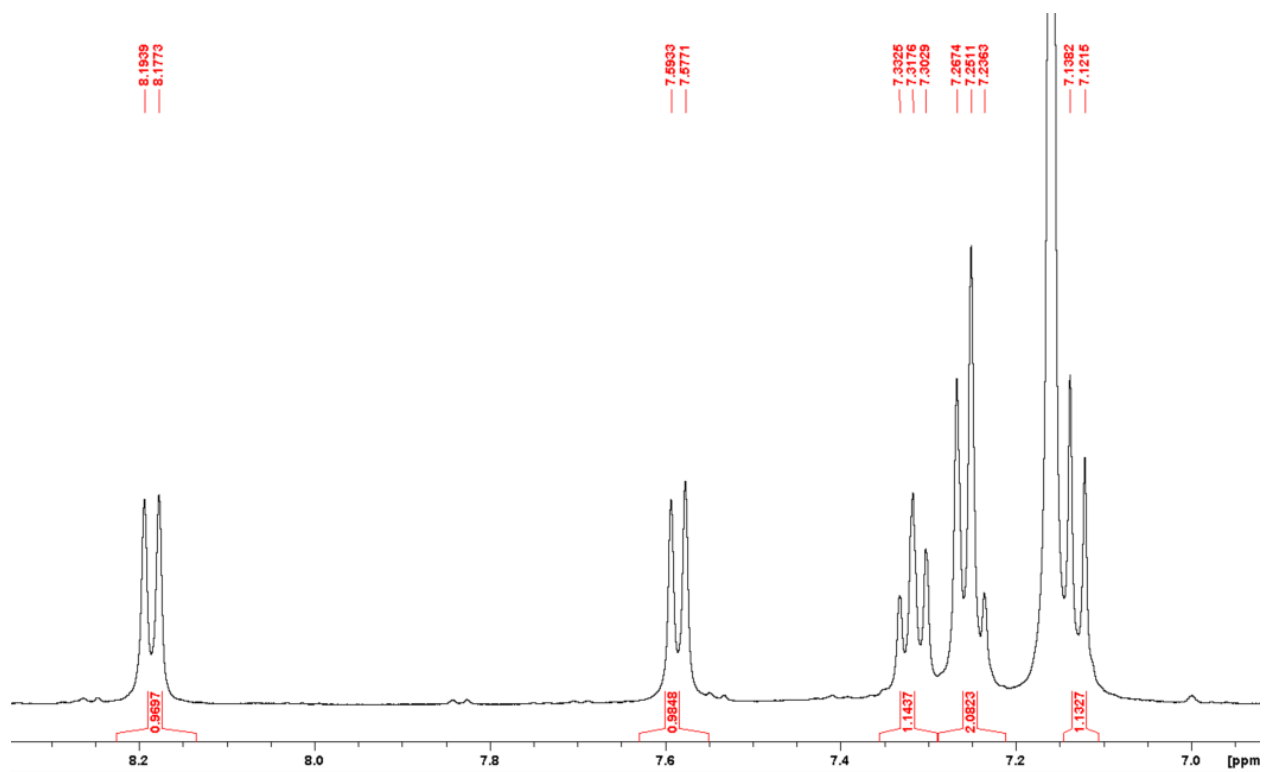
Figure S4.56: ^{1}H NMR spectrum of **2g** in C_6D_6, focus on the aromatic region.
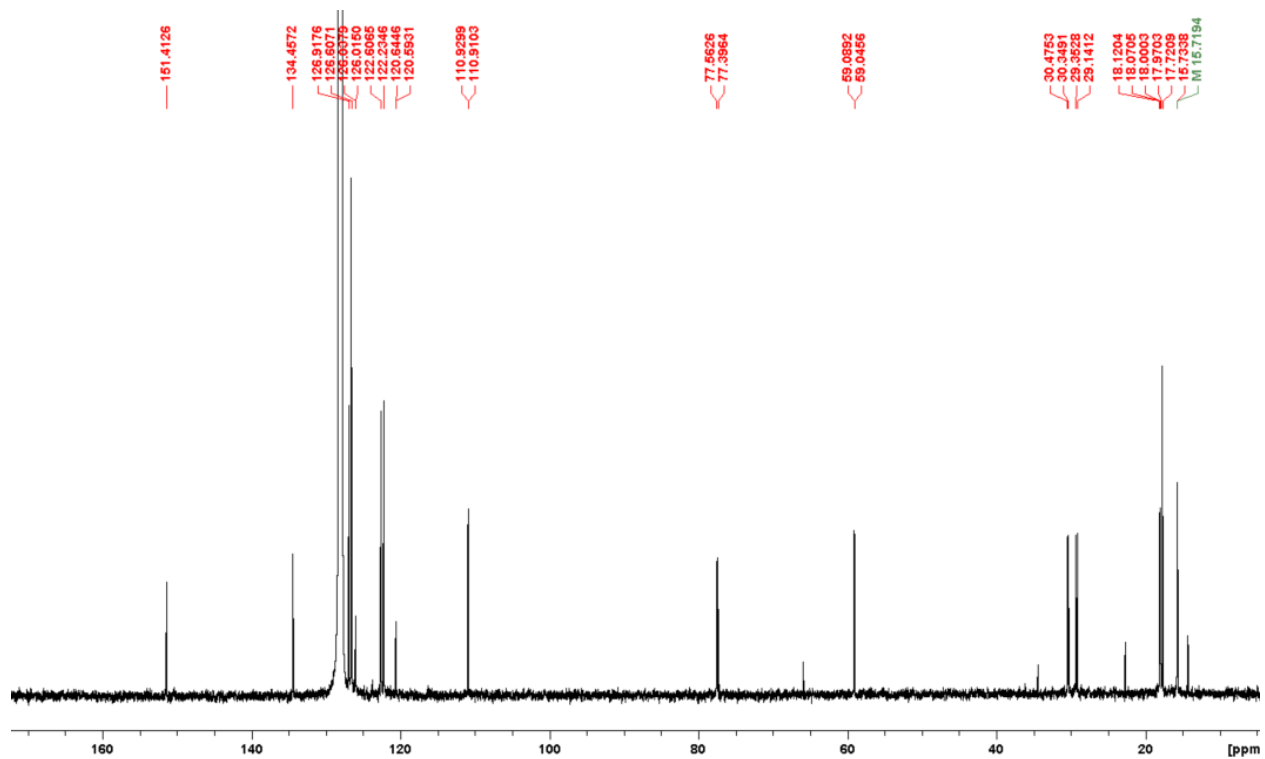
Figure S4.57: Full $^{13}C\{^1H\}$ NMR spectrum of **2g** in C_6D_6.
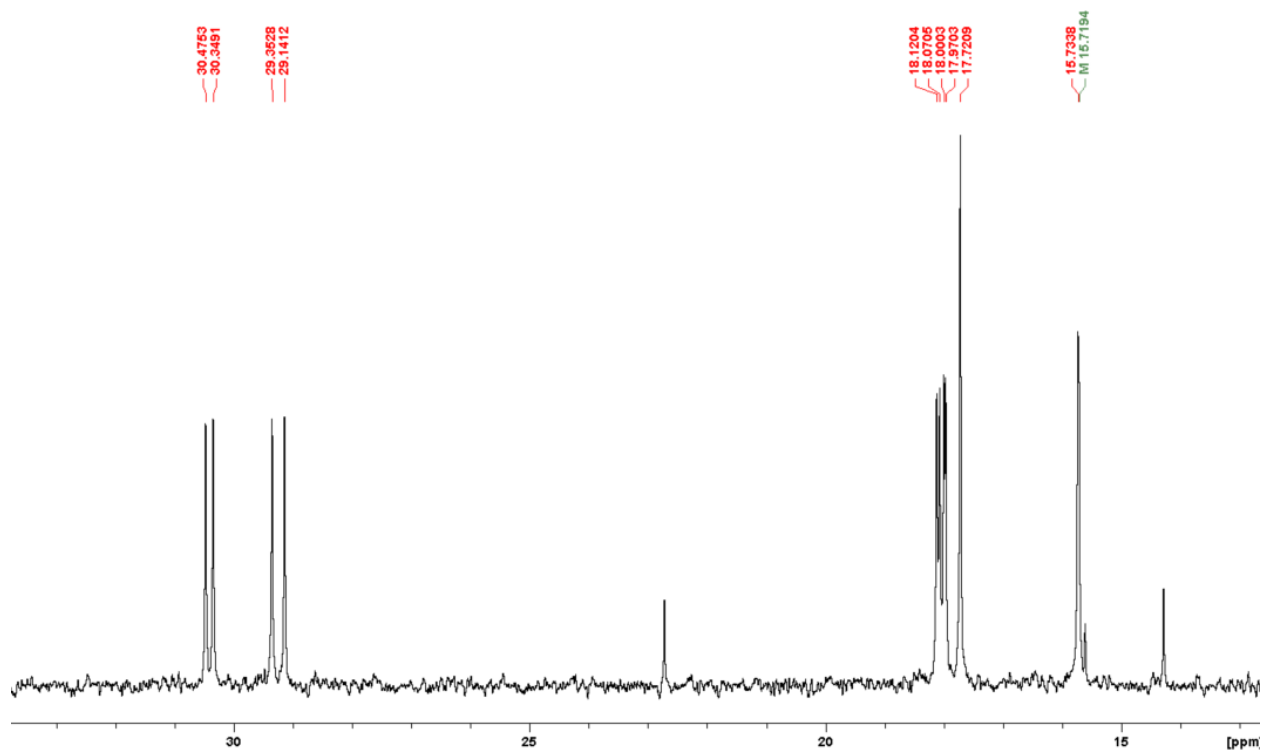
Figure S4.58: $^{13}C\{^1H\}$ NMR spectrum of **2g** in C_6D_6, focus on the aliphatic region.
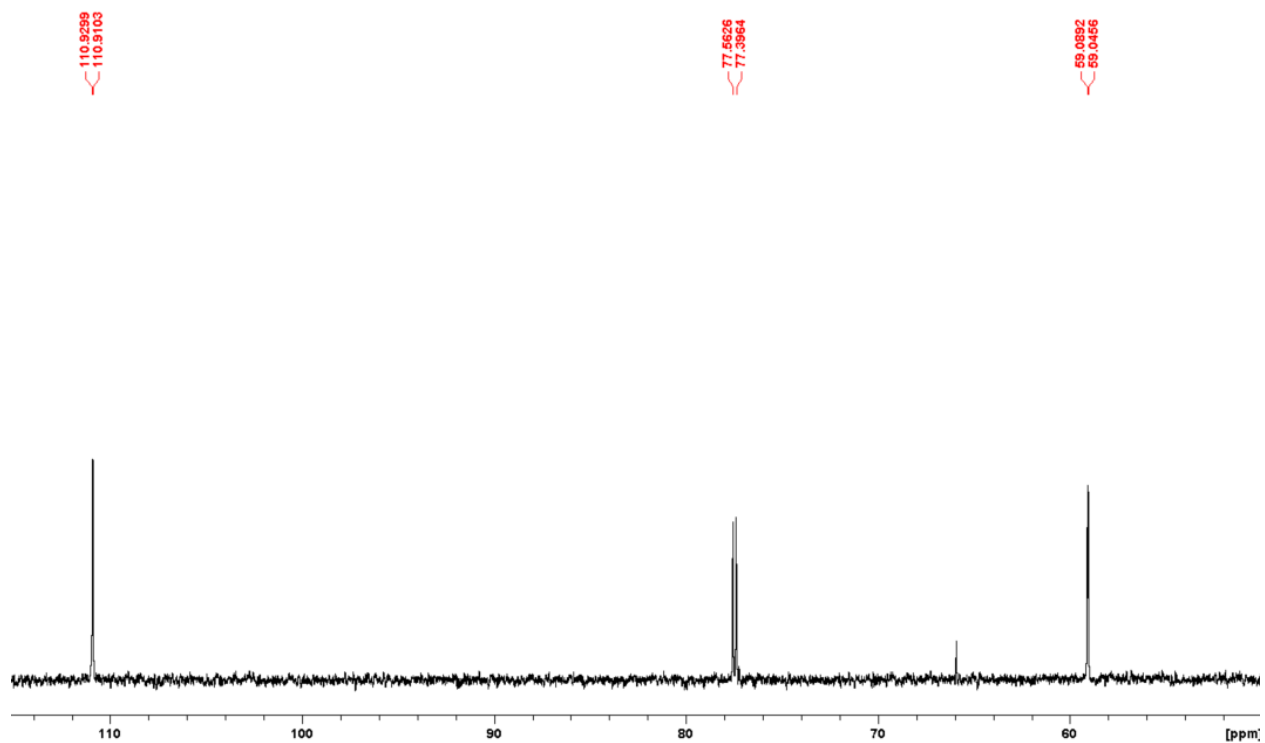
Figure S4.59: $^{13}\text{C}\{^1\text{H}\}$ NMR spectrum of **2g** in C_6D_6, focus on the allylic region.
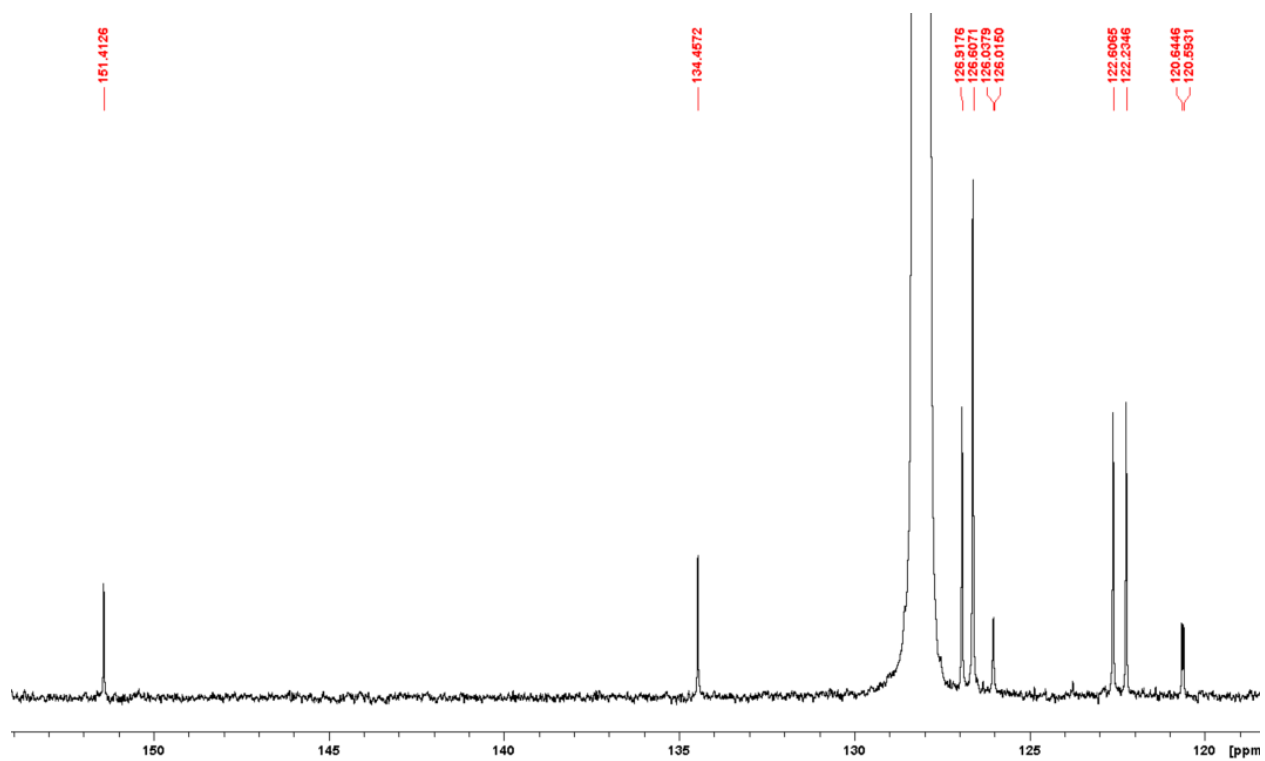
Figure S4.60: $^{13}\text{C}\{^1\text{H}\}$ NMR spectrum of **2g** in C_6D_6, focus on the aromatic region.
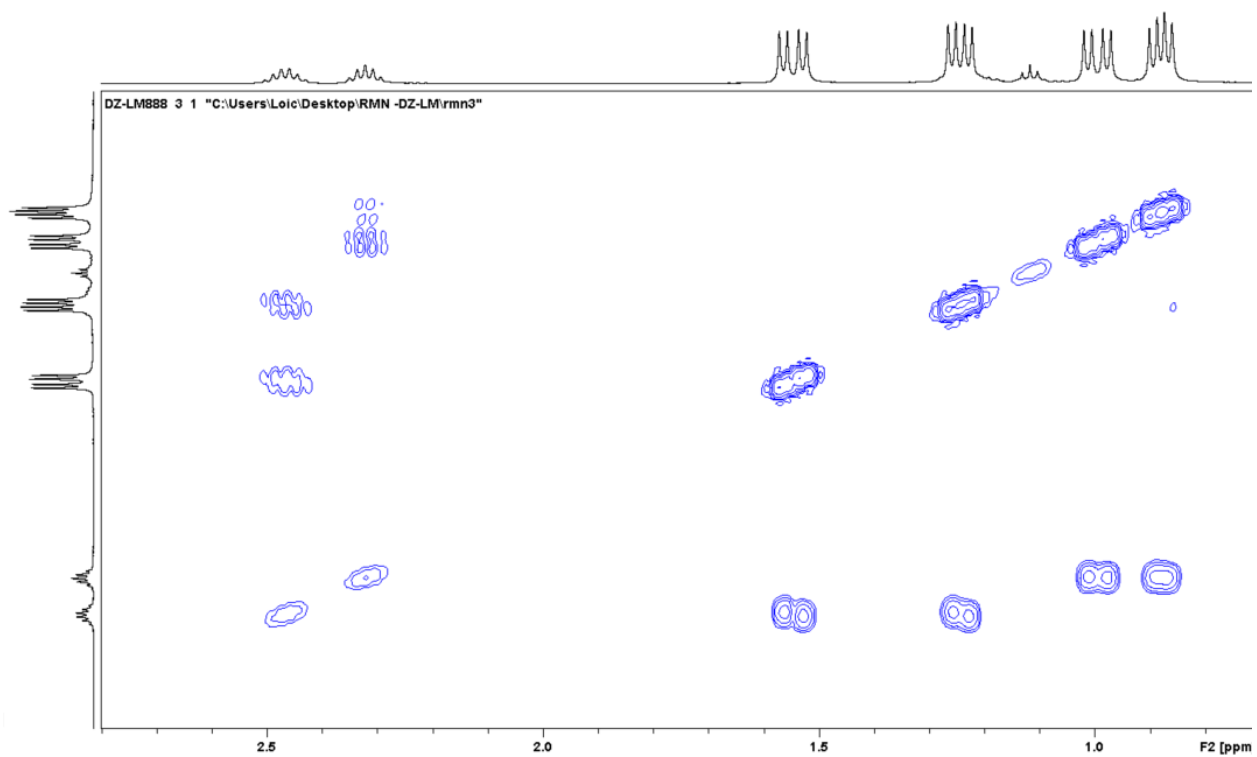
Figure S4.61: COSY NMR spectrum of **2g** in C_6D_6, focus on the aliphatic region.
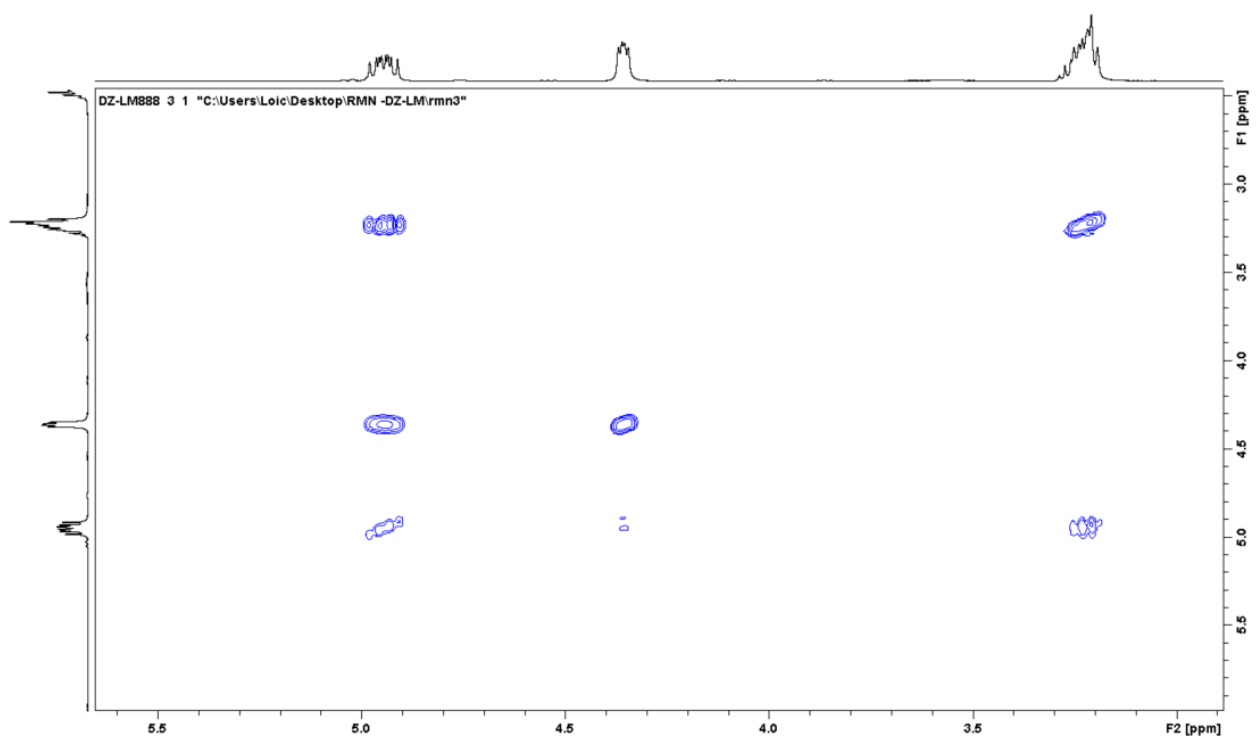
Figure S4.62: COSY NMR spectrum of **2g** in C_6D_6, focus on the allylic region.
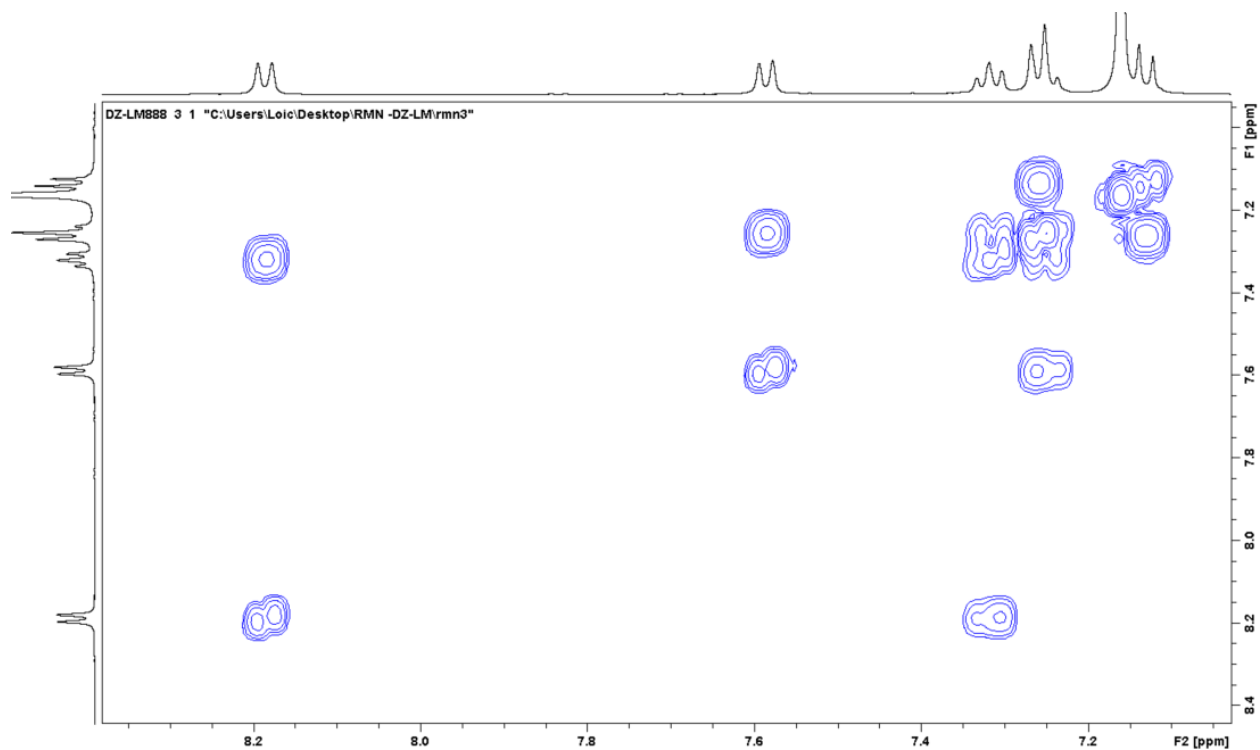
Figure S4.63: COSY NMR spectrum of **2g** in C_6D_6, focus on the aromatic region.
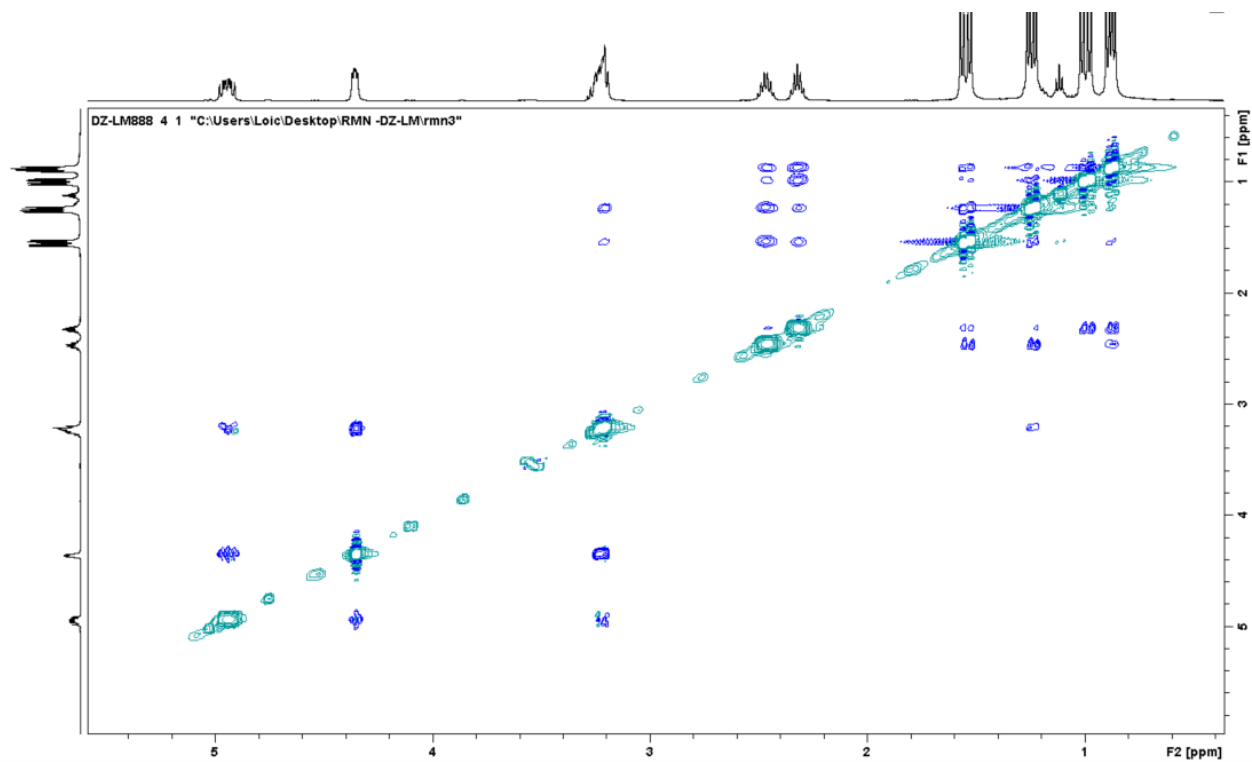
Figure S4.64: NOESY NMR spectrum of **2g** in C_6D_6, focus on the aliphatic/allylic and allylic/allylic interactions.
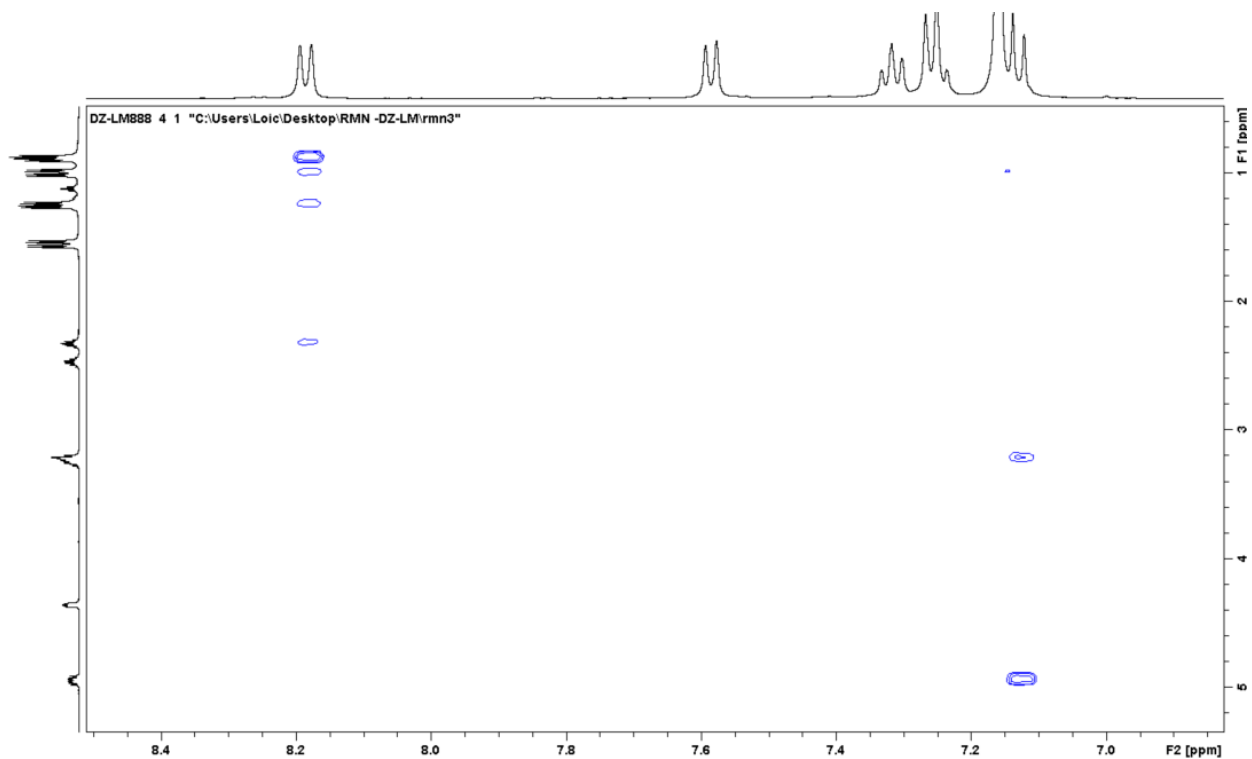
Figure S4.65: NOESY NMR spectrum of **2g** in C_6D_6, focus on the aromatic/aliphatic and aromatic/allylic interactions.
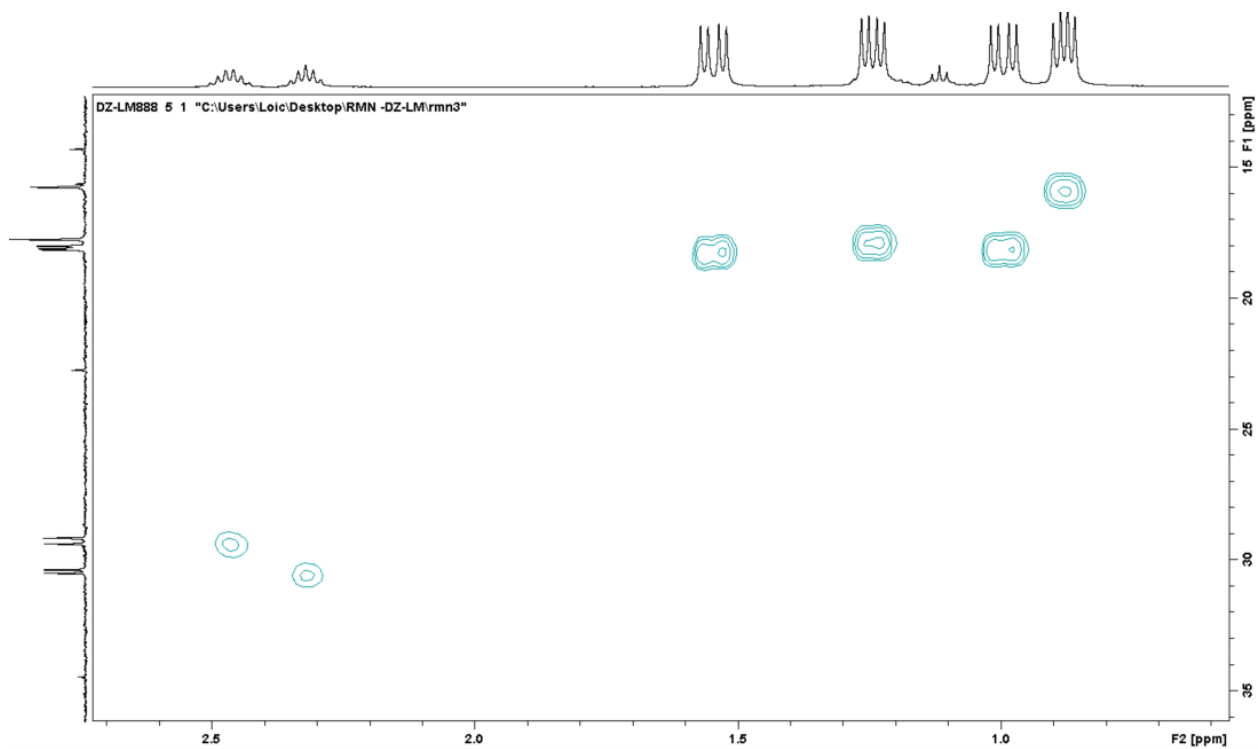
Figure S4.66: HSQC NMR spectrum of **2g** in C_6D_6, focus on the aliphatic region.
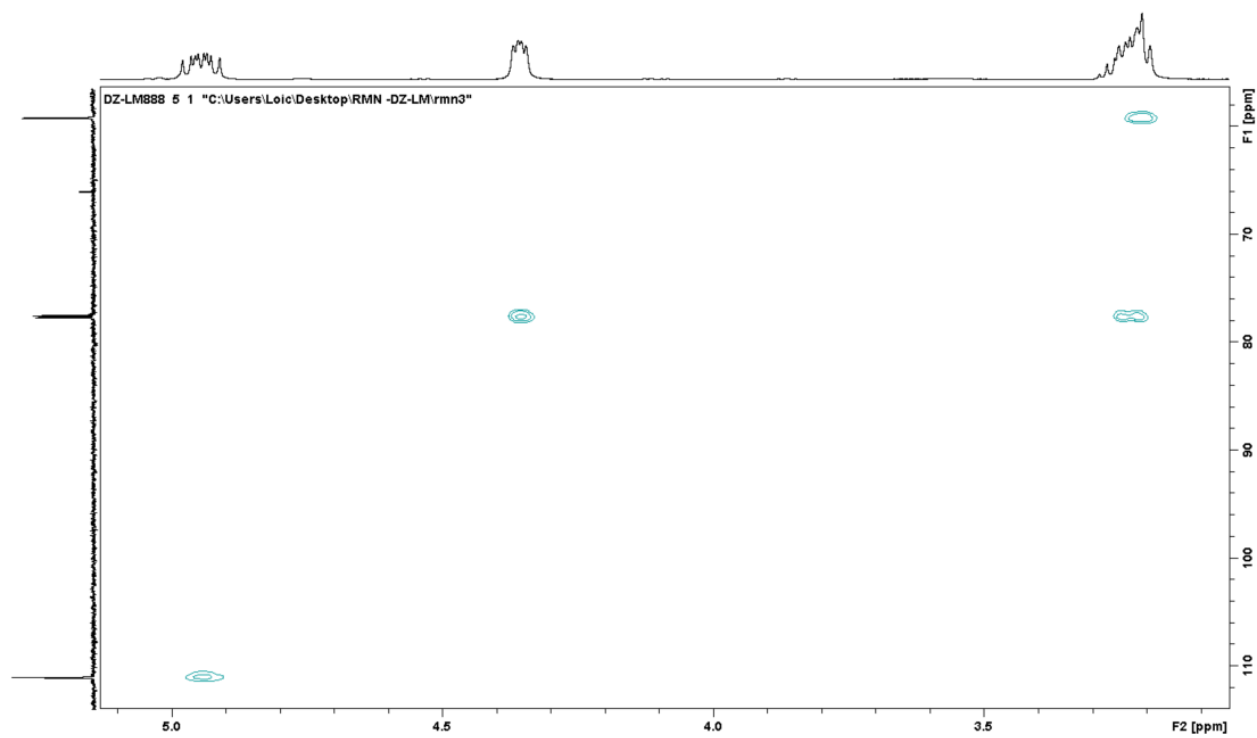
Figure S4.67: HSQC NMR spectrum of **2g** in C$_6$D$_6$, focus on the allylic region.
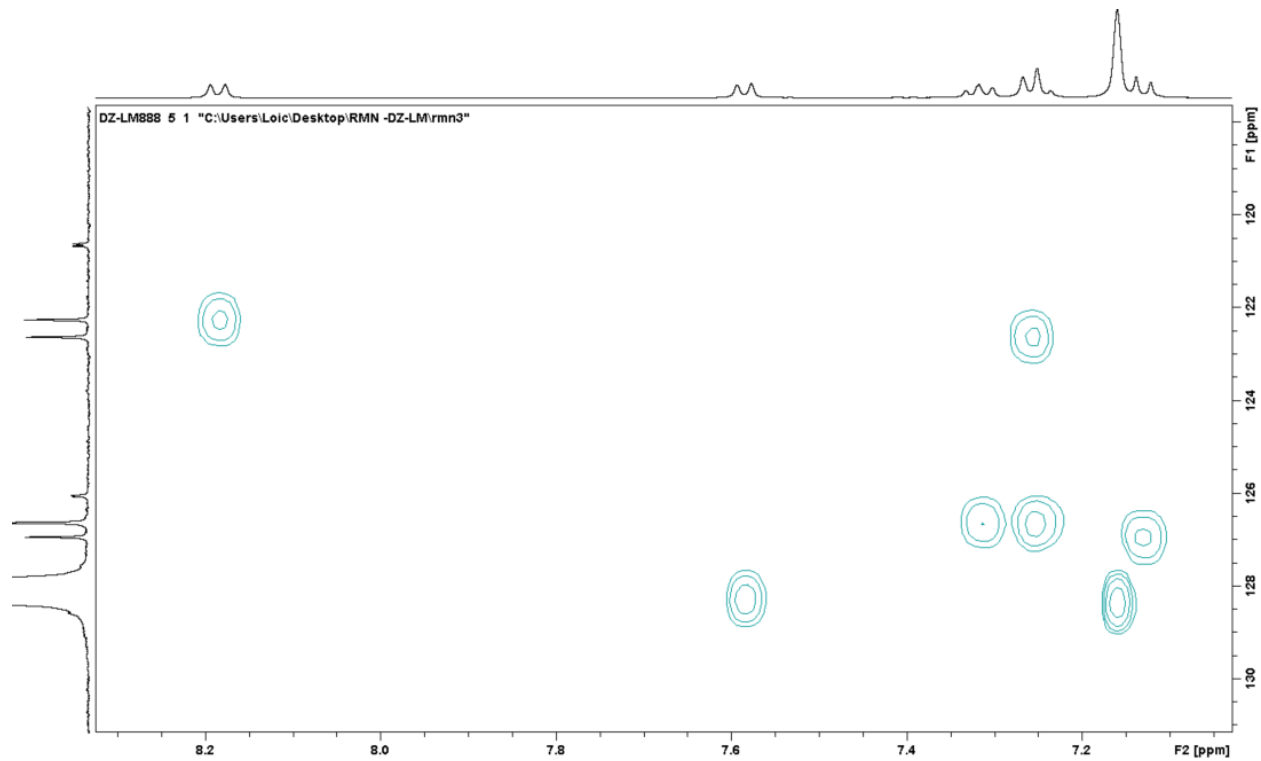
Figure S4.68: HSQC NMR spectrum of **2g** in C$_6$D$_6$, focus on the aromatic region
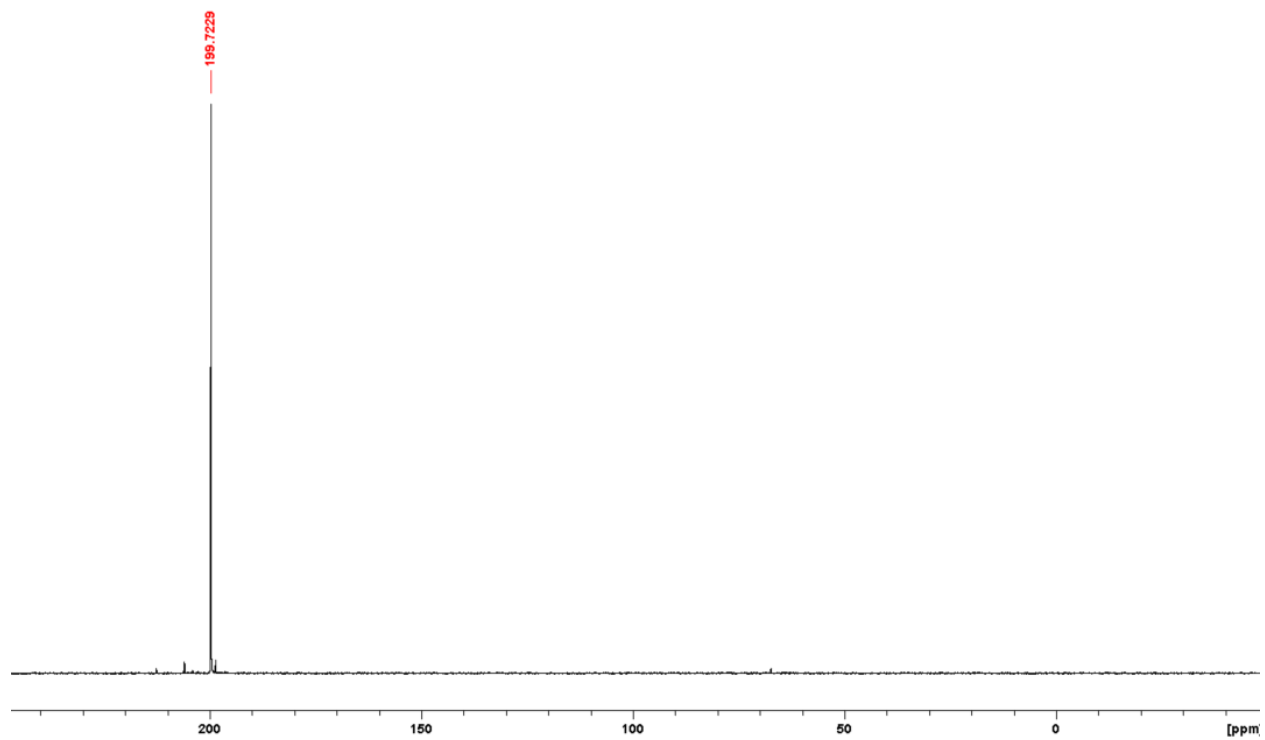
Figure S4.69: $^{31}P\{^1H\}$ NMR spectrum of **2g** in CDCl$_3$.
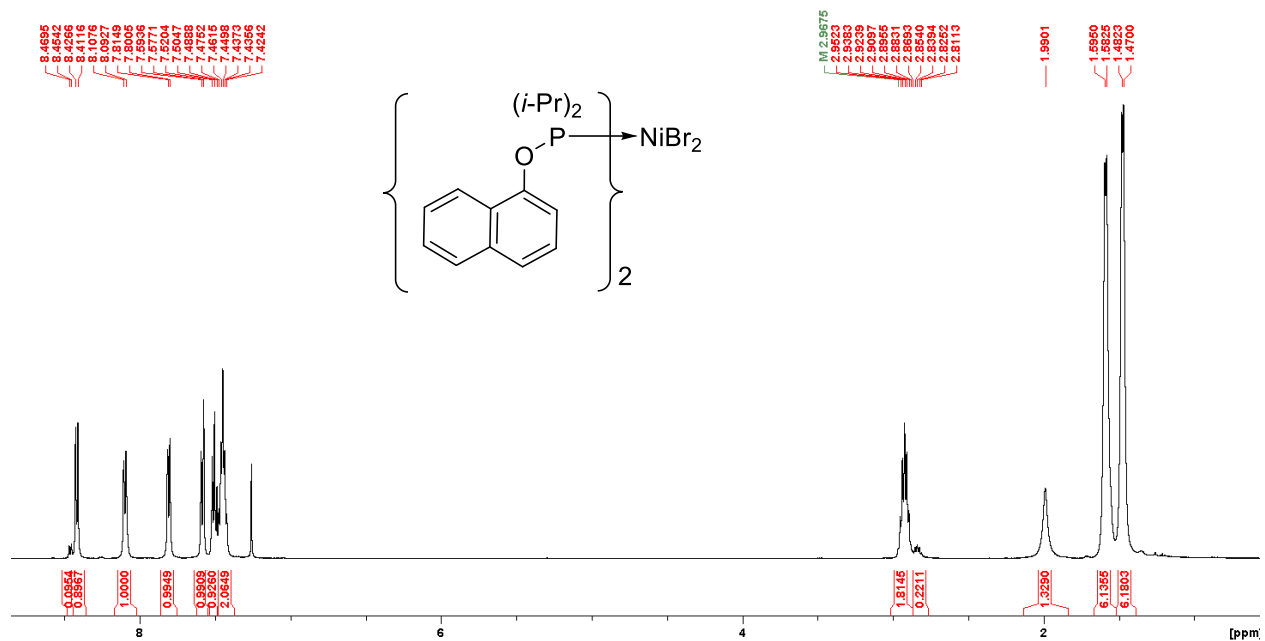
Figure S4.70: Full ^{1}H NMR spectrum of **3a·MeCN** in CDCl$_3$.
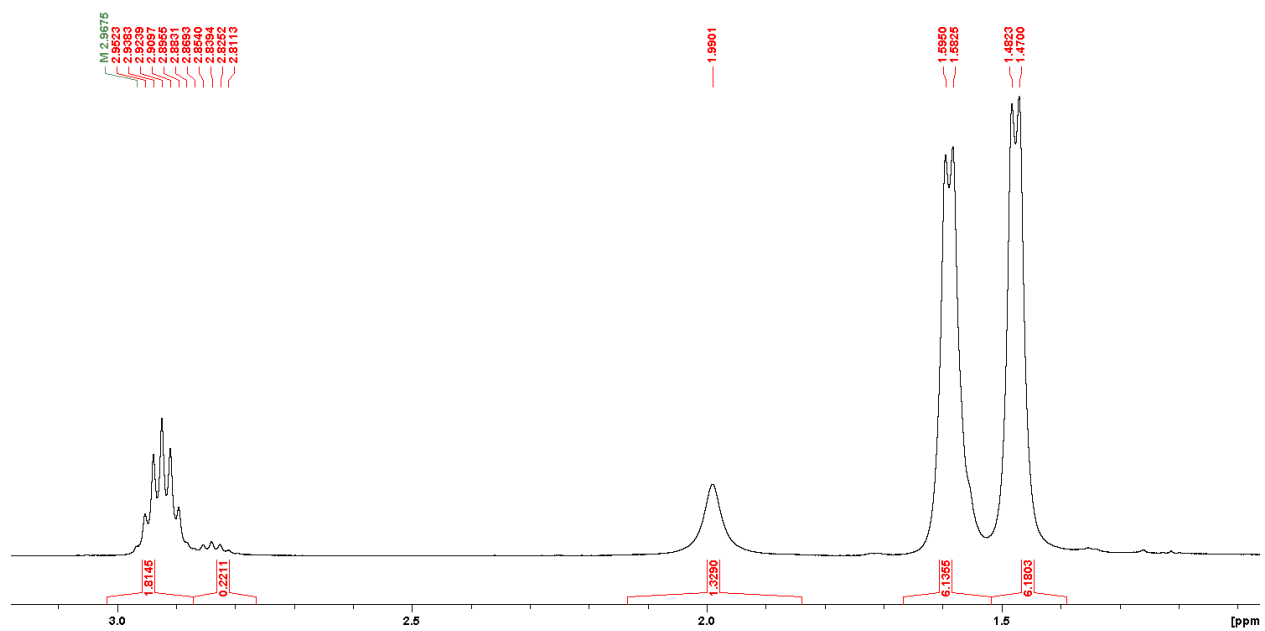
Figure S4.71: ^{1}H NMR spectrum of **3a·MeCN** in CDCl$_3$, focus on the aliphatic region.
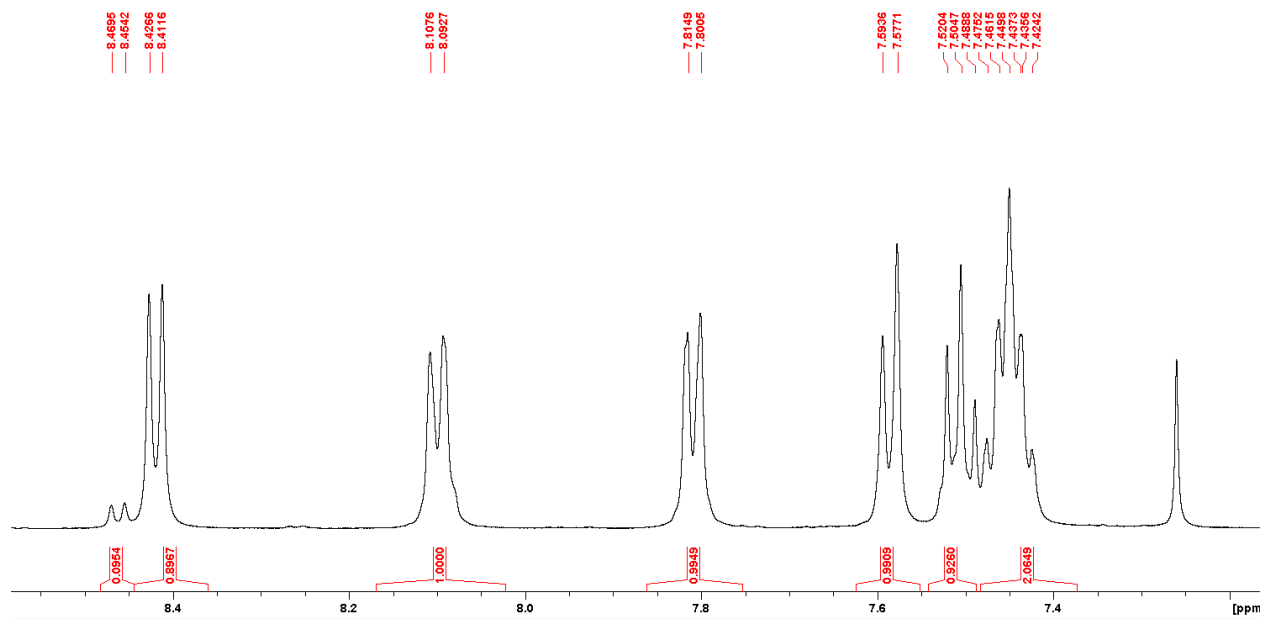
Figure S4.72: ^{1}H NMR spectrum of **3a·MeCN** in CDCl$_3$, focus on the aromatic region.
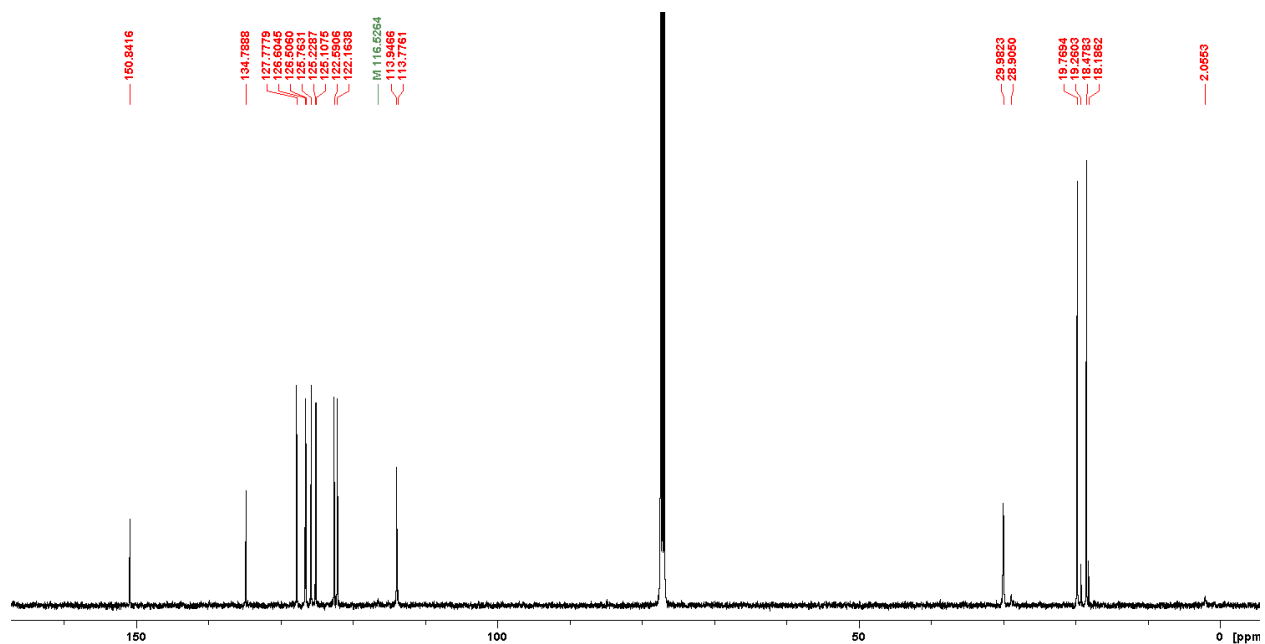
Figure S4.73: Full ^{13}C{^{1}H} NMR spectrum of **3a·MeCN** in CDCl$_3$.
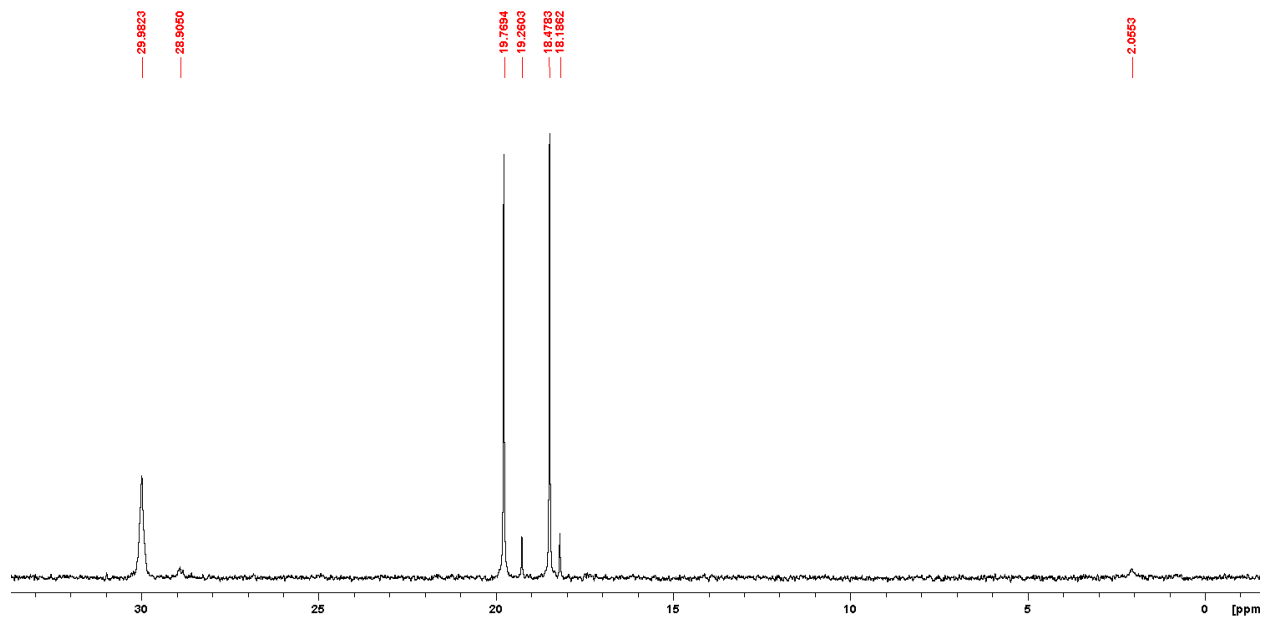
Figure S4.74: $^{13}C\{^1H\}$ NMR spectrum of **3a·MeCN** in CDCl$_3$, focus on the aliphatic region.
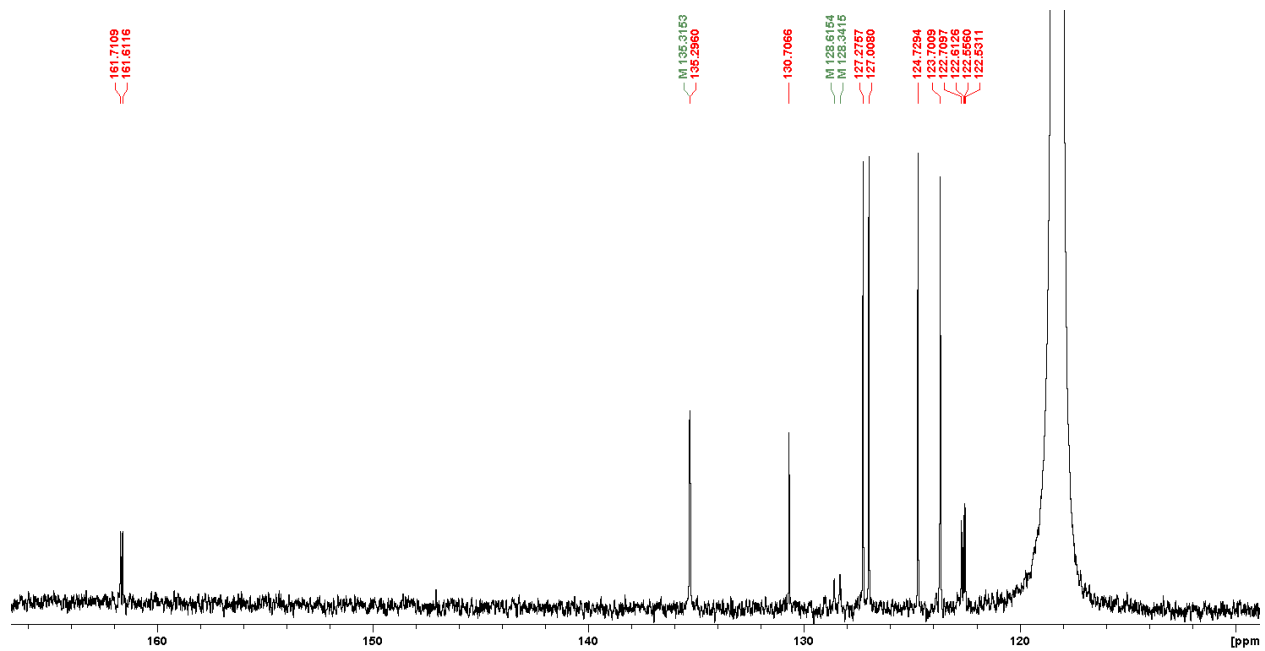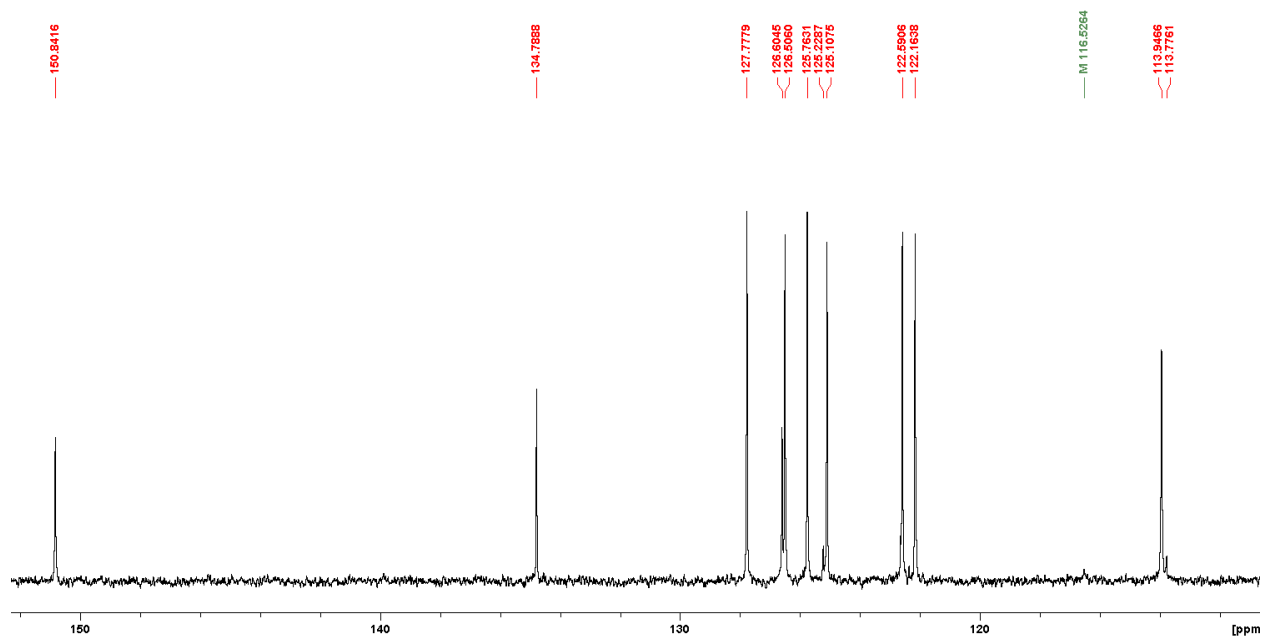

Figure S4.75: $^{13}C\{^1H\}$ NMR spectrum of **3a·MeCN** in CDCl$_3$, focus on the aromatic region.
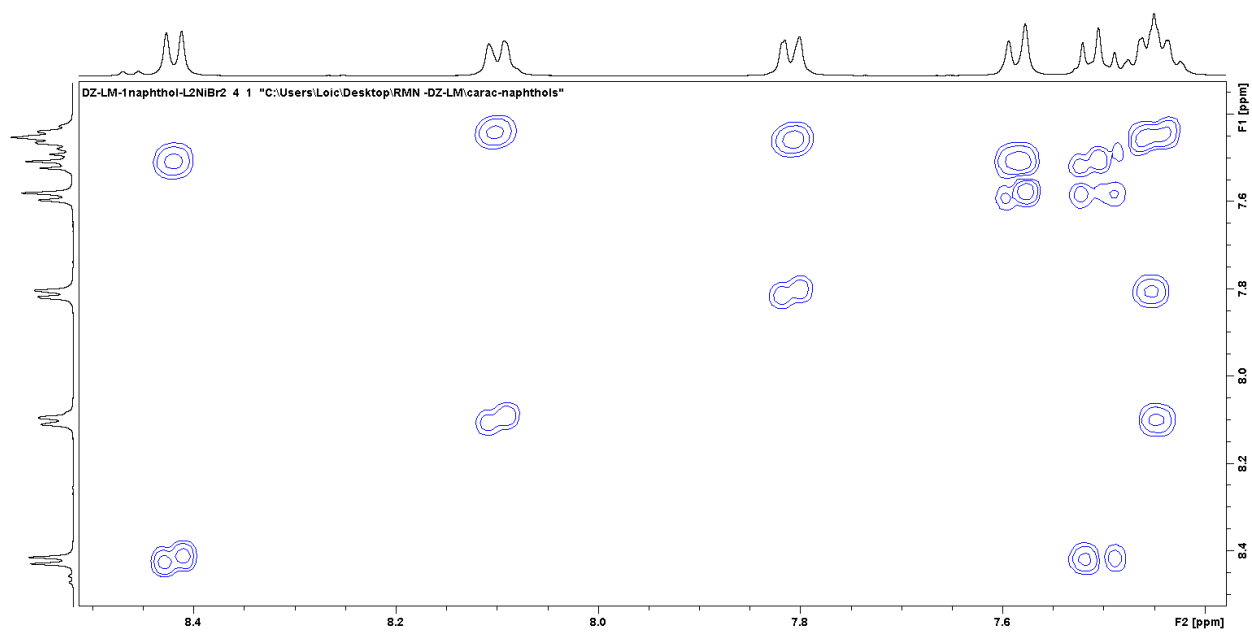
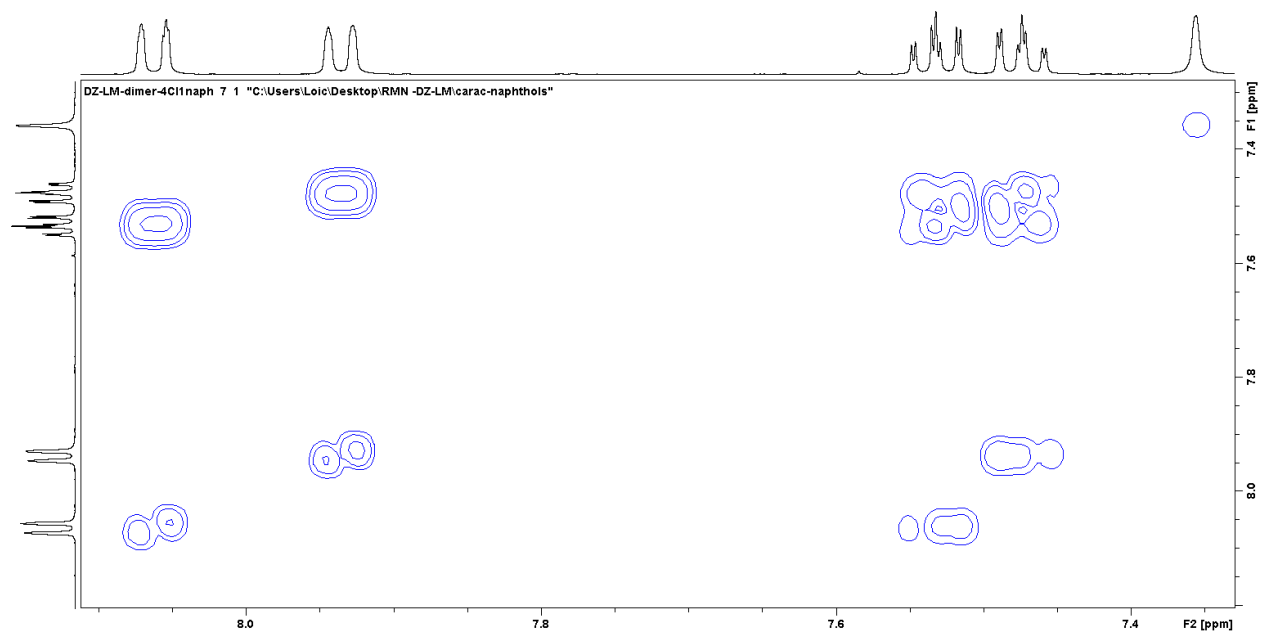Figure S4.76: COSY NMR spectrum of **3a·MeCN** in CDCl₃, focus on the aromatic region.
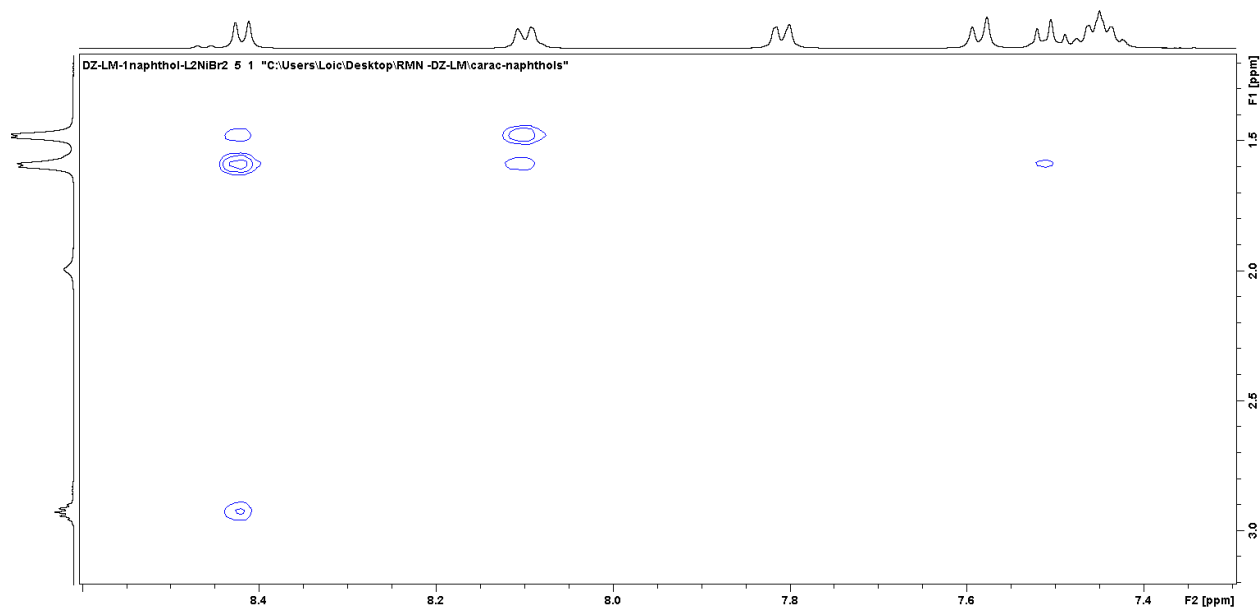
Figure S4.77: NOESY NMR spectrum of **3a·MeCN** in CDCl₃, focus on the aliphatic/aromatic interactions.
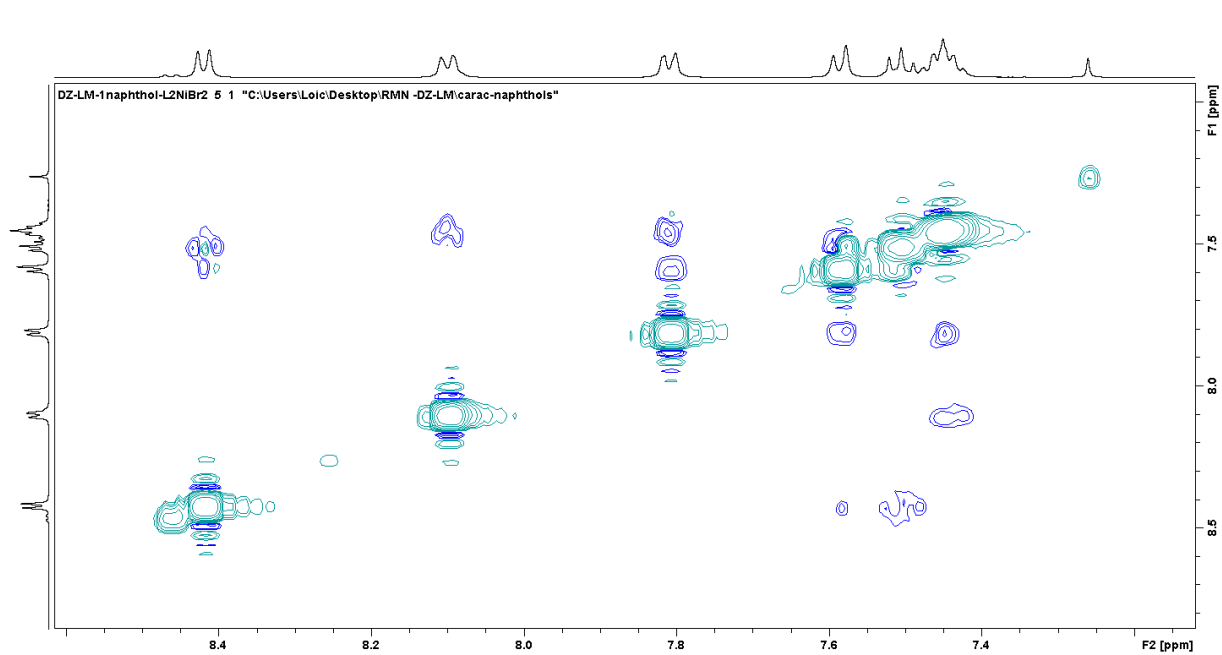
Figure S4.78: NOESY NMR spectrum of **3a·MeCN** in CDCl₃, focus on the aromatic/aromatic interactions.
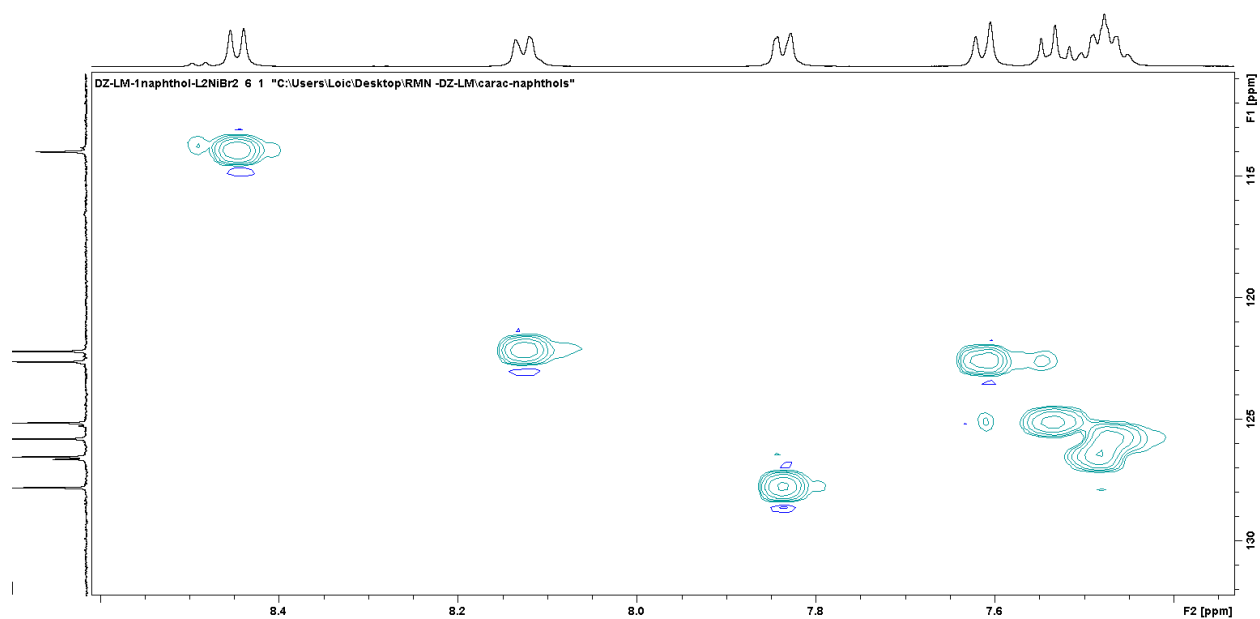
Figure S4.79: HSQC NMR spectrum of **3a·MeCN** in CDCl₃, focus on the aromatic region.
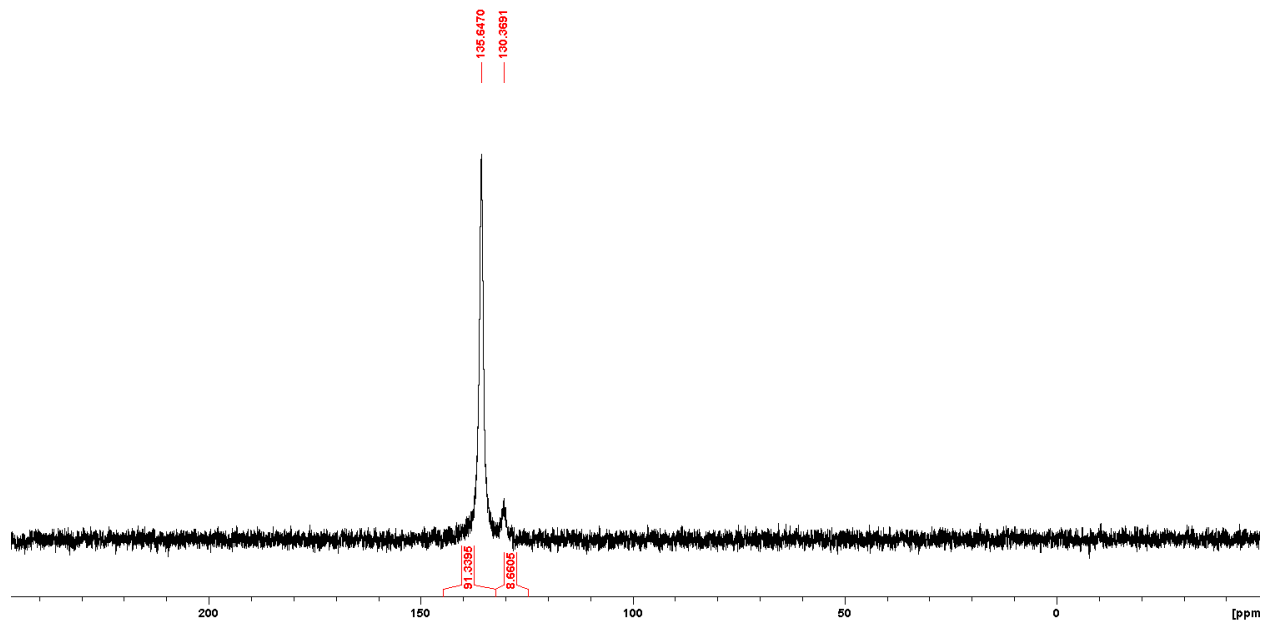
Figure S4.80: $^{31}P\{^1H\}$ NMR spectrum of **3a·MeCN** in CDCl$_3$.
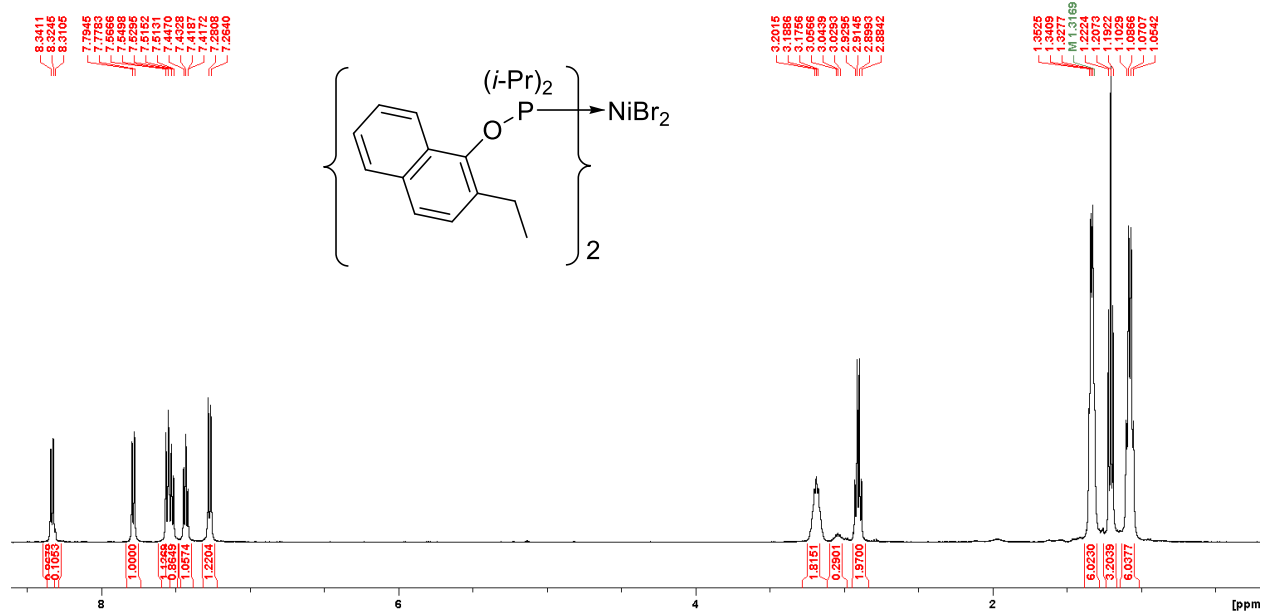
Figure S4.81: Full ^{1}H NMR spectrum of **3d** in CDCl$_3$.
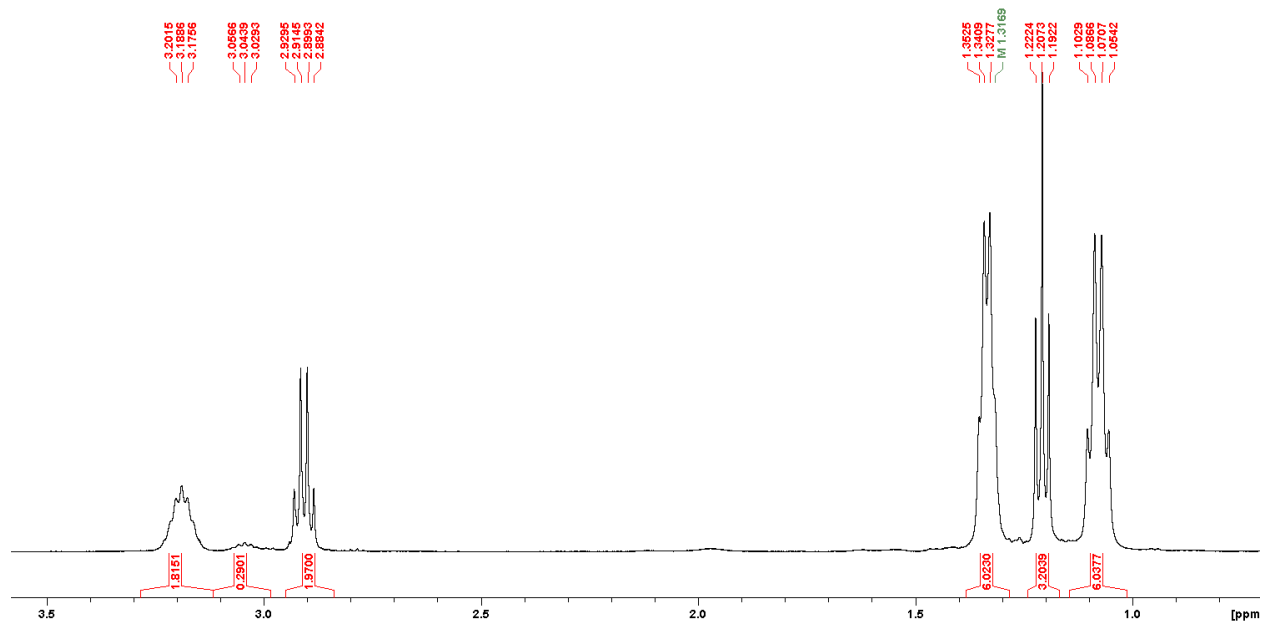
Figure S4.82: ^{1}H NMR spectrum of **3d** in CDCl$_3$, focus on the aliphatic region.
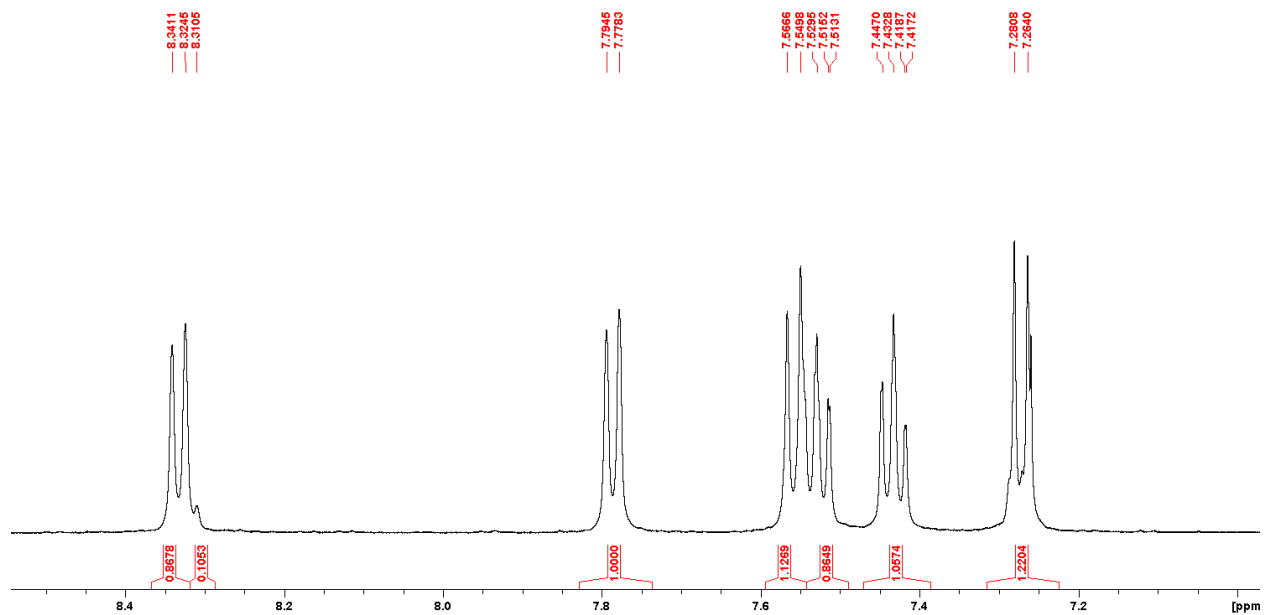
Figure S4.83: ¹H NMR spectrum of **3d** in CDCl₃, focus on the aromatic region.
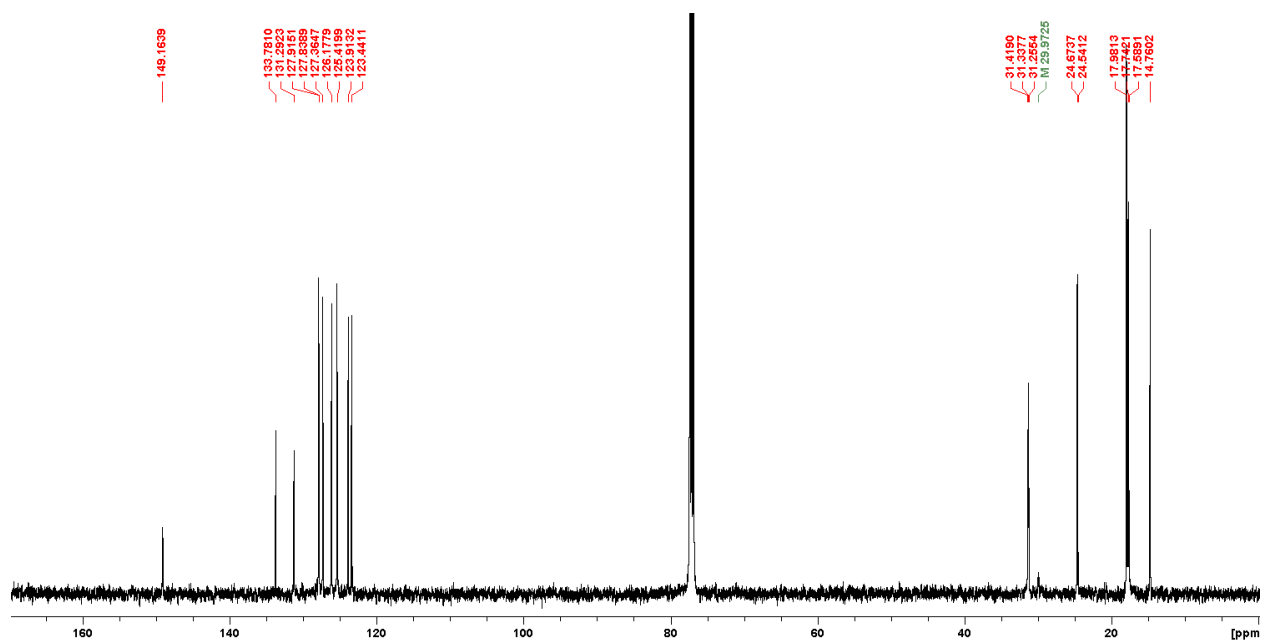
Figure S4.84: Full ¹³C{¹H} NMR spectrum of **3d** in CDCl₃.
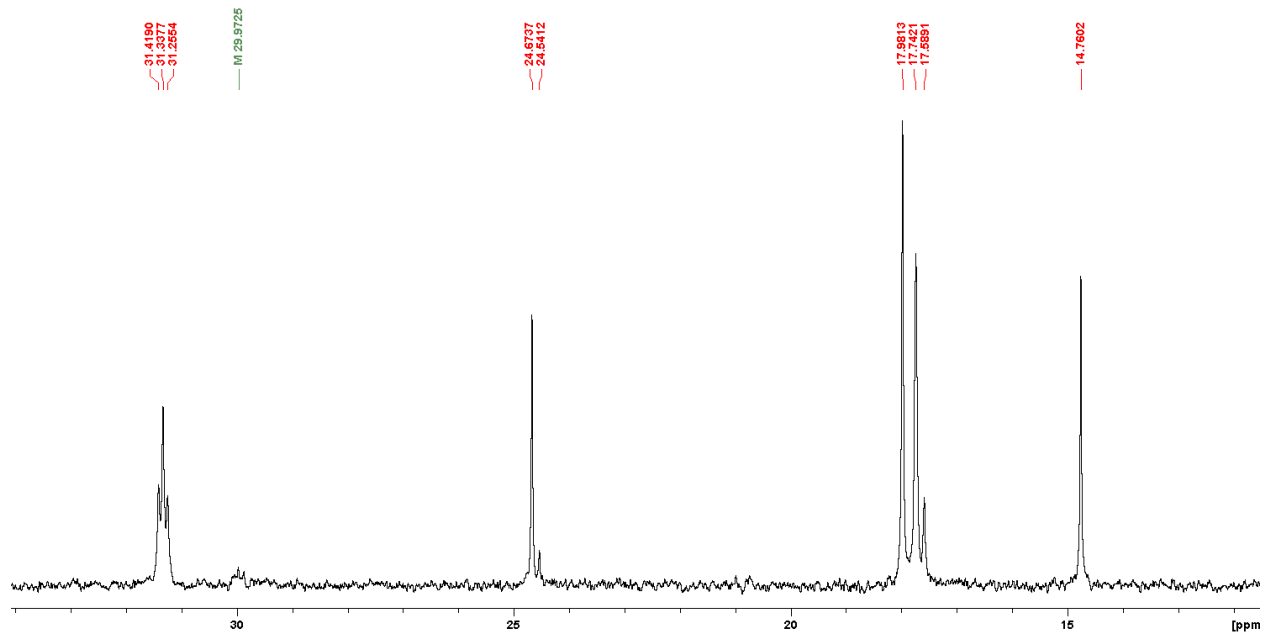
Figure S4.85: ^{13}C{^{1}H} NMR spectrum of **3d** in CDCl$_3$, focus on the aliphatic region.
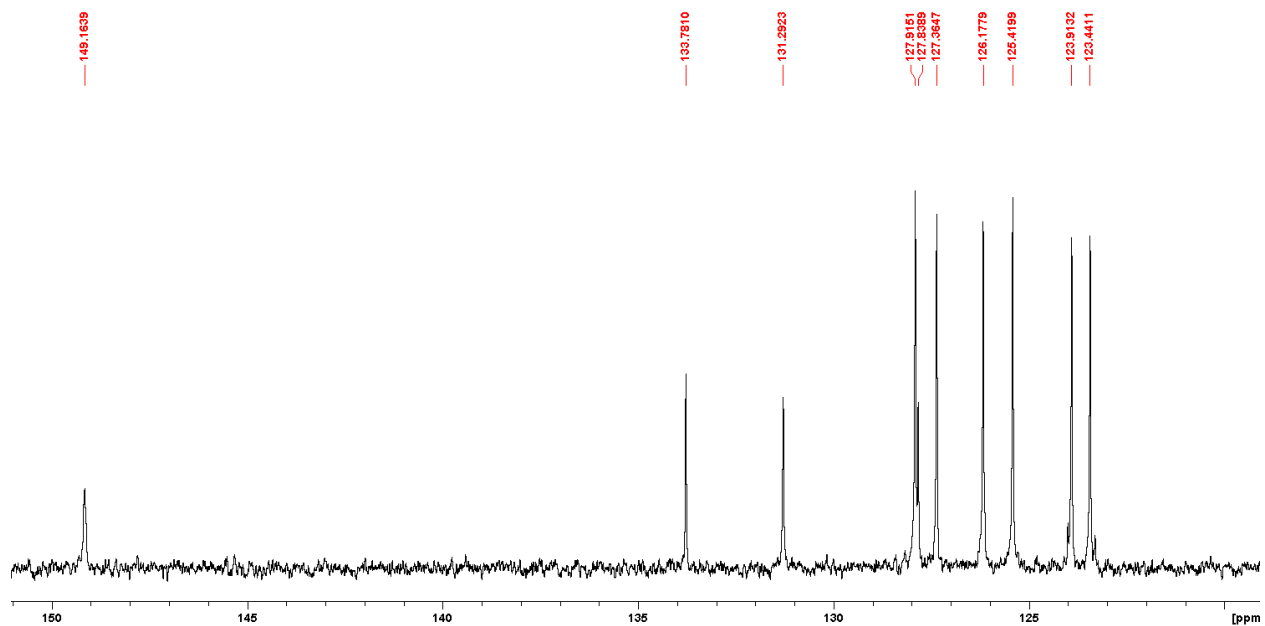
Figure S4.86: ^{13}C{^{1}H} NMR spectrum of **3d** in CDCl$_3$, focus on the aromatic region.
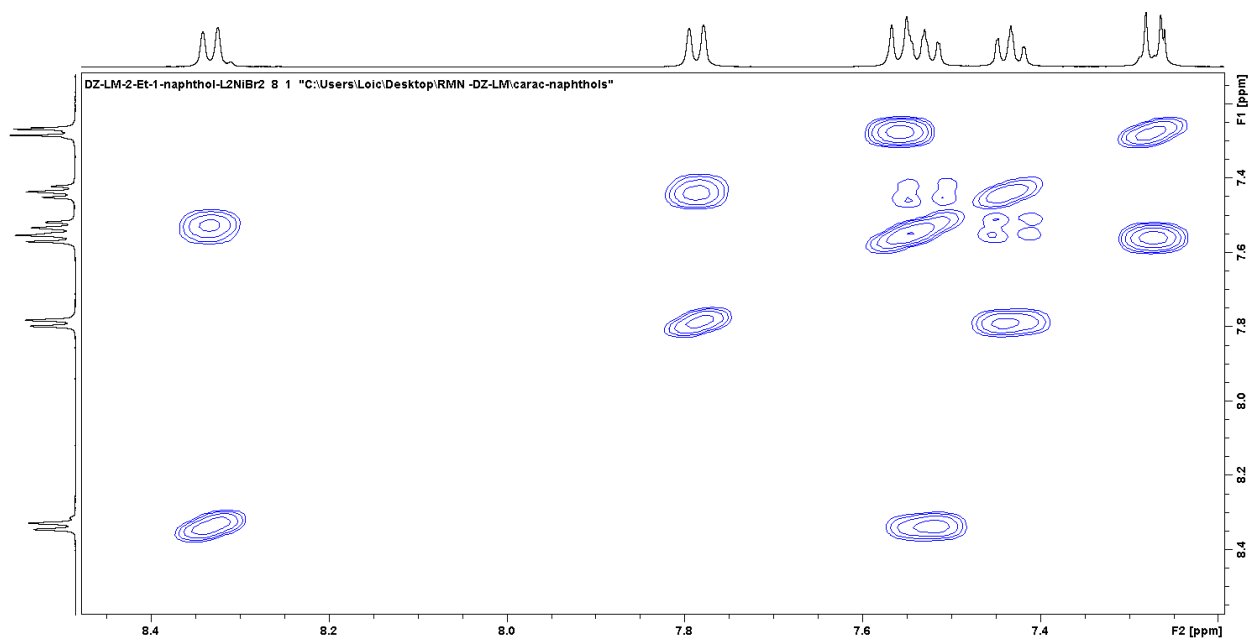
Figure S4.87: COSY NMR spectrum of **3d** in CDCl₃, focus on the aliphatic region.
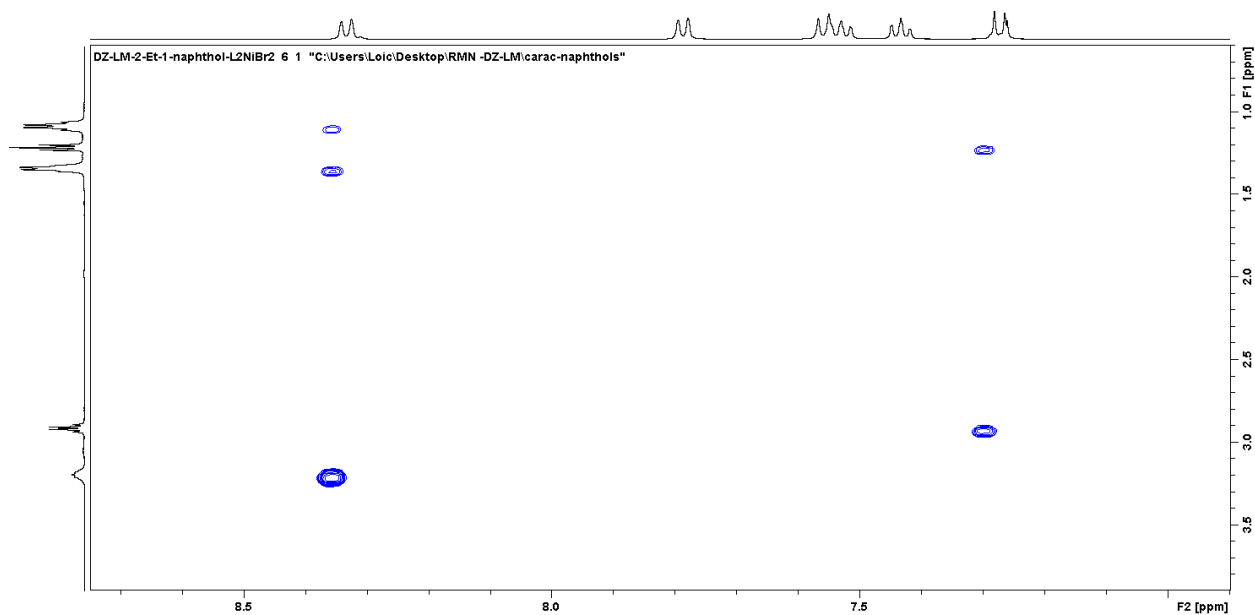
Figure S4.88: NOESY NMR spectrum of **3d** in CDCl₃, focus on the aliphatic/aromatic interactions.
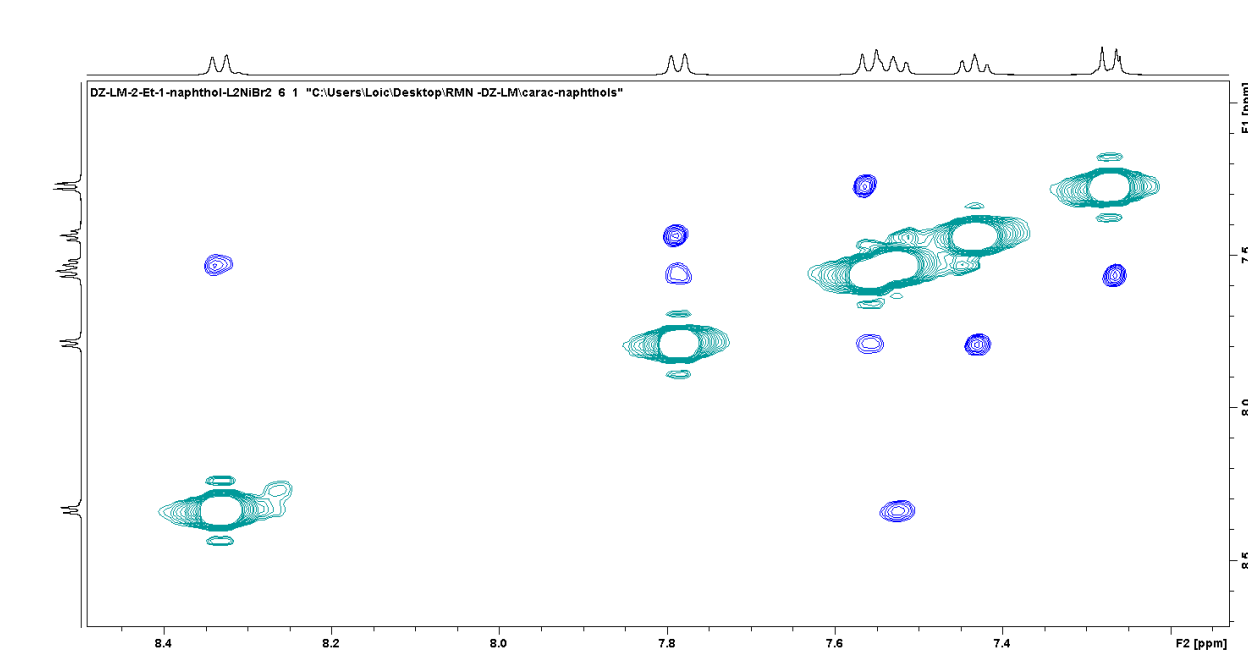
Figure S4.89: NOESY NMR spectrum of **3d** in CDCl$_3$, focus on the aromatic/aromatic interactions.
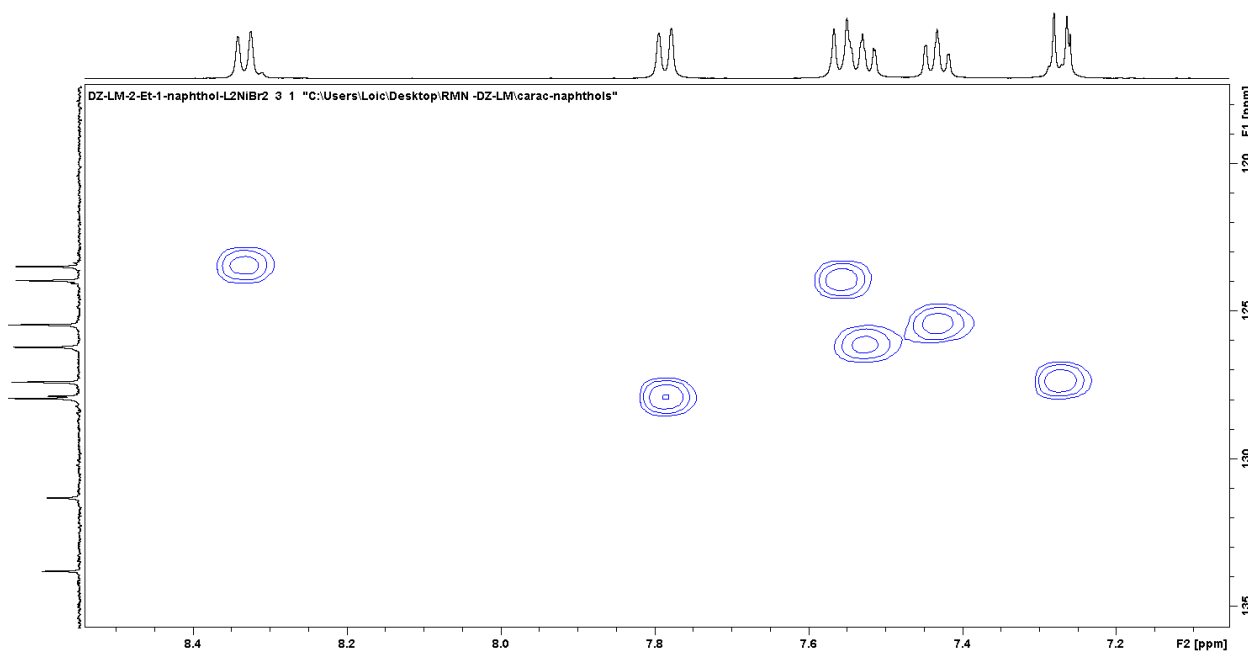
Figure S4.90: NOESY NMR spectrum of **3d** in CDCl$_3$, focus on the aromatic region.
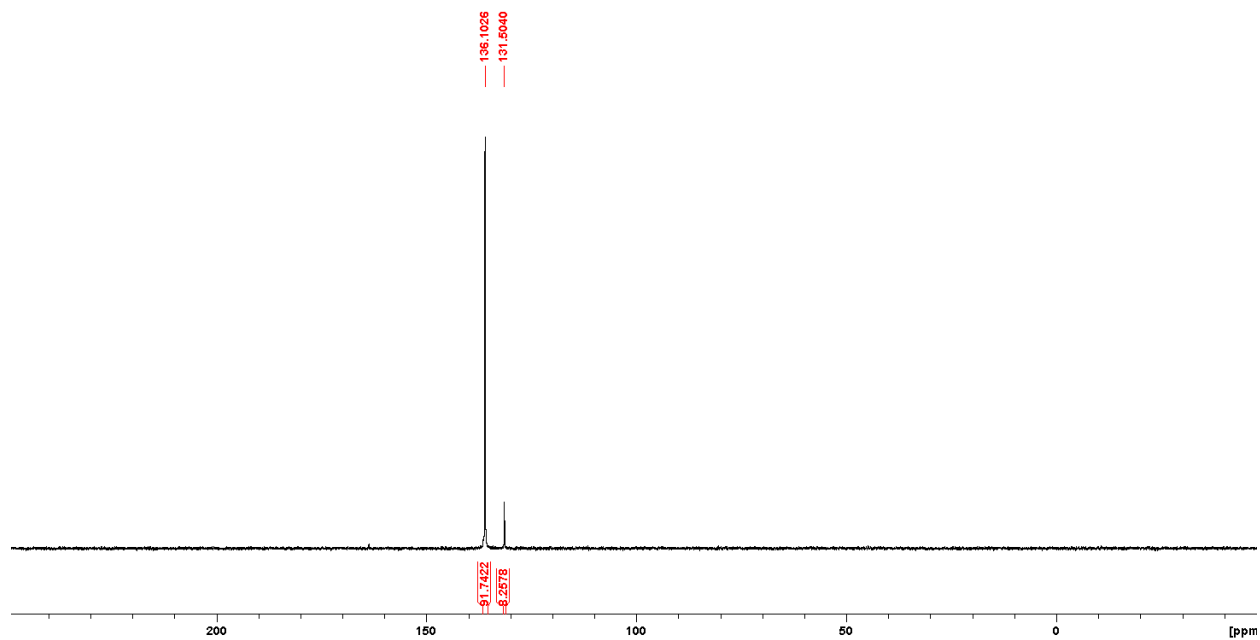
Figure S4.91: $^{31}P\{^1H\}$ NMR spectrum of **3d** in CDCl$_3$.
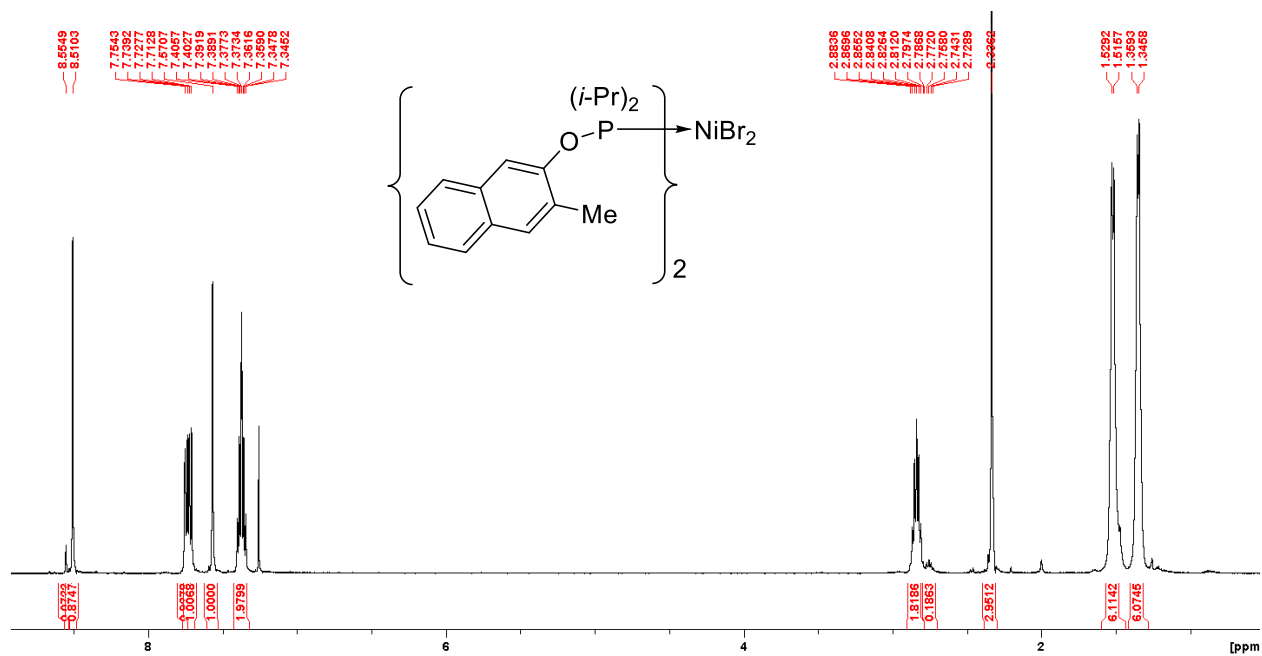
Figure S4.92: Full ^{1}H NMR spectrum of **3f** in CDCl$_3$.
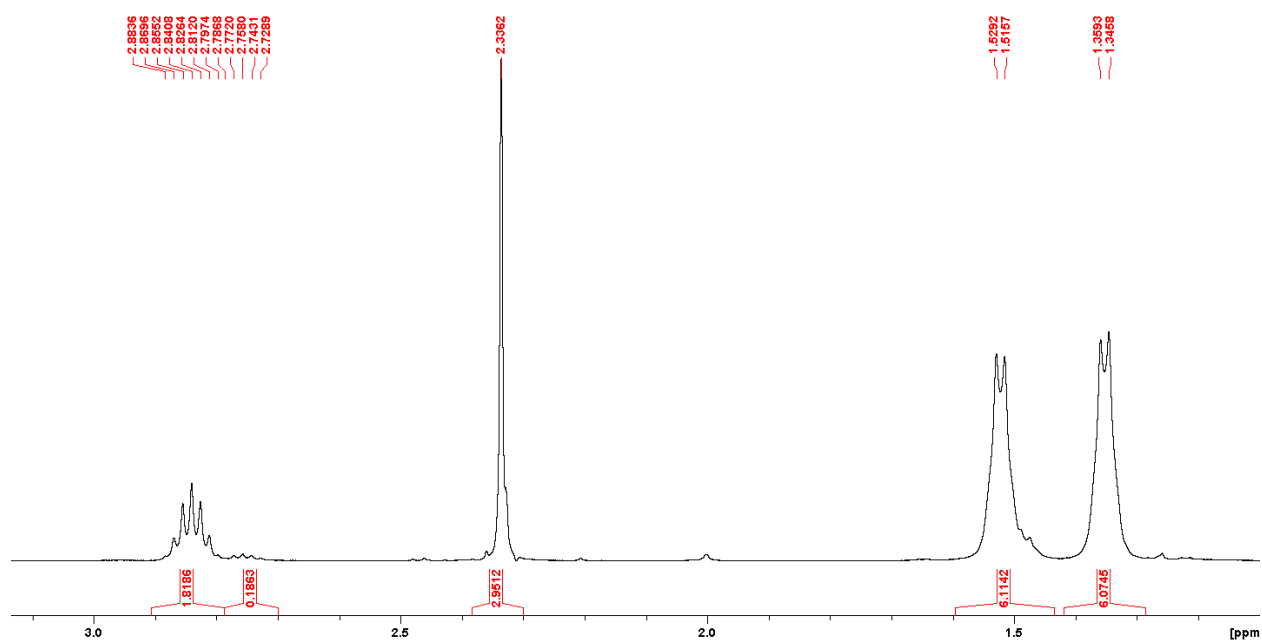
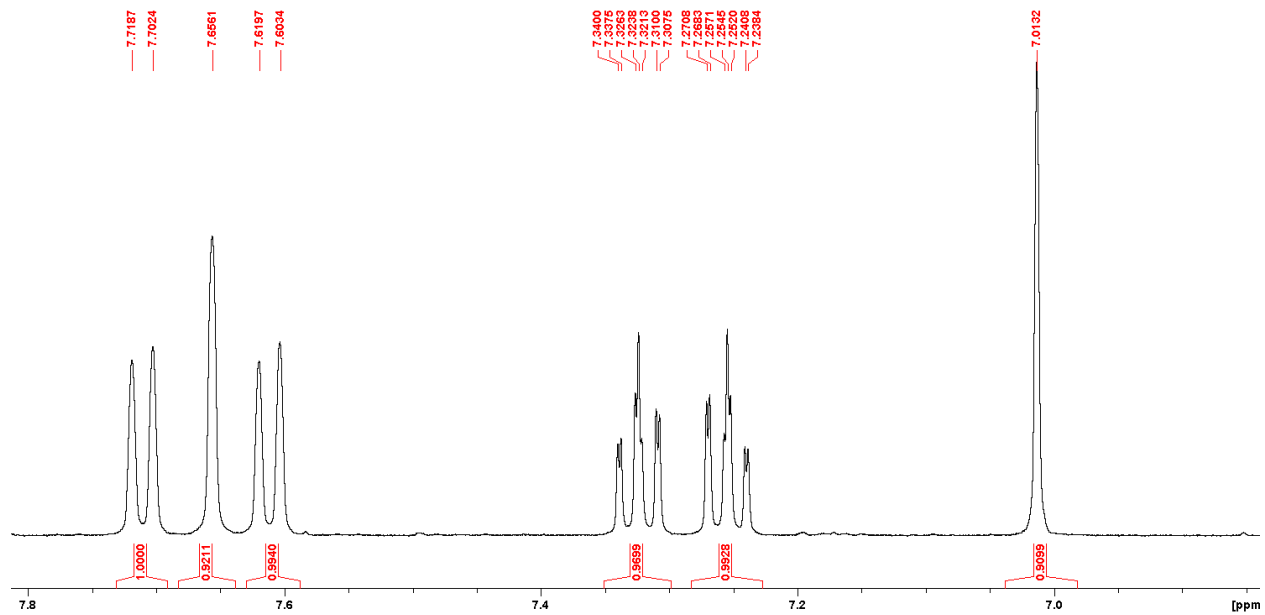Figure S4.93: ^{1}H NMR spectrum of **3f** in CDCl$_3$, focus on the aliphatic region.
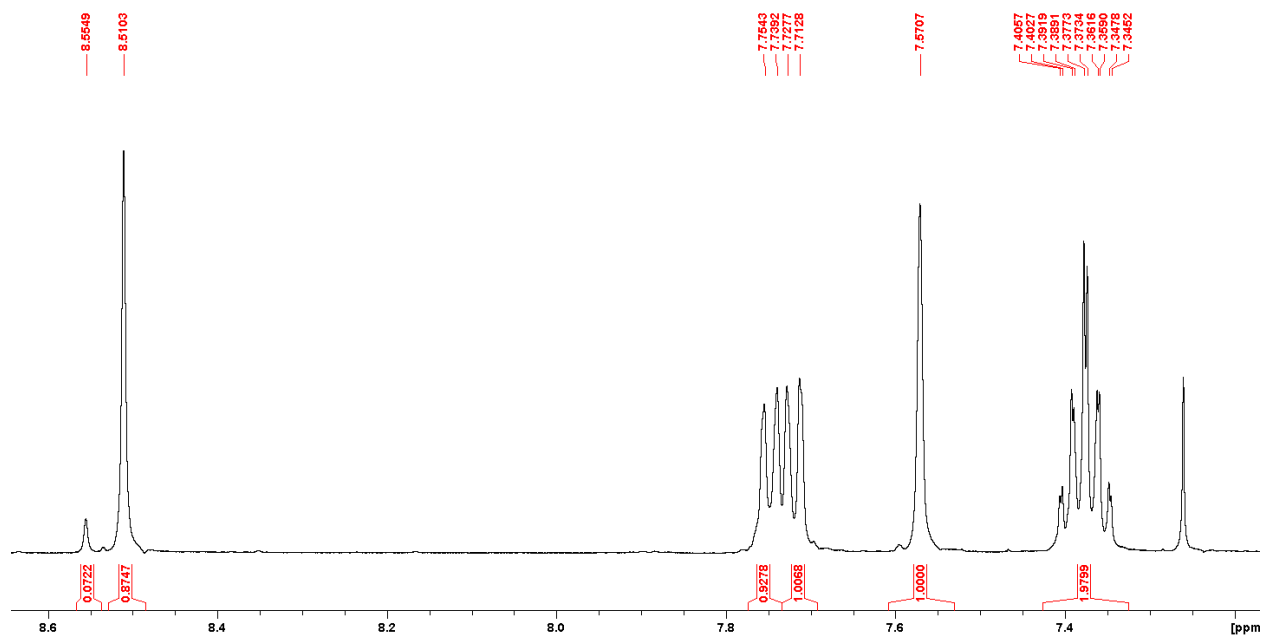
Figure S4.94: ^{1}H NMR spectrum of **3f** in CDCl$_3$, focus on the aromatic region.
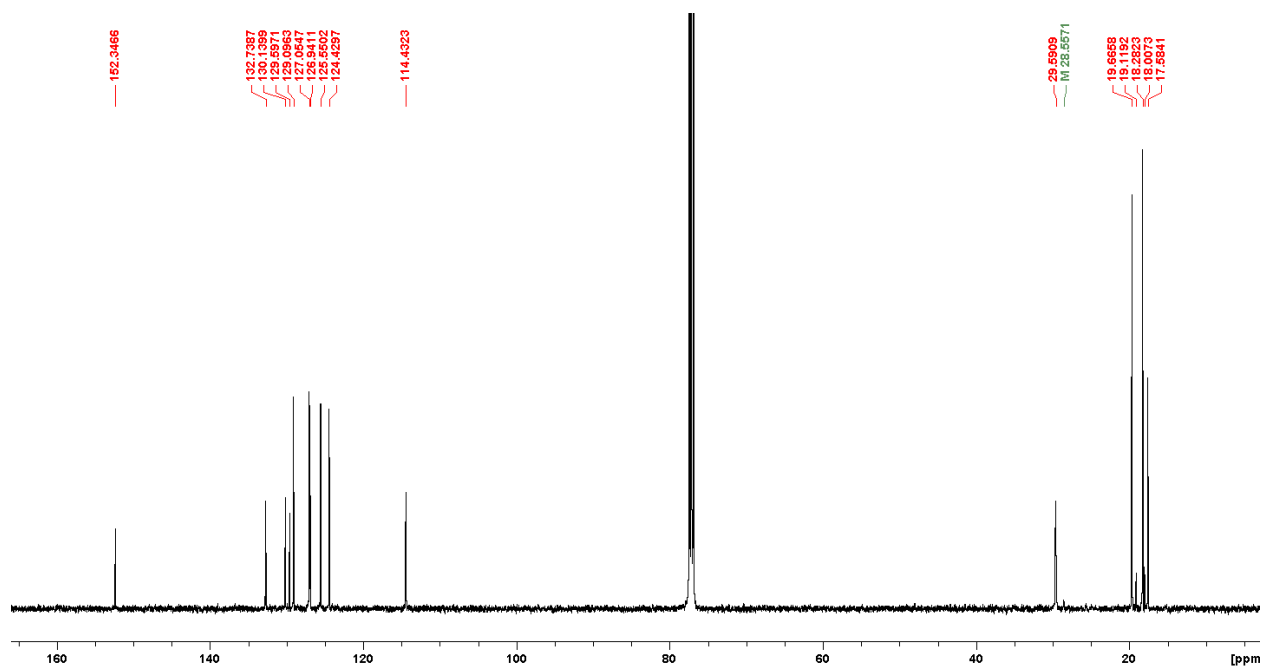
Figure S4.95: Full ^{13}C{^{1}H} NMR spectrum of **3f** in CDCl$_3$.
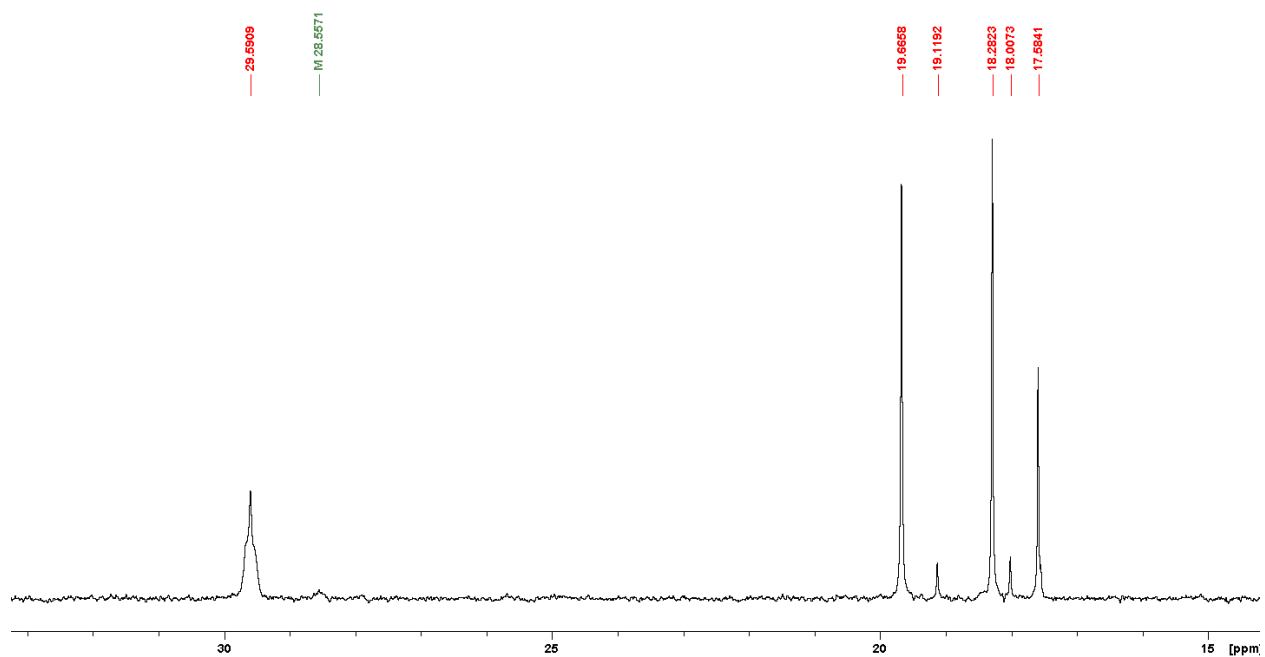
Figure S4.96: $^{13}C\{^1H\}$ NMR spectrum of **3f** in CDCl$_3$, focus on the aliphatic region.
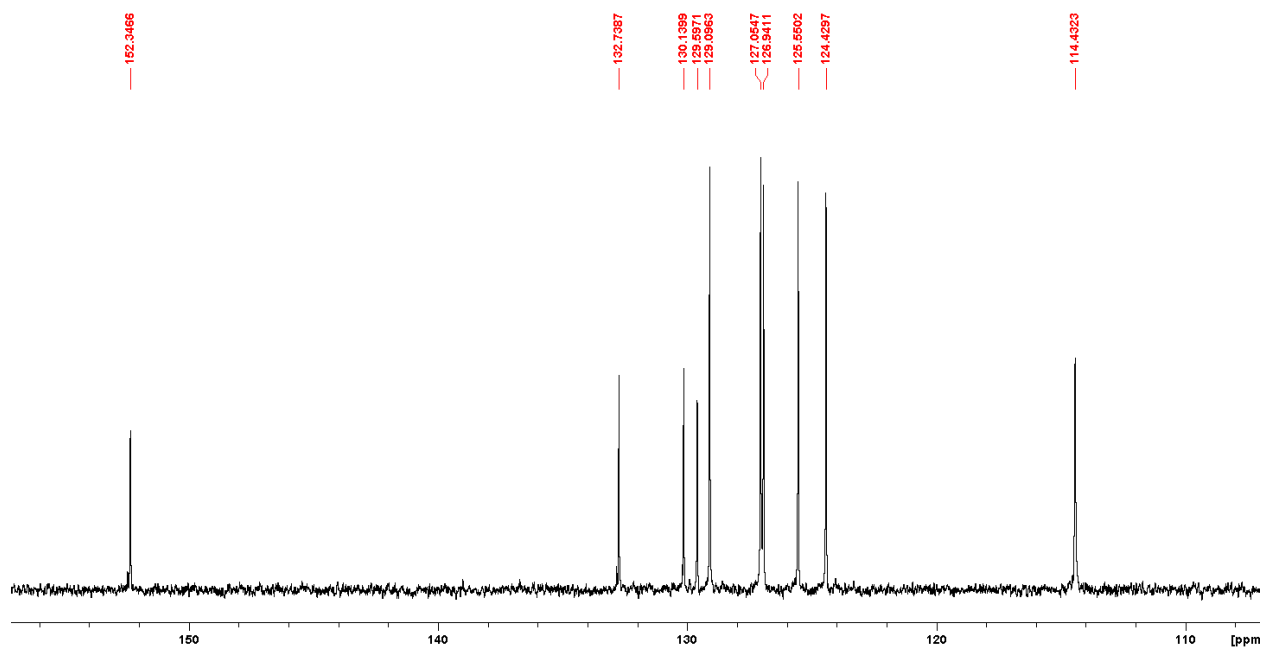
Figure S4.97: $^{13}C\{^1H\}$ NMR spectrum of **3f** in CDCl$_3$, focus on the aromatic region.

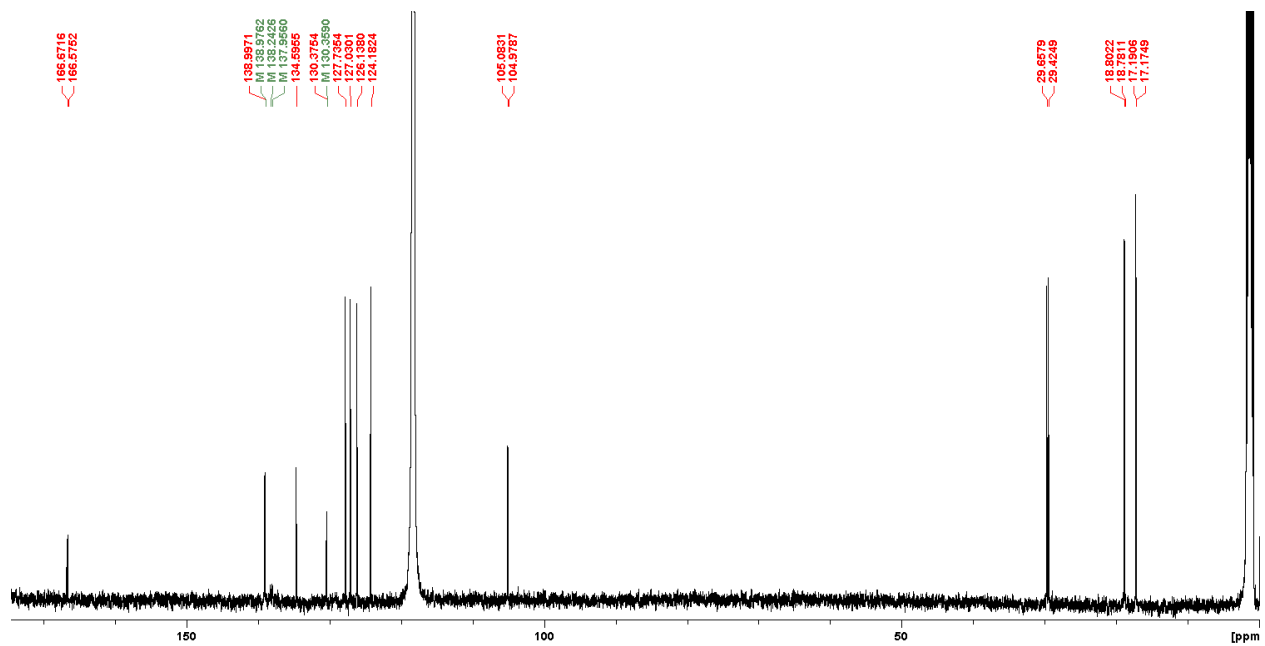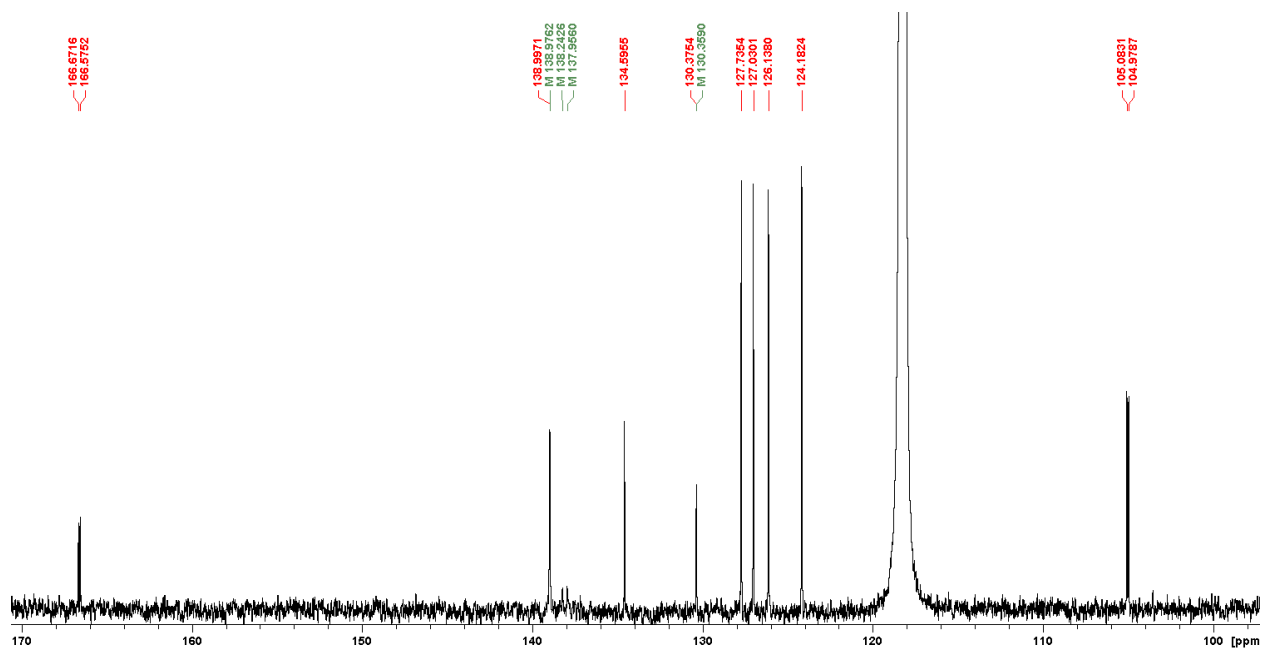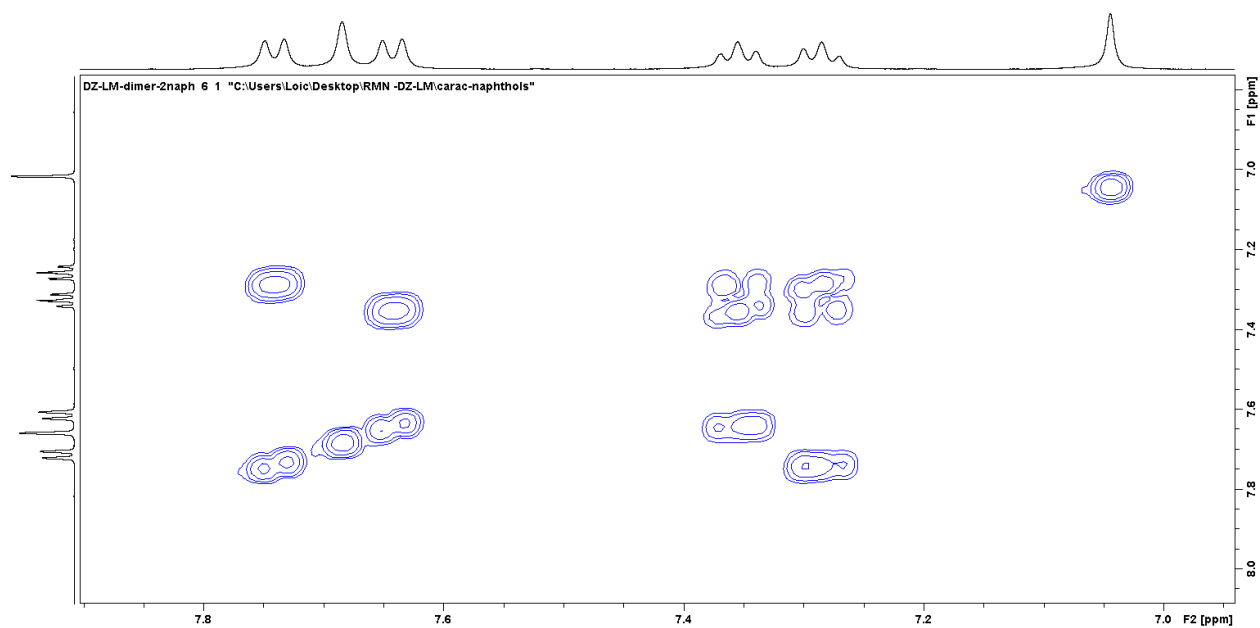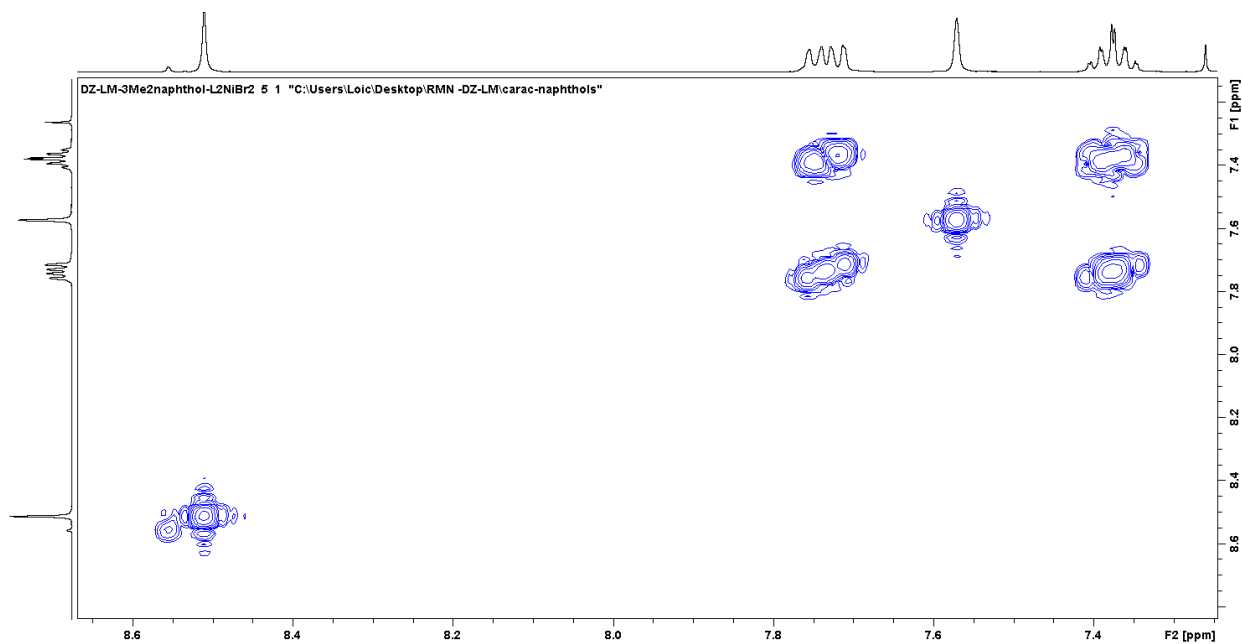Figure S4.98: COSY NMR spectrum of **3f** in CDCl₃, focus on the aromatic region.
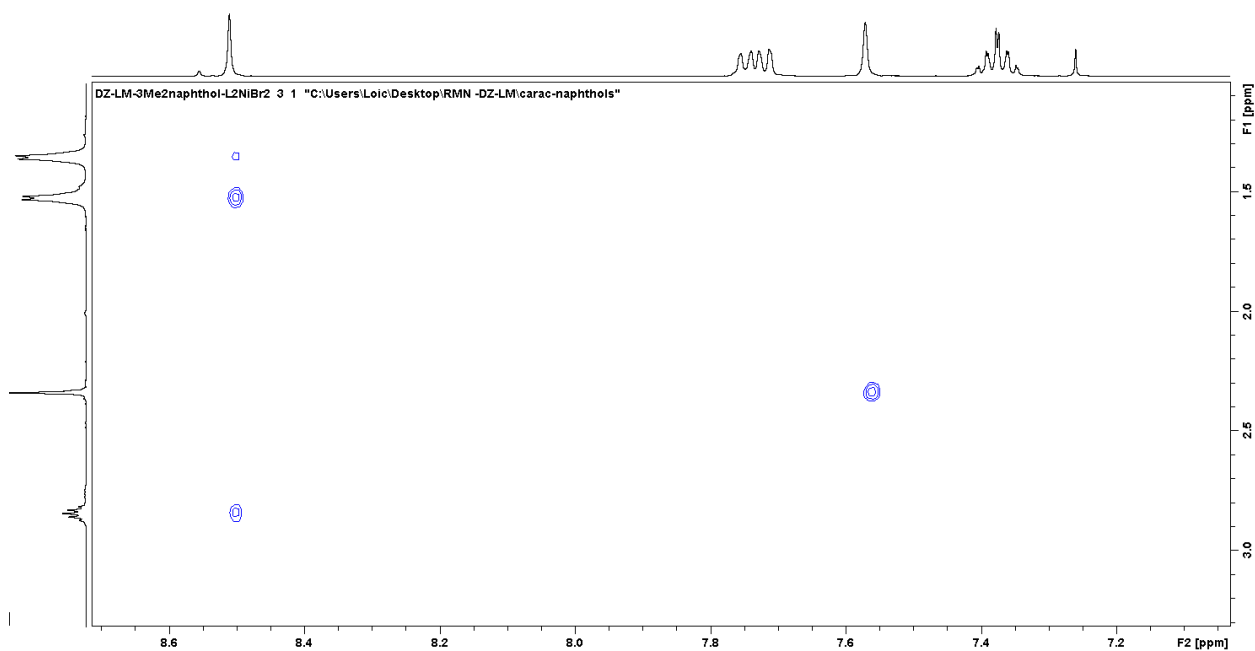
Figure S4.99: NOESY NMR spectrum of **3f** in CDCl₃, focus on the aliphatic/aromatic interactions.
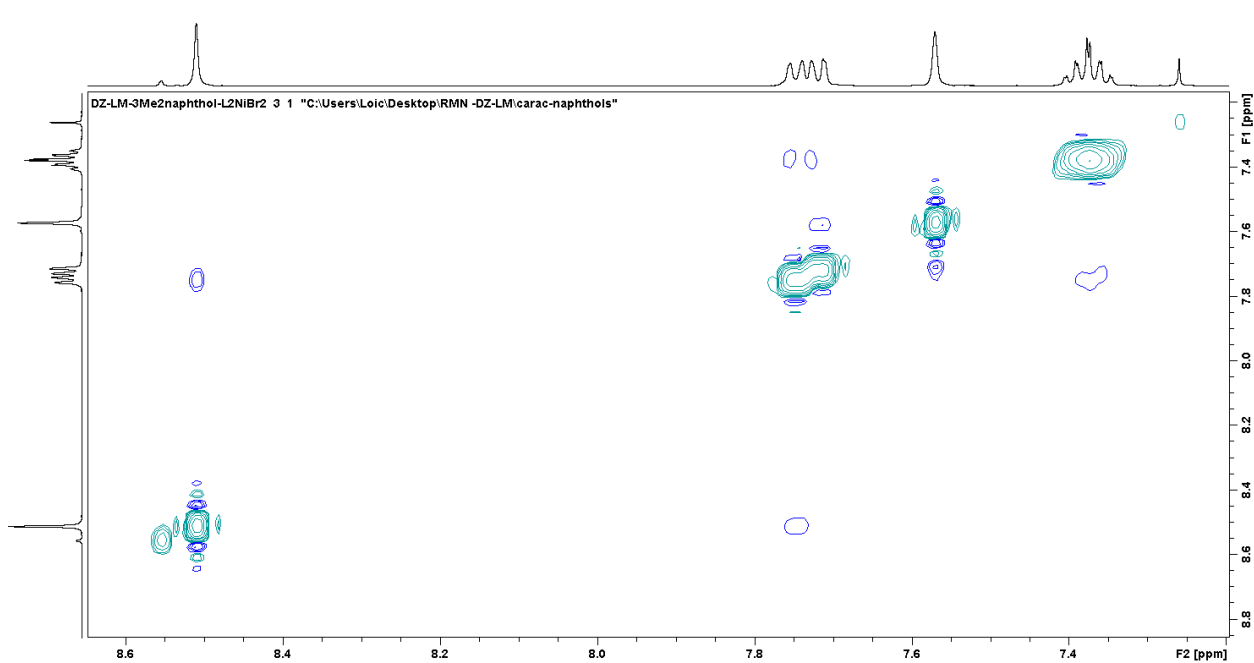
Figure S4.100: NOESY NMR spectrum of **3f** in CDCl₃, focus on the aromatic/aromatic interactions.
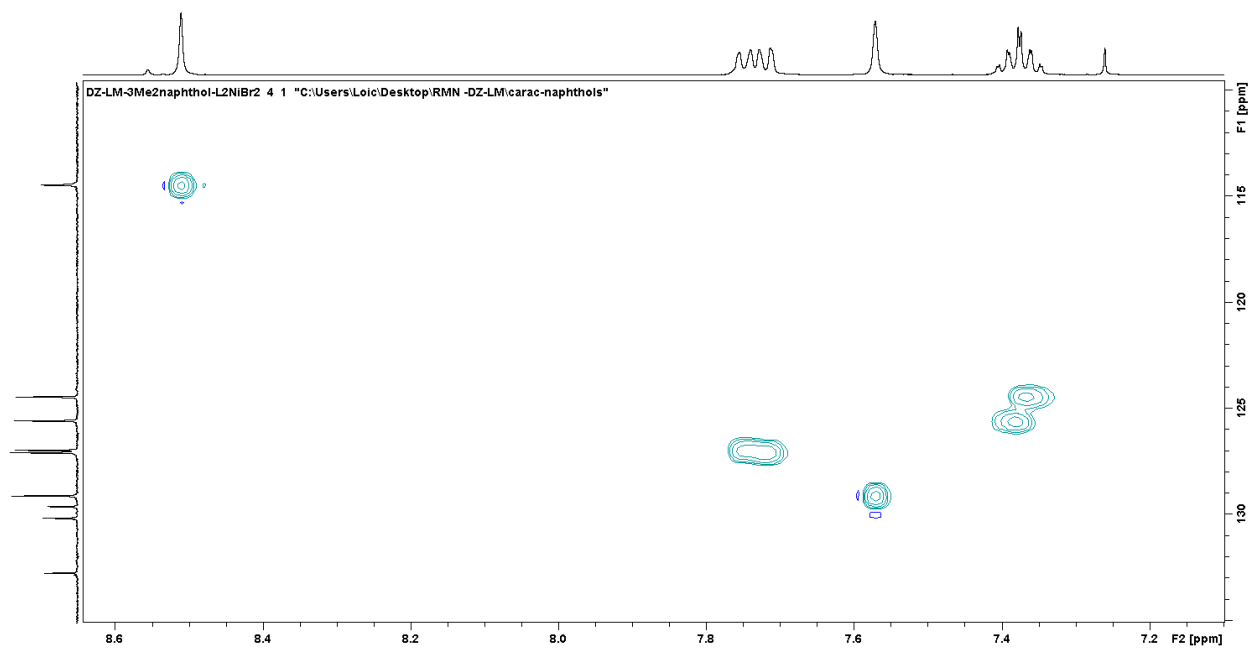
Figure S4.101: HSQC NMR spectrum of **3f** in CDCl₃, focus on the aromatic region.
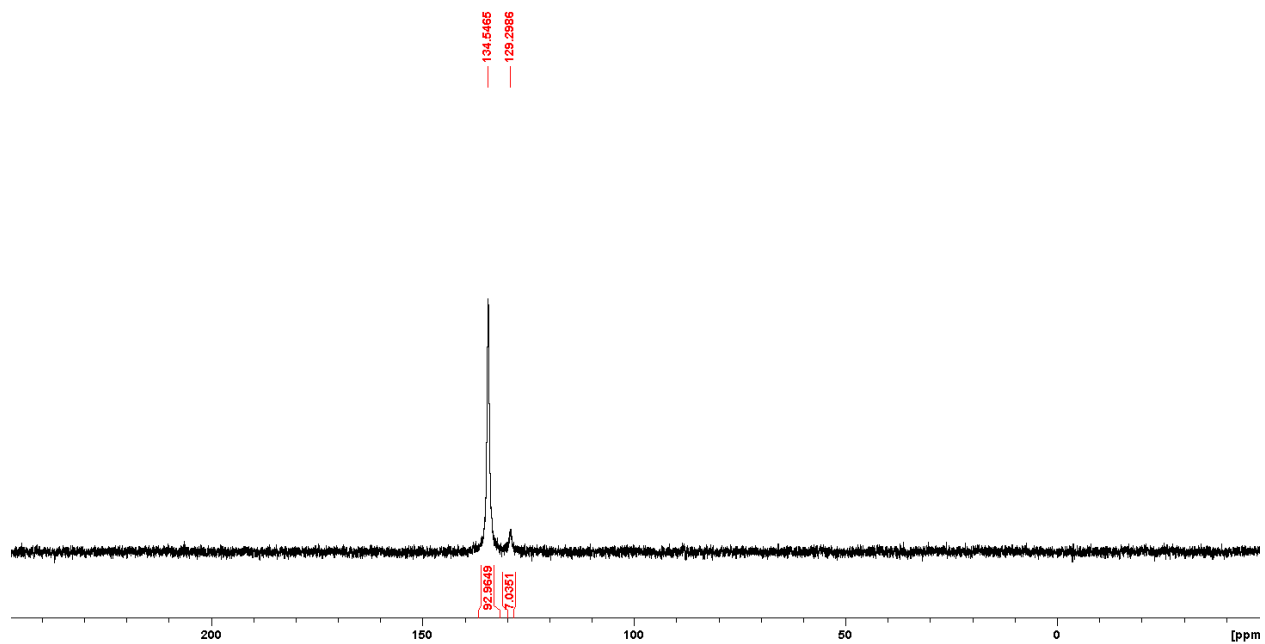
Figure S4.102: $^{31}P\{^1H\}$ NMR spectrum of **3f** in CDCl$_3$.
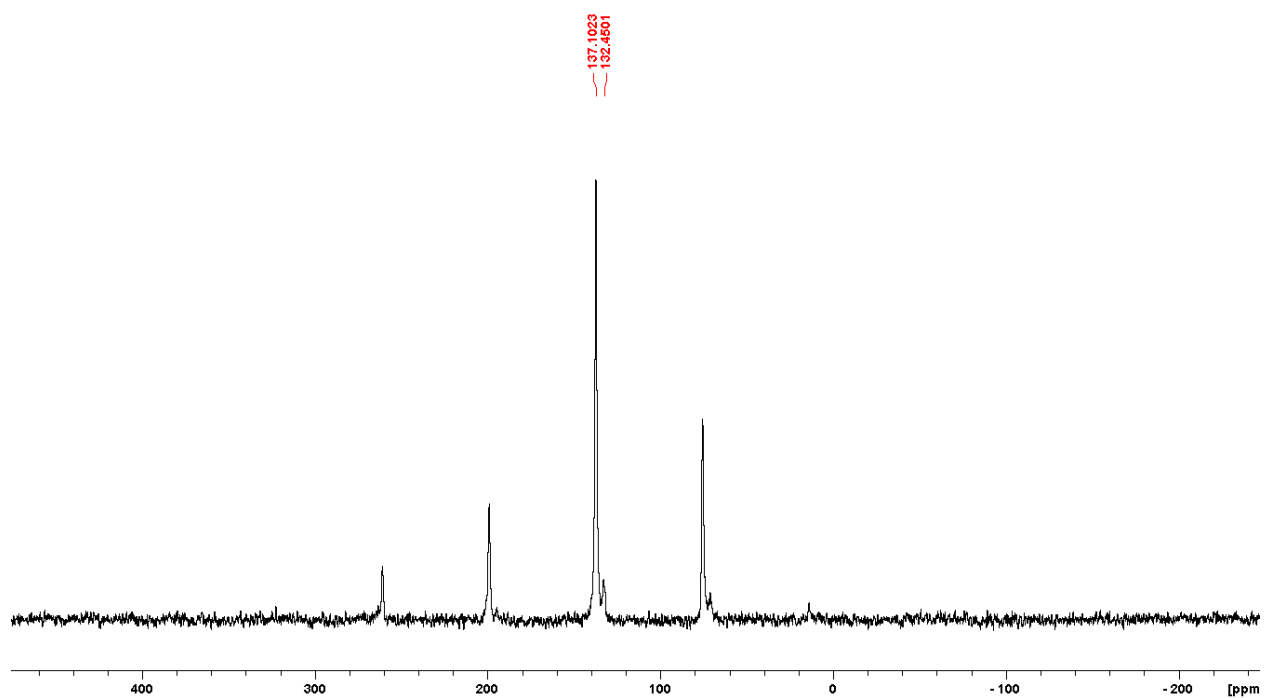
Figure S4.103: Solid-state ^{31}P NMR spectrum of compound **3f** showing two isomers at a spin rate of 10 kHz.

j. Compound **4**.
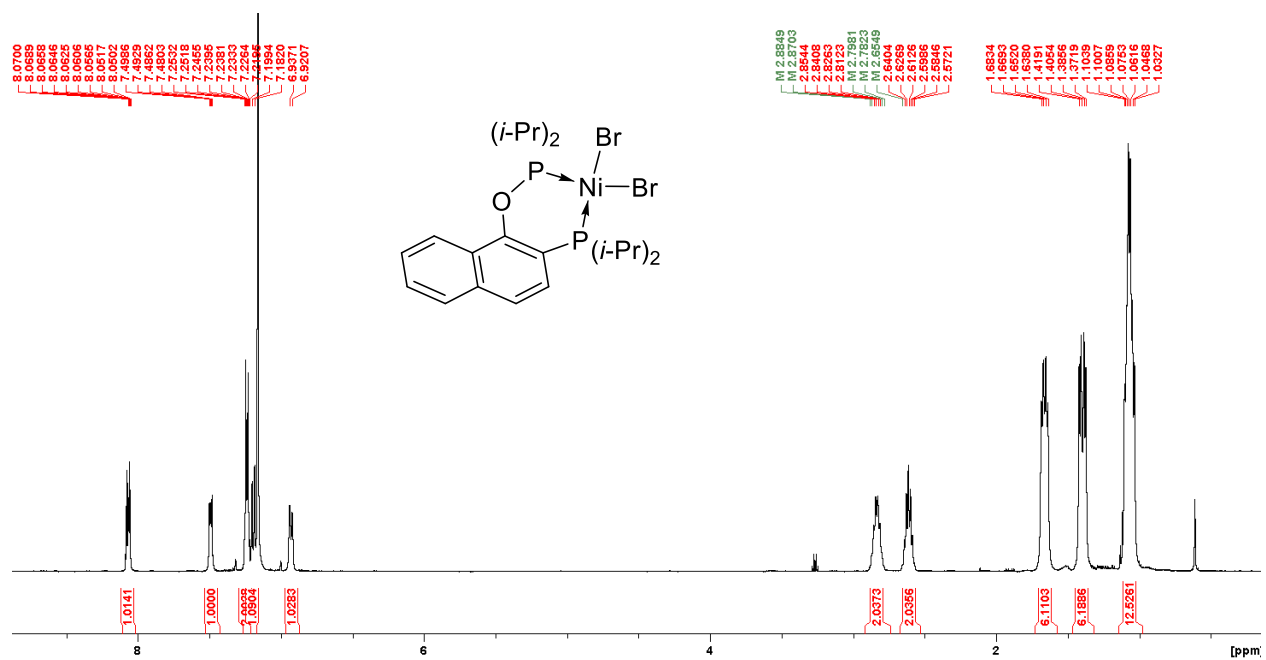
Figure S4.104: Full ^{1}H NMR of **4** in C$_6$D$_6$.
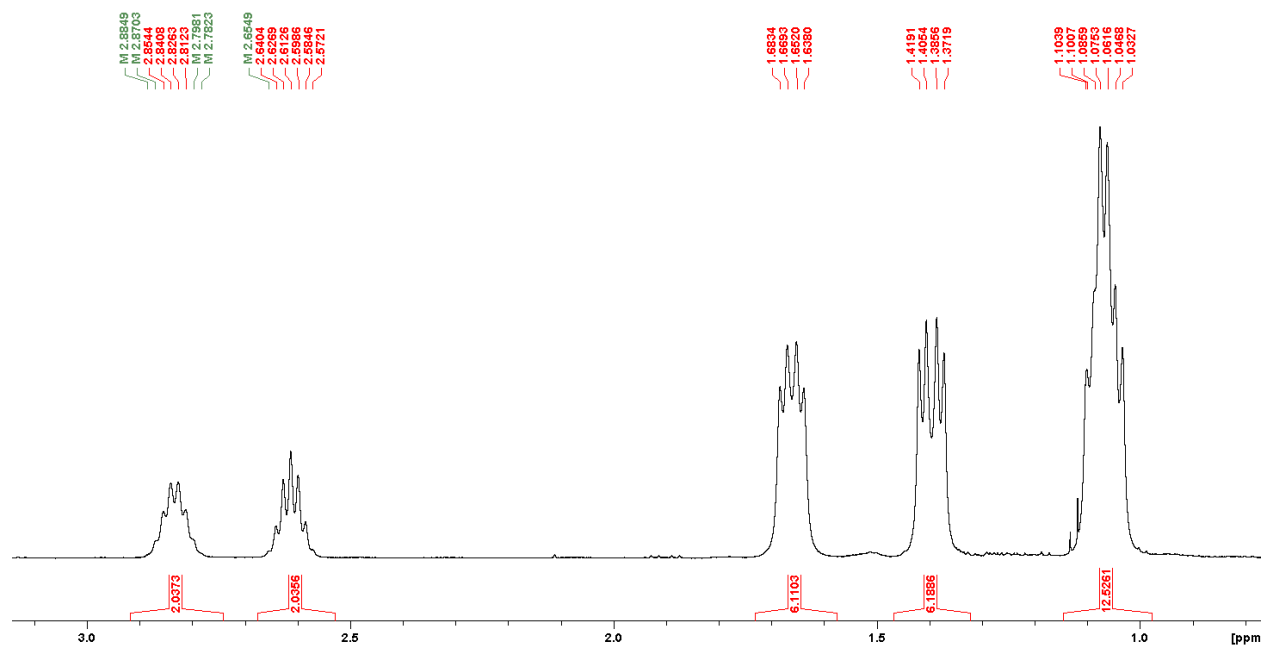
Figure S4.105: ^{1}H NMR of **4** in C$_6$D$_6$, focus on the aliphatic region.
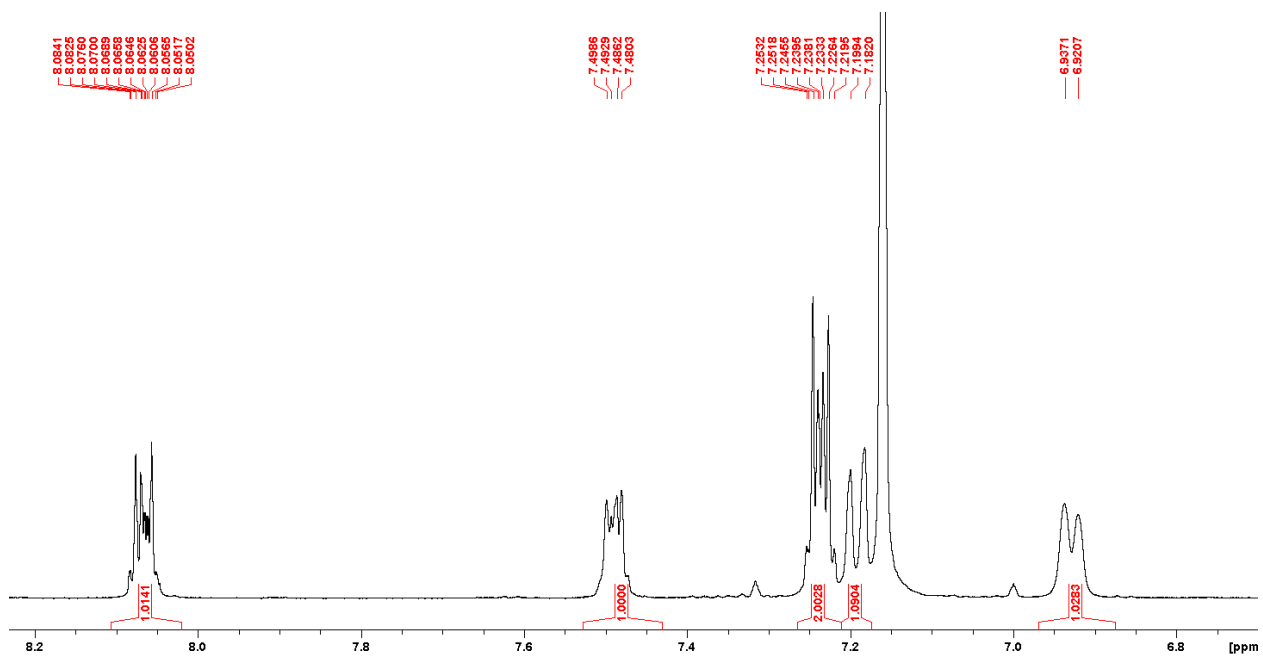
Figure S4.106: ^{1}H NMR of **4** in C_6D_6, focus on the aromatic region.
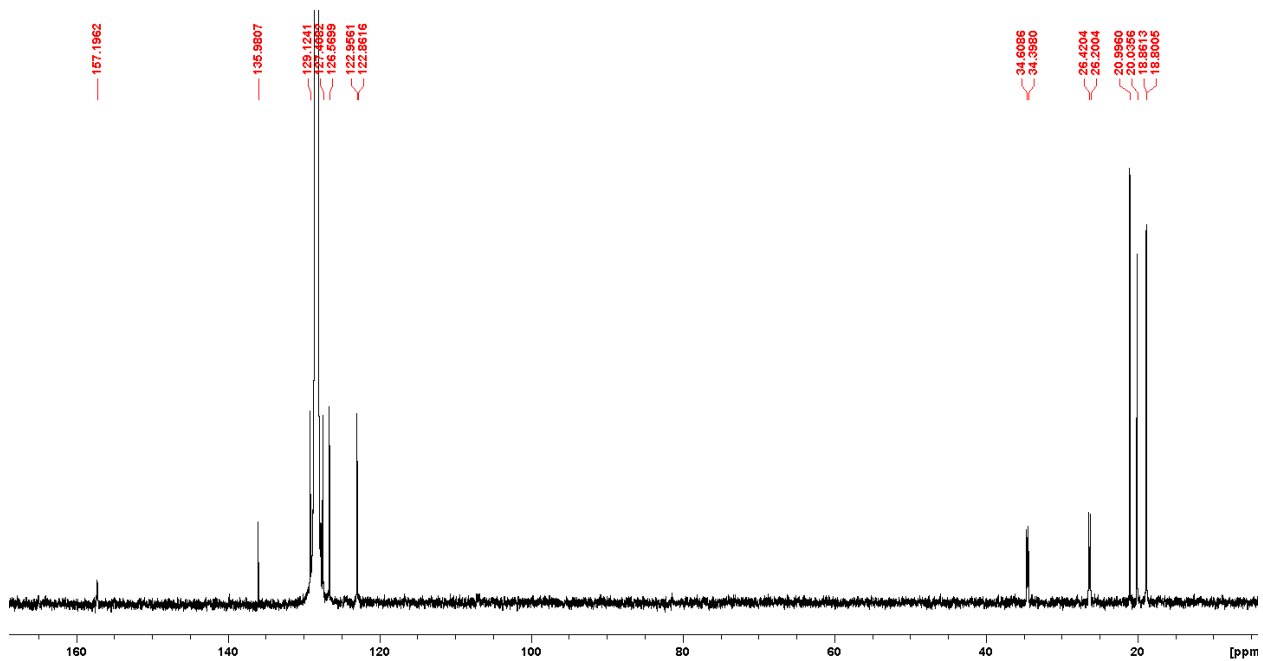
Figure S4.107: $^{13}C\{^1H\}$ NMR of **4** in C_6D_6, focus on the aliphatic region.
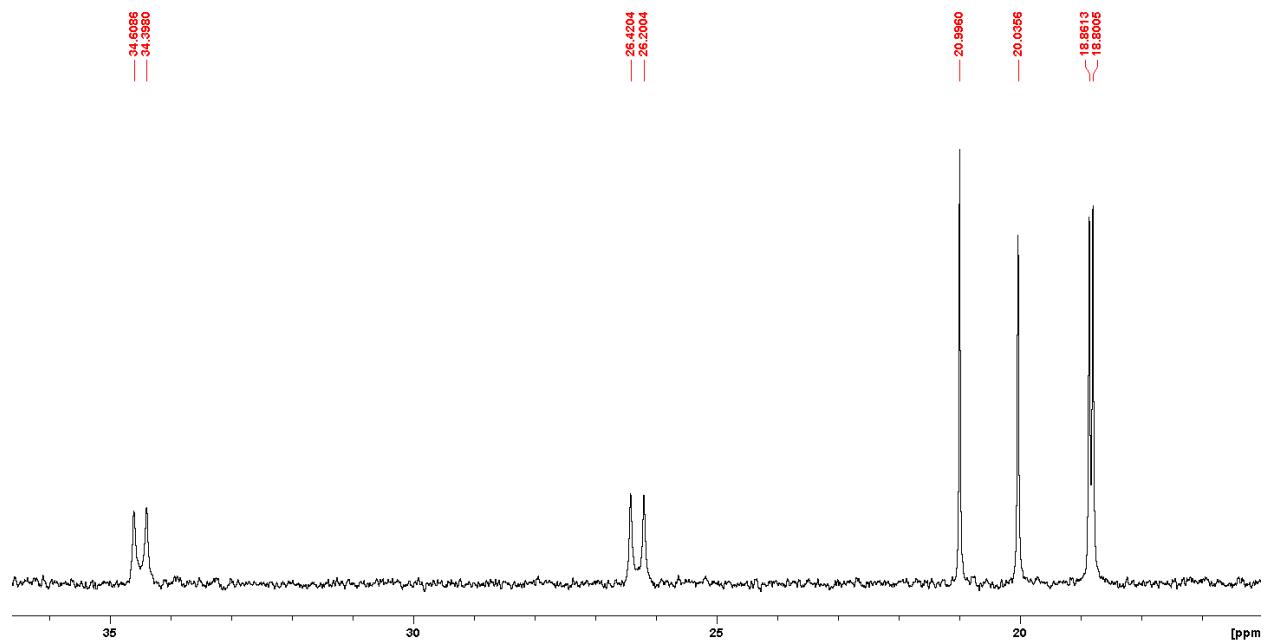
Figure S4.108: $^{13}C\{^1H\}$ NMR of **4** in C_6D_6, focus on the aliphatic region.
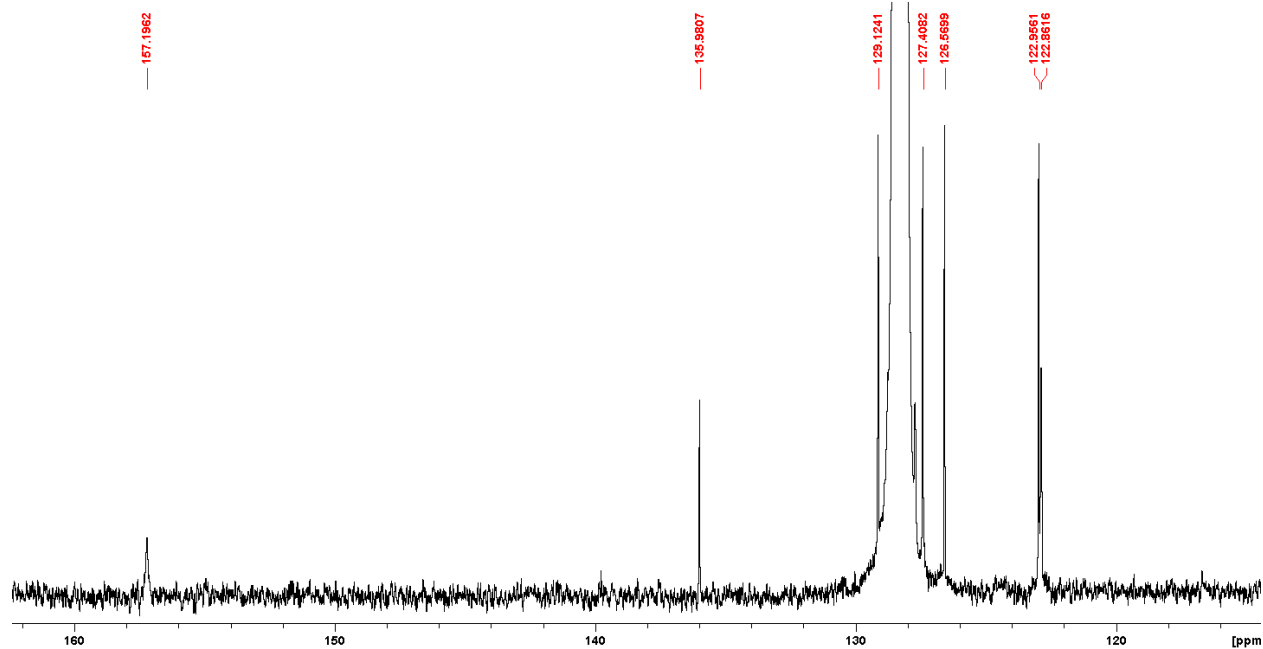
Figure S4.109: $^{13}C\{^1H\}$ NMR of **4** in C_6D_6, focus on the aromatic region.
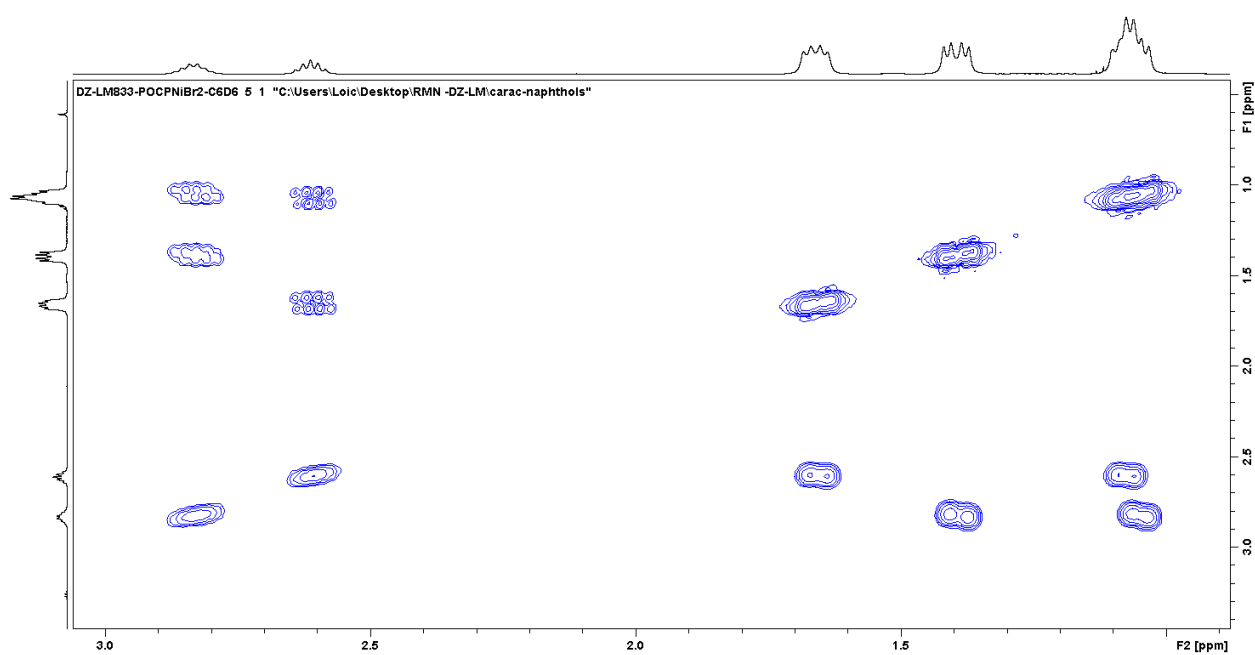
Figure S4.110: COSY NMR of **4** in C$_6$D$_6$, focus on the aliphatic region.
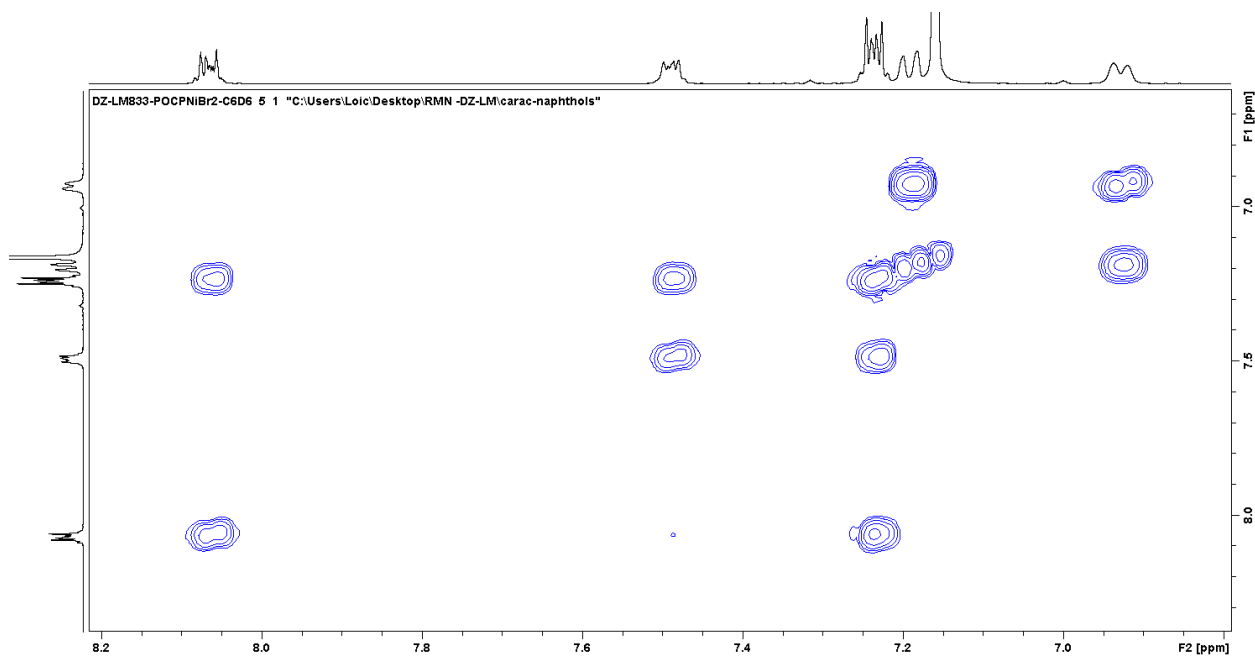
Figure S4.111: COSY NMR of **4** in C$_6$D$_6$, focus on the aromatic region.
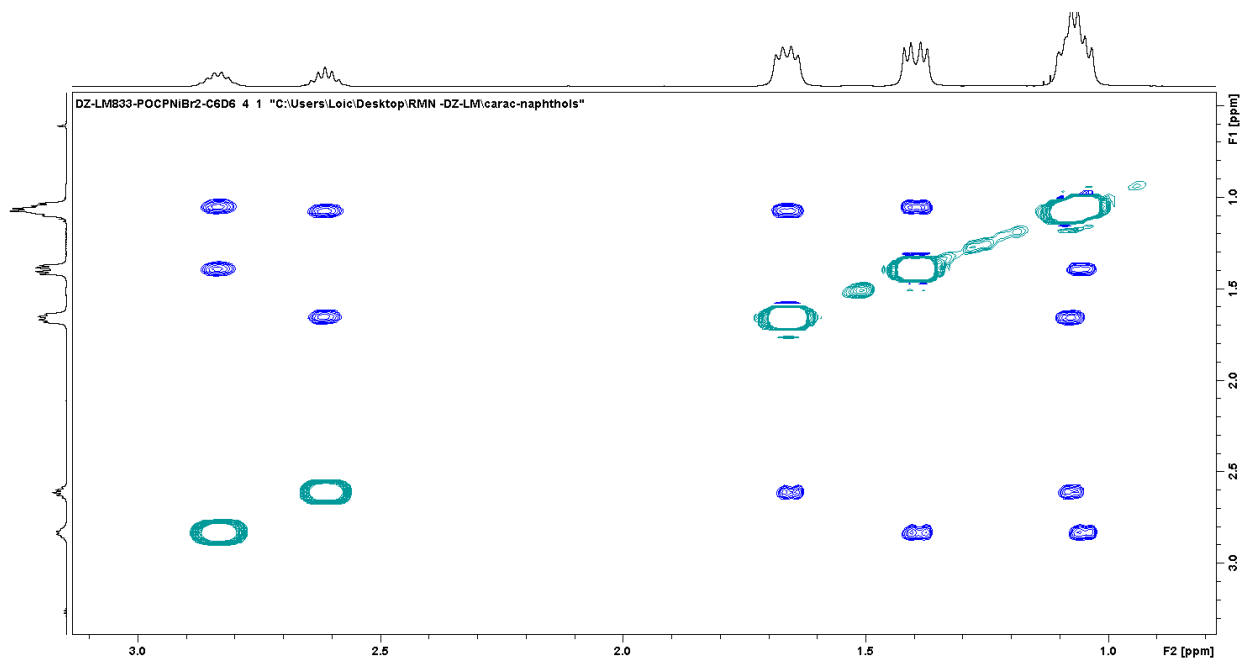
Figure S4.112: NOESY NMR of **4** in C_6D_6, focus on the aliphatic/aliphatic interactions.
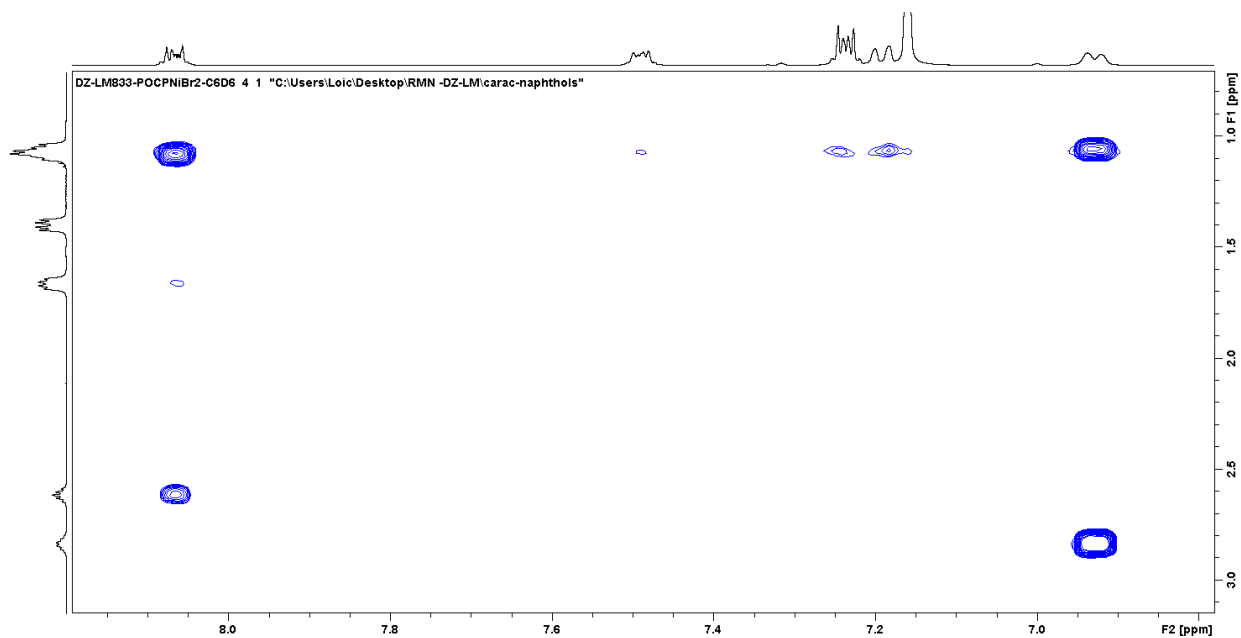
Figure S4.113: NOESY NMR of **4** in C_6D_6, focus on the aliphatic/aromatic interactions.
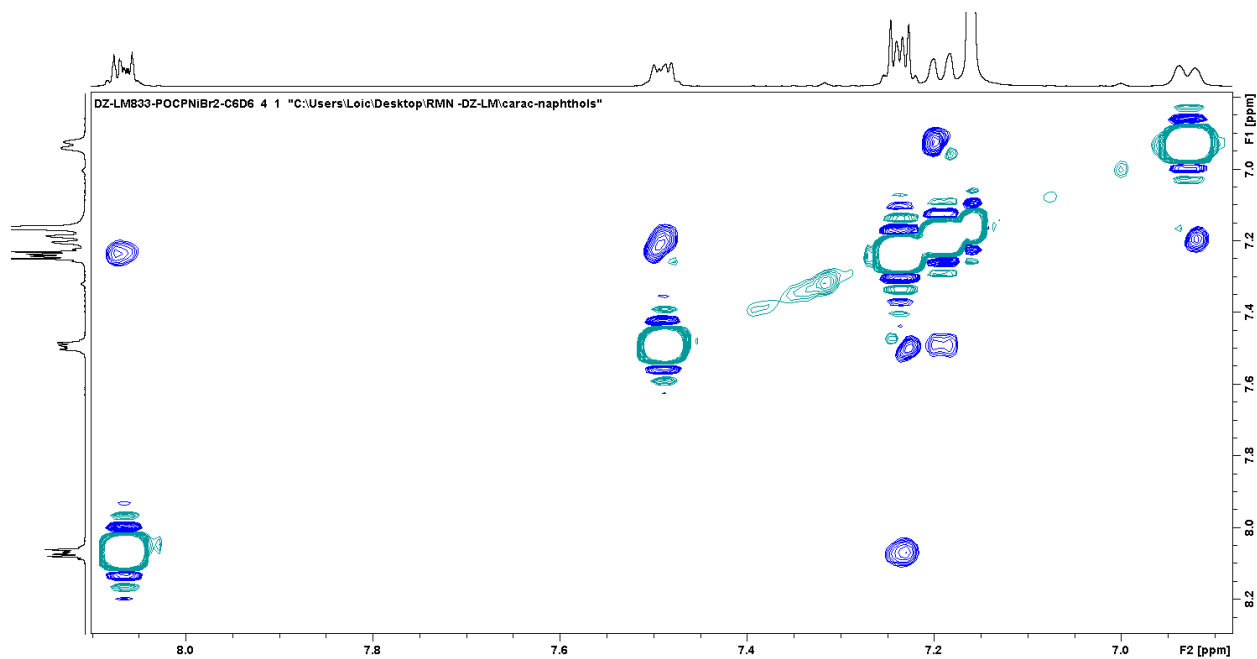
Figure S4.114: NOESY NMR of **4** in C$_6$D$_6$, focus on the aromatic/aromatic interactions.
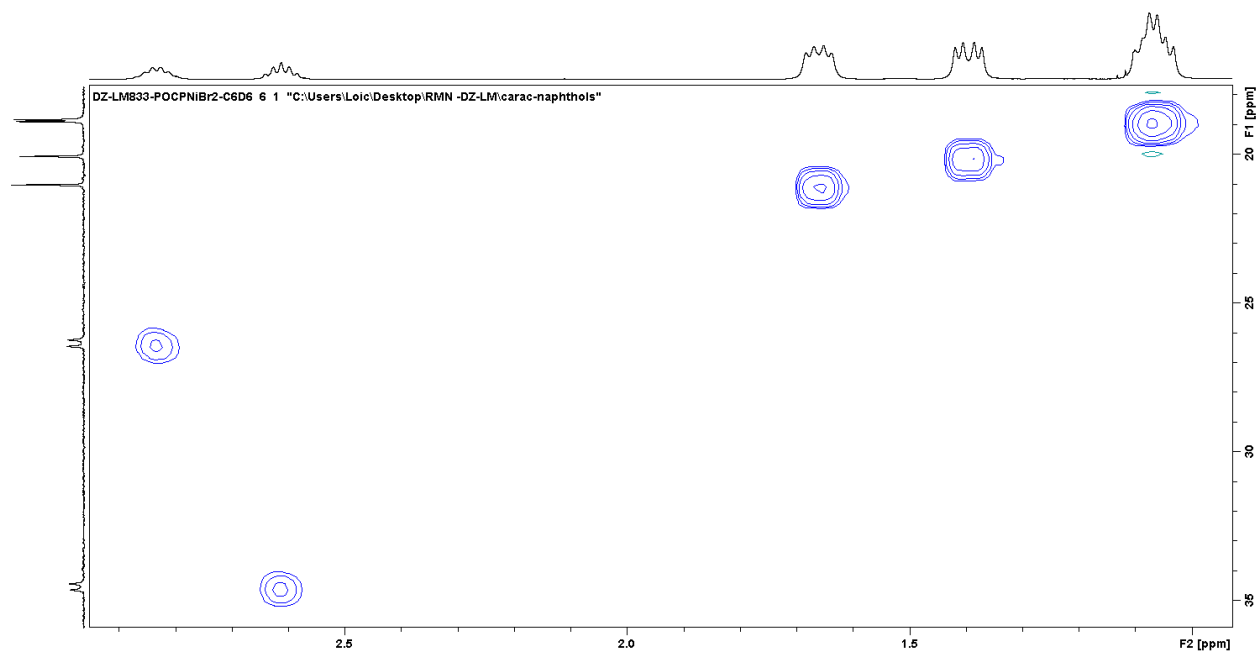
Figure S4.115: HSQC NMR of **4** in C$_6$D$_6$, focus on the aliphatic region.
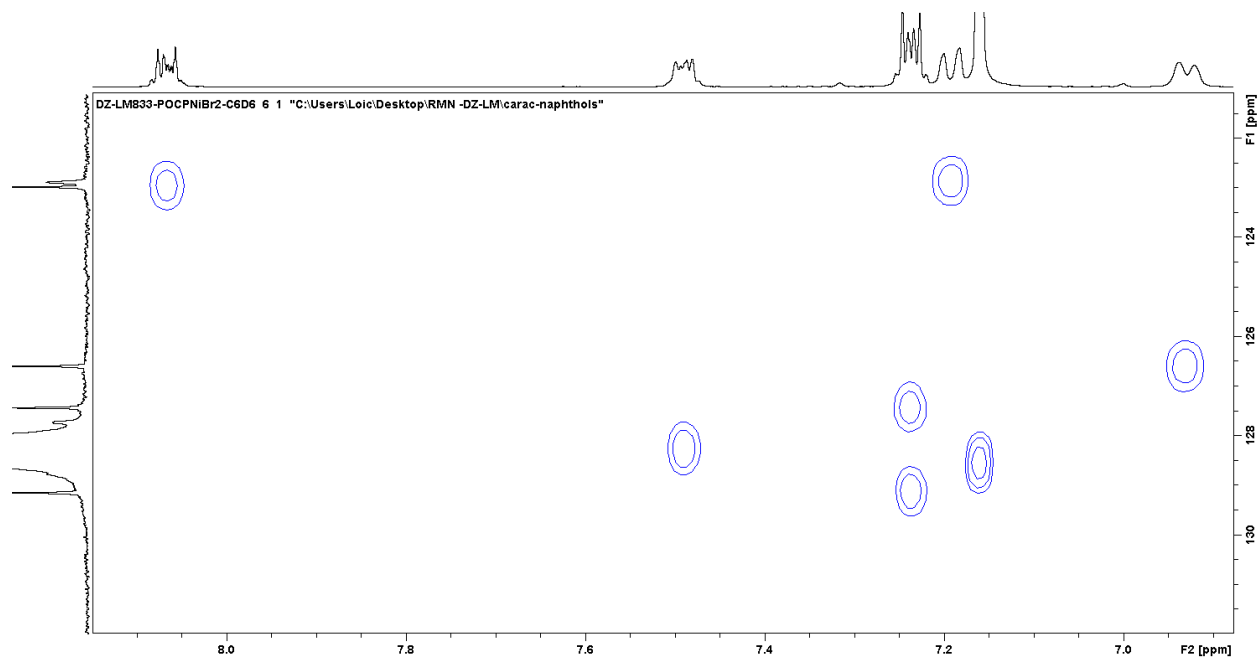
Figure S4.116: HSQC NMR of **4** in C$_6$D$_6$, focus on the aromatic region.
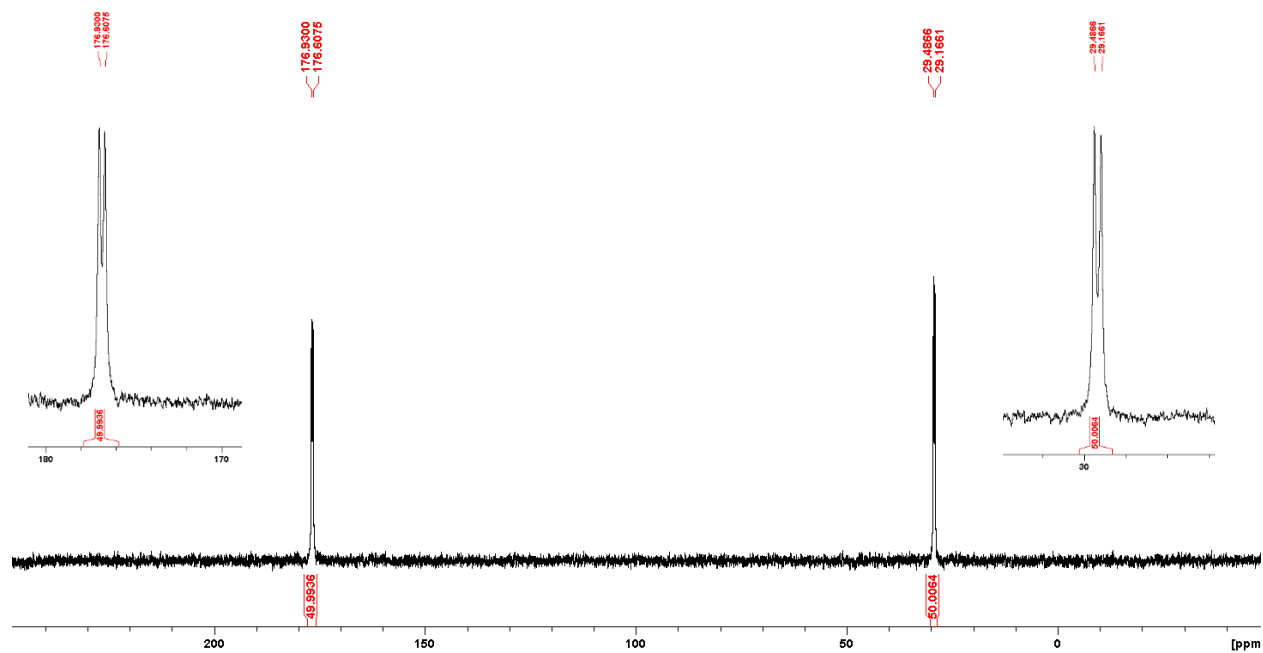
Figure S4.117: ^{31}P{^{1}H} NMR of **4** in C$_6$D$_6$.

k.   **(*i*-Pr₂PH)₂NiBr₂**
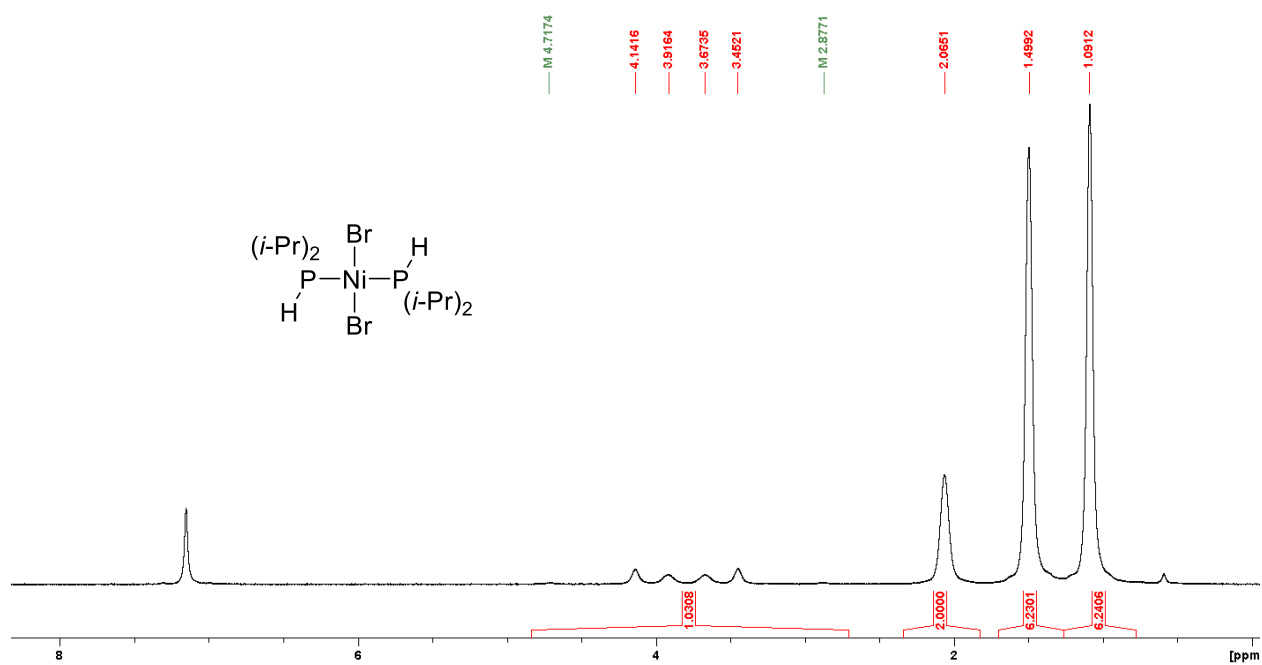
Figure S4.118: Full ^{1}H NMR spectrum of (*i*-Pr₂PH)₂NiBr₂ in C₆D₆.
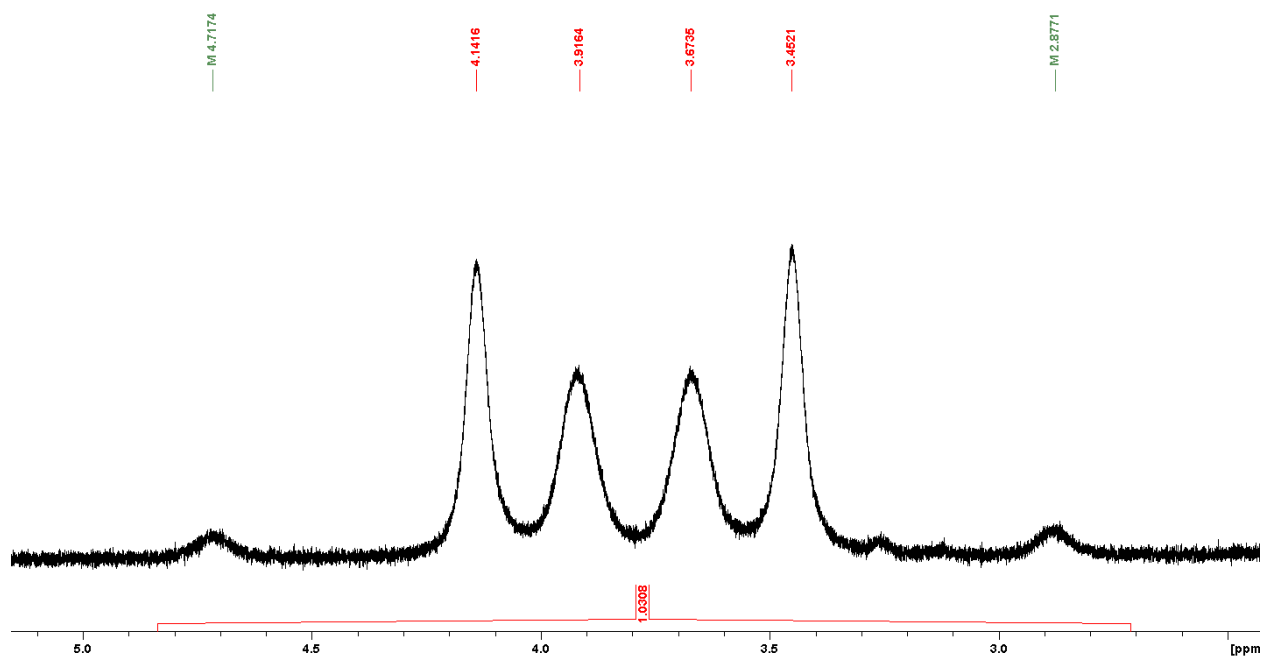
Figure S4.119: ^{1}H NMR spectrum of (*i*-Pr₂PH)₂NiBr₂ in C₆D₆, focus on the P*H* signals.
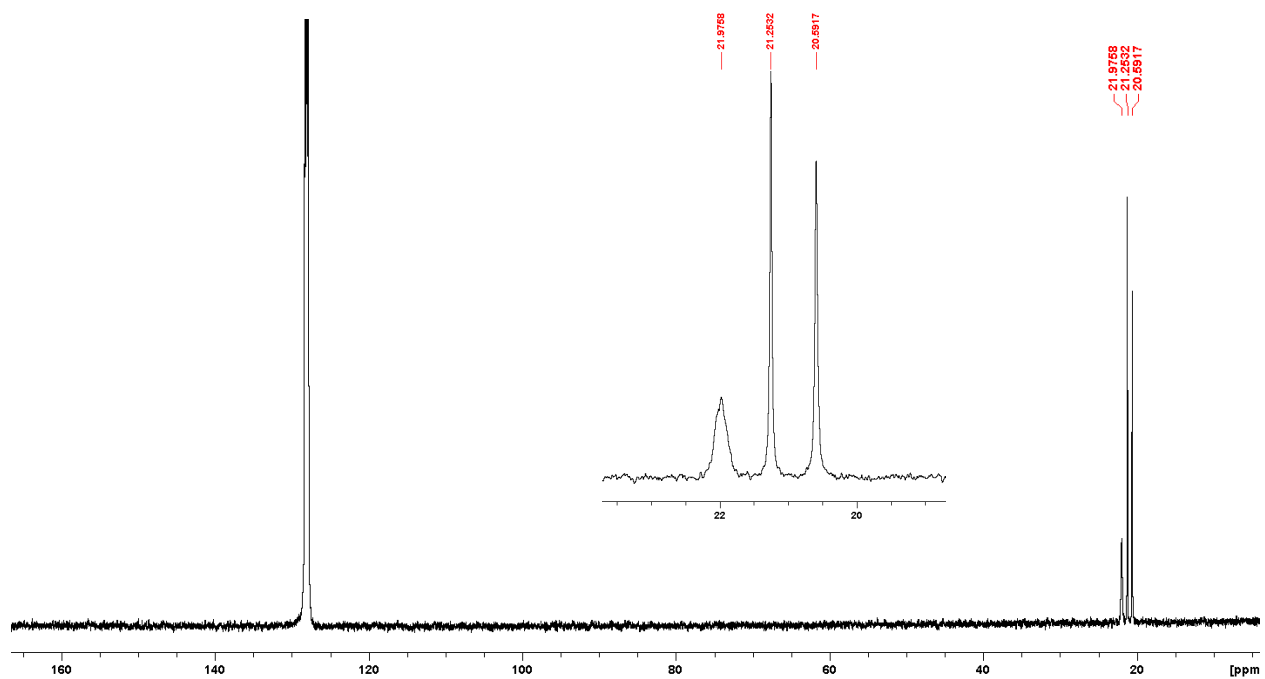
Figure S4.120: $^{13}C\{^1H\}$ NMR spectrum of (i-Pr$_2$PH)$_2$NiBr$_2$ in C$_6$D$_6$ and focus on the i-Pr signals.
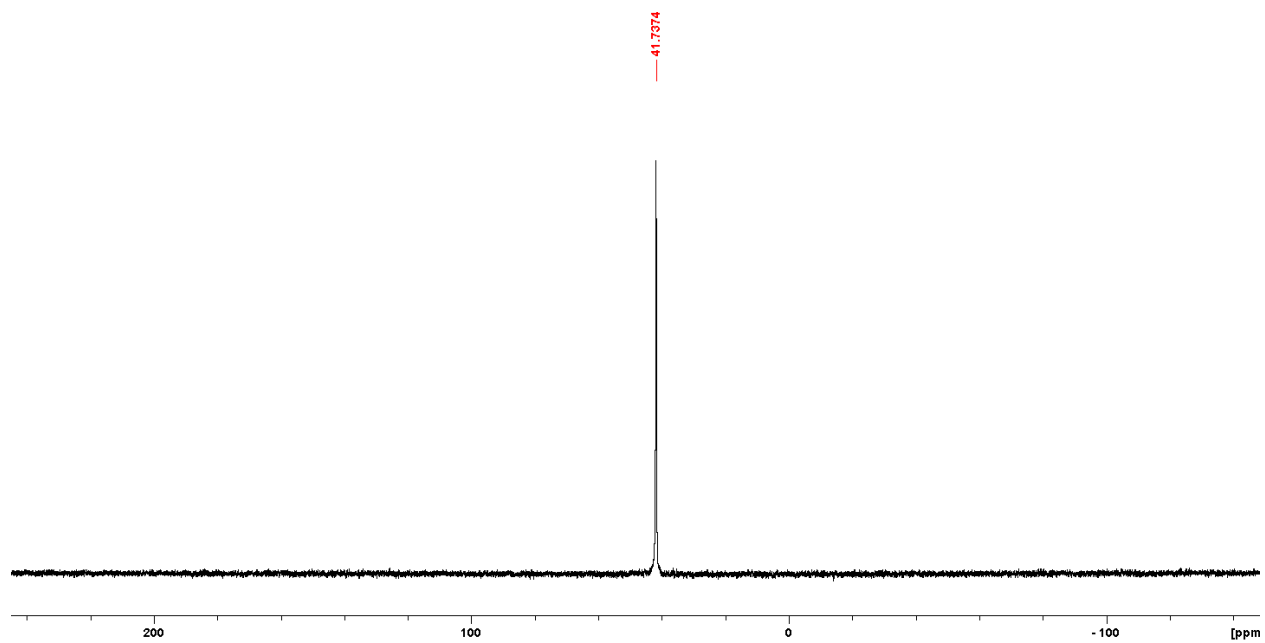
Figure S4.121: $^{31}P\{^1H\}$ NMR spectrum of (i-Pr$_2$PH)$_2$NiBr$_2$ in C$_6$D$_6$.
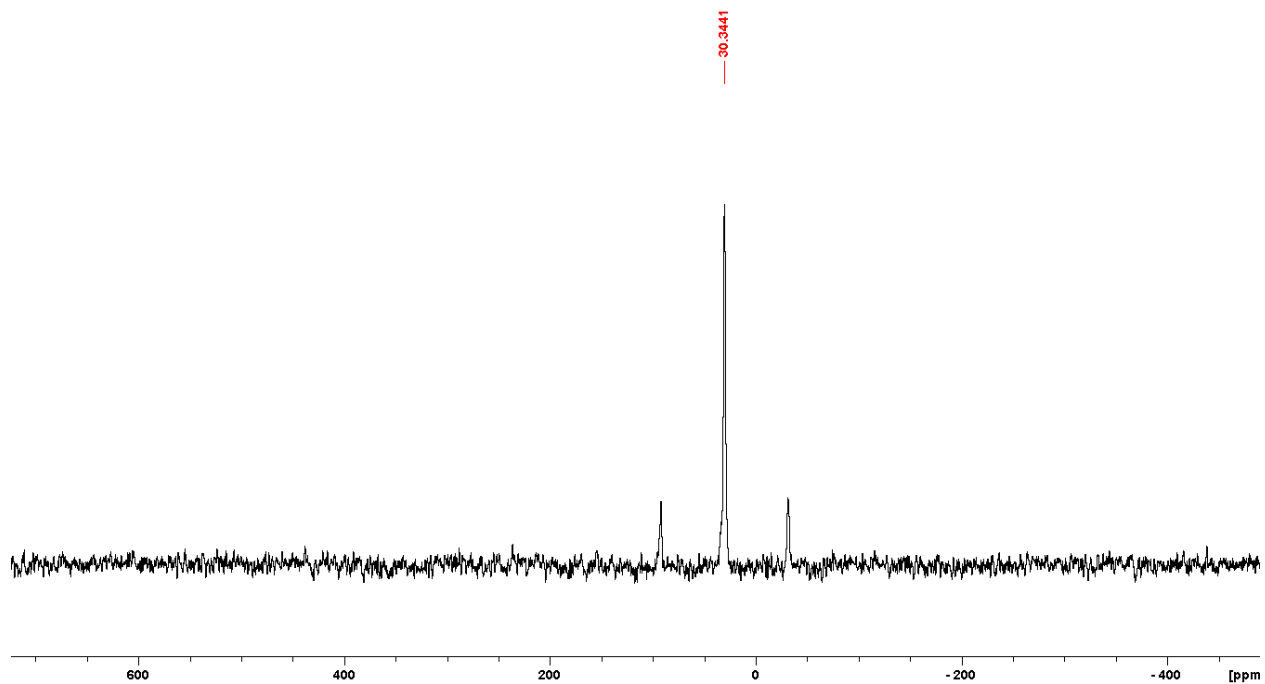
Figure S4.122: Solid-state ^{31}P NMR spectrum of $(i\text{-}Pr_2PH)_2NiBr_2$ at a spin rate of 10 kHz.

S4.4 Other relevant NMR spectra

a. Reaction mixtures at high temperatures
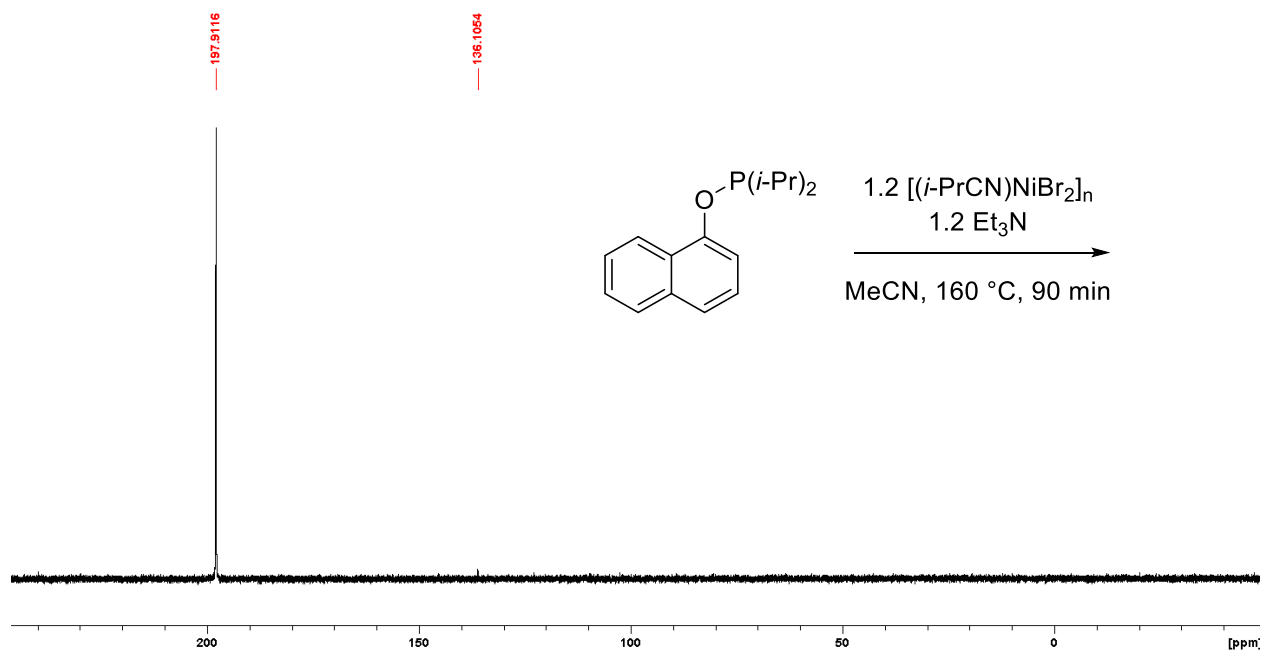
Figure S4.123: Crude reaction mixture for the nickelation of **1a** at 160 °C for 90 min with 1.2 equiv $[(i\text{-}PrCN)NiBr_2]_n$ and Et_3N.
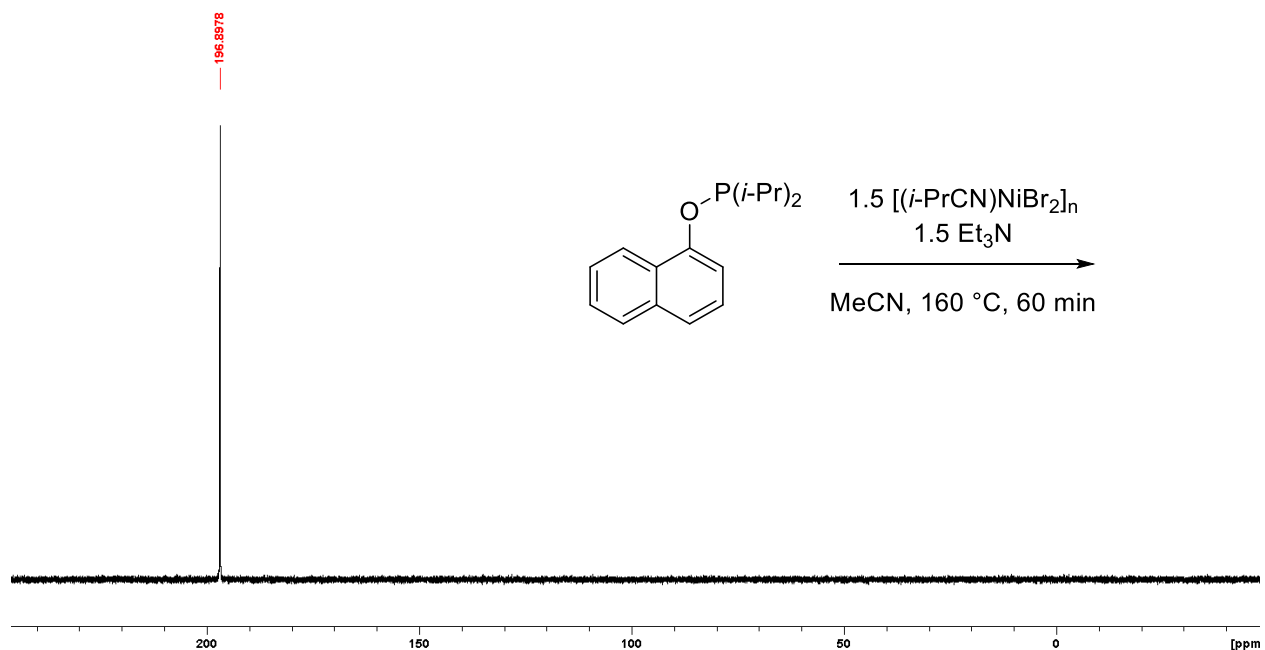
Figure S4.124: Crude reaction mixture for the nickelation of **1a** at 160 °C for 60 min with 1.5 equiv [(*i*-PrCN)NiBr$_2$]$_n$ and Et$_3$N.
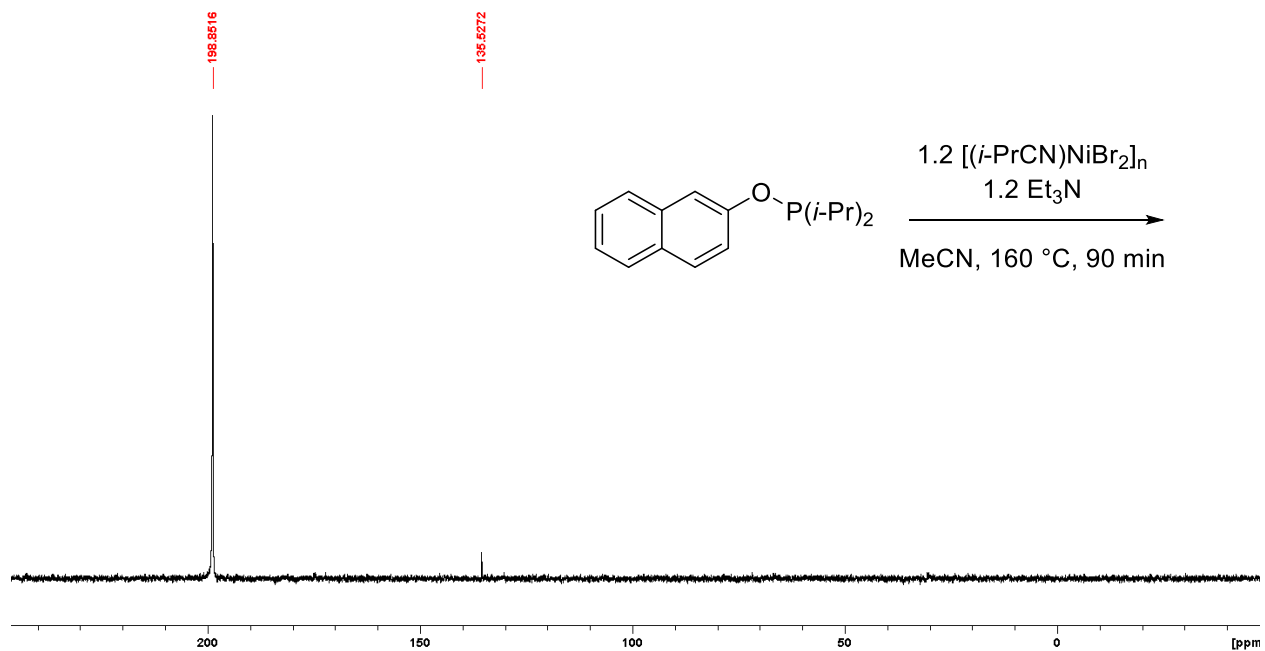
Figure S4.125: Crude reaction mixture for the nickelation of **1e** at 160 °C for 90 min with 1.2 equiv [(*i*-PrCN)NiBr$_2$]$_n$ and Et$_3$N.
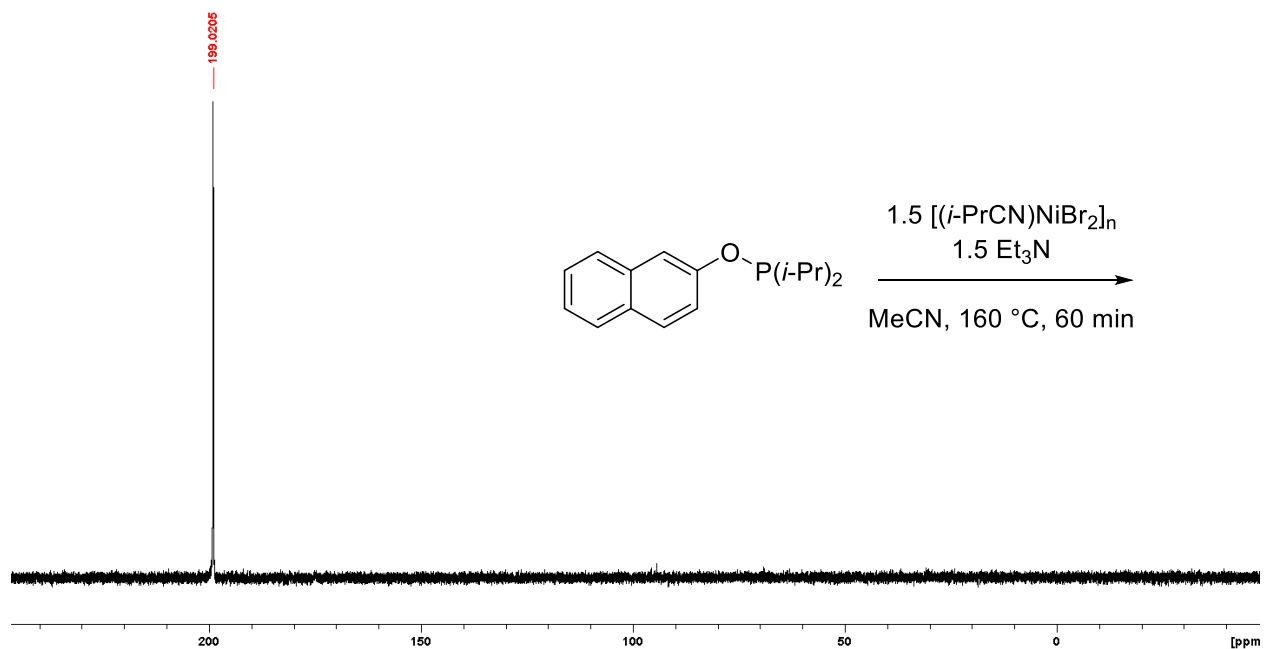
Figure S4.126: Crude reaction mixture for the nickelation of **1e** at 160 °C for 90 min with 1.5 equiv [(*i*-PrCN)NiBr$_2$]$_n$ and Et$_3$N.
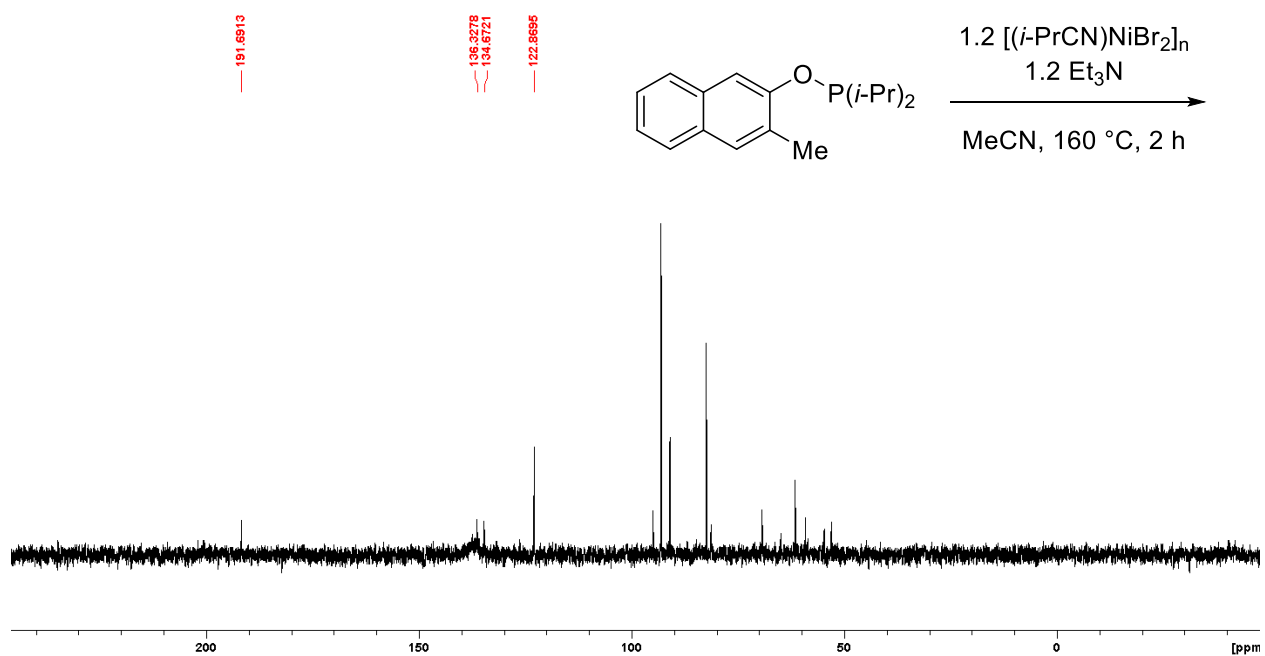
Figure S4.127: Crude reaction mixture for the nickelation of **1f** at 160 °C for 2 h with 1.2 equiv [(*i*-PrCN)NiBr$_2$]$_n$ and Et$_3$N.
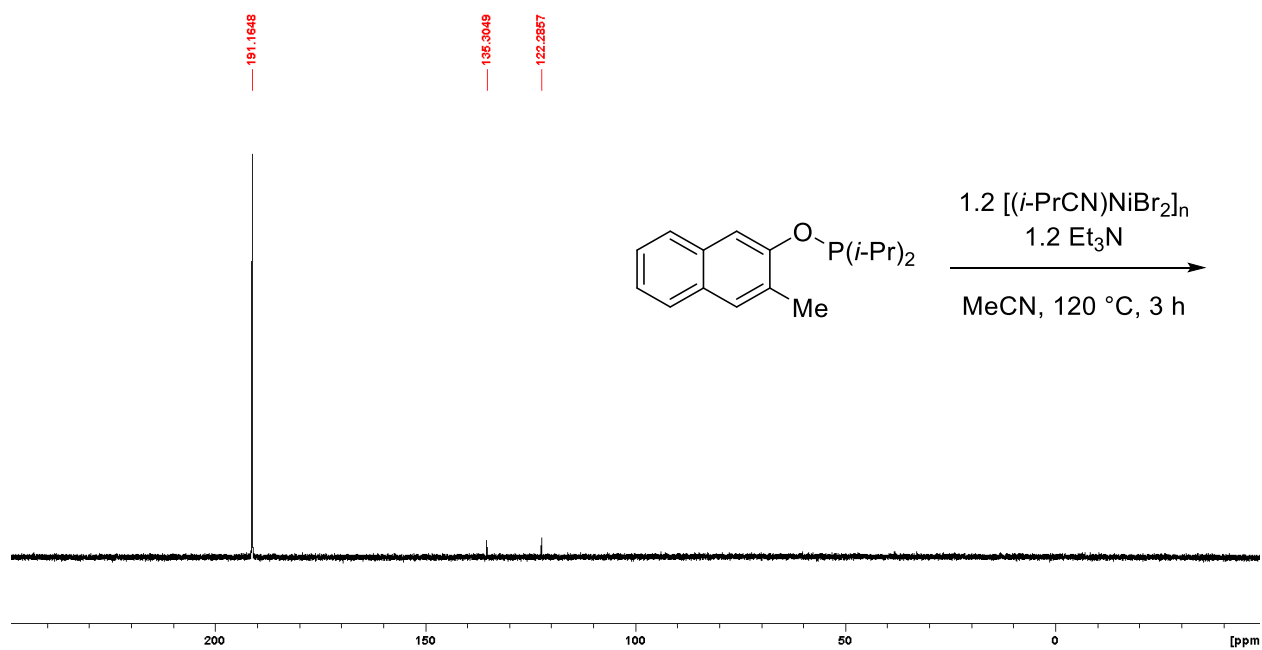
Figure S4.128: Crude reaction mixture for the nickelation of **1f** at 120 °C for 3 h with 1.2 equiv [(*i*-PrCN)NiBr$_2$]$_n$ and Et$_3$N.
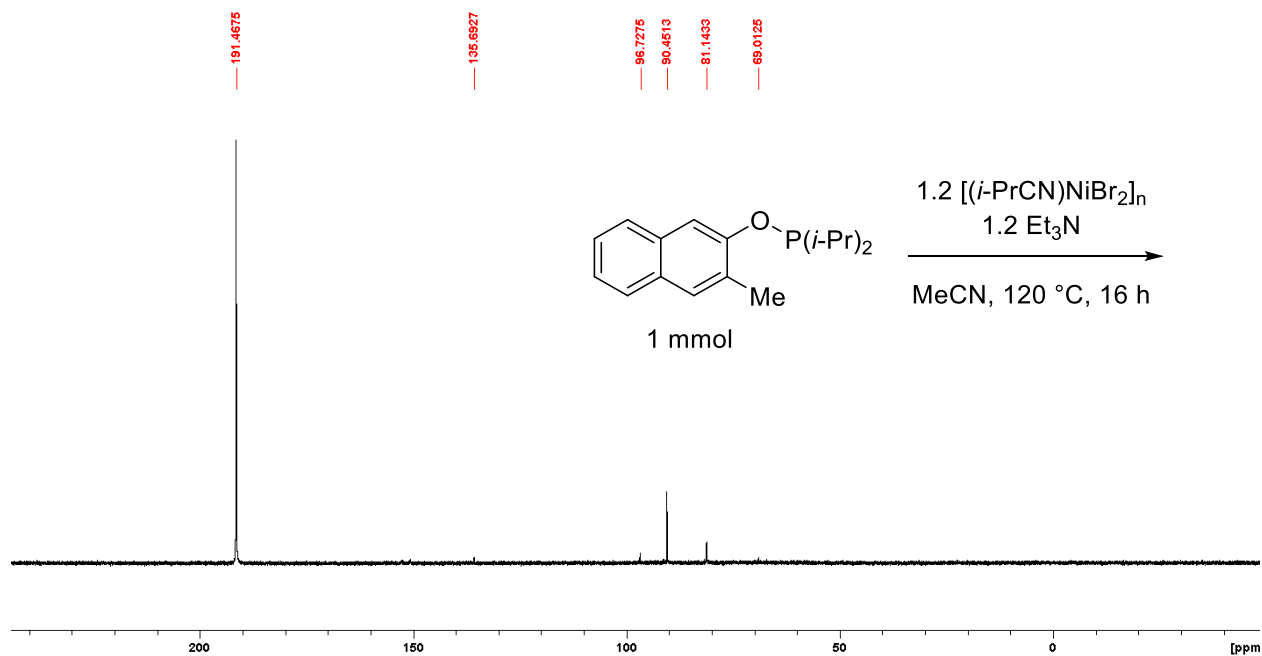
Figure S4.129: Crude reaction mixture for the nickelation of **1f** at 120 °C for 16 h with 1.2 equiv [(*i*-PrCN)NiBr$_2$]$_n$ and Et$_3$N.
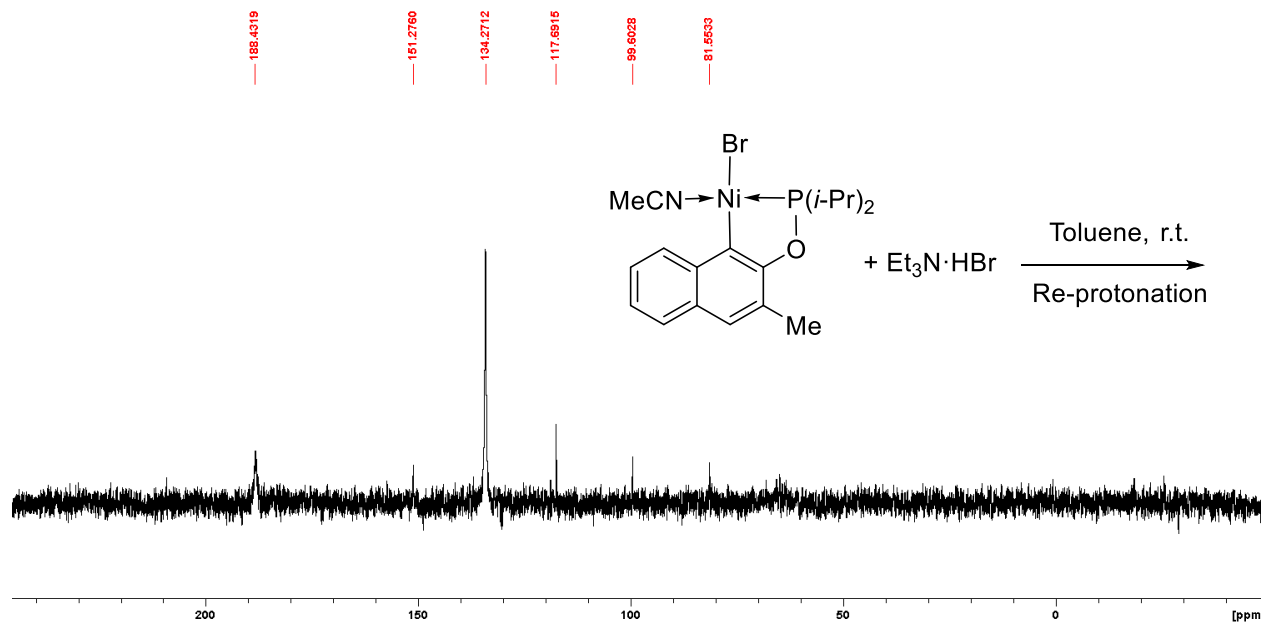
Figure S4.130: Toluene extracts after the nickelation of **1f** at 120 °C for 16 h with 1.2 equiv [(*i*-PrCN)NiBr₂]ₙ and Et₃N.
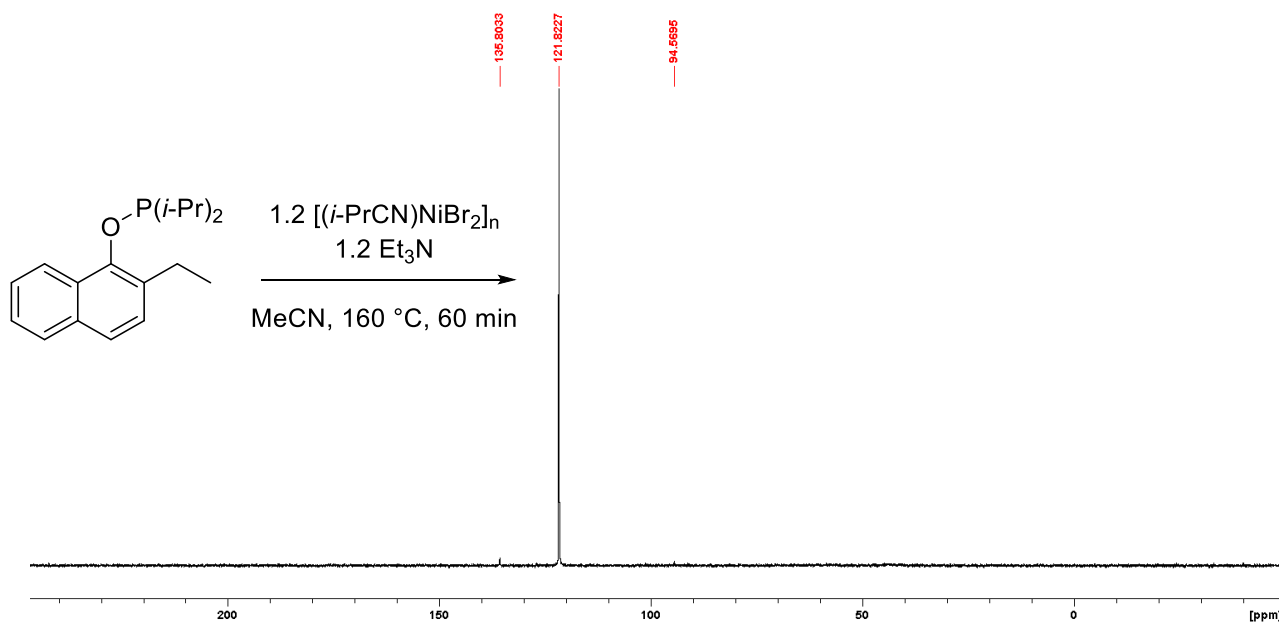
Figure S4.131: Crude reaction mixture for the nickelation of **1d** at 160 °C for 60 min with 1.2 equiv [(*i*-PrCN)NiBr₂]ₙ and Et₃N.
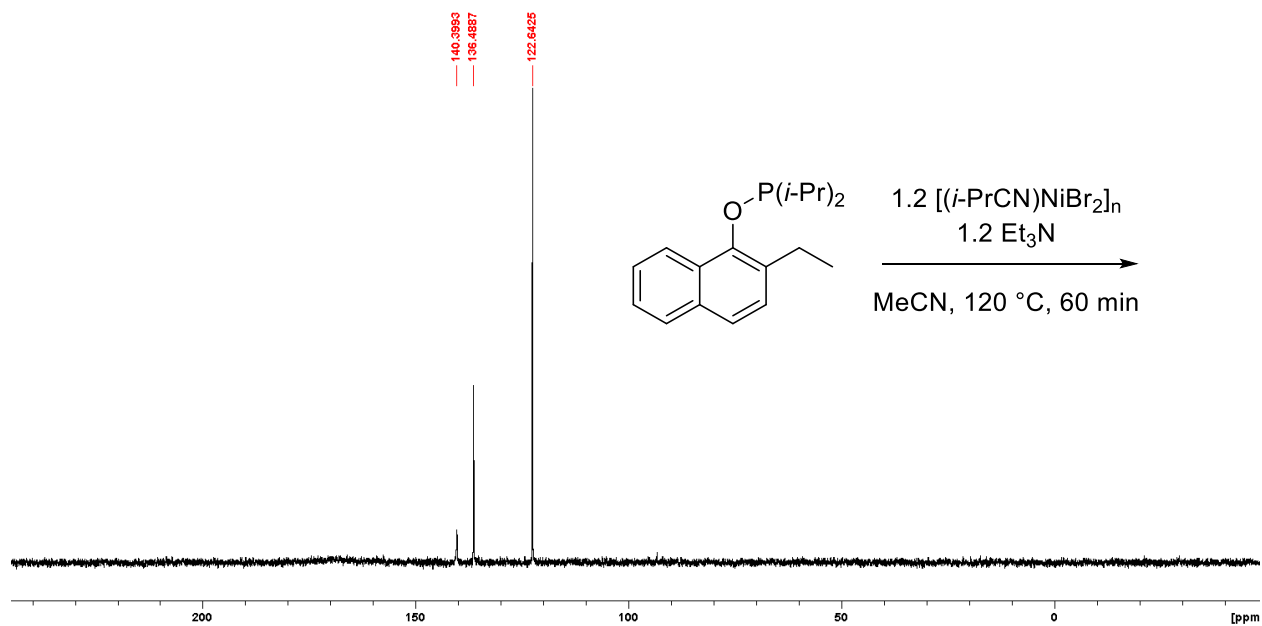
Figure S4.132: Crude reaction mixture for the nickelation of **1d** at 120 °C for 90 min with 1.2 equiv [(*i*-PrCN)NiBr$_2$]$_n$ and Et$_3$N.

b. Conversion quantification of nickelation and scrambling experiment
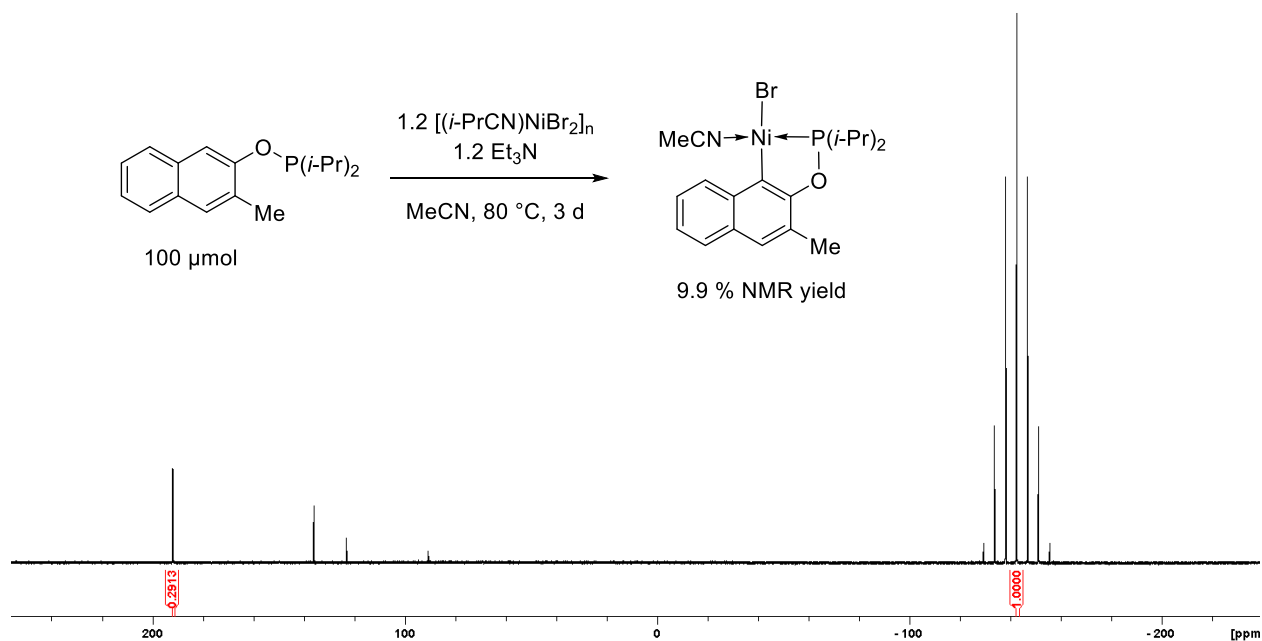
Figure S4.133: Quantification of the nickelation of 100 μmol **1f** against 42 mg TBAPF6 after 3 d at 80 °C.
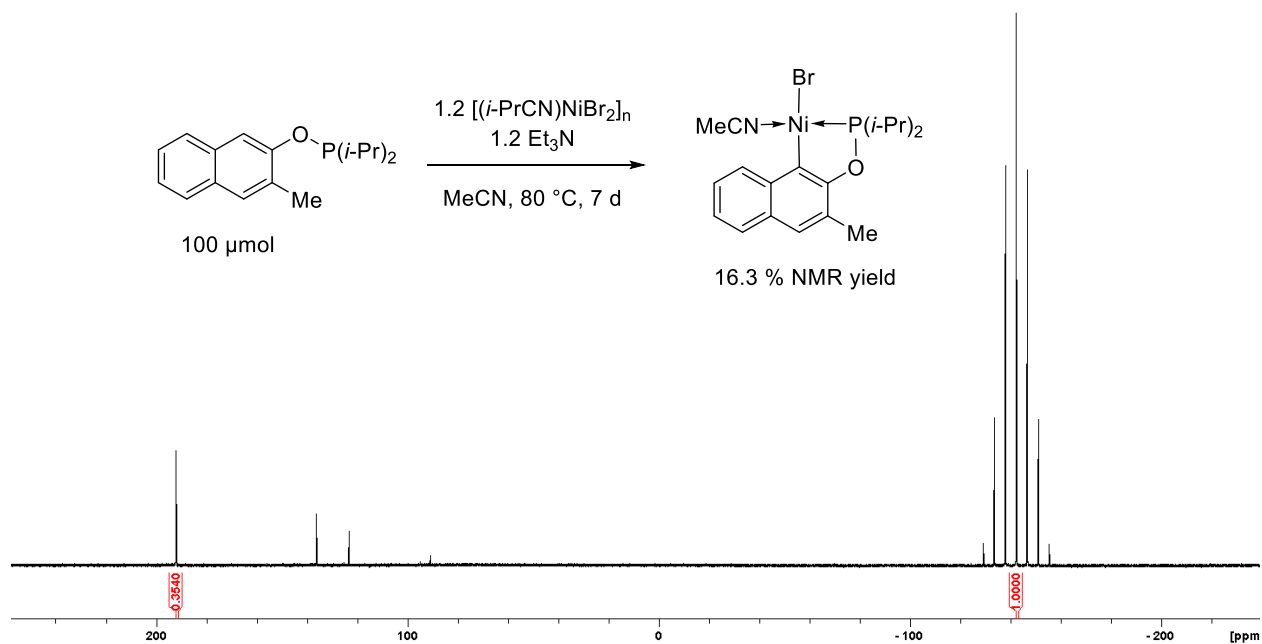
Figure S4.134: Quantification of the nickelation of 100 µmol **1f** against 57 mg TBAPF6 after 7 d at 80 °C.
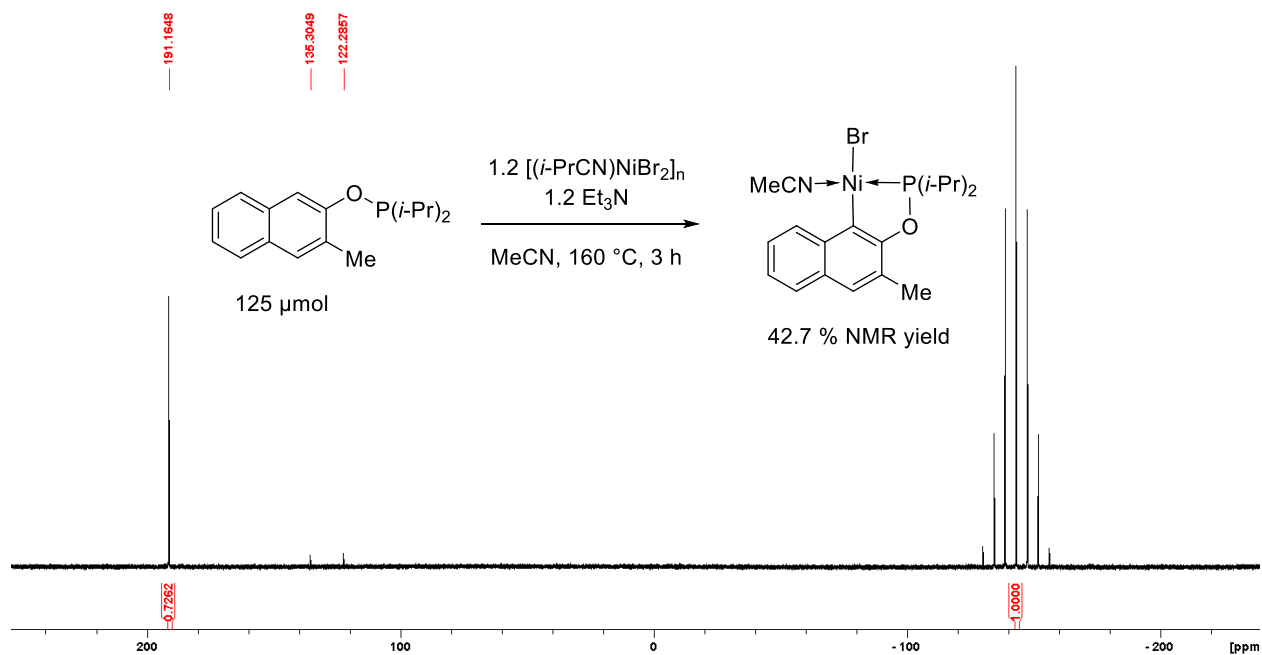
Figure S4.135: Quantification of the nickelation of 125 µmol **1f** against 91 mg TBAPF6 after 3 h at 160 °C.
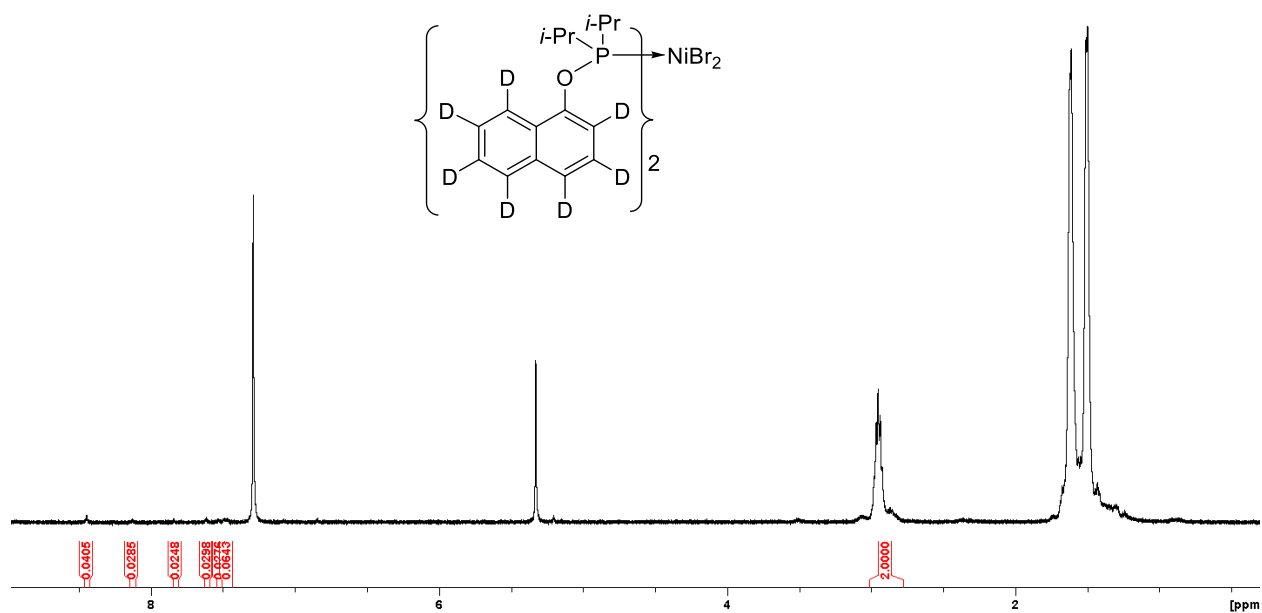
Figure S4.136: ^{1}H NMR spectrum of crude **3a-D$_7$** in CDCl3 prior to heating (* = residual CH$_2$Cl$_2$).
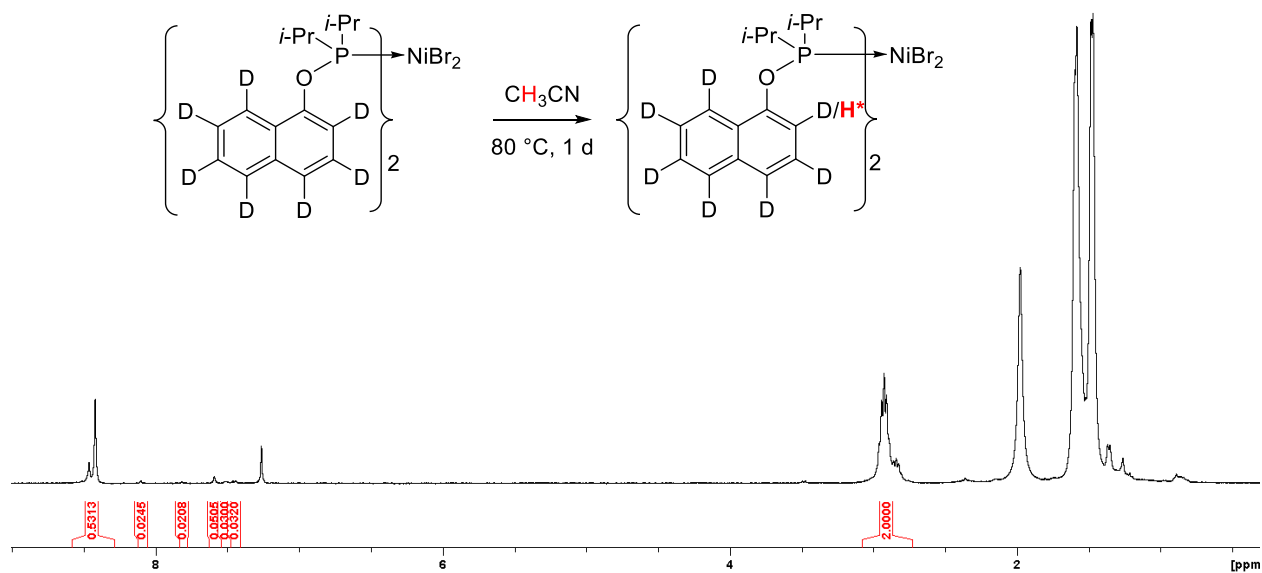
Figure S4.137: ^{1}H NMR in CDCl$_3$ of the crystals found after heating **3a-D7** at 80 °C for 1 d, showing 53 % H incorporation into C2.

c. Allyl complex-related spectra
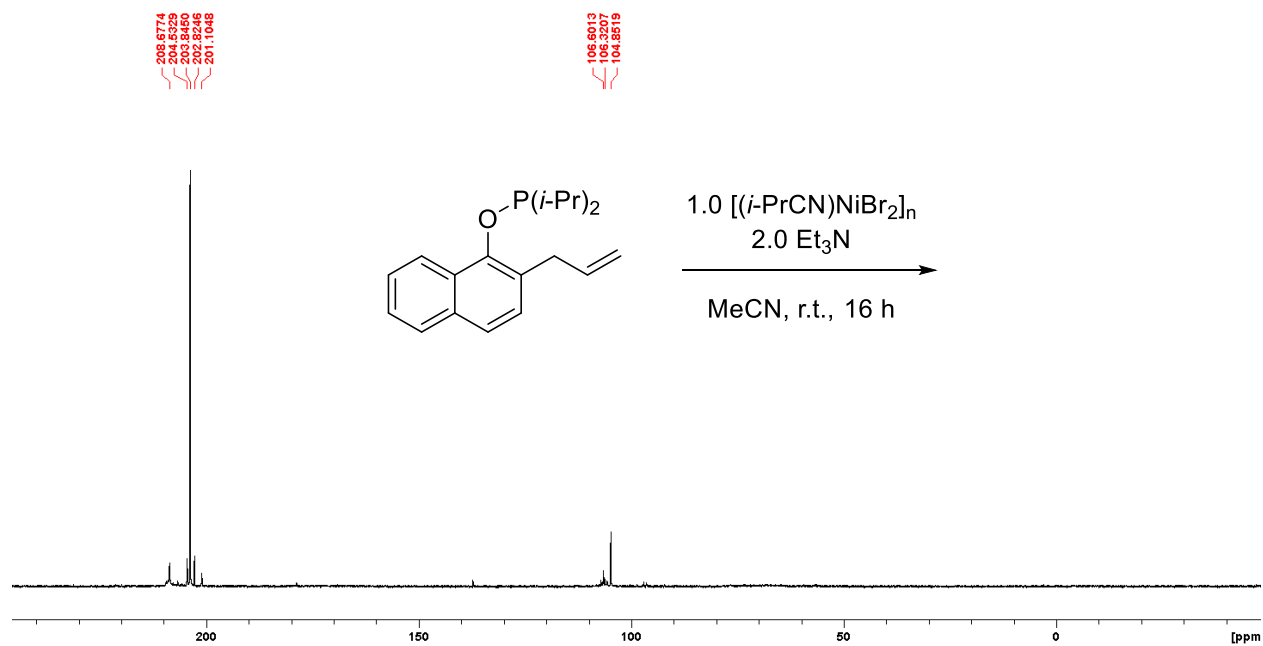
Figure S4.138: Crude reaction mixture for the nickelation of **1g** at r.t. for 16 h
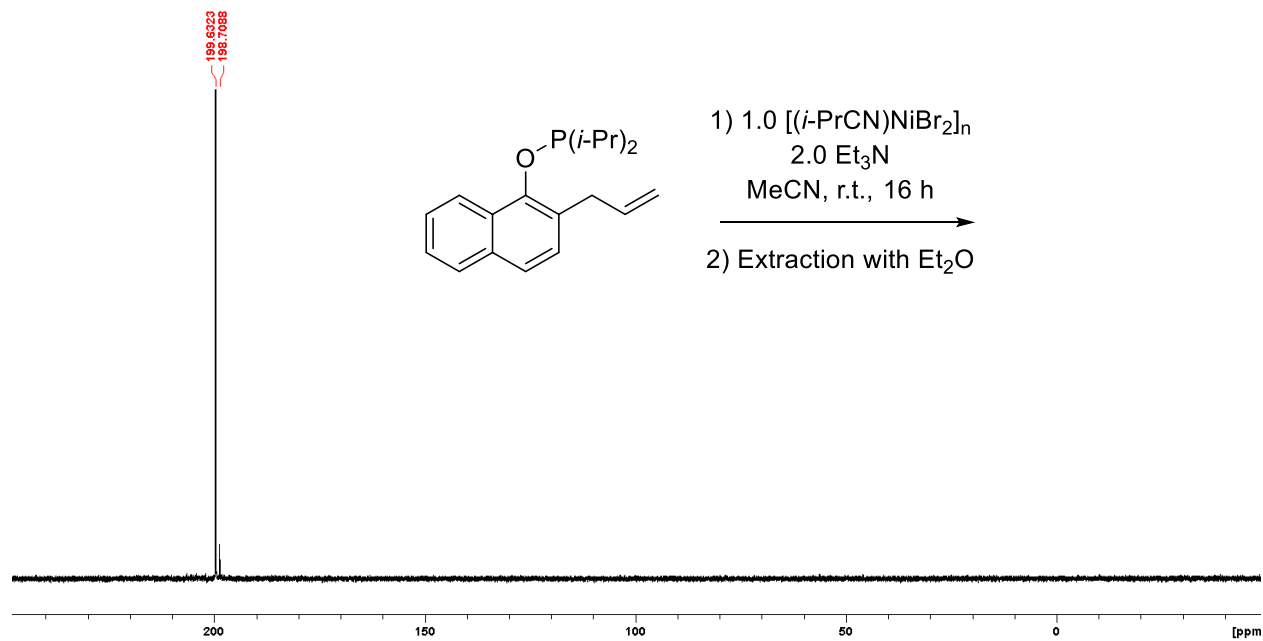
Figure S4.139: Et₂O extracts after the nickelation of **1g** at r.t. for 16 h in MeCN.

d. RMNs of experiments for the insertion product
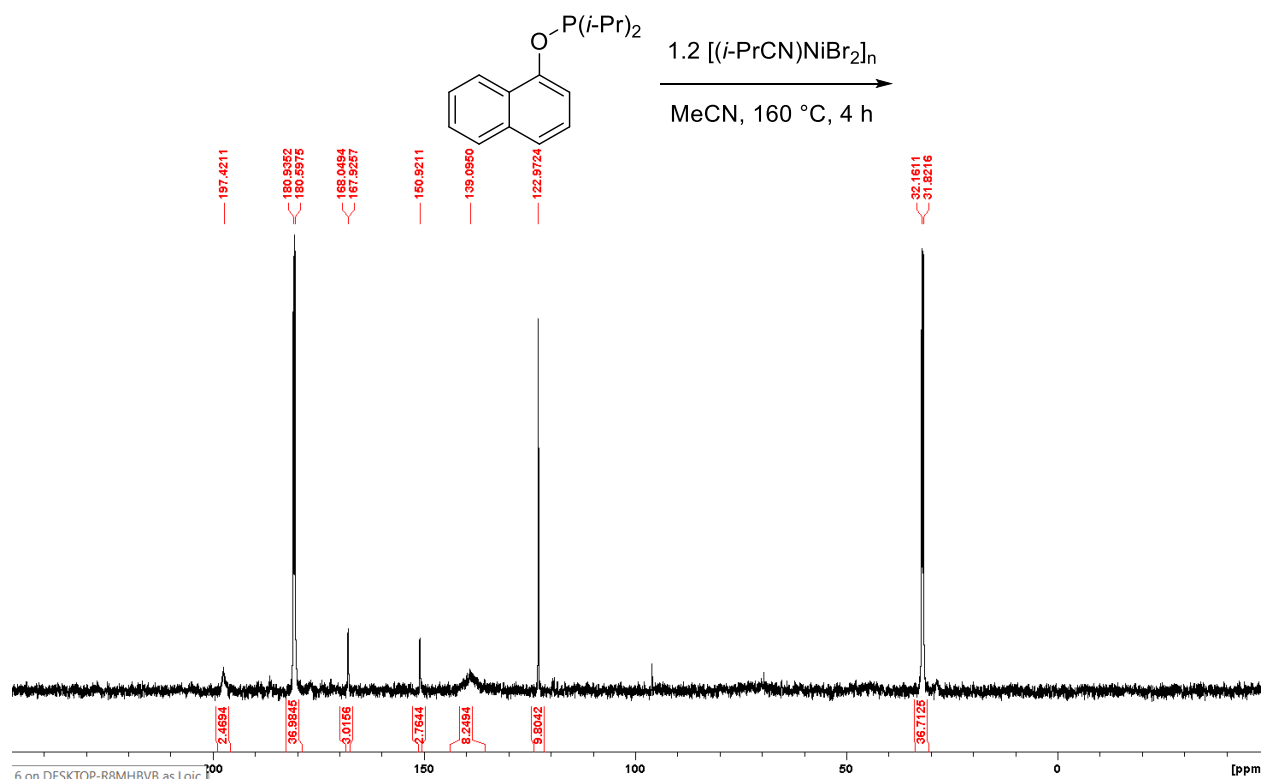
Figure S4.140: Crude reaction mixture of the insertion reaction for **1a** with 1.2 equiv [(*i*-PrCN)NiBr₂]ₙ after 4 h at 160 °C.
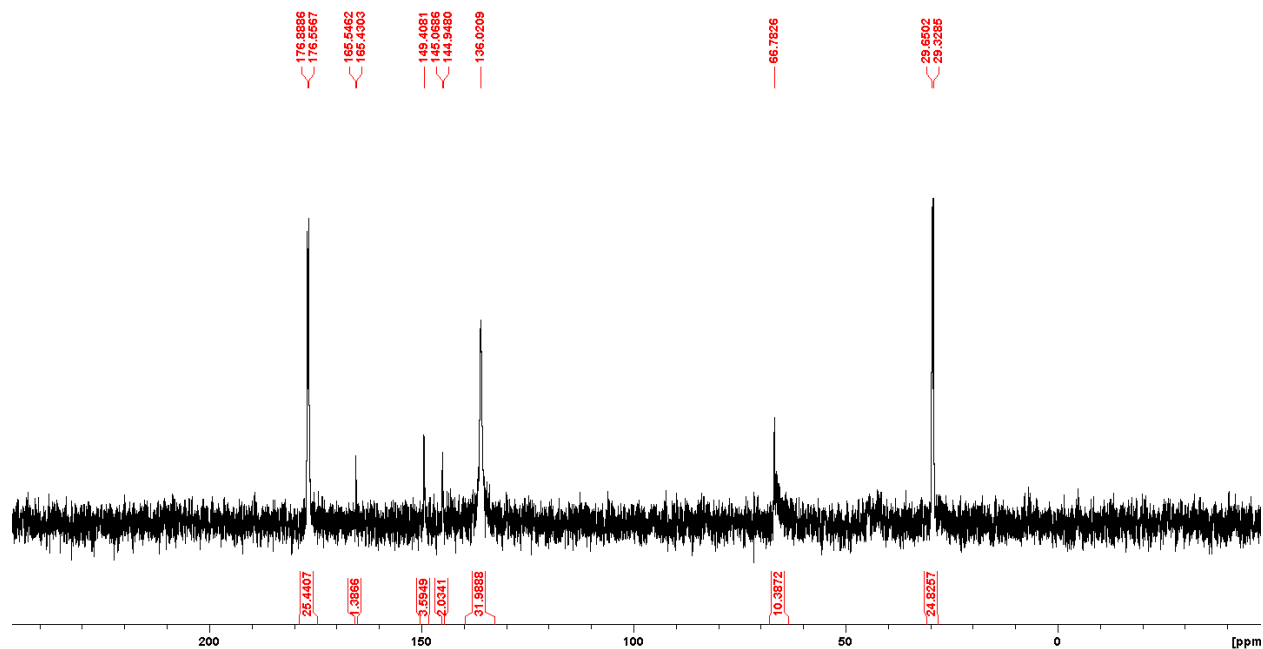
Figure S4.141: Toluene extracts of the insertion reaction for **1a** with 1.2 equiv [(*i*-PrCN)NiBr₂]ₙ after 4 h at 160 °C in MeCN.
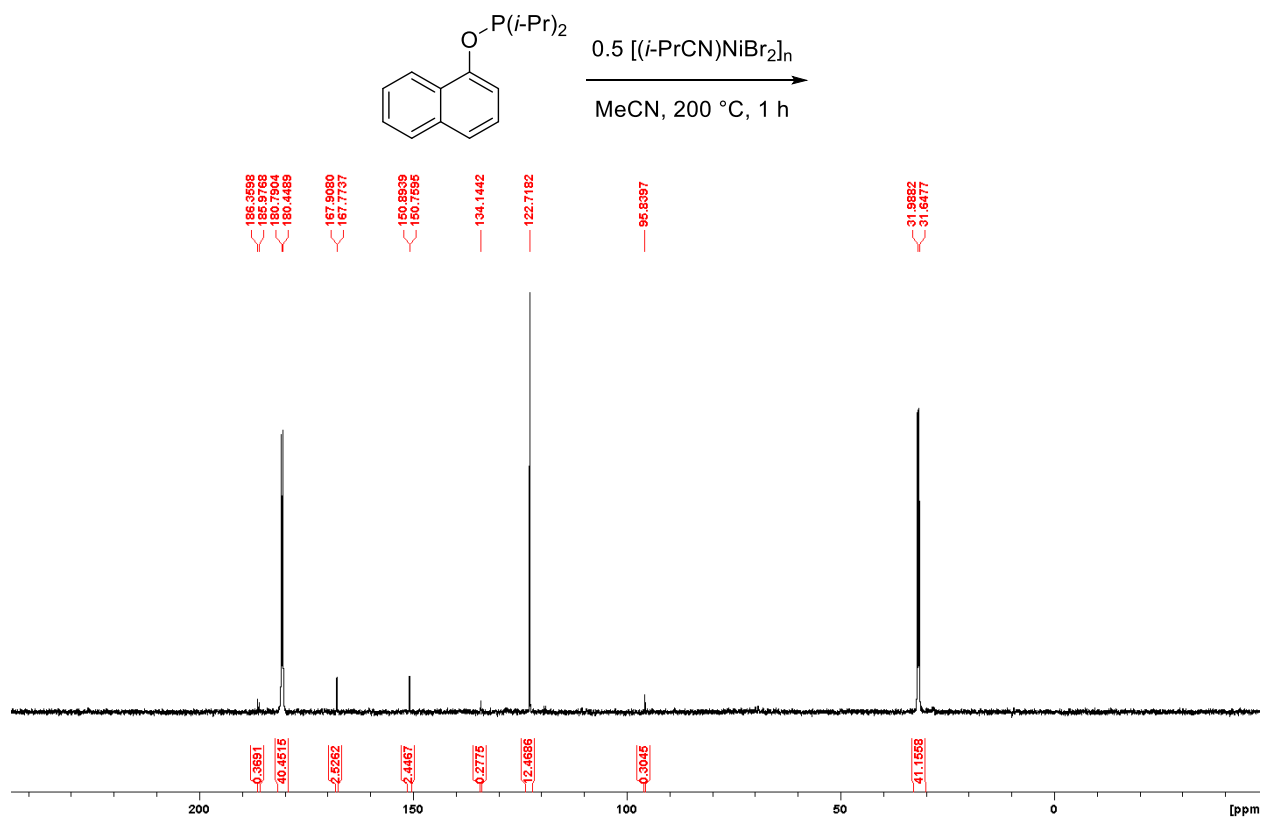
Figure S4.142: Crude reaction mixture of the insertion reaction for **1a** with 0.5 equiv [(*i*-PrCN)NiBr₂]ₙ after 1 h at 200 °C.
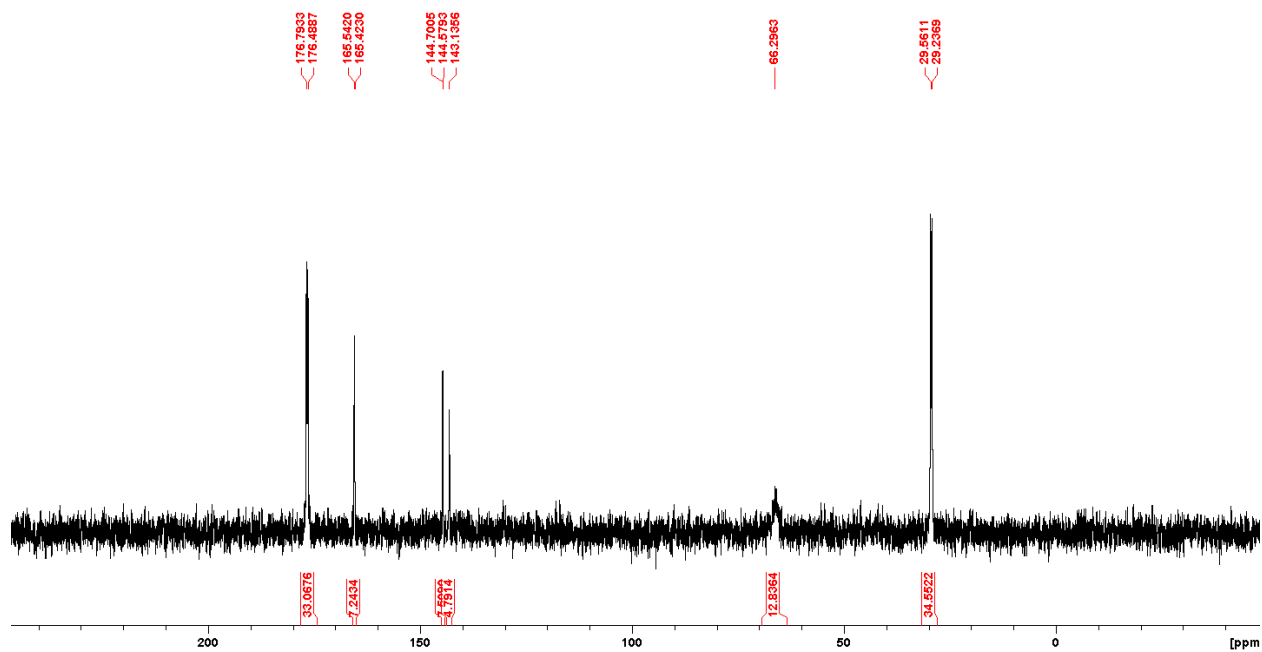
Figure S4.143: Toluene extracts of the insertion reaction for **1a** with 0.5 equiv [(*i*-PrCN)NiBr₂]ₙ after 1 h at 200 °C.
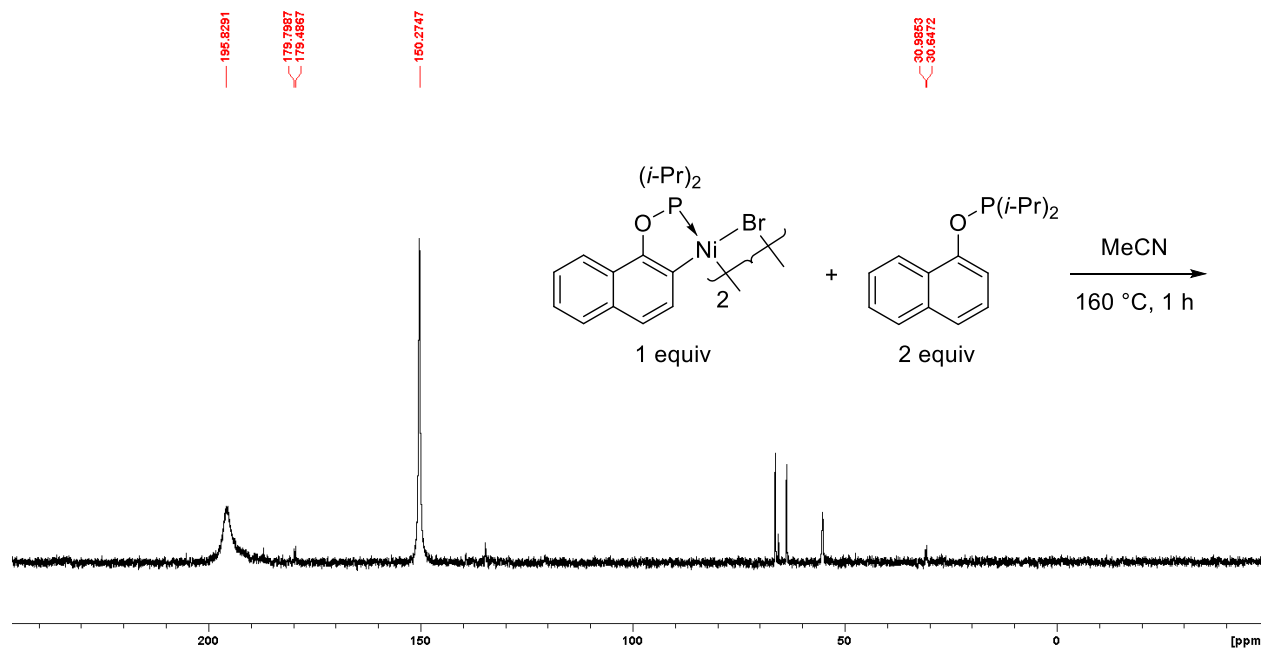
Figure S4.144: Crude reaction mixture of the reaction of **1a** and **2a** at 160 °C for 1h.
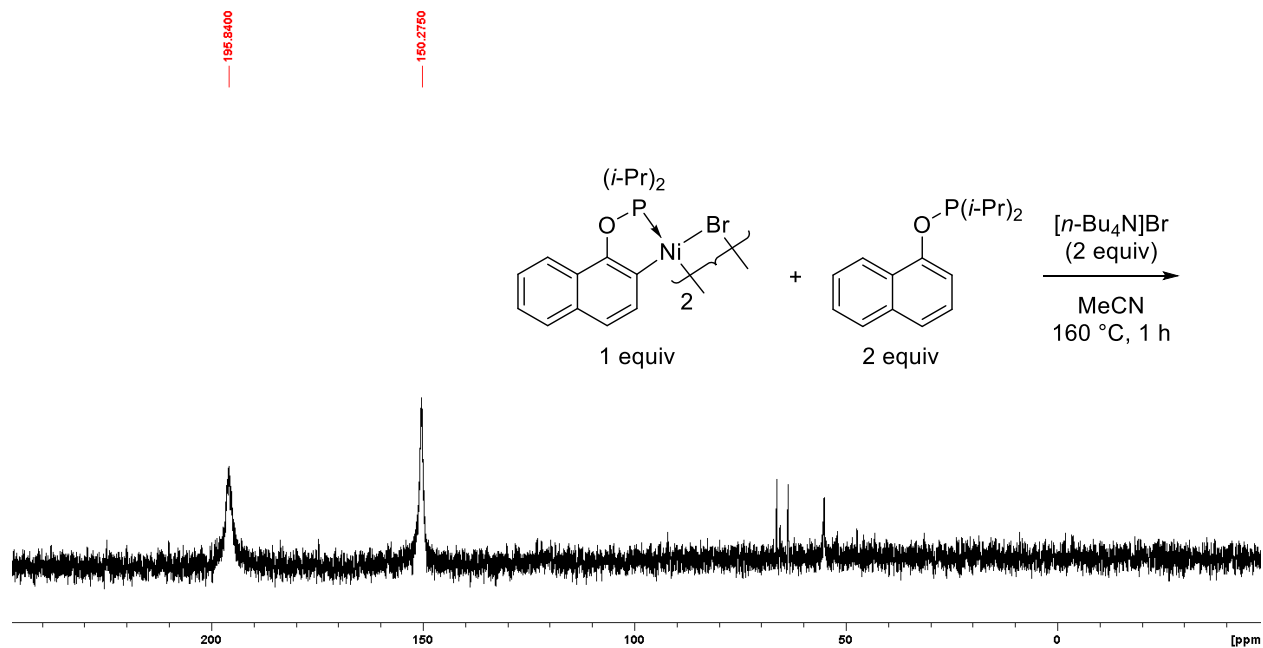
Figure S4.145: Crude reaction mixture of the reaction of **1a** and **2a** + 1 equiv [*n*-Bu₄N]Br at 160 °C for 1h.
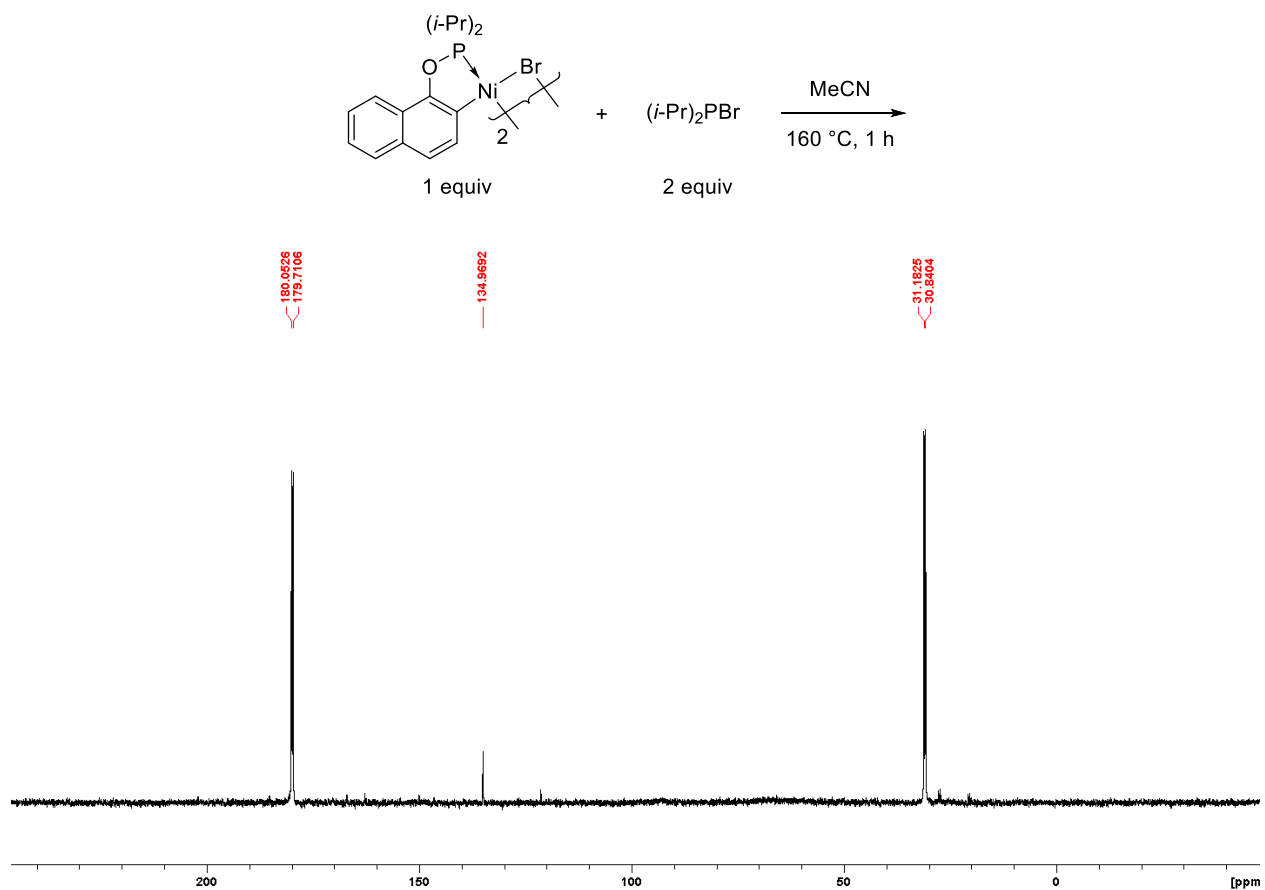
Figure S4.146: Crude reaction mixture of the reaction of **2a** and (*i*-Pr)₂PBr at 160 °C for 1h.

e. RMNs for the reactivity of **1d** at 160 deg
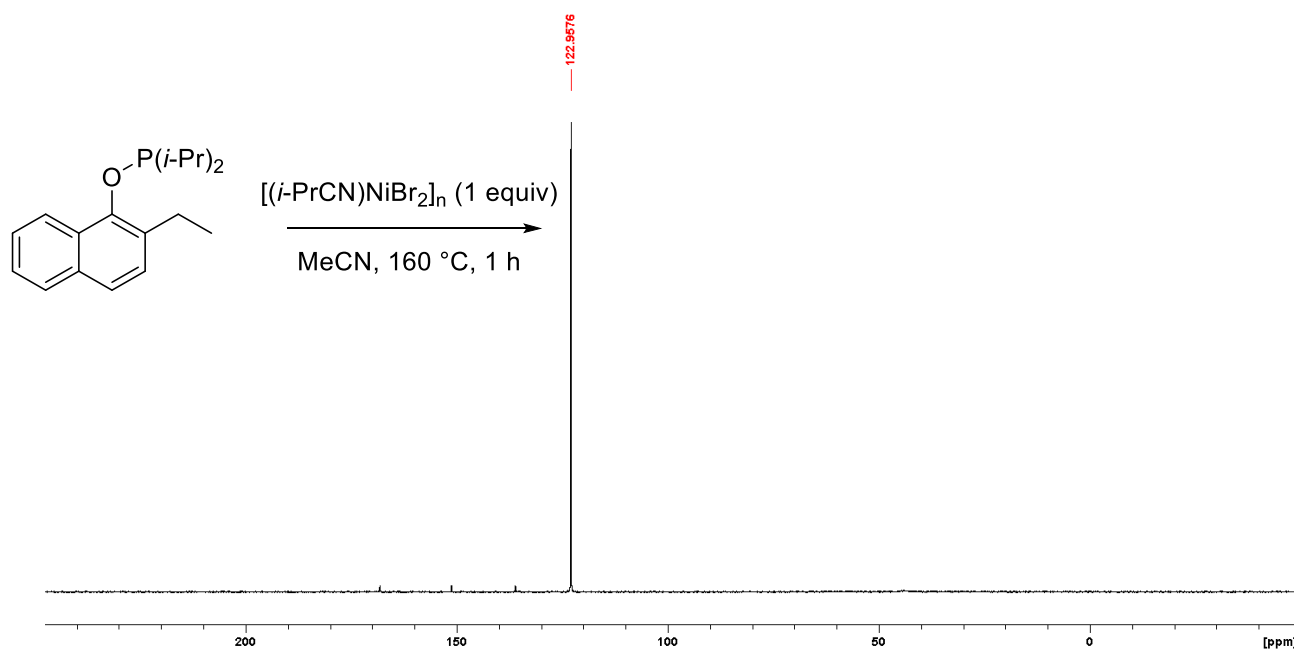
Figure S4.147: Crude mixture for the reaction of **1d** with 1 equiv [(*i*-PrCN)NiBr₂]ₙ at 160 °C for 1 h.
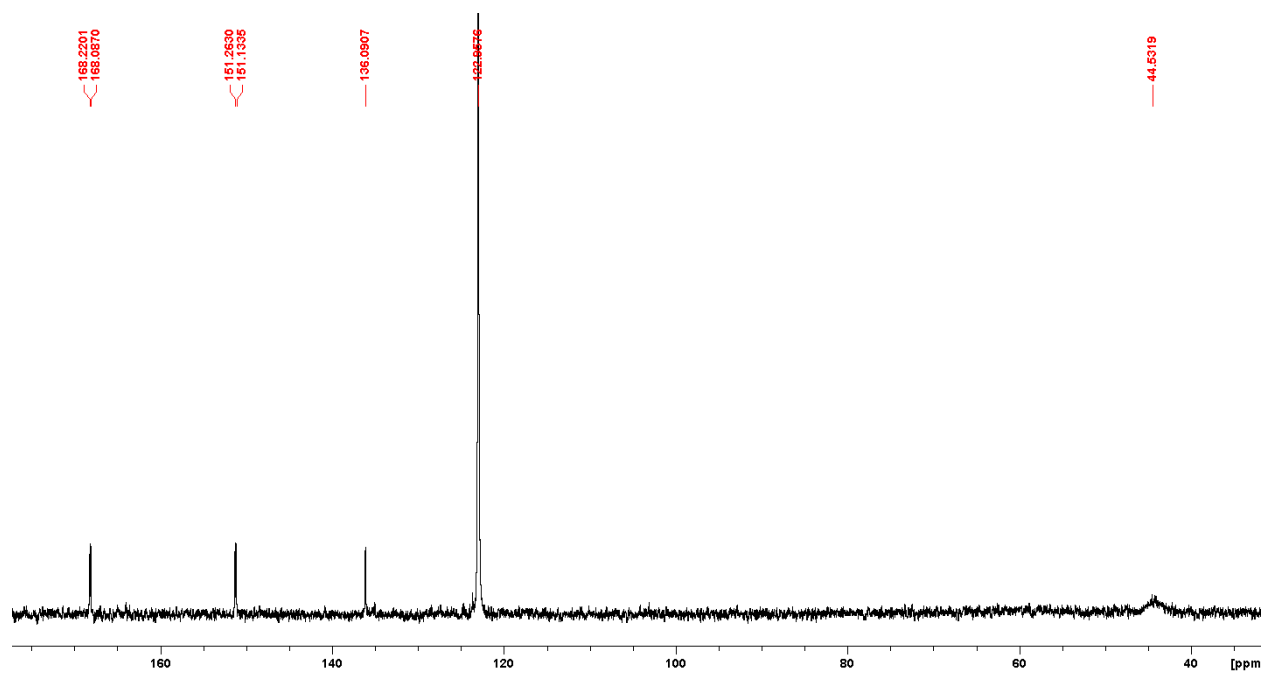
Figure S4.148: Crude mixture for the reaction of **1d** with 1 equiv [(*i*-PrCN)NiBr₂]ₙ at 160 °C for 1 h, with focus on byproducts.
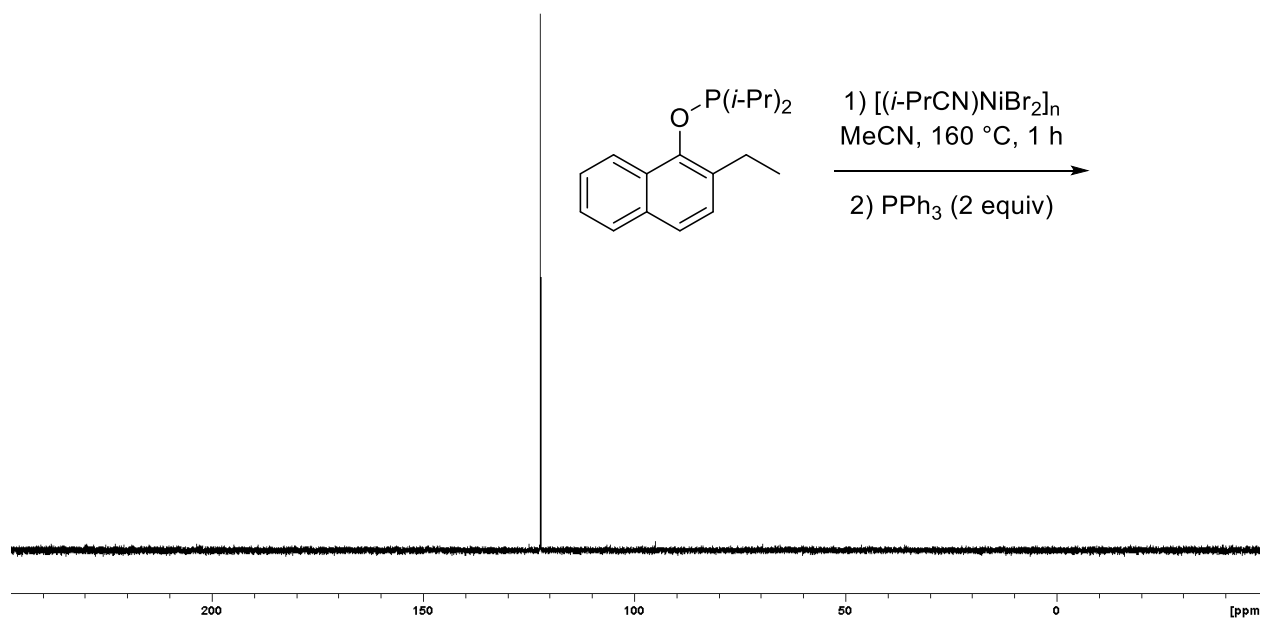
Figure S4.149: Crude mixture for the reaction of **1d** with 1 equiv [(*i*-PrCN)NiBr2]n at 160 °C for 1 h after addition of 2 equiv PPh3.
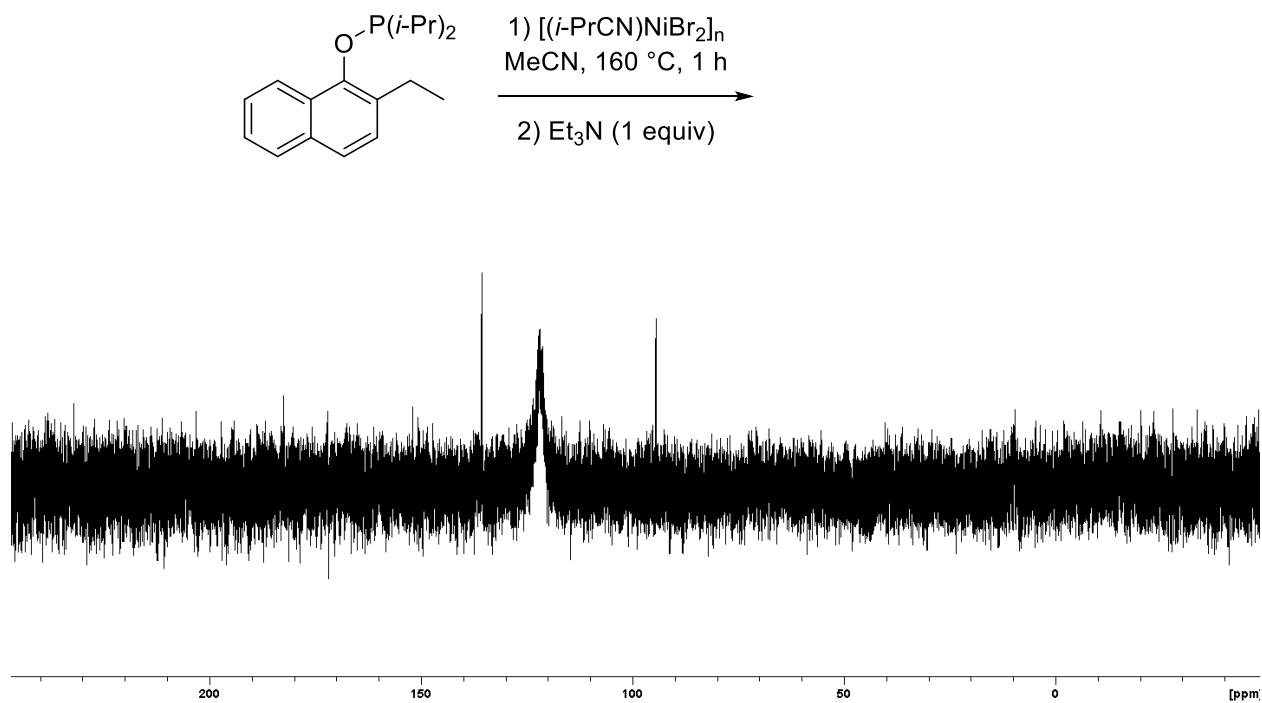
Figure S4.150: Crude mixture for the reaction of **1d** with 1 equiv [(*i*-PrCN)NiBr2]n at 160 °C for 1 h after addition of 1 equiv Et3N
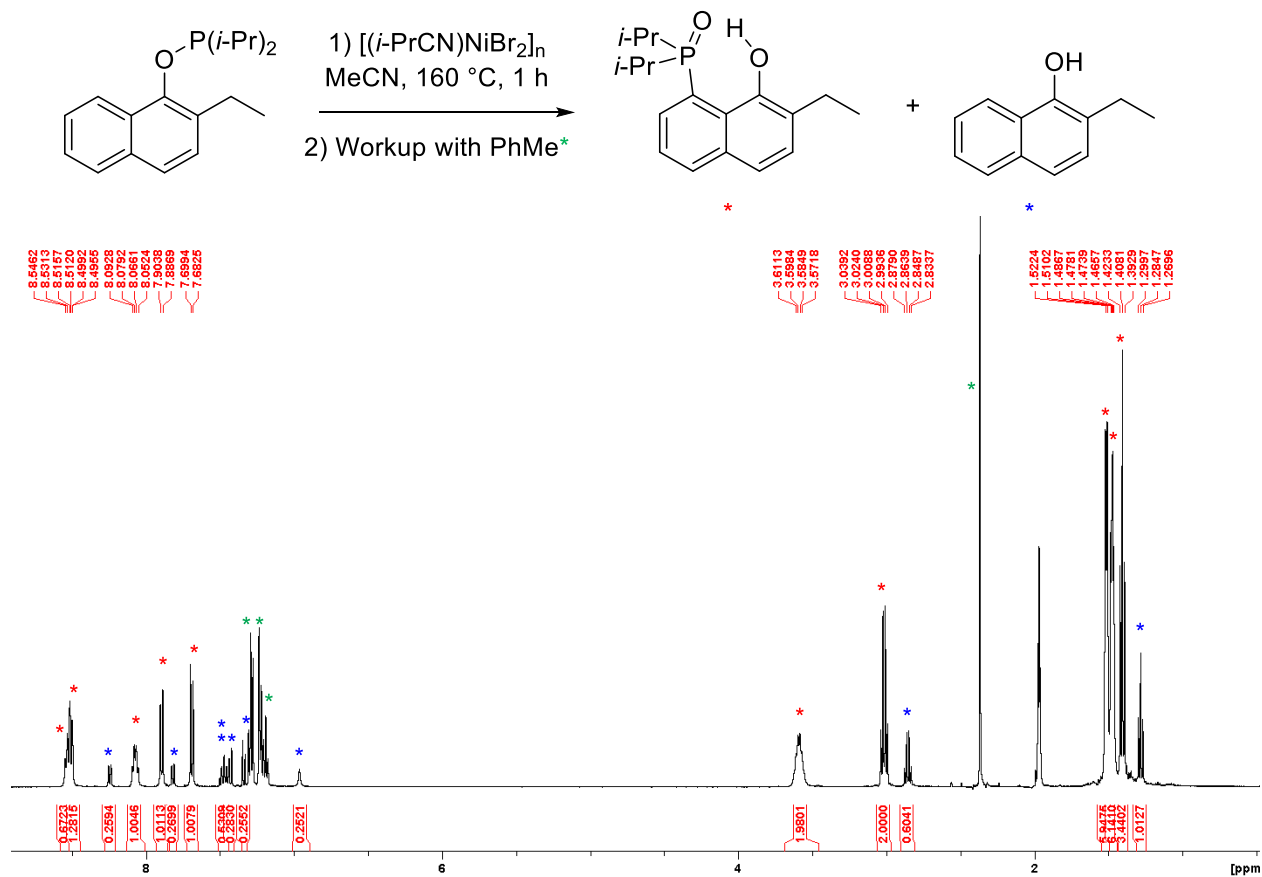
Figure S4.151: Full ^{1}H NMR spectrum in CD$_3$CN of the residues after PhMe workup of the reaction of **1d** with [(i-PrCN)NiBr$_2$]$_n$ at 160 °C for 1 h.
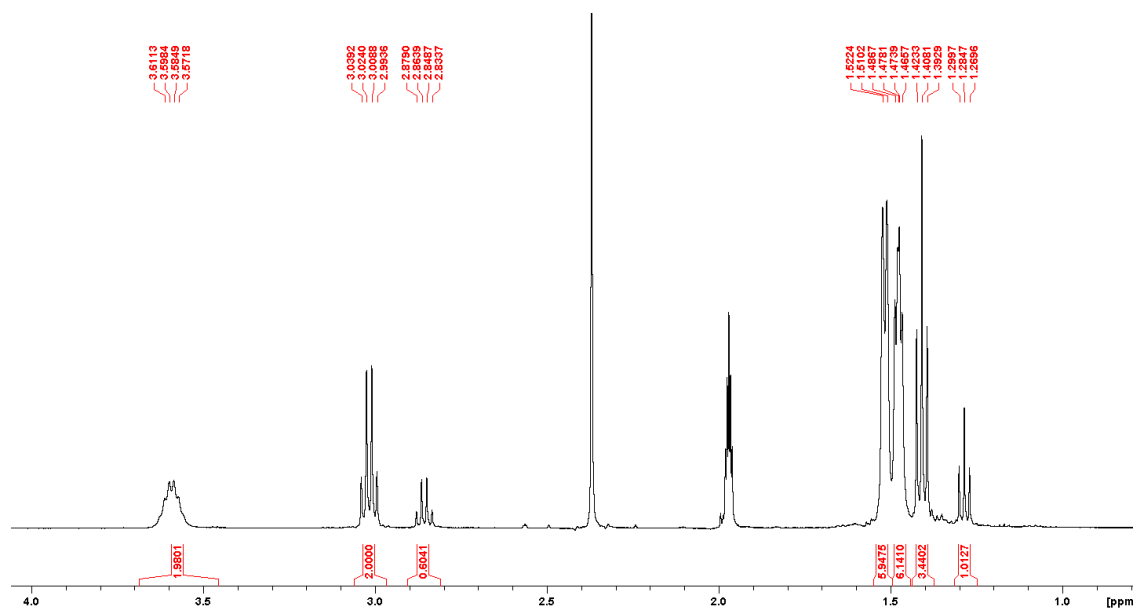
Figure S4.152: Aliphatic region of the ^{1}H NMR spectrum in CD$_3$CN of the residues after PhMe workup of the reaction of **1d** with [(i-PrCN)NiBr$_2$]$_n$ at 160 °C for 1 h.
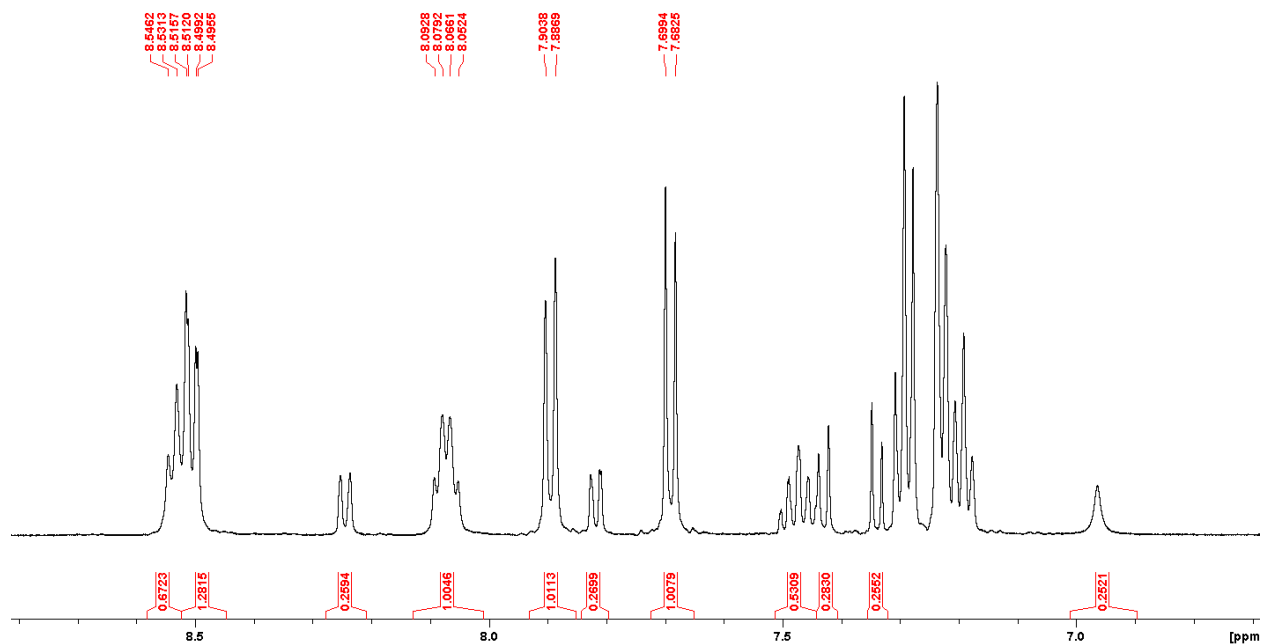
Figure S4.153: Aromatic region of the ^{1}H NMR spectrum in CD$_3$CN of the residues after PhMe workup of the reaction of **1d** with [(i-PrCN)NiBr$_2$]$_n$ at 160 °C for 1 h.
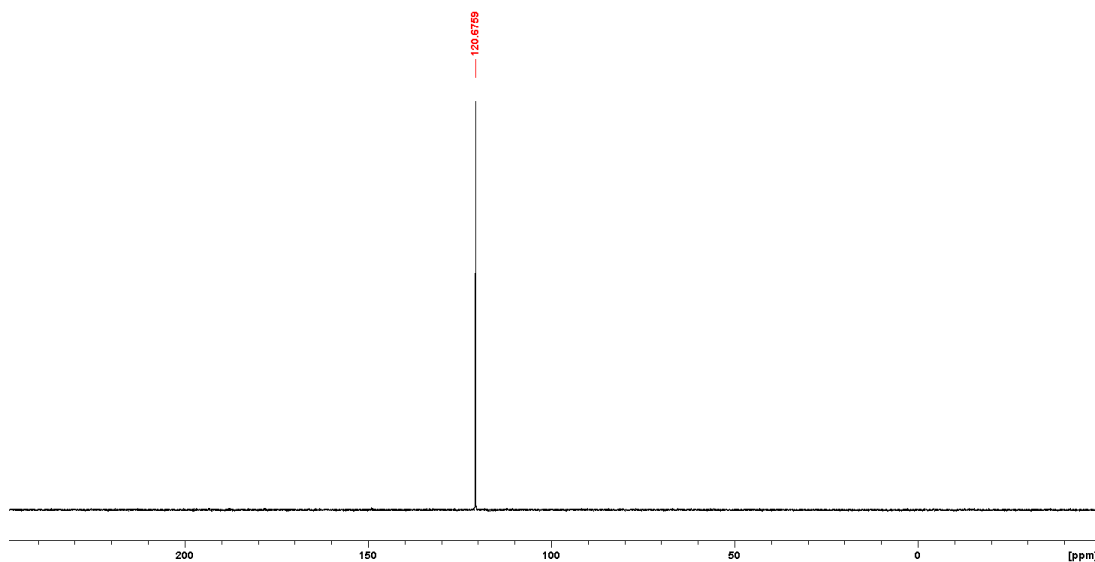
Figure S4.154: ^{31}P{^{1}H} NMR spectrum in CD$_3$CN of the residues after PhMe workup of the reaction of **1d** with [(i-PrCN)NiBr$_2$]$_n$ at 160 °C for 1 h.
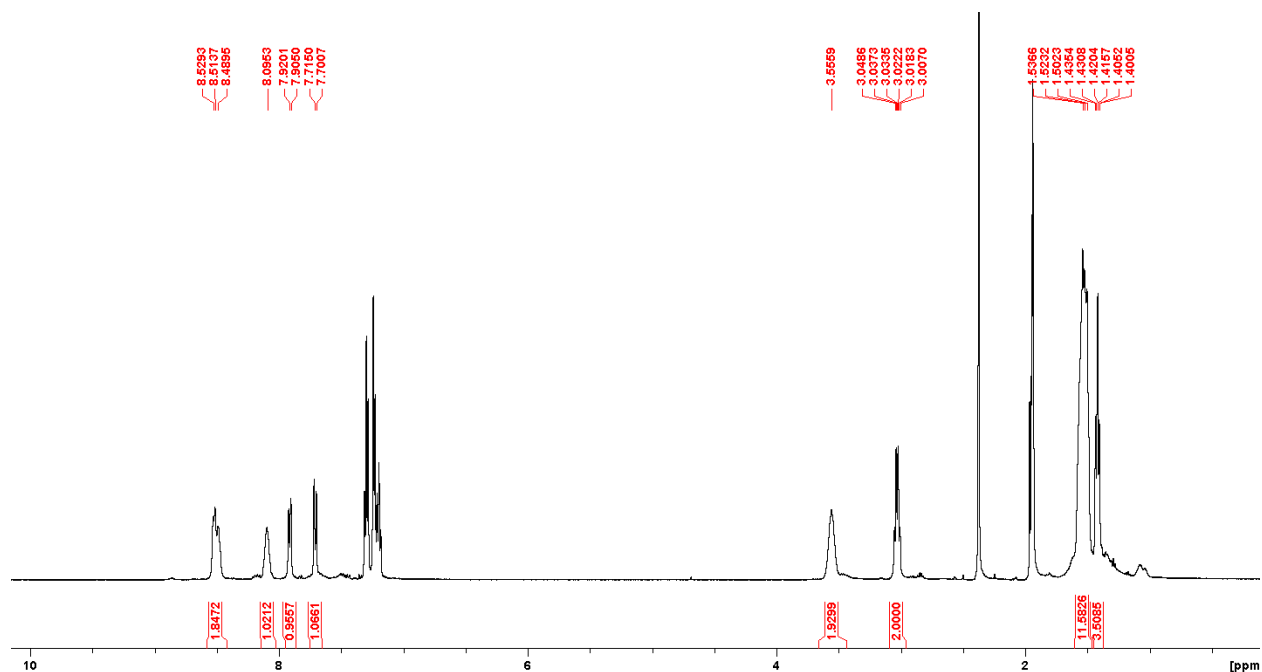
Figure S4.155: ^{1}H NMR in CD$_3$CN of other[1] residues found after PhMe workup of the reaction of **1d** with [(i-PrCN)NiBr$_2$]$_n$ at 160 °C for 1 h.　　　[1]This time, the ^{1}H NMR spectrum showed the same compound **5** (free of 2-Et-1-naphthol), and that the ethyl substituent found to be coupled to a P nucleus: a quadruplet of doublets at 3.03 ppm ($^6J_{HP} \approx 2.0$ Hz) and a triplet of doublets at 1.42 ppm ($^7J_{HP} \approx 2.3$ Hz) confirming the presence of a P substituent at C8 of naphthyl ring.
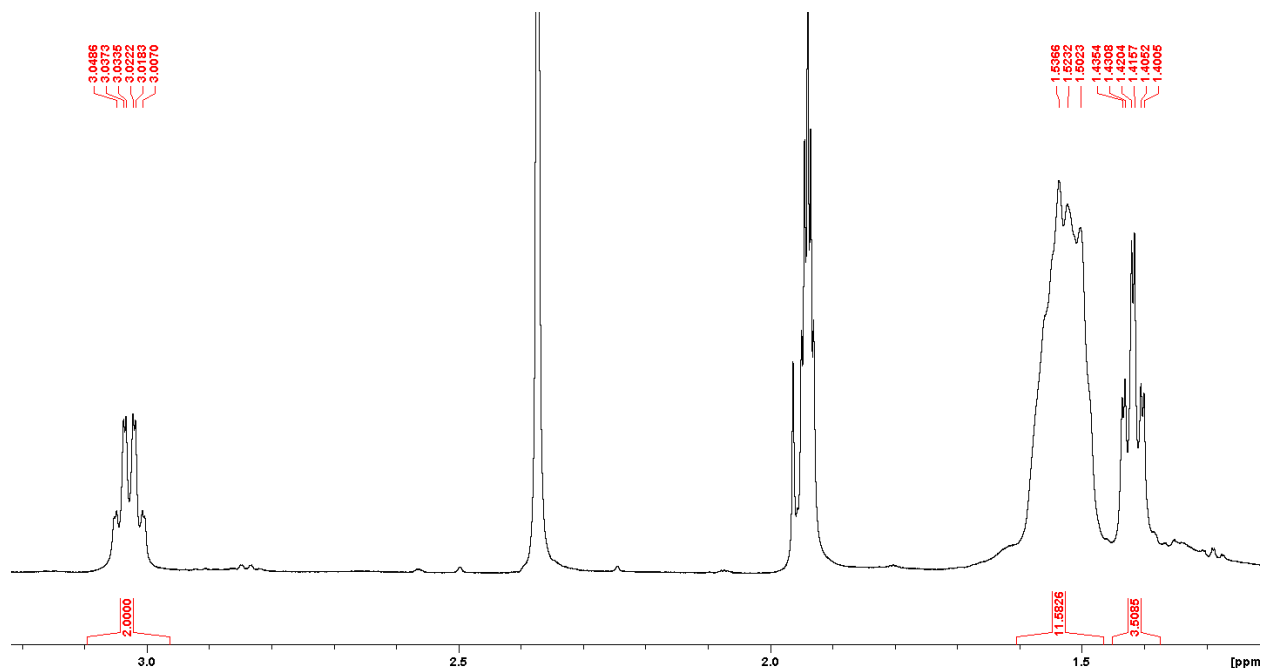
Figure S4.156. ^{1}H NMR in CD$_3$CN of other residues found after PhMe workup of the reaction of **1d** with [(i-PrCN)NiBr$_2$]$_n$ at 160 °C for 1 h, focus on the aliphatic region showing J_{HP} coupling between CH_2CH_3 and the C8-P(O)(i-Pr)$_2$.

S4.5 GC-MS Analysis
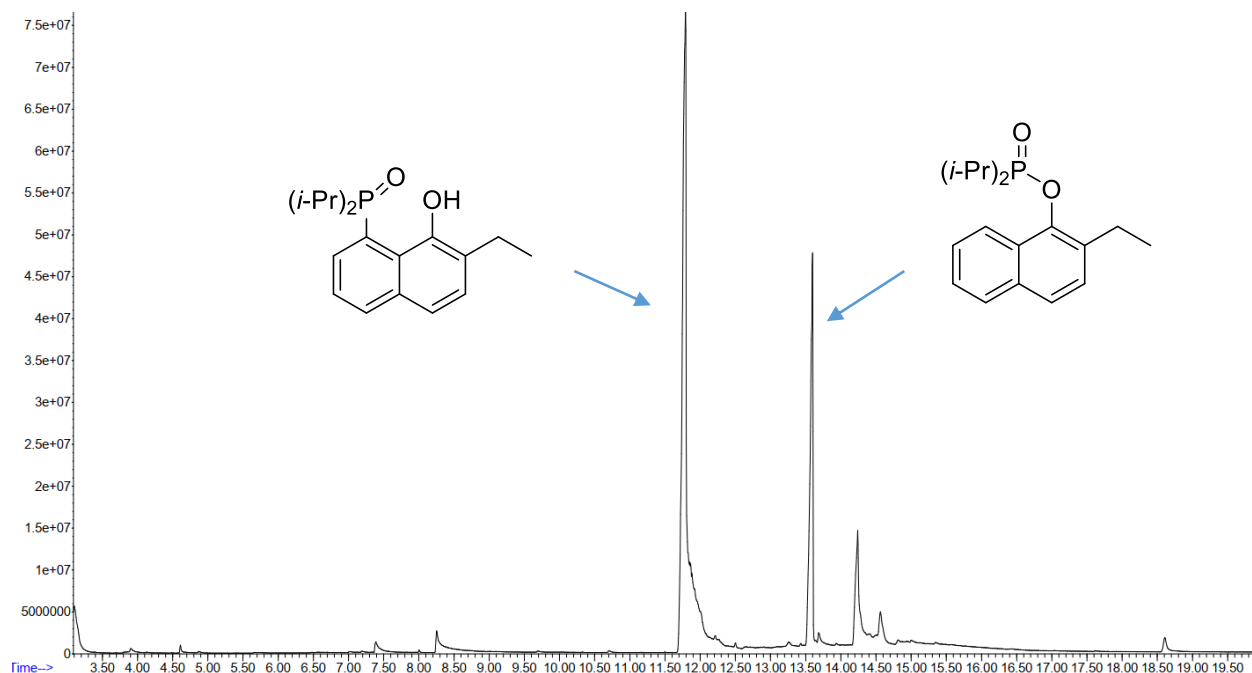
Figure S4.157: GC-MS chromatogram of the crude reaction mixture of **1d** + [(*i*-PrCN)NiBr$_2$]$_n$ in MeCN at 160 °C for 1 h
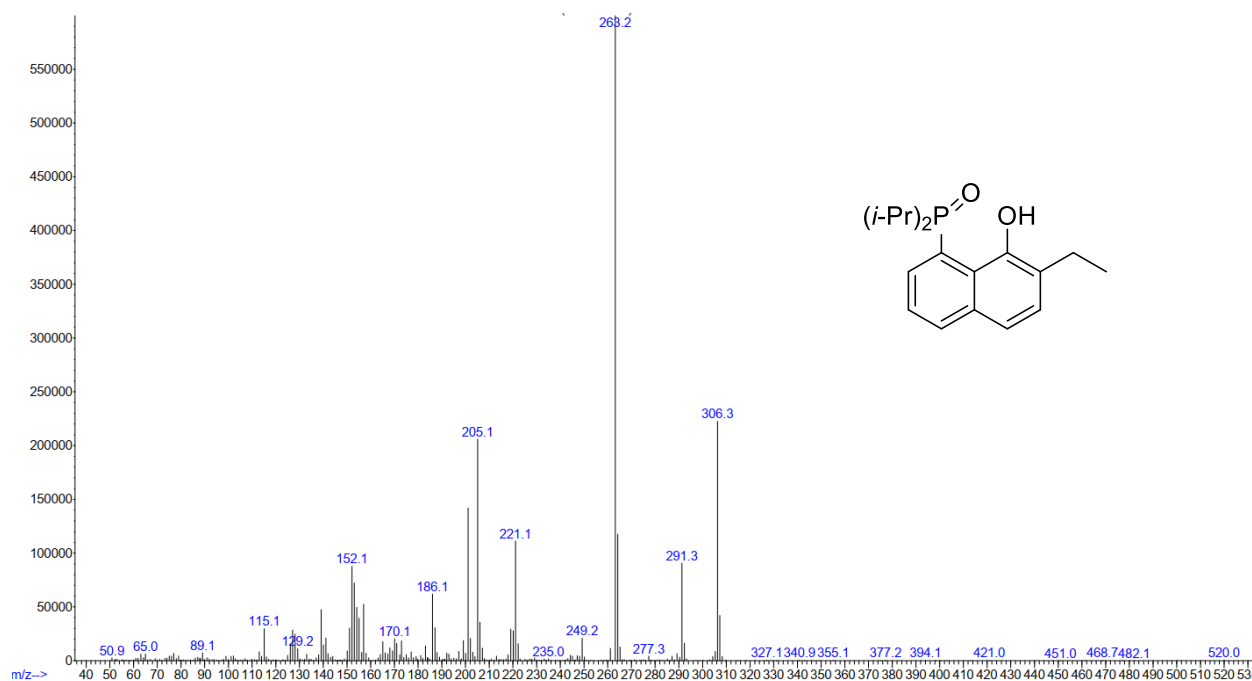
Figure S4.158: Mass spectrum of (2-Et-1-naphthol-8-yl)diisopropylphosphine oxide (Compound **5**).
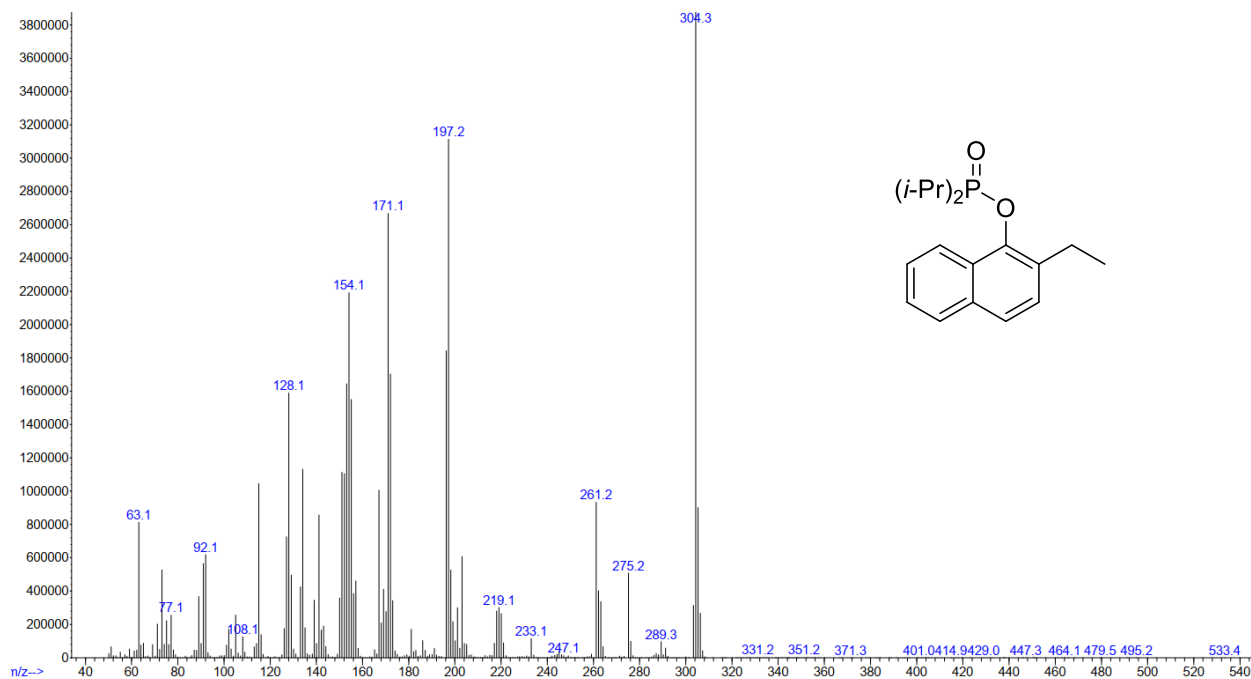
FigureS4.159: Mass spectrum of (2-Et-1-naphthyl)diisopropylphosphinate (Ligand **1d** oxidized).
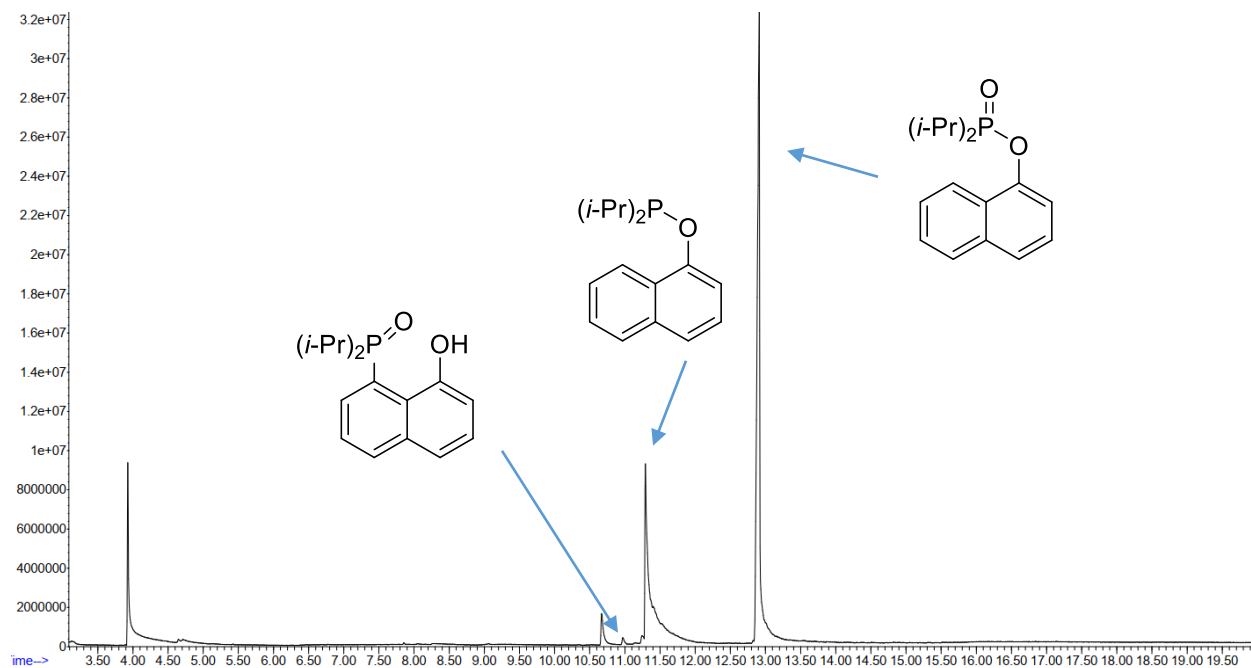
FigureS4.160: GC-MS chromatogram of the crude reaction mixture of **1a** + [(*i*-PrCN)NiBr$_2$]$_n$ in MeCN at 160 °C for 4 h
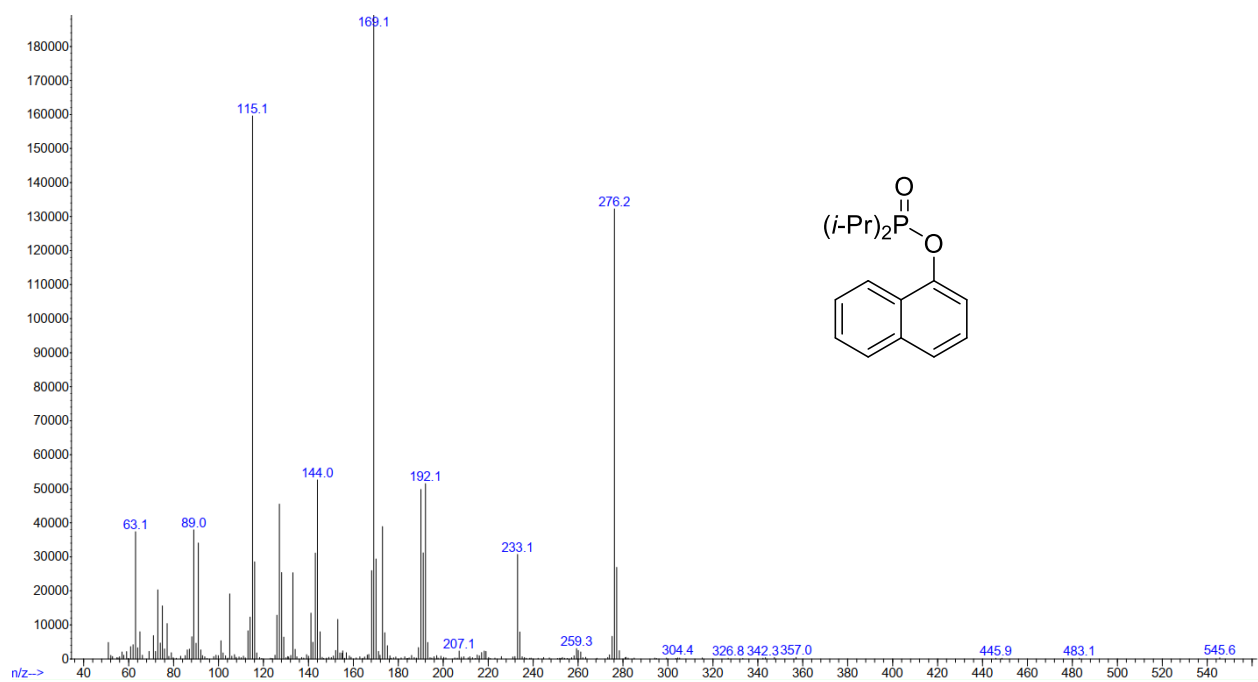
Figure S4.161: Mass spectrum of (1-naphthyl)diisopropylphosphinate (Ligand **1a** oxidized).
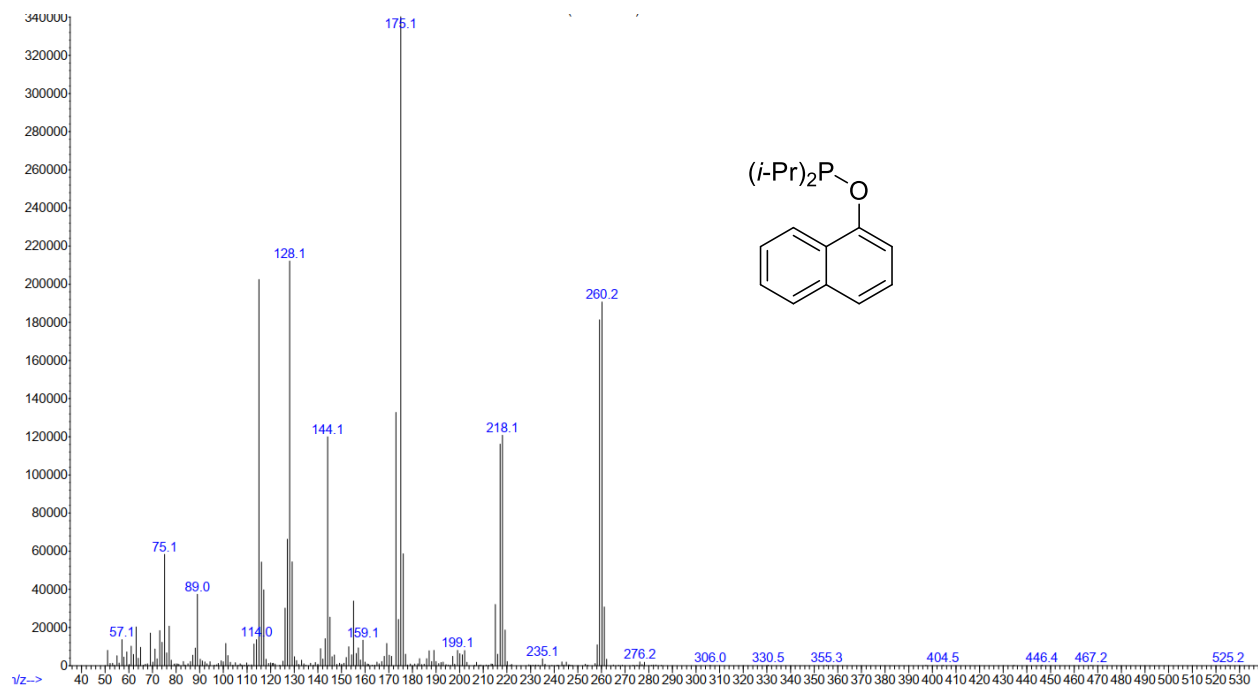
Figure S4.162: Mass spectrum of (1-naphthyl)diisopropylphosphinite (Ligand **1a**).
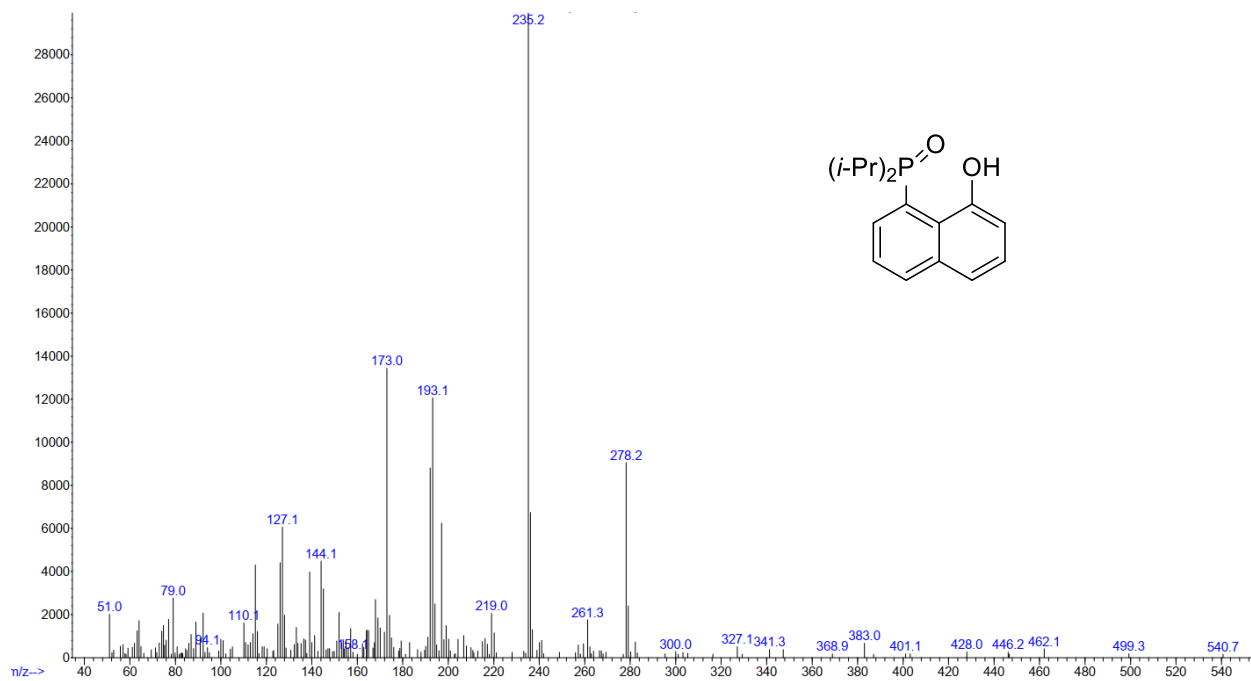
Figure S4.163: Mass spectrum of (1-naphthol-8-yl)diisopropylphosphine oxide (Compound **5**).

S4.6 Crystallographic data tables

Table S4.1 : Crystal description and refinement indicators for compounds **2a-2c**

	2a	2b	2c
chemical formula	$C_{32}H_{40}Br_2Ni_2O_2P_2$	$C_{34}H_{44}Br_2Ni_2O_4P_2$	$C_{32}H_{38}Br_2Cl_2Ni_2O_2P_2$
crystal color	orange	orange	orange
crystal size (mm)	$0.06 \times 0.12 \times 0.27$	$0.20 \times 0.20 \times 0.30$	$0.10 \times 0.12 \times 0.14$
index ranges	$-15 \le h \le 17$ $-9 \le k \le 9$ $-71 \le l \le 71$	$-23 \le h \le 23$ $-17 \le k \le 17$ $-31 \le l \le 31$	$-13 \le h \le 13$ $-14 \le k \le 14$ $0 \le l \le 16$
***Fw*; *F*(000)**	795.82; 3232	855.87; 3488	864.70; 872
***T* (K)**	100	100	100
wavelength (Å)	1.54178	1.54178	1.54178
space group	$Pca2_1$	Pbca	P-1
***a* (Å)**	14.3868(3)	18.8368(9)	11.1592(8)
***b* (Å)**	7.9633(2)	14.4998(7)	11.5729(8)
***c* (Å)**	57.8968(13)	25.8842(13)	13.1875(9)
α (deg)	90	90	92.908(3)
β (deg)	90	90	91.112(3)
γ (deg)	90	90	94.543(3)
Z	8	8	2
***V* (Å^3)**	6633.0(3)	7069.7(6)	1695.1(2)
ρ_{calcd} (g·cm^{-3})	1.594	1.608	1.694
μ (mm^{-1})	5.354	5.113	6.710
θ range (deg); completeness	$1.526 - 72.178$; 0.999	$3.415 - 72.237$; 0.998	$3.356 - 72.123$; 0.983
collected reflections; R_σ	261066; 0.0116	277524; 0.0066	68948; 0.0267
unique reflections; R_{int}	13028; 0.0352	6958; 0.0304	6406; 0.0503
R1^a; wR2^b [I > 2σ(I)]	0.0216; 0.0584	0.0298; 0.0779	0.0455; 0.1350
R1; wR2 [all data]	0.0216; 0.0584	0.0299; 0.0779	0.0467; 0.1372
GOOF	1.139	1.146	1.091
largest diff peak and hole	0.521 and -0.300	1.366 and -1.162	0.773 and -0.879

^{a} R$_1$=Σ(||F$_o$|-|F$_c$||)/Σ|F$_o$|

^{b} wR$_2$={Σ[w(F$_o$^{2}–F$_c$^{2})^2]/Σ[w(F$_o$^{2})^2]}^{½}

Table S4.2: Crystal description and refinement indicators for compounds **2e**, **2e-NCMe** and **2f-L**.

	2e	**2e-NCMe**	**2f-L**
chemical formula	$C_{32}H_{40}Br_2Ni_2O_2P_2$	$C_{18}H_{23}BrNNiOP$	$C_{34}H_{45}BrNiO_2P_2$
crystal color	orange	yellow	orange
crystal size (mm)	$0.16 \times 0.16 \times 0.32$	$0.15 \times 0.21 \times 0.27$	$0.04 \times 0.08 \times 0.12$
index ranges	$-15 \leq h \leq 15$ $-14 \leq k \leq 14$ $-16 \leq l \leq 17$	$-14 \leq h \leq 14$ $-15 \leq k \leq 15$ $-15 \leq l \leq 15$	$-13 \leq h \leq 14$ $-23 \leq k \leq 23$ $-21 \leq l \leq 20$
Fw; *F*(000)	795.82; 808	438.96; 896	686.26; 1432
T (K)	100	100	100
wavelength (Å)	1.34139	1.54178	1.34139
space group	P2$_1$/n	P2$_1$/c	P2$_1$/c
a (Å)	12.3164(7)	11.5439(4)	11.1245(4)
b (Å)	11.2308(7)	12.5404(4)	18.3974(6)
c (Å)	13.0845(8)	12.9313(5)	16.5321(6)
α (deg)	90	90	90
β (deg)	114.792(2)	93.8560(10)	102.647(2)
γ (deg)	90	90	90
Z	2	4	4
V (Å³)	1643.08(17)	1867.76(11)	3301.4(2)
ρ_{calcd} (g·cm⁻³)	1.609	1.561	1.381
μ (mm⁻¹)	8.900	4.829	4.889
θ range (deg); completeness	4.855 − 60.729; 0.999	4.918 − 72.287; 0.982	3.170 − 60.838; 1.000
collected reflections; R$_\sigma$	30737; 0.0309	50636; 0.0111	46673; 0.0388
unique reflections; R$_{int}$	3767; 0.0570	3616; 0.0298	7530; 0.0562
R1[a]; wR2[b] [I > 2σ(I)]	0.0305; 0.0793	0.0250; 0.0662	0.0500; 0.1266
R1; wR2 [all data]	0.0346; 0.0837	0.0250; 0.0662	0.0747; 0.1434
GOOF	1.086	1.151	1.023
largest diff peak and hole	0.826 and -0.520	0.415 and -0.429	0.936 and -1.418

[a] $R_1 = \Sigma(||F_o|-|F_c||)/\Sigma|F_o|$

[b] $wR_2 = \{\Sigma[w(F_o^2 - F_c^2)^2]/\Sigma[w(F_o^2)^2]\}^{1/2}$

Table S4.3: Crystal description and refinement indicators for compounds **3a·MeCN**, **3d** and **3f**.

	3a·MeCN	3d	3f
chemical formula	$C_{32}H_{42}Br_2NiO_2P_2,C_2H_3N$	$C_{36}H_{50}Br_2NiO_2P_2$	$C_{34}H_{46}Br_2NiO_2P_2$
crystal color	red	red	red
crystal size (mm)	$0.03 \times 0.05 \times 0.17$	$0.03 \times 0.10 \times 0.15$	$0.02 \times 0.04 \times 0.12$
index ranges	$-10 \le h \le 9$ $-17 \le k \le 17$ $-19 \le l \le 19$	$-16 \le h \le 17$ $-19 \le k \le 19$ $-19 \le l \le 19$	$-10 \le h \le 10$ $-29 \le k \le 28$ $-10 \le l \le 10$
Fw; *F*(000)	780.18; 800	795.23; 1640	767.18; 788
T (K)	100	100	100
wavelength (Å)	1.54178	1.54178	1.54178
space group	P-1	$P2_1/n$	$P2_1/c$
a (Å)	8.3521(4)	14.2676(4)	8.4388(3)
b (Å)	14.2132(6)	15.9314(5)	23.6016(7)
c (Å)	15.4975(6)	15.8391(5)	8.3785(2)
α (deg)	74.560(2)	90	90
β (deg)	89.119(2)	95.823(2)	93.3000(10)
γ (deg)	76.563(2)	90	90
Z	2	4	2
V (Å³)	1722.65(13)	3581.70(19)	1665.97(9)
ρ_{calcd} (g·cm⁻³)	1.504	1.475	1.529
μ (mm⁻¹)	4.643	4.467	4.780
θ range (deg); completeness	$2.962 - 72.203$; 0.972	$3.946 - 72.314$; 0.969	$3.746 - 71.983$; 1.000
collected reflections; R_σ	69751; 0.0252	94201; 0.0124	44436; 0.0135
unique reflections; R_{int}	6552; 0.0545	6811; 0.0319	3280; 0.0343
R1[a]; wR2[b] [I > 2σ(I)]	0.0449; 0.1210	0.0289; 0.0757	0.0273; 0.0767
R1; wR2 [all data]	0.0508; 0.1393	0.0328; 0.0849	0.0282; 0.0775
GOOF	1.073	1.083	1.040
largest diff peak and hole	1.076 and -0.839	0.543 and -0.372	0.444 and -0.430

[a] $R_1=\Sigma(||F_o|-|F_c||)/\Sigma|F_o|$

[b] $wR_2=\{\Sigma[w(F_o^2-F_c^2)^2]/\Sigma[w(F_o^2)^2]\}^{1/2}$

Table S4.4: Crystal description and refinement indicators for compounds **3g**, **2g** and **4·(1-naphthol)$_{0.5}$·MeCN**.

	3g	2g	4·(1-naphthol)$_{0.5}$·MeCN
chemical formula	$C_{38}H_{50}Br_2NiO_2P_2$	$C_{19}H_{24}BrNiOP$	$C_{22}H_{34}Br_2NiOP_2$,0.5($C_{10}H_8O$),C_2H_3N
crystal color	red	orange	red
crystal size (mm)	0.08 × 0.12 × 0.22	0.12 × 0.16 × 0.16	0.03 × 0.06 × 0.09
index ranges	-9 ≤ h ≤ 8	-24 ≤ h ≤ 24	-9 ≤ h ≤ 9
	-29 ≤ k ≤ 29	-10 ≤ k ≤ 10	-25 ≤ k ≤ 22
	-25 ≤ l ≤ 25	-27 ≤ l ≤ 27	0 ≤ l ≤ 16
Fw; ***F*(000)**	819.25; 1688	437.97; 1792	1416.19; 1448
***T* (K)**	100	100	100
wavelength (Å)	1.54178	1.54178	1.54178
space group	P2$_1$/n	P2$_1$/c	P-1
***a* (Å)**	7.63420(10)	19.5581(9)	7.5432(4)
***b* (Å)**	23.8674(3)	8.5915(4)	20.8491(9)
***c* (Å)**	20.5333(3)	22.5262(10)	21.6672(9)
α (deg)	90	90	117.132(2)
β (deg)	100.0170(10)	94.129(2)	90.463(3)
γ (deg)	90	90	93.294(3)
Z	4	8	2
***V* (Å^3)**	3684.31(9)	3775.3(3)	3025.3(2)
ρ$_{calcd}$ (g·cm^{-3})	1.477	1.541	1.555
μ (mm^{-1})	4.362	4.761	5.207
θ range (deg); completeness	2.864 − 71.703; 0.973	2.265 − 72.213; 0.998	2.293 − 72.207; 0.999
collected reflections; R$_σ$	93962; 0.0088	151698; 0.0095	76847; 0.0653
unique reflections; R$_{int}$	6979; 0.0229	7419; 0.0298	11784; 0.1309
R1^a; wR2^b [I > 2σ(I)]	0.0226; 0.0584	0.0337; 0.0899	0.0933; 0.2534
R1; wR2 [all data]	0.0229; 0.0595	0.0338; 0.0901	0.1196; 0.2882
GOOF	1.087	1.136	1.077
largest diff peak and hole	0.464 and -0.263	0.995 and -0.493	3.149 and -1.529

[a] $R_1 = \Sigma(||F_o|-|F_c||)/\Sigma|F_o|$

[b] $wR_2 = \{\Sigma[w(F_o^2 - F_c^2)^2]/\Sigma[w(F_o^2)^2]\}^{1/2}$

Table S4.5: Crystal description and refinement indicators for compounds **4, (i-Pr₂PH)₂NiBr₂** and **5·(2-Et-1-naphthol)₀.₅**.

	4	*cis*-(*i*-Pr₂PH)₂NiBr₂	5·(2-Et-1-naphthol)₀.₅
chemical formula	$C_{22}H_{34}Br_2NiOP_2$	$C_{12}H_{30}Br_2NiP_2$	$C_{18}H_{25}O_2P,0.5(C_{12}H_{12}O)$
crystal color	red	red	colorless
crystal size (mm)	0.05 × 0.12 × 0.17	0.05 × 0.08 × 0.17	0.04 × 0.07 × 0.09
index ranges	-13 ≤ h ≤ 11	-15 ≤ h ≤ 16	-21 ≤ h ≤ 21
	-15 ≤ k ≤ 15	-8 ≤ k ≤ 8	-9 ≤ k ≤ 9
	-22 ≤ l ≤ 22	-23 ≤ l ≤ 23	-20 ≤ l ≤ 20
Fw; *F*(000)	594.96; 1208	454.83; 920	390.46; 840
T (K)	100	100	100
wavelength (Å)	1.54178	1.54178	1.54178
space group	P2₁/n	C2/c	P2₁/c
a (Å)	11.1754(2)	13.1534(6)	17.4429(4)
b (Å)	12.3946(2)	7.2342(3)	7.3405(2)
c (Å)	18.0438(2)	19.1350(9)	16.6284(4)
α (deg)	90	90	90
β (deg)	103.0810(10)	97.951(2)	90.5770(10)
γ (deg)	90	90	90
Z	4	4	4
V (Å³)	2434.47(7)	1803.27(14)	2128.99(9)
ρ_calcd (g·cm⁻³)	1.623	1.675	1.218
μ (mm⁻¹)	6.313	8.256	1.281
θ range (deg); completeness	4.266 − 71.599; 0.970	7.232 − 72.139; 0.985	2.533 − 72.057; 1.000
collected reflections; R_σ	61151; 0.0085	16283; 0.0165	40499; 0.0158
unique reflections; R_int	4608; 0.0218	1749; 0.0327	4172; 0.0323
R1[a]; wR2[b] [I > 2σ(I)]	0.0194; 0.0507	0.0194; 0.0536	0.0411; 0.1142
R1; wR2 [all data]	0.0195; 0.0511	0.0194; 0.0537	0.0450; 0.1186
GOOF	1.140	1.135	1.044
largest diff peak and hole	0.347 and -0.247	0.491 and -0.289	0.362 and -0.233

[a] $R_1=\Sigma(||F_o|-|F_c||)/\Sigma|F_o|$

[b] $wR_2=\{\Sigma[w(F_o^2-F_c^2)^2]/\Sigma[w(F_o^2)^2]\}^{1/2}$

Table S4.6: Crystal description and refinement indicators for compounds **5·HBr** and **2f**.

	5·HBr	**2f**
chemical formula	Br,C$_{18}$H$_{26}$O$_2$P	C34H44Br2Ni2O2P2
crystal color	colorless	orange
crystal size (mm)	0.05 × 0.09 × 0.23	0.04 × 0.06 × 0.10
index ranges	-8 ≤ h ≤ 8 -18 ≤ k ≤ 17 -11 ≤ l ≤ 11	-12 ≤ h ≤ 12 -13 ≤ k ≤ 13 -19 ≤ l ≤ 19
***Fw*; *F*(000)**	385.27; 400	823.87; 840
***T* (K)**	100	100
wavelength (Å)	1.54178	1.54178
space group	P2$_1$	P2$_1$/n
***a* (Å)**	7.00080(10)	9.9076(5)
***b* (Å)**	14.6572(3)	11.2488(5)
***c* (Å)**	8.9994(2)	16.0069(8)
α (deg)	90	90
β (deg)	100.9820(10)	103.065(2)
γ (deg)	90	90
Z	2	2
***V* (Å^3)**	906.54(3)	1737.77(15)
ρ$_{calcd}$ (g·cm^{-3})	1.411	1.575
μ (mm^{-1})	3.954	5.130
θ range (deg); completeness	5.848 − 71.841; 0.988	4.813 − 72.091; 0.992
collected reflections; R$_\sigma$	23056; 0.0169	38646; 0.0138
unique reflections; R$_{int}$	3428; 0.0212	3373; 0.0317
R1^a; wR2^b [I > 2σ(I)]	0.0173; 0.0462	0.0215; 0.0543
R1; wR2 [all data]	0.0173; 0.0462	0.0233; 0.0556
GOOF	1.060	1.053
largest diff peak and hole	0.410 and -0.214	0.374 and -0.358

[a] **R$_1$=Σ(||F$_o$|-|F$_c$||)/Σ|F$_o$|**

[b] **wR$_2$={Σ[w(F$_o$^{2}–F$_c$^{2})^2]/Σ[w(F$_o$^{2})^2]}^{½}**

S4.7 Additional Thermal Ellipsoid Plots
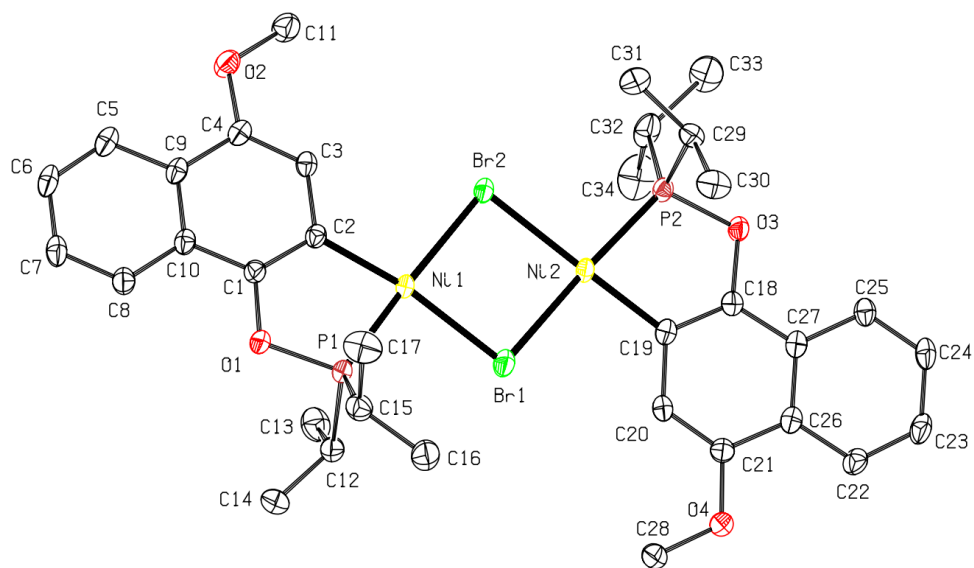
Figure S4.164: Top view of the molecular diagram for complex **2b**. Thermal ellipsoids are shown at the 50% probability level; hydrogen atoms are omitted for clarity.
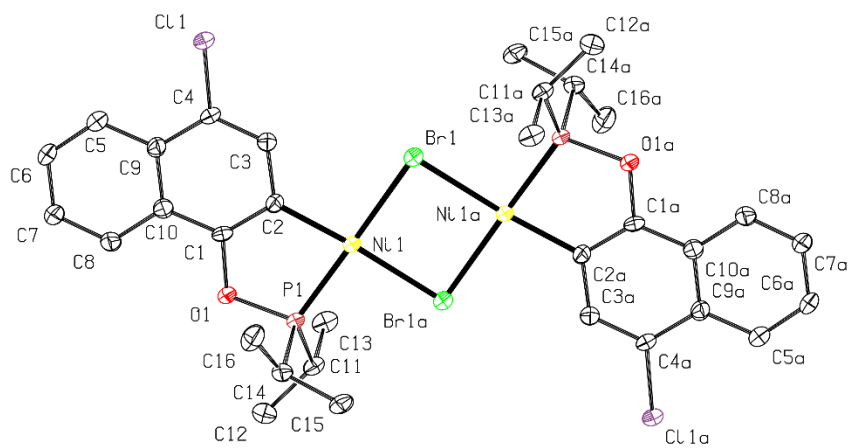
Figure S4.165: Top view of the molecular diagram for complex **2c**. Thermal ellipsoids are shown at the 50% probability level; hydrogen atoms are omitted for clarity.
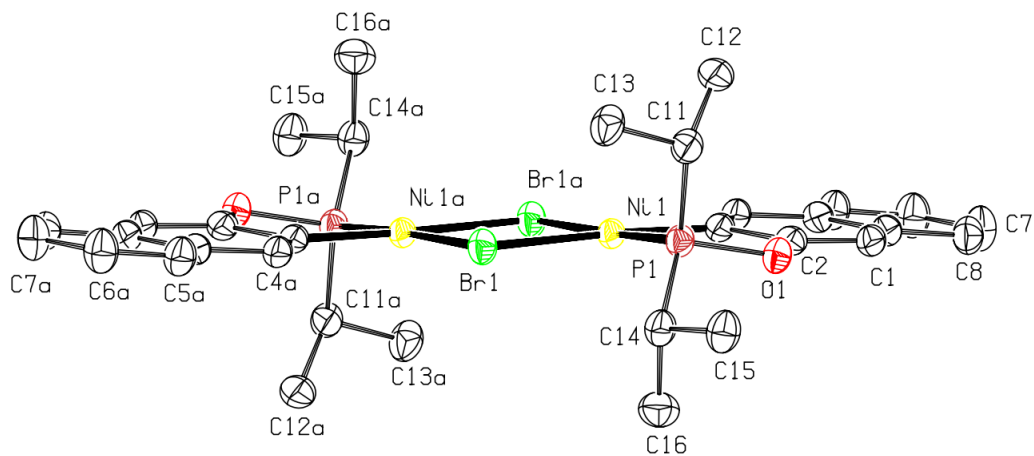
Figure S4.166: Side view of the molecular diagram for complex **2e**. Thermal ellipsoids are shown at the 50% probability level; hydrogen atoms are omitted for clarity.
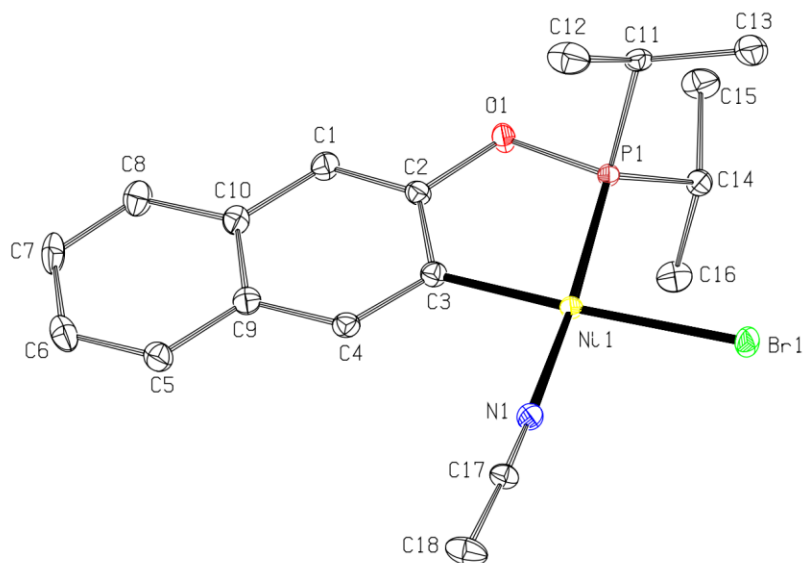
Figure S4.167: Molecular diagram for complex **2e-NCMe**. Thermal ellipsoids are shown at the 50% probability level; hydrogen atoms are omitted for clarity.
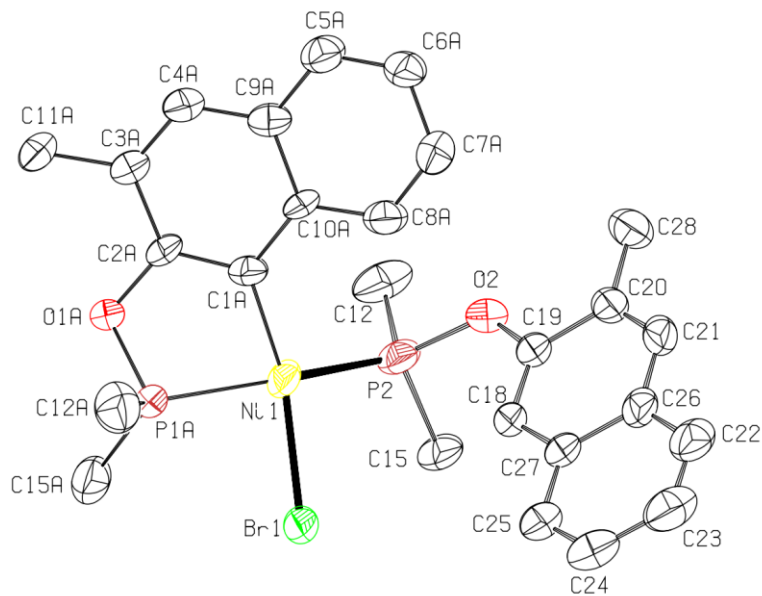
Figure S4.168: Top view of the molecular diagram for complex **2f-L**. Thermal ellipsoids are shown at the 50% probability level; hydrogen atoms and terminal methyls for P substituents are omitted for clarity.
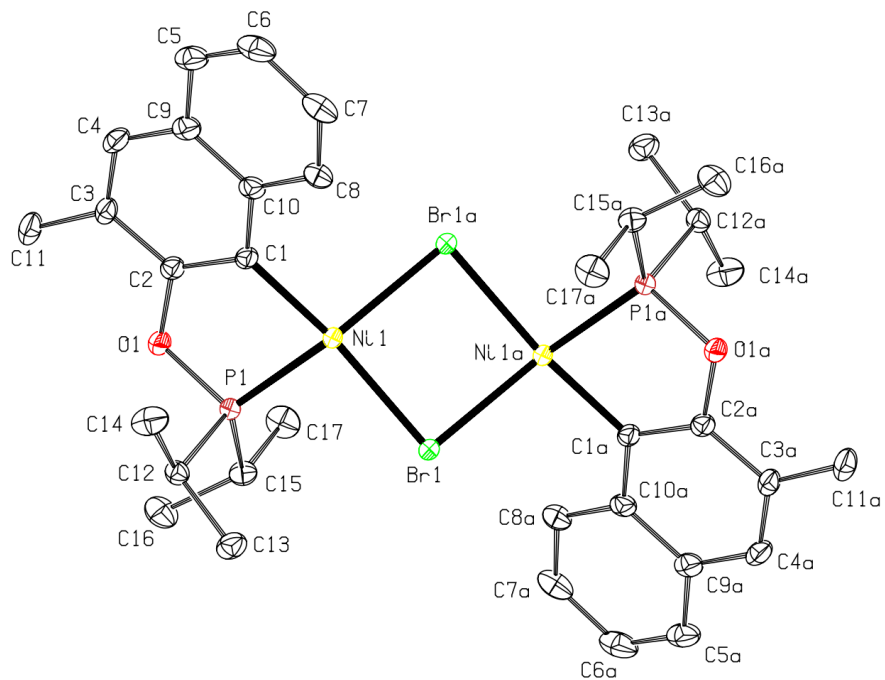
Figure S4.169: Top view of the molecular diagram for complex **2f**. Thermal ellipsoids are shown at the 50% probability level; hydrogen atoms are omitted for clarity.
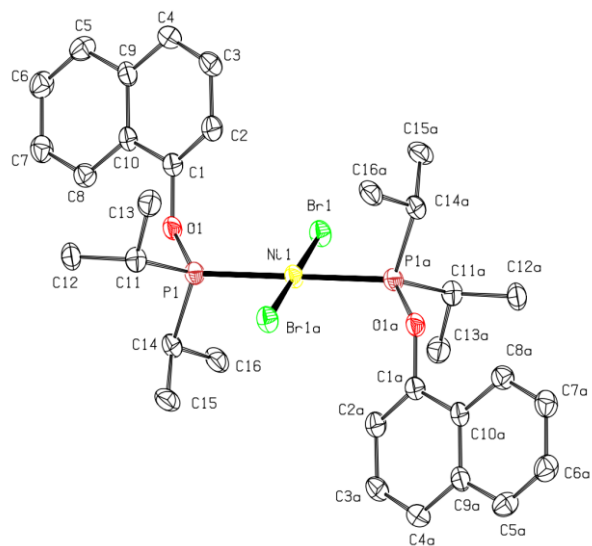
Figure S4.170: Molecular diagram for complex **3a·CH₃CN**. Thermal ellipsoids are shown at the 50% probability level; hydrogen atoms and co-crystallized CH₃CN molecule are omitted for clarity.
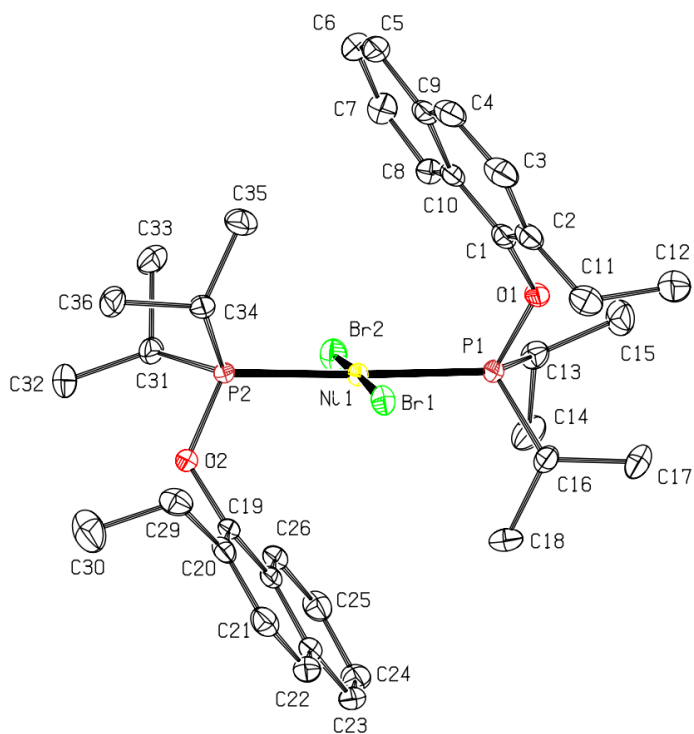
Figure S4.171: Molecular diagram for complex **3d**. Thermal ellipsoids are shown at the 50% probability level; hydrogen atoms are omitted for clarity.
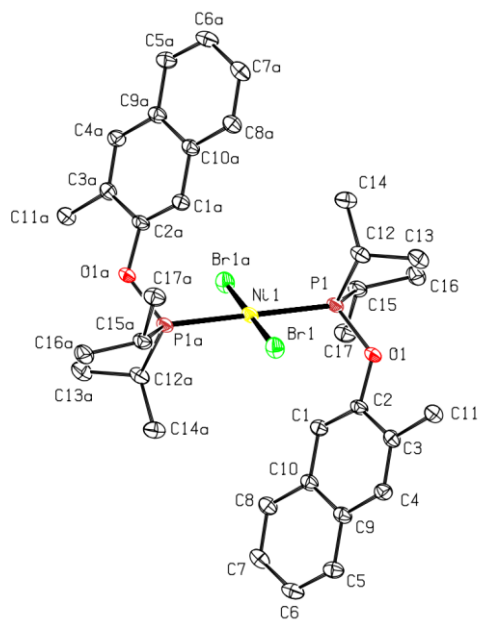
Figure S4.172: Molecular diagram for complex **3f**. Thermal ellipsoids are shown at the 50% probability level; hydrogen atoms are omitted for clarity.
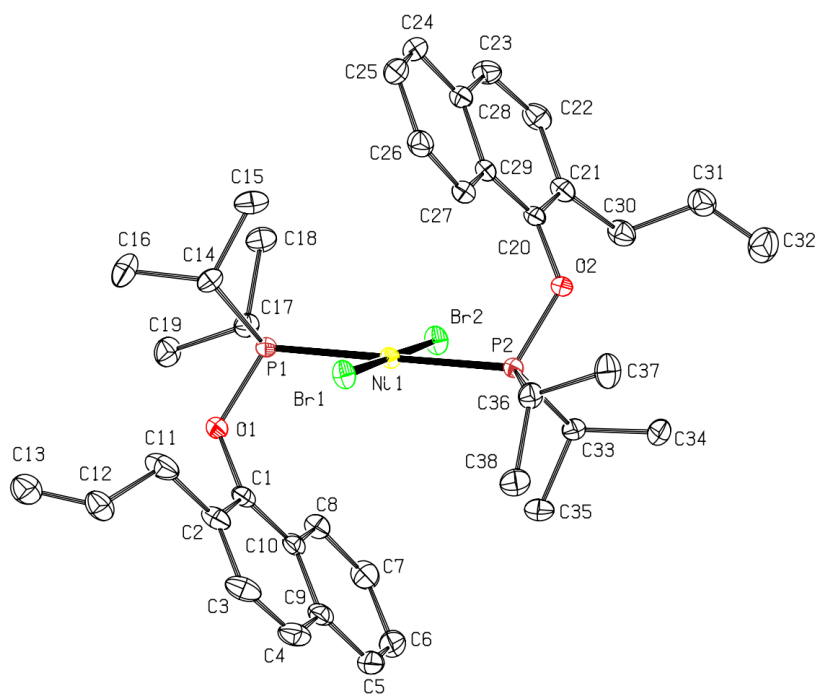
Figure S4.173: Molecular diagram for complex **3g**. Thermal ellipsoids are shown at the 50% probability level; hydrogen atoms are omitted for clarity.

369
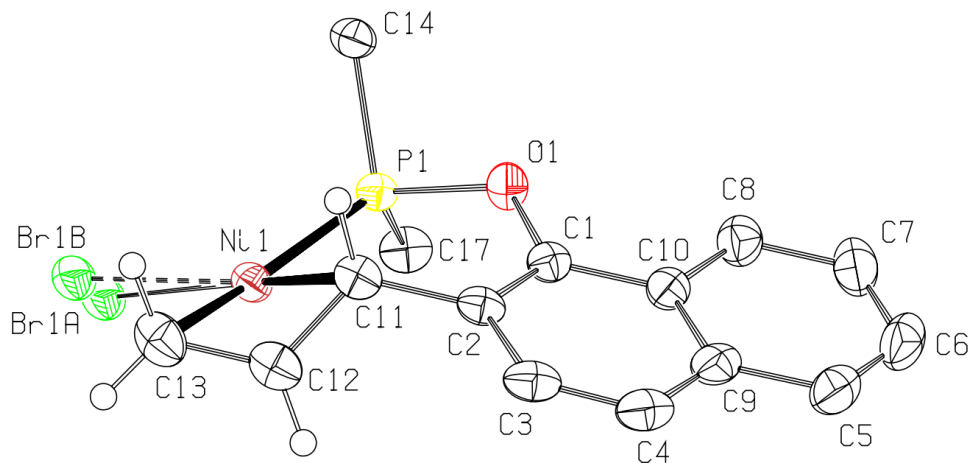
Figure S4.174: Side view of the molecular diagram for complex **2g**. Thermal ellipsoids are shown at the 50% probability level; non-allylic hydrogen atoms and methyl groups of the P substituents are omitted for clarity.
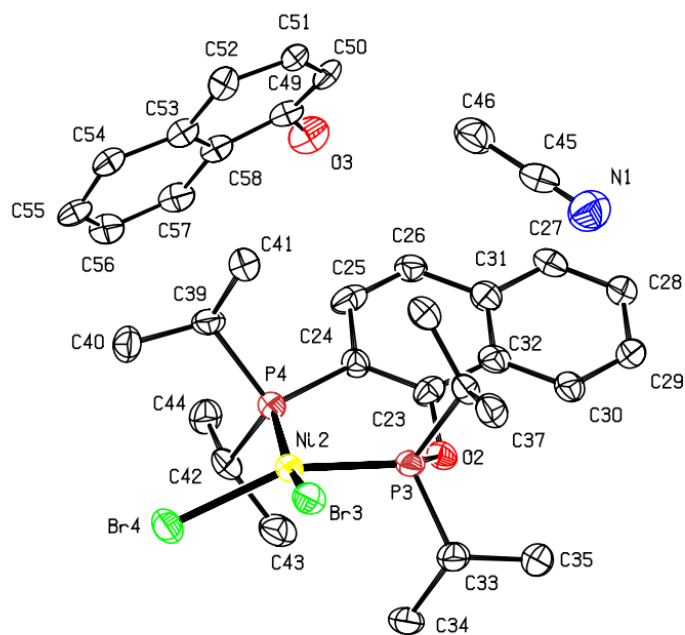
Figure S4.175: Molecular diagram for compound **4·(1-naphthol)₀.₅·MeCN**. Thermal ellipsoids are shown at the 50% probability level; hydrogen atoms are omitted for clarity.
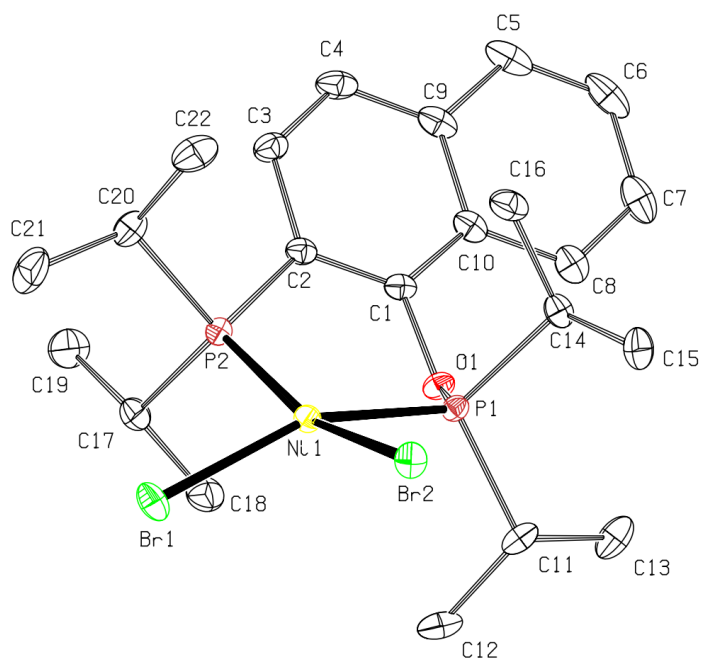
Figure S4.176: Other view the molecular diagram for complex **4**. Thermal ellipsoids are shown at the 50% probability level; hydrogen atoms are omitted for clarity.
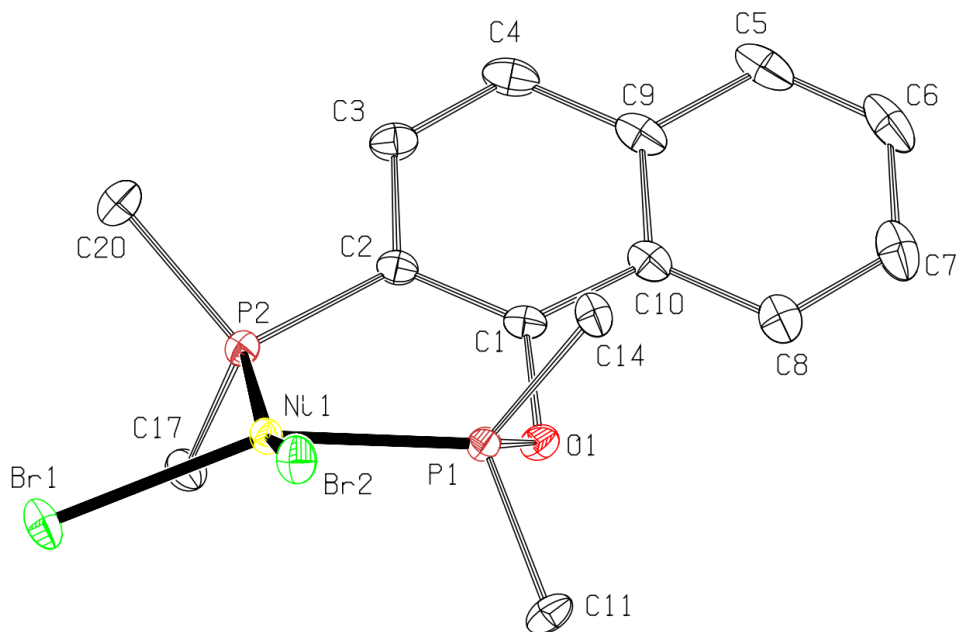
Figure S4.177: Side view (I) of the molecular diagram for complex **4**. Thermal ellipsoids are shown at the 50% probability level; hydrogen atoms and methyl groups of the P substituents are omitted for clarity.
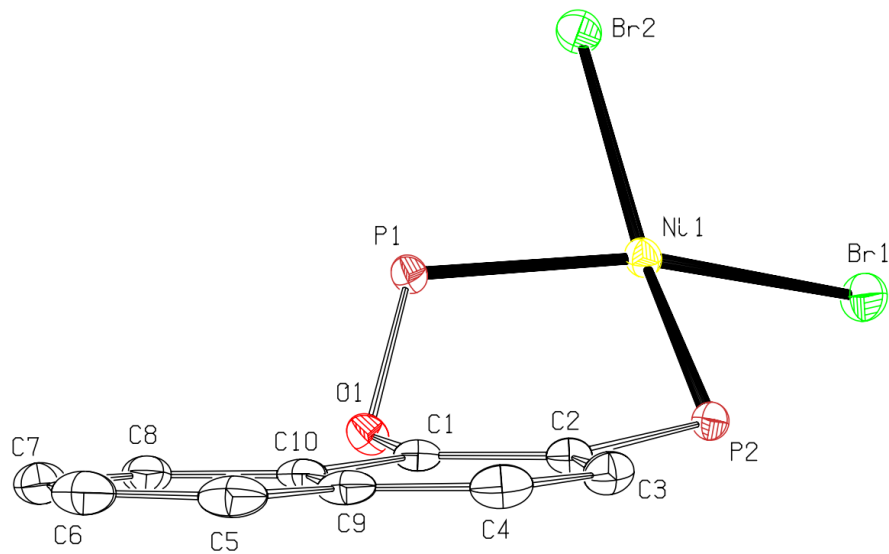
Figure S4.178: Side view (II) of the molecular diagram for complex **4**. Thermal ellipsoids are shown at the 50% probability level; hydrogen atoms and P substituents are omitted for clarity.
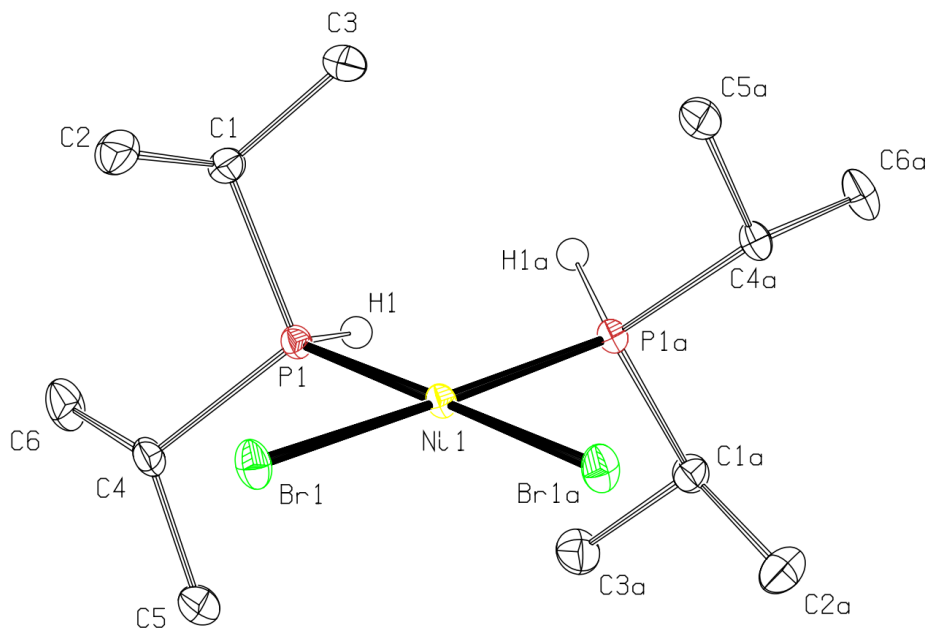
Figure S4.179: Molecular diagram for complex *cis*-(*i*-Pr₂PH)2NiBr2. Thermal ellipsoids are shown at the 50% probability level; alkyl hydrogen atoms are omitted for clarity.
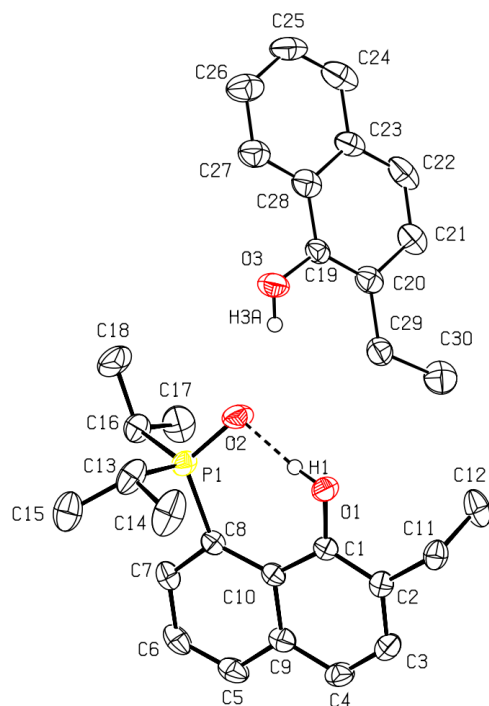
Figure S4.180: Molecular diagram for compound **5·(2-Et-1-naphthol)**$_{0.5}$. Thermal ellipsoids are shown at the 50% probability level; non protic hydrogens are omitted for clarity
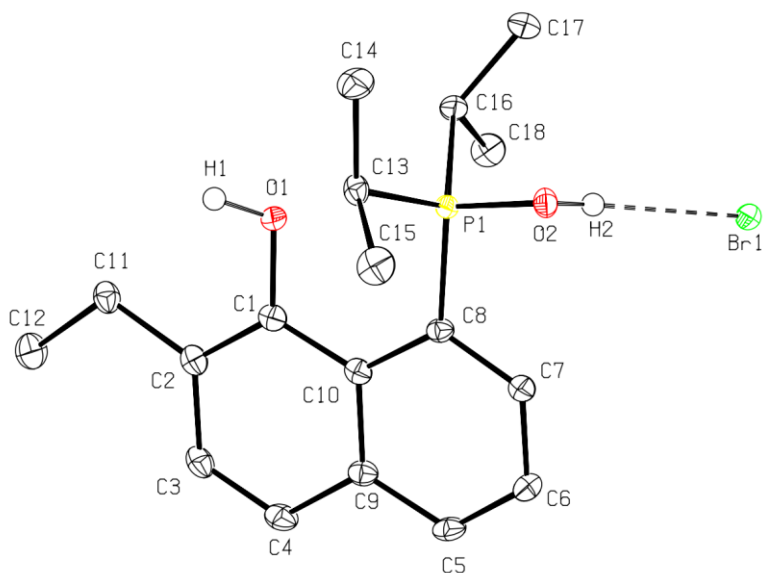
Figure S4.181: Molecular diagram for compound **5·HBr**. Thermal ellipsoids are shown at the 50% probability level; non protic hydrogens are omitted for clarity.

Chapitre 5 – A Versatile Umpolung Strategy for the Synthesis of New POC$_{sp^3}$E-Type Pincer Complexes of Nickel

Loïc P. Mangin[a], Guillaume Michaud[a] and Davit Zargarian[a]*

[a] Département de Chimie, Université de Montréal, Montréal, Canada H3T 1J4

Contributions :

Loïc P. Mangin : Conception du projet, Synthèse et caractérisation, Rédaction du manuscrit.

Guillaume Michaud : Optimisation de la synthèse du complexe **4** et exploration des différents nucléophiles.

5.1 Abstract

ECE-type pincer complexes have evolved into a diverse family of compounds possessing interesting structural/bonding features, reactivities, and practical applications. An important factor promoting the growth of pincer chemistry is the availability of versatile synthetic pathways that give access to ever-diverse pincer complexes. This report describes a new approach for the synthesis of pincer-Ni complexes possessing interesting structural features: a central Ni-C_{sp^3} linkage, two different peripheral donor moieties, and two differently sized metalacycles. The synthetic methodology reported herein is based on the reactivity of a substrate derived from 2-vinylphenol. Stirring the substrate 2-CH_2=CH-C_6H_4-OP(i-Pr)$_2$, **1**, with the Ni^{II} precursor {(i-PrCN)NiBr$_2$}$_n$ and Et$_3$N at room temperature gave the new 6,5-POC$_{sp^3}$PO-type pincer complex {$\kappa^O,\kappa^C,\kappa^P$-2-[OP($i$-Pr)$_2CH_2$CH]-$C_6H_4$-OP($i$-Pr)$_2$}NiBr, **2**. In addition to a Ni-C_{sp^3} moiety, this complex has phosphine-oxide and phosphinite donor moieties that define 6- and 5-membered metalacycles, respectively. It is interesting to note that the formation of **2** is hindered in the presence of an excess of **1**, the reaction giving instead the nickelacyclopropane complex {$\kappa^C,\kappa^{C'},\kappa^P$-2-[2-vinyl-$C_6H_4$-OP($i$-Pr)$_2$CHCH]-$C_6H_4$-OP($i$-Pr)$_2$}NiBr, **3**. Tests showed that formation of **2** and **3** involves a nucleophilic attack on the π-olefin moiety of the intermediate adduct ($\kappa^C,\kappa^{C'},\kappa^P$-**1**)NiBr$_2$ by the phosphinite moiety of a second, uncoordinated **1**. This generates a zwitterionic intermediate featuring new Ni-C_{sp^3} and P-C_{sp^3} bonds formed with the α and β carbons, respectively, of the vinyl moiety in **1**. This intermediate would then lead to complex **2** as the kinetic product via a reversible reaction with Et$_3$N, whereas complex **3** would be the thermodynamic product of the process. An altogether different reactivity is observed when the reaction of **1** with (i-PrCN)NiBr$_2$ and Et$_3$N is conducted in the presence of a second, stronger nucleophile. For instance, with HNR(R') as nucleophile we obtained the new 6,4-POC$_{sp^3}$N-type pincer complexes {$\kappa^N,\kappa^C,\kappa^P$-2-[NR(R')CH$_2$CH]-$C_6H_4$-OP($i$-Pr)$_2$}NiBr (NR(R')= N-morpholyl, **4**; NPh(Et), **5**; NH(i-Pr), **6**; NH(Ph), **7**; NH(Cy), **8**; NH(t-Bu), **9**) that have phosphinite and amine donor moieties defining 6- and 4-membered metalacycles, respectively. Analogous reactions with HPR$_2$ as the nucleophile led to 6,4-POC$_{sp^3}$P-type pincer complexes {$\kappa^P,\kappa^C,\kappa^{P'}$-2-[R$_2PCH_2$CH]-$C_6H_4$-OP($i$-Pr)$_2$}NiBr (R= Ph, **10**; i-Pr, **11**) having a phosphine and phosphinite donor moieties defining 6- and 4-membered metalacycles, respectively. Single crystal diffraction studies have established the solid-state structures of complexes **2-11**. Cyclic voltammetry measurements on complexes **2**, **4-6**, **10** and **11** have shown that these pincer-Ni complexes undergo facile one-electron oxidation.

5.2 Introduction

Since its inception more than four decades ago,[1] the field of pincer chemistry has evolved rapidly and made major contributions in diverse areas of application, including homogeneous and heterogeneous catalysis,[2] and preparation of functional materials.[3] A key element in the rapid development of pincer chemistry has been the successful elaboration of efficient synthetic strategies that have paved the way to a diverse array of different ligand platforms based on aromatic or aliphatic backbones. These synthetic methodologies have thus provided access to a variety of classical or novel pincer complexes featuring symmetrical and unsymmetrical architectures, different peripheral and central donor moieties, and different metallacycle sizes. This diversity has led, in turn, to the discovery of unique reactivities and properties that are the general hallmarks of pincer complexes today.[4]

By and large, the most commonly used synthetic strategy for the preparation of ECE-type tridentate, monoanionic pincer ligands rests on the activation/metalation of C-H or C-X bonds in EC(H)E- or EC(X)E-type proligands, respectively. Classical examples of this strategy include Shaw's synthesis of (PCP)NiCl from the PC(H)P-type proligands $1,3-(R_2PCH_2)_2C_6H_4$ via C-H nickelation (**Scheme 5.1**, **A**),[1a] and van Koten's synthesis of (NCN)ML complexes from the NC(X)N-type proligand $1,3-(Me_2NCH_2)_2,2-X-C_6H_3$ via Ar-X oxidative addition (X= Br or I, **Scheme 5.1**, **B**)[5] or transmetalation with Ar-Li[6] or Ar-AuL[7] (**Scheme 5.1**, **C** and **D**).

Scheme 5.1. Classical synthetic strategies for preparation of ECE-type pincer complexes based on a m-phenylene ligand platform.
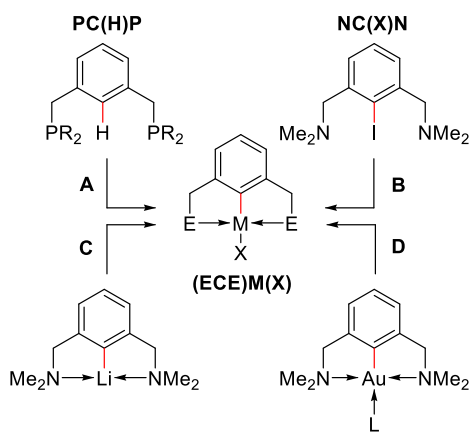
The success of synthetic routes based on activation/metalation of C-H bonds depends on many factors, including the nature of the donor moieties, the ligand backbone, and the type of metal precursor used. For instance, PCP-type pincer complexes of nickel are accessible via relatively facile C-H nickelation reactions with *m*-phenylene type proligands mentioned above (**Scheme 5.1**, **A**).[8] In contrast, analogous proligands featuring two amine moieties are much less amenable to pincer formation via C-H nickelation.[9] Moreover, C-H nickelation is generally more difficult with aliphatic proligands, even when they feature phosphine- or phosphinite-type donor groups. For instance, the aliphatic proligands $1,3\text{-}(R_2PO)_2\text{-}(CH_2)_3$ and $1,5\text{-}(R_2P)_2\text{-}(CH_2)_5$ require more forcing conditions to undergo C-H metalation in comparison to their counterparts based on *m*-phenylene backbones.[10] Although these limitations have not hindered the development of pincer-Ni systems, it would be advantageous to develop a synthetic strategy that sidesteps the (often-significant) barriers to C-H activation/metalation steps.

This report describes one such strategy that involves addition of nucleophiles to an olefin moiety coordinated to a divalent nickel precursor. This new synthetic methodology was discovered during our investigations on the C-H nickelation of phenyl and naphthyl phosphinites. Earlier studies had shown that in most cases nickelation of these substrates occurs regioselectively at the unsubstituted C−H moiety *ortho* to the OPR$_2$ position; moreover, *ortho* substituents were found to be largely inert to nickelation.[11] This regioselectivity is exemplified by the nickelation of 2-R-phenyl-OP(*i*-Pr)$_2$ (R= Me, Ph) and 3-Me-2-naphthyl-OP(*i*-Pr)$_2$, illustrated in **Scheme 5.2** (**A** and **B**).[12]

Scheme 5.2. Cyclonickelation of phosphinites derived from phenols and naphthols.
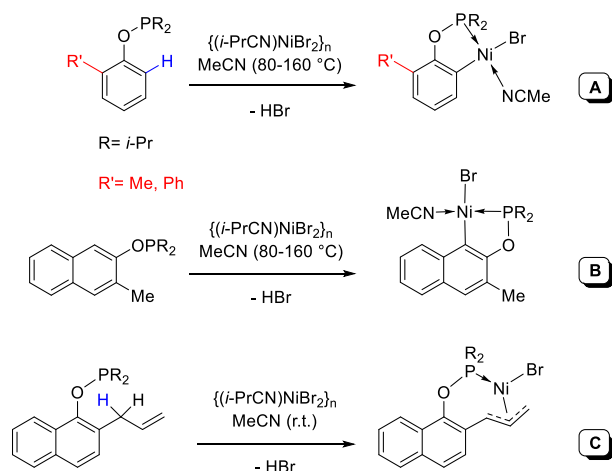
The only exception to the above-stated general trend, *i.e.* the only case wherein nickelation of a *substituent* C_{sp^3}−H moiety occurs in preference over reactivity at the C8-H aromatic proton, was observed with 2-allyl-1-naphthyl-OP(*i*-Pr)$_2$ (**Scheme 5.2**, **C**).[13] Indeed, the α C-H moiety in the allyl substituent of this substrate undergoes very facile nickelation (at room temperature), which is in stark contrast to the requirement of high temperatures (80-160 °C) for the nickelation of the aromatic C−H moieties in most phenyl and naphthyl phosphinites.[14] This observation prompted us to examine the reactivity of alkenyl-substituted aryl phosphinites to determine whether C−H nickelation would occur on the alkenyl substituent or the aryl ring. As will be described herein, studying the reactivities of the vinyl-substituted phenyl phosphinite 2-CH$_2$=CH-C$_6$H$_4$-OP(*i*-Pr)$_2$, **1**, led to the development of a new synthetic route that allows the facile formation of novel families of unsymmetrical pincer complexes without going through a C-H activation/metalation step.

5.3 Results and discussion

5.3.1 Initial exploration of the reactivity of 2-vinyl-phenylphosphinite

We began the present study by preparing our target substrate **1** and examining its reactivity under the conditions used for our previous nickelation studies.[11-13] Thus, **1** was treated in acetonitrile with {(*i*-PrCN)NiBr$_2$}$_n$ and Et$_3$N (molar ratio of 1:1.2:1.2), and the reaction progress was monitored by NMR. ^{31}P NMR analysis of the greenish mixture obtained after 2 h of stirring at room temperature showed that the initial signal for **1** had been replaced almost completely by two new ^{31}P resonances at ca. 103 and 202 ppm. The chemical shift of the latter signal was close to that observed for the π–allyl complex shown in **Scheme 5.2** (**C**, 201 ppm), thus hinting that nickelation might have occurred at the vinyl C−H moiety. However, the 1:1 intensity ratio of the new peaks suggested the formation of a complex bearing two different *P*-bearing moieties.

In order to isolate the product of the above reaction and characterize it unambiguously, we worked-up the reaction mixture as follows. Evaporation of the reaction solvent and extraction with toluene yielded an orange solution that displayed two ^{31}P peaks at 94 and 205 ppm in a 1:1 ratio; this mixture also contained ca. 15-20%[15] of the unreacted bis-phosphinite complex (**1**)$_2$NiBr$_2$. Evaporation of this toluene solution, followed by extraction of the residues in Et$_2$O and cooling the

379

ethereal extract to –35 °C afforded deep red crystals. The ^{31}P NMR (CDCl$_3$) of these crystals displayed two very weakly coupled doublets at 94 and 206 ppm ($J_{PP'}$ = 3 Hz), and XRD analysis revealed an unexpected product, the unsymmetrical ECE'-type pincer complex **2** shown in **Scheme 5.3**.

Scheme 5.3. Unanticipated formation of POCP(O)-NiBr pincer complex **2** and its molecular diagram.[a]
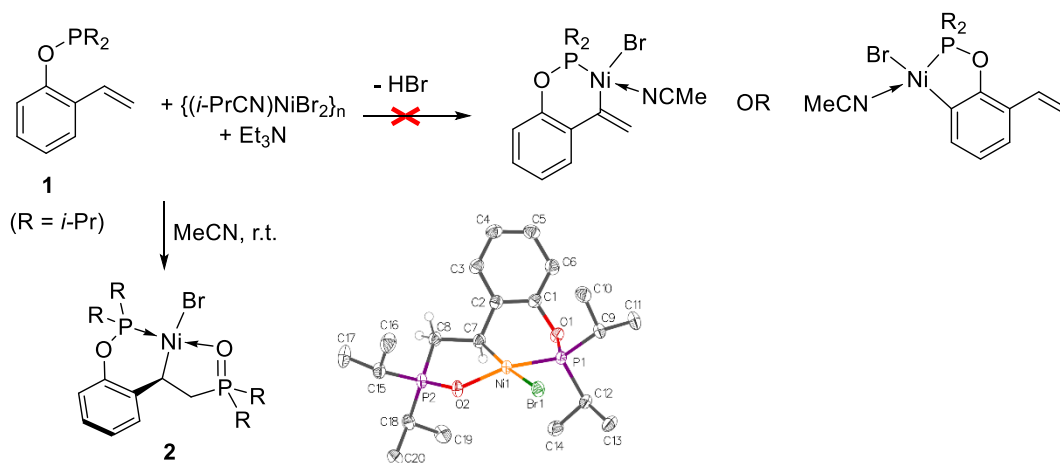
[a] Thermal ellipsoids are shown at the 50% probability level, and hydrogen atoms refined via the riding model and terminal Me substituents of P(*i*-Pr)$_2$ moieties are omitted for clarity.

The main structural parameters for complex **2** (and all the other solid-state structures presented herein) will be presented and discussed fully in the last section of this report. For now, it is worth noting that this complex features two metallacycles, a 6-membered ring formed by the coordination of the original phosphinite moiety in **1**, and a 5-membered ring defined by a newly formed phosphine oxide donor moiety. The latter originates from a second equivalent of **1** via a rearrangement that results in the expulsion of its aryl fragment. The overall transformation of **1** into **2** also converts the sp^2-hybridized α-C of the vinyl substituent in **1** into the sp^3-hybridized central carbon moiety of the new 6,4-POC$_{sp^3}$P(O)-type pincer complex. Hence, no net C−H nickelation has taken place during the formation of this unsymmetrical pincer complex.

The above considerations allowed us to envisage the following speculative scenario for the formation of **2**. First, π–coordination of the vinyl moiety in **1** to the Ni^{II} center would give an intermediate complex featuring a chelating phosphinite/vinyl ligand, as shown in **Scheme 5.4** (step

A). The coordinated vinyl moiety would thus become susceptible to an outer-sphere nucleophilic attack by a second equiv of **1**; this attack would generate two new bonds, one between the α-C and the Ni center and the other between the β-C and the phosphinite P (step B in **Scheme 5.3**). A subsequent SN$_{Ar}$-type nucleophilic attack by a bromide anion on the *ipso* carbon of the aryl ring of the newly generated phosphonium moiety would then break the Ar-O bond to generate the P(=O) moiety (step C in **Scheme 5.4**).

Scheme 5.4. Proposed mechanism for the formation of complex **2**.
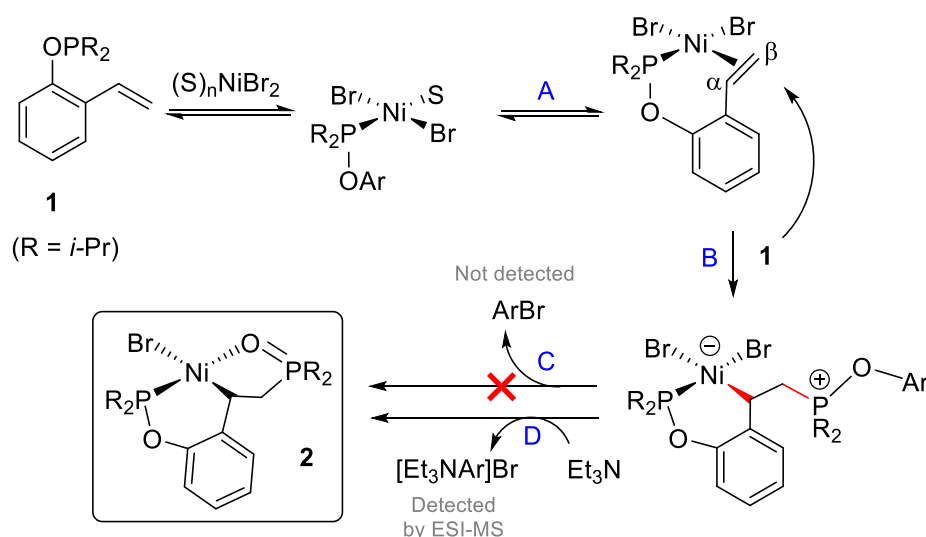
Although the sequence of steps illustrated in **Scheme 5.4** seemed feasible at first, subsequent tests generated a number of observations that cast doubt on the validity of step C in this transformation. First, the proposed SN$_{Ar}$-type nucleophilic attack by Br$^-$ resulting in the P(=O) moiety should have led to the concomitant formation of 2-Br-styrene, but GC-MS analysis of the final reaction mixture showed no trace of this by-product. Second, the proposed mechanism envisages no role for Et$_3$N, and yet a few experiments helped establish that a stoichiometric amount of Et$_3$N is necessary for the formation of **2**. For instance, treating **1** with 1.2 equiv {(*i*-PrCN)NiBr$_2$}$_n$ in the absence of Et$_3$N failed to give any conversion to **2**, even after 20 h, whereas the analogous reaction in the presence of 0.10 equiv of base led to partial conversion. And finally, stirring an acetonitrile mixture of **1**, {(*i*-PrCN)NiBr$_2$}$_n$, and Et$_3$N (1:1.2:1) for 2 h followed by ESI-MS analysis of the crude reaction mixture allowed us to detect the ammonium species [(2-vinylphenyl)NEt$_3$]Br at M$^+$ and [(2-vinyl-

381

phenyl)NEt$_3$]$_2$Br at [M-1]$^+$ (See **Figs. S5.1 and S5.2**). Altogether, these observations suggested that a stoichiometric amount of base is required for the reaction under discussion. We believe that the role of Et$_3$N is to promote the cleavage of the Ar-O bond required for the formation of the P(=O) moiety (step D in **Scheme 5.4)**.

Another aspect of the mechanism proposed in **Scheme 5.4** was puzzling at first: although the mechanism requires 2 equiv of substrate **1** relative to the metal precursor and Et$_3$N, tests showed that using more than 1 equiv of substrate slows down the formation of **2**. For instance, ^{31}P NMR monitoring of a reaction mixture containing 2 equiv of **1** (acetonitrile, room temperature) showed a much slower conversion of **1** to **2**, such that significant amounts of **1** remained in the reaction mixture even after 20 h. Similarly, a much slower reaction was observed when the reaction of **1** with the nickel precursor and Et$_3$N was conducted in THF instead of acetonitrile, either with 1 or 2 equiv of substrate.

The above observations were reminiscent of a phenomenon we had encountered during the course of our previous studies on the cyclonickelation of phenyl-phosphinites, namely: the nickelation of aryl phosphinites proceeded more slowly in the presence of 2 equiv of substrate due to the formation of less reactive bis-phosphinite intermediates. Using less polar solvents (THF, toluene, or Et$_2$O instead of acetonitrile) also had a similar impact even when 1 equiv of phosphinite substrate was present. We conclude, therefore, that the slower conversion of **1** to **2** in the presence of excess substrate, or when the reaction is run in less polar solvents, is also caused by the formation of the bis-phosphinite intermediate (**1**)$_2$NiBr$_2$.

An unexpected and interesting side-reaction was also observed during the above-noted experiments in the presence of 2 equiv of substrate, or when the reaction was conducted in less polar solvents. Thus, monitoring the reaction of **1** with the Ni precursor and Et$_3$N (2:1:1; acetonitrile; r.t.) showed the emergence of a second set of ^{31}P resonances in addition to those attributed to **2**. The observation of broad new resonances fairly close to those of **2** (i.e.,around 97 and 210 ppm vs. 103 and 202 ppm for **2** in MeCN) indicated the formation of a structurally similar side-product. Evaporation of this acetonitrile sample and extraction of the residues with THF caused these new resonances to appear at 78 and 195 ppm. (vs. 94 and 204 ppm for **2** in THF). Evaporation of the THF solution and extraction of the residues into Et$_2$O followed by cooling gave two sets of crystals that were

identified by XRD analyses as **2** (deep-red crystals) and the new zwitterionic complex **3** (**Scheme 5.5**) co-crystallized with **2** (bright orange crystals).

Scheme 5.5. Proposed mechanism leading to complex **3**.
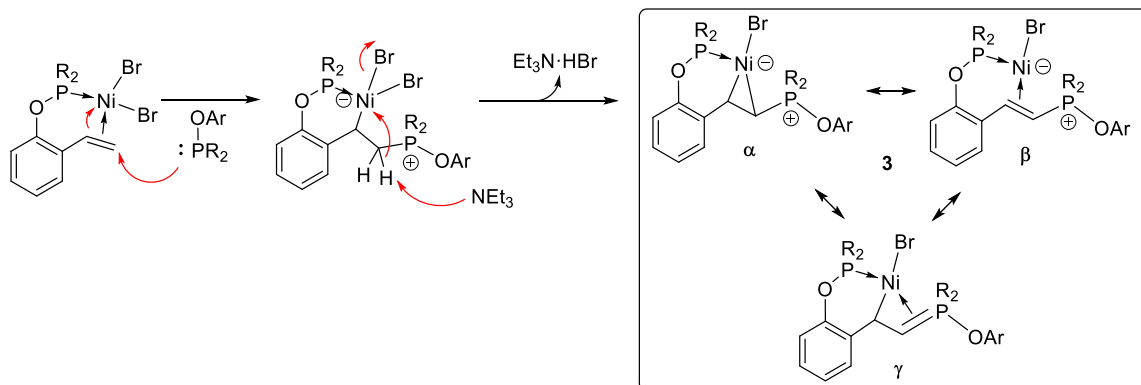
We propose that complex **3** forms via the same cationic intermediate that leads to **2**, i.e., the species arising from the nucleophilic attack by **1** on the complex bearing the chelating ligand (**Scheme 5.5**). The pathway leading to **3** involves a subsequent deprotonation of the proton adjacent to the phosphonium site. The structural discussion, which is presented later on in this report, will address the contributions of the three canonical representations of complex **3**, as illustrated in **Scheme 5.5**. The resonance structure **γ** featuring an ylide moiety is in theory possible, but the distance between the phosphorus and the metal center of > 3 Å in **3** rules out any P-Ni interaction. We conclude, therefore, that the zwitterionic species **α** and **β** are more likely to describe this complex. The ^{1}H and ^{13}C NMR spectra of **3** (**Figures S5.29 – S5.41**) indicate that the **α** form shown in **Scheme 5.5** and featuring a nickelacyclopropane moiety is the prevalent resonance structure of compound **3** in solution. Thus, the two C–H moieties bound to the metal center gave signals in the aliphatic region: δ ^{1}H at 2.04 and 2.95 ppm; δ ^{13}C at 18.63 and 37.17 ppm.

That the reaction of **1** with $\{(i\text{-PrCN})\text{NiBr}_2\}_n$ and Et_3N can lead to two different products, **2** and **3**, suggests two pathways accessible under kinetic and thermodynamic conditions. The pincer complex **2** is likely the kinetic product of the reaction of **1** since its formation appears to be favoured under conditions that accelerate this reaction (i.e., in acetonitrile and with only 1 equivalent of phosphinite). Conversely, complex **3** is likely the thermodynamic product because its formation

appears to be favoured when the reaction of the Ni precursor with **1** proceeds at slower rates (i.e., in THF, or with excess of phosphinite in acetonitrile). These assertions would also require that the reactions leading to **2** be reversible (**Scheme 5.6**). Indeed, NMR monitoring of the reaction of **1** with the Ni^{II} precursor and Et$_3$N showed the appearance of the ^{31}P signal for **2** during the early stages of the reaction (after 2 h), but over time the intensity of this signal decreased gradually as the signal for **3** emerged (after 16 h) and increased in intensity (after 40 h).[16] Near complete conversion to the thermodynamic product **3** required more than 60 h.

Scheme 5.6. Conversion of **1** to kinetic and thermodynamic products.
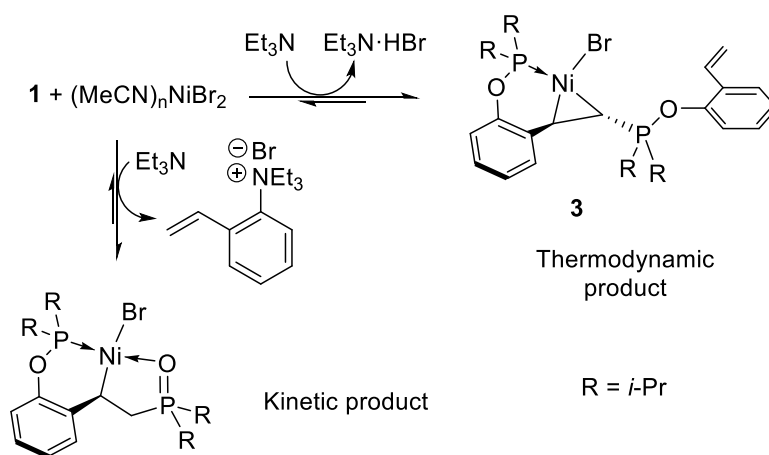
In order to isolate **3** in a pure form, we treated an acetonitrile solution of **1** with the Ni^{II} precursor and Et$_3$N (molar ratio of 1.0:0.6:2.0) over 4 days at room temperature. Evaporation, followed by extraction with Et$_2$O, cooling to –78 °C, and addition of hexanes allowed us to recover an orange solid. Analysis by quantitative ^{31}P NMR spectroscopy indicated that the orange solid consisted predominantly of **3**, but minor amounts of compound **2** (about 2%) were also present. Despite various attempts and workup procedures, we were unable to collect more than 20% yields of pure **3**, but this was sufficient for growing crystals and conducting a complete characterization of this compound.

5.3.2 Nucleophilic amines lead to 6,4-POCN-NiBr pincers

The previous section established that the coordination of the vinyl moiety in ligand **1** to the Ni^{II} center renders it susceptible to attack by even a weak Lewis base such as the phosphinite moiety in **1**. This attack generates a phosphonium-bearing intermediate that undergoes subsequent transformations to give either the 5,6-POCP(O)-type pincer complex **2** (without going through a C-H metalation step) or the zwitterionic nickelacyclopropane **3**. Based on these observations, we reckoned that conducting the reaction of **1** with the Ni^{II} precursor in the presence of a protic nucleophile might lead to new pincer complexes featuring a 4-membered nickelacycle, as illustrated in **Scheme 5.7**.

Scheme 5.7. Proposed Umpolung-based strategy leading to 6,4-POC$_{sp^3}$E-NiBr pincer complexes.
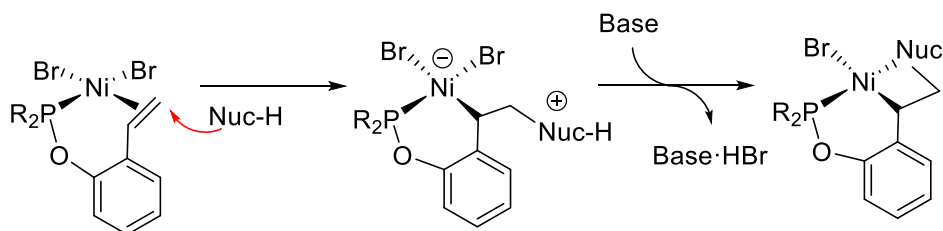
Morpholine was selected as nucleophile of choice for testing the above hypothesis, because our previous experience with the synthesis of 5,5-POCN-type pincer complexes of nickel had shown this amine to be a viable nucleophile for preparing stable pincer complexes.[17] Thus, treating **1** in acetonitrile for 1 h with 1.2 equiv of $\{(i\text{-PrCN})NiBr_2\}_n$ and 2.0 equiv of morpholine (as both nucleophile and base) resulted in complete disappearance of the ^{31}P signal for $(\mathbf{1})_2NiBr_2$ and emergence of a minor signal for complex **2** and a new, major, signal at 204 ppm. Varying the reaction conditions, including testing other solvents and bases, showed that the formation of **2** can be minimized by conducting the reaction in THF and using 1.2 equiv Et_3N as base. Under these conditions, the conversion of **1** was slower (16 h at room temperature) but led to the predominant formation of a new species represented by a ^{31}P resonance at ca. 204 ppm; three very minor resonances were also observed at ca. 207, 200, and 94 ppm (**Fig. S5.74**).

Evaporation of the volatiles, extraction with Et$_2$O, and addition of hexanes gave an orange powder for which the NMR spectra were consistent with the formation of the expected 6,4-POCN^{morph}-NiBr complex **4** (**Scheme 5.8**). For example, the ^{1}H NMR spectrum displayed signals at 1.59 for Ni-*CH* and at 3.42 and 3.68 ppm for Ni-CH-*CH$_2$*, with the corresponding ^{13}C signals at -1.12 and 64.72 ppm, respectively. In addition, we observed the anticipated ^{1}H resonances for 4 aromatic protons, the $\{(CH_3)_2CH\}_2$P resonances, and resonances for the 8 inequivalent protons of the morpholine ring.

Scheme 5.8. Synthesis of the 6,4-POCN pincer complex arising from morpholine (**4**) and its molecular diagram.^{a}
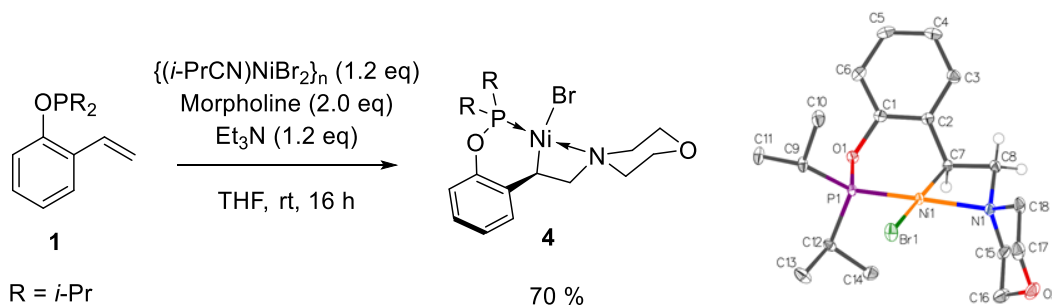
^{a} Thermal ellipsoids are shown at the 50% probability level, and hydrogen atoms refined via the riding model and terminal Me substituents of P(*i*-Pr)$_2$ moieties are omitted for clarity.

Single crystals obtained by slow evaporation of an Et$_2$O solution of the orange powder allowed us to conduct an XRD analysis that confirmed the identity of the product as the monomeric complex **4**. Inspection of the molecular diagram shown in **Scheme 5.8** reveals that this compound features the aforementioned unusual 4-membered ring metallacycle incorporating the amine moiety; it also has a 6-membered metallacycle incorporating the phosphinite moiety, similarly to what was observed in **2**. The absence of a plane of symmetry in this complex explains the inequivalence of all the protons (4 phosphinite Me groups, 4 aromatic protons, the 2 methylene protons in the pincer backbone, and all 8 morpholine protons).

Having established the competence of morpholine to intercept the formation of **2**, we moved next to test the reactivity with a less nucleophilic secondary amine to determine the lower threshold of

nucleophilicity required for hindering the formation of **2**. The substrate **1** was thus treated at room temperature and in acetonitrile with 2 equiv of *N*-ethylaniline and 1.2 equiv each of Et$_3$N and the Ni precursor. Monitoring the reaction by ^{31}P NMR spectroscopy showed the complete disappearance of the signal for **1** after 2 h,[18] and we observed the emergence of a new major signal at 208 ppm, along with minor resonances at 203, 200, 103, and 98 ppm. Conducting the reaction in THF proceeded more slowly (16 h), but gave a somewhat cleaner conversion.

As before, evaporation of the solvent, extraction with toluene, and addition of hexanes gave an orange powder, which was recrystallized in Et$_2$O (overnight at –35 °C) to afford crystals of the target complex **5**. ^{31}P NMR analysis of the crystals in C$_6$D$_6$ showed two singlets at 207 and 204 ppm in an 8:1 ratio, suggesting the existence of two isomers. The nucleophilic moiety N(Et)(Ph) being non-symmetrical, we infer that these isomers could arise from different orientations of the *N*-substituents relative to the aromatic cycle of the pincer ligand backbone. XRD analysis provided only the isomer featuring the Ph moiety pointing away from the aromatic cycle of the backbone (**Scheme 5.9**). Full NMR analysis revealed that this isomer is the major product in solution in a 9:1 ratio. An nOe analysis also showed cross peaks resulting from dynamic exchange between the two isomers, indicating that both isomers are in equilibrium at room temperature.

Scheme 5.9. Synthesis of complex **5** and observed diastereoisomers.
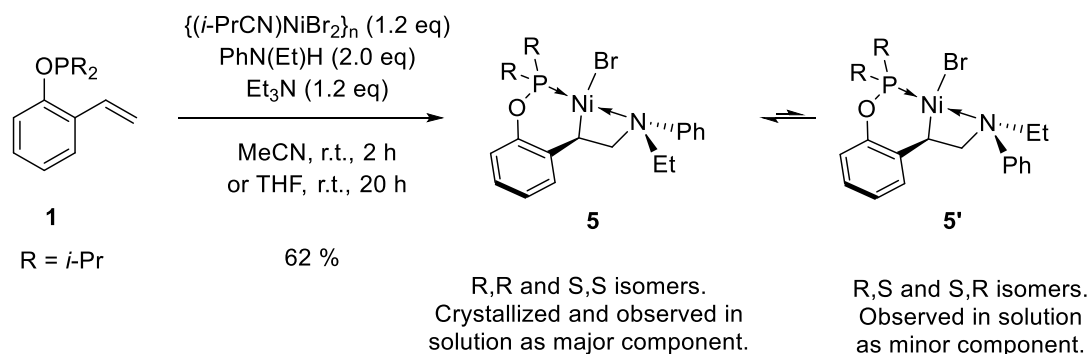
Next, we tested the reactivity of primary amines to see if the presence of a second N-H can hinder the formation of a 6,4-POCN pincer complex. Treating our usual Ni precursor with Et$_3$N and *i*-PrNH$_2$ as nucleophile (molar ratio 1.2:1.2: 2.0; THF, r.t.) led to a clean conversion. Analysis of the crude reaction mixture by ^{31}P NMR showed that the major product was the target 6,4-POCN^{iPr,H}

complex **6**, represented by two signals of similar intensities at 200.6 and 200.9 ppm; minor quantities of complex **2** were also detected. Recrystallization afforded crystals of the R,R and S,S isomers for **6**, i.e., the one with the *i*-Pr substituent of the amine moiety pointing away from the aromatic cycle of the backbone (**Scheme 5.10**).

Scheme 10. Synthesis of complex **6** and observation of diastereoisomers of similar energy.
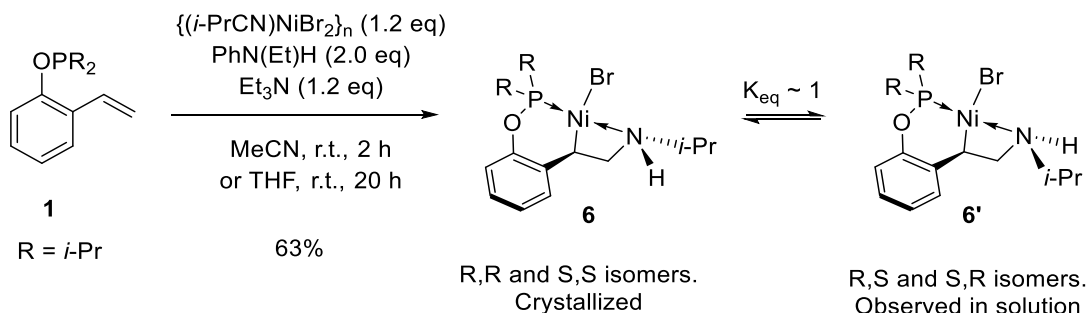
As described above for complex **5**, nOe cross peaks indicated that complex **6** was involved in a dynamic exchange process in solution at room temperature. This conclusion was corroborated by the following experiment. Analysis of a batch of crystals by powder XRD confirmed the presence of only isomer **6** (identified previously by single crystal XRD analysis). Re-dissolution of the powder in C_6D_6 and analysis by ^{31}P NMR showed again the presence of the two isomers in a close to 1:1 ratio. This finding establishes that the isomerization process occurs in solution at room temperature, likely owing to the hemi-lability of the amine arm. That the dissociation of the amine moiety is accessible at room temperature is presumably because it releases the strain in the 4-membered nickelacycle.

Repeating the reaction shown in **Scheme 5.10** with the less nucleophilic $PhNH_2$ in THF led to a less clean reaction, as evidenced by the appearance of several peaks in the 198-206 ppm region, none being dominant (**Fig. S5.128**). Nevertheless, as the starting material had completely disappeared, we undertook the work-up as before. Extraction with Et_2O followed by slow evaporation gave some crystals of the target 6,4-POCN^{Ph,H}-NiBr complex **7** (**Scheme 5.11**). XRD analysis of one of these crystals showed it to be the isomer with the Ph substituent of the amine moiety pointing away from the aromatic ring of the pincer backbone (see the last section for the structural diagram).

Scheme 5.11. Formation of 6,4-POCN-NiBr pincer complexes 7-9 from primary amines.
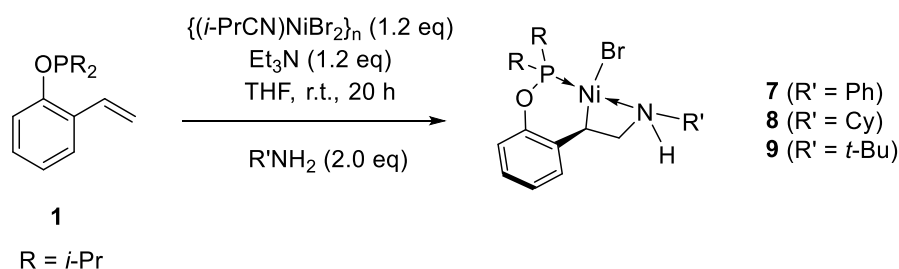
Similar reactions conducted with $CyNH_2$ and $t\text{-}BuNH_2$ proved not as clean as the reaction with $i\text{-}PrNH_2$, but still much cleaner than that with $PhNH_2$. Thus, the ^{31}P NMR spectra of the crude mixtures of these reactions indicated a similar outcome and we detected 2 major peaks in each case, at 200.7 and 201.0 ppm for the reaction with $CyNH_2$ and at 198.5 and 200.0 ppm for the reaction with $t\text{-}BuNH_2$. The intensities of these peaks were in a nearly 1:1 ratio, suggesting the co-existence of 2 isomers close in energy. It should be added that the reaction conditions for the synthesis of these complexes and the work-up processes have not been optimized, but XRD analyses were performed on crystals obtained from these reactions for the sole purpose of structural comparison. These analyses showed once again the formation of 6,4-POCN-NiBr complexes (**8** and **9**, **Scheme 5.11**); the isomers obtained in the solid state were those wherein the *N*-alkyl substituent was pointing away from the arene ring of the pincer backbone.

To gain some insight into the mechanism of the reactions with amine nucleophiles, we carried out a competition experiment between the two nucleophiles PhN(Et)H and $i\text{-}PrNH_2$. ^{31}P NMR monitoring of the reaction of **1** with 1.2 equiv each of the Ni precursor, $i\text{-}PrNH_2$, PhN(Et)H and Et_3N gave a surprising result. After 1 h of reaction in THF at room temperature, the ratio of the two complexes **5:6** was found to be 57:43, indicating that the less nucleophilic PhN(Et)H produces the 6,4-POCN-NiBr product slightly faster (**Scheme 5.11**). This observation can be rationalized as follows: the more nucleophilic amine binds preferentially to the Ni center, thus leaving more of the less nucleophilic amine to participate in an outer-sphere attack on the Ni-bound vinyl moiety group. Consistent with this assertion, during the synthesis of complex **8** in THF at 60 °C we isolated colourless crystals of the compound $(CyNH_2)_4NiBr_2$ (**Fig. S5.142** for its molecular diagram). Interestingly, when the above competition experiment was conducted over longer reaction times, the ratio of **5:6** reversed to 47:53 after 7 h and then 33:67 after 24 h (**Scheme 5.12**).[19] This indicates

that the formation of **6** is thermodynamically more favoured than that of **5** and that **6** can be converted to **5** in the reaction medium.

Scheme 5.12. Competitive formation of 6,4-POCN pincer complexes **5** and **6**.

	5	:	6
1 h	57	:	43
7 h	47	:	53
24 h	33	:	67
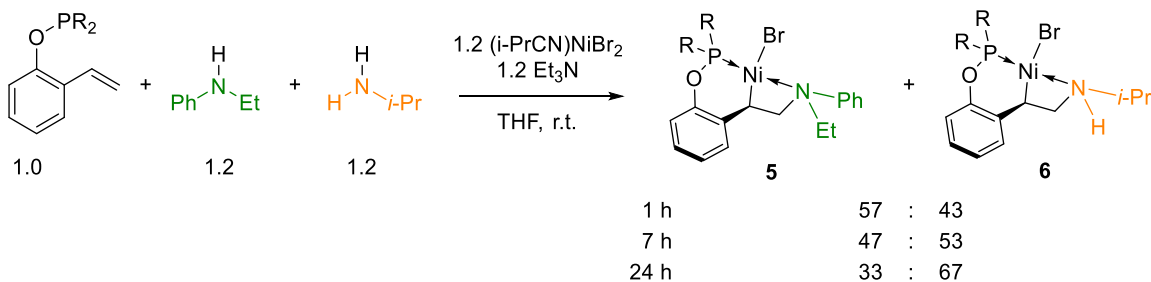
5.3.3 6,4-POCP-type pincer complexes from *P*-based nucleophiles

Having developed a relatively facile protocol for the synthesis of the above-discussed rare 6,4-POCN-type pincer complexes of Ni prompted us to test this approach for the synthesis of the corresponding compounds based on 6,4-POCP ligands that are also quite rare.[20] As a proof of concept for this idea, we stirred **1** in THF at room temperature with a 1.2:1.2:1 ratio of the Ni precursor, Et_3N and an Et_2O solution of i-Pr_2PH.[21] Analysis of the initial reaction mixture by ^{31}P NMR showed a number of signals after 4 h, including a major set of two AB doublets at 192 and –57 ppm. The large coupling constants of this set of signals ($J_{PP'}$ = 307 Hz) is typical of *trans* phosphines, allowing us to conclude that they represent the expected complex **10** (**Scheme 5.13**). The remaining minor resonances included the signals for complex **2** and (i-$Pr_2PH)_2NiBr_2$ as well as unidentified resonances at 117, 52, 27 and –12 ppm. Evaporation of the solvent, extraction with hexanes and precipitation at –78 °C afforded a light orange powder. Crystallization from a solution of hexanes cooled to –35 °C afforded orange crystals of the desired 6,4-POCP^{iPr}-NiBr complex **10**, which was characterized fully by NMR and XRD analysis (**Scheme 5.13**)

Scheme 5.13. Synthesis of the 6,4-POCP^{iPr}-NiBr, **10**, arising from *i*-Pr$_2$PH.
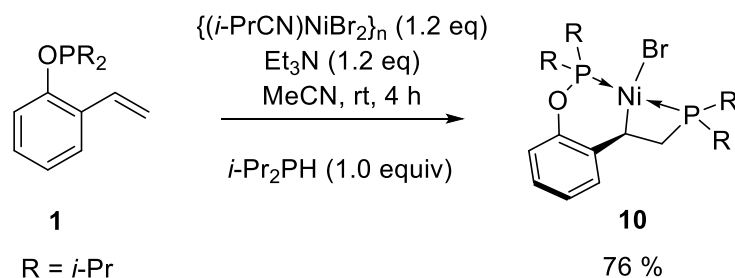
To limit the formation of by-product **2** in the above approach, we changed the source of nucleophile from free *i*-Pr$_2$PH to the complex (*i*-Pr$_2$PH)$_2$NiBr$_2$. This compound can be obtained treating an Et$_2$O solution of *i*-Pr$_2$PH containing the oxide impurity, (*i*-Pr$_2$P(O)H), with our Ni^{II} precursor, and removing from the less soluble blue species (*i*-Pr$_2$P(O)H)$_n$NiBr$_2$. Thus, reaction of **1** with 0.7 equiv of the new Ni precursor, 0.5 equiv (*i*-Pr$_2$PH)$_2$NiBr$_2$ and 1.2 equiv Et$_3$N allowed us to obtain complex **10** in 76% yield, along with minor amounts of **2**; the formation of the latter side-product could not be suppressed completely.

The formation of even minor quantities of **2** in the above reaction with *i*-Pr$_2$PH was somewhat surprising as this side-product was known to form much more slowly (16 h in THF). It occurred to us that formation of **2** might well arise from the reaction with small amounts of *i*-Pr$_2$P(O)H impurities generated during the synthesis of *i*-Pr$_2$PH.[22] To validate this hypothesis, we prepared *i*-Pr$_2$P(O)H via the reaction of *i*-Pr$_2$PCl with H$_2$O, followed by the addition of the base, which gave a light-yellow oil in 91 % yield. Reaction of **1** with 1.0 equiv *i*-Pr$_2$P(O)H and 1.2 equiv of both Et$_3$N and the Ni precursor in THF showed complete disappearance of the starting material after 3 h and appearance of the sharp resonance at 205 ppm and the broad one at 96 ppm attributed to the 6,5-POCP(O)-NiBr complex **2** (**Scheme 5.14**). It is noteworthy that this reaction was much cleaner than the synthetic approach described earlier with **1** only (**Scheme 5.3**). Applying this new synthetic route allowed us to isolate **2** in higher yields and, more importantly, uncontaminated by the side-product **3**.

Scheme 5.14. Direct preparation of complex **2** from i-Pr$_2$P(O)H.

1

R = *i*-Pr

2

75 %
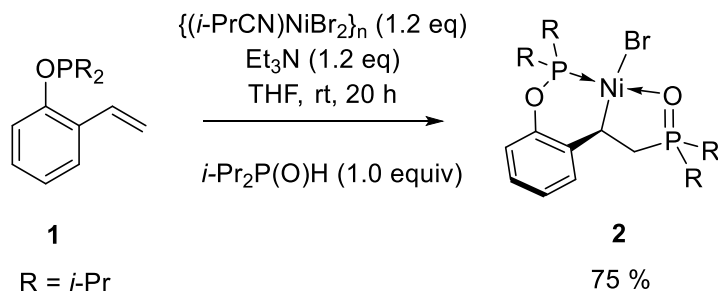
Finally, we studied the reaction of **1** with Ph$_2$PH as shown in **Scheme 5.15**. Analysis of the deep red crude reaction mixture by ^{31}P NMR confirmed the formation of the target complex after 4 h: the resonance for the starting material had been replaced by AB doublets at ca. 197 and –78 ppm with a $J_{PP'}$ of 320 Hz. Extraction with toluene, followed by crystallization of the resulting brown solids from hot acetonitrile afforded deep red crystals of the target product 6,4-POCP^{Ph}-NiBr, **11** in only 35% yields. Unfortunately, conducting the reaction in acetonitrile did not result in improved yields. XRD analyses and full NMR characterization confirmed its identity.

Scheme 5.15. Synthesis of the 6,4-POCP^{Ph}-NiBr, **11**, arising from Ph$_2$PH.

1

R = *i*-Pr

11

35 %
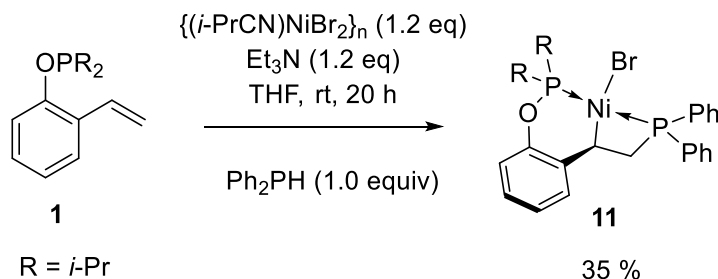
It is noteworthy that the above reaction also generated a mass of brick red solid that remained insoluble in either polar or nonpolar solvents (acetonitrile, THF, Et$_2$O, or toluene). One clue for this side reaction is the observation of minor resonances attributed to complex **10** in the crude reaction mixture, which suggests an exchange reaction between the nucleophile used, HPPh$_2$, and

substrate **1**, as shown in Eq. 1. Such an exchange equilibrium would also rationalize the poor isolated yield for complex **11**, if Ni complexes generated from the competitive Ph_2P-OAr ligand are less soluble.

$$i\text{-}Pr_2P\text{-}OAr \ + \ Ph_2P\text{-}H \ \rightleftarrows \ i\text{-}Pr_2P\text{-}H \ + \ Ph_2P\text{-}OAr \quad (\text{Eq. 1})$$
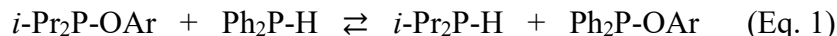
5.3.4 Electrochemical analysis

To the best of our knowledge, the pincer-type compounds described in the above sections, i.e., the $6,5\text{-}POC_{sp^3}P(O)$ complex **2**, the $6,4\text{-}POC_{sp^3}N$ compounds **4-9**, and the $6,4\text{-}POC_{sp^3}P$ compounds **10** and **11**, represent a new class of pincer-Ni complexes. Indeed, Scifinder and CCCD searches have revealed no previous example of POCN-Ni complexes featuring an aliphatic backbone, nor pincer-type Ni complexes based on POCP ligands (phosphinite/phosphine donor moieties) or POCP(O) ligands (phosphinite/phosphine oxide donor moieties) with either aliphatic or aromatic linking groups. The access to these unprecedented pincer-type Ni complexes led us, naturally, to investigate their structures and other properties relevant to reactivities.

Our long-standing interest in the synthesis and reactivities of high-valent Ni complexes[9a,23] prompted us to use cyclic voltammetry (CV) to measure the one-electron oxidation potentials of the above-mentioned $POC_{sp^3}N$ and $POC_{sp^3}P$ complexes. The main objective of this exercise was to study variations in redox potentials as a function of different structural features (e.g., aromatic vs. aliphatic ligand backbone or C_{sp^3}-Ni vs. C_{sp^2}-Ni; nature of donor moieties $R_3N{\rightarrow}Ni$, $R_3P{\rightarrow}Ni$, etc.). We hoped that any insight gleaned from such studies would facilitate design of thermally stable high-valent derivatives.

We began our CV measurements with complex **4** as this would provide a meaningful comparison of its redox potentials to that of a close relative of this complex, $5,5\text{-}\kappa^P,\kappa^C,\kappa^N\text{-}\{i\text{-}Pr_2\underline{P}OC_6H_3CH_2(\text{morphol-}\underline{N}\text{-yl})\}NiBr$, which we had studied previously.[17] Initial CV measurements conducted on CH_2Cl_2 solutions of **4** using $[n\text{-}Bu_4N]PF_6$ as supporting electrolyte[17] showed a distinct but irreversible oxidation wave attributed to Ni^{II}/Ni^{III} (**Fig. S5.3**). That this one-electron oxidation is irreversible implies that the in-situ generated 15-electron species $[6,4\text{-}POCN^{morph}\text{-}Ni^{III}Br]^+$ is unstable.

In an effort to favor reversibility of the redox events with **4**, the CV experiments were conducted in acetonitrile to see if the greater binding ability of this solvent might stabilize the in-situ formed trivalent cationic species. The CV trace obtained at a scan rate of 100 mV/s in acetonitrile was much cleaner, but the difference between the anodic and cathodic peak potentials in this trace was ca. 270 mV, which is much greater than the ideal value of 56.5 mV for $|E_{p,a}-E_{p,c}|$ of a fully reversible single electron redox process.[24] This larger-than-ideal potential difference is attributed to the likelihood that the redox process in question involves different species; in other words, the oxidation occurs with complex **4** whereas the reduction likely occurs with the in-situ generated penta- or hexacoordinate cationic MeCN adducts [{$\kappa^N,\kappa^C,\kappa^P$-2-[(morphol-$\underline{N}$-yl)CH$_2$$\underline{C}$H]-C$_6H_4$-OP($i$-Pr)$_2$}-NiBr(NCMe)$_n$]$^+$ (n= 1 or 2). Given that the various complexes under discussion are likely to give rise to $|E_{p,a}-E_{p,c}|$ values that might be more or less sensitive to this factor, we have opted to focus the comparison of redox potentials across the various compounds on the anodic peak potentials as opposed to the $E°_{1/2}$ potentials. Moreover, the $E_{p,a}$ values for all the compounds investigated here have been referenced to the $E°_{1/2}$ for ferrocene (Fc/Fc$^+$), which is used as the standard complex for calibrating our measurements. Representative CV traces for the complexes studied are shown in **Figure 5.1** and **Figure 5.2**, whereas the $E_{p,a}$ values measured for all complexes are listed in **Figure 5.3**.
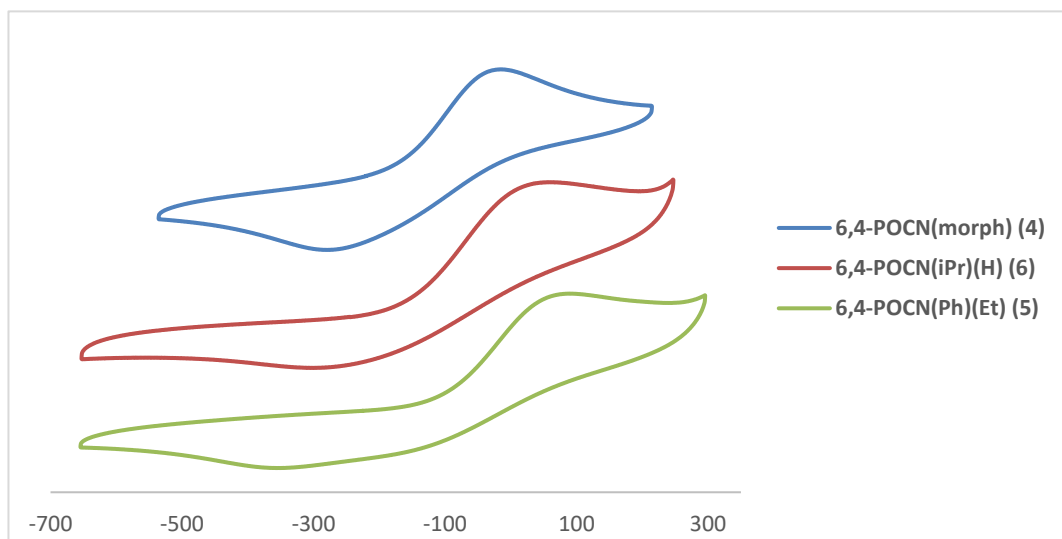
Figure 5.1. Cyclic voltammograms of complexes **4-6** (1 mM) in the presence of [n-Bu$_4$N]PF$_6$ (100 mM) in MeCN at a glassy carbon electrode. Potentials are referenced against the $E°_{1/2}$ of the Fc/Fc$^+$ redox couple.
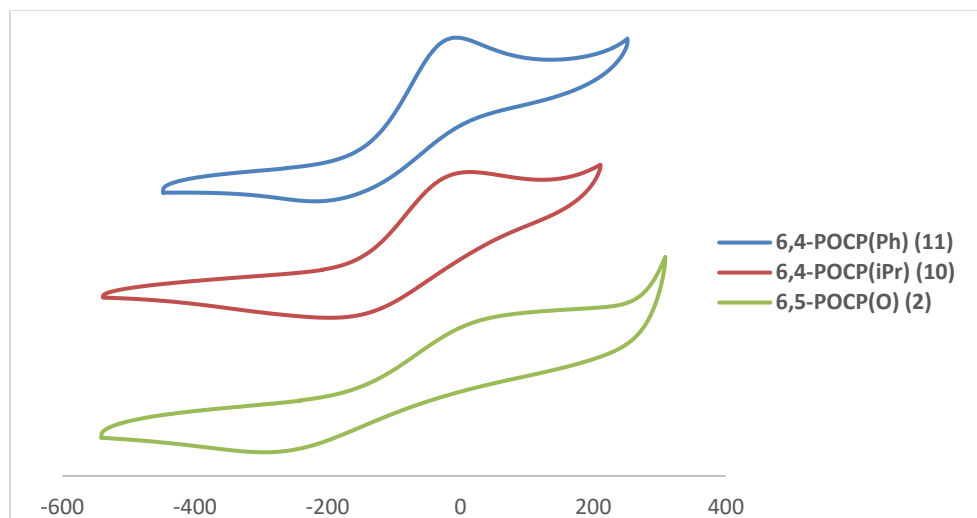
Figure 5.2. Cyclic voltammograms of complexes **9**, **10** and **2** (1 mM) in the presence of [*n*-Bu$_4$N]PF$_6$ (100 mM) in MeCN at a glassy carbon electrode. Potentials are referenced against the E°$_{1/2}$ of the Fc/Fc$^+$ redox couple.

The data gathered in **Figure 5.3** allow us to comment on the impact of various structural features on electrochemical oxidation potentials. For instance, the E$_{p,a}$ values for the 6,4-POC$_{sp^3}$N complexes **4** (-13 mV), **5** (+89 mV), and **6** (+57 mV) confirm that the morpholine moiety bestows a greater electron density to Ni relative to N(*i*-Pr)H and N(Ph)Et. It is also worth noting here that the CV traces for these complexes were all quasi-reversible, though decomposition of the Ni^{III} species is evident, implying that the presence/absence of an N-H moiety has no major influence on this phenomenon.

It is also instructive to compare the above data to the E$_{p,a}$ values for the complexes bearing donor moieties other than amine. Thus, the 6,4-POC$_{sp^3}$P pincer complexes **10** (–8 mV) and **11** (+14 mV) show anodic potentials that are quite comparable to the 6,4-POC$_{sp^3}$N-type complex **4**. These findings were somewhat surprising as we had anticipated that replacing a "hard" amine moiety in **4** by a "soft" phosphine moiety should be unfavorable to oxidation. We were also surprised that the E$_{p,a}$ values for these 6,4-POC$_{sp^3}$P-type complexes did not seem to follow the anticipated order: complex **11**, the one bearing the presumed better σ-donor CH$_2$P(*i*-Pr)$_2$ moiety, was found slightly more difficult to oxidize than its CH$_2$PPh$_2$ counterpart. This said, the difference is not large, and the oxidation potentials of both **10** and **11** are similar to the corresponding value for the analogous compound (5,5-PC$_{sp^3}$P)NiBr (**Figure 5.3**). That the latter can be converted to stable and isolable trivalent species[10b] bodes well for the prospects of accessing trivalent species from **10** and **11**.

395
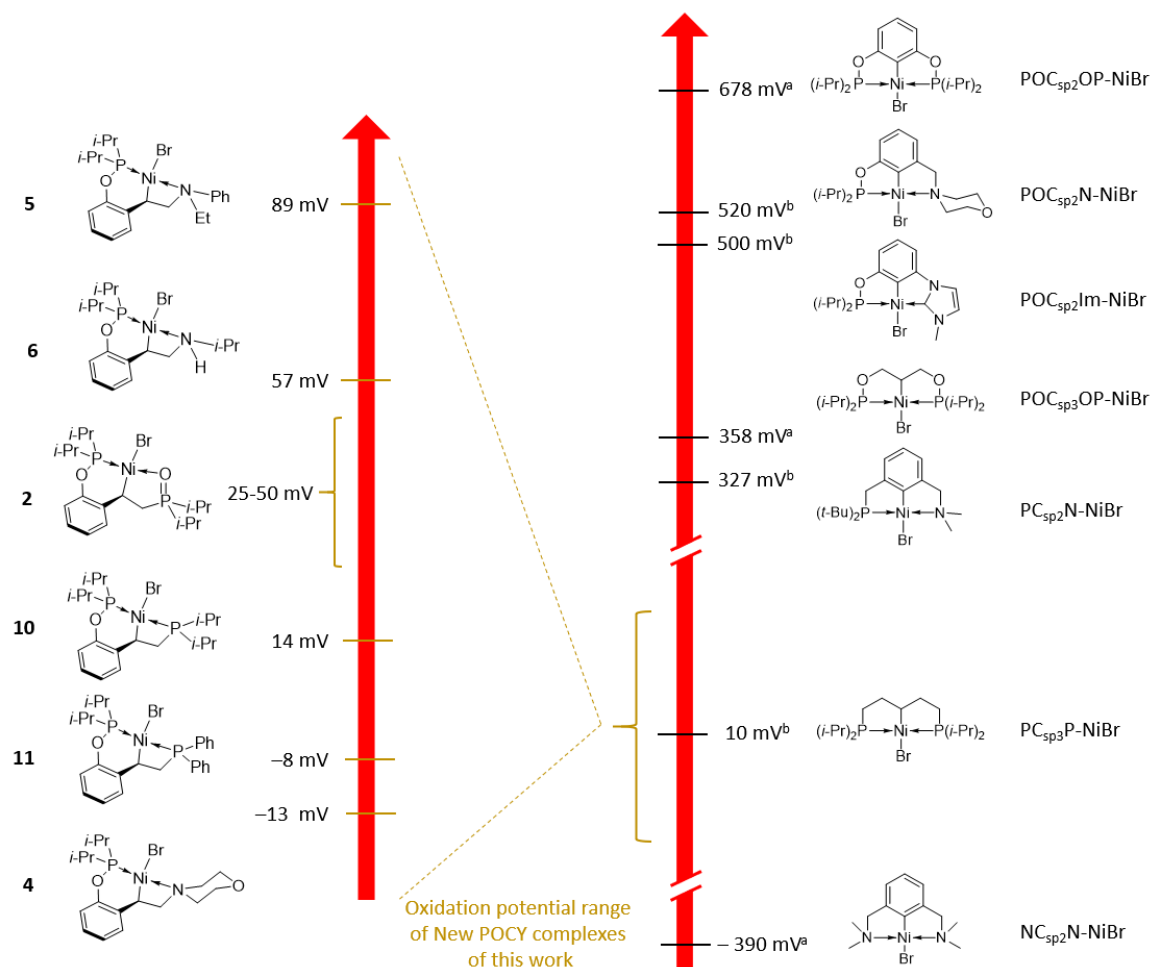
Figure 5.3. $E_{p,a}$ of new pincer complexes characterized by cyclic voltammetry and relative ease of oxidation vs. previously reported pincer NiBr complexes. All potentials are referenced against the $E°_{1/2}$ of the Fc/Fc$^+$ redox couple. [a] The CV of these complexes were measured in acetone. [b] The CV of these complexes were measured in dichloromethane.

The last complex studied by CV was the 6,5-POCP(O) compound **2**. The analysis of the data is complicated in this case owing to the flatness of the anodic wave: an oxidation event is evident, but a clear anodic peak is not revealed (i.e., dI/dE never reaches 0 around the oxidation event). Thus, we used the first derivative dI/dE = f(E) to approximate the $E_{p,a}$ closer to the inflexion point, which turned out to be between +25 and +50 mV vs. Fc/Fc$^+$. This uncertainty in the precise value of $E_{p,a}$ notwithstanding, we conclude that the P(O) donor moiety does not diminish the electrochemical oxidation prospects for the Ni center relative to the 6,4-POC$_{sp^3}$N complex bearing the strong σ-donor NH(i-Pr). This is presumably due to a strongly polarized phosphine oxide bond in which the R$_3$P$^+$-O$^-$ resonance form is prevalent.

Overall, the CV measurements presented above allow us to conclude that these 6,4-POC$_{sp^3}$N, 6,4-POC$_{sp^3}$P, and 5,5-POC$_{sp^3}$PO complexes are much easier to oxidize relative to the classical pincer-type complexes 5,5-POC$_{sp^2}$N-NiBr and 5,5-POC$_{sp^2}$OP-NiBr studied previously. For instance, the difference between the oxidation potentials of complex **4** and the closely analogous 5,5-POC$_{sp^2}$N^{morph}-NiBr mentioned above is about 530 mV. The analogous 5,5-POC$_{sp^2}$OP-NiBr complex is even harder to oxidize (by 700-800 mV depending on solvent), whereas the difference is smaller with the analogous POC$_{sp^3}$OP compound featuring an aliphatic backbone (ca. +358 mV). These observations confirm that a C$_{sp^3}$-Ni moiety bestows a great deal of electron density to the Ni center. On the other hand, van Koten's 5,5-NC$_{sp^2}$N-NiBr system is much easier to oxidize (–390 mV vs. Fc/Fc$^+$ in acetone) in spite of its aromatic backbone, establishing the superior oxidation prospects for pincer systems with two amine donor moieties. It is also noteworthy that the presumably strained 4-membered nickelacycle in **4** does not hinder the N→Ni bonding sufficiently to reduce the electron density at Ni^{II}.

5.3.5 Structural characterization of new complexes

As stated earlier, single crystal diffraction analyses have been performed for all the new complexes prepared in this study. The molecular diagrams for the complexes **2** and **4** were presented in the synthetic schemes discussed earlier (**Schemes 5.3**, and **5.8**). This section will present an alternative perspective on the structure of complex **2** (**Figure 5.4**), in addition to molecular diagrams for complexes **5** and **6** (**Figure 5.5**) and **10** and **11** (**Figure 5.6**). (The molecular diagrams for complexes **7-9** are presented in the Supporting Information)

The most pertinent structural parameters for all structures are tabulated in **Table 1**. All the complexes under discussion display a square planar geometry: the Ni center and the four atoms bound to it are located on or near the mean coordination plane. The 6-membered nickelacycle forces the aromatic ring originating from ligand **1** to lift off the mean coordination plane by about 51-66° (**Figure 5.4**). Some of the more relevant bond angles and distances are discussed below and compared to the corresponding parameters reported previously for other pincer-Ni systems.
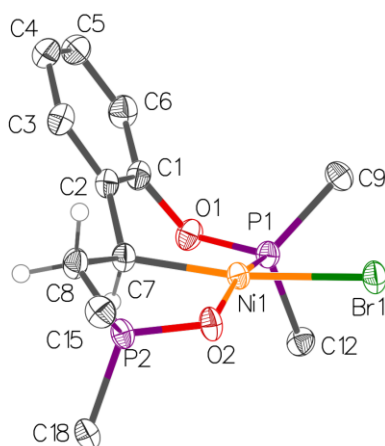
Figure 5.4. Side view of the molecular diagram for complex **2**. Thermal ellipsoids are shown at the 50% probability level, and hydrogen atoms refined via the riding model and terminal Me substituents of P(*i*-Pr)$_2$ moieties are omitted for clarity.

Table 5.1. Selected Structural Parameters for Complexes **2-11**.

	Ni-C7	Ni-P1	Ni-Br	Ni-E[a]	P-Ni-C	E-Ni-C	P-Ni-E	C-Ni-Br
2[b]	1.998(2)	2.1104(5)	2.3743(3)	1.9477(12)	90.41(5)	90.74(6)	165.08(4)	171.10(6)
	1.998(2)	2.1106(4)	2.3785(3)	1.9317(10)	88.39(5)	91.11(6)	177.47(4)	171.85(5)
3[c]	1.910(2)	2.1103(5)	2.3479(3)	2.0103(16)	92.46(5)	43.18(6)	135.02(5)	157.10(5)
	1.905(2)	2.1058(4)	2.3479(3)	2.0148(14)	90.47(4)	43.33(6)	133.61(4)	155.99(4)
4	1.9436(16)	2.1095(5)	2.3524(3)	2.0250(14)	90.22(5)	72.95(6)	158.13(4)	172.07(5)
5	1.943(2)	2.0967(7)	3.3533(4)	2.026(2)	90.06(7)	72.36(9)	156.80(6)	168.82(7)
6	1.943(2)	2.1141(4)	2.3734(3)	1.9884(13)	90.70(5)	73.91(6)	164.39(4)	175.64(5)
7	1.938(2)	2.1065(5)	2.3608(3)	1.9884(15)	89.14(6)	74.07(7)	162.41(5)	173.25(5)
8	1.945(2)	2.1154(6)	2.3727(4)	1.9828(18)	89.54(7)	73.83(8)	163.98(6)	175.25(7)
	1.951(2)	2.1130(6)	2.3864(4)	1.9836(18)	89.69(6)	73.69(8)	162.78(6)	174.41(6)
9	1.939(2)	2.1175(7)	2.3689(4)	2.004(2)	88.17(7)	73.68(9)	159.91(6)	173.95(8)
	1.942(2)	2.1214(6)	2.3753(4)	2.008(2)	89.19(7)	73.53(9)	161.45(6)	175.77(7)
10	1.991(3)	2.1501(8)	2.3562(5)	2.1762(8)	89.79(8)	73.07(8)	161.47(3)	174.89(8)
	1.998(3)	2.1509(8)	2.3604(5)	2.1650(8)	90.37(8)	73.44(8)	163.59(3)	173.42(8)
11	2.001(3)	2.1541(8)	2.3472(6)	2.1897(8)	90.30(8)	71.65(8)	155.44(4)	174.19(8)

[a] E refers to O2 in complex **2**, C8 in complex **3**, N1 in complexes **4-9** and P2 in complexes **10-11**. [b] The first row corresponds to value found in the structure of **2** only, and the second row to values found in co-crystals of **2** and **3**. [c] The first row corresponds to value found in the structure of **3** only, and the second row to values found in co-crystals of **2** and **3**.
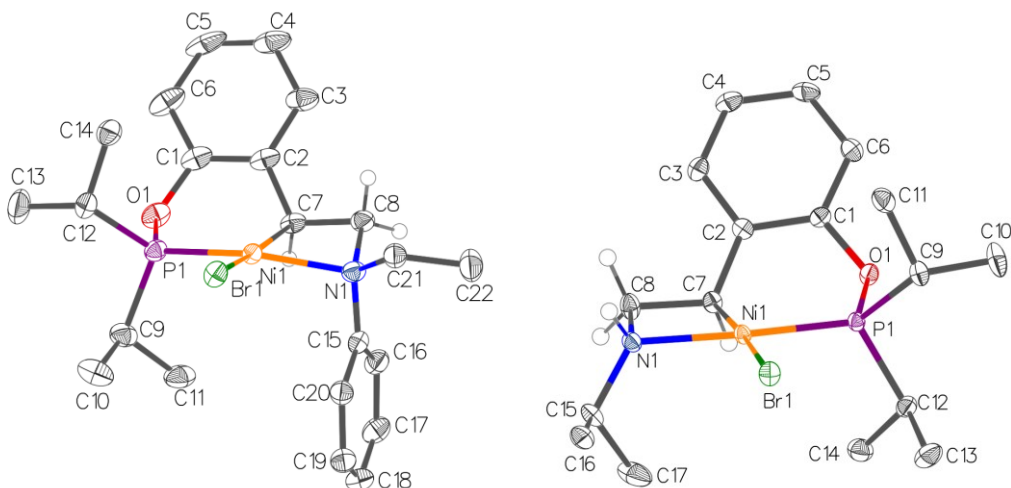
Figure 5.5. Molecular diagrams for complexes **5** & **6** that crystallized as R,R and S,S isomers. Thermal ellipsoids are shown at the 50% probability level; hydrogen atoms refined via the riding model are omitted for clarity.
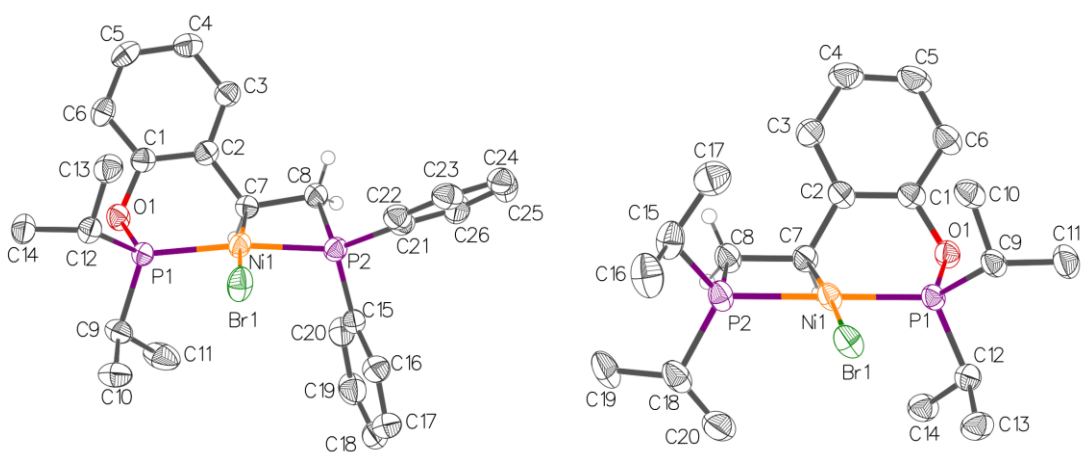
Figure 5.6. Molecular diagrams for complexes **10** and **11**. Thermal ellipsoids are shown at the 50% probability level; hydrogen atoms refined via the riding model are omitted for clarity.

Perhaps the most noteworthy feature of the 6,4-POCN complexes **4-9** and 6,4-POCP complexes **10** and **11** is the 4-membered nickelacycle. The acute *cis* angles C7-Ni1-N1 and C7-Ni1-P2 defining these 4-membered rings range from 71° to 74°, whereas the C7-Ni1-P1 angles defining the 6-membered nickelacycles are closer to the ideal right angles (88°-91°). By comparison, the C7-Ni1-O2 angle of 91° defining the 5-membered nickelacycle in complex **2** is also close to the ideal value expected for a square planar geometry, whereas the corresponding *cis* angles in the analogous 5,5-aromatic-pincer-Ni complexes reported previously range from 83° to 85°. The acute

cis angles observed in the 4-membered metalacycles in **4-11** might be expected to result in a weakening of the Ni-N and Ni-P bonds, but comparison of these distances to the corresponding values in the analogous 5,5-POCN,[17,25] 5,5-POCOP,[10a,26] 5,5-PCP,[10b,27] and PCN[28] complexes does not reveal significant differences: 1.983(2)-2.026(2) vs. 1.97-2.05 Å for Ni-N distances; 2.17-2.19 vs. 2.16-2.21 Å for Ni-P distances.

One remarkable feature of the 6,4- and 6,5-pincer complexes described here is the relative insensitivity of the 6-membered metalacycle to the size of the adjoining metalacycle, as well as to the identity of the donor moiety contained in it. This is reflected in the P1-Ni1-C7 angles that are in the narrow range of 88-91° over complexes **2** and **4-11**. In contrast, the P-Ni-C *cis* angles of typical 5,5-pincer-Ni complexes are more acute (80-85°[29]) whereas 5,6-POCOP-NiBr displays a wider *cis* angle of 93° for its 5-membered nickelacycle.[20b] The *trans* C7-Ni1-Br1 angles are greater than 169° in all complexes except in the more distorted compound **3** wherein it is much smaller (156°). Among the 6,4-POCN complexes **4-9**, those featuring a primary amine moiety show C7-Ni1-Br1 angles that are fairly close to the ideal value of 180°, whereas the corresponding angles in the analogous complexes with tertiary amine are somewhat narrower (174-176° vs. 169-172°).

Other Ni-ligand bond distances were also found to be nearly constant over the complexes in question, with only minor variations noted in certain cases. Thus, the Ni-Br distances range from 2.345 to 2.388 Å, which is in the same range as observed for the analogous POCOP, PCP, POCN, and PIMCOP complexes bearing P(i-Pr)$_2$ phosphinites. Among the 6,4-POCN complexes, those featuring a primary amine moiety display significantly longer Ni-Br distances (2.361-2.388 Å vs. 2.352-2.353). In the case of Ni1-C7 bond distances, all 6,4-POCN complexes **4-9** showed values ranging from 1.938(2) to 1.951(2) Å (the shorter for complex **7** and the longer for complex **8**); this is similar to the range of Ni-C distances reported for aliphatic 5,5-POCOP (1.94-1.96 Å), while significantly larger values were obtained for complexes **2** and **10-11** (ranging 1.99-2.00 Å). For compound **3**, the Ni1-C7 bond distance is significantly shorter with a value of 1.91 Å. Finally, the Ni1-P1 bond distances found in complexes **2-9** were in the same range as in the analogous 5,5-POCN-Ni complexes reported previously (2.11-2.12 vs. 2.10-2.11 Å). The somewhat longer Ni1-P1 bond distances of 2.150(1)-2.154(1) Å observed in complexes **10** and **11** are likely due to the greater *trans* influence of the phosphine moieties. Consistent with this assertion, similar Ni-P bond distances (2.14-2.16 Å) have been reported in the analogous aliphatic and aromatic 5,5-POCOP$^{i\text{-Pr}}$

complexes reported previously, whereas even longer Ni-P bond distances were found in the 6-membered nickelacycle of the 6,5-POCOP$^{i\text{-}Pr}$ (> 2.17 Å).

The Ni1-O2 bond distances of 1.932(1)-1.948(1) Å and P2-O2 of 1.523(1) Å in our 6,5-POCP(O) complex **2** is similar to those observed in PCP(O) pincer-Ni complexes featuring a R(*i*-Pr)$_2$P=O→Ni interaction (1.93-1.96 Å for Ni-O and 1.50-1.53 Å for P-O).[30] It is also worth noting that the P=O bond distance displayed in **2** is clearly longer than in reported crystallized free *i*-Pr$_2$P(O)-CH$_2$-R molecules (with P-O bonds ranging 1.48-1.50 Å,[31] indicating a bond order close to unity and thus strong polarization of the R3P$^+$-O$^-$ bond which gives this arm an almost X-ligand character.

Additional structural analysis is required for complex **3** (**Figure 5.7**), in particular regarding what the structural parameters of this compound might reveal regarding the interactions between the Ni center and the carbons C7 and C8 arising from the vinyl moiety of ligand **1**. We had argued earlier on the basis of NMR data that the **α** form of compound **3** shown in **Scheme 5.5** and featuring a nickelacyclopropane moiety is the prevalent resonance structure. Comparison of solid-state parameters to previously reported analogous complexes support this argument. A CCDC search of complexes considered as Ni(0) and featuring one alkene or *trans*-stillbene revealed that their C-C bond distances span the range of 1.410(4)-1.428(4) Å in spite of the presence of strong σ donors such as trialkylphosphines or NHC ligands.[32] Surprisingly, in our 6,3-POCC complex **3** that bears only moderate σ donors (phosphinite, bromide), the C7-C8 bond distance was found significantly longer with values of 1.446(2)-1.451(2) Å, which are more in line with a cyclopropane moiety as opposed to a coordinated olefin.

Another important consideration is the Ni-C bond lengths in the complexes under discussion. The Ni-C distances observed in mono-olefin-Ni^0 complexes span the range of 1.96-2.01 Å, whereas much shorter distances of 1.88-1.91 Å are reported for the highly π-acidic Ni-polyfluoroalkenes, which are regarded as essentially nickelacyclopropanes bound to Ni^{II}.[33] Given that the average C7-Ni1 bond length of 1.91 Å found in complex **3** is much shorter than C-Ni bonds in Ni-olefin complexes, the cyclopropane description for this moiety seems more reasonable. Indeed, the C7-Ni1 distance is even shorter than the corresponding distances in benzyl-NiX complexes (1.95-2.02 Å),[34] in the 6,4 pincer compounds **4-11** reported here (1.93-2.01 Å), and also in previously reported aromatic/aliphatic pincer-NiX complexes (1.94-1.96 Å). It should be acknowledged, however, that

the second Ni-C distance in the putative cyclopropane moiety of complex **3** is much longer (Ni1-C8 = 2.010(2)-2.015(2) Å); we believe that the greater steric bulk of the phosphonium substituent on C8 might be at least partially responsible for this lengthening.
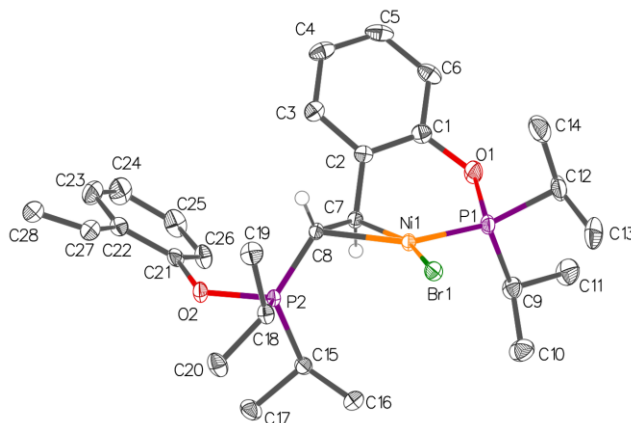
Figure 5.7. Molecular diagram for complex **3**. Thermal ellipsoids are shown at the 50% probability level; hydrogen atoms refined via the riding model and co-crystallized complex 3 are omitted for clarity.

5.4 Conclusion

The study presented herein has led to the development of a new synthetic strategy for the preparation of rather novel unsymmetrical ECE'-Ni pincer complexes. The key step in this synthetic route involves an outer-sphere nucleophilic addition onto the olefin moiety of the phosphinite **1**; chelation of an electrophilic Ni^{II} center by this substrate activates the olefin moiety toward the requisite nucleophilic attack (*umpulong* reactivity). This approach works with readily available precursors and proceeds at room temperature to give products that would be otherwise difficult to access without more elaborate starting materials such as zero-valent Ni precursors and proligands bearing one or more C-halide moieties. Thus, the new synthetic strategy under discussion obviates the need for C-H or C-X addition/metalation, frequently difficult steps that can constitute important obstacles for the synthesis of ECE'-type pincer complexes. Future studies will probe the possibility of extending this synthetic strategy for the preparation of analogous pincer complexes with other metals, as well as to other ligand platforms such as phosphinites derived from homoallylic alcohols.

An interesting and somewhat unexpected feature of the pincer-Ni complexes synthesized in the current study is the observed thermal stability of the 4-membered metallacycles, especially in the case of 6,4-POC$_{sp^3}$N complexes featuring the shorter Ni-N bond in the 4-membered ring. The observed solution isomerization that these complexes undergo underlines the hemilability of the N→Ni coordination bond; this hemilability bodes well for potential reactivities and catalytic applications of these complexes.

Another interesting aspect of the pincer complexes described in this report touches on the ligand/complex features that render the Ni^{II} center prone to relatively facile electrochemical oxidation. The CV measurements we have reported demonstrate the important impact of N→Ni, P→Ni, and C$_{sp^3}$–Ni moieties for facilitating single electron oxidation of the Ni centers in these complexes. Future efforts will be directed at exploiting the insights gleaned from these studies to prepare thermally stable high-valent analogues of these pincer complexes.

5.5 Experimental section

General considerations. All manipulations were carried out under a nitrogen atmosphere using standard Schlenk techniques and an inert-atmosphere box. The transfer/addition of all liquid reagents/reactants was performed with BRAND Transferpette® micropipettes (20-200 µL and 100-1000µL). Reported volumes should be considered to be within ±7 µL (for > 200 µL transfers) and ±3 µL (for < 200 µL transfers) of the measurements, with a >99% confidence level.[35] Solvents were dried by passage over a column of activated alumina, collected under nitrogen, and stored over 3 Å molecular sieves inside transfer/storage flasks equipped with high vacuum valves (Straus flasks). Et$_3$N was dried over CaH$_2$. The Ni^{II} precursor [(i-PrCN)NiBr$_2$]$_n$ used throughout this study was prepared as reported previously.[36] Other reagents were purchased from Sigma-Aldrich or FisherSci and used without further purification.

The NMR spectra were recorded at 500 MHz (^{1}H), 125.72 MHz (^{13}C), and 202.4 MHz (^{31}P). Chemical shift values are reported in ppm (δ) and referenced internally to the residual solvent signals (^{1}H and ^{13}C: δ = 7.26 and 77.16 for CDCl$_3$; 7.16 and 128.06 for C$_6$D$_6$) or externally (^{31}P: H$_3$PO$_4$ in D$_2$O, δ = 0). The minimal precision of the NMR spectra was found to be 0.3 Hz for ^{1}H, 0.7 Hz for ^{13}C and 2 Hz for ^{31}P.

Single crystals of the structurally characterized complexes were grown as follows: **2**, **3** and **2·3** from Et$_2$O solutions cooled to -35 °C, **4-9** by slow evaporation of Et$_2$O solutions under inert atmosphere, **10** from hot acetonitrile and **11** from hexanes solution cooled to -35 °C.

(2-vinyl-phenyl)-OP(*i*-Pr)$_2$ (1). The 23.0 mmol batch of 2-vinylphenolprepared as described in the Supporting Information (and still containing some AcOEt remaining from its purification step) was dissolved in 30 mL THF. To this solution was added Et$_3$N (3.53 mL, 25.3 mmol, 1.10 equiv), followed by dropwise addition of ClP(*i*-Pr)$_2$ (3.84 mL, 24.15 mmol, 1.05 equiv) which led to salt precipitation. The resulting mixture was stirred for 2 h at room temperature, followed by evaporation of volatiles and extraction of the residues with 3 × 25 mL Et$_2$O by cannula filtration. Evaporation of the volatiles afforded the target product as a pale yellow oil (4.99 g, 21.1 mmol, 92 %). ^{1}H NMR (500 MHz, 20 °C, CDCl$_3$): δ 1.10 (dd, 6H, CH(C*H$_3$*)(CH$_3$), $^3J_{HH}$ = 7.3, $^3J_{HP}$ = 15.8), 1.17 (dd, 6H, CH(CH$_3$)(C*H$_3$*), $^3J_{HH}$ = 7.0, $^3J_{HP}$ = 10.8), 1.96 (heptd, 2H, C*H*(CH$_3$)$_2$, $^3J_{HH}$ = 7.1, $^2J_{HP}$ = 2.8), 5.24 (dd, 1H, ArCH=C(*H*)(H), $^3J_{HH}$ = 11.2, $^2J_{HH}$ = 1.5, *cis* to ArC*H*=CH$_2$), 5.72 (dd, 1H, ArCH=C(H)(*H*), $^3J_{HH}$ = 17.8, $^2J_{HH}$ = 1.5, *trans* to ArC*H*=CH$_2$), 6.93 (tm, 1H, C4$_{Ar}$-*H*, $^3J_{HH}$ = 7.5), 7.09 (dd, 1H, ArC*H*=CH$_2$, $^2J_{HHtrans}$ = 17.8, $^3J_{HHcis}$ = 11.2), 7.18 (ddd, 1H, C5$_{Ar}$-*H*, $^3J_{HH}$ = 8.9, $^3J_{HH'}$ = 7.3, $^4J_{HH}$ = 1.7), 7.30 (ddd, 1H, C6$_{Ar}$-*H*, $^3J_{HH}$ = 8.3, $^4J_{HP}$ = 3.6, $^4J_{HH}$ = 1.1), 7.47 (dd, 1H, C3$_{Ar}$-*H*, $^3J_{HH}$ = 7.7, $^4J_{HH}$ = 1.7). ^{13}C{^{1}H} NMR (125.72 MHz, 20 °C, CDCl$_3$): δ 17.20 (d, 2C, CH(CH$_3$)(*C*H$_3$), $^2J_{CP}$ = 8.6), 17.80 (d, 2C, CH(*C*H$_3$)(CH$_3$), $^2J_{CP}$ = 19.7), 28.36 (d, 2C, *C*H(CH$_3$)$_2$, $^1J_{CP}$ = 17.8), 114.09 (s, 1C, ArCH=*C*H$_2$), 117.54 (d, 1C, *C*6$_{Ar}$-H, $^3J_{CP}$ = 21.3), 121.39 (d, 1C, *C*4$_{Ar}$-H, $^5J_{CP}$ = 1.3), 126.13 (s, 1C, *C*3$_{Ar}$-H), 127.96 (d, 1C, *C*2$_{Ar}$-CH=CH$_2$, $^3J_{CP}$ = 1.6), 128.77 (d, 1C, *C*5$_{Ar}$-H, $^4J_{CP}$ = 1.6), 137.74 (s, 1C, Ar*C*H=CH$_2$), 156.34 (d, 1C, *C*1$_{Ar}$-OP, $^2J_{CP}$ = 8.0). ^{31}P{^{1}H} NMR (202.4 MHz, 20 °C, CDCl$_3$): 147.63 (s, 1P).

{$\kappa^O,\kappa^C,\kappa^P$-2-[O*P*(*i*-Pr)$_2CH_2$*C*H]-C$_6H_4$-O*P*(*i*-Pr)$_2$}NiBr (2 or 6,5-POCP(O)-NiBr). To a solution of substrate **1** (236 mg, 1.00 mmol, 1.00 equiv) in 10 mL THF were added {(*i*-PrCN)NiBr$_2$}$_n$ (345 mg, 1.20 mmol, 1.20 equiv), *i*-Pr$_2$P(O)H (134 mg, 1.00 mmol, 1.00 equiv), and Et$_3$N (167 μL, 1.20 mmol, 1.20 equiv). The mixture was stirred at room temperature for 3 h, further diluted by addition of 15 mL Et$_2$O, followed by cannula filtration and evaporation of the volatiles down to a volume of ca. 5 mL. To the latter solution was slowly added 15 mL of hexanes to complete precipitation. The precipitated solid was separated by filtration, washed with 2 × 5 mL hexanes and dried under vacuum to give the target product as a purple powder. (Yield: 380 mg, 0.751 mmol, 75 %).^{1}H NMR

(500 MHz, 20 °C, C$_6$D$_6$): δ 0.66 (dd, 3H, P(O)[CH(CH_3)(CH$_3$)][CH(CH$_3$)$_2$], $^3J_{HH}$ = 7.1, $^3J_{HP}$ = 15.7), 0.80 (dd, 3H, P(O)[CH(CH$_3$)(CH_3)][CH(CH$_3$)$_2$], $^3J_{HH}$ = 7.2, $^3J_{HP}$ = 14.9), 0.89 (dd, 1H, Ni-CH-C(*H*)(H), $^2J_{HH'}$ = 15.1, $^3J_{HH}$ = 7.3, *cis* to Ni-C*H*), 1.05-1.12 (3x dd overlapping, 9H, 2x P(O)[CH(CH$_3$)$_2$][CH(CH_3)$_2$] and 1x ArO-P[CH(CH_3)(CH$_3$)][CH(CH$_3$)$_2$], $^3J_{HH}$ ≈ 7.2, $^3J_{HP}$ ≈ 14.8), 1.46 (dd, 3H, ArO-P[CH(CH$_3$)(CH_3)][CH(CH$_3$)$_2$], $^3J_{HH}$ = 7.3, $^3J_{HP}$ = 17.0), 1.69 (dd, 3H, ArO-P[CH(CH$_3$)$_2$][CH(CH_3)(CH$_3$)], $^3J_{HH}$ = 7.0, $^3J_{HP}$ = 14.9), 1.77 (dd, 3H, ArO-P[CH(CH$_3$)$_2$][CH(CH$_3$)(CH_3)], $^3J_{HH}$ = 7.3, $^3J_{HP}$ = 16.2), 1.92 (t, 1H, Ni-CH-C(H)(*H*), $^2J_{HH}$ ≈ $^2J_{HP}$ = 15.1, $^2J_{HH}$ = 10.2, *trans* to Ni-C*H*), 2.42 (dhept, 1H, ArO-P(CH(CH$_3$)$_2$)(C*H*(CH$_3$)$_2$), $^2J_{HP}$ = 10.9, $^3J_{HH}$ = 7.14), 2.60 (heptd, 1H, 1H, ArO-P(C*H*(CH$_3$)$_2$)(CH(CH$_3$)$_2$), $^3J_{HH}$ = 7.6, $^2J_{HP}$ = 1.3), 2.68 (dddd, 1H, Ni-C*H*, $^3J_{HHtrans}$ = 10.5, $^3J_{HP(OAr)}$ = 9.3, $^3J_{HHcis}$ = 7.6, $^3J_{HP(=O)}$ = 3.7), 6.85 (dd, 1H, C6$_{Ar}$-*H*, $^3J_{HH}$ = 7.8, $^4J_{HH}$ = 1.4), 6.99-7.08 (m, 2H, C4$_{Ar}$-*H* and C5$_{Ar}$-*H*, overlapping with δ 7.05), 7.05 (dd, 1H, C3$_{Ar}$-*H*, $^3J_{HH}$ = 6.1, $^4J_{HH}$ = 1.3, overlapping with δ 6.99-7.08), Resonances for P(O)[C*H*(CH$_3$)$_2$][CH(CH$_3$)$_2$] and P(O)[CH(CH$_3$)$_2$][C*H*(CH$_3$)$_2$] are hidden under the signals at 1.46 and 1.69 ppm, respectively. ^{13}C{^{1}H} NMR (125.72 MHz, 20 °C, C$_6$D$_6$): δ 14.99 (br d, 1C, Ni-*C*H, $^2J_{CP}$ = 22.7), 15.34 (d, 1C, P(O)[CH(*C*H$_3$)(CH$_3$)][CH(CH$_3$)$_2$], $^2J_{CP}$ = 3.2), 15.90 (d, 1C, P(O)[CH(*C*H$_3$)(CH$_3$)][CH(CH$_3$)$_2$], $^2J_{CP}$ = 1.7), 16.01 (d, 1C, P(O)[CH(CH$_3$)$_2$][CH(*C*H$_3$)$_2$] or ArO-P[CH(*C*H$_3$)(CH$_3$)][CH(CH$_3$)$_2$], $^2J_{CP}$ = 2.7), 16.33 (d, 1C, P(O)[CH(CH$_3$)$_2$][CH(*C*H$_3$)$_2$] or ArO-P[CH(*C*H$_3$)(CH$_3$)][CH(CH$_3$)$_2$], $^2J_{CP}$ = 2.2), 16.49 (d, 1C, P(O)[CH(CH$_3$)$_2$][CH(*C*H$_3$)$_2$] or ArO-P[CH(*C*H$_3$)(CH$_3$)][CH(CH$_3$)$_2$], $^2J_{CP}$ = 3.7), 18.56 (s, 1C, ArO-P[CH(CH$_3$)$_2$][CH(*C*H$_3$)(CH$_3$)]), 19.40 (d, 1C, ArO-P[CH(CH$_3$)$_2$][CH(CH$_3$)(*C*H$_3$)], $^2J_{CP}$ = 3.6), 18.87 (d, 1C, ArO-P[CH(CH$_3$)(*C*H$_3$)][CH(CH$_3$)$_2$], $^2J_{CP}$ = 2.1), 25.04 (d, 1C, P(O)[*C*H(CH$_3$)$_2$][CH(CH$_3$)$_2$], $^1J_{CP}$ = 61.0), 25.17 (br d, 1C, Ni-CH-*C*H$_2$, $^1J_{CP}$ = 69.4), 25.50 (d, 1C, P(O)[CH(CH$_3$)$_2$][*C*H(CH$_3$)$_2$], $^1J_{CP}$ = 59.7), 29.68 (d, 1C, ArO-P(CH(CH$_3$)$_2$)(*C*H(CH$_3$)$_2$), $^1J_{CP}$ = 32.7), 31.25 (br d, 1C, ArO-P(*C*H(CH$_3$)$_2$)(CH(CH$_3$)$_2$), $^1J_{CP}$ = 19.6), 119.53 (d, 1C, *C*6$_{Ar}$-H, $^5J_{CP}$ = 2.1), 123.36 (s, 1C, *C*3$_{Ar}$-H or *C*4$_{Ar}$-H), 123.87 (s, 1C, *C*3$_{Ar}$-H or *C*4$_{Ar}$-H), 124.27 (s, 1C, *C*5$_{Ar}$-H), 140.18 (dd, 1C, *C*2$_{Ar}$-CHNi, $^3J_{CP}$ = 11.2, $^3J_{CP'}$ = 7.2), 154.16 (d, 1C, *C*2$_{Ar}$-OP, $^2J_{CP(OAr)}$ = 3.0). ^{31}P{^{1}H} NMR (202.4 MHz, 20 °C, C$_6$D$_6$): 205.43 (d, 1P, (ArO)*P*-Ni, $^4J_{PP}$ = 3), 93.51 (br d, 1P, *P*(=O)-Ni, $^4J_{PP}$ = 3).

{κ^C,$\kappa^{C'}$,κ^P-2-[2-vinyl-C$_6$H$_4$-OP(*i*-Pr)$_2$C̲H̲C̲H̲]-C$_6$H$_4$-OP̲(*i*-Pr)$_2$}NiBr (3 or 6,3-POCC-NiBr). To a solution of substrate **1** (236 mg, 1.00 mmol, 1.00 equiv) in 10 mL THF were added {(*i*-PrCN)NiBr$_2$}$_n$ (173 mg, 0.60 mmol, 0.60 equiv), and Et$_3$N (279 μL, 2.00 mmol, 2.00 equiv). The mixture was stirred at room temperature for 4 days after which time the mixture was placed under

vacuum to remove the volatiles. The remaining residues were extracted with 3×10 mL Et$_2$O by cannula filtration, and the extracts concentrated to ca. 5 mL. To the latter was added 10 mL hexanes, the mixture concentrated to ca. 5 mL under vacuum, and cooled to -78 °C. Cannula filtration gave an orange solid, which was dried under vacuum (Yield: 61 mg, 0.10 mmol, 20 %). ^{1}H NMR (500 MHz, 20 °C, C$_6$D$_6$): δ 1.03 (br dd, 3H, C(Ni)(H)-P$^+$(OAr)[CH(CH_3)(CH$_3$)][CH(CH$_3$)$_2$], $^3J_{\mathrm{HH}} = 6.3$, $^3J_{\mathrm{HP}} = 15.9$), 1.11 (br dd, 3H, C(Ni)(H)-P$^+$(OAr)[CH(CH$_3$)$_2$][CH(CH_3)(CH$_3$)], $^3J_{\mathrm{HH}} = 8.0$, $^3J_{\mathrm{HP}} = 15.8$, hidden under residual Et$_2$O), 1.20 (dd, 3H, Ni-P[CH(CH_3)(CH$_3$)][CH(CH$_3$)$_2$], $^3J_{\mathrm{HH}} = 7.0$, $^3J_{\mathrm{HP}} = 11.8$), 1.33 (br dd, 3H, C(Ni)(H)-P$^+$(OAr)[CH(CH$_3$)(CH_3)][CH(CH$_3$)$_2$], $^3J_{\mathrm{HH}} = 6.2$, $^3J_{\mathrm{HP}} = 11.4$, overlapping with δ 1.37), 1.37 (dd, 3H, Ni-P[CH(CH$_3$)$_2$][CH(CH_3)(CH$_3$)], $^3J_{\mathrm{HH}} = 6.8$, $^3J_{\mathrm{HP}} = 13.2$, overlapping with δ 1.33 and 1.38), 1.38 (dd, 3H, Ni-P[CH(CH$_3$)(CH_3)][CH(CH$_3$)$_2$], $^3J_{\mathrm{HH}} = 7.3$, $^3J_{\mathrm{HP}} = 13.0$, overlapping with δ 1.37 and 1.41), 1.41 (dd, 3H, Ni-P[CH(CH$_3$)$_2$][CH(CH$_3$)(CH_3)], $^3J_{\mathrm{HH}} = 7.1$, $^3J_{\mathrm{HP}} = 17.5$, overlapping with δ 1.38), 1.81 (br dd, 3H, C(Ni)(H)-P$^+$(OAr)[CH(CH$_3$)$_2$][CH(CH_3)(CH$_3$)], $^3J_{\mathrm{HH}} = 6.6$, $^3J_{\mathrm{HP}} = 17.1$), 2.04 (br ddd, 1H, Ni-CH-P$^+$, $^3J_{\mathrm{HH}} = 10.9$, $^2J_{\mathrm{HP}} = 4.3$, $^3J_{\mathrm{HP}} = 6.2$), 2.27 (hept, 1H, Ni-P[CH(CH$_3$)$_2$][CH(CH$_3$)$_2$], $^3J_{\mathrm{HH}} = 7.2$), 2.35 (br s, 1H, C(Ni)(H)-P$^+$(OAr)[CH(CH$_3$)$_2$][CH(CH$_3$)$_2$], overlapping with δ 2.37), 2.37 (heptd, 1H, Ni-P[CH(CH$_3$)$_2$][CH(CH$_3$)$_2$], $^3J_{\mathrm{HH}} = 7.2$, $^3J_{\mathrm{HP}} = 10.6$, overlapping with δ 2.37), 2.95 (br q, 1H, Ni-CH-Ar, $^3J_{\mathrm{HH}} = 10.9$, $^3J_{\mathrm{HP^+}} = 12.3$, $^3J_{\mathrm{HP'}} = 10.2$), 3.40 (br s, 1H, C(Ni)(H)-P$^+$(OAr)[CH(CH$_3$)$_2$][CH(CH$_3$)$_2$]), 5.08 (d, 1H, Ar-CH=C(H)(H), $^3J_{\mathrm{HH}} = 11.0$, cis to Ar-CH), 4.58 (d, 1H, Ar-CH=C(H)(H), $^3J_{\mathrm{HH}} = 17.6$, $trans$ to Ar-CH), 6.50 (d, 1H, C3$_{\mathrm{Ar}}$-H, $^3J_{\mathrm{HH}} = 7.3$), 6.73 (td, 1H, C4$_{\mathrm{Ar}}$-H, $^3J_{\mathrm{HH}} = 7.4$, $^4J_{\mathrm{HH}} = 1.0$), 6.86 (td, 1H, C19$_{\mathrm{Ar}}$-H, $^3J_{\mathrm{HH}} = 7.3$, $^4J_{\mathrm{HH}} = 2.1$, overlapping with δ 6.89), 6.89 (td, 1H, C18$_{\mathrm{Ar}}$-H, $^3J_{\mathrm{HH}} = 7.4$, $^4J_{\mathrm{HH}} = 2.1$, overlapping with δ 6.86), 6.94 (dd, 1H, Ar-CH=CH$_2$, $^3J_{\mathrm{HH}trans} = 17.4$, $^3J_{\mathrm{HH}cis} = 10.1$, overlapping with C6$_{\mathrm{Ar}}$-$H$), 6.94 (d, 1H, C6$_{\mathrm{Ar}}$-$H$, $^3J_{\mathrm{HH}} = 7.3$, overlapping with Ar-CH=CH$_2$), 6.99 (d, 1H, C20$_{\mathrm{Ar}}$-H, $^3J_{\mathrm{HH}} \approx 7.3$, overlapping with C5$_{\mathrm{Ar}}$-$H$), 6.99 (dt, 1H, C5$_{\mathrm{Ar}}$-$H$, $^3J_{\mathrm{HH}} \approx 7.6$, $^4J_{\mathrm{HH}} \approx 1.5$, overlapping with C20$_{\mathrm{Ar}}$-$H$), 7.35 (dd, H, C17$_{\mathrm{Ar}}$-$H$, $^3J_{\mathrm{HH}} \approx 6.8$, $^4J_{\mathrm{HH}} \approx 2.4$). ^{13}C NMR (100.61 MHz, 20 °C, C$_6$D$_6$): δ 16.13 (d, 1C, Ni-P[CH(CH_3)(CH$_3$)][CH(CH$_3$)$_2$], $^2J_{\mathrm{CP}} = 2.3$), 16.33 (d, 1C, C(Ni)(H)-P$^+$(OAr)[CH(CH$_3$)(CH_3)][CH(CH$_3$)$_2$], $^2J_{\mathrm{CP}} = 5.9$), 16.58 (d, 1C, C(Ni)(H)-P$^+$(OAr)[CH(CH_3)(CH$_3$)][CH(CH$_3$)$_2$], $^2J_{\mathrm{CP}} = 4.4$), 17.29 (d, 1C, Ni-P[CH(CH$_3$)$_2$][CH(CH$_3$)(CH_3)], $^2J_{\mathrm{CP}} = 11.3$), 17.71 (d, 1C, C(Ni)(H)-P$^+$(OAr)[CH(CH$_3$)$_2$][CH(CH_3)(CH$_3$)], $^2J_{\mathrm{CP}} = 2.0$), 18.46 (d, 1C, Ni-P[CH(CH$_3$)$_2$][CH(CH$_3$)(CH_3)], $^2J_{\mathrm{CP}} = 2.9$), 18.63 (br dd, 1C, Ni-CH-P$^+$, $^1J_{\mathrm{CP}} = 79.0$, $^2J_{\mathrm{CP'}} = 16.0$), 18.75 (d, 1C, C(Ni)(H)-P$^+$(OAr)[CH(CH$_3$)$_2$][CH(CH_3)(CH$_3$)], $^2J_{\mathrm{CP}} = 1.3$, overlapping with

δ 18.76), 18.76 (d, 1C, Ni-P[CH(CH$_3$)(CH$_3$)][CH(CH$_3$)$_2$], $^2J_{CP}$ = 5.4, overlapping with δ 18.75), 24.54 (d, 1C, C(Ni)(H)-P$^+$(OAr)[CH(CH$_3$)$_2$][CH(CH$_3$)$_2$], $^1J_{CP}$ = 67.1), 25.33 (d, 1C, C(Ni)(H)-P$^+$(OAr)[CH(CH$_3$)$_2$][CH(CH$_3$)$_2$], $^1J_{CP}$ = 76.3), 28.69 (d, 1C, Ni-P[CH(CH$_3$)$_2$][CH(CH$_3$)$_2$], $^1J_{CP}$ = 22.7), 30.77 (d, 1C, Ni-P[CH(CH$_3$)$_2$][CH(CH$_3$)$_2$], $^1J_{CP}$ = 9.8), 37.17 (br s, 1C, Ni-CH-Ar), 116.50 (br s, 1C, Ar-CH=CH$_2$), 119.31 (d, 1C, C6$_{Ar}$-H, $^3J_{CP}$ = 2.7), 120.63 (br d, 1C, C20$_{Ar}$-H, $^3J_{CP}$ = 3.4), 122.66 (s, 1C, C4$_{Ar}$-H), 124.89 (s, 1C, C19$_{Ar}$-H), 126.73 (s, 1C, C5$_{Ar}$-H), 127.48 (s, 1C, C17$_{Ar}$-H), 127.81 (s, 1C, C3$_{Ar}$-H, hidden under the peak of C_6D_6), 129.25 (s, 1C, C18$_{Ar}$-H), 130.75 (d, 1C, C16$_{Ar}$-CH=CH$_2$, $^3J_{CP}$ = 4.0, overlapping with δ 130.80), 130.80 (br s, 1C, Ar-CH=CH$_2$), 133.02 (t, 1C, C2$_{Ar}$-CHNi, $^3J_{CP} \approx {}^3J_{CP'}$ = 8.9), 148.90 (d, 1C, C15$_{Ar}$-OP$^+$, $^2J_{CP}$ = 9.7), 158.08 (dd, 1C, C1$_{Ar}$-OPNi, $^2J_{CP}$ = 1.3, $^2J_{CP}$ = 0.8). ^{31}P{^{1}H} NMR (161.98 MHz, 20 °C, C_6D_6): δ 77.86 (br d, 1P, (i-Pr)$_2$(ArO)P^+CHNi, $^3J_{PP}$ = 10), 195.98 (d, 1P, ArO-P-Ni, $^3J_{PP}$ = 10).

{κ^N,κ^C,κ^P-2-[morphol-N-yl-CH$_2$CH]-C$_6$H$_4$-OP(i-Pr)$_2$}NiBr (4 or 6,4-POCN^{morph}-NiBr). To a solution of substrate **1** (236 mg, 1.00 mmol, 1.00 equiv) in 10 mL THF were added {(i-PrCN)NiBr$_2$}$_n$ (345 mg, 1.20 mmol, 1.20 equiv), morpholine (173 µL, 2.00 mmol, 2.00 equiv) and Et$_3$N (167 µL, 1.20 mmol, 1.20 equiv) and the mixture was stirred overnight at room temperature. Filtration of the final mixture followed by evaporation, extraction with 3 × 10 mL toluene, cannula filtration, and removal of the volatiles under vacuum gave a sticky residue. This was sonicated in 5 mL Et$_2$O and 10 mL hexanes and stirred vigorously. The volume of the resulting mixture was concentrated to ca. 5mL to complete the precipitation, and the precipitated solid was separated by cannula filtration and dried under vacuum. (Yield: 325 mg, 70 %). ^{1}H NMR (500 MHz, 20 °C, C_6D_6): δ 1.02 (dd, 3H, P[CH(CH_3)(CH$_3$)][CH(CH$_3$)$_2$], $^3J_{HH}$ = 7.0, $^3J_{HP}$ = 12.1), 1.44 (dd, 3H, P[CH(CH$_3$)(CH_3)][CH(CH$_3$)$_2$], $^3J_{HH}$ = 7.3, $^3J_{HP}$ = 17.1), 1.52 (dd, 3H, P[CH(CH$_3$)$_2$][CH(CH_3)(CH$_3$)], $^3J_{HH}$ = 7.3, $^3J_{HP}$ = 16.7, overlapping with δ 1.53), 1.53 (dd, 3H, P[CH(CH$_3$)$_2$][CH(CH$_3$)(CH_3)], $^3J_{HH}$ = 6.9, $^3J_{HP}$ = 15.1, overlapping with δ 1.52), 1.59 (q, 1H, Ni-CH, $^3J_{HHtrans} \approx {}^3J_{HHcis} \approx {}^3J_{HP}$ = 9.4), 1.96-2.05 (m, 1H, NiCHCH$_2$-N[C$_a$($H_{a'}$)($H_{a''}$)][C$_b$H$_2$]), 2.05-2.12 (m, 1H, NiCHCH$_2$-N[C$_a$H$_2$][C$_b$($H_{b'}$)($H_{b''}$)], overlapping with δ 2.12), 2.12 (hept, 1H, P[CH(CH$_3$)$_2$](CH(CH$_3$)$_2$], $^3J_{HH}$ = 9.4, overlapping with δ 2.05-2.12), 2.37 (heptd, 1H, P[CH(CH$_3$)$_2$](CH(CH$_3$)$_2$], $^3J_{HH}$ = 7.1, $^2J_{HP}$ = 0.6), 3.13-3.23 (m, 2H, NiCHCH$_2$-N[C$_a$H$_2$][C$_b$(H$_{b'}$)($H_{b''}$)] and NiCHCH$_2$-N[C$_c$H$_2$-C$_d$($H_{d'}$)(H$_{d''}$)O]), 3.27-3.37 (m, 2H, NiCHCH$_2$-N[C$_a$(H$_{a'}$)($H_{a''}$)][C$_b$H$_2$] and NiCHCH$_2$-N[C$_b$H$_2$-C$_d$($H_{d'}$)(H$_{d''}$)O]), 3.42 (ddd, 1H, Ni-CH-C(H)(H), $^2J_{HH}$ = 12.0, $^3J_{HHcis}$ = 8.5, $^4J_{HP}$ = 2.7, *cis* to Ni-CH), 3.68 (dd, 1H, Ni-CH-C(H)(H), $^2J_{HH}$ = 12.2,

$^3J_{\text{HH}trans}$ = 9.4, *trans* to Ni-C*H*), 3.87 (br s, 2H, NiCHC*H*$_2$-N[C$_a$H$_2$-C$_c$(H$_{c'}$)(*H$_{c''}$*)O] and NiCHC*H*$_2$-N[C$_b$H$_2$-C$_d$(H$_{d'}$)(*H$_{d''}$*)O]), 6.78 (dm, 1H, C2$_{\text{Ar}}$-*H*, $^3J_{\text{HH}}$ = 7.6, overlapping with δ 6.80), 6.80 (d, 1H, C6Ar-*H*, $^3J_{\text{HH}}$ = 8.3, overlapping with δ 6.78), 6.91 (td, 1H, C4$_{\text{Ar}}$-*H*, $^3J_{\text{HH}}$ = 7.6, $^4J_{\text{HH}}$ = 1.3), 6.98 (tm, 1H, C5$_{\text{Ar}}$-*H*, $^3J_{\text{HH}}$ = 7.7). ^{13}C{^{1}H} NMR (125.72 MHz, 20 °C, C$_6$D$_6$): δ -1.12 (d, 1C, Ni-*C*H, $^2J_{\text{CP}}$ = 16.1), 15.46 (d, 1C, P[CH(*C*H$_3$)(CH$_3$)][CH(CH$_3$)$_2$], $^2J_{\text{CP}}$ = 4.7), 18.08 (d, 1C, P[CH(CH$_3$)$_2$][CH(*C*H$_3$)(CH$_3$)], $^2J_{\text{CP}}$ = 6.2), 18.83 (s, 1C, P[CH(CH$_3$)$_2$][CH(CH$_3$)(*C*H$_3$)]), 19.16 (d, 1C, P[C$_a$H(CH$_3$)(*C*H$_3$)][CH(CH$_3$)$_2$], $^2J_{\text{CP}}$ = 2.7), 28.31 (d, 1C, P[*C*H(CH$_3$)$_2$](CH(CH$_3$)$_2$], $^1J_{\text{CP}}$ = 29.6), 29.95 (d, 1C, P[CH(CH$_3$)$_2$](*C*H(CH$_3$)$_2$], $^1J_{\text{CP}}$ = 17.8), 54.82 (s, 1C, NiCHCH$_2$-N[*C$_a$*H$_2$][C$_b$H$_2$]), 55.94 (s, 1C, NiCHCH$_2$-N[C$_a$H$_2$][*C$_b$*H$_2$]), 61.77 (s, 1C, O[*C$_c$*H$_2$][C$_d$H$_2$] or O[C$_c$H$_2$][*C$_d$*H$_2$]), 62.37 (s, 1C, O[*C$_c$*H$_2$][C$_d$H$_2$] or O[C$_c$H$_2$][*C$_d$*H$_2$]), 64.72 (s, 1C, Ni-CH-*C*H$_2$), 119.13 (d, 1C, *C*6$_{\text{Ar}}$-H, $^5J_{\text{CP}}$ = 2.4), 123.44 (s, 1C, *C*4$_{\text{Ar}}$-H), 124.40 (s, 1C, *C*3$_{\text{Ar}}$-H), 125.49 (s, 1C, *C*5$_{\text{Ar}}$-H), 153.53 (d, 1C, *C*2$_{\text{Ar}}$-CHNi, $^3J_{\text{CP}}$ = 8.4), 156.29 (d, 1C, *C*1$_{\text{Ar}}$-OP, $^2J_{\text{CP}}$ = 3.0). ^{31}P{^{1}H} NMR (202.4 MHz, 20 °C, C$_6$D$_6$): 203.92 (s, 1P).

{$\kappa^N,\kappa^C,\kappa^P$-2-[PhN(Et)CH$_2$CH]-C$_6H_4$-OP(i-Pr)$_2$}NiBr (5 or 6,4-POCN$^{\text{Ph,Et}}$-NiBr). To a solution of substrate **1** (236 mg, 1.00 mmol, 1.00 equiv) in 10 mL THF were added {(*i*-PrCN)NiBr$_2$}$_n$ (345 mg, 1.20 mmol, 1.20 equiv), PhN(Et)H (252 μL, 2.00 mmol, 2.00 equiv) and Et$_3$N (167 μL, 1.20 mmol, 1.20 equiv) and the mixture was stirred overnight at room temperature. The volatiles were removed under vacuum and the residues extracted with 2 x 10 mL toluene by cannula filtration. The solution was concentrated under vacuum, and the residues were treated with 8 mL Et$_2$O, filtered and the filtrate was cooled to –35 °C overnight. The deep orange crystals were separated, and washed with 2x 3 mL cold Et$_2$O. (Yield: 307 mg, 62 %). Major (crystallized) isomer: ^{1}H NMR (500 MHz, 20 °C, C$_6$D$_6$): δ 0.61 (t, 3H, N-CH$_2$-C*H$_3$*, $^3J_{\text{HH}}$ =7.1), 0.95 (dd, 3H, P[CH(C*H$_3$*)(CH$_3$)][CH(CH$_3$)$_2$], $^3J_{\text{HH}}$ = 7.1, $^3J_{\text{HP}}$ = 11.9), 1.20 (dd, 3H, P[CH(CH$_3$)$_2$][CH(C*H$_3$*)(CH$_3$)], $^3J_{\text{HH}}$ = 6.9, $^3J_{\text{HP}}$ = 15.9), 1.25 (dd, 3H, P[CH(CH$_3$)$_2$][CH(CH$_3$)(C*H$_3$*)], $^3J_{\text{HH}}$ = 7.2, $^3J_{\text{HP}}$ = 17.4), 1.41 (dd, 3H, P[CH(CH$_3$)(C*H$_3$*)][CH(CH$_3$)$_2$], $^3J_{\text{HH}}$ = 7.3, $^3J_{\text{HP}}$ = 17.3), 1.65 (ddd, 1H, Ni-C*H*, $^3J_{\text{HP}} \approx$ 12.5, $^3J_{\text{HH}trans}$ = 11.5, $^3J_{\text{HH}cis}$ 7.2), 1.93 (dhept, 1H, P[CH(CH$_3$)$_2$][C*H*(CH$_3$)$_2$], $^2J_{\text{HP}}$ = 14.3, $^3J_{\text{HH}}$ = 7.15), 2.38 (heptd, 1H, P[C*H*(CH$_3$)$_2$][CH(CH$_3$)$_2$], $^3J_{\text{HH}}$ = 7.2, $^2J_{\text{HP}}$ = 2.1), 3.04 (dq, 1H, N-C(*H*)(H)-CH$_3$, $^2J_{\text{HH}}$ = 14.3, $^3J_{\text{HH}}$ = 7.1), 3.58 (dq, 1H, N-C(H)(*H*)-CH$_3$, $^2J_{\text{HH}}$ = 14.4, $^3J_{\text{HH}}$ = 7.2), 4.10 (t, 1H, Ni-CH-C(*H*)(H), $^2J_{\text{HH}} \approx \, ^3J_{\text{HH}}$ = 11.9, *trans* to Ni-C*H*), 4.32 (ddd, 1H, Ni-CH-C(H)(*H*), $^2J_{\text{HH}}$ = 12.3, $^3J_{\text{HH}}$ = 7.1, $^4J_{\text{HP}}$ = 5.2, *cis* to Ni-C*H*), 6.79 (d, 1H, C6$_{\text{Ar}}$-*H*, $^3J_{\text{HH}}$ = 7.6), 6.82 (dm, 1H, C3$_{\text{Ar}}$-*H*, $^3J_{\text{HH}}$ = 7.5),

6.94 (td, 1H, C4$_{Ar}$-H, $^3J_{HH}$ = 7.6, $^4J_{HH}$ = 1.1, overlapping with δ 6.97), 6.97 (tm, 1H, N(*para*-C$_6$H$_5$), $^3J_{HH}$ = 7.3, overlapping with δ 6.94 and δ 7.01), 7.01 (tm, 1H, C5$_{Ar}$-H, $^3J_{HH}$ = 7.6, $^4J_{HH}$ = 1.1, overlapping with δ 6.97), 7.20 (tm, 2H, N(*meta*-C$_6$H$_5$), $^3J_{HH}$ = 7.9), 7.55 (d, 2H, N(*ortho*-C$_6$H$_5$), $^3J_{HH}$ = 8.0). ^{13}C{^{1}H} NMR (125.72 MHz, 20 °C, C$_6$D$_6$): δ 2.10 (d, 1C, Ni-CH, $^2J_{CP}$ = 17.1), 8.14 (d, 1C, N-CH$_2$-CH$_3$, $^4J_{CP}$ = 1.6), 15.12 (d, 1C, P[CH(CH$_3$)(CH$_3$)][CH(CH$_3$)$_2$], $^2J_{CP}$ = 5.5), 17.55 (d, 1C, P[CH(CH$_3$)$_2$][CH(CH$_3$)(CH$_3$)], $^2J_{CP}$ = 7.2), 18.41 (d, 1C, P[CH(CH$_3$)$_2$][CH(CH$_3$)(CH$_3$)], $^2J_{CP}$ = 1.6), 18.91 (d, 1C, P[CH(CH$_3$)(CH$_3$)][CH(CH$_3$)$_2$], $^2J_{CP}$ = 2.7), 27.89 (d, 1C, P[CH(CH$_3$)$_2$][CH(CH$_3$)$_2$], $^1J_{CP}$ = 17.6), 29.78 (d, 1C, P[CH(CH$_3$)$_2$][CH(CH$_3$)$_2$], $^1J_{CP}$ = 30.6), 54.85 (s, 1C, N-CH$_2$-CH$_3$), 59.89 (s, 1C, Ni-CH-CH$_2$), 118.99 (d, 1C, C6$_{Ar}$-H, $^5J_{CP}$ = 2.8), 123.07 (s, 2C, N(*ortho*-C_6H$_5$)), 123.36 (s, 1C, C4$_{Ar}$-H), 124.42 (s, 1C, N(*para*-C_6H$_5$)), 124.72 (s, 1C, C3$_{Ar}$-H), 125.77 (s, 1C, C5$_{Ar}$-H), 129.29 (s, 2C, N(*meta*-C_6H$_5$)), 134.44 (d, 1C, C2$_{Ar}$-CHNi, $^3J_{CP}$ = 8.9), 145.54 (d, 1C, N(*ipso*-C_6H$_5$), $^3J_{CP}$ = 2.1), 156.44 (d, 1C, C1$_{Ar}$-OP, $^2J_{CP}$ = 3.1). ^{31}P{^{1}H} NMR (202.4 MHz, 20 °C, C$_6$D$_6$): δ 207.05 (s, 1P). Minor isomer: ^{1}H NMR (500 MHz, 20 °C, C$_6$D$_6$): δ 1.00 (dd, 3H, P[CH(CH_3)(CH$_3$)][CH(CH$_3$)$_2$], $^3J_{HH}$ = 6.9, $^3J_{HP}$ = 12.2), 1.45 (dd, 3H, P[CH(CH$_3$)(CH_3)][CH(CH$_3$)$_2$], $^3J_{HH}$ = 6.4, overlapping with δ 1.41 of major), 1.53 (dd, 3H, P[CH(CH$_3$)$_2$][CH(CH_3)$_2$], $^3J_{HH}$ = 6.9, overlapping with δ 1.56), 1.56 (dd, 3H, P[CH(CH$_3$)$_2$][CH(CH_3)$_2$], $^3J_{HH}$ = 7.2, overlapping with δ 1.53 and δ 1.58), 1.58 (t, 3H, N-CH$_2$-CH_3, $^3J_{HH}$ =7.1, overlapping with δ 1.56), 1.80 (q, 1H, Ni-CH, $^3J_{HP}$ ≈ $^3J_{HHtrans}$ ≈ $^3J_{HHcis}$ ≈ 9-10), 2.16 (dhept, 1H, P[CH(CH$_3$)$_2$][CH(CH$_3$)$_2$], $^2J_{HP}$ = 13.3, $^3J_{HH}$ = 7.1), 2.29 (hept, 1H, P[CH(CH$_3$)$_2$][CH(CH$_3$)$_2$], $^3J_{HH}$ = 6.9), 3.27 (1H, N-C(H)(H)-CH$_3$, hidden under the peak for major), 3.26 (dq, 1H, N-C(H)(H)-CH$_3$, $^2J_{HH}$ = 14.2, $^3J_{HH}$ = 7.1), 3.98 (dd, 1H, Ni-CH-C(H)(H), $^2J_{HH}$ = 13.4, $^3J_{HH}$ = 9.1, *cis* to Ni-CH), 4.65 (dd, 1H, Ni-CH-C(H)(H), $^2J_{HH}$ = 13.1, $^3J_{HH}$ = 8.7, *trans* to Ni-CH), 7.08 (t, 2H, N(*meta*-C$_6$H$_5$), $^3J_{HH}$ = 7.9), 7.80 (d, 2H, N(*ortho*-C$_6$H$_5$), $^3J_{HH}$ = 7.9). Other peaks were hidden under the signals for the major isomers. ^{13}C{^{1}H} NMR (125.72 MHz, 20 °C, C$_6$D$_6$): δ 15.63 (1C, P[CH(CH$_3$)(CH$_3$)][CH(CH$_3$)$_2$]), 18.25 (2C, P[CH(CH$_3$)$_2$][CH(CH$_3$)$_2$]), 19.53 (1C, P[CH(CH$_3$)(CH$_3$)][CH(CH$_3$)$_2$], 28.62 (1C, P[CH(CH$_3$)$_2$][CH(CH$_3$)$_2$]), 30.06 (1C, P[CH(CH$_3$)$_2$][CH(CH$_3$)$_2$]), 51.36 (1C, N-CH$_2$-CH$_3$), 67.34 (1C, Ni-CH-CH2), 122.71 (2C, N(*ortho*-C$_6$H$_5$)), 129.01 (2C, N(*meta*-C$_6$H$_5$)). Other resonances were not detected or could not be attributed. ^{31}P{^{1}H} NMR (202.4 MHz, 20 °C, C$_6$D$_6$): δ 204.07 (s, 1P).

{κ^N,κ^C,κ^P-2-[i-Pr$\underline{N}$(H)CH$_2$$\underline{C}$H]-C$_6H_4$-O$\underline{P}$($i$-Pr)2}NiBr (6 or 6,4-POCN^{iPr,H}-NiBr). To a solution of substrate **1** (236 mg, 1.00 mmol, 1.00 equiv) in 10 mL THF were added {(i-PrCN)NiBr$_2$}$_n$ (345

mg, 1.20 mmol, 1.20 equiv), i-PrNH$_2$ (172 μL, 2.00 mmol, 2.00 equiv), and Et$_3$N (167 μL, 1.20 mmol, 1.20 equiv). The resulting mixture was stirred overnight at room temperature, filtered, evaporated, and extracted with 3 × 10 mL Et$_2$O by cannula filtration. The filtrate was concentrated under vacuum up to ca. 5 mL, then 10 mL hexanes were added, and this mixture was once again concentrated to ca. 5 mL and cooled to –78 °C. The precipitated solid was separated by cannula filtration and dried under vacuum. (Yield: 272 mg, 63 %). Major (crystallized) isomer: ^{1}H NMR (500 MHz, 20 °C, C$_6$D$_6$): δ 0.86 (br s, 1H, NH), 1.00 (d, 3H, N[CH(CH_3)(CH$_3$)], $^3J_{HH}$ = 6.5), 1.04 (dd, 3H, P[CH(CH_3)$_2$]$_2$, $^3J_{HH}$ = 7.1, $^3J_{HP}$ ≈ 12, overlapping with signal of minor), 1.39 (d, 3H, N[CH(CH$_3$)(CH_3)], $^3J_{HH}$ = 6.7), 1.47 (dd, 3H, P[CH(CH_3)$_2$]$_2$, $^3J_{HH}$ = 7.3, $^3J_{HP}$ ≈ 17.0), 1.51 (dd, 3H, P[CH(CH_3)$_2$]$_2$, $^3J_{HH}$ = 7.3, $^3J_{HP}$ ≈ 16.9), 1.55 (1H, Ni-CH, hidden under the signals for P[CH(CH_3)$_2$]$_2$ of major and minor), 1.56 (dd, 3H, P[CH(CH_3)$_2$]$_2$, $^3J_{HH}$ = 6.6, $^3J_{HP}$ ≈ 13.1), 2.15 (dhept, 1H, P[CH(CH$_3$)$_2$]$_2$, $^2J_{HP}$ = 14.2, $^3J_{HH}$ = 7.1, overlapping with signal of minor), 2.42 (heptd, 1H, P[CH(CH$_3$)$_2$]$_2$, $^3J_{HH}$ = 7.2, $^2J_{HP}$ = 1.2, overlapping with signal of minor), 2.82 (heptd, 1H, N[CH(CH$_3$)$_2$], $^3J_{HH(Me)}$ = 6.6, $^3J_{HH(N)}$ = 3.0), overlapping with signal of minor), 3.31 (dddd, 1H, Ni-CH-CH_2, $^2J_{HH}$ = 12.9, $^3J_{HH(C)}$ = 8.9, $^3J_{HH(N)}$ = 3.9, $^4J_{HP}$ = 1.0, $trans$ to Ni-CH), 3.87 (dt, 1H, $^2J_{HH}$ = 12.9, $^3J_{HH(C)}$ ≈ $^3J_{HH(N)}$ = 9.1, cis to Ni-CH), 6.81 (1H, C$_{Ar}$-H, overlapping with signals of minor), 6.83 (1H, C3$_{Ar}$-H, overlapping with signals of minor), 6.93 (1H, C$_{Ar}$-H, overlapping with signals of minor), 6.98 (t, 1H, C4$_{Ar}$-H or C5$_{Ar}$-H, $^3J_{HH}$ = 7.4). ^{13}C{^{1}H} NMR (125.72 MHz, 20 °C, C$_6$D$_6$): δ -1.94 (d, 1C, Ni-CH, 2JCP = 15.6), 15.32 (d, 1C, P[CH(CH_3)$_2$]$_2$, $^2J_{CP}$ = 6.9), 17.88 (d, 1C, P[CH(CH_3)$_2$]$_2$, $^2J_{CP}$ = 6.9), 18.70 (d, 1C, P[CH(CH_3)$_2$]$_2$, $^2J_{CP}$ = 1.2), 19.14 (d, 1C, P[CH(CH_3)$_2$]$_2$, $^2J_{CP}$ = 3.1), 20.59 (d, 1C, N[CH(CH_3)(CH$_3$)], $^4J_{CP}$ = 2.0), 21.41 (s, 1C, N[CH(CH$_3$)(CH_3)]), 28.48 (d, 1C, P[CH(CH$_3$)$_2$]$_2$, $^2J_{CP}$ = 29.0), 29.65 (d, 1C, P[CH(CH$_3$)$_2$]$_2$, $^2J_{CP}$ = 17.3), 49.40 (s, 1C, N[CH(CH$_3$)$_2$]), 52.31 (s, 1C, Ni-CH-CH$_2$), 119.21 (s, 1C, C_{Ar}-H), 123.26 (s, 1C, C_{Ar}-H), 124.58 (s, 1C, C3$_{Ar}$-H), 125.21 (s, 1C, C4$_{Ar}$-H or C5$_{Ar}$-H), 134.76 (d, 1C, C2$_{Ar}$-CHNi, $^3J_{CP}$ = 8.6), 156.40 (d, 1C, C1$_{Ar}$-OP, $^2J_{CP}$ = 3.1). ^{31}P{^{1}H} NMR (202.4 MHz, 20 °C, C$_6$D$_6$): δ 200.63 (s, 1P). Minor isomer. ^{1}H NMR (500 MHz, 20 °C, C$_6$D$_6$): δ 0.70 (br s, 1H, NH), 0.89 (d, 3H, N[CH(CH_3)(CH$_3$)], $^3J_{HH}$ = 6.5), 1.04 (dd, 3H, P[CH(CH_3)$_2$]$_2$, $^3J_{HH}$ = 7.1, $^3J_{HP}$ ≈ 12, overlapping with signal of major), 1.34 (d, 3H, N[CH(CH$_3$)(CH_3)], $^3J_{HH}$ = 6.6), 1.51 (dd, 3H, P[CH(CH_3)$_2$]$_2$, $^3J_{HH}$ = 7.2, $^3J_{HP}$ ≈ 16.9), 1.59 (dd, 3H, P[CH(CH_3)$_2$]$_2$, $^3J_{HH}$ = 7.0, $^3J_{HP}$ ≈ 13.3), 1.60 (dd, 3H, P[CH(CH_3)$_2$]$_2$, $^3J_{HH}$ = 7.4, $^3J_{HP}$ ≈ 16.6), 1.55 (q, 1H, Ni-CH, $^3J_{HH}$ ≈ $^3J_{HH'}$ ≈ $^3J_{HP}$ = 9.4), 2.18 (dhept, 1H, P[CH(CH$_3$)$_2$]$_2$, $^2J_{HP}$ = 14.2, $^3J_{HH}$ = 7.1, overlapping with signal of major), 2.35 (hept, 1H, P[CH(CH$_3$)$_2$]$_2$, $^3J_{HH}$ = 7.2, overlapping with

410

signal of major), 2.86 (heptd, 1H, N[CH(CH$_3$)$_2$], $^3J_{HH(Me)}$ = 6.6, $^3J_{HH(N)}$ = 3.0), overlapping with signal of major), 3.49 (dtd, 1H, Ni-CH-CH_2, $^2J_{HH}$ = 12.2, $^3J_{HH(C)}$ ≈ $^3J_{HH(N)}$ = 8.0, *trans* to Ni-CH), 3.75 (dt, 1H, Ni-CH-CH_2, $^2J_{HH}$ = 12.0, $^3J_{HH(C)}$ ≈ $^3J_{HH(N)}$ = 8.9, *cis* to Ni-CH), 6.79 (1H, C$_{Ar}$-H, overlapping with signals of major), 6.81 (1H, C3$_{Ar}$-H, overlapping with signals of major), 6.87 (t, 1H, C4$_{Ar}$-H or C5$_{Ar}$-H, $^3J_{HH}$ = 7.3), 6.95 (1H, C$_{Ar}$-H, overlapping with signals of major). ^{13}C{^{1}H} NMR (125.72 MHz, 20 °C, C$_6$D$_6$): δ -1.69 (d, 1C, Ni-CH, 2JCP = 16.3), 15.60 (d, 1C, P[CH(CH$_3$)$_2$]$_2$, $^2J_{CP}$ = 4.5), 18.20 (d, 1C, P[CH(CH$_3$)$_2$]$_2$, $^2J_{CP}$ = 6.1), 18.70 (d, 1C, P[CH(CH$_3$)$_2$]$_2$, $^2J_{CP}$ = 0.7), 19.12 (d, 1C, P[CH(CH$_3$)$_2$]$_2$, $^2J_{CP}$ = 3.6), 20.07 (d, 1C, N[CH(CH$_3$)(CH$_3$)], $^4J_{CP}$ = 2.2), 20.88 (s, 1C, N[CH(CH$_3$)(CH$_3$)]), 28.40 (d, 1C, P[CH(CH$_3$)$_2$]$_2$, $^2J_{CP}$ = 29.2), 30.11 (d, 1C, P[CH(CH$_3$)$_2$]$_2$, $^2J_{CP}$ = 17.2), 50.45 (s, 1C, N[CH(CH$_3$)$_2$]), 51.61 (s, 1C, Ni-CH-CH$_2$), 119.23 (s, 1C, C_{Ar}-H), 123.40 (s, 1C, $C4_{Ar}$-H or $C5_{Ar}$-H), 124.27 (s, 1C, $C3_{Ar}$-H), 125.20 (s, 1C, C_{Ar}-H), 134.30 (d, 1C, $C2_{Ar}$-CHNi, $^3J_{CP}$ = 8.5), 156.21 (d, 1C, $C1_{Ar}$-OP, $^2J_{CP}$ = 3.1). ^{31}P{^{1}H} NMR (202.4 MHz, 20 °C, C$_6$D$_6$): δ 200.88 (s, 1P).

{κ^P,κ^C,$\kappa^{P'}$-2-[i-Pr$_2$$\underline{P}CH_2$$\underline{C}$H]-C$_6H_4$-O$\underline{P}$($i$-Pr)2}NiBr (10 or 6,4-POCP^{iPr}-NiBr). To a solution of substrate **1** (236 mg, 1.00 mmol, 1.00 equiv) in 20 mL THF were added {(i-PrCN)NiBr$_2$}$_n$ (201 mg, 0.70 mmol, 0.70 equiv), (i-Pr$_2$PH)$_2$NiBr$_2$ (227 mg, 0.50 mmol, 0.50 equiv) and Et$_3$N (335 μL, 2.40 mmol, 1.20 equiv). The mixture was stirred at room temperature for 4 h, after which the solution was separated by cannula filtration, and the volatiles evaporated under vacuum. The residues were extracted with 3 × 15 mL hexanes, separated by cannula filtration, the filtrate was concentrated to ca. 10 mL and cooled to –78 °C. The precipitate was isolated by cannula filtration and washed with an extra 5 mL cold hexanes to give a dull orange powder. (Yield: 374 mg, 0.76 mmol, 76 %). ^{1}H NMR (500 MHz, 20 °C, C$_6$D$_6$): δ 1.03 (dd, 3H, CH$_2$-P[CH(CH_3)$_2$]$_2$, $^3J_{HH}$ = 7.0, $^3J_{HP}$ = 14.6), 1.08 (dd, 3H, ArO-P[CH(CH_3)(CH$_3$)][CH(CH$_3$)$_2$], $^3J_{HH}$ = 7.1, $^3J_{HP}$ = 11.4, overlapping with δ 1.03 and δ 1.11), 1.11 (dd, 3H, CH$_2$-P[CH(CH_3)$_2$]$_2$, $^3J_{HH}$ = 7.0, $^3J_{HP}$ = 14.6), 1.29 (dd, 3H, CH$_2$-P[CH(CH_3)$_2$]$_2$, $^3J_{HH}$ = 7.2, $^3J_{HP}$ = 16.9), 1.37 (dd, 3H, ArO-P[CH(CH$_3$)(CH_3)][CH(CH$_3$)$_2$], $^3J_{HH}$ = 7.2, $^3J_{HP}$ = 16.6, overlapping with δ 1.38), 1.38 (dd, 3H, CH$_2$-P[CH(CH_3)$_2$]$_2$, $^3J_{HH}$ = 7.2, $^3J_{HP}$ = 16.9, overlapping with δ 1.37), 1.57 (dd, 3H, ArO-P[CH(CH$_3$)$_2$][CH(CH_3)(CH$_3$)], $^3J_{HH}$ = 7.2, $^3J_{HP}$ = 15.9), 1.61 (dd, 3H, ArO-P[CH(CH$_3$)$_2$][CH(CH$_3$)(CH_3)], $^3J_{HH}$ = 7.0, $^3J_{HP}$ = 14.6), 1.74-1.87 (m, 2H, CH$_2$-P[CH(CH_3)$_2$]$_2$, $^3J_{HH}$ ≈ 7.0, $^2J_{HP}$ ≈ 3.1), 2.09 (dddd, 1H, Ni-CH-C(H)(H), $^2J_{HH}$ =1414.8 9.7, $^2J_{HP}$ = 7.6, $^4J_{HP}$ = 1.6, *cis* to Ni-CH), 2.24 (qd, 1H, Ni-CH, $^3J_{HH}$ ≈ $^3J_{HH'}$ ≈ $^3J_{HP(OAr)}$ = 9.7, $^3J_{HP(CH2)}$ = 4.0), 2.53 (td, 1H, Ni-CH-C(H)(H), $^2J_{HH}$ =14.8, $^3J_{HH}$ ≈ $^2J_{HP}$ = 9.4, *trans* to Ni-CH), 6.82-

6.88 (m, 1H, C6$_{Ar}$-*H*), 6.94-7.02 (m, 2H, C4$_{Ar}$-*H* and C5$_{Ar}$-*H*), 7.06-7.11 (m, 1H, C2$_{Ar}$-*H*). ^{13}C{^{1}H} NMR (125.72 MHz, 20 °C, C$_6$D$_6$): δ -0.81 (dd, 1C, Ni-*C*H, $^2J_{CP}$ = 44.2, $^2J_{CP'}$ = 8.7), 15.53 (dd, 1C, ArO-P[CH(*C*H$_3$)(CH$_3$)][CH(CH$_3$)$_2$], $^2J_{CP}$ = 3.7, $^4J_{CP}$ = 1.4), 17.65 (d, 1C, CH$_2$-P[CH(*C*H$_3$)$_2$]$_2$, $^2J_{CP}$ = 1.4), 17.77 (d, 1C, CH$_2$-P[CH(*C*H$_3$)$_2$]$_2$, $^2J_{CP}$ = 1.2), 18.20 (d, 1C, ArO-P[CH(CH$_3$)$_2$][CH(*C*H$_3$)(CH$_3$)], $^2J_{CP}$ = 6.4), 18.46 (d, 1C, ArO-P[CH(CH$_3$)$_2$][CH(CH$_3$)(*C*H$_3$)], $^2J_{CP}$ = 1.9), 18.69 (d, 1C, CH$_2$-P[CH(*C*H$_3$)$_2$]$_2$, $^2J_{CP}$ = 4.3), 18.92 (d, 1C, ArO-P[CH(CH$_3$)(*C*H$_3$)][CH(CH$_3$)$_2$] or CH$_2$-P[CH(*C*H$_3$)$_2$]$_2$, $^2J_{CP}$ = 4.8), 19.18 (d, 1C, ArO-P[CH(CH$_3$)(*C*H$_3$)][CH(CH$_3$)$_2$] or CH$_2$-P[CH(*C*H$_3$)$_2$]$_2$, $^2J_{CP}$ = 4.6), 22.14 (dd, 1C, Ni-CH-*C*H$_2$, $^2J_{CP}$ = 26.1, $^3J_{CP}$ = 2.5), 22.31 (dd, 1C, CH$_2$-P[*C*H(CH$_3$)$_2$]$_2$, $^1J_{CP}$ = 10.5, $^3J_{CP}$ = 5.7), 22.49 (dd, 1C, CH$_2$-P[*C*H(CH$_3$)$_2$]$_2$, $^1J_{CP}$ = 12.8, $^3J_{CP}$ = 3.6), 28.92 (dd, 1C, ArO-P[*C*H(CH$_3$)$_2$]$_2$, $^1J_{CP}$ = 10.3, $^3J_{CP}$ = 4.5, overlapping with δ 28.93), 28.93 (dd, ArO-P[*C*H(CH$_3$)$_2$]$_2$, $^1J_{CP}$ = 16.3, $^3J_{CP}$ = 2.5, overlapping with δ 28.92), 120.35 (t, 1C, C6$_{Ar}$-*H*, $^5J_{CP} \approx {}^5J_{CP'}$ = 1.8), 123.70 (d, 1C, *C*3$_{Ar}$-H, $^4J_{CP}$ = 0.7), 124.70 (m, 2C, *C*4$_{Ar}$-H and *C*5$_{Ar}$-H), 136.27 (t, 1C, *C*2$_{Ar}$-CHNi, $^3J_{CP} \approx {}^3J_{CP'}$ = 8.1), 155.85 (dd, 1C, *C*1$_{Ar}$-OP, $^2J_{CP(OAr)}$ = 2.5, $^4J_{CP(CH2CHNi)}$ = 1.7). ^{31}P{^{1}H} NMR (202.4 MHz, 20 °C, C$_6$D$_6$): δ 192.25 (d, 1P, CH$_2$-*P*(*i*-Pr)$_2$, $^2J_{PP}$ = 307), -57.15 (d, 1P, ArO-*P*(*i*-Pr)$_2$, $^2J_{PP}$ = 307).

{$\kappa^P,\kappa^C,\kappa^{P'}$-2-[Ph$_2PCH_2$CH]-C$_6H_4$-OP(*i*-Pr)2}NiBr (11 or 6,4-POCP^{Ph}-NiBr). To a solution of substrate **1** (473 mg 2.00 mmol, 1.00 equiv) in 20 mL THF were added {(*i*-PrCN)NiBr$_2$}$_n$ (690 mg, 2.40 mmol, 1.20 equiv), Ph$_2$PH (348 µL, 2.00 mmol, 1.00 equiv) and Et$_3$N (335 µL, 2.40 mmol, 1.20 equiv). The mixture was stirred at room temperature for 4 h, after which the volatiles were evaporated under vacuum. The residues were extracted with 3 × 10 mL toluene by cannula filtration and the solvent was again removed in vacuo. The dark brown residues were dissolved in refluxing acetonitrile (ca. 60 mL) and gradually cooled to –10 °C (after which crystallization started) and then to –35 °C overnight. The supernatant was removed by cannula filtration and the crystals were washed with 2 fractions of cold acetonitrile and dried under vacuum to give dark orange crystals. (Yield: 395 mg, 0.71 mmol, 35 %). ^{1}H NMR (500 MHz, 20 °C, C$_6$D$_6$): δ 1.07 (dd, 3H, P[CH(C*H*$_3$)(CH$_3$)][CH(CH$_3$)$_2$], $^3J_{HH}$ = 7.1, $^3J_{HP}$ = 11.5), 1.41 (dd, 3H, P[CH(CH$_3$)(C*H*$_3$)][CH(CH$_3$)$_2$], $^3J_{HH}$ = 7.4, $^3J_{HP}$ = 16.9), 1.46 (dd, 3H, P[CH(CH$_3$)$_2$][CH(C*H*$_3$)(CH$_3$)], $^3J_{HH}$ = 7.0, $^3J_{HP}$ = 14.9, overlapping with δ 1.50), 1.50 (dd, 3H, P[CH(CH$_3$)$_2$][CH(CH$_3$)(C*H*$_3$)], $^3J_{HH}$ = 7.3, $^3J_{HP}$ = 16.3, overlapping with δ 1.46), 2.27 (heptdd, 1H, P[CH(CH$_3$)$_2$](C*H*(CH$_3$)$_2$], $^3J_{HH}$ = 7.0, $^2J_{HP}$ = 12.9, $^4J_{HP}$ = 10.1), 2.39 (quint, 1H, Ni-C*H*, $^3J_{HH} \approx {}^3J_{HH'} \approx {}^3J_{HP} \approx {}^3J_{HP'}$ = 9.3), 2.53 (heptd, 1H, P[C*H*(CH$_3$)$_2$](CH(CH$_3$)$_2$], $^3J_{HH}$ = 7.3, $^2J_{HP}$ = 0.9), 3.03

(dddd, 1H, Ni-CH-C(H)(H), $^2J_{HH}$ = 14.0, $^3J_{HH}$ = 8.7, $^4J_{HP(Ph2)}$ = 7.0, $^4J_{HP(i\text{-}Pr2)}$ = 2.2, *cis* to Ni-CH,), 3.16 (ddd, 1H, Ni-CH-C(H)(H), $^2J_{HH}$ = 14.1, $^3J_{HH}$ = 9.7, $^4J_{HP(Ph2)}$ = 8.3, *trans* to Ni-CH), 6.82 (d, 1H, C6$_{Ar}$-H, $^3J_{HH}$ = 7.6), 6.87 (t, 1H, C4$_{Ar}$-H, $^3J_{HH}$ = 7.9), 6.92-6.97 (m, 2H, C3$_{Ar}$-H and C5Ar-H, $^3J_{HH}$ = 7.7), 6.96-7.01 (m, 3H, P(*para*- and *meta*-C$_6H_5$)(Ph), $^4J_{HP}$ = 2.1), 7.02-7.06 (tq, 1H, P(Ph)(*para*- C$_6H_5$), $^3J_{HH}$ = 7.4, $^4J_{HH} \approx {}^5J_{HP}$ = 1.4), 7.05-7.11 (overlapping tq and tq, 2H, P(Ph)(*meta*-C$_6H_5$), $^3J_{HH}$ = 7.4, $^4J_{HH} \approx {}^5J_{HP}$ = 2.0), 7.92-7.97 (m, 2H, P(*ortho*-C$_6H_5$)(Ph), $^2J_{HP}$ = 11.0, $^3J_{HH}$ = 7.0, $^4J_{HH}$ = 2.2), 7.96-8.00 (m, 2H, P(Ph)(*ortho*-C$_6H_5$), $^2J_{HP}$ = 10.6, $^3J_{HH}$ = 7.4, $^4J_{HH}$ = 1.7). $^{13}C\{^1H\}$ NMR (125.72 MHz, 20 °C, C$_6$D$_6$): δ 2.12 (dd, 1C, Ni-CH, $^2J_{CP}$ = 42.7, $^2J_{CP'}$ = 10.3), 15.45 (dd, 1C, P[C$_a$H(CH_3)(CH$_3$)][CH(CH$_3$)$_2$], $^2J_{CP}$ = 4.4, $^4J_{CP}$ = 1.7), 18.03 (d, 1C, P[CH(CH$_3$)$_2$][CH(CH$_3$)(CH_3)], $^2J_{CP}$ = 6.5), 18.51 (d, 1C, P[CH(CH$_3$)$_2$][CH(CH_3)(CH$_3$)], $^2J_{CP}$ = 1.9), 19.21 (d, 1C, P[C$_a$H(CH$_3$)(CH_3)][CH(CH$_3$)$_2$], $^2J_{CP}$ = 4.0), 28.68 (dd, 1C, P[CH(CH$_3$)$_2$](CH(CH$_3$)$_2$], $^1J_{CP}$ = 25.0, $^3J_{CP}$ = 2.4), 28.93 (dd, 1C, P[CH(CH$_3$)$_2$](CH(CH$_3$)$_2$], $^1J_{CP}$ = 11.7, $^3J_{CP}$ = 5.1), 31.76 (dd, 1C, Ni-CH-CH_2, $^3J_{CP}$ = 31.3, $^3J_{CP'}$ = 1.1), 119.91 (t, 1C, C6$_{Ar}$-H, $^5J_{HP} \approx {}^5J_{HP'}$ = 2.0), 123.81 (s, 1C, C4$_{Ar}$-H), 125.05 (s, 1C, C5$_{Ar}$-H), 125.20 (d, 1C, C3$_{Ar}$-H, $^4J_{CP}$ = 1.1), 128.93 (d, 2C, P(*meta*-C$_6H_5$)(Ph), $^3J_{CP}$ = 9.9), 129.11 (d, 2C, P(Ph)(*meta*-C$_6H_5$), $^3J_{CP}$ = 9.7), 130.36 (d, 1C, P(Ph)(*para*-C$_6H_5$), $^4J_{CP}$ = 2.4), 130.36 (d, 1C, P(*para*-C$_6H_5$)(Ph), $^4J_{CP}$ = 2.6), 131.53 (dd, 1C, P-C_{Ar}, $^1J_{CP}$ = 25.5, $^3J_{CP}$ = 8.1, overlapping with δ 131.56), 131.56 (dd, 1C, P-C'_{Ar}, $^1J_{CP}$ = 31.1, $^3J_{CP}$ = 3.2, overlapping with δ 131.53), 132.97 (dd, 2C, P(*ortho*-C$_6H_5$)(Ph), $^2J_{CP}$ = 11.4, $^4J_{CP}$ = 0.9), 133.54 (dd, 2C, P(Ph)(*ortho*-C$_6H_5$), $^2J_{CP}$ = 11.6, $^4J_{CP}$ = 1.4), 135.95 (dd, 1C, C2$_{Ar}$-CHNi, $^3J_{CP}$ = 10.8, $^3J_{CP'}$ = 8.0), 155.96 (dd, 1C, C1$_{Ar}$-OP, $^2J_{CP(iPr)2}$ = 2.4, $^4J_{CP(Ph)2}$ = 1.6). $^{31}P\{^1H\}$ NMR (202.4 MHz, 20 °C, C$_6$D$_6$): δ 196.79 (d, 1P, PPh$_2$, $^2J_{PP}$ = 322), -78.12 (d, 1P, OP(i-Pr)$_2$, $^2J_{PP}$ = 322).

Competition experiment. To a mixture of substrate **1** (118 mg, 0.50 mmol) and {(*i*-PrCN)NiBr$_2$}$_n$ (173 mg, 0.60 mmol) in 10 mL THF were added *i*-PrNH$_2$ (49 μL, 0.60 mmol), PhN(H)Et (76 μL, 0.60 mmol) and Et$_3$N 84 μL, 0.60 mmol). The internal standard [nBu4N]PF$_6$ was added (76 mg, 0.20 mmol) and the mixture was stirred at room temperature. Quantitative $^{31}P\{^1H\}$ NMR of the crude solution was recorded after 1h, 7h and 24 h, revealing ratios of complex **5** : complex **6** of 57:43, 47:53, and 33:67 respectively.

Cyclic voltammetry. Due to the air sensitivity of the studied compounds, the electrochemical cell was prepared in the glovebox. 25 μmol of the complex under study (1 mM) and 2.5 mmol of [*n*-Bu$_4$N]PF$_6$ (969 mg, 100 mM) were dissolved in 25.0 mL dried and deoxygenated MeCN. The

resulting solution was transferred to the cell, the Teflon electrode holder was placed on top and the cell was sealed with parafilm. At the last minute, the parafilm was punctured to allow insertion of the glassy-carbon working electrode, the Ag/AgCl reference electrode and the platinum wire counter electrode. Measurements were recorded outside the glovebox with a Bio-Logic SAS SP-50 potentiostat. After all the measurements were recorded, ca. 25 µmol ferrocene (4.6 mg) was introduced into the electrochemical cell and its cyclic voltammogram recorded in order to extract its $E_{1/2}$ in our conditions to serve as the reference.

5.6 Acknowledgements

5.7 References

[1] (a) Moulton, C. J.; Shaw, B. L., Transition metal–carbon bonds. Part XLII. Complexes of nickel, palladium, platinum, rhodium and iridium with the tridentate ligand 2,6-bis[(di-t-butylphosphino)methyl]phenyl. *Journal of the Chemical Society, Dalton Transactions* **1976,** (11), 1020-1024. (b) Al-Salem, N. A.; Empsall, H. D.; Markham, R.; Shaw, B. L.; Weeks, B., Formation of large chelate rings and cyclometallated products from diphosphines of type $But_2P(CH_2)_nPBut_2$ (n= 5–8) and $Ph_2P(CH_2)_5PPh_2$ with palladium and platinum chlorides: factors affecting the stability and conformation of large chelate rings. *Journal of the Chemical Society, Dalton Transactions* **1979,** (12), 1972-1982. (c) Crocker, C.; Errington, R. J.; Markham, R.; Moulton, C. J.; Odell, K. J.; Shaw, B. L., Large-ring and cyclometallated rhodium complexes from some medium-chain α,ω-diphosphines. *Journal of the American Chemical Society* **1980,** *102* (13), 4373-4379. (d) Grove, D. M.; Van Koten, G.; Zoet, R.; Murrall, N. W.; Welch, A. J., Unique stable organometallic nickel(III) complexes; syntheses and the molecular structure of $[Ni[C_6H_3(CH_2NMe_2)2-2,6]I_2]$. *Journal of the American Chemical Society* **1983,** *105* (5), 1379-1380. (e) Grove, D. M.; Van Koten, G.; Mul, P.; Zoet, R.; Van der Linden, J. G. M.; Legters, J.; Schmitz, J. E. J.; Murrall, N. W.; Welch, A. J., Syntheses and characterization of unique organometallic nickel(III) aryl species. ESR and electrochemical studies and the x-ray molecular study of square-pyramidal $[Ni\{C_6H_3(CH_2NMe_2)_2-o,o'\}I_2]$. *Inorganic Chemistry* **1988,** *27* (14), 2466-2473.
[2] (a) Ohff, M.; Ohff, A.; van der Boom, M. E.; Milstein, D., Highly Active Pd(II) PCP-Type Catalysts for the Heck Reaction. *Journal of the American Chemical Society* **1997,** *119* (48), 11687-11688. (b) Miyazaki, F.; Yamaguchi, K.;

Shibasaki, M., The synthesis of a new palladacycle catalyst. Development of a high performance catalyst for Heck reactions. *Tetrahedron Letters* **1999,** *40* (41), 7379-7383. (c) Bedford, R. B.; Draper, S. M.; Noelle Scully, P.; Welch, S. L., Palladium bis(phosphinite) 'PCP'-pincer complexes and their application as catalysts in the Suzuki reaction. *New Journal of Chemistry* **2000,** *24* (10), 745-747. (d) Dijkstra, H. P.; Meijer, M. D.; Patel, J.; Kreiter, R.; van Klink, G. P. M.; Lutz, M.; Spek, A. L.; Canty, A. J.; van Koten, G., Design and Performance of Rigid Nanosize Multimetallic Cartwheel Pincer Compounds as Lewis-Acid Catalysts. *Organometallics* **2001,** *20* (14), 3159-3168. (e) Sebelius, S.; Olsson, V. J.; Szabó, K. J., Palladium Pincer Complex Catalyzed Substitution of Vinyl Cyclopropanes, Vinyl Aziridines, and Allyl Acetates with Tetrahydroxydiboron. An Efficient Route to Functionalized Allylboronic Acids and Potassium Trifluoro(allyl)borates. *Journal of the American Chemical Society* **2005,** *127* (30), 10478-10479. (f) Goldman, A. S.; Roy, A. H.; Huang, Z.; Ahuja, R.; Schinski, W.; Brookhart, M., Catalytic Alkane Metathesis by Tandem Alkane Dehydrogenation-Olefin Metathesis. *Science* **2006,** *312* (5771), 257-261. (g) Naghipour, A.; Sabounchei, S. J.; Morales-Morales, D.; Canseco-González, D.; Jensen, C. M., A highly active two six-membered phosphinite palladium PCP pincer complex [PdCl{C$_6$H$_3$(CH$_2$OPPr^i)2-2,6}]. *Polyhedron* **2007,** *26* (7), 1445-1448. (h) Gunanathan, C.; Ben-David, Y.; Milstein, D., Direct Synthesis of Amides from Alcohols and Amines with Liberation of H$_2$. *Science* **2007,** *317* (5839), 790-792. (i) Bernskoetter, W. H.; Brookhart, M., Kinetics and Mechanism of Iridium-Catalyzed Dehydrogenation of Primary Amines to Nitriles. *Organometallics* **2008,** *27* (9), 2036-2045. (j) Zweifel, T.; Naubron, J.-V.; Grützmacher, H., Catalyzed Dehydrogenative Coupling of Primary Alcohols with Water, Methanol, or Amines. *Angewandte Chemie International Edition* **2009,** *48* (3), 559-563.

[3] (a) Batema, G. D.; Lutz, M.; Spek, A. L.; van Walree, C. A.; Donegá, C. d. M.; Meijerink, A.; Havenith, R. W. A.; Pérez-Moreno, J.; Clays, K.; Büchel, M.; Dijken, A. v.; Bryce, D. L.; van Klink, G. P. M.; Koten, G. v., Substituted 4,4′-Stilbenoid NCN-Pincer Platinum(II) Complexes. Luminescence and Tuning of the Electronic and NLO Properties and the Application in an OLED. *Organometallics* **2008,** *27* (8), 1690-1701. (b) Albrecht, M.; Lutz, M.; Spek, A. L.; van Koten, G., Organoplatinum crystals for gas-triggered switches. *Nature* **2000,** *406* (6799), 970-974. (c) Rivera, E. J.; Figueroa, C.; Colón, J. L.; Grove, L.; Connick, W. B., Room-Temperature Emission from Platinum(II) Complexes Intercalated into Zirconium Phosphate-Layered Materials. *Inorganic Chemistry* **2007,** *46* (21), 8569-8576. (d) Tastan, S.; Krause, J. A.; Connick, W. B., Synthesis, structures and spectroscopic properties of palladium(II) complexes with tridentate piperidyl-containing pincer ligands. *Inorganica Chimica Acta* **2006,** *359* (6), 1889-1898.

[4] (a) Albrecht, M.; van Koten, G., Platinum Group Organometallics Based on "Pincer" Complexes: Sensors, Switches, and Catalysts. *Angewandte Chemie International Edition* **2001,** *40* (20), 3750-3781. (b) van der Boom, M. E.; Milstein, D., Cyclometalated Phosphine-Based Pincer Complexes: Mechanistic Insight in Catalysis, Coordination, and Bond Activation. *Chemical Reviews* **2003,** *103* (5), 1759-1792. (c) Singleton, J. T., The uses of pincer complexes in organic synthesis. *Tetrahedron* **2003,** *59* (11), 1837-1857. (d) Slagt, M. Q.; Zwieten, D. A. P. v.; Moerkerk, A. J. C. M.; Gebbink, R. J. M. K.; Koten, G. v., NCN–pincer palladium complexes with multiple anchoring points for functional groups. *Coordination Chemistry Reviews* **2004,** *248* (21), 2275-2282. (e) Liang, L.-C., Metal complexes of chelating diarylamido phosphine ligands. *Coordination Chemistry Reviews* **2006,** *250* (9), 1152-1177. (f) Nishiyama, H., Synthesis and use of bisoxazolinyl-phenyl pincers. *Chemical Society Reviews* **2007,** *36* (7), 1133-1141. (g) Benito-Garagorri, D.; Kirchner, K., Modularly Designed Transition Metal PNP and PCP Pincer Complexes based on Aminophosphines: Synthesis and Catalytic Applications. *Accounts of Chemical Research* **2008,** *41* (2), 201-213. (h) Leis, W.; Mayer, H. A.; Kaska, W. C., Cycloheptatrienyl, alkyl and aryl PCP-pincer complexes: Ligand backbone effects and metal reactivity. *Coordination Chemistry Reviews* **2008,** *252* (15), 1787-1797. (i) Selander, N.; Szabó, K. J., Catalysis by Palladium Pincer Complexes. *Chemical Reviews* **2011,** *111* (3), 2048-2076.

[5] (a) Grove, D. M.; Van Koten, G.; Ubbels, H. J. C.; Zoet, R.; Spek, A. L., Organonickel(II) complexes of the tridentate monoanionic ligand o,o'-bis[(dimethylamino)methylphenyl (N-C-N). Syntheses and the x-ray crystal structure of the stable nickel(II) formate [Ni(N-C-N)O2CH]. *Organometallics* **1984,** *3* (7), 1003-1009. (b) van de Kuil, L. A.; Luitjes, H.; Grove, D. M.; Zwikker, J. W.; van der Linden, J. G. M.; Roelofsen, A. M.; Jenneskens, L. W.; Drenth, W.; van Koten, G., Electronic tuning of arylnickel(II) complexes by para substitution of the terdentate monoanionic 2,6-bis[(dimethylamino)methyl]phenyl ligand. *Organometallics* **1994,** *13* (2), 468-477.

[6] Kleij, A. W.; Gossage, R. A.; Klein Gebbink, R. J. M.; Brinkmann, N.; Reijerse, E. J.; Kragl, U.; Lutz, M.; Spek, A. L.; van Koten, G., A "Dendritic Effect" in Homogeneous Catalysis with Carbosilane-Supported Arylnickel(II) Catalysts: Observation of Active-Site Proximity Effects in Atom-Transfer Radical Addition. *Journal of the American Chemical Society* **2000,** *122* (49), 12112-12124.

[7] Contel, M.; Stol, M.; Casado, M. A.; van Klink, G. P. M.; Ellis, D. D.; Spek, A. L.; van Koten, G., A Bis(ortho-amine)aryl−Gold(I) Compound as an Efficient, Nontoxic, Arylating Reagent. *Organometallics* **2002,** *21* (21), 4556-4559.

[8] Other examples of pincer-type nickel complexes easily accessible through C-H metalation include POCOP- and POCN-type pincer complexes of nickel featuring two phosphinite or one phosphinite and one amine donor moieties. For representative reports of this type of complexes see: (a) Gómez-Benítez, V.; Baldovino-Pantaleón, O.; Herrera-Álvarez, C.; Toscano, R. A.; Morales-Morales, D., High yield thiolation of iodobenzene catalyzed by the phosphinite nickel PCP pincer complex: [NiCl{C$_6$H$_3$-2,6-(OPPh$_2$)$_2$}]. *Tetrahedron Letters* **2006,** *47* (29), 5059-5062. (b) Benito-Garagorri, D.; Bocokić, V.; Mereiter, K.; Kirchner, K., A Modular Approach to Achiral and Chiral Nickel(II), Palladium(II), and Platinum(II) PCP Pincer Complexes Based on Diaminobenzenes. *Organometallics* **2006,** *25* (16), 3817-3823. (c) Chakraborty, S.; Krause, J. A.; Guan, H., Hydrosilylation of Aldehydes and Ketones Catalyzed by Nickel PCP-Pincer Hydride Complexes. *Organometallics* **2009,** *28* (2), 582-586. (d) Chakraborty, S.; Zhang, J.; Krause, J. A.; Guan, H., An Efficient Nickel Catalyst for the Reduction of Carbon Dioxide with a Borane. *Journal of the American Chemical Society* **2010,** *132* (26), 8872-8873. (e) Vabre, B.; Lindeperg, F.; Zargarian, D., Direct, one-pot synthesis of POCOP-type pincer complexes from metallic nickel. *Green Chemistry* **2013,** *15* (11), 3188-3194. (f) Mougang-Soumé, B.; Belanger-Gariépy, F.; Zargarian, D., Synthesis, Characterization, and Oxidation of New POCNimine-Type Pincer Complexes of Nickel. *Organometallics* **2014,** *33* (21), 5990-6002. (g) For a recent review on ECE-type pincer complexes of nickel see: Zargarian, D.; Castonguay, A.; Spasyuk, D. M., ECE-Type Pincer Complexes of Nickel. In *Organometallic Pincer Chemistry*, van Koten, G.; Milstein, D., Eds. Springer Berlin Heidelberg: Berlin, Heidelberg, 2013; pp 131-173.

[9] (a) Cloutier, J.-P.; Vabre, B.; Moungang-Soumé, B.; Zargarian, D., Synthesis and Reactivities of New NCN-Type Pincer Complexes of Nickel. *Organometallics* **2015,** *34* (1), 133-145. (b) Shao, D.-D.; Niu, J.-L.; Hao, X.-Q.; Gong, J.-F.; Song, M.-P., Neutral and cationic chiral NCN pincer nickel(ii) complexes with 1,3-bis(2′-imidazolinyl)benzenes: synthesis and characterization. *Dalton Transactions* **2011,** *40* (35), 9012-9019.

[10] (a) Pandarus, V.; Zargarian, D., New Pincer-Type Diphosphinito (POCOP) Complexes of Nickel. *Organometallics* **2007,** *26* (17), 4321-4334. (b) Castonguay, A.; Beauchamp, A. L.; Zargarian, D., Preparation and Reactivities of PCP-Type Pincer Complexes of Nickel. Impact of Different Ligand Skeletons and Phosphine Substituents. *Organometallics* **2008,** *27* (21), 5723-5732. (c) Pandarus, V.; Castonguay, A.; Zargarian, D., Ni(II) complexes featuring non-metallated pincer-type ligands. *Dalton Transactions* **2008,** (35), 4756-4761.

[11] Mangin, L. P.; Zargarian, D., C–H nickellation of phenol-derived phosphinites: regioselectivity and structures of cyclonickelated complexes. *Dalton Transactions* **2017,** *46* (46), 16159-16170.

[12] Mangin, L. P.; Zargarian, D., C–H Nickelation of Aryl Phosphinites: Mechanistic Aspects. *Organometallics* **2019,** *38* (7), 1479-1492.

[13] Mangin, L. P.; Zargarian, D., C–H Nickelation of Naphthyl Phosphinites: Electronic and Steric Limitations, Regioselectivity, and Tandem C–P Functionalization. *Organometallics* **2019,** *38* (24), 4687-4700.

[14] (a) Estudiante-Negrete, F.; Hernández-Ortega, S.; Morales-Morales, D., Ni(II)–POCOP pincer compound [NiCl{C$_{10}$H$_5$-2,10-(OPPh$_2$)$_2$}] an efficient and robust nickel catalyst for the Suzuki–Miyaura coupling reactions. *Inorganica Chimica Acta* **2012,** *387*, 58-63. (b) Lefèvre, X.; Spasyuk, D. M.; Zargarian, D., New POCOP-type pincer complexes of Nickel(II). *Journal of Organometallic Chemistry* **2011,** *696* (4), 864-870. (c) Vabre, B.; Petiot, P.; Declercque, R.; Zargarian, D., Fluoro and Trifluoromethyl Derivatives of POCOP-Type Pincer Complexes of Nickel: Preparation and Reactivities in S(N)$_2$ Fluorination and Direct Benzylation of Unactivated Arenes, *Organometallics* **2014,** *33*, 5173-5184.

[15] It should be noted that the amount of this adduct is a rough estimate based on the integration of the broad peak at ca. 135 ppm against that of the product.

[16] It should be emphasized that the ^{31}P signals for complexes **2** and **3** overlap in the crude reaction mixture (in acetonitrile). To distinguish and quantify the signals, an aliquot of the reaction mixture was evaporated and redissolved in THF before recording the spectrum.

[17] Spasyuk, D. M.; Zargarian, D.; van der Est, A., New POCN-Type Pincer Complexes of Nickel(II) and Nickel(III). *Organometallics* **2009,** *28* (22), 6531-6540.

[18] It should be noted that conducting this reaction in THF gave similar results, but the conversion was slower, requiring 20 h to go to completion.

[19] It is worth noting here that quantification by ^{31}P NMR against [n-Bu$_4$N][PF$_6$] as the internal standard confirmed that complex **5** was not simply decomposing in the medium.

[20] (a) For a previously reported 6,4-system see: Gwynne, E. A.; Stephan, D. W., Nickel(II) and Palladium(II) Bis-Aminophosphine Pincer Complexes. *Organometallics* **2011,** *30* (15), 4128-4135. (b) For a previously reported 6,5-system see: Salah, A.; Corpet, M.; ul-Hassan Khan, N.; Zargarian, D.; Spasyuk, D. M., Synthesis of unsymmetrical 5,6-POCOP′-type pincer complexes of nickel(ii): impact of nickelacycle size on structures and spectroscopic properties. *New Journal of Chemistry* **2015,** *39* (8), 6649-6658.

[21] *i*-Pr$_2$PH was prepared from *i*-Pr$_2$PCl and LiAlH$_4$ followed by H$_2$O quenching. See ESI for details.

[22] Indeed, NMR analysis of the reaction mixture from the synthesis of *i*-Pr$_2$PH showed about 8% *i*-Pr$_2$P(OH). See ESI.

[23] (a) Cloutier, J.-P.; Zargarian, D., Functionalization of the Aryl Moiety in the Pincer Complex (NCN)Ni^{III}Br$_2$: Insights on NiIII-Promoted Carbon–Heteroatom Coupling. *Organometallics* **2018**, *37* (9), 1446-1455. (b) Cloutier, J.-P.; Rechignat, L.; Canac, Y.; Ess, D. H.; Zargarian, D., C–O and C–N Functionalization of Cationic, NCN-Type Pincer Complexes of Trivalent Nickel: Mechanism, Selectivity, and Kinetic Isotope Effect. *Inorganic Chemistry* **2019**, *58* (6), 3861-3874.[24] Note that by comparison, the Fc/Fc$^+$ couple used under the same conditions as the reference in these measurements gives a |E$_{p,a}$-E$_{p,c}$| value of 68-72 mV, which is close to the ideal values.

[25] (a) Spasyuk, D. M.; Zargarian, D., Monomeric and Dimeric Nickel Complexes Derived from a Pincer Ligand Featuring a Secondary Amine Donor Moiety. *Inorganic Chemistry* **2010**, *49* (13), 6203-6213. (b) Sanford, J.; Dent, C.; Masuda, J. D.; Xia, A., Synthesis, characterization and application of pincer-type nickel iminophosphinite complexes. *Polyhedron* **2011**, *30* (6), 1091-1094. (c) Smith, J. B.; Miller, A. J. M., Connecting Neutral and Cationic Pathways in Nickel-Catalyzed Insertion of Benzaldehyde into a C–H Bond of Acetonitrile. *Organometallics* **2015**, *34* (19), 4669-4677. (d) Smith, J. B.; Kerr, S. H.; White, P. S.; Miller, A. J. M., Thermodynamic Studies of Cation–Macrocycle Interactions in Nickel Pincer–Crown Ether Complexes Enable Switchable Ligation. *Organometallics* **2017**, *36* (16), 3094-3103. (e) Gudun, K. A.; Segizbayev, M.; Adamov, A.; Plessow, P. N.; Lyssenko, K. A.; Balanay, M. P.; Khalimon, A. Y., POCN Ni(ii) pincer complexes: synthesis, characterization and evaluation of catalytic hydrosilylation and hydroboration activities. *Dalton Transactions* **2019**, *48* (5), 1732-1746.

[26] (a) Pandarus, V.; Zargarian, D., New pincer-type diphosphinito (POCOP) complexes of NiII and NiIII *Chemical Communications* **2007**, (9), 978-980. (b) Vabre, B.; Spasyuk, D. M.; Zargarian, D., Impact of Backbone Substituents on POCOP-Ni Pincer Complexes: A Structural, Spectroscopic, and Electrochemical Study. *Organometallics* **2012**, *31* (24), 8561-8570. (c) Chen, T.; Yang, L.; Li, L.; Huang, K.-W., Homocoupling of benzyl halides catalyzed by POCOP–nickel pincer complexes. *Tetrahedron* **2012**, *68* (31), 6152-6157. (d) Vabre, B.; Lindeperg, F.; Zargarian, D., Direct, one-pot synthesis of POCOP-type pincer complexes from metallic nickel. *Green Chemistry* **2013**, *15* (11), 3188-3194. (e) Adhikary, A.; Krause, J. A.; Guan, H., Configurational Stability and Stereochemistry of P-Stereogenic Nickel POCOP-Pincer Complexes. *Organometallics* **2015**, *34* (14), 3603-3610. (f) García-Eleno, M. A.; Padilla-Mata, E.; Estudiante-Negrete, F.; Pichal-Cerda, F.; Hernández-Ortega, S.; Toscano, R. A.; Morales-Morales, D., Single step, high yield synthesis of para-hydroxy functionalized POCOP ligands and their Ni(II) pincer derivatives. *New Journal of Chemistry* **2015**, *39* (5), 3361-3365. (g) Lapointe, S.; Vabre, B.; Zargarian, D., POCOP-Type Pincer Complexes of Nickel: Synthesis, Characterization, and Ligand Exchange Reactivities of New Cationic Acetonitrile Adducts. *Organometallics* **2015**, *34* (14), 3520-3531. (h) Li, H.; Meng, W.; Adhikary, A.; Li, S.; Ma, N.; Zhao, Q.; Yang, Q.; Eberhardt, N. A.; Leahy, K. M.; Krause, J. A.; Zhang, J.; Chen, X.; Guan, H., Metathesis reactivity of bis(phosphinite) pincer ligated nickel chloride, isothiocyanate and azide complexes. *Journal of Organometallic Chemistry* **2016**, *804*, 132-141. (i) Joksch, M.; Haak, J.; Spannenberg, A.; Beweries, T., Synthesis, Characterisation and Hydrogen Bonding of Isostructural Group 10 Metal Halido Complexes Bearing a POCOP Ligand. *European Journal of Inorganic Chemistry* **2017**, *2017* (32), 3815-3822. (j) Salomón-Flores, M. K.; Bazany-Rodríguez, I. J.; Martínez-Otero, D.; García-Eleno, M. A.; Guerra-García, J. J.; Morales-Morales, D.; Dorazco-González, A., Bifunctional colorimetric chemosensing of fluoride and cyanide ions by nickel-POCOP pincer receptors. *Dalton Transactions* **2017**, *46* (15), 4950-4959. (k) Wellala, N. P. N.; Dong, H. T.; Krause, J. A.; Guan, H., Janus POCOP Pincer Complexes of Nickel. *Organometallics* **2018**, *37* (21), 4031-4039.

[27] (a) Bachechi, F., X-Ray Structural Analysis of Ni^{II}, Pd^{II}, and Pt^{II} Complexes with the Potentially Tridentate Ligand 1,3-Bis(diphenylphosphinomethyl)benzene, 1,3-C$_6$H$_4$(CH$_2$PPh$_2$)$_2$. *Structural Chemistry* **2003**, *14* (3), 263-269. (b) van der Boom, M. E.; Liou, S.-Y.; Shimon, L. J. W.; Ben-David, Y.; Milstein, D., Nickel promoted C–H, C–C and C–O bond activation in solution. *Inorganica Chimica Acta* **2004**, *357* (13), 4015-4023. (c) Castonguay, A.; Sui-Seng, C.; Zargarian, D.; Beauchamp, A. L., Syntheses and Reactivities of New PCsp^{3}P Pincer Complexes of Nickel. *Organometallics* **2006**, *25* (3), 602-608. (d) Castonguay, A.; Beauchamp, A. L.; Zargarian, D. New Derivatives of PCP-Type Pincer Complexes of Nickel, *Inorganic Chemistry* **2009**, *48*, 3177-3184. (e) Rossin, A.; Peruzzini, M.; Zanobini, F., Nickel(ii) hydride and fluoride pincer complexes and their reactivity with Lewis acids BX$_3$·L (X = H, L = thf; X = F, L = Et$_2$O). *Dalton Transactions* **2011**, *40* (17), 4447-4452. (f) Duncan, D.; Hope, E. G.; Singh, K.; Stuart, A. M., A recyclable perfluoroalkylated PCP pincer palladium complex. *Dalton Transactions* **2011**, *40* (9), 1998-2005. (g) Schmeier, T. J.; Nova, A.; Hazari, N.; Maseras, F., Synthesis of PCP-Supported Nickel Complexes and their Reactivity with Carbon Dioxide. *Chemistry – A European Journal* **2012**, *18* (22), 6915-6927. (h) Jonasson, K. J.; Wendt, O. F., Synthesis and characterisation of new PCsp^{3}P-supported nickel complexes. *Journal of Organometallic Chemistry* **2014**, *759*, 15-18. (i) Yang, Z.; Liu, D.; Liu, Y.; Sugiya, M.; Imamoto, T.; Zhang, W., Synthesis and Structural Characterization of Nickel Complexes Possessing P-Stereogenic Pincer Scaffolds and Their Application in Asymmetric Aza-Michael Reactions. *Organometallics* **2015**, *34* (7), 1228-1237. (j) Yang, X.-Y.; Tay, W. S.; Li, Y.; Pullarkat, S. A.; Leung, P.-H., Versatile Syntheses of Optically Pure PCE Pincer Ligands: Facile Modifications of the

Pendant Arms and Ligand Backbones. *Organometallics* **2015**, *34* (8), 1582-1588. (k) Gibbons, S. K.; Xu, Z.; Hughes, R. P.; Glueck, D. S.; Rheingold, A. L., Chiral Bis(Phospholane) PCP Pincer Complexes: Synthesis, Structure, and Nickel-Catalyzed Asymmetric Phosphine Alkylation. *Organometallics* **2018**, *37* (13), 2159-2166. (l) Zhang, J.; Liu, T.; Wei, C.; Chang, J.; Ma, Q.-Q.; Li, S.; Ma, N.; Chen, X., The Reactivity of Mercapto Groups against Boron Hydrides in Pincer Ligated Nickel Mercapto Complexes. *Chemistry – An Asian Journal* **2018**, *13* (21), 3231-3238.

[28] Mousa, A. H.; Bendix, J.; Wendt, O. F., Synthesis, Characterization, and Reactivity of PCN Pincer Nickel Complexes. *Organometallics* **2018**, *37* (15), 2581-2593.

[29] The bite angles for the 5,5-pincer-Ni complexes bearing at least one phosphinite moiety are as follows: 81-83° for the POCOP complexes based on aromatic or aliphatic backbones; 80-82° for the POCN^{imine}, POCN^{amine}, and NHCCOP systems featuring aromatic backbones; and 83-85° for PIMCOP systems. See refs 8-10, 12, 15 for POCOP and POCN systems, and the following reports NHCCOP and PIMCOP systems: (a) Vabre, B.; Canac, Y.; Duhayon, C.; Chauvin, R.; Zargarian, D., Nickel(II) complexes of the new pincer-type unsymmetrical ligands PIMCOP, PIMIOCOP, and NHCCOP: versatile binding motifs. *Chemical Communications* **2012**, *48* (84), 10446-10448. (b) Vabre, B.; Canac, Y.; Lepetit, C.; Duhayon, C.; Chauvin, R.; Zargarian, D., Charge Effects in PCP Pincer Complexes of Ni^{II} bearing Phosphinite and Imidazol(i)ophosphine Coordinating Jaws: From Synthesis to Catalysis through Bonding Analysis. *Chemistry – A European Journal* **2015**, *21* (48), 17403-17414.

[30] LaPierre, E. A.; Clapson, M. L.; Piers, W. E.; Maron, L.; Spasyuk, D. M.; Gendy, C., Oxygen Atom Transfer to Cationic PCPNi(II) Complexes Using Amine-N-Oxides. *Inorganic Chemistry* **2018**, *57* (1), 495-506.

[31] (a) Čermák, J.; Kvíčalová, M.; Šabata, S.; Blechta, V.; Vojtíšek, P.; Podlaha, J.; Shaw, B. L., Diphosphinoazines (Z,Z)-R$_2$PCH$_2$C(But)–NN–C(But)CH$_2$PR$_2$ with R groups of various sizes and complexes {[[(Z,Z)-R$_2$PCH$_2$C(But)–NN–C(But)CH$_2$PR$_2$]-[η^3-CH$_2$C(CH$_3$)–CH$_2$PdCl]$_2$}. *Inorganica Chimica Acta* **2001**, *313* (1), 77-86. (b) Kiyoshi Matsumoto; Mitsuo Toda; Hirokazu Iida; Hiroshi Hamana, IS THERE ANY EFFECT OF PRESSURE ON METAL CATION EXTRACTION PROPERTIES OF 7,13-BIS (2'-THIAZOYL)-1,4,10-TRIOXA-7,13-DIAZA-CYCLOPENTADECANE? **2007**, *13* (1), 13. (c) Rieckborn, T. P.; Karakoc, E.; He, J.; Prosenc, M. H., Chlorido{[2-(dicyclohexylphosphanoyl)ethyl]bis[2-(dicyclohexylphosphanyl)ethyl]phosphane}platinum(II) chloride dichloromethane hemisolvate tetrahydrate. *Acta Crystallographica Section E* **2009**, *65* (1), m57-m58. (d) Martínez-Prieto, L. M.; Melero, C.; del Río, D.; Palma, P.; Cámpora, J.; Álvarez, E., Synthesis and Reactivity of Nickel and Palladium Fluoride Complexes with PCP Pincer Ligands. NMR-Based Assessment of Electron-Donating Properties of Fluoride and Other Monoanionic Ligands. *Organometallics* **2012**, *31* (4), 1425-1438. (e) Morales-Becerril, I.; Flores-Álamo, M.; Tlahuext-Aca, A.; Arévalo, A.; García, J. J., Synthesis of Low-Valent Nickel Complexes in Aqueous Media, Mechanistic Insights, and Selected Applications. *Organometallics* **2014**, *33* (23), 6796-6802. (f) Hao, J.; Vabre, B.; Mougang-Soumé, B.; Zargarian, D., Small Molecule Activation by POCOP-Nickel Complexes. *Chemistry – A European Journal* **2014**, *20* (39), 12544-12552. (g) Kovács, T.; Fülöp, L. S.; Mucsi, Z.; Karaghiosoff, K.; Czugler, M.; Keglevich, G., Revisiting the 7-Phosphanorbornene Family: New P-Alkyl Derivatives. *Heteroatom Chemistry* **2015**, *26* (5), 335-347.

[32] (a) Brunker, T. J.; Blank, N. F.; Moncarz, J. R.; Scriban, C.; Anderson, B. J.; Glueck, D. S.; Zakharov, L. N.; Golen, J. A.; Sommer, R. D.; Incarvito, C. D.; Rheingold, A. L., Chiral Palladium(0) trans-Stilbene Complexes: Synthesis, Structure, and Oxidative Addition of Phenyl Iodide. *Organometallics* **2005**, *24* (11), 2730-2746. (b) Schaub, T.; Radius, U., Efficient C–F and C–C Activation by a Novel N-Heterocyclic Carbene–Nickel(0) Complex. *Chemistry – A European Journal* **2005**, *11* (17), 5024-5030. (c) Barrios-Francisco, R.; García, J. J., Stereoselective Hydrogenation of Aromatic Alkynes Using Water, Triethylsilane, or Methanol, Mediated and Catalyzed by Ni(0) Complexes. *Inorganic Chemistry* **2009**, *48* (1), 386-393. (d) Harrold, N. D.; Hillhouse, G. L., Strongly bent nickel imides supported by a chelating bis(N-heterocyclic carbene) ligand. *Chemical Science* **2013**, *4* (10), 4011-4015. (e) Kruckenberg, A.; Wadepohl, H.; Gade, L. H., Bis(diisopropylphosphinomethyl)amine Nickel(II) and Nickel(0) Complexes: Coordination Chemistry, Reactivity, and Catalytic Decarbonylative C–H Arylation of Benzoxazole. *Organometallics* **2013**, *32* (18), 5153-5170. (f) Brendel, M.; Braun, C.; Rominger, F.; Hofmann, P., Bis-NHC Chelate Complexes of Nickel(0) and Platinum(0). *Angewandte Chemie International Edition* **2014**, *53* (33), 8741-8745. (g) Gendy, C.; Mansikkamäki, A.; Valjus, J.; Heidebrecht, J.; Hui, P. C.-Y.; Bernard, G. M.; Tuononen, H. M.; Wasylishen, R. E.; Michaelis, V. K.; Roesler, R., Nickel as a Lewis Base in a T-Shaped Nickel(0) Germylene Complex Incorporating a Flexible Bis(NHC) Ligand. *Angewandte Chemie International Edition* **2019**, *58* (1), 154-158. (h) Nattmann, L.; Saeb, R.; Nöthling, N.; Cornella, J., An air-stable binary Ni(0)–olefin catalyst. *Nature Catalysis* **2020**, *3* (1), 6-13.

[33] (a) Ohashi, M.; Saijo, H.; Shibata, M.; Ogoshi, S., Palladium-Catalyzed Base-Free Suzuki–Miyaura Coupling Reactions of Fluorinated Alkenes and Arenes via a Palladium Fluoride Key Intermediate. *European Journal of Organic Chemistry* **2013**, *2013* (3), 443-447. (b) Ohashi, M.; Shibata, M.; Saijo, H.; Kambara, T.; Ogoshi, S., Carbon–Fluorine Bond Activation of Tetrafluoroethylene on Palladium(0) and Nickel(0): Heat or Lewis Acidic Additive Promoted Oxidative Addition. *Organometallics* **2013**, *32* (13), 3631-3639. (c) Xu, W.; Sun, H.; Xiong, Z.; Li, X., Acid-Promoted

Selective Carbon–Fluorine Bond Activation and Functionalization of Hexafluoropropene by Nickel Complexes Supported with Phosphine Ligands. *Organometallics* **2013,** *32* (23), 7122-7132. (d) Giffin, K. A.; Pua, L. A.; Piotrkowski, S.; Gabidullin, B. M.; Korobkov, I.; Hughes, R. P.; Baker, R. T., Generation of Hydrofluoronickelacycles from Trifluoroethylene and Ni(0): Ligand Effects on Regio-/Stereoselectivity and Reactivity. *Journal of the American Chemical Society* **2017,** *139* (11), 4075-4086.

[34] (a) van der Boom, M. E.; Liou, S.-Y.; Shimon, L. J. W.; Ben-David, Y.; Milstein, D., Nickel promoted C–H, C–C and C–O bond activation in solution. *Inorganica Chimica Acta* **2004,** *357* (13), 4015-4023. Sujith, S.; Noh, E. K.; Lee, B. Y.; Han, J. W., Synthesis, characterization, and norbornene polymerization of η3-benzylnickel(II) complexes of N-heterocyclic carbenes. *Journal of Organometallic Chemistry* **2008,** *693* (12), 2171-2176. (b) Azerraf, C.; Shpruhman, A.; Gelman, D., Diels–Alder cycloaddition as a new approach toward stable PC(sp^3)P-metalated compounds. *Chemical Communications* **2009,** (4), 466-468. (c) Gutsulyak, D. V.; Piers, W. E.; Borau-Garcia, J.; Parvez, M., Activation of Water, Ammonia, and Other Small Molecules by PCcarbeneP Nickel Pincer Complexes. *Journal of the American Chemical Society* **2013,** *135* (32), 11776-11779. (d) Borau-Garcia, J.; Gutsulyak, D. V.; Burford, R. J.; Piers, W. E., Selective hydration of nitriles to amides catalysed by PCP pincer supported nickel(ii) complexes. *Dalton Transactions* **2015,** *44* (27), 12082-12085. (e) LaPierre, E. A.; Clapson, M. L.; Piers, W. E.; Maron, L.; Spasyuk, D. M.; Gendy, C., Oxygen Atom Transfer to Cationic PCPNi(II) Complexes Using Amine-N-Oxides. *Inorganic Chemistry* **2018,** *57* (1), 495-506. (f) LaPierre, E. A.; Piers, W. E.; Gendy, C., Divergent Reactivity of CO2, CO, and Related Substrates at the Nickel Carbon Double Bond of (PCcarbeneP)Ni(II) Pincer Complexes. *Organometallics* **2018,** *37* (20), 3394-3398.

[35] *Post-facto* calibration of the 100-1000 µL micropipette with 20 × 500 µL aliquots of deionized H$_2$O revealed that we must allow an accuracy (systematic error) of +4 µL and a precision of ±3 µL for our measurements, with > 99% confidence. The 20-200 µL micropipette was calibrated by the same procedure, with 150 µL aliquots, and revealed an accuracy of +0.3 µL and a precision of ±3 µL for our measurements, with > 99% confidence.

[36] (a) Vabre, B.; Spasyuk, D. M.; Zargarian, D., Impact of Backbone Substituents on POCOP-Ni Pincer complexes: A Structural, Spectroscopic and Electrochemical Study, *Organometallics* **2012,** *31* (24), 8561-8570. (b) Vabre, B.; Lindeperg, F.; Zargarian, D., Direct, one-pot synthesis of POCOP-type pincer complexes from metallic nickel, *Green Chemistry* **2013,** *15* (11), 3188-3194.

Chapitre 5 – Annexes

S5.1 General information and references

The MS experiments were acquired on a benchtop Bruker micrOTOF instrument equipped with an ESI source and supplied with a syringe pump. The polarity of ions was set to positive with an m/z range of 50-3000.

The crystallographic data for all resolved structures were collected on either a Bruker Microsource (Cu source) or a Bruker Venture Metaljet (Ga source) via the Bruker APEX II or APEX III[1] software packages. Cell refinement and data reduction were performed using SAINT.[2] An empirical absorption correction, based on multiple measurements of equivalent reflections, was applied using the program SADABS or TWINABS.[3] The space group was confirmed by the XPREP[4] routine in APEX. The structures were solved in OLEX[5] using the SHELX[6] suite and refined by full-matrix least squares with SHEXL.[7] All non-hydrogen atoms were refined with anisotropic displacement parameters, whereas hydrogen atoms were set in calculated positions and refined via the riding model, with thermal parameters being 1.5 times that of the carbon bearing the H in question. All Thermal ellipsoid plots were drawn using OLEX.

---

[1] Bruker (2012). APEX2 / Bruker (2016) APEX3, Bruker AXS Inc., Madison, WI, USA.

[2] Bruker (2012). "SAINT Integration Software for Single Crystal Data", Bruker AXS Inc., Madison, WI, USA.

[3] (a) Sheldrick, G. M. (1996). *SADABS/TWINABS.* University of Göttingen, Germany. (b) Bruker (2001). *SADABS/TWINABS.* Bruker AXS Inc., Madison, Wisconsin, USA.

[4] Bruker (2012). Data Preparation and Reciprocal Space Exploration Program, Bruker AXS Inc., Madison, WI, USA.

[5] A: O. V. Dolomanov, L. J. Bourhis, R. J. Gildea, J. A. K. Howard and H. Puschmann. "OLEX2: a complete structure solution, refinement and analysis program". *J. Appl. Cryst.* 2009, *42*, 339-341.

[6] Sheldrick, G. M., "SHELXT - Integrated space-group and crystal structure determination", *Acta Cryst.*, 2015, A71, 3-8.

[7] Sheldrick, G. M., Crystal structure refinement with SHELXL, *Acta Cryst.*, 2015, C71, 3-8.

S5.2 Experimental procedure for the synthesis of precursors

2-vinyl-phenol. This known compound was prepared by a slightly modified version of the procedure reported by Zhu *et al.*[8] The main modification touched on the number of phosphonium equivalents used: we reasoned that the presence of the phenolic OH group did not justify the use of > 2 equiv phosphonium, as required in the published procedure. A suspension of [Ph$_3$PMe]Br (10.7 g, 30 mmol, 1.2 equiv) in THF (100 mL) was stirred in an ice/water bath for a few min followed by addition of KO^{t}Bu (6.17 g, 55 mmol, 2.2 equiv) in one portion. The resulting heterogeneous mixture was stirred in the ice bath for 30 min, followed by dropwise addition of salicylaldehyde (2.85 mL, 25 mmol, 1.0 equiv) over a 5 min period, allowing the mixture to warm to room temperature, and continued stirring for 16 h. The final mixture was cooled again in the ice/water bath, and 25 mL water was carefully added, followed by 25 mL saturated aqueous NH$_4$Cl until the pH was around 8. To the mixture was added 50 mL Et$_2$O and the two phases were separated. The aqueous phase was extracted with 2 × 50 mL AcOEt, the organic extracts combined, dried over MgSO$_4$, and concentrated under vacuum. The thick oily residues (containing a lot of residual Ph$_3$PO) were purified over silica gel starting with 1:9 AcOEt:Hexanes as eluent. The eluent was switched to 1:5 AcOEt:Hexanes as soon as the desired product began eluting. Evaporation of the combined fractions on the rotovap at 50 °C gave 3.591 g of a pale-yellow oil that still contained residual EtOAc. Analysis of this oil by ^{1}H NMR was in accord with the spectral data reported in the literature, and revealed the presence of 0.409 molecule of AcOEt per molecule of 2-vinylphenol. This allowed us to estimate a yield of ca. 23.0 mmol or 92% for the synthesis. No further attempt was made to remove residual AcOEt in order to avoid sublimating the title compound or inducing polymerization. It is also worth noting that this product is immune to polymerization or decomposition over months if it is stored in a freezer away from light. Moreover, phosphination of the phenol moiety proceeded without complication despite the presence of AcOEt to give the substrate **1** that could be stored at room temperature in the glovebox over months without polymerizing or decomposition.

---

[8] Zhu, Y.; Colomer, I.; Thompson, A. L.; Donohoe, T. J., HFIP Solvent Enables Alcohols To Act as Alkylating Agents in Stereoselective Heterocyclization. *Journal of the American Chemical Society* **2019,** *141* (16), 6489-6493.

***i*-Pr₂PH Solution.** This compound has been prepared according to the following procedure that represents a modified version of a reported protocol.[9] To a suspension of $LiAlH_4$ (380 mg, 10 mmol, 0.5 equiv) in 10 mL Et_2O cooled to 0 °C was added (dropwise over 10 min) a solution of $ClP(i\text{-}Pr)_2$ (3.18 mL, 20 mmol, 1.0 equiv) in 10 mL Et_2O. The resulting mixture was slowly warmed to room temperature and vigorously stirred overnight. The final mixture was cannula filtered, the solid residues were stirred in 10 mL Et_2O and cannula filtered again. Degassed H_2O (722 μL 40 mmol, 2.0 equiv) was added dropwise to the combined filtrates and the mixture stirred for 10 min at room temperature, followed by careful addition of anhydrous $MgSO_4$ and continued stirring for a few min. The solution was filtered again, and an aliquot of the filtrate was used to quantify the yield by quantitative $^{31}P\{^1H\}$ NMR against Ph_2PH as an internal standard. This analysis showed that the solution was 0.34 M in the title compound, but also contained some of the phosphine oxide $i\text{-}Pr_2P(O)H$ (ca. 0.029 M) due to oxidation during the filtration. This mixture was used without further purification for the preparation of the desired $NiBr_2$ adduct (vide infra).

(*i*-Pr₂PH)₂NiBr₂. To a stirred suspension of $\{(i\text{-}PrCN)NiBr_2\}_n$ (1.15 g, 4.0 mmol, 1.0 equiv) in 10 mL Et_2O was added some of the of $i\text{-}Pr_2PH$ solution prepared as described above (11.7 mL of a 0.34 M solution in Et_2O, 4.0 mmol, 1.0 equiv). The green color of the original suspension turned deep red immediately; stirring was continued at room temperature for 30 min. Cannula filtration of the final mixture allowed us to separate the solids (excess Ni(II) precursor), which were extracted with 2 × 15 mL Et_2O. Evaporation of the combined filtrates yielded a deep Burgundy-red powder (906 mg, 2.00 mmol, quant. yield). The crude product could be further purified from hot hexanes or acetonitrile in > 80% yields. The NMR spectra of this material matched that of the desired product reported in the literature.[10]

***i*-Pr₂P(O)H.** To a solution of $ClP(i\text{-}Pr)_2$ (835 μL, 5.00 mmol, 1.00 equiv) in 15 mL THF were added H_2O (180 μL, 10.0 mmol, 2.00 equiv) and the resulting mixture was stirred at room temperature for 1 h. Analysis of an aliquot of this mixture by ^{31}P NMR confirmed disappearance of the starting material. Et_3N (767 μL, 5.50 mmol, 1.10 equiv) was then added carefully while stirring, which resulted in precipitation of a colorless solid (Et_3NHCl). (*N. B. Addition of Et₃N must*

[9] Habraken, E. R. M.; Jupp, A. R.; Brands, M. B.; Nieger, M.; Ehlers, A. W.; Slootweg, J. C., Parallels between Metal-Ligand Cooperativity and Frustrated Lewis Pairs. *European Journal of Inorganic Chemistry* **2019,** *2019* (19), 2436-2442.

[10] Mangin, L. P.; Zargarian, D., C–H Nickelation of Naphthyl Phosphinites: Electronic and Steric Limitations, Regioselectivity, and Tandem C–P Functionalization. *Organometallics* **2019,** *38* (24), 4687-4700.

be done after complete disappearance of ClP(i-Pr)₂ to avoid the attack of the [i-Pr₂P(O)]⁻ anion on the unreacted chlorophosphine.) Addition of anhydrous $MgSO_4$ and 15 mL Et_2O, followed by stirring and cannula filtration allowed us to separate the solid residues, which were extracted with 2×15 mL Et_2O. Evaporation of the combined filtrates under vacuum gave the desired product as a pale yellow oil (608 mg of 4.53 mmol, 91 % yield). The NMR spectra of this material matched literature data.[11]

---

[11] Brück, A.; Ruhland, K., Investigation of the Dynamic Solution Behavior of Chloro(diene)rhodium(I) Phosphine Complexes with a Pendant Unsaturated Heterocycle at Phosphorus (2-pyridyl, 2-imidazyl; diene = COD, NBD). *Organometallics* **2009,** *28* (22), 6383-6401.

S5.3 ESI-MS Results

Full acquisition parameters:

Acquisition Parameter					
Source Type	ESI	Ion Polarity	Positive	Set Nebulizer	0.4 Bar
Focus	Active			Set Dry Heater	180 °C
Scan Begin	50 m/z	Set Capillary	4500 V	Set Dry Gas	4.0 l/min
Scan End	3000 m/z	Set End Plate Offset	-500 V	Set Divert Valve	Waste
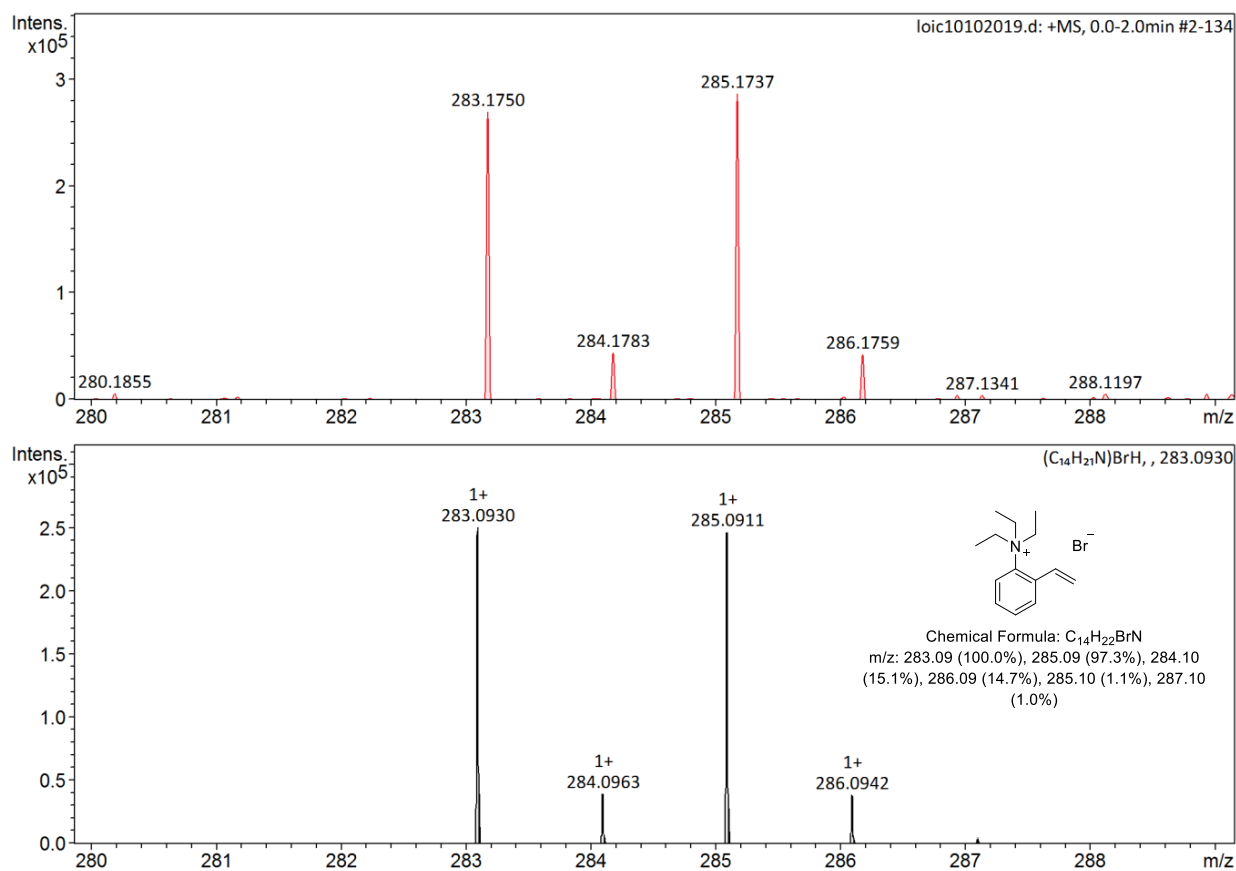
Figure S5.1: Experimental (top) and Theoretical (bottom) mass spectra of the ion pair $[C_{14}H_{22}N]Br$ that was detected at M^+.
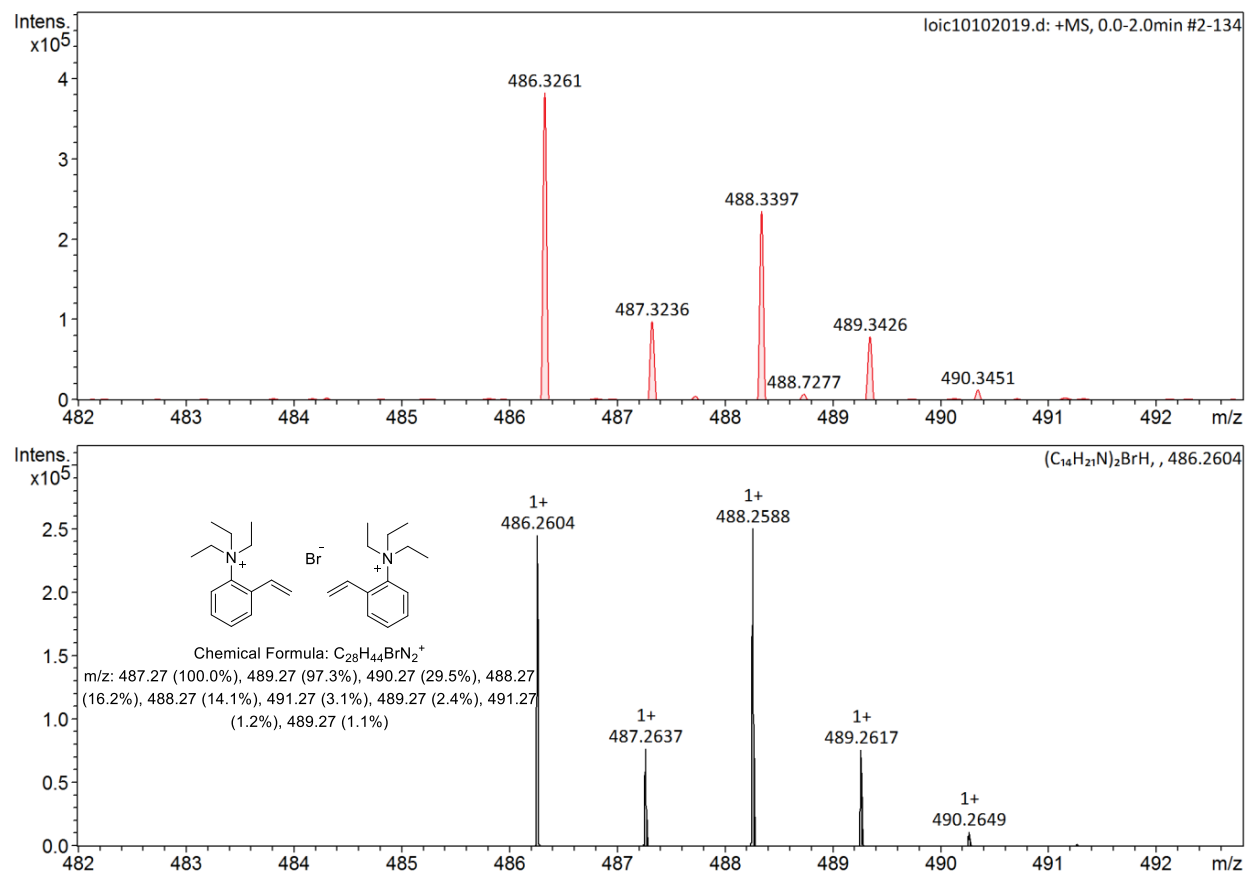
Figure S5.2: Experimental (top) and Theoretical (bottom) mass spectra of the ion group [[C14H22N]2Br]+ that was detected at [M-1]+.

S5.4 Additional cyclic voltammograms
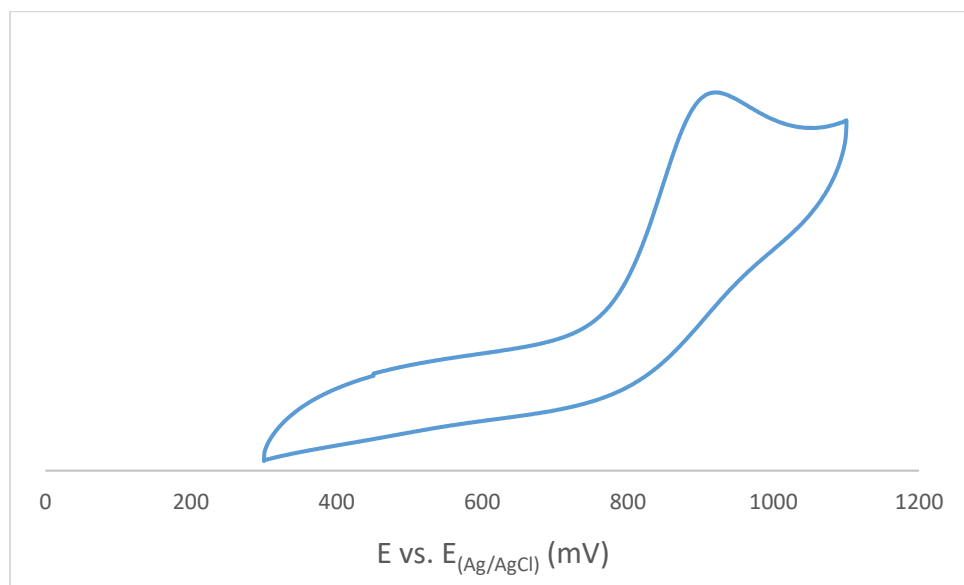
Figure S5.3: Cyclic voltammograms of complex 4 (1 mM) in the presence of [n-Bu4N]PF6 (100 mM) in DCM at a glassy carbon electrode. Potentials are referenced against the Ag/AgCl reference electrode.
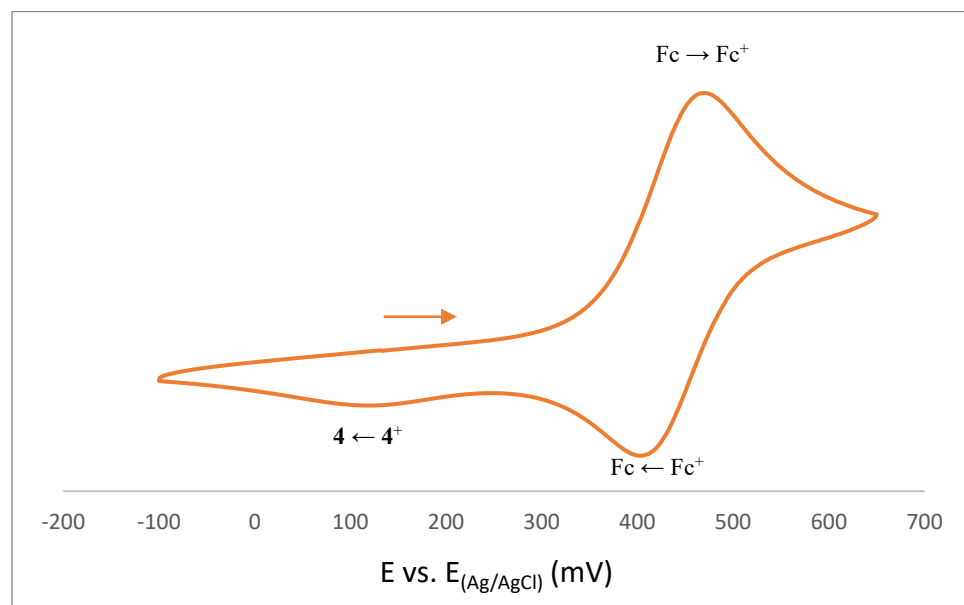
Figure S5.4: Cyclic voltammograms of complex 4 (1 mM) in the presence of [n-Bu4N]PF6 (100 mM) in MeCN at a glassy carbon electrode, with added ca 3 equiv Cp2Fe (= Fc). Potentials are referenced against the Ag/AgCl reference electrode.

S5.5 NMR of characterized compounds

a. Ligand **1**
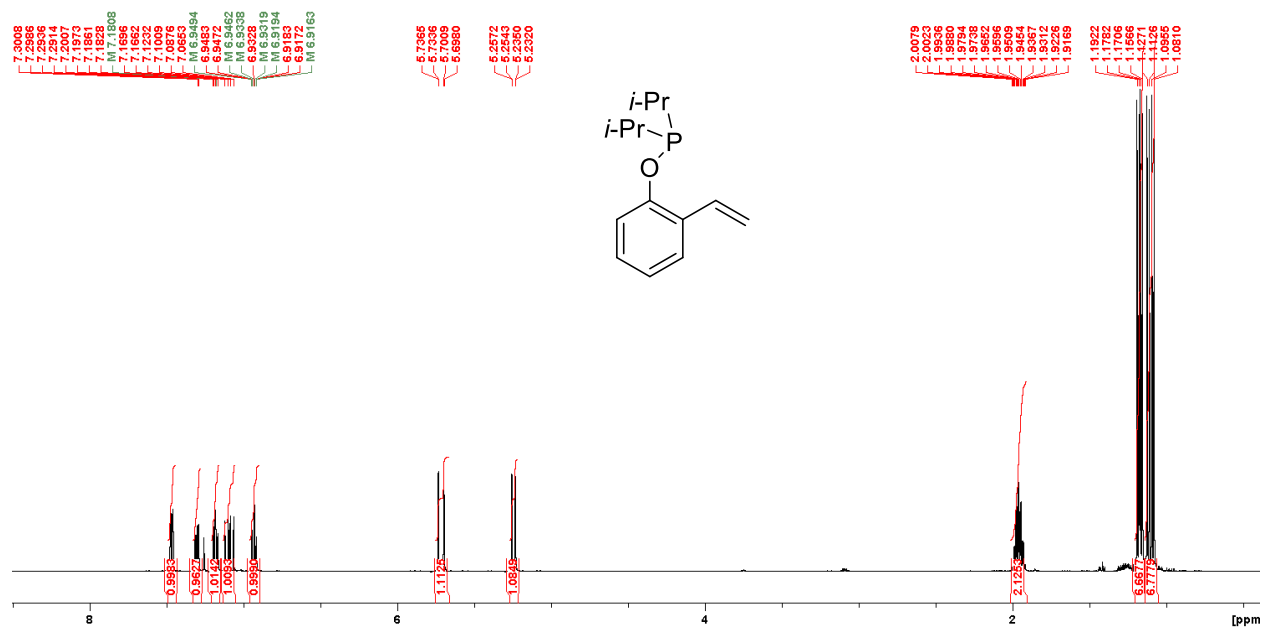

Figure S5.5: Full ^{1}H NMR spectrum of **1** in CDCl$_3$.
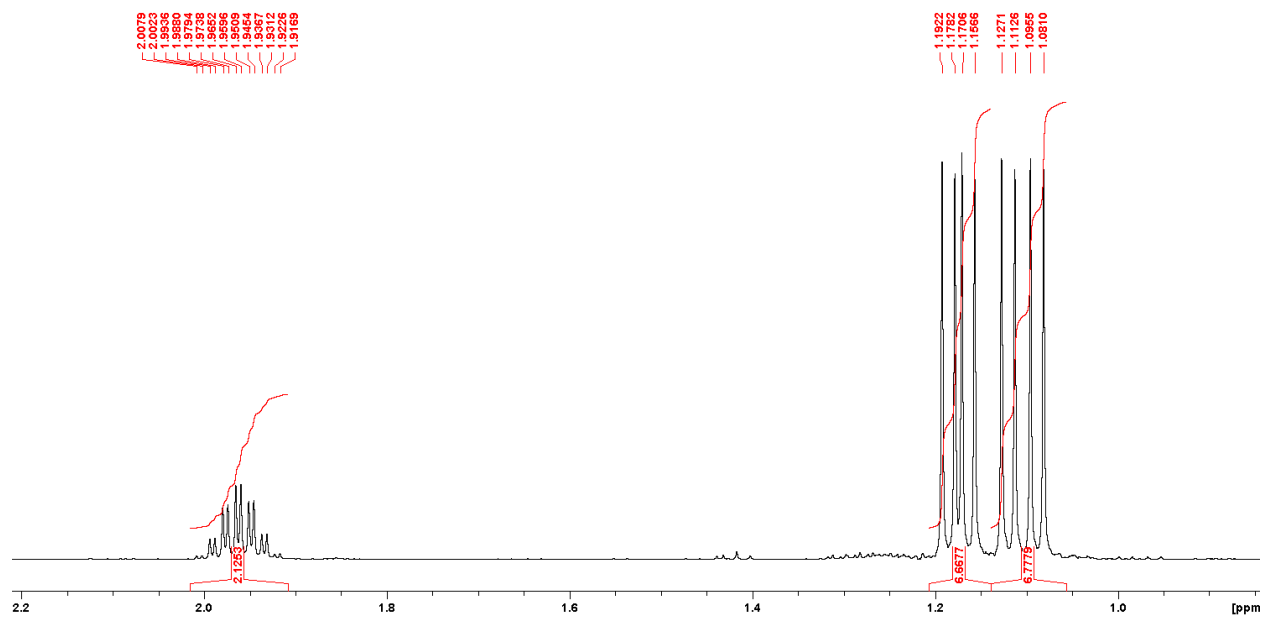
Figure S5.6: The expanded aliphatic region of the ^{1}H NMR spectrum of **1** in CDCl$_3$.
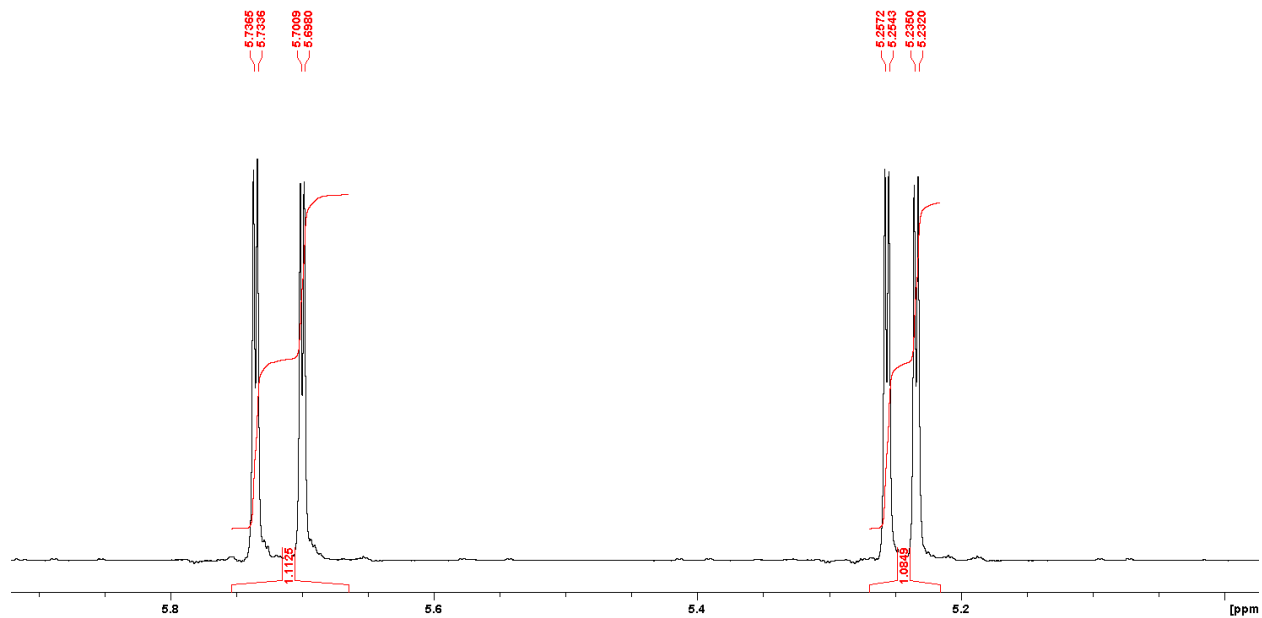
Figure S5.7: The expanded olefinic region of the ^{1}H NMR spectrum of **1** in CDCl$_3$.
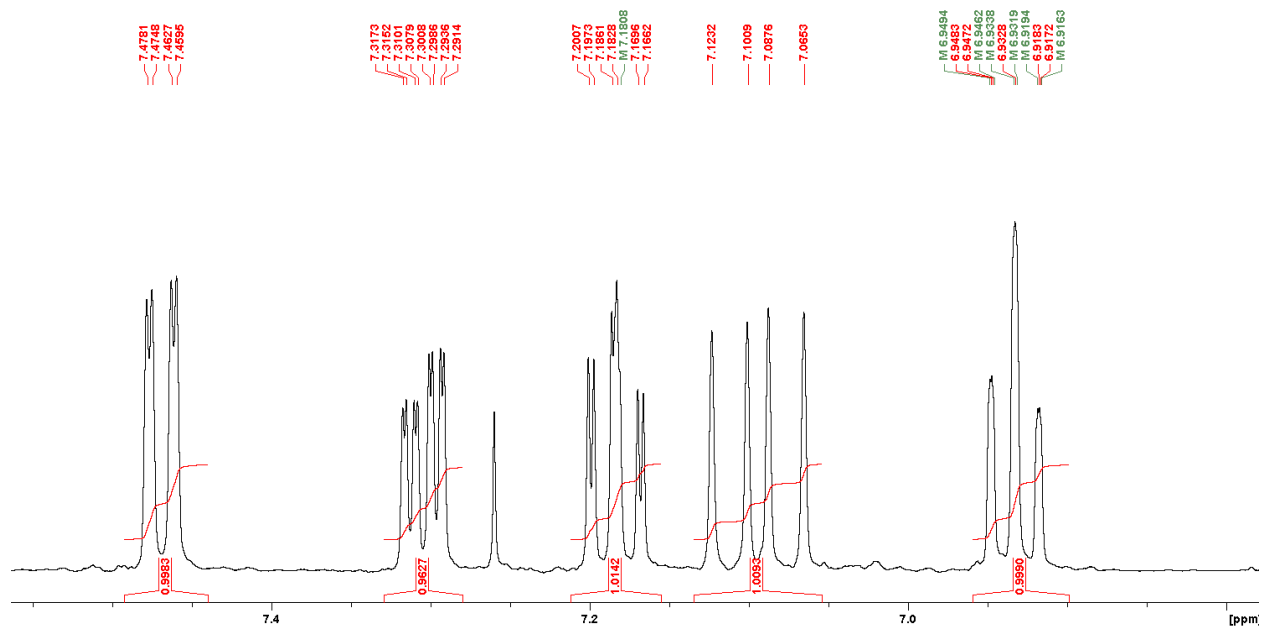
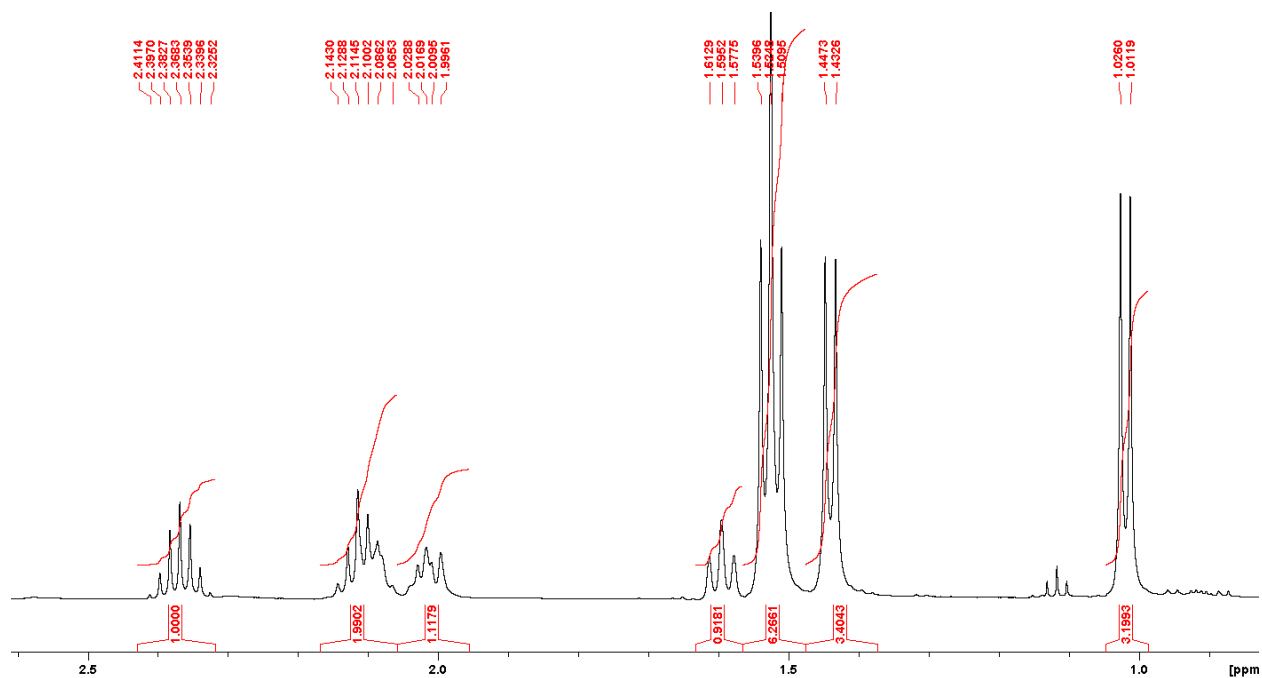Figure S5.8: The expanded aromatic region of the ^{1}H NMR spectrum of **1** in CDCl$_3$.
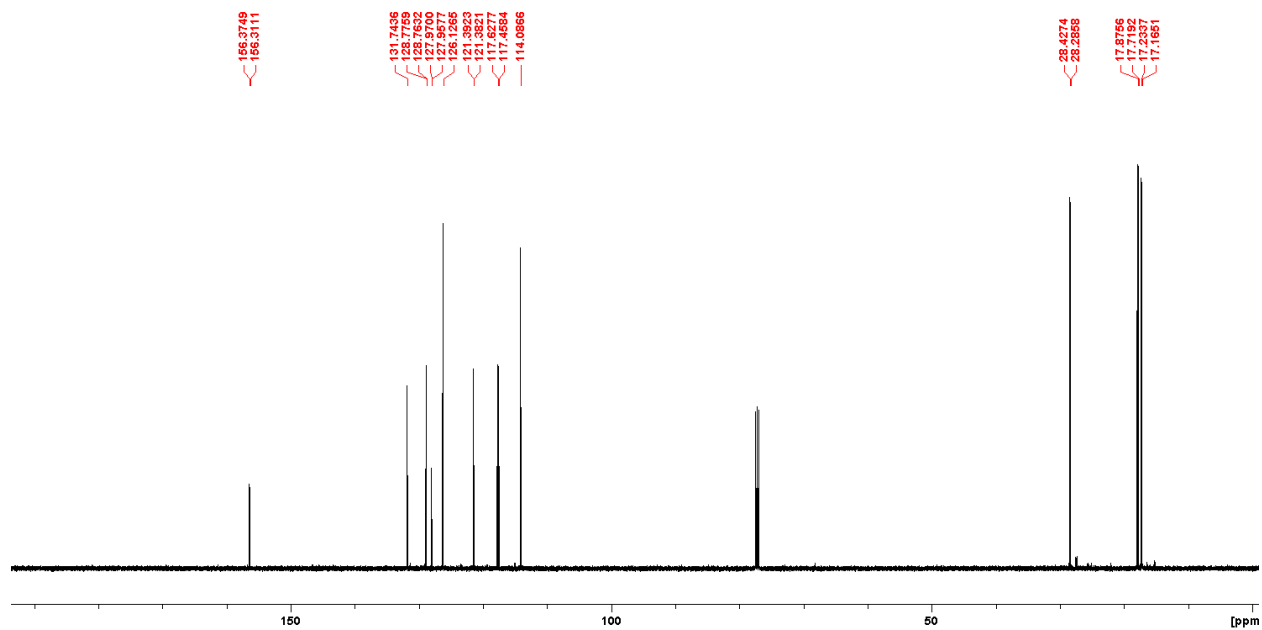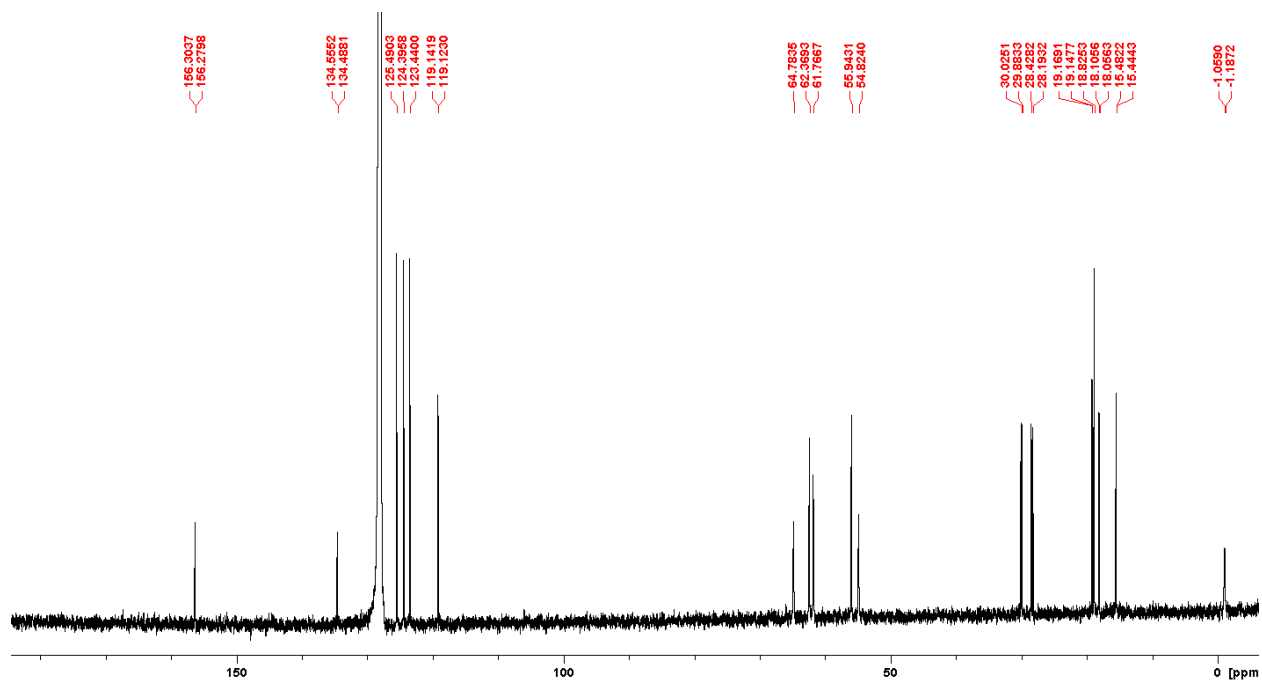
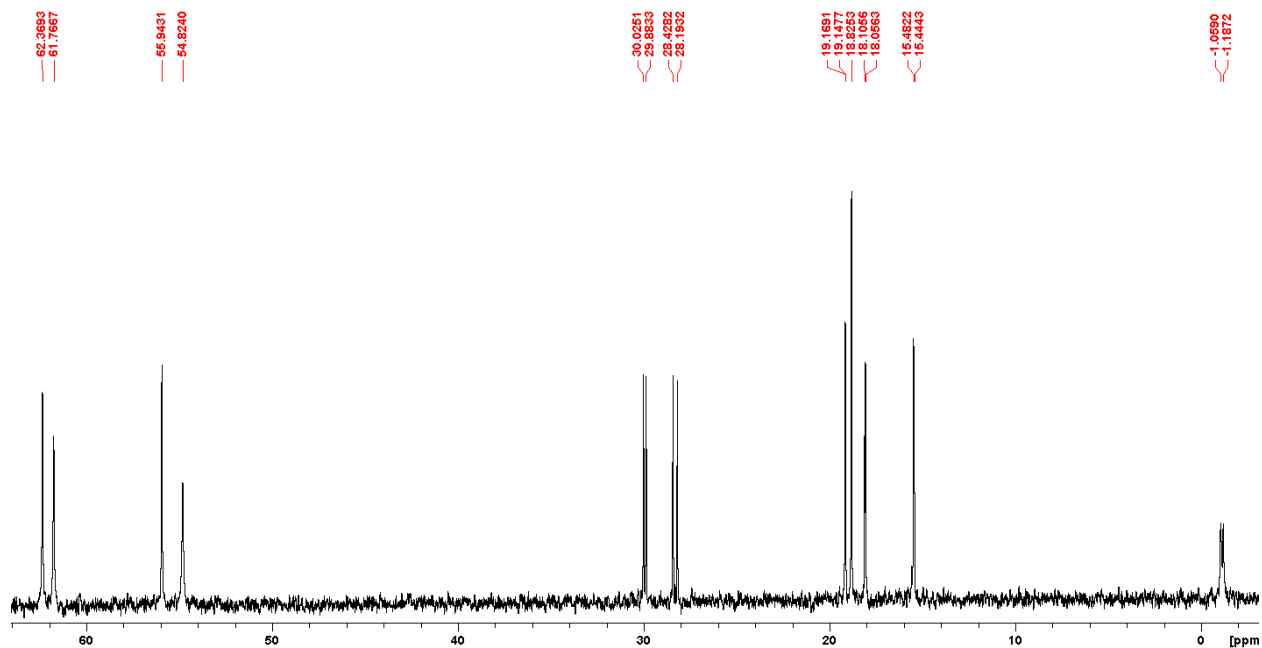Figure S5.9: Full ^{13}C NMR spectrum of **1** in CDCl$_3$.
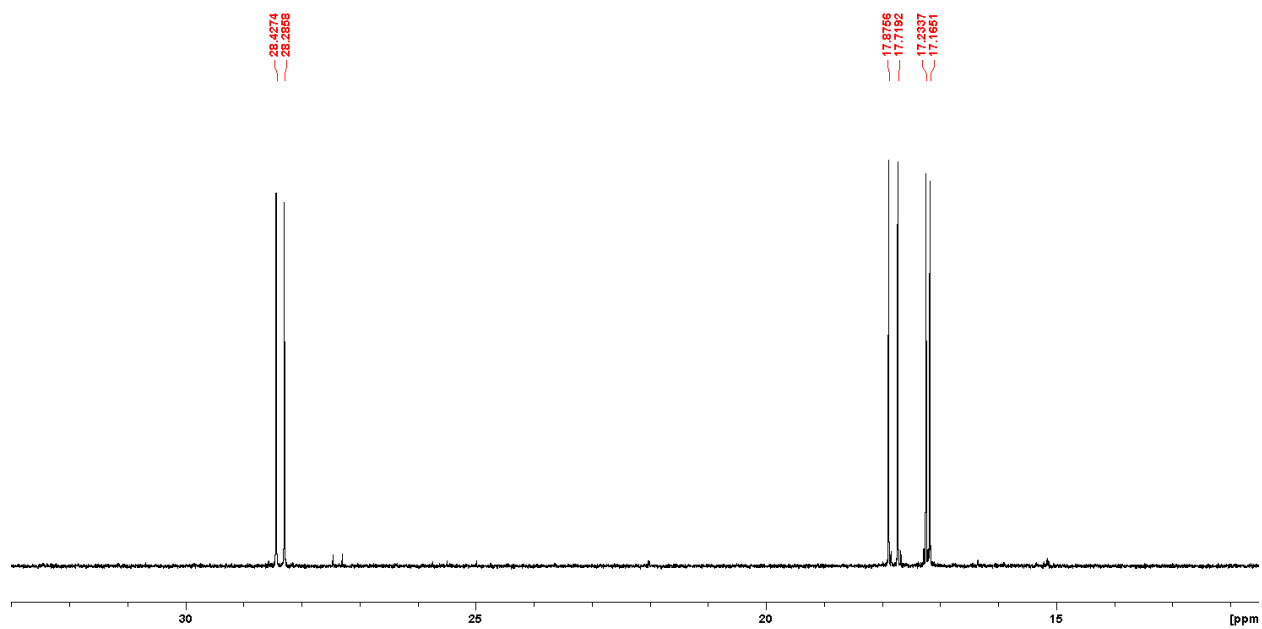
Figure S5.10: The expanded aliphatic region of the ^{13}C NMR spectrum of **1** in CDCl$_3$.
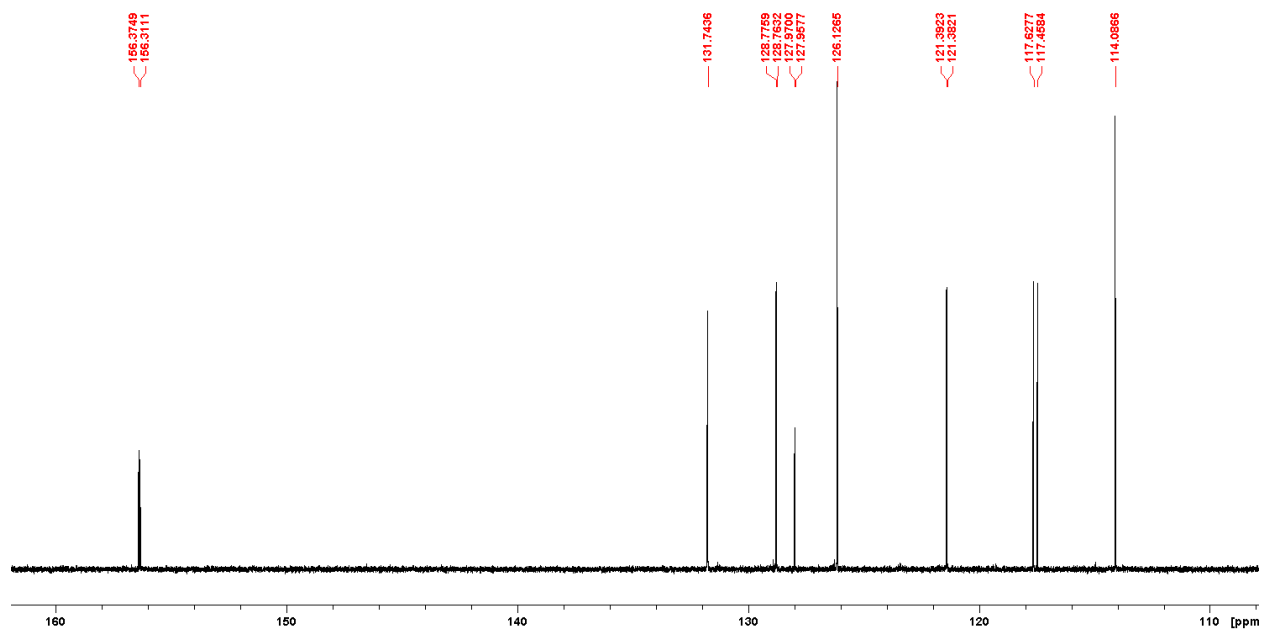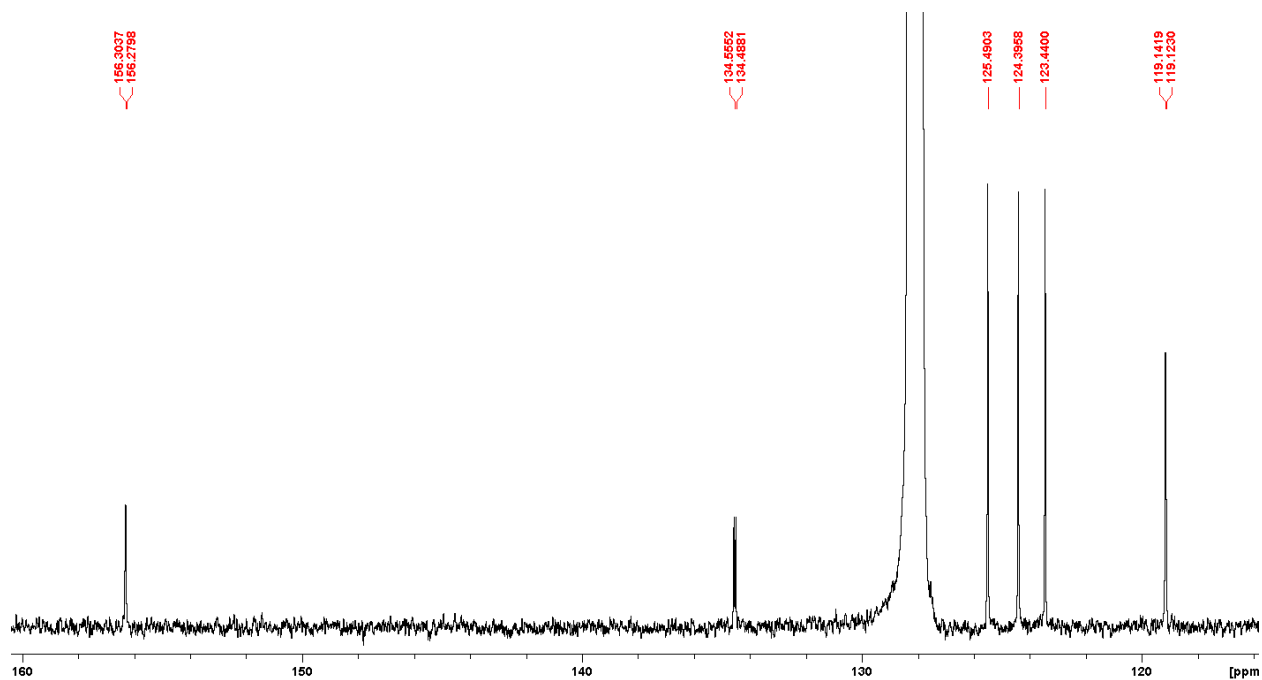
Figure S5.11: The expanded aromatic region of the ^{13}C NMR spectrum of **1** in CDCl₃.
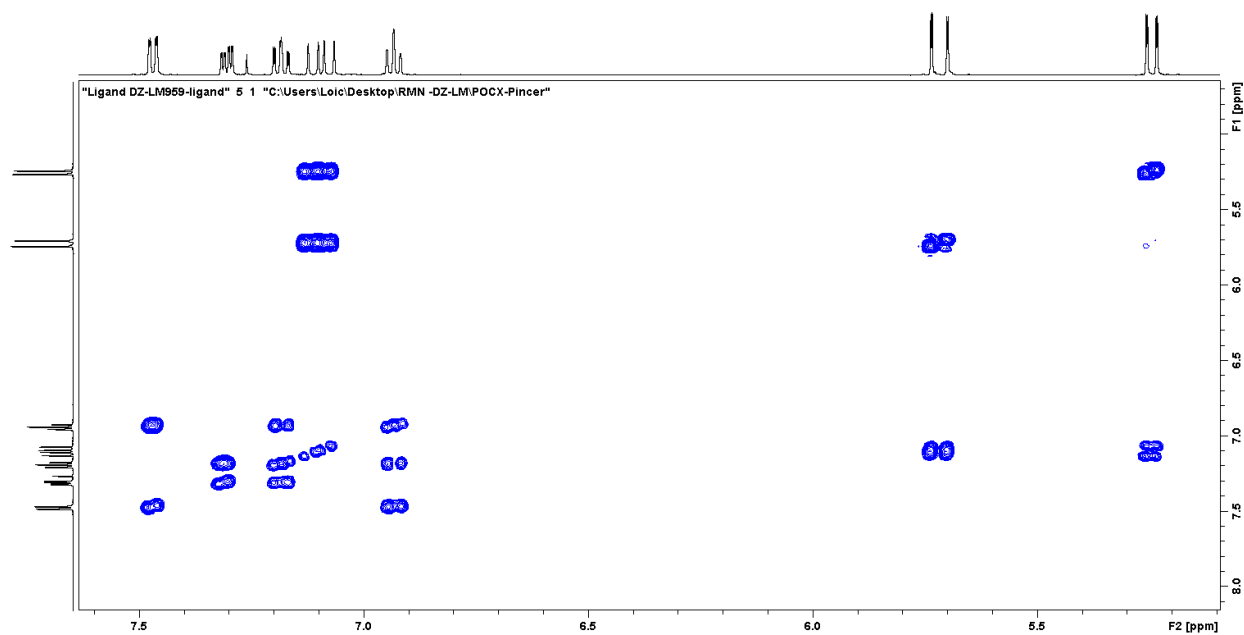
Figure S5.12: The expanded olefinic/aliphatic region of the COSY NMR spectrum of **1** in CDCl₃.
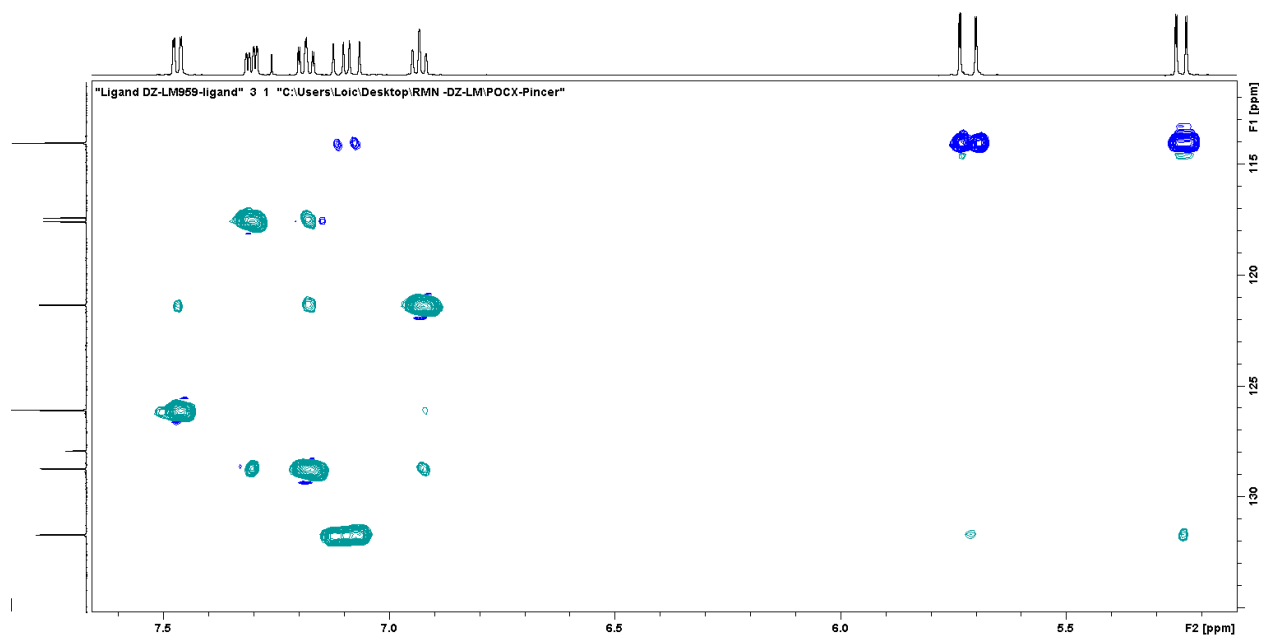
Figure S5.13: The expanded olefinic/aliphatic region of the COSY NMR spectrum of **1** in CDCl₃.
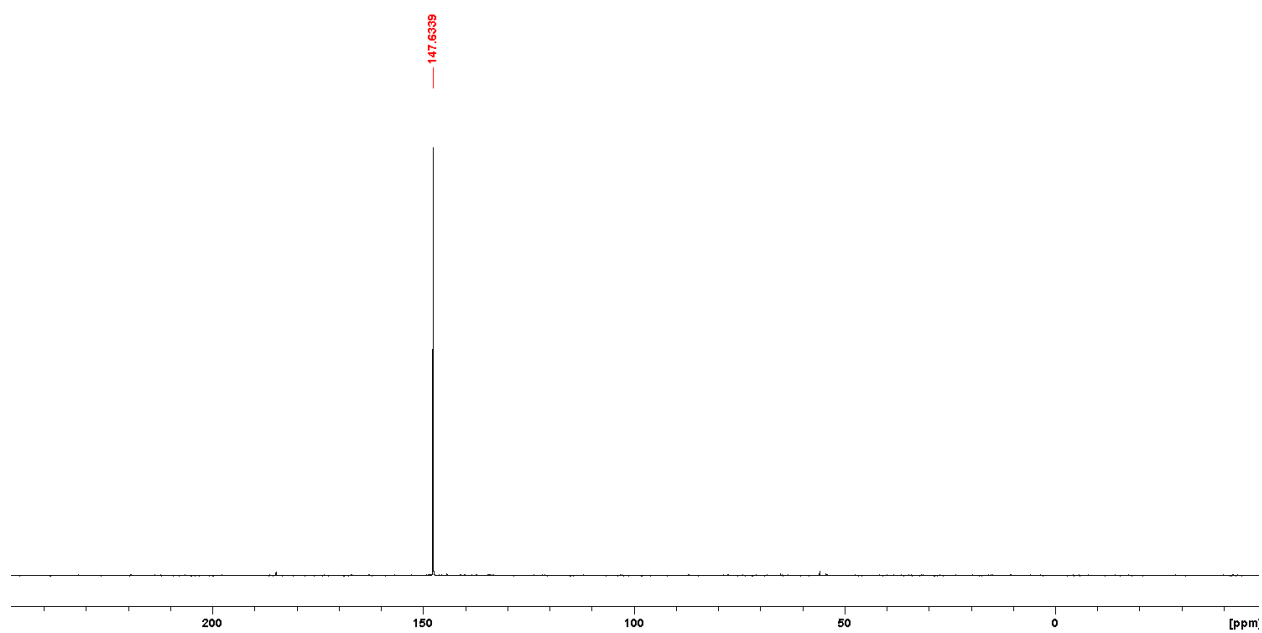
Figure S5.14: ³¹P{¹H} NMR spectrum of **2** in C₆D₆.

b. Complex **2**

Figure S5.15: Full ^{1}H NMR spectrum of 2 in C6D6.

Figure S5.16: The expanded aliphatic region of the ^{1}H NMR spectrum of **2** in C$_6$D$_6$.
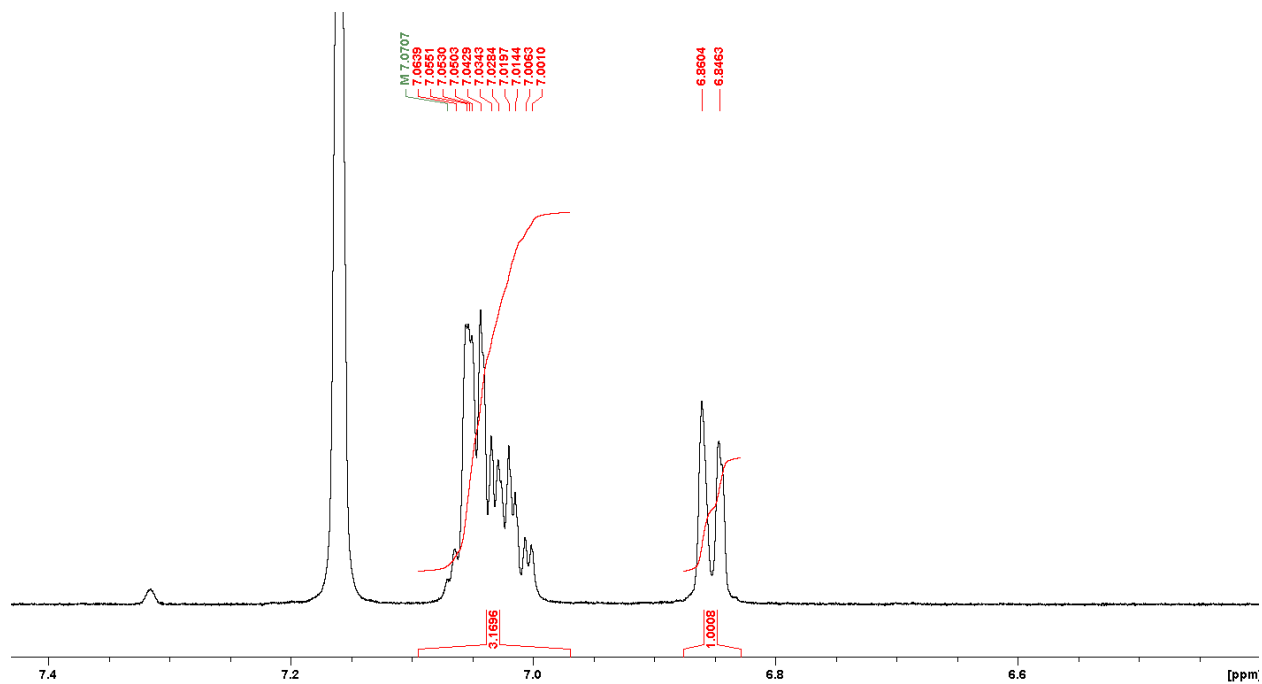
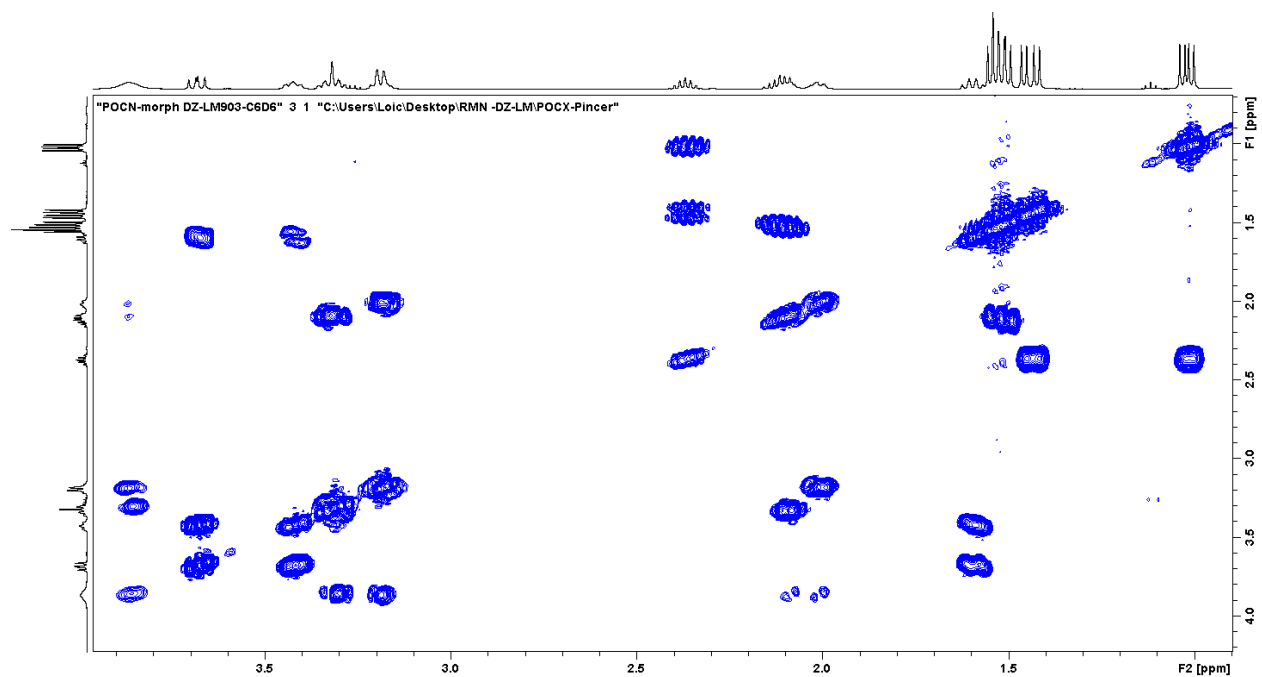Figure S5.17: The expanded aromatic region of the ^{1}H NMR spectrum of **2** in C_6D_6.
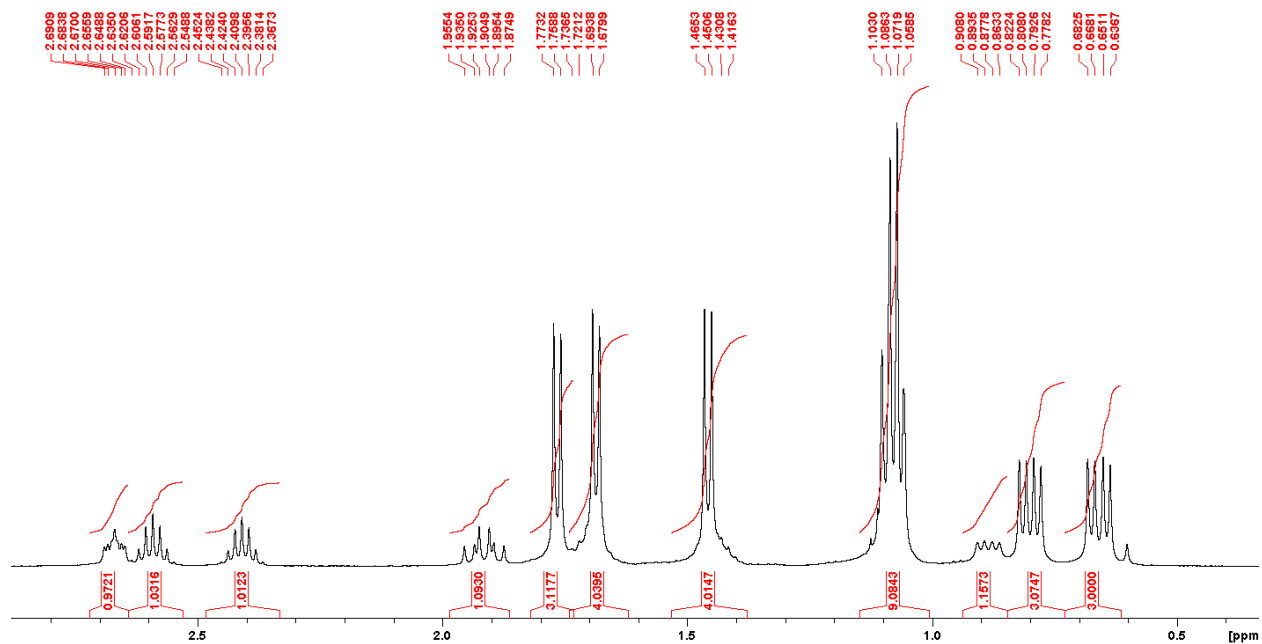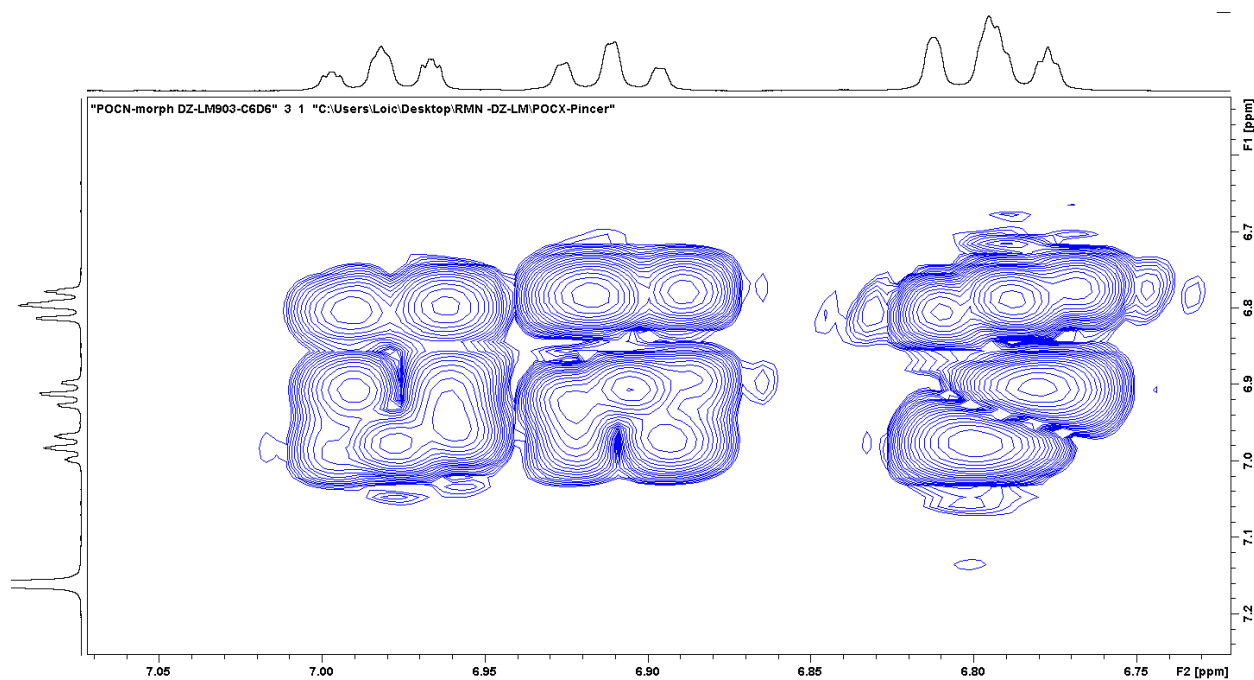

Figure S5.18: The expanded aliphatic region of the ^{1}H$\{^{31}$P, δ 205.43$\}$ NMR spectrum of **2** in C_6D_6.
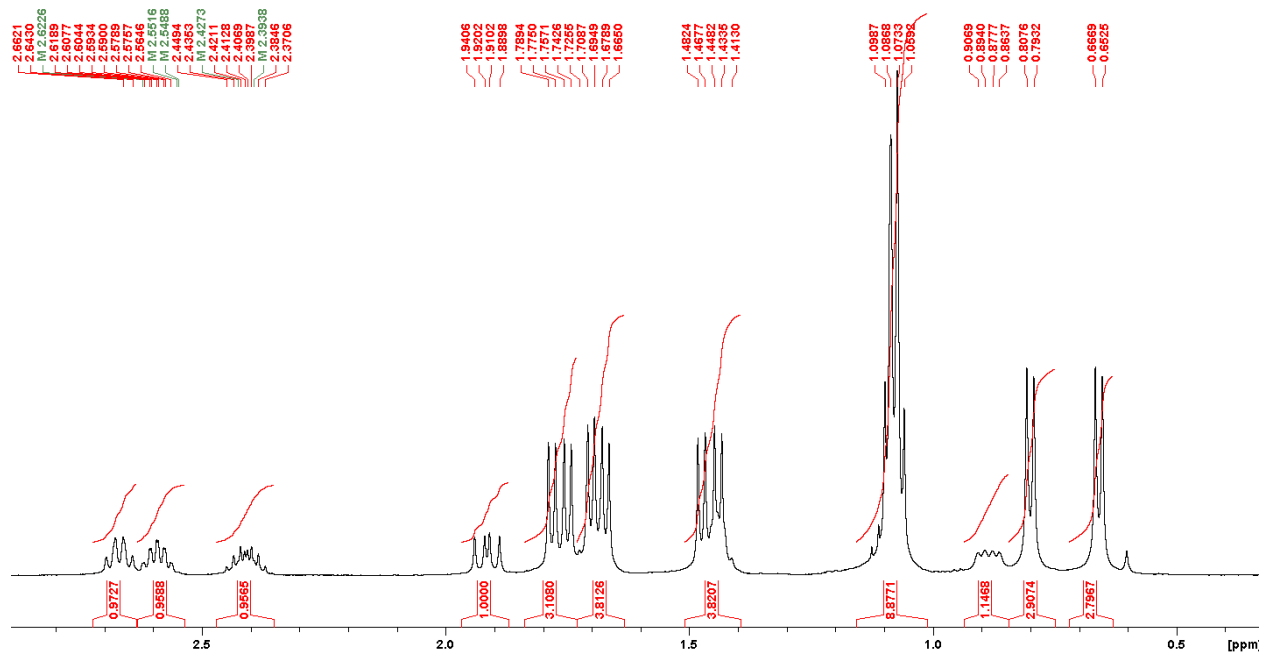
Figure S5.19: The expanded aliphatic region of the ^{1}H{^{31}P, δ 93.51} NMR spectrum of **2** in C_6D_6.
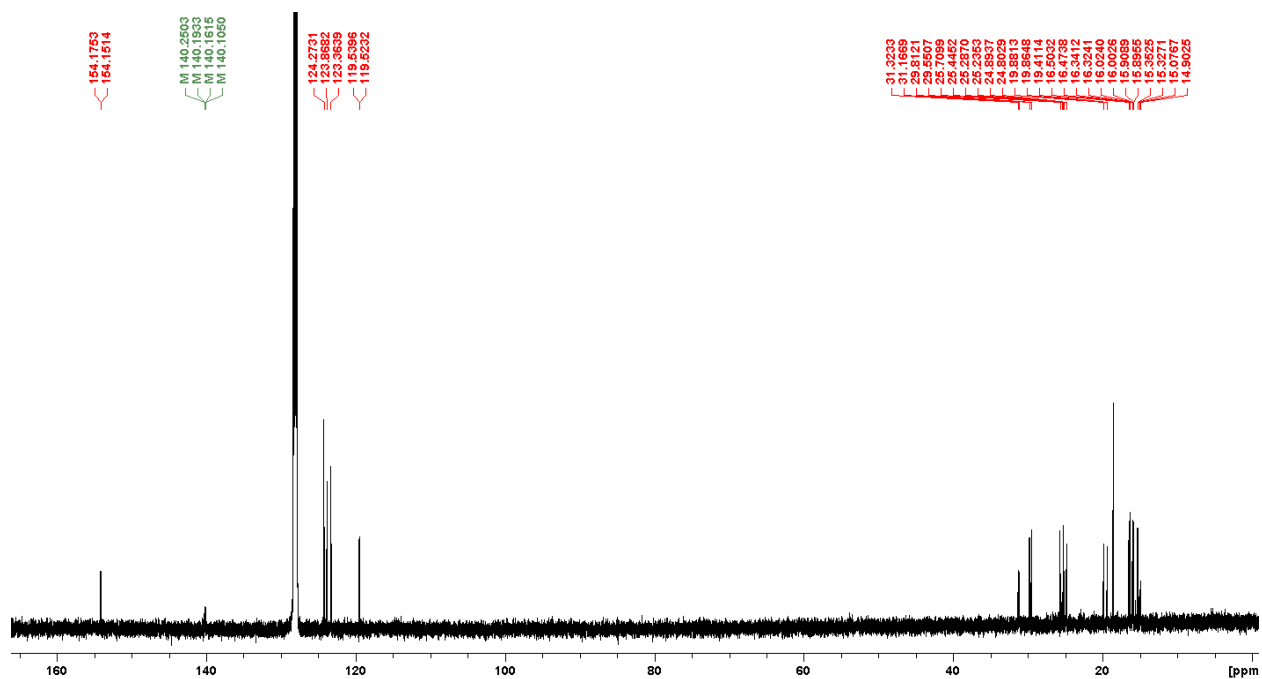
Figure S5.20: Full ^{13}C NMR spectrum of **2** in C_6D_6.
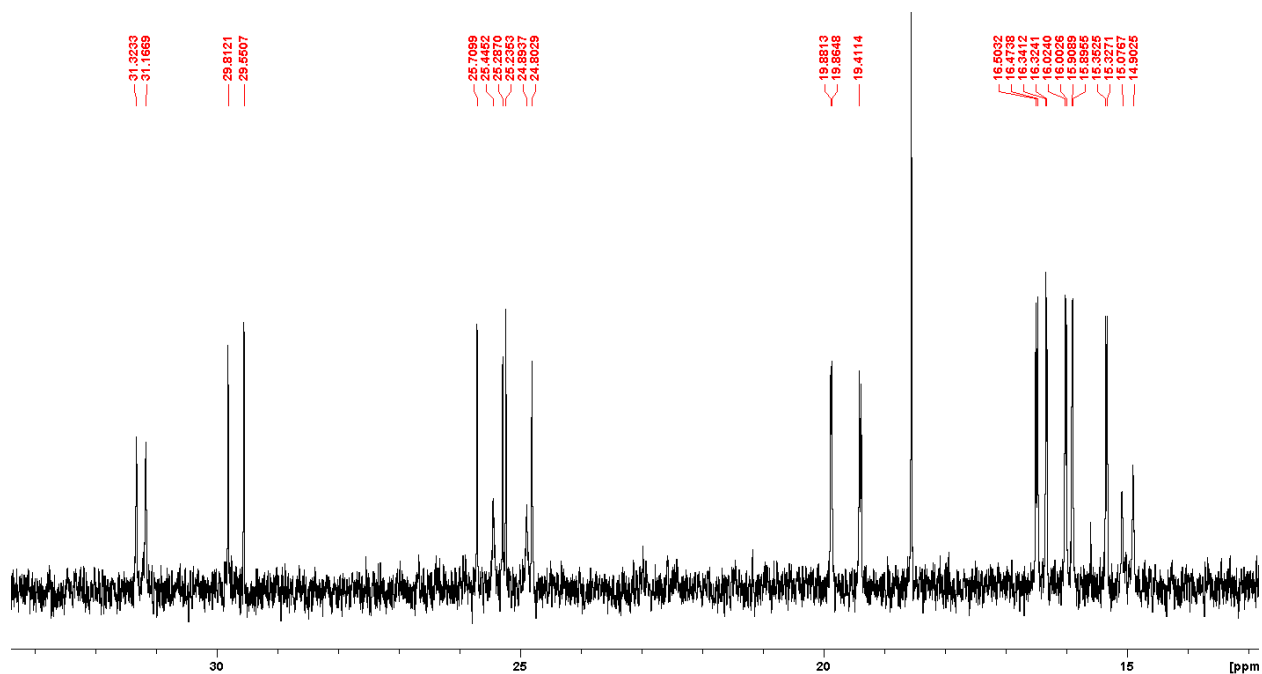
Figure S5.21: The expanded aliphatic region of the ^{13}C NMR spectrum of **2** in C_6D_6.
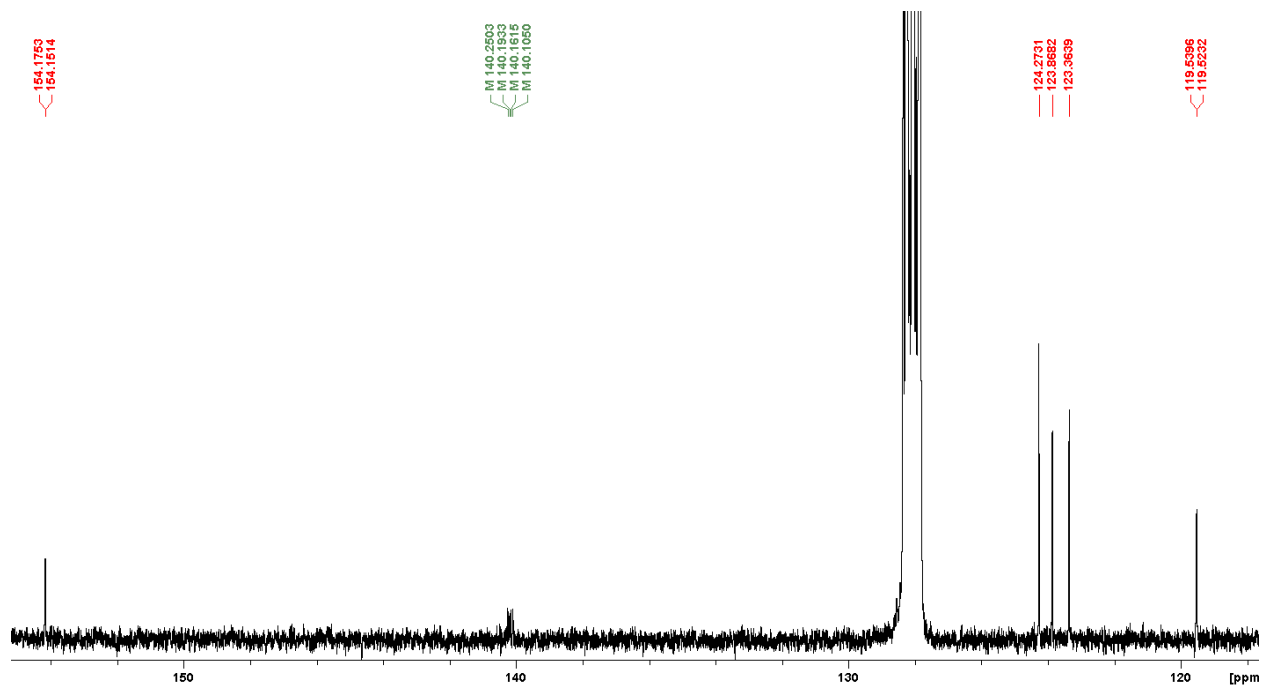
Figure S5.22: The expanded aromatic region of the ^{13}C NMR spectrum of **2** in C_6D_6.
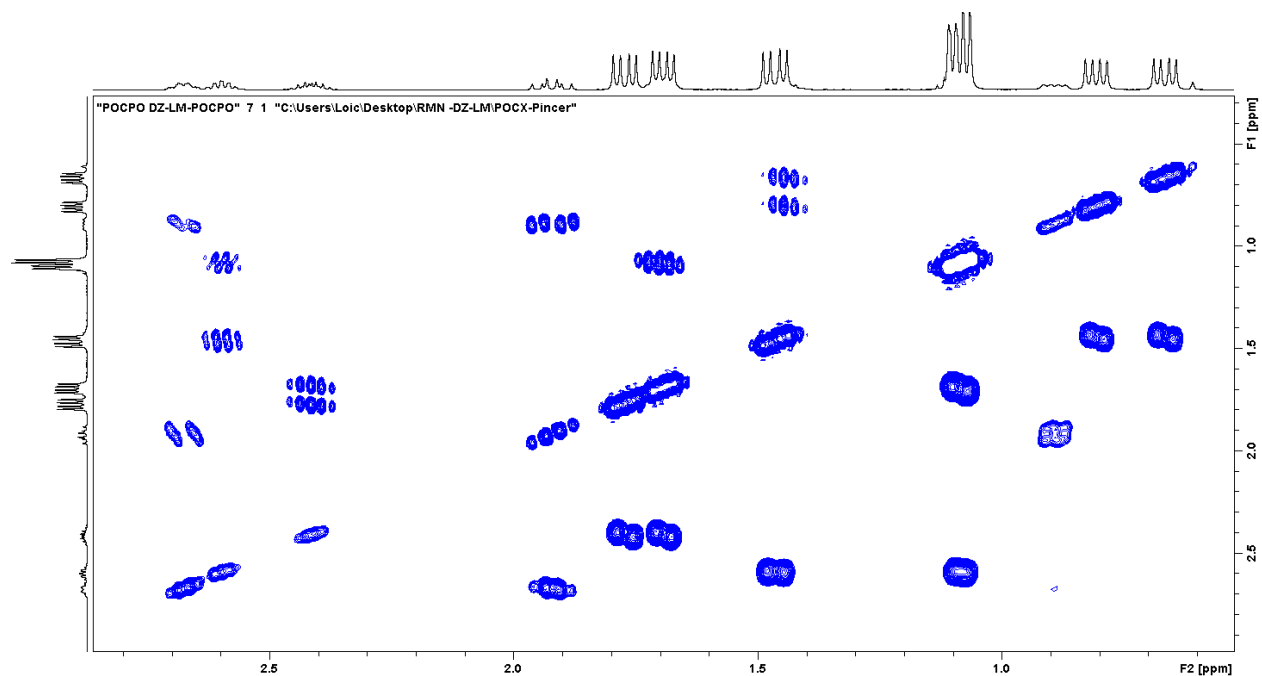
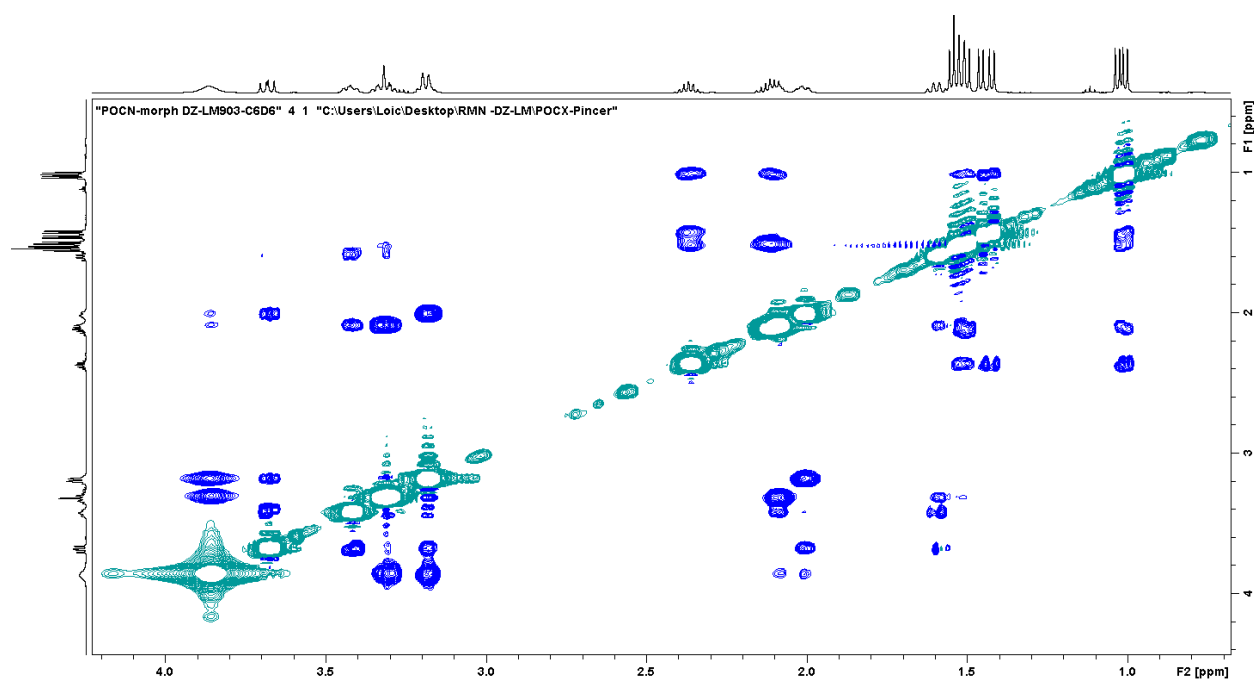Figure S5.23: The expanded aliphatic region of the COSY NMR spectrum of **2** in C_6D_6.
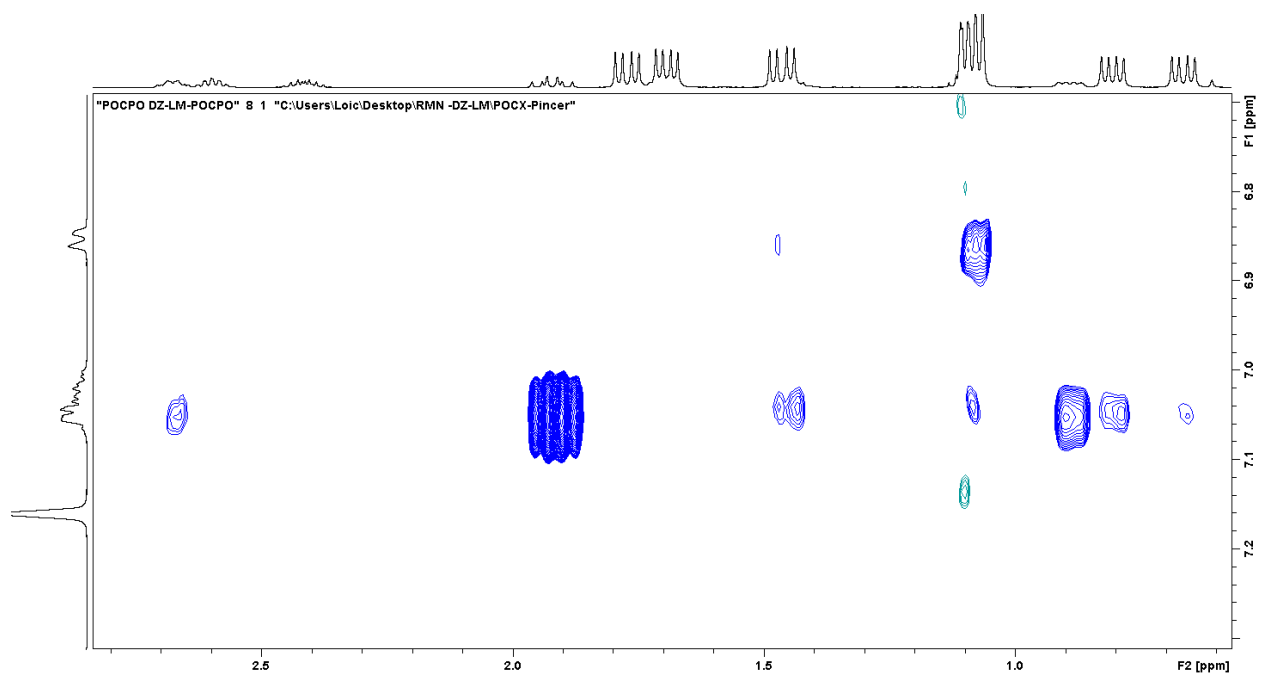
Figure S5.24: Partial NOESY NMR spectrum of **2** in C_6D_6 showing the aliphatic/aromatic interactions.
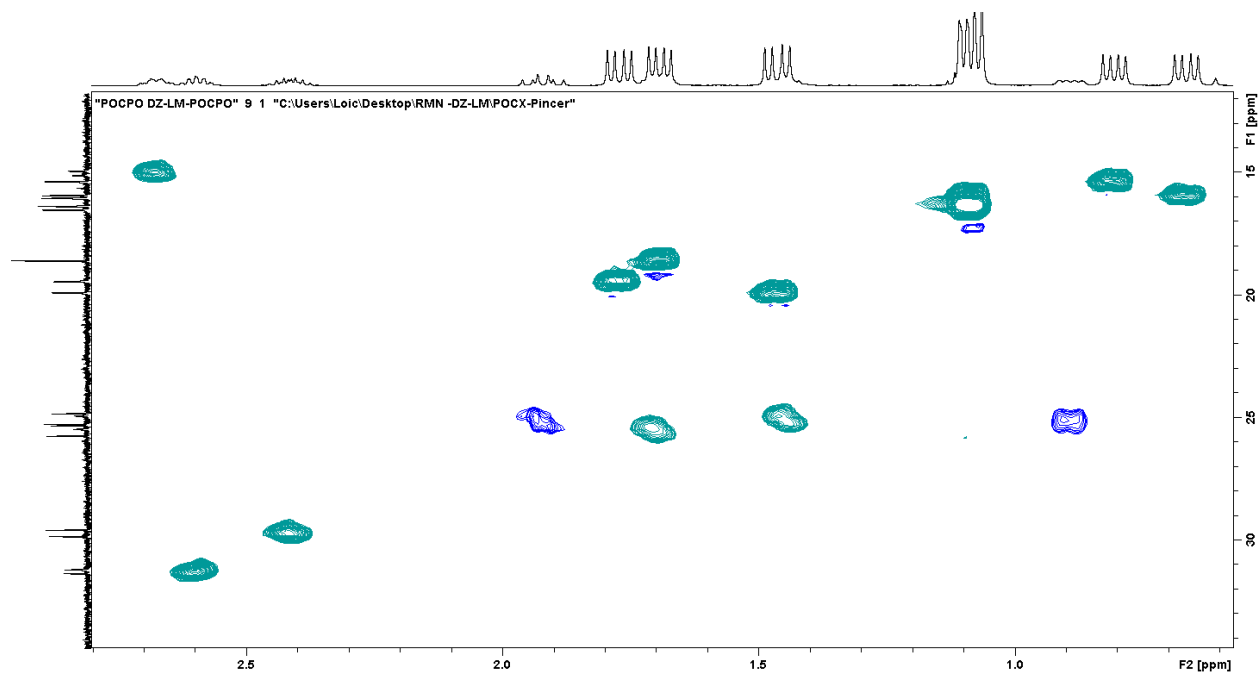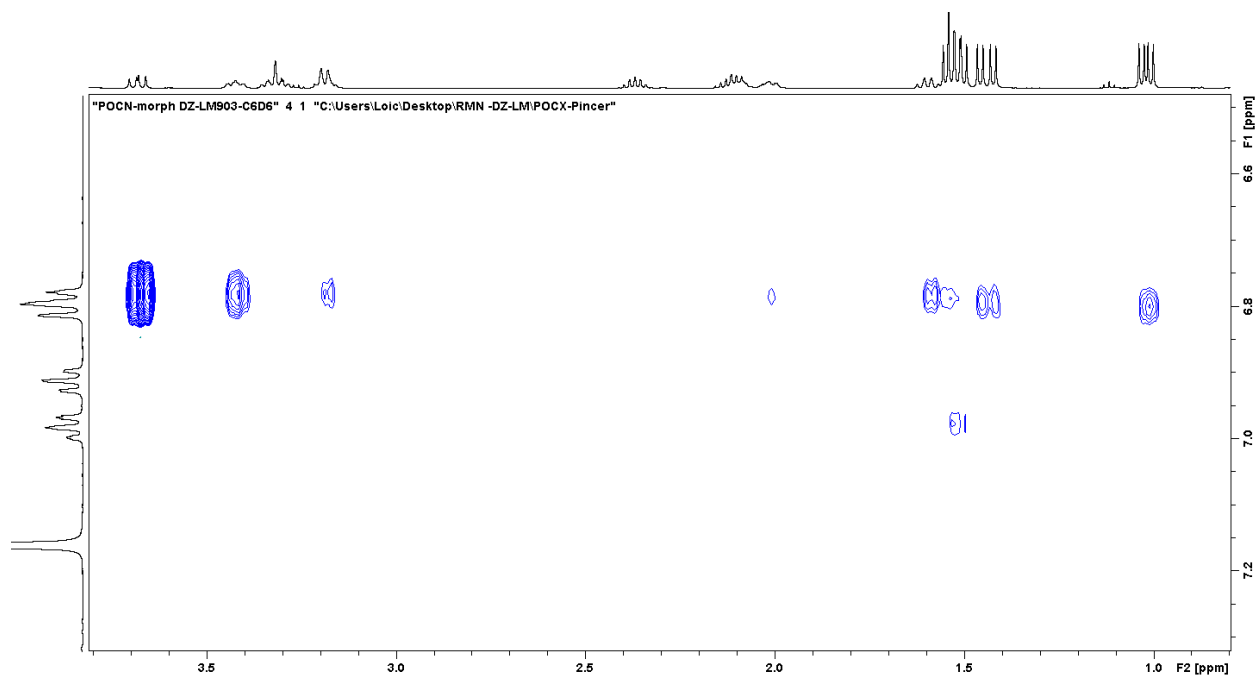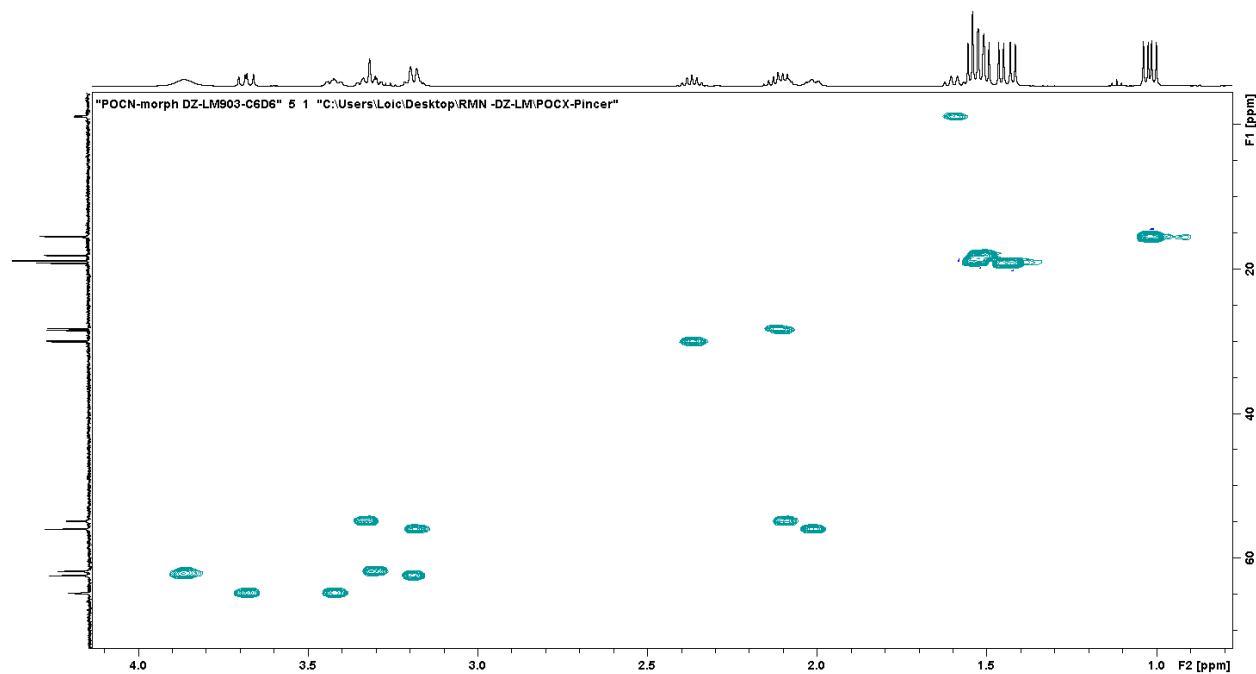
Figure S5.25. The expanded aliphatic region of the HSQC NMR spectrum of **2** in C_6D_6.
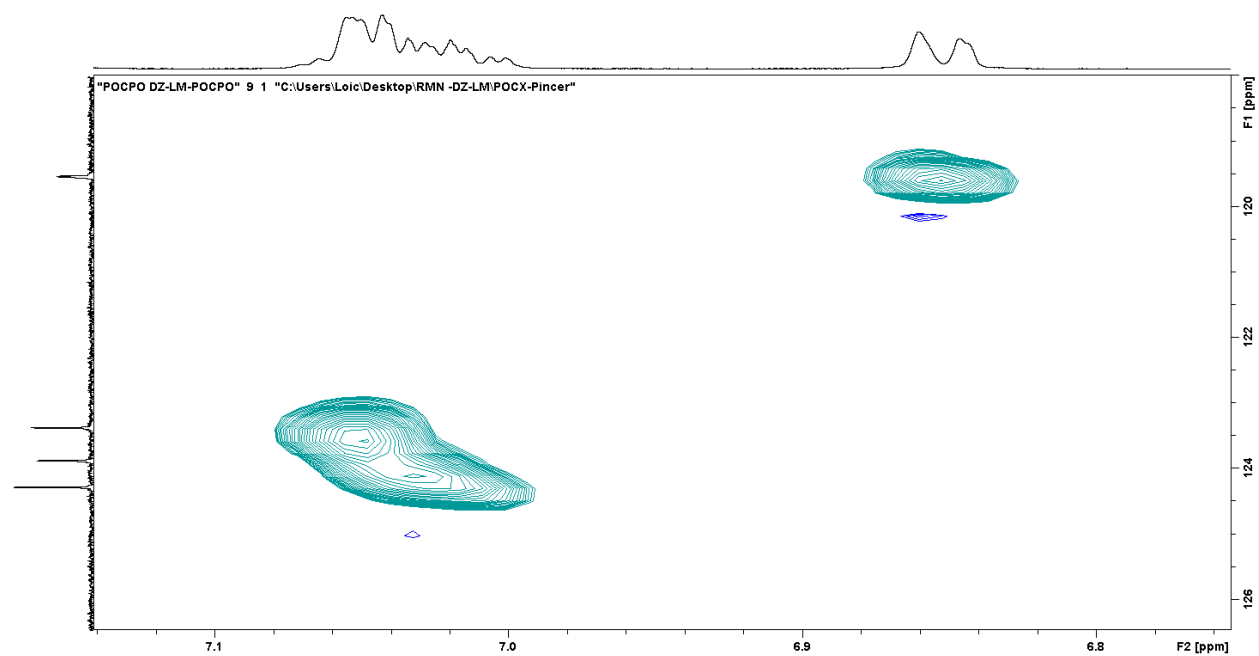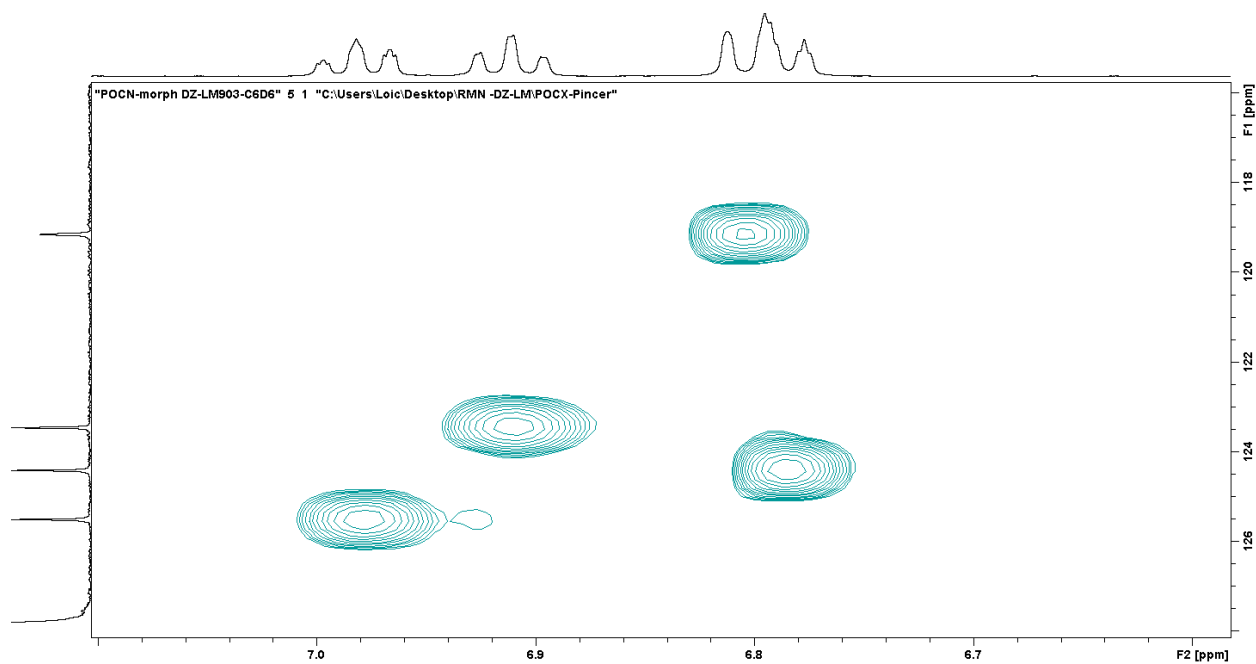

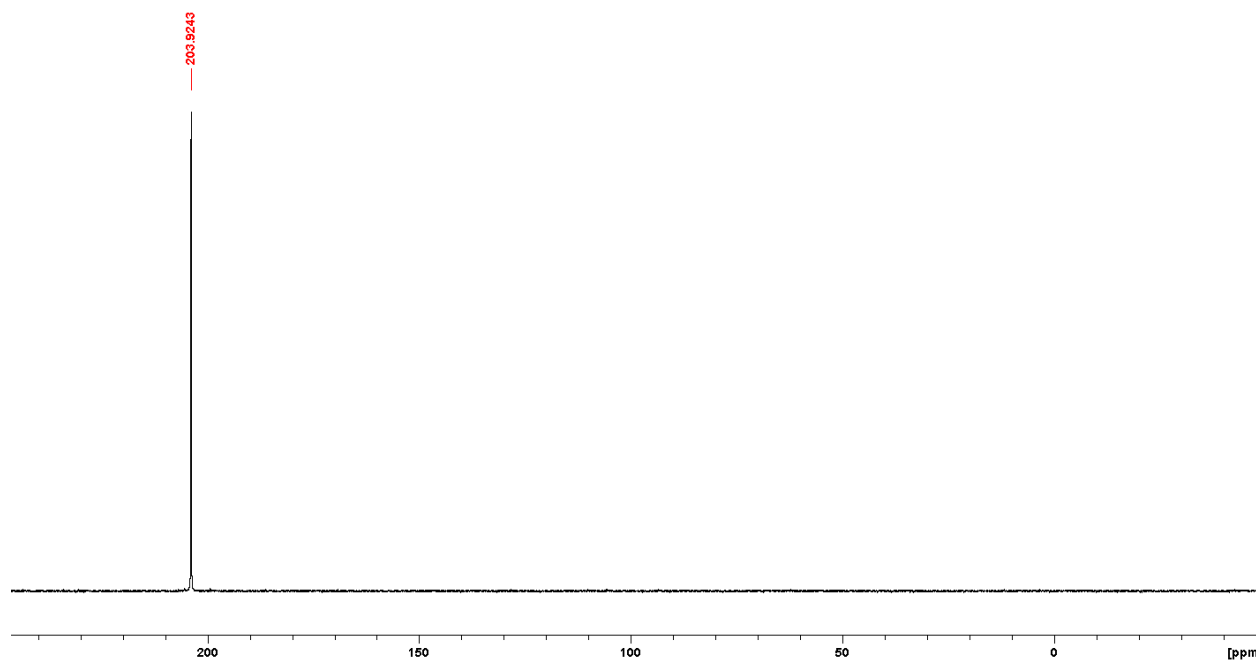Figure S5.26: The expanded aromatic region of the HSQC NMR spectrum of **2** in C_6D_6.
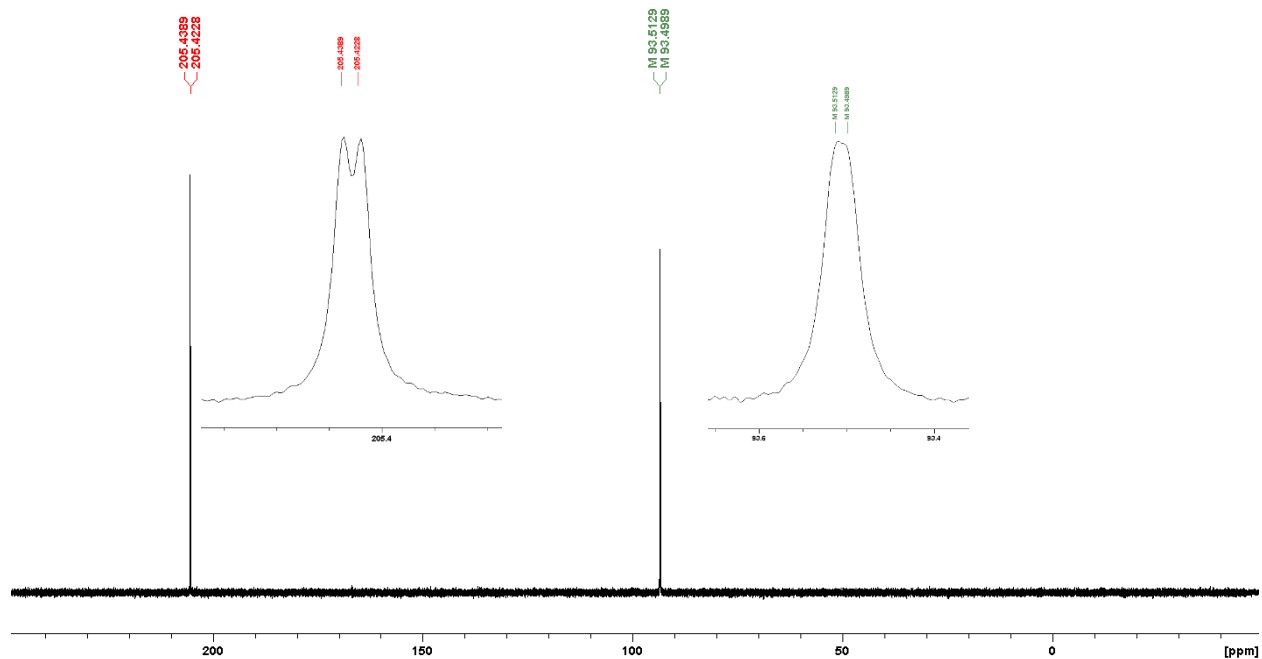
Figure S5.27: $^{31}P\{^1H\}$ NMR spectrum of **2** in C_6D_6.
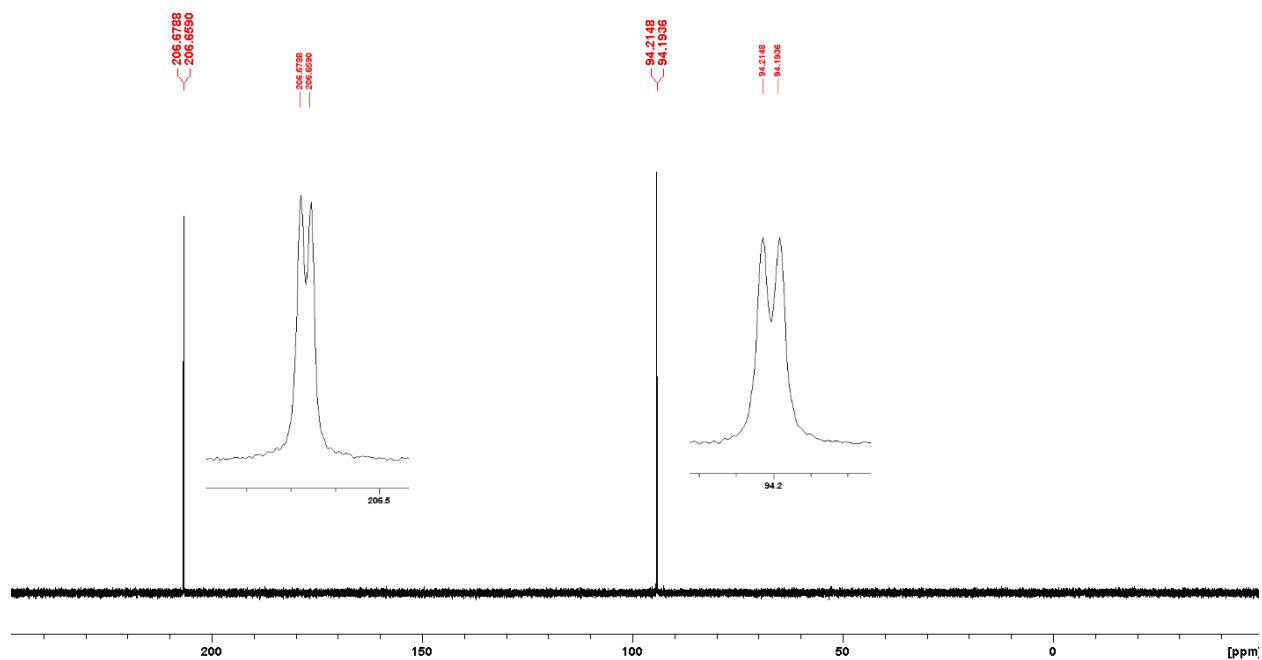
Figure S5.28: $^{31}P\{^1H\}$ NMR spectrum of **2** in $CDCl_3$.

c. Complex **3**
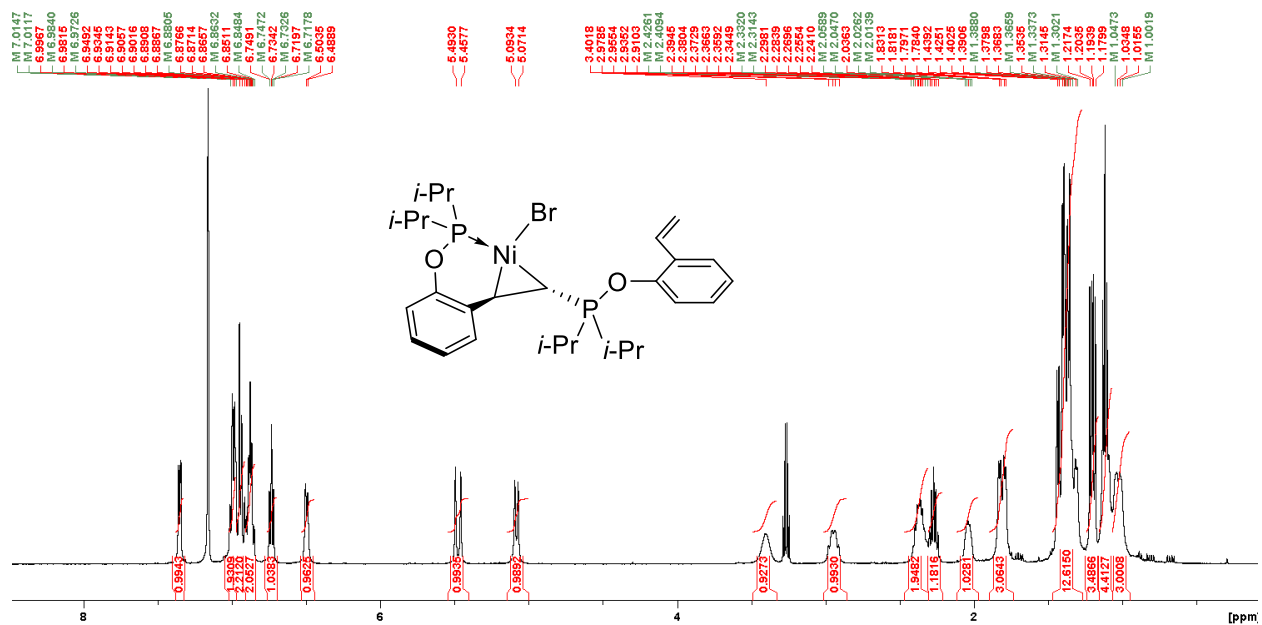
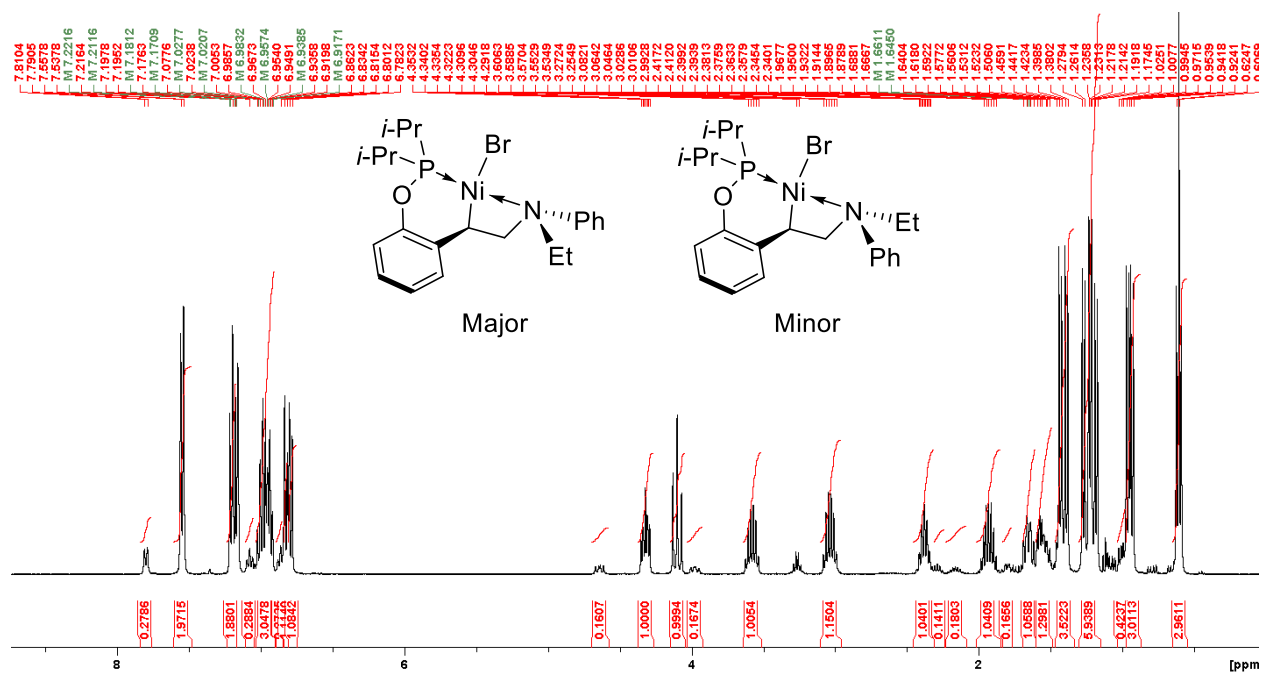Figure S5.29: Full ^{1}H NMR spectrum of **3** in C$_6$D$_6$.
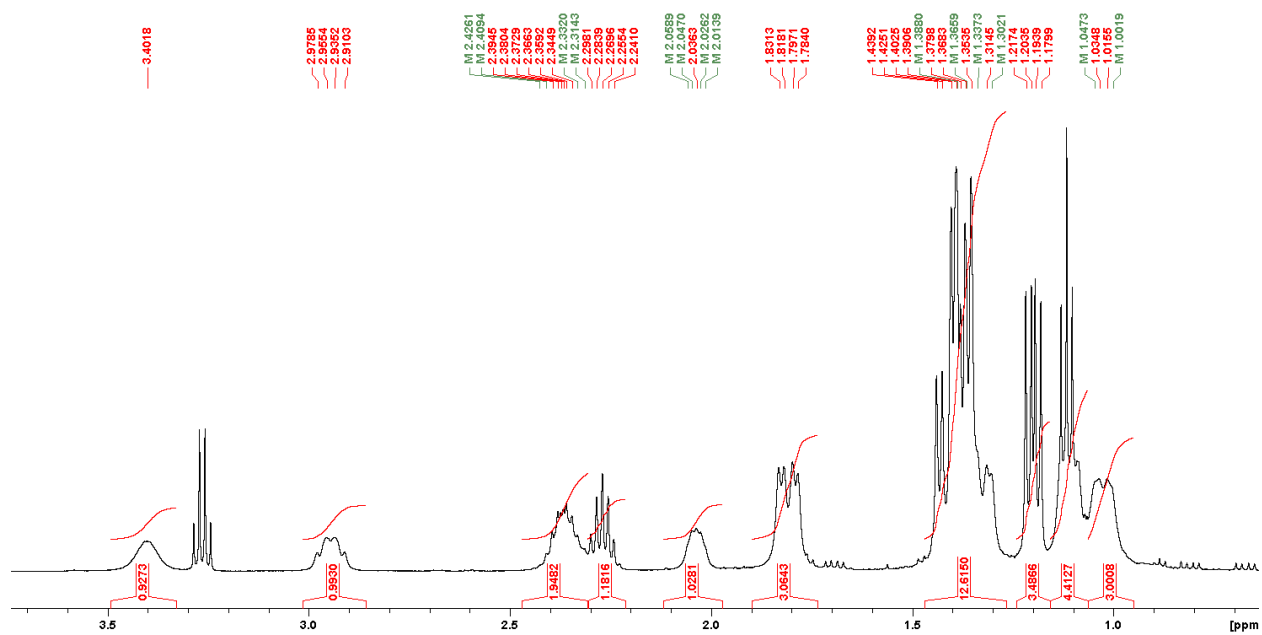
Figure S5.30: The expanded aliphatic region of the ^{1}H NMR spectrum of **3** in C$_6$D$_6$.
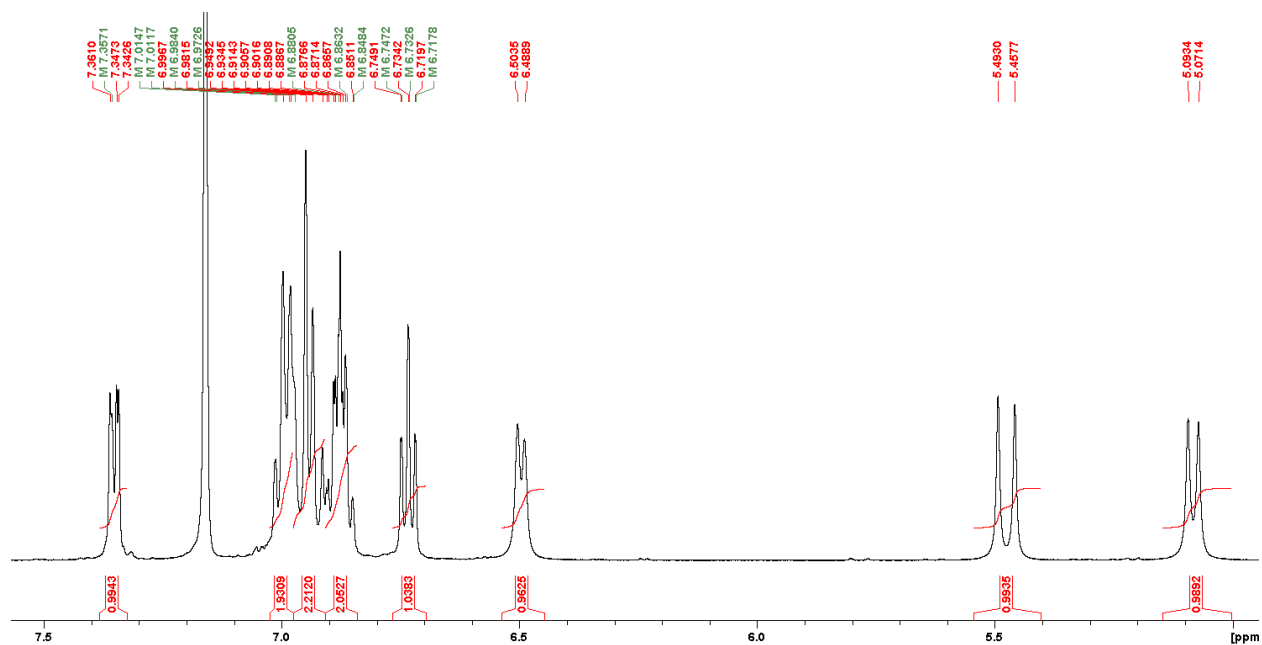
Figure S5.31: The expanded aromatic region of the ^{1}H NMR spectrum of **3** in C$_6$D$_6$.
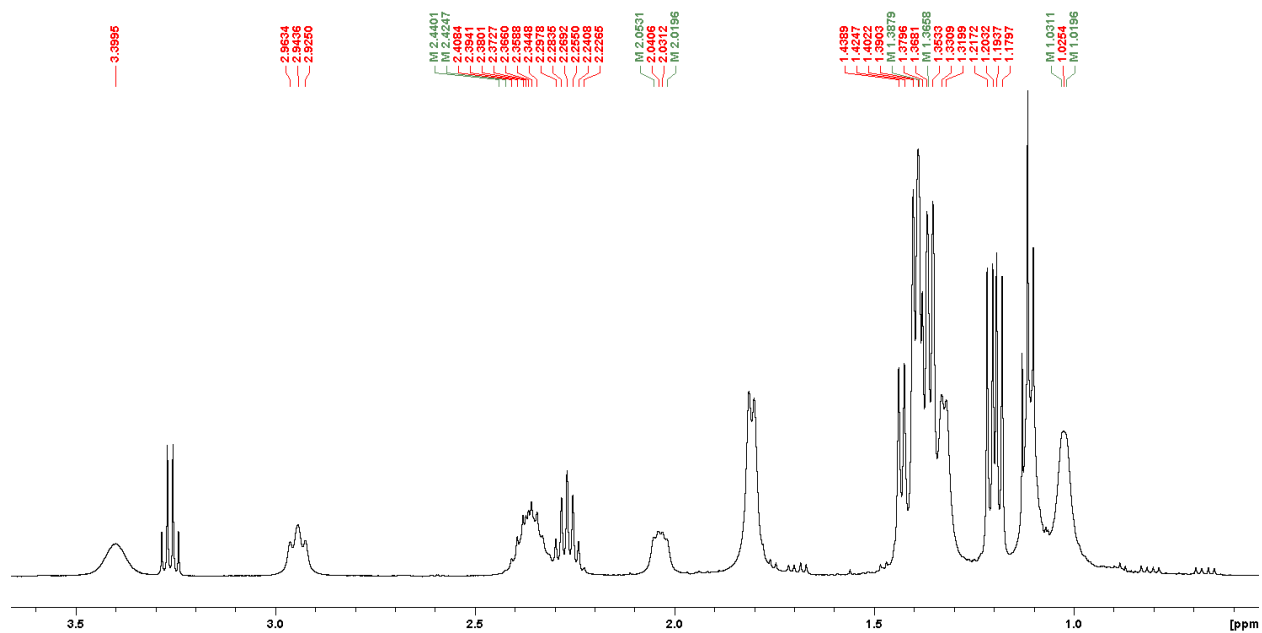
Figure S5.32: The expanded aliphatic region of the ^{1}H{^{31}P, δ 78.18} NMR spectrum of **3** in C$_6$D$_6$.
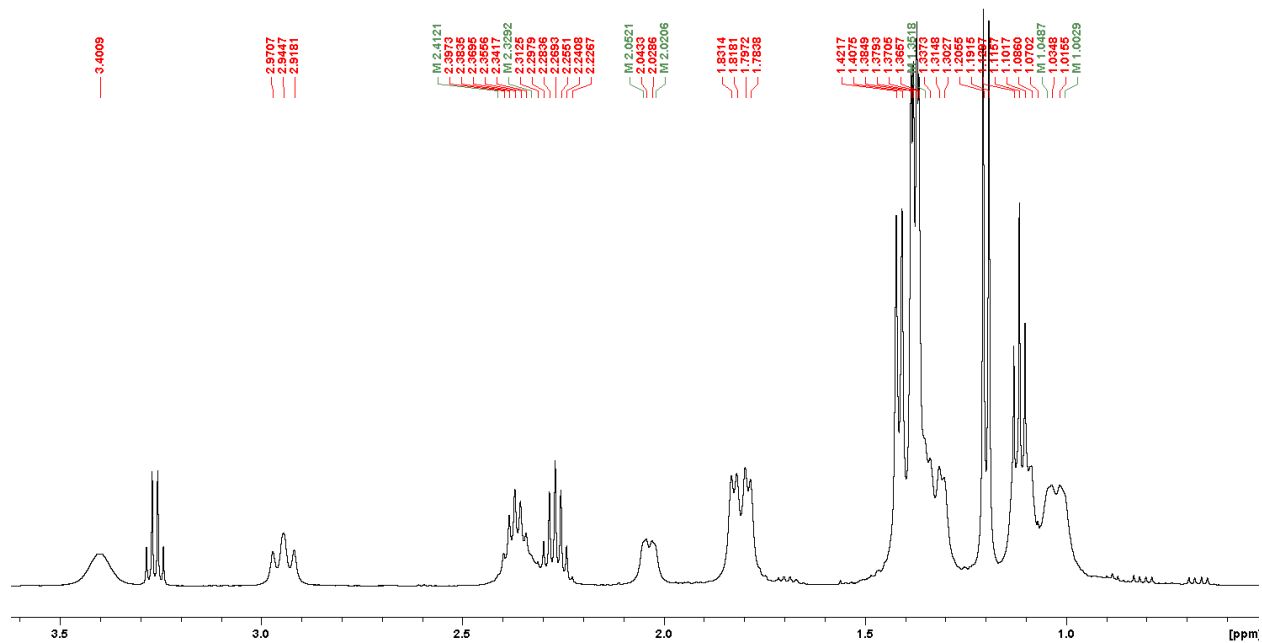
Figure S5.33: The expanded aliphatic region of the $^1H\{^{31}P, \delta\ 193.35\}$ NMR spectrum of **3** in C_6D_6.
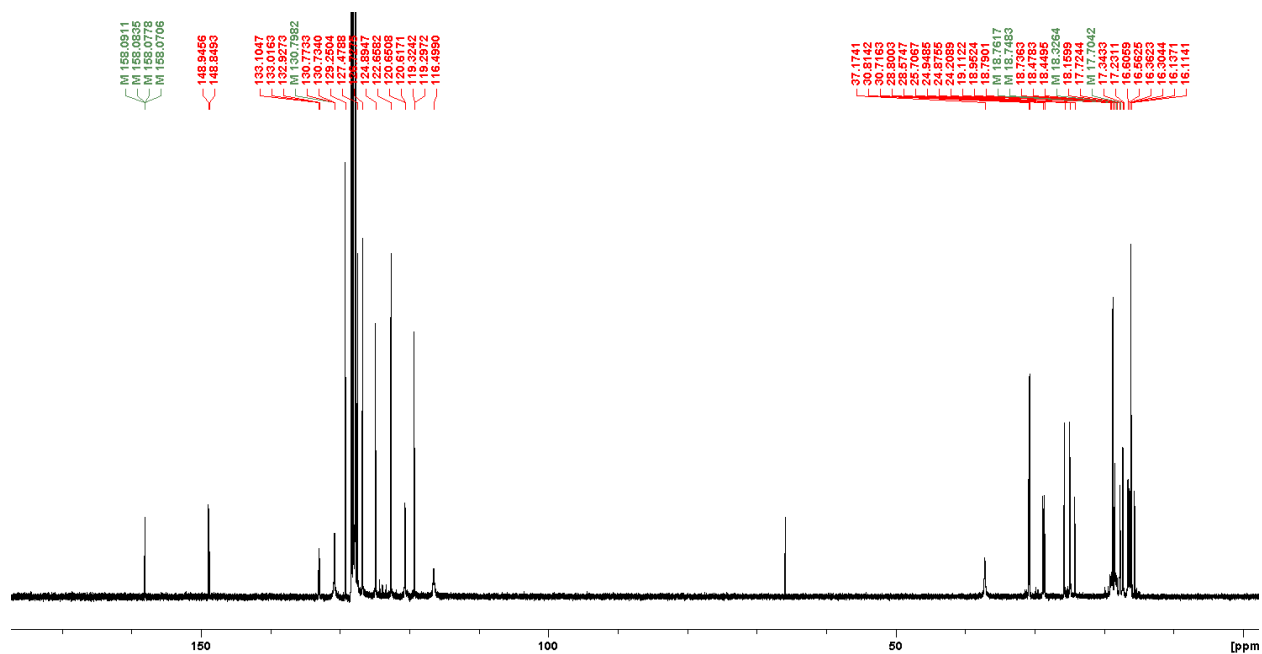
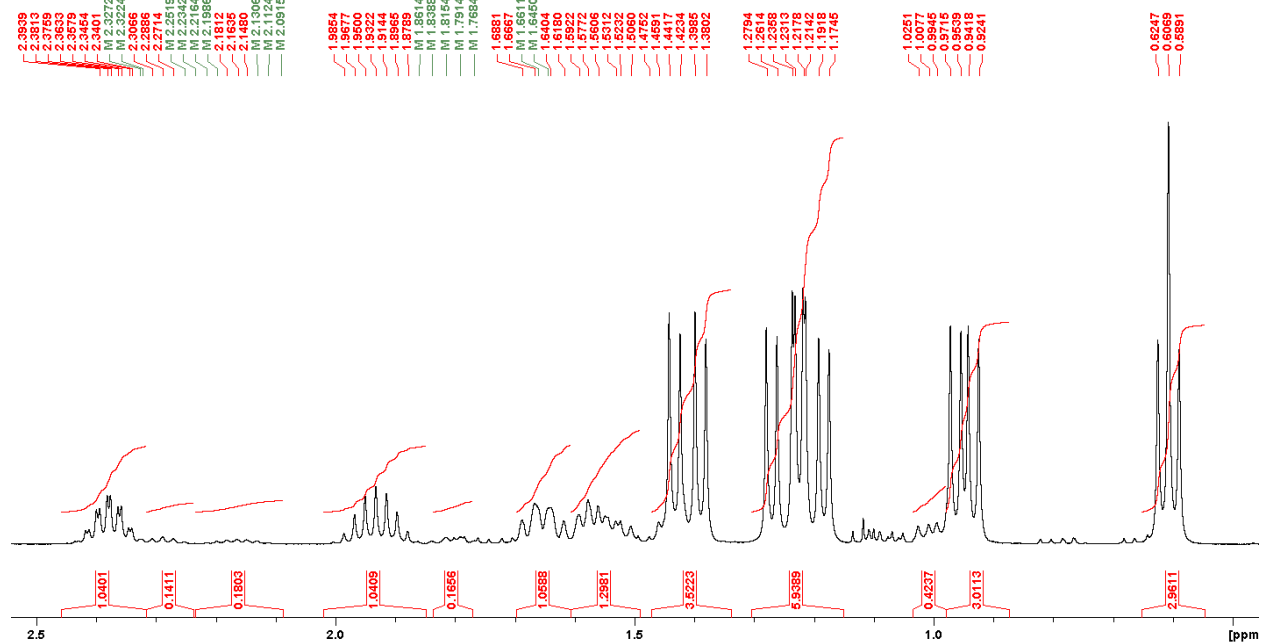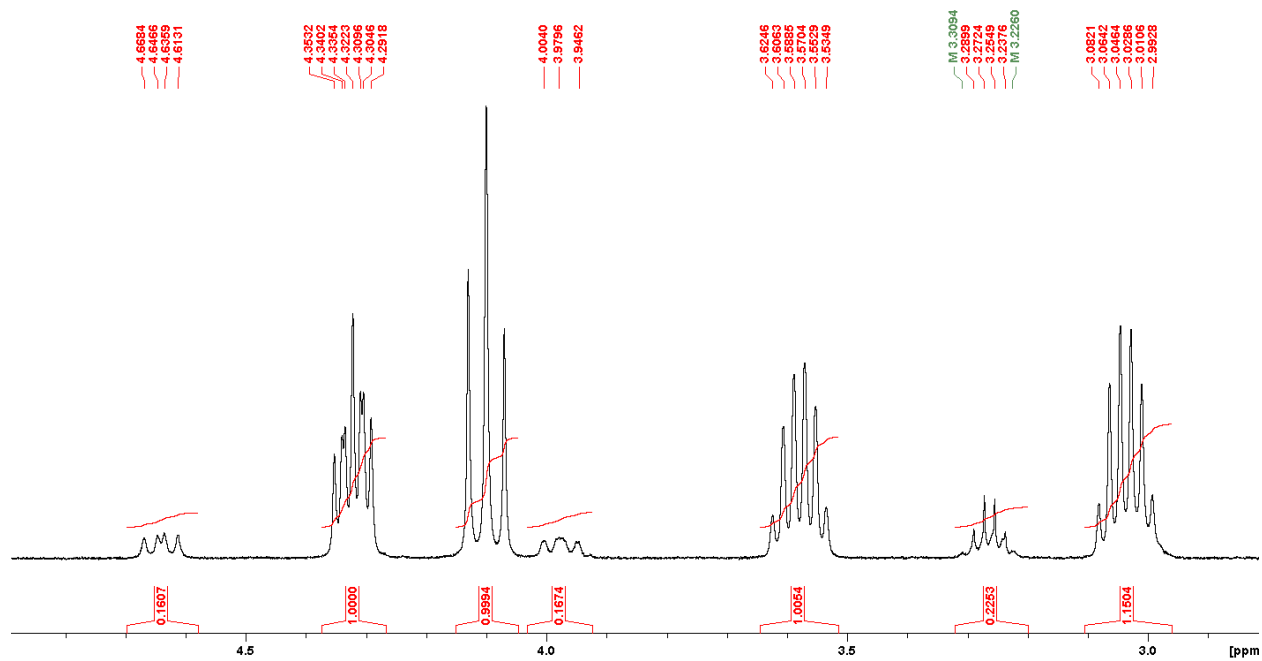Figure S5.34: Full ^{13}C NMR spectrum of **3** in C_6D_6.
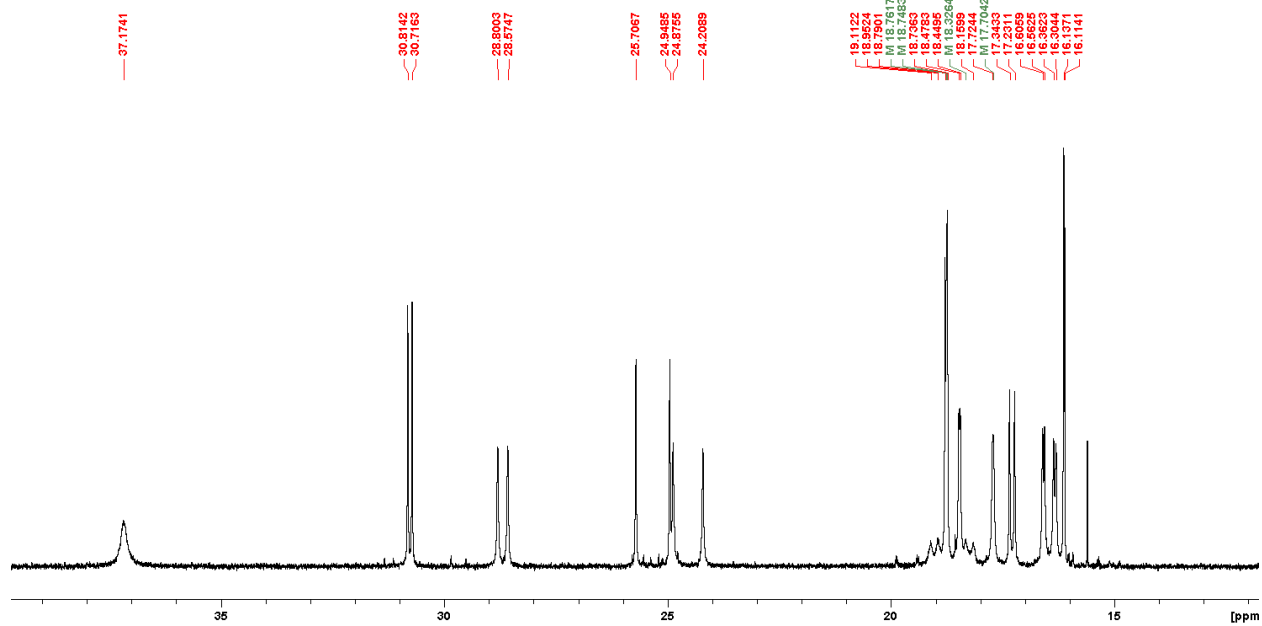
Figure S5.35: The expanded aliphatic region of the ^{13}C NMR spectrum of **3** in C$_6$D$_6$.
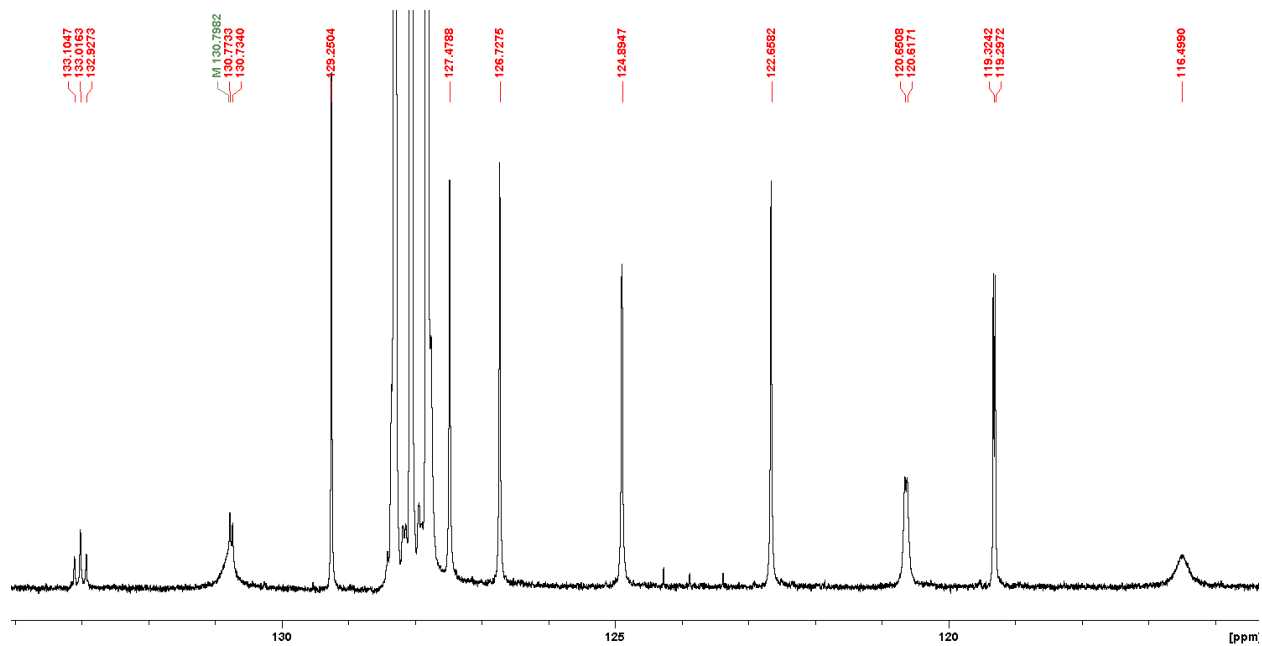
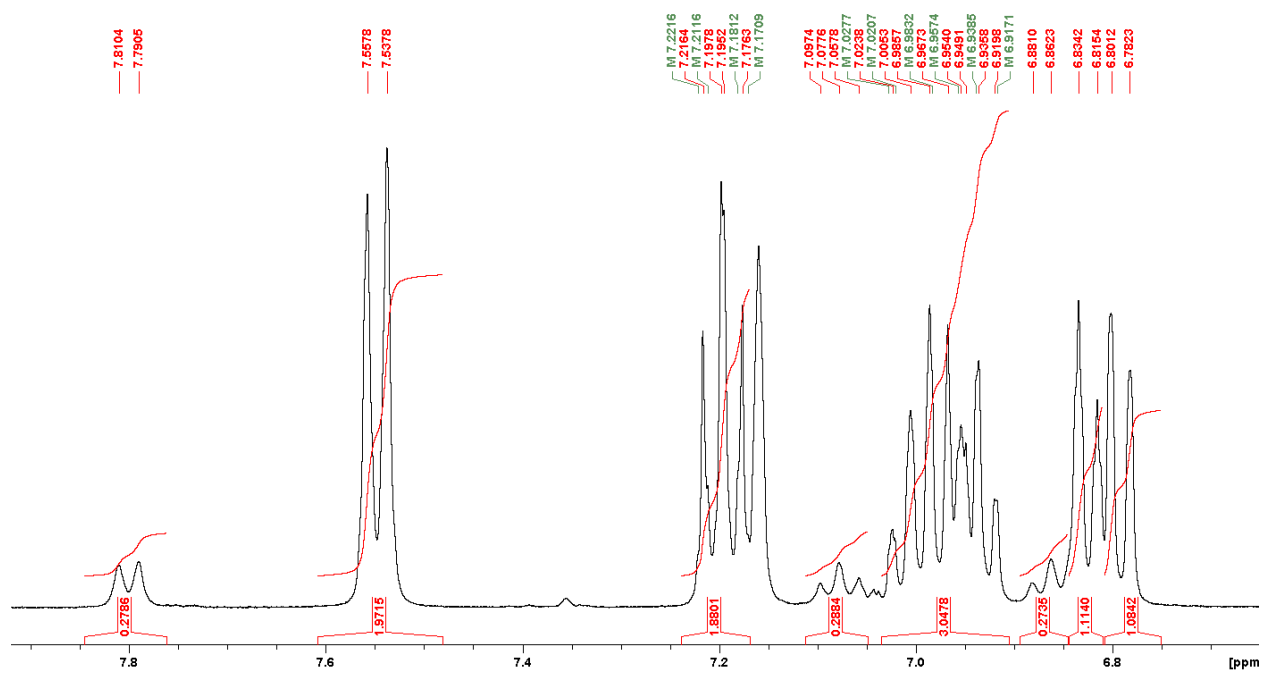

Figure S5.36: The expanded aromatic region of the ^{13}C NMR spectrum of **3** in C$_6$D$_6$.
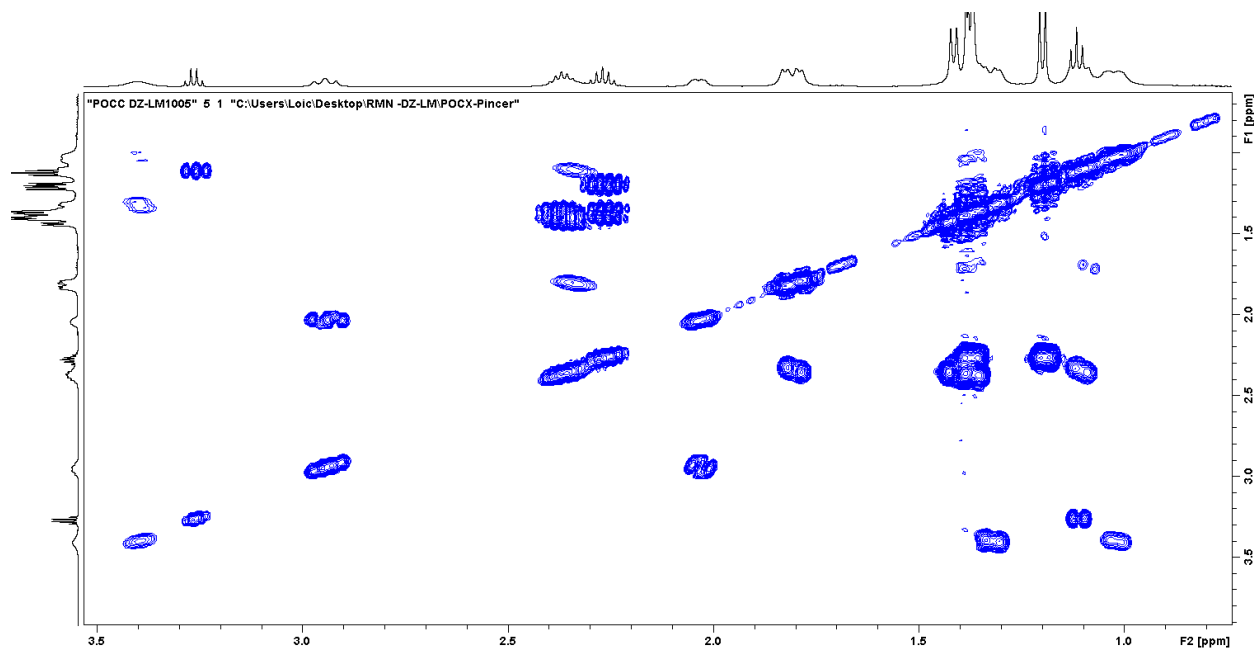
Figure S5.37: The expanded aliphatic region of the COSY NMR spectrum of **3** in C$_6$D$_6$.
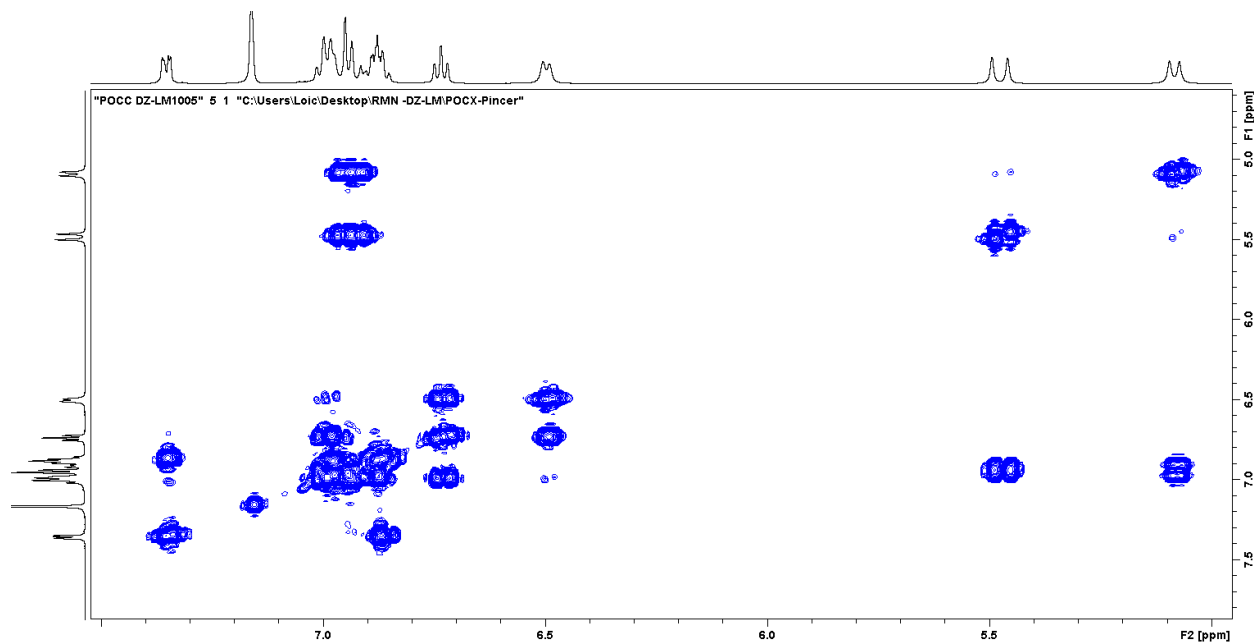
Figure S5.38: The expanded aromatic region of the COSY NMR spectrum of **3** in C$_6$D$_6$.
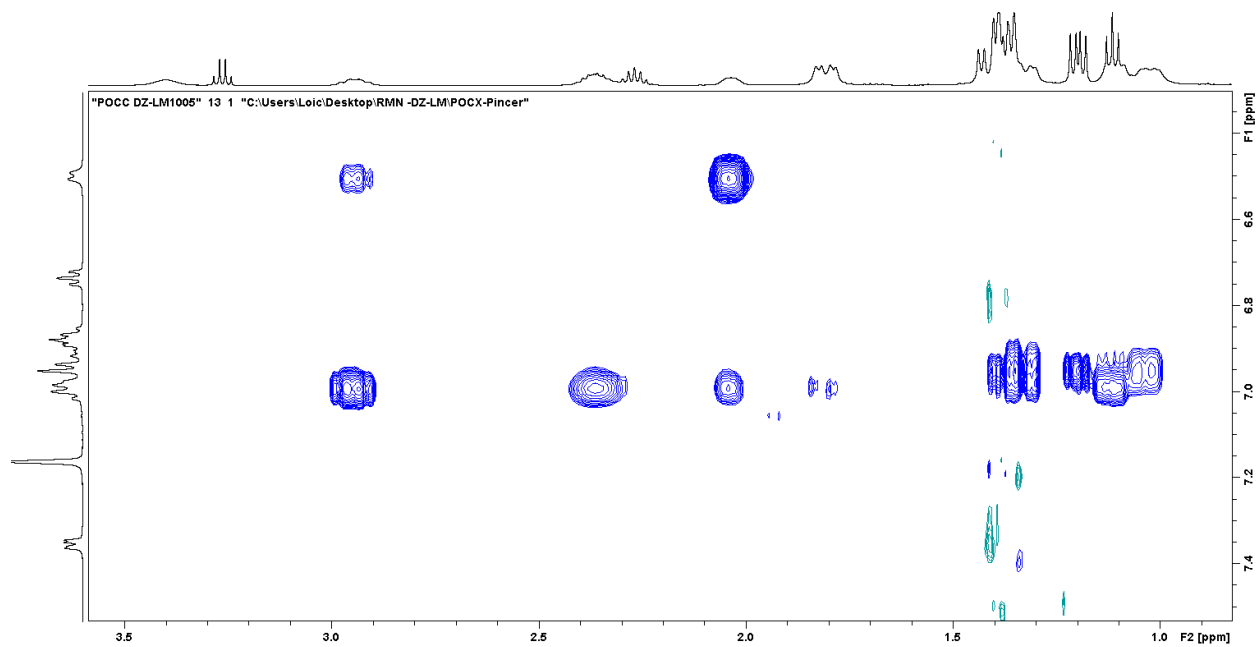
Figure S5.39: Partial NOESY NMR spectrum of **3** in C_6D_6 showing the aliphatic/aromatic interactions.
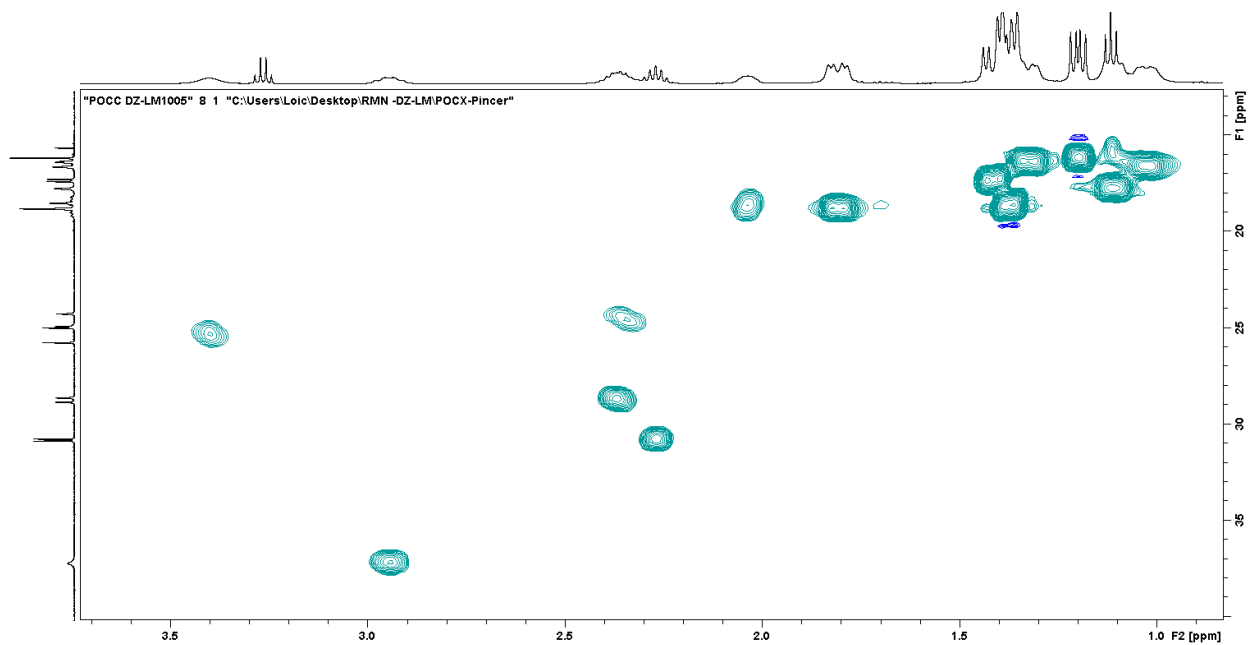
Figure S5.40: The expanded aliphatic region of the HSQC NMR spectrum of **3** in C_6D_6.
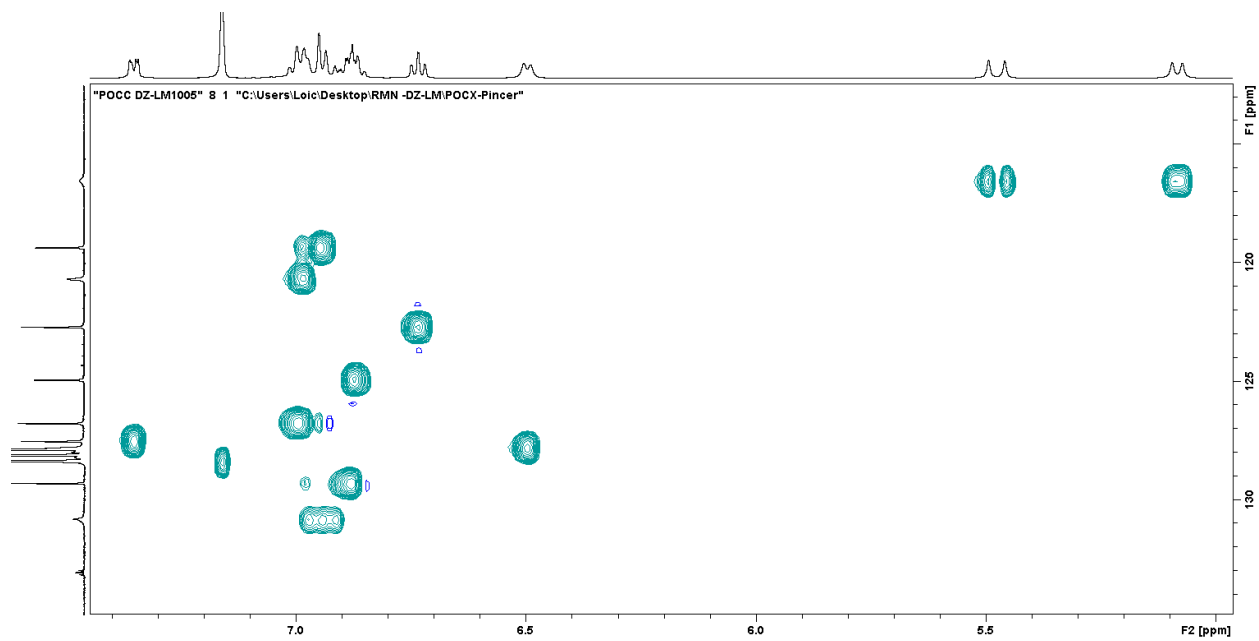
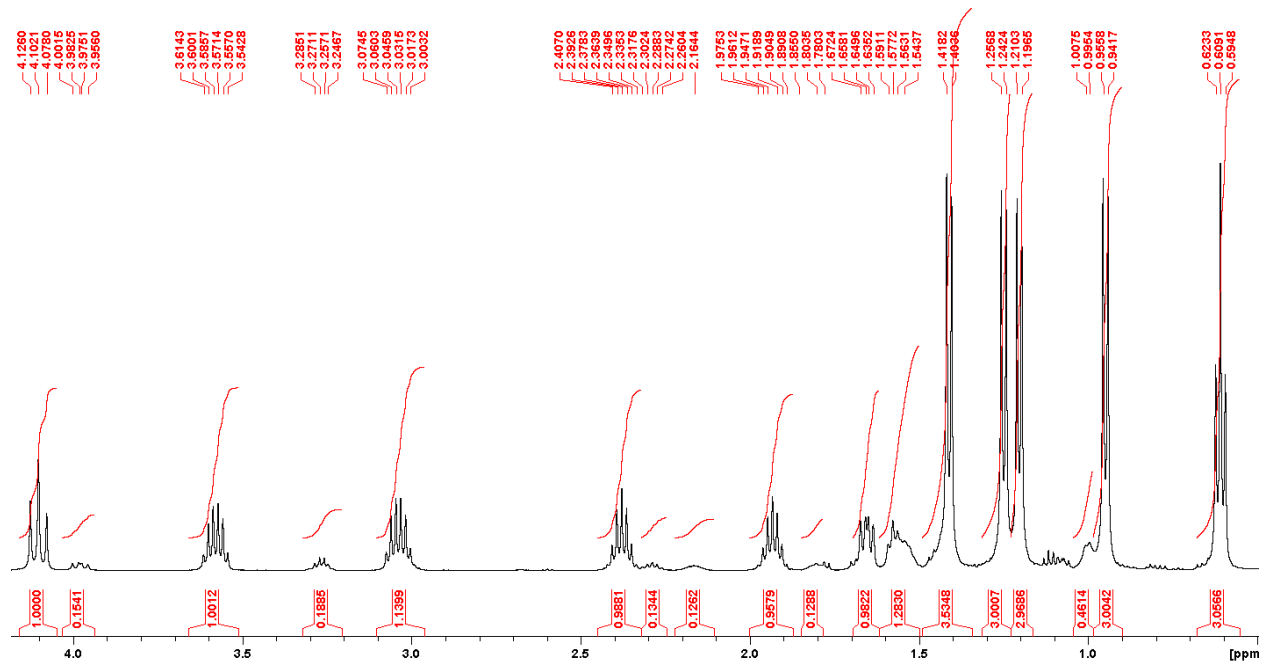Figure S5.41: The expanded aromatic region of the HSQC NMR spectrum of **3** in C$_6$D$_6$.
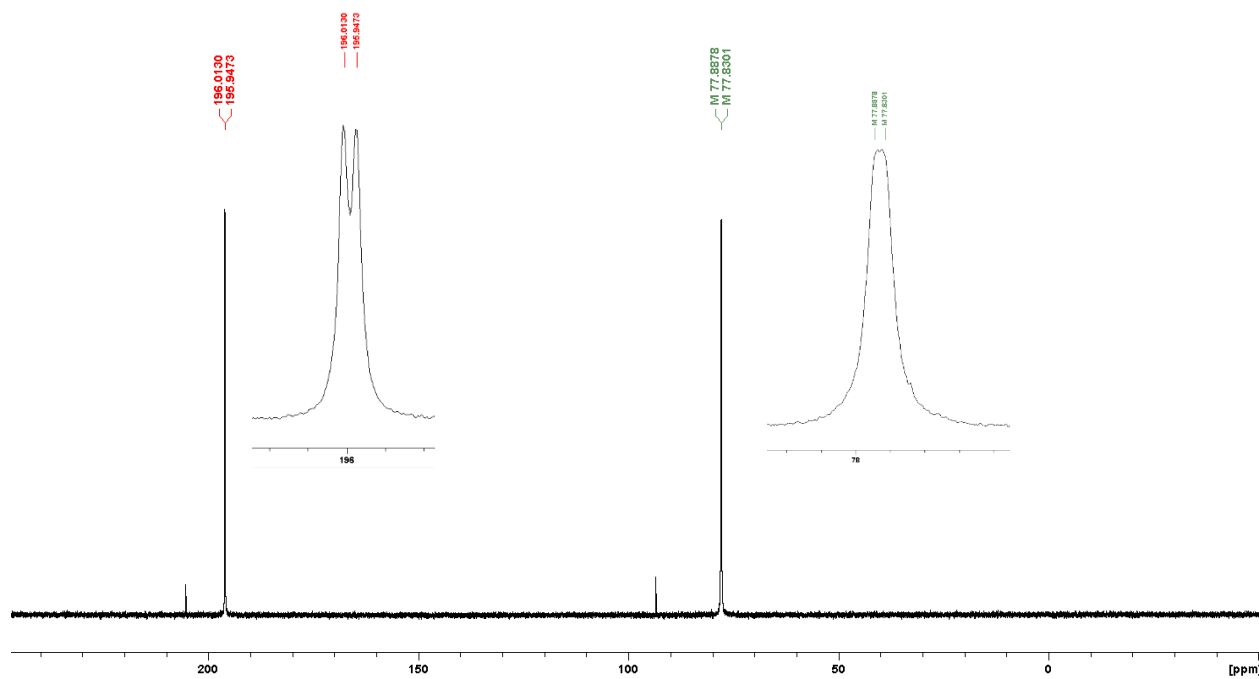
Figure S5.42: ^{31}P{^{1}H} NMR spectrum of **3** in C$_6$D$_6$.

d. Complex **4**
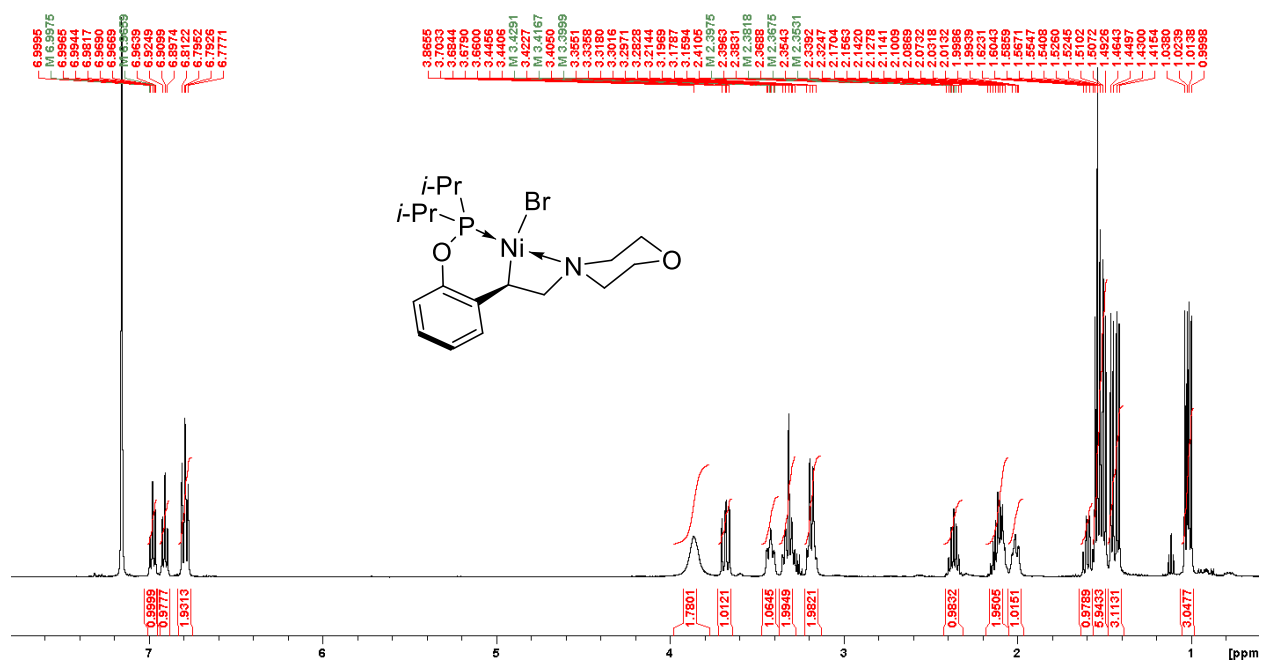
Figure S5.43: Full ^{1}H NMR spectrum of **4** in C_6D_6.
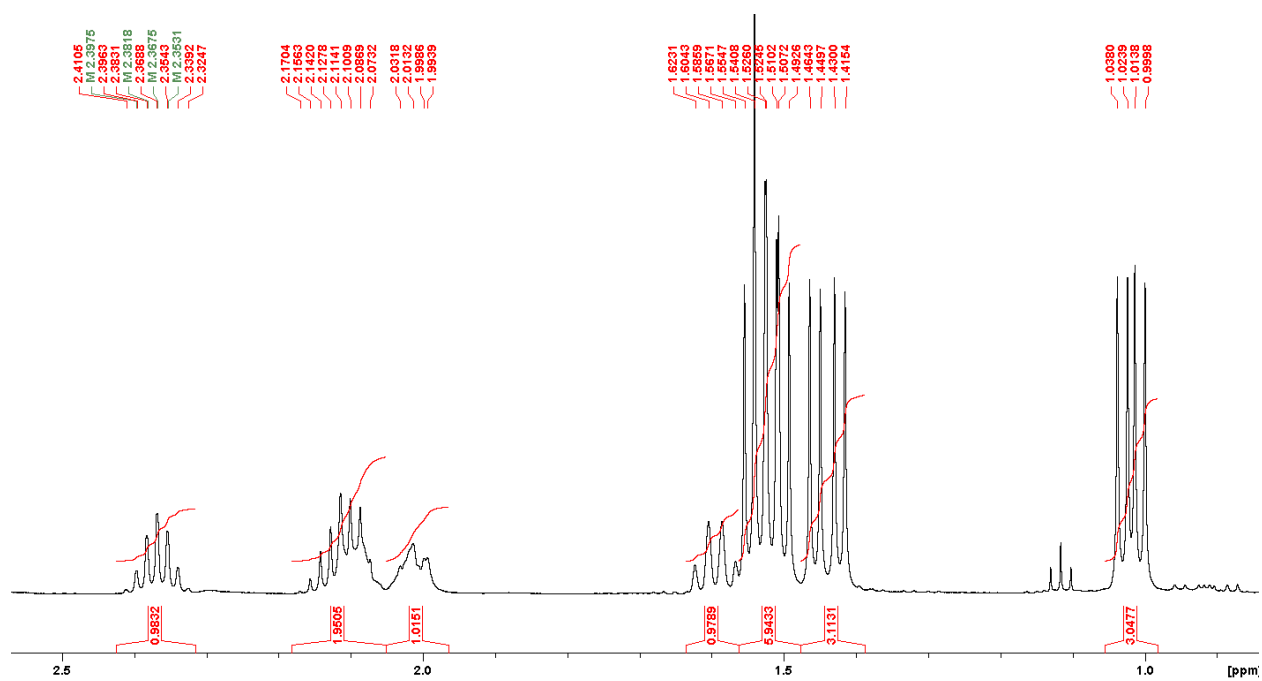
Figure S5.44: The expanded aliphatic region (I) of the ^{1}H NMR spectrum of **4** in C_6D_6.
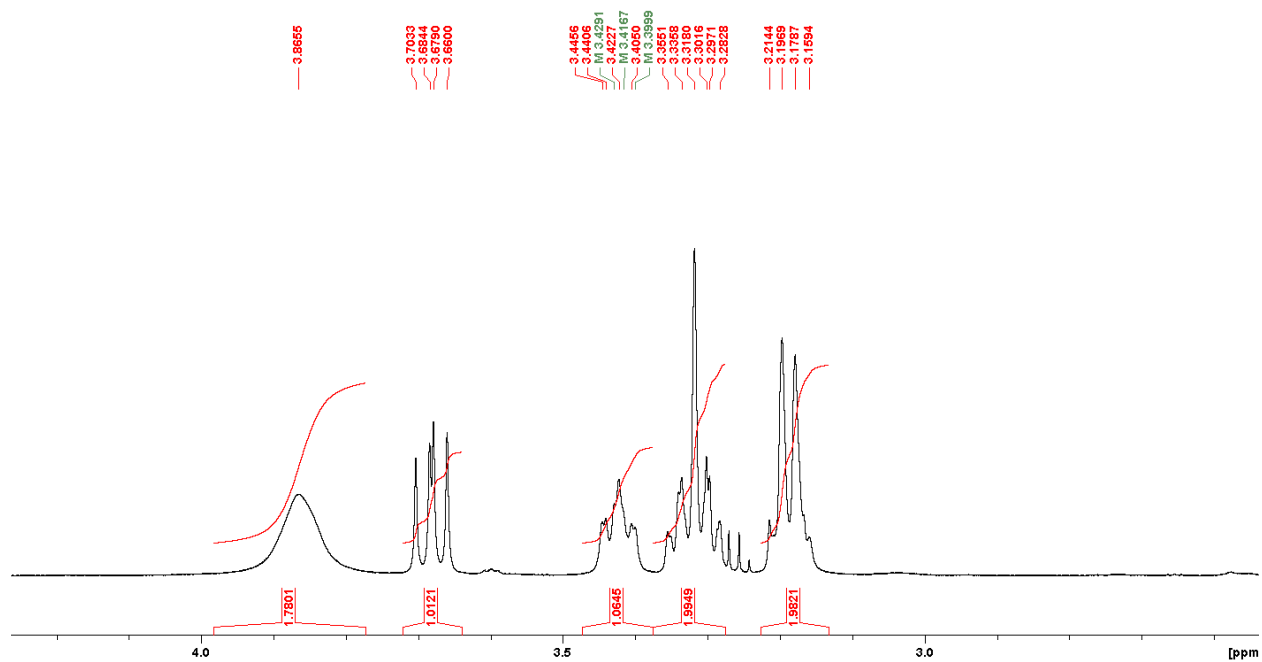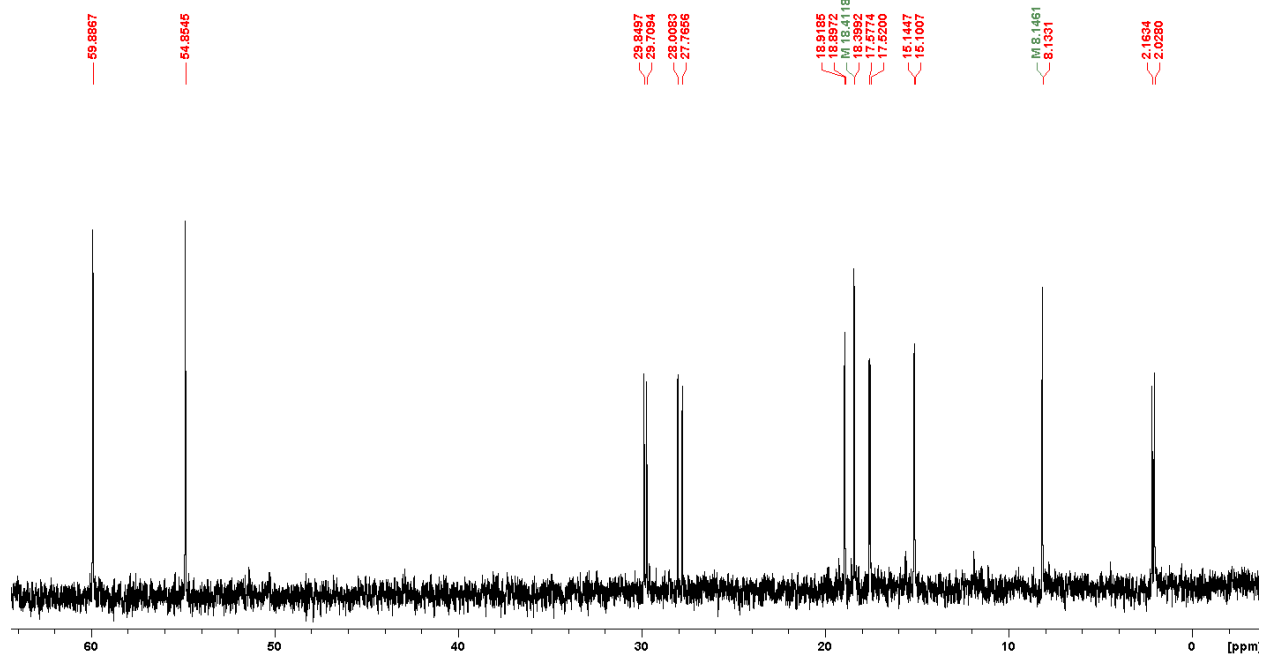
Figure S5.45: The expanded aliphatic region (II) of the ^{1}H NMR spectrum of **4** in C_6D_6.
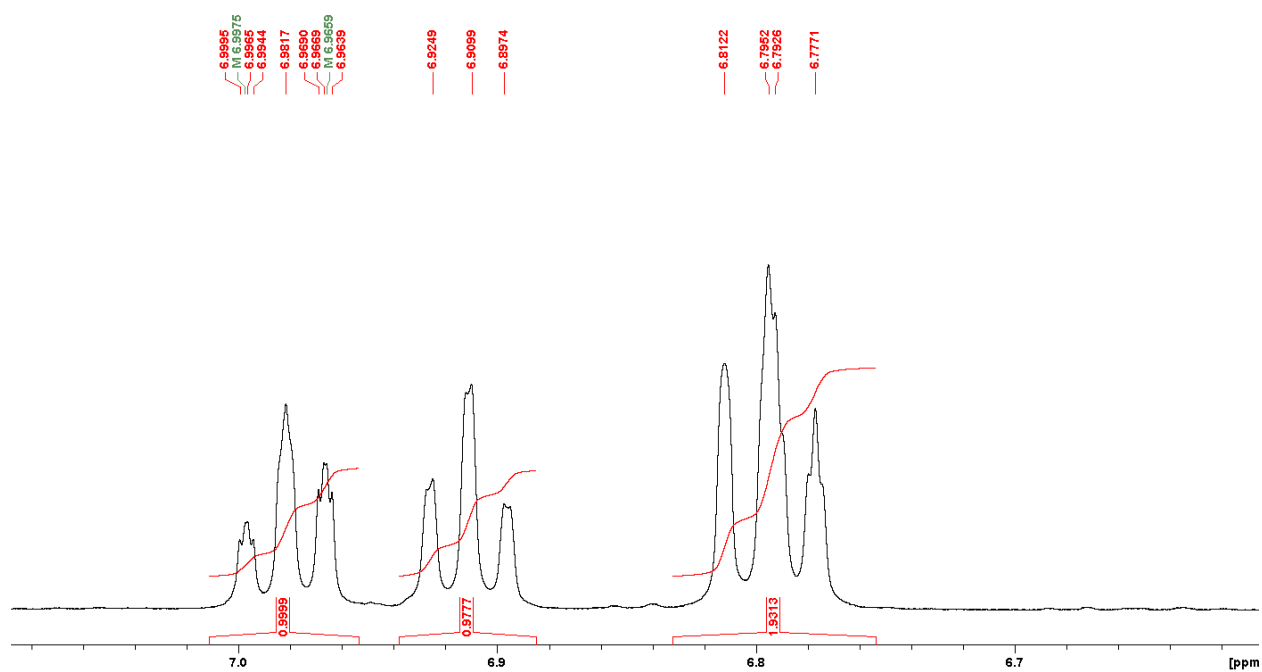
Figure S5.46: The expanded aromatic region of the ^{1}H NMR spectrum of **4** in C_6D_6.

Figure S5.47: The expanded aliphatic region (I) of the ^{1}H{^{31}P} NMR spectrum of **4** in C$_6$D$_6$.
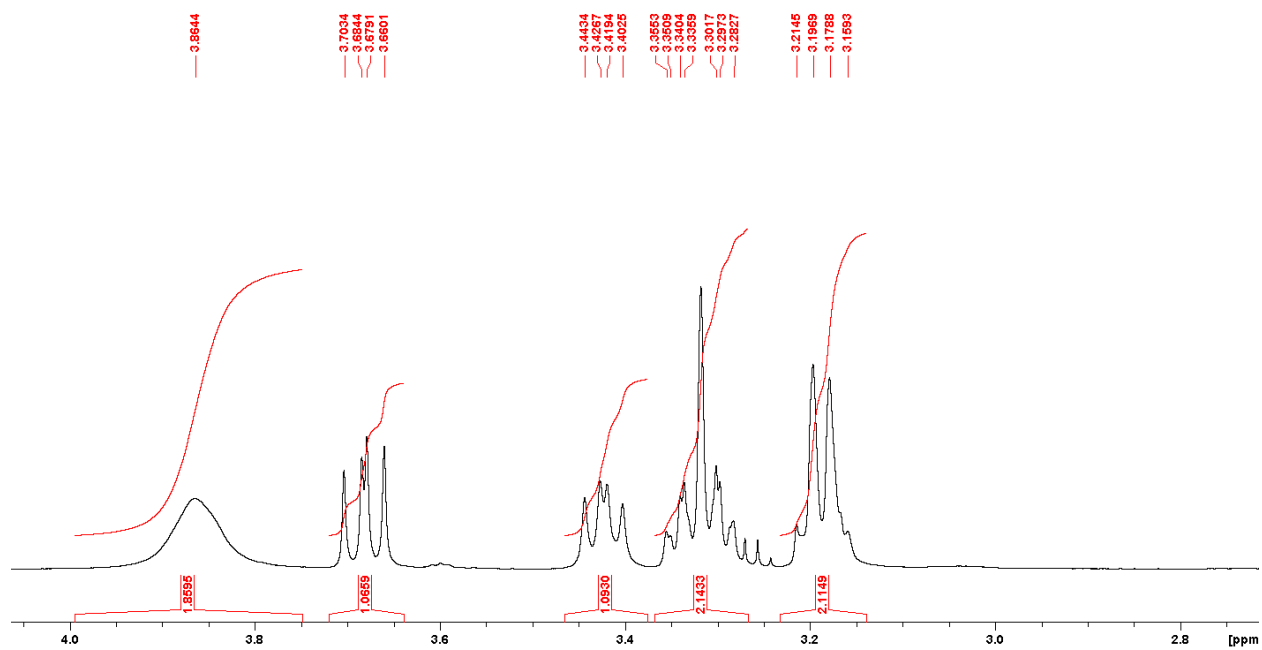
Figure S5.48: The expanded aliphatic region (II) of the ^{1}H{^{31}P} NMR spectrum of **4** in C$_6$D$_6$.

Figure S5.49: Full ^{13}C NMR spectrum of **4** in C_6D_6.

Figure S5.50: The expanded aliphatic region of the ^{13}C NMR spectrum of **4** in C_6D_6.
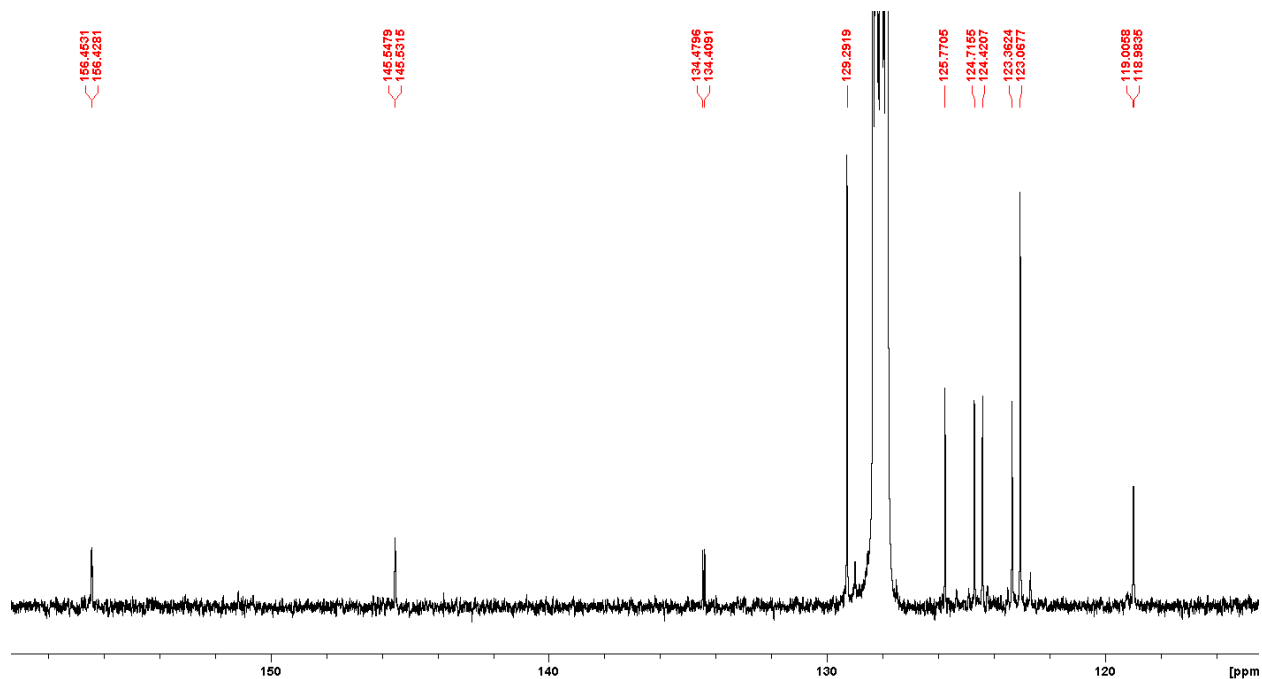
Figure S5.51: The expanded aromatic region of the ^{13}C NMR spectrum of **4** in C_6D_6.
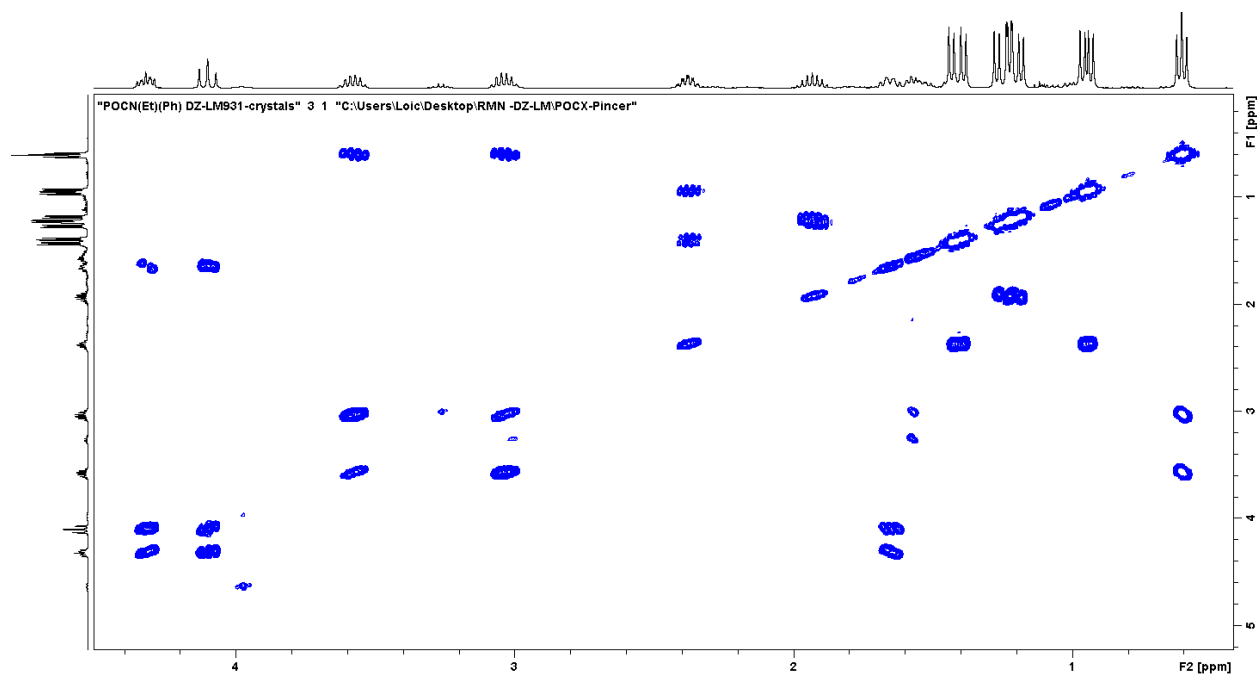

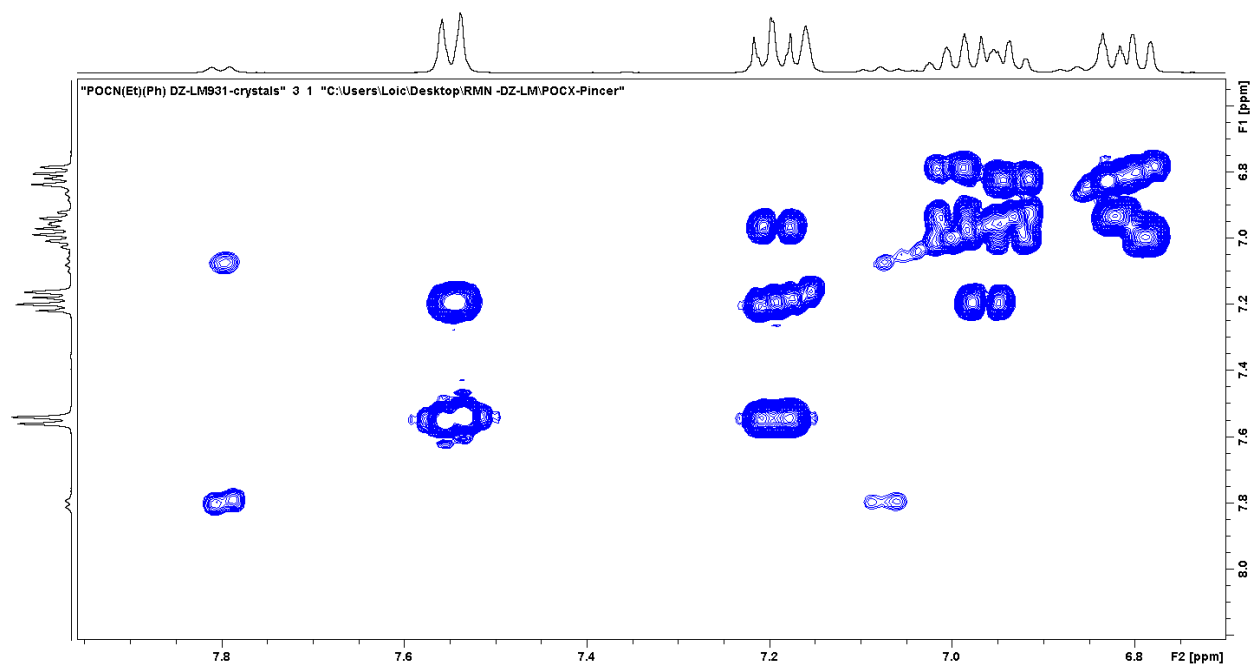Figure S5.52: The expanded aliphatic region of the COSY NMR spectrum of **4** in C_6D_6.

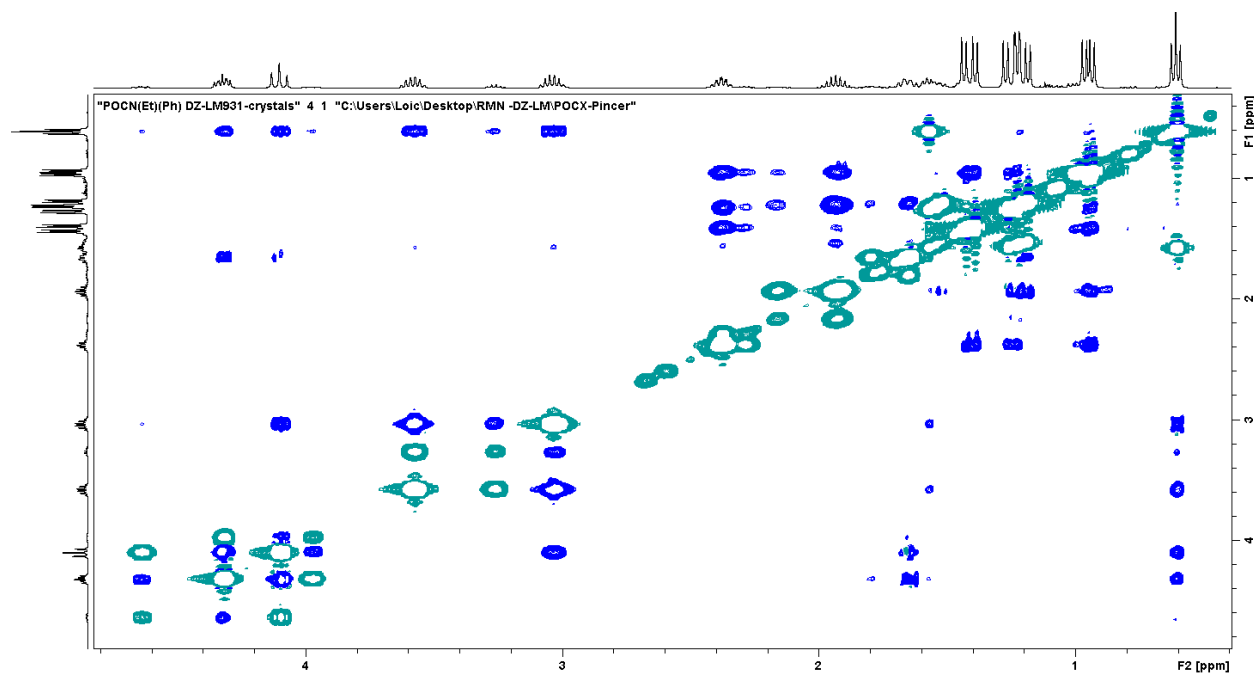Figure S5.53: The expanded aromatic region of the COSY NMR spectrum of **4** in C$_6$D$_6$.

Figure S5.54: Partial NOESY NMR spectrum of **4** in C$_6$D$_6$ showing the aliphatic/aliphatic interactions.
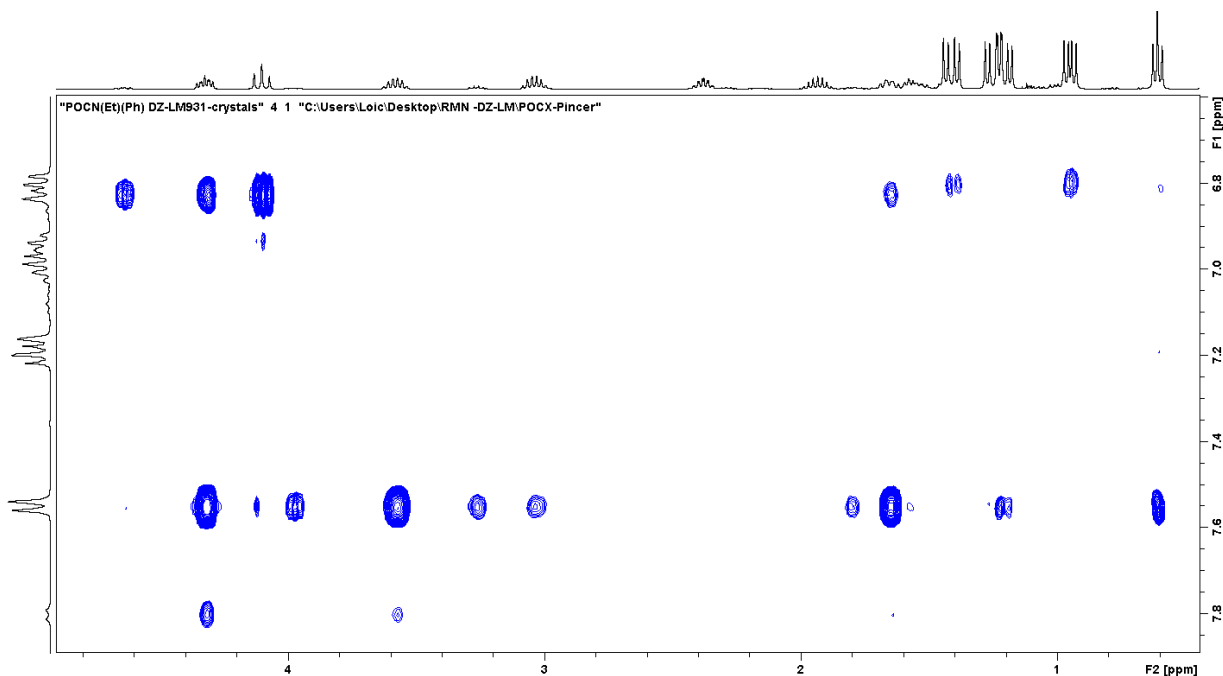
Figure S5.55: Partial NOESY NMR spectrum of **4** in C_6D_6 showing the aliphatic/aliphatic interactions.
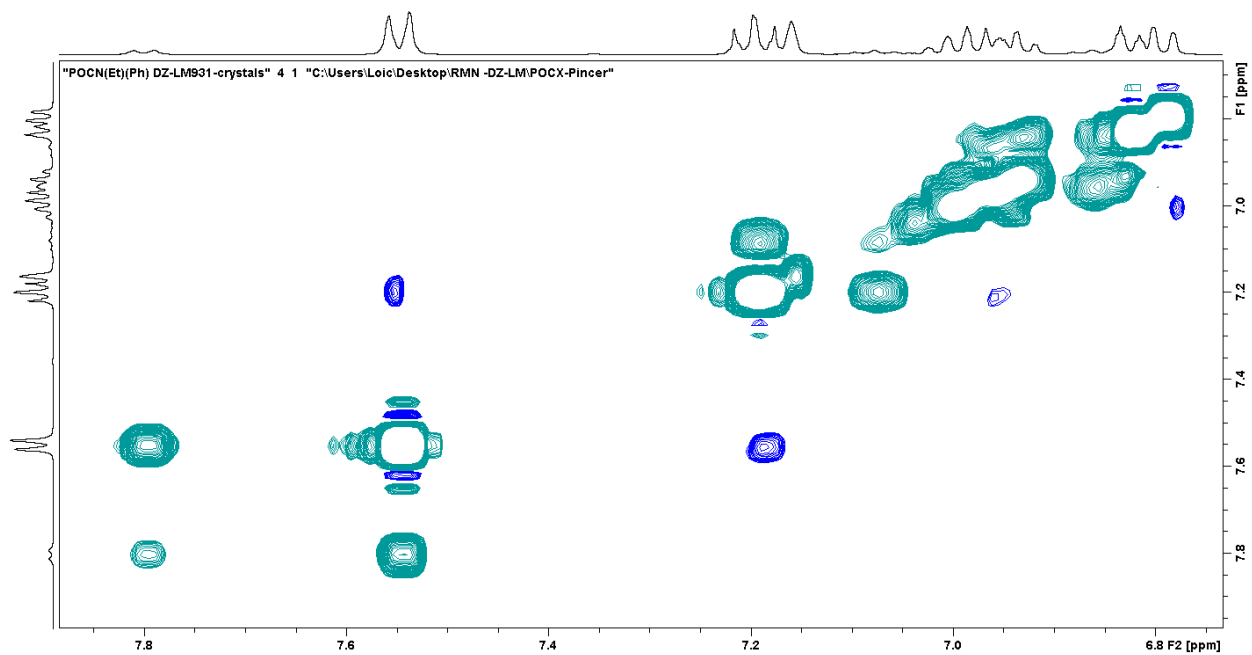

Figure S5.56: The expanded aliphatic region of the HSQC NMR spectrum of **4** in C_6D_6.

Figure S5.57: The expanded aromatic region of the HSQC NMR spectrum of **4** in C$_6$D$_6$.

Figure S5.58: ^{31}P{^{1}H} NMR spectrum of **4** in C$_6$D$_6$.

e. Complex **5**

Figure S5.59: Full ^{1}H NMR spectrum of **5** in C$_6$D$_6$.

Figure S5.60: The expanded aliphatic region (I) of the ^{1}H NMR spectrum of **5** in C$_6$D$_6$.
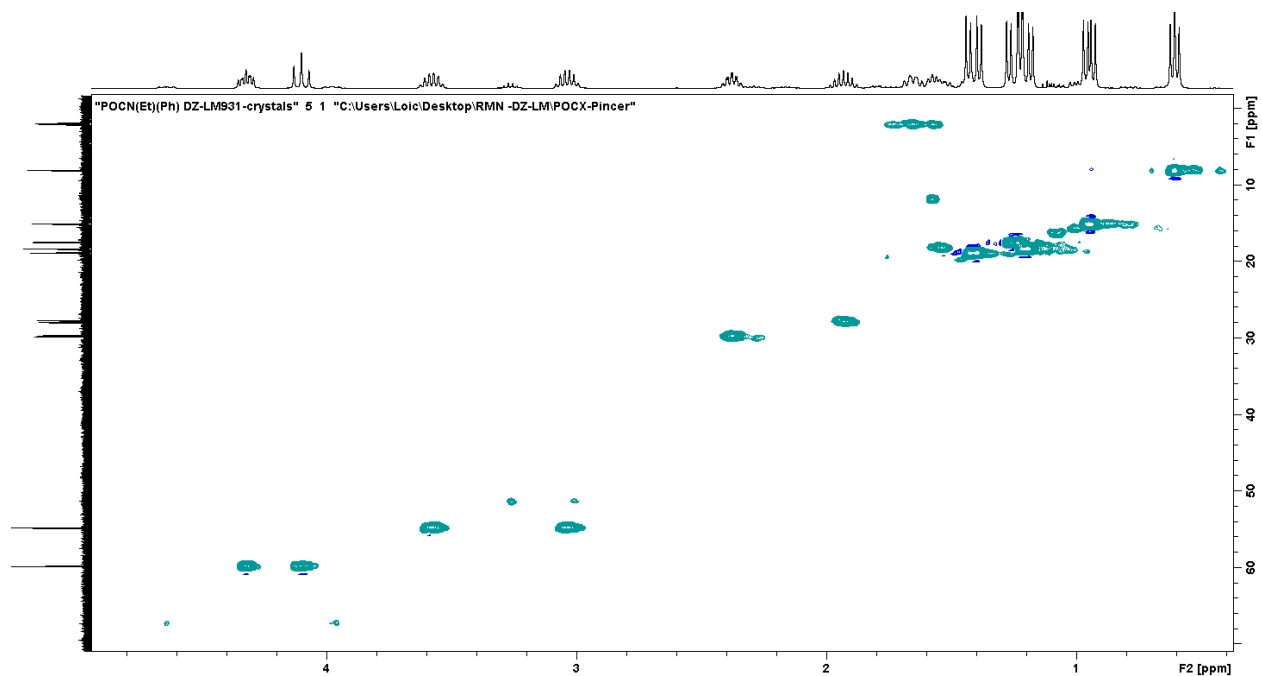
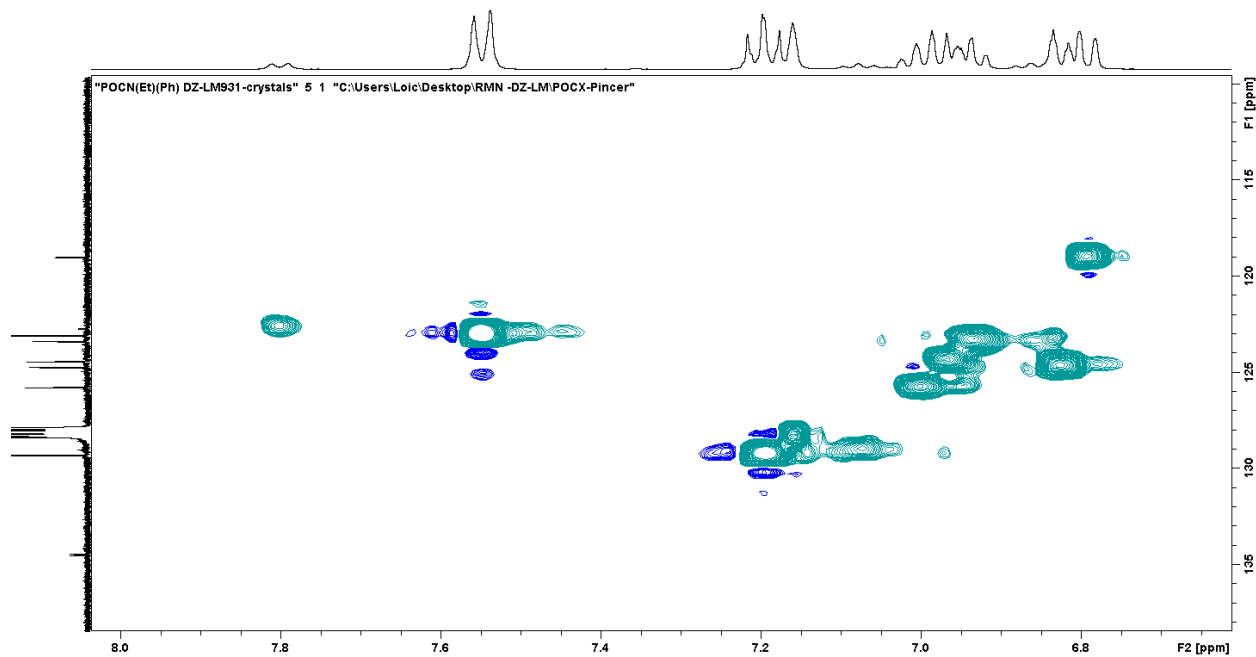Figure S5.61: The expanded aliphatic region (II) of the ^{1}H NMR spectrum of **5** in C$_6$D$_6$.

Figure S5.62: The expanded aromtaic region of the ^{1}H NMR spectrum of **5** in C$_6$D$_6$.

Figure S5.63: The expanded aliphatic region of the ^{1}H{^{31}P} NMR spectrum of **5** in C$_6$D$_6$.
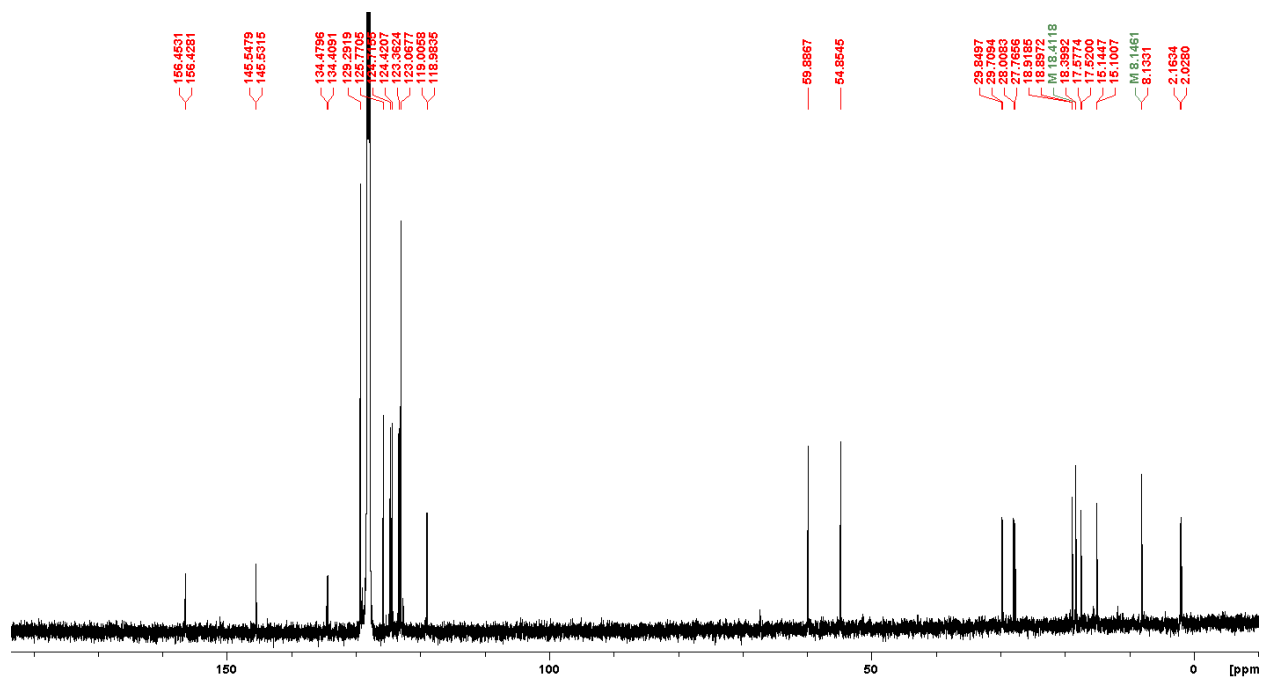
Figure S5.64: Full ^{13}C NMR spectrum of **5** in C$_6$D$_6$.

Figure S5.65: The expanded aliphatic region of the ^{13}C NMR spectrum of **5** in C_6D_6.

Figure S5.66: The expanded aromatic region of the ^{13}C NMR spectrum of **5** in C_6D_6.

Figure S5.67: The expanded aliphatic region of the COSY NMR spectrum of **5** in C$_6$D$_6$.

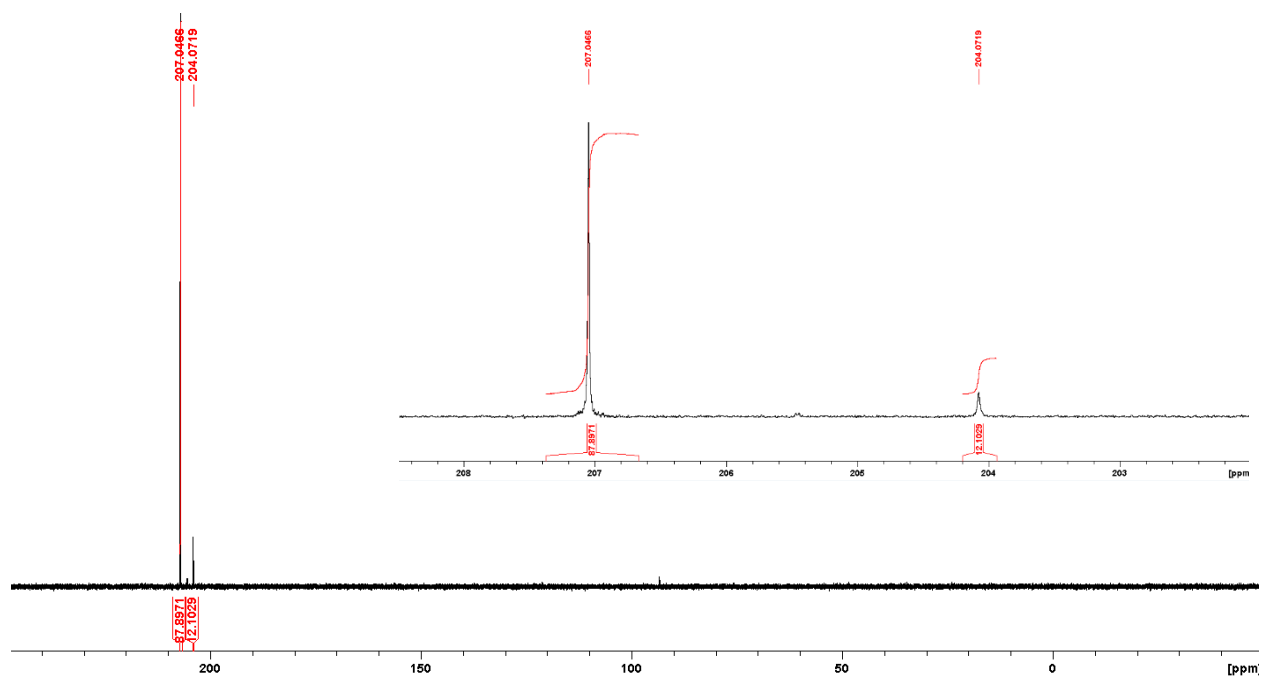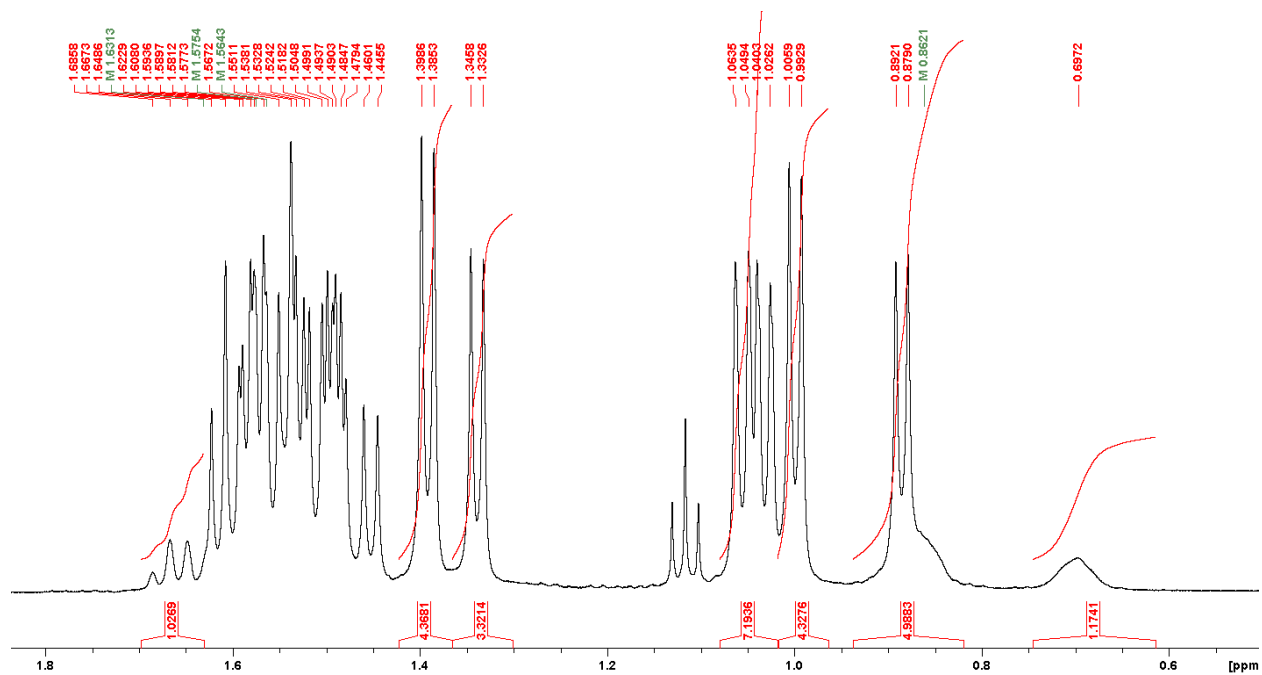Figure S5.68: The expanded aromatic region of the COSY NMR spectrum of **5** in C$_6$D$_6$.

459

Figure S5.69: Partial NOESY NMR spectrum of **5** in C_6D_6 showing the aliphatic/aliphatic interactions.

Figure S5.70: Partial NOESY NMR spectrum of **5** in C_6D_6 showing the aliphatic/aromatic interactions.

Figure S5.71: Partial NOESY NMR spectrum of **5** in C_6D_6 showing the aromatic/aromatic interactions.

Figure S5.72: The expanded aliphatic region of the HSQC NMR spectrum of **5** in C_6D_6.

Figure S5.73: The expanded aromatic region of the HSQC NMR spectrum of **5** in C_6D_6.

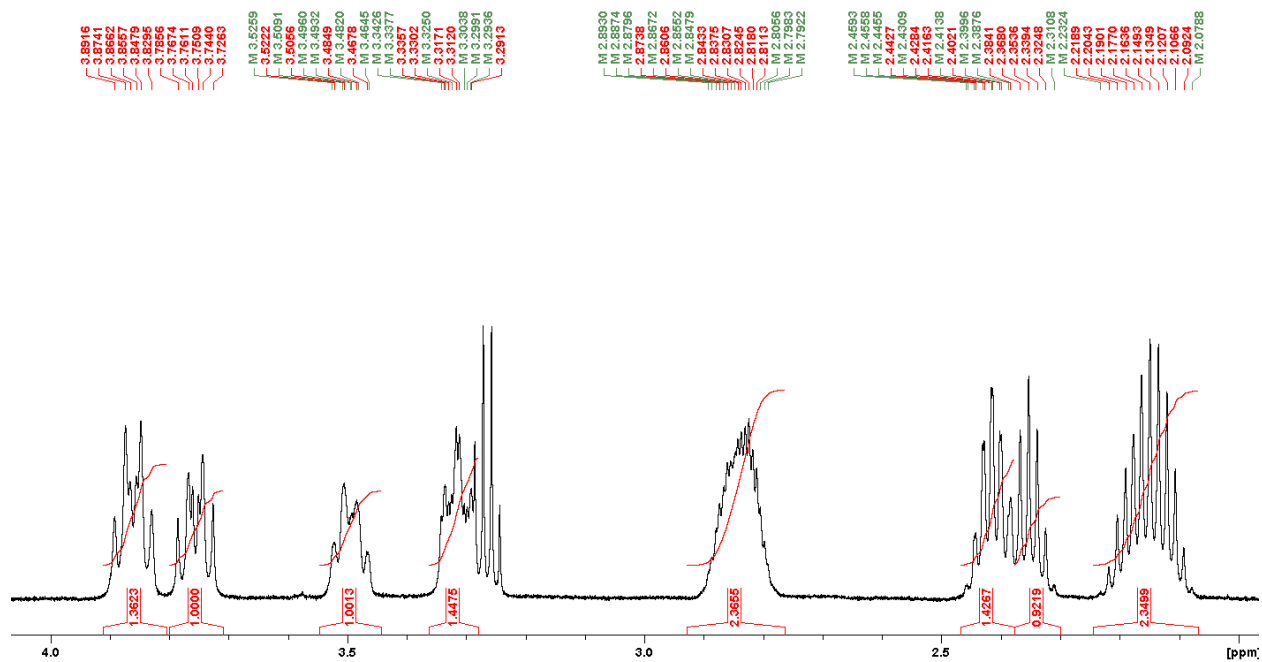Figure S5.74: $^{31}P\{^1H\}$ NMR spectrum of **5** in $CDCl_3$.

f. Complex **6**

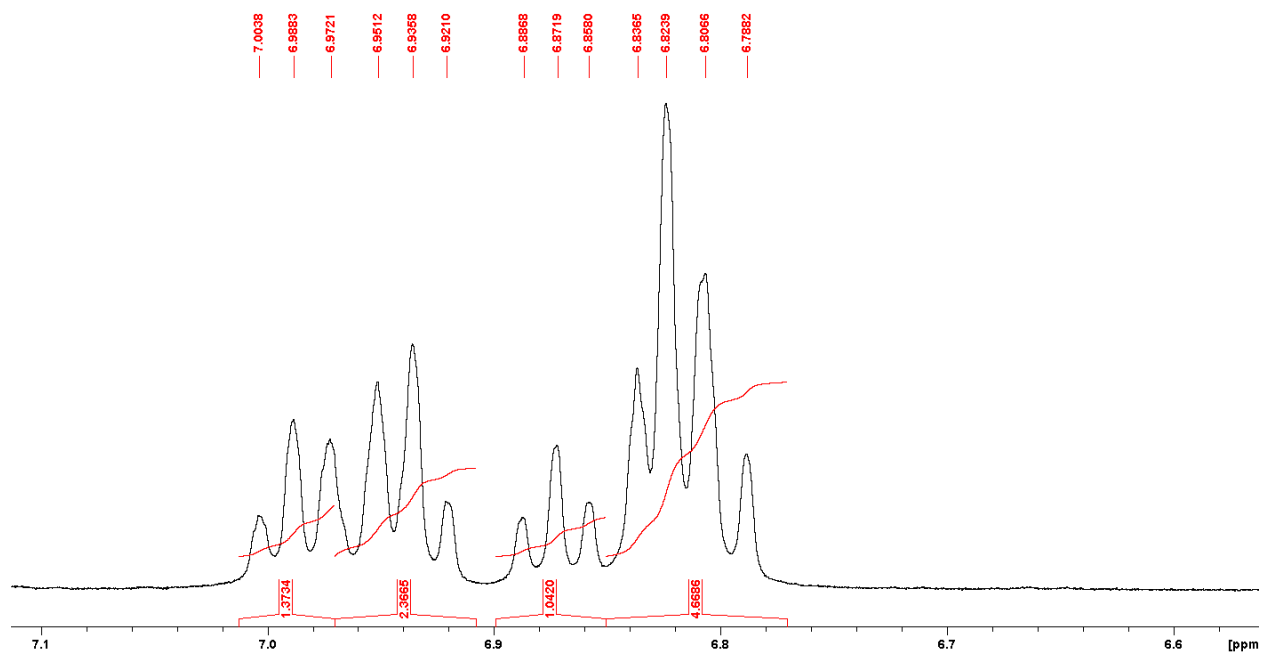Figure S5.75: Full ^{1}H NMR spectrum of **6** in C_6D_6.

Figure S5.76: The expanded aliphatic region of the ^{1}H NMR spectrum of **6** in C_6D_6.
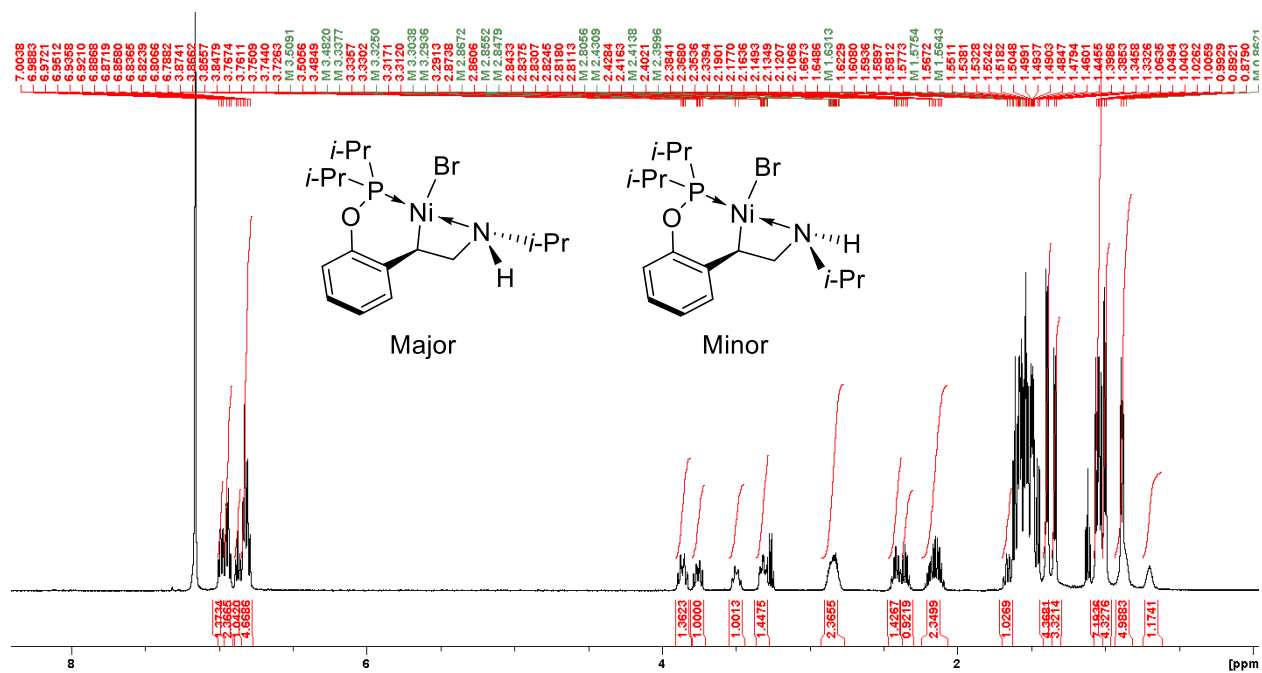
Figure S5.77: The expanded aliphatic region of the ^{1}H NMR spectrum of **6** in C$_6$D$_6$.

Figure S5.78: The expanded aromatic region of the ^{1}H NMR spectrum of **6** in C$_6$D$_6$.
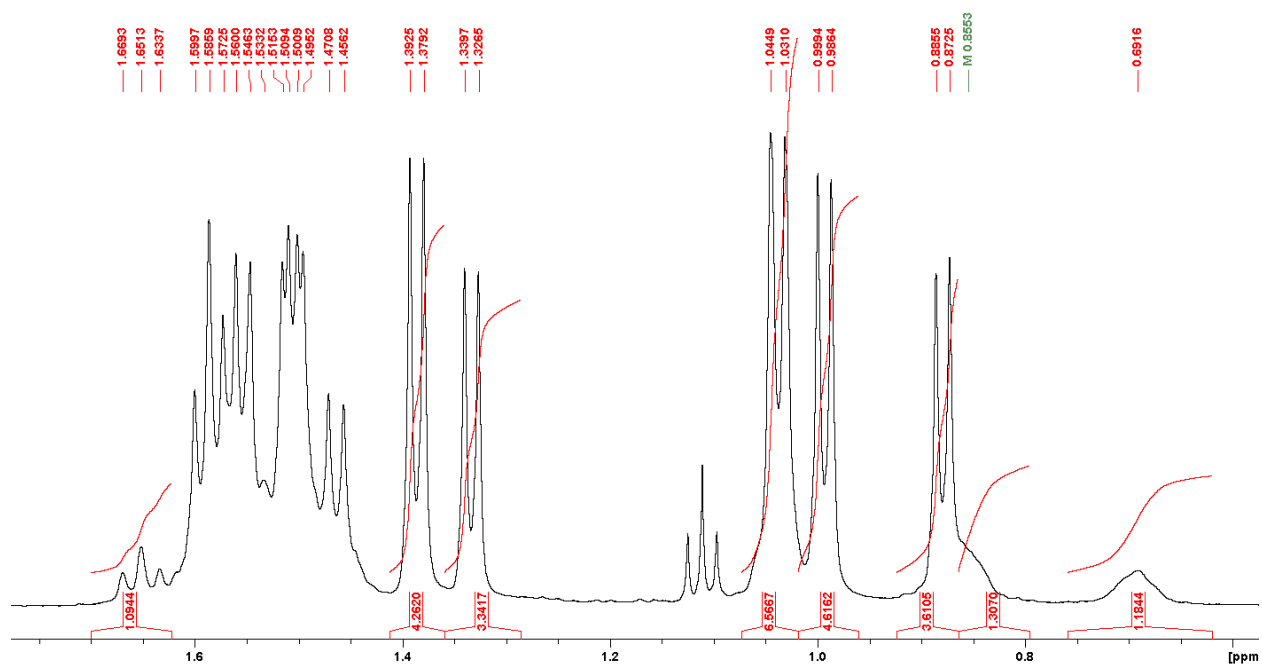

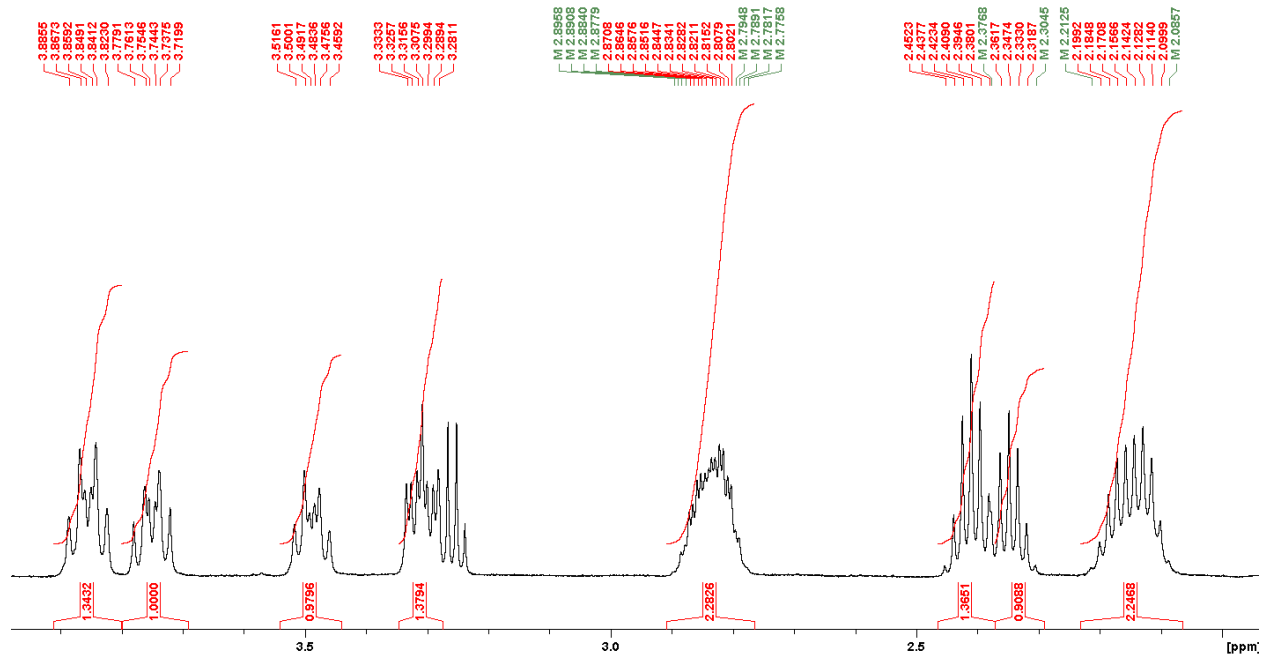Figure S5.79: The expanded aliphatic region (I) of the ^{1}H{^{31}P} NMR spectrum of **6** in C$_6$D$_6$.

Figure S5.80: The expanded aliphatic region (II) of the ^{1}H{^{31}P} NMR spectrum of **6** in C$_6$D$_6$.
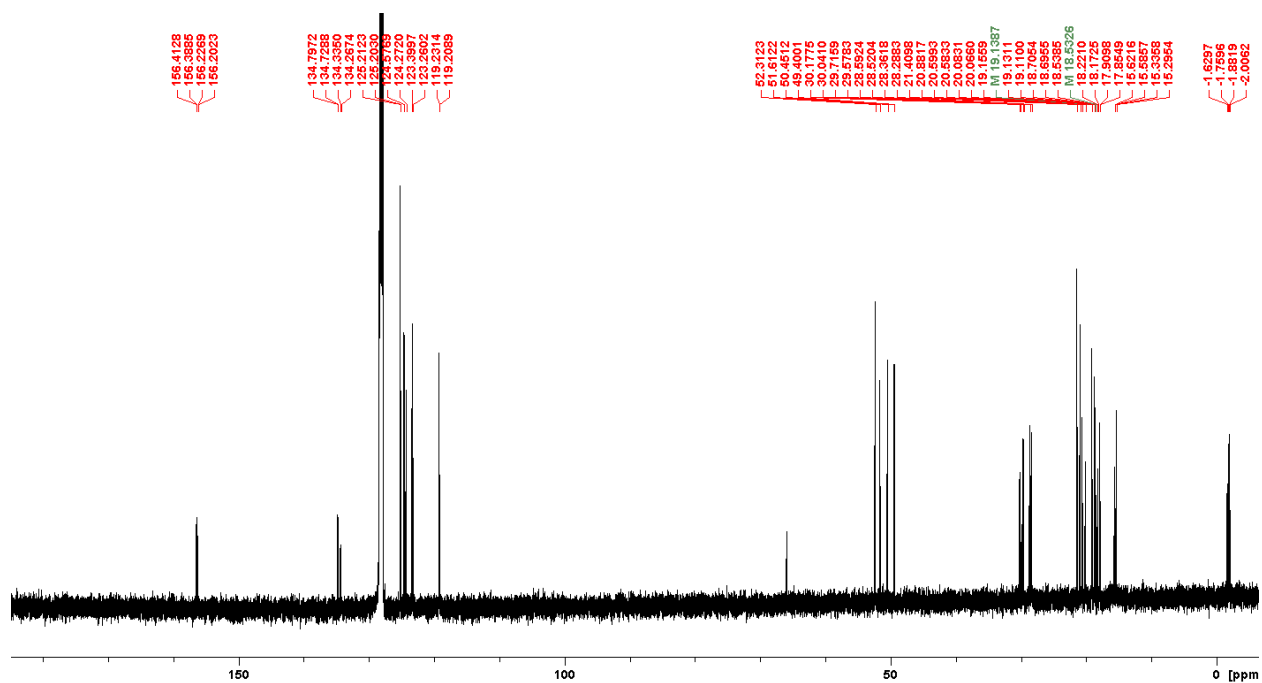

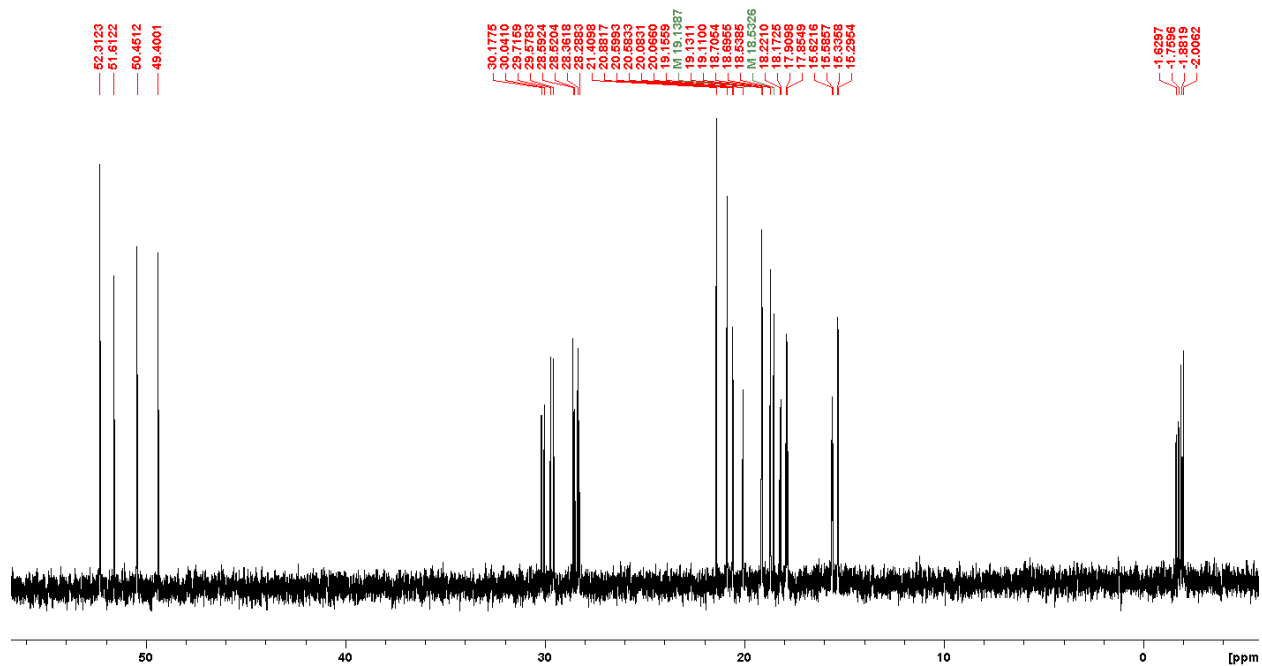Figure S5.81: Full ^{13}C NMR spectrum of **6** in C$_6$D$_6$.

Figure S5.82: The expanded aliphatic region of the ^{13}C NMR spectrum of **6** in C_6D_6.
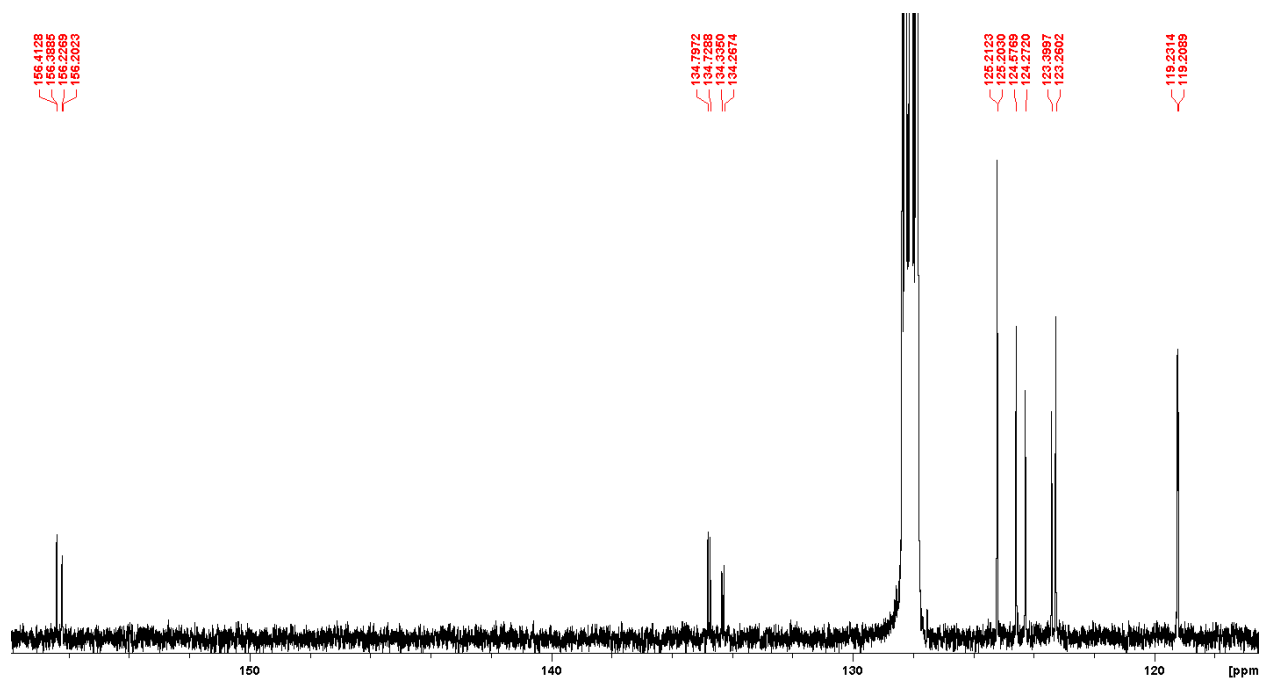

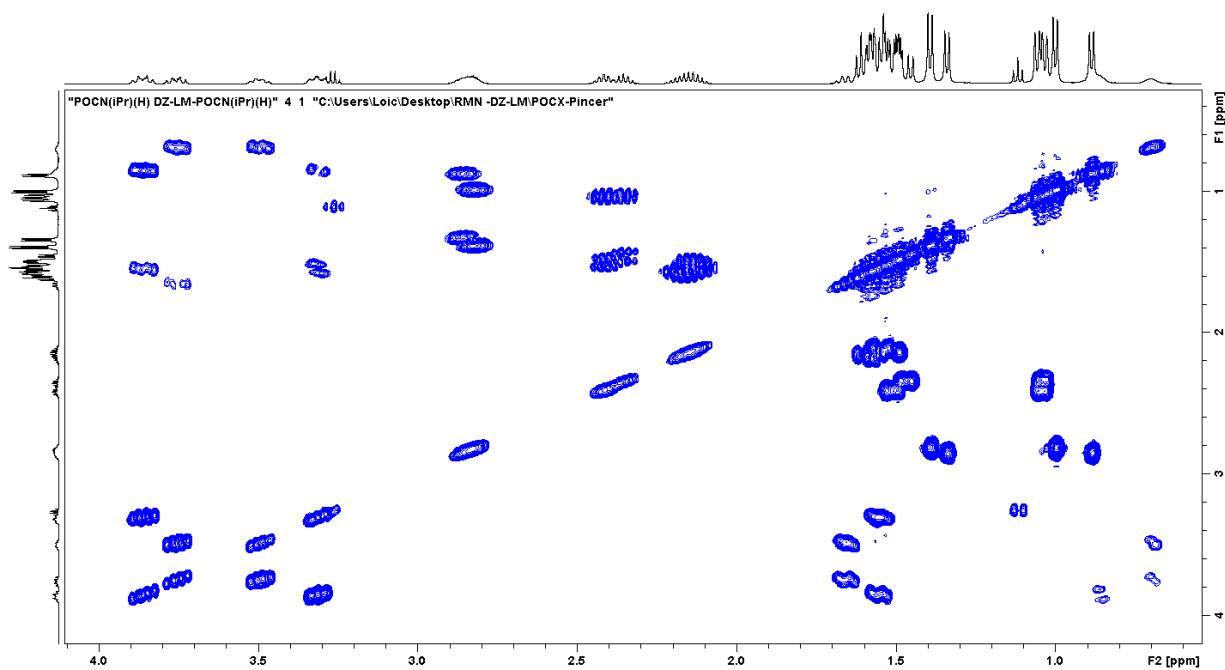Figure S5.83: The expanded aromatic region of the ^{13}C NMR spectrum of **6** in C_6D_6.

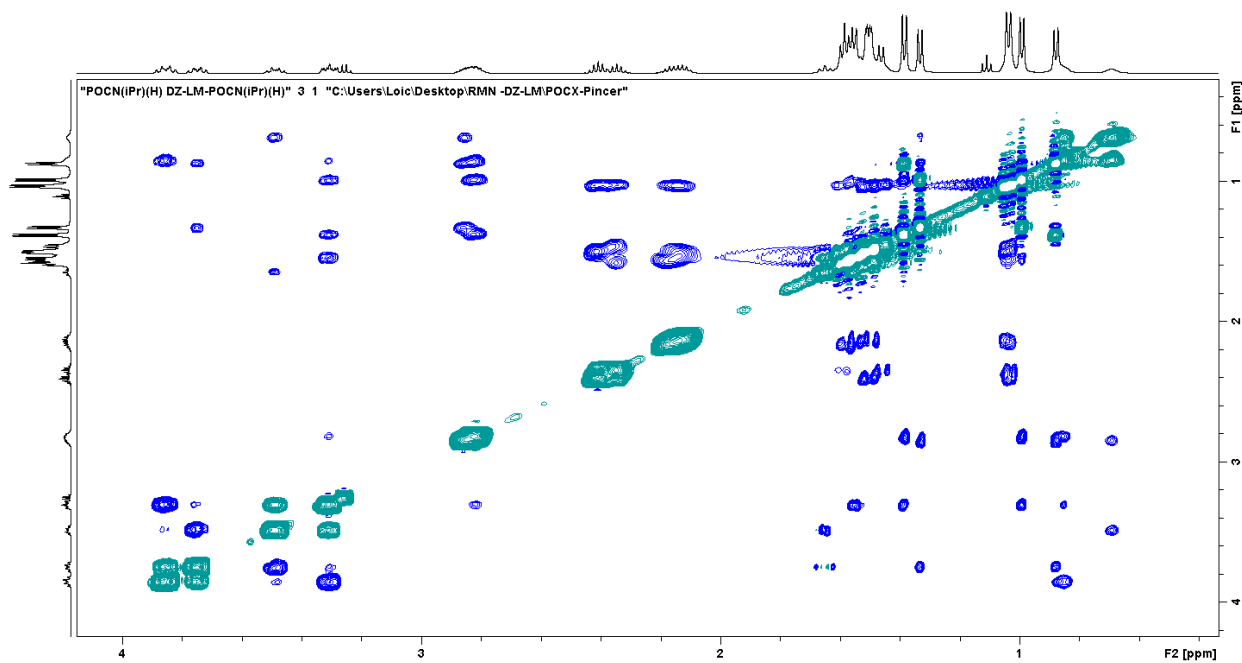Figure S5.84: The expanded aliphatic region of the COSY NMR spectrum of **6** in C₆D₆.

Figure S5.85: Partial NOESY NMR spectrum of **6** in C₆D₆ showing the aliphatic/aliphatic interactions.
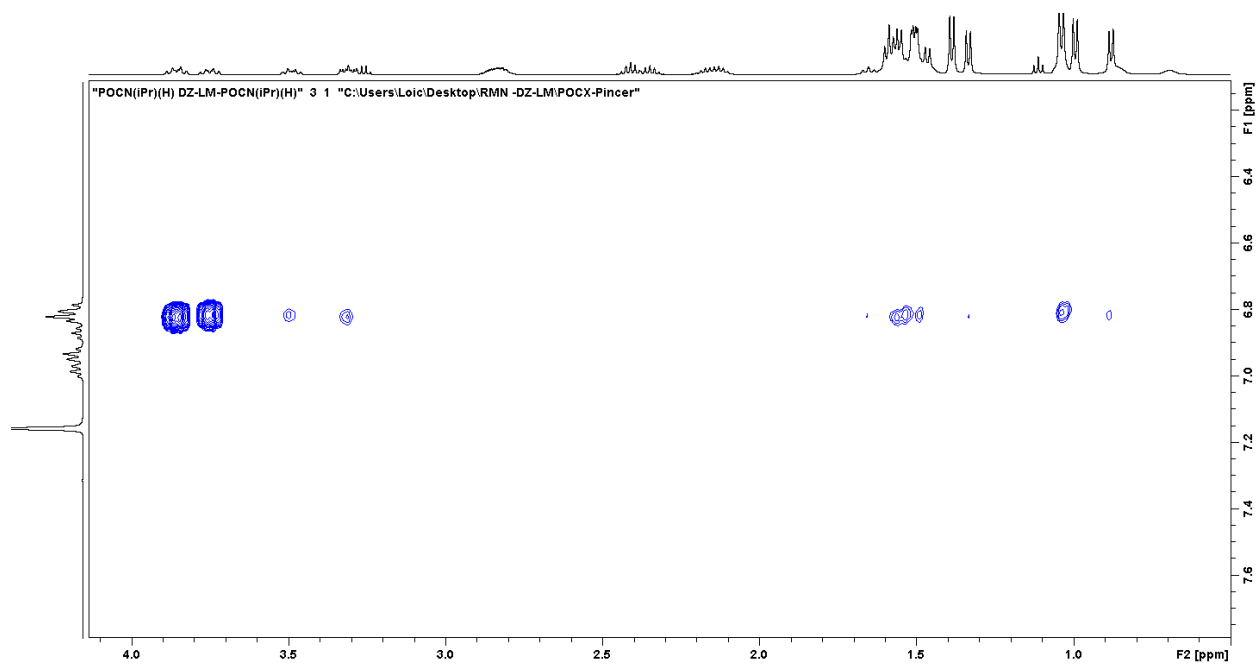
Figure S5.86: Partial NOESY NMR spectrum of **6** in C_6D_6 showing the aliphatic/aromatic interactions.
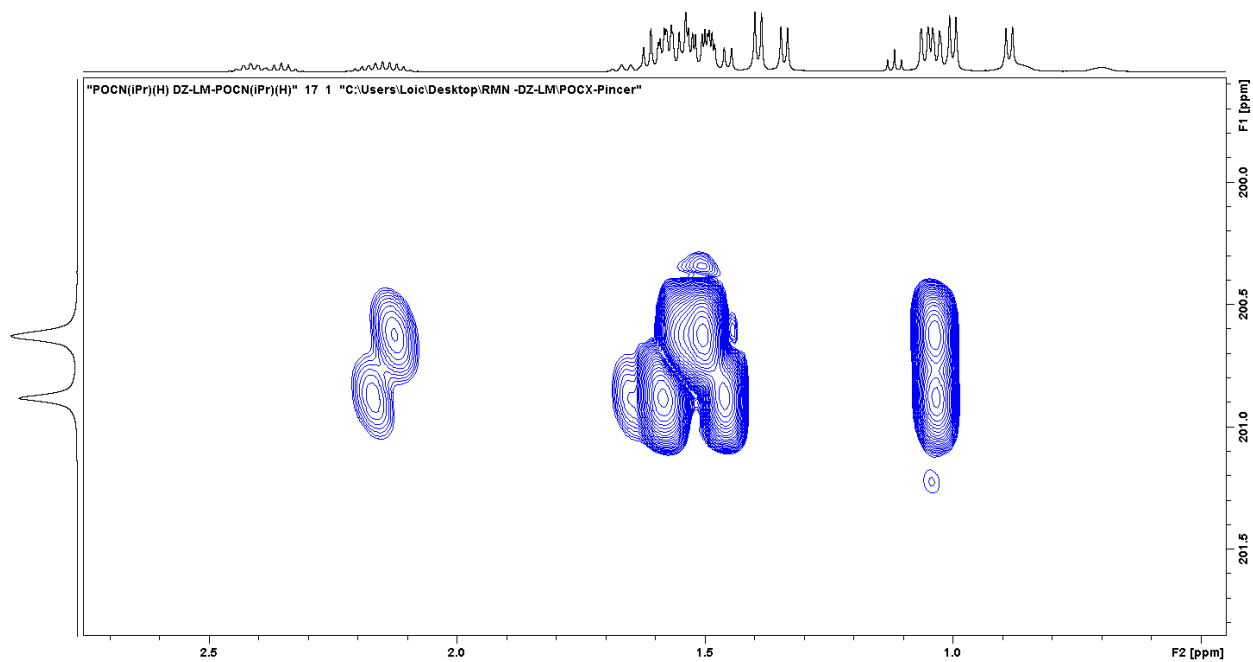
Figure S5.87: HMQC ($^{31}P/^1H$) NMR spectrum of **6** in C_6D_6 (I).
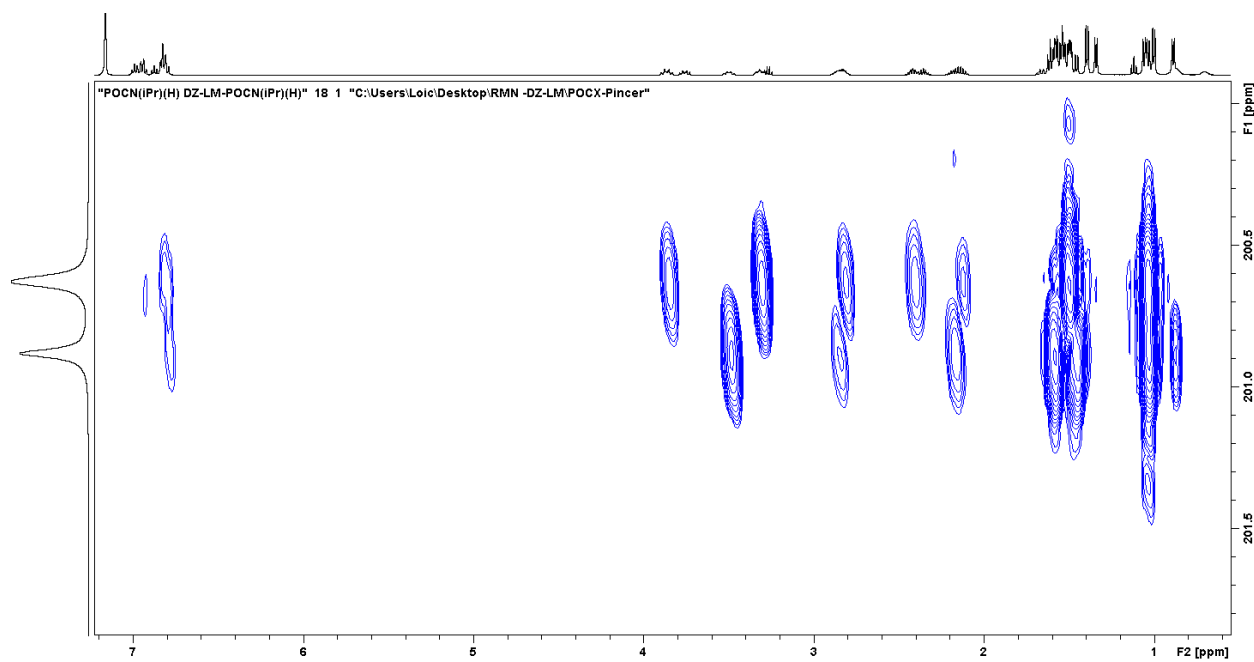
Figure S5.88: HMQC (^{31}P/^{1}H) NMR spectrum of **6** in C_6D_6 (II).

Figure S5.89: The expanded aliphatic region of the HSQC NMR spectrum of **6** in C_6D_6.
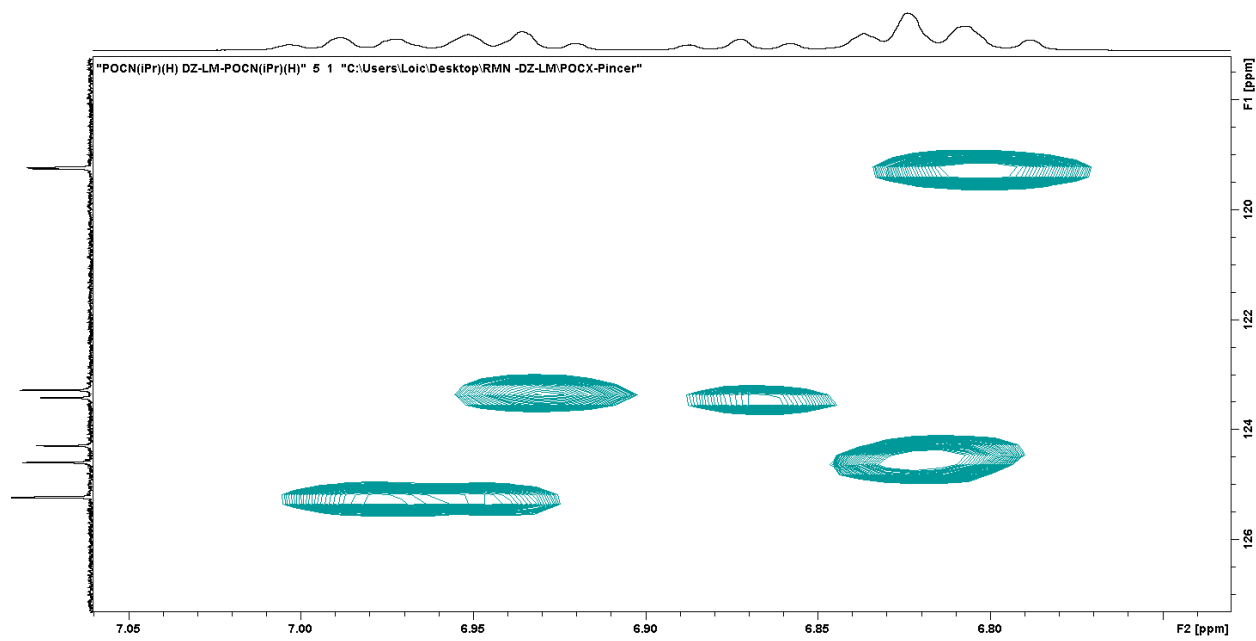
Figure S5.90: The expanded aromatic region of the HSQC NMR spectrum of **6** in C_6D_6.

Figure S5.91: Full $^{31}P\{^1H\}$ NMR spectrum of **6** in C_6D_6.

Figure S5.92: The expanded $^{31}P\{^1H\}$ NMR spectrum of **6** in C_6D_6.

g. Complex **10**

Figure S5.93: Full ^{1}H NMR spectrum of **10** in C$_6$D$_6$.

Figure S5.94: The expanded aliphatic region of the ^{1}H NMR spectrum of **10** in C$_6$D$_6$.

473
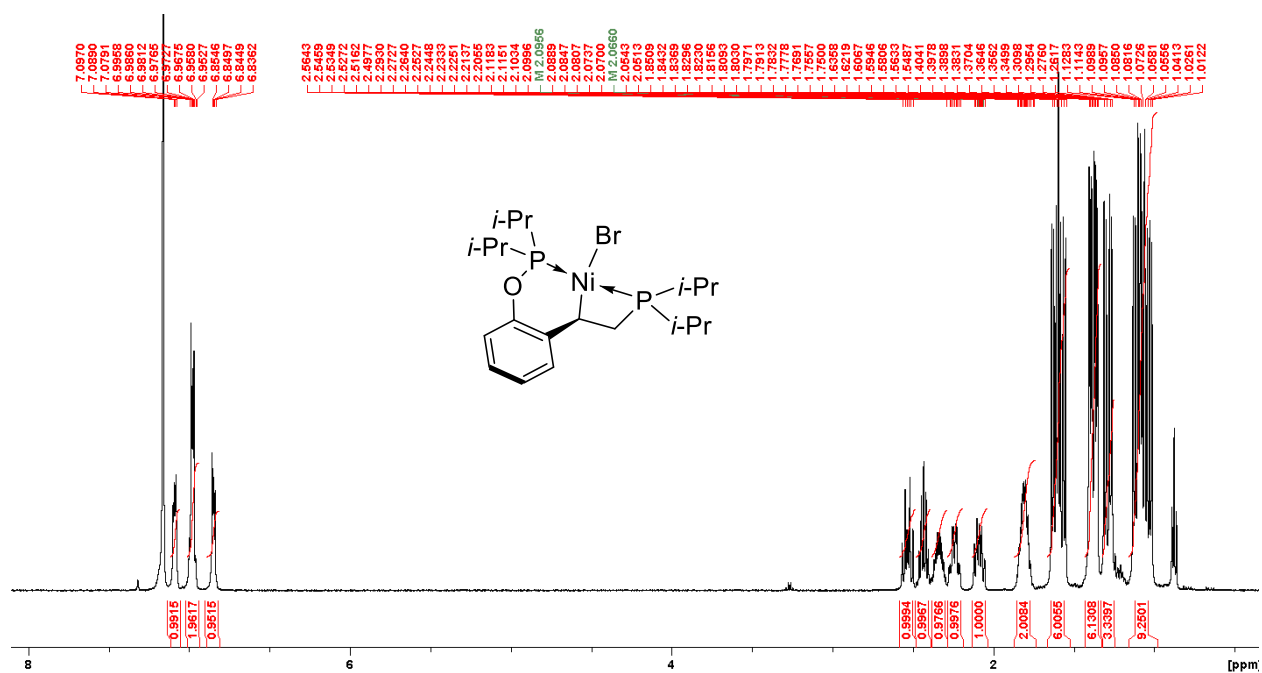
Figure S5.95: The expanded aromatic region of the ^{1}H NMR spectrum of **10** in C$_6$D$_6$.

Figure S5.96: The expanded aliphatic region of the ^{1}H{^{31}P, δ -57.1} NMR spectrum of **10** in C$_6$D$_6$.

Figure S5.97: The expanded aromatic region of the ^{1}H$\{^{31}$P, δ 192.3$\}$ NMR spectrum of **10** in C$_6$D$_6$.

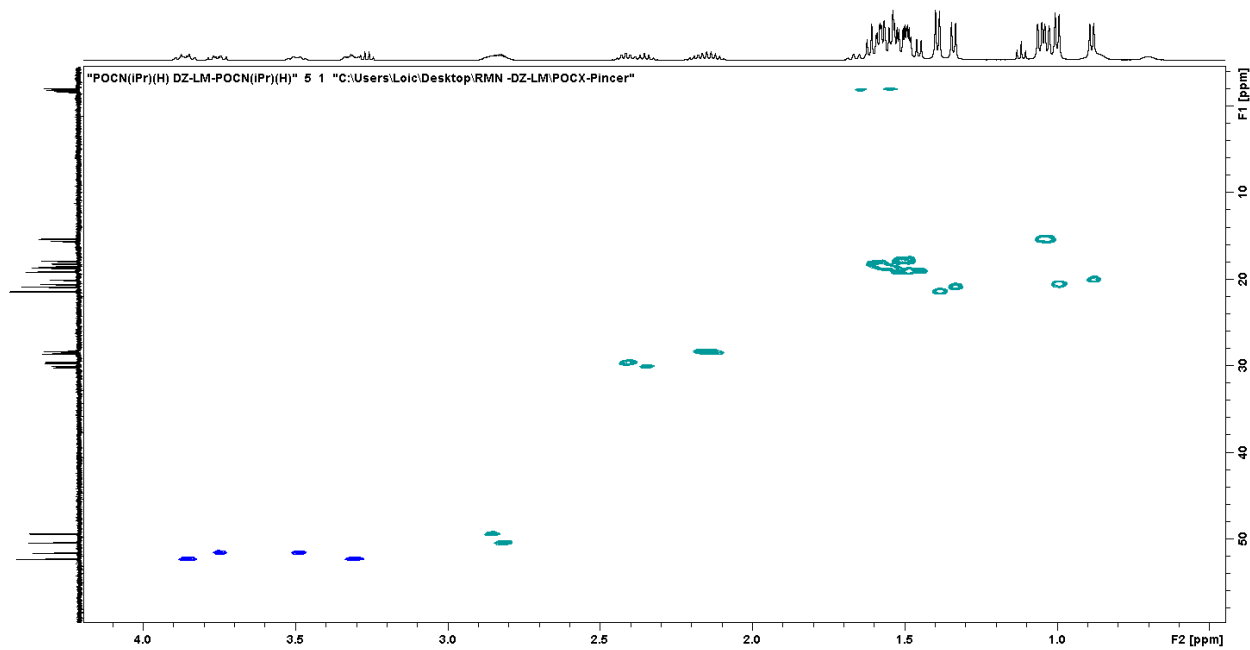Figure S5.98: Full ^{13}C NMR spectrum of **10** in C$_6$D$_6$.

Figure S5.99: The expanded aliphatic region of the ^{13}C NMR spectrum of **10** in C$_6$D$_6$.

Figure S5.100: The expanded aromatic region of the ^{13}C NMR spectrum of **10** in C$_6$D$_6$.

Figure S5.101: The expanded aliphatic region of the COSY NMR spectrum of **10** in C$_6$D$_6$.

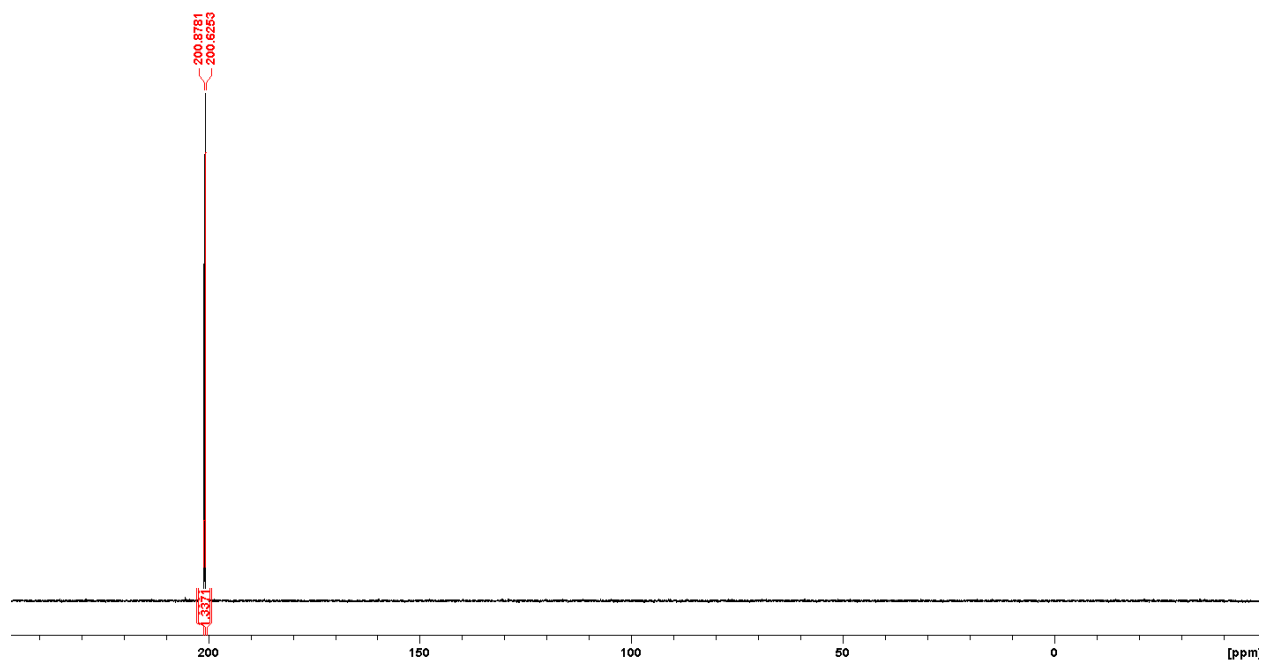Figure S5.102: The expanded aromatic region of the COSY NMR spectrum of **10** in C$_6$D$_6$.
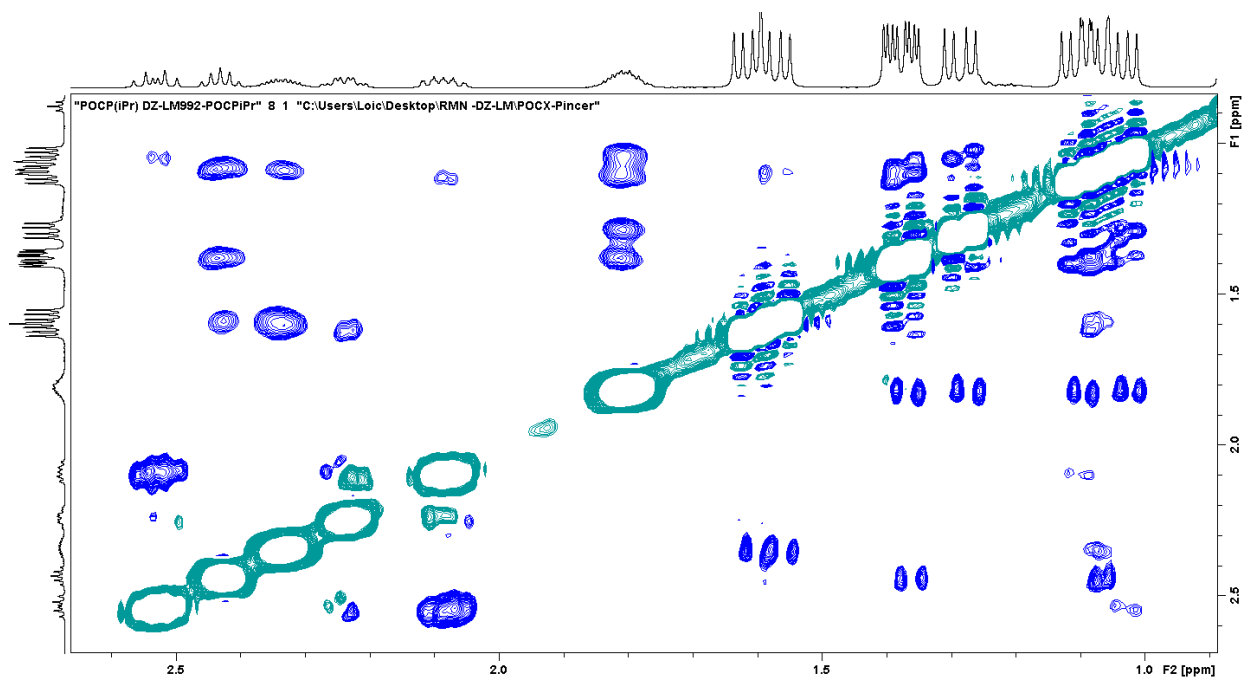
Figure S5.103: Partial NOESY NMR spectrum of **10** in C_6D_6 showing the aliphatic/aliphatic interactions.
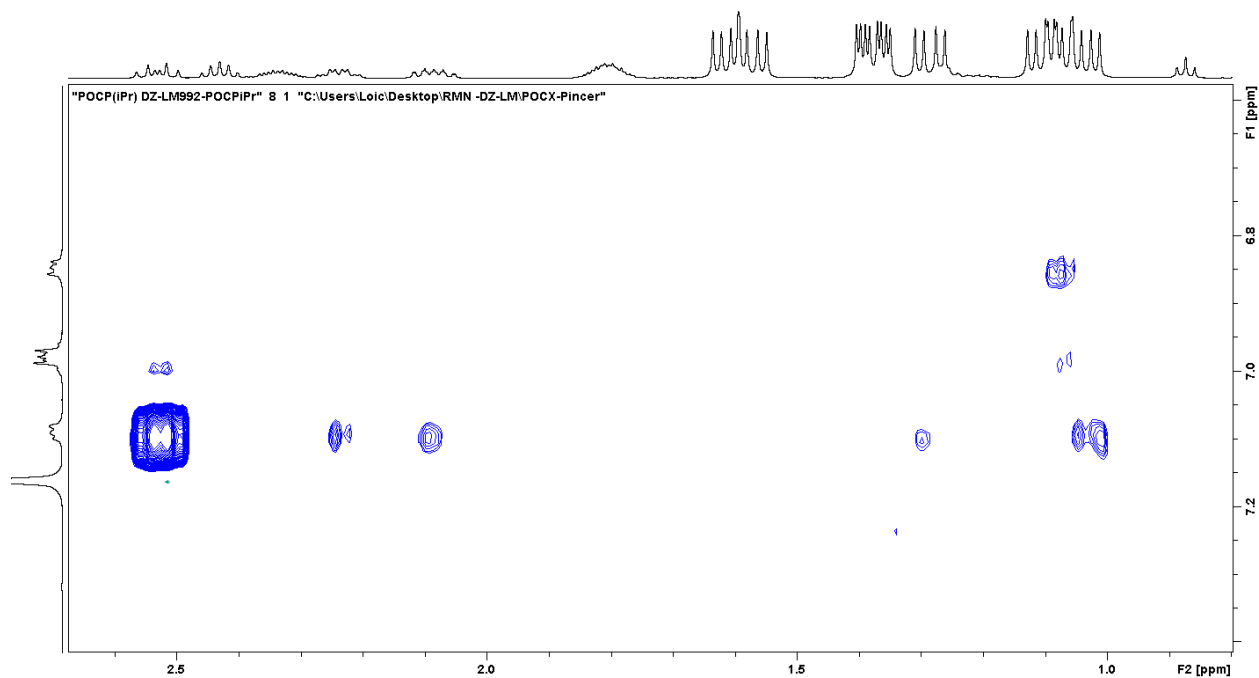
Figure S5.104: Partial NOESY NMR spectrum of **10** in C_6D_6 showing the aliphatic/aromatic interactions.
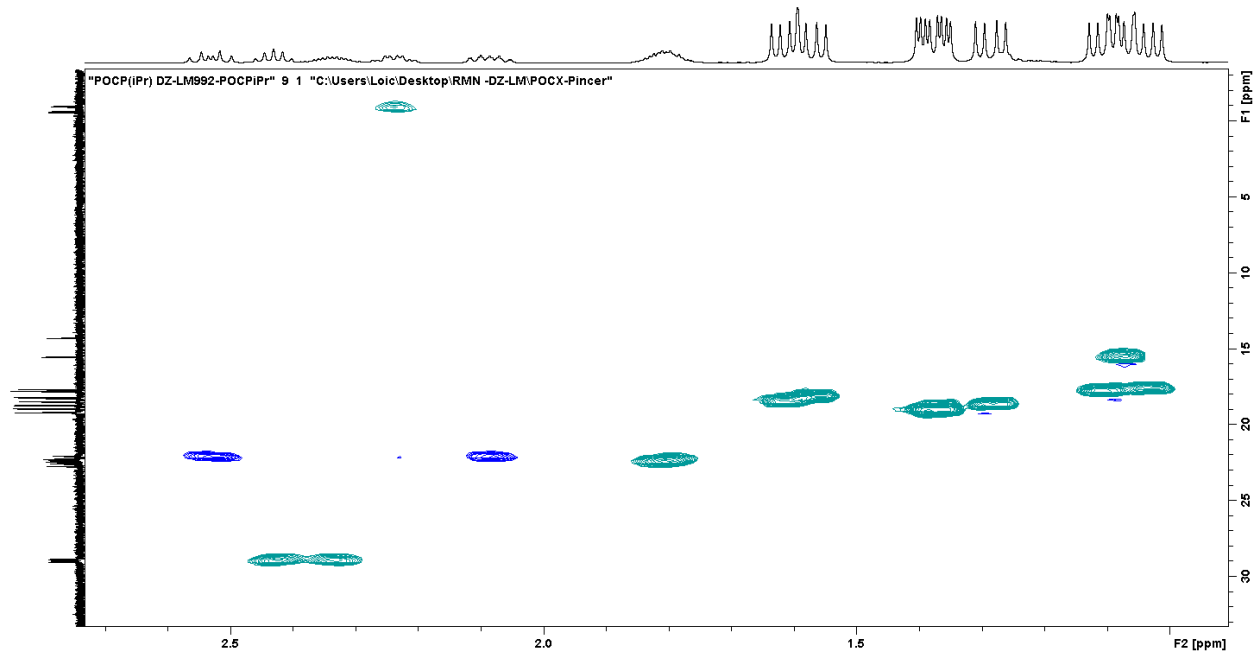
Figure S5.105: The expanded aliphatic region of the HSQC NMR spectrum of **10** in C$_6$D$_6$.
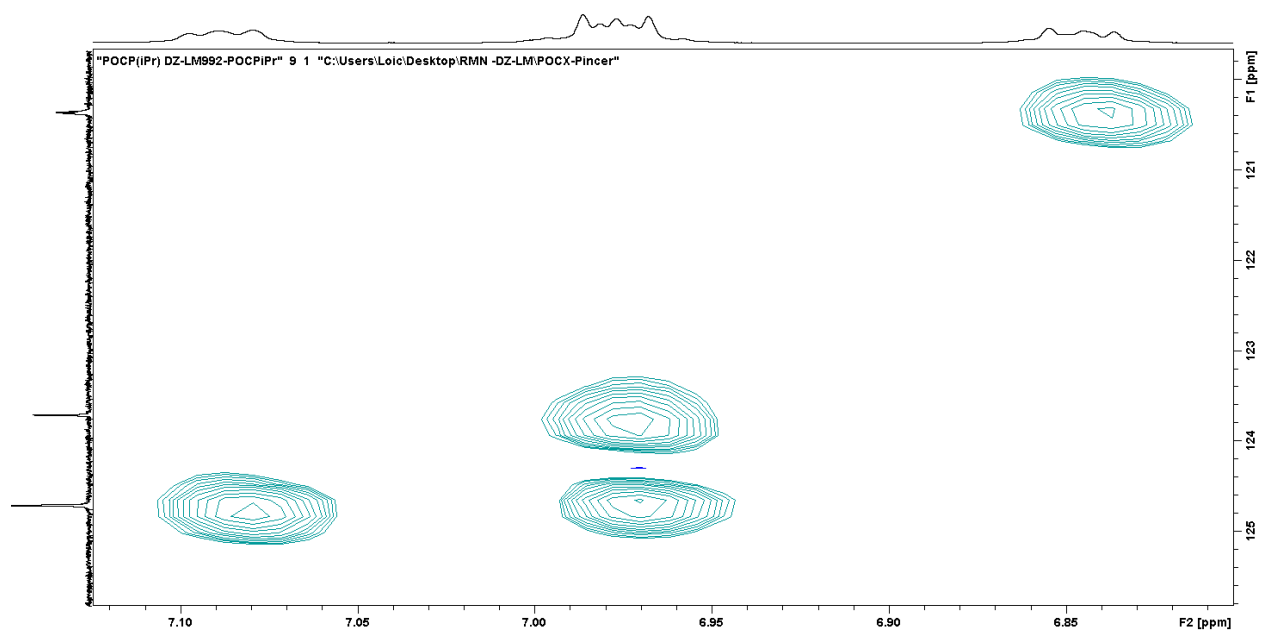
Figure S5.106: The expanded aromatic region of the HSQC NMR spectrum of **10** in C$_6$D$_6$.
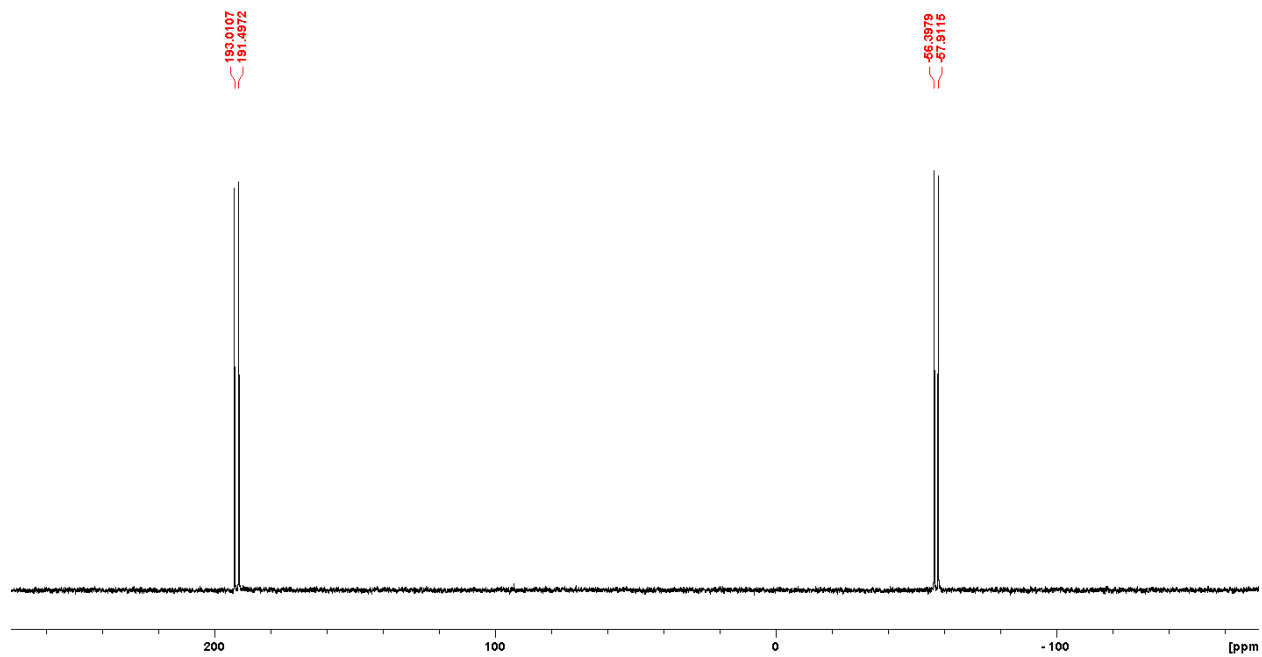
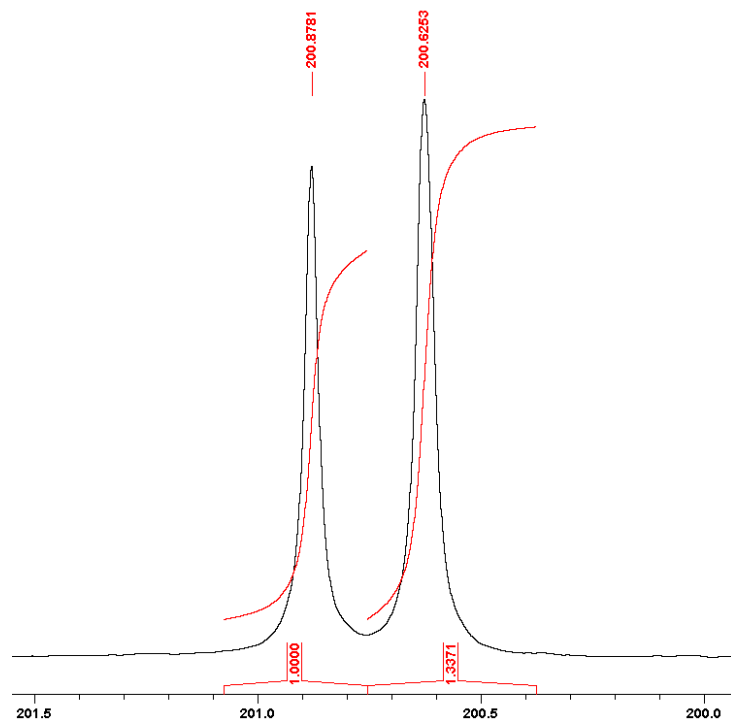Figure S5.107: $^{31}P\{^1H\}$ NMR spectrum of **10** in CDCl$_3$.

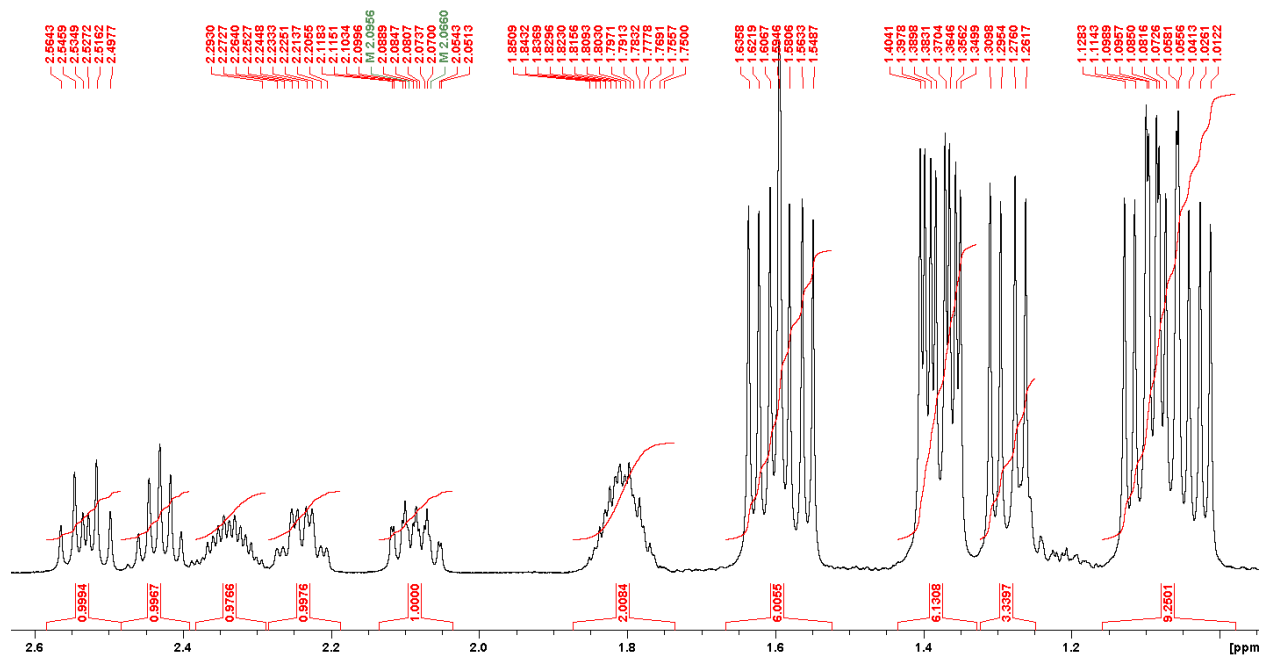h. Complex **11**
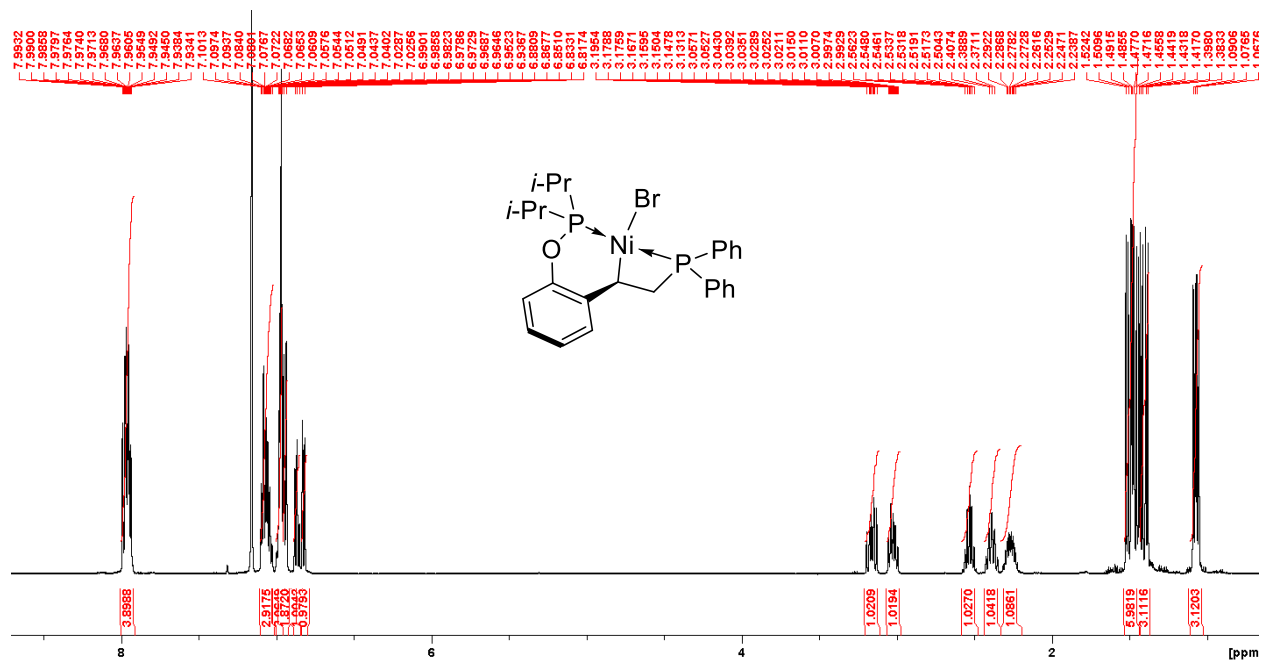
Figure S5.108: Full ^{1}H NMR spectrum of **11** in C$_6$D$_6$.
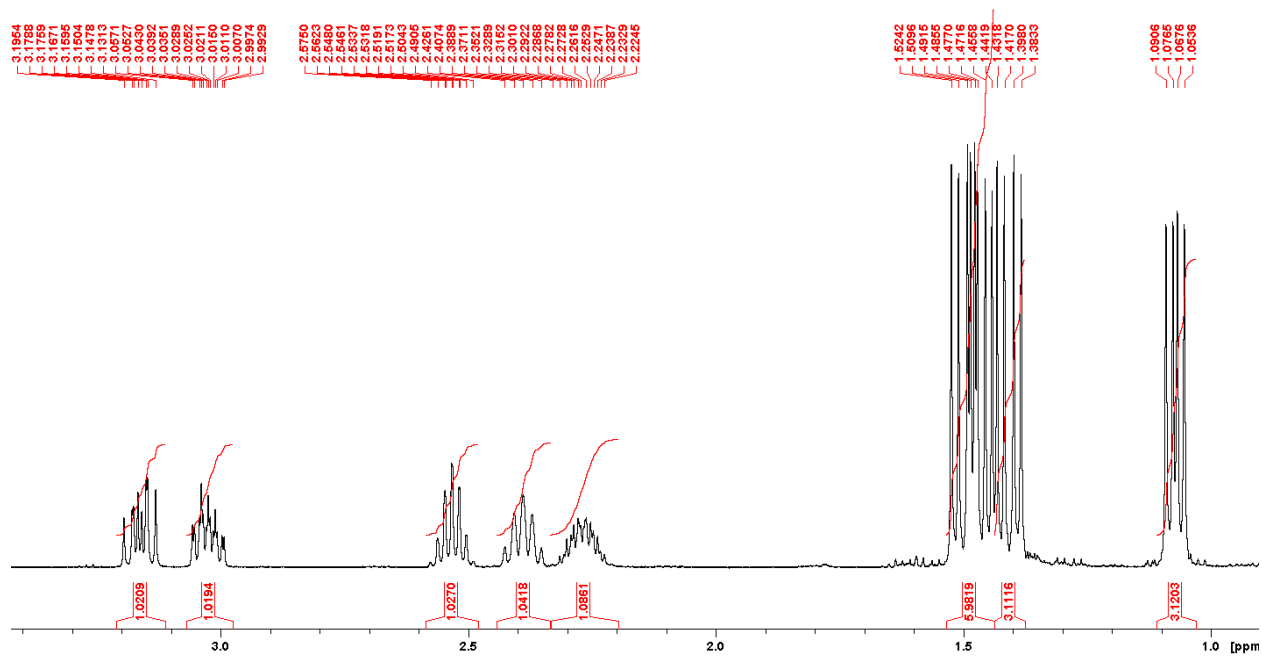
Figure S5.109: The expanded aliphatic region of the ^{1}H NMR spectrum of **11** in C$_6$D$_6$.
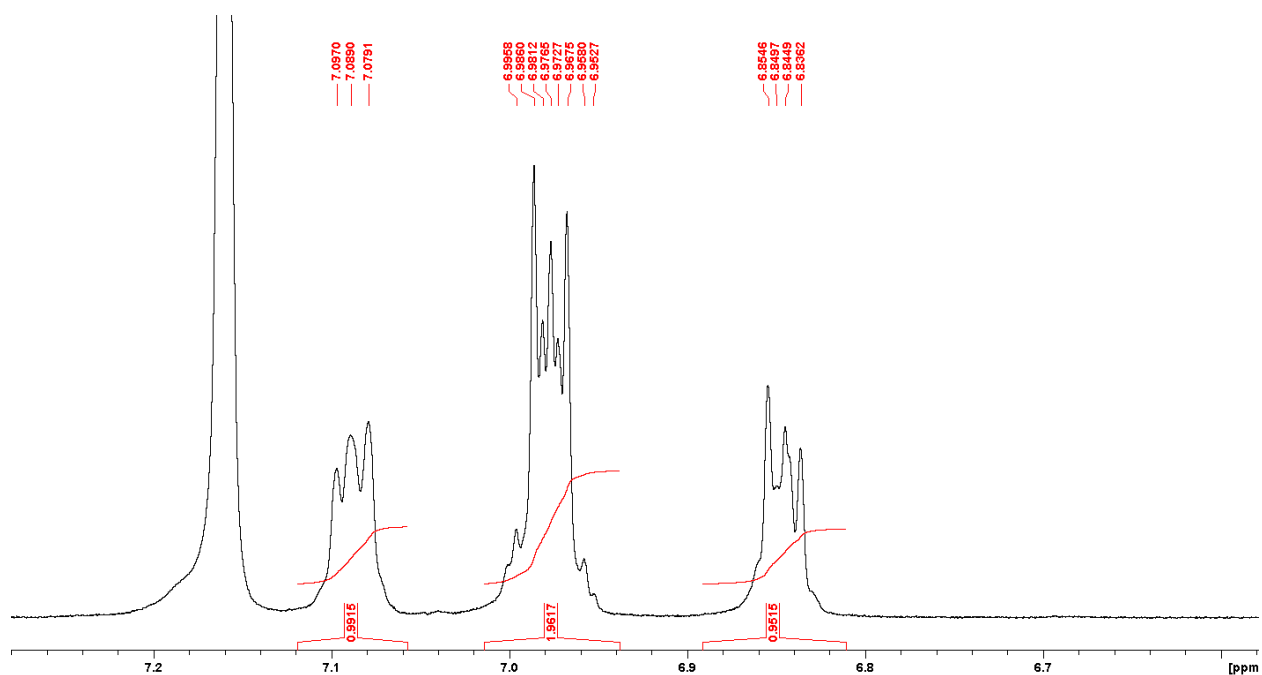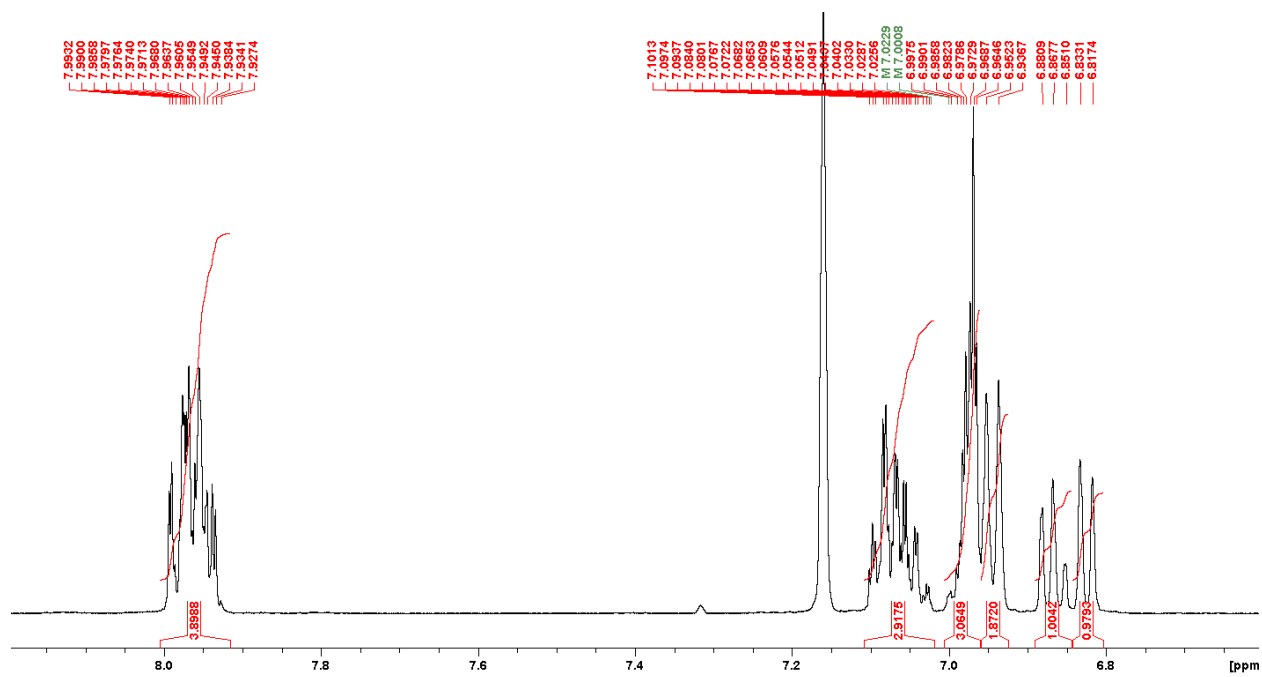
Figure S5.110: The expanded aromatic region of the ^{1}H NMR spectrum of **11** in C$_6$D$_6$.
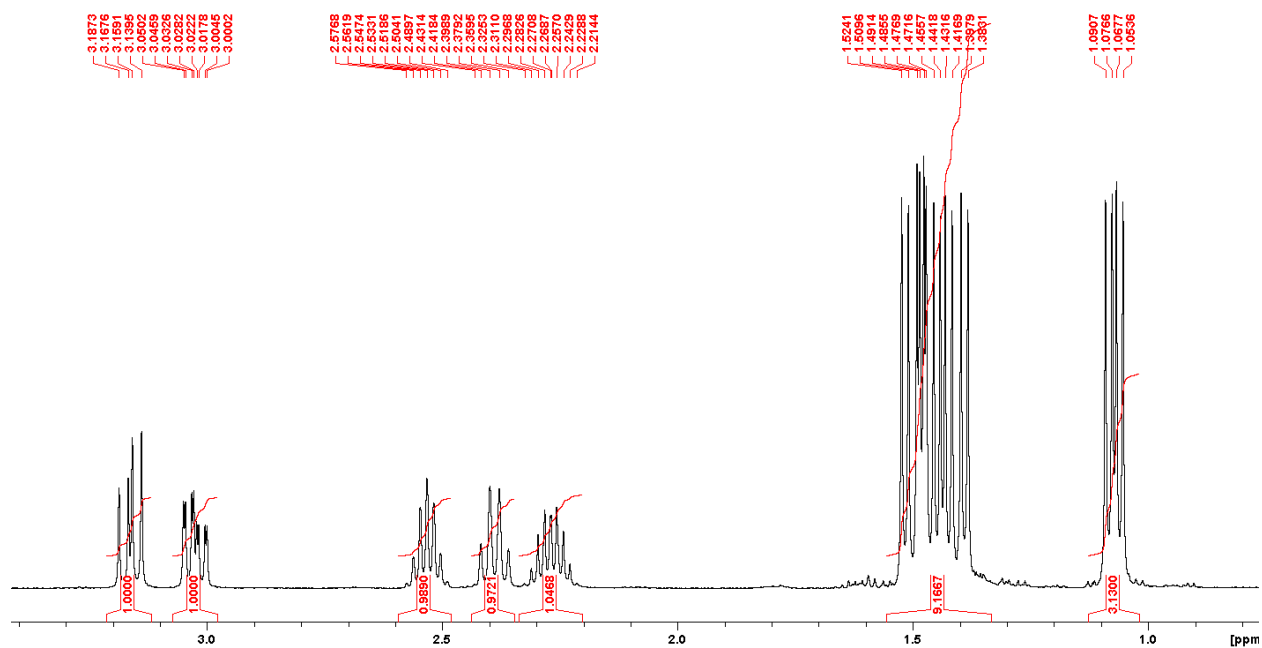
Figure S5.111: The expanded aliphatic region of the ^{1}H{^{31}P, δ -78.20} NMR spectrum of **11** in C$_6$D$_6$.

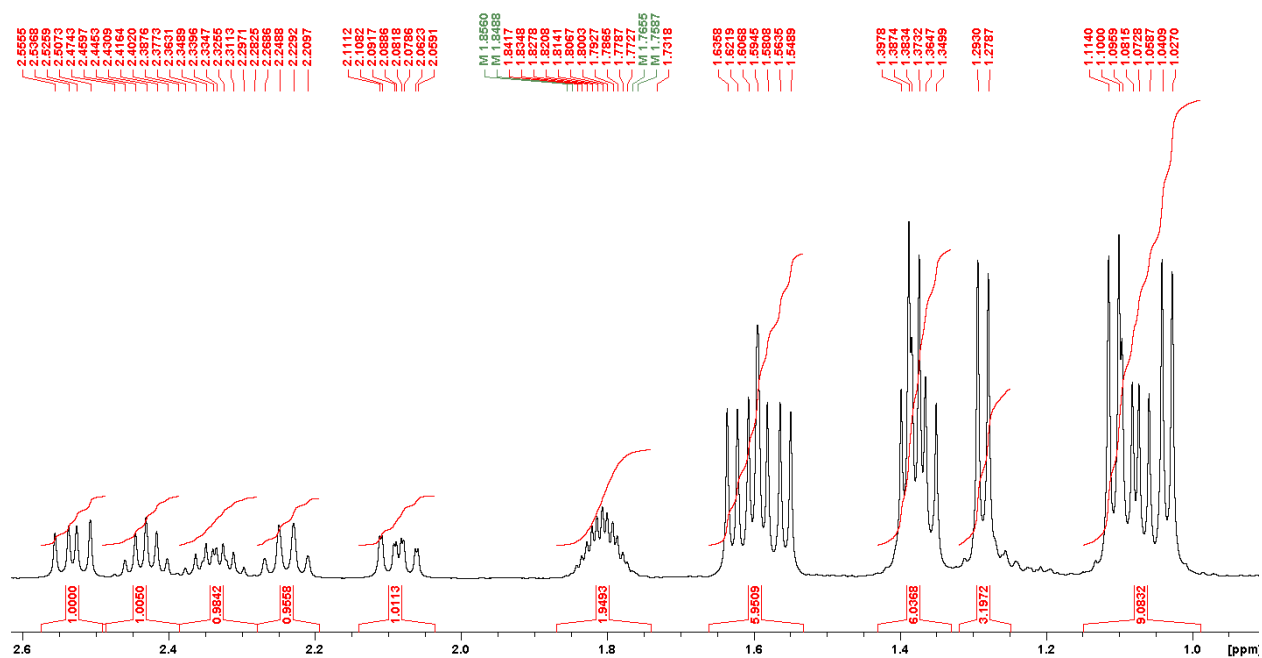Figure S5.112: The expanded aromatic region of the $^1H\{^{31}P, \delta$ -78.20$\}$ NMR spectrum of **11** in C_6D_6.
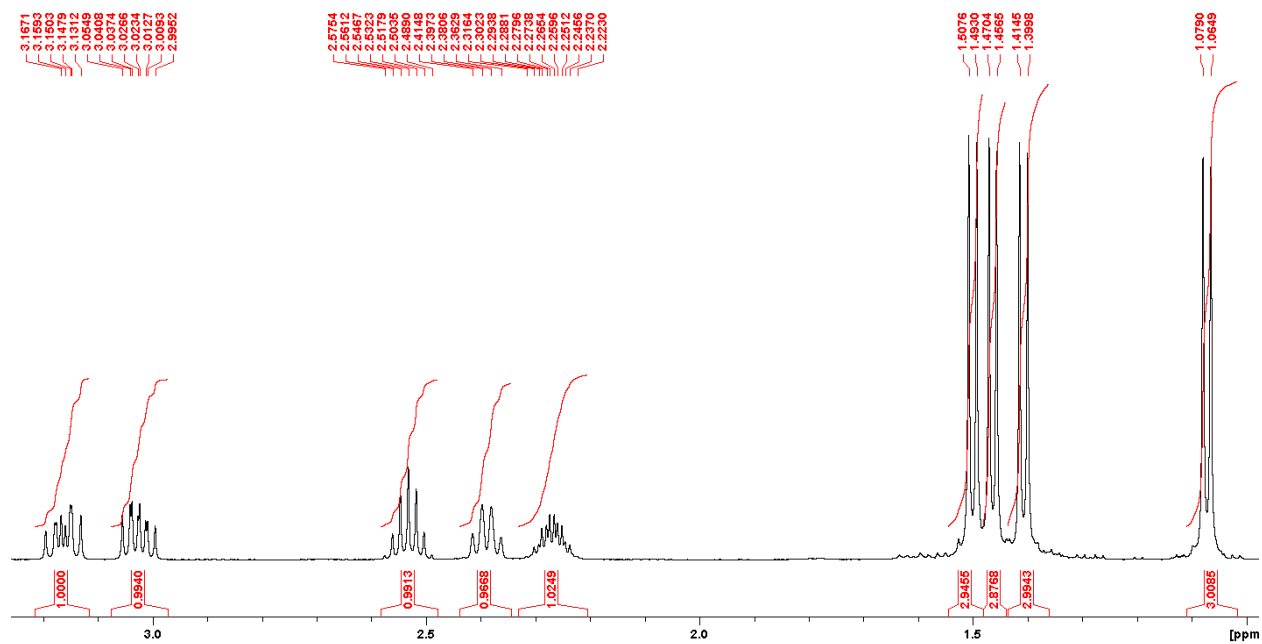
Figure S5.113: The expanded aliphatic region of the $^1H\{^{31}P, \delta$ 196.7$\}$ NMR spectrum of **11** in C_6D_6.
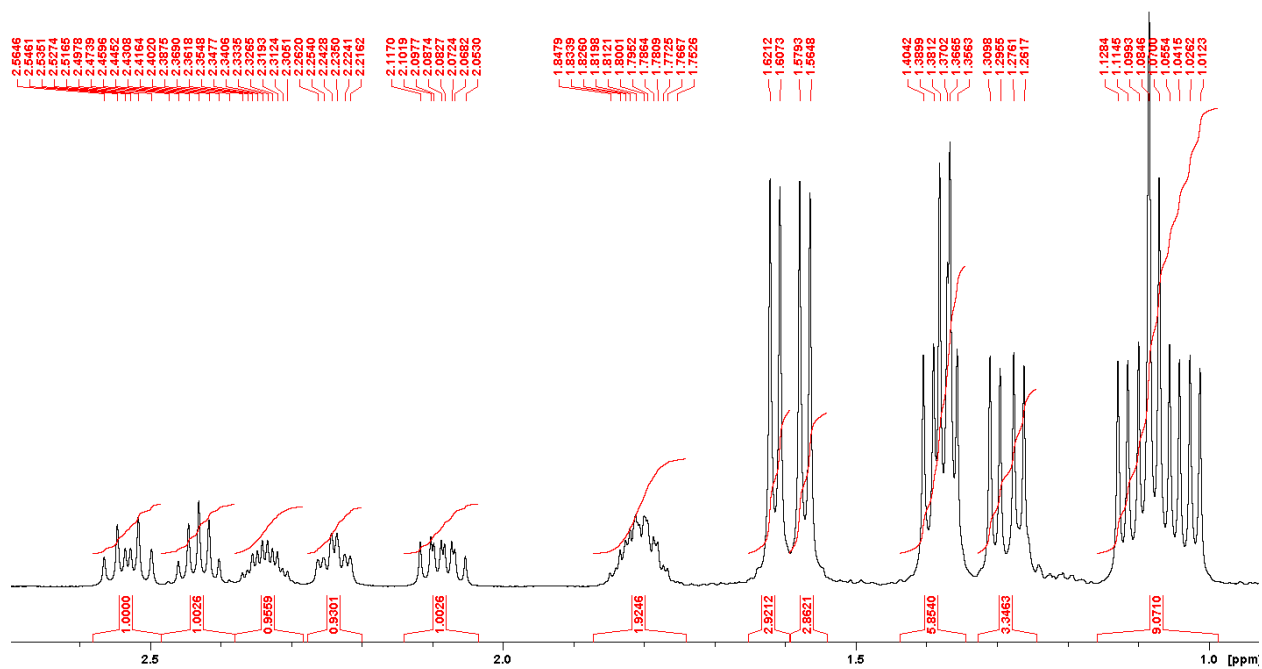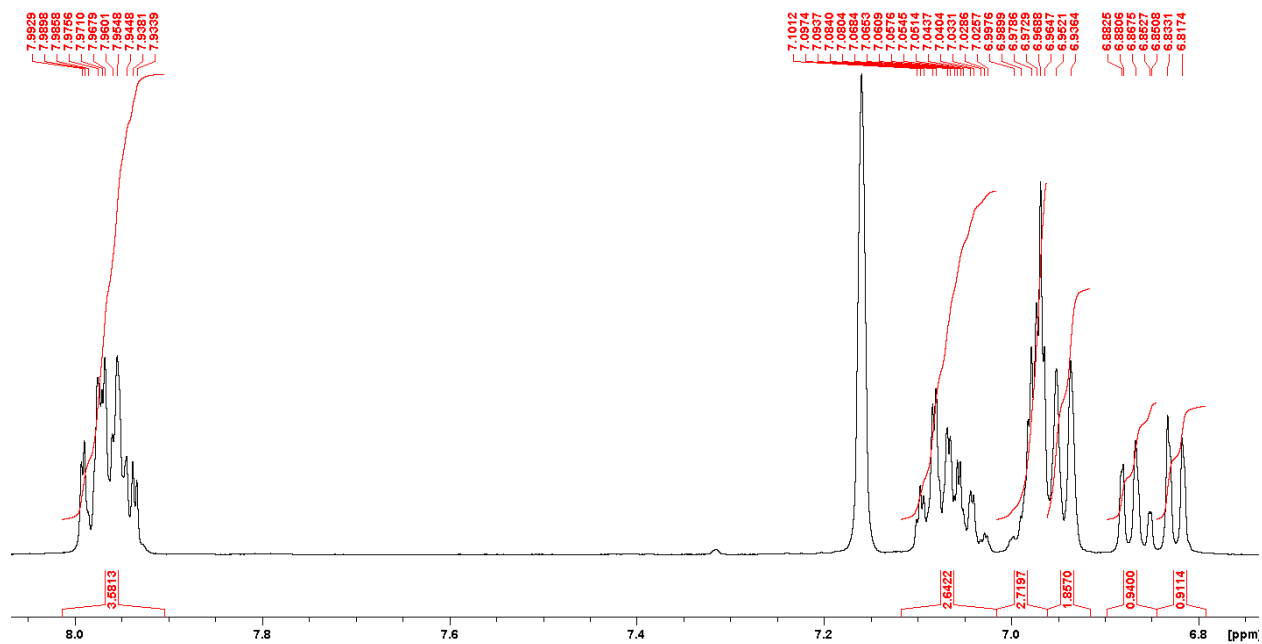
Figure S5.114: The expanded aromatic region of the ^{1}H$\{{}^{31}$P, δ -196.7$\}$ NMR spectrum of **11** in C$_6$D$_6$.
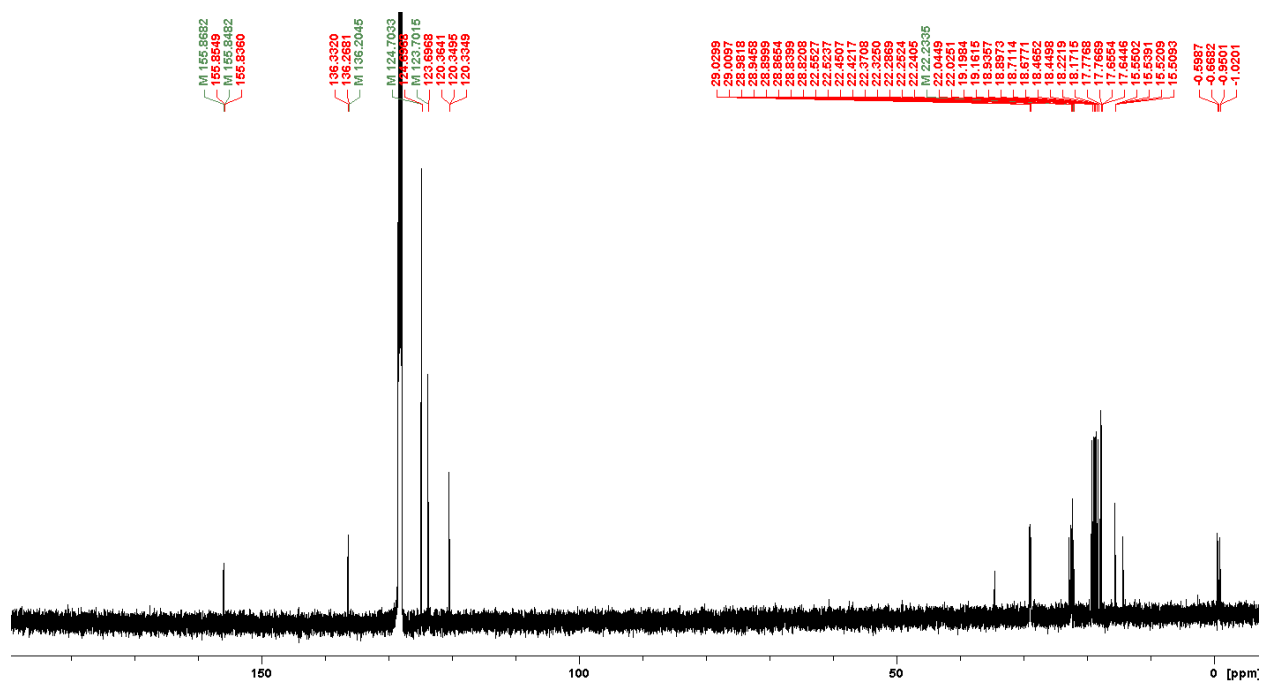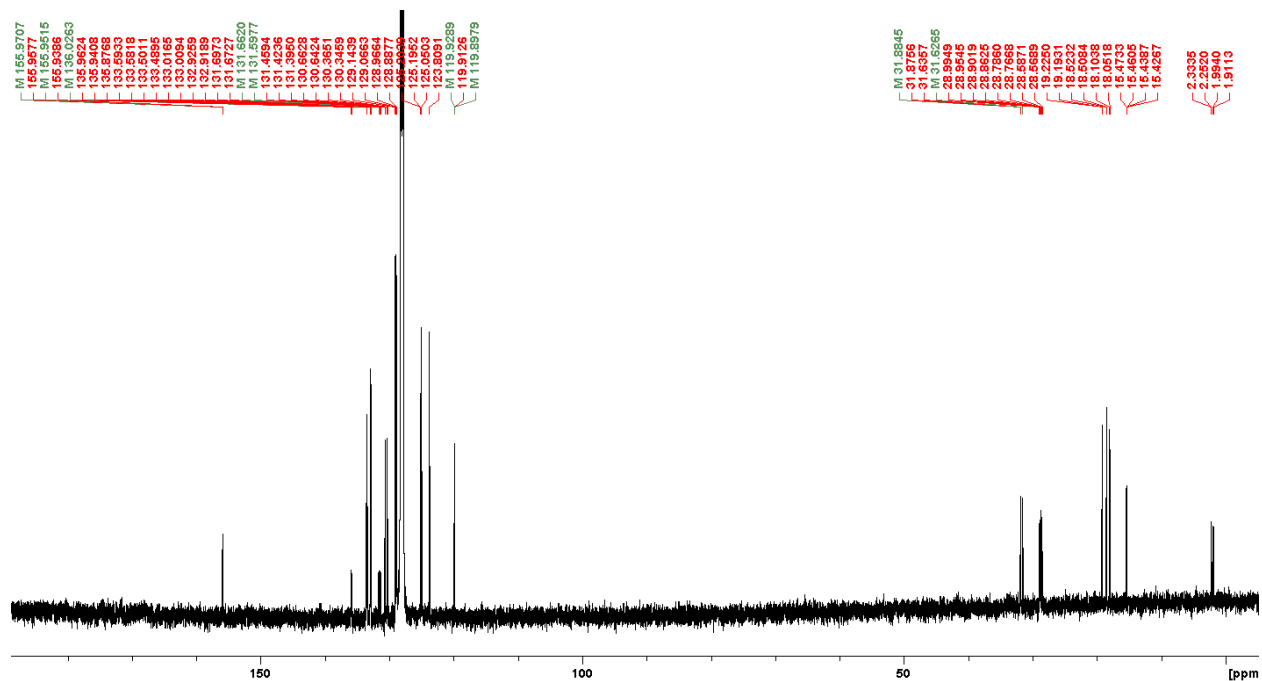

Figure S5.115: Full ^{13}C NMR spectrum of **11** in C$_6$D$_6$.
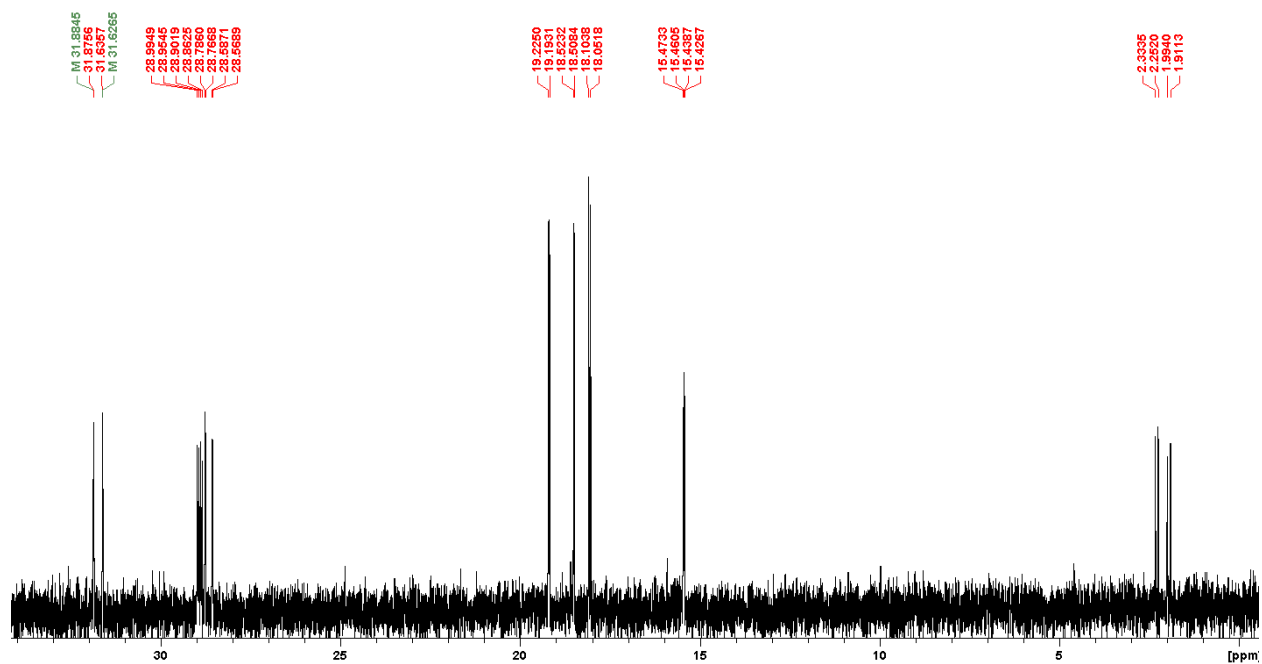
Figure S5.116: The expanded aliphatic region of the ^{13}C NMR spectrum of **11** in C_6D_6.
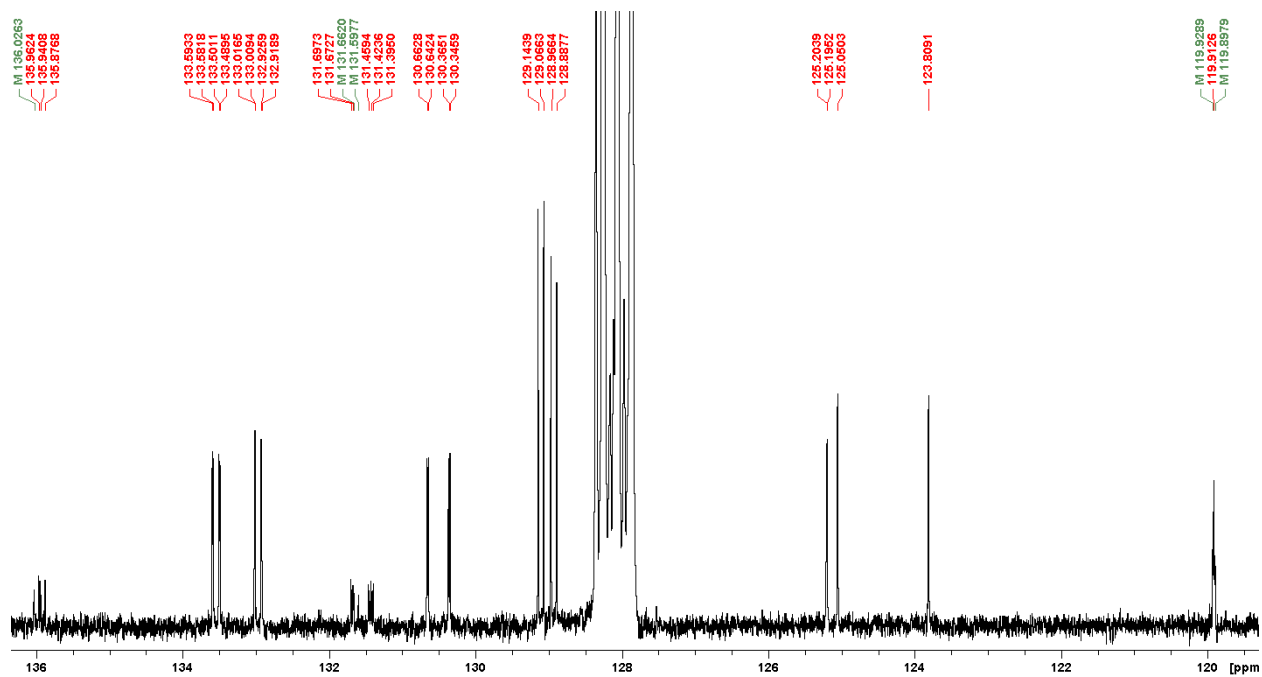
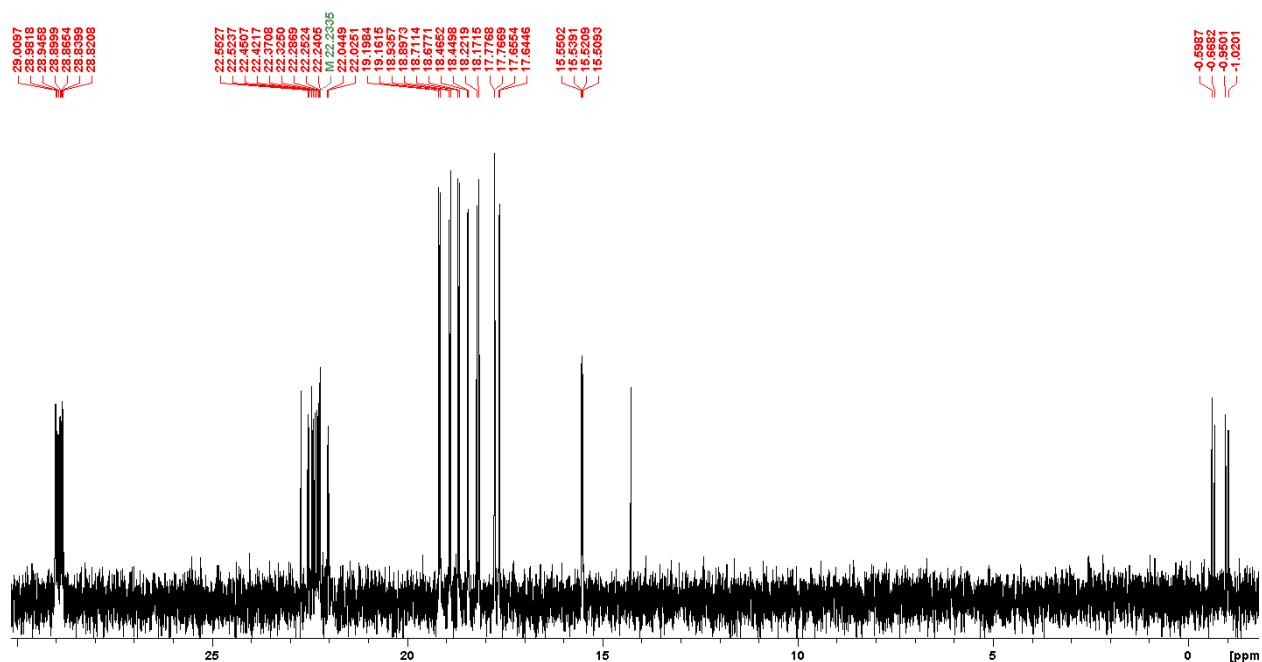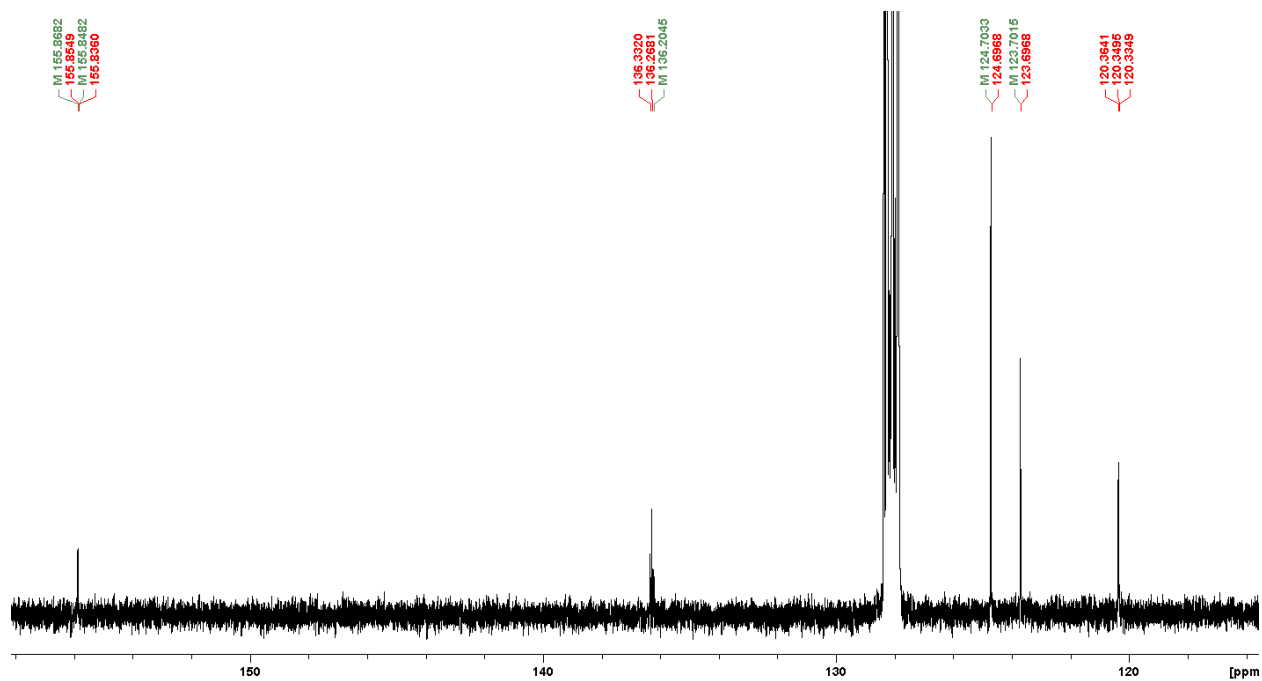Figure S5.117: The expanded aromatic region of the ^{13}C NMR spectrum of **11** in C_6D_6.
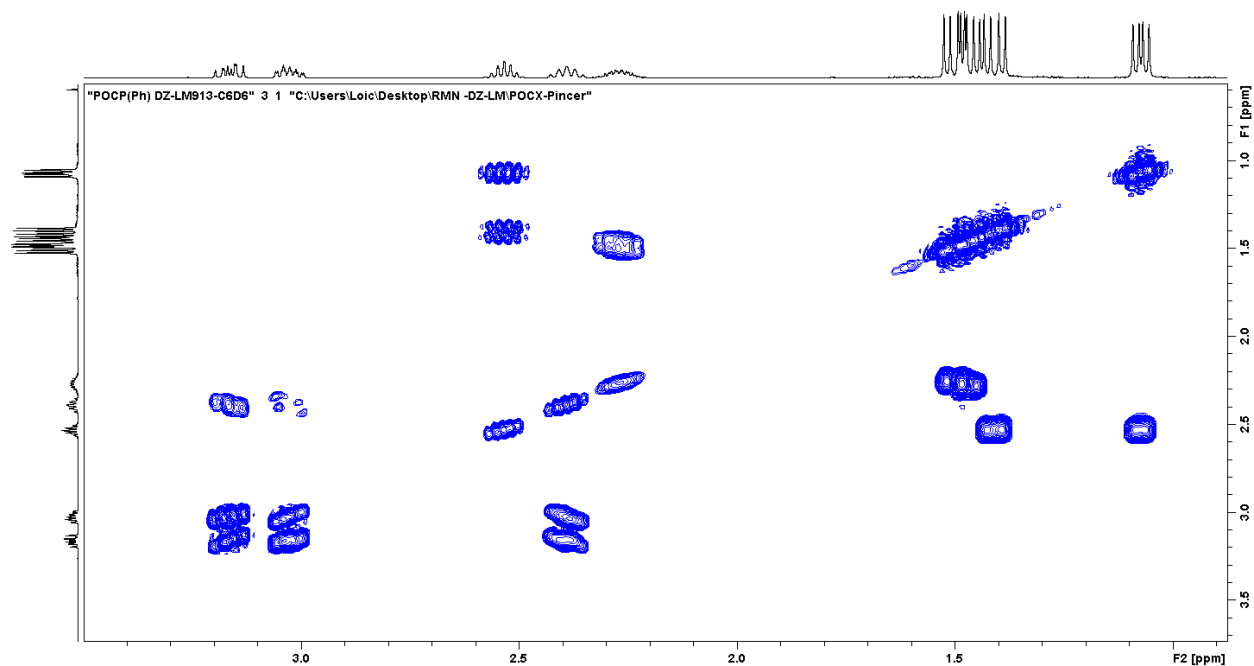
Figure S5.118: The expanded aliphatic region of the COSY NMR spectrum of **11** in C$_6$D$_6$.
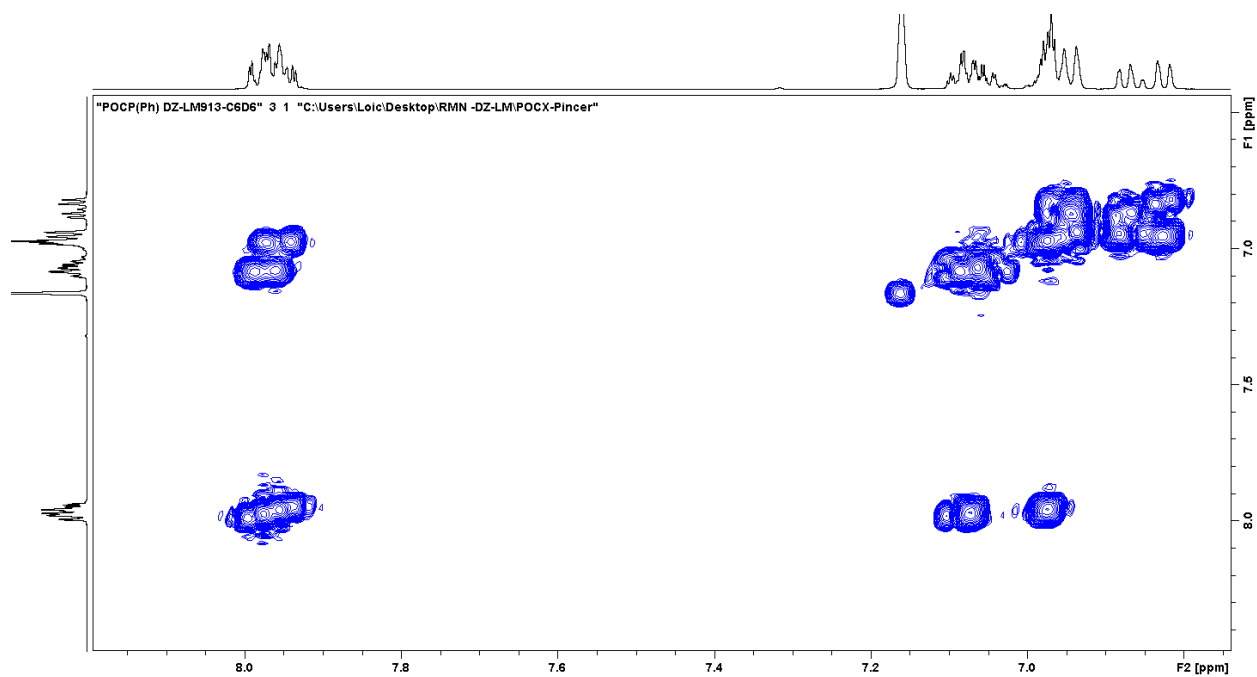
Figure S5.119: The expanded aromatic region of the COSY NMR spectrum of **11** in C$_6$D$_6$.
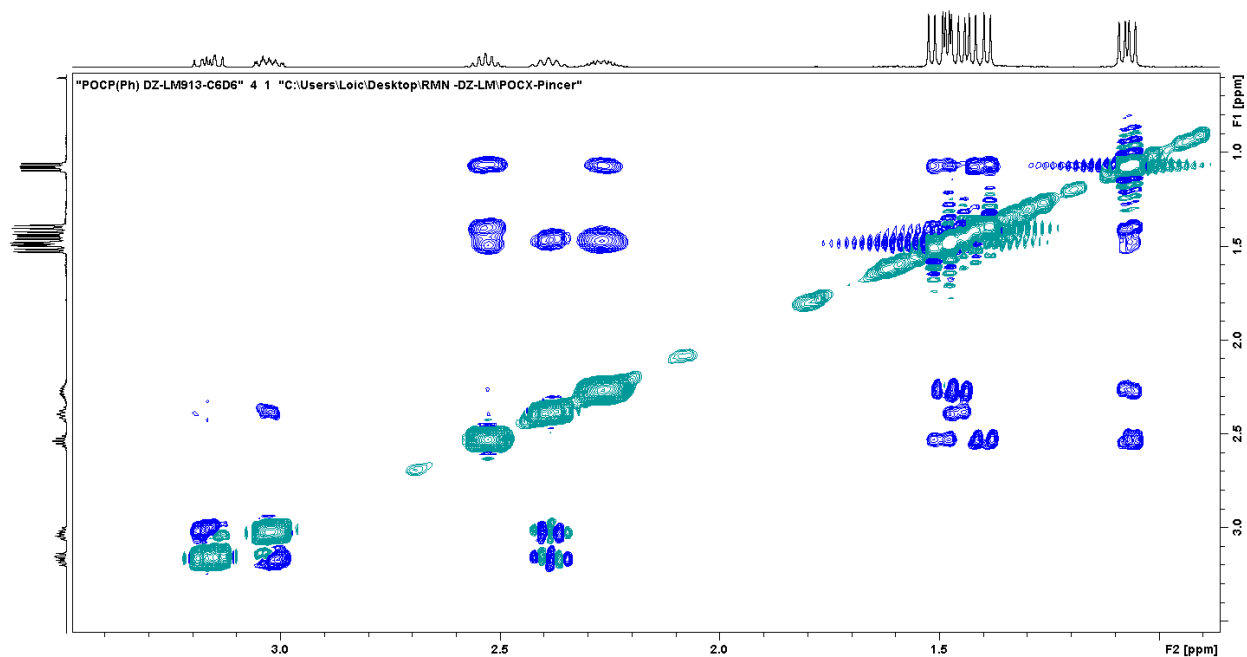
Figure S5.120: Partial NOESY NMR spectrum of **11** in C_6D_6 showing the aliphatic/aliphatic interactions.
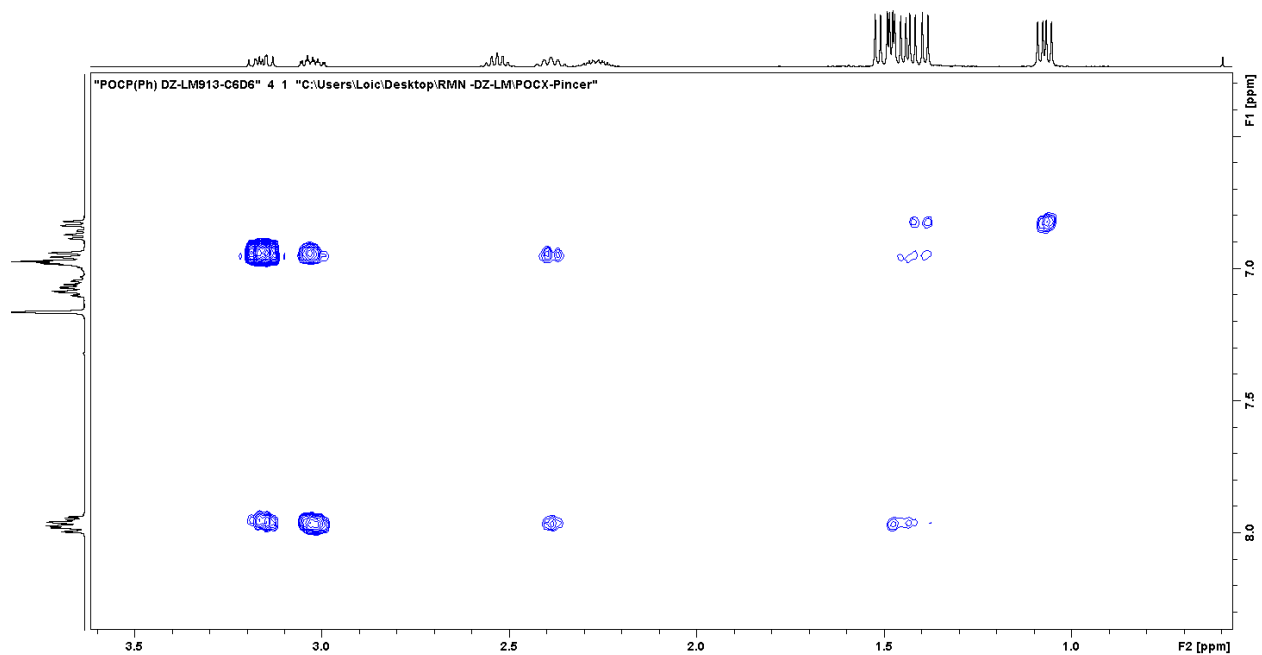
Figure S5.121. Partial NOESY NMR spectrum of **11** in C_6D_6 showing the aliphatic/aromatic interactions.
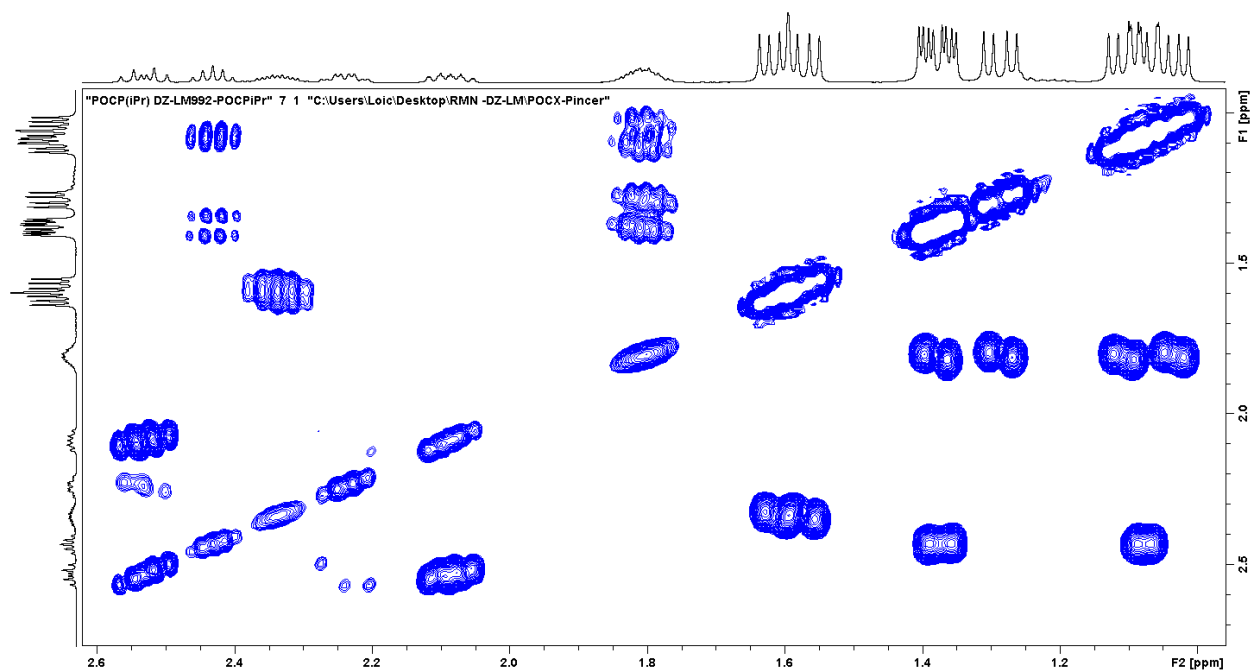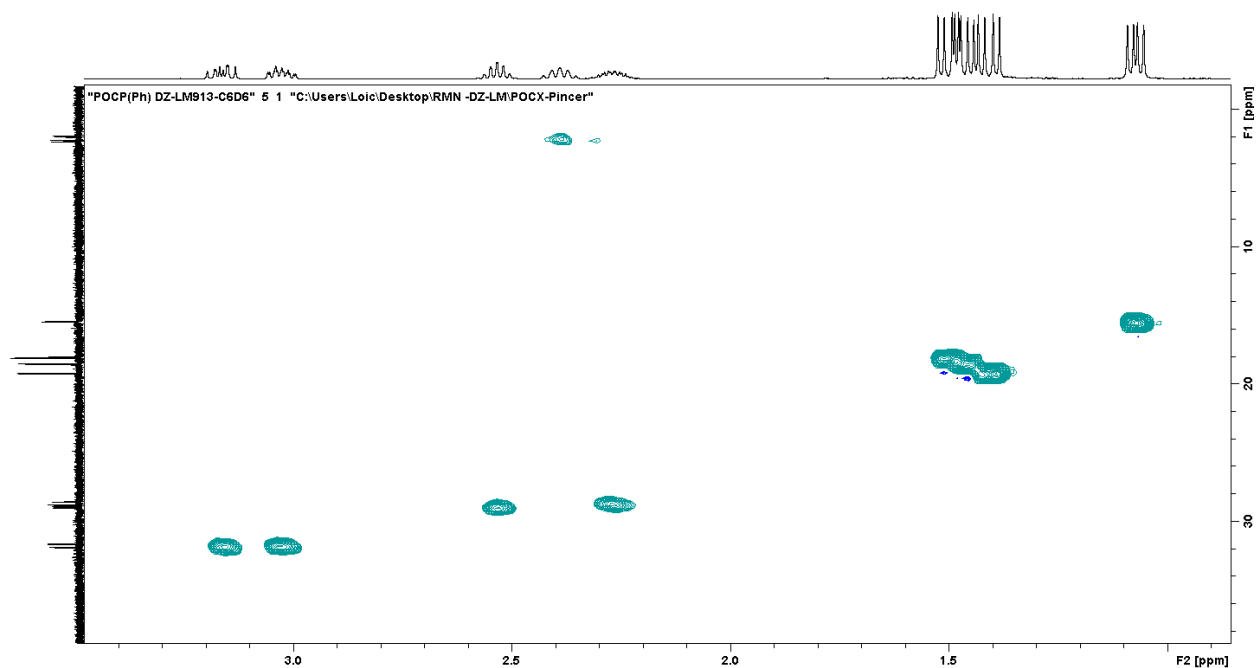
Figure S5.122: The expanded aliphatic region of the HSQC NMR spectrum of **11** in C_6D_6.

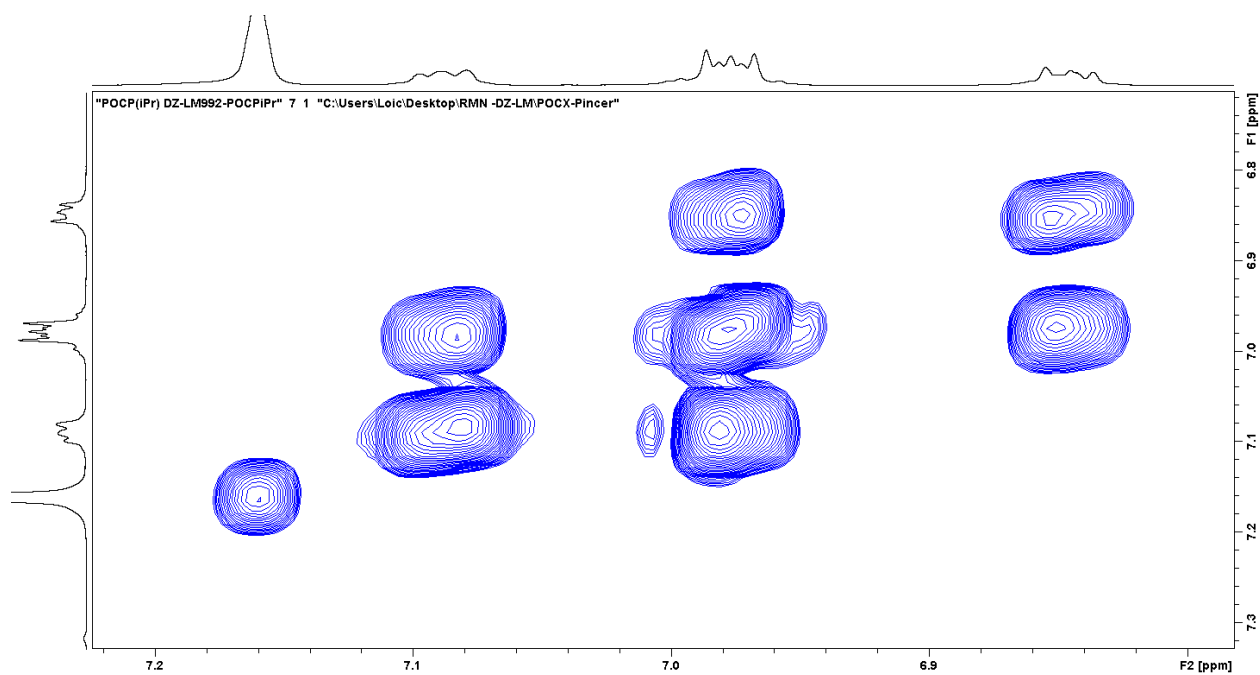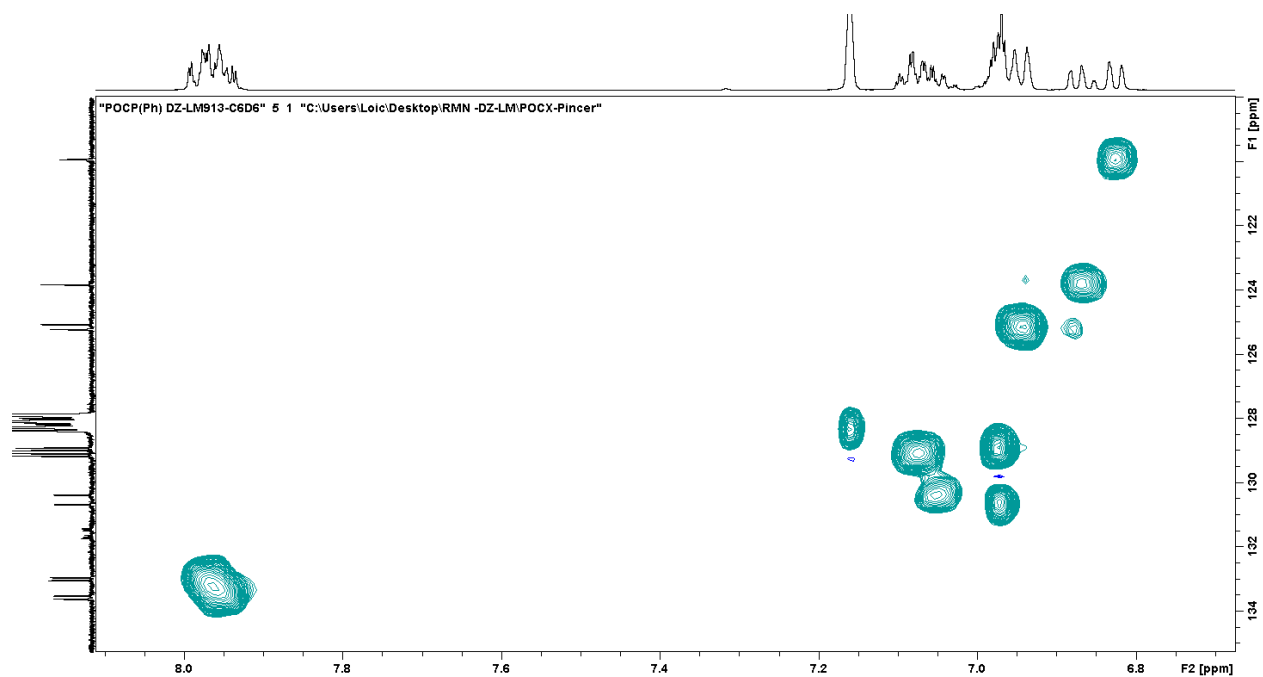Figure S5.123: The expanded aromatic region of the HSQC NMR spectrum of **11** in C_6D_6.
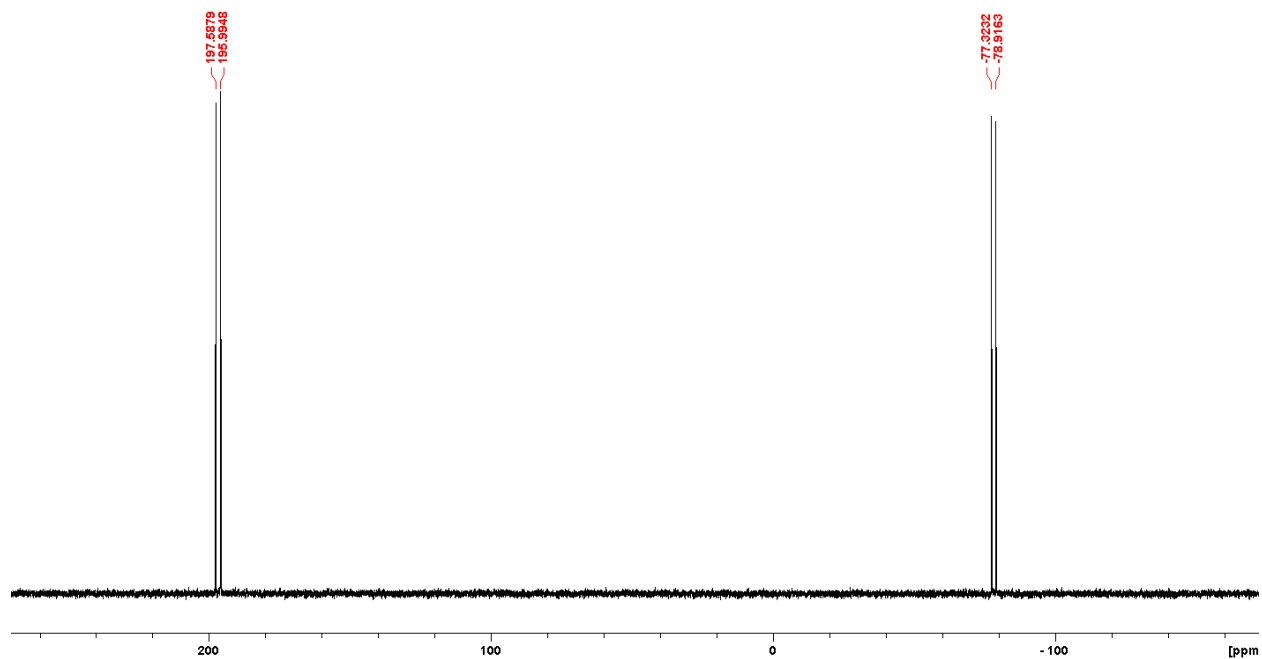
Figure S5.124: $^{31}P\{^{1}H\}$ NMR spectrum of **11** in C$_6$D$_6$.

S5.6 Other relevant NMR spectra
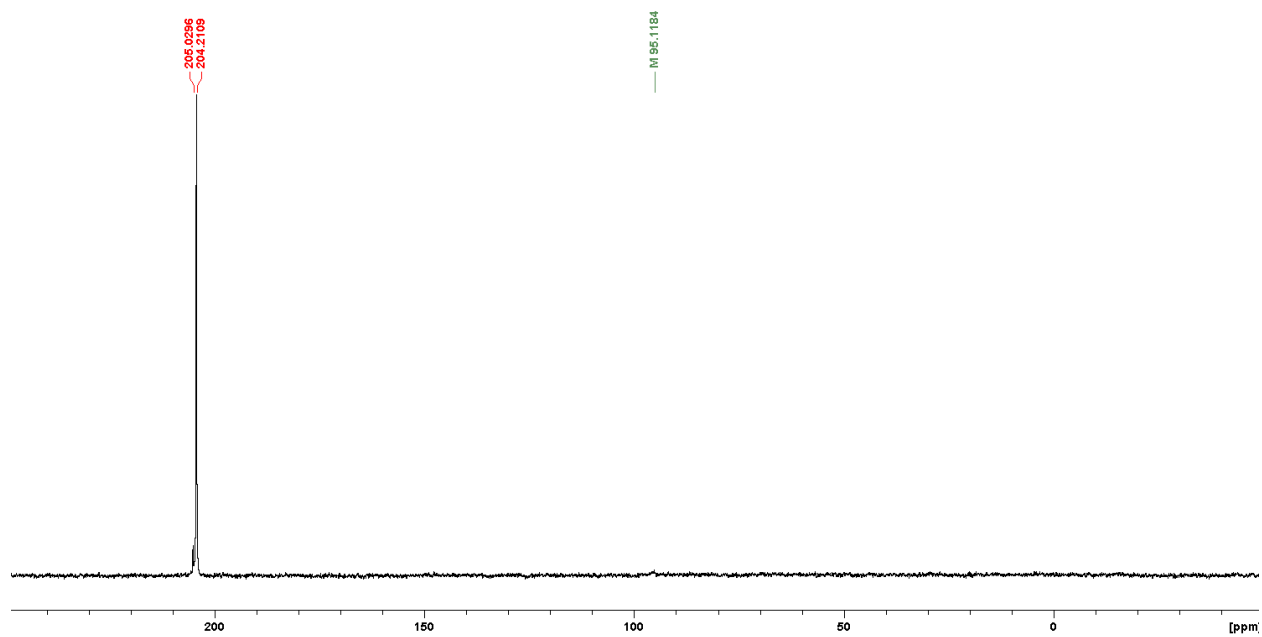
Figure S5.125: $^{31}P\{^1H\}$ NMR spectrum of the crude mixture for the formation of complex **4**.
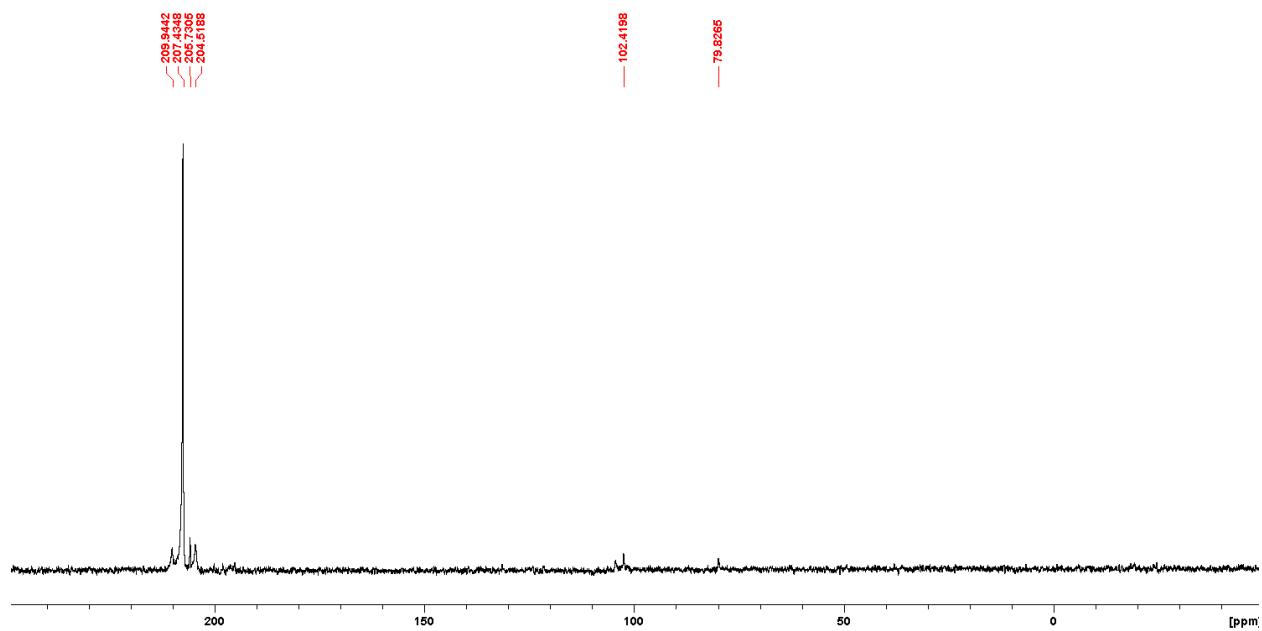
Figure S5.126: $^{31}P\{^1H\}$ NMR spectrum of the crude mixture for the synthesis of complex **5**.
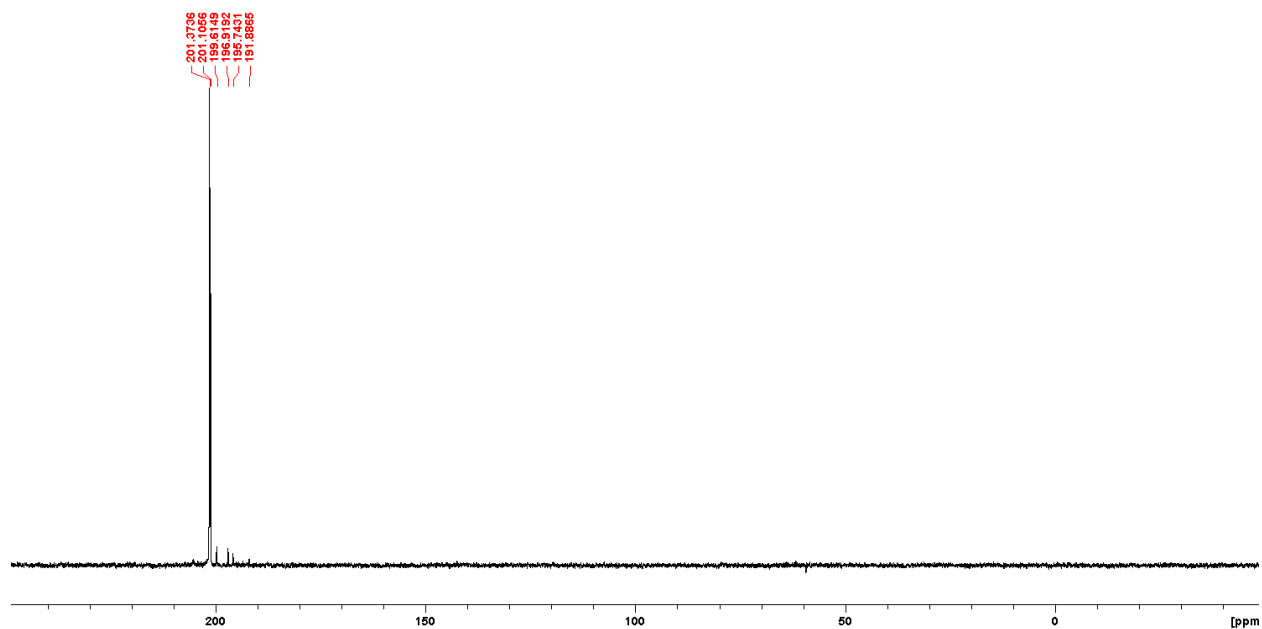
Figure S5.127: ^{31}P{^{1}H} NMR spectrum of the crude mixture for the synthesis of complex **6**.
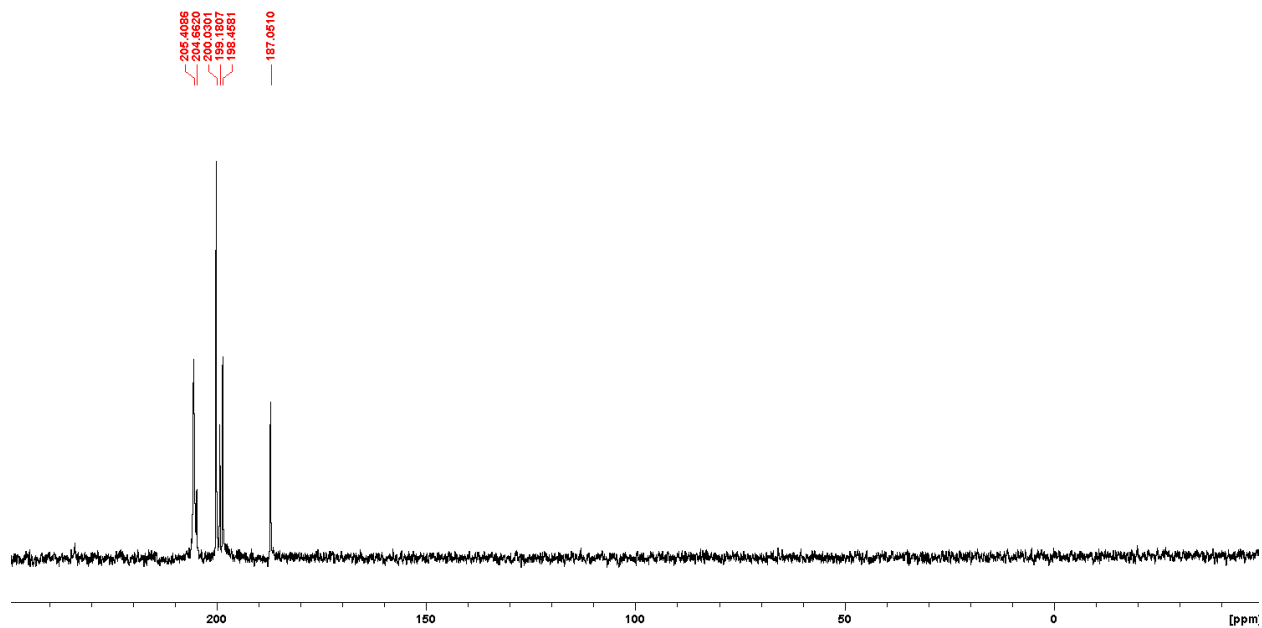
Figure S5.128: ^{31}P{^{1}H} NMR spectrum of the crude mixture for the synthesis of complex **7**.
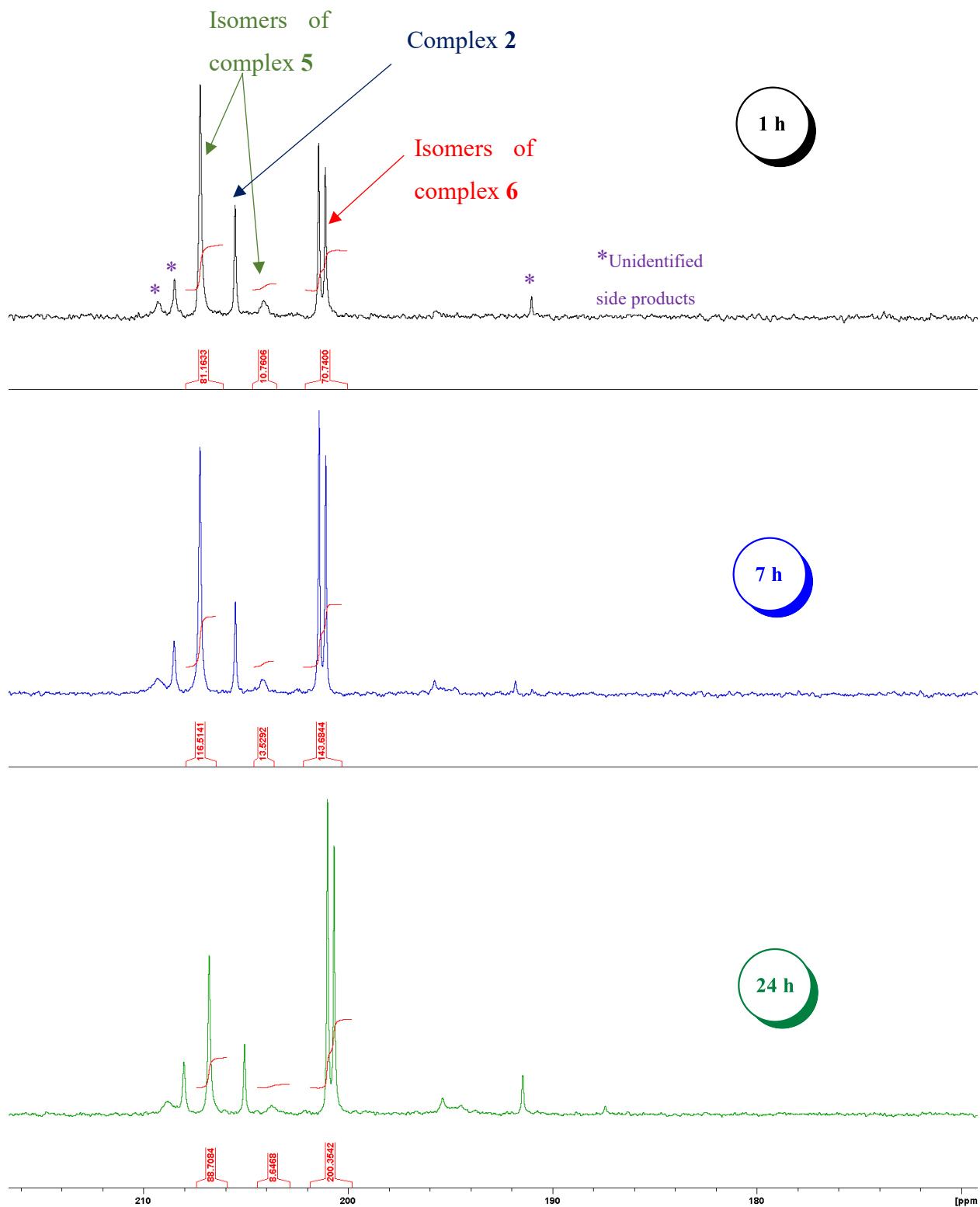
Figure S5.129: Kinetic monitoring the competition reaction between PhN(Et)H and *i*-PrNH₂. The integrals are referenced to the median peak of the PF6⁻ set to ∫ = 100.

S5.7 Powder XRD Results
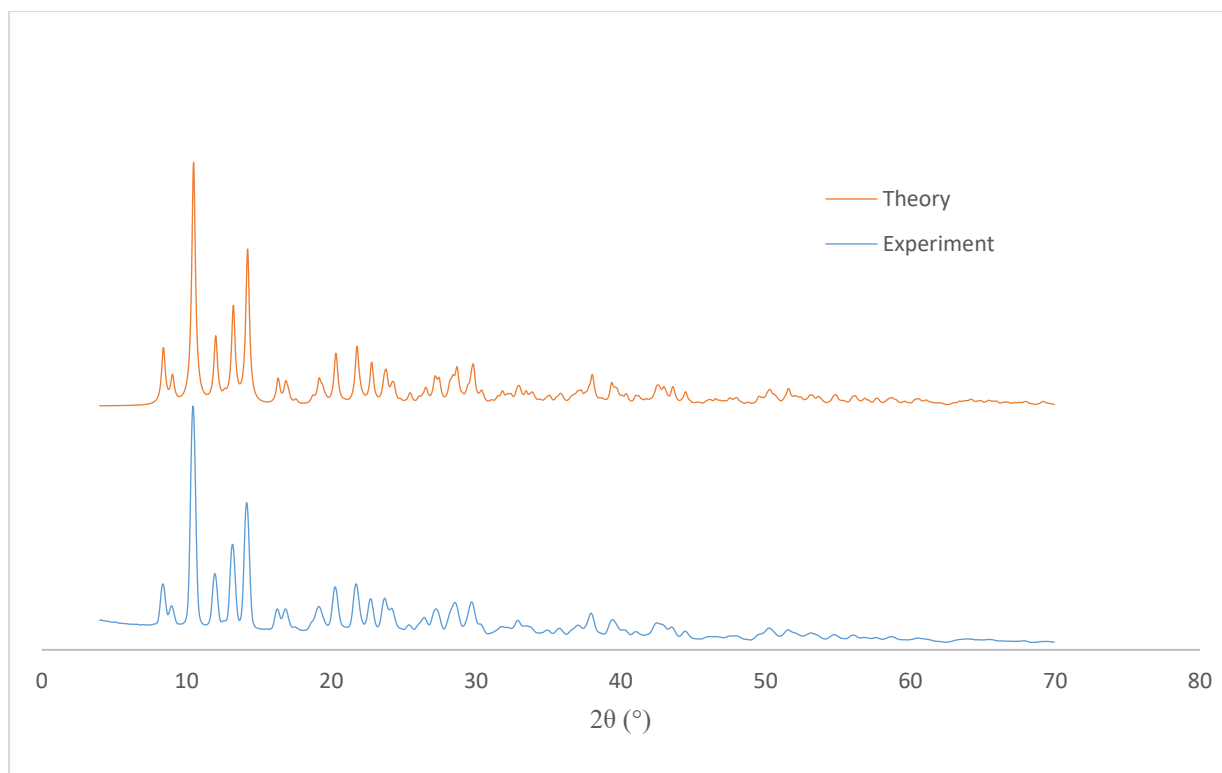
Figure S5.130: Experimental and Theoretical powder XRD diagrams of complex **6**.

S5.8 Crystallographic data tables

Table S5.1: Crystal description and refinement indicators for compounds **2-4**.

	2	2·3	4
chemical formula	$C_{20}H_{35}BrNiO_2P_2$	$C_{28}H_{41}BrNiO_2P_2,C_{20}H_{35}BrNiO_2P_2$	$C_{18}H_{29}BrNNiO_2P$
crystal colour	red	orange	orange
crystal size (mm)	$0.04 \times 0.04 \times 0.08$	$0.08 \times 0.10 \times 0.14$	$0.16 \times 0.18 \times 0.24$
index ranges	$-16 \le h \le 15$ $-14 \le k \le 14$ $-22 \le l \le 22$	$-12 \le h \le 12$ $-18 \le k \le 18$ $-22 \le l \le 22$	$-11 \le h \le 10$ $-13 \le k \le 13$ $-22 \le l \le 22$
Fw; *F*(000)	508.04; 1056	1118.20; 1164	461.01; 952
T (K)	150	100	100
wavelength (Å)	1.34139	1.54178	1.54178
space group	$P2_1/c$	P-1	$P2_1/n$
a (Å)	12.9589(7)	10.1678(2)	10.1636(2)
b (Å)	10.8672(6)	14.8302(3)	10.6763(2)
c (Å)	17.2475(9)	18.3511(4)	18.5212(4)
α (deg)	90	94.2580(10)	90
β (deg)	110.863(2)	92.3890(10)	96.2830(10)
γ (deg)	90	109.7560(10)	90
Z	4	2	4
V (Å^3)	2269.7(2)	2590.53(9)	1997.66(7)
ρ_{calcd} (g·cm^{-3})	1.487	1.434	1.533
μ (mm^{-1})	6.970	4.186	4.577
θ range (deg); completeness	$3.175 - 60.714$; 0.999	$2.420 - 72.162$; 0.978	$4.788 - 72.277$; 0.978
collected reflections; R_σ	24651; 0.0362	71924; 0.0121	53705; 0.0103
unique reflections; R_{int}	5209; 0.0496	9927; 0.0225	3835; 0.0281
R1[a]; wR2[b] [I > 2σ(I)]	0.0268; 0.0704	0.0221; 0.0588	0.0224; 0.0578
R1; wR2 [all data]	0.0290; 0.0720	0.0225; 0.0591	0.0225; 0.0578
GOOF	1.036	1.063	1.111
largest diff peak and hole	0.781 and -0.558	0.640 and -0.301	0.411 and -0.408

[a] $R_1 = \Sigma(||F_o|-|F_c||)/\Sigma|F_o|$

[b] $wR_2 = \{\Sigma[w(F_o^2-F_c^2)^2]/\Sigma[w(F_o^2)^2]\}^{\frac{1}{2}}$

Table S5.2: Crystal description and refinement indicators for compounds **5**-**7**.

	5	6	7
chemical formula	$C_{22}H_{31}BrNNiOP$	$C_{17}H_{29}BrNNiOP$	$C_{20}H_{27}BrNNiOP$
crystal colour	orange	orange	orange
crystal size (mm)	$0.06 \times 0.13 \times 0.22$	$0.13 \times 0.14 \times 0.24$	$0.12 \times 0.16 \times 0.16$
index ranges	$-10 \leq h \leq 10$ $-23 \leq k \leq 23$ $-17 \leq l \leq 17$	$-11 \leq h \leq 11$ $-13 \leq k \leq 13$ $-13 \leq l \leq 12$	$-9 \leq h \leq 9$ $-12 \leq k \leq 12$ $-17 \leq l \leq 17$
Fw; *F*(000)	495.07; 1024	433.00; 448	467.01; 480
T (K)	100	100	100
wavelength (Å)	1.54178	1.54178	1.54178
space group	$P2_1/c$	P-1	P-1
a (Å)	8.1369(2)	9.2201(2)	7.5034(2)
b (Å)	19.2702(6)	10.6029(2)	9.9905(3)
c (Å)	14.3864(4)	10.6404(2)	14.5552(4)
α (deg)	90	90.3200(10)	97.5230(10)
β (deg)	91.1200(10)	112.7990(10)	100.4150(10)
γ (deg)	90	96.2890(10)	104.3160(10)
Z	4	2	2
V (Å^3)	2255.35(11)	951.85(3)	1021.99(5)
ρ_{calcd} (g·cm^{-3})	1.458	1.511	1.518
μ (mm^{-1})	4.064	4.720	4.449
θ range (deg); completeness	$3.835 - 72.074$; 0.998	$4.514 - 72.261$; 0.962	$6.076 - 72.244$; 0.976
collected reflections; R_σ	60624; 0.0091	37984; 0.0088	28755; 0.0167
unique reflections; R_{int}	4415; 0.0246	3606; 0.0203	3909; 0.0338
R1[a]; wR2[b] [I > 2σ(I)]	0.0305; 0.0721	0.0200; 0.0497	0.0328; 0.0914
R1; wR2 [all data]	0.0305; 0.0721	0.0201; 0.0498	0.0329; 0.0916
GOOF	1.186	1.106	1.080
largest diff peak and hole	1.053 and -0.396	0.393 and -0.308	1.071 and -0.675

[a] $R_1 = \Sigma(||F_o| - |F_c||)/\Sigma|F_o|$

[b] $wR_2 = \{\Sigma[w(F_o^2 - F_c^2)^2]/\Sigma[w(F_o^2)^2]\}^{1/2}$

Table S5.3: Crystal description and refinement indicators for compounds **8**, **9** and **3**.

	8·(Et₂O)₀.₅	9	3
chemical formula	2($C_{20}H_{33}BrNNiOP$),0.5($C_4H_{10}O$)	$C_{18}H_{31}BrNNiOP$	$C_{28}H_{41}BrNiO_2P_2$
crystal colour	orange	orange	orange
crystal size (mm)	0.06 × 0.07 × 0.075	0.08 × 0.14 × 0.29	0.06 × 0.08 × 0.14
index ranges	$-13 \leq h \leq 13$	$-13 \leq h \leq 12$	$-15 \leq h \leq 15$
	$-27 \leq k \leq 27$	$-13 \leq k \leq 13$	$-21 \leq k \leq 20$
	$-27 \leq l \leq 27$	$-21 \leq l \leq 19$	$-17 \leq l \leq 17$
Fw; *F*(000)	983.18; 2052	447.03; 928	610.17; 1272
T (K)	150	100	100
wavelength (Å)	1.34139	1.54178	1.54178
space group	P2₁/c	P-1	P2₁/n
a (Å)	10.2094(3)	10.5516(3)	12.9498(5)
b (Å)	21.2046(7)	10.7031(3)	17.0373(7)
c (Å)	20.9367(7)	17.9010(5)	14.3613(6)
α (deg)	90	94.5490(10)	90
β (deg)	95.3510(10)	99.3800(10)	116.631(2)
γ (deg)	90	91.5130(10)	90
Z	4	4	4
V (Å³)	4512.8(3)	1986.74(10)	2832.4(2)
ρ_{calcd} (g·cm⁻³)	1.447	1.495	1.431
μ (mm⁻¹)	6.561	4.541	3.880
θ range (deg); completeness	2.586 − 60.748; 0.999	2.511 − 72.228; 0.977	3.827 − 72.078; 1.000
collected reflections; R_σ	68487; 0.0258	54975; 0.0141	77862; 0.0135
unique reflections; R_{int}	10398; 0.0410	7583; 0.0262	5567; 0.0361
R1[a]; wR2[b] [I > 2σ(I)]	0.0316; 0.0813	0.0307; 0.0783	0.0267; 0.0701
R1; wR2 [all data]	0.0384; 0.0855	0.0310; 0.0788	0.0282; 0.0716
GOOF	1.001	1.124	1.043
largest diff peak and hole	0.971 and -0.707	1.486 and -0.428	1.167 and -0.587

[a] $R_1 = \Sigma(||F_o|-|F_c||)/\Sigma|F_o|$

[b] $wR_2 = \{\Sigma[w(F_o^2–F_c^2)^2]/\Sigma[w(F_o^2)^2]\}^{½}$

Table S5.4: Crystal description and refinement indicators for compounds **10**, **11** and $(CyNH_2)_4NiBr_2$.

	10	11	$(CyNH_2)_4NiBr_2$
chemical formula	$C_{20}H_{35}BrNiOP_2$	$C_{26}H_{31}BrNiOP_2$	$C_{24}H_{52}Br_2N_4Ni$
crystal colour	orange	red	colourless
crystal size (mm)	$0.10 \times 0.14 \times 0.17$	$0.08 \times 0.10 \times 0.12$	$0.04 \times 0.06 \times 0.22$
index ranges	$-19 \leq h \leq 19$	$-13 \leq h \leq 13$	$-7 \leq h \leq 7$
	$-24 \leq k \leq 24$	$-16 \leq k \leq 16$	$-12 \leq k \leq 12$
	$-18 \leq l \leq 18$	$-22 \leq l \leq 22$	$-13 \leq l \leq 13$
Fw; *F*(000)	492.04; 2048	560.07; 1152	615.22; 322
T (K)	100	296(2)	100
wavelength (Å)	1.54178	1.54178	1.54178
space group	$P2_1/c$	$P2_1/c$	P-1
a (Å)	15.8105(5)	13.4188(3)	6.2521(2)
b (Å)	19.9910(6)	10.5227(2)	10.3484(3)
c (Å)	15.3797(5)	17.8245(4)	11.3769(3)
α (deg)	90	90	85.1680(10)
β (deg)	108.9380(10)	90.4370(10)	74.2280(10)
γ (deg)	90	90	81.4670(10)
Z	8	4	1
V (Å³)	4597.9(3)	2516.78(9)	699.78(4)
ρ_{calcd} (g·cm⁻³)	1.422	1.478	1.460
μ (mm⁻¹)	4.601	4.288	4.465
θ range (deg); completeness	$2.955 - 72.212$; 1.000	$3.293 - 72.333$; 1.000	$4.325 - 72.290$; 0.999
collected reflections; R_σ	125825; 0.0155	105674; 0.0138	35589; 0.0457
unique reflections; R_{int}	9044; 0.0393	4957; 0.0516	2735; 0.0486
R1[a]; wR2[b] [$I > 2\sigma(I)$]	0.0381; 0.0996	0.0419; 0.1144	0.0461; 0.1219
R1; wR2 [all data]	0.0387; 0.1001	0.0442; 0.1164	0.0471; 0.1235
GOOF	1.107	1.092	1.060
largest diff peak and hole	2.457 and -0.582	1.643 and -0.441	0.721 and -0.678

[a] $R_1 = \Sigma(||F_o|-|F_c||)/\Sigma|F_o|$

[b] $wR_2 = \{\Sigma[w(F_o^2 - F_c^2)^2]/\Sigma[w(F_o^2)^2]\}^{1/2}$

S5.5 Additional Thermal ellipsoid plots

Figure S5.131: Top view of the molecular diagram of compound **3**. Thermal ellipsoids are shown at the 50% probability level; hydrogen atoms refined via the riding model, terminal Me substituents of P(i-Pr)$_2$ moieties and co-crystallized complex **2** are omitted for clarity.
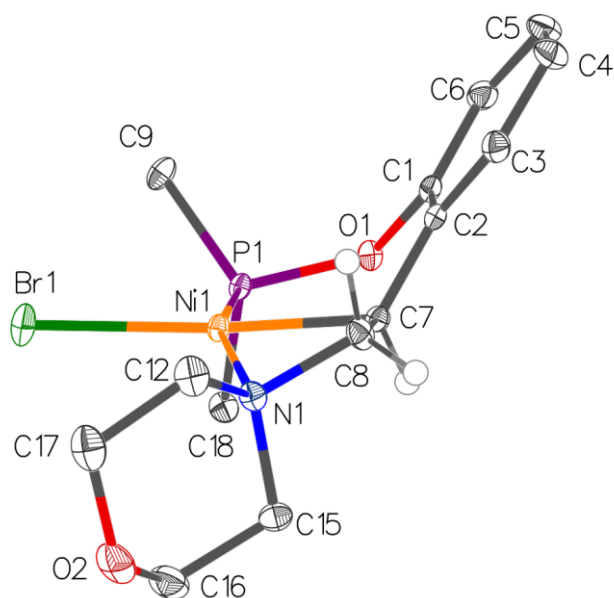
Figure S5.132: Side view of the molecular diagram of compound **4**. Thermal ellipsoids are shown at the 50% probability level; hydrogen atoms refined via the riding model and terminal Me substituents of P(i-Pr)$_2$ are omitted for clarity.

Figure S5.133: Side view of the molecular diagram of compound **5** that crystallized as R,R and S,S isomers. Thermal ellipsoids are shown at the 50% probability level; hydrogen atoms refined via the riding model and terminal Me substituents of P(*i*-Pr)$_2$ are omitted for clarity.

Figure S5.134: Top view of the molecular diagram of compound **6** that crystallized as R,R and S,S isomers. Thermal ellipsoids are shown at the 50% probability level; hydrogen atoms refined via the riding model are omitted for clarity.

Figure S5.135: Side view of the molecular diagram of compound **6** that crystallized as R,R and S,S isomers. Thermal ellipsoids are shown at the 50% probability level; hydrogen atoms refined via the riding model and terminal Me substituents of P(*i*-Pr)$_2$ are omitted for clarity.

Figure S5.136: Side view of the molecular diagram of compound **7** that crystallized as R,R and S,S isomers. Thermal ellipsoids are shown at the 50% probability level; hydrogen atoms refined via the riding model and terminal Me substituents of P(*i*-Pr)$_2$ are omitted for clarity.
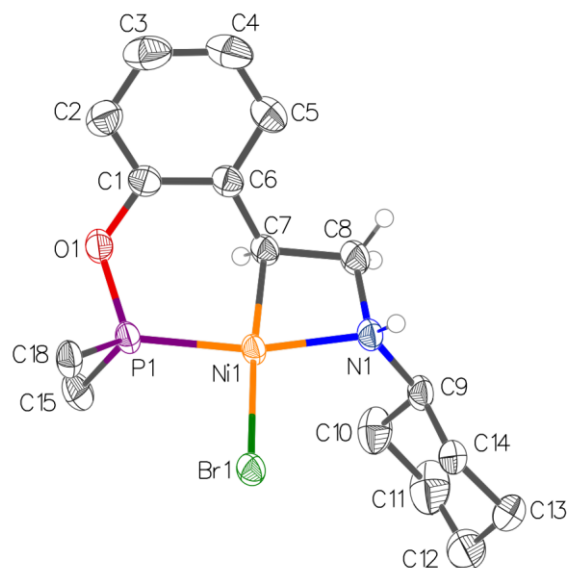
Figure S5.137: Top view of the molecular diagram of compound **8** that crystallized as R,R and S,S isomers. Thermal ellipsoids are shown at the 50% probability level; hydrogen atoms refined via the riding model and terminal Me substituents of P(i-Pr)$_2$ are omitted for clarity.
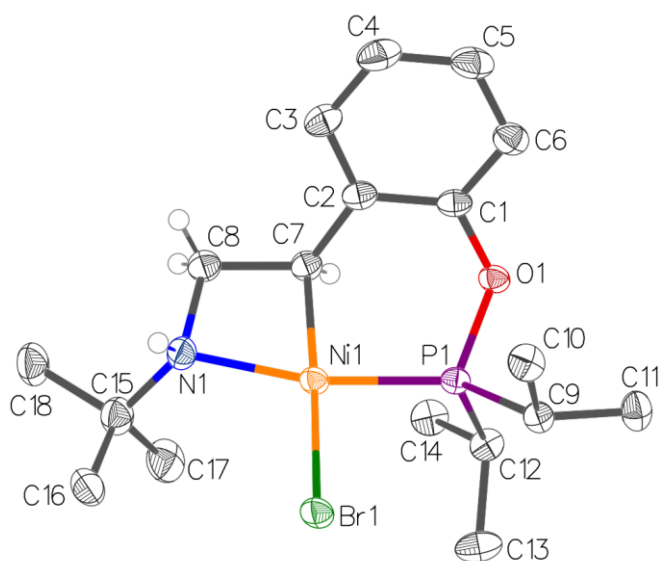
Figure S5.138: Top view of the molecular diagram of compound **9** that crystallized as R,R and S,S isomers. Thermal ellipsoids are shown at the 50% probability level; hydrogen atoms refined via the riding model and terminal Me substituents of P(i-Pr)$_2$ are omitted for clarity.
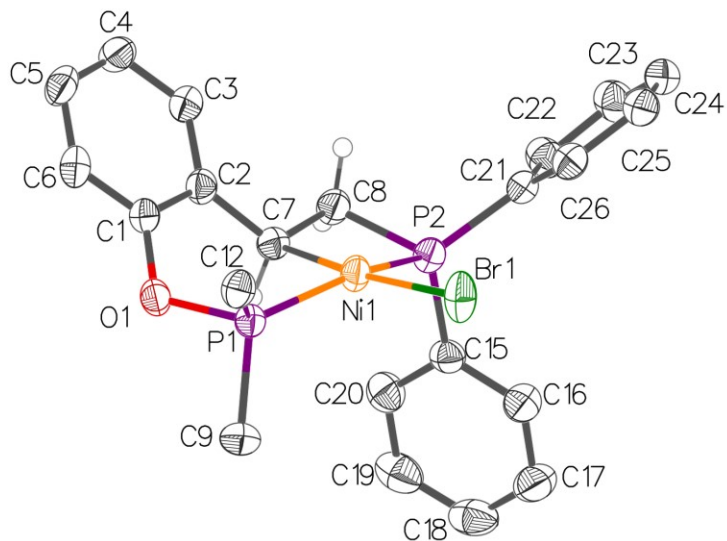
Figure S5.139: Side view of the molecular diagram of compound **10**. Thermal ellipsoids are shown at the 50% probability level; hydrogen atoms refined via the riding model and terminal Me substituents of P(*i*-Pr)$_2$ are omitted for clarity.
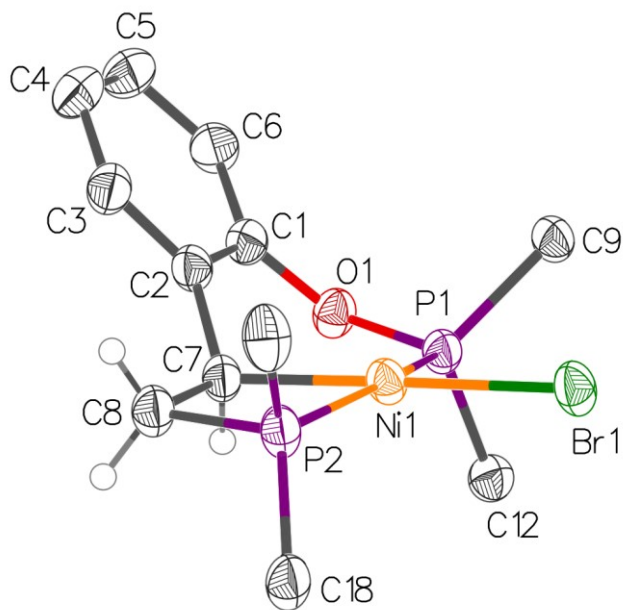
Figure S5.140: Side view of the molecular diagram of compound **11**. Thermal ellipsoids are shown at the 50% probability level; hydrogen atoms refined via the riding model and terminal Me substituents of P(i-Pr)2 are omitted for clarity.
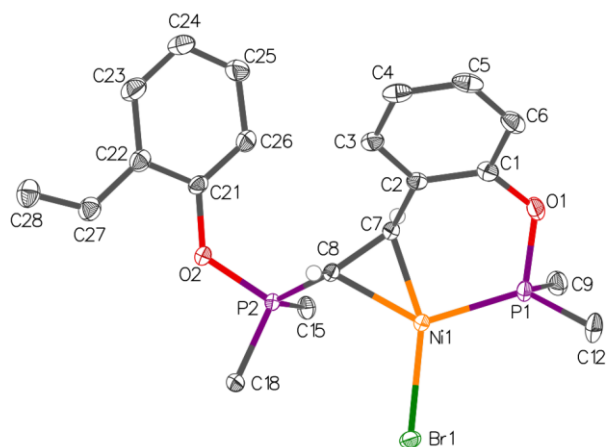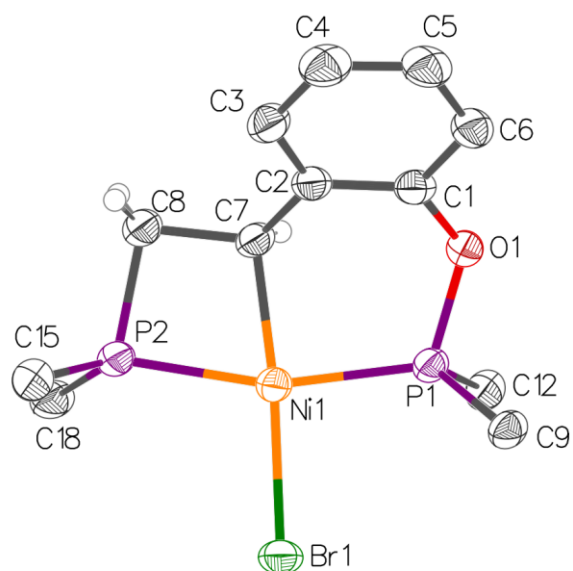
Figure S5.141: Top view of the molecular diagram of compound **11**. Thermal ellipsoids are shown at the 50% probability level; hydrogen atoms refined via the riding model and terminal Me substituents of P(i-Pr)$_2$ are omitted for clarity.
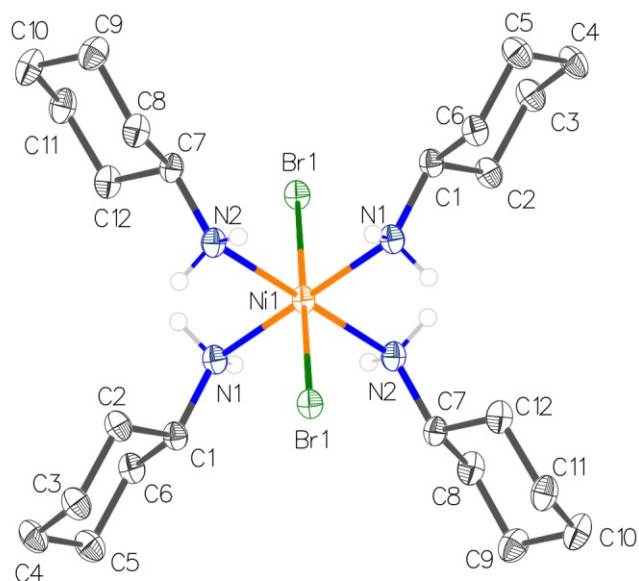
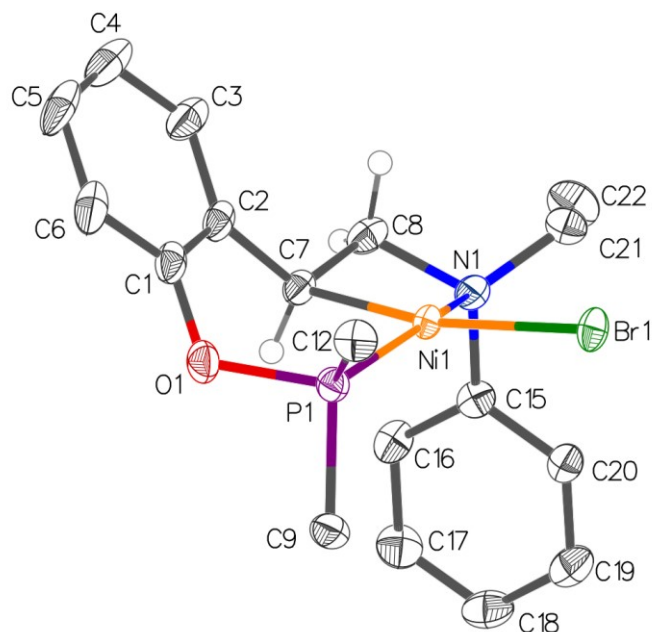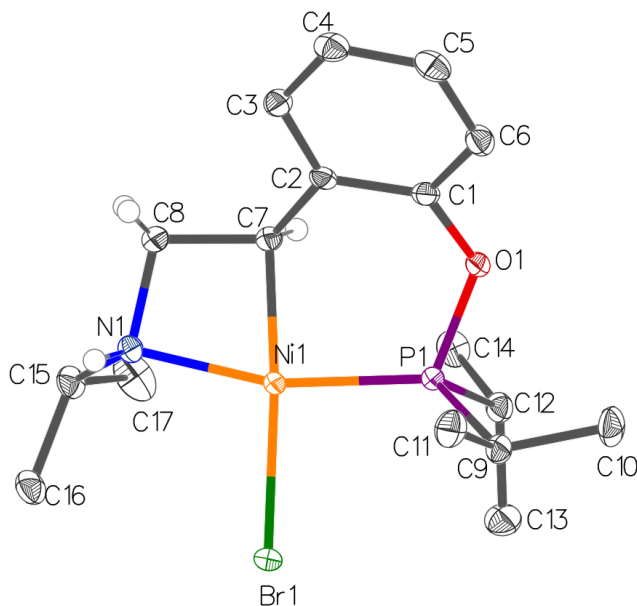Figure S5.142: Molecular diagram of (CyNH$_2$)$_4$NiBr$_2$. Thermal ellipsoids are shown at the 50% probability level; hydrogen atoms refined via the riding model are omitted for clarity.

# Chapitre 6 – Résultats additionnels préliminaires

Ce chapitre présente des résultats additionnels acquis au laboratoire durant mon doctorat : ces résultats sont très préliminaires mails ils permettent d'ouvrir des perspectives sur les projets présentés aux chapitres précédents. Ainsi, bien que les procédés de synthèse n'aient pas été optimisés et que les caractérisations soient incomplètes, l'identification des produits par simple RMN ^{31}P, par l'obtention de cristaux ou par détection GC-MS atteste des réactivités présentées en s'appuyant sur les preuves dévoilées aux Chapitres 2–5.

6.1 Cyclométallation du ligand 3,5-Me$_2$-C$_6$H$_3$-OP(i-Pr)$_2$

Le Chapitre 2 a démontré que lorsqu'une position *ortho* C-H est encombrée par un substituant, la cyclonickellation des arylphosphinites est possible jusqu'à une certaine limite de taille du substituant voisin. Ainsi, dans les conditions standard (1,2 equiv Et$_3$N, 1,2 equiv [(i-PrCN)NiBr$_2$]$_n$, MeCN, 80 °C), le ligand 3,5-Me$_2$-C$_6$H$_3$OP(i-Pr)$_2$ (**1a**) n'a démontré aucun signe de métallation, même après 3 jours de réaction. Cependant, les conditions plus rudes proposées au Chapitre 4 (à 160 °C) permettaient d'accélérer considérablement la cyclonickellation. En appliquant cette nouvelle procédure, le ligand **1** a démontré des signes de métallation très encourageants : après un chauffage de seulement 30 minutes à 160 °C, un singulet à 192 ppm apparait comme majeur et témoigne de la nickellation (**Fig. 6.1**), bien que la réaction ne soit pas complète (pic mineur à 135 ppm).

Ceci prouve que les limitations stériques peuvent être aisément surpassées par des conditions plus rudes, et montre également que le complexe hypothétique **1b-NCMe** est stable à haute températures. Bien que la structure de l'adduit d'acétonitrile ou de son dimère hypothétique correspondant, **1b**, n'ait été isolée, on peut imaginer qu'il y aura une distorsion significative autour du centre métallique. L'affaiblissement de la liaison C-Ni dans un tel composé devrait entrainer une plus grande réactivité (augmentation de l'énergie interne du réactif), ce qui pourrait constituer un modèle d'étude pour la fonctionnalisation du lien C-Ni.
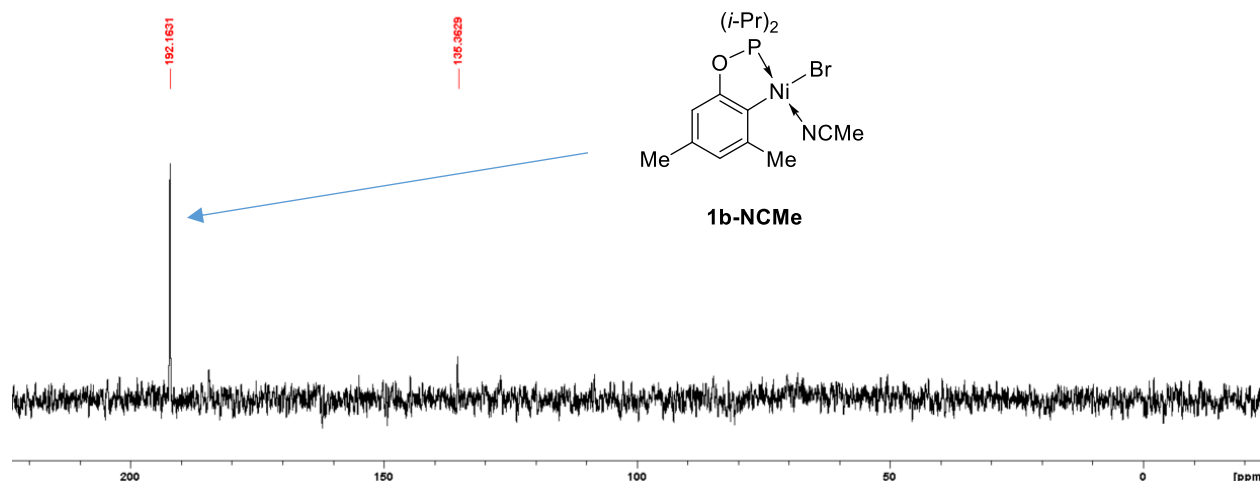
Figure 6.1. RMN ^{31}P du mélange brut la cyclonickellation du ligand **1a** après 30 minutes à 160 °C.

6.2 Métallation des liens carbone-halogène

Au cours de nos études sur la régiosélectivité de la nickellation (Chapitre 2), la réactivité des phosphinites portant un ou deux substituants méthyle en position *ortho* a été étudiée. Dans le cas de mono-substitution, la préférence est allée, telle qu'attendue, vers la position *ortho* C-H non substituée, alors que dans le cas de la di-substitution (aucun lien *ortho* C-H disponible), aucune réactivité n'a malheureusement été observée. La réactivité attendue était alors soit la nickellation C_{sp^2}-H du substituant Me, ou encore la nickellation par bris du lien C_{sp^2}-C_{sp^3}, les deux réactivités ayant été observées dans les systèmes pinceurs PCP de rhodium présentés par le groupe de D. Milstein.[1] Notre regard s'est alors porté vers des phosphinites mono- ou di-substitués par le brome, les liens C-Br étant généralement thermodynamiquement et cinétiquement plus faciles à briser que les liens C-C ou C-H.

Ainsi, la phosphinite dérivée du 2-bromophénol (**2a**) a été soumise aux conditions de cyclonickellation standard (1,2 equiv Et$_3$N, 1,2 equiv [(*i*-PrCN)NiBr$_2$]$_n$, MeCN, 80 °C). Après 20 h, le suivi RMN ^{31}P a démontré que le produit de départ a disparu laissant place, cette fois, à deux singulets à 197.1 et 196.8 ppm, dans la région correspondant aux phosphinites cyclonickellées (**Fig. 6.2**). Le signal à plus haut champ est trouvé comme majeur, avec un ratio de 2:1 par rapport au signal à plus bas champ. Ce dernier est identifié comme le produit de cyclonickellation de la

phosphinite PhOP(*i*-Pr)$_2$ sous forme de l'adduit d'acétonitrile, **2c-NCMe**[2] (présenté au Chapitre 2) et dont le dimère correspondant **2c** était également connu.
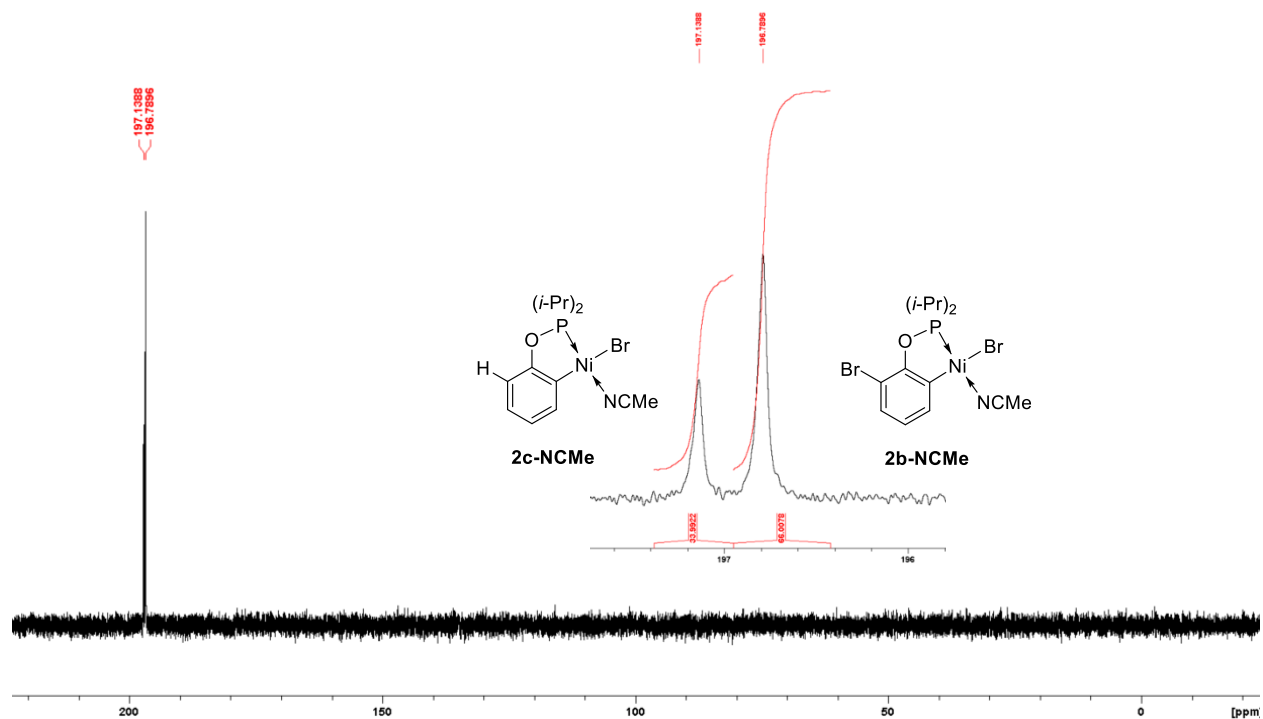
Figure 6.2. RMN ^{31}P du mélange brut de la cyclonickellation pour le ligand **2a** dans les MeCN à 80°C après 20 h.

Ce résultat indique que la réaction du ligand **2a** a mené à une compétition entre le bris des liens C-H et C-Br, à des vitesse réactionnelles semblables, bien que la nickellation C-H ait été légèrement favorisée (**Schéma 6.1**). La preuve de cette dernière est d'ailleurs apportée par l'obtention de cristaux, après *workup*, du produit de cyclonickellation C-H sous forme de l'adduit d'acétonitrile **2b-NCMe** (**Fig. 6.3**).

Schéma 6.1. Compétition entre la nickellation du lien C-H et du lien C-Br pour le ligand **2a**.
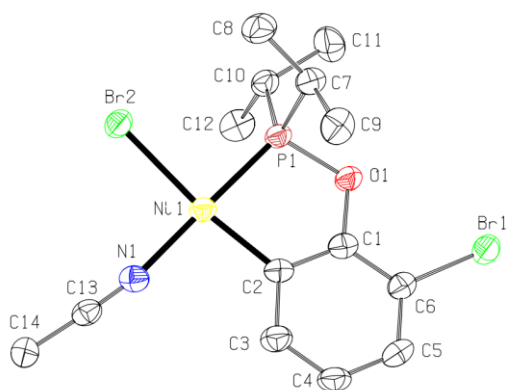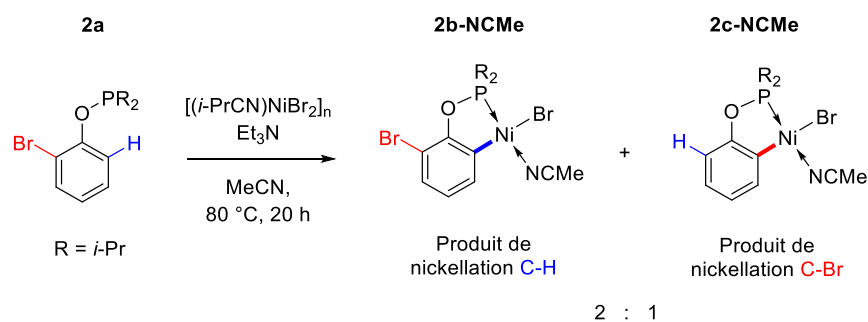
Figure 6.3. Diagramme moléculaire du composé **2b-NCMe**. Les ellipsoïdes thermiques sont montrées avec une probabilité de 50%; les atomes d'hydrogène sont cachés pour plus de clarté.

Nous avons par la suite testé la réactivité de la phosphinite **3a**, issue du 2,4,6-tribromophénol, afin de ne permettre que l'activation ortho d'un lien C-Br. En principe, la métallation d'un tel lien, ne nécessite pas la présence de base de Brønsted car elle ne génère pas de proton; à la place, la réaction formelle devrait générer du dibrome, selon l'équation 1.

$$C\text{-}Br \ + \ NiBr_2 \ \rightarrow \ C\text{-}Ni\text{-}Br \ + \ Br_2 \qquad (Eq.\ 1)$$

Étonnamment, lorsque **3a** est chauffée avec 1.2 equiv précurseur de nickel dans l'acétonitrile à 80 °C en l'absence de Et$_3$N, aucune réactivité (*i.e.* aucun signal dans la région 190-200 ppm) n'est observée après 20 h. La RMN ^{31}P du mélange réactionnel est alors dominée par un singulet à 135 ppm (attribué au matériel non réagi (**3a**)$_2$NiBr$_2$, **Fig. S6.12**), et deux signaux mineurs vers 100 ppm sont observés. Cependant, lorsque 2 equiv Et$_3$N sont ajoutés au milieu suivi d'un chauffage à 80

°C pendant 20 h, le produit de départ et les résonances autour de 100 ppm disparaissent totalement, pour laisser place à un seul signal à 197 ppm (**Fig. 6.4**, **Schéma 6.2**), indiquant une cyclonickellation fructueuse (**3b-NCMe**). L'identité du produit comme étant le composé de nickellation C-Br est par ailleurs confirmée par l'obtention de cristaux du dimère correspondant, **3b**.
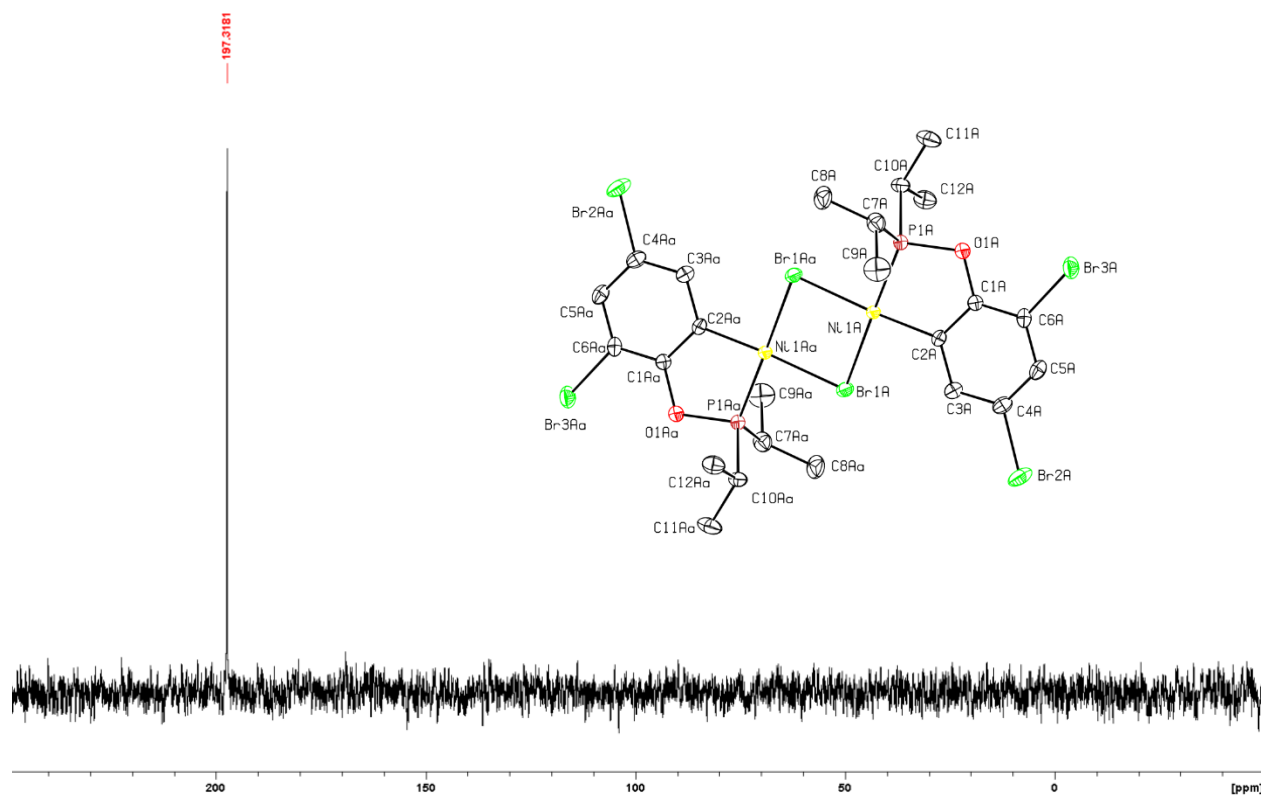
**Figure 6.4.** RMN ^{31}P du mélange brut de la cyclonickellation pour le ligand **3a**, après l'ajout de base, et diagramme moléculaire du dimère **3b**. Les ellipsoïdes thermiques sont montrées avec une probabilité de 50%; les atomes d'hydrogène sont cachés pour plus de clarté.

Schéma 6.2. La cyclonickellation par métallation C-Br du ligand **3a** requiert la présence d'une base.
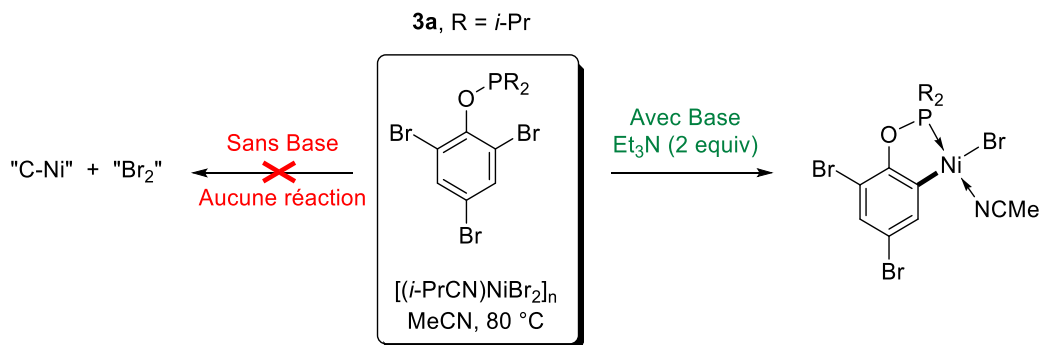
Cette réaction nécessitant un chauffage, tout comme pour la cyclonickellation des phosphinites par métallation C-H, nous nous sommes tournés vers le système pinceur correspondant, qui mène aux composés (POCOP)NiX rapidement à température ambiante en partant du proligand POC(H)OP. Afin de tester la facilité de la réaction de métallation des liens carbone-halogène, le proligand **4a** substitué par un iode en position 2, POC(I)OP, a été préparé : avant que les stratégies de métallation directe C-H dominent la préparation des *pincer*, ces complexes métalliques étaient généralement préparés par addition oxydante C-X sur des métaux de basse valence (Ni^0, Rh^I, Ir^I *etc.*).

Lorsque le ligand **4a** est réagi dans le THF à 60 °C avec le précurseur [(*i*-PrCN)NiBr$_2$]$_n$, le produit de départ disparait totalement après 1 h. Deux singulets sont alors apparus à 186 et 192 ppm, correspondant respectivement aux complexes (POCOP)NiBr et (POCOP)NiI, en un ratio de 1.3:1, légèrement en faveur du NiBr (**Fig. 6.5**). Cette fois ci, la réaction fonctionne proprement en l'absence de base, et ce même à température ambiante (bien que requérant un temps > 6 h). Avec le précurseur (dme)NiCl$_2$, la nickellation s'est montrée tout autant efficace, et mène encore une fois à un ratio d'environ 1:1 pour les complexes (POCOP)NiCl et (POCOP)NiI.
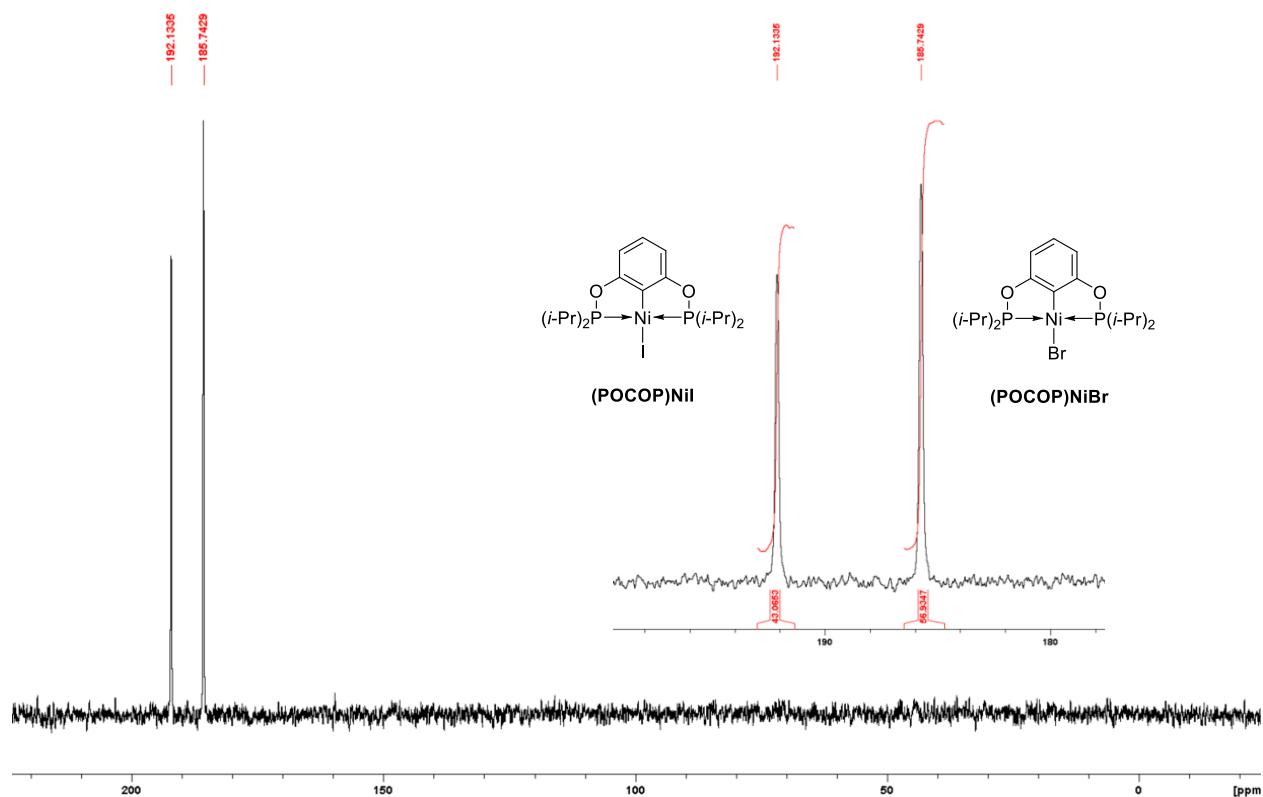
Figure 6.5. RMN ^{31}P du mélange brut de la nickellation pour le ligand **4a** avec le précurseur [(*i*-PrCN)NiBr$_2$]$_n$ dans le THF.

Afin d'investiguer un peu plus dans le mécanisme, et d'en comprendre où le dihalogène généré par la métallation C-X se retrouve, le proligand **4a** a été réagi avec le précurseur (Ph$_3$P)$_2$Ni(Ar)(Br). Cette fois ci, la réaction dans le THF à 60 °C est légèrement moins propre, mais elle mène toujours à l'obtention des complexes (POCOP)NiBr et (POCOP)NiI, cette fois en un ratio d'environ 1:2, alors que le composé (POCOP)Ni(Ph), attendu à 187 ppm,[3] n'est pas observé (**Fig. 6.6**).
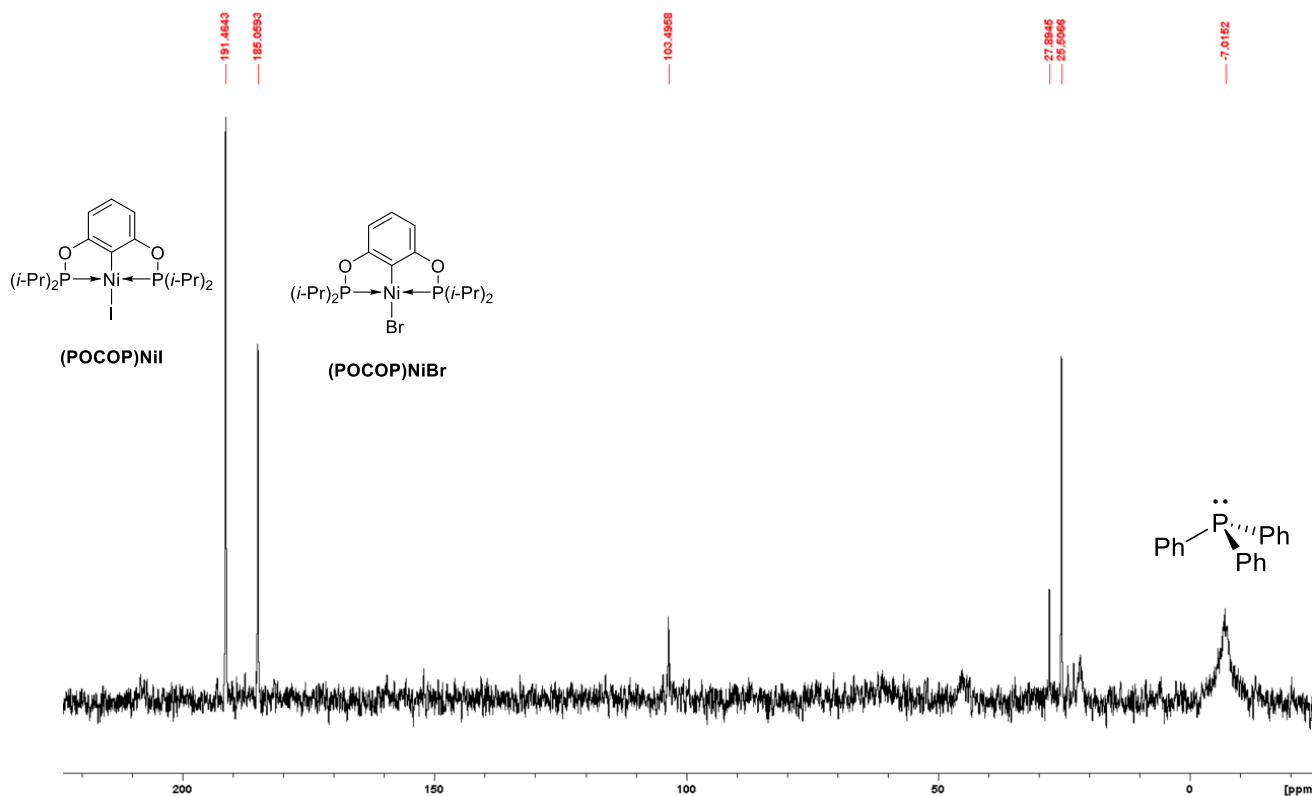
Figure 6.6. RMN ^{31}P du mélange brut de la nickellation pour le ligand **4a** avec le précurseur (Ph$_3$P)$_2$Ni(Ph)(Br) dans le THF.

L'analyse GC-MS du mélange réactionnel (**Fig. S6.16**) montre la présence de PhBr et de PhI, qui semble indiquer que la métallation C-X sur le centre Ni^{II} passe probablement par des espèces de haute valence (*i.e.* Ni^{III} ou Ni^{IV}), lesquelles sont connues pour leur compétence dans le couplage carbone-hétéroatome/halogène[4] (**Schéma 6.3**). La détection de biphényle, obtenu par homocouplage, indique également que des espèces radicalaires sont impliquées dans le mécanisme global, soit pour l'oxydation du centre métallique, soit pour sa réduction, ou pour les deux.

Schéma 6.3. Réaction du proligand **4a** avec le précurseur (Ph$_3$P)$_2$Ni(Ar)(Br).
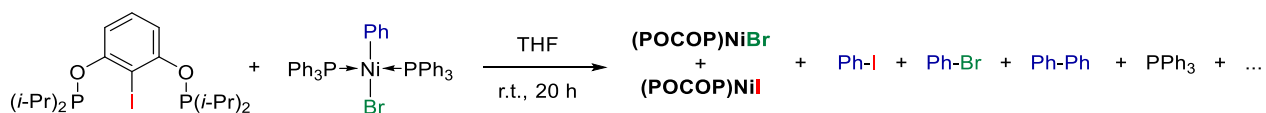
6.3 Fonctionnalisation des liens C-Ni dans les espèces cyclonickellées

Le Chapitre 4 a dévoilé un exemple de la fonctionnalisation du lien C-Ni dans les phosphinites cyclonickellées, par réaction avec BrP(i-Pr)$_2$ formée in situ, et qui mène à l'insertion formelle du phospènium [i-Pr$_2$P]$^+$ dans le lien carbone-nickel. Cette réaction nécessite l'usage d'une haute température (160 °C) afin de convertir la phosphinite en chlorophosphine (Eq. 2, R = i-Pr) à une vitesse suffisante pour permettre la réaction d'insertion.

$$ArO\text{-}PR_2 \; + \; HBr \; \rightleftharpoons \; ArOH \; + \; BrPR_2 \qquad (Eq.\ 2)$$
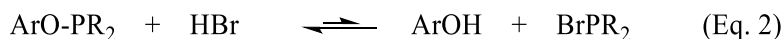
Lors de mon doctorat, j'ai été amené à étudier la cyclonickellation des diphényl-phosphinites, en particulier celle de PhOPPh$_2$ (**5a**) comme modèle de travail. Dans les conditions classiques, nous n'avons jamais été capable d'isoler le produit cyclonickellé, et le suivi RMN ^{31}P des réactions offrait un mauvais rapport signal/bruit. Ainsi, l'on distinguait à peine deux signaux vers 145 et 20 ppm (**Fig. 6.7**), mais l'obtention de cristaux a permis d'identifier cette espèce comme étant le complexe du ligand bidenté phosphine-phosphinite (**5b-PPh$_2$**), *i.e.* formellement le produit d'insertion du phosphènium [Ph$_2$P]$^+$ dans le lien C-Ni de la diphényl-phosphinite cyclonickellée (**Fig. 6.8**). Le fait que cette réaction se produise à 80 °C et que le composé cyclométallé ne soit pas détecté comme intermédiaire suggère que ce dernier est plus réactif ou que l'échange entre avec HBr (Eq. 2, R = Ph) est rapide, en contraste à ce qui est observé avec les diisopropyl-phosphinites.
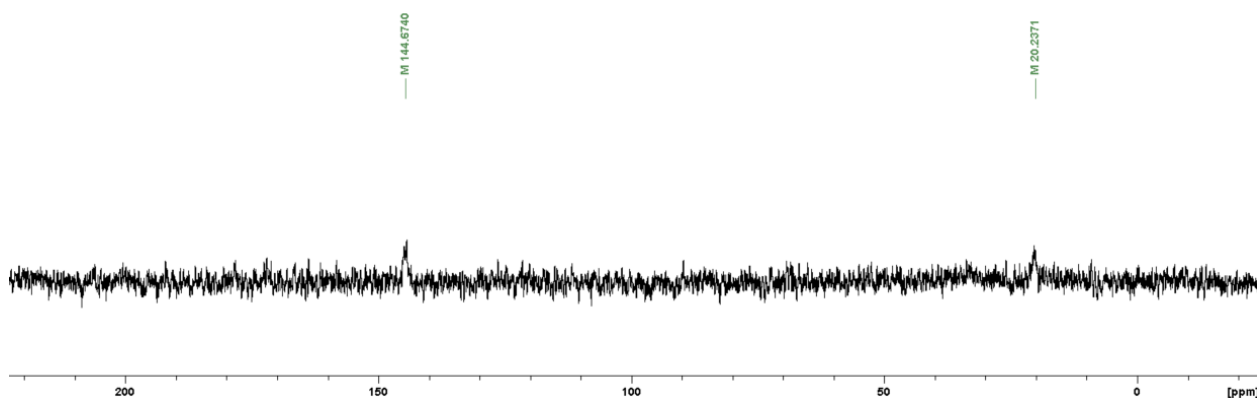
Figure 6.7. RMN ^{31}P du mélange brut de la cyclonickellation pour le ligand **5a** dans les conditions normales.
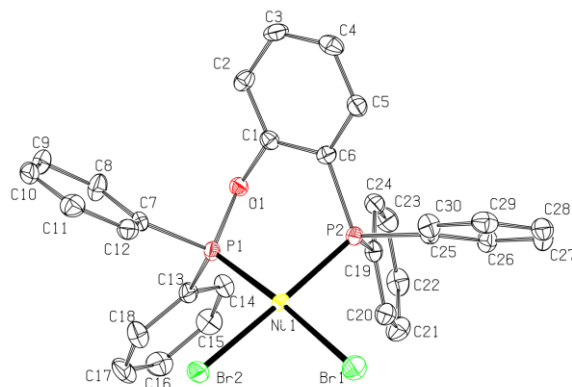
Figure 6.8. Diagramme moléculaire du composé **5b-PPh₂**. Les ellipsoïdes thermiques sont montrées avec une probabilité de 50%; les atomes d'hydrogène sont cachés pour plus de clarté.

Ainsi, nous avons pu montrer, à l'instar de ce qui est présenté au Chapitre 4, que les diisopropyl-phosphinites cyclonickellées pouvaient mener également à l'insertion formelle de [Ph₂P]⁺ dans leur lien carbone nickel. Lorsque le dimère issu de PhOP(*i*-Pr)₂ est chauffé en présence de ClPPh₂ pendant 24 h, la RMN ³¹P montre 4 sets de doublets AB d'intensités semblables vers 170-180 ppm et 10-20 ppm avec des constantes $^2J_{PP'}$ de l'ordre de 60-70 Hz, caractéristique des couplages pour les ligands phosphorés *cis* (**Fig. S6.13**). Ceci indique la formation d'un nouveau ligand bidenté triarlyphosphine-dialkylphosphinite lié au nickel, les 4 différents sets de doublets correspondant aux 4 combinaisons Ni(Br)(Br), Ni(Br)(Cl), Ni(Cl)(Br) et Ni(Cl)(Cl) (halogènes *cis* ou *trans* par rapport à l'un ou l'autre des phhosphores). L'identité de ce nouveau composé a été confirmée par diffraction des rayons X, où le fragment NiX₂ possède un désordre d'identité pour X = Br ou Cl, indiquant que les 4 complexes sont isostructuraux et co-cristallisent tous ensemble (**Fig. 6.9**).
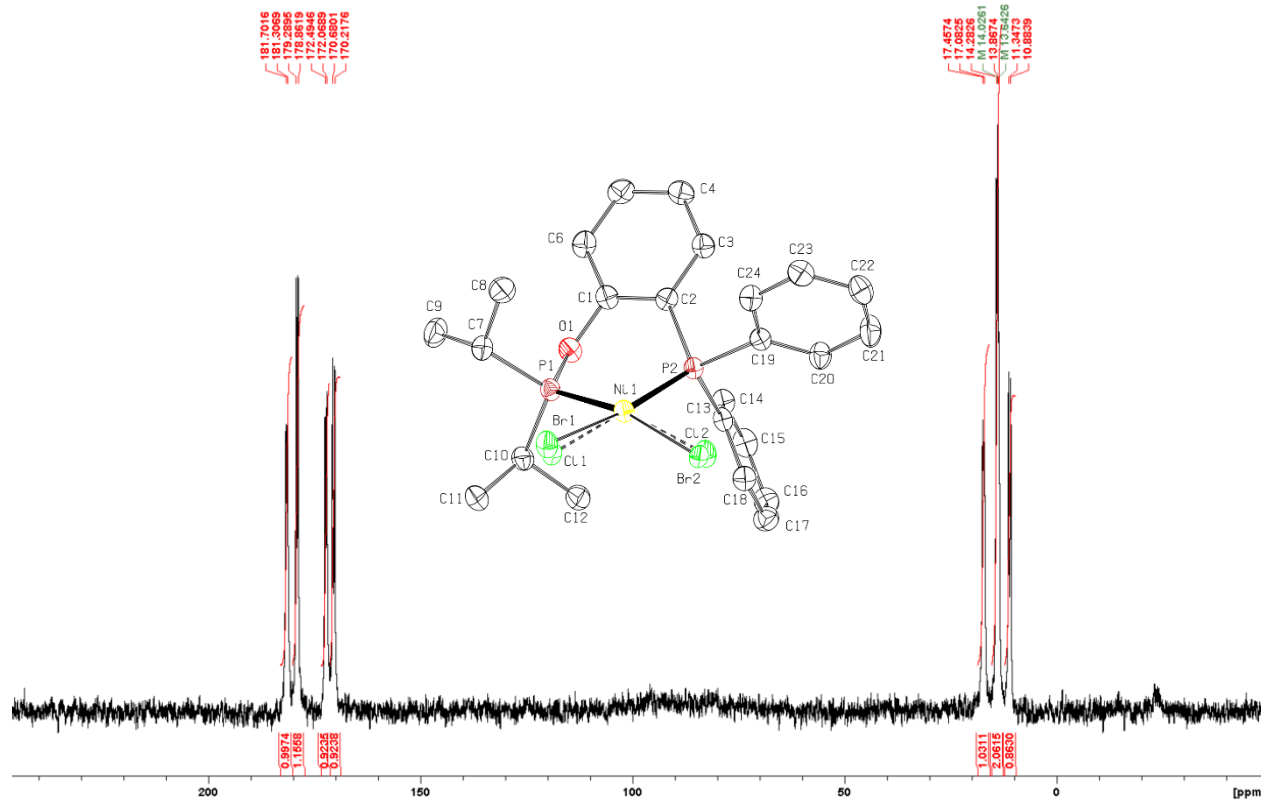
Figure 6.9. RMN ^{31}P du mélange brut de la réaction entre le dimère **3c** et Ph₂PCl, et diagramme moléculaire du composé **3c-PPh₂**. Les ellipsoïdes thermiques sont montrées avec une probabilité de 50%; les atomes d'hydrogène sont cachés pour plus de clarté.

Durant mon doctorat, j'ai effectué plusieurs essais de fonctionnalisation des liens C-H avec des composés neutres (alcènes, alcynes, CO *etc.*), avec des nucléophiles (R-MX$_n$, R-BX$_n$, R₂NH, CN⁻ *etc.*) ou avec des électrophiles ([R4N]X, R₂CO *etc.*). La plupart de ces tentatives se sont révélées infructueuses, menant soit à la décomposition du complexe sans que la phosphinite fonctionnalisée ne soit détectée, soit à un manque total de réactivité. Le fait que les halophophsines (ajoutées comme réactifs, ou générées in-situ) aient réagi aussi proprement nous a mené à penser que la coordination de ces dernières au métal était cruciale pour une fonctionnalisation efficace des liens C-Ni. Ainsi, notre regard s'est tourné vers la fonctionnalisation par des électrophiles capables de se coordonner, en l'occurrence des amines portant un groupe partant. Nous avons donc préparé le composé Et₂N-OTs, qui peut être vu comme la combinaison de l'anion tosylate et du nitrènium [Et₂N]⁺, lequel est isolobal aux phosphèniums et devrait avoir un potentiel d'insertion dans les liens C-Ni.

Lorsque le dimère issu de PhPO(*i*-Pr)$_2$ (**2c**) est réagi avec 2 equiv N-tosyloxy-diéthylamine dans le toluène à température ambiante, le signal du composé cyclonickellé (à 197 ppm) disparait totalement après 20 h. En fait, la RMN ^{31}P du mélange devient silencieuse, indiquant la transformation en une espèce paramagnétique : on propose que ce serait le complexe [κ^N,κ^P-2-Et$_2$N-C$_6$H$_4$-OP(*i*-Pr)$_2$]NiX$_2$ (X = Br ou OTs) issu de l'insertion de [Et$_2$N]$^+$ dans le lien carbone-nickel. Cette proposition est supportée par la préparation indépendante du ligand 2-Me$_2$N-C$_6$H$_4$-OP(*i*-Pr)$_2$ par mon stagiaire Xuecong Li, et la réaction du composé de NiBr$_2$ correspondant qui est paramagnétique et présente une structure tétraédrique en phase solide (**Fig. 6.10**).
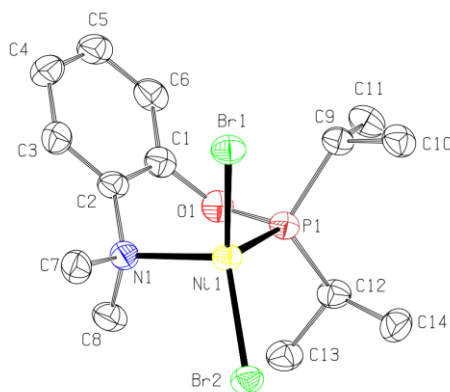
Figure 6.10. Diagramme moléculaire du composé **[κ^N,κ^P-2-Me$_2$N-C$_6$H$_4$-OP(*i*-Pr)$_2$]NiBr$_2$**. Les ellipsoïdes thermiques sont montrées avec une probabilité de 50%; les atomes d'hydrogène sont cachés pour plus de clarté.

Après réaction du dimère **2c** avec Et$_2$NOTs, un workup dans H$_2$O à l'air ambiant a été réalisé, suivi d'une extraction a l'acétate d'éthyle. L'analyse GC-MS de la phase organique (**Fig S6.22**) a permis de détecter des produits de fonctionnalisation sous forme du phénol 2-Et$_2$N-C$_6$H$_4$OH ou du ligand fonctionnalisé et oxydé 2-Et$_2$N-C$_6$H$_4$OP(O)(*i*-Pr)$_2$ (**Schéma 6.4**).

Schéma 6.4. Mécanisme propose pour la fonctionnalisation du lien C-Ni par le réactif Et$_2$NOTs.
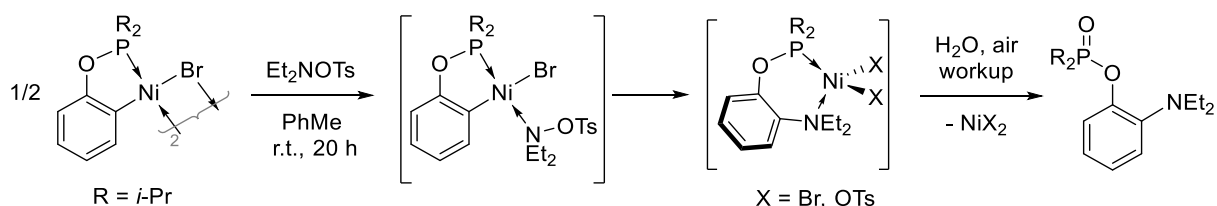
La réaction est toutefois incomplète (détection du ligand non fonctionnalisé et oxydé), et semble donner des sous-produits (détection de composés non identifiés), mais il est encourageant de voir que la réaction est possible à température ambiante. Il faut noter également que la préparation de Et$_2$N-OTs est assez difficile dû à la sensibilité de ce composé à la chaleur et à la lumière : bien que la réaction ait été conduite à l'abri de la lumière, un mécanisme radicalaire impliquant le bris homolytique du lien N-O ne peut pas définitivement être exclus.

6.4 Stabilité des composés 6,4-POCN-NiBr

Les nouveaux composés pinceurs présentés au Chapitre 5 sont produits par une réaction de « couplage » entre la 2-vinyl-phénylphosphinite qui sert d'électrophile, et une amine ou une phosphine comme nucléophile (NuH). Par protonation du lien C-Ni, on devrait obtenir un nouveau proligand du type 2-(Nu-CH$_2$CH$_2$)-C$_6$H$_4$-OP(*i*-Pr)$_2$ qui pourrait servir à préparer des composés pinceurs de divers métaux de transition portant le même squelette POCNu-MX$_n$. Formellement, la réaction est une hydro-amination ou -phosphination du groupe vinyle dans la phosphinit, et dans une optique de rendre cette réaction catalytique, il convenait d'étudier si la protonation du lien carbone-nickel est faisable in-situ.

Puisqu'un tel procédé requiert la présence de phénols comme substrat (*i.e.* 2-vinyl-phénol), le premier acide considéré a été le 3-fluorophénol. Lorsque 2 equiv de cet acide faible en sont ajoutés à une solution des 6,4-POCN-NiBr (N = morpholyl ou CyN(H)), aucun changement dans le spectre RMN ^{31}P n'a été observé après 24 h à température ambiante. Même après chauffage à 80 °C pendant 20 h, aucun signe de décomposition des pinceurs n'a été observé (**Fig. S6.14**). Cela dit, face à un acide organique légèrement plus fort, tel que l'acide 3-chlorobenzoïque, le lien C-Ni se protone à température ambiante (**Schéma 6.5**), et le signal du composé *pincer* disparait au profit d'un signal vers 148 ppm, indiquant une phosphinite libre (**Fig. S6.15**). Ceci contraste avec la stabilité de la plupart des composés pinceurs 5,5 de nickel, et laisse entrevoir que les composés présentés au Chapitre 5 ont une plateforme où la réactivité peut être centrée sur le ligand.

Schéma 6.5. Stabilité des complexes 6,4-POCN-NiBr face à divers acides.
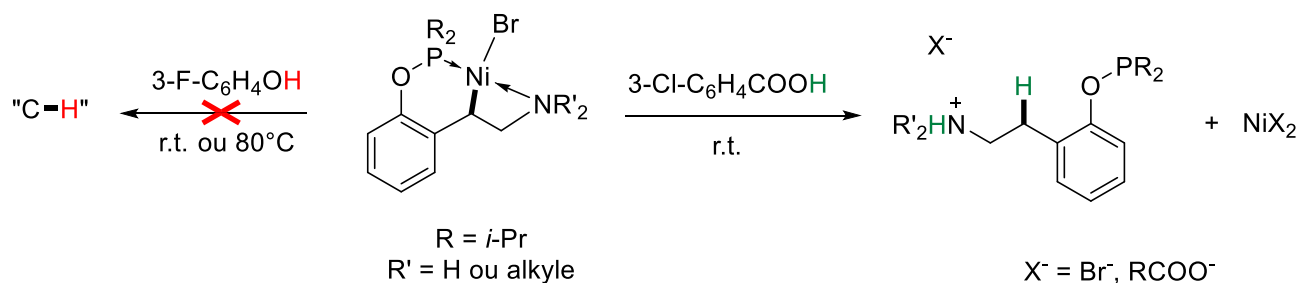
6.5 Partie expérimentale

Considérations générales. Toutes les manipulations ont été réalisées sous atmosphère d'azote via les techniques standard de Schlenk et de boite à gants. Les solvants ont été séchés par un passage à travers des colonnes d'alumine activée et stockés sur des tamis moléculaires 3 Å dans des Straus flasks. La triethylamine a été séchée par distillation sur CaH₂. Le nickel, [(*i*-PrCN)NiBr₂]ₙ a été synthétisé selon une procédure épouvée,[5] et la phosphination des alcools aromatiques a été réalisée selon le même protocole décrit aux Chapitres 2-5. Le précurseur (Ph₃P)₂Ni(Ar)(Br) a été préparé selon une procédure connue.[6] Tous les autres réactifs ont été achetés de Sigma-Aldrich ou FisherSci, et ont été utilisés tel quels. La précision minimale des spectres RMN ^{1}H est de 0.3 Hz.

3,5-Me₂-C₆H₃OP(*i*-Pr)₂ (1a). Préparé à partir de 5.0 mmol 3,5-diméthylphénol pour donner une huile jaune pâle. Rendement : 726 mg (61%) qui contiennent < 5% d'oxydes comme impuretés. RMN ^{1}H (400 MHz, 20 °C, CDCl₃): δ 1.09 (dd, 6 H, PCH(C*H₃*)(CH₃), $^3J_{HH}$ = 7.3, $^3J_{HP}$ = 15.9), 1.16 (dd, 6H, PCH(CH₃)(C*H₃*), $^3J_{HH}$ = 7.0, $^3J_{HP}$ = 10.8), 1.91 (heptd, 2H, PC*H*(CH₃)₂, $^3J_{HH}$ = 7.2, $^2J_{HP}$ = 2.1), 2.27 (d, 6H, Ar-C*H₃*, $^4J_{HH}$ = 0.6), 6.61 (s, 1H, *para*-C$_{Ar}$-*H*), 6.72 (s, 2H, *ortho*-C$_{Ar}$-*H*). RMN ^{31}P (161.98 MHz, 20 °C, CDCl₃): δ 147.84 (s, 1P).

2-Br-C₆H₄OP(*i*-Pr)₂ (2a). Préparé à partir de 4.0 mmol 2-bromophénol pour donner une huile jaune pâle. Rendement : 764 mg (66%) qui contiennent environ < 10% d'oxydes comme impuretés. RMN ^{1}H (400 MHz, 20 °C, CDCl₃): δ 1.11 (dd, 6H, PCH(C*H₃*)(CH₃), $^3J_{HH}$ = 7.2, $^3J_{HP}$ = 15.9), 1.21 (dd, 6H, PCH(CH₃)(C*H₃*), $^3J_{HH}$ = 7.0, $^3J_{HP}$ = 10.9), 1.99 (heptd, 2H, PC*H*(CH₃)₂, $^3J_{HH}$ = 7.1, $^2J_{HP}$ = 3.0), 6.82 (td, 1H, C4$_{Ar}$-*H* ou C5$_{Ar}$-*H*, $^3J_{HH}$ = 7.8, $^4J_{HH}$ = 1.5), 7.21 (td, 1H, C4$_{Ar}$-*H* ou C5$_{Ar}$-

H, $^3J_{HH}$ = 7.4, $^4J_{HH}$ = 1.6), 7.31 (ddd, 1H, C6$_{Ar}$-*H*, $^3J_{HH}$ = 8.2, $^4J_{HP}$ = 3.4, $^4J_{HH}$ = 1.5), 7.49 (dd, 1H, C3$_{Ar}$-*H*, $^3J_{HH}$ = 7.9, $^4J_{HH}$ = 1.5).RMN ^{31}P (161.98 MHz, 20 °C, CDCl$_3$): δ 153.52 (s, 1P).

2,4,6-Br$_3$-C$_6$H$_2$OP(*i*-Pr)$_2$ (3a). Préparé à partir de 5.0 mmol 2,4,6-tribromophénol pour donner une huile incolore très épaisse. Rendement : 2.23 g (79%). RMN ^{1}H (400 MHz, 20 °C, CDCl$_3$): δ 1.17 (dd, 6H, PCH(C*H$_3$*)(CH$_3$), $^3J_{HH}$ = 7.2, $^3J_{HP}$ = 13.8), 1.19 (dd, 6H, PCH(CH$_3$)(C*H$_3$*), $^3J_{HH}$ = 7.1, $^3J_{HP}$ = 12.0), 2.17 (heptd, 2H, PC*H*(CH$_3$)$_2$, $^3J_{HH}$ = 7.1, $^2J_{HP}$ = 3.2), 7.62 (s, 2H, C$_{Ar}$-*H*). RMN ^{31}P (161.98 MHz, 20 °C, CDCl$_3$): δ 173.60 (s, 1P).

2-I-1,6-(*i*-Pr$_2$PO)C$_6$H$_3$ (4a). Le 2-iodorésorcinol a été préparé à partir de résorcinol, de I$_2$ et de NaHCO$_3$ dans l'eau selon une procédure connue[7] dans une rendement de 87%. Le ligand a été préparé à partir de 3.0 mmol de 2-iodorésorcinol. Rendement : 1.18 g (84%). RMN ^{1}H (400 MHz, 20 °C, CDCl$_3$): δ 1.11 (dd, 12H, PCH(C*H$_3$*)(CH$_3$), $^3J_{HH}$ = 7.2, $^3J_{HP}$ = 15.8), 1.21 (dd, 12H, PCH(CH$_3$)(C*H$_3$*), $^3J_{HH}$ = 7.0, $^3J_{HP}$ = 10.9), 1.99 (heptd, 4H, PC*H*(CH$_3$)$_2$, $^3J_{HH}$ = 7.1, $^2J_{HP}$ = 4.0), 6.90 (dd, 2H, *meta*-C$_{Ar}$-*H*, $^3J_{HH}$ = 8.2, $^4J_{HP}$ = 3.4), 6.90 (t, 2H, *para*-C$_{Ar}$-*H*, $^3J_{HH}$ = 8.2). RMN ^{31}P (161.98 MHz, 20 °C, CDCl$_3$): δ 150.03 (s, 1P).

PhOPPh$_2$ (5a). Préparé à partir de 10.0 mmol de phénol, et en remplaçant 1.05 equiv *i*-Pr$_2$PCl par 1.00 equiv Ph$_2$PCl, pour donner une huile incolore. Rendement : 2.43 g (87 %). RMN ^{1}H (400 MHz, 20 °C, CDCl$_3$): δ 7.02 (t, 1H, *para*-C$_{Ar(OP)}$-*H*, $^3J_{HH}$ = 7.3), 7.13 (d, 2H, *ortho*-C$_{Ar(OP)}$-*H*, $^3J_{HH}$ = 8.2), 7.28 (t, 2H, *meta*-C$_{Ar(OP)}$-*H*, $^3J_{HH}$ = 7.7), 7.35-7.45 (m, 6H, *ortho*- et *para*-C$_{Ar(P)}$-*H*), 7.60 (td, (td, 4H, *para*-C$_{Ar(P)}$-*H*, $^3J_{HH}$ = 7.8, $^4J_{HP}$ = 1.8). RMN ^{31}P (161.98 MHz, 20 °C, CDCl$_3$): δ 111.40 (s, 1P).

N-tosyloxy-diéthylamine. Une solution de 2.06 mL N-hydroxy-diéthylamine (20.0 mmol, 1.0 equiv) et de 3.07 mL Et$_3$N (22.0 mmol, 1.1 equiv) dans 25 mL de dichlorométhane est refroidie à –40 °C au bain de MeCN/CO$_2$. Sous agitation, 3.81 g de *p*-TsCl (20.0 mmol, 1.0 equiv) sont ajoutés, et le mélange est laissé doucement revenir à une température de 0 °C sur une période de 3 h. La réaction est neutralisée par l'ajout de 25 mL d'eau glacée, et le tout agité pendant encore 5 min à 0 °C. La phase organique est séparée de la phase aqueuse, et cette dernière est extraite avec encore 2 x 25 mL Et$_2$O froid. Les phase organiques sont combinées, séchées sur MgSO4, évaporées et séchées sous vide. 2.75 g d'une poudre blanc cassé sont obtenus (Rendement : 11.3 mmol, 56%). Le produit est conservé à l'abri de la lumière dans un freezer à –35 °C. RMN ^{1}H (400 MHz, 20 °C, CDCl$_3$): δ 0.89 (t, 6H, N(CH$_2$C*H$_3$*)$_2$, $^3J_{HH}$ = 7.1), 2.45 (s, 3H, Ar-C*H$_3$*), 2.92 (q, 4H,

N(CH_2CH$_3$)$_2$, $^3J_{HH}$ = 7.1), 7.32 (d, 2H, Ar-*H*, *meta* à SO$_2$, $^3J_{HH}$ = 8.3), 7.86 (d, 2H, Ar-*H*, *ortho* à SO$_2$, $^3J_{HH}$ = 8.3).

6.6 Remerciements

Je tiens à remercier M. Mehrban Ashiq pour l'étude de la nickellation de la phosphinite **2a** et M. Xuecong Li pour la préparation du composé [2-Me$_2$N-C$_6$H$_4$-OP(*i*-Pr)$_2$]NiBr, durant leur stage respectif au sein du groupe. Je remercie également Dr. Michel Simard pour avoir résolu le désordre dans la structure du composé **3b**, où l'unité asymétrique contient deux demi-dimères, chacun totalement désordonnés dans une proportion de 0.05:0.95.

6.7 Références

[1] Gandelman, M.; Vigalok, A.; Konstantinovski, L.; Milstein, D., The First Observation and Kinetic Evaluation of a Single Step Metal Insertion into a C−C Bond. *Journal of the American Chemical Society* **2000,** *122* (40), 9848-9849.

[2] Le signal à 197.1 ppm a été identifié comme étant le composé **2c-NCMe** en ajoutant une quantité du dimère **2c** dans le milieu après réaction, menant à l'augmentation de ce signal en RMN ^{31}P (**Fig. S6.11**).

[3] Cao, B.; Ding, Y.; Fang, F.; Chang, J.; Zhang, J.; Li, S.; Chen, X., The stability of group 10 metal POCOP pincer complexes: decomposition/reconstruction pathways of the pincer backbone. *Dalton Transactions* **2019,** *48* (36), 13760-13768.

[4] Cloutier, J.-P.; Zargarian, D., Functionalization of the Aryl Moiety in the Pincer Complex (NCN)Ni^{III}Br$_2$: Insights on Ni^{III}-Promoted Carbon–Heteroatom Coupling. *Organometallics* **2018,** *37* (9), 1446-1455.

[5] (a) Vabre, B.; Spasyuk, D. M.; Zargarian, D., Impact of Backbone Substituents on POCOP-Ni Pincer complexes: A Structural, Spectroscopic and Electrochemical Study, *Organometallics* **2012,** *31* (24), 8561-8570. (b) Vabre, B.; Lindeperg, F.; Zargarian, D., Direct, one-pot synthesis of POCOP-type pincer complexes from metallic nickel, *Green Chemistry* **2013**, *15* (11), 3188-3194.

[6] Smeets, A.; Van den Bergh, K.; De Winter, J.; Gerbaux, P.; Verbiest, T.; Koeckelberghs, G., Incorporation of Different End Groups in Conjugated Polymers Using Functional Nickel Initiators. *Macromolecules* **2009,** *42* (20), 7638-7641.

[7] Greig, L. M.; Slawin, A. M. Z.; Smith, M. H.; Philp, D., The dynamic covalent chemistry of mono- and bifunctional boroxoaromatics. *Tetrahedron* **2007,** *63* (11), 2391-2403.

Chapitre 6 – Annexes

S6.1 Spectres RMN de caractérisation des ligands et de Et₂NOTs
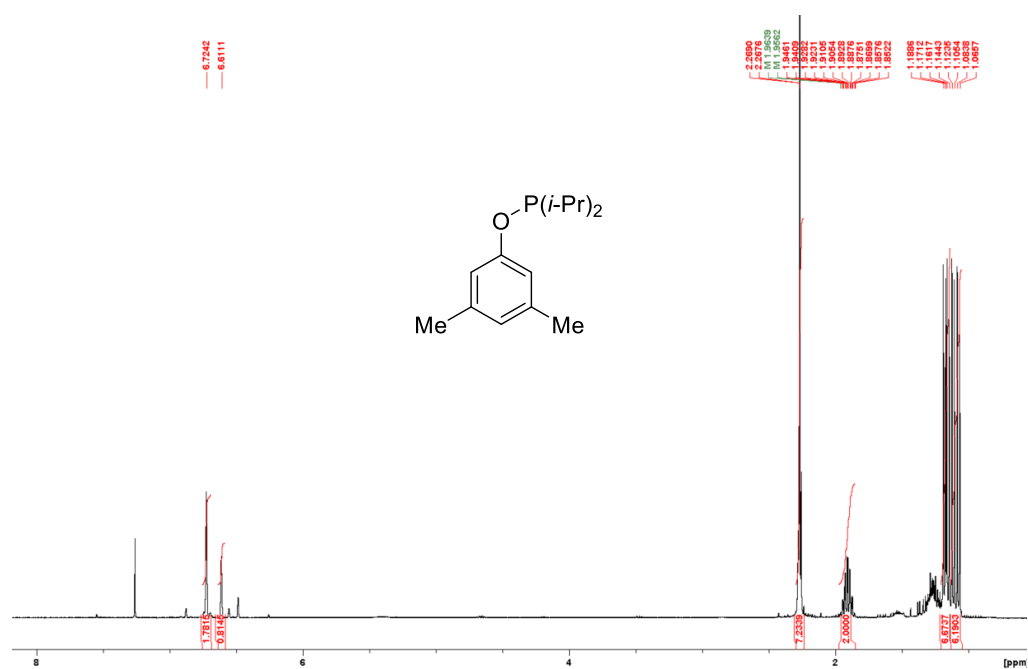
Figure S6.1 : Spectre RMN ^{1}H du ligand **1a** dans CDCl$_3$.
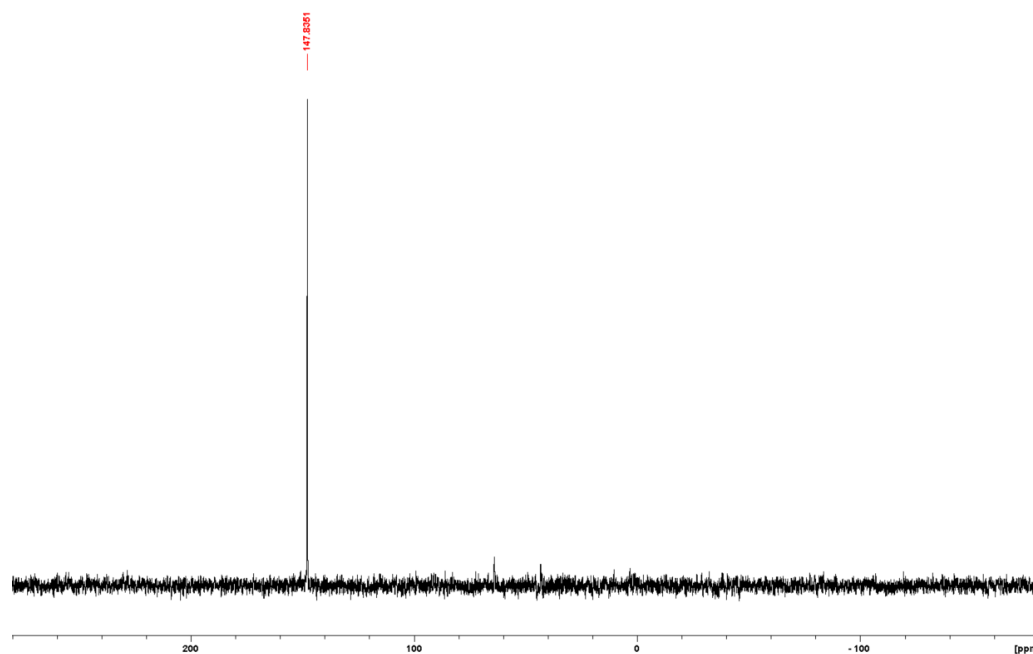
Figure S6.2 : Spectre RMN ^{31}P{^{1}H} du ligand **1a** dans CDCl$_3$.
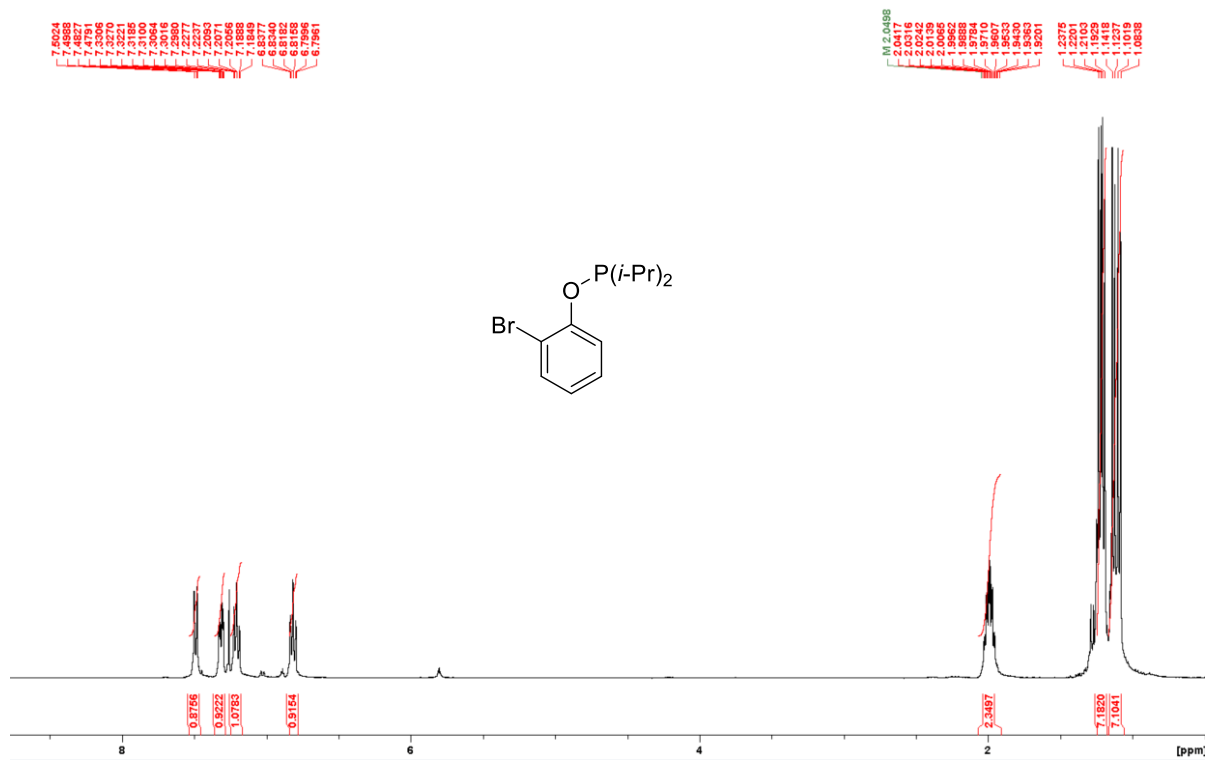
Figure S6.3 : Spectre RMN ^{1}H du ligand **2a** dans CDCl$_3$.
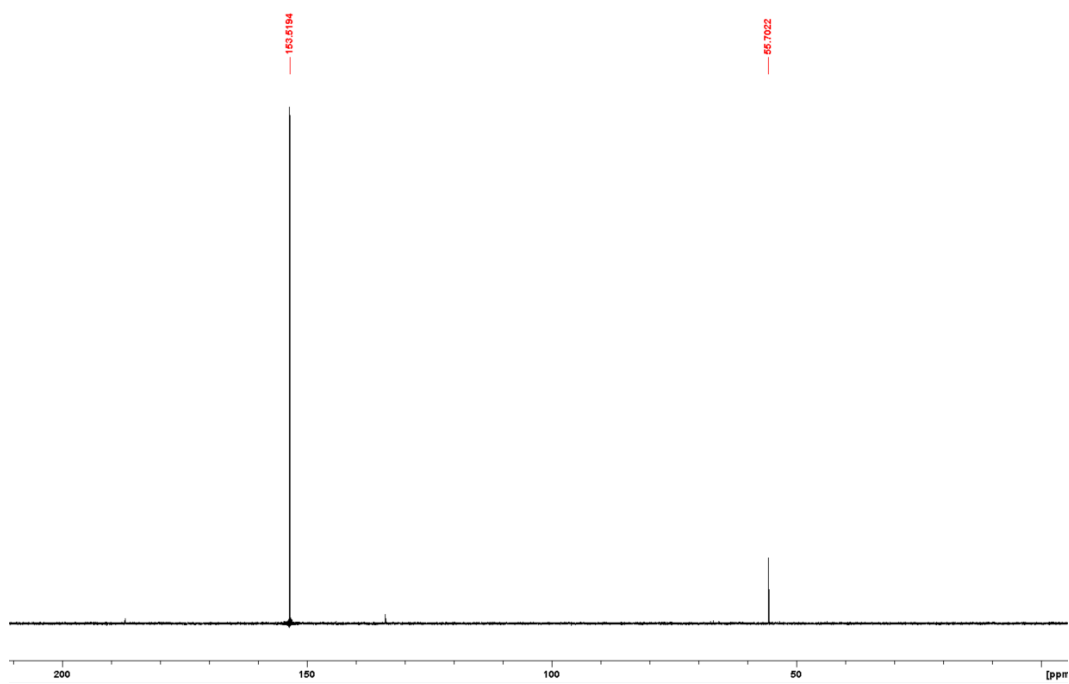
Figure S6.4 : Spectre RMN ^{31}P{^{1}H} du ligand **1b** dans CDCl$_3$.
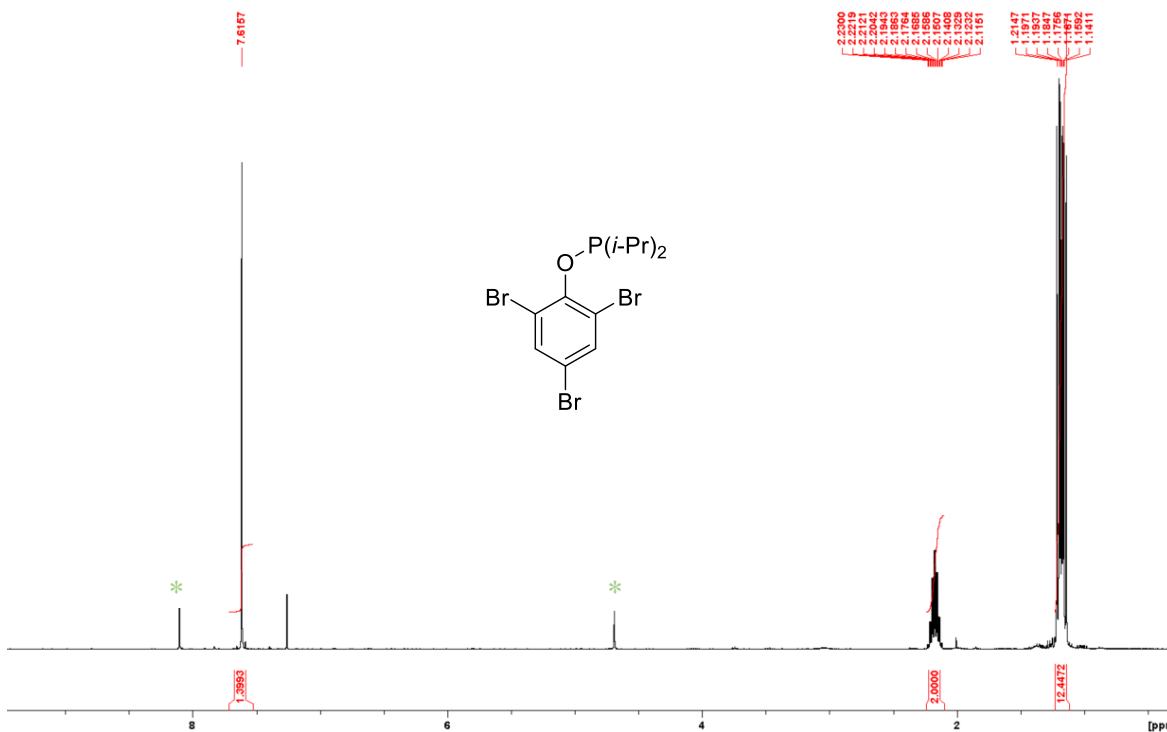
Figure S6.5 : Spectre RMN ^{1}H du ligand **3a** dans CDCl$_3$. *Impuretés contenues dans le solvant deutéré.
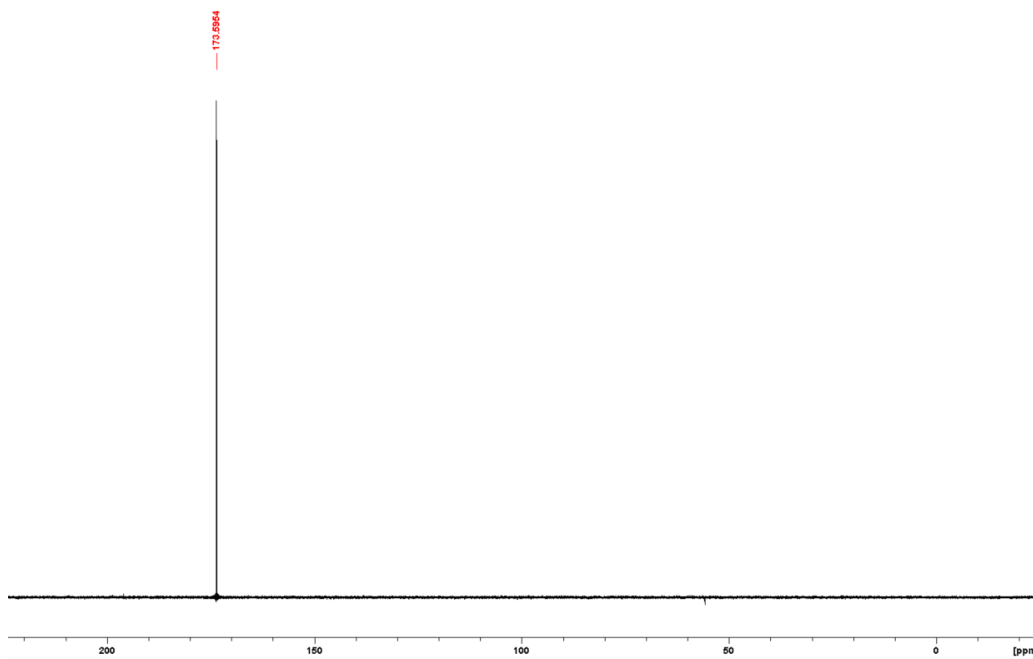
Figure S6.6 : Spectre RMN ^{31}P{^{1}H} du ligand **3a** dans CDCl$_3$.
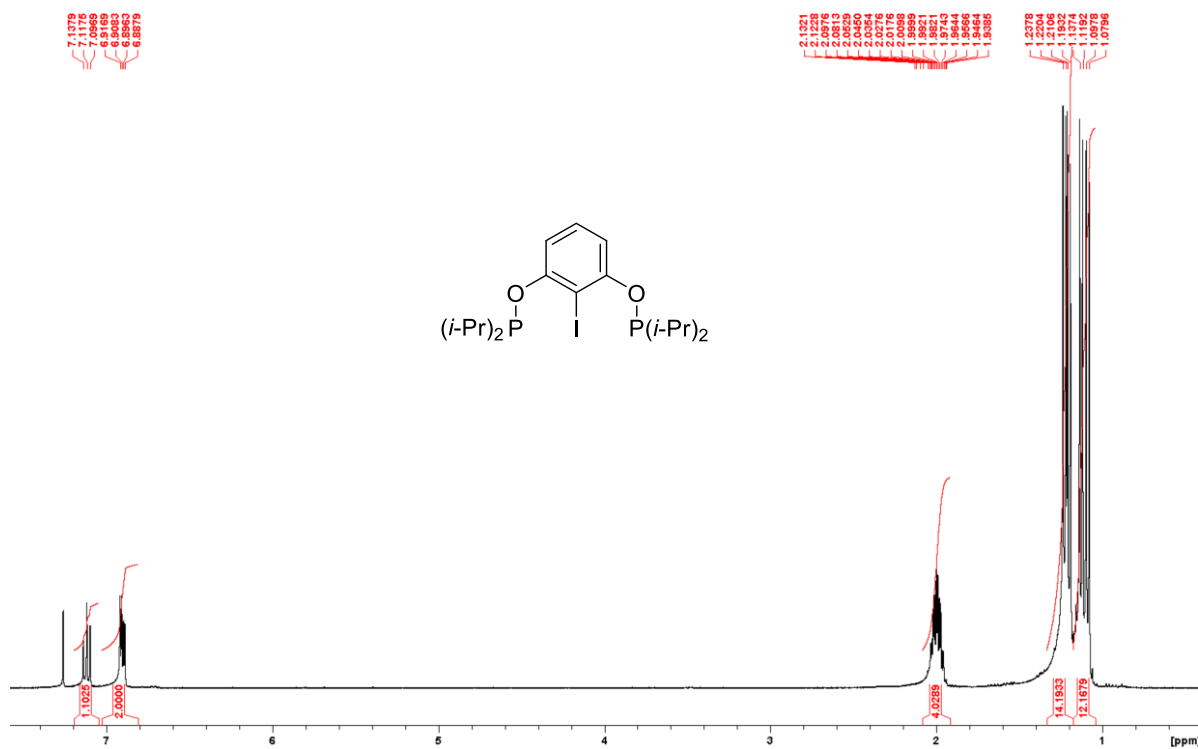
Figure 7 : Spectre RMN ^{1}H du ligand **4a** dans CDCl$_3$.
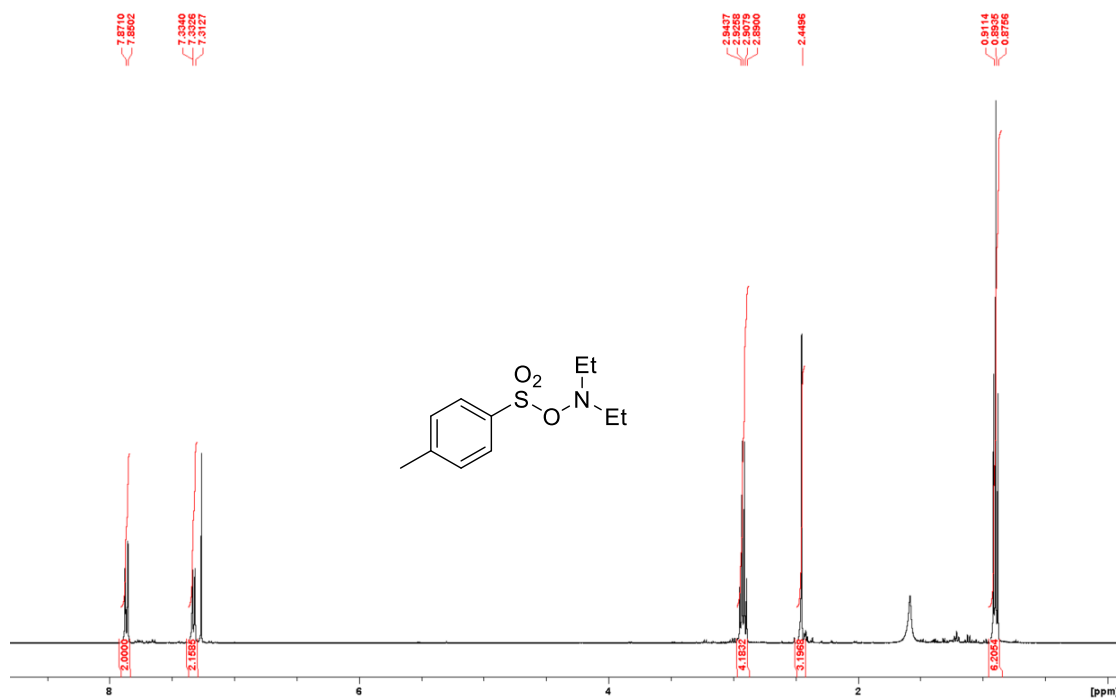
Figure S6.8 : Spectre RMN ^{1}H du réactif Et$_2$NOTs dans CDCl$_3$.

524
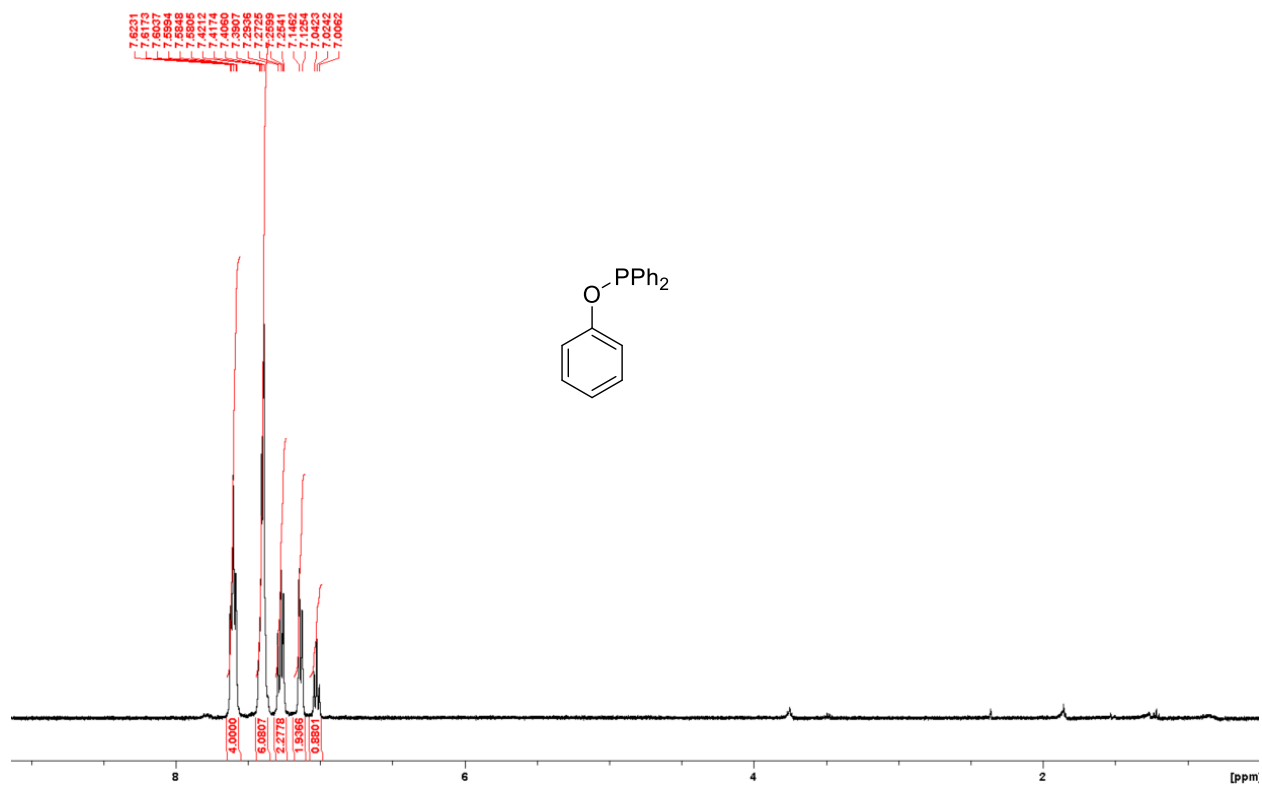
Figure S6.9 : Spectre RMN ^{1}H du ligand **5a** dans CDCl$_3$.
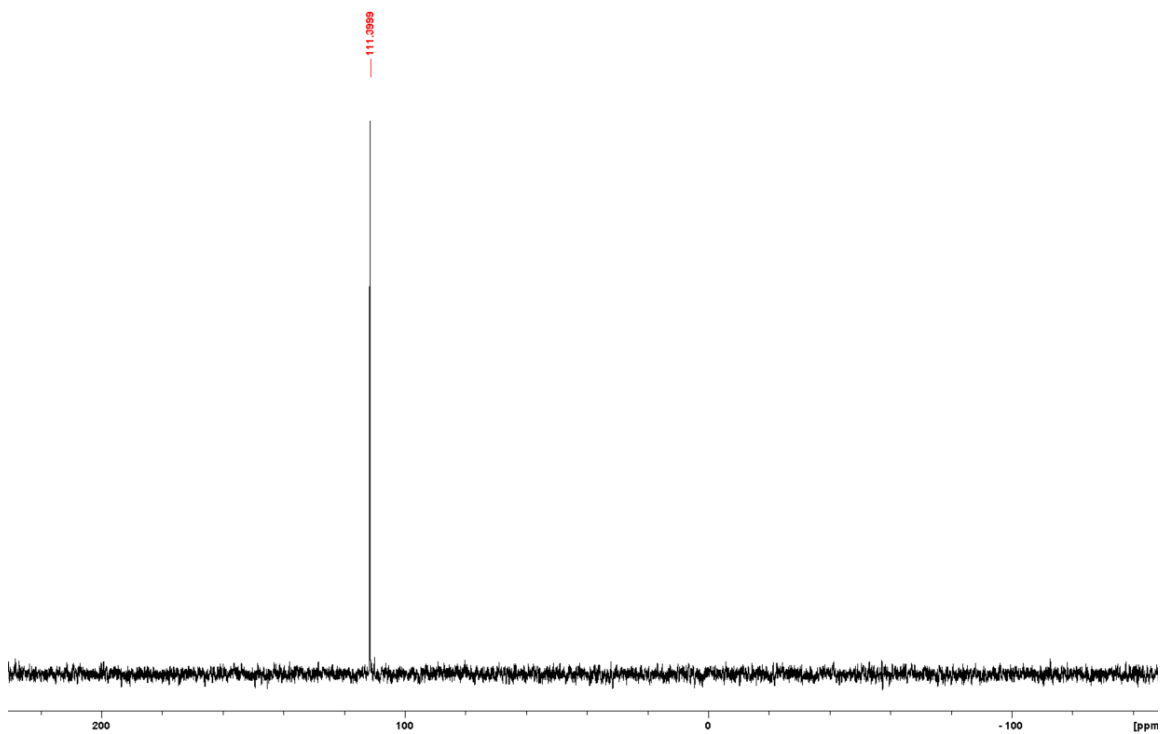
Figure S6.10 : Spectre RMN ^{31}P{^{1}H} du ligand **5a** dans CDCl$_3$.

S6.2 Spectres RMN ^{31}P additionnels des réactions
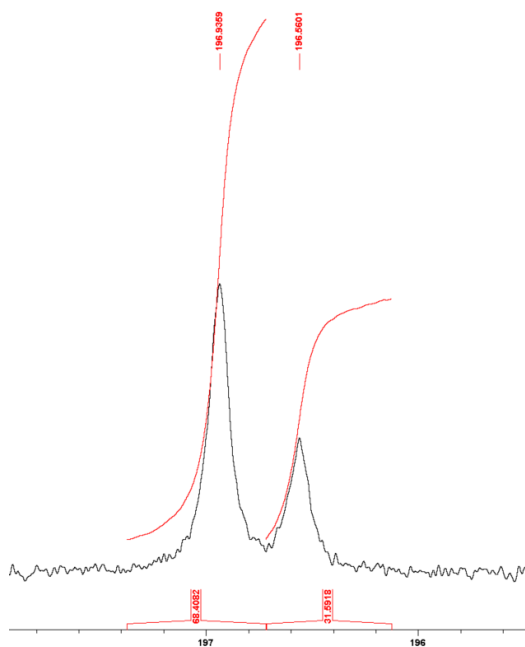
Figure S6.11 : RMN ^{31}P{^{1}H} du mélange brut de la cyclonickellation pour le ligand **2a**, après addition du dimère **2c**.
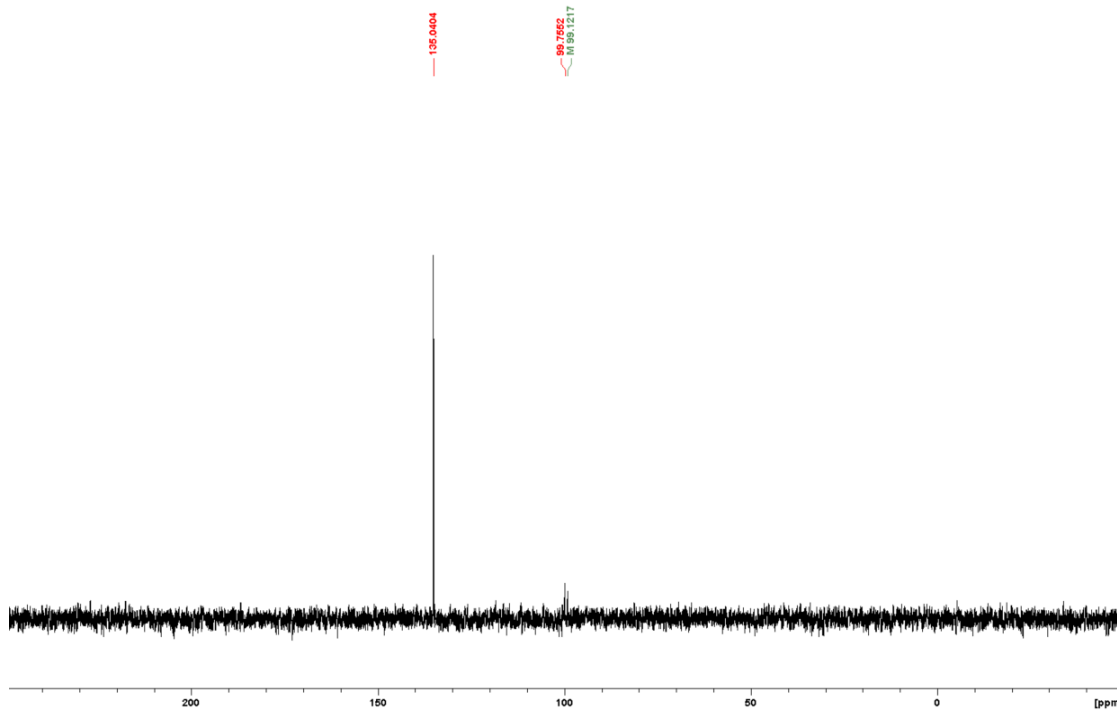
Figure S6.12 : Spectre RMN ^{31}P{^{1}H} du mélange brut de réaction du ligand **3a** avec [(i-PrCN)NiBr$_2$]$_n$ dans l'acétonitrile à 80 °C pendant 20h, en l'absence de base externe.
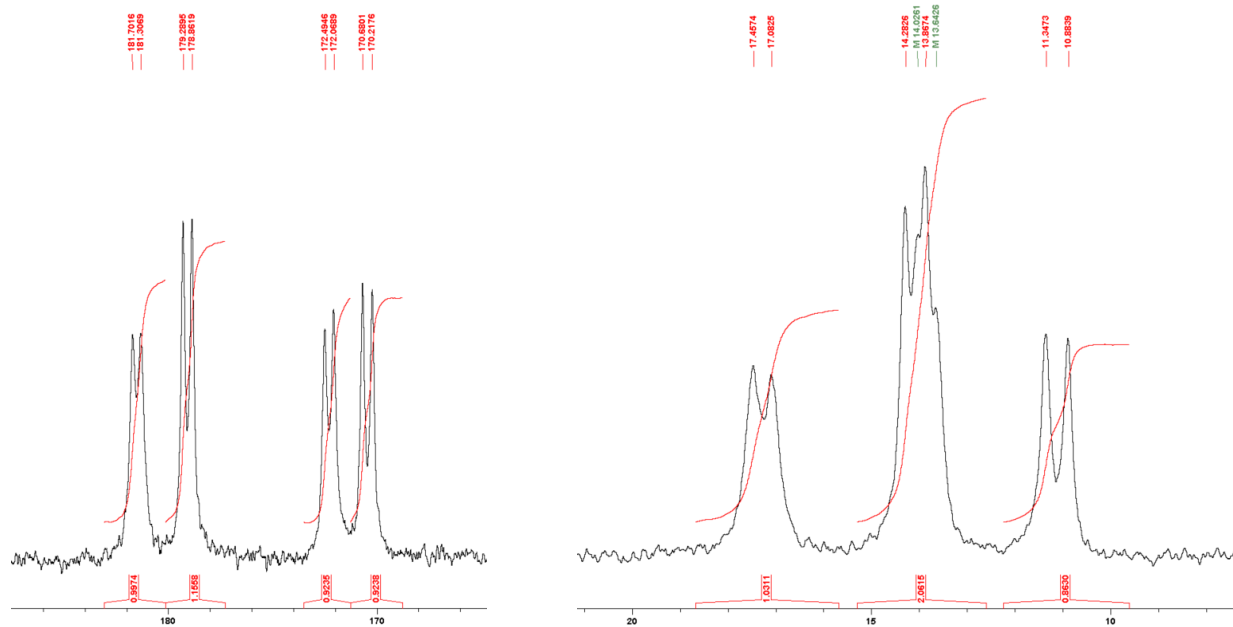
Figure S6.13 : Spectre RMN ^{31}P{^{1}H} du composé **3c-PPh₂** : emphase sur les signaux (ArO)(*i*-Pr)₂P→Ni (à gauche) et Ar₃P→Ni (à droite).
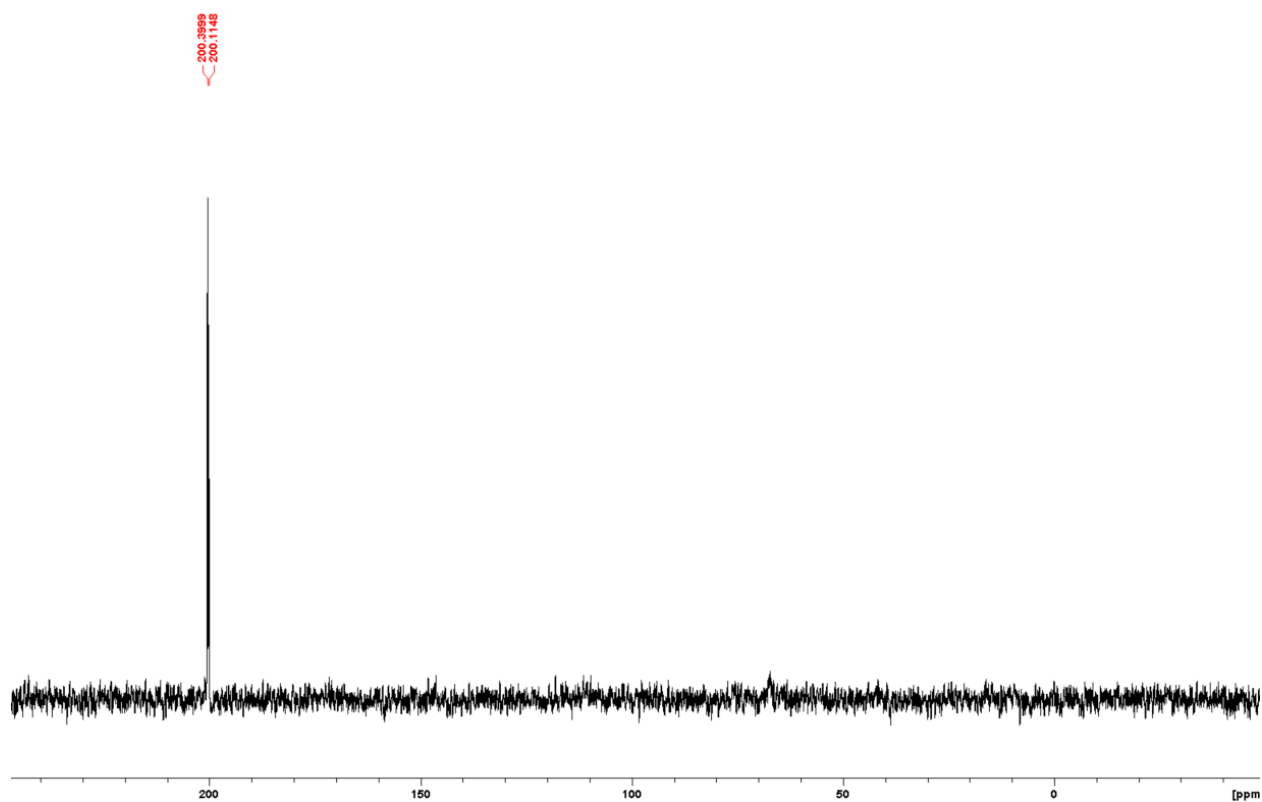
Figure S6.14 : Spectre RMN ^{31}P{^{1}H} de la réaction du complexe 6,4-POCN^{Cy,H}-NiBr avec le 3-fluorophénol après 20 h à 80 °C.
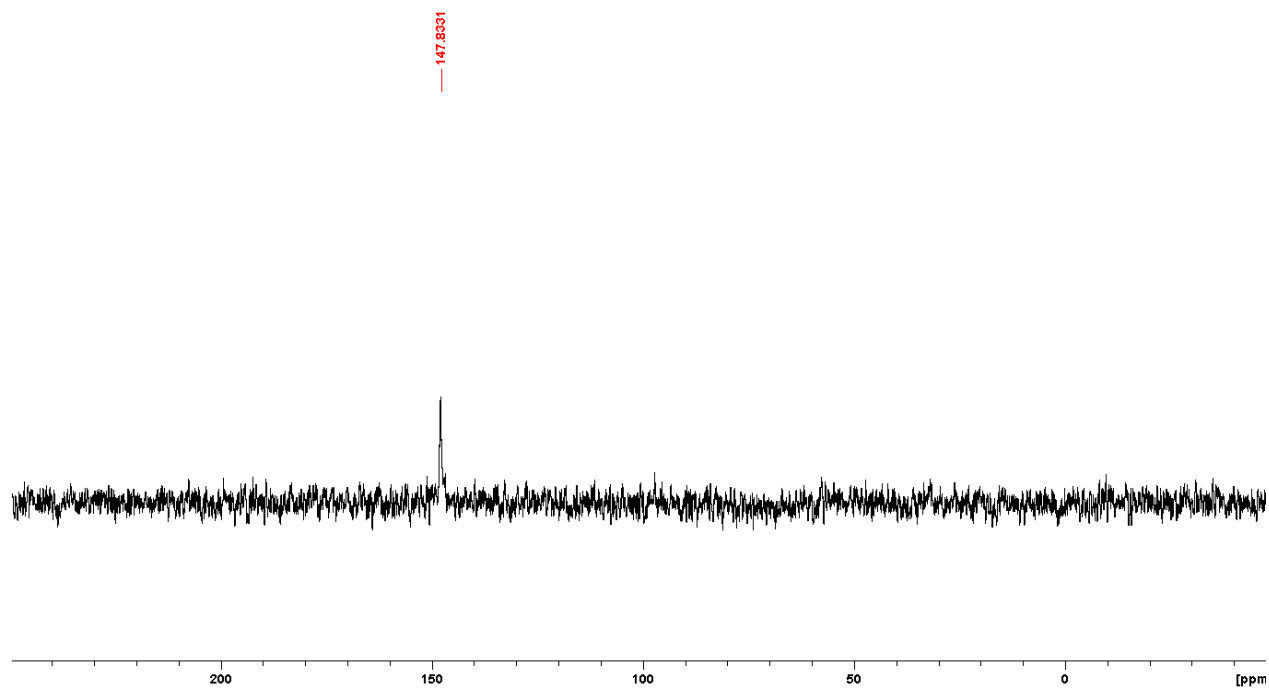
Figure S6.15 : Spectre RMN ^{31}P{^{1}H} de la réaction du complexe 6,4-POCN^{morph}-NiBr avec l'acide 3-chlorobenzoïque après 20 h à température ambiante.

S6.3 Chromatogrammes GC-MS et spectres de masse instantanés

S6.3.1 Réaction du proligand 4a avec le précurseur (Ph₃P)₂Ni(Ph)(Br)
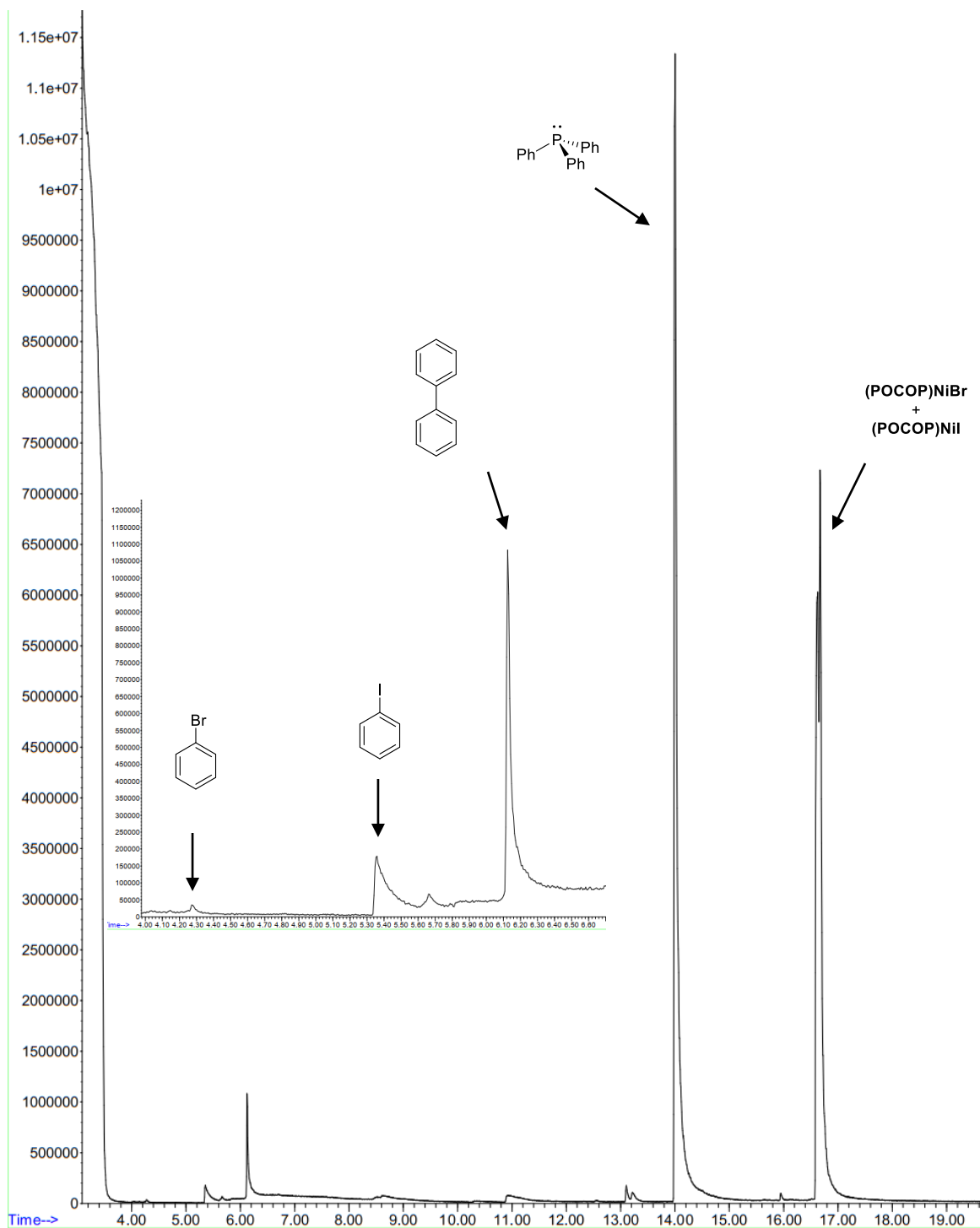
Figure S6.16 : Chromatogramme du brut de la réaction.
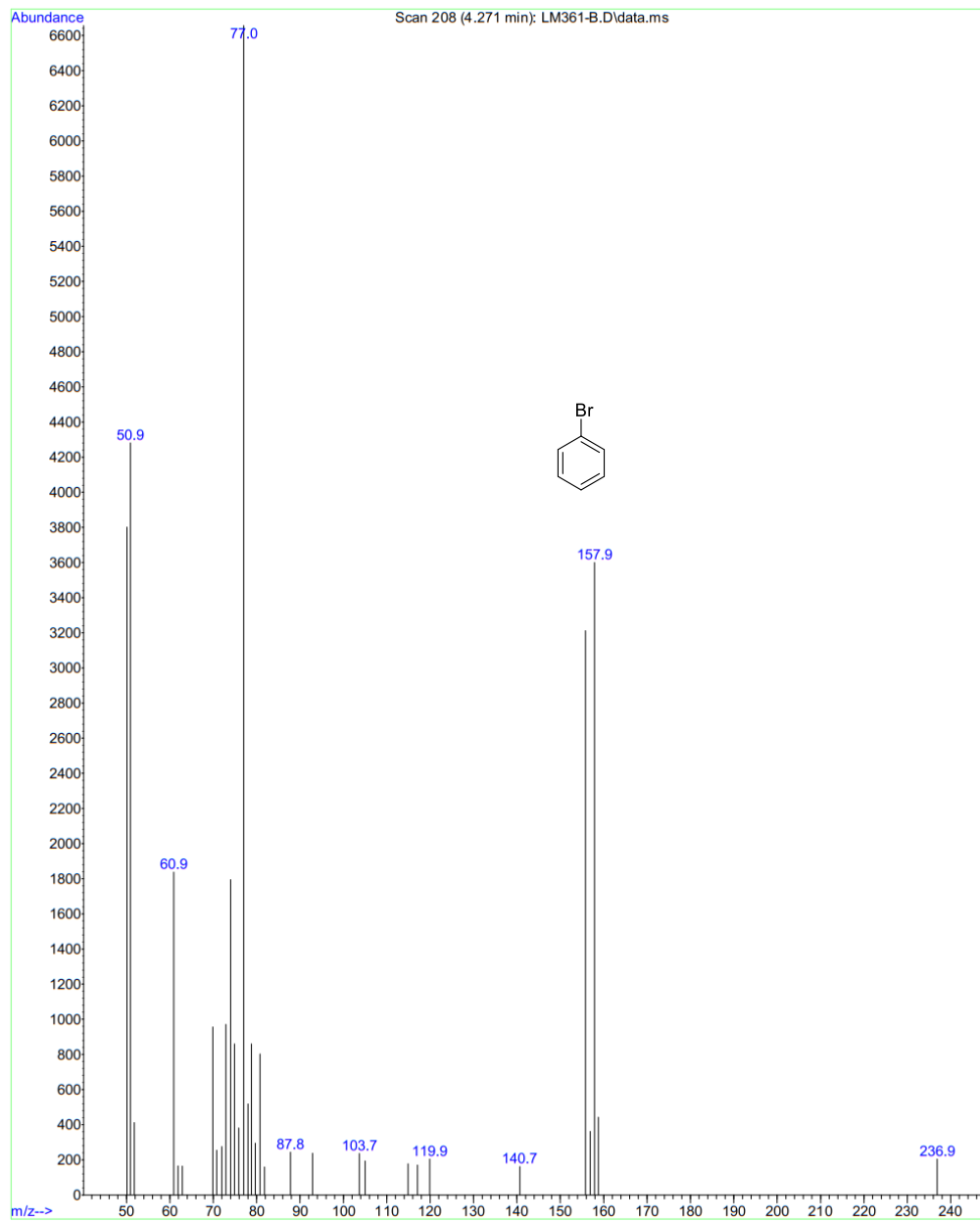
Figure S6.17 : Spectre de masse à t = 4.27 min, montrant la présence du PhBr.
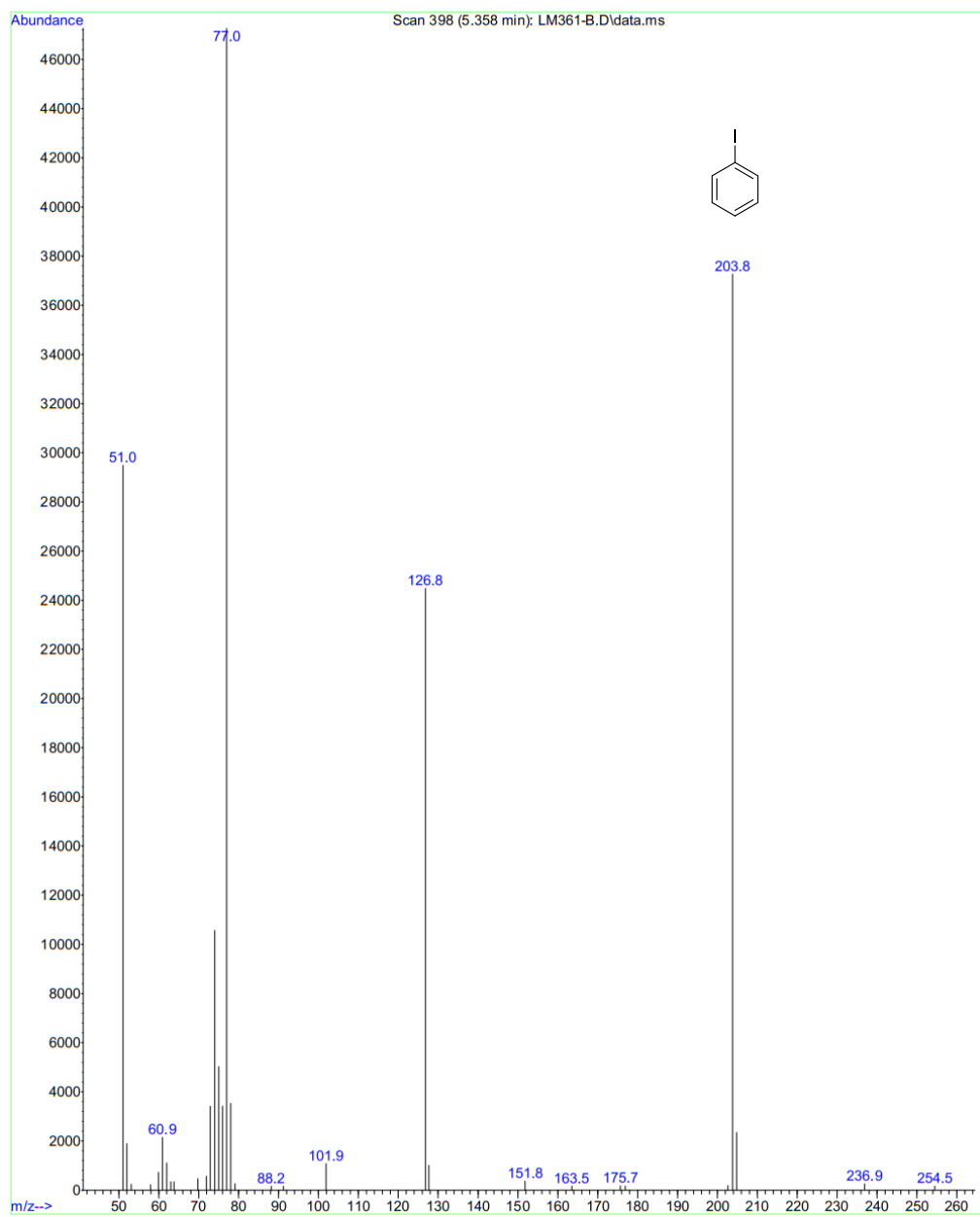
Figure S6.18 : Spectre de masse à t = 3.56 min, montrant la présence du PhI.
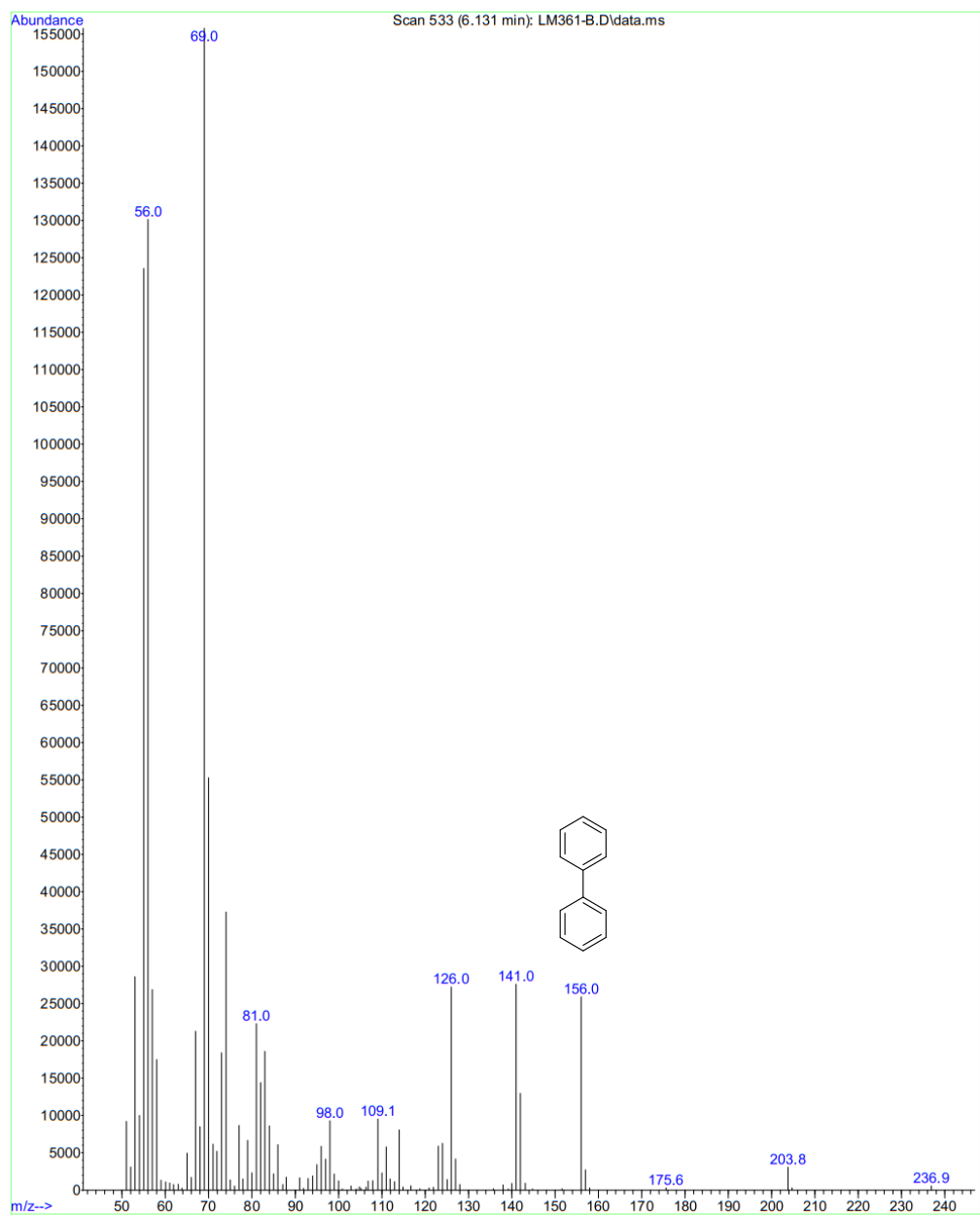
Figure S6.19 : Spectre de masse à t = 6.13 min, montrant la présence du biphényle.
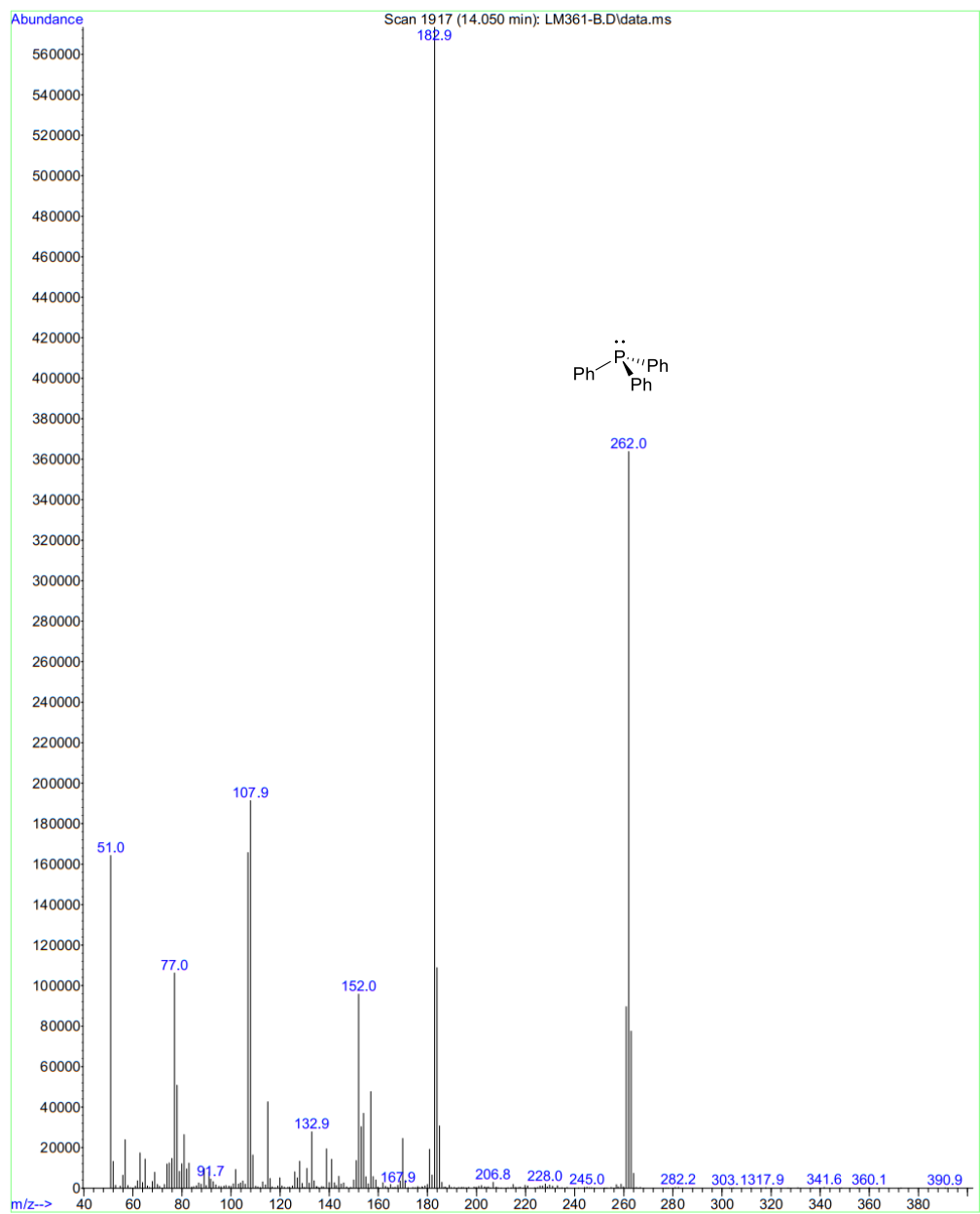
Figure S6.20 : Spectre de masse à t = 14.05 min, montrant la présence de PPh$_3$.
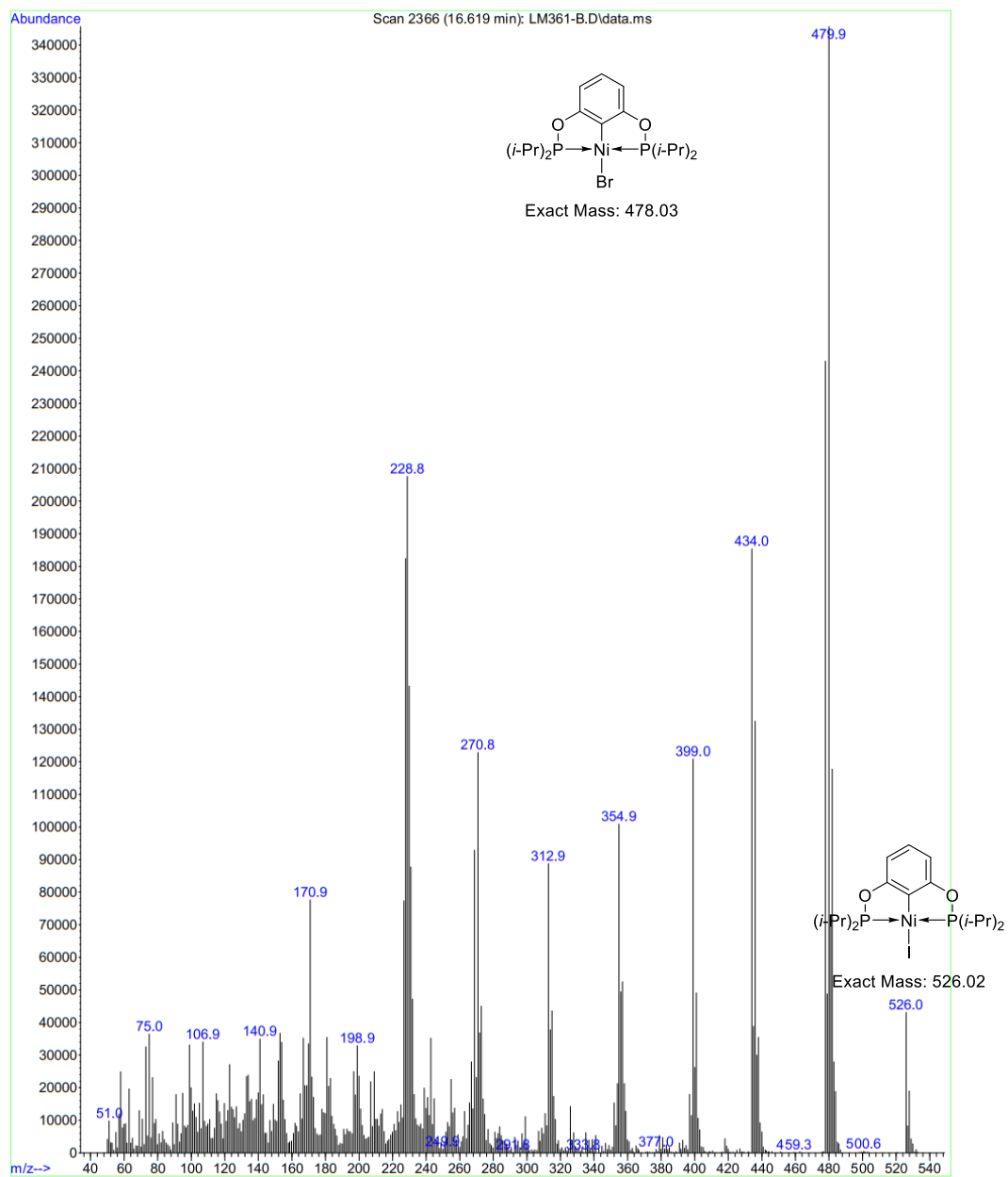
Figure S6.21 : Spectre de masse à t = 16.62 min, montrant la présence de (POCOP)NiBr et de (POCOP)NiI.

S6.3.2 Réaction du dimère 3c avec le réactif Et₂NOTs

Figure S6.22 : Chromatogramme de la réaction, après workup à H₂O et extraction à AcOEt.
*Composés non identifiés.
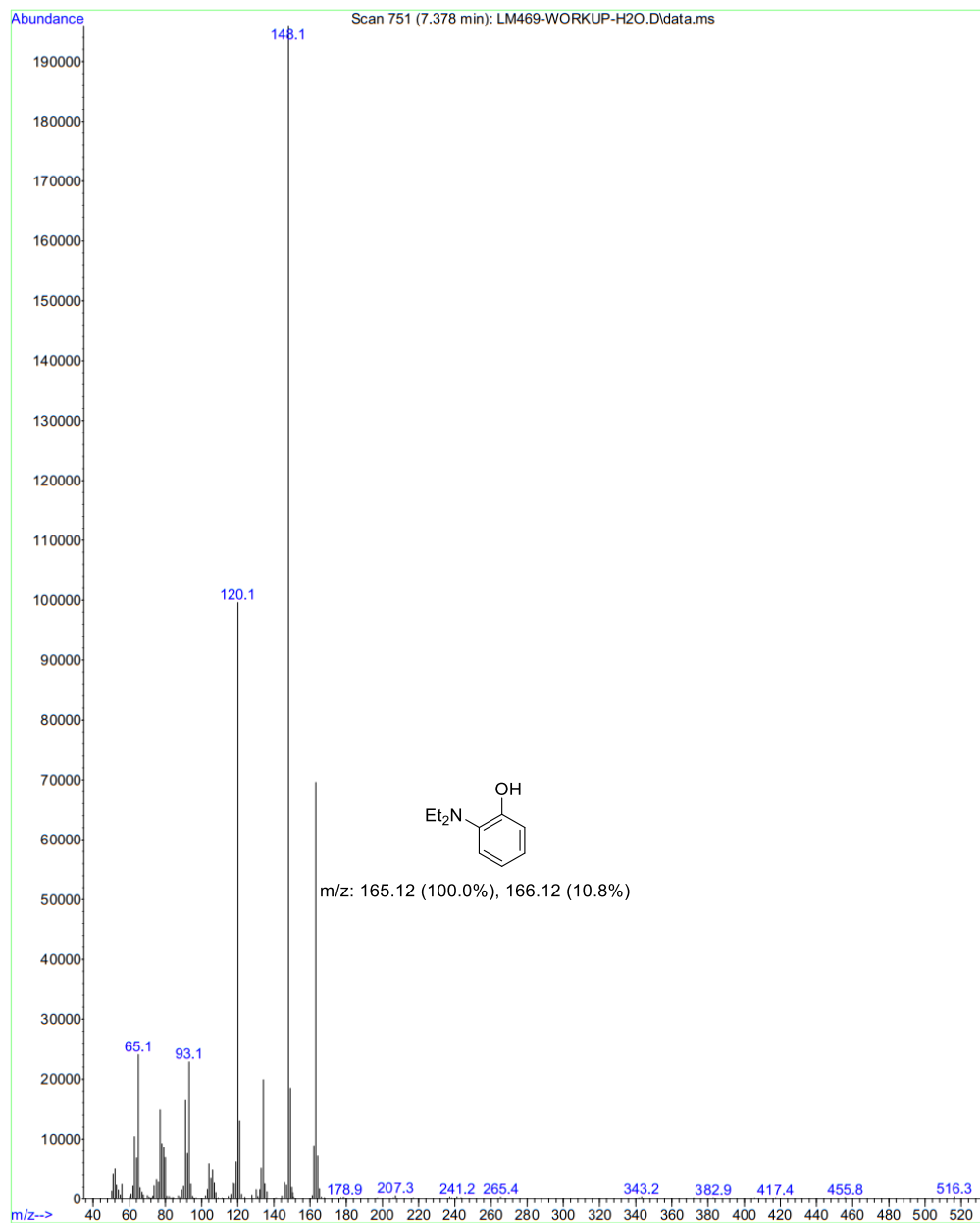
Figure S6.23 : Spectre de masse à t = 7.38 min, montrant la présence de 2-diéthylamino-phénol.
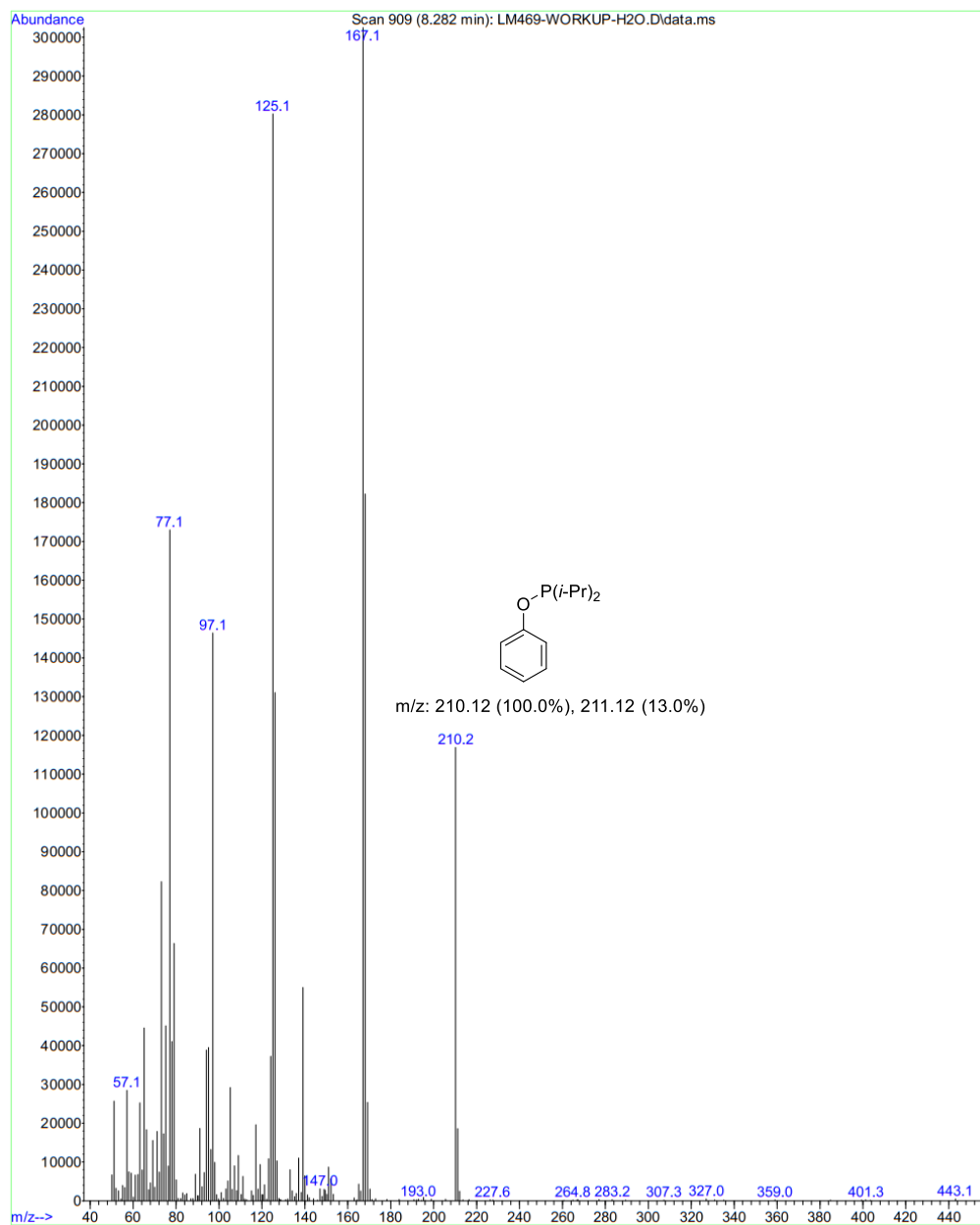
Figure S6.24 : Spectre de masse à t = 8.28 min, montrant la présence de PhOP(*i*-Pr)₂.
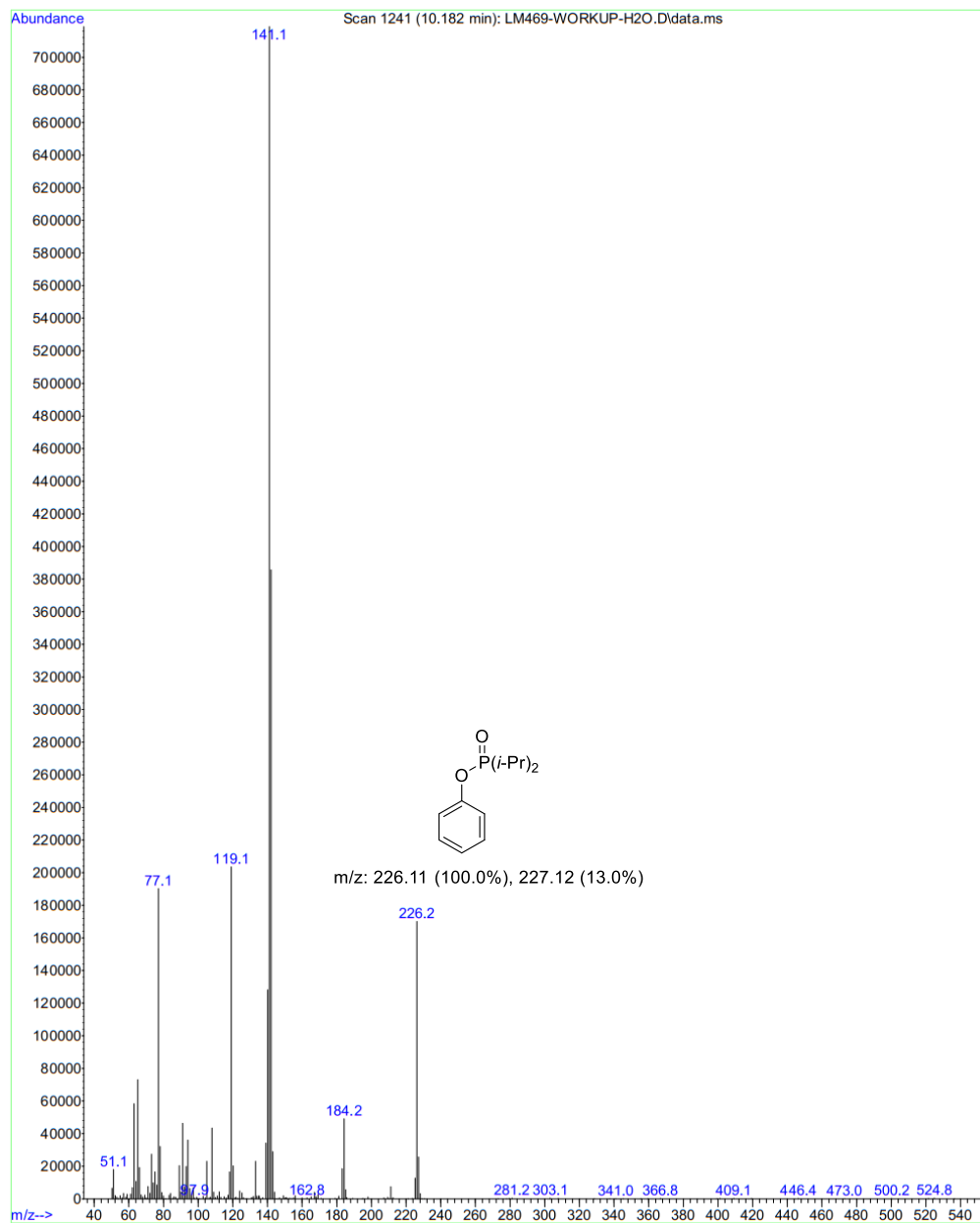
Figure S6.25 : Spectre de masse à t = 10.18 min, montrant la présence de PhOP(O)(*i*-Pr)₂.
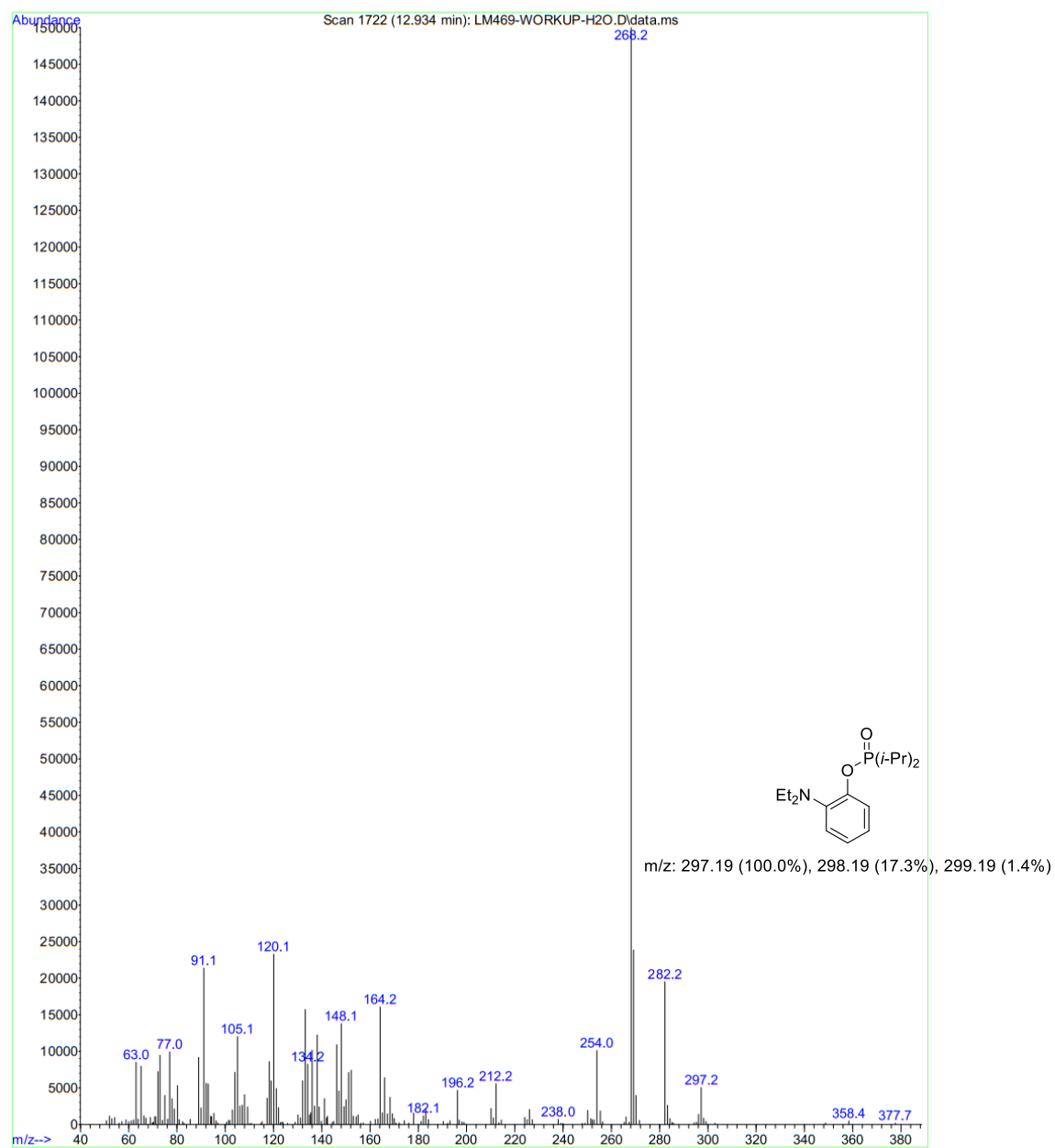
Figure S6.26 : Spectre de masse à t = 12.93 min, montrant la présence de 2-Et$_2$N-C$_6$H$_4$OP(O)(i-Pr)$_2$.

6.4 Tableaux des données cristallographiques

Tableau S6.1 : Description des cristaux et indicateurs d'affinement pour les composés **2b-NCMe**, **3b** et **5b-PPh₂**.

|	2b-NCMe	3b	5b-PPh₂
chemical formula	$C_{14}H_{20}Br_2NNiOP$	$C_{24}H_{32}Br_6Ni_2O_2P_2$	$C_{30}H_{24}Br_2NiOP2$
crystal colour	orange	Orange	orange
crystal size (mm)	0.06 × 0.18 × 0.20	0.12 × 0.17 × 0.18	0.06 × 0.06 × 0.12
index ranges	$-12 \leq h \leq 12$ $-15 \leq k \leq 15$ $0 \leq l \leq 17$	$-23 \leq h \leq 25$ $-11 \leq k \leq 11$ $-26 \leq l \leq 26$	$-12 \leq h \leq 12$ $-12 \leq h \leq 12$ $-18 \leq h \leq 18$
Fw; *F*(000)	467.81; 928	1011.31; 1952	680.96; 680
T (K)	100.0	100	100
wavelength (Å)	1.54178	1.34139	1.34139
space group	P-1	P2₁/n	P-1
a (Å)	10.369(3)	19.4474(10)	9.7846(2)
b (Å)	12.945(3)	8.9144(5)	9.8566(2)
c (Å)	14.557(4)	19.5696(10)	14.5986(3)
α (deg)	113.279(4)	90	105.3973(12)
β (deg)	101.086(4)	106.615(2)	92.8885(13)
γ (deg)	91.099(4)	90	99.4103(12)
Z	4	8	2
V (Å³)	1751.7(7)	3251.0(3)	1332.60(5)
ρ_{calcd} (g·cm⁻³)	1.774	2.066	1.697
μ (mm⁻¹)	7.761	12.798	7.168
θ range (deg); completeness	3.386 − 72.265; 0.999	2.050 − 63.594; 0.999	2.745 − 60.690; 1.000
collected reflections; R_σ	121666; 0.0171	117488; 0.0255	38490; 0.0258
unique reflections; R_{int}	6875; 0.0691	8070; 0.0623	6129; 0.0381
R1ᵃ; wR2ᵇ [I > 2σ(I)]	0.0498; 0.1433	0.0316; 0.0834	0.0500; 0.1425
R1; wR2 [all data]	0.0510; 0.1442	0.0319; 0.0836	0.0584; 0.1479
GOOF	1.126	1.042	1.062
largest diff peak and hole	0.936 and -0.913	0.836 and -0.843	3.054 and -1.001

ᵃ $R_1 = \Sigma(||F_o|-|F_c||)/\Sigma|F_o|$

ᵇ $wR_2 = \{\Sigma[w(F_o{}^2 - F_c{}^2)^2]/\Sigma[w(F_o{}^2)^2]\}^{1/2}$

Tableau S6.2 : Description des cristaux et indicateurs d'affinement pour les composés **3c-PPh₂** et
[2-NMe₂-PhOP(i-Pr)₂]NiBr₂.

	3c-PPh₂	[2-NMe₂-PhOP(*i*-Pr)₂]NiBr₂
chemical formula	$C_{24}H_{28}Br_{1.201}Cl_{0.799}NiOP_2$	$C_{14}H_{24}Br_2NNiOP$
crystal colour	Orange	purple
crystal size (mm)	0.01 × 0.02 × 0.012	0.04 × 0.08 × 0.09
index ranges	-11 ≤ h ≤ 11 -12 ≤ k ≤ 12 -15 ≤ l ≤ 15	-12 ≤ h ≤ 12 -10 ≤ k ≤ 10 -26 ≤ l ≤ 26
Fw; *F*(000)	577.36; 587	471.84; 944
T (K)	100	100.0
wavelength (Å)	1.54178	1.54178
space group	P-1	P2₁/c
a (Å)	9.3983(3)	10.0474(5)
b (Å)	10.4295(3)	8.3838(4)
c (Å)	12.8756(4)	21.4876(11)
α (deg)	94.3970(10)	90
β (deg)	90.7420(10)	95.540(2)
γ (deg)	104.5700(10)	90
Z	2	4
V (Å³)	1217.20(6)	1801.56(15)
ρ_calcd (g·cm⁻³)	1.575	1.740
μ (mm⁻¹)	5.612	7.547
θ range (deg); completeness	3.445 − 72.135; 0.975	4.134 − 72.212; 0.999
collected reflections; R_σ	33985; 0.0168	34833; 0.0260
unique reflections; R_int	4637; 0.0306	3547; 0.0509
R1ᵃ; wR2ᵇ [I > 2σ(I)]	0.0262; 0.0713	0.0405; 0.1164
R1; wR2 [all data]	0.0263; 0.0714	0.0444; 0.1215
GOOF	1.075	1.056
largest diff peak and hole	0.490 and -0.354	1.042 and -0.691

ᵃ $R_1=\Sigma(||F_o|-|F_c||)/\Sigma|F_o|$
ᵇ $wR_2=\{\Sigma[w(F_o^2-F_c^2)^2]/\Sigma[w(F_o^2)^2]\}^{½}$

Chapitre 7 – Conclusion générale et perspectives

7.1 Remarques sur la régiosélectivité de la cyclonickellation des phosphinites

Le **Chapitre 2** a démontré que la cyclonickellation des phosphinites dérivées des phénols substitués se produit préférablement à la position la moins encombrée, peu importe les facteurs électroniques des groupes fonctionnels. On peut forcer les positions encombrées par un substituant à subir la nickellation à 80 °C si ce substituant impose peu de contraintes stériques comme F ou MeO, mais la réaction ne se produit pas lorsque le substituant voisin est un Me ou un Cl. Dans le cas de F et MeO, les structures montrent cependant une distorsion autour du lien C-Ni qui témoigne de la gêne stérique, et dans le cas du MeO, l'encombrement stérique ne permet pas à l'adduit d'acétonitrile de dimériser. Le **Chapitre 4** a montré que les phosphinites dérivées des 1- et 2-naphthols produisent des nickellacycles à 5 chainons, et que la position C3 du 2-naphtol est favorisée mais qu'elle peut être forcée à la position C1 davantage encombrée, menant à une distorsion importante accompagnée d'une faible stabilité comparée aux complexes homologues non distordus. Dans le cas du 1-naphtol, la cyclométallation à la position C8 produirait un cycle à 6 chainons qui n'est pas favorable et ne permet pas l'isolation d'un complexe portant un lien Carbone-Nickel. Cet intermédiaire présumé est supposé instable, et seule une réaction de fonctionnalisation à haute température laisse une trace de la cyclonickellation à cette position. De la même manière, la nickellation sur le substituant aryle de la 2-Ph-phényl-phosphinite ou de son homologue di-substituée n'a pas été détectée, probablement car la cyclométallation requiert un état de transition tendu et que le nickellacycle généré (à 7 chainons) pourrait être instable.

Le **Chapitre 4** a également démontré que la cyclonickellation peut être accélérée de manière spectaculaire lorsque la réaction est conduite à des hautes températures (120 °C, 160 °C). Dans ces conditions, la nickellation à la position C8 du 1-naphtol a pu être – indirectement – observée, indiquant que les positions C-H non réactives dans les conditions standard (80 °C) pouvait subir la nickellation en fournissant davantage d'énergie au milieu. Ainsi, des résultats préliminaires ont montré que les limites stériques de la nickellation sur des positions encombrés

par des substituants voisins peuvent être surmontées par un chauffage intense. En effet, alors que la phosphinite dérivée du 3,5-diméthylphénol ne montrait aucun signe de réactivité dans les conditions standards, même après 3 jours, sa cyclonickellation s'est avérée quasiment complète à 160 °C après seulement 2 heures, indiquant une forte dépendance du système face à la température (**Schéma 7.1**). De plus, l'obtention d'un signal en majeur RMN ^{31}P dans la région des complexe nickellés témoigne de la stabilité thermodynamique du nickellacycle. Ainsi, ce type de procédures permettrait d'isoler des de nouveaux complexes de phosphinites *ortho*-nickellées ou des nickellacycles à 6 ou 7 chainons, qui pourrait être plus réactifs face à la fonctionnalisation (*i.e.* dans des conditions moins rudes avec une meilleure efficacité), en raison de leur plus faible stabilité cinétique.

Schéma 7.1. Nickellation des positions encombrés à haute température. FG = Groupe fonctionnel.
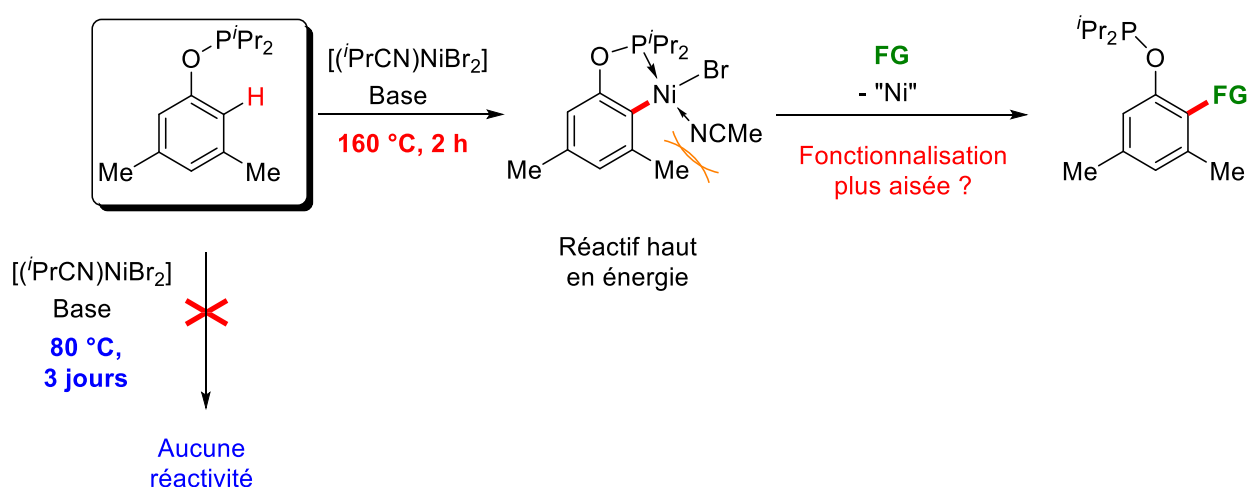
Si le **Chapitre 2** a démontré que la mesityl-phosphinite ne permettaient pas l'isolation de complexes issus de la nickellation des liens C_{sp^3}-H, les tentatives d'échange H/D présentées au **Chapitre 4** indiquent que l'existence elle-même de ce type de complexes est très peu probable, ou du moins que leur temps de survie ne permet par leur détection, même indirecte. Ainsi, la fonctionnalisation de ces liens par des intermédiaires phosphinites cyclonickellées est largement compromise. Cependant, un complexe π-allyle généré formellement par métallation d'un C_{sp^3}-H en position benzylique et allylique a été isolé. On pense que la nickellation est favorisée cinétiquement par la coordination de l'oléfine (produisant un analogue de ligand *pincer*) et thermodynamiquement

par la formation d'une complexe tridenté. Malgré cela, le complexe était relativement instable, suggérant qu'un des liens C-Ni du fragment allyle-Ni serait un bon candidat pour la fonctionnalisation soit par des électrophiles, ou par des nucléophiles menant à la réduction du centre métallique (**Schéma 7.2**).

Schéma 7.2. Mécanismes possibles de fonctionnalisation des composés π-allyle-Ni cyclométallés
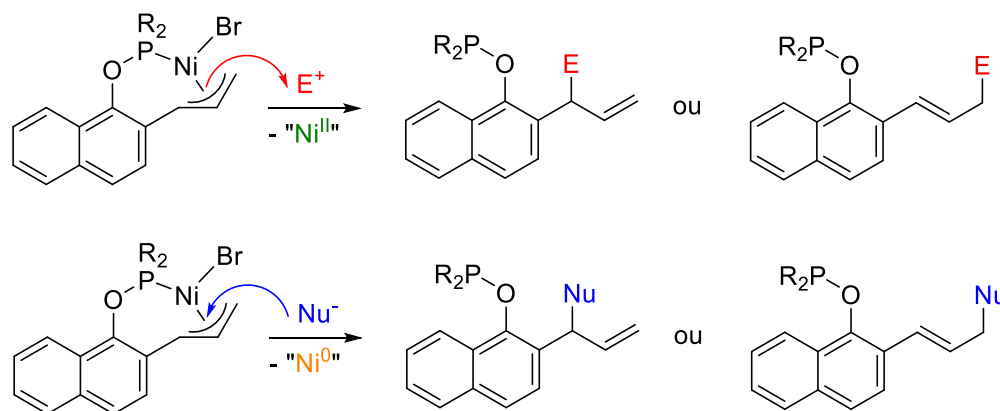
Ce résultat ouvre également la voie à la cyclonickellation de phosphinites dérivées des alcools aliphatiques portant une insaturation : les alcools allyliques sont de mauvais candidats car leurs phosphinites se réarrangent (**Schéma 7.3**), mais les alcools homoallyliques et leurs dérivés sont des candidats intéressants (**Schéma 7.4**).

Schéma 7.3. Réarrangement des allyl-phohsphinites.

Schéma 7.4. Cyclonickellation des phosphinites dérivées des alcools homo-allyliques.

7.2 Notes sur les mécanismes de la nickellation

L'étude des milieux réactionnels dans le toluène et dans l'acétonitrile a permis de prouver que ce dernier était un meilleur solvant parce qu'il permet de générer des espèces différentes, qui sont plus réactives. Dans le cas de la cyclonickellation des phosphinites monodentées, l'utilisation d'une base externe est nécessaire pour isoler le lien C-Ni, à l'inverse des ligands *pinceurs* (POCOP, POCN, PCP) p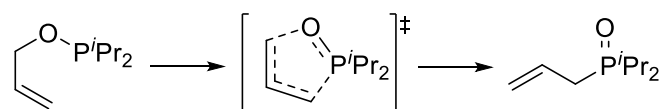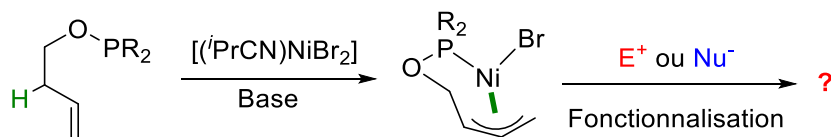our lesquels la nickellation est tellement favorable thermodynamiquement que le ligand lui-même est capable de capter l'acide généré. Cependant, l'utilisation d'un excès de base inhibe la réaction car elle génère des espèces non compétentes dans le procédé de nickellation C-H (les composés bis-phosphinites de $NiBr_2$), en se coordonnant au centre métallique.

Ainsi, les études cinétiques présentées dans le **Chapitre 3** ont montré que lorsqu'une base idéale (*i.e.* suffisamment basique mais non coordonnante) est utilisée, la cinétique est de 1er ordre, ce qui indique une étape de nickellation unimoléculaire. Les études d'échange H/D ont d'ailleurs prouvé que la base n'est pas nécessaire, cinétiquement, à générer l'espèce cyclométallée, indiquant que la base cinétique est le ligand Br^- et que le HBr généré est capté par la triéthylamine en dehors de la sphère de coordination.

La lenteur des réactions, en comparaison avec les systèmes POCOP et PCP, a permis de faire une étude des vitesses de réaction dans différentes conditions et avec différents substrats. Cette étude expérimentale a permis de montrer que la métallation est radicalement plus rapide quand le cycle aromatique porte des substituants électrodonneurs (pente de Hammett $\rho \approx -4$), ce qui pointe vers un mécanisme de nickellation électrophile impliquant la coordination du carbone au nickel afin de faciliter l'abstraction du proton. De plus, l'effet cinétique isotopique normal observé est très grand ($k_H/k_D \approx 11$) indiquant que le bris du lien C-H est l'étape limitante de la nickellation. L'étude de Eyring a également permis d'extraire les paramètres d'activation ($\Delta H^{\ddagger} = 18(1)$ kcal·mol^{-1} and $\Delta S^{\ddagger} = -27(4)$ cal·mol^{-1}·K^{-1}), indiquant un état de transition ordonné et qui mènent à une énergie de Gibbs d'activation de de $\Delta G^{\ddagger} = 27(3)$ kcal·mol^{-1}.

Les études DFT ont permis de confirmer que les espèces présentes avant la cyclométallation sont des espèces tétraédriques portant un seul ligand phosphinite, et appuie la théorie selon laquelle l'utilisation de l'acétonitrile comme solvant permet de générer des espèces différentes et plus

réactives. L'étude théorique écarte un mécanisme impliquant un intermédiaire Ni^{IV} (*i.e.* addition oxydante C-H), et appuie la thèse d'une métallation électrophile donnant lieu à une parie d'ions comme intermédiaire, où l'anion bromure dissocié réalise la déprotonation par mécanisme CMD. L'énergie de Gibbs d'activation trouvée par les méthodes computationnelles est d'ailleurs proche de celle déterminée expérimentalement.

Bien que les **Chapitres 2** et **4** montrent l'efficacité de la formation des composés cyclonickellés par métallation directe C-H sur le Ni^{II} et que le **Chapitre 3** décrit le mécanisme et les caractéristiques de ce procédé, des résultats préliminaires nous ont montré que liens Carbone-Halogène pouvaient également être métallés par les précurseurs de Ni^{II}, tout en menant à des complexes cyclonickellés de même valence. En effet, les études sur la régiosélectivité nous ont mené à tester la nickellation d'une phényl-phosphinite portant un hydrogène à une position *ortho* et un brome à la seconde position *ortho*. La réaction dans les conditions normales de cyclométallation a montré l'apparition de deux signaux distincts dans la région attendue dans des ratios de 2:1 : le signal majeur a été attribué au produit d'*ortho*-nickellation C-H, et le signal mineur a été identifié comme le produit d'ortho-nickellation C-Br, puisque ce produit était déjà connu et caractérisé (**Schéma 7.5**). La présence de ces deux signaux dans des ordre de grandeur semblables indiquerait que la nickellation des liens C-Br est d'une vitesse similaire à celle des liens C-H.

Schéma 7.5. Cyclonickellation du ligand 2-Br-C$_6$H$_4$-OP(*i*-Pr)$_2$.
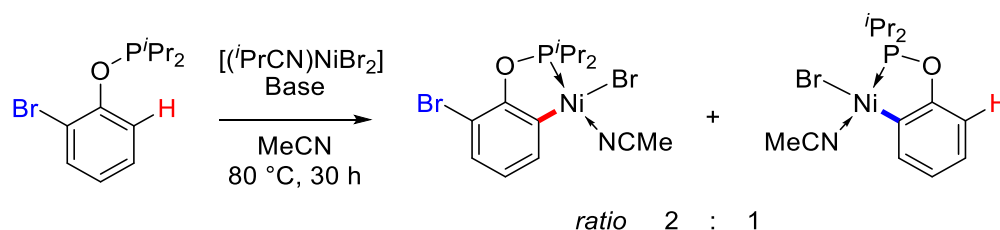
Pour confirmer, cette théorie, le ligand dérivé du 2,4,6-tribromophénol a été placé en conditions de standard, menant à l'obtention et à la caractérisation d'un dimère de phosphinites *ortho*-cyclonickellées, indiquant que la métallation du lien C-Br était bien réelle. Étonnamment, le signal à 197 ppm témoignant de la formation du lien C-Ni n'apparait que lorsque qu'une base est

547

introduite dans le milieu. La réaction formelle de nickellation étant C-Br + Ni-Br → C-Ni + Br$_2$. Il serait donc important de comprendre le rôle de la base dans ce processus et de déterminer où le Br$_2$ généré formellement se retrouve à la fin de la réaction. Ainsi, cette voie est une nouvelle stratégie probable pour la formation de liens C-Ni, et les régiosélectivités observées par nickellation Carbone-Halogène pourraient sûrement différer de celles de l'activation C-H, et dépendre de l'identité de l'halogène.

Schéma 7.6. Cyclonickellation du ligand 2,4,6-Br$_3$-C$_6$H$_2$-OP(i-Pr)$_2$.
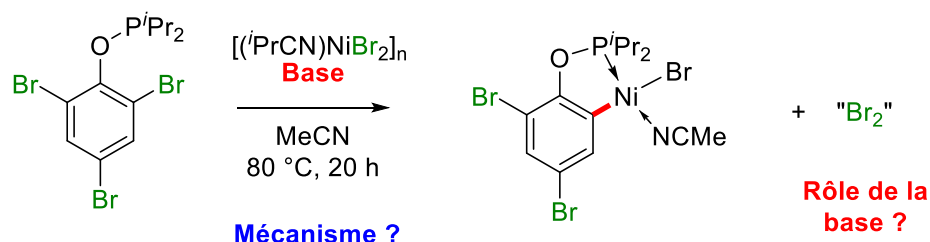
Tout comme les pinceurs ont souvent servi de modèles pour l'étude des composés cyclométallés, des résultats préliminaires sur le ligand pinceur POCOP portant un iode en position 2 ont montré que le pinceur POCOP-NiX est également obtenu en 1 h à 60 °C ou en 16 h à température de la pièce (**Schéma 7.7**). Avant que le concept de métallation C-H apparaisse, les procédés les plus utilisés pour la formation de pinceurs impliquaient l'addition oxydante C-X sur des précurseurs de basse valence. Il est donc drôle de penser que les chimistes auraient simplement pu utiliser des précurseurs déjà oxydés, qui sont généralement moins chers, plus stables et plus faciles à manipuler.

Schéma 7.7. Formation des complexes POCOP-NiX par nickellation Carbone-Halogène.
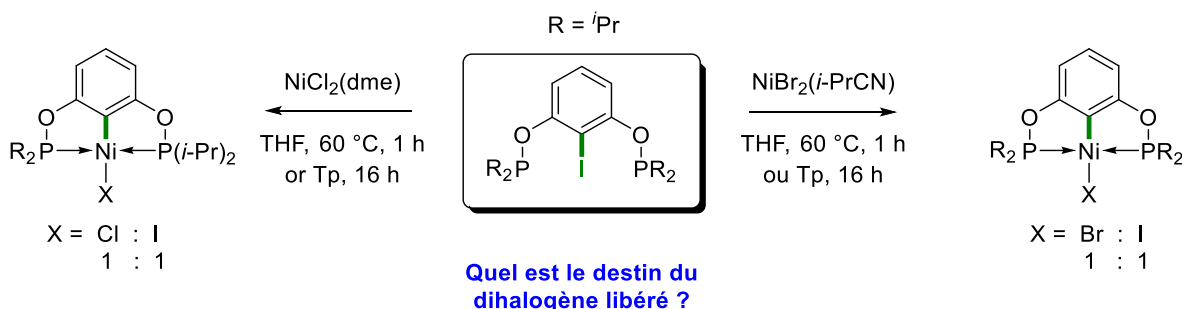
Bien que l'utilisation de lien C-X comme précurseur est aujourd'hui surpassée (économiquement et écologiquement) par la nickellation directe C-H, le mécanisme et les caractéristiques de la nickellation directe Carbone-Halogène mérite d'être étudié. On peut proposer que les mécanismes probables soient le SET (menant à des intermédiaires Ni^{III}) ou l'addition oxydante (menant à des intermédiaires Ni^{IV}), et la compréhension de ces mécanisme pourrait même mener à la capture de ces intermédiaires. Leur isolation serait une avancée scientifique importante, car aucun procédé à ce jour n'a mené à l'isolation de composés cyclonickellés de haute valence (Ni^{III} ou Ni^{IV}) par addition oxydante Carbone-Halogène.

7.3 La fonctionnalisation des liens C-Ni des phosphinites cyclonickellées

Le **Chapitre 4** a démontré que les phosphinites cyclonickellées étaient capable de réagir avec la bromophosphine – introduite directement ou générée *in situ* – par insertion formelle d'un phosphènium dans le lien Carbone-Nickel. Bien que les résultats aient été démontré à des hautes températures, cette réaction se produit également à 80 °C en 16 h, indiquant que la vitesse de cette insertion est similaire à la vitesse de cyclonickellation. De plus, cette réaction s'est avérée efficace dans l'acétonitrile, mais elle est beaucoup plus lente dans les solvant non polaires. Ainsi, on peut penser que le mécanisme implique la coordination du ligand R_2P-Br sur le centre métallique suivi d'une dissociation homolytique P-Br, qui mène à un phosphènium coordonné au nickel. Ce dernier s'insèrerait ensuite dans le lien Carbone-Nickel.

Schéma 7.8. Mécanisme proposé pour la réaction d'une espèce cyclonickellée avec une bromophosphine.
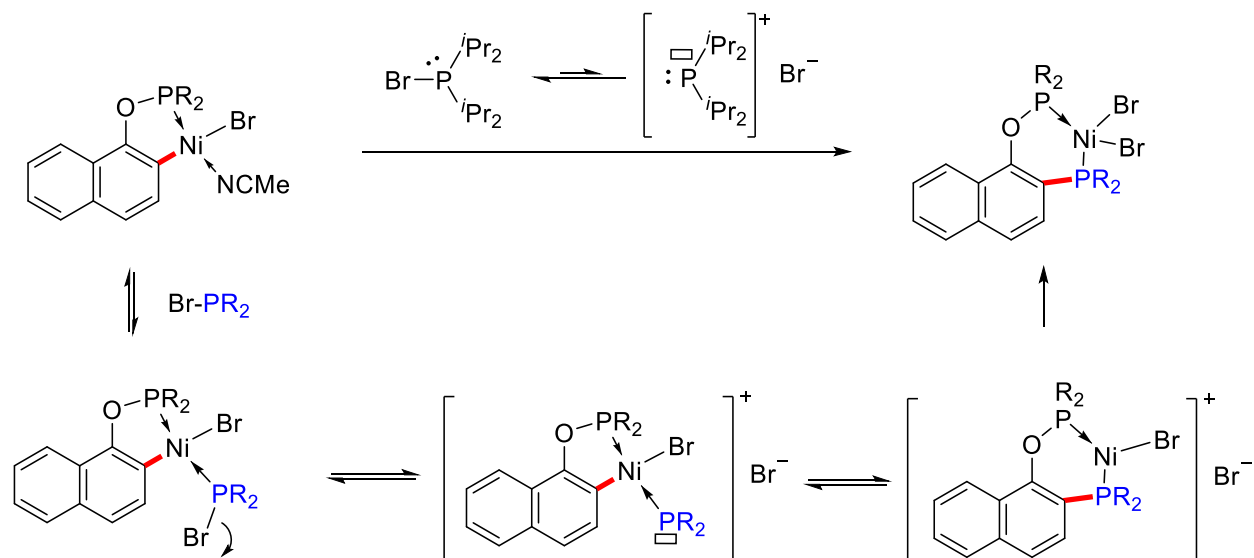
Le produit de fonctionnalisation – un ligand phosphine-phosphinite – quant à lui obtenu sous forme d'un complexe de NiBr$_2$. Cependant, on peut imaginer que la réaction globale (**Eq. 7.1**) peut se produire avec un défaut de nickel : dans ce cas le métal serait essentiellement un catalyseur et le procédé mènerait à l'obtention du ligand bidenté libre. Le défi ici serait bien sûr l'inhibition par le produit (*product inhibition*), car les ligands bidentés se lient en général plus fortement au métal que les ligands monodentés, ce qui impliquerait de conduire la réaction à plus haute température afin de faciliter les étapes de dissociation.
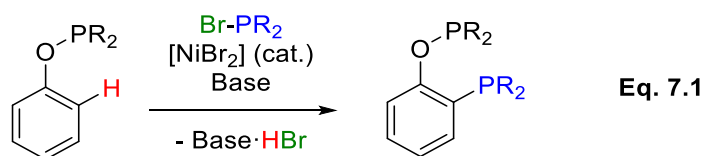
Nous pensons que les bromophosphines sont compétentes dans la fonctionnalisation du lien C-Ni car elles sont à la fois des nucléophiles qui peuvent se lier au métal, et des électrophiles car le substituant Br est un bon groupe partant : on peut donc dire que c'est un phosphènium protégé. Ainsi, les meilleurs candidats pour la fonctionnalisation sont probablement des composés qui cachent des phosphèniums ou des composés isolobaux. Toutes les composés du phosphore(III)

possédant un lien P-Cl ou P-Br sont donc à considérer afin de créer toute une variété de nouveaux ligands. L'éventail des di-alkyle/aryle-halophosphines permettrait de préparer d'autre types de ligands phosphine-phosphinite, incluant des halophosphines chirales qui mèneraient à des nouveaux complexes chiraux. Les composés phosphorés de type (RO)R'P-X et (RO)$_2$P-X permettraient quant à eux de générer des composés bidentés de type bis-phosphinite et phosphinie-phosphonite respectivement (**Schéma 7.9**).

Schéma 7.9. Synthèse de divers ligands phosphorés bidentés par l'insertion de phosphèniums.
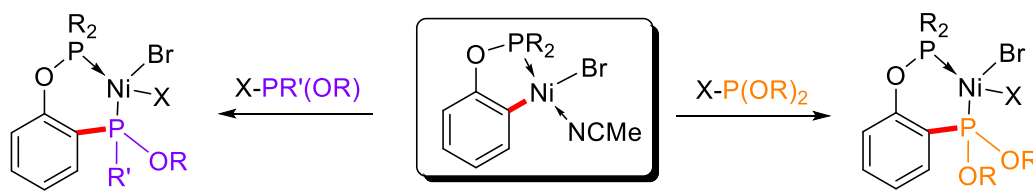

Dans la série des composés isoélectroniques du groupe des pnictogènes, les nitrèniums sont également des candidats à considérer, puisque les couplages Carbone-Azote sont d'une grande valeur commerciale. Les nitrèniums, au contraire de certains phosphèniums, ne peuvent pas être isolés mais ils sont quand même considérés comme des intermédiaires réactionnels et générés *in situ*. Les haloamines sont donc des précurseurs de nitrèniums mais leur toxicité et les précautions nécessaires à leur manipulation devraient nous pousser à chercher des amines portant d'autres groupes partants que les halogènes, tels que les pseudohalogènes. Par exemple, des résultats préliminaires nous ont démontré que la N-tosyloxy-diéthylamine réagissait avec des phosphinites cyclonickellées pour donner le ligand portant le fragment -NEt$_2$ en position *ortho*, et ce à température ambiante (**Schéma 7.10**). Dû à l'instabilité des liens N-O, il est difficile d'en conclure si la réaction implique (a) la coordination de l'azote sur le nickel, puis le départ du groupe TsO$^-$ suivi de l'insertion du nitrènium supporté par le métal dans le lien C-Ni ou (b) la dissociation homolytique du lien N-O pour générer un nitrène, sa coordination au métal pour donner un intermédiaire Ni^{III} suivie d'une élimination réductrice C-N. Dans les deux cas, le résultats global est tout de même la transformation d'un lien C-H en lien C-Ni suivi d'une fonctionnalisation en lien C-N.

Schéma 7.10. Fonctionnalisation d'un lien C-Ni par insertion formelle d'un nitrènium.
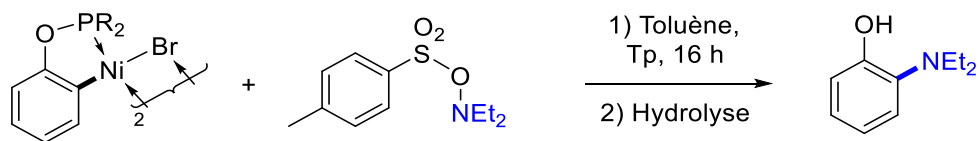
Enfin, les composés isoélectroniques aux phosphèniums/nitrèniums mais de charge neutre, tels que les carbènes (incluant CO) ou les nitrènes peuvent constituer des candidats intéressants pour la fonctionnalisation C-H des phosphinites, via cyclonickellation. Dans ces cas, l'insertion de ces composés mènerait à des ligands bidentés de type LX (monoanionique) qui peuvent donner le produit de fonctionnalisation par protonation du lien Nickel-Alkyle ou Nickel-Amidure (**Schéma 7.11**). Une des méthodes commune pour générer les carbènes et les nitrènes et d'utiliser les précurseurs diazoalcanes ou azotures, respectivement, par abstraction d'une molécule d'azote.

Schéma 11. Stratégies possibles de fonctionnalisation des liens C-Ni par des carbènes et des nitrènes.
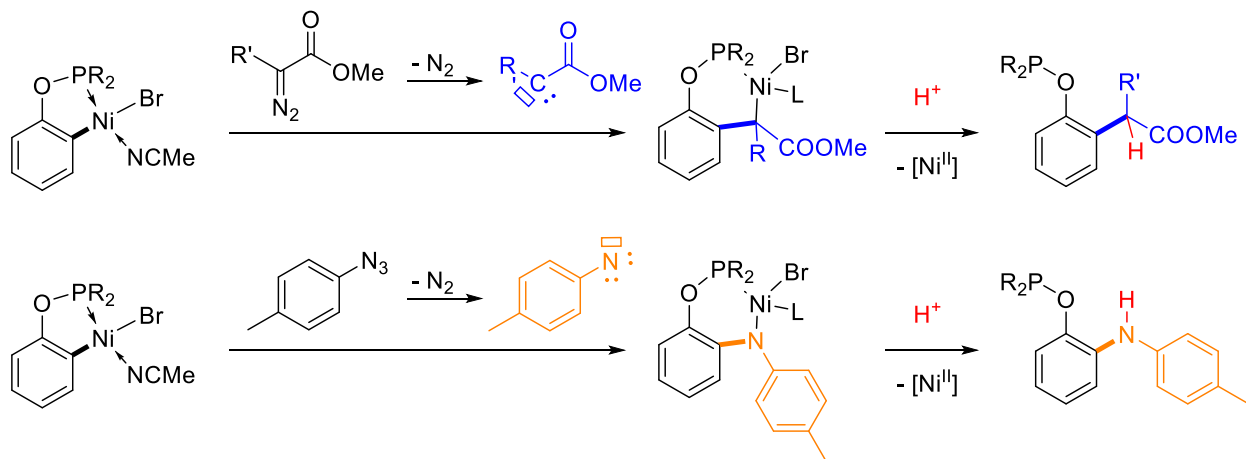
La méthode d'insertion de nitrène dans le lien Carbone-Nickel a, par exemple, été utilisée par G. Hillhouse qui a pu isoler le produit d'insertion dans un lien C$_{sp^3}$-Ni d'un nickellacyclopentane (**Schéma 1.45**). D'autres procédés d'amination directe des liens C-H avec d'autres métaux que le nickel impliquent également la formation de nitrènes *in situ* par diverses méthodes.

7.4 Fonctionnalisation des oléfines

Le **Chapitre 5** de cette thèse a démontré que la 2-vinyl-phenylphosphinite ne réagit pas préférablement par nickellation C-H comme les autres aryl-phosphinites. À la place, les nucléophiles (incluant ce ligand lui-même) attaquent la position β du vinyle, ce qui crée en même temps un lien C-Ni avec le carbone α, et ce à température de la pièce. Cette stratégie a permis de former des nouveaux *pinceurs* comprenant un premier nickellacycle à 6 chainons portant un bras phosphinite et un second nickellacycle à 4 chainons portant un bras amine ou phosphine, selon que le nucléophile est une amine ou une phosphine portant au moins un lien N-H ou P-H. Cette voie de synthèse permet également l'emploi d'une grande variété de nucléophiles, afin d'ajuster les propriétés des composés pinceurs, incluant des nucléophiles chiraux qui mèneraient à des complexes chiraux, alors que l'emploi de substituants sur le groupe vinyle permettrait d'ajuster la richesse électronique du centre métallique.

Ces nouveaux composés son intéressants puisque le lien C_{sp^3}-Ni enrichit le centre métallique, et permet au composé de s'oxyder à des potentiels relativement bas (de l'ordre du couple ferrocène/ferrocènium) en dépit du bras phosphinite qui est un donneur mou et relativement faible. Ainsi, ces nouveaux composés *pincer* pourraient être étudiés comme catalyseurs dans les réactions nécessitant le passage à des états d'oxydation plus élevés tels que l'addition de Kharasch ou les couplages croisés avec des halogénures organiques impliquant des intermédiaires Ni^{III}. L'hémi-labilité du donneur azoté dans les composés 6,4-POCN pourraient être avantageuse pour placer les partenaires de couplage en position *cis* et planaire et faciliter leur élimination réductrice.

Ce cycle à 4 chainons constitue également un désavantage : durant la prise des mesures électrochimiques, les complexes ont tous montré des signes de décomposition rapide lorsque mis au contact de l'air, contrairement autre composés de type 5,5-*pincer*-Ni. Cependant, cette faiblesse, incluant l'instabilité du lien C_{sp^3}-Ni, peut être retournée en avantage si l'on désire que la réactivité soit centrée sur le ligand et non sur le métal. Ainsi, la protonation du lien Carbone-Nickel mène formellement à un ligand fonctionnalisé, donnant formellement les produits d'hydro-amination ou d'hydro-phosphination anti-Markovnikov du fragment styrène (**Schéma 7.12**). Si la protonation du lien C-Ni provient d'une entité 2-vinylphénol, ce dernier une fois déprotoné peut s'échanger avec

le fragment vinylphénol fonctionnalisé sur le phosphore, et le nickel ainsi que le groupe directeur phosphinites peuvent être utilisés en quantités catalytiques (**Schéma 7.13**).

Schéma 7.12. Hydroamination et Hydrophosphination des 2-vinylphényl-phosphinites.
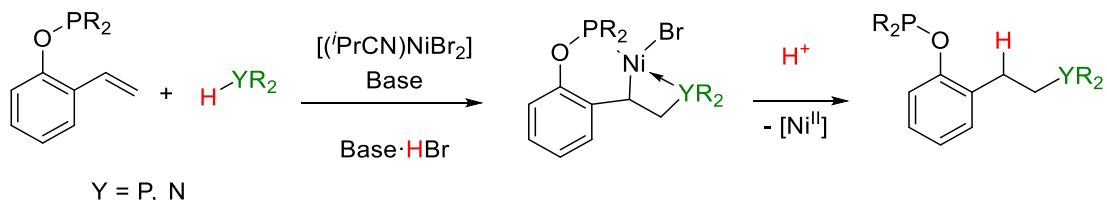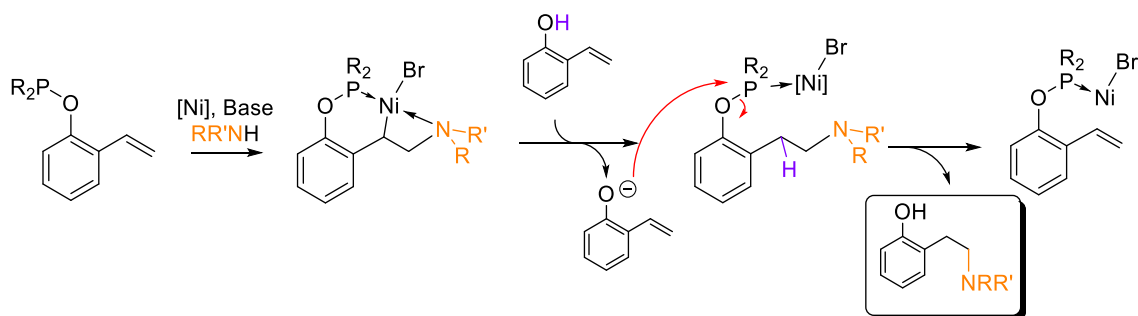

**Schéma 7.13.** Concept d'hydroamination catalytique des 2-vinyl-phénols.

Des résultats préliminaires indiquent que les complexes 6,4-POCN-NiBr sont protonés à température de la pièce par l'acide 3-chlorobenzoïque, mais qu'ils sont stables au 3-fluorophénol, même en chauffant. Ainsi, bien que la plupart des phénols ne soient pas capables de mener thermodynamiquement à la protolyse des liens C-Ni pour les nouveaux complexes décrits dans le **Chapitre 5**, il n'est pas impossible qu'un processus catalytique soit conduit par la protonation de la fonction amine du fragment fonctionnalisé, ce qui tuerait son caractère de proligand *pincer* et inhiberait sa nickellation comme tel. Pour cela, il est nécessaire de conduire la réaction en absence d'un excès de base, ou même en présence d'un acide.

D'autres réactivités menant formellement à la fonctionnalisation du groupe vinyle sont envisageables pour ces composés pinceurs, en particulier celles qui conservent le taux d'insaturation du composé. La première consiste donc à cliver le lien Carbone-Nickel par abstraction d'un proton, à l'inverse de la protolyse. L'utilisation des amines en excès dans les

synthèses menant aux composés 6,4-POC(N/P)-NiBr ne semble pas réagir plus loin, indiquant que les bases à considérer pour ces réactions sont des bases plus fortes (*i.e.* alcoolates, amidures, organo-magnésiens *etc.*). Par exemple, la déprotonation du ligand au carbone β peut entrainer la reformation de la liaison π du fragment oléfine, et serait accompagnée d'une réduction du centre Ni^{II} en Ni^{0}. Alternativement, la déprotonation du carbone β peut mener à la formation d'un nouveau lien Carbone-Nickel, menant à un nickellacyclopropane tel qu'observé dans un des composés présentés au **Chapitre 5**. Afin de relâcher l'oléfine fonctionnalisée, par élimination réductrice, une oxydation du centre Ni^{II} en Ni^{IV} peut s'avérer utile au déclenchement de la réaction (**Schéma 6.14**).

Schéma 6.14. Stratégie de fonctionnalisation des 2-vinylphénylphosphinites par déprotonation
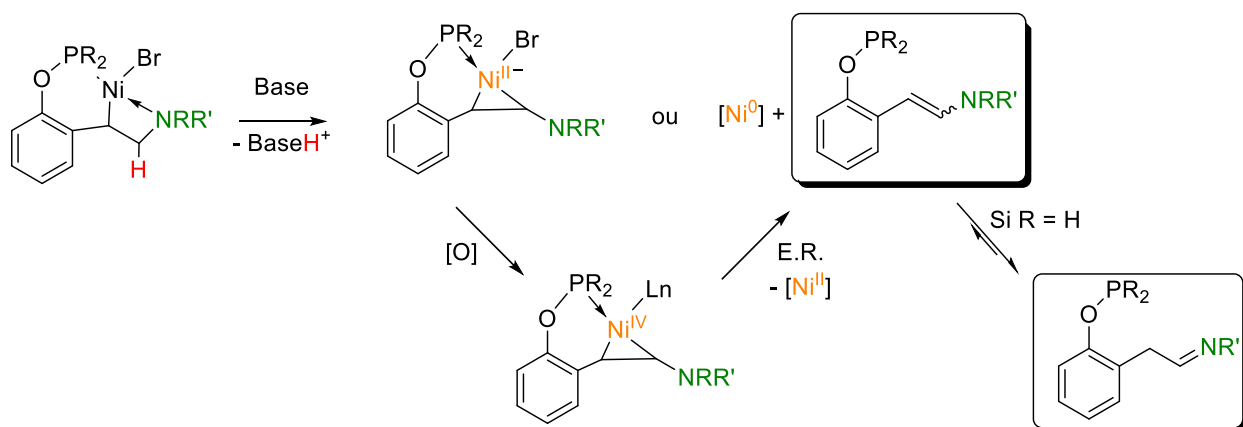

Une autre stratégie conservant le taux d'insaturation à considérer est l'élimination réductrice entre le carbone lié au nickel et l'atome d'azote des POCN portant un lien N-H, menant formellement à la formation des aziridines correspondantes, après déprotonation. Encore une fois, à l'instar des travaux publiés par D. Zargarian sur les *pincers* NCN-Ni, une oxydation du centre métallique peut s'avérer nécessaire au déclenchement du couplage C-N (**Schéma 6.15**).

Schéma 6.15. Stratégie de préparation des aziridines par oxydation des complexes 6,4-POCN-Ni
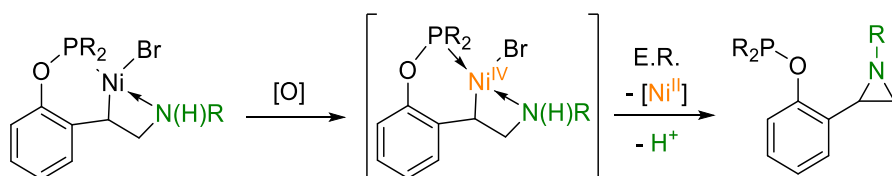
Enfin, cette stratégie de formation des pinceurs portant un lien Csp³-Ni pourrait être étendue à la préparation différents composés de type *pincer*, à partir de ligands portant des oléfines greffées sur des chainons aliphatiques ou aromatiques. Non seulement les phosphinites sont à considérer, mais les phosphines et les amines également, puisque la nickellation de ces dernières est généralement très difficile par métallation directe des liens C-H (**Schéma 6.16**).

Schéma 6.16. Exemple d'application de la stratégie à la synthèse de composés *pincers*.
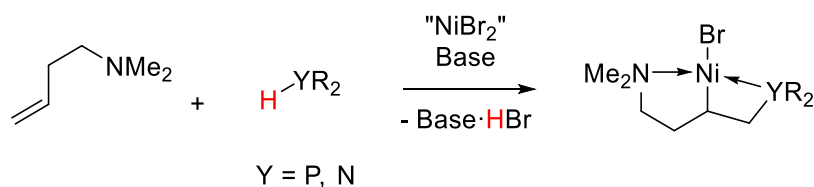
7.5 Aperçu final

Cette thèse a permis d'accumuler des connaissances sur les phosphinites cyclonickellées, en isolant ces espèces qui peuvent jouer un rôle dans les procédés de fonctionnalisation catalysées par le nickel. L'étude systématique a permis d'établir la régiosélectivité et les limites de la nickellation des phosphinites dérivées des phénols et des naphtols, en explorant une gamme de composés substitués, qui ont été totalement caractérisées par RMN et par cristallographie aux rayons X. Les données présentées ont contribué à comprendre les aspects synthétiques menant à ces nickellacycles, et les conditions réactionnelles optimales (solvant, base, température *etc.*) ont été justifiées par diverse expériences. De plus, le mécanisme de la cyclométallation et les intermédiaires impliqués a été décrit par des études cinétiques expérimentales agrémentées par un argument computationnel. La proposition d'un mécanisme de nickellation électrophile C-H est appuyée par des données quantitatives sur cette étape, données qui font souvent défaut aux procédés catalytiques contournant l'isolation des intermédiaires réactionnels. En outre, un exemple de fonctionnalisation du lien carbone-nickel dans les espèces isolées a été dévoilé et ouvre la voie à d'autres procédés de fonctionnalisation des phosphinites cyclonickellées. Cette thèse a également démontré la préparation efficace et versatile d'une nouvelle classe de composés de type *pincer*, en

présentant une stratégie alternative à celles déjà connues et qui contourne les limitations liées au bris de liens carbone-hydrogène. Cette contribution a permis d'enrichir le monde de la chimie des pinceurs, par la caractérisation de ces nouvelles espèces aux particularités structurelles indéniables. Non seulement la caractérisation par RMN et par cristallographie a été présentée, mais une étude électrochimique a mis en lumière la facilité d'oxydation de ces nouveaux *pincers* en dépit du fragment phosphinite qui est un donneur relativement pauvre. L'ensemble des travaux a ainsi démontré quelques aperçus du potentiel qu'ont la combinaison nickel-phosphinite pour faciliter la formation des liens carbone-nickel et pour les faire réagir, et a donc contribué à approfondir la connaissance fondamentale en chimie organométallique.